Ignác Capek

Noble Metal Nanoparticles

Preparation, Composite Nanostructures, Biodecoration and Collective Properties

Springer

Nanostructure Science and Technology

Series editor

David J. Lockwood, FRSC
National Research Council of Canada
Ottawa, Ontario, Canada

Ignác Capek

Noble Metal Nanoparticles

Preparation, Composite Nanostructures,
Biodecoration and Collective Properties

Springer

Ignác Capek
Slovak Academy of Sciences
Bratislava
Slovakia

For my daughters Jana and Martina

Preface

This book focuses on the experimental, and to a lesser extent, theoretical, status of research on the preparation and characterization of noble metal nanoparticles and their conjugates, especially those of silver and gold. As such, this book starts with a brief overview of the foundation work concerned with the chapter topics which include nanomaterials, nanoscience, surface-capping molecules, and traditional and nontraditional reduction agents. Although not an exhaustive study, this book examines and summarizes existing achievements in the methods of noble metal nanoparticle synthesis with mainly spherical morphologies, highlighting how their physical and chemical properties are influenced by their change in the size, shape, and morphology.

The book is organized into five chapters. Efforts have been made to develop one-phase, two-phase, and multiphase syntheses in which the reduction of a metal takes place homogeneously or heterogeneously in a selected organic solvent. High-temperature solution-phase synthesis, which is a very reproducible method, can be used for the large-scale synthesis of organoamine-protected gold and silver monodisperse nanoparticles. Most hydrophobic gold nanoparticles (also sometimes called monolayer protected clusters (MPCs)) with diameters below 10 nm are prepared via the Brust–Schiffrin method: a two-phase liquid/liquid system or a suitable single-phase solvent. The Brust–Schriffin in situ biphasic gold nanoparticle synthesis introduces the use of a quaternary ammonium ion stabilized by a bromide anion—as a stabilizing agent and a phase-transfer catalyst. A new method combining both concepts, the surfactant-free synthesis and the introduction of (functionalized) ligands, controls the particle size well. The resulting, weakly protected nanoparticles can straightforwardly be stabilized and functionalized by the addition of a variety of ligands. The influence of alkylthiol chain lengths on the colloidal and localized surface plasmon resonance (LSPR) properties of AuNPs is summarized. It is concluded that under slow reduction conditions, nanoparticle growth is controlled also by Ostwald ripening. The generation of silver and gold nanoparticles was investigated under various reaction conditions such as with weak and strong reducing and capping agents, low and high temperatures, various additives (ionic

liquid-surfactants, steric surfactants, acids, polysaccharides, polyakrylamides), as well as synthetic approaches.

Templates were used as an effective method for preparing metal nanocrystals with morphologies similar to, or complementary to, those of the template. Both soft and hard templates can be employed for shape-controlled synthesis of metal nanocrystals. Self-assembled, biological, and synthetic structures such as micelles (or reverse micelles), microemulsions, liposomes and vesicles, biological macro-molecules, viruses, etc., belong to the soft template group. Multilayered polymer films and block copolymer films were used as nanoreactors or templates for the formulation of noble metal nanoparticles. Microwave irradiation was found to be a new technique for coating AgNPs onto the surface of polymer beads. A new template method for the preparation of flexible silver/cross-linked poly(vinyl alcohol) (PVA) nanocables via a one-step, in situ reduction of Ag^+ and Ag^+-catalyzed cross-linking PVA chains under hydrothermal conditions is discussed. In fact, the formation of such elegant nanocables was controlled by a synergistic growth mechanism called a synergistic soft–hard template mechanism (SSHM). Colorless floccular precipitates formed when commercial polyacrylamide was added to the aqueous solution of silver nitrate at room temperature. This indicated the coordination of silver ions with NH_2 groups in polyacrylamide (PAAm), with silver ions serving as weak cross-linkers, attaching polymer chains. A thermosensitive water-soluble polymer, poly(N-isopropylacrylamide) (PNIPAM) was also used for the immobilization and stabilization of noble metal nanoparticles. The grafting-onto method, to coat gold nanoparticles with PNIPAM chains of end-functionalized SH groups, was used. Poly(N-isopropylacrylamide-acrylic acid-2-hydroxyethyl acrylate) microgel particles acted as a scaffold to form fluorescent silver nanoclusters. Nevertheless, linear polyacrylates or poly-methacrylates such as poly(methacrylic acid) also act as excellent scaffolds for the preparation of silver nanoclusters in a water solution, by photoreduction with vis-ible light, UV-light, or sonochemically. Microgels of poly(N-isopropylacrylamide-co-acrylic acid-co-acrylamide) can be used to template the formation of fluorescent silver nanoparticles. A poly(ethylene glycole) (PEG)-based, non-ionic block copolymer (poly(ethylene oxide)–poly(propylene oxide)–poly(ethylene oxide) (PEO–PPO–PEO)) templated the synthesis of luminescent silver particles, with a mean diameter of ca. 8 nm. Infinite coordination polymer particles (ICPs) are a class of emerging functional materials that are formed by bridging repeating organic ligands with metallic nodes. Metal-organic frameworks (MOFs) represent another form of mesoporous materials that are thermally robust and in many cases highly porous.

The polymers known as polyelectrolytes (PE) can be used as reducing/stabilizing agents in one single-step syntheses. The building-up of multifunctional core@shell nanostructures is one of the great advantages of using PE assemblies. In this case, the PE forming the multilayers can be functionalized with drugs, organic dyes, contrast agents, radionuclides, catalysts, organic dyes, and proteins—namely anti-bodies—allowing the application of the ensuing structures in areas such as drug/gene delivery, biosensing, bioimaging, and photodynamic therapy.

Dendrimers are highly branched, nearly size monodisperse polymers with several structural properties. These structural features include the incorporation of metal nanoparticles, with precise control over nanoparticle size and their defined number of terminal groups for each generation with multiple branch ends, which are available for consecutive conjugation reactions. Moreover, they are able to form stable, dense, well-organized, and closely packed arrays on surfaces. The encapsulation of metal ions inside dendrimers involves, variously, electrostatic and complexation interactions—the dendrimer interior includes coordinating groups such as –OH, NH$_2$, or –COOH. One unique approach to the preparation of gold nanoparticles is through the use of poly(amidoamine) (PAMAM) dendrimers. The addition of HAuCl$_4$ to neutral G4-PAMAM dendrimers resulted in a protonated dendrimer with AuCl$_4^-$ counterions, which were then reduced to metallic gold. The stable brown–red solution of the resulting colloidal gold indicated that the metal colloids were stabilized by the dendrimer. The advantage of using dendrimers as templates to prepare gold nanoparticles lies in the fact that the surface of the particles can be modified with various functional moieties (e.g., targeting ligands and dyes) through dendrimer chemistry for practical biomedical applications (e.g., cancer-cell targeting and imaging).

Silica is widely used as an inorganic coating and templates for nanoparticles of different composition (e.g., quantum dots (QDs), magnetic nanoparticles, lanthanide nanoparticles, and noble metal nanoparticles (especially AuNPs), or as a nanoparticle-based carrier of functional molecules. Using the diversity of silane chemistry, a silica shell, coating, or template can be tailored to have functional groups that can include, but are not limited to, amine, aldehyde, carboxyl, epoxy, and thiol groups. In addition to the use of silica as a structural shell on other template materials, nanoparticles composed of silica can be prepared with sizes that typically range between tens and hundreds of nanometers.

The nanoclusters (nanodots) have a discrete electronic state and exhibit strong size-dependent fluorescence over the region from ultraviolet to near-infared. The excellent fluorescing properties of these clusters means they are suitable for chemical sensing, bioimaging, and single-molecule. Gold clusters have been studied for decades, and many gold clusters with well-defined compositions such as Au$_8$, Au$_{13}$, Au$_{25}$, and Au$_{38}$ have been prepared. Thus, having spectral properties that distinguish them from their larger nanoparticle counterparts, as well as organic chromophores, noble metal clusters are a new class of small, innocuous, and bright fluorophores whose spectral properties can be tuned. A more sophisticated design of protection groups (ligands) is required to obtain water-soluble luminescent nanodots. Nanodots can be prepared by chemical reduction or photoactivation in the presence of protection groups. Some biological molecules have shown great potential as protection groups. Single-stranded DNA (ssDNA) is also a good scaffold to obtain luminescent silver nanodots with outstanding photophysics, such as large extinction coefficients, high luminescence quantum yields, and excellent photostability. Biomolecules (proteins) are also utilized for luminescent gold nanodot protection. Thiolate-monolayer protected gold (sub) nanoparticles (nanoclusters (NCls) or QDs) are stable when efficiently passivated by organothiolate monolayers.

Further research in template-based synthetic strategies has led to the preparation of highly fluorescent, water-soluble AuNCls and AgNCls when using PAMAM dendrimers, polyglycerol-block-poly(acrylic acid) copolymers, proteins, and DNA as templates. In these hybrid systems the preparation of various nanocomposites by different synthetic routes. The one-pot sonochemical route was taken for the preparation of gold nanocomposites (AuNCos) with near-infrared emission and Au/AgNCos with high quantities of yellow-emission under mild conditions. The obtained Au-AgNCo was yellow under visible light (with 365 nm excitation) and emitted a strong yellow fluorescence. The emitted wavelength of Au–AgNCo blue-shifted to 565 nm compared to that of AuNCos.

Fluorescent silver subnanoparticles can be produced by photogenerated ketyl radicals that reduce Ag^+ from silver trifluoroacetate in the presence of cyclohexylamine as a stabilizer. AuNPs and AgNPs can act as the quencher of the fluorescence emission of many organic molecules. The quenching of the tryptophan emission, e.g., by AuNPs was analyzed in terms of the Stern–Volmer equation. The AuNPs were synthesized using a direct reduction process (by laser) in sodium citrate. The absorption curve of the citrate-capped AuNPs showed a plasmon resonance at 520 nm. On addition of $AgNO_3$, there was a decrease in absorption. On excitation with a 532-nm laser for 60 minutes, another peak, at 400 nm, was formed which corresponded to the formation of AgNPs. Also, there was an overall increase in the absorbance which suggested the formation of a core@shell structure.

Poly(vinyl alcohol) (PVA) as a matrix component was based, in part, on the ability of this polymer to serve as an electron donor during the reduction of metal ions. In addition, optically transparent films of PVA can be employed to study the optical properties of noble metal nanoparticles. Incorporation of Ag^+ into polymer templates was found to be more reproducible when poly(acrylic acid) (PAAc) was present, probably owing to the known ability of this polymer to bind silver ions. A very simple method was used to prepare AuNPs with block copolymer shell structures in situ, using a UV irradiation method with the copolymers (polystyrene-block-poly (2-vinyl pyridine) (PSt-b-PVP)) as templates. AuNPs of ∼28 nm in diameter were covered by PSt-b-PVP copolymer shells. The UV–visible absorption band corresponding to the surface plasmon resonance (SPR) energy of the core–shell nanoparticles is 530 nm, which is larger than that (522 nm) of free AuNPs of the same diameter (20 nm).

In "silica-directed photosynthesis" the metal nanoparticles formed after irradiation of metal ion solutions are nested into mesoporous silica. The silica framework was chosen because of its transparence meaning that the ionizing radiation would penetrate homogeneously within the solid and ensure a homogeneous initial distribution of reducing radiolytic radicals formed by ionization and excitation of the solvent. The silver or gold ions can then interact with the Si–OH groups on the internal pore surfaces of the silica framework. The silver–silica samples irradiated with lower doses displayed a plasmon resonance absorption centered at about 420 nm. In silicas, the plasmon resonance maximum of silver particles is often observed in the 400–440-nm region.

In "reactive species-directed synthesis" the nanoparticles are prepared by reduction of metal ions by gamma irradiation which first induces ionization and excitation of the aqueous solvent, generating radiolytic molecular and radical species—such as solvated electrons (e^-), hydroxyl radicals ($OH^\bullet$), and hydrogen atoms ($H^\bullet$). The solvated electrons and hydrogen atoms reduce the metal ions to metal atoms, which eventually coalesce to form nanoparticles. Pulse-radiolysis is another "bottom-up" method that involves gamma-ray irradiation for the reduction of Au^{III} instead of the traditional addition of a chemical reductant.

"Biomolecule mediated synthesis" covers the preparation of metal nanoparticles in the presence of biomolecules acting both as reducing and capping agents. Photoreduction has been widely used as a route for synthesis of metal NPs either in solution or in polymeric films. The photochemical synthesis used to obtain such nanoparticles in an aqueous medium with biocompatible reducing agents, therefore, has special significance as the NPs can then be readily used in physiological conditions. Additionally, for biolabeling applications, the size of the fluorophore is crucial for an efficient bioconjugation and targeted delivery. Though several methods have demonstrated for the synthesis of metal nanoclusters, the presence of biopolymeric macromolecules on the nanoclusters negates the size advantage. As a result, though the achieved metal core size is very small, the actual hydrodynamic radius including the stabilizing molecules is comparatively large.

Laser ablation synthesis in solution (LASiS) can be an effective technique for obtaining noble metal nanoparticles (NMNPs). In the LASiS method, nanoparticles are produced during the condensation of a plasma plume formed by the laser ablation of a bulk metal plate dipped into a liquid solution. LASiS is usually considered a top-down physical approach, it is free of the usual disadvantages of chemical procedures and can be complementary to the bottom-up chemical methods for production of NMNPs. Moreover, LASiS has the potential of being a unique method for the synthesis of nanoparticles of different metals, with different surface coatings (if any) and in different solvents. Nanoparticles of gold, silver, platinum, copper, and other materials have been obtained by LASiS in water and organic solvents through this one-step, simple procedure. By irradiation of organic microcrystals suspended in water, photothermal or photomechanical ablation mechanisms with nanosecond or femtosecond laser pulses, respectively, were observed. Nanoparticle stability is a crucial aspect of LASiS in pure solvents. Despite the absence of stabilizers, NMNPs obtained in water and in several organic solvents remain stable for days, months, or even longer time periods. If using NMNPs obtained in the absence of stabilizing agents one should always take into consideration the stability time frame for each set of metal nanoparticles and solvent. In general, the presence of electrolytes (surfactants) during LASiS has negative effects on the stability of NMNPs, due to the screening of particle surface charges.

Ionic liquids (ILs) are well-known and intensively explored for their unique properties such as their wide electrochemical windows, good thermal and chemical stability, as well as their good ionic conductivity and non-volatility. Recently, ILs have been used to replace classic organic solvents for the electrodeposition of

metallic nanocrystallines or nanoparticles. Metal-organic frameworks (MOFs), also called coordination polymers or coordination networks, are a class of hybrid materials formed by the self-assembly of metal ions or clusters and polydentate bridging ligands typically under mild conditions. Solvothermal synthesis of MOFs can be achieved with either conventional heating or a microwave. Because high reaction temperatures are involved in the solvothermal method, more extensive transformations of the precursors typically occur before the formation of the MOFs nanoparticles. Temperatures and heating rates provide additional parameters to control MOFs particle nucleation and growth. Surfactant molecules can also be used to template the MOFs synthesis under solvothermal conditions by coating the surfaces of growing MOFs particles. Surfactant molecules play an important role in defining MOFs morphologies. Because of their unique characteristics, microscale plasmas (i.e., microplasmas) offer specific advantages both for nanomaterial synthesis and for interacting with liquids. Microplasma-induced synthesis and the surface engineering of nanomaterials directly in liquids has also been investigated.

Silver nanoparticles with different structures, such as single-crystal cubes with sharp corners, single-crystal cubes with truncated corners, multiply twinned particles, and single-crystal cuboctahedrons, have been used as sacrificial templates. When silver nanocubes with sharp corners are used as templates, the reaction starts pitting on one of its six faces. Through an alloying and dealloying process, pin-hole-free nanoboxes with hollow interiors and porous nanocages can be obtained along the reaction process. If a silver nanocube with truncated corners is used as a template, the reaction starts at all the corners producing cubic nanocages with holes at their corners. Multipodal, spike-radiating, and dentritic shapes are a few examples of the branched morphologies which can be obtained. Branched NMNPs have been prepared under widely different reaction conditions. Starting with seed structure and leading on to factors such as fast-reaction kinetics, preferential binding effects of capping agents and additives, and relative surface growth have all been invoked to explain their branch-formation mechanisms. Submicrometer-sized hollow silver spheres, using PEO-b-PMAA(poly(methacrylic acid))-SDS complex micelles as soft templates, can be prepared. The fabrication of two- and three-dimensional ordered structures of hollow silver spheres using colloidal crystal hard templates can also be undertaken. In addition, monodisperse hollow silver spheres have been prepared with phase-transformable emulsions, composed of natural beeswax used as a hard template. Each method has several intrinsic advantages and disadvantages. Templating against hard (solid) templates is arguably the most effective, and certainly the most common, method for synthesizing hollow microstructures/nanostructures, however, the template-removal step not only significantly complicates the process but also diminishes the quality of the product particles. Preparation of non-spherical hollow structures introduces additional challenges, because the synthetic approaches for spherical hollow structures does not generally apply to the synthesis of non-spherical hollow structures. Furthermore, the fabrication of silver nanoshells has proven more difficult than other types, such as gold nanoshells. Cubic NaCl crystals serve as unconventional non-spherical hard templates, easily coated by AgCl particles around the cube

surfaces because of their similar crystalline structures. Polycrystalline silver nanoparticles, synthesized by thermal reduction of silver ions in a glycine matrix, are stable in aqueous solution and exhibit bright luminescence. Solution plasma, a novel technology, has the potential for the advancement of nanomaterial production and the decomposition of organic-based compounds.

The combination of the magnetic and optical properties of nanoparticles into a single platform has gained further attention due to diagnostic, therapeutic uses and immunomagnetic separation (IMS), drug delivery, and sensing. Therefore, the rationale design, synthesis, and surface modification of multifunctional nanoparticles represent the most important steps. One of the examples of a multifunctional nanoparticle results from a core@shell structured Fe_3O_4@Au nanoparticle. Chitosan acts as a soft template in the formation of multibranched magnetic nanoparticles, and the gold-coating process was carried out in the presence of chitosan to give a better particle dispersity and to avoid agglomeration problems. In addition, the main advantage of using a chitosan matrix is that it acts as a stabilizing agent in the formation of nanoparticles due to the presence of hydroxyl and primary amino groups. The addition of silver ions provides an anisotropic-shaped nanostructure. Gold bimetallic nanoparticles are classified by two types of mixing pattern: core@shell NPs and alloy bimetallic NPs. The alloy bimetallic NPs consist of a homogeneous mixture of gold and another metal in the NP. Many Au bimetallic NPs are alloyed with Ag, Pd, Pt, Zn, Cu, ZrO_2, CdS, Fe_2O_3, Eu, Ni, and Rh. The core@shell NPs consist of a metal shell surrounding a gold core, or gold shell surrounding another metal core. The Au-Fe_3O_4 bimetallic NPs are considered as attractive materials for both biological and medical uses, due to their theranostic (therapy + diagnostic) properties involving magnetic resonance imaging (MRI) and hyperthermia. The Au–Fe_3O_4 bimetallic NPs are attractive materials for biological and medical areas, due to their theranostic (therapy + diagnostic) properties involving magnetic resonance imaging (MRI) and hyperthermia.

Bratislava, Slovakia   Ignác Capek
March 2017

Contents

About the Author

Ignác Capek Emeritus Professor of polymer and metal colloids and nano(bio)technology, researcher in Slovak academy of sciences (Polymer Institute and Institute of Measurement Sciences (Slovakia), Waterloo university (Canada), Stuttgart university (Germany), Kagoshima university (Japan), Sendai university (Japan) and Toyohasi university (Japan), lecturer in Comenius and Trenčin Universities and Principal of M.Sc. and Ph.D. studies. He has been the principle investigator of some basic and industrial projects, he published some patents, scientific and review articles, chapters and scientific books in polymer chemistry, polymer and metal colloids and nanobiotechnology. He spent several long-term visits as a postdoc and visiting professor at foreign universities and scientific institutes in Canada, Germany, Japan, Taiwan, Turkey and France.

Chapter 1
Nanofield

Abstract Gold and silver that are beautiful and resistant to water and air were always fascinating for people. Metals and noble metals remain important even in the present ages of wood, polymer, carbon, and silicon. Different pathways have been proposed for the preparation of noble metal nanoparticles with tailor-made size and shape in the present decades. The nanometer regime covers the transition from condensed matter behavior to atomic and molecular properties and thus is a very rich but also very demanding area in materials science. Decreasing the dimension of nanoparticles has pronounced effect on the physical properties that significantly differ from the bulk material. They represent the missing link between metal atoms and microparticles. The role of interfaces is rapidly increasing in science and nanotechnology and they are the key to new functions. Separation and purification techniques play important role in separation of the nanomaterials (NMs) and their conjugates from the original reactants and by-products. Characterization includes assessment of composition, morphology, dimensionality, and physical and chemical properties. Size, volume, aspect ratio, perimeter, projected area, surface roughness, etc., are typical morphology parameters that are assessed. A variety of well-developed techniques which already have been successfully applied to the characterization of bare NMs are now being extended to examining NM-conjugates. These include separation-based, scattering, microscopy, spectroscopy, mass spectroscopy, and thermal techniques. Dialysis, filtration, extraction, and differential precipitation represent the most common methods applied to nanoparticle-(bio)conjugate purification. Chemical extraction and differential precipitation are other potentially efficient but largely underused purification techniques. Top-down approaches, such as photolithography, e-beam lithography (EBL), and Focused ion beam (FIB), offer high fidelity and high controllability in terms of design and prediction. Some bottom-up approaches based on self-assembly can produce high-resolution (sub)nanostructures over a large area with a low cost. The utilization of spectroscopic techniques for the detection of cancerous and precancerous lesions is based on the analysis of specific light-tissue interactions to assess the state of biological tissue. As light illuminates the targeted tissue, these biomolecules, termed fluorophores, absorb the energy in the illuminating light and respond by emitting fluorescent light of lower energy (and longer

wavelength). Advances in bioengineering and the continued refinement of optical detection techniques have led to the development of multimodal optical detection systems. The ultimate goal of the optical detection systems centers on the achievement of an "optical biopsy." Nanotechnology is increasingly gaining a foothold in clinical medicine, especially in oncology. The fabrication of nanodevices as probes is complex, most likely the assembly of building blocks including nanoparticles, nanowires, nanotubes, and substrates.

Keywords Nanotechnology · Nanomaterials · Noble metal nanoparticles · Metal colloids · Separation and purification techniques · Procedures

Abbreviations

1D	One-dimensional
^{1}H-NMR	Proton nuclear magnetic resonance
2D	Two-dimensional
3D	Three-dimensional
9-BBN	9-borabicyclo [3.3.1] nonane
AAO	Anodized aluminum oxide
AFM	Atomic force microscopy
AgNPs	Silver nanoparticles
Ag–PfFt	Ferritin protein
AOT	Sodium di(2-ethylhexyl) sulphosuccinate
APS	Aminopropyltrimethoxysilane
APTES	(Aminopropyl)triethoxysilane
APTMS	Aldehyde propyltrimethoxysilane
AU	Analytical ultracentrifugation
AuDENP	Dendrimer-entrapped gold nanoparticles
AuDSNPs	Dendrimer-stabilized gold nanoparticles
AuNDs	Gold nanodots
AuNPs	Gold nanoparticles
BAC	Benzyldimethyltetradecylammonium chloride
BDAC	Benzyldimethylhexadecylammonium chloride
BHDAC	Benzylhexadecylammonium chloride
C_{AuNP}	AuNP concentrations
CD	Cyclodextrin
CE	Capillary electrophoresis
CEA	Carcinoembryonic antigen
CMC	Critical micellar concentration
CMT	Critical micellar temperature
CNT	Carbon nanotube
CSPI	Cross-sectional perimeter integration
CT	Computed tomography
CTAB	Cetyltrimethylammonium bromide
CTAC	Cetyltrimethylammonium chloride

Cys	Cysteine
DanArg	Dansylated arginine
DDA	Discrete dipole approximation
DDT	1-dodecanethiol
DENPs	Dendrimer-entrapped nanoparticles
DFM	Dark-field microscopy
DLS	Dynamic light scattering
DNA	Deoxyribonucleic acid
DOS	Density of states
DOTAP	1,2-dioleoyl-3-trimethylammonium propane
DSC	Differential scanning calorimetry
DSNPs	Dendrimer-stabilized nanoparticles
DVLO	Derjaguin-Verway-Landau-Overbeek theory
E	Efficiency
EBL	E-beam lithography
EDAX	Energy-dispersive X-ray analysis
EDS	Energy-dispersive X-ray spectroscopy
EDX	Energy-dispersive X-ray spectroscopy
EDXRF	Energy-dispersive X-ray fluorescence
EELS	Electron energy loss spectroscopy
EET	Electronic energy transfer
EG	Ethylene glycol
EIS	Electrochemical impedance spectroscopy
ELISA	Enzyme-linked immunosorbent assay
EM	Electromagnetic
EPR	Enhanced permeability and retention
ES-DMA	Electrospray-differential mobility analysis
ESEM	Environmental SEM
Et_3P	Three ethyl phosphine
FA	Folic acid
FAR	Folic acid receptor
FCS	Fluorescence correlation spectroscopy
FE	Field emission
FESEM	Field emission scanning electron microscopy
FFF	Field flow fractionation
FI	Fluorescein isothiocyanate
FIB	Focused ion beam
FRET	Förster (fluorescence) resonance energy transfer
FTIR	Fourier transform infrared
FWHM	Half the maximum intensity
GE	Gel electrophoresis
Glu	Glutamic acid
Gly	Glycine
GO	Graphene oxide

Gp	Graphene peak
GSH	Glutathione
HAuCl$_4$ × 3H$_2$O	Gold(III)-chloride-trihydrate
HDT	1-hexadecanethiol
HEIS	High-energy ion scattering
His	Histidine
HLB	Hydrophilic-lipophilic balance
HMTS	Heptamethyltrisiloxane
HOPG	Highly ordered (oriented) pyrolytic graphite
HPLC	High-performance liquid chromatography
HRTEM	High-resolution transmission electron microscopy
HSA	Human serum albumin
HTAB	*N*-hexadecyltrimethylammonium bromide
IBBC	Integrated blood barcode chip
ICP-AES	Inductively coupled plasma-atomic emission spectrometry
ICP-OES	Inductively coupled plasma-optical emission spectroscopy
ICPs	Infinite coordination polymer particles
IL	Ionic liquid
IR	Infrared
ITC	Isothermal titration calorimetry
Lac	*P*-aminophenyl-β-D-lactopyranoside
LBL	Layer-by-layer
LDOS	Local density of states
L-PEI	Linear polyethylenimine
LSP	Localized surface plasmon
LSPR	Localized surface plasmon resonance
mAbs	Monoclonal antibodies
MBA	*P*-mercaptobenzoic acid
MBI	2-mercaptobenzimidazole
MC@MNPs	Metal nanoparticles decorated microcapsule
MDR	Multidrug resistance
MEF	Metal-enhanced fluorescence
Met	Methionine
NIR	Near-infrared
MMT	Montmorillonite
MOFs	Metal-organic frameworks
MPA	3-mercaptopropionic acid
mPEG-SH	Monofunctional methoxy PEG
MPTMS	Mercaptopropyltrimethoxysilane
MRI	Magnetic resonance imaging
MS	Mass spectrometry
MW	Microwave
MWCNTs	Multi-walled carbon nanotubes
MwCO	Molecular weight cutoff

$Na_2H(C_3H_5O(COO)_3)$	Sodium citrate
$NaAuCl_4$	Gold salt
$NaBH_4$	Sodium borohydride
N_{ap}	Average number of particles
NBI	Narrowband imaging
NICISS	Neutral impact collision ion scattering spectroscopy
NIL	Nanoimprint lithography
NMHs	Noble metal-based hybrids
NMNPs	Noble metal nanoparticles
NMR	Nuclear magnetic resonance
NMs	Nanomaterials
NPs	Nanoparticles
NSOM	Near-field scanning optical microscopy
NSOM (SNOM)	Near-field scanning optical microscopy
NT	1-nonanethiol
o/w	Oil-in-water
o/w/o	Oil-in-water-in-oil
OA	Oriented attachment
OCT	Optical coherence tomography
OR	Ostwald ripening
PA	Amino polymers
PAA	Poly(allylamine)
PAM	Polyacrylamide
PAH	Poly(allylamine hydrochloride)
PAMAM	Poly(amidoamine)
PAN	Poly(amidoamine), polyacrylate, polyacrylonitrile
PAT	Process analytical technology
PCS	Photon correlation spectroscopy
PBS	Phosphate buffer saline
PDHPMA	Poly(2,3-dihydroxypropyl methacrylate)
PDMS	Polydimethylsiloxane
PDPAEMA	Poly[2-(diisopropylamino) ethyl methacrylate]
PDT	Photodynamic therapy
PEG	Poly(ethylene glycole)
PEI	Polyethyleneimine
PEO	Poly(ethylene oxide)
PEs	Polyelectrolytes
PET	Positron emission tomography
PES	Polyethersulfone
PEU	Poly(ether)urethane
PfFt	Ferritin protein
PG	Polyguanidino oxanorbornene
PLGA	Poly(L-glutamic acid)
PLL	Poly(L-lysine)

PNIPAM	Poly(*N*-isopropylacrylamide)
PPO	Poly(propylene oxide)
PSA	Prostate-specific antigen
PSD	Particle size distribution
PSt	Polystyrene
PTA	Photothermal ablation therapy
PVA	Poly(vinyl alcohol)
PVPo	Polyvinylpyrrolidone
QD	Quantum dot
RBS	Rutherford backscattering spectrometry
RCA_{120}	Recinus communis agglutinin
RET	Resonance energy transfer
RF	Relative frequency
RGD	Arginine-glycine-aspartic acid
ROMP	Ring-opening metathesis polymerization
r_p	Particle radius
S	Sedimentation coefficient
S/V	Surface-to-volume
SAED	Selected-area electron diffraction
SAMs	Self-assembled monolayers
SANS	Small-angle neutron scattering
S_{area}	Surface area
SAXS	Small-angle X-ray scattering
SEC	Size exclusion
SEM	Scanning electron microscopy
SERRS	Surface-enhanced resonance Raman scattering
SERS	Surface-enhanced Raman scattering
SET	Surface energy transfer
SiNWs	Silicon nanowires
SLS	Static light scattering
SNOM	Scanning near-field optical microscopy
(sp)FRET	Single-pair or particle
SPM	Scanning probe microscopy
SPR	Surface plasmon resonance
STM	Scanning tunneling microscopy
SWCNTs	Single-walled carbon nanotubes
TAPP	Tetra(4-aminophenyl) porphyrin
TDT	1-tetradecanethiol
TED	Transmission electron diffraction
TEM	Transmission electron microscopy
TEOS	Tetraethylorthosilicate, tetraethoxysilane
T_g	Glass transition temperature
TGA	Thermal gravimetric analysis
TG-DTA	Thermal gravimetric and differential thermal analysis

TLC	Thin-layer chromatography
TOA	Trioctylamine
TOAB	Tetraoctylammonium bromide
Trp	Tryptophan
Tween 20	Polyoxyethylene sorbitan monolaurate
UPD	Underpotential deposition
v_f	Volume fractions
VFT	Vogel-Fulcher-Tammann
w/o	Water-in-oil
w/o/w	Water-in-oil-in-water
XPS	X-ray photoelectron spectroscopy
XRD	X-ray diffraction
v_a	Volume of action

1.1 Introduction

Although enjoying a history dating back to the days of Faraday's pioneering work [1], noble metal nanoparticles (NMNPs) are still intensively studied in current research [2, 3]. After the seminal report by Faraday in 1857 [1] of the reduction of a tetrachloroaurate solution by phosphorus in carbon disulfide, the preparation of gold nanoparticles (AuNPs) with controlled sizes and shapes has raised increased attention during the second half of the twentieth century. The breakthroughs have been those by Turkevich in 1951 with the citrate method improved by Frens in 1973, then in 1981 with Schmid's report of a Au_{55}-phosphine cluster and the notion of quantum dot, then by Mulvaney and Giersing in 1993 with the first synthesis and stabilization of AuNPs by thiolates, and finally by the Schiffrin group in 1994 with the report of the illustrious and most convenient Brust-Schiffrin biphasic method of thiolate-stabilized AuNPs [2]. Sophistications of these methods during the last decade, especially the seed-growth synthesis, have now led to promising applications. This is mainly due to their applications in catalysis [4], chemical sensing [5], biolabeling [6], and photonics [7]. Additionally, AuNPs have served as building blocks for self-assembled two- and three-dimensional superlattices [8, 9].

Hardly any other material has contributed more in the human civilization than (noble) metals. Metals remain important even in the present ages of wood, polymer, carbon, inorganics and silicon. Applications of metallic materials range from household items to space ships due to their useful properties including strength and toughness, thermal and electrical conductivity, different colors, jewels, ductility, and high melting points. One of the key features of metallic materials is that they can be crafted into numerous useful shapes and forms. "Gold will be slave or master" as Horace once said. Gold, because of being rare, beautiful, and resistant to chemical modification, was always fascinating for people. Centuries of human

civilization passed, and gold was present since the earliest known traces of it. Even today we can observe beautiful golden jewelry and other gold items, made in Ancient Egypt. Gold is popularly associated with wealth and power. The first medical use of gold is dated to the Chinese in 2500 BC. Since then, multiple therapeutic effects were assigned to gold. There were attempts to treat nervous disorders, tuberculosis, rheumatic disorders, and tumors usually with rather toxic, not therapeutic effect. In our endeavor of exploring new materials with better performance and new functionality, the researches have invented many techniques for manipulating metallic materials. Currently, noble metal nanomaterials with a variety of morphologies and sizes can be synthesized by various procedures [10].

The miniaturization of structures by conventional [11] and electron-beam lithography [12] is reaching the theoretical limits of about 50 nm. For the further miniaturization of chemical objects, alternative approaches must be developed. Following Feynman's vision, one may employ atoms and molecules as building units for the "bottom-up" assembly and construction of architectures with nanometer dimensions. Nanoparticles that consist of metals [13] (e.g., gold, silver, platinum, and copper) seem to be attractive units for the engineering of such structures. A variety of synthetic methodologies for the preparation of various metal nanoparticles within a designed size distribution are available. Often, the metal nanoparticles are prepared by "wet chemistry" procedures, in which clusters of metal atoms are formed in the presence of a surface-capping ligand (surfactant or surface active molecule). This capping ligand binds to the metal atom clusters, prevents aggregation of the particles into bulk material, and controls the final dimensions of the nanoparticles. Many capping (agents) systems are available: hydrophobic monolayers [14], positively or negatively charged hydrophilic monolayers [15, 16], surface active (macro)molecules, and (bio)polymer layers [17].

Nanoparticles exhibit completely new or improved properties as compared to the larger particles of the bulk material that they are composed of based on specific characteristics such as size, distribution, and morphology [18]. Certainly, finding new materials is always an important part of progress, but we should also focus on the much larger domain of novel functions that we can give to existing or modified materials. Various techniques are involved in nanoparticle preparation like chemical and physical methods which may successfully produce pure, well-defined nanoparticles, but these are quite expensive and potentially can be dangerous to the environment [19]. Green chemistry-based eco-friendly methods for synthesis of nanoparticles could be an alternative for chemical synthesis. Numerous naturally derived materials and biopolymers have been successfully used for well-organized and speedy green synthesis of silver [20]. Nanomaterial synthesis is emerging as a crucial technology in nanotechnology to develop building blocks for nanometer-scale devices. The synthesis of noble metal nanoparticles with controlled chemical composition, size, and shape distributions is an important first step toward the realization of nanotechnology. Size and shape are pivotal in determining the physical and chemical properties of materials on the nanoscale [21]. A wide variety

of physical and chemical processes have been employed for the synthesis of metal nanoparticles [22–24].

Separation and purification techniques separate the nanomaterials (NMs) and their conjugates from the original reactants and by-products [25]. Characterization, an important step in the morphology-controlled synthesis of nanoparticles, includes assessment of composition, morphology, dimensionality, and physical (such as optical and spectroscopic characteristics) and chemical properties (such as surface charge and functionality). Size (diameter, length, width, and height), volume, aspect ratio, perimeter, projected area, surface roughness, etc., are typical morphology parameters that are assessed [26]. A variety of well-developed techniques which already have been successfully applied to the characterization of bare NMs are now being extended to examining NMNPs and their nanoconjugates. These include separation-based, scattering, microscopy, spectroscopy, mass spectroscopy, and thermal techniques [27].

Current methods for determining noble metal nanoparticle size can be divided into several subcategories. The first is light scattering method that includes dynamic light scattering (DLS), static light scattering (SLS), and small-angle X-ray scattering (SAXS). The second category is the microscopy method including atomic force microscopy (AFM), transmission electron microscopy (TEM), and scanning electron microscopy (SEM). The third is the localized surface plasmon resonance (LSPR) method, which takes advantage of the fact that the LSPR features of AuNPs depend on the size, shape, and concentration of the AuNPs [28, 29]. Fractional precipitation has often been used for size and shape estimation of nanoparticles.

Chromatography separation techniques are based upon the differing affinities of the multiple sample components for the chosen chromatographic mobile and/or stationary/solid phase [30]. For High-performance liquid chromatography (HPLC) coupled with reverse-phase ion-exchange and size exclusion (SEC), stationary phases have been extensively used for purification of nanomaterial conjugate from excess (bio)molecules [31]. Size exclusion chromatography has also shown its feasibility for the separation of various metallic nanoparticles according to their size and shape. Field flow fractionation (FFF) provides information on charge, size (peak height position), and size distribution (peak width) [32]. Centrifugation is a relatively simple and cheap technique that can be used to purify functionalized nanomaterials and their conjugates from unconjugated ligand (molecule).

Of all the scattering techniques available, DLS, also known as photon correlation spectroscopy (PCS), is probably the most commonly used for characterizing the hydrodynamic size of nanoparticles (NPs) and their conjugates, given that it is simple, noninvasive, nondestructive, and relatively cheap to apply [33]. The concentration of particle gold in solution, for example, can be measured by inductively coupled plasma-optical emission spectroscopy (ICP-OES) [34]. The Scherrer equation, in X-ray diffraction and crystallography, is a formula that relates the size of submicrometer particles, or crystallites, in a solid to the broadening of a peak in a diffraction pattern [35].

Fluorescence correlation spectroscopy (FCS) is similar to DLS, in that it measures signal fluctuations due to diffusion, aggregation, interactions, etc., and has

already been successfully applied to accurately estimate the hydrodynamic radius of fluorescent NPs and fluorescent beads [36]. Surface-enhanced Raman scattering (SERS) is an ultrasensitive vibrational spectroscopic technique that can be used for the detection of molecules on or in close proximity to the surface of metal nanostructures. When a dye resonant with the interrogating laser is investigated, a further enhancement that results in surface-enhanced resonance Raman scattering (SERRS) can be achieved [37]. Förster resonance energy transfer (FRET), fluorescence resonance energy transfer (FRET), resonance energy transfer (RET), or electronic energy transfer (EET) is a mechanism describing energy transfer between two light-sensitive molecules (chromophores) [38].

X-ray diffraction (XRD) is typically used to provide structural information about crystalline samples [39]. Thermal techniques can aid in determining the amount of conjugated molecule as well as both the nanoparticle and the molecule's (polymer's) thermal stability. Typically, for techniques such as differential scanning calorimetry (DSC), microgram amounts of sample are required for analysis (depending on composition). Thermal gravimetric analysis (TGA) is a method that utilizes a high-precision balance to determine changes in the weight of a bulk sample relative to changes in temperature and has been used to characterize a variety of NPs functionalized with biomolecules [40].

Environmental SEM (ESEM) does allow sample imaging under low pressure, fairly high humidity, and without the requirement of a conducting overcoat but has found limited use to date for the study of nanoparticles and their bioconjugates. Dark-field microscopy (DFM) and near-field optical microscopy allow direct examination of single particles, providing deeper understanding of the optical properties of individual nanoparticles [41]. Experimental techniques, such as electron energy loss spectroscopy (EELS), have been proven to be successful in imaging localized optical excitations with high resolution to reveal their dramatic spatial variation over single nanoparticle by using photons and electron beams [42, 43]. The discrete dipole approximation (DDA) technique was used to model the silica-coated nanoprisms [44]. Mass spectrometry (MS) is an analytical chemistry technique that helps identify the amount and type of chemicals present in a sample by measuring the mass-to-charge ratio and abundance of gas-phase ions. Dialysis, filtration, extraction, and differential precipitation represent the most common methods applied to NP-(bio)conjugate purification.

A ligand adsorption method is used for determining the surface areas, concentrations, and sizes of colloidal gold. Preformed-seed-mediated growth is a popular colloid-chemical method for the preparation of a wide variety of NMNPs [45]. A variant of preformed-seed-mediated growth method is the "in situ seeding method." Solution plasma, a novel technology, has potentials for advancement in production of nanomaterials and decomposition of organic-based compounds as well as control of microorganisms. Liquid chemistry initiated by microplasma at the plasma-liquid interface is ultimately responsible for the nucleation and corresponding synthesis of AuNPs in liquid. Electric discharge technique is one of the classical colloid preparation methods [46]. There are two general methods for producing a polymer shell around noble metal nanoparticles: the "grafting to" and

the "grafting from" methods [47]. Top-down approaches, such as photolithography, e-beam lithography (EBL), and Focused ion beam (FIB), offer high fidelity and high controllability in terms of design and prediction. Some bottom-up approaches based on self-assembly, such as nanosphere lithography, anodized aluminum oxide (AAO) template, and block copolymer lithography, can produce high-resolution (sub)nanostructures over a large area with a low cost, but it is difficult to obtain highly uniform and controllable structures of arbitrary symmetries across whole area [48].

Advances in bioengineering and the continued refinement of optical detection techniques have led to the development of multimodal optical detection systems. These multimodal devices often function in real time to provide complementary diagnostic information and wide tissue surveillance capability. The ultimate goal of the optical detection systems centers on the achievement of an "optical biopsy."

The combination of nano-objects, nanotools, and nanotemplates with biomolecules yields new facets of bioelectronics to open new horizons of nanobioelectronics. Many nanogold(silver)-based environmental technologies (e.g., sensors, sorbents, reactants) are under very active research and development and are expected to emerge as the next-generation environmental technologies to improve or replace various conventional environmental technologies in the near future [49]. Some of the most promising near-term realizations of nanotechnology are at the interface of physical, chemical, and biological systems. Because many biomolecules have specific binding properties in self-assembly processes, they are attractive materials for nanotechnology.

1.2 Book's Features

This book will focus on the experimental, and to a lesser extent, theoretical, status of research on the preparation and characterization of noble metal nanoparticles and their conjugates, especially of silver and gold nanoparticles. As such, this book starts with a brief history of gold materials. Without making any attempt to be exhaustive, this book examines and summarizes the existing achievements in the methods of synthesis of NMNPs mainly with both spherical and partly with non-spherical morphologies, highlighting how their physical and chemical properties are influenced by the reaction procedure and change in morphology.

This book is organized into five chapters and many subchapters and sections. The first chapter "Nanofield" consists of seven subchapters. In the first subchapter, the short history and introduction to this field are presented. Noble metal nanoparticles appeared early in human history, probably since the fifth century BC in China and Egypt for medical or decorative purposes, which persisted until now. The second subchapter introduces the short content of all chapters. In the third subchapter, the general characteristics of nanomaterials and their preparations are described, with an emphasis on gold and silver nanoparticles. The synthesis of nanomaterials or nanoparticles was summarized to be carried out in the solid,

liquid, or gaseous state, following two basic approaches, as "top-down" and "bottom-up." A variety of colloid-chemical strategies involving a wide spectrum of reagents and reaction conditions has been employed in order to prepare noble metal nanomaterilas of controlled morphologies. The fourth subchapter, "Nanometria and nanotechnology," summarizes the approaches of manipulating and controlling things on a small scale. The nanometer regime covers the transition from condensed matter behavior to atomic and molecular properties and thus is a very rich but also very demanding area in materials science. Properties and functions change qualitatively or quantitatively by orders of magnitude when the dimensions become smaller than a critical size in the nanometer range. The key to the future lies in the functions that we give to materials, not just in finding "novel functional nanomaterials". Certainly, finding new materials is always an important part of progress, but we should also focus on the much larger domain of novel functions that we can give to existing or modified materials. Nanotechnology is the culmination of many facets of developments in the nanorealm, including nanofabrication, nanomachineries, quantum devices, molecular machines, and molecular computers. Various synthetic strategies to prepare noble metal nanoparticles and major techniques to characterize nanoparticles are summarized in the fifth subchapter. Herein, separation and purification techniques are reviewed for the separation of the nanomaterials (NMs) and their conjugates from the original reactants and by-products. Characterization includes assessment of composition, size, volume, aspect ratio, perimeter, projected area, surface roughness, morphology, dimensionality, and physical and chemical properties. These include scattering, microscopy, spectroscopy, mass spectroscopy, and thermal techniques. Current methods for determining NMNP size include light scattering methods such as dynamic light scattering (DLS), static light scattering (SLS), and small-angle X-ray scattering; the microscopy methods include atomic force microscopy (AFM), transmission electron microscopy (TEM), and scanning electron microscopy (SEM); the localized surface plasmonic resonance (LSPR) method; and the fractionation, centrifugation, and chromatographic methods. X-ray diffraction (XRD) is typically used to provide structural information about crystalline samples. Förster resonance energy transfer (FRET), fluorescence resonance energy transfer (FRET), resonance energy transfer (RET), or electronic energy transfer (EET) is a mechanism describing energy transfer between two light-sensitive molecules (chromophores). Thermal techniques can aid in determining the amount of conjugated molecule as well as both the nanoparticle and the molecule's (polymer's) thermal stability. Typically, for techniques such as differential scanning calorimetry (DSC), microgram amounts of sample are required for analysis (depending on composition). Thermal gravimetric analysis (TGA) is a method that utilizes a high-precision balance to determine changes in the weight of a bulk sample relative to changes in temperature. The electron diffraction pattern obtained from high-resolution TEM (HRTEM) and sometimes selected-area electron diffraction (SAED) techniques may provide information regarding the atomic structure of the particles, lattice plane fringes, and the nature of the facets such as twinning, twinning planes, and surface reconstruction. Energy-dispersive X-ray analysis (EDAX) available with analytical TEM

or SEM and X-ray photoelectron spectroscopy (XPS) can be used to determine surface elemental and surface compound composition. Indeed, these techniques provide extremely detailed information on the target molecules or atoms at an atomic scale, while they are used under ultrahigh vacuum or under extremely low temperatures for precise control of the mechanical drift or diffusion of the samples. Some are already routinely used to purify NP-conjugates and can also be quite effectively used for characterization purposes. The further subchapter deals with the medical diagnostics. This field comprises a variety of techniques designed to characterize the relationship between the physical (chemical) and biological properties of tissue. Through the detection of changes in light, for example, after interaction with tissue, optical technologies provide information on the physiologic condition of the tissue at a molecular level. Spectroscopic techniques, such as fluorescence spectroscopy, light scattering spectroscopy, optical coherence tomography, and Raman spectroscopy, utilize the unique spectral patterns that are created as tissue progresses toward cancer to offer the potential to detect diseased tissue during the initial stages of carcinogenesis. Advances in bioengineering and the continued refinement of optical detection techniques have led to the development of multimodal optical detection systems. These multimodal devices—mainly based on nanotechnology—often function in real time to provide complementary diagnostic information and wide tissue surveillance capability. The ultimate goal of the optical detection systems centers on the achievement of an "optical biopsy." Nanotechnology is garnering widespread recognition not only as a scientific subdiscipline, but an entity in its own right that encompasses physics, chemistry, and biology. It seems that nanotechnology is increasingly gaining a foothold in clinical medicine, especially in oncology. Nanoparticles, such as super paramagnetic iron fluids, noble metal nanoparticles, and quantum dots, are emerging as viable contrast agents to be used in medical imaging platforms, for instance CT or MRI. Small nanoparticles display superior fluorescent properties with less photobleaching compared with conventional chromophores. Nanoparticles have been of significant interest over the last decade as they offer great benefits for drug delivery to overcome limitations in conventional radiation or chemotherapy. Image-guided therapies could be designed based on multifunctional noble metal nanoparticles. Such NPs have a strong and tunable surface plasmon resonance absorption in the near-infrared region and can be detected using multiple imaging modalities (magnetic resonance imaging, nuclear imaging, and photoacoustic imaging). These novel nanostructures, once introduced, are expected to home in on solid tumors either via a passive targeting mechanism (i.e., the enhanced permeability and retention effect) or via an active targeting mechanism facilitated by ligands bound to their surfaces. Conclusion remarks about history, preparation, and characterization of noble metal nanoparticles are included in the last subchapter. Herein, the rich variety of synthetic techniques, routes, and morphologies in NMNPs briefly summarized are highlighted. We have seen that the progress has been rapid and inspiring toward the innovative synthesis methods and sophisticated characterization techniques. We finish off by showing new directions research is taking in this new and fascinating area.

The second chapter "Noble metal nanoparticles" consists of five subchapters. The first subchapter shows the general features about massive generation and usage of engineered nanomaterials (or nanoparticles) even though the potential nanostructure impacts of these materials are largely unknown. NMNPs play important roles in different branches of science, such as chemical catalysis, catalysts for the growth of nanowires, nanomedicines, and nanoelectronics. For most of those applications, their size and size distribution control are of key importance. Research involving the use of different types and designs of nanomaterials continues to evolve with the growth of nanotechnology for applications in such fields as drug delivery, medical imaging, diagnostics, and engineering technology. The second subchapter covers the basic knowledge about the reaction precursors. Control over the shape and size of the NMNPs is usually achieved through the careful selection of the experimental conditions, namely reducing agent (strong or weak), reaction time, temperature, UV light, template, (co)solvent, and capping agent (surfactant). Upon the addition of strong reductants, gold cations are reduced rapidly, resulting in an immediate color change of the reaction mixture from colorless or yellow to dark red. With the use of weaker reductants applied in these syntheses, a much slower but continuous color change from colorless to yellow, pink, brown, and finally to purple-red is observed, which indicates a relatively slow reducing rate of Au(I). The third subchapter deals with some factors contributing to the kinetics of particle nucleation, growth, and modification. There are several methods for the preparation of noble metal nanoparticles such as citric acid reduction, electrochemical synthesis, photoreduction, and radiation. The activation of the reaction to produce silver nanoclusters can be performed following several routes. The silver ions from dissolved silver salts can be reduced, either by a chemical reductant (e.g., sodium borohydride, sodium hypophosphite), by light (photoreduction with visible or ultraviolet light), or by γ-rays (by radiolysis of water). The chemical reduction and the photoreduction are the most commonly used methods. The sensitivity of gold and silver nanoclusters to the local environment can be exploited for sensing purposes; though it represents a difficulty when designing the synthesis, the proper recipe for the production of these nanoclusters with a certain scaffold might not be useful when using a different scaffold. Vast studies have concerned aqueous solutions of the amphiphilic "pluronics" type of triblock copolymers, PEO-PPO-PEO. It is well established that the pluronic copolymers with higher PEO/PPO ((poly(ethylene oxide)/poly(propylene oxide)) ratio self-assembly into micelles composed of a PPO-rich core and a PEO-rich corona above the critical micellar concentration (CMC) and a critical micellar temperature (CMT). PEO-PPO-PEO block copolymers can act as very efficient reductants/stabilizers in the single-step synthesis and stabilization of gold nanoparticles. In aqueous systems, the effects of metal ion/stabilizer mixing ratio, reaction temperature, reaction time, and energy input on the formation of colloidal particles typically have been considered. Formation of gold nanoparticles from $AuCl_4^-$ in aqueous PEO-PPO-PEO block copolymer solutions includes three main steps including complexation, reduction, and stabilization. Environmentally friendly, single-step/single-phase synthesis of core@shell noble metal NPs can be mediated

by polymers that simultaneously play the roles of reductant and stabilizer while imparting unique properties to the resulting hybrid material. To date, the above strategy has been applied successfully mainly to pluronics and polyacrylates with amino groups, which have a strong ability to coordinate on metal surfaces. Furthermore, it has been observed that foreign ions (metal, halides, etc.) play important roles in the morphology control of the NMNPs. They generally adsorb onto a certain set of facets of the growing particle more strongly than others. Such preferential adsorption affects the growth rate of a particle in an anisotropic fashion or may influence the formation of defect structure of the seeds, resulting in the modification of the final crystal shape. Often modifiers (e.g., surfactants) are added to moderate the growth rate or influence the final crystal habit. Growth of gold nanocrystals in solution also relies on surfactants to control unwanted cluster aggregation during chemical reduction of ionic precursors or thermal decomposition of metalorganics. Continuous fluctuations in the sizes of these clusters occur via the incorporation of additional atoms or molecules and their detachment. Depending on the surface-to-volume ratio of a developing particle, the resultant energy varies and, therefore, there will be an energy barrier for nucleation. Growth of metal nanocrystals in solution also relies on surfactants to control unwanted cluster aggregation during chemical reduction of ionic precursors or thermal decomposition of metalorganics. The homogeneous nucleation of nanoparticles is based on the supersaturation of solution by reactants such as precursors, reducing agent, stabilizers, costabilizers, and additives. The supersaturation state can be then reached by the reduction in temperature. Generation of supersaturation through in situ chemical reactions by converting highly soluble chemicals into less soluble chemicals is a good example of this approach. In a typical homogeneous nucleation synthesis consisting of one-step process in which precursor(s), stabilizer(s) and other additives are stirred in the oil- or water-continuous phase and then treated by the heat. The heterogeneous nucleation of metal particles consists of several steps' process. In a typical heterogeneous nucleation, the first step is the formation of the primary (seed) metal particles and then the growth of particles is achieved via further steps, for example, by the further addition of precursor(s), stabilizer(s), and additives. The noble metal nanoparticle growth is generally categorized by two processes: diffusion-controlled Ostwald ripening and aggregation/coalescence. The digestive-ripening process contributes to the regulation of the particle growth and particle distribution. Modifications in temperature influence the reaction by changing the stabilization of the complexes formed between metal precursors and the surface modifiers, e.g., polyvinylpyrrolidone (PVPo), and the nucleation rate of the reduced metallic atoms. Seed-mediated growth method has been demonstrated to be a powerful synthetic route to generate a range of different types of metal nanoparticles. This method separates the nucleation and growth stage of nanoparticle syntheses by introducing presynthesized small seed particles into a growth solution typically containing a metal precursor, reducing agent, surfactants, and some additives. Dissolution is one of the main processes that controls metal nanoparticles behavior in aquatic systems. This is not the case for the metal microparticles or bulk metal fragments. Dissolution of silver nanoparticles, for

example, occurs through oxidation of metallic silver and release of Ag^+ into solution (or dissolution rate is accelerated). The further subchapter based on bioapproach indicates that some surfactants find their way to various environmental segments and thus pose serious health hazards. Long exposure to quaternary ammonium compounds (QAC) can cause sensitization, hemolysis, and toxic effects by all routes of exposure including inhalation, ingestion, dermal application, and irrigation of body cavities. Toxicity is a major nuisance of anticancer drugs. Most of the clinically used anticancer drugs have a narrow therapeutic index, with a small difference in their dose for antitumor effect and toxicity. One promising example of such materials is presented by a class of pluronic block copolymers. These block copolymers consist of hydrophilic poly(ethylene oxide) (PEO) and hydrophobic poly(propylene oxide) (PPO) blocks arranged in ABA triblock structure. Passive drug targeting is a validated method for improving the delivery of low molecular weight (chemo)therapeutic agents to tumors. Prominent examples of macromolecular drug carrier systems evaluated in patients are albumin, poly(ethylene glycol), dextran, poly(L-glutamic acid), poly[N-(2-hydroxypropyl)methacrylamide], and others. These formulations were found to be 4–5 times higher than that of free doxorubicin (DOX), no cardiotoxicity was detected (in spite of the relatively high overall doses administered), and several clear responses were observed, in patients with nonsmall cell lung cancer, with colon cancer and with doxorubicin-resistant breast cancer. Furthermore, these copolymers have also been employed to improve the treatment of noncancerous disorders, such as rheumatoid arthritis and bacterial infections, which are also characterized by a strong inflammation component and leaky blood vessels, and which are therefore also highly amenable to EPR-mediated passive drug targeting. The last subchapter (conclusion) attempted to give an outline of the colloid-chemical synthesis approach for controlling morphology in NMNPs. These NPs with intriguing and novel morphologies, and sometimes with near-perfect shape control, have been produced by colloid-chemical synthesis. The influences of various synthesis parameters, processes, and approaches in manipulating the nanometer features in all three dimensions of NPs have been discussed.

The surfactant-mediated preparation of noble metal nanoparticle studies summarized in the third chapter consists of four subchapters. The literature review to this topic is shortly introduced in the first subchapter. The second subchapter deals with the basic knowledge concerning of the preparation of metal nanoparticles in reverse micelles (six sections). The surfactants that coat a micelle are typically amphiphilic in nature, meaning that micelles may be stable either as droplets of aprotic solvents, such as oil in water, or as protic solvents such as water in oil. The shape of the aggregates depends on the chemical structure of the surfactants, namely the balance in size between hydrophilic head and hydrophobic tail. A measure of this is the hydrophilic-lipophilic balance (HLB). Of the chemical processes, a reverse micelle (water-in-oil (w/o) microemulsion) synthesis has been demonstrated to be a viable method for producing a wide array of noble metals and metal (oxide) nanoparticles over a relatively narrow particle size distribution in different organic media. The w/o microemulsion method offers a lot of advantages

with respect to others (coprecipitation in solution, sol-gel, flame-spray pyrolysis, laser evaporation, high-energy milling), namely the use of a simple equipment, homogeneous mixing, high degree of particles size and composition control, formation of NMNPs with high surface area, and the use of soft condition of synthesis near ambient temperature and pressure. As the preparation of metal nanoparticles using reverse micelles does not require extreme conditions of temperature and pressure, it is comparatively easy to expand the scale of reverse micellar reaction system. A reverse microemulsion utilizes the natural phenomenon involving the formation of spheroidal aggregates in a solution when a surfactant is introduced to an organic solvent, formed either in the presence or in the absence of water. Micelle formation allows for a unique encapsulated volume of controllable size through which reactions and subsequent development of metal nanostructures or nanoparticles proceed in the soft template. However, large amounts of surfactant are required to stabilize the metal nanoparticles, which introduces impurities. The use of microemulsion template is one of the most advantageous ways to synthesize AuNP in a "bottom-up" approach. Different structure can be formed as such: water-in-oil (w/o) or oil-in-water (o/w) droplets, and bicontinuous structure, over a wide range of composition depending of the properties of the surfactant and the oil. The preparation of silver nanoparticles by the inverse microemulsion is summarized in the second section. Silver nanoparticles are of particular interest because of their wide applications resulting from the unique properties that depend on their shape and size. Synthesis of silver nanoparticles in the presence of various (coating) agents, such as amino acids or small peptides, often produces nanoparticles with variable dimensions, which depend on the concentration of the coating agent and on reaction conditions. AgNPs have been gaining significant research interest due to their unique shape and size-dependent optical, antimicrobial, and catalytic properties. Silver nitrate aqueous solution was directly used to prepare silver nanoparticles in AOT (sodium di(2-ethylhexyl) sulphosuccinate)-based microemulsions. The particles are spherical in shape, and there is narrower in the size distribution at lower water content. More elongated rodlike (anisotropic) micelles and/or wormlike micelle structures are formed at higher water content and in the presence of various additives. Surfactant molecules can be used as "simple" capping, soft template, and stabilizing agents. They also grew successive generations of metal alloy nanoparticles from seeds formed in ionic and anionic inverse micelles using the inverse micelle solution used to grow the seeds as the feedstock for each stage of growth. Dodecanethiol-capped silver "quantum dot" particles (QD-particles) have been synthesized using a novel biphasic microemulsion. AOT as the anionic surfactant due to its higher solubility in organic phase helps to extract metal cations from the aqueous to reverse micellar phase. An alternative new approach to monodisperse silver nanocubes by a HTAB (hexadecyltrimethylammonium bromide)-modified silver mirror reaction was discussed. The growth of silver nanoparticles should be a result of the interplay of the faceting tendency of the stabilizing agent of HTAB and the growth kinetics of silver metal. A number of 1D arrays of aligned silver colloids were found in the prolate HTAB micelles. Meanwhile, some nanowires that formed along the arrays were also observed. The simplest approaches for gold nanoparticle

synthesis are various surfactant-based methods, mainly microemulsion approach
described in the third section. Controlled nucleation and separation of nucleation
from growth are the keys to synthesizing near-monodisperse gold nanoparticles.
This can be achieved either by providing a controlled number of preformed gold
nanoparticles as nucleation centers in a growth medium where no secondary
nucleation can occur—the seeding growth method—or by varying the ratio of
strong and weak reducing agents. Surfactant molecules can be used as "simple"
capping, soft template, and stabilizing agents as in the organometallic precursor
decomposition reactions. A micelle template mechanism can explain the origin of
various shapes of gold nanoparticles. The $AuCl_4^-$ ions are quantitatively bound to
cetyltrimethylammonium bromide (CTAB) micelles and can be used to vary the
particle size and shape. The crystal growth can be manipulated and spatially con-
trolled by CTAB if the active solution species that deposits onto the growing
particle surface is adsorbed onto the CTAB micelles. The formed gold nanoparticles
exist in several morphologies (spheres, rhombs, triangles, popcorn, and polygons).
The organic coating was also performed in nonionic surfactant (Igepal)-cyclohex-
ane reverse micelle medium. Igepal produces 1–10-nm-size spherical reverse
micelles, depending on the water-surfactant molar ratio. In the fourth section
"Hybrid nanoparticles," composite nanomaterial studies were summarized. The soft
template formed by reverse micelles was effective to prepare the composite (hybrid)
gold-coated metal nanoparticles. The gold or silver shell was suggested to grow by
nucleating from small nanoparticles on the iron-core surface before it develops the
shell structure. These nanoparticle nucleation sites form islands for the growth and
coalescence of the thin gold or silver overlayer. Laser ablation of solvent-suspended
metal powders can be used for synthesis of gold/silver alloy and core@shell
nanoparticles of predetermined composition. Highly spherical nanoparticles with a
core comprising multiple gold nanodots and a silica shell ($\{Au@SiO_2\}NPs$) were
synthesized via a reverse (water-in-oil) microemulsion-based method. When the
multi-$Au@SiO_2$ NPs were stirred in aqueous polyvinylpyrrolidone solution at room
temperature, the multiple gold nanodots (AuNDs) within the silica matrix were
merged together and changed to a single gold nanoparticle. In the next (fourth)
section, the preparation and stabilization of noble metal nanoparticles by (co)
polymer surfactants (micelles) are discussed as an interesting route for the fabri-
cation of nanoparticle systems with a metal core@polymer shell structure.
A number of methods have been described for preparing and stabilizing NMNPs,
including soft micelle templates of ionic and nonionic polymeric surfactants such
polyoxyethylene sorbitan monolaurate (Tween 20), direct attachment of bolaam-
phiphile surfactants or thiolated polymers, and layer-by-layer deposition of poly-
mers using charge interactions on the surface of NMNPs as a driving force. Modern
macromolecular engineering knowledge is applied to synthesize next-generation
polymer coatings for noble metal nanoparticles that may feature
stimulus-responsiveness (pH, temperature, ionic strength, and light) and sponta-
neously form versatile supramolecular structures. The incorporation of amphiphilic
copolymers into the gold nanoparticle fabrication process has led to the interesting
discovery that both the formation and the stability of colloids are dictated by the

chemical structure of macromolecular chains. Environmentally friendly, single-step/single-phase synthesis of core@shell NMNPs can be mediated by surface active polymers that simultaneously play the roles of reductant and stabilizer while imparting unique properties to the resulting hybrid material. For instance, PEO-PPO-PEO-stabilized AuNPs were prepared in an efficient one-pot aqueous-phase synthesis from the reduction of gold salts by using PEO-PPO-PEO both as a reducing agent and as a stabilizer. The self-organized morphology comprises spherical micelles with a three-layer onion-like core@-shell-corona architecture, with the PDPAEMA block occupying the micelle core and the PDHPMA and PEO block forming the inner shell and corona, respectively, as a template. In the sixth section (five subsections), "Stabilizers-mediated nanoparticle syntheses," the effect of various reactants (solvents, reducing and capping agents, impurities, etc.) on the reaction mechanism of new nanoparticle generation is highlighted. The first, and older one, involves the reduction of metal (tetrachloroaurate) ions in aqueous media. The second concept involves the synthesis in organic solvents. The most popular method is the two-phase synthesis which involves the transfer of tetrachloroaurate ions into toluene with the use of tetraalkylammonium bromide and subsequent reduction with sodium borohydride in the presence of thiols. The surfactant tetraoctylammonium bromide (TOAB) is normally used in the Brust-Schiffrin two-phase method as a phase-transfer agent, and it also acts as metal nanoparticle stabilizer. The TOAB-capped AuNPs is obtained by the Brust-Schiffrin two-phase method without adding the additional stabilizer and utilized in further functionalization or self-assembly. The ionic liquid (IL) that use benzyldimethyltetradecylammonium chloride (BAC) stabilizes the nanoparticles noncovalently via electrostatic interactions. A proposed model is based on differential anion stabilization of metal nanoparticles in a certain order. The anion must be at the surface of the metal, because the stabilization of the nanoparticles correlates with the sterics of the anion.

A facile one-step one-phase synthetic route to achieve a variety of metallic nanoparticles by using amine-borane complexes as reducing agents is discussed. With the use of different metal sources, both mono- and alloyed metallic nanoparticles with a narrow size distribution can be obtained in a single step. An amine-borane complex was used to reduce metal cations. The reducing rate was varied by the reaction temperature and concentration of reactants including the type of solvent. A high-temperature solution-phase synthesis as an inexpensive, versatile, and very reproducible method can be used for the large-scale synthesis of organoamine-protected gold and silver nanoparticles in the 5–30 nm size ranges and with polydispersities as low as 7%. Alkylamines as stabilizers for silver nanoparticles have weaker interactions with silver. These weak interactions can potentially be broken up at significantly lower temperatures, thus enabling the "stripped" silver nanoparticles to coalesce to form a continuous conductive layer. The coordination of silver ions with NH_2 groups in polyacrylamide (PAM) served as weak cross-linkers to attach silver ions and later atoms to polymer chains. Fast formation of silver nanoparticles occurred upon exposing the above mixture to ambient (indoor) light. These observations highlighted the significant role that the polymer plays in the

present photoreactions. The Brust-Schiffrin method was improved by procedure upon which the alkylthiolate-stabilized AuNPs were synthesized in methanol solution without the phase-transfer agent. It has been shown that alkylthiolate-coated nanoparticles form a 2D assembly due to a combination of electrostatic repulsion and van der Waals interaction. The nanoparticles are suggested to form assemblies in solution and that a similar spatial arrangement of nanoparticles may exist in solution. 9-borabicyclo [3.3.1] nonane (9-BBN) was introduced as a mild reducing agent for the synthesis of a series of functionalized alkylthiolate-stabilized AuNPs. Other thiolate ligands such as bifunctional alkanethiolate, arenethiolate, and other functional thiolate-stabilized have been used to synthesize functional AuNPs from the corresponding thiols. The monodispersed spherical silver nanoparticles were formed by reduction of Ag salt in toluene using the mild reducing agent heptamethyl-trisiloxane (HMTS) in the presence of the stabilizing ligand trioctylamine (TOA). Thiols used are strong, stabilizing ligands, and the formation of thiolate-protected gold nanoparticles is very complex. The introduction of strong capping agents during nanoparticle synthesis has the effect of stopping the growth of the NPs, whereas weakly associated ligands allow for continued growth. The versatility and usefulness of soft-ligand-coated AuNPs are further demonstrated by replacing the soft ligands with alkylthiols, which results in 2D assembly of the AuNPs. Soft-ligand-stabilized nanoparticles can be used as precursors to obtain nanoparticles with different surface chemistry by replacing the soft ligands with other desired ligands. A new method of producing gold nanoparticles is a surfactant-free synthesis, high variability in the introduction of (functionalized) ligands, and good control over the particle size. It was found that a solution of hydrogen tetra-chloroaurate in diethylene glycol dimethyl ether can be reduced by a solution of sodium naphthalenide in diglyme to form gold nanoparticles. The citrate reduction method is well known for its simple procedure, yielding stable and reproducible gold nanoparticles of narrow size distribution. The citrate method produces nearly monodisperse gold nanoparticles. Nearly, monodispersed AuNPs with sizes ranging from 20 to 40 nm have been synthesized upon variation of the solution pH. Other improvements of the Turkevich method involved the control of the reaction temperature, the introduction of fluorescent light irradiation, and the use of high-power ultrasound. An intriguing result concerns citrate-stabilized AuNPs that appeared by using D_2O as the solvent instead of H_2O during the synthesis of AuNPs. It was concluded that D_2O increased the reducing strength of citrate. Incorporation of low molecular mass drugs into pluronic micelles can increase drug solubility and drug stability, and can improve drug pharmacokinetics and biodistribution (the third subchapter). Dilution in the blood upon injection would quickly dissolve the micelle and prematurely release the drug into the bloodstream, which limits their practical uses for systemic delivery of DOX. To enhance stability of micelles in the bloodstream upon dilution, pluronic micelles were cross-linked through their hydrophilic shells. Pluronics cause drastic sensitization of multidrug resistance (MDR) tumors to various anticancer agents, enhance drug transport across the blood-brain and intestinal barriers, and cause transcriptional activation of gene expression both in vitro and in vivo. Pluronics have a broad spectrum of biological response

modifying activities which make it one of the most potent drug targeting systems available, resulting in a remarkable impact on the emergent field of nanomedicine. The versatility of the micellar liposomal structure lies in its capacity to cargo drug molecules and biological macromolecules that are either hydrophilic, therefore entrapped in the liposome inner aqueous core, or hydrophobic, therefore incorporated within the lipid bilayer. Hydrophobic nanoparticles can be embedded in the lipid bilayer, whereas hydrophilic nanoparticles can be encapsulated within the internal liposome aqueous core. Alternatively, various types of nanoparticles can be chemically or physically adsorbed onto the external liposome surface. The liposome-nanoparticle hybrids have been designed for use as diagnostic probes. In addition, various types of liposome-nanoparticle hybrids have shown promise in significantly stabilizing colloidal dispersions of otherwise unstable nanoparticle systems in vitro and in vivo. There are multiple examples of liposome systems with diverse characteristics and capabilities that incorporate therapeutics or imaging agents. Encapsulation of doxorubicin and MRI contrast agents in temperature-sensitive liposomes allowed noninvasive and dynamic imaging of drug release during hyperthermia application. PEO-modified gold nanomaterials except of self-assembling have also several attractive characteristics for diagnostic applications, including (1) biocompatibility and stability, (2) unique tunable optical properties (LSPR), and (3) easy conjugation of biomolecules (i.e., ssDNA) to the surface for tumor-specific targeting. More complex shapes with excitation wavelengths of 800–1200 nm could absorb the NIR light and then be converted to heat. By changing the shape of gold nanoparticles to nanorods, the absorption wavelength and scattering wavelength change from the visible to the (near-infrared) NIR region, and their absorption and scattering cross sections also increase. Another type of multifunctional nanoparticles is the combination of metallic nanoparticles and magnetic nanoparticles, which likely will lead new applications in biomedicine because metallic nanoparticles hold the intrinsic properties and functions as optical contrast agents and probes. A novel class of molecules, referred to as nucleic acid ligands (aptamers), has been developed for noble metal stabilization and therapeutic and diagnostic applications. Aptamers are DNA or RNA oligonucleotides or modified DNA or RNA oligonucleotides that fold by intramolecular interaction into unique conformations with ligand-binding characteristics. Since these nanoparticles are 100- to 10,000-fold smaller than cancer cells, they can easily pass through cell barriers. In addition, they preferentially accumulate at the tumor sites because of hallmarks of tumors such as the fenestrated vasculature and poorly lymphatic drainage, resulting in an enhanced permeability and retention (EPR) effect. In the last subchapter (conclusion), various variants corresponding to various combinations of metal precursors, solvents, reducing agents, stabilizing molecules, complexing agents and reaction conditions, and their effects on the reaction mechanism of noble metal nanoparticles formation in the short are summarized. The generation of silver and gold nanoparticles was investigated under various reaction conditions such as using weak and strong reducing and capping agents, the low and high temperatures, various additives (ionic liquid surfactants, steric surfactants, acids, polyacrylamides, etc.), and synthetic approaches.

The fourth chapter consisting of five subchapters deals with the use of spatially and dimensionally constrained structures—polymer templates as an effective method to prepare metal nanocrystals with a morphology similar or complementary to that of the template (the first introductory subchapter). Some functional polymers have found special mention for their ease of handling, effective capping, mild reducing ability, and human-friendly nature. These methods are expected to result in a very narrow particle size distribution and particles of uniform shape. Most syntheses describe the use of suitable surface-capping agents in addition to the reducing agents for synthesis of nanoparticles. Templating synthesis is a powerful method for the controlled synthesis of shaped nanocrystals; however, the available templates for colloidal synthesis of gold nanocrystals are still rather limited. The second subchapter (two sections) summarizes the direct synthesis of nanoparticles in polymer matrixes. Direct synthesis of nanoparticles in so (co)polymer matrixes is discussed in the first section. This field is attracting and increasing interest in terms of practical applications and synthetic challenges. These spatially and dimensionally constrained structures can serve as reaction cages to control the growth of the particles. By varying the shape of the sacrificial template nanoparticle and its ratio to the more noble metal precursor added, one can obtain a variety of morphologies such as triangular rings, wires, tubes, boxes, or cages. Multilayered polymer films and block copolymer films were used as nanoreactors for the generation of noble metal nanoparticles. Bimetallic alloy nanoparticles consisting of two noble metals were successfully prepared by ethylene glycol (EG) agent. A new template method for the preparation of flexible silver/cross-linked poly(vinyl alcohol) (PVA) nanocables via one-step in situ reduction of Ag^+ and Ag^+-catalyzed cross-linking of PVA chains under hydrothermal conditions was discussed. A synthesis of positively charged silver nanoparticles via photoreduction of silver nitrate in branched polyethyleneimine (PEI) solution was reported. A further polymers such as polyvinylpyrrolidone, poly(amidoamine), polyacrylate, and polyacrylonitrile (PAN) are also popular stabilizing agents. A thermosensitive water-soluble polymer, poly(N-isopropylacrylamide) (PNIPAM), and its copolymers were also used for the immobilization and stabilization of noble metal nanoparticles (fluorescent silver nanoparticles). Nevertheless, also linear polyacrylates or polymethacrylates such as poly(methacrylic acid) can act as an excellent scaffold for the preparation of silver nanoclusters in water solution, by photoreduction with visible light, UV light or sonochemically. The sonochemical process was as well successfully used with scaffolds as poly(acrylic acid) and poly(acrylic acid-co-maleic acid). Microgels of poly(N-isopropylacrylamide-co-acrylic acid-co-acrylamide) can be used to template the formation of fluorescent silver nanoparticles. Block copolymers (di- and triblock), especially amphiphilic, have been used to prepare aggregation-free NMNPs. A PEG-based nonionic block copolymer (poly(ethylene oxide)-poly(propylene oxide)-poly(ethylene oxide) (PEO-PPO-PEO)) templates the synthesis of luminescent silver particles. There is a great diversity of polymers that can be used to produce surface-capped AuNPs with adequate chemical functionalities toward a specific (bio)application. The most used polymers in AuNPs synthesis and stabilization include poly(ethylene oxide), diamine-terminated poly(ethylene oxide),

linear poly(ethyleneimine) (L-PEI), amine-functionalized poly(propylene imine)-dendrimers, poly(dimethylsiloxane), poly(vinyl pyrrolidone), poly(allylamine) (PAA), and poly(allylamine hydrochloride) (PAH). All these polymers are water soluble, thus allowing the preparation of hydrosols of AuNPs. The polymers known as polyelectrolytes (PEs) can be used as reducing/stabilizing agents. The optimal coating/stabilization of nanoparticles, i.e., the best adsorption of the polyelectrolyte onto the oppositely charged nanoparticles, depends on some key parameters such as the PE molecular weight (chain length), the nature of the repeating units, the concentration and charge density of the polyelectrolyte, particle size, concentration and surface properties (e.g., charge density) of the nanoparticle, as well as the ionic strength, pH, and temperature of the medium. The building-up of multifunctional core@shell nanostructures is one of the great advantages of using PE assemblies. In this case, the PE forming the multilayers can be functionalized with drugs, organic dyes, contrast agents, radionuclides, catalysts, organic dyes, and proteins, namely antibodies, allowing the application of the ensuing structures in areas such as drug/gene delivery, biosensing, bioimaging, and photodynamic therapy. The cationic polymers were made from oxanorbornene monomers via ring-opening metathesis polymerization (ROMP). Polyguanidino oxanorbornene (PG) has been shown previously to have a remarkable combination of potent antimicrobial activity and low membrane-disruptive properties. Microgels of poly(*N*-isopropylacrylamide-co-acrylic acid-co-acrylamide), for example, can be used to template the formation of fluorescent silver nanoparticles (the second section). These nanoparticles as a scaffold were also used to fabricate the composite structures with fluorescent silver nanoclusters. The microgel particles contain not only NH_2- and OH-groups but also COOH-groups. Additionally, the scaffold exhibits stimuli-responsive volume changes under variation of external factors such as temperature and pH, facilitating the application of nanoclusters. Infinite coordination polymer particles (ICPs) are a class of emerging functional materials that are formed by bridging repeating organic ligands with metallic nodes. The ICPs have attracted enormous research interest in chemistry and materials science, because they can be made from readily available and highly tailorable metal and ligand precursors, have chemically adjustable porosities and high internal surface areas, and provide with a network structure that can be deliberately and easily modified for many applications. Metal-organic frameworks (MOFs) are another form of mesoporous materials that are thermally robust and in many cases highly porous. It is expected that the crystalline porous structures of MOFs limit the migration and aggregation of AuNPs. Such metal nanoparticles decorated microcapsule (MC@MNPs) structures are of both scientific and technological importance because of the wide range of potential applications, such as catalyst, controlled delivery of drugs, sensor, and imaging. The incorporation of metal nanoparticles in polymer microcapsules is an effective way to combine the unique optical, electrical, and catalytic properties of metal nanoparticles.

Dendrimers' structural features include the incorporation of metal nanoparticles with precise control over the nanoparticle size and a defined number of terminal groups for each generation with multiple branch ends, which can be available for consecutive conjugation reactions (the third subchapter). The encapsulation of

metal ions inside dendrimers involves, variously, electrostatic and complexation interactions—the dendrimer interior includes coordinating groups such as −OH, NH$_2$, or −COOH. One unique approach to the preparation of noble metal nanoparticles is through the use of various poly(amidoamine) (PAMAM) dendrimers. The advantage of using dendrimers as templates to prepare metal nanoparticles lies in the fact that the surface of the particles can be modified with various functional moieties (e.g., targeting ligands and dyes) through dendrimer chemistry for practical biomedical applications (e.g., cancer cell targeting and imaging). A wide range of metal ions can be preorganized with dendrimers, especially PAMAM dendrimers to form metal DENPs. Likewise, bimetallic core@shell or alloy DENPs (dendrimer-entrapped) can be prepared by coreduction of the metal ions in the presence of dendrimer templates. AuDSNPs (dendrimer-stabilized) were found to be fluorescent and display strong blue photoluminescence. The size of the AuDSNPs decreases with the increase in the number of dendrimer generations, suggesting the different nucleation and growth mechanisms for gold nanocrystals in the presence of PAMAM dendrimers. Specifically, unique bimetallic materials can be synthesized by dendrimer templating method such as AuAg alloys, core@shell Au@Ag, and AuAg alloy@Ag structures. The encapsulation of metal ions inside dendrimers involves, variously, electrostatic and complexation interactions. Stable monodisperse gold nanoparticles can be synthesized using quaternary ammonium-terminated fourth- and sixth-generation (G4 and G6) dendrimers without further purification steps. Nontraditional nanostructures consisting of noble metals are often fabricated by depositing thin layers of metals (or their precursors) on some silica beads existing templates, followed by calcination or wet chemical etching to remove the solid cores. Another method was based on the layer-by-layer adsorption of polyelectrolytes and charged gold nanoparticles to build shell-like structures around colloidal templates whose surfaces had been derivatized with appropriately charged groups. Amine-terminated fourth-generation PAMAM dendrimers functionalized with thiophene dendrons are synthesized, and their application in the preparation of dendrimer-encapsulated nanoparticles has been demonstrated. AFM images reveal that the functionalized PAMAM dendrimer is an efficient host for immobilizing and stabilizing hybrid nanoparticles on HOPG. The complex dendrimer-like gold assembly was spontaneously formed. These assemblies have great potential for even larger structures and for utilization as engineered materials. A supramolecular procedure was introduced for the stepwise construction of multilayer thin films. The procedure, based on the LBL assembly of guest-functionalized dendrimers and {Au@CDs}NPs, was demonstrated to yield multilayer thin films with thickness control at the nanometer level. Characterization by means of SPR, UV-Vis spectroscopy, ellipsometry, and AFM showed a well-defined multilayer formation, an accurate thickness control, and the need of specific host-guest interactions. Such protocols can potentially be used for obtaining various structures, whose assembly is driven by multiple supramolecular interactions. This constitutes a general nanofabrication paradigm for the integration of organic, inorganic, metallic, and biomolecular components while retaining the interfacing supramolecular

specificity. The cyclodextrin (CD) self-assembled monolayers (SAMs) constitute a molecular printboard for the positioning of thermodynamically and kinetically stable assemblies of multivalent systems, for example, dendrimers. The supramolecular cages generated by hydrophilic dendritic polyols can be utilized as templates for the kinetically controlled growth of faceted silver nanoparticles with low aspect ratios. These polyester-type polyols consist of a multifunctional core, and the large number of terminal hydroxyl groups makes them hydrophilic. A "green" advantage of using hydrophilic polymers is that one can avoid using hazardous organic solvents for nanoparticle synthesis. Most of the dendritic containers reported so far use the concept of closing the dendritic box in order to keep the guest molecules (particles) inside the dendrimer host. Folic acid (FA)- and fluorescein isothiocyanate (FI)-modified G5 dendrimers with neutral surface charge can specifically target to cancer cells overexpressing folic acid receptor (FAR). It is anticipated that using FA- and FI-modified G5 dendrimers to synthesize AuDSNPs using the developed spontaneous approach may provide a means to create an AuNP-based multifunctional nanoplatform for cancer cell targeting and imaging. Arginine-glycine-aspartic acid (RGD) peptide-functionalized generation 5 dendrimers can be used as templates to form AuDENPs with a size of 3 nm, which can specifically target tumor vasculature-related endothelial cells overexpressing $\alpha_V\beta_3$ integrin. These studies have clearly indicated that PAMAM dendrimers are promising templates for the generation of multifunctional AuDENP-based nanoplatforms for various biomedical applications. The next to the last chapter deals with (water-soluble) functional nanomaterials and nanoparticles as a possible template. Their amine, hydroxyl, or carboxyl groups can be used as the conjugation reagent for the formation of bioconjugates showing their biochemical activity toward various, for example, glycoproteins. Among the myriad possibilities, dendrimers (DMs) can find applications in drug delivery due to the opportunity of their internal niches to host a variety of (bio)molecules. Incorporation of photoactive components in either the core or the periphery of these nanostructures enriches them with new functionalities opening new perspectives in nanomedicine. Dendrimer modification with chemically inert polyethylene glycol (PEG) or fatty acids is one of the most attractive ways to reduce dendrimer toxicities in vitro. Furthermore, G4 dendrimers conjugated to Arg-Gly-Asp (RGD) were much less toxic compared to unconjugated G4 dendrimers. Photoactivated DMs for the targeted delivery of an anticancer drug were also developed based on the photocaging strategy. For targeted imaging of cancer cells in vitro and in vivo, it would be ideal to assemble targeting ligand-modified dendrimer molecules onto the metal nanoparticles. Gold-based nanoparticles have been developed that strongly absorb light in the near-infrared region, facilitating deep optical penetration into tissues, generating a localized lethal dose of heat at the site of a tumor. The advantage of using dendrimers as templates to prepare gold nanoparticles lies in the fact that the surface of the particles can be modified with various functional moieties (e.g., targeting ligands and dyes) through dendrimer chemistry for practical biomedical applications. The last subchapter summarizes the polymer and dendrimer templates

as the shape-controlled synthesis of metal nanoparticles, bioconjugates, and the stabilizers as well.

The last fifth chapter summarizes the preparation of metal nanoparticles and their conjugates via various hard template-directed approaches, and it consists of five subchapters. The first subchapter presents readers the literature review in detail on the preparation of metal nanoparticles using template systems based on inorganic matrixes. Templating can also be done against existing nanoparticles with a well-controlled shape. In the preformed-seed-mediated method, a similar or identical seed particle becomes part of the resultant nanoparticle, whereas the template is often a dissimilar material that does not become part of the nanoparticle. There are also some reports on the deposition of various inorganic nanoparticles onto silica microspheres. The second subchapter consists of three sections. The first section describes silica as a robust, hydrophilic, and biocompatible material that can be readily modified with diverse chemical functionality. Silica is widely used as a template for the development of various nanostructures to its characteristic high surface area, thermal and chemical resistance, the presence of reactive silanol groups (Si–OH), and pores with diameters between 2 and 50 nm. Using the diversity of silane chemistry, a silica shell, coating or template, can be tailored to have functional groups that can include, but are not limited to, amine, aldehyde, carboxyl, epoxy, and thiol groups. In addition to the use of silica as a structural shell on other template materials, nanoparticles composed of silica can be prepared with sizes that typically range between tens and hundreds of nanometers. These spatially and dimensionally constrained structures can serve as reaction cages to control the nucleation and growth of the particles (and impart stability), leading to the formation of nanoparticles with a morphology complementary to that of the template. Polyol process was applied to form and immobilize silver nanoparticles onto the silica surface functionalized with thiol groups (the second section). Generally, polyvinylpyrrolidone (PVPo) acts not only as a nucleation-promoting agent for silver ions but also as a stabilizer for silver nanoparticles in polyol process. When ethylene glycol solution containing silver ions and silica particles functionalized with thiol groups was heated with reflux in the absence of PVPo, few particles were formed and immobilized onto the silica surface. On the contrary, when the same reaction proceeded in the presence of PVPo, silver nanoparticles were successfully formed and immobilized onto the surface of silica particles. Silver nanoparticles can be also synthesized by using thermal decomposition method. Ag–SiO_2 (SiO_2@AgNPs) nanoparticles are synthesized by using well-known Stober method at low-temperature route for coating SiO_2 nanoparticles with silver nanoparticles. Silica nanoparticles were synthesized by hydrolysis and condensation of tetraethylorthosilicate (TEOS) in a mixture of ethanol with water, using ammonia as catalyst to initiate the reaction. TEM image shows SiO_2 nanoparticles were homogeneously impregnated with silver nanoparticles. Silica-silver heterogeneous nanocomposite structures have been prepared by alcohol reduction method. The size-controlled immobilization route is explained by following two steps: (1) Small silver particles are firstly formed on the silica surface, and (2) these small silver particles homogeneously grow to larger ones. These two steps are completely

conducted in one pot by polyol process, which is attributed to the slower and more easily controllable reaction rate of the polyol reduction method than that of general chemical reduction method using reducing agent such as hydrazine or sodium borohydride. Microwave-assisted synthesis of different AgNPs to MMT ratios nanocomposite was developed. Paraformaldehyde and citric acid are used as stabilizing and reducing agent for synthesizing silver nanoparticles through the reduction in silver ions by the oxidation of hydroxyl groups of paraformaldehyde to aldehyde groups using strong base, NaOH. The stable MMT@AgNPs nanocomposites exhibited card-like and ball-like homogeneous surface fractions and form one-phase morphology. The stable MMT@AgNPs nanocomposites were synthesized by microwave method. XRD analyses and TEM observations confirmed the formation of nanoparticles on the clay surfaces. The FT-IR analysis suggested that the interaction between AgNPs and the MMT surfaces was weak due to the presence of van der Waals interactions. The synthesized MMT@AgNPs suspensions were found to be stable over a long time without any sign of precipitation (or detachment). The silver ions released explain the antimicrobial properties found in the investigated the stable MMT@AgNPs nanocomposites.

When aminopropyltrimethoxysilane (APS) monolayers were immersed into the suspension of AuNPs, their top amino groups were protonated since the pKa of amino groups of aminopropyltrimethoxysilane monolayers is smaller than the pH of the suspension (the third section, the second subsection). Therefore, negatively charged gold nanoparticles can be assembled on APS monolayers with positively charged amino groups by electrostatic interaction. Using this concept, a binary pattern can be generated with two groups with different affinities for gold nanoparticles. Gold clusters nucleate and grow at defect sites on SiO_2 thin films. There is a straightforward sol-gel method for the preparation of gold nanoparticles via in situ-doped silica aerogels using hydroxylamine as a reducing agent (the second subsection). The monolithic gold-doped silica aerogels were comprised of crystalline gold nanoparticles with sizes at the 5–7 nm range. Samples possessed high surface area and pore diameters of about 15 nm. The SEM images revealed the morphologies of the SiO_2@Au composite nanoparticles, which showed distinctly that AuNPs were attached to the surfaces of the functionalized silica microspheres. The results revealed that the lower pH values led to a denser gold layer on silica microspheres, while the higher pH values led to a lower gold coverage. The prepared SiO_2@Au composite nanoparticles using various reductants exhibited the plasmon absorption peaks at 551 nm for sodium citrate, 551 nm for formaldehyde, and 548 nm for sodium hypophosphite. They all had a little redshift compared with the absorption peak of the SiO_2@Au composite particles prepared at room temperature. Mercapto-functionalized ordered mesoporous silica with pore sizes ranging from 2.1/2.1 to 7.2/.59 nm (adsorption/desorption branch) are used as matrixes for gest noble metal nanoparticles. Instead of using a post-diffusion process, monolithic gold-silica nanocomposites were synthesized through a one-step sol-gel reaction in the presence of a colloidal gold sol and a nonsurfactant template in the starting precursor sol mixtures (the third subsection). After the template was removed through calcinations, the materials exhibited mesoporosity with a high

surface area up to 600 m^2/g, a pore volume of 0.5 cm^3/g and relatively narrow pore size distributions with a pore diameter of 3–4 nm. Gold particles ranging in diameters of 2–8 nm were homogeneously dispersed throughout the silica matrix. The annealed gold-silica nanocomposites retain a distinctive wine-red color, which arises from the surface plasmon resonance (SPR) of gold particles. SPR is characteristic of mesoscale (2–50 nm) particle surfaces because, at this dimension, the electron cloud can oscillate on the particle surfaces and absorb electromagnetic radiation at a particular level of energy. Mesoporous carbon-supported gold nanoparticles have been obtained by replication of gold-containing mesoporous silicas. Au/SiO$_2$ templates were prepared by contacting a functionalized SBA-15 silica material with an aqueous solution of HAuCl$_4$, followed by chemical reduction (the fourth subsection). Alkylammonium grafts led to the direct formation of gold nanoparticles located in the pores of SBA-15, with a size limited by the pore opening. Thus, gold-containing mesostructured carbons by replication of gold-supported mesoporous silicas were prepared. The use of mercaptopropyltrimethoxysilane (MPTMS) as grafting molecule afforded the possibility to control the particle size inside the mesopores. The use of task-specific ligands with calcining as post-treatment provides AuNPs that are encapsulated into the mesoporous channels or loaded on the surface of silica spheres. Gold nanorods were observed to grow on a Si(100) surface functionalized with MPTMS. Small gold nanoparticles could be adsorbed onto the surfaces of silica spheres that had been premodified with self-assembled monolayers of (3-aminopropyl)triethoxysilane. Another method was based on the layer-by-layer adsorption of polyelectrolytes and charged gold nanoparticles to build shell-like structures around colloidal templates whose surfaces had been derivatized with appropriately charged groups. Noble metal nanoparticles can be synthesized in mesoporous silica films and in ultrathin nanoporous films. Surface area, average pore size, and pore volume were determined for silica aerogels and gold-doped silica aerogels. In comparison with the results obtained without SiO$_2$, it can be noted that in the presence of silica, the rate of formation of silver particles decreases drastically. The use of task-specific ligands with calcining as post-treatment provides AuNPs that are encapsulated into the mesoporous channels or loaded on the surface of silica spheres. Task-specific ligands containing a cetylammonium moiety act as structure-directing agent with AuNPs containing a trialkoxysilyl group. The latter co-condenses with tetraethoxysilane (TEOS) to form mesoporous silica. The silica nanoparticles were used as the templates of interior cores of metal nanoshells and as the interior templates for the deposition of the external noble metal shell layer by layer. A straightforward sol-gel method can be utilized for the preparation of gold nanoparticles via in situ-doped silica aerogels using a reducing agent. Metal nanoparticles were used as sacrificial templates to react with an aqueous gold salt solution, resulting in the formation of gold nanoshells with hollow interiors and smooth and pinhole-free surfaces, as well as homogeneous and highly crystalline walls. Similar changes in morphology, composition, and structure were observed no matter whether silver nanocubes, nanowires, or nanospheres were used as the templates. Polycrystalline gold colloids can be deformed by ion irradiation

indirectly, if they are embedded in an amorphous silica glass matrix that does deform under the ion beam (the fifth subsection). TEM image of a gold@silica particle before irradiation showed spherically shaped, with the 14-nm-diameter gold core centered inside. The deformation of the silica shell is consistent with other work on ion beam deformation of pure silica colloids. To explain the shape change of the gold core due to the silica shell, the indirect deformation scenario was proposed. Gold nanodots deposited on silicon are of significant importance because this material presents a large number of applications such as subwavelength antennas in plasmonic applications, or as catalysts for the growth of silicon nanowires (SiNWs), or even as electrical contacts in Si nanodevices.

The third subchapter introduces the inorganic scaffolds as possible stabilizers available for noble metal nanoclusters in five sections. Noble metal nanoparticles were used as sacrificial templates to react with an aqueous gold precursor solution, resulting in the formation of gold nanoshells with hollow interiors and smooth and pinhole-free surfaces, as well as homogeneous and highly crystalline walls. In addition, recent success in synthesizing silver nanostructures with well-defined shapes and surfaces (e.g., nanocubes bounded by {100} (crystallographic planes)) also provides a number of model systems to systematically investigate the template-engaged replacement reaction on the nanometer-scale—nanomaterials (the first section). Matrix-isolation is a method to produce few-atom ligand-free metal nanoclusters. The most widely used procedure for the preparation of gold nanoparticles supported on the insoluble oxides solids is the precipitation-deposition method. Rigid templates such as membranes have been used wherein metal ions are reduced/reacted inside their nanoscale pores. An alternative method for the synthesis of metal hybrids lies in the use of bimetallic nanocrystals by means of seed-grow processes to obtain heterogeneous nanoparticles. There is a simple and reproducible method for the activation of monodispersed silver nanoparticles by introducing the concentrated NaCl solution into the AgNP dispersion (the second section). Immediately after the addition of NaCl solution to AgNPs, there was a considerable change in the color of the dispersion of AgNPs with corresponding changes in its absorption spectrum. The absorption spectra obtained a very flat course without any pronounced maximum, which is characteristic of silver particles with dimensions of about 200 nm and larger with various shapes. The discovery of surface-enhanced raman scattering (SERS) on colloidal silver particles started the extensive development of a new and very sensitive analytical method enabling to detect molecules in the concentration range from pico- to femtomoles. Some studies have shown that the highest value of enhancement is achieved only on the silver particles of a certain size which are referred to as "hot particles." The most frequently used activation agents of the silver nanoparticles prepared by the common reduction procedures include halide ions, particularly chlorides. A simple and reproducible method for the activation of monodispersed AgNPs was insertion of the concentrated NaCl solution into the AgNP dispersion. Similar experiments were performed with NaBr and NaI solutions. The synthetic procedure involves the preparation of small gold seed nanoparticles ($d \sim 5$ nm), and the subsequent three-step growth of seeds in an

aqueous solution containing the capping agent (CTAB), gold ions, reducing agent (ascorbic acid), and NaOH generates the gold nanoprisms (the third section). A facile, high-yield synthesis of unique porous gold nanobelts by morphology-preserved transformation from metal-surfactant complex precursor nanobelts formed by $HAuCl_4$, and the capping agent is discussed. Such porous gold nanobelts combine the advantages of both 1D structures and nanoporous structures and may be an appealing material in application areas including catalysis. The remarkable behavior of core@shell gold@silver composite nanostructures stabilized with aspartame (Asm) was reported. A seed-mediated growth procedure was employed for the formation of Au@Ag core@shell nanoparticles. Moreover, in addition to the synthesis and characterization of aspartame-stabilized Au/Ag nanostructures (Au@Ag@Asm), representative in vitro experiments were carried out as a first indication of their antibacterial properties. Bimetallic core-shell nanoparticles allow for the exploitation of properties characteristic for monometallic (Au and Ag) nanoparticles. Under irradiation, Au@Ag@Asm particles presented effective inhibitory microbial properties. We suggest that thanks to the core-shell nanoparticles' synergistic properties, the material proposed represents attractive photothermal properties. Aspartame stabilization provides a good shelf life for particles with a material that is nontoxic, inexpensive, and water soluble. In addition to the traditional templates acting as spatially confined reaction media, certain reactive solids with a specific shape can be used as sacrificial templates for the production of metal nanocrystals, which adopt the underlying shape of the template (the fourth section). In particular, silver nanocubes can be used as sacrificial templates for the fabrication of novel gold nanocages and nanoframes through a galvanic displacement reaction. The introduction of silver seeds can lead to fast and high-yield syntheses of two highly anisotropic metal nanoparticles: ultrathin metal nanowires and triangular gold nanoprisms. Low-dimensional nanoparticles can be readily synthesized in high yields by adopting silver seed particles in combination with an aromatic surfactant, benzyldimethylhexadecylammonium chloride (BDAC), and gold precursor. Silver seeds play an important role for the high-yield formation of anisotropic triangular nanoprisms. Gold seeds, on the other hand, generate a mixture of nanoparticles with different shapes due to the lack of shape reconfiguration mechanism. It is worth noting that the quasispherical gold particles formed from silver seeds and silver-free growth solution show very little defects, while gold spheres made from gold seeds at the same condition show many defect-induced contrasts. While triangular nanoprisms could be generated with cetyltrimethylammonium chloride (CTAC), the yield of nanoprisms was lower and the size distribution was broader with CTAC. The use of BDAC was particularly important for the formation of nanowires; nanowires were rarely observed in CTAC samples. When BDAC was replaced with cetyltrimethylammonium bromide (CTAB), a mixture of different shapes (spheres, rods, etc.) were formed instead of triangles or wires presumably due to bromide ions interfering with silver under-potential deposition (UPD). We have reported that ultrathin gold/silver nanowires and sub-50-nm gold triangular nanoprisms can be readily synthesized by adopting small silver seeds and BDAC in the seed-growth method. Large silver particles

(over 25 nm) have been actively used for synthesizing hollow gold nanostructures such as nanoframes or nanocages. Large silver triangular nanoprisms (~ 50 nm edge length) have been used as a template for the synthesis of gold hexagonal bipyramids. However, small silver seed particles have rarely been exploited for synthesizing gold nanostructures because the use of gold seeds is a natural choice for making gold nanostructures and gold seeds are easier to make in narrow size distribution. Here, small silver seeds are a versatile choice for generating anisotropic gold nanostructures because they can undergo structure evolution through various mechanisms including galvanic replacement reaction. The seed shape repopulation along with the structure-directing ability of silver UPD and BDAC is responsible for the formation of uniform triangular nanoprisms. These results underscore the importance of the chemical nature of seeds in controlling the shape of metal nanoparticles in the seed-growth method. Silver seeds can significantly speed up the growth rate of ultrathin nanowires. A majority of existing synthetic procedures for ultrathin nanowires take much longer times ranging from hours to days because they rely on slow processes to ensure the formation of highly anisotropic wires. The introduction of silver seeds and BHDAC (benzylhexadecylammonium chloride) in the seed-growth method reported here opens a new pathway to high-yield syntheses of anisotropic metal nanoparticles. A versatile colloidal synthesis method appears to assemble noble metal NP heterodimers based on electrostatic interactions. The phase diagrams of the relevant individual dimer components were investigated to derive a stability zone where both components were stable in solution despite opposite surface charge, in order to find the optimal conditions for selective self-assembly of the targeted heterodimers. Using this approach, we have successfully assembled plasmonic heterodimers of Au and Ag spheres$_{90\text{ nm}}$ paired with Au$_{30\text{ nm}}$ cubes and Au$_{50\text{ nm}}$ rhombic dodecahedron. The demonstrated electrostatic assembly mechanism was explained using theoretical modeling. This analysis proved that the maximum theoretical yields for dimeric heterostructures were achieved in the presented experiments by tuning the experimental conditions in the narrow mutual-stability zone for the binary NP system and used surfactants. TiO$_2$ is the most promising material in the field of photocatalysis because of its superior photocatalytic activity, chemical stability, low cost, and nontoxicity (the fifth section). As such, its performances in photocatalytic degradation of chemical pollutants and solar energy conversion have been widely studied in the past decades, and its practical application has been seriously considered. The most widely used procedure for the preparation of AuNPs supported on these insoluble oxides solids is the precipitation-deposition method. A controlled growth of AgNPs on TiO$_2$ templates is expected in tuning the optical response of the Ag–TiO$_2$ hybrids. In addition, these silver nanoplates are mobile and easily stripped from the substrates. After nucleation, the AgNPs grow through two mechanisms, Ostwald ripening (OR) and oriented attachment (OA). TiO$_2$ assembled with AgNPs has received much attention because such a hybrid can effectively separate the charges and redshift the absorption to visible light via plasmonic resonance. The silver reduction rate is determined by the parameters related to UV irradiation, reduction activity of TiO$_2$ film, AgNO$_3$ concentration of solution, etc. The growth

model can explain the phenomenon of Ag nanoplates lying on the small AgNPs. The growth model is consistent with the conclusion that the OA growth is facilitated in high-density primary particles. Similarly, the formation of silver nanoplates using $AgNO_3$ ethanol solution or using oil-decorated TiO_2 films can also be attributed to the increase in the Ag reduction rate due to the photodegradation of organic molecules. According to this growth model, a smooth TiO_2 film facilitates the formation of large-scale silver nanoplates. If the brownish-gray Ag–TiO_2 film is irradiated with colored (e.g., red) light in air, the photo-oxidatively generated Ag^+ is retained in the nanopores, so that the colored (e.g., red) film turns original brownish-gray under UV light. This should be because the silver nanoparticles absorbing the colored (e.g., red) light form again in the nanopores. In contrast, if the Ag–TiO_2 film is irradiated with colored (e.g., red) light in water, the generated Ag^+ is removed from the pores, so that the film retains its color (e.g., red) even under UV light. It was also revealed that we can control the multicolor photochromic behavior and the chromogenic properties by regulating irradiation conditions as well as geometry and matrix materials of nanopores. Thus, silver nanoparticles of various sizes and shapes should be prerequisite to displaying various colors. Furthermore, nanopores of various sizes and shapes present in the TiO_2 films act as molds for Ag nanoparticles with various sizes and shapes. We call this a "molding effect." A controlled growth of silver nanoparticles on TiO_2 templates is expected in tuning the optical response of the Ag–TiO_2 hybrids. The photocatalytic growth of anisotropic AgNPs on the nanoparticulate TiO_2 films in the $AgNO_3$ ethanol solution was reported, and the vertical growth of silver nanoplates was attributed to the surface roughness and random features of the substrate. The oil-decorated TiO_2 films successfully induce the anisotropic growth of AgNPs. The number of silver nanoplates increases with an increase in the oil-decoration time. Two kinds of AgNPs, isotropic nanoparticles and anisotropic nanoplates, were obtained using the oil-decorated films. Most of the Ag nanoplates pile up over each other or lay over the irregularly shaped AgNPs. In addition, these Ag nanoplates are mobile and easily stripped from the substrates. The oriented attachment (OA) mechanism is a particle-mediated mesoscopic transformation process and has been demonstrated to be one of the important mechanisms leading to the anisotropic growth of AgNPs in solution-phase synthesis. AgNPs synthesized by photocatalytic reduction generally exhibit irregular spherelike shapes. By increasing the $AgNO_3$ concentration, we found that the increased Ag reduction rate gave rise to a change in AgNP growth, resulting in the formation of Ag nanoplates in the product. The Ag nanoplates were formed in the early period of coalescence, rather than gradually grew up with the increase in the growth time.

The bioconjugates subchapter describes the morphological changes of HeLa cells obtained by optical microscopy by the photodynamic killing effect of the Pt/TiO_2 nanocomposite on the cancer cells. The live HeLa cells treated in the absence of Pt/TiO_2 nanocomposite may remain attached to the substrate with elongated shapes, so UV irradiation on the cells with no Pt/TiO_2 nanocomposite involved is harmless to the cancer cells. The nanosemiconductor, the gold-doped nanocomposite and the Pt/TiO_2 nanocomposite have similar effects on the cancer cells. It was observed that

in the presence of Pt/TiO$_2$ nanocomposite, the death mode of cells is undergone by both apoptosis and necrosis. An interesting approach to introduce theranostic functionalities into a nanosystem is to covalently attach a palladium (Pd)-porphyrin chelate (PdTPP) to mesoporous silica nanoparticles (MSNs) which are readily taken up by cells. MSNs have several advantages over normal silica nanoparticles and, thus, are used in a wide array of applications, including chemical catalysis, drug delivery, controlled release of therapeutics, and cell labeling. Pd-porphyrin has a long phosphorescence lifetime and has been used for in vivo oxygen sensing and imaging. By changing the energy of photoirradiation, the functionalities of MSN-PdTPP can be "switched" between a phosphorescence probe for oxygen sensing/imaging (diagnostics) and a photosensitizer for PDT (therapy). The conclusion (last) subchapter summarizes in short hard template for the shape-controlled synthesis of metal nanocrystals and the stabilization of hybrid nanostructures.

1.3   Nanomaterial Basics

The synthesis of nanomaterials or nanoparticles can be carried out in the solid, liquid, or gaseous state, following two basic approaches, classified as "top-down" and "bottom-up." Top-down approach uses the physical and lithographic principles of micro- and nanotechnology and achieves structure sizes in the medium to lower nanometer range, starting from a large materials entity. On the other hand, in the bottom-up approach, ionic, atomic, or molecular units are assembled through various processes to form structures in the nanometer range. From generation of the constituents to their growth into a nanoentity, the bottom-up approach is governed primarily by the chemical synthesis principles. If the process of assembling of the starting elements into a nanoentity is understood, the bottom-up approach allows, in principle, the design and formation of nanoparticles of any size and morphology. Further, this approach can shed light on the atomic-/molecular-level aspects of the morphology development and structure-property relationship in a particle. The bottom-up colloid-chemical methods involve the precipitation of nanometer-sized particles within a continuous solvent matrix to form a colloidal sol. These methods are inexpensive, versatile, and technologically simple to implement. Nanoparticles as well as nanocomposites of a wide range of materials (e.g., metals, alloys, intermetallics, and ceramics) can be prepared by the colloid-chemical methods.

A variety of colloid-chemical strategies involving a wide spectrum of reagents and reaction conditions has been employed in order to prepare noble metal nanoparticles of controlled morphologies. Since the field of morphology-controlled synthesis is in a developing stage, many of the reported methodologies are not well established in terms of the particle yield, formation mechanism, reproducibility, etc. Except a few cases, no straightforward relationship between the synthesis strategy and the particle morphology has been observed. Furthermore, particles with the same morphology can be obtained from widely varying reaction conditions and strategies, and on the other hand, particles with a wide variety of morphologies can

also form under a given synthesis condition. However, there are certain methodologies such as the preformed-seed-mediated growth approach, high-temperature synthesis, template-based electrochemical synthesis, and photochemical techniques, which are emerging as popular ways of developing isometric and anisometric nanoparticles. Furthermore, formation of nanoparticles with controlled morphology has so far remained, excepting a few cases, primarily a matter of "mix and try" approach. Before one can reproducibly grow nanoparticles of desired shape, orientation, and crystallinity, the factors that influence these parameters and the mechanism of particle development have to be comprehensively understood. Therefore, one of the major goals of current nanomaterials research has been to understand how various morphologies develop in nanoparticles, starting from their nucleation in solution.

The miniaturization of structures by conventional [11] and electron-beam lithography [12] is reaching the theoretical limits of about 50 nm. For the further miniaturization of chemical objects, alternative approaches must be developed. Following Feynman's vision, one may employ atoms and molecules as building units for the "bottom-up" assembly and construction of architectures with nanometer dimensions. Nanoparticles that consist of metals [13] (e.g., gold, silver, platinum, and copper) seem to be attractive units for the engineering of such structures. A variety of synthetic methodologies for the preparation of various metal nanoparticles within a designed size distribution are available. Often, the metal nanoparticles are prepared by "wet chemistry" procedures, in which clusters of metal atoms are formed in the presence of surfactant. This capping ligand binds to the metal atoms clusters, prevents aggregation of the particles into bulk material, and controls the final dimensions of the noble metal nanoparticles. Many capping (agents) systems are available: hydrophobic monolayers [14], positively or negatively charged hydrophilic monolayers [15, 16], surface active (macro)molecules, and (bio)polymer layers [17].

While most describe an upper size limit of approximately 100 nm in at least one dimension, there is currently limited scientific evidence to strictly support this value for all nanomaterials. What is not in dispute is that many of these nanomaterials display unique nanoscale size-dependent properties that are of interest to various applications. These can include, for example, intrinsic properties such as the quantum confinement displayed by quantum dots, the paramagnetism of iron oxide, and other metal alloy nanoparticles [50], along with the conductivity and ballistic transport found in nanoscale carbon allotropes [51]. Beyond photophysical and electronic properties, nanomaterials (NMs), and nanoparticles (NPs) in particular, have extremely high surface-to-volume (S/V) ratios (e.g., at <2 nm the S/V atomic ratio exceeds 50%), along with nontrivial surface areas [25]. This can allow for the display of multiple biological entities on their surface which can cumulatively provide increased avidity in certain configurations [27].

Chemists are aware of the intimate relationships among valence, stoichiometry, molecular geometry (the way the atoms or molecules arrange themselves), and reactivity of molecules, colloids, and solids. It has long been recognized that the molecular morphology exerts a direct impact on the properties of polymeric

materials. Similarly, in nanomaterials where a few hundreds to thousands atoms (or molecules) are combined as a single entity, the resultant particle shape is expected to be a crucial factor in determining the properties of a nanoparticle. However, it should be noted here that nanoparticles are often larger than molecules (and small clusters). Therefore, the surface energy factor plays a major role in determining the shapes of the nanoparticle, unlike the bond energy in the molecules (and clusters). It has been experimentally and theoretically found that deviations from spherical geometry strongly affect the properties of nanoparticles. Strict control of the particle morphology is therefore required in order to fine-tune the properties of the nanoparticles. Conversely, this allows for the generation of particles with new properties from the same materials by simply tuning the particle size and morphology. In addition, there are other motivations for morphology-controlled preparation of nanoparticles. For example, an ability to engineer materials on a nanometer length scale enables the investigation into the fundamental size- and shape-dependent properties of matter. Furthermore, studies of the growth mechanism leading to nanoparticle anisotropy are important in the elucidation of the crystal-growth mechanism. Isotropic and anisotropic nanoparticles can also be used as templates for further generation of novel materials. Sometimes, particle anisotropy offers features and functionalities that are either difficult to obtain or not obtained by simple size-tuning in spherical nanoparticles. For example, a slight change in particle geometry can produce great changes in the plasmon peak position, which can hardly be achieved in the spherical systems through a similar change in their physical dimensions. Further, an important design criterion for future devices is to keep the building blocks relatively small in the nanometer regime while obtaining useful new properties. This can be accomplished by tuning the geometry of nanoparticles. It is also necessary to fabricate nanoparticles into one-, two-, or tree-dimensional (1D, 2D, or 3D) functional structures in order to utilize their collective properties. The particle morphology influences the assembly structure through their joining behaviors and mutual interaction [52, 53]. Anisotropic nanoparticles offer several crystal surfaces, different surface roughness, and a plethora of corners, steps, edges, and defects. Since each crystallographic plane provides different atomic arrangements and surface terminations, the particle geometry can markedly affect the chemical and physical properties of a nanoparticle. Moreover, noble metal colloids may be tuned to create wide range of sizes and forms of nanoparticles by adjustment of local dielectric environment in the process of nanoparticles production. Chen described way in which surface area or shape of the gold nanoparticles (AuNPs) may be controlled [54]. Colloid of AuNPs is usually formed by use of passivating ligands, chemical or electric reduction, with further stabilization with capping agent, i.e., citrate [55, 56].

Sphere (and sometimes spheroidal)-shaped colloidal particles have been of broad research interest. The present quest for shape-controlled colloidal particles can be traced back to the work of Matijevic [57]. Later, this field has witnessed significant advances due to numerous contributions. The high resistance to oxidation and corrosion, the unique optical properties, and the ease of preparation of noble metal nanoparticles (NMNPs) have made these systems interesting for fundamental

scientific studies, including exploration of particle-growth mechanisms. NMNPs find interesting applications in the fields of optics [58], chemical and biosensing [59–61] catalysis [62], electronics [63], and so forth [64, 65]. Currently, NMNP systems are being studied extensively in the context of anisotropic particles with a variety of shapes from simple cubes to branched multipods [65, 66]. However, noble metal nanoparticles have a high surface area that results in poor colloidal stability and subsequent aggregation in solution [67]. To overcome this instability, oligomeric (bio)polymers have often been used as an outer shell coating to the gold cores, providing a steric (or sometimes electrostatic or electrosteric) barrier to aggregation [68].

The synthesis of metal nanoparticles with well-defined size and shape can be also classified broadly into wet and dry methods. They essentially fall into three categories: condensation from a vapor, chemical synthesis, and solid-state processes [69]. Other novel production techniques have been reported based on the use of microwaves, ultrasound, and biomimetics. The interesting functional nanoparticles with narrow size distribution and low crystalline defects have been generally synthesized in nonpolar solvents by thermal decomposition of organometallic species at high temperature [70]. Because many organic (macro)molecules have specific binding properties in self-assembly processes, they are attractive materials for nanotechnology. In recent years, nanoscale materials in the most important types of nanomaterials, including gold, silver, and platinum, have been extensively investigated [71], due to their unusual plasmonic [72], optical [73], chemical [74], photoelectrochemical [75], and electronic [76] properties. Moreover, metal/metal nanocomposites are synthesized to further improve their specific properties [77]. Most existing approaches explore the strong affinity of thiols to gold and silver [78] and the use of disulfides [79] and thioethers [80] as capping agents as well. Polymers functionalized with molecular recognition groups [81], thioacetate groups [82], and tetradentate thioether ligands [83] have been used to mediate the formation of spherical or related assemblies of noble metal nanoparticles. However, the most common method is the chemical reduction of metal ions, which involves the addition of a reducing agent to a metal salt solution in the presence of a stabilizer. Chemical reduction in solution is advantageous over other processes, because of its simplicity, low reaction temperature, and solubility of metal salts in water. The most used reducing agents are sodium borohydride, ethylene glycol, and formamide [84–86]. On the other hand, the stabilizing agents bind to the nanoparticle surface, improving stability and wettability, which are needed to prevent aggregation [87]. Different pathways have been proposed for the preparation of noble metal nanoparticles with tailor-made size and shape. The physical method involves radiation reduction of silver ions by γ-ray, microwave, ultraviolet, or visible light [88–90].

Of the wet chemical processes, a reverse micelle (microemulsion) synthesis has been demonstrated to be a viable method for producing a wide array of noble metal colloids and metal (oxide) nanoparticles [91, 92], over a relatively narrow particle size distribution in different organic media. The w/o microemulsion method offers a lot of advantages with respect to others (coprecipitation in solution, sol-gel,

flame-spray pyrolysis, laser evaporation, high-energy milling), namely the use of a simple equipment, homogeneous mixing, high degree of particles size and composition control, formation of gold nanoparticles with high surface area, and the use of soft condition of synthesis near ambient temperature and pressure [93–95]. An emulsion is a colloidal system with one liquid dispersed in another. Emulsions are widely used in cosmetics, food, drilling muds, and pharmaceutical products. Emulsions are thermodynamically unstable, and surfactants or surface active polymers are normally used to help form a kinetically stable system [96]. However, surfactant-stabilized emulsions have a short shelf life and they may be toxic and relatively expensive and are not environmentally friendly [96].

Pickering emulsions or solid-stabilized emulsions are colloidal emulsions that are stabilized by particles instead of organic surfactants [97, 98]. A new interface is created by the particles that assemble at the fluid interface, and at the same time, the reduction of the interfacial energy brought about by the new particle-liquid interface replaces the liquid–liquid interface and ensures the stability of the Pickering emulsion [98]. Compared with classical emulsions which are stabilized by surfactants, Pickering emulsions which are stabilized by particles use less surfactants and polymers and have increased stabilities [99]. However, particles with wettabilities that are similar to oil or water can improve the stability of a Pickering emulsion. In general, the hydrophilicity or the hydrophobicity of the particles will determine the type of emulsions. For example, when particles are more hydrophilic, they tend to form oil-in-water (o/w) emulsions [100]. In some cases, phase inversions in emulsions may happen [101]. Sometimes, an oil-in-water-in-oil (o/w/o) or a water-in-oil-in-water (w/o/w) multiple emulsion can be obtained when the emulsion is emulsified by a mixture of hydrophilic and hydrophobic surfactants or by a combination of small particles and surfactants.

Noble metal nanoparticles have been widely employed in the development of electrochemical sensors by deploying them to form new materials that have different properties by virtue of having a reduced size compared with the same materials in bulk form. NMNPs characteristically facilitate the process of electron transfer in the surfaces of materials used in electrocatalysis [102]. Among noble metal nanoparticles, silver and gold nanoparticles have been widely used in the development of (bio)electrochemical sensors due to their biocompatibility with various biomolecules. They also present antibacterial properties and excellent conductive properties, improving the sensitivity of (bio)electrochemical sensors with respect to analytes studied [103, 104].

Templates can be used as a matrix for a preparation of metal nanocrystals with morphology similar or complementary to that of the template. Both soft and hard templates can be employed for the shape-controlled synthesis of metal nanocrystals [105]. The template can also serve as a scaffold. The metal ions are reduced within or around the confined volume or space of the template. Self-assembled, biological, and synthetic structures such as micelles, microemulsions, liposomes and vesicles, viruses, etc., belong to the soft templates [106, 107]. In general, specific templates such as metal oxides [108] or activated carbon [109] have been used to improve the activity in the adsorption of reactants, stability of noble metal nanoparticles, and

reusability of sensors. The adsorption reactivity of molecules on the surface of gold nanocatalysts can be a result of the quantum effects of gold nanoparticles, which interact with oxide supports [110]. Significant effort has been made to develop NMNPs nanocatalytic systems that mainly include discovering adequate oxide supports and efficient deposition methodologies [111], fabricating core@shell type morphologies [112], and integrating active nanoparticles [113]. In particular, controlled assemblies of colloidal nanoparticles are expected to exhibit collective properties that are distinctly different from those of the corresponding individual particles [114].

Dendrimers have been used as ideal templates or stabilizers for the synthesis and modification of various hybrid, (noble) metal, and semiconductor nanoparticles. Dendrimer-entrapped nanoparticles (DENPs) are formed using dendrimers as templates, where each metal or other inorganic nanoparticle is entrapped within each dendrimer molecule, while dendrimer-stabilized nanoparticles (DSNPs) are formed using dendrimers as stabilizers, where each metal or other inorganic nanoparticle is surrounded or protected by multiple dendrimer molecules on its surface [115, 116].

Single- and multi-walled carbon nanotubes (SW- and MWCNTs) hard templates are considered as promising materials for various applications in electrochemistry due to their outstanding special electronic properties [117]. However, to optimize the use of MWCNTs in various applications, it is necessary to attach either functional groups or various nanoparticles onto their surfaces. It was also shown that electronic states away from the Fermi level can contribute to the kinetics of electron transfer between carbon nanotubes and solution [118]. In particular, defect- and dopant-induced states enhance the electron transfer kinetics at low-dimensional carbons [119]. Another approach to increase the efficiency of carbon nanotube-based electrodes is the construction of hybrid structures. The combination of MWCNTs with other nanomaterials is expected to be very useful for electrocatalysis and consequently for the design of novel selective sensors [120].

Several different colloidal silver nanoparticles (AgNPs) were prepared in situ by reducing the silver cations in solutions of polyamino and polyguanidino oxanorbornenes with sodium borohydride. Lin and coworkers reported [121] a AgNP–nanosilicate platelet hybrid, and these were further blended with water-soluble poly (ether)urethane (PEU). These conjugates promoted antimicrobial activity as well as reduce the inflammatory response [121]. Santos et al. [122] introduced new AgNP conjugates stabilized by linear polyethylenimine (L-PEI). They systematically modified the L-PEI framework to create new ligands of polymer stabilizers. They also tested the catalytic activity in the reduction reaction of 4-nitrophenol, and their kinetics were fully analyzed [122]. In another very recent study by again Lin and coworkers [123], they emphasized the importance of the existence of polymeric coatings on both AgNPs surfaces and the surfaces they interact with in stabilizing nanoparticles against deposition. This study suggested that although polymeric coatings are stabilizers of AgNPs, they might stabilize AgNPs against deposition unless the collector surface is also polymer coated [123]. Polymers reported in this work stabilize AgNPs and kept them in aqueous solutions for more than a month.

Compared with the amino polymers (PA), the guanidino analogues (PG) better stabilized the silver colloids as evident from the spectroscopic data. Also, there seems to be a polymer size dependence on stability with the shorter PG being more effective than the longer PG. These nanoparticles could be very useful in catalytic applications. Furthermore, the polymers PG and PA being biocompatible, polymer-bound silver nanoparticles could be integrated into various biomedical and biosensor applications and worth studying in the future.

Hybrid materials based on the mesoporous silica/carbon/noble metal combination have attracted the attention of many researchers due to the possibility of combining the main features that silica- and carbon-based materials may be present in a single material. Graphene is considered to be the newest member of the carbon family, which consists of a single sheet of graphite containing carbon atoms linked together by pi (π) linkages and trigonal planar geometry [124], and each atom has a π orbital structure contributing to the formation of a delocalized electron network. Graphene has a single atomic plane, giving it a 2D structure and thus may exhibit metallic and semiconducting properties [125, 126], beyond excellent conductivity, high surface area, high elasticity, adjustable band gap, biocompatibility, robustness, and, especially, endless possibilities for modification or functionalization of its carbon chain [127], making it an excellent substrate for the development of electrochemical sensors [128].

Combining multiple components into one nanostructure is useful for various materials with numerous applications [129]. Designing hybrids consisting of various organic and inorganic materials has attracted great attention in the past few years [130]. Materials used range from the noble metals, carbon nanoparticles and nanotubes, graphene, metal oxides, and silica nanowires to small organic molecules and polymers [131]. Among the multitude of multicomposites investigated, magnetic nanomaterials and noble metal-based hybrids (NMHs) attracted the most attention due to their unique properties demonstrated theoretically and experimentally [132]. Nowadays, hybrid nanomaterials comprised of two or more different components (core@shell, composite, alloys) with potential to perform several technological tasks of biomedicine simultaneously, especially the superparamagnetic/plasmonic hybrid nanoparticles [133–135], have attracted a lot of attention. Noble metals are low cytotoxic [136] and facile for bioconjugation and possess outstanding optical properties that could be tuned through varying their size, shape, and thickness and composition of the shell [137]. These features make gold nanoparticles potential candidates for novel noninvasive targeting and imaging agents [41, 138] and photothermal therapy agents [139]. In terms of catalysis, coupling with magnetic materials enables the nanosized noble metal-based catalysts to be easily recycled by external magnetic field [140]. Meanwhile, the contamination of the reaction solution is also avoided. For bioapplications, such as drug delivery [141], imaging [135], and therapy [142], NMHs have significant advantages over other hybrids because of the robust interaction between noble metals and thiol groups.

The particle hybrids can be prepared by various approaches. For example, the (core@shell) gold@SiO_2 nanoparticles could be etched by heating to give other

hybrids gold@mesoporous-SiO$_2$ nanoparticles. The mesopores in the silica shell were easily observed. In addition, the empty space around the gold nanoparticle in the single-Au@SiO$_2$ NPs expanded, which generates a distinct core-shell structure. Although various synthetic strategies have been employed to generate core-shell {Au@SiO$_2$}NPs [143–145]. Nanoparticles tend to aggregate when fabricated alone, and therefore, a supporting material is needed to grow and anchor the metal nanoparticles, and graphene oxide (GO) has been used as a support material for many types of NPs including Au, Ag, Pd, Pt, and Ni [146, 147]. The prepared AuNP/GO hybrid particles were then used to stabilize Pickering emulsions. Furthermore, the Pickering emulsions were used to fabricate AuNP/GO-supported polystyrene microspheres and their catalytic performance for the reduction of 4-nitrophenol was investigated. This investigation provides guidance for the fabrication of functional materials, which may find applications in catalytic reactions and composite materials [148].

The properties of nanocomposites (nanostructures or nanoparticles) depend on the microscopic and macroscopic states of the composites and provide information on the interaction of individual components inside composite material systems. In a mixture between a dielectric and a conducting component, for example, the conductivity of this mixture shows a critical behavior if the fraction of the conducting component reaches the percolation threshold [149].

Following early developments in wet chemistry methods, such as the well-known reduction of silver or gold salts by different reducing agents in the presence of low molecular weight additives (surfactants) to provide colloidal stability and/or specific functionality, the use of (co)polymers is clearly an interesting route for the fabrication of noble metal nanoparticle systems with a core@shell microgel structure [23, 24]. The external polymeric coating of gold cores defines both the spacing and the interactions in nanoparticle systems with this type of architecture. We can synthesize next-generation polymer coatings for gold nanoparticles that may feature stimulus-responsiveness (pH, temperature, ionic strength, and light) and spontaneously form versatile supramolecular structures. The fabrication of metal core@polymer shell nanoparticle architectures has been the focus of research owing to potential applications in various fields of research [150–152].

Polymer nanocomposites are an important class of materials that have numerous applications in a number of different industrial sectors, which is why they have been extensively studied in recent decades. Bionanocomposites are formed by the combination of natural polymers with organic and/or inorganic solids; they show at least one dimension on the nanometer scale. The use of bionanocomposites has been preferred because most of the synthetic polymers are not biocompatible, so natural polymers and biopolymers are ideal components in this type of composite material. A slightly different approach to polymer-metal hybrid nanoparticles has also been taken, where inorganic nanoparticles (e.g., AuNPs, magnetic nanoparticles) have been attached to the surface of polymeric microparticles yielding composites with demonstrated potential in cancer therapy and photovoltaic applications [153, 154].

Among selective and sensitive chemosensors, gold nanoparticles and silver nanoparticles have attracted great attention as colorimetric probes, which can enable the direct detection of analytes through the monitoring of color changes with the naked eye as well as fluorescent and UV-Vis spectroscopy. Recently, more and more research about AgNPs was reported. Sun et al. detected Hg^{2+} in blood and wastewater with AgNPs [155]. Duan et al. have reported an investigation of a facile colorimetric sensor for Hg^{2+} in aqueous solution based on the antiaggregation of AgNPs [156]. Rastogi et al. reported a highly sensitive and selective method for the colorimetric detection of Hg^{2+} in an aqueous system by using label-free AgNPs [157, 158].

Several known properties of noble metal nanoparticles stimulated the research reported here: (a) Upon light absorption, AuNPs can deliver energy with pinpoint precision [159], with high efficiency, and in subpicosecond timescales. This property has been proposed as a powerful tool for photodynamic therapy (PDT), a light-mediated form of clinical treatment [160, 161]. (b) AgNPs have excellent antimicrobial properties that exceed those of silver ions themselves, and it has been proposed that the AgNP themselves are strongly anti-infective, beyond any effect due to Ag^+ leaching [162–164]. And (c) some (bio)molecules can stabilize metal nanoparticles, such as AgNP, while they retain their anti-infective properties and show excellent biocompatibility [165].

Noble metal-nanostructured materials have attracted considerable attention scientifically and industrially, owing to their numerous applications that include surface plasmon resonance (SPR, surface-enhanced Raman scattering (SERS), as well as chemical and biological sensing [166–168]. The intrinsic properties of a metal nanocrystal are determined by a set of physical parameters that may include its size, shape, composition, and structure (e.g., solid or hollow) [65, 169]. For example, in the case of a gold or silver nanocrystal, both computational and experimental studies have demonstrated that their shape and structure play important roles in determining the number, position, and intensity of LSPR modes, as well as the spectral region or polarization dependence for effective molecular detection by SERS [28, 170]. Therefore, preparation of metal nanostructures with controllable morphologies is essential in order to fully exploit their peculiar properties and unique applications.

Shem et al. have investigated the influence of alkylthiol chain lengths on the LSPR properties of the AuNPs (H_3C–$(CH_2)_{nc}$–SH (where nc represents the number of methylene (–CH_2–) groups). TEM images confirm the formation of the thiol coated nearly monodisperse AuNPs. It has been shown that alkylthiolate-coated nanoparticles form a 2D assembly due to a combination of electrostatic repulsion and van der Waals interaction. The nanoparticles were suggested to form assemblies in solution and that a similar spatial arrangement of NPs may exist in solution. The LSPR bands are clearly dependent on the thiol chain length, where the largest LSPR shift was observed for the shorter chain thiol and lowest LSPR peak shift (18 nm) was exhibited when the longer chain thiol was used [171].

A wealth of chemical methods have been developed for the synthesis of silver and gold various nanostructures that have well-controlled morphologies, including nanoplates [172, 173], cubes [21, 174], belts [175, 176], wires [177, 178], rods

[179], and branched multipods [180, 181]. Silver nanoparticles have been gaining significant research interest due to their unique shape- and size-dependent optical [182], antimicrobial [183], and catalytic properties [184]. Nanostructures of silver such as monodispersed nanoparticles [185], nanoprisms [186], nanocubes [187], nanowires [188], and nanodisks [189] have potential applications in optics, catalysis, and SERS detection [190]. They are usually obtained from colloidal dispersions and, according to the method used during the synthesis, may have a variety of morphologies, such as nanocubes, nanoprisms, nanospheres, triangular nanoplates, and wires [191–193]. The interest in silver nanoparticles is increasing because when compared to their bulk counterparts, the nanoparticles possess greater surface area per mass [194].

The synthesis of silver nanoparticles involves three broadly defined routes. AgNPs can form in the presence of strong reducing agents, such as sodium borohydride [195], hydrazine [196], and tetrabutylammonium borohydride [196]. A second route can involve the UV irradiation [197], γ-irradiation [198], ultrasound irradiation [199], or microwave [200] heating of silver ions in solution in the presence of capping agents. A third route involves prolonged heating of silver ions in solution in the presence of weak reducing agents, such as sodium citrate [201], glucose [202], dimethylformamide [203], potassium bitartrate [204], ascorbic acid [205], and polyols [177]. A wide variety of capping agents have been used to control size, shape, stability, and solubility of silver nanostructures. Organic thiol compounds [206] are the most commonly used capping agents to stabilize colloidal silver. Long-chain amine [207], aniline [201], surfactant [208], carboxylates [185], and starch [209] have been also used to stabilize silver nanostructures.

Nanomaterials can also act as a carrier for an insoluble agent such as a drug. Alternatively, the nanomaterials can display multiple different biomolecules, thus imbuing the composite with multifunctionality. Indeed, one of the current engineering goals is to create viable nanotheranostic agents where a NM would provide inherent fluorescent or magnetic contrast while displaying multiple targeting agents such as tumor-specific antibodies along with cell-penetrating peptides and a chemotherapeutic agent. This nanomedicine concept is being pursued to overcome many of the issues associated with current systematically delivered medicines [27, 210].

1.4 Nanometria and Nanotechnology

The nanometer regime covers the transition from condensed matter behavior to atomic and molecular properties and thus is a very rich but also very demanding area in materials science. Close to the condensed matter side, properties and functions might still very well be scalable, whereas close to the atomic and molecular side, the scalability is mostly lost. Properties and functions change qualitatively or quantitatively by orders of magnitude when the dimensions become smaller than a critical size in the nanometer range. Examples are the ballistic regime for electron or spin transport at dimensions below the mean free path, near-field

effects in scanning near-field optical microscopy, and quantum wells when the dimensions are below an appropriate wavelength, novel electronic, mechanical, and chemical properties when the number of bulk atoms becomes smaller than that of surface atoms, quantum conduction, and Coulomb blockade. Thus, by going below a certain size, an abundance of novel properties and functions is at one's disposal, or, in other words, we can functionalize materials simply by reducing their size to the nanoscale [211].

Unlike bulk materials, nanomaterials or nanoparticles have characteristic physical, chemical, electronic, electrical, mechanical, magnetic, thermal, dielectric, optical, and biological properties [2]. Decreasing the dimension of nanoparticles has pronounced effect on the physical properties that significantly differ from the bulk material. These physical properties are caused by their large surface atom, large surface energy, spatial confinement, and reduced imperfections. Nanoparticles have advantages over bulk materials due to their surface plasmon resonance, enhanced Rayleigh scattering, and surface-enhanced Raman scattering in metal nanoparticles, quantum size effect in semiconductors, and supermagnetism in magnetic nanomaterials. Therefore, nanoparticles are considered as building blocks of the next generation of optoelectronics, electronics, and various chemical and biochemical sensors [212].

Although the term "nanotechnology" had not appeared on the horizon, Feynman said: "What I want to talk about is the problem of manipulating and controlling things on a small scale… What I have demonstrated is that there is room-that you can decrease the size of things in a practical way… I will not discuss how we are going to do it, but only what is possible in principle… We are not doing it simply because we haven´t yet gotten around to it" (Nobel Laureate Richard Feynman in his visionary lecture "There is plenty of room at the bottom") [213, 214]. Several decades later, scientists have learnt that the manipulation of atoms, molecules, and clusters on surfaces is feasible and that new fundamental physics governs the properties of nano-objects [215]. The unique electronic, optical, and catalytic properties of metal nanoparticles, together with the different methods available for the preparation of nanoparticles (nano-objects) of controlled shape and size, provide exciting building blocks for nanoscale assemblies, nanostructures, and nanodevices. They show often radically different properties from their constituents or bulk counterparts. Richard Feynman in his visionary lecture inspired the concepts for the rapidly exploding research topic of nanotechnology. Nanoparticles are described herein as discrete particles with at least one characteristic dimension: the size in nanometers, typically in the range of $\sim$1–100 nm [216]. 1 nm is $\sim$6 times the atom size of gold and $\sim$4.5 times the atomic spacing in noble metals. In addition to the material composition, the size and shape are two other important factors that determine properties of a nanoparticle.

Nanotechnology—the science and engineering of creating functional materials and devices between 0.1 and 100 nm in scale—is the most commercially viable technology of the twenty-first century due to its very wide applications from health science to electronics. This new emerging technology has attracted great interest from the scientific community around the world and is predicted to be an over—

$1 trillion worldwide market by 2015. Early envisioning of nanotechnology was put forward by Richard Feynman in the 1960s [213]. However, the discovery of fullerene C_{60} in 1985 by Kroto et al. [217] initiated great interest in the field of nanotechnology. Two decades after the initial discovery of fullerenes, man-made nanostructured materials are now globally produced in the quantity of tens of tonnes per year. Laboratory-synthesized and pilot-level plant-produced nanomaterials include fullerenes, nanoparticles, nanotubes, nanowires, nanorods, quantum dots, dendrimers, nanoclusters, nanocrystals, nanocoatings, and nanocomposites, all of which exhibit significantly improved and unique properties over their counterpart bulk materials. The applications of nanomaterials are increasing tremendously day-by-day nearly in all industries.

In the twenty-first century, nanotechnology has become one of the most rapidly developing fields of science and technology [218]. Numerous nanomaterials have been manufactured to have characteristic electrical, mechanical, magnetic, thermal, dielectric, optical, and catalytic properties [219]. The broad range of functionalities associated with these materials has led to them being used in electronics, computing, communications, materials science, transport, and energy-based sectors of the economy, as well as by the pharmaceutical and cosmetic industries [219]. In recent years, a great deal of attention has been drawn to the fabrication of biomimetic or bioinspired nanomaterials. A variety of highly organized nanoscale biological structures have evolved which have inspired researchers to design new systems for producing novel nanomaterials, and viruses are perfect examples of such materials.

The pace of scientific research and technological advancement in the recent times is mostly due to the entry of nanotechnology. With the birth of nanotechnology, all fields of science have come up with a new dimension to the research in their respective fields of study. However, it is of recent times it made heavy strides and hastened the research activity in the areas of all sciences more so in the area of life sciences. "Nanotechnology" mainly consists of the processing, separation, consolidation, and deformation of materials by one atom or one molecule. Nanoparticles of noble metals such as gold, silver, and platinum are widely applied in products that directly come in contact with the human body such as shampoos, soaps, detergents, shoes, cosmetic products, and toothpaste, besides medical and pharmaceutical applications. Nanoparticle exhibits completely new or improved properties as compared to the larger particles of the bulk material that they are composed of based on specific characteristics such as size, distribution, and morphology [18].

Bulk metals are electrically conducting and good optical reflectors, as caused by the sea of freely moving delocalized electrons in the conduction band. On the other hand, metal nanoparticles display intense colors due to surface plasmon resonance, a feature attributed to the collective oscillation of conduction electrons upon interaction with light (Scheme 1.1). When the size of metals is further reduced to around 1 nm or less, down to a few atoms, the band structure becomes discontinuous and is broken down into discrete energy levels, somewhat similar as the energy levels of molecules. Therefore, these metal nanoclusters are said to have
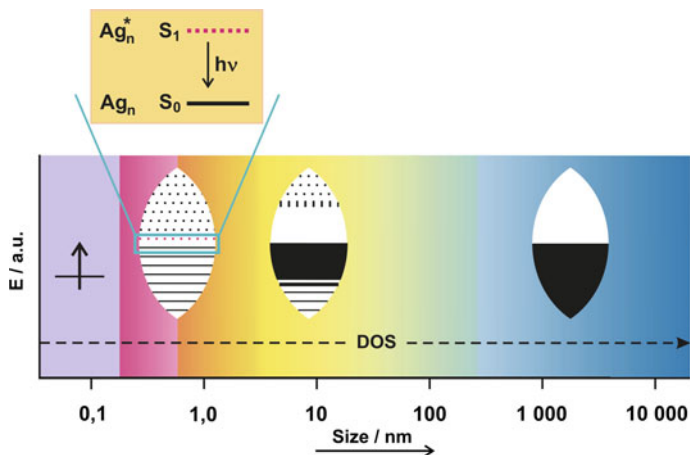
Scheme 1.1 Variations of energy (E/a.u) level with the atom agglomeration and DOS. The effect of metal particle size, single valence electron (below 0.1 nm), discrete energy levels by quantum confinement (below 1 nm), and bulk metal freely moving electrons (above ca. 1 μm). Ag_n herein n means a number of silver atoms [222]

molecule-like properties and do not anymore exhibit plasmonic properties. They represent the missing link between metal atoms and nanoparticles. Nonetheless, metal nanoclusters can still interact with light via electronic transitions between energy levels, resulting in intense light absorption and emission [220, 221].

In solid-state and condensed matter physics, the density of states (DOS) of a system describes the number of states per interval of energy at each energy level that are available to be occupied. Unlike isolated systems, like atoms or molecules in gas phase, the density distributions are not discrete like a spectral density but continuous. A high DOS at a specific energy level means that there are many states available for occupation. A DOS of zero means that no states can be occupied at that energy level. In general, a DOS is an average over the space and time domains occupied by the system. Local variations, most often due to distortions of the original system, are often called local density of states (LDOS). If the DOS of an undisturbed system is zero, the LDOS can locally be nonzero due to the presence of a local potential [222, 223].

The key to the future lies in the functions that we give to materials, not just in finding "novel functional nanomaterials." Certainly, finding new materials is always an important part of progress, but we should also focus on the much larger domain of novel functions that we can give to existing or modified materials. A good example is semiconductors: They were not of widespread interest and use until the transistor changed their destiny into being the central material in the information technology revolution. Interfaces gave them their functions, shaping them into ever-smaller functional components made them indispensably omnipresent as transistors produced in billions per person and per year, and they are no doubt the rulers of today's technical world. These nanomaterials serve as an inspiring

example of functionalizing materials. The developments of microelectronics profited very much from scalability; that is, the properties and functions do not change significantly with size. Therefore, every step toward smaller dimensions was a technical and commercial challenge with risks well under control. The transition to the nanoscale, however, is discontinuous. Examples of this transition are the local probe methods that exploit the mechanically controlled proximity to the object under consideration and that have become indispensable as microscopes and as measuring and modifying tools, the size of molecular components that are much smaller than the smallest possibly achievable transistor, the properties and functions of materials below a critical size, the continuum properties versus discrete ones, and novel concepts inspired by living nature. It is these discontinuous steps that make the nanoscale different, not just smaller. They pose exciting challenges and open great opportunities and nearly unlimited possibilities, but they also carry serious technical, commercial, environmental, and health risks [211].

The role of interfaces is rapidly increasing in science and nanotechnology, and they are the key to new functions. Think of the simple "mechanical" interface responsible for the lotus effect where wetting is prevented by the rapidly changing surface curvature due to nanoparticles. Think of all the connections of a nanometer-sized area between very different materials, for example, for electron or spin transport. Think of the delicate interfaces that protect nanofunctional units from the environment but allow for communication of various types with other nanocomponents or with the macroscopic world. Interfaces are the "faces of action," and nanoscale materials science will be, to a great extent, "interface science."

The main focus of nanotechnology is to synthesize nanoparticles with predictable shape, size, polymeric coating, and fine distribution for potential biomedical applications. Various techniques are involved in nanoparticles preparation like chemical and physical methods which may successfully produce pure, well-defined nanoparticles, but these are quite expensive and potentially dangerous to the environment [19]. Green chemistry-based eco-friendly methods for synthesis of nanoparticles could be an alternative for chemical synthesis. Numerous naturally derived materials and biopolymers have been successfully used for well-organized and speedy green synthesis of silver [20], copper oxide [224], zinc oxide [225], selenium [226], platinum [227], and gold nanoparticles [228–230].

Many nanogold- and nanosilver-based environmental technologies (e.g., sensors, sorbents, reactants, and different agents) are under very active research and development and are expected to emerge as the next generation of environmental technologies to improve or replace various conventional environmental technologies in the near future [231]. For environmental applications, nanotechnology offers the potential of novel functional materials, processes, and devices with unique activity toward, for example, enhanced mobility in environmental media and desired application flexibility [231]. Some of the most promising near-term realizations of nanotechnology are at the interface of physical, chemical, and biological systems. Nanotechnology has been receiving increased attention in the past decade due to its extensive applications in the field of catalysis, electronics, high-density

magnetic recording media, sensors, different reactive agents, and biotechnology [232]. It is the engineering and art of manipulating matter at the nanoscale [233, 234]. Synthesis of metallic nanoparticles with controllable properties for biological, chemical, optical, and electronic applications has been a major focus of nanomaterials research [234]. One of the most important considerations during the synthesis of nanoparticles is surface chemistry which plays a vital role in determining the characteristics of the NPs [235].

Nanomaterial synthesis is emerging as a crucial technology in nanotechnology to develop building blocks for nanometer-scale devices. The synthesis of noble metal nanoparticles with controlled chemical composition, size, and shape distributions is an important first step toward the realization of nanotechnology. A wide variety of physical and chemical processes have been employed for the synthesis of metal nanoparticles [22], but these methods have certain disadvantages due to the involvement of toxic chemicals and radiations. So the development of reliable experimental protocols for the synthesis of nanomaterials over a range of chemical compositions, sizes, and high monodispersity is one of the challenging issues in current nanotechnology. There is a need to develop an environment-friendly approach for nanomaterial synthesis and assembly that should be fast and devoid of the use of toxic chemicals in the synthesis protocol. As a result, for the development of clean and environmentally acceptable green procedures, nature-made systems are fast gaining attention of the researchers.

It is well recognized that properties of metal nanoparticles depend largely on the size, shape, composition, structure, and crystallinity. Therefore, various approaches have been developed to control these parameters and, hence, meet the requirements for various applications. This has been leading to the synthesis of a spectacular variety of nanoparticles of different shapes, compositions, patterns, and functionalities through physical, chemical, and biological methods, though nanomaterials can be generated by physical (top-down) (such as evaporation, arc discharge, and laser ablation) and chemical (bottom-up) approaches. The latter is one of the preferred methods for fabricating a wide variety of nanoparticles. The colloid-chemical methods of noble metal nanoparticle preparation basically involve the (bio)chemical reduction of metal salts, photochemical and electrochemical pathways, or sonochemical/thermal decomposition of metallic precursors (salts) in aqueous or organic solvents in the presence of a variety of additives such as surfactants, reducing agents, ligands, polymers [236].

In particular, it is the myriad of properties such as the ease of synthesis, functionalization, small size, nontoxicity, stability, interesting optical, and electrical properties that make the nanomaterials so attractive. Their capacity to carry high payloads has drawn attention to gold nanoparticles as potential sensing, delivery, and imaging agents [237–239]. The facile ability to functionalize gold nanoparticles with stabilizing ligands has made them very attractive for biomedical applications [240]. The modification of gold nanoparticles with polymeric capping agents such as polyethylene glycol, amino- or mercaptodextrans affords long-circulating nanoparticles, known as nanocarriers, that are desired for passive targeting to tumor and inflammatory sites [241]. The production and applications of noble metal

nanoparticles have rapidly been increased, since their novel physical and chemical properties are not only different from those of bulk substances, but also metal nanoparticles exhibit specific colors due to localized surface plasmon resonance (LSPR) [242]. The colors of gold and silver nanoparticles result from changes of LSPR induced by their size and shape. In particular, the applications of these nanoparticles have widely been investigated, since they exhibit some profitable properties such as catalysis [243], antibacterial agent [244], nanoparticle colorant [245], nanopaste for electrical circuits and electrodes [246], and substrates for surface-enhanced Raman scattering [247].

Noble metal nanoparticle chemistry and physics has emerged as a broad new subdiscipline in the domain of colloids and particle surfaces. The unusual optical properties of small gold and silver particles, their size-dependent electrochemistry, and their high chemical stability have made them the model system of choice for exploring a wide range of phenomena including self-assembly, biolabeling, electron transfer theories, phase transfer, DNA melting and assays, and crystal growth. These nanoparticles when stabilized or protected by a shell of thiolate ligands display good stability toward aggregation and other modes of decay, which enables attempts at isolating different nanoparticle sizes and the exploration of how nanoparticle properties depend on size (including quantization effects). Gold nanoparticles with fewer than 300 gold atoms can display distinct optical and electronic properties compared to the bulk metal or even to larger nanoparticles. The thiolated nanoparticle stability further enables treating the ligand shell as a chemical platform that can be manipulated to exhibit desired reactivities, poly-functionalization, and optical properties. The consequence for the past couple of decades has been a very active field of basic nanoscience research and applications of these nanoparticles. An important aspect of gold nanoparticles has been the breadth of their impact applications ranging from photonic device fabrications, to sensing of organic and biomolecules, to charge storage systems [248].

The synthesis of noble metal nanoparticles is a focus of current interest as they exhibit unique properties due to their unique size and shape [249, 250]. Because of their stability, oxidation resistance, and biocompatibility [251], noble metal nanoparticles find wide applications in a number of areas. However, their characteristic properties can be tailored for potential application by controlling the size and shape of the nanoparticles [252]. Thus, new methodologies for designing shape-controlled synthesis of gold nanoparticles are essential for the advancement of nanotechnology [253, 254]. Synthetic chemical methods for obtaining noble metal nanoparticles of different sizes and shapes are being continuously modified and improved. Conventionally, nanomaterials of different shapes and sizes having reasonably good monodispersity are usually synthesized by reducing a gold salt with sodium citrate or sodium borohydride, followed by surface modification of the produced particles with suitable capping ligands, occasionally using an organic solvent, which often raises environmental questions [255]. At the same time, these approaches produce multishaped nanoparticles requiring purification by different approaches [256, 257]. Thus, there is a constant drive for new methodologies to produce the shape-controlled synthesis of gold nanoparticles.

Generally, nanoparticles are divided into spherical and nonspherical. No commonly accepted nomenclature and classification exist for nonspherical nanocolloids. Nanomaterials are generally classified according to their composition (mono-, bimetallic, multimetallic, metal oxide, magnetic, semiconductor, hybrid, functional, composite, etc.), size, and/or shape/morphology. Glotzer and Solomon attempted to put forward several possible classifying principles as a way of unifying the practically infinite number of different particle shapes and types that are already made or will be made in the near future [258]. One can classify anisometric nanomaterials into three families according to their growth dimensionality: (i) 1D nanoparticles growth confined in two dimensions, i.e., major growth occurred in one dimension (e.g., rods, wires, tubes); (ii) 2D nanoparticles growth confined in one dimension (e.g., planar triangles, hexagons, plates, disks, ribbons belts); and (iii) 3D nanoparticles where major growth occurred in all three dimensions [e.g., Platonic, Archimedean, and Poison shapes such as tetrahedra, octahedra, decahedra, icosahedra, cubes, prisms, nanocages, or branched nanoparticles (bipod, tripod, tetrapod, multi, bumpy, thorny, sea urchin, etc.)]. Figure 1.1 shows a few examples of 1D, 2D, and 3D nonspherical NMNPs.

Characterization is an important step in the morphology-controlled synthesis of nanoparticles that includes assessment of composition, morphology, dimensionality, and physical (such as optical and spectroscopic characteristics) and chemical properties (such as surface charge and functionality). Size (diameter, length, width, and height), volume, aspect ratio, perimeter, projected area, surface roughness, etc., are typical morphology parameters that are assessed [26]. Multiple techniques are often applied in tandem for comprehensive characterization of nanoparticle systems [259]. These include separation-based, scattering, microscopy, spectroscopy, mass
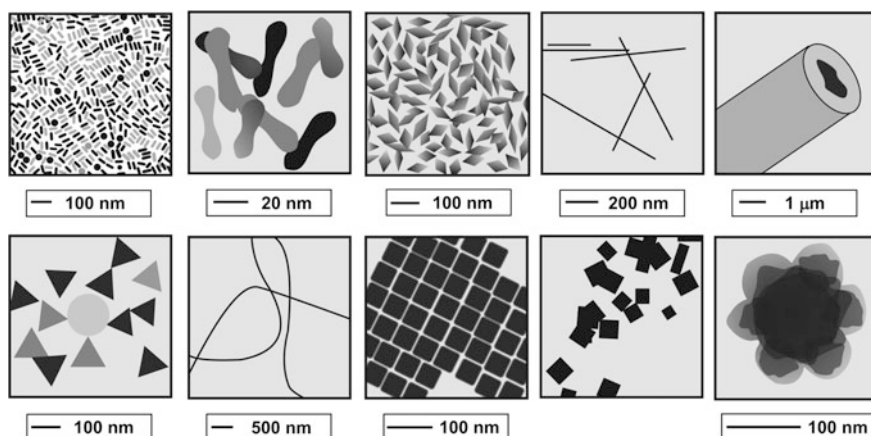
Fig. 1.1 A few representative examples of nonspherical 1D, 2D, and 3D noble metal nanoparticles synthesized by the colloid-chemical synthetic approach. The TEM or SEM images of nanoparticles: nanorods, nanoshuttles, nanobipyramids, nanowires, nanotubule, triangular nanoplates, nanocubes, ribbons, and star-shaped particles [236]

spectroscopy, and thermal techniques. The colloid-chemical synthesis, for example, often results in nanoparticles with a distribution in size, shape, composition, etc. Determination of these distributions is important in order to improve the synthesis protocols and assess their effects on the overall property of the particle ensemble.

Commonly used light scattering techniques provide information about particle size, size distribution, and relative dispersion directly in the reaction medium but do not provide direct information on the morphology of particles. The nanometer-scale architecture of the particle-based surfaces has been characterized by a wide range of analytical techniques including atomic force microscopy (AFM) [260], field emission scanning electron microscopy (FESEM) [261], transmission electron microscopy (TEM) [262], near-field scanning optical microscopy (NSOM) [263], scanning tunneling microscopy (STM) [264], and photon STM [265]. Microscopy techniques are based on visualizing a sample using light, electrons, or a scanning probe [266]. Traditional optical light microscopy (sometimes referred to as bright field microscopy) and its myriad of fluorescent derivatives were until recently, however, unable to resolve nanoscale features <200 nm due to diffraction limitations. As a result, they found limited application in the characterization of individual NM-conjugates. Conventional TEM is used for the determination of size, size distribution, and the number density of the particles easily and accurately.

Nanoparticle purity is important when it comes to more precise determination of optical and electronic properties, in assessing structure-function relationships in toxicology studies and for determining the functional role of the ligand on the nanoparticle surface. A number of techniques can be used to purify nanoparticles such as extensive washing with solvents or fractional crystallization. In cases where the nanomaterials and ligands are water-soluble, dialysis has shown to be effective.

1.5 Techniques, Procedures, and Approaches

Separation and purification techniques separate the nanomaterials (NMs) and their conjugates from the original reactants and by-products [25]. While certain nanomaterials, such as those that are magnetic, provide inherent properties that make purification relatively simple (i.e., collection using a permanent magnet) [267], most rely on several commonly utilized methods to minimally separate the unbound additives from the NM products. Characterization is an important step in the morphology-controlled synthesis of nanoparticles. It is essential in order to validate the synthesis, decipher the evolution of particle morphologies, and improve the synthesis protocols [26]. Multiple techniques are often applied in tandem for comprehensive characterization of nanoparticle systems [259]. The ultimate test of successful NM-conjugation is of course functionality in the desired application, and while the very nature of activity infers the presence and activity of the ligand (surfactant, biomolecule, etc.) on the NM surface, this does not reflect any specific details of the underlying NM-conjugate architecture. A variety of well-developed techniques which already have been successfully applied to the characterization of

bare nanomaterials are now being extended to examining NM-conjugates. These include separation-based, scattering, microscopy, spectroscopy, mass spectroscopy, and thermal techniques. In general, the separation techniques are relatively cheap and widely available. Some are already routinely used to purify NP-conjugates and can also be quite effectively used for characterization purposes. Indeed, they have been shown to be particularly useful for confirming molecular attachment to the NM surface and providing information on approximate hydrodynamic radius, NM-to-ligand (surfactant, (bio)molecule) conjugation ratio, and insight into post-production degradation (i.e., stability) [27].

The particle size and concentration are important parameters of nanotechnology area. Current methods for determining NMNP size can be divided into several subcategories. The first is light scattering methods that include dynamic light scattering (DLS), static light scattering (SLS) [268, 269], and small-angle X-ray scattering (SAXS) [270]. The second category is the microscopy method including atomic force microscopy (AFM), transmission electron microscopy (TEM) [271], and scanning electron microscopy (SEM). The third is the localized surface plasmonic resonance (LSPR) method, which takes advantage of the fact that the LSPR features of AuNPs depend on the size, shape, and concentration of the AuNPs [28, 29]. A more recent method is electrospray-differential mobility analysis (ES-DMA) that involves the conversion of AuNP suspension into the gas phase using electrospray ionization. In ES-DMA, the charged particles are sorted based on their electrical mobility and the number average diameter is measured after counting [272]. While TEM, SEM, and AFM images allow direct AuNP visualization [271, 273], these measurements require tedious sample preparation, sophisticated equipment, and lengthy and often subjective data analysis to determine particle size and size distribution. Since only a small population of the nanoparticles is probed, the results are statistically less representative [274].

The size of nanoparticles can also be determined by the fractionation processes. They are usually effective in controlling the particle sizes over a wide range. Particularly, gold nanoparticles functionalized with thiol ligands behave similarly as charged biomolecules and thus can be easily fractionated using traditional biomolecular separation methods, such as gel electrophoresis [275], capillary electrophoresis [276], membrane filtration [277], and size exclusion chromatography [278]. In most of these approaches, gold nanoparticles of different sizes were separated from each other as a result of different electrophoretic migration velocities in gel matrices. Although a high resolution of about 1–5 nm has been achieved [279, 280], chromatography- and electrophoresis-based technologies still suffer from the inherent low throughputs and the low recovery, caused by the nonspecific interaction between AuNPs and supporting substrates. In comparison, size-selective precipitation is more effective and applicable for high-throughput fractionation of nanoparticles [281]. This technique utilizes the balance between the size-dependent van der Waals attraction of nanoparticles and the capping ligand-induced solubilization/dispersion of AuNPs in certain solvents. When the ligands are not sufficiently solvated by the solvent, nanoparticles aggregate and precipitate from the solution. Larger particles have stronger van der Waals attractions between them and

therefore are subject to greater driving force for precipitation [282]. Thus, size differentiation of NMNPs can be achieved through precise tuning of the solvent property (e.g., the solvent composition) or the solvent conditions (e.g., the solvent pressure and temperature [283]) in supercritical fluid-based separations. Mirkin's group reported a size-selective precipitation in aqueous media based on the intrinsic particle size-dependent aggregation/dissociation properties of DNA functionalized AuNPs [284]. Fractional precipitation has often been used for size and shape estimation of nanoparticles. Researchers are employing established separation techniques, which have been commonly applied to separate small species such as viruses, organelles, or macromolecules. For example, density-gradient centrifugation has been used to separate differently shaped gold nanoparticles [285].

Chromatography techniques separate based upon the differing affinities of the multiple sample components for the chosen chromatographic mobile and/or stationary/solid phases. The actual separation mechanism depends on the chromatographic method utility, but, in all cases, care should be taken to limit non-specific interactions with the stationary phase or denaturation due to solvents which can be problematic for sensitive or labile biomolecules. Ion-exchange, size exclusion, and affinity chromatography, run under either gravity or low-pressure conditions, are commonly applied to nanomaterial conjugate purification and can even be extended to materials of quite large mass [30]. High-performance liquid chromatography (HPLC) [286] coupled with reverse-phase ion-exchange [287], size exclusion (SEC) [31], and stationary phases have been extensively used for purification of nanomaterial conjugate from excess (bio)molecules. Size-exclusion chromatography [288] has also shown its feasibility for the separation of various metallic nanoparticles according to their size and shape. Chromatography techniques, in particular HPLC coupled with anion exchange or reverse-phase columns, has demonstrated the exquisite ability to resolve nanomaterial conjugates with different nanomaterial-to-ligand ratios, providing both the distribution and overall average ratio of NM-to-molecule per sample [289]. In an especially challenging characterization example, Mullen and coworkers recently demonstrated the use of reverse-phase HPLC to investigate poly(amidoamine) (PAMAM) dendrimers modified with alkyne ligands which are important for subsequent conjugation using click chemistry (Fig. 1.2) [290]. Distinct peaks within each HPLC trace were observed, and deconvolution revealed the different dendrimer-ligand species allowing them to be quantified.

Field flow fractionation (FFF) encompasses a family of analytical techniques in which the sample is introduced into a pressure-driven mobile phase contained within an open channel (no stationary phase) demonstrating a parabolic flow profile, and an alternate field is applied perpendicular to the direction of flow [291]. The principles of separation are dependent on the applied field, but the technique has demonstrated the ability to purify NM-conjugates from both unmodified NM and free molecules [32]. FFF provides information on charge, size (peak height position), and size distribution (peak width) [32]. FFF has already been used by a number of researchers to provide size information on various unmodified nanoparticles, including AuNPs and AuNPs modified with PEG ligands [292].

Fig. 1.2 Chromatographic techniques. HPLC trace monitored at 210 nm of sample G5-... is shown. Five different peaks (0–4) were observed in the sample's trace [27, 290]
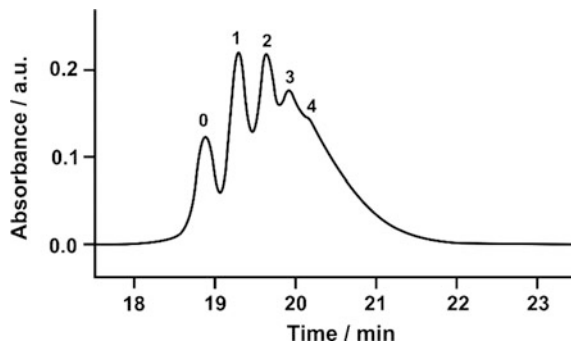
Centrifugation is a relatively simple and cheap technique that can be used to purify functionalized nanomaterials and their conjugates from unconjugated ligand (molecule). Depending on the density, size, and structure of the nanomaterials and molecules, application can sometimes be as straight forward as using a benchtop centrifuge to separate functionalized NMs from the reaction mixture and then either removing the soluble conjugate or, alternatively, resuspending the conjugate precipitate in the buffer of choice. For smaller NMs, or those with a lower density, ultracentrifugation may also be useful for separation and purification.

Analytical ultracentrifugation (AU) can be used to estimate the colloidal stability of gold colloids. The two principle modes used in AU are sedimentation velocity and sedimentation equilibrium. While the technique can be applied to the purification of NM-conjugates, it is more commonly used for characterization of these composites. To establish the utility of analytical ultracentrifugation, we can estimate sedimentation coefficients for two different sizes of gold nanocrystals from different sources and compared the results to measured S-values. The theoretical sedimentation coefficient (S), for a smooth, compact, and spherical particle, is given by Eq 1.1:

$$S = M_{\mathrm{W}}(1-\overline{\upsilon}\rho s)/N_{\mathrm{A}}6\pi\eta_{\mathrm{S}}rf \tag{1.1}$$

where M_{w} is molecular weight, υ is the partial specific volume of the particle, ρ_{s} is the density of the solvent, N_{A} is Avogadro's number, $\pi\eta_{\mathrm{s}}$ is the viscosity of the solvent, r is the radius of the particle, and f is the frictional coefficient ($f = 1$ for a sphere). In the case of a nonspherical particle, the frictional coefficient can alter the S-value substantially [293].

Assuming a spherical particle, a gold nanocrystal density of 17 g/cm^3 in Eq. 1.1 [294], and using the diameter and polydispersity as determined from TEM, theoretical S-values were estimated in ranges for sample A (650–1010 S, $d \sim 10.1$ nm) and sample B (940–2260, $d \sim 13.8$ nm), respectively. The nanocrystals were then analyzed with AU. Figure 1.3 shows S-value distributions calculated from van Holde-Weischet analysis of the resulting AU data from samples A and B. The smaller nanocrystals in sample A (Fig. 1.3, curve 1) show a sedimentation

coefficient range between 500 and 1200 S, with a peak at approximately 670 S. The measured and theoretical S-values are therefore in good agreement, considering the severity of the assumptions made for the theoretical calculations.

An important advantage of AU in nanocrystal analysis is that it is a nonde-structive method; samples can be recovered after sedimentation, permitting further analysis or purification. The dashed line in Fig. 1.3 illustrates this feature directly. After sedimentation, sample A was recovered, resuspended, and rerun in the AU under the same conditions. The samples show a broad (>500) S-value distribution. Larger S-value species, presumably aggregated material, cannot be resuspended in the recovered sample and therefore disappear from the analyzed data. The prepared nanocrystals in sample B (curve 3) have a larger diameter and therefore a larger S-value than the purchased nanocrystals in sample A.

The S-value of the recovered sample (Fig. 1.3, curve 2) is comparable to the initial sample, having a maximum of 660 S. The most significant change is the decrease in the amount of larger species (or aggregates) at higher S-values, pre-sumably due to difficulty in their resuspension after the initial sedimentation. These data illustrate that the integrity of the sample is not disrupted by sedimentation, and samples can thus be recovered for further use and analysis. Compared to sample A, the larger gold nanocrystals in sample B (Fig. 1.3, curve 3) have a broader and higher S-value range, 1000–2500 S, with a peak at 1380 S. This breadth is expected given the larger 3.0 nm standard deviation in size for sample B. For sample A, we find that theoretical S-values are in reasonably good agreement with the experimentally obtained S-values. In effect, these sedimentation data capture the polydispersity of gold nanocrystals and accurately reflect the distribution of sizes seen from TEM data.

Analytical ultracentrifugation is also a fractionating technique that allows determination of molar mass and particle size distribution with high statistical relevance as every particle contributes to the sedimentation profile [295]. The particle size distribution of the Ag–PfFt (the ferritin protein—from the hyperther-mophilic archaeon Pyrococcus furiosus) nanoconjugate [296] was calculated by

Fig. 1.3 *S*-values derived for sample A ($d \sim 10.1$ nm, *curve 1*) and sample B ($d \sim 13.8$ nm, *curve 3*). The relative frequency (RF) of different *S*-values is plotted. Sample A (*black line*, 1) and a recovered sample rerun in the AU under the same conditions (*dotted line*, 2) [293]
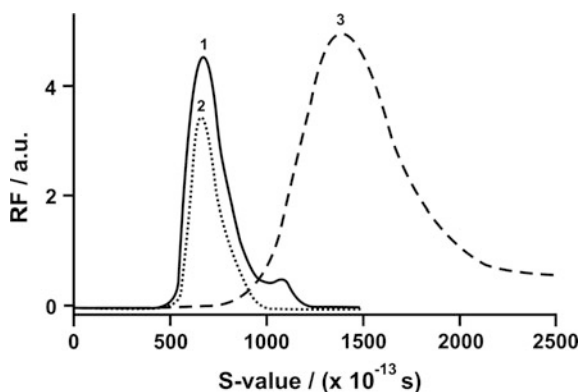
taking into account the densities of the protein (1.35 g/cm^3) and of bulk silver particles (10.5 g/cm^3) and the thickness (2 nm) of the protein shell [297, 298]. The size distribution of the Ag–PfFt solution thus calculated has its maximum at 2.1 nm and a standard deviation of 0.4 nm (Fig. 1.4). Together with the high stability reported above, the high homogeneity of AgNPs encapsulated in PfFt shown by these studies is one of the required, as well as difficult to achieve, features of AgNPs for practical applications [296].

Microfluidic and increasingly nanofluidic devices have much to offer researchers from improved synthesis to characterization as well as reduced sample volumes. Stravis and coworkers recently demonstrated a nanofluidic size exclusion device for on-chip nanoparticle size separation and characterization [299]. Currently, the device is capable of separating particles in the 80–620 nm range with a step size resolution of 18 nm, although potential exists down to <10 nm.

A number of electrophoretic methods have demonstrated wide utility in the characterization of nanoparticles and their (bio)conjugates [300]. Gel and capillary electrophoresis (GE and CE) are the two principle types of electrophoretic techniques commonly applied to the purification of nanoparticles and their conjugates [300]. Gel electrophoresis monitors the electrophoretic mobility of charged species in a gel matrix, typically agarose or polyacrylamide, when an electric field is applied across it. For both nanoparticles and NP-conjugates, the overall size, shape, and charge density influences the direction and distance moved in the gel [301]. Capillary electrophoresis [302] and gel electrophoresis [303] have also shown their feasibility for the separation of various metallic nanoparticles according to their size and shape. Separated NP-sample bands can also be extracted from the gels for subsequent application or further characterized using techniques such as AFM, mass spectrometry [304].

Fig. 1.4 Particle size distribution (PSD) of AgNPs encapsulated in PfFt. The *solid* (*curve 1*) and *dotted* (2) *lines* were estimated from the AU and SAXS data, respectively [296]
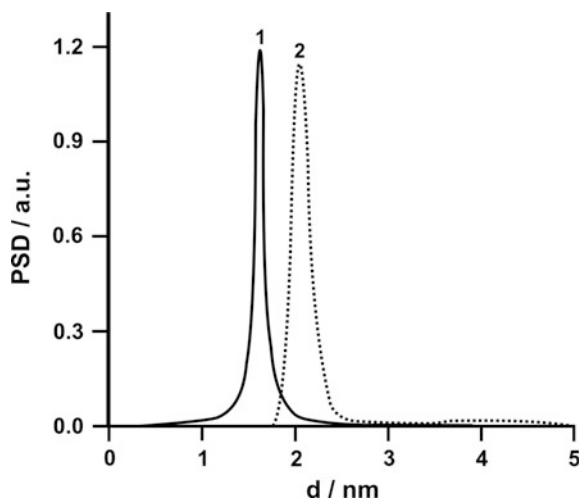
A systematic approach to studying the mobility and physicochemical properties of metal nanoparticles is gel electrophoresis. Several studies involving quantum dots have shown how hydrodynamic radius [305], ligand density [306], and chain length influence mobility [307]. Other groups have used electrophoresis for the analysis of AuNPs, including glycocationic-modified AuNPs [308], DNA-AuNP conjugates [287], and human serum albumin (HSA)-modified AuNPs [309]. Hanauer et al. used electrophoresis for efficient separation of PEGylated gold nanoparticles and AuNPs based on size, shape, and functionalization [310]. Gel electrophoresis has also been used to determine the extent to which a gold nanoparticle surface is capped by monofunctional methoxy-PEG (mPEG-SH) ligands (ligand density) [311]. The stability and aggregation of dispersions are affected by the zeta potential of those colloidal dispersions [312]. Zeta potential (ζ) is a scientific term for the electrokinetic potential in a colloidal system. The zeta potential indicates the degree of repulsion between adjacent similarly charged particles in dispersion and is therefore related to the stability of that dispersion. The zeta potential of dispersion can be used to investigate how charged particles affect the behavior of dispersion such as aggregation, flow, sedimentation, and filtration [312]. When the magnitude of the potential is small, attraction exceeds repulsion and the dispersion will break and flocculate.

When metallic fillers are dispersed in an insulating matrix, percolation theory predicts that the DC conductivity of the composite in the vicinity of the percolation threshold varies as follows [313]:

$$\sigma \alpha (x - x_\mathbf{c})^t \tag{1.2}$$

where x is the weight percent of the conductive phase; x_c is the critical concentration at the percolation threshold; and t is a critical exponent that depends only on the dimensionality of the percolation system with values typically at 1.3 and 2.0 for two and three dimensions, respectively [314]. This dependence produces a straight line with a slope equal to t in a double log–log plot of the electrical conductivity versus $x - x_c$.

Ferguson analysis of gel electrophoretic data can be further used to infer the ζ (electrokinetic) potential of NP-conjugates, as demonstrated for AuNP-DNA and QD-MBP bioconjugates [315, 316]. The mobility of the unknown sample in the gel series can be converted either to its retardation coefficient to yield its ζ potential [316]. The ζ potential is commonly determined by applying an electric field across a sample and measuring the velocity at which charged species move toward the electrode; this is proportional to the ζ potential [305]. The ζ potential can also be used to infer particle stability with a value of ± 30 mV often selected as an arbitrary delineation of stability. Values >30 mV indicate stability, while values <30 mV represent particles with a tendency toward agglomeration or instability [317]. The magnitude of the zeta potential, thus, indicates the degree of electrostatic repulsion between adjacent, similarly charged particles in dispersion. For molecules and particles that are small enough, a high zeta potential will confer stability; i.e., the solution or dispersion will resist aggregation. When the potential is small,

attractive forces may exceed this repulsion and the dispersion may break and flocculate. So, colloids with high zeta potential (negative or positive) are electrically stabilized while colloids with low zeta potentials tend to coagulate or flocculate. Many factors can influence NP stability (and hence the ζ potential) including pH, concentration, ionic strength of the solution, temperature, radiation, and the nature of the surface ligands. ζ potential measurements have been used to study the stability and particle size of biofunctionalized nanoparticles as a function of pH [318], the surface coverage of ligands bioconjugated to AuNPs [319], and various capping agents [305]. In other words, the zeta potential ζ is the potential difference between the dispersion medium and the stationary layer of fluid attached to the dispersed particle.

Scattering techniques exploit the scattering of radiation (e.g., light or energetic particles) through its interaction with a sample. Depending on the scattering technique applied, information about the nanoparticle structure, morphology, hydrodynamic size, and aggregation state as well as the molecular conformation and the NP-conjugate stability post-production can be obtained. Fluctuations in the scattered light intensity, due to the Brownian motion of the particles, are used to determine the particle diffusion coefficient which is then related to its hydrodynamic radius via the Stokes-Einstein relationship [320]. Dynamic light scattering (DLS) has a size range of $\sim$10–1000 nm, respectively; however, its sixth power dependence on scattering versus particle size means that wide NP-conjugate size distributions can obscure the presence of smaller materials in the sample [320]. Similarly, analytical ultracentrifugation can be used for characterization of NPs and their (bio)conjugates (Fig. 1.5).

Of all the scattering techniques available, DLS, also known as photon correlation spectroscopy (PCS), is probably the most commonly used for characterizing the hydrodynamic size of NPs and their conjugates, given that it is simple, noninvasive, nondestructive, and relatively cheap to apply (Fig. 1.6) [305].

One key advantage of light scattering (e.g., SLS or DLS) and LSPR-based methods is their ability to probe the gold nanoparticle in situ, that is, the AuNP in solution, eliminating the tedious sample preparation required for imaging-based methods. Unfortunately, DLS and SLS suffer from poor robustness and accuracy. For example, large uncertainties in particle size analysis can occur in both DLS and SLS induced by variations in the viscosity and refractive index of the solvent, particulate contaminants in the sample, and fluctuations in the solution temperature. Although DLS proves to be a useful tool for monitoring slow aggregation processes, Khlebtsov et al. reported that false peaks appear in the size range of 5–10 nm in DLS measurements of colloidal AuNPs [269]. A critical limitation of the LSPR method is its insensitivity to small changes in particle size, which is particularly problematic for AuNPs smaller than 35 nm in diameter [324]. Theoretical calculations have shown that the change in the peak LSPR wavelength is less than 5 nm when the particle size changes from 5 to 35 nm in diameter [324]. Because of their limited reliability, light scattering and LSPR methods are better suited to study big changes in AuNP sizes induced by AuNP aggregation than to determine the exact particle size.

Fig. 1.5 Analytical ultracentrifugation for characterization. Progression of the sedimentation coefficient (S) distribution (Conc.rel/a.u. vs. S) for bare 10 nm gold particles and 10 nm AuNPs modified with thymidine homo-oligomers decreasing from 30 bases (SH-T30) to 5 bases (SH-T5) in size (Conc.rel/a.u.). *Curve 1* (SH-T30), *2* (SH-T20), *3* (SH-T10), *4* (SH-T5), and *5* (bare AuNPs) [321, 322]
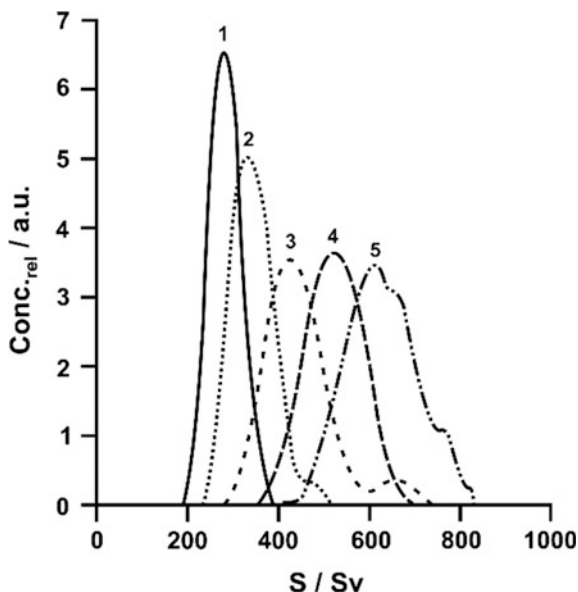
Fig. 1.6 Dynamic light scattering for characterization. Hydrodynamic diameter (d_h) of noble metal particle-based bioconjugates as a function of the average number ($N_{aver.prot}$) of proteins (His$_5$ or luc$_6$) per nanoparticle [305, 323]
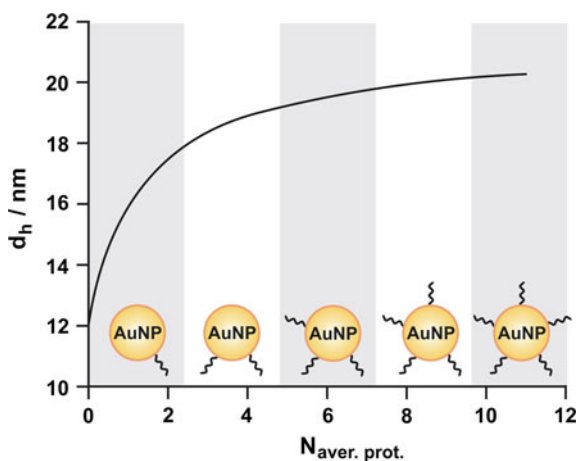
The concentration of particle gold in solution, for example, can be measured by inductively coupled plasma-optical emission spectroscopy (ICP-OES). The distribution of gold particle sizes can be determined by TEM and DLS. The average number of gold atoms in a particle, $N_{av,atoms}$, is a further important parameter determining the properties of colloid solution. It can be evaluated from the Gaussian fit to the distribution of particle diameters [34]:

$$N_{\text{average}} = (\text{Total volume Au})/V_{\text{atom}}(\text{number of particles})$$

$$= \pi \int_{\infty}^{0} x^3 \exp\left(-\left(x - \mu/\sqrt{2}\sigma\right)^2 \mathrm{d}x\right)/6V_{\text{atom}} \int_{\infty}^{0} \exp\left(-\left(x - \mu/\sqrt{2}\sigma\right)^2 \mathrm{d}x\right)$$

$$(1.3)$$

where V_{atom} is the volume of a gold atom, 0.0169 nm [325]. The Gaussian distribution was characterized by mean, μ (10.39 nm), and standard deviation, σ (0.78 nm). The number density of particles in the protein/metal conjugation preparations was thus calculated to be $\sim 3.8 \times 10^{12}$ particles/mL.

The number of gold atoms in each nanoparticle (N_{ap}) was also calculated according to Eq. (1.4) [326], where α refers to the edge of a unit cell (~ 0.40786 nm) and d refers to the diameter of the AuNP:

$$N_{\text{ap}} = (2/3)\pi(\mathrm{d}/\alpha)^3 \tag{1.4}$$

The concentration of AuNPs measured by the number of nanoparticles (C_{AuNP}) was calculated using Eq. (1.5), where n_{final} refers to the final concentration of HAuCl$_4$ precursor:

$$C_{\text{AuNP}} = n_{\text{fina}}/N_{\text{ap}} \tag{1.5}$$

The concentration of the surfactant on the surface of AuNPs (C_{DD}) was calculated according to Eq. (1.6), where S refers to the area of the stabilizer (DDAB) polar head (~ 0.65 nm^2) [327]:

$$C_{\text{DD}} = 2C_{\text{AuNP}}\left(\text{pd}^2/S\right) \tag{1.6}$$

The concentration of the original prepared AuNPs ($d \sim 9$ nm) was calculated as 10 nM (6.02×10^{12} particles/ml). They showed maximal absorption about ~ 1.07 at 540 nm. The nitrogen on the surface of AuNPs was calculated as 9.4 µM.

The polydispersity index is dimensionless and scaled such that values smaller than 0.05 are rarely seen other than with highly monodisperse samples. A polydispersity index of 0.1 is suggested as a suitable limit of monodispersity, and values greater than 0.7 indicate that the sample has a very broad size distribution [328].

Assuming a spherical shape and a uniform fcc structure (from high-resolution TEM analysis) [329], the average number of gold atoms (N_{ap}) for each type of nanosphere was also calculated by Eq. (1.7), where ρ is the density for fcc gold (19.3 g/cm^3) and M_{w} stands for atomic weight of gold (197 g/mol) [330]:

$$N_{\text{ap}} = \pi\rho\mathrm{d}^3/6 M_{\text{w}} = 30.89602 \ \mathrm{d}^3 \tag{1.7}$$

The molar concentration of the nanosphere solutions was calculated by dividing the total number of gold atoms (N_{total}, equivalent to the initial amount of gold salt

added to the reaction solution) over the average number of gold atoms per nanosphere (N_{ap}) according to Eq. (1.8), where V is the volume of the reaction solution in liter and N_A is Avogadro's constant. It is assumed that the reduction from gold(III) to gold atoms was 100% complete. The concentrations of each diluted solution may be calculated from this initial concentration according to their relative concentration:

$$C = N_{Total}/N_{ap} V N_A \tag{1.8}$$

The Scherrer equation, in X-ray diffraction and crystallography, is a formula that relates the size of submicrometer particles, or crystallites, in a solid to the broadening of a peak in a diffraction pattern. It is used in the determination of size of particles of crystals in the form of powder [35]. Scherrer Eq. (1.9) can be written as:

$$t = \frac{K\lambda}{\beta \cos\theta} \tag{1.9}$$

where $\tau(d)$ is the mean size of the ordered (crystalline) domains, which may be smaller or equal to the grain size; K is a dimensionless shape factor, with a value close to unity. The shape factor has a typical value of about 0.9, but varies with the actual shape of the crystallite; λ is the X-ray wavelength; β is the line broadening at half the maximum intensity (FWHM), after subtracting the instrumental line broadening, in radians. This quantity is also sometimes denoted as $\Delta(2\theta)$ and θ is the Bragg angle.

The Scherrer equation is limited to nanoscale particles. It is not applicable to grains larger than about 0.1–0.2 μm, which precludes those observed in most metallographic and ceramographic microstructures. It is important to realize that the Scherrer formula provides a lower bound on the particle size. The reason for this is that a variety of factors can contribute to the width of a diffraction peak besides instrumental effects and crystallite size; the most important of these are usually inhomogeneous strain and crystal lattice imperfections. If all of these other contributions to the peak width were zero, then the peak width would be determined solely by the crystallite size and the Scherrer formula would apply. If the other contributions to the width are nonzero, then the crystallite size can be larger than that predicted by the Scherrer formula, with the "extra" peak width coming from the other factors. The concept of crystallinity can be used to collectively describe the effect of crystal size and imperfections on peak broadening.

The number of silver atoms per nanoparticle (n_{ap}), particle radius (r_p), or silver nanoparticle/TAPP ratio can be also estimated by following (1.10) and (1.11) equations [331].

$$n = \frac{4}{3}\pi r_p^3 (\rho_{Ag}/M_{wAg}) N_A \tag{1.10}$$

$$\frac{1}{n}\left[Ag^0\right]/[TAPP] = [Ag\ nanoparticle]/[TAPP] \tag{1.11}$$

where ρ_{Ag} is the density of silver, M_{wAg} is the molecular weight of silver, $[Ag^0]$ is the concentration of silver atoms (assuming complete reduction), and TAPP is tetra (4-aminophenyl) porphyrin. The approximate diameter, ~ 10 nm, of the Ag nanoparticles is estimated by the position of the surface plasmon peak, ~ 390 nm. This estimate is in agreement with TEM measurements that indicate a distribution of Ag nanoparticle sizes ~ 7–20 nm in diameter.

Li et al. have reported that the asymmetric distribution of the AgNPs' size can be well fitted with the extreme function [332]:

$$y = A\exp(-\exp(-z) + z + 1) \tag{1.12}$$

where y is the percentage of the AgNPs with the size of x:

$$z = (x - x_c)/\sigma \tag{1.13}$$

x_c AgNP is the feature size at the most probable value, and σ is the standard deviation. The feature size (x_c) is ~ 80 nm at 5 min growth time, for example (Fig. 1.7). With the increase in growth time (t), the feature size is on the increase (Fig. 1.7). The average size (d) of AgNPs fits the relation:

$$d^3 - d_0^3 = kt \tag{1.14}$$

indicating that the Ostwald ripening (OR) mechanism dominates the crystal growth of AgNPs (Fig. 1.8) [333]. Such Ag–TiO$_2$ hybrids have been reported in the photocatalytic synthesis of AgNPs and adopted in the studies related to LSPR-assisted TiO$_2$ photocatalysis and SERS [334].

Small-angle X-ray scattering (SAXS) and small-angle neutron scattering (SANS) have been applied to elucidating information on the structure, morphology,
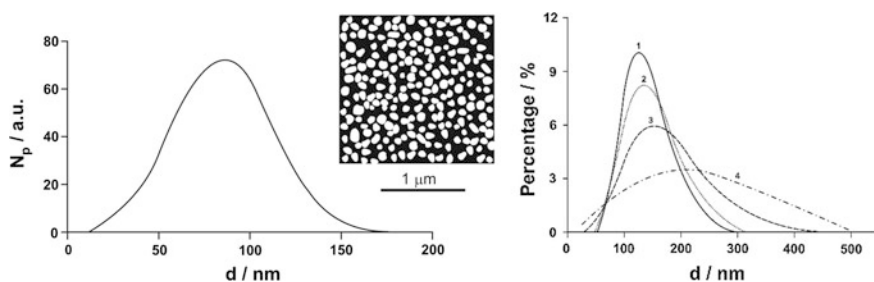
Fig. 1.7 Distribution of the AgNPs' size estimated with the extreme function Eq. (1.12). The *left panel* number of particles (N_p/a.u.) and *the inset* at *top-right corner*—typical SEM image, the size distribution of AgNPs grown on fresh TiO$_2$ films in the AgNO$_3$ solution. The *right panel (curves 1–4)* 10 min (x_c = 124 nm, σ = 39 nm), 16 min (x_c = 133 nm, σ = 51 nm), 30 min (x_c = 150 nm, σ = 67 nm), and 60 min (x_c = 203 nm, σ = 171 nm) [332]

Fig. 1.8 Fluorescent fluctuations fitted to an autocorrelation function used to determine diffusion coefficients, binding kinetics between unilamellar vesicles, and fluorescently labeled peptides: (*1*) 90% bound peptide, (*2*) 74, (*3*) 57, (*4*) 15 and (*5*) 0 [27]
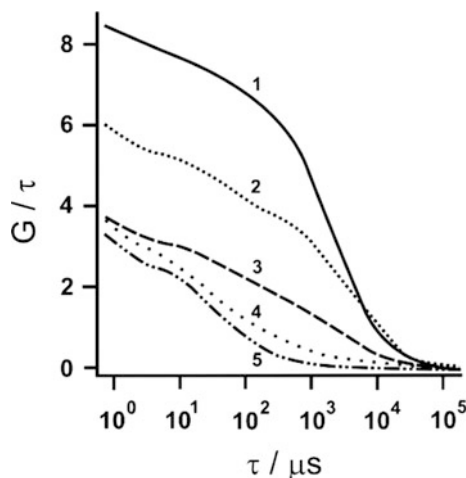
and characteristic intra-assembly spacings of a variety of polymer and biological based nanomaterials [335]. The principle mechanistic difference between SAXS and SANS is that X-rays are scattered by the electrons while neutrons are scattered by the nucleus. This has a direct impact on what can be observed and the magnitude of the observation (e.g., in neutron scattering, the scattering factor of carbon and hydrogen is of approximately equal magnitude but opposite sign while with X-rays, there is about a sixfold difference between carbon and hydrogen). A study by McKenzie and coworkers demonstrated a microscale flow system for simultaneous in situ monitoring of SAXS and UV-Visible spectra [336]. The system was used for the real-time size determination of thiol stabilized AuNPs (0.8–5 nm), and while no bioconjugates were investigated here, the technique could quite readily be applied to the characterization of nanoparticles and their conjugates. SANS was also used in combination with DLS and static light scattering (SLS) to elucidate the structure and core morphology of nanoparticles [337].

Energy-dispersive X-ray fluorescence (EDXRF) and energy-dispersive X-ray spectroscopy (EDX, EDS)) are all acronyms for instruments that use X-ray fluorescence to obtain elemental composition of materials such as soils, solids, sludges, liquids, or powders. Elemental analysis is the process of either qualitatively (which elements) or quantitatively (concentration levels of each element) identifying composition of a sample of material. From ppm (parts per million) to percentages, it is possible to obtain a complete breakdown of the composition of known or unknown material with instruments that use EDXRF, EDX, or EDS technology. Each of these acronyms refers to the same basic analytical technique which uses some form of X-ray excitation in order to obtain chemical characterization of a sample. The acronyms EDS and EDX are typically used when describing SEM systems that, when integrated with EDS/EDX, allow one to obtain the structure, texture, chemical, and elemental composition of a sample. It can be written as SEM/EDS or SEM/EDX.

The energy-dispersive X-ray fluorescence spectrometer, for example, irradiates the sample with X-rays and measures the energy (wavelength) and intensity of the generated fluorescent X-rays to determine the type and content of the elements comprising the sample. X-ray fluorescence spectrometry permits the nondestructive elemental analysis of solid, powder, and liquid samples as well as rapid, nondestructive testing for harmful elements in printed circuit boards and other electronic devices.

Neutral impact collision ion scattering spectroscopy (NICISS) uses detection of backscattered projectiles to determine concentration depth profiles of the elements. The NICISS technique uses noble gas ions (usually He^+) of energy 1–5 keV. When the projectile ions are within a few angstrom of the surface, they are neutralized and proceeded to penetrate into the surface. The projectiles may be backscattered (at an angle of up to 180°) upon collision with a target atom. This backscattering causes the projectiles to lose energy proportional to the mass of the target and is of the order of a few hundred eV. The final energy of the projectiles is determined via time of flight (TOF). Hence by knowing the initial and final energies of the projectile, it is possible to determine the identity of the target atom. The projectiles also experience an additional energy loss while penetrating through the bulk of the order of a few eV per angstrom. Hence, the depth that each target atom was hit can also be determined. From the TOF spectrum, it is then possible to gain the concentration depth profiles of the elements present in the sample. NICISS is able to probe to a depth of approximately 20 nm with a resolution of only a few angstrom.

Rutherford backscattering spectrometry (RBS) is an analytical technique used in materials science. Sometimes referred to as high-energy ion scattering (HEIS) spectrometry, RBS is used to determine the structure and composition of materials by measuring the backscattering of a beam of high-energy ions (typically protons or alpha particles) impinging on a sample. The energy loss of a backscattered ion is dependent on two processes: the energy lost in scattering events with sample nuclei and the energy lost to small-angle scattering from the sample electrons. The first process is dependent on the scattering cross section of the nucleus and thus on its mass and atomic number. The second energy loss process, the stopping power of the sample electrons, does not result in large discrete losses such as those produced by nuclear collisions. Instead, it creates a gradual energy loss dependent on the electron density and the distance traversed in the sample. In practice, then, a compositional depth profile can be determined from an RBS measurement. The elements contained by a sample can be determined from the positions of peaks in the energy spectrum. Depth can be determined from the width and shifted position of these peaks, and relative concentration from the peak heights. This is especially useful for the analysis of a multilayer sample, for example, or for a sample with a composition which varies more continuously with depth.

Fluorescence correlation spectroscopy (FCS) is similar to DLS in that it measures signal fluctuations due to diffusion, aggregation, interactions, etc., and has already been successfully applied to accurately estimate the hydrodynamic radius of fluorescent nanoparticles and fluorescent beads [36]. With the use of confocal microscopy, a laser interrogates a sample containing a small number of particles

and the fluorescent fluctuations observed within a confined optical volume are fitted to an autocorrelation function that can then be used to determine diffusion coefficients (Fig. 1.8). The diffusion coefficient can be correlated to the particle hydrodynamic radius via the Stokes-Einstein equation. In terms of NP-conjugates, FCS has also been used to determine binding kinetics between 100 nm unilamellar vesicles and fluorescently labeled peptides [338]. This technique has even been extended to observing metal-enhanced fluorescence (MEF) resulting from Cy5-labeled DNA hybridizing to DNA-modified silver nanoparticles by using the modified technique of fluorescence lifetime correlation spectroscopy [27]. Popular derivatives of FCS include dual-color FCS, which allows the user to cross-correlate data from two different fluorescent channels simultaneously [339] and Förster resonance energy transfer (FRET)-FCS, commonly called single-pair or particle (sp)FRET.

X-ray diffraction (XRD) is typically used to provide structural information about crystalline samples. It is also frequently used to characterize materials containing nanosized components embedded in an extended biological matrix, such as those found in tissue scaffolds and bone cements [39] or nanobioconjugate layered materials such as nanobiohybrids [340] where analysis of d-spacing changes upon bioconjugation between layers of the nanomaterial can be used to assess reaction completion or investigate the biomolecular orientation [341].

Raman and Krishnan observed that certain molecules scatter a small fraction of light which is different from the energy of the incident beam [342]. The scattered photons either gain or lose energy due to the vibrational and rotational modes of the molecules, which is known as Raman scattering, and the resulting Raman spectrum (scattering intensity vs wavelength) is characteristic of the chemical structure of the molecule. Albrecht and Creighton later recognized surface-enhanced Raman scattering (SERS) and reported the mechanism of enhancement based on the now well-known electromagnetic effect and chemical effect, respectively [343]. The electromagnetic field enhancement is due to the excitation of localized surface plasmons within the metal, which enhances the incident electric field intensity $|E^2|$ in the vicinity of the metals by 10^2–10^4 [344].

Raman techniques commonly applied to characterization include Raman spectroscopy and SERS. Raman spectroscopy measures the inelastic scattering of monochromatic radiation (UV, visible, or near IR) by a sample. The incident light becomes either Stokes or anti-Stokes shifted in wavelength resulting in sharp fingerprint Raman bands that are characteristic of the sample and complementary to infrared (IR) spectroscopy. This technique can be used to detect the effect of the surrounding environment on the molecule. Various types of surface enhancement-based techniques have been used to enhance the signal ranging from the magnetooptic Kerr effect in Fe_3O_4 nanoparticles [345] to surface-enhanced infrared absorption [346]. UV-V is absorption [347], fluorescence [348], circular dichroism [349], and Raman spectroscopy [350]. Among these techniques, surface-enhanced Raman spectroscopy has been particularly popular recently as people are still discovering better enhancement by experimenting with the surface structure and type of metals.

Surface-enhanced Raman scattering is an ultrasensitive vibrational spectroscopic technique that can be used for the detection of molecules on or in close proximity to the surface of metal nanostructures. The enhancement usually originates from chemical and electromagnetic (EM) contributions [37]. When a dye resonant with the interrogating laser is investigated, a further enhancement that results in surface-enhanced resonance Raman scattering (SERRS) [37] can be achieved. EM enhancement depends on the large local field enhancements that occur close to metallic surfaces when localized surface plasmon (LSP) resonances are excited and is the dominant enhancement mechanism in the case of a nonresonant absorbate [351]. "Hot spots" are the regions where the EM field is significantly enhanced beyond the average field intensity surrounding a nanoparticle and results in much greater SERS activity from these areas [352].

Furthermore, research on SERS has turned from roughened metal surfaces to the use of well-defined metallic nanoparticles to better understand and control the enhancement. Gold and gold nanoparticles are the most commonly used because of their strong LSPR band in the visible range. Researchers have studied the effect of the size, shape, and composition of the metal NPs on the SERS signal with the metal NPs dissolved in solution with the analyte or with the metal NPs attached to solid supports. It is well accepted that "hot spots" exist where the Raman enhancement is particularly strong at sharp regions of the metal with a high curvature or between metal nanoparticles coupled together. Some studies have even demonstrated single molecule sensitivity with SERS. Molecules that are not Raman active can be detected with SERS by using Raman labels and for molecules which cannot bind chemically to a metal surface, but dwell within close proximity to the metal surface, a partition layer can be used to increase the concentration of the analyte in close proximity to the metal surface [37]. Carbon nanotubes, for example, exhibit strong Raman scattering which has been found to be sensitive to isotope composition [353].

Spectroscopic techniques exploit the interaction of electromagnetic radiation with a sample material resulting in the wavelength-dependent absorption, and in the case of fluorescence re-emission, of radiation. Typically, a wavelength-dependent spectrum is produced with characteristic absorption/emission peaks inherent to the sample. The intrinsic UV-Visible absorbance properties of many nanoparticles can be used to monitor pertinent properties, such as concentration, size, and aggregation state. Both direct and in-direct analysis of UV-Visible spectroscopy data can also provide information on the NP-conjugate. Direct characterization is possible when the molecule has a distinct UV-Visible profile that remains discernible upon conjugation to the nanoparticle.

Fluorescence spectroscopy in both steady-state and time-resolved modes offers a powerful and sensitive technique for determining a number of the parameters associated with the immobilization of molecules to a nanoparticle surface including fluorophore local environment, molecule-NM coupling ratio, conformational state, and, in some instances, intra-assembly molecular distances [354]. Fluorescence techniques are of course limited to NP-bioconjugate components that have some form of either intrinsic or extrinsic fluorescence (or fluorescence quenching)

capacity. Obviously if conjugation of a fluorophore to the NP is desired as part of the final application, then fluorescence is an excellent method to determine the average number of fluorophores per nanoparticle, as demonstrated for cellulose and viral NMs [355].

Förster resonance energy transfer (FRET), fluorescence resonance energy transfer (FRET), resonance energy transfer (RET), or electronic energy transfer (EET) is a mechanism describing energy transfer between two light-sensitive molecules (chromophores). A donor chromophore, initially in its electronic excited state, may transfer energy to an acceptor chromophore through nonradiative dipole–dipole coupling. The efficiency of this energy transfer is inversely proportional to the sixth power of the distance between donor and acceptor, making FRET extremely sensitive to small changes in distance (Scheme 1.2). Measurements of FRET efficiency can be used to determine whether two fluorophores are within a certain distance of each other. Such measurements are used as a research tool in fields including biology and chemistry. FRET is analogous to near-field communication, in that the radius of interaction is much smaller than the wavelength of light emitted. In the near-field region, the excited chromophore emits a virtual photon that is instantly absorbed by a receiving chromophore. These virtual photons are undetectable, since their existence violates the conservation of energy and momentum, and hence, FRET is known as a radiationless mechanism. Quantum electrodynamical calculations have been used to determine that radiationless (FRET) and radiative energy transfer are the short- and long-range asymptotes of a single unified mechanism [38].
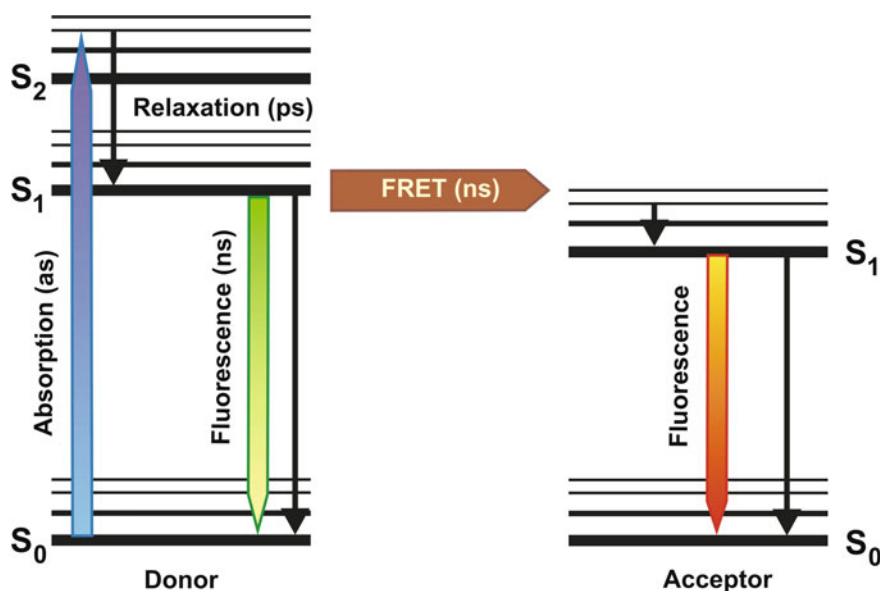
Scheme 1.2 Jablonski diagram of FRET with typical timescales

Förster resonance energy transfer is an increasingly popular microscopy technique used to measure the proximity of two fluorophores. Resonance energy transfer occurs only over very short distances, typically within 10 nm, and involves the direct transfer of excited state energy from the donor fluorophore to an acceptor fluorophore as an alternative to fluorescence emissive decay from the donor. Upon transfer of energy, the acceptor molecule enters an excited state from which it decays emissively (always of a longer wavelength than that of the acceptor emission). Thus, by exciting the donor and then monitoring the relative donor and acceptor emissions, either sequentially or simultaneously, one can determine when FRET has occurred and at what efficiency. Since fluorophores can be employed to specifically label biomolecules and the distance condition for FRET is of the order of the diameter of most biomolecules, FRET is often used to determine when and where two or more biomolecules, often proteins, interact within their physiological surroundings. Since energy transfer occurs over distances of 1–10 nm, a FRET signal corresponding to a particular location within a microscope image provides an additional distance accuracy surpassing the optical resolution (~ 0.25 mm) of the light microscope. Aside from spatial proximity, for efficient FRET to take place the FRET dye pair must also exhibit significant overlap of the donor's excitation spectrum with the acceptor's absorption spectrum. Herein though lies one of the experimental paradoxes of FRET. The spectral profiles of the FRET pair cannot be so separated that we have poor overlap, yet one wants to avoid "cross talk" between the two imaging channels; i.e., ideally, the donor emission filter set must collect only the light from the donor and none from the acceptor and vice versa. In practice, this can be somewhat realized by employing short bandpass filters that collect light from only the shorter wavelength side of the donor emission and the longer wavelength side of the acceptor emission. This can limit somewhat the photon flux from both donor and acceptor during a typical exposure, especially when we bear in mind that these measurements are best performed under conditions of reduced excitation power, such that we do not accelerate the rates of bleaching.

A number of researchers have used gold nanoparticle acceptors as quenchers in energy transfer studies with fluorescent donor species, and the resulting putative surface energy transfer (SET) process observed has been shown to have a nontraditional r^4 distance dependency, allowing in essence the ability to extend the reach of the molecular ruler [356]. In the process of FRET, initially a donor fluorophore absorbs the energy due to the excitation of incident light and transfer the excitation energy to a nearby chromophore, the acceptor. Energy transfer manifests itself through decrease or quenching of the donor fluorescence and a reduction of excited state lifetime accompanied also by an increase in acceptor fluorescence intensity. Scheme 1.2 is a Jablonski diagram that illustrates the coupled transitions involved between the donor emission and acceptor absorbance in FRET. In the presence of suitable acceptor, the donor fluorophore can transfer its excited state energy directly to the acceptor without emitting a photon.

There are few criteria that must be satisfied in order for FRET to occur. These are as follows: (i) the fluorescence emission spectrum of the donor molecule must overlap the absorption or excitation spectrum of the acceptor chromophore

(Fig. 1.9). The degree of overlap is referred to as spectral overlap integral (J). (ii) The two fluorophore (donor and acceptor) must be in the close proximity to one another (typically 1–10 nm). (iii) The transition dipole orientations of the donor and acceptor must be approximately parallel to each other. (iv) The fluorescence lifetime of the donor molecule must be of sufficient duration to allow the FRET to occur. Förster [357] showed that the efficiency of the FRET process (E_{FRET}) depends on the inverse sixth power of the distance between the donor and acceptor pair (r_{DA}).

When an electron in a molecule with a singlet ground state is excited (via absorption of radiation) to a higher energy level, either an excited singlet state or an excited triplet state will form. A singlet state is a molecular electronic state such that all electron spins are paired. That is, the spin of the excited electron is still paired with the ground state electron (a pair of electrons in the same energy level must have opposite spins, per the Pauli exclusion principle). In a triplet state, the excited electron is no longer paired with the ground state electron; that is, they are parallel (same spin). Since excitation to a triplet state involves an additional "forbidden" spin transition, it is less probable that a triplet state will form when the molecule absorbs radiation. Intersystem crossing is a radiationless process involving a transition between two electronic states with different spin multiplicity (Scheme 1.3).

One can approximate the fluorescence decays by considering them equal to a sum of exponential functions to get lifetime according to the equation [358].

$$D(t) = \sum_{i=1}^{n} a_i \exp(-t/\tau_i) \qquad (1.15)$$

where τ_i are the fluorescence lifetimes of various fluorescent forms and a_i are the pre-exponential factors depending on the molar extinction coefficients of the respective fluorophores. The mean lifetime is defined as:

Fig. 1.9 Absorption and fluorescence spectra of an ideal donor–acceptor pair. *Weak blue colored* region is the spectral overlap between the fluorescence spectrum of donor (absorption: *red full line*; emission: *dotted red line*) and absorption spectrum (absorption: *blue full line*; emission: *dotted line*) of acceptor [357]
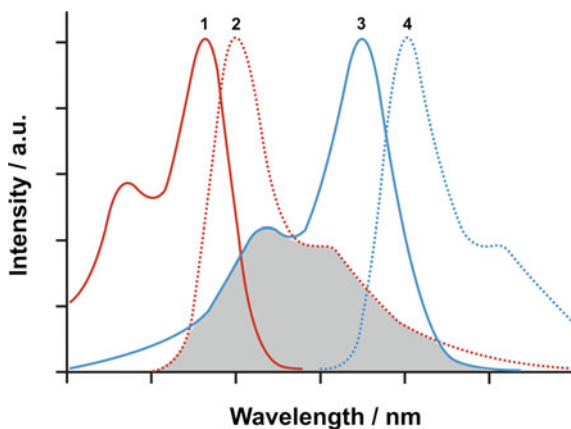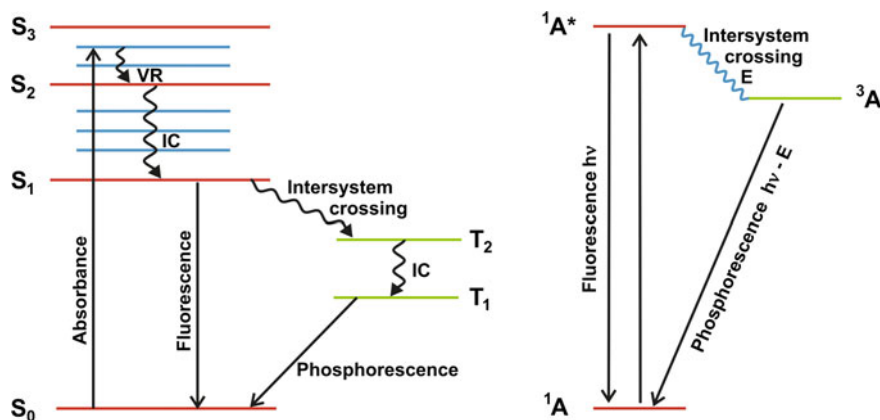
Scheme 1.3 Diagram illustrating the radiation (fluorescence and phosphorescence) and radiationless [internal vibrational redistribution (*IVR*), internal conversion (*IC*) and intersystem crossing (*ISC*)] processes

$$\tau_{av} = \sum_{i=1}^{n} f_i \tau_i \tag{1.16}$$

where $f_i = a_i \tau_i / \Sigma_j a_j \tau_j$, and the amplitude-weighted lifetime is calculated as:

$$\langle \tau \rangle = \sum_{i=1}^{n} a_i \tau_i \tag{1.17}$$

The fitting procedure uses an iterative fitting procedure based on the Marquardt algorithm [359]. Deviation from the best fit is characterized by the reduced chi-square statistic, χ^2, calculated by measuring the "noise" at a time t and applying a special procedure developed for the case of the stroboscopic optical boxcar [360]. Steady-state fluorescence and fluorescence binding experiments were performed with 295 nm excitation wavelength to select tryptophan (Trp) residues. The dissociation constants were calculated from the saturation curves using the method described in Ref. [361].

The intensity decay of the molecules provides an easy accuracy for the determination of averaged lifetimes. Fluorescence resonance energy transfer parameters can be estimated using steady-state information. The FRET efficiency (*E*) was determined by measuring the decrease of the fluorescence intensity of the donor (D, protein) in the presence of acceptor (A, emodin):

$$E = 1 - F/F_0 \tag{1.18}$$

where F_0 represents the maximum of the fluorescence emission intensity of the protein in the absence of ligand and F the maximum of the fluorescence emission

intensity of the 1:1 protein-ligand complex. The Förster critical radius, $r_0 = 0.2180$ $(\kappa^2 \Phi_D n^{-4} J_{D-A})^{1/6}$, is the D–A distance corresponding to an energy transfer efficiency of 50%. $\kappa^2 = 0.66$ as the orientation factor, $\Phi_D = 0.15$ as the quantum yield of the Trp, and $n = 1.33$ for the refraction index of the medium were used. J_{D-A} is the spectral overlap integral between the excitation spectrum of A and the emission spectrum of the D.

The overlap integral J_{D-A} was calculated using the expression:

$$J_{D-A} = C \int_0^\infty I_D(\lambda) E_A(\lambda) \lambda^4 d\lambda \tag{1.19}$$

where I_D is the emission spectrum of the D, E_A is the excitation spectrum of the A, and C is the normalization factor. The distance between D and A, r_{D-A}, was calculated using the relation:

$$r_D - A = (1/E - 1)^{1/6} r_0 \tag{1.20}$$

and the FRET rate constant, k_{ET}, was calculated according to:

$$k_{ET} = \frac{1}{\tau D} (r_0/r)^6 \tag{1.21}$$

Thermal techniques can aid in determining the amount of conjugated molecule as well as both the nanoparticle and the molecule's (polymer's) thermal stability. Typically, for techniques such as differential scanning calorimetry (DSC), microgram amounts of sample are required for analysis (depending on composition). Thermal gravimetric analysis (TGA) is a method that utilizes a high-precision balance to determine changes in the weight of a bulk sample relative to changes in temperature and has been used to characterize a variety of nanoparticles functionalized with biomolecules, including AuNPs functionalized with dendrons, hydroxyapatite grown on Au-fibrin NPs, as well as the amount of paclitaxel bound to a nanoparticle drug delivery system [40]. DSC and isothermal titration calorimetry (ITC) are other thermally based methods that can provide bulk information about the NP-conjugate. DSC is used to study various material transitions including melting, crystallization, glass transition, and decomposition. Subsequent analysis can indicate the state of the NP-conjugate including the stability of the biomolecule and structural information on both the NP and molecule including underlying crystallinity and how the different components are interacting with each other. DSC has also been used to help elucidate the structure and stability of surface coatings of NP-conjugates as well as the state of their therapeutic payloads. For example, DSC has been used to probe the stability of lipid bilayers when the bilayers were embedded with silver NPs [362]. ITC provides further potential to investigate the stoichiometry, affinity, and enthalpy of the NM-biomolecule

interaction, as demonstrated by studying the corona layering mechanism for various polymeric NPs and binding proteins.

Thermophoresis or thermodiffusion involves localized heating of a sample and monitoring the resulting motion of the particles due to the temperature gradient [306, 363]. Sperling and coworkers compared thermophoresis to various other analytical techniques for their ability to determine the size of various PEG-functionalized quantum dots (QDs) [306]. They found that the reported particle diameters were highly dependent upon the particular technique applied along with the underlying physical principles and assumptions used to determine particle size.

The thermal gravimetric and differential thermal analysis (TG-DTA) obtained in nitrogen gas provided additional evidence for the relationship between the redox reaction and structural stability. As expected, the TG-DTA of $[Na(H_2O)_2]_{0.25}MoO_3$, for example, showed two stages of weight loss with distinct endothermic peaks at 100 and 240 °C, which were assigned to the dehydration on the external surface and the interlayer [364].

A recent comparison of four techniques, AFM, FESEM, TEM, and NSOM, concluded that a combination of at least one scanning probe method (AFM, NSOM) and one accelerated electron method (TEM, FESEM) is required to obtain the most accurate information regarding the nanometer-scale architecture of the particle-based surfaces [365]. Sample preparation is also a key and crucial factor for obtaining good AFM imaging. The formation of self-assembled monolayers (SAMs) on various surfaces such as glass [366], silicon [367], and gold [368] has been previously examined. The morphologies and crystallographic data of the three-dimensional nanoparticle superlattices are determined using scanning electron microscopy (SEM), high-resolution transmission electron microscopy (HRTEM), transmission electron diffraction (TED), and small-angle X-ray diffraction (XRD). As nanoparticles are too small to be seen by conventional optical microscopes, SEM and scanning probe microscopy (SPM), such as scanning tunneling microscopy (STM) and atomic force microscopy, as well as TEM are used for size and topography characterization of metal nanoparticles. The basic concept of SPM techniques is the detection of interactions between a scannable nanoscale probe and a nearby surface, in order to map and measure local surface properties. STM technique has been used for imaging the atomic structure of supported NMNPs [369]. Atomic force spectroscopy (AFM) can also be used for surface force information, fabrication of nanosystems, sensing, etc. [370]. Contact-mode AFM technique is used to obtain lattice resolution, whereas the noncontact mode can give the atomic resolution of surfaces. Unlike other microscopy techniques, AFM can be used for both dry and wet samples of individual ensembles and clusters of nanoparticles at ambient conditions.

Characterization of the morphology and the internal structure of nanocrystals are routinely done by microscopy techniques [371]. These techniques are based on visualizing a sample using light, electrons, or a scanning probe [266]. Traditional

optical light microscopy (sometimes referred to as bright field microscopy) and its myriad of fluorescent derivatives were until recently, however, unable to resolve nanoscale features <200 nm due to diffraction limitations. As a result, they found limited application in the characterization of individual NP-conjugates.

Conventional TEM is used for the determination of size, size distribution, and the number density of the particles easily and accurately. However, TEM often provides only partial information about the actual particle shape. The various profiles observed in the images may correspond to various projections of a particle. For example, a truncated octahedra with {111} and {100} facets seen along a [372] axis perpendicular to the sample show a square profile [373]. A square outline can also mean a cube or square pyramid. When the same nanocrystal sits on one of its edges between two {111} facets, the particle image presents a rhomboid shape with two corners cut off [373].

The electron diffraction pattern obtained from high-resolution TEM (HRTEM) and sometimes selected-area electron diffraction (SAED) techniques may provide information regarding the atomic structure of the particles, lattice plane fringes, and the nature of the facets such as twinning, twinning planes, surface reconstruction. Energy-dispersive X-ray analysis (EDAX) available with analytical TEM or SEM and X-ray photoelectron spectroscopy (XPS) can be used to determine surface elemental and surface compound composition. In combination with HRTEM, elemental mapping emerges as a very useful technique for imaging nanoparticles at high magnification to determine their local compositions at specific areas of interest [236, 374].

TEM and SEM readily obtain single particle resolution and are more frequently applied to characterizing the nanoparticle core along with core@shell size and/or structure. Both techniques rely on the wave nature of electrons to directly illuminate a sample in either transmission or reflectance modes, respectively, and generate an image [266]. Since SEM uses electrons to image a surface in reflectance mode, it is mainly used to image nanoparticle core materials [139] but has the added advantage of a larger imaging field of view than the TEM [375]. SEM has less resolving power for features <20 nm than TEM, although the technology is steadily improving even in this area. SEM is often combined with energy-dispersive X-ray spectroscopy (EDX) analysis to confirm elemental composition of the nanoparticle [376]. Environmental SEM (ESEM) does allow sample imaging under low pressure, fairly high humidity, and without the requirement of a conducting overcoat but has found limited use to date for the study of NPs and their bioconjugates [377].

However, the particle sizes obtained with different techniques vary widely, illustrating the difficulties in reliable AuNP characterization. The differences are particularly large for the 30, 50, and 90-nm citrate-capped AuNPs, where the polydispersities are relatively high. These differences can be attributed to the inherent bias associated with different techniques. For example, the DLS particle sizes are consistently larger than those obtained with other techniques [274].

Nominal particle sizes 10 and 50 nm estimated by following techniques:

$$10.1 \ (TEM, \ a), \ 8.8 \ (TEM, \ b), \ 9.7 \ (MBI), \ 11.6 \ (DLS, \ c), \ 19.3 \ (DLS, \ d) \ and \ 10 \ (LSPR)$$

$$(1.22)$$

$$49.6 \ (TEM, \ a), \ 38.4 \ (TEM, \ b), \ 40.2 \ (MBI), \ 46.7 \ (DLS, \ c), \ 54.1 \ (DLS, \ d) \ and \ 51 \ (LSPR)$$

$$(1.23)$$

where

(a)   TEM particle sizes provided by the vendors,
(b)   TEM CSPI (cross-sectional perimeter integration) approach,
(c)   DLS particle sizes based on mass histogram, and
(d)   DLS particle sizes based on intensity histogram.

This may be related to the fact that DLS measures the hydrodynamic radius of the AuNP and its surface adsorbates. Because the AuNP surface is usually coated with citrate or other stabilizing agent in the solution, DLS measurement is expected to give larger particle sizes. The deviation of the DLS results, in particular the ones obtained with intensity histograms from that of TEM, might also have resulted from the artifacts related to DLS measurement procedure or data analysis. The relatively larger LSPR particle sizes are not surprising either as the molar extinction coefficients of larger nanoparticles are significantly higher than those of smaller nanoparticles. Importantly, the results obtained from the TEM analysis using the CSPI method and the 2-mercaptobenzimidazole (MBI) adsorption method are remarkably similar for all the AuNPs we tested. The largest relative difference between the particle sizes from these two methods is less than 10%. In addition, AuNP surface areas per unit volume of AuNP solutions determined with these two methods are consistently larger than that obtained with other techniques with the only exception being the DLS result for the 90-nm AuNP. This result provides critical cross-validation of these two analytical methods. It should not be surprising because by design the CSPI method and ligand adsorption method can both accommodate some morphological irregularity of the AuNPs. However, compared to the TEM CSPI method, the MBI adsorption technique is much simpler to implement. The excellent agreement between the TEM CSPI results and that obtained with MBI ligand adsorption method indicates that the MBI packing density on the AuNPs is independent of the particle size of AuNPs in the size ranging from 10 to 100 nm in diameter. This result is consistent with what was reported by Elzey et al. who demonstrated that the packing densities of 3-mercaptopropionic acid (MPA) on AuNPs are the same for AuNPs in the size range from 5 to 100 nm [378]. MBI and MPA adsorption results suggest that the difference in the curvature of AuNPs with diameter equal to or larger than 5 nm does not have significant impact on the organothiol packing density. This result is not surprising, given the subsquare-nanometer footprint of MBI and MPA on the AuNP surfaces [378, 379].

The AuNP solution was characterized with the MBI adsorption method and ICP-OES determination of the Au^{3+} concentration, and the results were compared with data obtained using the other techniques [274]:

Particle size in nm (method) is:

$$10.2 \ (TEM, \ a), \ 9.5 \ (MBI), \ 12.6 \ (DLS, \ c), \ 15.9 \ (DLS, \ d) \ and \ 12.6 \ (LSPR) \tag{1.24}$$

AuNP concentrations in nM are:

$$13 \ (TEM, \ a), \ 16 \ (MBI), \ 7 \ (DLS, \ c), \ 3.4 \ (DLS, \ d) \ and \ 8 \ (LSPR) \tag{1.25}$$

Surface area per unit volume AuNP in cm^2/ml is:

$$25.6 \ (TEM, \ a), \ 27.4 \ (MBI), \ 20.7 \ (DLS, \ c), \ 16.4 \ (DLS, \ d) \ and \ 20.7 \ (LSPR) \tag{1.26}$$

Again, TEM analysis by CSPI and the MBI adsorption method give the smallest particle size and highest AuNP surface area per unit volume of AuNP solution.

The LSPR particle sizes were determined from the peak UV-Vis absorption wavelength (λ_{SPR}) using the formula reported by Haiss et al. [324], while the LSPR AuNP concentrations were calculated according to Liu et al. [330]. It should be noted that the equivalent spherical particle size and AuNP concentration for this MBI adsorption method are calculated on the assumption that all the nanoparticles are spherical and monodispersed, which is the same assumption used by the current AuNP LSPR method.

Dark-field microscopy (DFM) and near-field optical microscopy allow direct examination of single particles, providing deeper understanding of the optical properties of individual nanoparticles [41]. Silver and gold nanoparticles, due to their localized surface plasmon resonance modes, absorb and scatter light so intensely that single nanoparticles are easily detected by eye using DFM. Rayleigh scattering spectra of single metal particles can be recorded with an optical microscope using either total internal reflection or dark-field illumination, allowing measurement of the single-particle spectral properties [380]. Experimental techniques, such as electron energy loss spectroscopy (EELS), have been proven to be successful in imaging localized optical excitations with high resolution to reveal their dramatic spatial variation over single nanoparticle by using photons and electron beams [42, 43]. Another surface probe microscopy technique, near-field scanning optical microscopy (NSOM also known as SNOM), breaks the optical resolution limit of light microscopy by placing the detection probe extremely close (at distances much smaller than the wavelength of light) to the surface to be analyzed. Scanning near-field optical microscopy (SNOM), which combines the SPM technique with the principle of the near-field optical method, has been applied to obtain spectroscopic information with nanometer spatial resolution [381]. NSOM has the advantage of combining optical and/or spectroscopic data with

high-resolution surface topographical information. Contrast properties, such as phase contrast, polarization, fluorescence, staining, that are available through traditional optical microscopy are also available with NSOM.

SEM and its variants, such as field emission (FE)-SEM and ultrahigh-resolution FESEM, can produce high-resolution images of sample surfaces [174]. EE-SEM involves the analysis of the energy distribution of primary electrons that are inelastically scattered upon interaction with the specimen in the TEM [382].

The discrete dipole approximation (DDA) technique has been extensively used, and the mathematical formalism, advantages, disadvantages, and recent developments of this technique have been thoroughly described [44]. In the present application, the DDA technique calculates the extinction spectrum by representing the SiO_2-encapsulated gold prism structure with a cubic array of polarizable dipoles. The polarizability of each dipole is a function of the local dielectric constant, either gold or SiO_2. Each dipole is polarized upon application of an electromagnetic plane wave and then self-consistently coupled to determine overall particle optical properties such as extinction.

Mass spectrometry (MS) is an analytical chemistry technique that helps identify the amount and type of chemicals present in a sample by measuring the mass-to-charge ratio and abundance of gas-phase ions. A mass spectrum (plural spectra) is a plot of the ion signal as a function of the mass-to-charge ratio. The spectra are used to determine the elemental or isotopic signature of a sample, the masses of particles and of molecules, and to elucidate the chemical structures of molecules, such as peptides and other chemical compounds. Mass spectrometry works by ionizing chemical compounds to generate charged molecules or molecule fragments and measuring their mass-to-charge ratios. In a typical MS procedure, a sample, which may be solid, liquid, or gas, is ionized, for example, by bombarding it with electrons. This may cause some of the sample's molecules to break into charged fragments. These ions are then separated according to their mass-to-charge ratio, typically by accelerating them and subjecting them to an electric or magnetic field: Ions of the same mass-to-charge ratio will undergo the same amount of deflection.

Nuclear magnetic resonance (NMR) spectroscopy and magnetic resonance imaging (MRI) measure the intrinsic magnetic moment of certain nuclei, typically either hydrogen (^{1}H) or carbon (^{13}C), in the presence of an applied magnetic field [383]. NMR spectroscopy is an analytical chemistry technique used in quality control and research for determining the content and purity of a sample as well as its molecular structure. For example, NMR can quantitatively analyze mixtures containing known compounds. For unknown compounds, NMR can either be used to match against spectral libraries or to infer the basic structure directly. Once the basic structure is known, NMR can be used to determine molecular conformation in solution as well as studying physical properties at the molecular level such as conformational exchange, phase changes, solubility, and diffusion. In order to achieve the desired results, a variety of NMR techniques are available. NMR spectroscopy, thus, can provide physical, chemical, structural, or environmental

information about the species under study as well as information concerning the dynamic interactions of many molecules, including proteins and nucleic acids.

Nanoparticle purity is important when it comes to more precise determination of optical and electronic properties, in assessing structure-function relationships in toxicology studies and for determining the functional role of the ligand on the nanoparticle surface. A number of techniques can be used to purify nanoparticles such as extensive washing with solvents or fractional crystallization. In cases where the nanomaterials and ligands are water soluble, dialysis has shown to be effective.

Dialysis, filtration, extraction, and differential precipitation represent the most common methods applied to NP-(bio)conjugate purification. Dialysis and membrane filtration methods in particular are relatively cheap, commercially available, and simple to use. Both use some form of permeable or semipermeable membrane with a given size or molecular weight cutoff (MwCO) value to separate the biomolecule from the NP-conjugate. In the case of dialysis, the membrane containing the sample to be purified is immersed in a large excess volume of liquid and species of Mw < membrane MwCO (typically the biomolecule) flow in the direction of high to low concentration [384]. Filtration devices can be gravity driven, but generally centrifugation is used to increase the speed and efficiency of the process [385].

Diafiltration has been shown to be an effective method for purifying water-soluble nanoparticles with low polydispersity, high purity, minimal waste generation, and improved yield [386]. In addition, ultracentrifugation using PES (polyethersulfone) membrane-supported concentrators with selected nominal MwCOs minimizes membrane blockage and is also 98% effective in separating biomolecules from nanomaterials [387].

Chemical extraction and differential precipitation are other potentially efficient but largely underused purification techniques. In a relatively simple strategy that highlights the possibilities available, Zhang and coworkers recently used a biphasic cap exchange extraction method to generate amino acid functionalized QDs [388]. The purification and separation of water-soluble thiolated 3-nm AuNPs is possible according to Sweeney et al. [386]. In this procedure, the solution of AuNPs is removed using a peristaltic pump through a diafiltration membrane. Small molecule impurities or small NPs are eluted in the permeate, while the large nanoparticles are retained. The expanded view is that of a hollow-fiber-type diafiltration membrane depicting the elution of small impurities and nanoparticles and the retention of larger particles. Kornberg's group [389] introduced the precipitation method in order to obtain $Au_{102}(MBA)_{44}$ (p-mercaptobenzoic acid (MBA)). The prepared MBA-protected AuNPs were precipitated by the addition of ammonium acetate or NaCl and methanol and then collected in a microfuge by several centrifugation steps to yield purified $Au_{102}(MBA)_{44}$.

^{1}H-NMR spectroscopy and thin-layer chromatography (TLC) were used to assess the amount of excess precursor molecules or impurities in the samples. For example, representative TLCs of unpurified and purified Au–GSH and Au–GSH–$(Trp)_2$ nanoparticles as well as free amino acids and GSH (glutathione) were shown. Two spots were observed in the TLC with unpurified nanoparticles corresponding

to AuNPs, free amino acids, or GSH, whereas only one spot was observed with purified nanoparticles. This was also observed with all the peptide-capped AuNP derivatives, demonstrating that TLC is a convenient method to confirm nanoparticle purity. UV-Vis and fluorescence spectroscopies were also used to confirm the absence of tryptophan (Trp), methionine (Met), histidine (His), and dansylated arginine (DanArg), which absorb in the UV-Vis region (200–330 nm). Analysis was performed on samples collected after ultracentrifugation. No characteristic absorption in this region of free ligands was observed. Analysis of the permeate by fluorescence also showed no spectroscopic evidence of unconjugated Trp (λ_{ex} = 280 nm, λ_{em} = 356 nm) and DanArg (λ_{ex} = 330 nm, λ_{em} = 541 nm) ligands. These techniques confirm that ultracentrifugation produces highly pure materials [390].

The ^{1}H-NMR spectra of unpurified peptide-stabilized AuNPs exhibited a complicated spectrum with sharp signals corresponding to protons of the peptide-capped AuNPs and free amino acids, which is consistent with free ligands present in the sample [386]. In contrast, the concentrated pure peptide-capped AuNPs in 100% D_2O showed line broadening and loss of splitting patterns from proton–proton coupling, making it difficult to assign any proton signals. To confirm conjugation of terminal amino acids, the ^{1}H-NMR spectra of samples were taken of AuNPs etched with cyanide in water and then dissolved in methanol. These samples showed proton signals between 7 and 8 ppm corresponding to amines, amides, and aromatic protons. For example, the ^{1}H-NMR spectra of etched Au–GSH–(Trp)$_2$ in methanol showed characteristic signals of the –CH groups of Trp (7.70–7.35 ppm) shifted downfield from free tryptophan, amide protons on the peptide backbone (8.03 ppm), and the amine group of Glu residue (8.55 ppm). Note that the amide proton signal is small because of its rapid exchange rate [391]. When compared to etched Au–GSH and free oxidized GSH, Au–GSH–(Trp)$_2$ showed a set of multiplets between 3.55 and 2.90 ppm that corresponds to the –CH and –CH$_2$ groups of glutamic acid (Glu), cysteine (Cys), and Trp on the peptide backbone. The –CH bond (–NH–CH–C(O)–) of Trp was shifted downfield from free Trp and overlaps with the D_2O signal. While the high signal-to-noise ratio and the baseline made it difficult to perform integration, these spectral changes in ^{1}H-NMR are consistent with amide bond formation upon Trp coupling to the Glu and glycine (Gly) residues. Although there were small unidentified signals that indicate non-bonded impurity, based on the splitting pattern, the predominant product was determined to be the disulfide species, Trp$_2$–GS–SG–Trp$_2$, which has a white appearance [390].

Reported herein is a ligand adsorption method for determining the surface areas, concentrations, and sizes of colloidal AuNPs, using 2-mercaptobenzimidazole (MBI) as the probe ligand [274]. The general principles for the determination of the surface area and particle size of AuNPs using quantitative ligand adsorption are outlined below. The amount of MBI adsorbed per milliliter of AuNP solution, Γ_{MBI} (nanomoles per milliliter of AuNP solution), was determined as the difference between the amount of MBI added and the excess MBI in the supernatant. The

surface area (S_{area}) afforded per milliliter of AuNP solution (in square centimeters per milliliter of AuNP solution) is then calculated using Eq. 1.27 (see also Eq. 1.26):

$$S_{area} = \Gamma_{MBI}/P_{MBI} \qquad (1.27)$$

where P_{MBI} (0.574 nmol/cm^2) is the MBI packing density on AuNPs. The equivalent spherical particle diameter d_{AuNP}, that is, the diameter of the AuNPs that are assumed perfectly spherical and monodispersed, can be calculated with Eq. 1.28. d_{Au} (19.3 g/cm^3) is the density of gold and $a = 60$ was obtained from unit conversions. The total gold ion content (C_{Au}^{3+} in parts per million) is experimentally quantified by inductively coupled plasma-optical emission spectroscopy (ICP-OES) after digestion of a known volume of AuNP solution with aqua regia.

$$d_{AuNP} = aP_{MBI}C_{Au}^{3+}/\Gamma_{MBI}\,\rho_{Au} \qquad (1.28)$$

The AuNP concentrations (C_{AuNP}) can also be easily calculated using Eq. 1.29. The results of this ligand adsorption method are compared with those obtained using the DLS, LSPR, and TEM methods for a series of commercial citrate-capped AuNPs with nominal particle sizes of 10, 30, 50, and 90 nm in diameter:

$$C_{AuNP} = 3.17 \times 10^3 \left(C_{Au}^{3+}/D_{AuNP}^3\,d_{Au}\right) \qquad (1.29)$$

The advantage of this cross-sectional perimeter integration (CSPI) method is that the AuNP does not have to be perfectly spherical, as long as the cross section of the AuNP can be approximated to be circular. After determining the surface areas of individual AuNPs, the average equivalent spherical AuNP diameter d is determined using Eq. 1.30:

$$d_{CSPI} = \sqrt{(S_{area}/\pi)} \qquad (1.30)$$

where S_{area} is the average surface area of the AuNPs analyzed using the CSPI method [274].

The results show that the amounts of MBI adsorbed onto AuNPs are essentially the same over the entire investigated pH range (over three pH units), indicating the applicability of this MBI adsorption method for general AuNP characterization. The near-perfect linear correlation between the amounts of MBI adsorbed and the volume fraction of AuNPs indicates that this ligand adsorption method can be used to predict the AuNP surface area afforded by AuNPs in the sample volume or the nanoparticle concentration if the equivalent AuNP size is known (Fig. 1.10).

The diffraction band centered around at 2θ of 15°, 21.6°, 25.3°, and 29.3° correspond to reflections of graphene (002), Au (111), Ni (111), and Ni (200), respectively (for graphene sample coated with 2.5 nm Au, Fig. 1.11, left panel). In this X-ray spectra, diffraction peak corresponding to substrate Si is not observed as X-rays effectively stopped in Ni layer for a grazing angle of 0.3°. A continuous shift

Fig. 1.10 AuNP concentration dependence of MBI adsorbed onto AuNPs. The AuNP solutions were prepared by mixing the concentrated 30-nm AuNPs with water to yield AuNP volume fractions (v_f) from 0.2 to 1 [274]
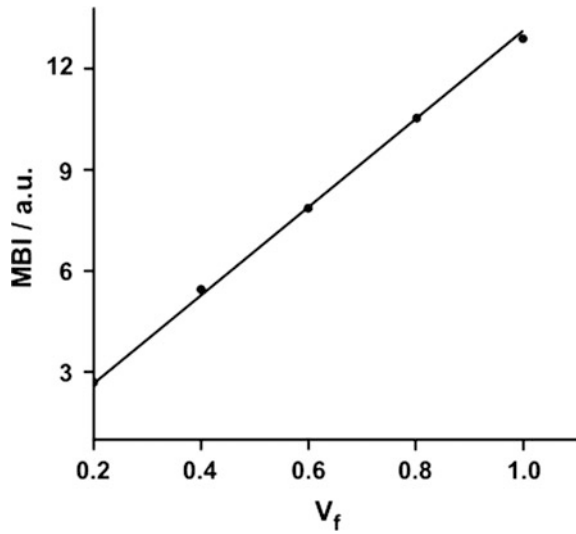
Fig. 1.11 Stacked XRD pattern of graphene peak with different Au film thickness (pristine (*1*), 0.5 nm Au (*2*), and 2.5 nm Au (*3*) (*left panel*) and graphene peak (*G*p) position and relative strain (ε_{rel})(%) with respect to pristine sample versus Au film thickness (*right panel*) [394]
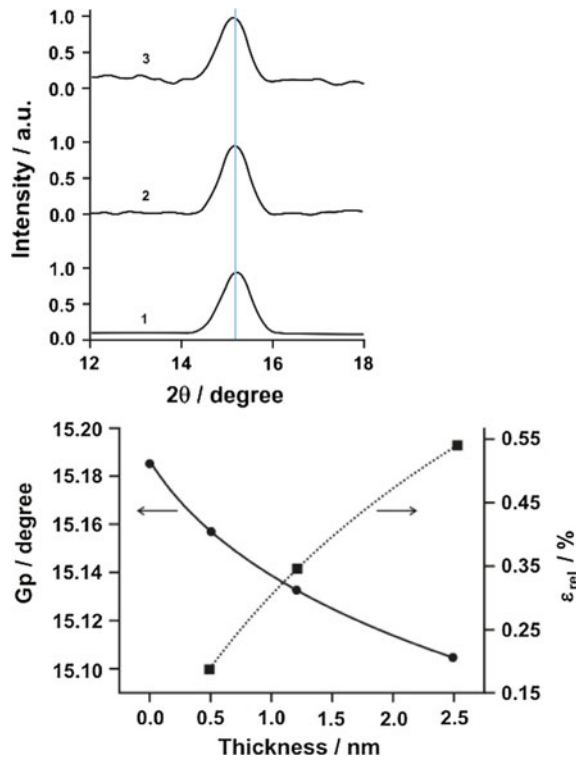
in the graphene peak position toward the lower 2θ angle with increase in Au film thickness is observed. The positions of all other peaks in the spectra remain same. The graphene peak position versus Au film thickness is plotted in Fig. 1.11, right panel. A continuous shift in peak position in Fig. 1.11, right panel, clearly indicates that the lattice constant of graphene increases with increase in Au content on surface of graphene. The change in lattice constants in diffraction spectra results from the strain arising due to interaction of deposited gold atoms with graphene [392]. The peak shift is toward the lower 2θ angle, and therefore, the strain is compressive in nature. The strain in graphene lattice can be calculated quantitatively by differentiating Bragg's law. According to Bragg's law:

$$2d \, \sin\theta = n\lambda \tag{1.31}$$

where d is interlayer spacing, θ is Bragg diffraction angle, n is an integer, and λ is X-ray wavelength. The strain (ε) in graphene lattice is calculated by differentiating Bragg's law with respect to d and θ, keeping λ constant and Eq. (1.31) becomes [392]

$$2d \, \cos\theta\delta\theta + 2 \, \sin\theta\delta d = 0 \tag{1.32}$$

$$\varepsilon = \Delta d/d = -\Delta\theta \, \cot\theta \tag{1.33}$$

$$\varepsilon = (d - d_0)/d_0 = -\Delta\theta \, \cot\theta \tag{1.34}$$

here d_0 is the interlayer spacing in the unstrained lattice, d is the interlayer spacing of strained lattice, and $\Delta\theta$ is the shift in the X-ray reflection resulting from strain. The values of strain (ε) calculated using Eqs. (1.31–1.34) are 0.19, 0.35, and 0.54% for 0.5, 1.2, and 2.5 nm gold film thickness, respectively. Thus, engineering of the strain in graphene is possible by simply adding the gold content on graphene. The origin of stress generation in substrate upon which thin film is deposited arises from intrinsic stresses in thin films [393].

In the early stage of growth known as nucleation or pre-coalescence, the film consists of individual islands or nuclei. The nature of chemical bonding of atoms at the surface is different from that of interior atoms in islands. Due to the difference in bonding, equilibrium interatomic distance between surface atoms is different from interior atoms. As a result, interior atoms exert a force on surface atoms known as surface stress. This surface stress exerts a pressure equal to the difference between the pressure of island and surrounding vapor known as Laplace pressure [395] (ΔP):

$$\Delta P = \frac{2f}{r} \tag{1.35}$$

where f is surface stress and r is the radius of spherical island. In the pre-coalescence regime, Laplace pressure on the surface induces compressive stress in the islands and this compressive stress is measured by substrate curvature [396].

The nonlinear α-relaxation can be well described by the Vogel-Fulcher-Tammann (VFT) relationship:

$$\sigma_{dc} = \sigma_0 \exp(-D/T - T_0) \tag{1.36}$$

where σ_0 is the pre-exponential factor; D_{mc} is a material constant; and T_0 is the so-called Vogel temperature related to the glass transition temperature [397]. From the fitting of the experimental data to this model, T_0 can be calculated and the glass transition temperature (T_g) can be assigned as previously described [398] (where T_0 is 50 K below T_g) [399].

Preformed-seed-mediated growth is a popular colloid-chemical method for the preparation of a wide variety of noble metal nanoparticles [45, 374, 400, 401]. In the seeding growth, fine metal particles are first produced by reducing metal ions with a suitable reducing agent. These fine metal particles are called seed particles, since in a subsequent step they are added to growth solutions containing the same or different metal ions along with other additives such as dopants, ligands, and surfactants. Here, the metal ions of the growth solutions are reduced at the surface of the seeds via heterogeneous nucleation during the particle-growth reaction. By varying the concentration and nature of the seeds in the growth solution, NMNPs of different size and shape can be prepared. This seed-mediated growth protocol has been known for decades and has been used to prepare spherical particles of desired sizes through step-wise enlargement [402]. This approach has been used to synthesize a spectacular variety of shapes such as linear, bent, planar, 3D, and branched geometries, from various metals. Amount and features of the seed (such as internal structures, facets, composition, size) can be varied to produce various different shapes [403]. A variant of preformed-seed-mediated growth method is the "in situ seeding method." In this approach, a small quantity of relatively strong reducing agent is introduced into the reaction medium, in which a mild reducing agent is already present. The purpose of the strong reducing agent is to initiate homogeneous nucleation in the reaction medium. The growth of the seed created in situ from the reduction of metal ions by the strong reducing agent is then carried forward by the mild reducing agent present in the reaction medium. Nanorods/nanowires, rectangle-, cube-, or tetrapod-like gold nanoparticles and silver nanoplates and disks have been synthesized in aqueous solution at room temperature by this method [404]. Furthermore, Sajanlal and Pradeep reported an electrical-potential-assisted preformed-seed-mediated growth method providing uniform equilateral triangular gold nanoparticles [405]. Duraiswamy and Khan have reported a dual-stage continuous-flow seedless method that leverages the unique advantages of microfluidic reactors to spatially and temporally segregate the in situ synthesis of incipient nanoparticle seeds, which are subsequently grown by further addition of reagents within microfluidic droplets [406]. This method might overcome the challenges posed by both seeded and one-pot seedless methods, and allows facile gold nanocrystal synthesis and screening with tunable particle shape and size in rapid "on-demand" fashion.

An alternative way to produce metallic nanoparticles avoiding the use of organometallic precursors is the polyol method. This simple, one-step, nonaqueous method produces metal or alloy nanoparticles either in powder or film form using readily available and environmentally benign metal salts. The reduction of metal precursors is usually carried out in refluxing ethylene glycol, which serves both as solvent and as reducing agent for the formation of metal nanoparticles without the problems from hydrolysis and oxidation encountered in aqueous media. The method has been successfully applied to prepare finely dispersed metallic particles, bimetallic powders, or thin films including Cu, NiCo, NiFe, and MoS_2 [407].

Solution plasma, a novel technology, has potentials for advancement in production of nanomaterials and decomposition of organic-based compounds as well as control of microorganisms and has been expected to be developed as a green strategy due to its unique characteristics [408, 409]. Plasma can be created in liquid under atmospheric conditions, and it is beneficial in the aspects of minimal usage of chemical agents, short process time, and easy handling [410]. Since plasma is generated in aqueous solution by supplying high voltage, a variety of radicals (H•, O•, OH•), gases (H_2, O_2, H_2O_2), electrons, and radiation (UV rays) could be generated via association, excitation, and ionization of water molecules during discharge [411, 412]. The outputs of solution plasma can be controlled by changing various factors, i.e., physical parameters of power supply (voltage, frequency, duty ratio, and electrode geometry) and chemical parameters of discharge media (polarity and pH). With high energetic and active outputs, reaction rate can be enhanced, making it superior to commercial chemical reactions. Although various active species are generated physically, selective reaction can be achieved. For an example, hydrogen radicals play a crucial role in the formation of nanometallic particles by reducing metal ions to nanoparticle precursors, making usage of chemical reducing agent unnecessary.

Liquid chemistry initiated by microplasma at the plasma-liquid interface is ultimately responsible for the nucleation and corresponding synthesis of AuNPs in liquid. Several studies have reported on the reaction mechanisms leading to AuNP synthesis from the reduction of $HAuCl_4$ in aqueous solution; salt reduction was generally attributed to plasma electrons [413], hydrogen radicals in liquid [414], hydrated electrons e_{aq}^- [414], and hydrogen peroxide [415].

In order to synthesize surfactant-free AuNPs, atmospheric pressure microplasma is generated at the surface of a gold (III)-chloride-trihydrate ($HAuCl_4 \times 3H_2O$) aqueous solution [416]. The interactions of the gas-phase plasma with the solution initiate liquid-based reactions that determine the nucleation and growth of AuNPs from the reduced gold precursor ($HAuCl_4$). The plasma-liquid interface is possibly represented by a gas/water vapor plasma environment where electrons are believed to be responsible for initiating reactions that then cascade into the liquid solution. This method can be easily implemented in a continuous-flow process, compared to batch-based chemical synthesis, which would bring about unprecedented and industrially viable nanomanufacturing capabilities. Overall, the features offered by this microplasma-liquid system could allow the synthesis to be highly environmentally friendly, low cost, and accessible to a wide range of nonspecialist users.

Room-temperature ionic liquids are attracting much interest in many fields of chemistry and industry, due to their potential as a "green" recyclable alternative to the traditional organic solvents. They are nonvolatile and provide an ultimately polar environment for chemical synthesis. Some ionic liquids are immiscible with water and organic solvents, giving biphasic ionic liquid systems, which enables easy extraction of products from the ionic liquid. The miscibility with organic solvents or water is mostly dependent on the appropriate anions.

Electric discharge technique is one of the classical colloid preparation methods. The electrochemical method of nanoparticle preparation induces chemical reactions in an electrolyte solution via the use of an applied voltage. This technique has the advantage of being compatible with a wide variety of materials. Metallic nanoparticles have been prepared by electrochemical pathways with and without the use of nanoporous hard templates. Hard templates consist of nanoporous materials such as track-etched polymers and anodized aluminum oxides [46, 417, 418]. Electrochemical deposition is carried out by coating one face of the membrane with a metal film, which acts as a cathode for electroplating. Appropriate metal ions are then electrochemically reduced and deposited within the pores of the template membranes [419, 420].

Sonochemistry has been proven to be an effective route for the synthesis of nanoparticles [421]. The chemical effects of high intensity ultrasound derive from cavitation: formation, growth, and collapse of a bubble in the liquid, leading to localized hot spots with high temperature, high pressure, and extremely rapid cooling rates [422]. Such a remarkable environment provides a platform for the growth of materials with an abundance of energy with extremely fast kinetics, promoting chemical reactions. The advantages of sonochemistry include nonhazardous, rapid reaction rate, controllable reaction conditions, and the ability to form nanoparticles with uniform shapes, narrow size distribution, and high purity.

There are two general methods for producing a polymer shell around noble metal nanoparticles: the "grafting to" and the "grafting from" methods. In the "grafting to" method, a polymer molecule is grafted (covalently bonded) to the surface of the AuNP [47]. In the "grafting from" method, however, the preferred polymer is grown from the surface of the nanoparticles via a process known as "surface-induced" of "surface-initiated" polymerization [423, 424]. To generate a polymer shell using the "grafting from" method, a polymerization initiator is immobilized on the surface of the AuNPs, and preferred monomers are polymerized on the surface of the particles using the immobilized initiators. This process typically leads to a high polymer chain density on the surface of the nanoparticle because the relatively small initiator molecules can completely cover the gold surface. Furthermore, the uniformity and thickness of the polymer shell can also be controlled, allowing the fabrication of well-designed composite nanoparticles.

The cryo-electron-tomography [425] was used to locate the forming gold particles in 3D (Fig. 1.12). This technique has definitive advantages over classical TEM since it allows the direct visualization of the vesicles in a fully hydrated environment, which maintains the shape and structure of the ethosomes, and therefore allows the use of tomographic reconstruction techniques. The gold

particle within the ethosome membrane can be either inserted into the bilayer but protruding from it and being exposed to the polar environment [Fig. 1.12(left panel)] or embedded into the lipid bilayer and interacting with the internal sides of the two monolayers [Fig. 1.12(right panel)].

Top-down approaches, such as photolithography, e-beam lithography (EBL), and Focused ion beam (FIB), offer high fidelity and high controllability in terms of design and prediction. However, top-down approaches are low throughput and need expensive instruments. Some bottom-up approaches based on self-assembly, such as nanosphere lithography [426, 427], anodized aluminum oxide (AAO) template [428], and block copolymer lithography [429], can produce high-resolution (sub)-nanostructures over a large area with a low cost, but it is difficult to obtain highly uniform and controllable structures of arbitrary symmetries across whole area [48]. The details of fabrication of the hybrid mold have been reported by Masuda et al. [430]. Scheme 1.4 shows the hybrid mold fabrication process. AAO template surface was first modified with alkyl silanes by vapor-phase deposition. A polydimethylsiloxane (PDMS) support was placed on resist film spin coated on a silicon wafer. After the PDMS kept contacting with the resist film, the PDMS was removed from the silicon wafer and then placed against the AAO template. The sample was exposed to UV radiation in nitrogen ambient. After a brief exposure to O_2 plasma, the surface of the hybrid mold was coated with a self-assembled monolayer of silane by vapor-phase deposition. The resulting mold was ready to be used for UV-curing imprint process. These issues of conventional fabrication techniques can be solved by nanoimprint lithography (NIL) which is a high-throughput fabrication technique capable to replicate nanopatterns from a master mold over a large area with nanometer precision and high fidelity at a low cost [431–433].
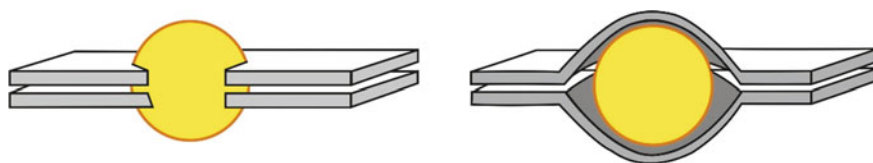
Fig. 1.12 Cryo-electron-tomography and proposed models of the ethosome-nanoparticles hybrids. (*Left panel*) Possible model of the hybrid with the particle exposed to the internal and external ethosome environment (**a**, *left panel*). Possible sandwich model of the hybrid with the particle protected by the hydrophobic sides of lipid bilayer (*right panel*) [425]
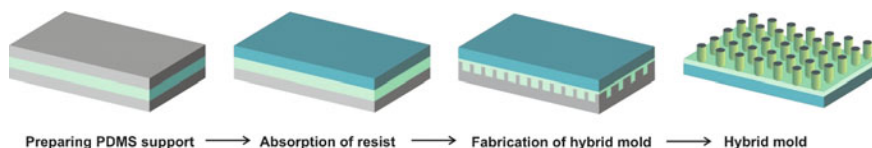
Scheme 1.4 Schematic of the hybrid mold fabrication process [48]

Ion implantation is the commonly used technique to introduce dopants into (nano)materials irrespective of chemical solubility of the dopant material. However, the implantation process is always accompanied with sputtering causing the modification of the surface morphology. Despite the increasing interest in Ge, sputtering-induced structure formation on Ge has been studied to a much lesser extent and also less understood. Irradiation of Ge surface with keV ion energies results in amorphization of the material at fluences $\approx 5 \times 10^{13}$ ions cm^{-2} [434] followed by void formation within the amorphous layer with increasing fluence and finally the transformation to a sponge-like surface over a critical fluence of $\approx 10^{15}$ ions cm^{-2} [435]. Although the spongy or porous morphology is the most common feature of ion-sputtered Ge surfaces, some recent studies [436] show that the heavy ion (Bi and its clusters) sputtering at energies $\geq$ 10 keV can generate a different morphology, e.g., dotlike pattern on Ge. Irradiation of Ge by inert gas ions at sub-keV energy with simultaneous supply of Au, Al, or Ge can also produce various types of nanostructures as reported by Miyawaki et al. [437].

AuNPs with precise number of gold atoms and ligands such as $Au_{140}(SC6)_{53}$ (SC6 = hexanethiol) [438] and $Au_{144}(SCH_2CH_2Ph)_{60}$ [439] have been synthesized using the Brust-Schiffrin method. Murray's group [440, 441] has prepared $Au_{25}(SCH_2CH_2Ph)_{18}$ by a modified version of the Brust-Schiffrin procedure. In this synthesis, $AuCl_4^-$ was phase-transferred from water to toluene, reacted with $HSCH_2CH_2Ph$, and then reduced by adding aqueous $NaBH_4$. The crude product $Au_m(SCH_2CH_2Ph)_n$ (between 1 and 2 nm) was purified by precipitation. For instance, the clusters $Au_{25}(SCH_2CH_2Ph)_{18}$ and $Au_{140}(SCH_2CH_2Ph)_{53}$ were isolated from the crude product by precipitation in acetonitrile, $Au_{25}(SCH_2CH_2Ph)_{18}$ being soluble in acetonitrile unlike $Au_{140}(SCH_2CH_2Ph)_{53}$. The formation of $[oct_4N^+]$ $[Au_{25}(SCH_2CH_2Ph)_{18}^-]$ was confirmed by ^1H NMR, UV-Vis, and mass spectrometry [442].

In order to probe the immobilization of 1,2-dioleoyl-3-trimethylammonium propane (DOTAP)-AuNP complex on the gold, highly sensitive electrochemical impedance spectroscopy (EIS) technique that indicates the changes at the electrode/film/electrolyte interface is used. The impedance data are modeled using the equivalent $[R_s(C_1R_1)(C_2R_2)W]$ circuit, in which R_s is solution resistance; C_1R_1 are capacitance and resistance of the gold electrode; C_2R_2 are capacitance and resistance of the lipid-AuNP layers; and W is Warburg element. Surface coverages from Nyquist plot are calculated using two different relations:

$$\theta_{IS}^R = 1 - \left(R_{CT}^{Au} / R_{CT}^{SAM} \right) \quad \text{and} \quad \theta_{IS}^P = 1 - (\sigma_W / m - \sigma_w) \tag{1.37}$$

which is proposed for partially covered monolayers [443]. In these relations, σ_w is the Warburg diffusion coefficient obtained for the unmodified electrode and m is the slope of the Z′ versus $\omega^{-1/2}$ plot in the higher frequency region [444].

The conventional method of AgNP synthesis requires the reductive reaction to occur in an oil bath, which must be held at a constant temperature of ~ 80 °C for 5 h (on average). Due to excessive heating and extended reaction time, more eco-friendly means of AgNP synthesis are desired. An alternative green AgNP

synthesis technique employs the use of microwaves. In general, microwave (MW) heating is better than a conventional oil bath when it comes to consistently yielding nanostructures with smaller sizes, narrower size distributions, and a higher degree of crystallization [445]. Heating samples with microwaves is a practical method for the greener synthesis of nanomaterials. MW heating is advantageous as it has shorter reaction times, reduced energy consumption, and better product yields which prevents the agglomeration of the particles formed. Nadagouda and Varma [445] have discussed the production of silver nanostructures at length through a MW-assisted synthetic approach which shows that the one-pot synthesis of metallic nanostructures in solutions can be conducted efficiently via MW heating. Silver, gold, platinum, and gold-palladium nanostructures have been prepared through this method, which illustrates the generality of this approach. Through MW heating conditions, spherical nanoparticles can be prepared within a few minutes and single crystalline polygonal plates, sheets, rods, wires, tubes, and dendrites can also be formed. By altering some experimental parameters such as the concentration of metallic precursors, surfactant polymers, and solvents, or the operational temperature, parameters such as morphology and nanostructure size could be controlled. Other than the elimination of the oil bath, MW-assisted techniques, in conjunction with benign reaction media, can also drastically reduce chemical wastes and reaction times in several organic syntheses and chemical transformations [446].

As a heating method, microwave irradiation has found a number of applications in chemistry and recently shown a very rapid growth in its application in materials science due to its unique reaction effects such as rapid volumetric heating and the consequent dramatic increase in reaction rates [447]. As a quick, simple, and energy-efficient heating method, the microwave irradiation was combined with many conventional methods such as a traditional hydrothermal method and a solvothermal process [448] and has been widely used in many fields such as molecular sieve and inorganic complex preparations, organic reactions, and catalysis and lately extended to the synthesis of nanocrystalline particles. Microwaves are electromagnetic waves and being used for the development of different materials. In microwave applications, heating is caused by the interaction of permanent dipole moment of molecules with high-frequency electromagnetic radiation. In comparison with conventional heating, this method shortens reaction time by factor of approximately 20 with uniformly spread through the entire bulk of the reaction medium.

According to the extended Derjaguin-Verway-Landau-Overbeek theory (DVLO), the interaction energy between two nanoparticles A and B can be divided into three contributions (for bottom-up building of nanoparticles (hetero)dimers) [449]:

$$V_T^{AB} = V_{elec}^{AB} + V_{VdW}^{AB} + V_{solvT}^{AB} \tag{1.38}$$

The last term in Eq. 1.38 (V_{solv}^{AB}) is the solvation repulsion potential, describing a short-range repulsive interaction that depends on the properties of the solvent. This

interaction, even at very short interparticle distances, is of the same order of magnitude as the thermal energy and decays very fast as the interparticle distance increases. The second term ($V_{\text{VdW}}^{\text{AB}}$) accounts for the contribution of van der Waals and London attraction forces to the interaction energy. This contribution can be neglected for long distances but becomes significant as the interparticle distance decreases, reaching more than 10 k_BT. The first term in Eq. 1.38 ($V_{\text{elec}}^{\text{AB}}$) is related to electrostatic interactions between the electric double layers of the NPs and depends on the electric surface potential of the NPs (i.e., the zeta potential) [449]. This contribution determines the limiting behavior of the interaction energy for large interparticle distances, and the sign depends on the surface charges of the particles. In the case of particles with the same charge, this interaction is repulsive ($V_{\text{elec}}^{\text{AB}} > 0$) and creates an energy barrier for aggregation, while for particles oppositely charged, the electrostatic contribution is attractive ($V_{\text{elec}}^{\text{AB}} < 0$).

From the theoretical point of view, the formation of multimers can be understood considering a stepwise aggregation process. We have calculated the pairwise interaction energy for the combination of AuNPs (sphere$_{90\ \text{nm}}$, NP-A) and Pd nanocubes$_{25}$ nm (NP-B) forming multimers. In this case, the electrostatic interactions between the multimers AB$_n$ and one NP-B are attractive for low NP-B-occupancy numbers (A, AB, AB$_2$, and AB$_3$). However, they become repulsive if the number of NP-B's in the multimer is larger than 3. Moreover, the energy barrier for aggregation becomes higher than the thermal energy for occupancy numbers larger than 4. Therefore, we can conclude that the formation of multimers with large number of NP-Bs is energetically disfavored, and the yield of such structures is expected to be low. This theoretical result is consistent with the results observed during the self-assembly experiments and DLS characterization. In the presence of irreversible aggregation, the formation of nanoparticle aggregates can be related to the collision rates depending on the NPs interaction energy and on the cross section of collision. If we consider that the driving force for aggregation has an effective volume of action (v_a), and assuming that the average distance between two NPs of type A is sufficiently large, we can infer that if n NP-B are within effective volume of action of one particle NP-A, they will lead to the formation of an aggregate of the type ABn. Under these conditions, the relative amounts of single NPs as well as dimeric and multimeric aggregates can be expressed as:

$$\widehat{P}_A = e^{-([B]v_a)} \tag{1.39}$$

$$\hat{P}_{AB} = ([B]v_a)e^{-([B]v_a)} \tag{1.40}$$

$$\widehat{P}_m = 1 - \left(\widehat{P}_A + \widehat{P}_{AB}\right) \tag{1.41}$$

where $[B]$ is the concentration of NP-B and v_a is the effective volume of action of NP-A that can be obtained from the experimental data. The agreement between the theoretical data (calculated from Eqs. 1.39–1.41) and the experimental values

Fig. 1.13 Experimental (*dots*) and theoretical (*lines*) population abundance for (*1*) single Au sphere$_{90\ nm}$, (*3*) heterodimers Au sphere$_{90\ nm}$−Pd cube$_{25\ nm}$, and (*2*) multimers Au sphere$_{90\ nm}$−Pd cube$_{25\ nm}$; as a function of the average number of Pd cube$_{25\ nm}$ in the effective volume of action of Au sphere$_{90\ nm}$ ($\langle B \rangle = [B]v_a$) [451]
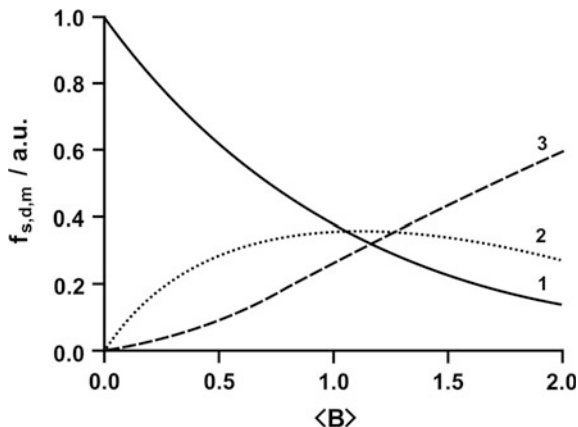
determined in the self-assembly experiments suggests that this set of equations accurately describes the formation of the aggregates, especially for low concentrations of NP-B (Fig. 1.13). The major features of these equations are shown in Fig. 1.13. The fraction of single NP-As decreases monotonically while increasing the concentration of NP-B (Fig. 1.13, curves 1 and 3). The relative abundance of dimeric heteroaggregates (AB) initially increases and reaches a maximum when the average number of NP-Bs within the effective volume of action is equal to 1 (Fig. 1.13, curve 2). It is interesting to notice that according to Eq. 1.40, the relative yield of dimeric aggregates is theoretically expected to be lower than 37%. Therefore, we can conclude that the maximum yields of dimers obtained in the optimal experimental conditions (ranging from 30 to 40%) correspond to the theoretical limit of our electrostatic self-assembly method. Moreover, these yields are comparable with other state-of-the-art methods for self-assembly of NP heterodimers (see Chap. 5, Schemes 5.14 and 5.15) [450]. The Poisson fluctuation model describing the population of single NP-A as well as dimeric and multimeric aggregates was found to be universal for the combinations of NPs A and B investigated.

1.6   Bionanostructures

The field of optical diagnostics comprises a variety of techniques designed to characterize the relationship between the optical and biological properties of tissue. Through the detection of changes in light after interaction with tissue, optical technologies provide information on the physiologic condition of the tissue at a molecular level. The utilization of spectroscopic techniques for the detection of cancerous and precancerous lesions is based on the analysis of specific light-tissue interactions to assess the state of biological tissue. As tissue undergoes the carcinogenic sequence from normal to neoplasia, complex morphological and

molecular transformations occur that modify the manner in which light is absorbed and reflected in the tissue. Spectroscopic techniques such as fluorescence spectroscopy, light scattering spectroscopy, and Raman spectroscopy utilize the unique spectral patterns that are created as tissue progresses toward cancer to offer the potential to detect diseased tissue during the initial stages of carcinogenesis [452].

Fluorescence spectroscopy is based on the biological emission of fluorescent light from tissue exposed to ultraviolet or short wavelength visible light. Light is formed by packages of energy termed photons. When tissue is exposed to light, photons may be absorbed, reflected, or scattered by specific molecules within the tissue. As light illuminates the targeted tissue, these biomolecules, termed fluorophores, absorb the energy in the illuminating light and respond by emitting fluorescent light of lower energy (and longer wavelength). The change in wavelength then allows fluorescent light to be differentiated from illuminating light (UV or Vis light). Each group of fluorophores will respond to specific excitation wavelengths and, in turn, emit a different range of wavelengths resulting in a spectral pattern that ideally represents the biochemical and metabolic status of the tissue undergoing optical interrogation. As tissue undergoes the biochemical and morphological progression to neoplasia, the concentration and distribution of the fluorophores is transformed. Though complex, tissue autofluorescence patterns reflect changes in tissue composition and have been shown to be capable of distinguishing benign from malignant tissue [453].

Fluorescent imaging systems utilize spectroscopic principles to capture fluorescence emission spectra from a larger tissue sampling area than is possible with point spectroscopy. The acquisition of an image requires tissue illumination with a light source, often in the near UV to green range [454].

Elastic scattering spectroscopy, also known as diffuse reflectance spectroscopy, utilizes the principle of white light (400–700 nm) reflectance to determine the structural characteristics of illuminated tissue. Dysplastic change is often characterized by enlarged nuclei, crowding, and hyperchromicity. These changes lead to characteristic reflectance spectra used to identify the structural composition of tissue and aid in clinical diagnosis [455].

Raman spectroscopy is a novel optical technique employed to provide detailed information about the molecular composition of tissue. In contrast to elastic scattering spectroscopy, Raman spectra are generated from the molecule-specific inelastic scattering of light. Following exposure to a light source (generally near-infrared light 700–1300 nm), a minute fraction of the scattered light undergoes a wavelength shift due to the energy transfer between incident photons and tissue molecules. The wavelength shift (and change in energy) is achieved when the incident photon alters the vibrational state of an intramolecular bond. Though Raman spectroscopy is sensitive to a wide range of specific biomolecules such as proteins, lipids, and nucleic acids, the Raman effect only compromises a small fraction (1 in a million) of scattering events and signals may be weak and difficult to implement [456].

Optical coherence tomography (OCT) is an innovative optical imaging technique designed to provide high-resolution (~ 10–20 nm) cross-sectional images of

microscopic subsurface tissue structures. As the optical analogue of high-frequency B-scan ultrasonography, a imaging technique that detects backscattered sound waves, OCT images are generated by measuring the intensity of backscattered light after tissue is probed with a low-power near-infrared light source (wavelengths ranging from 750 to 1300 nm). Despite this high resolution, OCT imaging is limited by a depth of penetration of 1–3 mm [457].

Narrowband imaging (NBI) is a recently developed optical technique designed to enhance the visualization of microvasculature on the mucosal surface. Developed to improve the quality of endoscopic images, NBI systems limit the depth of light penetration into tissue through red, green, and blue optical interference filters. These three filters divide the visible wavelength ranges into three shorter wavelength bands, while increasing the relative contribution of blue-filtered light. The increased contribution of blue light is fundamental to creating a narrowband image, as blue light corresponds to the peak absorption of hemoglobin. The resulting image demonstrates preferential enhancement of the vascular network of the superficial mucosa. To differentiate normal from dysplastic tissue, the microvascular patterns present in the narrowband image are analyzed [458].

Advances in bioengineering and the continued refinement of optical detection techniques have led to the development of multimodal optical detection systems. These multimodal devices often function in real time to provide complementary diagnostic information and wide tissue surveillance capability. The ultimate goal of the optical detection systems centers on the achievement of an "optical biopsy."

The synthesis and properties of biomolecule-nanoparticle hybrid systems as well as the organization of these systems as functional devices are shown in Scheme 1.5. We follow their properties and the methods to assemble two-dimensional and three-dimensional nanoparticle structures on surfaces, and we describe the operation of these biomolecule-nanoparticle structures as functional devices. Specifically, one can discuss the use of the systems as sensors, as building blocks for electronic circuitry, and as electronic and optoelectronic elements. We highlight the findings
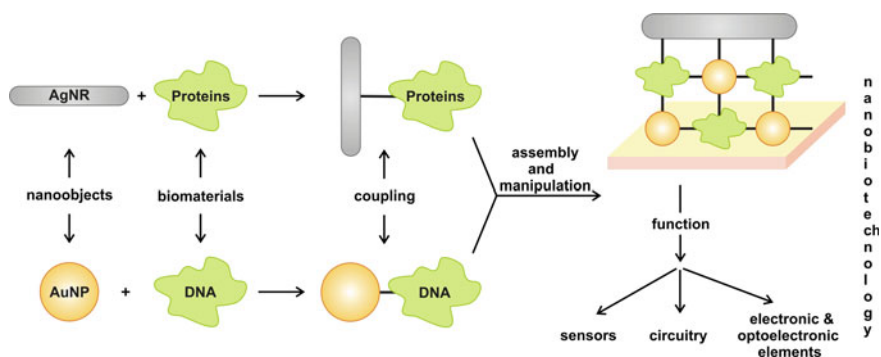
Scheme 1.5 The conceptual generation of biomolecule-nanoparticle conjugates to yield functional devices [215]

of the past few years that have already established the core elements of the new research area—nanobiotechnology. The combination of nano-objects, nanotools, and nanotemplates [459–461] with biomolecules yields new facets of bioelectronics to open new horizons of nanobioelectronics.

The convergence of biotechnology and nanotechnology has led to the development of hybrid nanomaterials that incorporate the highly selective catalytic and recognition properties of biomaterials, such as proteins/enzymes and DNA, with the unique electronic, photonic, and catalytic features of nanoparticles. The conjugation of NPs and other nano-objects (e.g., nanorods, nanoshells, and carbon nanotubes) with biomolecules is an attractive area of research within nanobiotechnology [462–464]. Biomolecules are fascinating macromolecular structures in terms of their unique recognition, transport, and catalytic properties. The conjugation of NPs with biomolecules could provide electronic or optical transduction of biological phenomena in the development of novel biosensors [465–467]. Enzymes, antigens and antibodies, and biomolecular receptors have dimensions in the range of 2–20 nm, similar to those of NPs; thus, the two classes of materials are structurally compatible.

Modern efforts in biotechnology involve the application of combinatorial methods for the synthesis of new biocatalysts or drugs. The simultaneous analysis of many pathogens, mutants, or therapeutic drugs is a major challenge in bioanalytical chemistry. Thus, the unique optical or electronic properties of metal NPs are of key interest for the development of high-throughput techniques for the parallel analysis of numerous components in samples. The possibility to control and tune these unique optical and electronic properties of metal NPs through their dimensions paves the way to the application of NPs as versatile analytical probes. That is, the application of size-controlled noble metal nanoparticles as libraries of probes for different analytes promises a great potential in future biosensing assays.

Nanotechnology is garnering widespread recognition not only as a scientific subdiscipline, but an entity in its own right that encompasses physics, chemistry, and biology. It seems that nanotechnology is increasingly gaining a foothold in clinical medicine, especially in oncology. Nanoparticles, such as superparamagnetic iron fluids and quantum dots, are emerging as viable contrast agents to be used in medical imaging platforms, for instance computed tomography (CT) or magnetic resonance imaging (MRI) [468]. QDs display superior fluorescent properties with less photobleaching compared with conventional chromophores [469]. In the past few years, with the advent of nanotechnology, there has been a dramatic increase in the development of novel nanoparticulate materials. Nanometer-sized particles such as magnetic iron oxides, gold, and semiconducting nanocrystals (quantum dots) possess novel magnetic and optical properties that can be used as imaging probes. However, their surface hydrophobicity or poor colloidal stability at physiological conditions frequently renders them inappropriate for clinical use. Carbon nanotubes (CNTs) are allotropes of carbon in a honeycomb-like lattice, and they are essentially "rolled up" sheets of graphene with internal diameters of 1 nm [470].

The fabrication of nanodevices as probes is complex, most likely the assembly of building blocks including nanoparticles, nanowires, nanotubes, and substrates [471,

472]. Typical examples of nanodevices are nanofluidic arrays and protein nano-biochips. One of the most promising uses of nanofluidic devices is isolation and analysis of individual biomolecules, such as DNA, which could lead to new detection schemes for cancer [473].

Devices based on nanowires are emerging as a powerful and general platform for ultrasensitive, direct electrical detection of biological and chemical species. Lieber's group developed the silicon (Si) nanowire field-effect devices in which distinct nanowires and surface receptors are incorporated into arrays. The surface chemistry of nanowire devices can affect the electric changes, which is the basic mechanism of this approach for the development of a viable multiplexed detection technology. The Si-nanowire probes have been used for detection of various bio-logical species and their interactions, including small molecules, proteins, DNAs, viruses, and even neuronal signals [474–476]. There are three key steps for the fabrication of a nanowire device array: first, the couple of aldehyde propy-ltrimethoxysilane (APTMS) and Si-nanowires to present terminal aldehyde groups at the nanowire surface; second, the conjugation of aldehyde groups with mono-clonal antibodies (mAbs) to endow with the specificity; third, the block of unre-acted free aldehyde groups by reaction with ethanolamine [477]. Selective interaction of cancer biomarkers with surface-linked mAbs will produce a con-ductance change in the corresponding receptor-modified Si-nanowire devices but not in devices lacking of the specific antibodies. For example, the results showed that the conductance change was directly proportional to the solution of prostate-specific antigen (PSA) concentration from ~ 5 ng/mL down to 90 fg/mL. Using Si-nanowire devices functionalized with mAbs for PSA, carcinoembryonic antigen (CEA), and mucin-1, respectively, one can achieve the multiplexed, real-time, label-free biomarker detection with sensitivity to the femtomolar level. The nanodevices were also successful for the detection of PSA in donkey and human serum samples with high sensitivity and selectivity [477]. The capability of Si-nanowire probes for multiplexed real-time monitoring of protein markers with high sensitivity and selectivity in clinically relevant samples opens up substantial possibilities for diagnosis and treatment of cancer and other complex diseases. For example, the combination of Si nanoprobes and microfluidic purification chips may provide point-of-care diagnostics for the specific and quantitative detection of disease biomarkers in physiological fluid samples, positioning this technology for rapid translation to clinical settings [478].

For in vitro diagnostics, because the intrinsic complexity of the plasma pro-teome, the heterogeneity of human diseases, and the rapid degradation of proteins in sampled blood, it is very necessary to do the in situ test of blood within a short period of time. Fan et al. developed a device so-called integrated blood barcode chip (IBBC) to integrate on-chip plasma separations from microliter quantities of whole blood with rapid in situ measurements of multiple plasma proteins [479]. The immunoassay region of the chip is a microscopic barcode, integrated into a microfluidics channel and customized for the detection of many proteins and/or for the quantification of a single or few proteins over a broad concentration range. The IBBC enabled on-chip blood separation and rapid measurement (with 10 min)

of a panel of plasma proteins from tiny amount of blood sample. Although the issue of sensitivity may be of concern, this device is inexpensive, noninvasive, and robust, which may represent a realistic in vitro diagnostic platform for point-of-care use, particularly in remote locations [480].

Nanoparticles have been of significant interest over the last decade as they offer great benefits for drug delivery to overcome limitations in conventional chemotherapy [210]. They can not only be formed in a range of sizes (1–1000 nm) but also be made using a variety of materials including polymers (e.g., biodegradable polymeric nanoparticles, dendrimers), lipids (e.g., solid-lipid nanoparticles, liposomes), inorganic materials (e.g., metal nanoparticles, quantum dots), and biological materials (e.g., viral nanoparticles, albumin nanoparticles). In addition, they can be tailored to simultaneously carry both drugs and imaging probes and designed to specifically target molecules of diseased tissues. Nanoparticles for anticancer drug delivery had reached the first clinical trial in the mid-1980 s, and the first nanoparticles (e.g., liposomal with encapsulated doxorubicin) had entered the pharmaceutical market in 1995. Since then, numerous new nanoparticles for cancer drug delivery have been approved and/ or are currently under development due to their many advantages. Their advantages include enhancing solubility of hydrophobic drugs, prolonging circulation time, minimizing nonspecific uptake, preventing undesirable off-target and side effects, improving intracellular penetration, and allowing for specific cancer-targeting [481]. For example, nanoparticles via either passive targeting or active targeting have been shown to enhance the intracellular concentration of drugs/genes in cancer cells while avoiding toxicity in normal cells. In addition, the targeted nanoparticles can also be designed as either pH-sensitive or temperature-sensitive carriers.

Although targeted nanoparticles have emerged as one strategy to overcome the lack of specificity of conventional chemotherapy, there are also potential risks and challenges associated with this novel strategy. For instance, some cancer cell types would develop drug resistance over the drug treatment course, thereby rendering drugs released from the targeted nanoparticles to be ineffective. Combined therapies, such as the use of targeted nanoparticles for delivering both chemotherapeutics and gene therapeutics, might be effectively delivered and specifically targeted to cancer cells and tissues to overcome this drug resistance and to stop the tumor growth. Another strategy to overcome this drug resistance is to develop multi-functional targeted nanoparticles.

Besides developing new materials and selecting appropriate materials for each specific treatment, other factors need to be optimally selected in order to design better targeted nanoparticles. These factors include the particles size, shape, sedimentation, drug encapsulation efficacy, desired drug release profiles, distribution in the body, circulation, and cost. For instance, in the case of particle size, it has been well-known that the clearance rate of very small nanoparticles might be high, and most of these nanoparticles might end up in the liver and spleen, thus making the use of targeted nanoparticles impractical and ineffective. On the other hand, larger nanoparticles might be too big to go through small capillaries for drug delivery.
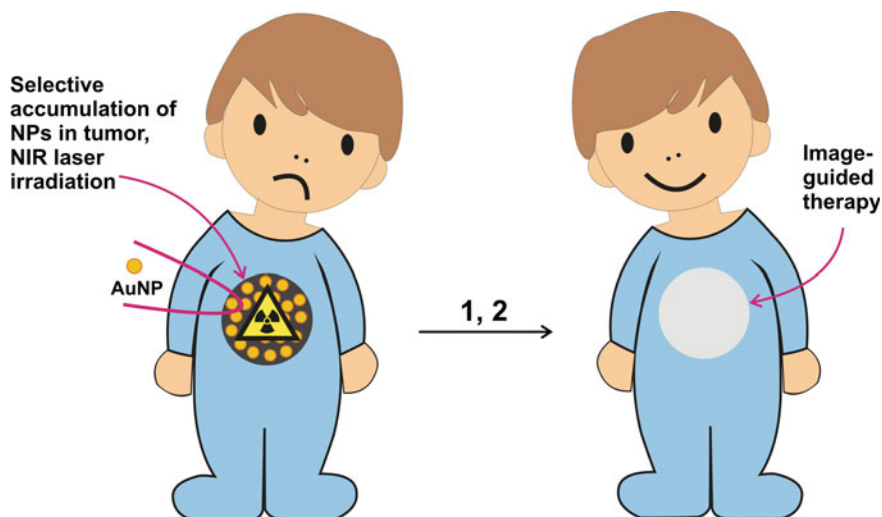
Scheme 1.6 Selective accumulation of nanoparticles in tumor followed by NIR laser irradiation. (*1*) Detection processes (PET, PAT, MRI, optical…) and (*2*) phototherapy (PTA therapy, light-activated drug release) [483]

Thus, selecting the right materials and particle size is another important aspect in targeted NPs for cancer therapy [482].

Nanomaterials that interact with light provide a unique opportunity for applications in biophotonic nanomedicine. Image-guided therapies could be designed based on multifunctional noble metal nanoparticles (Scheme 1.6). Such NPs have a strong and tunable surface plasmon resonance absorption in the near-infrared region and can be detected using multiple imaging modalities (magnetic resonance imaging, nuclear imaging, and photoacoustic imaging). These novel nanostructures, once introduced, are expected to home in on solid tumors either via a passive targeting mechanism (i.e., the enhanced permeability and retention effect) or via an active targeting mechanism facilitated by ligands bound to their surfaces. Once the NPs reach their target tissue, their activity can then be turned on using an external stimulus. For example, photothermal conducting NPs primarily act by converting light energy into heat. As a result, the temperature in the treatment volume is elevated above the thermal damage threshold, which kills the cells. This process, termed photothermal ablation therapy (PTA), is effective, but it is also unlikely to kill all tumor cells when used alone. In addition to PTA, photothermal conducting NPs can also efficiently trigger the release of drugs and activate RNA interference. A multimodal approach, which permits simultaneous PTA therapy, chemotherapy, and therapeutic RNA interference, has the potential to completely eradicate residual diseased cells [483].

To assist i.v. applied anticancer agents in achieving proper circulation times and tumor concentrations, and to improve the balance between their efficacy and their

toxicity, a large number of drug delivery systems have been designed and evaluated over the years [484]. Clinically relevant examples of such nanometer-sized carrier materials are liposomes, polymers, micelles, polymer and metal particles and antibodies (Scheme 1.7). These nanomedicine systems primarily aim to improve the circulation time of the conjugated or entrapped active agent and to improve its tumor accumulation by means of enhanced permeability and retention (EPR)-mediated passive drug targeting (Scheme 1.8). The latter, on the other hand, are primarily designed to improve target cell recognition and target cell uptake and to improve the efficacy of the attached active agent by means of active drug targeting. In addition to this, various different types of hybrid systems have been developed over the past two decades, including antibody-modified liposomes or peptide-functionalized polymers, which are intended to combine passive and active targeting, to initially localize to tumors by means of EPR, and to subsequently stimulate tumor cell-specific uptake by selectively binding to surface receptors (over) expressed by cancer cells.

Upon i.v. injection, a low molecular weight anticancer agent is generally rapidly cleared from the circulation, and only low levels of the drug accumulate in tumors
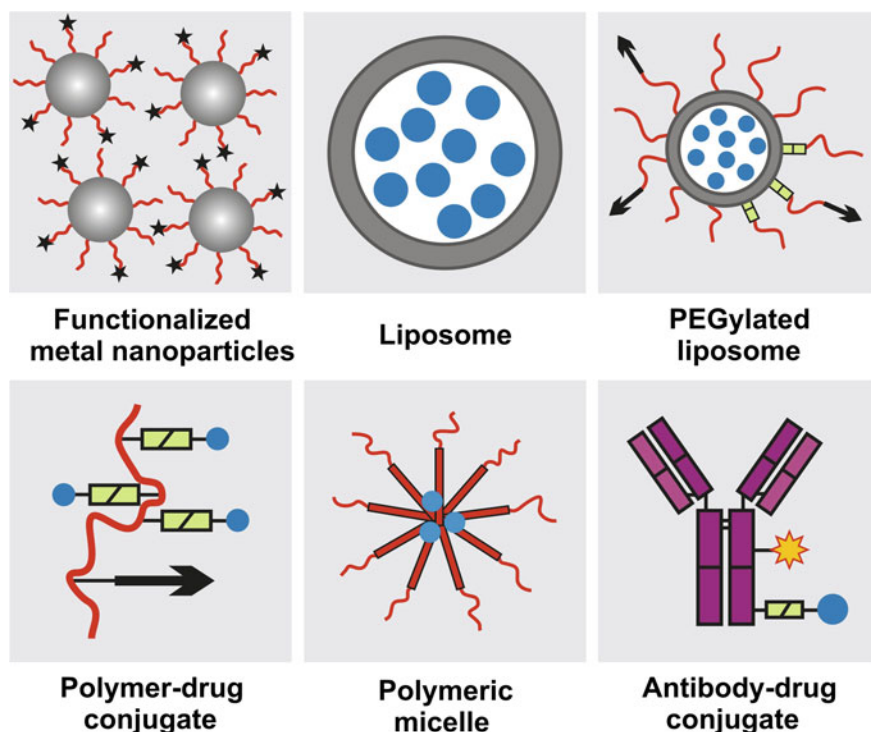
Scheme 1.7 Schematic of some drug targeting systems. Liposomes, polymers, and polymer coatings, linkers allowing for drug release and for sheddable stealth coatings, targeting ligands, antibody fragment, radionuclides, and conjugated or entrapped active agents [485]
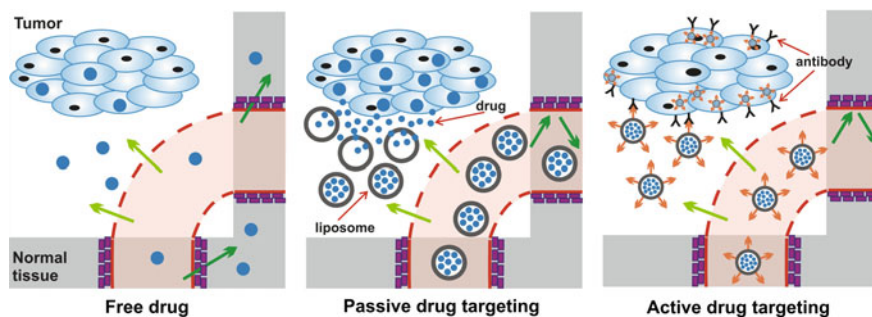
Scheme 1.8 Principles of passive and active drug targeting to tumors [485]

and in tumor cells (Schemes 1.7 and 1.8). At the same, due to its small size, its high hydrophobicity, and/or its large volume of distribution, significant levels of the agent accumulate in healthy tissues. Upon encapsulation in (or conjugation to) a long-circulating and passively tumor-targeted drug delivery system, the concentration of the active agent in tumors can be increased substantially (by means of the EPR effect), while its accumulation in healthy organs and tissues can be attenuated. Upon the incorporation of targeting ligands, such as antibodies and peptides, the interaction between the drug and/or drug delivery system and cancer cells can be improved, resulting in a more selective target site localization and/or target cell uptake [485].

Passively and actively targeted nanomedicine formulations have been used to treat various different diseases. PEGylated proteins, for instance, have been approved for improving the treatment of hepatitis (PegIntron), of acromegaly (PegVisomant), and of severe combined immunodeficiency (SCID; Adagen) [486]. Liposomal nanomedicines are, for example, routinely implemented in the management of fungal infections (AmBisome) and of lymphomatous meningitis (DepoCyt) [487]. By far, the most progress in this regard, however, has been made in the field of oncology. Two different liposomal doxorubicin formulations, i.e., Myocet (unPEGylated) and Doxil (PEGylated; Caelyx in Europe), are for instance being used to treat Kaposi sarcoma, multiple myeloma, metastatic breast cancer and ovarian carcinoma, and liposomal vincristine (Onco-TCS) to treat non-Hodgkin's lymphoma [488]. PEGylated L-asparaginase (Oncaspar) and poly (styrene-co-maleic acid)-modified neocarzinostatin (SMANCS) have been implemented in the treatment of acute lymphoblastic leukemia hepatocellular carcinoma, respectively, and albumin- and poly(L-glutamic acid)-based paclitaxel (i.e., Abraxane and Xyotax) in the management of breast and nonsmall cell lung cancer [489]. Examples of antibody-based actively targeted nanomedicines approved for clinical use are Zevalin (yttrium-90-labeled ibritumomabtiuxetan) and Ontak (denileukin diftitox), which are used for non-Hodgkin's lymphoma and cutaneous T-cell lymphoma, respectively [490].

Many nanogold(silver)-based environmental technologies (e.g., sensors, sorbents, reactants) are under very active research and development and are expected to emerge as the next-generation environmental technologies to improve or replace various conventional environmental technologies in the near future [231]. Some of the most promising near-term realizations of nanotechnology are at the interface of physical, chemical, and biological systems. Because many biomolecules have specific binding properties in self-assembly processes, they are attractive materials for nanotechnology.

The OEO acetal ligand group was converted to aldehyde by gentle acid treatment, followed by the reaction with sugar derivatives having *p*-aminophenyl moieties at the C-1 position (*p*-aminophenyl-β-D-lactopyranoside: Lac) in the presence of $(CH_3)_2NHBH_3$ and gold salt. Reaction of the prepared Lac-derivatized gold nanoparticles with bivalent galactose-binding lectin (ricinus communis agglutinin, RCA_{120}) [491] was followed as a function of time through optical changes in the surface plasmon band in the UV-Vis spectrum. These solutions were initially a pinkish-red color due to the well-dispersed nature of the particles. After introduction of the RCA_{120} lectin in PBS (phosphate buffer saline), the color gradually changes from red to purple. In line with this directly observable change in appearance, significant differences in the optical spectra over time were observed, specifically a broadening and redshift in the particle surface plasmon resonance from 523 nm to longer wavelength. This is attributed to distance-dependent changes in the optical properties of three-dimensionally aggregated gold nanoparticles cross-linked by RCA_{120} lectin which recognizes lactose residues on the OEOylated gold surface. Images of two-dimensional, single-layer aggregates revealed close-packed assemblies of the colloids with uniform particle separations of about 20 nm, which corresponds to the length of the combination of lectin and PEO linker. The aggregation by the RCA_{120} lectin was reversible, recovering the original dispersed phase and color by addition of excess galactose. Notably, the degree of aggregation was proportional to lectin concentration, allowing the system to be utilized to quantitate lectin concentration with nearly the same sensitivity as enzyme-linked immunosorbent assay (ELISA).

1.7   Conclusion

Noble metal nanoparticles appeared early in human history, probably since the fifth century BC in China and Egypt for medical or decorative purposes, which persisted until now. The synthesis of nanomaterials or nanoparticles was summarized to be carried out in the solid, liquid, or gaseous state, following two basic approaches, classified as "top-down" and "bottom-up." A variety of colloid-chemical strategies involving a wide spectrum of reagents and reaction conditions has been employed in order to prepare noble metal nanomaterials of controlled morphologies. The nanometer regime covers the transition from condensed matter behavior to atomic and molecular properties and thus is a very rich but also very demanding area in

materials science. Nanotechnology is garnering widespread recognition not only as a scientific subdiscipline, but an entity in its own right that encompasses physics, chemistry, and biology. Properties and functions change qualitatively or quantitatively by orders of magnitude when the dimensions become smaller than a critical size in the nanometer range. The key to the future lies in the functions that we give to materials smart properties, not just in finding "novel functional nanomaterials." Certainly, finding new materials is always an important part of progress, but we should also focus on the much larger domain of novel functions that we can give to existing or modified materials. Nanotechnology is the culmination of many facets of developments in the nanorealm, including nanofabrication, nanomachineries, quantum devices, molecular machines, molecular computers. Colloid-chemical synthesis very often results in a mixture of nanoparticles, and constant efforts must be directed to gain exquisite control of the size and the shape of various types of nanoparticles. Achieving high yield and successful scaling up of the synthesis process is necessary for the synthesis to be commercially viable. New tools will be required to characterize noble metal nanoparticles more comprehensively and adequately. Nanoparticles of the same chemical composition but with different morphologies can show considerably different physicochemical properties. This warrants individual nanoparticle characterizations. Single-particle techniques have appeared to be very valuable tools for direct exploration of structure-property relationships. It is not clear how nanoparticles evolve from the seed nuclei. Studies on the nucleation and seed formation in the context of shape control in nanoparticles deserve immediate attention. Formidable challenges exist for direct real-time monitoring of the events of development from precursors to final particle formation, such as defect formations, surface-interface interactions of auxiliaries, diffusion and incorporation kinetics of growth units. Development of simple, nondestructive characterization tools for direct visualization of morphology development in reaction medium will certainly be a milestone in the field of nanoscience. Advances in theory and computational techniques are essential for a quantitative understanding of the morphology development and associated properties. This will open up new avenues in the development of nanoparticles of desired size and shape. Clearly, the bottom-up colloid-chemical syntheses are likely to emerge as powerful and economical design tools for morphology control in nanoparticles. However, most of the methods are limited to synthesis in small quantities and often have poor yield of a given morphology. Colloid-chemical synthesis very often results in a mixture of nanoparticles, and constant efforts must be directed to gain exquisite control of the size and the shape of various types of nanoparticles. Achieving high yield and successful scaling up of the synthesis process are necessary for the synthesis to be commercially viable. At the same time, there is need for the development of advanced techniques for separation or elimination of the unwanted shapes.

Herein, separation and purification techniques are reviewed for the separation of the nanomaterials (NMs) and their conjugates from the original reactants and by-products. Characterization includes assessment of composition, size, volume, aspect ratio, perimeter, projected area, surface roughness, morphology, dimensionality, and physical and chemical properties. These include scattering,

microscopy, spectroscopy, mass spectroscopy, thermal techniques. Current methods for determining NMNP size include light scattering methods such as dynamic light scattering (DLS), static light scattering (SLS), and small-angle X-ray scattering; the microscopy methods include atomic force microscopy (AFM), transmission electron microscopy (TEM), and scanning electron microscopy (SEM); the localized surface plasmonic resonance (LSPR) method; and the fractionation, centrifugation, and chromatographic methods. X-ray diffraction (XRD) is typically used to provide structural information about crystalline samples. Förster resonance energy transfer (FRET), fluorescence resonance energy transfer (FRET), resonance energy transfer (RET), or electronic energy transfer (EET) is a mechanism describing energy transfer between two light-sensitive molecules (chromophores). Thermal techniques can aid in determining the amount of conjugated molecule as well as both the nanoparticle and the molecule's (polymer's) thermal stability. Typically, for techniques like differential scanning calorimetry (DSC), microgram amounts of sample are required for analysis. Thermal gravimetric analysis (TGA) is a method that utilizes a high-precision balance to determine changes in the weight of a bulk sample relative to changes in temperature. The electron diffraction pattern obtained from high-resolution TEM (HRTEM) and sometimes selected-area electron diffraction (SAED) techniques may provide information regarding the atomic structure of the particles, lattice plane fringes, and the nature of the facets such as twinning, twinning planes, and surface reconstruction. Energy-dispersive X-ray analysis (EDAX) available with analytical TEM or SEM and X-ray photoelectron spectroscopy (XPS) can be used to determine surface elemental and surface compound composition, and so on. Some are already routinely used to purify NP-conjugates and can also be quite effectively used for characterization purposes. Spectroscopic techniques, such as fluorescence spectroscopy, light scattering spectroscopy, optical coherence tomography, and Raman spectroscopy, utilize the unique spectral patterns that are created as tissue progresses toward cancer to offer the potential to detect diseased tissue during the initial stages of carcinogenesis. Nanoparticles, such as superparamagnetic iron fluids, noble metal nanoparticles, and quantum dots, are emerging as viable contrast agents to be used in medical imaging platforms, for instance CT or MRI. Small nanoparticles display superior fluorescent properties with less photobleaching compared with conventional chromophores. Nanoparticles have been of significant interest over the last decade as they offer great benefits for drug delivery to overcome limitations in conventional radiation or chemotherapy. Image-guided therapies could be designed based on multifunctional noble metal nanoparticles. Such NPs have a strong and tunable surface plasmon resonance absorption in the near-infrared region and can be detected using multiple imaging modalities (magnetic resonance imaging, nuclear imaging, and photoacoustic imaging). These novel nanostructures, once introduced, are expected to home in on solid tumors either via a passive targeting mechanism (i.e., the enhanced permeability and retention effect) or via an active targeting mechanism facilitated by ligands bound to their surfaces. A variety of techniques designed to characterize the relationship between the optical and biological properties of tissue is discussed. Through the detection of changes in light after

interaction with tissue, optical technologies provide information on the physiologic condition of the tissue at a molecular level. The utilization of spectroscopic techniques for the detection of cancerous and precancerous lesions is based on the analysis of specific light-tissue interactions to assess the state of biological tissue. Spectroscopic techniques, such as fluorescence spectroscopy, light scattering spectroscopy, and Raman spectroscopy, utilize the unique spectral patterns that are created as tissue progresses toward cancer to offer the potential to detect diseased tissue during the initial stages of carcinogenesis. Advances in bioengineering and the continued refinement of optical detection techniques have led to the development of multimodal optical detection systems. These multimodal devices often function in real time to provide complementary diagnostic information and wide tissue surveillance capability. The ultimate goal of the optical detection systems centers on the achievement of an "optical biopsy." We have seen that the progress has been rapid and inspiring toward the innovative synthesis methods and sophisticated characterization techniques. It seems that nanotechnology is increasingly gaining a foothold in clinical medicine, especially in oncology. We finish off by showing new directions research is taking in this new and fascinating area.

Glossary

Biomarker, or biological marker	generally refers to a measurable indicator of some biological state or condition. The term is also occasionally used to refer to a substance the presence of which indicates the existence of a living organism.
Fluorophore (or fluorochrome, similarly to a chromophore)	is a fluorescent chemical compound that can re-emit light upon light excitation. Fluorophores typically contain several combined aromatic groups, or planar or cyclic molecules with several π bonds.
Immunodeficiency (or immune deficiency)	is a state in which the immune system's ability to fight infectious disease and cancer is compromised or entirely absent.
Monoclonal antibodies (mAb or moAb)	are antibodies that are made by identical immune cells that are all clones of a unique parent cell. Monoclonal antibodies can have monovalent affinity, in that they bind to the same epitope (the part of an antigen that is recognized by the antibody).

Non-Hodgkin lymphoma (sometimes called NHL, or just lymphoma)	is a cancer that starts in cells called lymphocytes, which are part of the body's immune system.
Photothermal therapy (PTT)	refers to efforts to use electromagnetic radiation (most often in infrared wavelengths) for the treatment of various medical conditions, including cancer. This approach is an extension of photodynamic therapy, in which a photosensitizer is excited with specific band light. This activation brings the sensitizer to an excited state, where it then releases vibrational energy (heat), which is what kills the targeted cells.
Premalignant (precancerous) lesions	are morphologically atypical tissue which appears abnormal under microscopic examination, in which cancer is more likely to occur than in its apparently normal counterpart.

References

1. Faraday M (1857) The bakerian lecture: experimental relations of gold (and other metals) to light. Philos Trans R Soc 147:145–181
2. Daniel MC, Astruc D (2004) Gold nanoparticles: assembly, supramolecular chemistry, quantum-size-related properties, and applications toward biology, catalysis, and nanotechnology. Chem Rev 104:293–346
3. Schmid G (ed) (2004) Nanoparticles. Wiley-VCH, Weinheim
4. Haruta M (2002) Catalysis of gold nanoparticles deposited on metal oxides. Cattech 6:102–115
5. Zayats M, Kharitonov AB, Pogorelova SP, Lioubashevski O, Katz E, Willner I (2003) Probing photoelectrochemical processes in Au–CdS nanoparticle arrays by surface plasmon resonance: Application for the detection of acetylcholine esterase inhibitors. J Am Chem Soc 125:16006–16014
6. Jahn W (1999) Review: chemical aspects of the use of gold clusters in structural biology. J Struct Biol 127:106–112
7. Maier SA, Brongersma ML, Kik PG, Meltzer S, Requicha AAG, Atwater HA (2001) Plasmonics—a route to nanoscale optical devices. Adv Mater 13:1501–1505
8. Wang SH, Sato S, Kimura K (2003) Preparation of hexagonal-close-packed colloidal crystals of hydrophilic monodisperse gold nanoparticles in bulk aqueous solution. Chem Mater 15:2445–2448
9. Kiely CJ, Fink J, Brust M, Bethell D, Schiffrin DJ (1998) Spontaneous ordering of bimodal ensembles of nanoscopic gold clusters. Nature 396:444–446
10. Bhattacharya R, Mukherjee P (2008) Biological properties of "naked" metal nanoparticles. Adv Drug Deliv Rev 60:1289–1306

11. Qin D, Xia YN, Rogers JA, Jackman RJ, Zhao XM, Whitesides GM (1998) Microfabrication, microstructure and microsystems. Top Curr Chem 194:1–20

12. Tennant DM, Feder K, Dreyer KF, Gnall RP, Koch TL, Koren U, Miller BI, Young MG (1995) Phase grating masks for photonic integrated circuits fabricated by e-beam writing and dry etching: Challenges to commercial applications. Microelectron Eng 27:427–434

13. Feldheim DL, Foss CA Jr (2002) Metal nanoparticles; synthesis, characterization, and applications. Marcel Dekker Incorporated, New York

14. Badia A, Singh S, Demers L, Cuccia L, Brown GR, Lennox RB (1996) Self-assembled monolayers on gold nanoparticles. Chem Eur J 2:359–363

15. Yao H, Momozawa O, Hamatani T, Kimura K (2001) Stepwise size-selective extraction of carboxylate-modified gold nanoparticles from an aqueous suspension into toluene with tetraoctylammonium cations. Chem Mater 13:4692–4697

16. Hussain N, Singh B, Sakthivel T, Florence AT (2003) Formulation and stability of surface-tethered DNA-gold-dendron nanoparticles. Int J Pharm 254:27–31

17. Miyazaki A, Nakano Y (2000) Morphology of platinum nanoparticles protected by poly(N-isopropylacrylamide). Langmuir 16:7109–7111

18. Taniguchi N (1974) On the basic concept of nanotechnology. In Proceedings of the international conference on production engineering. Tokyo (Part II) Japan Society of Precision Engineering, pp 18–23

19. Bhattacharya D, Rajinder G (2005) Nanothechnology and potential of microorganisms. Crit Rev Biotechnol 25:199–204

20. Sanpui P, Chattopadhyay A, Ghosh SS (2011) Induction of apoptosis in cancer cells at low silver nanoparticle concentrations using chitosan nanocarrier. ACS Appl Mater Interfaces 3:218–228

21. Sau TK, Murphy CJ (2004) Room temperature, high-yield synthesis of multiple shapes of gold nanoparticles in aqueous solution. J Am Chem Soc 126:8648–8649

22. Shankar SS, Ahmad A, Pasricha R, Sastry M (2003) Bioreduction of chloroaurate ions by geranium leaves and its endophytic fungus yields gold nanoparticles of different shapes. J Mater Chem 13:1822–1826

23. Liu S, Weaver JVM, Save M, Armes SP (2002) Synthesis of pH-responsive shell cross-linked micelles and their use as nanoreactors for the preparation of gold nanoparticles. Langmuir 18:8350–8357

24. Tatarchuk VV, Sergievskaya AP, Druzhinina IA, Zaikovsky VI (2011) Kinetics and mechanism of the growth of gold nanoparticles by reduction of tetrachloroauric acid by hydrazine in Triton N-42 reverse micelles. J Nanopart Res 13:4997–5007

25. Aubin-Tam ME, Hamad-Schifferli K (2008) Structure and function of nanoparticle-protein conjugates. Biomed Mater 3:034001

26. Wong Ch, West PE, Olson KS, Mecartney ML, Starostina N (2007) Tip Dilation and AFM Capabilities in the Nanoparticle Characterization. J Mater 59:12–16

27. Sapsford KE, Tyner KM, Dair BJ, Deschamps JR, Medintz IL (2011) Analyzing nanomaterial bioconjugates: a review of current and emerging purification and characterization techniques. Anal Chem 83:4453–4488

28. Jain PK, Lee KS, El-Sayed IH, El-Sayed MA (2006) Calculated absorption and scattering properties of gold nanoparticles of different size, shape, and composition: applications in biological imaging and biomedicine. J Phys Chem B 110:7238–7248

29. Amendola V, Meneghetti M (2009) Size evaluation of gold nanoparticles by UV-vis spectroscopy. J Phys Chem C 113:4277–4285

30. Trapiella-Alfonso L, Montoro Bustos AR, Encinar JR, Costa-Fernandez JM, Pereiro R, Sanz-Medel A (2011) New integrated elemental and molecular strategies as a diagnostic tool for the quality of water soluble quantum dots and their bioconjugates. Nanoscale 3:954–957

31. Wu C, Schneider T, Zeigler M, Yu J, Schiro PG, Burnham DR, McNeill JD, Chiu DT (2010) Bioconjugation of ultrabright semiconducting polymer dots for specific cellular targeting. J Am Chem Soc 132:15410–15417

32. Williams SKR, Runyon JR, Ashames AA (2011) Field-Flow fractionation: addressing the nano challenge. Anal Chem 83:634–642

33. Jans H, Liu X, Austin L, Maes G, Huo Q (2009) Dynamic light scattering as a powerful tool for gold nanoparticle bioconjugation and biomolecular binding studies. Anal Chem 81:9425–9432

34. Swift J, Butts CA, Cheung-Lau J, Yerubandi V, Dmochowski IJ (2009) Efficient self-assembly of Archaeoglobus fulgidus ferritin around metallic cores. Langmuir 25:5219–5225

35. Patterson A (1939) The scherrer formula for X-Ray particle size determination. Phys Rev 56:978–982

36. Müller CB, Loman A, Richtering W, Enderlein J (2008) Dual-focus fluorescence correlation spectroscopy of colloidal solutions: influence of particle size. J Phys Chem B 112:8236–8240

37. Stiles PL, Dieringer JA, Shah NC, Van Duyne RP (2008) Surface-enhanced Raman spectroscopy. Annu Rev Anal Chem 1:601–626

38. Andrews DL, Bradshaw DS (2004) Virtual photons, dipole fields and energy transfer: A quantum electrodynamical approach. Eur J Phys 25:845–858

39. Brunner TJ, Bohner M, Dora C, Gerber C, Stark WJ (2007) Comparison of amorphous TCP nanoparticles to micron-sized alpha-TCP as starting materials for calcium phosphate cements. J Biomed Mater Res, Part B 83B:400–407

40. Shon YS, Choi D, Dare J, Dinh T (2008) Synthesis of nanoparticle-cored dendrimers by convergent dendritic functionalization of monolayer-protected nanoparticles. Langmuir 24:6924–6931

41. Durr NJ, Larson T, Smith DK, Korgel BA, Sokolov K, Ben-Yakar A (2007) Two-photon luminescence imaging of cancer cells using molecularly targeted gold nanorods. Nano Lett 7:941–945

42. Imura K, Okamoto H (2008) Development of novel near-field microspectroscopy and imaging of local excitations and wavefunctions of nanomaterials. Bull Chem Soc Jpn 81:659–675

43. N'Gom M, Ringnalda J, Mansfield JF, Agarwal A, Kotov N, Zaluzec NJ, Norris TB (2008) Single particle plasmon spectroscopy of silver nanowires and gold nanorods. Nano Lett 8:3200–3204

44. Yurkin MA, Hoekstra AG (2007) The discrete dipole approximation: an overview and recent developments. J Quant Spectrosc Radiat Transfer 106:558–589

45. Millstone JE, Wei W, Jones MR, Yoo H, Mirkin CA (2008) Iodide ions control seed-mediated growth of anisotropic gold nanoparticles. Nano Lett 8:2526–2529

46. Yu JS, Kim JY, Lee S, Mbindyo JKN, Martin BR, Mallouk TE (2000) Template synthesis of polymer-insulated colloidal gold nanowires with reactive ends. J Chem Soc, Chem Comm 24:2445–2446

47. Mossmer S, Spatz JP, Möller M, Aberle T, Schmidt J, Burchard W (2000) Solution behavior of poly(styrene)-block-poly(2-vinylpyridine) micelles containing gold nanoparticles. Macromolecules 33:4791–4798

48. Yang T, Fu X, Zhang Q, Cui Y, Yuan C, Zhang W, Ge H, Chen Y (2014) Fabrication of Ag nanodot array over large area for surface-enhanced Raman scattering using hybrid nanoimprint mold made from AAO template. Appl Phys A 117:909–915

49. Li J, Zhu Z, Liu F, Zhu B, Ma Y, Yan J, Lin B, Ke G, Liu R, Zhou L, Tu S, Yang C (2016) DNA-mediated morphological control of silver nanoparticles. Small 12:5449–5487

50. Figuerola A, Di Corato R, Manna L, Pellegrino T (2010) From iron oxide nanoparticles towards advanced iron-based inorganic materials designed for biomedical applications. Pharmacol Res 62:126–143

51. Schnorr JM, Swager TM (2011) Emerging applications of carbon nanotubes. Chem Mater 23:646–657

52. Sau TK, Murphy CJ (2005) Self-assembly patterns formed upon solvent evaporation of aqueous cetyltrimethylammonium bromide-coated gold nanoparticles of various shapes. Langmuir 21:2923–2929

53. Yang SM, Kim SH, Lim JM, Yi GR (2008) Synthesis and assembly of structured colloidal particles. J Mater Chem 18:2177–2190

54. Chen Y, Preece JA, Palmer RE (2008) Processing and characterization of gold nanoparticles for use in plasmon probe spectroscopy and microscopy of biosystems. Ann NY Acad Sci 1130:201–206

55. Zhou M, Wang B, Rozynek Z, Xie Z, Fossum JO, Yu X, Raaen S (2009) Minute synthesis of extremely stable gold nanoparticles. Nanotechnology 20:505606

56. Kim YG, Yang SY (2010) Nanoparticle syntheses using non-porous and porous polyelectrolyte multilayers for biological applications. J Nanosci Nanotechnol 10:6892–6895

57. Matijevic E (1981) Monodispersed metal (hydrous) oxides—a fascinating field of colloid science. Acc Chem Res 14:22–29

58. Zijlstra P, Chon JWM, Gu M (2009) Five-dimensional optical recording mediated by surface plasmons in gold nanorods. Nature 459:410–413

59. Chen PC, Mwakwari SC, Oyelere AK (2008) Gold nanoparticles: From nanomedicine to nanosensing. Nanotechnol Sci Appl 1:45–66

60. Anker JN, Hall WP, Lyandres O, Shah NC, Zhao J, Van Duyne RP (2008) Biosensing with plasmonic nanosensors. Nat Mater 7:442–453

61. Burgin J, Liu M, Guyot-Sionnest P (2008) Dielectric sensing with deposited gold bipyramids. J Phys Chem C 112:19279–19282

62. Astruc D, Lu F, Aranzaes JR (2005) Nanoparticles as recyclable catalysts: the frontier between homogeneous and heterogeneous catalysis. Angew Chem Int Ed 44:7852–7872

63. Crespo-Biel O, Ravoo BJ, Huskens J, Reinhoudt DN (2006) Writing with molecules on molecular printboards. Dalton Trans 23:2737–2741

64. Skrabalak SE, Chen J, Au L, Lu X, Li X, Xia Y (2007) Gold nanocages for biomedical applications. Adv Mater 19:3177–3184

65. Xia Y, Xiong Y, Lim B, Skrabalak SE (2008) Shape-controlled synthesis of metal nanocrystals: simple chemistry meets complex physics? Angew Chem Int Ed 48:60–103

66. Nehl CL, Hafner JH (2008) Shape-dependent plasmon resonances of gold nanoparticles. J Mater Chem 18:2415–2419

67. Zhou J, Ralston J, Sedev R, Beattie DA (2009) Functionalized gold nanoparticles: synthesis, structure and colloid stability. J Colloid Interface Sci 331:251–262

68. Boyer C, Whittaker MR, Luzon M, Davis TP (2009) Design and synthesis of dual thermoresponsive and antifouling hybrid polymer/gold nanoparticles. Macromolecules 42:6917–6926

69. Huang L, Wang H, Wang Z, Mitra A, Bozhilov KN, Yan Y (2002) Nanowire arrays electrodeposited from liquid crystalline phases. Adv Mater 14:61–64

70. Redl FX, Black CT, Papaefthymiou GC, Sandstrom RL, Yin M, Zeng H, Murray CB, O'Brien SP (2004) Magnetic, electronic, and structural characterization of nonstoichiometric iron oxides at the nanoscale. J Am Chem Soc 126:14583–14599

71. Zhu M, Lanni E, Garg N, Bier ME, Lin R (2008) Kinetically controlled, high-yield synthesis of Au25 clusters. J Am Chem Soc 130:1138–1139

72. Qian X, Zhou X, Nie S (2008) Surface-enhanced Raman nanoparticle beacons based on bioconjugated gold nanocrystals and long range plasmonic coupling. J Am Chem Soc 130:14934–14935

73. Akola J, Walter M, Whetten RL, Häkkinen H, Grönbeck H (2008) On the structure of thiolate-protected Au25. J Am Chem Soc 130:3756–3757

74. Yang KH, Liu YC, Yu CC (2009) Temperature effect of electrochemically roughened gold substrates on polymerization electrocatalysis of polypyrrole. Anal Chim Acta 631:40–46

75. Zhang H, Wang G, Chen D, Lv X, Li J (2008) Tuning photoelectrochemical performances of Ag–TiO$_2$ nanocomposites via reduction/oxidation of Ag. Chem Mater 20:6543–6549

76. Yamauchi Y, Takai A, Nagaura T, Inoue S, Kuroda K (2008) Pt fibers with stacked donut-like mesospace by assembling Pt nanoparticles: Guided deposition in physically confined self-assembly of surfactants. J Am Chem Soc 130:5426–5427

77. Virel A, Saa L, Pavlov V (2009) Modulated growth of nanoparticles. Application for sensing nerve gases. Anal Chem 81:268–272

78. Brust M, Walker M, Bethell D, Schiffrin DJ, Whyman R (1994) Synthesis of thiol-derivatised gold nanoparticles in a two-phase liquid-liquid system. J Chem Soc, Chem Commun 801–802

79. Shon YS, Mazzitelli C, Murray RW (2001) Unsymmetrical disulfides and thiol mixtures produce different mixed monolayer-protected gold clusters. Langmuir 17:7735–7741

80. Li XM, de Jong MR, Inoue K, Shinkai S, Huskens J, Reinhoudt DN (2001) Formation of gold colloids using thioether derivatives as stabilizing ligands. J Mater Chem 11:1919–1923

81. Boal AK, Ilhan F, DeRouchey JE, Thurn-Albrecht T, Russell TP, Rotello VM (2000) Self-assembly of nanoparticles into structured spherical and network aggregates. Nature 404:746–748

82. Brousseau LC, Novak JP, Marinakos SM, Feldheim DL (1999) Assembly of phenylacetylene-bridged gold nanocluster dimers and trimers. Adv Mater 11:447–449

83. Maye MM, Chun SC, Han L, Rabinovich D, Zhong CJ (2002) Novel spherical assembly of nanoparticles mediated by a thioether. J Am Chem Soc 124:4958–4959

84. Mohan YM, Vimala K, Thomas V, Varaprasad K, Sreedhar B, Bajpai SK, Raju KM (2010) Controlling of silver nanoparticles structure by hydrogel networks. J Colloid Interface Sci 342:73–82

85. da Costa LP, Formiga ALB, Mazali IO, Sigoli FA (2011) Spontaneous formation of highly dispersed spheroidal metallic silver nanoparticles in surfactant-free N, N-dimethylacetamide. Synth Met 161:1517–1521

86. Pastoriza-Santos I, Liz-Marzán LM (2009) N, N-dimethylformamide as a reaction medium for metal nanoparticle synthesis. Adv Func Mater 19:679–688

87. Nath S, Jana S, Pradhan M, Pal T (2010) Ligand-stabilized metal nanoparticles in organic solvent. J Colloid Interface Sci 341:333–352

88. Huang NM, Radiman S, Lim HN, Khiew PS, Chiu WS, Lee KH, Syahida A, Hashim R, Chia CH (2009) γ-ray assisted synthesis of silver nanoparticles in chitosan solution and the antibacterial properties. Chem Eng J 155:499–507

89. Darmanin T, Nativo P, Gilliland D, Ceccone G, Pascual C, De Berardis B, Guittard F, Rossi F (2012) Microwave-assisted synthesis of silver nanoprisms/nanoplates using a modified polyol process. Colloids Surf A 395:145–151

90. Hsu YC, Chen YM, Lin WL, Lan YF, Chan YN, Lin JJ (2010) Hierarchical synthesis of silver nanoparticles and wires by copolymer templates and visible light. J Colloid Interface Sci 352:81–86

91. Capek I (2006) Nanocomposite structures and dispersions. In: Mobius D, Muller R (eds). Elsevier, London

92. Misra RDK, Gubbala S, Kale A, Egelhoff WF (2004) A comparison of the magnetic characteristics of nanocrystalline nickel, zinc, and manganese ferrites synthesized by reverse micelle technique. J Mater Sci Eng B 111:164–174

93. Dominguez MS, Pemartin K, Boutonnet M (2012) Preparation of inorganic nanoparticles in oil-in-water microemulsions: a soft and versatile approach. Curr Opin Colloid Interface Sci 17:297–305

94. Trickett K, Brice H, Myakonkaya O, Eastoe J, Rogers SE, Heenan RK, Grillo I (2010) Microemulsion-based organogels containing inorganic nanoparticles. Soft Matter 6:1291–1296

95. Boutonnet M, Lögdberg S, Svensson E (2008) Recent developments in the application of nanoparticles prepared from w/o microemulsions in heterogeneous catalysis. Curr Opin Colloid Interface Sci 13:270–286

96. Cui YN, Threlfall M, Van Duijneveldt JS (2011) Optimizing organoclay stabilized Pickering emulsions. J Colloid Interface Sci 356:665–671

97. Pickering SU (1907) Emulsions. J Chem Soc Trans 91:2001–2021
98. Ma C, Bi X, Ngai T, Zhang GZ (2013) Polyurethane-based nanoparticles as stabilizers for oil-in-water or water-in-oil Pickering emulsions. J Mater Chem A 1:5353–5360
99. Melle S, Lask M, Fuller GG (2005) Pickering emulsions with controllable stability. Langmuir 21:2158–2162
100. Leal-Calderon F, Schmitt V (2008) Solid-stablized emulsions. Curr Opin Colloid Interface Sci 13:217–227
101. Zhao ZH, Liu WX, Liu ZY, Ding PX, Li HD (2013) Phase inversion of TiO_2 nanoparticle stabilized emulsions of alkenyl succinic anhydride. Chem Eng Sci 87:246–257
102. Chazalviel JN, Allongue P (2011) On the origin of the efficient nanoparticle mediated electron transfer across a self-assembled monolayer. J Am Chem Soc 133:762–764
103. He Y, Su S, Xu TT, Zhong YL, Zapien JA, Li J, Fan CH, Lee ST (2011) Silicon-based highly efficient SERS-active platform for sensitive and sequence-specific dna detection. Nano Today 6:122–130
104. Canevari TC, Raymundo-Pereira PA, Landers R, Machado SAS (2013) Direct synthesis of Ag nanoparticles incorporated on a mesoporous hybrid material as a sensitive sensor for the simultaneous determination of dihydroxybenzenes isomers. Eur J Inorg Chem 33:5746–5754
105. Huo Z, Tsung CK, Huang W, Zhang X, Yang P (2008) Sub-two nanometer single crystal Au nanowires. Nano Lett 8:2041–2044
106. Wei G, Zhou H, Liu Z, Song Y, Wang L, Sun L, Li Z (2005) One-step synthesis of silver nanoparticles, nanorods, and nanowires on the surface of DNA network. J Phys Chem B 109:8738–8743
107. Zhang J, Liu H, Wang Z, Ming N (2007) Shape-selective synthesis of gold nanoparticles with controlled sizes, shapes, and plasmon resonances. Adv Func Mater 17:3295–3303
108. Gong J (2012) Structure and surface chemistry of gold-based model catalysts. Chem Rev 112:2987–3054
109. Önal Y, Schimpf S, Claus P (2004) Structure sensitivity and kinetics of D-glucose oxidation to D-gluconic acid over carbon-supported gold catalysts. J Catal 223:122–133
110. Bond GC (2002) Gold: a relatively new catalyst. Catal Today 72:5–9
111. Bond GC, Louis C, Thompson DT (2006) Catalysis by gold. Catalytic science series 6. Imperial College Press, London
112. Zhang Q, Lee I, Joo JB, Zaera F, Yin Y (2012) Core-shell nanostructured catalysts. Acc Chem Res 46:1816–1824
113. Zeng HC (2013) Integrated nanocatalysts. Acc Chem Res 46:226–235
114. Huang HY, Chen WF, Kuo PL (2005) Self-assembly of gold nanoparticles induced by poly (oxypropylene) diamines. J Phys Chem B 109:24288–24294
115. Scott RWJ, Wilson OM, Crooks RM (2005) Synthesis, characterization, and applications of dendrimer-encapsulated nanoparticles. J Phys Chem B 109:692–704
116. Esumi K (2003) Dendrimers for Nanoparticle Synthesis and Dispersion Stabilization. Top Curr Chem 227:31–52
117. Sanghavi BJ, Srivastava AK (2011) Adsorptive stripping differential pulse voltammetric determination of venlafaxine and desvenlafaxine employing Nafion-carbon nanotube composite glassy carbon electrode. Electrochim Acta 56:4188–4196
118. Szroeder P (2011) Electron transfer kinetics at single-walled carbon nanotube paper: the role of band structure. Physica E 44:470–475
119. Szroeder P, Górska A, Tsierkezos N, Ritter U, Strupiński W (2013) The role of band structure in electron transfer kinetics in lowdimensional carbon. Mat wiss u Werkstofftech 44:226–230
120. Sanghavi BJ, Sitaula S, Griep MH, Karna SP, Ali MF, Swami NS (2013) Real-time electrochemical monitoring of adenosine triphosphate in the picomolar to micromolar range using graphene-modified electrodes. Anal Chem 85:8158–8165

121. Lin JJ, Lin WC, Li SD, Lin CY, Hsu SH (2013) Evaluation of the antibacterial activity and biocompatibility for silver nanoparticles immobilized on nano silicate platelets. ACS Appl Mater Interfaces 5:433–443

122. Santos KO, Elias WC, Signori AM, Giacomelli FC, Yang H, Domingos JB (2012) Synthesis and catalytic properties of silver nanoparticle-linear polyethylene imine colloidal systems. J Phys Chem C 116:4594–4604

123. Lin S, Cheng Y, Liu J, Wiesner MR (2012) Polymeric coatings on silver nanoparticles hinder autoaggregation but enhance attachment to uncoated surfaces. Langmuir 28:4178–4186

124. Chen D, Feng HB, Li JH (2012) Graphene Oxide: preparation, functionalization, and electrochemical applications. Chem Rev 112:6027–6053

125. Tang LH, Wang Y, Li YM, Feng HB, Lu J, Li JH (2009) Preparation, structure and electrochemical properties of reduced graphene sheet films. Adv Func Mater 19:2782–2789

126. Zhu YW, Murali S, Cai WW, Li XS, Suk JW, Potts JR, Ruoff RS (2010) Graphene and graphene oxide: synthesis, properties, and applications. Adv Mater 22:3906–3924

127. Sreejith S, Ma X, Zhao YL (2012) Graphene oxide wrapping on squaraine-loaded mesoporous silica nanoparticles for bioimaging. J Am Chem Soc 134:17346–17349

128. Kuila T, Bose S, Khanra P, Mishra AK, Kim NH, Lee JH (2011) Recent advances in graphene-based biosensors. Biosens Bioelectron 26:4637–4648

129. Bardhan R, Chen WX, Bartels M, Perez-Torres C, Botero MF, McAninch RW, Contreras A, Schiff R, Pautler RG, Halas NJ, Joshi A (2010) Tracking of multimodal therapeutic nanocomplexes targeting breast cancer in vivo. Nano Lett 10:4920–4928

130. Xiao YH, Li CM (2008) Nanocomposites: from fabrications to electrochemical bioapplications. Electroanalysis 20:648–662

131. Yuan WY, Li CM (2009) Direct modulation of localized surface plasmon coupling of Au nanoparticles on solid substrates via weak polyelectrolyte-mediated layer-by-layer self assembly. Langmuir 25:7578–7585

132. Lu Y, Shi C, Hu MJ, Xu YJ, Yu L, Wen LP, Zhao Y, Xu WP, Yu SH (2010) Magnetic alloy nanorings loaded with gold nanoparticles: synthesis and applications as multimodal imaging contrast agents. Adv Func Mater 20:3701–3706

133. Xu ZC, Hou YL, Sun SH (2007) Magnetic core/shell Fe3O4/Au and Fe_3O_4/Au/Ag nanoparticles with tunable plasmonic properties. J Am Chem Soc 129:8698–8699

134. Choi SH, Na HB, Park YI, An K, Kwon SG, Jang Y, Park MH, Moon J, Son JS, Song IC, Moon WK, Hyeon T (2008) Simple and generalized synthesis of oxide-metal heterostructured nanoparticles and their applications in multimodal biomedical probes. J Am Chem Soc 130:15573–15580

135. Jiang J, Gu HW, Shao HL, Devlin E, Papaefthymiou GC, Ying JY (2008) Bifunctional Fe_3O_4-Ag heterodimer nanoparticles for two-photon fluorescence imaging and magnetic manipulation. Adv Mater 20:4403–4407

136. Connor EE, Mwamuka J, Gole A, Murphy CJ, Wyatt MD (2005) Gold nanoparticles are taken up by human cells but do not cause acute cytotoxicity. Small 1:325–327

137. Weissleder R (2001) A clearer vision for in vivo imaging. Nat Biotechnol 19:316–317

138. Lu X, Tuan HY, Chen J, Li ZY, Korgel BA, Xia Y (2007) Mechanistic studies on the galvanic replacement reaction between multiply twinned particles of Ag and $HAuCl_4$ in an organic medium. J Am Chem Soc 129:1733–1742

139. Skrabalak SE, Chen J, Sun Y, Lu X, Au L, Cobley CM, Xia YN (2008) Gold nanocages: synthesis, properties, and applications. Acc Chem Res 41:1587–1595

140. Shylesh S, Schunemann V, Thiel WR (2010) Magnetically separable nanocatalysts: bridges between homogeneous and heterogeneous catalysis. Angew Chem Int Ed 49:3428–3459

141. Xu CJ, Wang BD, Sun SH (2009) Dumbbell-like Au–Fe_3O_4 nanoparticles for target-specific platin delivery. J Am Chem Soc 131:4216–4217

142. Chen W, Xu NF, Xu LG, Wang LB, Li ZK, MaW ZhuYY, Xu CL, Kotov NA (2010) Multifunctional magnetoplasmonic nanoparticle assemblies for cancer therapy and diagnostics (theranostics). Macromol Rapid Commun 31:228–236

143. Liu J, Qiao SZ, Chen JS, Lou XW, Xing X, Lu GQ (2011) Yolk/shell nanoparticles: new platforms for nanoreactors, drug delivery and lithium-ion batteries. Chem Commun 47:12578–12591
144. Park JC, Song H (2011) Metal@Silica yolk-shell nanostructures as versatile bifunctional nanocatalysts. Nano Res 4:33–49
145. Yin Y, Rioux RM, Erdonmez CK, Hughes S, Somorjai GA, Alivisatos AP (2004) Formation of hollow nanocrystals through the nanoscale Kirkendall effect. Science 304:711–714
146. Wang H, Liu J, Wu X, Tong Z, Deng Z (2013) Tailor-made Au@Ag core-shell nanoparticle 2D arrays on protein-coated graphene oxide with assembly enhanced antibacterial activity. Nanotechnology 24:205102
147. Li SS, Lv JJ, Hu YY, Zheng JN, Chen JR, Wang AJ, Feng JJ (2014) Facile synthesis of porous Pt-Pd nanospheres supported on reduced graphene oxide nanosheets for enhanced methanol electrooxidation. J Power Sour 247:213–218
148. Tang M, Wang X, Wu F, Liu Y, Zhang S, Pang X, Li X, Qiu H (2014) Au nanoparticle/graphene oxide hybrids as stabilizers for pickering emulsions and Au nanoparticle/graphene microspheres. Carbon 71:238–248
149. Efros AL, Shklovskii BI (1976) Critical behaviour of conductivity and dielectric constant near the metal-non-metal transition threshold. Phys Status Solid B 76:475–485
150. Chen S, Sommers JM (2001) Alkanethiolate-protected copper nanoparticles: spectroscopy, electrochemistry, and solid-state morphological evolution. J Phys Chem B 105:8816–8820
151. Klein DL, Roth R, Lim AKL, Alivisatos AP, McEuen PL (1997) A single-electron transistormade from a cadmiumselenide nanocrystal. Nature 389:699–701
152. Bergbreiter DE, Case BL, Liu YS, Caraway JW (1998) Poly(N-isopropylacrylamide) soluble polymer supports in catalysis and synthesis. Macromolecules 31:6053–6062
153. Kubo S, Diaz A, Tang Y, Mayer TS, Khoo IC, Mallouk TE (2007) Tunability of the refractive index of gold nanoparticle dispersions. Nano Lett 7:3418–3423
154. Lee JH, Kim DO, Song GS, Lee Y, Jung SB, Nam JD (2007) Direct metallization of gold nanoparticles on a polystyrene bead surface using cationic gold ligands. Macromol Rapid Commun 28:634–640
155. Sun ZZ, Zhang N, Si YM, Li S, Wen JW, Zhu XB, Wang H (2014) High-throughput colorimetric assays for mercury(II) in blood and wastewater based on the mercury-stimulated catalytic activity of small silver nanoparticles in a temperature-switchable gelatin matrix, vol 50. Chemical Communications Cambridge, UK, pp 9196-9199
156. Duan JL, Yin HZ, Wei RR, Wang WW (2014) Facile colorimetric detection of Hg^{2+} based on anti-aggregation of silver nanoparticles. Biosens Bioelectron 57:139–142
157. Rastogi L, Sashidhar RB, Karunasagar D, Arunachalam J (2014) Gum kondagogu reduced/stabilized silver nanoparticles as direct colorimetric sensor for the sensitive detection of Hg^{2+} in aqueous system. Talanta 118:111–117
158. Jain PK, Huang XH, EI-Sayed IH, EI-Sayed MA (2007) Review of some interesting surface plasmon resonance-enhanced properties of noble metal nanoparticles and their applications to biosystems. Plasmonics 2:107–118
159. Fasciani C, Bueno Alejo CJ, Grenier M, Netto-Ferreira JC, Scaiano JC (2011) High-temperature organic reactions at room temperature using plasmon excitation: decomposition of dicumyl peroxide. Org Lett 13:204–207
160. Agostinis P, Berg K, Cengel KA, Foster TH, Girotti AW, Gollnick SO, Hahn SM, Hamblin MR, Juzeniene A, Kessel D, Korbelik M, Moan J, Mroz P, Nowis D, Piette J, Wilson BC, Golab J (2011) Photodynamic therapy of cancer: an update. CA: Cancer J Clin 61:250–281
161. Sperandio F, Huang Y, Hamblin M (2013) Antimicrobial photodynamic therapy to kill gram-negative bacteria. Antiinfect Drug Discov 8:108–120
162. Alarcon E, Bueno-Alejo C, Noel C, Stamplecoskie K, Pacioni N, Poblete H, Scaiano JCJ (2013) Human serum albumin as protecting agent of silver nanoparticles: role of the protein conformation and amine groups in the nanoparticle stabilization. Nanopart Res 15:1–14

163. Kalishwaralal K, BarathManiKanth S, Pandian SRK, Deepak V, Gurunathan S (2010) Silver nanoparticles impede the biofilm formation by pseudomonas aeruginosa and staphylococcus epidermidis. Colloids Surf B: Biointerfaces 79:340–344

164. Mukherjee S, Chowdhury D, Kotcherlakota R, Patra S, Vinothkumar B, Bhadra MP, Sreedhar B, Patra CR (2014) Potential theranostics application of bio-synthesized silver nanoparticles (4-in-1 system). Theranostics 4:316–335

165. Vignoni M, de Alwis Weerasekera H, Simpson MJ, Phopase J, Mah TF, Griffith M, Alarcon EI, Scaiano JC (2014) LL37 peptide@silver nanoparticles: combining the best of the two worlds for skin infection control. Nanoscale 6:5725–5728

166. Tran ML, Centeno SP, Hutchison JA, Engelkamp H, Liang D, Van Tendeloo G, Sels BF, Hofkens J, Uji-i H (2008) Control of surface plasmon localization via self-assembly of silver nanoparticles along silver nanowires. J Am Chem Soc 130:17240–17241

167. Dadosh T, Sperling J, Bryant GW, Breslow R, Shegai T, Dyshel M, Haran G, Bar-Joseph I (2009) Plasmonic control of the shape of the Raman spectrum of a single molecule in a silver nanoparticle dimer. ACS Nano 3:1988–1994

168. Peng H, Strohsahl CM, Leach KE, Krauss TD, Miller BL (2009) Label-free DNA detection on nanostructured Ag surfaces. ACS Nano 3:2265–2273

169. Tao AR, Habas S, Yang P (2008) Shape control of colloidal metal nanocrystals. Small 4:310–325

170. Wiley BJ, Im S, Li Z, McLellan J, Siekkinen A, Xia Y (2006) Maneuvering the surface plasmon resonance of silver nanostructures through shape-controlled synthesis. J Phys Chem B 110:15666–15675

171. Shem PM, Sardar R, Shumaker-Parry JS (2014) Soft ligand stabilized gold nanoparticles: incorporation of bipyridyls and two-dimensional assembly. J Colloid Interface Sci 426:107–116

172. Jin R, Cao C, Hao E, Metraux GS, Schatz GC, Mirkin CA (2003) Controlling anisotropic nanoparticle growth through plasmon excitation. Nature 425:487–490

173. Washio I, Xiong Y, Yin Y, Xia Y (2006) Reduction by the end groups of poly(vinyl pyrrolidone): a new and versatile route to the kinetically controlled synthesis of Ag triangular nanoplates. Adv Mater 18:1745–1749

174. Sun Y, Xia Y (2002) Shape-controlled synthesis of gold and silver nanoparticles. Science 298:2176–2179

175. Sun Y, Mayers B, Xia Y (2003) Transformation of silver nanospheres into nanobelts and triangular nanoplates through a thermal process. Nano Lett 3:675–679

176. Zhao N, Wei Y, Sun N, Chen Q, Bai J, Zhou L, Qin Y, Li M, Qi L (2008) Controlled synthesis of gold nanobelts and nanocombs in aqueous mixed surfactant solutions. Langmuir 24:991–998

177. Sun Y, Yin Y, Mayers BT, Herricks T, Xia Y (2002) Uniform silver nanowires synthesis by reducing $AgNO_3$ with ethylene glycol in the presence of seeds and poly(vinyl pyrrolidone). Chem Mater 14:4736–4745

178. Sun Y, Mayers B, Herricks T, Xia Y (2003) Polyol synthesis of uniform silver nanowires: a plausible growth mechanism and the supporting evidence. Nano Lett 3:955–960

179. Pietrobon B, McEachran M, Kitaev V (2009) Synthesis of size-controlled faceted pentagonal silver nanorods with tunable plasmonic properties and self-assembly of these nanorods. ACS Nano 3:21–26

180. Hao E, Bailey RC, Schatz GC, Hupp JT, Li S (2004) Synthesis and optical properties of 'three-pointed' star-shaped gold nanoparticles. Nano Lett 4:327–330

181. Han Y, Liu S, Han M, Bao J, Dai Z (2009) Fabrication of hierarchical nanostructure of silver via a surfactant-free mixed solvents route. Cryst Growth Des 9:3941–3947

182. El-Sayed MA (2001) Some interesting properties of metals confined in time and nanometer space of different shapes. Acc Chem Res 34:257–264

183. Wang L, Luo J, Shan S, Crew E, Yin J, Zhong CJ, Wallek B, Wong SSS (2011) Bacterial inactivation using silver-coated magnetic nanoparticles as functional antimicrobial agents. Anal Chem 83:8688–8695

184. Tang S, Vongehr S, Meng X (2010) Carbon spheres with controllable silver nanoparticle doping. J Phys Chem C 114:977–982

185. Yamamoto M, Kashiwagi Y, Nakamoto M (2006) Size-controlled synthesis of monodispersed silver nanoparticles capped by long- chain alkyl carboxylates from silver carboxylate and tertiary amine. Langmuir 22:8581–8586

186. Kim JY, Lee JS (2010) Synthesis and thermodynamically controlled anisotropic assembly of dna-silver nanoprism conjugates for diagnostic applications. Chem Mater 22:6684–6691

187. Zhang Q, Li W, Moran C, Zeng J, Chen J, Wen LP, Xia Y (2010) Seed-mediated synthesis of Ag nanocubes with controllable edge lengths in the range of 30-200 nm and comparison of their optical properties. J Am Chem Soc 132:11372–11378

188. Netzer NL, Gunawidjaja R, Hiemstra M, Zhang Q, Tsukruk VV, Jiang C (2009) Formation and optical properties of compression-induced nanoscale buckles on silver nanowires. ACS Nano 3:1795–1802

189. Tang B, An J, Zheng X, Xu S, Li D, Zhou J, Zhao B, Xu W (2008) Silver nanodisks with tunable size by heat aging. J Phys Chem C 112:18361–18367

190. Halvorson RA, Vikesland PJ (2010) Surface-enhanced raman spectroscopy (SERS) for environmental analyses. Environ Sci Technol 44:7749–7755

191. Chang S, Chen K, Hua Q, Ma Y, Huang W (2011) Evidence for the growth mechanisms of silver nanocubes and nanowires. J Phys Chem C 115:7979–7986

192. Huang L, Zhai Y, Dong S, Wang J (2009) Efficient preparation of silver nanoplates assisted by non-polar solvents. J Colloid Interface Sci 331:384–388

193. Sarkar A, Kapoor S, Mukherjee T (2005) Synthesis of silver nanoprisms in formamide. J Colloid Interface Sci 287:496–500

194. Schneider OD, Loher S, Brunner TJ, Uebersax L, Simonet M, Grass RN, Merkle HP, Stark WJ (2008) Cotton wool-like nanocomposite biomaterials prepared by electrospinning: In vitro bioactivity and osteogenic differentiation of human mesenchymal stem cells. J Biomed Mater Res, Part B 84:350–362

195. Shon YS, Cutler E (2004) Aqueous synthesis of alkanethiolate- protected Ag nanoparticles using bunte salts. Langmuir 20:6626–6630

196. Jana NR, Peng X (2003) Single-phase and gram-scale routes toward nearly monodisperse Au and other noble metal nanocrystals. J Am Chem Soc 125:14280–14281

197. Tan S, Erol M, Attygalle A, Du H, Sukhishvili S (2007) Synthesis of positively charged silver nanoparticles via photoreduction of AgNO$_3$ in branched polyethyleneimine/HEPES solutions. Langmuir 23:9836–9843

198. Zhu Y, Qian Y, Li X, Zhang M (1997) γ-Radiation synthesis and characterization of polyacrylamide-silver nanocomposites. Chem Commun 10:1081–1082

199. Jiang LP, Xu S, Zhu JM, Zhang JR, Zhu JJ, Chen HY (2004) Ultrasonic-assisted synthesis of monodisperse single-crystalline silver nanoplates and gold nanorings. Inorg Chem 43:5877–5883

200. Hu B, Wang SB, Wang K, Zhang M, Yu SH (2008) Microwave-assisted rapid facile "green" synthesis of uniform silver nanoparticles: self-assembly into multilayered films and their optical properties. J Phys Chem C 112:11169–11174

201. Tan Y, Li Y, Zhu D (2003) Preparation of silver nanocrystals in the presence of Aniline. J Colloid Interface Sci 258:244–251

202. Yu D, Yam VWW (2004) Controlled synthesis of monodisperse silver nanocubes in water. J Am Chem Soc 126:13200–13201

203. Giersig M, Pastoriza-Santos I, Liz-Marzan LM (2004) Evidence of an aggregative mechanism during the formation of silver nanowires in N, N-dimethylformamide. J Mater Chem 14:607–610

204. Tan Y, Dai X, Li Y, Zhu D (2003) Preparation of gold, platinum, palladium and silver nanoparticles by the reduction of their salts with a weak reductant-potassium bitartrate. J Mater Chem 13:1069–1075

205. Lee GJ, Shin SI, Kim YC, Oh SG (2004) Preparation of silver nanorods through the control of temperature and pH of reaction medium. Mater Chem Phys 84:197–204

206. Baram-Pinto D, Shukla S, Perkas N, Gedanken A, Sarid R (2009) Inhibition of herpes simplex virus type 1 infection by silver nanoparticles capped with mercaptoethane sulfonate. Bioconjugate Chem 20:1497–1502
207. Chen M, Feng YG, Wang X, Li TC, Zhang JY, Qian DJ (2007) Silver nanoparticles capped by oleylamine: formation, growth, and self-organization. Langmuir 23:5296–5304
208. Khan Z, Al-Thabaiti SA, Obaid AY, Khan ZA, Al-Youbi AO (2011) Effects of solvents on the stability and morphology of CTAB stabilized silver nanoparticles. Colloids Surf A 390:120–125
209. Mohanty S, Mishra S, Jena P, Jacob B, Sarkar B, Sonawane A (2012) An investigation on the antibacterial, cytotoxic, and antibiofilm efficacy of starch-stabilized silver nanoparticles. Nanomed Nanotechnol 8:916–924
210. Subbiah R, Veerapandian M, Yun KS (2010) Nanoparticles: functionalization and multifunctional applications in biomedical sciences. Curr Med Chem 17:4559–4577
211. Rohrer H (2010) Nanomaterials science. Sci Technol Adv Mater 11(3):050301
212. Ramanaviciusa A, Kausaite A, Kausaite A, Ramanaviciene A (2005) Biofuel cell based on direct bioelectrocatalysis. Biosens Bioelect 20:1962–1967
213. Feynman R (1959) There's plenty of room at the bottom. Caltech Institute Archives, Pasadena, California
214. Feynman R (1999) The pleasure of finding things out: the best short works of Richard P. Feynman (Helix Books). Robbins J (ed). Perseus Books
215. Katz E, Willner I (2004) Integrated nanoparticle-biomolecule hybrid systems: synthesis, properties, and applications. Angew Chem Int Ed 43:6042–6108
216. Hunt W (2004) Nanomaterials: nomenclature, novelty, and necessity. J Miner Met Mater Soc 56:13–18
217. Kroto HW, Heath JR, O'Brien SC, Curl RF, Smalley RE (1985) C_{60}: Buckminsterfullerene. Nature 318:162–163
218. Mangematin V, Walsh S (2012) The future of nanotechnologies. Technovation 32:157–160
219. Chaturvedi S, Dave PN (2013) Design process for nanomaterials. J Mater Sci 48:3605–3622
220. Xu HX, Suslick KS (2010) Water-soluble fluorescent silver nanoclusters. Adv Mater 22:1078–1082
221. Jin RC (2010) Quantum sized, thiolate-protected gold nanoclusters. Nanoscale 2:343–362
222. Díez I, Ras RHA (2011) Fluorescent silver nanoclusters. Nanoscale 3:1963–1970
223. Díez I, Ras RHA (2010) Advanced fluorescence reporters in chemistry and biology II. Demchenko AP (ed). Springer, Heidelberg, pp 307–332
224. Gunalan S, Sivaraj R, Venckatesh R (2012) Aloe barbadensis Miller mediated green synthesis of mono-disperse copper oxide nanoparticles: optical properties. Spectrochim Acta A Mol Biomol Spectrosc 97:1140–1144
225. Vimala K, Sundarraj S, Paulpandi M, Vengatesan S, Kannan S (2014) Green synthesized doxorubicin loaded zinc oxide nanoparticles regulates the Bax and Bcl-2 expression in breast and colon carcinoma. Process Biochem 49:160–172
226. Ramamurthy CH, Sampath KS, Arunkumar P, SureshKumar M, Sujatha V, Premkumar K, Thirunavukkarasu C (2013) Green synthesis and characterization of selenium nanoparticles and its augmented cytotoxicity with doxorubicin on cancer cells. Bioprocess Biosyst Eng 36:1131–1139
227. Zheng B, Kong T, Jing X, Odoom-Wubah T, Li X, Sun D, Lu F, Zheng Y, Huang J, Li Q (2013) Plant-mediated synthesis of platinum nanoparticles and its bioreductive mechanism. J Colloid Interface Sci 396:138–145
228. Bhuvanasree SR, Harini D, Rajaram A, Rajaram R (2013) Rapid synthesis of gold nanoparticles with Cissus quadrangularis extract using microwave irradiation. Spectrochim Acta A 106:190–196
229. Aswathy Aromal S, Philip D (2012) Green synthesis of gold nanoparticles using Trigonella foenum-graecum and its size-dependent catalytic activity. Spectrochim Acta A 97:1–5

230. Sujitha MV, Kannan S (2013) Green synthesis of gold nanoparticles using Citrus fruits (Citrus limon, Citrus reticulata and Citrus sinensis) aqueous extract and its characterization. Spectrochim Acta A 102:15–23
231. Modi A, Koratkar N, Lass E, Wei BQ, Ajayan PM (2003) Miniaturized gas ionization sensors using carbon nanotubes. Nature 424:171–174
232. Heath JR (1999) Nanoscale materials. Acc Chem Res 32:388
233. Mohamed H, Hassan A (2005) Small things and big changes in the developing world. Science 309:65–66
234. Mahmoud MA, Saira F, El-Sayed MA (2010) Experimental evidence for the nanocage effect in catalysis with hollow nanoparticles. Nano Lett 10:3764–3769
235. Somorjai GA, Park JY (2008) Molecular factors of catalytic selectivity. Angew Chem Int Ed 47:9212–9228
236. Sau TK, Rogach AL (2010) Nonspherical noble metal nanoparticles: colloid-chemical synthesis and morphology control. Adv Mater 22:1781–1804
237. Boisselier E, Astruc D (2009) Gold nanoparticles in nanomedicine: preparations, imaging, diagnostics, therapies and toxicity. Chem Soc Rev 38:1759–1782
238. Gu Y, Cheng J, Lin C, Lam Y, Cheng S, Wong W (2009) Nuclear penetration of surface functionalized gold nanoparticles. Toxicol Appl Pharmacol 237:196–204
239. Hosta L, Pla-Roca M, Arbiol J, Lopez-Iglesias C, Samitier J, Cruz L, Kogan M, Albericio F (2009) Conjugation of Kahalalide F with gold nanoparticles to enhance in vitro antitumoral activity. Bioconjug Chem 20:138–146
240. Park J, Lee S, Kim J, Park K, Kim K, Kwon I (2008) Polymeric nanomedicine for cancer therapy. Prog Polym Sci 33:113–137
241. Peer D, Karp J, Hong S, Farokhzad O, Margalit R, Langer R (2007) Nanocarriers as an emerging platform for cancer therapy. Nat Nanotechnol 2:751–760
242. Fendler JH (1998) Nanoparticles and nanostructured films: Preparation, characterization and applications. Wiley-VCH, Weinheim
243. Zhang JP, Chen P, Sun CH, Hu XJ (2004) Sonochemical synthesis of colloidal silver catalysts for reduction of complexing silver in DTR system. Appl Catal A 266:49–54
244. Lee HJ, Yeo SY, Jeong SH (2003) Antibacterial effect of nanosized silver colloidal solution on textile fabrics. J Mater Sci 38:2199–2204
245. Zhang Q, Tan YN, Xie J, Lee JY (2009) Colloidal synthesis of plasmonic metallic nanoparticles. Plasmonics 4:9–22
246. Sridhar A, van Dijk DJ, Akkerman R (2009) Inkjet printing and adhesion characterization of conductive tracks on a commercial printed circuit board material. Thin Solid Films 517:4633–4637
247. Chen J, Luo Y, Liang Y, Jiang J, Shen G, Yu R (2009) Surface-enhanced Raman scattering for immunoassay based on the biocatalytic production of silver nanoparticles. Anal Sci 25:347–352
248. Sardar R, Funston AM, Mulvaney P, Murray RW (2009) Gold nanoparticles: past, present, and future. Langmuir 25:13840–13851
249. Chen S, Yang YJ (2002) Magnetoelectrochemistry of gold nanoparticle quantized capacitance charging. J Am Chem Soc 124:5280–5281
250. Cao YC, Jin R, Mirkin CA (2002) Nanoparticles with raman spectroscopic fingerprints for DNA and RNA detection. Science 297:1536–1540
251. Huang H, Yang X (2005) One-step, shape control synthesis of gold nanoparticles stabilized by 3-thiopheneacetic acid. Colloids Surf A 255:11–17
252. Ji Q, Acharya S, Hill PJ, Richards G, Ariga K (2008) Multi-dimensional control of surfactant-guided assemblies of quantum gold particles. Adv Mater 20:4027–4032
253. Tang ZY, Kotov NA, Giersig M (2002) Spontaneous organization of single CdTe nanoparticles into luminescent nanowires. Science 297:237–240
254. Grubbs RB (2007) Nanoparticle assembly: solvent-tuned structures. Nat Mater 6:553–555

255. Lévy R, Thanh NTK, Doty RC, Hussain I, Nichols RJ, Schiffrin DJ, Brust M, Ferning DG (2004) Rational and combinatorial design of peptide capping ligands for gold nanoparticles. J Am Chem Soc 126:10076–10084

256. Murphy CJ (2002) Nanocubes and nanoboxes. Science 298:2139–2141

257. Puntes VF, Krishnan KM, Alivisatos AP (2001) Colloidal nanocrystal shape and size control: the case of cobalt. Science 291:2115–2117

258. Glotzer SC, Solomon MJ (2007) Anisotropy of building blocks and their assembly into complex structures. Nat Mater 6:557–562

259. Jiang XC, Brioude A, Pileni MP (2006) Gold nanorods: limitations on their synthesis and optical properties colloids and surfaces a: physicochemical and engineering aspects. Colloids Surf A 277:201–206

260. de Hollander RBG, van Hulst NF, Kooyman RPH (1995) Near field plasmon and force microscopy. Ultramicroscopy 57:263–269

261. Naitoh M, Shoji F, Oura K (1992) Direct observation of the growth process of Ag thin film on a hydrogen-terminated Si(111) surface. Jpn J Appl Phys 31:4018–4019

262. Arai M, Mitsui M, Ozaki JL, Nishiyama Y (1994) Dispersion and optical absorption of Au and Ag particles supported on an amorphous SiO_2 substrate. J Colloid Interface Sci 168:473–477

263. Fischer UC (1986) Submicrometer aperture in a thin metal film as a probe of its microenvironment through enhanced light scattering and fluorescence. J Opt Soc Am B 3:1239–1244

264. Rucker M, Knoll W, Rabe JP (1992) Surface-plasmoninduced contrast in scanning tunneling microscopy. J Appl Phys 72:5027–5031

265. Dawson P, de Fornet F, Goudonnet JP (1994) Imaging of surface plasmon propagation and edge interaction using a photon scanning tunneling microscope. Phys Rev Lett 72:2927–2930

266. Jin SE, Bae JW, Hong S (2010) Multiscale observation of biological interactions of nanocarriers: from nano to macro. Microsc Res Tech 73:813–823

267. Medley CD, Bamrungsap S, Tan W, Smith JE (2011) Aptamer-conjugated nanoparticles for cancer cell detection. Anal Chem 83:727–734

268. Cornelia MK (2010) Particle size analysis of nanocrystals: improved analysis method. Int J Pharm 390:3–12

269. Khlebtsov B, Khlebtsov N (2011) On the measurement of gold nanoparticle sizes by the dynamic light scattering method. Colloid J 73:118–127

270. Bienert R, Emmerling F, Thünemann A (2009) The size distribution of 'gold standard' nanoparticles. Anal Bioanal Chem 395:1651–1660

271. Pyrz WD, Buttrey DJ (2008) Particle size determination using TEM: a discussion of image acquisition and analysis for the novice microscopist. Langmuir 24:11350–11360

272. Guha S, Li M, Tarlov MJ, Zachariah MR (2012) Electrospray- differential mobility analysis of bionanoparticles. Trends Biotechnol 30:291–300

273. Couteau O, Roebben G (2011) Measurement of the size of spherical nanoparticles by means of atomic force microscopy. Meas Sci Technol 22:065101

274. Gadogbe M, Ansar SM, He G, Collier WE, Rodriguez J, Liu D, Chu IW, Zhang D (2013) Determination of colloidal gold nanoparticle surface areas, concentrations, and sizes through quantitative ligand adsorption. Anal Bioanal Chem 405:413–422

275. Xu X, Caswell KK, Tucker E, Kabisatpathy S, Brodhacker KL, Scrivens WA (2007) Size and shape separation of gold nanoparticles with preparative gel electrophoresis. J Chromatogr A 1167:35–41

276. Lo CK, Paau MC, Xiao D, Choi MMF (2008) Application of capillary zone electrophoresis for separation of water-soluble gold monolayer-protected clusters. Electrophoresis 29:2330–2339

277. Akthakul A, Hochbaum AI, Stellacci F, Mayes AM (2005) Size fractionation of metal nanoparticles by membrane filtration. Adv Mater 17:532–535

278. Gautier C, Taras R, Gladiali S, Bürgi T (2008) Chiral 1,1-binaphthyl-2,2-dithiol-stabilized gold clusters: size separation and optical activity in the UV-vis. Chirality 20:486–493

279. Liu FK, Wei GT (2004) Adding sodium dodecylsulfate to the running electrolyte enhances the separation of gold nanoparticles by capillary electrophoresis. Anal Chim Acta 510:77–83

280. Al-Somali AM, Krueger KM, Falkner JC, Colvin VL (2004) Recycling size exclusion chromatography for the analysis and separation of nanocrystalline gold. Anal Chem 76:5903–5910

281. Murray CB, Norris DJ, Bawendi MG (1993) Synthesis and characterization of nearly monodisperse CdE (E = sulfur, selenium, tellurium) semiconductor nanocrystallites. J Am Chem Soc 115:8706–8715

282. McLeod MC, Anand M, Kitchens CL, Roberts CB (2005) Precise and rapid size selection and targeted deposition of nanoparticle populations using CO_2 gas expanded liquids. Nano Lett 5:461–465

283. Williams DP, Satherley J (2009) Size-selective separation of polydisperse gold nanoparticles in supercritical ethane. Langmuir 25:3743–3747

284. Lee JS, Seferos DS, Giljohann DA, Mirkin CA (2008) Thermodynamically controlled separation of polyvalent 2-nm gold nanoparticle-oligonucleotide conjugates. J Am Chem Soc 130:5430–5431

285. Kumar SA, Peter YA, Nadeau JL (2008) Facile biosynthesis, separation and conjugation of gold nanoparticles to doxorubicin. Nanotechnol 19:495101

286. Otto DP, Vosloo HCM, de Villiers MM (2007) Application of size exclusion chromatography in the development and characterization of nanoparticulate drug delivery systems. J Liq Chromatogr Relat Technol 30:2489–2514

287. Claridge SA, Liang HW, Basu SR, Fréchet JMJ, Alivisatoes AP (2008) Isolation of discrete nanoparticle-DNA conjugates for plasmonic applications. Nano Lett 8:1202–1206

288. Wei GT, Liu FK, Wang CR (1999) Shape separation of nanometer gold particles by size-exclusion chromatography. Anal Chem 71:2085–2091

289. Mullen DG, Desai AM, Waddell JN, Cheng X, Kelly CV, McNerny DQ, Majoros IJ, Baker JR Jr, Sander LM, Orr BG, Banaszak Holl MM (2008) The implications of stochastic synthesis for the conjugation of functional groups to nanoparticles. Bioconjugate Chem 19:1748–1752

290. Mullen DG, Fang M, Desai AM, Baker JR, Orr BG, Banaszak Holl MM (2010) A quantitative assessment of nanoparticle-ligand distributions: implications for targeted drug and imaging delivery in dendrimer conjugates. ACS Nano 4:657–670

291. Schimpf M, Caldwell KD, Giddings JC (eds) (2000) Field flow fractionation handbook. Wiley Interscience, New York

292. Cho TJ, Hackley VA (2010) Fractionation and characterization of gold nanoparticles in aqueous solution: asymmetric-flow field flow fractionation with MALS, DLS, and UV-Vis detection. Anal Bioanal Chem 398:2003–2018

293. Calabretta M, Jamison JA, Falkner JC, Liu Y, Yuhas BD, Matthews KS, Colvin VL (2005) Analytical ultracentrifugation for characterizing nanocrystals and their bioconjugates. Nano Lett 5:963–967

294. Baudhuin P, Van der Smissen P, Beauvois S, Courtoy PJ (1989) In colloidal gold: principles, methods and applications. In: Hayat MA (ed) Academic Press, San Diego, CA 2:2-18

295. Mächtle W, Börger L (2006) Analytical ultracentrifugation of polymers and nanoparticles. Springer, Berlin

296. Kasyutich O, Ilari A, Fiorillo A, Tatchev D, Hoell A, Ceci P (2010) Silver ion incorporation and nanoparticle formation inside the cavity of pyrococcus furiosus ferritin: structural and size-distribution analyses. J Am Chem Soc 132:3621–3627

297. Jamison JA, Krueger KM, Yavuz CT, Mayo JT, LeCrone D, Redden JJ, Colvin VL (2008) Size-dependent sedimentation properties of nanocrystals. ACS Nano 2:311–319

298. Goertz V, Dingenouts N, Nirschl H (2009) Comparison of nanometric particle size distributions as determined by SAXS, TEM and analytical ultracentrifuge. Part Part Syst Charact 26:17–24

299. Stavis SM, Geist J, Gaitan M (2010) Separation and metrology of nanoparticles by nanofluidic size exclusion. Lab Chip 10:2618–2621
300. Pyell U (2010) Characterization of nanoparticles by capillary electromigration separation techniques. Electrophoresis 31:814–831
301. Surugau N, Urban PL (2009) Electrophoretic methods for separation of nanoparticles. J Sep Sci 32:1889–1906
302. Liu FK, Ko FH, Huang PW, Wu CH, Chu TC (2005) Studying the size/shape separation and optical properties of silver nanoparticles by capillary electrophoresis. J Chromatogr A 1062:139–145
303. Mock JJ, Smith DR, Schultz S (2003) Local refractive index dependence of plasmon resonance spectra from individual nanoparticles. Nano Lett 3:485–491
304. Bücking W, Massadeh S, Merkulov A, Xu S, Nann T (2010) Electrophoretic properties of BSA-coated quantum dots. Anal Bioanal Chem 396:1087–1094
305. Pons T, Uyeda HT, Medintz IL, Mattoussi H (2006) Hydrodynamic dimensions, electrophoretic mobility, and stability of hydrophilic quantum dots. J Phys Chem B 110:20308–20316
306. Sperling RA, Liedl T, Duhr S, Kudera S, Zanella M, Lin CAJ, Chang WH, Braun D, Parak WJ (2007) Size determination of (bio)conjugated water-soluble colloidal nanoparticles: a comparison of different techniques. J Phys Chem C 111:11552–11559
307. Daou TJ, Li L, Reiss P, Josserand V, Texier I (2009) Effect of poly(ethylene glycol) length on the in vivo behavior of coated quantum dots. Langmuir 25:3040–3044
308. Ahmed M, Deng Z, Narain R (2009) Study of transfection efficiencies of cationic glyconanoparticles of different sizes in human cell line. ACS Appl Mater Interfaces 1:1980–1987
309. Lôpez-Viota J, Mandal S, Delgado A, Toca-Herrera JL, Moller M, Zanuttin F, Balestrino M, Krol S (2009) Electrophoretic characterization of gold nanoparticles functionalized with human serum albumin (HSA) and creatine. J Colloid Interface Sci 332:215–223
310. Hanauer M, Pierrat S, Zins I, Lotz A, Sönnichsen C (2007) Separation of nanoparticles by gel electrophoresis according to size and shape. Nano Lett 7:2881–2885
311. Perrault SD, Chan WCW (2009) Synthesis and surface modification of highly monodispersed, spherical gold nanoparticles of 50–200 nm. J Am Chem Soc 131:17042–17043
312. Bremmel KE, Jameson GJ, Biggs S (1999) Adsorption of ionic surfactants in particulate systems: flotation, stability, and interaction forces. Colloids Surf A 146:75–87
313. Kirkpatrick S (1973) Percolation and conduction. Rev Mod Phys 45:574–588
314. Stauffer D, Aharony A (1994) Introduction to percolation theory. Taylor & Francis, London
315. Pellegrino T, Sperling RA, Alivisatoes AP, Parak WJ (2007) Gel electrophoresis of gold-DNA nanoconjugates. J Biomed Biotechnol 26796–26804
316. Park S, Hamad-Schifferli K (2008) Evaluation of hydrodynamic size and zeta-potential of surface-modified Au nanoparticle-DNA conjugates via Ferguson analysis. J Phys Chem C 112:7611–7616
317. Dair BJ, Tyner K, Sapsford KE (2009) Techniques for the characterization of nanoparticle-bioconjugates. In: Rege K, Medintz IL (ed) Methods in bioengineering: nanoscale bioengineering and nanomedicine, 1st edn. Artech House, London, pp 293–331
318. Bergman L, Rosenholm J, Öst AB, Duchanoy A, Kankaanpää P, Heino J, Lindén M (2008) On the importance of surface chemical engineering for controlling nanoparticle suspension stability in biotargeting and imaging applications. J Nanomater 712514:9
319. Gomes I, Santos NC, Oliveira MA, Quintas A, Eaton P, Pereira E, Franco R (2008) Probing surface properties of cytochrome c@Au bionanoconjugates. J Phys Chem C 112:16340–16347
320. Filipe V, Hawe A, Jiskoot W (2010) Critical evaluation of nanoparticle tracking analysis (NTA) by NanoSight for the measurement of nanoparticles and protein aggregates. Pharm Res 27:796–810

321. Falabella JB, Cho TJ, Ripple DC, Hackley VA, Tarlov MJ (2010) Characterization of gold nanoparticles modified with single-stranded DNA using analytical ultracentrifugation and dynamic light scattering. Langmuir 26:12740–12747

322. Lees EE, Gunzburg MJ, Nguyen TL, Howlett GJ, Rothacker J, Nice EC, Clayton AHA, Mulvaney P (2008) Experimental determination of quantum dot size distributions, ligand packing densities, and bioconjugation using analytical ultracentrifugation. Nano Lett 8:2883–2890

323. Xing Y, So MK, Koh AL, Sinclair R, Rao J (2008) Improved QD-BRET conjugates for detection and imaging. Biochem Biophys Res Commun 372:388–394

324. Haiss W, Thanh NTK, Aveyard J, Fernig DG (2007) Determination of size and concentration of gold nanoparticles from UV-vis spectra. Anal Chem 79:4215–4221

325. Cedervall T, Lynch I, Lindman S, Berggard T, Thulin E, Nilsson H, Dawson KA, Linse S (2007) Understanding the nanoparticle-protein corona using methods to quantify exchange rates and affinities of proteins for nanoparticles. Proc Natl Acad Sci USA 104:2050–2055

326. Chithrani BD, Ghazani AA, Chan WCW (2006) Determining the size and shape dependence of gold nanoparticle uptake into mammalian cells. Nano Lett 6:662–668

327. Ricoul F, Dubois M, Zemb T, Plusquellec D (1998) Micelles-smetic phase coexistence: origin of the maximum swelling of a mixed lamellar phase. Eur Phys J B 4:333–340

328. Baalousha M, Lead JR (2012) Rationalizing nanomaterial sizes measured by atomic force microscopy, flow field-flow fractionation, and dynamic light scattering: Sample preparation, polydispersity, and particle structure. Environ Sci Technol 46:6134–6142

329. Mucic RC, Storhoff JJ, Mirkin CA, Letsinger RL (1998) DNA-directed synthesis of binary nanoparticle network materials. J Am Chem Soc 120:12674–12675

330. Liu X, Atwater M, Wang J, Huo Q (2007) Extinction coefficient of gold nanoparticles with different sizes and different capping ligands. Colloids Surf B 58:3–7

331. Murphy S, Huang L, Kamat PV (2011) Charge-transfer complexation and excited-state interactions in porphyrin-silver nanoparticle hybrid structures. J Phys Chem C 115:22761–22769

332. Li S, Tao Q, Li D, Zhang Q (2014) Controlled anisotropic growth of Ag nanoparticles on oil-decorated TiO_2 films with photocatalytic reduction method. J Mater Res 29:2497–2504

333. Viswanatha R, Santra PK, Dasgupta C, Sarma DD (2007) Growth mechanism of nanocrystals in solution: ZnO, a case study. Phys Rev Lett 98:255501

334. Li DW, Pan LJ, Li S, Liu K, Wu SF, Peng W (2013) Controlled preparation of uniform TiO_2-catalyzed silver nanoparticle films for surface-enhanced Raman scattering. J Phys Chem C 117:6861–6871

335. Hammouda B (2010) SANS from polymers—review of the recent literature. Polymer Rev 50:14–39

336. McKenzie LC, Haben PM, Kevan SD, Hutchison JE (2010) Determining nanoparticle size in real time by small-angle X-ray scattering in a microscale flow system. J Phys Chem C 114:22055–22063

337. Castelletto V, Newby GE, Zhu Z, Hamley IW (2010) Self-assembly of pegylated peptide conjugates containing a modified amyloid β-peptide fragment. Langmuir 26:9986–9996

338. Rusu L, Gambhir A, McLaughlin S, Rädler J (2004) Fluorescence correlation spectroscopy studies of peptide and protein binding to phospholipid vesicles. Biophys J 87:1044–1053

339. Ruan Q, Tetin SY (2008) Applications of dual-color fluorescence cross-correlation spectroscopy in antibody binding studies. Anal Biochem 374:182–195

340. Wang X, Du Y, Luo J (2008) Biopolymer/montmorillonite nanocomposite: preparation, drug-controlled release property and cytotoxicity. Nanotechnology 19:065707–065714

341. Tyner KM, Schiffman SR, Giannelis EP (2004) Nanobiohybrids as delivery vehicles for camptothecin. J Control Release 95:501–514

342. Raman CV, Krishnan KS (1928) A new type of secondary radiation. Nature 121:501–502

343. Albrecht MG, Creighton JA (1977) Anomalously intense Raman spectra of pyridine at a silver electrode. J Am Chem Soc 99:5215–5217

344. Haes AJ, Haynes CL, McFarland AD, Zou S, Schatz GC, Van Duyne RP (2005) Plasmonic materials for surface-enhanced sensing and spectroscopy. MRS Bull 30:368–375
345. Shemer G, Markovich G (2002) Enhancement of magneto-optical effects in magnetite nanocrystals near gold surfaces. J Phys Chem B 106:9195–9197
346. Wang H, Kundu J, Halas NJ (2007) Plasmonic nanoshell arrays combine surface-enhanced vibrational spectroscopies on a single substrate. Angew Chem Int Ed 46:9040–9044
347. Elghanian R, Storhoff JJ, Mucic RC, Letsinger RL, Mirkin CA (1997) Selective colorimetric detection of polynucleotides based on the distance-dependent optical properties of gold nanoparticles. Science 277:1078–1081
348. Chu LQ, Förch R, Knoll W (2007) Surface-plasmon-enhanced fluorescence spectroscopy for DNA detection using fluorescently labeled PNA as "DNA indicator". Angew Chem Int Ed 46:4944–4947
349. Lieberman I, Shemer G, Fried T, Kosower EM, Markovich G (2008) Plasmon-resonance-enhanced absorption and circular dichroism. Angew Chem Int Ed 47:4855–4857
350. Michaels AM, Nirmal M, Brus LE (1999) Surface enhanced raman spectroscopy of individual rhodamine 6G molecules on large Ag nanocrystals. J Am Chem Soc 121:9932–9939
351. Le Ru EC, Etchegoin PG (2009) Principles of surface-enhanced raman spectroscopy and related plasmonic effects, vol 23. Elsevier, Amsterdam, pp 209–214
352. Farcau C, Astilean S (2010) Mapping the SERS efficiency and hot-spots localization on gold film over nanospheres substrates. J Phys Chem C 114:11717–11722
353. Liu Z, Li X, Tabakman SM, Jiang K, Fan S, Dai H (2008) Multiplexed multi-color raman imaging of live cells with isotopically modified single walled carbon nanotubes. J Am Chem Soc 130:13540–13541
354. Lakowicz JR (2006) Principles of fluorescence spectroscopy, 3rd edn. New York, Springer
355. Nielson LJ, Eyley S, Thielemans W, Aylott JW (2010) Dual fluorescent labelling of cellulose nanocrystals for pH sensing. Chem Commun 46:8929–8931
356. Sen T, Haldar KK, Patra A (2008) Au nanoparticle-based surface energy transfer probe for conformational changes of BSA protein. J Phys Chem C 112:17945–17951
357. Förster T (1959) 10th spiers memorial lecture. Transfer mechanisms of electronic excitation, Th. Förster, Discuss Faraday Soc 27:7–17
358. De-Llanos R, Sanchez-Cortes S, Domingo C, Garcia-Ramos JV, Sevilla P (2011) Surface plasmon effects on the binding of antitumoral drug emodin to bovine serum albumin. J Phys Chem C 115:12419–12429
359. Bevington PR (2002) Data reduction and error analysis for the physical sciences. McGraw-Hill, New York
360. James DR, Siemiarczuk A, Ware WR (1992) Stroboscopic optical boxcar technique for the determination of fluorescence lifetimes. Rev Sci Instrum 63:1710–1716
361. Sevilla P, Rivas JM, Garcia-Blanco F, Garcia-Ramos JV, Sanchez-Cortes S (2007) Identification of the antitumoral drug emodin binding sites in bovine serum albumin by spectroscopic methods. BBA-Proteins Proteomics 1774:1359–1369
362. Bothun GD (2008) Hydrophobic silver nanoparticles trapped in lipid bilayers: Size distribution, bilayer phase behavior, and optical properties. J Nanobiotechnol 6:13
363. Piazza R, Parola A (2008) Thermophoresis in colloidal suspensions. J Phys: Condens Matter 20:153102
364. Dong WJ, Feng SH, Shi Z, Li LS, Xu YH (2003) A well-confined redox route to silver nanoparticles on the surface of MoO_3. Chem Mater 15:1941–1943
365. Graber KC, Brown KR, Keating CD, Stranick SJ, Tang SL, Natan MJ (1997) Nanoscale characterization of gold colloid monolayers: a comparison of four techniques. Anal Chem 69:471–477
366. Fendler JH (2001) Chemical self-assembly for electronic applications. Chem Mater 13:3196–3210

367. Tang Z, Wang Y, Kotov N (2002) Semiconductor nanoparticles on solid substrates: film structure, intermolecular interactions and polyelectrolyte effects. Langmuir 18:7035–7040
368. Xe HX, Zhang H, Li QG, Zhu T, Li SFY, Liu ZF (2000) Fabrication of designed architectures of Au nanoparticles on solid substrate with printed self-assembled monolayers as templates. Langmuir 16:3846–3851
369. Henry CR (2005) Morphology of supported nanoparticles. Prog Surf Sci 80:92–116
370. Huey B, Sigmund W (2007) The application of scanning probe microscopy in materials science studies. J Miner Met Mater Soc 59:11
371. Wang ZL (2000) Transmission electron microscopy of shape-controlled nanocrystals and their assemblies. J Phys Chem B 104:1153–1175
372. Klajn R, Pinchuk A, Schatz GC, Grzybowski BA (2007) Synthesis of heterodimeric sphere-prism nanostructures via metastable gold suprasheres. Angew Chem Int Ed 46:8363–8367
373. Yin Y, Erdonmez C, Aloni S, Alivisatos AP (2006) Faceting of nanocrystals during chemical transformation: from solid silver spheres to hollow gold octahedra. J Am Chem Soc 128:12671–12673
374. Seo D, Yoo CI, Jung J, Song H (2008) Ag–Au–Ag heterometallic nanorods formed through directed anisotropic growth. J Am Chem Soc 130:2940–2941
375. Cobley CM, Skrabalak SE, Campbell DJ, Xia Y (2009) Shape-controlled synthesis of silver nanoparticles for plasmonic and sensing applications. Plasmonics 4:171–179
376. Wang Y, Shen Y, Xie A, Li S, Wang X, Cai Y (2010) A simple method to construct bifunctional Fe_3O_4/Au hybrid nanostructures and tune their optical properties in the near-infrared region. J Phys Chem C 114:4297–4301
377. Gatti AM, Kirkpatrick J, Gambarelli A, Capitani F, Hansen T, Eloy R, Clermont G (2008) ESEM evaluations of muscle/nanoparticles interface in a rat model. J Mater Sci Mater Med 19:1515–1522
378. Elzey S, Tsai DH, Rabb S, Yu L, Winchester M, Hackley V (2012) Quantification of ligand packing density on gold nanoparticles using ICP-OES. Anal Bioanal Chem 403:145–149
379. Ansar SM, Haputhanthri R, Edmonds B, Liu D, Yu L, Sygula A, Zhang D (2010) Determination of the binding affinity, packing, and conformation of thiolate and thione ligands on gold nanoparticles. J Phys Chem C 115:653–660
380. Novo C, Gomez D, Perez-Juste J, Zhang Z, Petrova H, Reismann M, Mulvaney P, Hartland GV (2006) Contributions from radiation damping and surface scattering to the linewidth of the longitudinal plasmon band of gold nanorods: a single particle study. Phys Chem Chem Phys 8:3540–3546
381. Imura K, Nagahara T, Okamoto H (2004) Plasmon mode imaging of single gold nanorods. J Am Chem Soc 126:12730–12731
382. Khan I, Cunningham D, Lazar S, Graham D, Smith WE, McComb DW (2006) A TEM and electron energy loss spectroscopy (EELS) investigation of active and inactive silver particles for surface enhanced resonance Raman spectroscopy (SERRS). Faraday Discuss 132:171–178
383. Pavia DL, Lampman GM, Kriz GS, Vyvyan JA (2008) Introduction to spectroscopy, 4th edn. Brooks/Cole, Belmont, CA
384. Tiwari DK, Tanaka SI, Inouye Y, Yashizawa K, Watanabe TM, Jin T (2009) Synthesis and characterization of anti-HER2 antibody conjugated CdSe/CdZnS quantum dots for fluorescence imaging of breast cancer cells. Sensors 9:9332–9354
385. Vannoy CH, Xu J, Leblanc RM (2010) Bioimaging and self-assembly of lysozyme fibrils utilizing CdSe/ZnS quantum dots. J Phys Chem C 114:766–773
386. Sweeney SF, Woehrle GH, Hutchison JE (2006) Rapid purification and size separation of gold nanoparticles via diafiltration. J Am Chem Soc 128:3190–3197
387. Rytting E, Bur M, Cartier R, Bouyssou T, Wang X, Krüger M, Lehr CM, Kissel T (2010) In vitro and in vivo performance of biocompatible negatively-charged salbutamol-loaded nanoparticles. J Control Release 141:101–107

388. Zhang Y, Schnoes AM, Clapp AR (2010) Dithiocarbamates as capping ligands for water-soluble quantum dots. ACS Appl Mater Interfaces 2:3384–3395

389. Kalisman YL, Jadzinsky PD, Kalisman N, Tsunoyama H, Tsukuda T, Bushnell DA, Kornberg RD (2011) Synthesis and characterization of Au102(p-MBA)44 nanoparticles. J Am Chem Soc 133:2976–2982

390. Wu RH, Nguyen TP, Marquart GW, Miesen TJ, Mau T, Mackiewicz MR (2014) A facile route to tailoring peptide-stabilized gold nanoparticles using glutathione as a synthon. Molecules 19:6754–6775

391. Zhang YZ, Roder H, Paterson Y (1995) Rapid amide proton exchange rates in peptides and proteins measured by solvent quenching and two-dimensional NMR. Protein Sci 4:804–814

392. Cullity BD, Stock SR (2001) Elements of X-Ray diffraction, 3rd edn. Prentice Hall, Upper Saddle River, NJ

393. Henein GE, Wagner WR (1983) Stresses induced in GaAs by TiPt ohmic contacts. J Appl Phys 54:6395–6400

394. Pannu C, Singh UB, Kumar S, Tripathi A, Kabiraj D, Avasthi DK (2014) Engineering the strain in graphene layers with Au decoration. Appl Surf Sci 308:193–198

395. Cammarata RC, Trimble TM, Srolovitz DJ (2000) Surface stress model for intrinsic stresses in thin films. J Mater Res 15:2468–2474

396. Friesen C, Seel SC, Thompson CV (2004) Reversible stress changes at all stages of Volmer-Weber film growth. J Appl Phys 95:1011–1020

397. Raju GG (2003) Dielectrics in electrical fields. Marcel Dekker, Inc., New York, p 260

398. González-Campos JB, Prokhorov E, Luna-Bárcenas G, Fonseca-García A, Sanchez IC (2009) Dielectric relaxations of chitosan: the effect of water on the α-relaxation and the glass transition temperature. J Polym Sci, Part B: Polym Phys 47:2259–2271

399. Hernández-Vargas J, González-Campos JB, Lara-Romero J, Prokhorov E, Luna-Bárcenas G, Aviña-Verduzco JA, González-Hernández JC (2014) Chitosan/MWCNTs-Decorated with silver nanoparticle composites: dielectric and antibacterial characterization. J Appl Polym Sci 131:40213

400. Lee H, Habas SE, Somorjai GA, Yang P (2008) Localized Pd overgrowth on Cubic Pt nanocrystals for enhanced electrocatalytic oxidation of formic acid. J Am Chem Soc 130:5406–5407

401. Wu HL, Chen CH, Huang MH (2008) Seed-mediated synthesis of branched gold nanocrystals derived from the side growth of pentagonal bipyramids and the formation of gold nanostars. Chem Mater 21:110–214

402. Sau TK, Pal A, Jana NR, Wang ZL, Pal T (2001) Size controlled synthesis of gold nanoparticles using photochemically prepared seed particles. J Nanopart Res 3:257–261

403. Kumar PS, Pastoriza-Santos I, Rodriguez-Gonzalez B, de Abajo FJG, Liz-Marzan LM (2008) High-yield synthesis and optical response of gold nanostars. Nanotechnol 19:015606 (1–5)

404. Sau TK, Murphy CJ (2007) Role of ions in the colloidal synthesis of gold nanowires. Philos Mag 87:2143–2158

405. Sajanlal PR, Pradeep T (2008) Electric-field-assisted growth of highly uniform and oriented gold nanotriangles on conducting glass substrates. Adv Mater 20:980–983

406. Duraiswamy S, Khan SA (2014) Dual-stage continuous-flow seedless microfluidic synthesis of anisotropic gold nanocrystals. Part Part Syst Charact 31:429–432

407. Kurihara LK, Chow GM, Schoen PE (1995) Nanostruct Mater 5:607

408. Cho SP, Bratescu MA, Saito N, Takai O (2011) Microstructural characterization of gold nanoparticles synthesized by solution plasma processing. Nanotechnology 22:455701

409. Hu X, Cho SP, Takai O, Saito N (2012) Rapid synthesis and structural characterization of well-defined gold clusters by solution plasma sputtering. Cryst Growth Des 12:119–123

410. Tseng KH, Chen YC, Shyue JJ (2011) Continuous synthesis of colloidal silver nanoparticles by electrochemical discharge in aqueous solutions. J Nanopart Res 131865–1872

411. Heo YK, Lee SY (2011) Effects of the gap distance on the characteristics of gold nanoparticles in nanofluids synthesized using solution plasma processing. Met Mater Int 17:431–434

412. Nandagiri VK, Gentile P, Chiono V, Tonda-Turo C, Matsiko A, Ramtoola Z, Montevecchi FM, Ciardelli G (2011) Incorporation of PLGA nanoparticles into porous chitosan-gelatin scaffolds: influence on the physical properties and cell behavior. J Mech Behav Biomed 4:1318–1327

413. McKenna J, Patel J, Mitra S, Soin N, Švrček V, Maguire P, Mariotti D (2011) Silicon-based quantum dots: synthesis, surface and composition tuning with atmospheric pressure plasmas. Eur Phys J Appl Phys 56:24020

414. Chen Q, Kaneko T, Hatakeyama R (2012) Rapid synthesis of water-soluble gold nanoparticles with control of size and assembly using gas-liquid interfacial discharge plasma. Chem Phys Lett 521:113–117

415. Chen Q, Kaneko T, Hatakeyama R (2011) Plasma induced synthesis of water-soluble DNA conjugated gold nanoparticles. In: 30th international conference on phenomena in ionized gases, Belfast, UK

416. Patel J, Němcová L, Maguire P, Graham WG, Mariotti D (2013) Synthesis of surfactant-free electrostatically stabilized gold nanoparticles by plasma-induced liquid chemistry. Nanotechnology 24:245604 (11)

417. Martin CR (1996) Membrane-based synthesis of nanomaterials. Chem Mater 8:1739–1746

418. Preston CK, Moskovits M (1993) Optical characterization of anodic aluminum oxide films containing electrochemically deposited metal particles. 1. Gold in phosphoric acid anodic aluminum oxide films. J Phys Chem 97:8495–8503

419. Payne EK, Shuford KL, Park S, Schatz GC, Mirkin CA (2006) Multipole plasmon resonances in gold nanorods. J Phys Chem B 110:2150–2154

420. Wang J (2008) Barcoded metal nanowires. J Mater Chem 18:4017–4020

421. Xu H, Suslick KS (2010) Sonochemical synthesis of highly fluorescent Ag nanoclusters. ACS Nano 4:3209–3214

422. Buffat PA, Flueli M, Spycher R, Stadelmann P, Borel JP (1991) Crystallographic structure of small gold particles studied by high-resolution electron microscopy. Faraday Discuss 92:173–187

423. Raula J, Shan J, Nuopponen M, Niskanen A, Jiang H, Kauppinen EI, Tenhu H (2003) Synthesis of gold nanoparticles grafted with a thermoresponsive polymer by surface-induced reversible-addition fragmentation chain-transfer polymerization. Langmuir 19:3499–3504

424. Mandal TK, Fleming MS, Walt DR (2002) Preparation of polymer coated gold nanoparticles by surface-confined living radical polymerization at ambient temperature. Nano Lett 2:3–7

425. De la Presa P, Rueda T, del Puerto Morales M, Javier Chichón F, Arranz R, Valpuesta JM, Hernando A (2009) Gold nanoparticles generated in ethosome bilayers, as revealed by cryo-electrontomography. J Phys Chem B 12(113):3051–3057

426. Jensen TR, Duval ML, Kelly KL, Lazarides AA, Schatz GC, Van Duyne RP (1999) Nanosphere lithography: effect of the external dielectric medium on the surface plasmon resonance spectrum of a periodic array of silver nanoparticles. J Phys Chem B 103:9846–9853

427. Jensen TR, Malinsky MD, Haynes CL, Van Duyne RP (2000) Nanosphere lithography: tunable localized surface plasmon resonance spectra of silver nanoparticles. J Phys Chem B 104:10549–10556

428. Zhou WM, Zhang J, Li XL, Liu YB, Min GQ, Song ZT, Zhang JP (2009) Replication of mold for UV-nanoimprint lithography using AAO membrane. Appl Surf Sci 255:8019–8022

429. Park M, Harrison C, Chaikin PM, Register RA, Adamson DH (1997) Block copolymer lithography: periodic arrays of ∼1011 holes in 1 square centimeter. Science 276:1401–1404

430. Masuda H, Fukuda K (1995) Ordered metal nanohole arrays made by a two-step replication of honeycomb structures of anodic alumina. Science 268:1466–1468

431. Chou SY, Krauss PR, Renstrom PJ (1996) Nanoimprint lithography. J Vac Sci Technol B 14:4129–4133

432. Sotomayor Torres CM, Zankovych S, Seekamp J, Kam AP, Cedeno CC, Hoffmann T, Ahopelto J, Reuther F, Pfeiffer K, Bleidiessel G, Gruetzner G, Maximov MV, Heidari B (2003) Nanoimprint lithography: an alternative nanofabrication approach. Mater Sci Eng C 23:23–31

433. Guo LJ (2007) Nanoimprint lithography: methods and material requirements. Adv Mater 19:495–513

434. López P, Pelaz L, Santos I, Marqués LA, Aboy M (2012) Molecular dynamics simulations of damage production by thermal spikes in Ge. J Appl Phys 111:033519

435. Romano L, Impellizzeri G, Grimaldi MG (2013) Influence of microstructure on voids nucleation in nanoporous Ge. Mater Lett 96:74–77

436. Böttger R, Bischoff L, Heinig KH, Schmidt B, Pilz W, Schmidt B (2012) From sponge to dot arrays on (100) Ge by increasing the energy of ion impacts. J Vac Sci Technol B 30:06FF12

437. Miyawaki A, Hayashi T, Tokunaga T, Hayashi A, Hayashi Y, Tanemura M (2012) Low-temperature fabrication of germanium nanostructures by ion irradiation: effect of supplied particle species. Jpn J Appl Phys 51:01AB05

438. Miles DT, Murray RW (2003) Temperature-dependent quantized double layer charging of monolayer-protected gold clusters. Anal Chem 75:1251–1257

439. Quinn BM, Liljeroth P, Ruiz V, Laaksonen T, Kontturi K (2003) Electrochemical resolution of 15 oxidation states for monolayer protected gold nanoparticles. J Am Chem Soc 125:6644–6645

440. Parker JF, Fields-Zinna CA, Murray RW (2010) The story of a monodisperse gold nanoparticle: Au25L18. Acc Chem Res 43:1289–1296

441. Donkers RL, Lee D, Murray RW (2004) Synthesis and isolation of the molecule-like cluster Au38(PhCH2CH2S)24. Langmuir 20:1945–1952

442. Zhao P, Li N, Astruc D (2013) State of the art in gold nanoparticle synthesis. Coord Chem Rev 257:638–665

443. Wu J, Campuzano S, Halford C, Haake DA, Wang J (2010) Ternary surface monolayers for ultrasensitive (zeptomole) amperometric detection of nucleic acid hybridization without signal amplification. Anal Chem 82:8830–8837

444. Bhuvana M, Dharuman V (2016) Influence of alkane chain lengths and head groups on tethering of liposome-gold nanoparticle on gold surface for electrochemical DNA sensing and gene delivery. Sensors Actuators B 223:157–165

445. Nadagouda MN, Speth TF, Varma RS (2011) Microwave-assisted green synthesis of silver nanostructures. Acc Chem Res 44:469–478

446. Polshettiwar V, Nadagouda MN, Varma RS (2009) Microwaveassisted chemistry: a rapid and sustainable route to synthesis of organics and nanomaterials. Aust J Chem 62:16–26

447. Wang H, Zhang J, Zhu JJ (2001) A microwave assisted heating method for rapid synthesis of sphalrite-type mercury sulfide nanocrystals with different sizes. J Cryst Growth 233:829–836

448. Lu QY, Gao F, Komarneni SJ (2004) Microwave-assisted synthesis of one-dimensional nanostructures. Mater Res 19:1649–1655

449. Kim T, Lee CH, Joo SW, Lee K (2008) Kinetics of gold nanoparticle aggregation: experiments and modeling. J Colloid Interface Sci 318:238–243

450. Lombardi A, Grzelczak M, Crut A, Mioli P, Isabel PS, Liz-Marzán LM, Del Fatti N, Vallée F (2013) Optical Response of Individual Au–Ag@SiO$_2$ Heterodimers. ACS Nano 7:2522–2531

451. Gschneidtner T, Diaz-Fernandez YA, Syrenova S, Westerlund F, Langhammer C, Moth-Poulsen KA (2014) Versatile self-assembly strategy for the synthesis of shape-selected colloidal noble metal nanoparticle heterodimers. Langmuir 30:3041–3050

452. Sokolov K, Follen M, Richards-Kortum R (2002) Optical spectroscopy for detection of neoplasia. Curr Opin Chem Biol 6:651–658

453. Crow P, Stone N, Kendall CA, Persad RA, Wright MPJ (2003) Optical diagnostics in urology: Current applications and future prospects. BJU Int 92:400–407

454. De Veld DCG, Witjes MJH, Sterenborg HJCM, Roodenburg JLN (2005) The status of in vivo autofluorescence spectroscopy and imaging for oral oncology. Oral Oncol 41:117–131

455. Swinson B, Jerjes W, El-Maaytah M, Norris P, Hopper C (2006) Optical techniques in diagnosis of head and neck malignancy. Oral Oncol 42:221–228

456. Wong KSLM, Molckovsky A, Wang KK, Dolenko B, Somorjai RL, Wilson BC (2005) Diagnostic potential of Raman spectroscopy in Barrett's esophagus. Proc SPIE 5692:140–146

457. Zysk AM, Nguyen FT, Oldenburg AL, Marks DL, Boppart SA (2007) Optical coherence tomography: a review of clinical development from bench to bedside. J Biomed Opt 12:051403

458. Watanabe A, Tsujie H, Taniguchi M, Hosokawa M, Fujita M, Sasaki S (2006) Laryngoscopic detection of pharyngeal carcinoma in situ with narrowband imaging. Laryngoscope 116:650–654

459. Hamley IW (2003) Nanotechnology with soft materials. Angew Chem Int Ed 42:1692–1712; Angew Chem 115:1730–1752

460. Cölfen H, Mann S (2003) Higher-order organization by mesoscale self-assembly and transformation of hybrid nanostructures. Angew Chem 115:2452–2468

461. van Bommel KJC, Friggeri A, Shinkai S (2003) Organic templates for the generation of inorganic materials. Angew Chem 115:1010–1030; Angew Chem Int Ed 42:980–999

462. Niemeyer CM (2003) Functional hybrid devices of proteins and inorganic nanoparticles. Angew Chem Int Ed 42:5796–5800; Angew Chem 115:5974 –5978

463. Parak WJ, Gerion D, Pellegrino T, Zanchet D, Micheel C, Williams SC, Boudreau R, Le Gros MA, Larabell CA, Alivisatos AP (2003) Biological applications of colloidal nanocrystals. Nanotechnology 14:R15–R27

464. Csaki A, Maubach G, Born D, Reichert J, Fritzsche W (2002) DNA-based molecular nanotechnology. Single Mol 3:275–280

465. Penn SG, Hey L, Natan MJ (2003) Nanoparticles for bioanalysis. Curr Opin Chem Biol 7:609–615

466. West JL, Halas NJ (2003) Engineered nanomaterials for biophotonics applications: improving sensing, imaging, and therapeutics. Ann Rev Biomed Eng 5:285–292

467. Alivisatos P (2004) The use of nanocrystals in biological detection. Nat Biotechnol 22:47–52

468. Thiesen B, Jordan A (2008) Clinical applications of magnetic nanoparticles for hyperthermia. Int J Hyperthermia 24:467–474

469. Iga AM, Robertson JH, Winslet MC, Seifalian AM (2007) Clinical potential of quantum dots. J Biomed Biotechnol 10:76087

470. Tan A, De La Pena H, Seifalian AM (2010) The application of exosomes as a nanoscale cancer vaccine. Int J Nanomedicine 5:889–900

471. Roy S, Gao ZQ (2009) Nanostructure-based electrical biosensors. Nano Today 4:318–334

472. Yan H, Choe HS, Nam SW, Hu YJ, Das S, Klemic JF, Ellenbogen JC, Lieber CM (2011) Programmable nanowire circuits for nanoprocessors. Nature 470:240–244

473. Napoli M, Eijkel JCT, Pennathur S (2010) Nanofluidic technology for biomolecule applications: a critical review. Lab Chip 10:957–985

474. Patolsky F, Zheng G, Lieber CM (2006) Nanowire sensors for medicine and the life sciences. Nanomedicine 1:51–65

475. Tian BZ, Cohen-Karni T, Qing QA, Duan XJ, Xie P, Lieber CM (2010) Three-dimensional, flexible nanoscale field-effect transistors as localized bioprobes. Science 329:830–834

476. Lin SP, Pan CY, Tseng KC, Lin MC, Chen CD, Tsai CC, Yu SH, Sun YC, Lin TW, Chen YT (2009) A reversible surface functionalized nanowire transistor to study protein-protein interactions. Nano Today 4:235–243

477. Zheng G, Patolsky F, Cui Y, Wang WU, Lieber CM (2005) Multiplexed electrical detection of cancer markers with nanowire sensor arrays. Nat Biotechnol 23:1294–1301

478. Stern E, Vacic A, Rajan NK, Criscione JM, Park J, Ilic BR, Mooney DJ, Reed MA, Fahmy TM (2010) Label-free biomarker detection from whole blood. Nat Nanotechnol 5:138–142

479. Fan R, Vermesh O, Srivastava A, Yen BK, Qin L, Ahmad H, Kwong GA, Liu CC, Gould J, Hood L, Heath JR (2008) Integrated barcode chips for rapid, multiplexed analysis of proteins in microliter quantities of blood. Nat Biotechnol 26:1373–1378

480. Wang J, Ahmad H, Ma C, Shi Q, Vermesh O, Vermesh U, Heath J (2010) A self-powered, one-step chip for rapid, quantitative and multiplexed detection of proteins from pinpricks of whole blood. Lab Chip 10:3157–3162

481. Heidel JD, Davis ME (2011) Clinical developments in nanotechnology for cancer therapy. Pharm Res 28:187–199

482. Nguyen KT (2011) Targeted nanoparticles for cancer therapy: promises and challenges. J Nanomedic Nanotechnol 2:1–2

483. Melancon MP, Zhou M, Li C (2011) Cancer theranostics with nearinfrared light-activatable multimodal nanoparticles. Acc Chem Res 44:947–956

484. Lammers T, Hennink WE, Storm G (2008) Tumour-targeted nanomedicines: principles and practice. Br J Cancer 99:392–397

485. Lammers T, Subr V, Ulbrich K, Hennink WE, Storm G, Kiessling F (2010) Polymeric nanomedicines for image-guided drug delivery and tumor-targeted combination therapy. Nano Today 5:197–212

486. Duncan R (2003) The dawning era of polymer therapeutics. Nat Rev Drug Discovery 2:347–360

487. Torchilin VP (2005) Recent advances with liposomes as pharmaceutical carriers. Nat Rev Drug Discovery 4:145–160

488. Hofheinz RD, Gnad-Vogt SU, Beyer U, Hochhaus A (2005) Liposomal encapsulated anti-cancer drugs. Anticancer Drugs 16:691–707

489. Duncan R (2006) Polymer conjugates as anticancer nanomedicines. Nat Rev Cancer 6:688–701

490. Allen TM (2002) Ligand-targeted therapeutics in anticancer therapy. Nat Rev Cancer 2:750–763

491. Sweeney EC, Tonevitsky AG, Temiakov DE, Agapov II, Saward S, Palmer RA (1997) Preliminary crystallographic characterization of ricin agglutinin. Proteins 28:586–589

Chapter 2
Noble Metal Nanoparticles

Abstract To synthesize noble metal nanomaterials in controlled sizes and dimensions, various approaches and mechanisms have been developed. The successful utilization of noble metal nanoparticles (NMNPs) relies on the availability of synthetic methods generating nanoparticles with the desired characteristics, namely high solubility in water, adequate morphology, and surface functionalities. Control over the shape and size of the nanoparticles is usually achieved through the careful selection of the experimental conditions, namely reducing agents, type and concentration of precursors, reaction time, temperature, UV light, (co)solvent, and capping agents. Depending on the reduction potentials of the metal precursor and the reducing-agent systems, reduction can occur at room temperature or at elevated temperatures. In general, citrate plays a role as a stabilizing agent with preparations of gold nanoparticles requiring relatively high temperatures due to its weak reducing strength. The use of amine–borane complexes is essential for the syntheses of monodisperse metallic nanoparticles. Upon the addition of strong reductants, such as $NaBH_4$, metal cations are reduced rapidly, resulting in an immediate color change of the reaction mixture. Rationally designed molecular building blocks allow for the precise control of particle size and morphology of the supramolecular aggregate, and various defined structures, including spherical micelles, rodlike micelles, or vesicles. Molecules which control the overall crystal growth are known as "capping agents," the term frequently used for specific adsorption of surface-active molecules on selective crystal planes of a particular geometry. Additives such as surfactants, polymers, foreign ions, ligands, and impurities present in the reaction medium have been observed to play important roles in controlling the morphology of particles produced. Surfactants, ligands, or polymers were commonly added as stabilizers to impart stability to nanoparticles against aggregation, since colloidal particles tend to aggregate to decrease the overall surface area and energy. In a typical liquid-phase synthesis, the nanoparticle formation process undergoes three distinct stages as follows: (1) reduction and generation of active nuclei; (2) formation of seed particles upon collision of active nuclei; and (3) formation of larger nanoparticles via a growth process, which may be Ostwald ripening or aggregation. The nanoparticle growth is generally categorized by two processes: diffusion-controlled Ostwald-ripening and

aggregation/coalescence. Nowadays, a molecule which can act both as a reducing and capping agent is preferred so that the reaction takes place in one step and there is no need for an external reducing agent. Multifunctional amines and nitrogen-containing polymers have also been tested for the synthesis of nanoparticles. Poly(ethylene oxide)-poly(propylene oxide)-based block copolymers are well known as dispersion stabilizers and templates for the synthesis of mesoporous materials and nanoparticles. Coordination chemistry offers simplicity, stable bonding, and ligand-metal specificity, enabling ligand-bearing components to be assembled into supramolecular structures using appropriate metal ions. This approach is particularly compatible with surface chemistry, as binding of metal ions activates the surface toward ligand binding, and vice versa. Some stabilizing agents can also be used as a reducing agent. Ionic liquids (ILs) are a viable option as stabilizing agents because of their ionic character and can be easily made task-specific as phase-transfer catalysts due to their tunable nature. Ligand exchange reactions have proven a particularly powerful approach to incorporate functionality in the ligand shell of thiol-stabilized nanoparticles and are widely used to produce organic- and water-soluble nanoparticles with various core sizes and functional groups. NMNPs can be intercalated into the gallery regions of montmorillonite and formed hybrid framework. Models of particle (crystal) development consider two basic steps: nucleation and growth. The creation of a new phase from a metastable state is nucleation. Seed-mediated growth method has been demonstrated to be a powerful synthetic route to generate a range of different types of metal nanoparticles. This method separates the nucleation and growth stage of nanoparticle syntheses by introducing presynthesized small seed particles into a growth solution typically containing a metal precursor, reducing agent, surfactants, and some additives. Dissolution of silver nanoparticles, for example, occurs through oxidation of metallic Ag and release of Ag^+ into solution (or dissolution rate is accelerated). Release of Ag^+ is determined by intrinsic physicochemical properties of silver nanoparticles and by those of the solution. Parameters that either enhance or suppress silver nanoparticle dissolution are ionic strength, pH, dissolved oxygen concentration, temperature, dissolved complexing ligands (organic matter, sulfur, chlorine), silver surface coating, shape, and size. The surfactants find their way to various environmental segments and thus pose serious health hazards. Several different polymer-based anticancer agents have been approved for clinical use, for passive tumor targeting. Prominent examples of macromolecular drug carrier systems evaluated in patients are poly(ethylene glycol), poly(L-glutamic acid), poly[N-(2-hydroxypropyl)methacrylamide], and their copolymers. Copolymers based on N-(2-hydroxypropyl)methacrylamide (i.e., HPMA) were used to improve the tumor-directed delivery of doxorubicin.

Abbreviations

3D	Three-dimensional
AA	Ascorbic acid
AFM	Atomic force microscopy
AgNPs	Silver nanoparticles
AuNPs	Gold nanoparticles
AuNRs	Gold nanorods
BDAC	Benzyldimethylhexadecylammonium chloride
[BMIM][BF$_4$]	1-butyl-3-methylimidazolium tetrafluoroborate
BSA	Bovine serum albumin
CHIT	Chitosan
CMC	Critical micellar concentration
CMT	Critical micellar temperature
CTAB	Cetyltrimethylammonium bromide
CTAC	Cetyltrimethylammonium chloride
DMEM	Dulbecco's minimum media
DMF	N,N-dimethylformamide
DNA	Deoxyribonucleic acid
DSC	Differential scanning calorimetry
fcc	Face-centered cubic
FDTD	Finite-difference time domain
F-faces	Flat faces
FTIR	Fourier transform infrared spectroscopy
GCE	Glassy carbon electrode
GFLG	Glycylphenylalanylleucylglycine
GO	Graphene oxide
GSH	Glutathione
HAADF	High-angle annular dark field
HCPA	Hexachloroplatinic acid
HPMA	N-(2-hydroxypropyl)methacrylamide
HRTEM	High-resolution TEM
HSA	Human serum albumin
HTAB	Hexadecyltrimethylammonium bromide
ILs	Ionic liquids
K-faces	Kinked faces
LB	Langmuir–Blodgett
LbL	Layer-by-layer
LCST	Lower critical solution temperature
LED	Light-emitting diode
LMWT	Low molecular weight thiol
LSPR	Localized surface plasmon resonance
MC@AgNPs	Silver nanoparticle-decorated microcapsules
MC@AuNPs	Gold nanoparticle-decorated microcapsules
MC@PtNPs	Platinum nanoparticle-decorated microcapsules

MCs	Microcapsules
MES	2-(N-morpholino)ethanesulfonic acid
MIES	Metastable impact electron spectroscopy techniques
MMT	Montmorillonite
MNPs	Metal nanoparticles
NaBH$_4$	Sodium borohydride
NaPA	Sodium polyacrylate
NaOC$_2$H$_5$	Sodium ethoxide
NMNPs	Noble metal nanoparticles
NMs	Nanomaterials
NPs	Nanoparticles
NRs	Nanorods
o/w	Oil-in-water
PA	Polyacrylate
PAM	Polyacrylamide
PAN	Polyacrylonitrile
PBS	Phosphate buffer saline
PCS	Photon correlation spectroscopy
PDPAEMA	Poly2-(diisopropylamino) ethyl methacrylate
PEG-SH	Thiol-PEG
PEO	Poly(ethylene oxide)
PEO-b-PDHPMA-b-PDPAEMA	(poly(ethyleneoxide)-b-poly (2,3-dihydroxypropyl methacrylate)-b-poly[2-(diisopropylamino) ethyl methacrylate]
PIC	Polyion complex
Pl	Pullulan
pNIPAM	Poly(N-isopropylacrylamide)
POSS	Polyhedral oligomeric silsesquioxane
PPDO	(poly(p-dioxanone)
PPO	Poly(propylene oxide)
PtNPs	Platinum nanoparticles
PTPS	Amphiphilic polyhedral oligomeric silsesquio-xane-containing thiol groups
PVA	Poly(vinyl alcohol)
PVP	Polyvinylpiridine
PVPo	Polyvinylpyrrolidone, poly(N-vinyl-2-pyrrolidone)
SERS	Surface-enhanced Raman scattering
S-faces	Stepped faces
sMNPs	Spherical metal nanoparticles
SPB	Surface plasmon band
SPEEK	Sulfonated poly(ether–ether) keton
SPL	Scanning probe lithography

SPR	Surface plasmon resonance
STM	Scanning tunneling microscopy
TEM	Transmission electron microscope
TGA	Thermal gravimetric analysis
TMPTA	Trimethylolpropane triacrylate
tTEM	Real-time TEM
UPD	Underpotential deposition
UPS	Ultraviolet photoelectron spectroscopy
UV	Ultraviolet
VOCs	Volatile organic chemicals
XANES	X-ray absorption near-edge spectroscopy
XPS	X-ray photoelectron spectroscopy
XRD	X-ray diffraction
γ	Surface energy

2.1 Introduction

The rapid development of nanotechnology worldwide is accompanied by massive generation and usage of engineered nanomaterials (NMs) or nanoparticles (NPs) even though the potential nanostructure impacts of these materials are largely unknown. The interest in nanomaterials is a result of the extreme dependence of properties (electronic, magnetic, optical, mechanical, etc.) on particle size and shape in the 1–100-nm regime. These interesting new properties at the nanoscale are the basis of the nanomaterial's various applications. Reducing a material's size to the nanometer length scale (which is the length scale of the electronic motion that determines the material's properties) makes it sensitive to further reduction in size or a change in shape. The molecular design of functional materials at nanoscale supports innovation expected to revolutionize present technology and overcome societal challenges including sustainable energy supply, information storage, and the advancement of medical treatments. Research involving the use of different types and designs of nanomaterials continues to evolve with the growth of nanotechnology for in vivo applications in such fields as drug delivery, medical imaging, diagnostics, and engineering technology.

Noble metal nanoparticles (NMNPs) can be prepared by both "top–down" and "bottom–up" approaches. For "top–down" procedures, a bulk state metal is systematically broken down to generate metal nanoparticles of desired dimensions. In this case, particle assembly and formation is controlled by a pattern or matrix. However, the "top–down" method is limited concerning the control of the size and shape of particles as well as further functionalization [1]. In contrast, in the "bottom–up" strategy, the formation of nanoparticles originates from individual molecules (atoms), because it involves a chemical or biological reduction [2]. Classical

procedure for nanoparticle synthesis is based on the chemical reduction of metal salts with sodium citrate (Turkevich method) and requires high temperature. Biological reduction is considered a green approach and leads to stable nanoparticle, but they are not uniform and are synthesized fairly slowly. A number of techniques have been used for producing metal nanoparticles, including vapor-phase techniques [3], sol-gel methods [4], sputtering [5], coprecipitation [6], chemical reduction [7], sonochemical reduction [8], laser ablation [9], annealing from high-temperature solutions [10], metal evaporation [11], Ar^+ ion sputtering [12], sonoelectrochemical reduction [13], and solvothermal and surfactant-templated solvothermal reactions. Furthermore, two main colloidal methods are broadly employed for the preparation of NMNPs: (co or nano)pre-cipitation and chemical reduction. In some cases, the presence of surfactant (capping agent) is required to control the particle nucleation, growth, and stability. Typically, the coprecipitation reactions involve the thermal decomposition of organometallic precursors and the precipitation of new reaction materials or compounds [14]. The chemical reduction occurring in colloidal assemblies is another approach for the formation of size- and shape-controlled nanoparticles [15]. A major benefit of chemical methods is their relatively inexpensive investment of capital equipment. Gold and silver nanocolloids have also been synthesized using a variety of above-mentioned methods, including chemical and bioreduction and synthesis in micellar solutions [16, 17]. The chemical reduction method involves two steps: nucleation and successive growth. When the nucleation and successive growth are completed in the same process, it is called in situ synthesis; otherwise, it is called the seed-growth method.

The successful utilization of NMNPs (e.g., silver or gold nanoparticles, AgNPs, or AuNPs) in biological assays relies on the availability of synthetic methods generating nanoparticles with the desired characteristics, namely high solubility in water, adequate morphology, size dispersion, and surface functionalities. Most commonly, NMNPs are synthesized by chemical or electrochemical reduction of noble metal precursor compounds (e.g., Au(III) and Ag(I) salts) in the presence of a capping agent, i.e., a compound able to bind to the nanoparticle surface blocking its growth beyond the nanometer range and stabilizing the colloid in the particular solvent used. Control over the shape and size of the NPs is usually achieved through the careful selection of the experimental conditions, namely reducing agent, reaction time, temperature, UV light (co)solvent, and capping agent. A common approach is to use capping agents with weak or strong affinities or both for noble metals. This mostly allows the synthesis of gold nanoparticles with good size dispersion but usually only soluble in organic solvents [18] requiring an additional step of extraction of the particles into water. In addition, exchange of strongly binding capping agents is usually cumbersome, which makes this type of gold nanoparticle less versatile for biological applications. Due to its simplicity and high yield, the most commonly used method for preparation of spherical AuNPs for biological assays is the citrate reduction method [19]. The use of citrate as a capping agent is very convenient due to its easy postsynthesis treatment, since it can be

easily replaced by other capping agents, e.g., thiol capping agents, bearing an appropriate functionality for binding of the biological analyte of interest.

NMNPs play important roles in different branches of science [20], such as chemical catalysis, catalysts for the growth of nanowires, nanomedicines, nanoelectronics. For most of those applications, their size and size distribution control are of key importance. Furthermore, composite and alloy nanoparticles exhibit unique electronic, optical, and catalytic properties that are different from those of the corresponding individual metal particles [21]. Research into NMNPs is a very active field in both fundamental scientific studies and applications—nanoscale materials [22]. A number of groups have been involved in synthesizing metal nanoparticles of different shapes, such as spheres [23], rods [24], triangular-shaped particles [25], prisms [26], nanowires [27], tripods, and tetrapods [28], using both chemical synthesis and lithography techniques, while other groups have investigated the optical [29] and electronic [30] properties of metal nanoparticles. The combination of these fields of research may lead to applications, such as optical data storage devices [31], biosensors [32], and new catalysts [33]. These applications are based on combining two principles: (1) surface functionalization for providing the colloidal stability and biocompatibility of particles, the molecular recognition of conjugates, etc., and (2) the excitation of plasmon resonances in the visible or near-IR region in order to obtain unique optical properties.

It is now well understood that the shape of the nanoparticles plays an important role in modulating their electronic and optical properties and, consequently, synthesis procedures that yield different shapes such as nanodisks [34], nanorods [35], nanowires [27], cubes [36], triangles [25], frames [37], and shells [38] are receiving considerable attention. The exciting electronic and optical properties displayed by metal nanoparticles [39] has resulted in their exploitation in a number of applications that include single-electron tunneling devices [40], nonlinear optical devices [41], electron microscopy markers [42], and the emerging area of plasmonics [43]. Some NMNPs are being studied in detail and are known to be excellent substrates for surface-enhanced Raman scattering (SERS) to probe single molecules [44].

Colloids of gold nanoparticles are one of the most stable and easiest to manipulate. However, preparing monodisperse gold nanoparticles is still not easily accomplished on a useful synthetic scale, especially if the stabilizing ligand of these particles is changed from the often used alkylthiols. The general synthetic procedure to prepare nearly monodisperse gold colloids involves the reduction of metal salts in the presence of surfactants and then stabilizing the particles with a capping ligand present in the solution [18]. In general, particle size and size distribution play a significant role in controlling the properties of any colloid based upon a nanomaterial [45, 46]. As a result, many groups have developed a variety of approaches to achieve particle separation and to narrow the size distribution of particles in a colloidal solution. Unlike molecular systems, it is often difficult to employ crystallization for colloidal structures, and the methods that have been used successfully are performed primarily in organic media. In such media, precipitation methods have been developed and used with great success for certain compositions [47]. Such methods, however, require an empirical tuning of the experimental conditions

to effect optimum size-selective precipitation or crystallization. The size distribution is further narrowed by size-selective precipitation [48]. Some authors demonstrated the advantage of a "digestive-ripening" procedure to prepare monodisperse colloids directly, avoiding the size-selective precipitation [49]. Other postsynthetic methods for refining particle size or separating a mixture of particles of different sizes in organic media include digestive ripening [50], use of supercritical fluids [51], gas pressurization [52], high-performance liquid chromatography [53], and size-exclusion chromatography [54]. In contrast, the improvement of the particle size distribution in aqueous media has been a more challenging task and is usually performed by filtration [55] or chromatographic methods such as size-exclusion chromatography [56] and capillary electrophoresis [57]. Such techniques, however, are somewhat limited in throughput and the types of compositions that can be used due to different degrees of interactions with column supports or filtration membranes and the need for specialized equipment (see more in the previous chapter). For particles dispersed in aqueous media, it would be a major advance if one could utilize the inherent chemical recognition properties of biomolecules [58–60] to size-selectively assemble particles.

Fendler and coworkers demonstrated that surface-modified hydrophobic colloidal nanoparticles may also be organized at the air–water interface—more specifically, on the surface of water—and that multilayer films of the nanoparticles could be formed on suitable substrates by the Langmuir–Blodgett (LB) technique [61]. A number of other groups have now used this method to form multilayer films of gold particles [62], polymer-capped platinum colloidal particles [63], buckyballs [64]. The Brust synthesis procedure [18] wherein gold nanoparticles are synthesized and capped with alkanethiols in a nonpolar organic phase continues to be the most popular means of obtaining hydrophobic gold nanoparticles that are readily dispersible in different nonpolar/weakly polar organic solvents [65, 66]. It was demonstrated an alternative method for obtaining hydrophobic gold nanoparticles synthesized in water by electrostatic coupling with fatty amine molecules present in nonpolar organic solvents [67]. The alkylamine-stabilized colloidal gold particles could be separated out in the form of a powder and dissolved in different organic solvents [67].

Spherical noble metal nanoparticles (sNMNPs) (gold, silver, SiO_2@Au or Au@SiO_2 core@shell, etc.) have been the primary choice of colorimetric probes and nanocomposites. Numerous assays have been developed for a wide range of analytes (e.g., DNA, protein, metal ions, enzyme, and small molecular drugs) [68]. These assays exploit interparticle cross-linking and noncross-linking aggregation mechanisms that usually involve receptor-conjugated sNMNPs and unmodified sNMNPs, respectively. Compared to the extensive research with the spherical nanoparticles, the use of nonspherical particles with anisotropic configuration to construct plasmon coupling-based colorimetric assays has been less well demonstrated, except for a few examples using gold nanorods (AuNRs) [69, 70]. The traditional in situ synthesis provides spherical or quasispherical NMNPs. The disadvantage is, however, that when the size increases, it becomes out of control, and the shape is not controlled either. Therefore, the seed-growth strategy has emerged

as a very efficient method to synthesize monodispersed AuNPs with large sizes (up to 300 nm) precisely and with well-defined shapes [71, 72].

In the course of the seed-growth synthesis of NMNPs, the formation of seeds takes a significant place correlated to the size, shape, and surface properties that are controlled by the amount and nature of reducing agent and stabilizer, and their ratio to the metal precursor. The earliest gold nanoseeds were proposed by Natan [73] using citrate reductant and capped spherical gold nanoseeds for the overgrowth of spherical AuNPs. Murphy's group [74, 75] reported the synthesis of 3.5-nm citrate-capped gold seeds by dropping an ice-cold aqueous solution of $NaBH_4$ into a solution of a mixture of $HAuCl_4$ and citrate. These seeds were originally used for the formation of AuNRs. This procedure of gold seed formation was modified by El-Sayed [76] using hexadecyltrimethylammonium bromide (HTAB) as the stabilizer instead of citrate. These gold seeds with a diameter smaller than 4 nm were used to promote the narrow dispersity of AuNRs. Subsequently, this seed formation was regarded as the most primary nucleation process in the synthesis of AuNPs. Other monodispersed, large-sized, spherical, or quasispherical AuNPs, AuNRs, and other shaped AuNPs have been synthesized using the seed-growth method.

Natan and coworkers [73, 77] prepared gold nanoparticles between 20 and 100 nm by adding citrate-capped, $NaBH_4$-reduced seeds into a "growth" solution containing a mild reducing agent such as citrate [77, 78] or hydroxylamine [79]. These results provided an improvement of physical properties compared with the Turkevich and Frens method. However, this synthetic route also generated a small population of rod-shaped AuNPs as impurities. Later, Murphy's group [80] improved the method by using ascorbic acid as a reducing agent as mild as citrate in growth solution and using cetyltrimethylammonium bromide (CTAB) as a stabilizer to synthesize monodispersed spherical AuNPs up to 40 nm (the citrate-stabilized AuNPs with a relative standard deviation that was lower than 10% were considered as monodisperse) [80, 81]. This method was later used by Han's group for the synthesis of icosahedral AuNPs having controlled size (from 10 to 90 nm) (Scheme 2.1) [82].

Later, Liz-Marzan's group first reported the synthesis of gold nanoparticles via the seed-growth method up to 200 nm, also showing optical properties with quadrupolar modes [79]. Highly monodispersed, spherical, citrate-stabilized AuNPs were synthesized up to 300 nm by using hydroquinone [71] or ascorbic acid [84] as
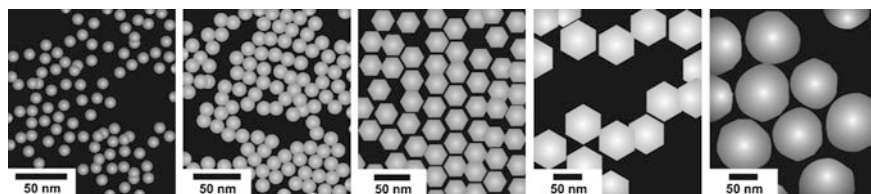
Scheme 2.1 TEM-like images of AuNPs (diameter) in solution (*from a left side*) ~ 11.0, ~ 13.3, ~ 32.2, ~ 69.0 nm, and (*to the right side*) 87.3 nm [82, 83]

reducing agent in the seed-growth process. Reaction conditions such as temperature [72], pH [72], gold precursors to seed particle concentration [72] and citrate concentration [81] were considered to affect the size distribution and shape of the AuNPs.

The formation of gold clusters by chemical reduction of $HAu^{III}Cl_4$ has been well described by Gachard et al. [85]. The gold salt reduction may occur either by UV irradiation or by chemical reduction. To evaluate the effect of light on gold reduction, the synthesis was performed in the dark, and gold nanoparticles were generated, which ruled out light as a reducing agent. Regev et al. [86] have proposed that the lipid monoolein, the onion supplier of OH groups, acts as a reductant for the gold salt:

$$R-CH-(OH)-CH_2(OH) \text{ being oxidized to } R-CH(OH)-CO_2H \qquad (2.1)$$
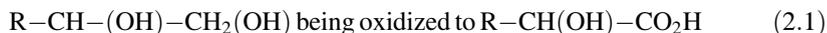
when Au(III) ions are reduced to Au(0). On the other hand, it was proposed that ethanol as well as water can act as very weak reducer agents [87].

A number of reports are available in the literature for the synthesis of silver nanoparticles by the chemical reduction of silver ions by sodium citrate or sodium borohydride [88], reduction in reverse micelles [89], biological methods [90, 91], electrochemical methods [92], photochemical methods [93], radiation methods [94], laser ablation [95], solvent reduction in the presence of surfactants [96], sonochemical methods [97], and reduction at two-phase liquid–liquid interfaces [98]. The unique size- and shape-dependent optical [99, 100] and antimicrobial [101, 102] properties of silver nanoparticles have prompted increasing interest of chemists, physicists, and materials scientists. Especially silver materials with zero-, one-, or two-dimensional nanostructures such as monodisperse nanoparticles [103, 104], nanowires [27], nanodisks [105], nanoprisms [106], nanoplates [107], and nanocubes [108] are believed to have great potential for applications in optics, catalysis, and other fields. Reduction routes involved in these studies fall into three broadly defined categories. The first one involves the use of relatively strong reducing agents, such as sodium borohydride [109], hydrazine [110], and tetrabutylammonium borohydride [110] to prepare silver nanoparticles. The second one is the irradiation of the solution containing silver ions with γ-ray [111], ultraviolet or visible light [112], and microwave [113] and ultrasound irradiation [107, 114]. The third route involves heating the solution of silver salt without commonly used reductants [115] or prolonged reflux silver solution in the presence of a weak reducing agent, such as glucose [116], sodium citrate [117], dimethylformamide (DMF) [118], potassium bitartrate [119], ascorbic acid [120], and alcohols or polyols [121, 122].

A variety of stabilizers or coating agents have been used in the silver particle preparation to achieve the best control of size, size distribution, shape, stability, and solubility of nanoparticles. Thiol derivatives [113] are the most common coating agents employed to stabilize silver colloids, even though aniline [123], long-chain amines [103, 110], surfactants [89], starch [124], and carboxylic compounds [110] have also been used. Polymers such as poly(vinyl pyrrolidone) (PVPo) [36, 121],

fourth-generation poly(amido amine) [125], polyacrylate [126], polyacrylonitrile (PAN) [115], and polyacrylamide (PAM) [111] are also important protective agents, which can effectively control shape, size, and stability of silver nanoparticles. For example, with the refluxing method, PVPo can direct the growth of silver into nanowires [121] and nanocubes [36]. Dickson and coworker have reported that photostable water-soluble silver nanodots created in dendrimers are quite stable and highly fluorescent [127]. Polymer-initiated photogeneration of silver nanoparticles in SPEEK/PVA (SPEEK = sulfonated poly(ether–ether) keton, PVA = poly(vinyl alcohol)) was anticipated to allow direct metal photopatterning [128]. Montmorillonite clay (MMT, as a reducing and stabilizing agent), as lamellar clay, has been used as carriers for silver nanoparticles with good results because of their high ion-exchange capacity, high surface area and sportive capacity, chemical lifelessness, and low or null toxicity [129]. Silver nanoparticles were synthesized onto the surface of MMT by a simple microwave-assisted process from an aqueous solution of silver nitrate; silver nanoparticles with a narrow size distribution on MMT surface were obtained without using any reducing agents [130].

The chitosan-mediated aqueous synthesis method was used for the preparation of high-yield monodisperse multibranched shaped gold-coated iron oxide nanoparticles. The growth of gold coating was achieved in the presence of chitosan and silver ions at room temperature. The plasmon band can be tuned with increasing branch length and gold shell thickness [131]. Further [132] have been synthesized silver nanoparticles protected with bovine serum albumin (BSA) where the BSA itself functions as the reducing agent leading to an undesired protein oxidation. Additional reports have also documented that BSA is able to interact with AgNP electrostatically [133] affecting the binding capacity of the protein with small molecules [133]. Nevertheless, research on the interaction between human serum albumin (HSA), the most abundant protein in the human plasma [134] and AgNP has been scarcely explored [135] though a deep understanding of the phenomenon is relevant for potential biomedical applications. It has also been shown that HSA can effectively interact with quantum dots and gold nanoparticles [136].

Palladium constitutes the most important model system for fundamental studies of metal–hydrogen interaction, which is central in areas such as hydrogen storage [137], heat storage [138], metal hydride batteries [139], hydrogen sensors [140], smart windows [141], and switchable mirrors [142]. Hydrogen forms a stable hydride with Pd, basically without activation barriers. During absorption, H_2 dissociates on the Pd surface and subsequently occupies surface, subsurface, and interstitial lattice sites according to their specific energetics.

The used surfactants find their way to various environmental segments and thus pose serious health hazards. They have the ability to adsorb strongly onto negatively charged suspended particulates and sludge. Intensive investigations have been carried out on their behavior, fate, and biological effects [143]. Long exposure to quaternary ammonium compounds (QACs) can cause sensitization, hemolysis, and toxic effects by all routes of exposure including inhalation, ingestion, dermal application, and irrigation of body cavities.

Polymer-based drug delivery systems emerged from the laboratory bench in the 1990s as a promising therapeutic strategy for the treatment of cancer and other devastating diseases [144]. Polymer–drug conjugates are nanosized hybrid constructs that covalently combine a bioactive agent with a polymer to ensure not only its efficient delivery to the required intracellular compartment but also its availability within a specific period of time. It has already been demonstrated that polymer–drug conjugation promotes tumor targeting by the enhanced permeability and retention effect and its capability of escaping from reticuloendothelial system.

2.2   Precursors and Their Conjugates

Nanoparticles typically grow in nonequilibrium conditions, and their final shapes are influenced by many factors contributing to the kinetics of growth. Factors such as the size, structure, composition of the seed, nature and concentration of metal precursor and reducing agent, molar ratio of precursor to additives, the selective adsorption of additives to different crystal facets, contact with an external support are all clearly capable of influencing the kinetics of particle growth and, hence, the particle morphology. The effects of these factors on the particle morphology are usually quite complex and are not yet completely understood. Therefore, it is a little early to formulate any general mechanism for growth in metallic nanocrystals. However, some preliminary trends have started to evolve. The basic principle of realizing anisometric growth in nanoparticles is that (synthesis) conditions have to be created so that the growth kinetics does not favor equal growth of all facets of the growing nanocrystal. A simple strategy is to use templates (rigid matrices) that will confine particle growth in various directions. When there is no physical template, the nature of the seed and/or the reaction kinetics must ensure dimension-specific growth during the particle formation. In addition to several polyhedral shapes, nanoparticles with highly anisotropic rod-, wire-, plate-, disk-, belt-, ribbon, branched-, or flowerlike morphologies have been prepared. In the related fields, it is essential to gain deeper understanding of the role of nanosizing because nanomaterial engineering provides a powerful means to optimize material performance [145].

The preparation of NMNPs by a chemical reduction approach contains two major parts: (i) reduction using agents such as borohydrides, aminoboranes, hydrazine, formaldehyde, hydroxylamine, saturated and unsaturated alcohols, citric and oxalic acids, polyols, sugars, hydrogen peroxide, sulfites, carbon monoxide, hydrogen, acetylene, and monoelectronic reducing agents including electron-rich transition-metal sandwich complexes; (ii) stabilization by agents such as trisodium citrate dihydrate, sulfur ligands (in particular thiolates), phosphorus ligands, nitrogen-based ligands (including heterocycles), oxygen-based ligands, dendrimers, polymers, copolymers, and surfactants (in particular cetyltrimethylammonium bromide, CTAB) . The in situ synthesized gold nanoparticles are also used for the seed-growth or further functionalization. Bolaamphiphiles (also known as bolaform

surfactants, bolaphiles, or alpha-omega-type surfactants) are amphiphilic molecules that have hydrophilic groups at both ends of a sufficiently long hydrophobic hydrocarbon chain. Compared to single-headed amphiphiles, the introduction of a second head- group generally induces a higher solubility in water, an increase in the critical micelle concentration (CMC), and a decrease in aggregation number. The aggregate morphologies of bolaamphiphiles include spheres, cylinders, disks, and vesicles. Bolaamphiphiles are also known to form helical structures that can form microtubular self-assemblies.

The formation and stabilization of silver nanoclusters in solution have been accomplished in various ways (Figs. 2.1, 2.2 and 2.3) [146–149]. The proper choice of parameters for the reaction, including the temperature, the reducing method, the stabilizers, and the initial ratio of metal salt (precursor) : stabilizer (capping agent, poly(methacrylic acid), surfactant, surface-active additive (mercaptosuccinic acid, DNA oligonucleotides, etc.)), reaction medium (water, water/ethanol, and ethanol) plays a crucial role in the successful synthesis of metal nanoclusters. Small variations in the synthetic procedure may change, for example, the collective properties such as fluorescent plasmonic silver nanoparticles to larger nonfluorescent plasmonic silver nanoparticles. Despite the many reports of the last few years about the synthesis of silver nanoclusters, it remains difficult to design general rules for the synthesis of silver nanoclusters, as similar reagents and reaction conditions may lead to silver nanoparticles instead of nanoclusters.

The activation of the reaction to produce silver nanoclusters can be performed following several routes. The silver ions from dissolved silver salts can be reduced, either by a chemical reductant (e.g., sodium borohydride, sodium hypophosphite), by light (photoreduction with visible or ultraviolet light), or by γ-rays (by radiolysis of water). The chemical reduction and the photoreduction are the most commonly used methods. The radiolytic method was also used to produce silver nanoclusters in solution [150]. It is well known that the specific properties of silver nanoclusters, such as the stability and fluorescence quantum yield, depend largely on the scaffold
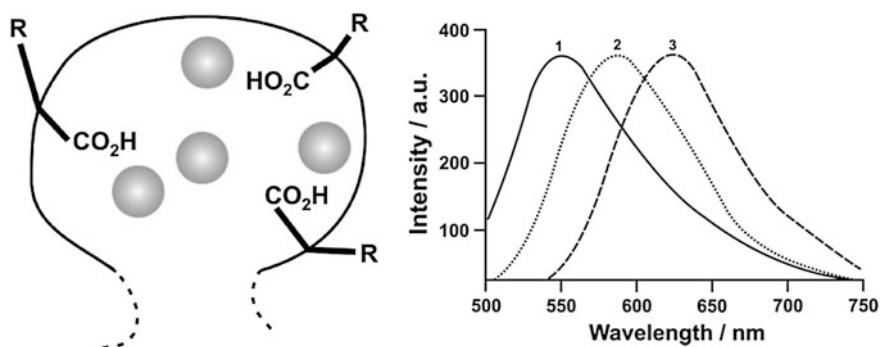
Fig. 2.1 Schematic drawing of silver nanoclusters protected by carboxyl groups of poly (methacrylic acid esters) where R means alkyl ester (*left panel*). Emission spectra of the samples imaged [water (*1*), water/methanol (*2*) and methanol (*3*)] [146]
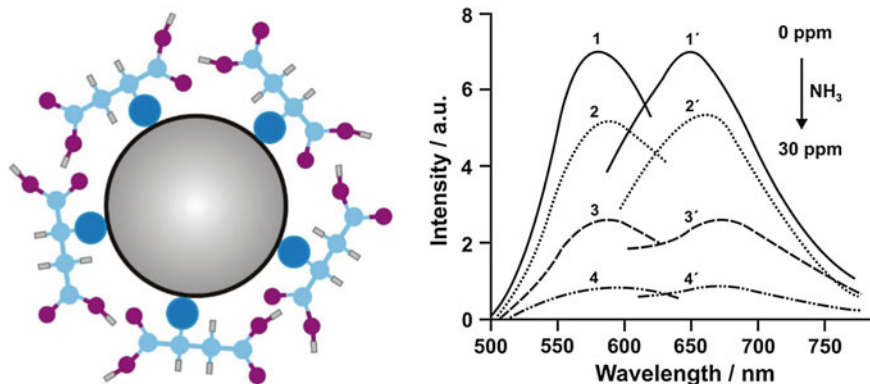
Fig. 2.2 Silver nanoclusters prepared by interfacial etching from silver nanoparticles and stabilized with small molecules (i.e., mercaptosuccinic acid). Fluorescence quenching by addition of quencher (NH₃) [147]
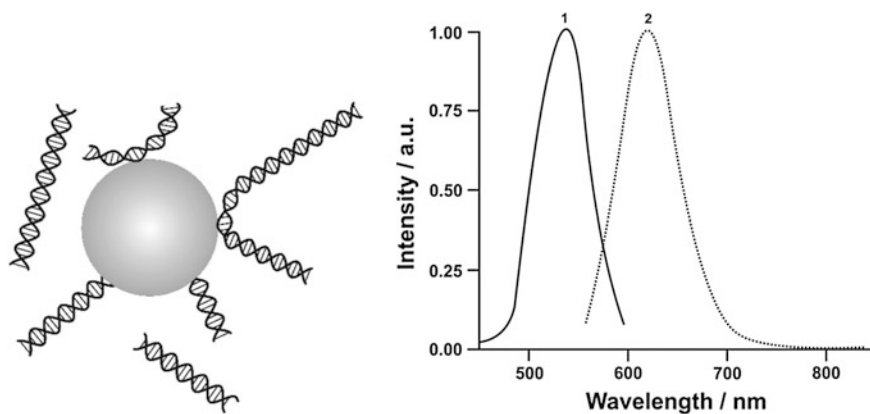
Fig. 2.3 Representation of silver nanoclusters encapsulated in DNA oligonucleotides. Emission spectra of the sample, showing red emitters [148, 149]

used during reduction. The largest fluorescence quantum yield reported for silver nanoclusters prepared in organic scaffolds is achieved using nucleic acid (quantum yield of 64%) [151] while polyacrylates provide stable solutions over years (Figs. 2.1, 2.2 and 2.3) [152]. The sensitivity of silver nanoclusters to the local environment can be exploited for sensing purposes, though it represents a difficulty when designing the synthesis, the proper recipe for the production of silver nanoclusters with a certain scaffold might not be useful when using a different scaffold. Silver nanoparticles larger than 2 nm exhibit plasmon resonance effects and typically do not present fluorescence. However, there are recent reports about luminescent silver nanoparticles. The emission of light from large silver particles is

likely produced from surface-bound nanoclusters or subnanodomains within silver nanoparticles. For gold nanoclusters, the ligands play a major role in enhancing the fluorescence of the nanoclusters in two different ways, by charge transfer from the ligands to the gold core through direct bonding or by direct donation of delocalized electrons of electron-rich atoms or groups of the ligands to the gold core [153]. In the case of silver, the role of ligands or scaffolds on the fluorescence properties is not yet understood.

The nature and concentration of a precursor affect the particle formation in various ways [154–156]. For example, while making platinum nanoparticles through hydrogen reductions of three different platinum precursors ($K_2[Pt(C_2O_4)_2]$, K_2PtCl_4, or K_2PtCl_6), Fu et al. [157] have observed that nanoparticles prepared from $K_2[Pt(C_2O_4)_2]$ exhibit quite narrow size and shape distributions and the selectivity of cubic nanoparticles is greater than 90%. Yu and Xu [156] reported that the use of K_2PtCl_6 and K_2PtCl_4 has a strong influence on the particle-formation reaction and the particle morphology. The result of the synthesis with K_2PtCl_4 was difficult to reproduce due to rapid hydrolysis of the Pt(II)-precursor (K_2PtCl_4) in aqueous solution unlike Pt(IV)-precursor (K_2PtCl_6) [158].

One common method of platinum nanoparticle formation is the in situ reduction of platinum salts by reducing agents to produce a nanoparticulate powder [159], which can then be supported on a low-cost, high-surface-area support. This method has been previously discussed in the literature, and a number of different reducing agents have been employed, for example, formate, formaldehyde, hydrazine, borohydride, formic acid, sodium citrate, and sodium thiosulfate [160]. The alkoxide route allows the properties of the platinum nanoparticles to be easily optimized, by varying the amount of water employed, the ratio of reactants, the synthesis temperature, and the time; the resulting film thickness and porosity can also be modified by varying the substrate withdrawal rate from the sol, the number of coatings, and the film drying temperature and time. The specific synthesis used here for platinum sol formation was shown to produce a precipitate phase and a sol containing suspended metallic PtNPs ca. 1–3 nm in diameter. The purpose is to characterize all of the species formed in the synthesis of several hexachloroplatinic acid (HCPA)/sodium ethoxide ($NaOC_2H_5$)-formed Pt sols. As well, a mechanism of in situ Pt sol formation via HCPA reduction by $NaOC_2H_5$ is proposed, with a goal of enhancing the yield of PtNPs for use as an electrocatalyst in fuel cell reactions. Considering the reactants employed in the synthesis, both metallic Pt and NaCl, among other species, can be expected to form (Eq. 2.2). As neither of these is appreciably soluble in ethanol, it was anticipated that both would be found, to varying extents, in the precipitate phase [161].

$$H_2PtCl_6 + NaOC_2H_5 \rightarrow Pt(0) + NaCl + acetaldehyde + ? \qquad (2.2)$$

It was that two phases appear: a precipitate, which ranges from white to black in color, depending on the HCPA to ethoxide ratio, and a yellow- or orange-colored solution phase. From the cyclic voltammetry, X-ray diffraction (XRD), and thermal gravimetric analysis/differential scanning calorimetry (TGA/DSC) results, it has

been shown that the precipitate is composed entirely of small platinum particles (average diameter of 6 nm) and NaCl. The TGA/DSC data showed that the darker precipitates contain a higher percentage of metallic Pt than do the lighter-colored ones. As well, in the optimized sol synthesis (type 1, with a 2:1 sodium ethoxide-to-HCPA ratio), only 1% of the Pt is lost to the precipitate. Electrochemical and inductively coupled plasma spectroscopic results showed that, of the Pt species retained in the sol, 75% was in the form of platinum nanoparticles (1–3 nm diameter) and 25% existed in a Pt(II) form (seen by X-ray photoelectron spectroscopy (XPS) and X-ray absorption near-edge spectroscopy (XANES)). The Pt(II) species was identified, by NMR spectroscopy, as being a Na^+ analogue of Zeise's salt [$KPtCl_3(C_2H_4)$], which exhibited a greater stability in both ethanol and air than the typical K^+ form of Zeise's salt. The $NaPtCl_3(C_2H_4)$ species, which arises from a side reaction of H_2PtCl_6 and ethanol, rather than as an intermediate formed during the in situ Pt(IV) reduction reaction, may serve as a stabilizer for the PtNPs in the sol phase. The mechanism of PtNP formation from the ethoxide/hexachloroplatinic acid synthesis is proposed to involve a metathesis reaction (a chloride in H_2PtCl_6 is exchanged with an ethoxide group from $NaOC_2H_5$, resulting in an unstable $PtCl_5(OC_2H_5)^{2-}$ intermediate and NaCl), followed by a hydride elimination step, producing acetaldehyde and $PtCl_5H_2^-$. Finally, a rapid reductive elimination step produces HCl and $PtCl_4^{2-}$. The process is repeated, reducing the Pt(II) species to Pt(0) nanoparticles.

The typical route for solution-phase synthesis of PtNPs is the simple reduction of metal salts. A wide range of reducing agents have been used in colloid-chemical synthesis of metal nanoparticles of practically all transition metals. For example, H_2 or hydrazine, hydroxyl amine, hydrides (e.g., $NaBH_4$), ascorbic acid (AA) or ascorbate, citric acid or citrate, oxidizable polymers [e.g., polyvinylalcohol (PVA)], solvents (such as alcohols, aldehydes, and DMF), etc., have been used to prepare various NMNPs [162]. Depending on the reduction potentials of the metal precursor and the reducing-agent systems, reduction can occur at room temperature or at elevated temperatures [163]. Hydrogen is one of the most widely used reducing agents to prepare palladium and platinum nanoparticles. For example, the first shape-controlled colloid-chemical synthesis of platinum nanoparticles used hydrogen reduction of K_2PtCl_4 in the presence of sodium polyacrylate (NaPA: $M_w \sim 2100$) [156, 158]. Similar reduction techniques have been used by several other authors to prepare differently shaped platinum nanocrystals in the presence of a number of other capping polymers [156, 157].

The alcohol-reduction process introduced by Toshima et al. is widely used for the preparation of colloidal noble metals [164]. Alcohols with alpha-hydrogen atoms are oxidized to the corresponding carbonyl compound during the metal-salt reduction. A variation of the alcohol method is found in Figlarz's polyol method, which consists of refluxing a solution of the metal precursor in ethylene glycol or larger polyols [165]. Xia et al. have used this method to synthesize a plethora of anisometric NMNPs [166]. Like alcohols, DMF has been used to reduce Ag^+ ions forming various-shape silver nanoparticles [155]. Reducing agents are not equally effective in generating anisometry in nanoparticles. Often, milder reducing agents

are prescribed for generating anisometric particles [167]. Beyond mere reduction of metal ions, reducing agents affect the nucleation and growth as well as stabilization of nanoparticles [168].

The strength of the reducing agent used in Brust–Schiffrin method is much larger than that of citrate used in the Turkevich method, and according to Marcus theory, the reaction rate in gold nanoparticles synthesis using sodium borohydride ($NaBH_4$) is much larger than that of the Turkevich gold nanoparticle synthesis using citrate reduction. A direct consequence is that the size of the AuNPs synthesized using the borohydride reductant is much smaller than that of Turkevich method using the citrate reductant. In general, citrate plays a role as a stabilizing agent with preparations of gold nanoparticles requiring relatively high temperatures due to its weak reducing strength. The method pioneered by Turkevich et al. is the simplest one available. In general, it is used to produce modestly monodisperse spherical gold nanoparticles suspended in water of around 10–20 nm in diameter. Larger particles can be produced, but this comes at the cost of monodispersity and shape. It involves the reaction of small amounts of hot chloroauric acid with small amounts of sodium citrate solution. The colloidal gold will form because the citrate ions act as both a reducing agent and a capping agent. To produce larger particles, less sodium citrate should be added. The reduction in the amount of sodium citrate will reduce the amount of the citrate ions available for stabilizing the particles, and this will cause the small particles to aggregate into bigger ones (until the total surface area of all particles becomes small enough to be covered by the existing citrate ions). Slot discovered a new way to prepare gold nanoparticles using a mixture of tannic acid/citrate solution whereby tannic acid plays the role of a reducing agent instead of citrate, and the AuNPs are obtained at 60 °C [169]. Then, Natan's group introduced a method using citrate as a stabilized agent only and borohydride as a reducing agent [170]. The AuNPs were obtained upon adding the $NaBH_4$/citrate mixture into the $HAuCl_4$ solution at room temperature. With this method, the size of AuNPs is tailored to 6 nm, which compares with sizes beyond 20 nm using the traditional Turkevich method. Remarkable modification of the Turkevich method involved the reversed order of addition that was conducted by adding $HAuCl_4$ to the citrate solution, producing monodispersed AuNPs with relatively small size (less than 10 nm) [171]. The further simple method generates nearly monodisperse "naked" gold nanoparticles in water. Precisely controlling the reduction stoichiometry by simply adjusting the ratio of $NaBH_4$–$NaOH$ ions to $HAuCl_4$–HCl ions within the "sweet zone," along with heating, enables reproducible diameter tuning between 3 and 6 nm. The aqueous particles are colloidally stable due to their high charge from the excess ions in solution. These particles can be coated with various hydrophilic functionalities, or mixed with hydrophobic molecules for applications in nonpolar solvents. Interestingly, in nonpolar solvents the nanoparticles curiously remain highly charged and self-assemble on liquid droplets to form 2D monolayer films of monodisperse nanoparticles.

There are several methods for the preparation of silver nanoparticles such as citric acid reduction, electrochemical synthesis, photoreduction, and radiation (see also above). However, silver nanoparticles prepared from these methods can only

be kept for a maximum of 2–3 months [172]. Many experiments have shown that the growth of silver nanoparticles in solution is sensitive to the presence of citric acid or sodium citrate but the exact role of citric acid is still unidentified. Later, [173] reported that using citric acid as a reducing agent made the reduction reaction take one week longer and led to a wide size distribution. They also reported that the use of sodium citrate did not result in the formation of silver nanoparticles. As far as stabilizers are concerned, citrate ions can bind on silver surfaces for shape control, but their ability to stabilize silver particles is weaker than thiols [174]. Nowadays, a molecule which can act both as a reducing and capping agent is preferred so that the reaction takes place in one step and there is no need for an external reducing agent. This will reduce the number of steps involved in metal nanoparticle synthesis. The physical method involves radiation reduction of silver ions by γ-ray, microwave, ultraviolet, or visible light [175]. Chemical reduction in solution is advantageous over other processes, because of its simplicity, low reaction temperature, and solubility of metal salts in water. The most used reducing agents are $NaBH_4$, ethylene glycol, DMF, dimethylacetamide, and formamide [176].

Several methods have been used to synthesize silver nanoparticles such as chemical reduction; Tollen's reagent; photoreduction; and biochemical, sol-gel and polyol approaches [177]. Paraformaldehyde and citric acid are used as stabilizing and reducing agents for synthesizing silver nanoparticles through the reduction in silver ions by the oxidation of hydroxyl groups of paraformaldehyde to aldehyde groups using strong base, NaOH. The addition of silver nitrate to the NaOH solution leads to the formation of Ag^+ as $[Ag(H_2O)_4]^+$, which then change to silver oxide (Ag_2O) through the reaction of OH^- ions with Ag^+ ions. A dark cream solution is produced because of the formation of a large amount of silver oxide (Ag_2O) sediment (Eq. 2.3) [178].

Paraformaldehyde is deprotonated $[-O(CH_2O)_nH]$, and electrostatic interaction between silver ions and free deprotonated paraformaldehyde shielded the formed nanoparticles and grabbed silver clusters to the nanoparticles (Eq. 2.3). Increasing temperature-using microwave in the presence of NaOH solution (pH 12) leads to fast hydrolysis paraformaldehyde to oligomers that capped more Ag^+ ions and cause high dispersion on template surface (Eq. 2.4). The addition of citric is obligatory because of the removal silver ions by NaOH (redox reaction), which inhibits further reduction reaction of the silver particle surface (Eqs. 2.5 and 2.6) [179].

$$2AgNO_3 + 2NaOH \longrightarrow Ag_2O + 2NaNO_3 + H_2O$$
$$\downarrow \qquad\qquad (2.3, 2.4)$$
$$2Ag^+ + O^{2-}$$

$$HO \left[\begin{array}{c} | \\ C - O \\ | \end{array} \right]_n H + nOH^- \longrightarrow {}^-O \left[\begin{array}{c} | \\ C - O \\ | \end{array} \right] H + nH_2O + ne^- \qquad (2.5)$$

$$Ag^+ + ne^- \rightarrow Ag^0 \tag{2.6}$$
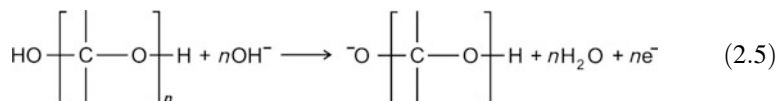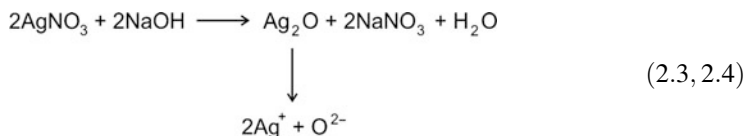
Liz-Marzan et al. [155] have shown that silver nanoparticles can be prepared in DMF without adding any reductant. It has been suggested that the reduction rate can be enhanced at high temperatures. Because most of the organic reactions take place in organic solvents, it is desirable to develop synthetic methods that lead to the formation of particles having different morphology in addition to the stabilization of metal nanoparticles in such solvents. In addition, if one can design a synthetic method to prepare different morphological particles in the same medium without adding reductants from outside, this may have its own important implications. Formamide is one of the most common solvents used to study various processes such as formation of metal nanoparticles, interaction with alcohols. [180]. It is known that formamide–water and formamide–methanol complexes can serve as model systems for protein–water and protein–solvent interactions. Photocatalytic oxidation of volatile organic chemicals (VOCs) constitutes one of the most promising methods for the removal of these pollutants in an enclosed atmosphere. Generally, metal oxides are being explored for such purposes. As silver is known to have bactericidal properties, it is important to assess its effect on VOCs. We have described the preparation of silver nanoparticles by reduction of silver ions with formamide in the absence and presence of stabilizers such as PVPo and SiO_2 nanoparticles. In addition, attempts have been made to see the effect of addition of methanol, VOCs, and a complexing agent on the stability of silver nanoparticles. The reaction of silver nanoparticles with $CHCl_3$ is indicative of the strong reducing power of the particles. As the nanoparticles have more surface atoms, the unsaturation at the surface is very high. In the presence of an organic molecule, which is an electrophile, the surface atom acquires an excess positive charge and the rest of the nanoparticles a corresponding negative charge. In the presence of oxygen, this excess negative charge is removed and the oxidation of the silver particles can proceed. This could be the reason for observing fast oxidation of silver particles in an aerated solution as compared to that in a N_2-bubbled solution. Similarly, the reactivity of silver nanoparticles with toluene was investigated. After addition of toluene to a silver dispersion in formamide, the color of the silver sol gradually faded due to oxidation in the formamide layer. However, in a N_2-bubbled solution, the oxidation of particles was very slow. It is known that oxidation of toluene leads to the formation of benzaldehyde. As metal particles can act as a sink for electrons, it appears that in the presence of silver particles, there is a possibility of oxidation of toluene, which is facilitated by the presence of oxygen [181].

The use of amine–borane complexes is essential for the syntheses of monodisperse metallic nanoparticles. Compared to commonly used reducing agents (e.g., $NaBH_4$, $LiBH_4$), amine–borane complexes have a weaker reducing ability, which can slow the reducing rate of gold cations and allow control over the growth of nanoparticles [182]. Upon the addition of strong reductants, such as $NaBH_4$, gold cations are reduced rapidly, resulting in an immediate color change of the reaction mixture from colorless or yellow to dark red. With the use of weaker reductants

applied in these syntheses, a much slower but continuous color change from colorless to yellow, pink, brown, and finally to purple–red is observed, which indicates a relatively slow reducing rate of Au(I). In addition to tert-butylamine-borane, other amine (i.e., triethylamine, morpholine, and ammonia)–borane complexes can be used. While the triethylamine complex is a reducing agent comparable to the tertbutylamine complex, the morpholine complex exhibits much weaker reducing ability and requires longer reaction time to complete the reaction. In comparison, the reducing ability of ammonia-borane is much stronger, so that it is difficult to obtain nanoparticles with a narrow size distribution.

The reducing power of the amines of several different structures was studied by Newman and Blanchard [183], who showed, very clearly, that the oxidation potential of the reducing agent should lie between the oxidation of Au(0)–Au(I) and the reduction of Au(III)–Au(0) for the reaction to proceed. Outside this range, the reaction is not spontaneous. Multifunctional amines and nitrogen-containing polymers have also been tested for the synthesis of gold nanoparticles [184, 185]. Indeed, the potential scan started immediately above the point at which the reduction of Au(III) occurs and firstly toward the cathodic direction. At pH 4.0 (Fig. 2.4, left panel), the reduction of Au(III)–Au(0) occurs at 0.72 V (peak I), and the oxidation of the main product Au(0) generated in this process appears in the opposite scan at 1.14 V (peak III).

Under the same experimental conditions, the cationic polyelectrolyte form of the block copolymer does not exhibit prominent electrochemical activity, and no more than a weak oxidation signal appears at 1.00 V (shoulder I*). In principle, the polymer oxidation potential is located within the range required for a spontaneous redox reaction with Au(III) to occur, but still no AuNPs are formed. One can attribute this finding to the onset oxidation potential of Au(0) of 0.92 V (arrow
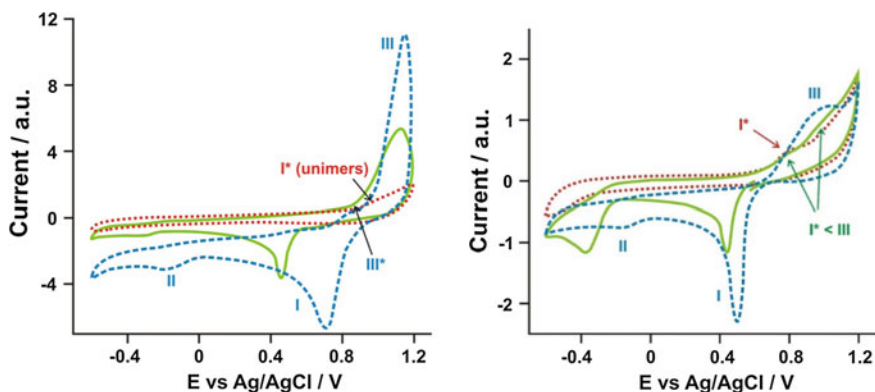
Fig. 2.4 Cyclic voltammograms recorded at 50 mV/s in aqueous media during selected experimental steps that ultimately lead to the spontaneous AuNP nucleation and growth mediated by pH-responsive triblock 1 copolymer, as indicated. [Au(III)] = 0.275 mM; [NR_3 groups] = 0.275 mM; $C_{triblock1}$ = 1.0 mg.mL^{-1}; *Left* pH 4.0 with 0.1 M KCl as electrolyte, *Right* pH 6.8 with 0.1 M KH_2PO_4/K_2HPO_4 as electrolyte [186]

labeled III*), which is lower than that of the polymer, implying that Au(0) would be oxidized before the polymer. The latter, however, strongly influences the reduction of Au(III), the potential of which shifts toward cathodic values from 0.72 V down to 0.45 V in the presence of the electrochemically inert cationic polyelectrolyte.

When the pH is controlled by using phosphate buffer solutions at pH 6.8, the electrochemical potentials of reactions involving the reactants Au(III), Au(0), and polymer micelles shift to lower values (Fig. 2.4, right panel). Au(III) is reduced to Au(0) at 0.50 V, which, in the absence of polymer, is oxidized at 1.00 V. Polymeric micelles undergo an oxidation reaction that gives a current density increase with a peak at 0.81 V. The oxidation potential of the polymer also lies within the range necessary for a spontaneous redox reaction with Au(III) to occur. When the individual cyclic voltammograms of Au(III) and polymer micelles are compared, one would expect the reaction not to take place because the onset of the polymer and Au(0) oxidation processes superimpose at 0.66 V.

The voltammogram recorded for a mixture of Au(III) and polymer reveals interesting new features. On addition of this buffer solution, the amino groups of the PDPAEMA (poly2-(diisopropylamino) ethyl methacrylate) segment are neutralized, and the polymer is rendered amphiphilic. Furthermore, the polymer chains become better electron donors through the presence of a lone pair of electrons on the nitrogen atoms of the amino groups after deprotonation. The self-assembled micelles feature a hydrophobic core with nitrogen atoms coordinated to Au(III); the affinity of gold for nitrogen is higher than that for the other possible atom-donor species in solution. These core@shell-type nanostructures can interact with the electrode surface and exhibit electrochemical activity in spite of having a stabilizing interface (shell) that is electrochemically inactive. The coil-like chains forming the hydrated shell can deform or rearrange to facilitate contact with the electrode surface. In fact, a few studies have been carried out on redox-active block copolymer micelles in which electrochemical reactions involved centers of an organic or organometallic nature, located in the hydrophobic core [187]. Depending on the reaction pathway and products, spherical micelles can be either disrupted or transformed into other morphologies [188].

The most important information obtained from the voltammogram recorded for the mixture is that the oxidation potential for the polymer in the form of micelles (peak I* micelles) is lower than the oxidation of Au(0) (peak III). As a result, gold nanoparticle synthesis is mediated solely by polymers with tertiary amino groups situated in the micelle core (the reaction microenvironment), without the need for any other reactant. Cyclic voltammograms recorded for AuNP@triblock 1 (poly (ethylene oxide)-b-poly(2,3-dihydroxypropyl methacrylate)-b-poly[2-(diisopropylamino) ethyl methacrylate] (PEO-b-PDHPMA-b-PDPAEMA) [186] after reaching a stable plateau in the characteristic absorption wavelength demonstrated that the Au(III) species were almost quantitatively converted into nanoparticles, since no reduction peak typical of their reduction was observed. Essentially, the same behavior was also observed using sodium tetraborate buffer solutions at pH 9.1.

The controlled self-assembling of amphiphilic block copolymers into micellar structures (Schemes 2.2, 2.3, 2.4, 2.5 and 2.6) has attracted substantial interest for

various potential applications, including particle syntheses, drug and gene delivery, catalysis, templates, metal particle synthesis, and biosensors [189–192]. Rationally designed molecular building blocks allow for the precise control of particle size and morphology of the supramolecular aggregate, and various defined structures, including spherical micelles, rodlike micelles, or vesicles [193, 194].

Vast studies have concerned aqueous solutions of the amphiphilic "pluronics" type of triblock copolymers, PEO-PPO-PEO, for pharmaceutical use and drug delivery systems [195]. It is well established that the pluronic copolymers with higher PEO/PPO [(poly(ethylene oxide)/poly(propylene oxide)] ratio self-assembly into micelles composed of a PPO-rich core and a PEO-rich corona above the critical micellar concentration and a critical micellar temperature (CMT) [196]. Amphiphilic block copolymers (AB or ABA-type) with large solubility differences between hydrophilic and hydrophobic moieties, in aqueous medium are able to self-assemble into polymeric micelles characterized by mesoscopic size range. These structures consist of water-insoluble cores and water-soluble shells. Depending on blocks' length, the core can assemble into various supramolecular structures characterized by different morphologies (Scheme 2.7). Poly(ethylene oxide)-poly(propylene oxide)-poly(ethylene oxide) (PEO-PPO-PEO) block copolymers are well known as dispersion stabilizers and templates for the synthesis of mesoporous materials and nanoparticles [197]. Variation of the PEO-PPO-PEO block copolymer molecular characteristics, concentration, and temperature allows for unique tunability of block copolymer self-assembly in the presence of selective solvents such as water. It was found that PEO-PPO-PEO block copolymers can act as very efficient reductants/stabilizers in the single-step synthesis and stabilization of gold nanoparticles from hydrogen tetrachloroaureate(III) hydrate (in air-saturated aqueous solutions) at ambient temperature in the absence of additional reductant or energy input [198]. This synthesis proceeds fast to completion and is environmentally benign and economical since it involves only water and nontoxic commercially available polymers (poloxamers or pluronics). The gold nanoparticle dispersions remain highly stable for several months. On the contrary, PEO
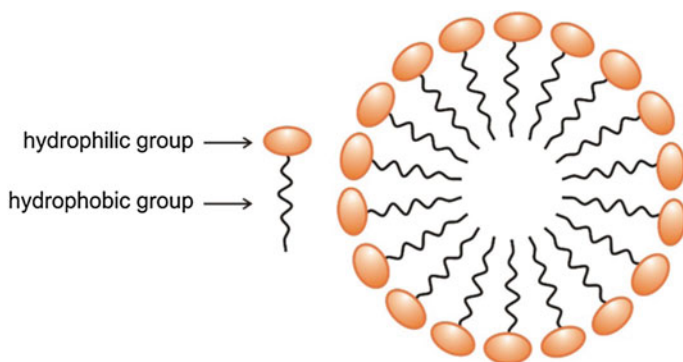
Scheme 2.2 Schematic of self-assembly of copolymer blocks into micelles
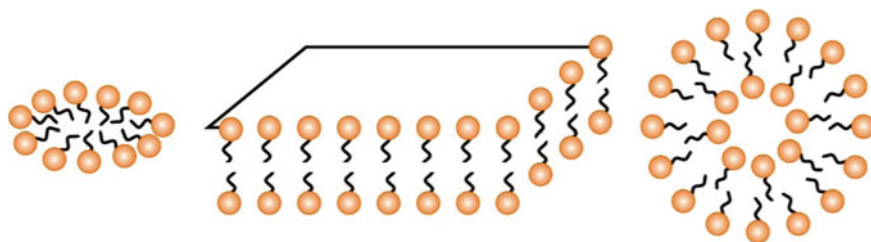
Scheme 2.3 Various defined structures, including disk-like, lamellar, and spherical vesicles
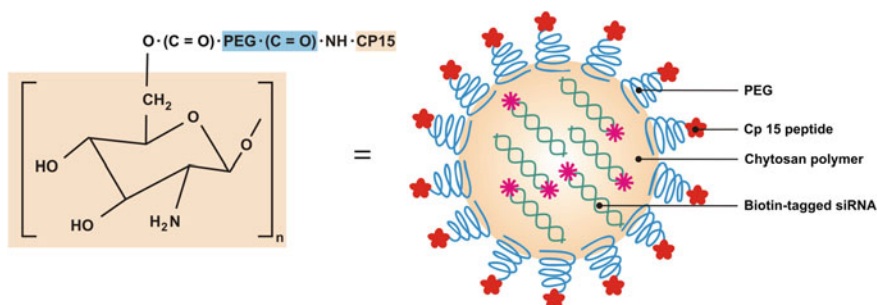
Scheme 2.4 Mechanistic view of drug delivery systems

homopolymer, of molecular weight comparable to that of the PEO-PPO-PEO block copolymers, was very slow in producing particles (more than 2 days were needed) and inadequate for their colloidal stabilization. Compared to recently reported single-step methods for gold nanoparticle synthesis, this method offers the advantages of ambient conditions, fast completion, being economical, and resulting in a "ready-to-use" product. The contributions of block copolymer molar concentration, PEO concentration, PPO concentration, and CMC are addressed by examining a range of PEO-PPO-PEO block copolymers. These polymers have the ability to form temperature-dependent micellar aggregates and, after a further temperature increase, gels due to micelles aggregation or packing. Therefore, with these polymers it is possible to mix drugs in the sol state and at room temperature and the solution can be injected into a target tissue. It forms an in situ gel depot at body temperature and provides controlled drug release. A formulation which is in the form of injectable liquid at room temperature, but changes into gel at body temperature, with a pH close to neutrality and having a certain biocompatibility and biodegradability surely represents an ideal system.

In general, different kinds of synthetic copolymers are made of poly(ethylene oxide) as hydrophilic block, and of a wider range of hydrophobic blocks. The combination of different PEO-hydrophobic blocks has given rise to several micelle systems with differing physicochemical properties, such as loading capacity,
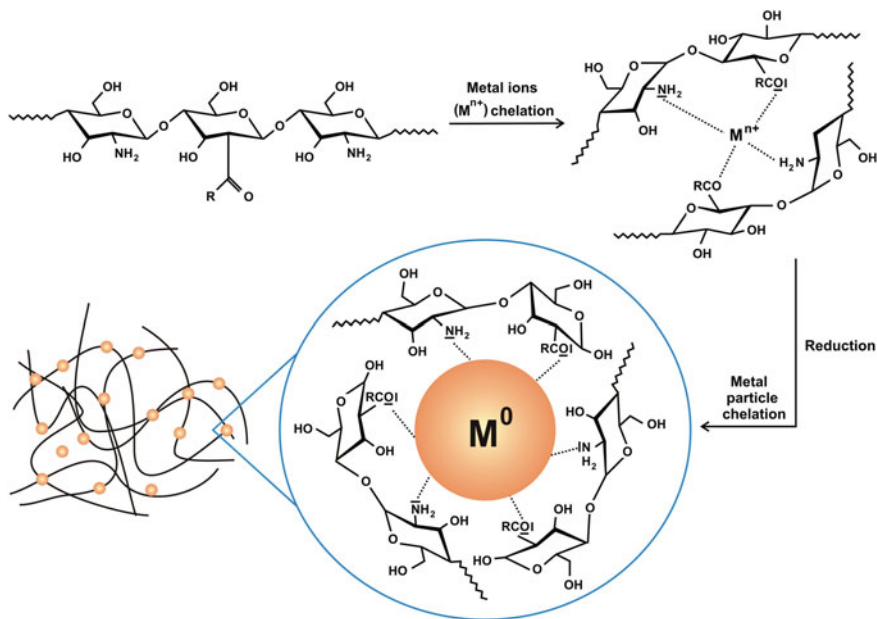
Scheme 2.5 Nucleation of metal nanoparticles via complexation of precursors followed by reduction of metal salts by functional polymer [189–192]

morphology, gel, biodistribution, size, release kinetics, and specificity against different kinds of drugs (Scheme 2.7).

In aqueous systems, the effects of metal ion/stabilizer mixing ratio, reaction temperature, reaction time, and energy input on the formation of colloidal particles typically have been considered. Formation of gold nanoparticles from $AuCl_4^-$ in aqueous PEO-PPO-PEO block copolymer solutions includes three main steps: (1) reduction of metal ions in aqueous block copolymer solution, (2) absorption of block copolymer on gold clusters because of amphiphilic character (hydrophobicity of PPO) and reduction of further metal ions on the surface of gold clusters, and (3) growth of gold particles and stabilization by block copolymers (refer to Scheme 2.8):

(1) reduction of metal ions facilitated by block copolymers in solution,

$$AuCl_4^- + nPEO\text{-}PPO\text{-}PEO \rightarrow (AuCl_4^-)\text{-}(PEO\text{-}PPO\text{-}PEO)n \qquad (2.7)$$

where $(AuCl_4^-)$-$(PEO\text{-}PPO\text{-}PEO)_n$ represents $AuCl_4^-$ ions bound to cavities that are formed from hydrated PEO and PPO coils. Reduction of bound $AuCl_4^-$ ions
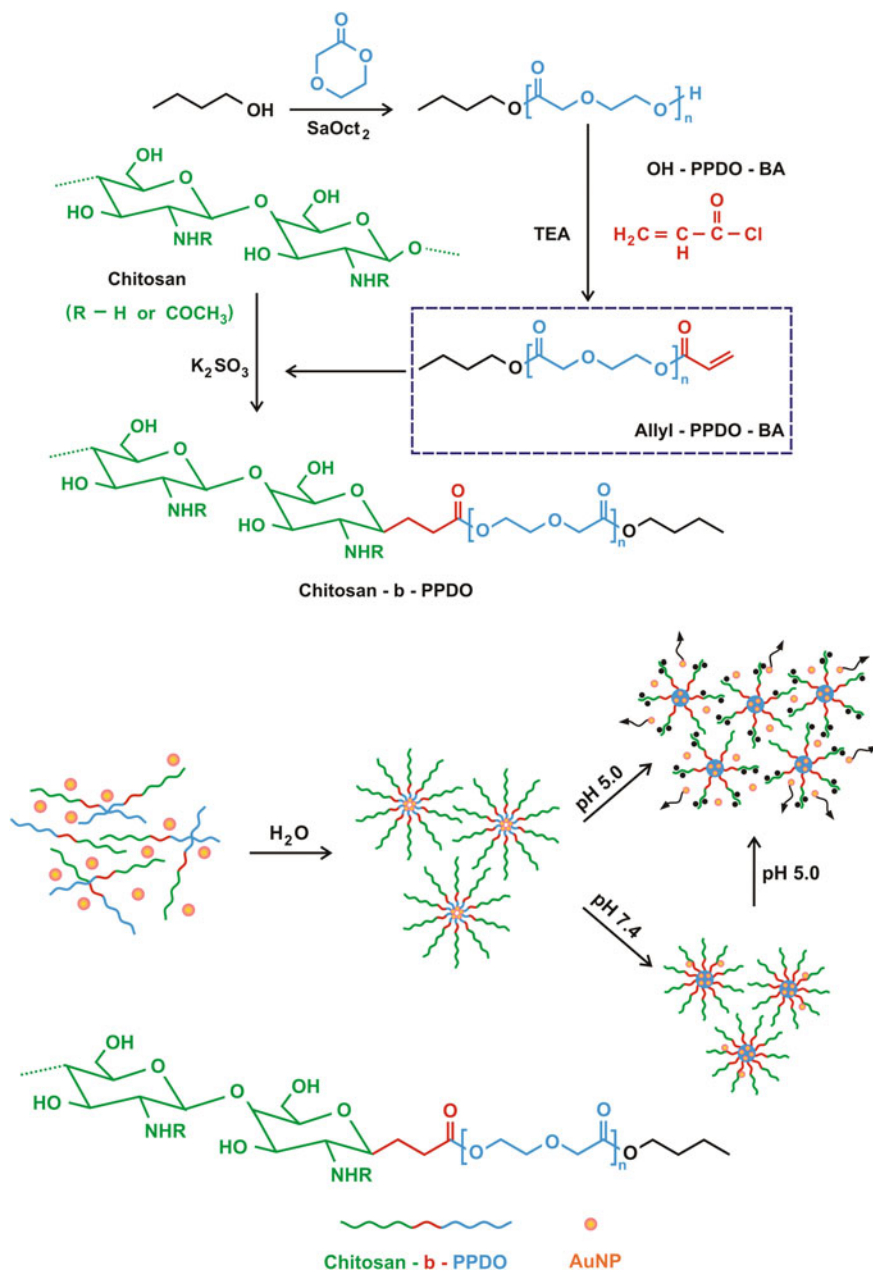
Scheme 2.6 Encapsulation of nanoparticles by the micellar aggregation via varied solubility and pH [poly(p-dioxanone) (PPDO)] [189–192]
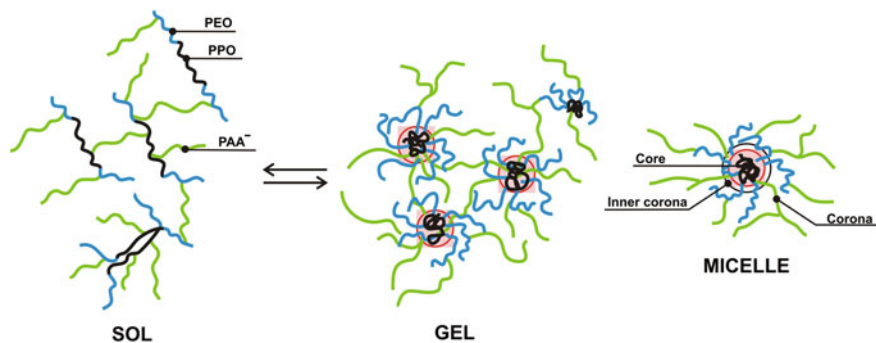
Scheme 2.7 Amphiphilic "pluronics" nanostructures based on PAA$^-$ Na$^+$ [197]
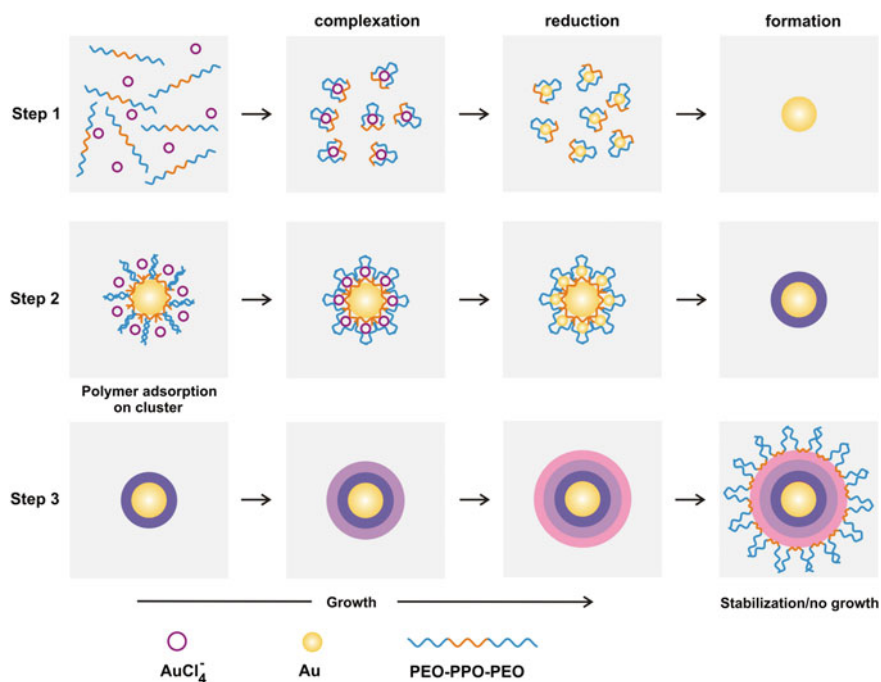
Scheme 2.8 Schematic of proposed mechanism of AuCl$_4$$^-$ reduction and particle formation [200, 203]

proceeds via oxidation of the polymer by the metal center. Oxidation products (carboxylate groups) have been identified by Fourier transform infrared spectroscopy (FTIR) in PEO homopolymer systems1 [199] after AuCl$_4$$^-$ reduction:

$$(AuCl_4^-)\text{-}(PEO\text{-}PPO\text{-}PEO)n \rightarrow Au + 4Cl^- + 2H^+ + oxidation\ products \quad (2.8)$$

Following the formation of gold clusters through reduction of $AuCl_4^-$ ions in solution, block copolymers adsorb on the surface of gold clusters, Au_m, due to the amphiphilic character of the PEO-PPO-PEO block copolymers:

$$Au_m + pPEO\text{-}PPO\text{-}PEO \rightarrow Au_m\text{-}(PEO\text{-}PPO\text{-}PEO)_p \quad (2.9)$$
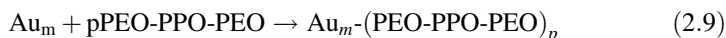
where Au_m-(PEO-PPO-PEO)$_p$ represents a gold cluster with adsorbed block copolymers. The adsorbed block copolymers can form pseudo-crown ether structures that bind with $AuCl_4$-ions, Au_m-(PEO-PPO-PEO)$_l$–$AuCl_4^-$, and facilitate their reduction.

(2) absorption of block copolymers on gold clusters and reduction of metal ions comparison of various PEO-PPO-PEO block copolymers reveal that the overall block copolymer (i.e., both PEO and PPO blocks) contributes to $AuCl_4^-$ reduction and particle formation. The third step is the growth of gold particles and stabilization by block copolymers (refer to Scheme 2.8).

PEO is more dominant than PPO in the initial stages of reduction. PPO facilitates block copolymer adsorption on gold clusters and reduction of $AuCl_4^-$ ions on the surface of these gold clusters and/or particles. The difference in particle formation observed between PEO-PPO-PEO block copolymer systems and PEO homopolymer systems is attributed to the block copolymer adsorption and $AuCl_4^-$ reduction processes on the surface of gold clusters and/or particles (steps 2 and 3) [200].

To improve the stability of polymeric micelles against dilution in the stream, various methods, by chemically cross-linking either in the inner core domain or within the outer shell layer, have been developed [201]. For example, Park et al. have reported on the shell cross-linked pluronic micelles using gold nanoparticles that exhibit a reversibly thermosensitive swelling/shrinking behavior [196]. The study on the evolution and morphology transition of the shell cross-linked micelles is, however, scarce. Xu et al. [202] have demonstrated that the gold nanoparticle-stabilized pluronic micelles spontaneous evolve and reassemble into large "vesicular"-like nanocapsules using glutathione as an effective trigger. It was also demonstrated that the evolved nanocapsules showed obvious temperature responsibility.

The incorporation of copolymers into the gold nanoparticles fabrication process has led to the interesting discovery that both the formation and the stability of colloids are dictated by the chemical structure of macromolecular chains. Environmentally friendly, single-step/single-phase synthesis of core@shell NMNPs can be mediated by polymers that simultaneously play the roles of reductant and stabilizer while imparting unique properties to the resulting hybrid material (Scheme 2.8). To date, the above strategy has been applied successful mainly to pluronics and polyacrylates with amino groups, which have a strong ability to coordinate on metal surfaces [203]. The reduction of Au(III) species is induced by

the poly(propylene oxide) (PPO) segment and nitrogen atoms, respectively. Polymer chains chemisorb onto the newly generated particle, being consequently tethered from the surface into the solvent phase. Despite their simplicity (one-pot, two-reactants, and no workup), this class of reactions still offers a number of possibilities in relation to tweaking the experimental conditions (concentration of reactants, polymer composition and architecture, temperature, and additives) to generate particles with controlled dimensions and properties. A comprehensive understanding of the kinetics and chemical environment around the gold cores is obviously relevant in such an endeavor, and more data in this respect are required to provide a clearer picture of these systems.

Furthermore, copolymers (as capping agents) with stimulus responsibility have attracted growing attention due to their diverse self-assembly behavior in response to stimuli, such as pH, temperature, salt [204]. The stimulus responsibility allows for tailoring the supramolecular aggregates with desirable morphologies and properties from the same precursory copolymers (Scheme 2.9). Poly(*N*-iso-propylacrylamide) (pNIPAM) is a stimulus responsive polymer that undergoes a reversible, inverse phase transition at a lower critical solution temperature (LCST) of about 32 °C in pure water. In addition to temperature, cosolvents can also cause an inverse phase transition in pNIPAM. For example, the addition of 50% methanol by volume to aqueous pNIPAM solutions leads to cononsolvency, effectively lowering the LCST of pNIPAM to below 0 °C. The functionality of pNIPAM on surfaces can be separated into two categories: (1) triggered changes in polymer conformation and (2) triggered changes in polymer surface energetics. Below the LCST, pNIPAM is hydrated and the chains are in an extended conformational state. Above the LCST, pNIPAM is in a hydrophobically collapsed conformational state. Polymer brushes with triggerable phase-transition behavior, such as pNIPAM, can be exploited in devices on the nano- and microscales, with potential applications for protein affinity separations and in micro- and nanofluidics [205].

It was demonstrated the surface-initiated polymerization of stimulus-responsive pNIPAM brushes from monolayers on gold-coated surfaces. By adopting low methanol concentrations during polymerization, the growing pNIPAM chains were maintained in a hydrophilic and an extended conformational state, yielding thick polymer brush layers. In addition, the prototypical fabrication of nanopatterned, surface-confined, stimulus-responsive pNIPAM brushes in a grafting-from approach using a simple strategy that combines nanoshaving, an SPL (scanning probe lithography) method, with surface-initiated polymerization were presented. The reversible, stimulus-responsive conformational height change of these bulk and nanopatterned polymer brushes is consistent with the behavior of surface-confined polymer chains, where chain mobility is restricted largely to one dimension perpendicular to the substrate. The polymerization and patterning approach is generic and can likely be extended to a wide variety of monomers [206].

The nature of precursor species in actual reaction mixture may not be as simple as it appears from molecular formula. For example, Xia and coworkers reported that
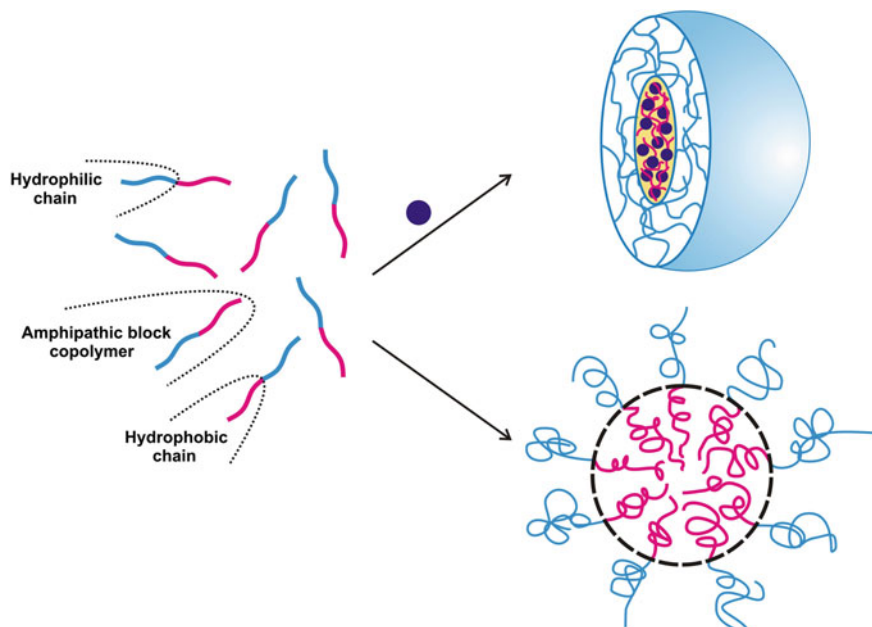
Scheme 2.9 Self-assembly behavior in response to stimuli effect. Via the formation of a nanoparticle proceeds the drug encapsulation [204]

a freshly prepared aqueous solution of $AgNO_3$ contains trimeric $Ag_3{}^+$ or Ag_3 species that acted as nuclei and led to the development of a triangular morphology [207]. The concentration of trimeric clusters of silver decreased as the $AgNO_3$ solution was aged in air under ambient conditions. Icosahedrons and cuboctahedrons were formed by reducing either Ag^+ ions or complexes such as $[Ag_2(NO_3)]^+$ and $[Ag_3(NO_3)_2]^+$ with polyvinylpyrrolidone. Further, the by-product ions, molecules, etc., formed from the precursor during particle-formation reaction can, for example, change the pH, the ionic strength, or can influence the activities of tailor-made additives. The seed-nuclei size can be determined by the strength of the metal–metal bonds and the difference between the redox potentials of the metal precursor and the reducing agent used [208]. Specific chemical reactions, such as the disulfide reduction, have emerged as an alternative stimulus for tuning the self-assembling of copolymers. For example, monodispersed polymeric nanocapsules have spontaneously evolved from reducible hetero-PEG PIC (polyion complex) micelle disulfide bond reduction [209].

In a next report, a simple solid-phase asymmetrical functionalization technique was introduced to construct gold nanoparticles with reactive ligands localized on a small confined surface [210]. This approach highlights that (i) the ligands decorated on a spatially limited surface can be used for further chemistry, and the rest of the ligands can be selected to remain unreactive during the coupling process. (ii) It was applicable to a wide size range of nanoparticles, e.g., the functionalization of gold

nanoparticles with the diameter of 16–41 nm was demonstrated. They used 3-aminopropyltriethoxysilane as the bifunctional ligand to "catch" the gold nanoparticles onto the glass substrate. Owing to the strong interaction between the AuNPs and the amino-silanized glass surface, a second ligand with a thiol functional group was required to replace the amino-binding sites under severe sonication so as to "release" the AuNPs from the substrate. However, the introduction of a second ligand to the AuNPs confines further chemistry to some extent. Additionally, biomolecules, such as DNAs and proteins, may be damaged during the sonication process. Therefore, asymmetric AuNPs decorated with biomolecules was almost impossible to be obtained [211].

Coordination chemistry offers simplicity, stable bonding, and ligand-metal specificity, enabling ligand-bearing components to be assembled into supramolecular structures using appropriate metal ions. This approach is particularly compatible with surface chemistry, as binding of metal ions activates the surface toward ligand binding, and vice versa. The use of different building blocks containing similar ligand functionalities provides a universal, LEGO-type binding scheme, where the same chemistry is used for binding different components into a composite nanostructure. This strategy is attractive for LbL schemes, adding one coordinated layer in each step. Murray and coworkers investigated coordinated nanoparticle films prepared by repetitive adsorption of carboxylate-modified AuNPs and divalent metal ions (Cu^{2+}, Zn^{2+}, Pb^{2+}) [212, 213]. In these systems, several nanoparticle monolayers are deposited in each dip cycle, while the interparticle spacing was shown to be lower than expected for coordinative carboxylate-metal ion binding. Chen and coworkers obtained similar results with pyridine-functionalized AuNPs and Cu^{2+} ions, studied by quartz crystal microbalance measurements [214]. These observations suggest that Cu^{2+}-based coordination systems induce insertion of excess ions to the periphery of the nanoparticles, resulting in poorly controlled growth (Scheme 2.5).

As a promising nanobiomaterial, gold nanoparticles have found a burst of research interest in biological applications, for example, transfection vectors, DNA-binding agents, protein inhibitors, and spectroscopic markers [215, 216]. Among the unique features of gold particles, facile place-exchanging reaction makes them well suited for biomedical applications [30]. As the most abundant thiol species in the cytoplasm and the major reducing agent in biochemical processes, glutathione (GSH, a tripeptide is a peptide consisting of three amino acids joined by peptide bonds, L-glutamine, L-cysteine, and glycine) showed special interest for the manipulation of place-exchanging reaction [217]. The glutathione-mediated selective intracellular release system has been developed on the basis of the fact that the intracellular GSH concentration is substantially higher than extracellular levels [217]. GSH is the most abundant low molecular weight thiol (LMWT) and is widely accepted to be the main cellular redox buffer.

For an effective shape-controlled synthesis, the surface activity of biomolecules at the liquid–solid interface plays a significant role. Molecules which control the overall crystal growth are known as "capping agents," the term frequently used for specific adsorption of surface-active molecules on selective crystal planes of a

particular geometry [218]. In addition to the stabilizing ability of some stabilizing agents, these additives can also be used as a reducing agent. This is case of bovin serum albumin (BSA) [219] for synthesizing NMNPs. Several other proteins and enzymes have shown the reducing ability of gold and silver ions into their respective nanoparticles [220]. If a stabilizing agent also provides reducing ability, then it becomes quite easy to understand the nucleation process and subsequently shape-directing effects as well. A protein macromolecule contains several amino acids such as cysteine, tryptophan, lysine which can act as weak reducing agents. All these amino acids can reduce gold or silver ions independently even at room temperature (Scheme 2.10).

However, when amino acid is present in a macromolecule, the reducing ability is significantly compromised by the steric screening of other nonreducing amino acids in the vicinity. Then, the reducing ability of a particular amino acid is purely related to its location in the native state of protein. As the globular form unfolds, more and more hidden cysteine amino acids come into contact with the aqueous phase whereby they provide a stronger reducing potential to BSA. Hence, unfolding not only facilitates the reduction but also provides required amphiphilic character necessary for the surface activity to produce desired shape-directing effects and is true for almost all globular proteins. Like PbSNPs and SeNPs, the unfolded BSA is also responsible for the synthesis of gold nanoplates with preserved {100} crystal planes of fcc geometry [219]. High temperature (around 70–80 °C) and sufficient acidic environment provide BSA with enhanced reducing as well as shape-directing abilities which are not observed close to the isoelectric point or room temperature.

HSA instead of BSA can be employed as model for exploring how proteins interact with silver nanoparticle since it has been reported before the different binding capabilities of HSA and BSA in spite of their structural similarities [221] by manipulating the biomacromolecule conformation, and/or selectively blocking NH_2 groups the authors have shown that there is a combination of several non-covalent electrostatic interactions involved in such phenomenon, where NH_2 residues play a key role in the observed poststabilization and synthesis of AgNPs. Alarcon et al. [222] have also explored to what extent surface plasmon band (SPB) excitation with 405-nm light-emitting diode (LED) can affect the protein conformation in the AgNP@HSA hybrid. Ketyl radicals formed by the photolysis of photoinitiator (I-2959) acted as reductants of silver salt leading to the formation of

Scheme 2.10 Schematic of the reducing and stabilizing ability of amino acids [220]
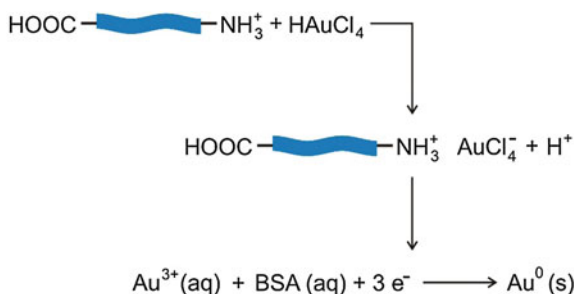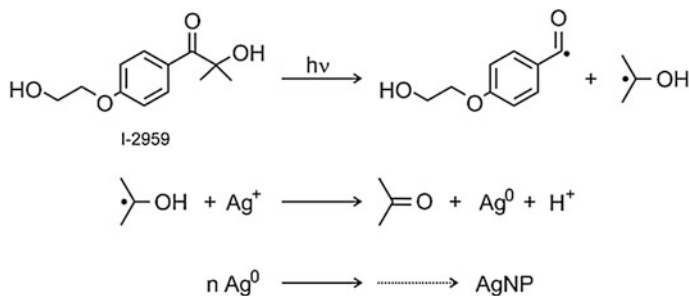
Scheme 2.11 Overall reaction for the formation of silver nanoparticles. Sodium citrate as a stabilizer has been employed [222]

AgNPs. This approach is based on the Norrish Type I photocleavage of carbonyl-type initiator leading to ketyl radicals [223]. Silver cations, Ag^+, scavenge the $(CH_3)_2C^.OH$ radical (ketyl) and reduce Ag^+ to Ag^0 (Scheme 2.11).

The bimodal behavior in the fluorescence of denatured HSA can be explained by the formation of protein corona arrangements [224] that at silver nanoparticle concentrations lower than 0.38 nM leads to a marked emission enhancement as they locate in the plasmon enhancement region. This enhanced emission becomes a smaller fraction of the total emission as the concentration of AgNP increases due to the finite availability of nanoparticle surface. Effectively, the ratio of HSA/AgNP at the maximum enhancement is close to 160,000 molecules per AgNP, while at AgNP concentrations >0.5 nM this will be less than 16,000 molecules per AgNP. These data are fully compatible with the formation of corona arrangement where there is a considerable excess of "free protein" in the aqueous phase. This corona arrangement is obviously different from the one formed for the native protein since no effect on the fluorescence emission was observed for the nonde-natured protein; the changes for denatured HSA, while modest ($\sim 20\%$), are outside error limits and are not observed for the native protein. The most likely explanation is that the formation of an initial shell of the unfolded HSA surrounding the metal surface facilitates the sequential association of more denatured protein.

It was postulated that this protecting effect depends on the number of available NH_2 groups, rather than the macromolecule conformation. These data suggest that electrostatic interactions confer protection to the silver nanoparticle surface [224]. Additionally, it was reported that protein protection against NaCl, and other salts, was not significantly affected by the presence of (≤ 0.5 mM sodium citrate or I-2959. This indicates that these components are not involved in the formation of the corona arrangement. Recognizing that NaCl is not the only substance that can potentially decrease the AgNP stability, we also assessed their stability with different buffers such as phosphate buffer saline (PBS, pH 7.0), glucose supplemented phosphate buffer (Hank's buffer), Dulbecco's minimum media (DMEM) buffer, MES (2-(N-morpholino)ethanesulfonic acid) buffer (pH 7.0), and Tris–HCl buffer (pH 7.0). Results show that even at low protein concentrations, AgNP becomes

stable in all the buffers assessed, with a concomitant PBS redshift of ∼8.0 nm. Remarkably, as the buffer complexity increases, the protein protection efficacy seems to decrease. In particular, the minimum protein concentration needed for conferring protection to AgNP becomes greater as the number of components in the buffer increases (DMEM > Hank's buffer > PBS). The most noteworthy difference within the buffers was found in the 18-h stability experiments for DMEM, where AgNP PBS clearly decreases after only 3 h, probably due to protein oxidation promoted by the components in the medium (amino acids, vitamins, minerals, etc.). Protein protection was also observed for AgNP in Tris–HCl buffer and to a lesser extent if MES buffer is employed [222].

The effectiveness of native HSA as a stabilizer for silver nanoparticles was also demonstrated by the changes in the PBS absorption upon protein addition. The redshift of PBS in the presence of HSA is a clear indication of dielectric constant changes at the nanoparticle surface. Further, AgNPs are unstable in the presence of chloride ions. Surprisingly, it was found that even relatively low concentrations of HSA can protect AgNP@citrate from different salts/ions such as NaCl or common buffers. Nevertheless, long-term stability for AgNP conferred by HSA is apparently controlled by the medium complexity where an increase in the number of components in the buffer causes the particles to be less stable. Silver nanoparticles can be readily prepared in aqueous solutions under mild conditions using a photo-chemical method with HSA as protecting agent. The protein is more than just a mere protecting agent, since it could also complex Ag^+ ions and affect the ratio of Ag^+ between the aqueous solution and the macromolecule structure as HSA shows a remarkable affinity for silver ions. Long-term stability experiments have shown that amine-blocked HSA is far less stable than when using native HSA or even the protein alone. The hydrodynamic size measurements for the nanoparticles showed that the nanocomposite size is highly modified when the NH_2 groups in HSA are blocked. It is also of note that when NH_2-blocked HSA is employed as a stabilizer, in the presence of other AgNP shapes (primarily cubes and plates) and sizes (5–15 nm), these are different from those obtained using native HSA.

Ganeshkumar et al. have exploited the reducing, stabilizing, and biocompatible nature of a biopolymer, pullulan (Pl), for the synthesis of gold nanoparticles (PlAuNPs or Au@PlNPs, pullulan-covered gold nanoparticle core) [225]. PlAuNPs allowed the attachment of a large number of small molecules. AuNPs were formed during microwaving only. The λ_{max} of PlAuNPs remained at 525 nm before and after autoclaving indicating that PlAuNPs were stable even after autoclaving. The stability of PlAuNPs at various temperatures was checked and found to be stable at all the temperatures, which was also confirmed by visible spectroscopy by taking SPR. The peak appeared at 525 nm confirmed the formation of gold nanoparticles. The zeta potential of PlAuNPs, AuNP@5-Fu (5-Fluorouracil, and 5-Fu) was measured by dynamic light scattering method, showed ∼−27.6 mV, respectively. PCS method was used to confirm the mean particle size of PlAuNPs and it was observed to be ∼71 nm. PCS measurements yield a significantly larger average gold nanoparticles diameter (∼71 nm) than the TEM analysis (∼20 nm); TEM visualizes the dried gold nanoparticles core of the particles, whereas PCS measures

their hydrodynamic diameter in liquid medium, which can be enhanced by hydrophilic pullulan coated on the gold nanoparticles surface.

Chitosan (CHI) acts as a soft template for the formation of multibranched magnetic nanoparticles, and gold coating process was carried out in the presence of chitosan to give better particle dispersity and to avoid agglomeration problems (Chart 2.1). Chitosan is a linear polysaccharide consisting of β-(1 → 4)-linked 2-amino-2- deoxy-D-glucose residues, originating from deacetylated derivative of chitin, which is the second most abundant polysaccharide in nature after cellulose. It was nontoxic, biodegradable, biofunctional, and biocompatible. In addition, the main advantage of chitosan matrix is to act as stabilizing agent in the formation of nanoparticles due the presence of hydroxyl and primary amino groups. The stabilizing agent used in chitosan and the addition of gold chloride salt solution to a mixture of water lead to the formation of a complex containing both chitosan primary amino group and gold (III) which appeared as an orange color solution. At room temperature, chitosan-based reduction kinetics is low, and Au^{3+} ions were complexed on the surface of chitosan; after the addition of ascorbic acid to this solution, the dark orange color of solution is turned to the clear solution due to the reduction of Au^{3+} into Au^+ ions in chitosan matrix [131].

In the presence of chitosan, the sequential addition of ascorbic acid, $HAuCl_4$, and seed as $Fe_3O_4@Au$ gave the anisotropic-shaped nanostructure. Indeed, it was reported that the role of Ag^+ is to assist the anisotropic growth of gold branches on certain crystallographic facets (Scheme 2.12) [226]. The directed surface growth and the particle dimension are also related to the presence of silver ions in the
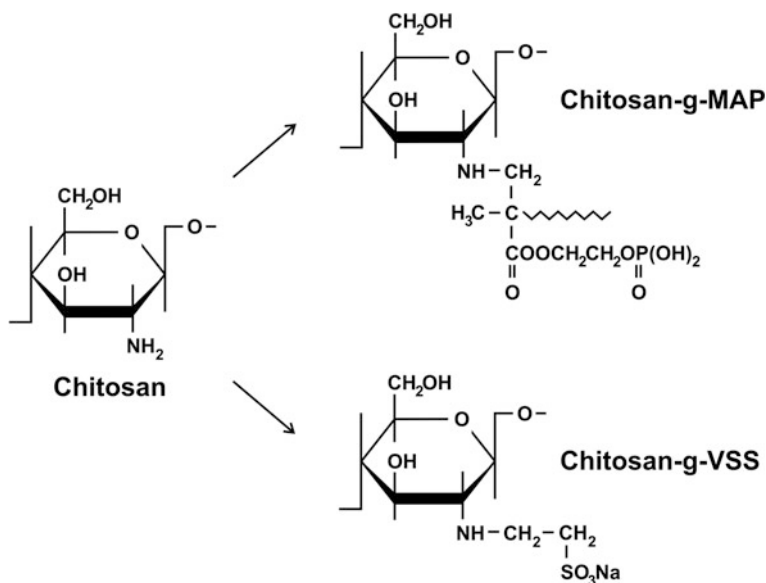
Chart 2.1 Chitosan-type templates

growth solutions. The presence of Ag^+ is necessary for branched nanocrystal formation. In the absence of silver ion in growth solution, the observed extinction spectrum is characterized by a plasmon resonance band around 550 nm of gold layer since in other study, the wide plasmon resonance band of gold layer is located at approximately 800 nm. This redshift is due to the increase of surface area of the magnetic nanoparticles. Plasmonic metallic nanoparticles are characterized by the presence of localized surface plasmon resonance, and this plasmon field is generated on the surface of the nanoparticles, which enhances both absorption and scattering. For nanoparticles of similar shapes, a redshift of the LSPR peak is observed as the nanoparticle size is increased [227].

Additives such as surfactants (e.g., CTAB, sodium dodecyl sulfate) [167, 228], polymers (e.g., PVP, PVPo, PVA, …) [229], foreign ions (e.g., Ag^+, Cu^{2+}, Cl^-, Br^-, I^-) [230, 231], ligands (e.g., inorganic ions, thiols, amines …) [232], and impurities [230] present in the reaction medium have been already partly discussed to play important roles in controlling the morphology of particles produced. Surfactants, ligands, or polymers were commonly added as stabilizers to impart stability to nanoparticles against aggregation, since colloidal particles tend to aggregate to decrease the overall surface area and energy. Later these species were used during synthesis as growth-arresting agents to control the particle size, morphology, and surface properties. That is why nowadays a general term, capping agent, is used to refer them. Through their interactions with particle surfaces, capping agents can inhibit the incorporation rate of growth units onto the particle surfaces, change the surface free energies of different facets, and, thereby, change relative growth rates of the facets [233].
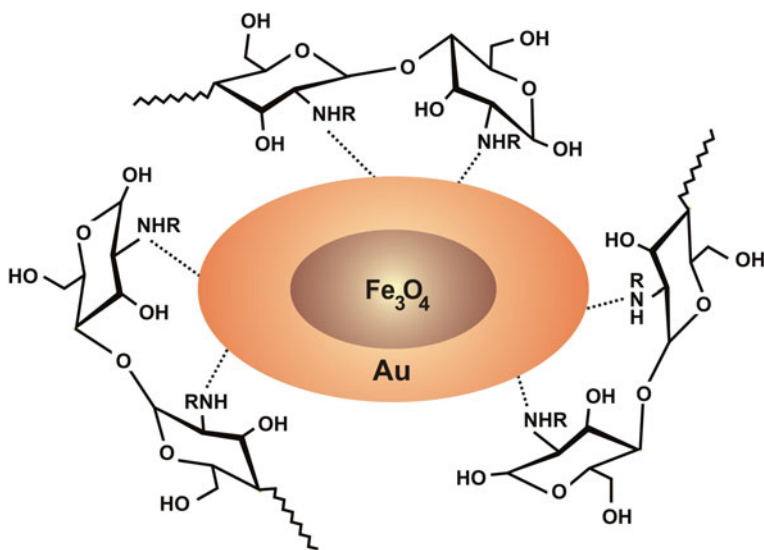
Scheme 2.12 {Fe$_3$O$_4$@Au}@CHI the anisotropic-shaped nanostructure [226]

Nanocrystal growth is a complicated process, and it is the combination of many ingredients that leads to the final shape. CTAB is known as the most suitable reagent to control the formation of AuNPs [234]. It was found that the type of surfactant was critical for the formation of highly anisotropic particles. While triangular nanoprisms could be generated with cetyltrimethylammonium chloride (CTAC), for example, the yield of nanoprisms was lower and the size distribution was broader with CTAC (Scheme 2.13; Fig. 2.5). The use of benzyldimethylhexadecylammonium chloride (BDAC) was particularly important for the formation of nanowires; nanowires were rarely observed in CTAC samples. When BDAC was replaced with CTAB, a mixture of different shapes (spheres, rods, etc.) was formed instead of triangles or wires presumably due to bromide ions interfering with silver underpotential deposition (UPD). Therefore, it is the combination of two unusual ingredients, silver seeds and BDAC, that is responsible for the formation of highly anisotropic nanoparticles reported here. Compared to CTAC and CTAB, which have been commonly used in seed-mediated growth method, BDAC has a greater tendency to crystallize due to the aromatic head group. Therefore, they can act as a more rigid organic template and promote the anisotropic growth of nanoparticles by slowing down the growth of (111) facets. Other factors such as reduction potential of surfactant-metal complexes and the affinity of aromatic groups to metal can also impact the growth of nanoparticles [235].
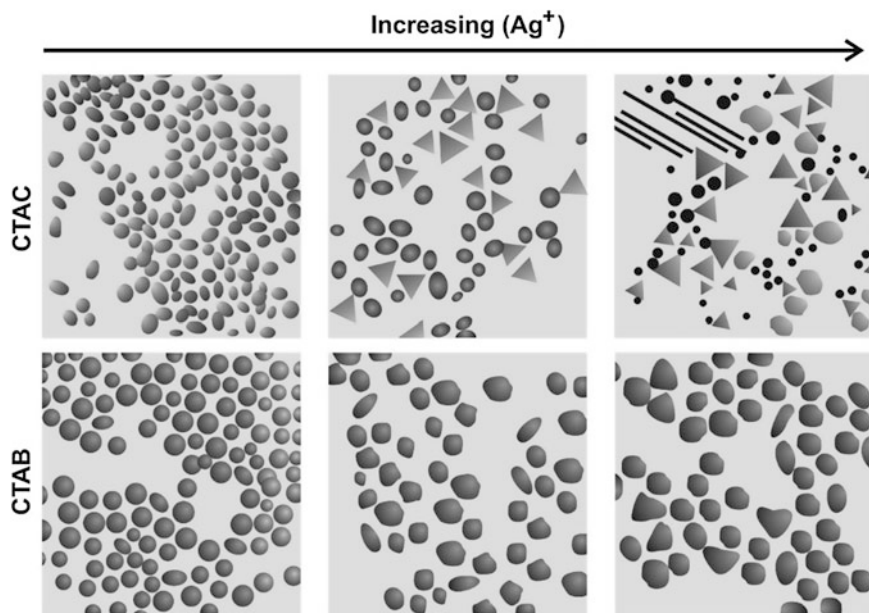
Scheme 2.13 TEM-like images for CTAC and CTAB—variations of particle size and shape with increasing silver salt concentration [234]
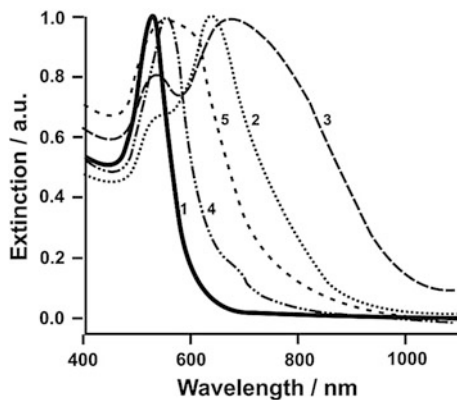
Fig. 2.5 Variations of extinction spectra (CTAC lines *2* and *3*, CTAB lines *4* and *5*, the black full line (*1*) is for both systems with the initial silver salt concentration) of nanoparticles synthesized using different surfactants (CTAB and CTAC) with increasing silver salt concentration. BDAC-stabilized silver seeds were used for all syntheses [235]

Fig. 2.6 Extinction spectra showing the growth process for Ag seed particles (*1*, *2*, and *3*) and Au seed particles (*4*, *5*, and *6*) (*Left panel*). Plot of time-dependent maximum extinction change for the two syntheses shown in (AgNPs) and (AuNPs) (*Right panel*) [235]
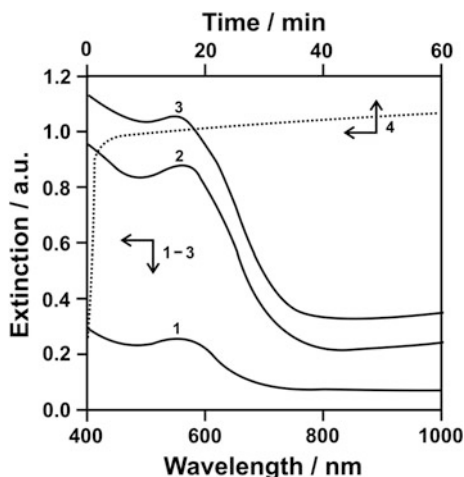
The fast growth kinetics with silver seeds was further verified by the sudden initial jump of the extinction in the UV–Vis spectra (Fig. 2.6, curve 4).

Gold nanorods have been extensively investigated as support, due to their well-established synthesis routes, tunable surface plasmon resonance property, and super catalytical activity. To obtain the dispersed platinum nanostructures, one of the effective routes is to chemically fabricate Pt on preformed nanostructured (nanorods (NRs)) surfaces, to form a core@shell structure. The Au@Pt nanostructure has been synthesized by using gold nanorods as support [236], which can catalyze the oxidation of some organic molecules. The CTAB was also involved in

the synthesis of the core@shell nanostructures in which platinum nanodots (PtNDs) appeared on the surface of seed AuNPs [237]. PtNDs were formed by the reduction of Pt salt (H_2PtCl_6) by ascorbic acid (AA). On the one hand, the CTAB covered the special lattice plane of the AuNRs though a moderate combination of bromide ion with metal; the long hydrocarbon chains of the absorbed CTAB formed a very stable bilayer on the AuNRs, which acted as the directing agents for growing PtNDs on AuNRs (Scheme 2.14). On the other hand, the interaction between the CTAB and Pt surface was significantly weaker, which offered a possibility to control the morphology and preserve the catalytic activity of the PtNDs [238] via a similar approach without using the AuNRs.

Ionic liquids (ILs) are a viable option as stabilizing agents because of their ionic character and can be easily made task-specific as phase-transfer catalysts due to their tunable nature. However, ILs are generally used as temporary stabilizing agents. They are used to halt aggregation of Au(0) produced in the reduction of $HAuCl_4$, thus limiting the size of the gold aggregates that form nanoparticles [239]. Several studies have reported the synthesis of transition metal nanoparticles using ILs as the media and stabilizers [240]. The earliest mention in the literature of an IL with a nitrogen cation used as the capping agent for AuNPs was an imidazolium-based cation IL reported by Itoh et al. [241]. Several other imidazolium ILs followed, however, these ILs contained sulfur functional groups which provided permanent covalent stabilization of the gold; these were effectively task-specific ILs that combined the phase-transfer catalyst and permanent stabilizer into one molecule by functionalizing the IL with an aurophilic capping agent (sulfur) [242].

Room-temperature ionic liquids are attracting much interest in many fields of chemistry and industry, due to their potential as a "green" recyclable alternative to the traditional organic solvents. They are nonvolatile and provide an ultimately polar environment for chemical synthesis. Some ionic liquids are immiscible with water and organic solvents, giving biphasic ionic liquid systems, which enables easy extraction of products from the ionic liquid. The miscibility with organic solvents or water is mostly dependent on the appropriate anions.

The ionic liquids based on the imidazolium cation are broadly used for the synthesis of gold nanoparticles [243]. Hydrophilic and hydrophobic properties will
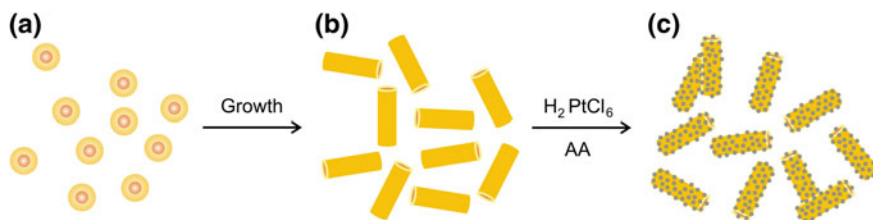
Scheme 2.14 Illustration of preparation processes of AuNR@PtNDs structures, AuNPs (**a**), AuNRs (**b**) and AuNR@PtNDs-HD (**c**) [237]

be tuned by anion exchange of the ionic liquid moiety. The use of the aggregation-induced color changes the gold nanoparticles in aqueous solutions as an optical sensor for anions via anion exchange of the ionic liquid moiety. Among various known ionic liquids, ionic liquids containing imidazolium cation and PF_6^- have a particularly useful set of properties, being virtually insoluble in water. Such biphasic ionic liquid systems have been used to enable simple extraction of products. The transfer of the gold nanoparticles across a phase boundary (water to ionic liquid) via the anion exchange of the ionic liquid by addition of HPF_6 to an aqueous solution of the 1-modified gold nanoparticles was investigated. When HPF_6 was added to the aqueous solution containing the 1-modified gold nanoparticles with stirring, the ionic liquid phase (1-methyl-3-hexylimidazolium hexafluorophosphate) quickly became colored, drawing from the original deep red color of the aqueous nanoparticle solution. The complete phase transfer of the gold nanoparticles was achieved. Before addition of HPF_6, the surface plasmon absorbance of the gold nanoparticles was observed around 526 nm. In contrast, the absorption disappeared completely after addition of HPF_6. The transferred nanoparticles displayed no signs of degradation or aggregation. Herein, HPF_6 acts as an efficient phase-transfer agent for the 1-modified gold nanoparticles and allows their solubilization in the ionic liquid phase through the solubility change by the anion exchange from Cl^- to PF_6^- [241].

A one-pot green process is based on the reduction of gold salts in the presence of surfactant, organic polymer and IL, etc. [244], which regulate the shape and size of nanomaterials and avoid their aggregation or precipitation. For instance, Li et al. used microwave to heat $HAuCl_4$ in IL (1-butyl-3-methylimidazolium tetrafluoroborate, [BMIM][BF$_4$]) to prepare gold nanosheet [245], and IL was thought to act as the structure-directing agent. Zhu et al. [246] prepared anisotropic gold nanoparticles by photochemical reduction of $HAuCl_4$ in [BMIM][BF$_4$] and pointed out that IL was the critical factor for the formation of anisotropic shape. Tsuda et al. fabricated anisotropic gold nanoparticles in bis(trifluoromethanesulfonyl)amide anion-based IL using accelerated electron beam irradiation and γ-ray [247]. These methods are free of additional capping agents, but the reaction conditions are relatively severe. Later, Yang et al. prepared gold networks@IL ([BMIM][BF$_4$]) by directly reducing $HAuCl_4$ with sodium citrate in [BMIM][BF$_4$] aqueous solution [248]. Similar technologies such as photochemical reduction [249], atmospheric plasma [250], and laser irradiation [251] were also utilized to prepare AuNPs using chitosan as the structure-directing agent. In these cases, CHIT was proved to act as a template agent for the formation of anisotropic shape. However, the density of AuNPs obtained was low [249, 250] comparing with physical reduction, the chemical method was easy to achieve under simple conditions. For instance, Carlo et al. used organic acids to reduce $HAuCl_4$ in CHIT aqueous solution, and the obtained solution was coated on electrode surface to form CHIT–AuNP hybrid film [252]. However, the layout of AuNP on electrode surface is agglomerate.

Yang et al. [253] have utilized IL and chitosan to regulate the formation of anisotropic gold nanoparticle and the shape of hybrid films. As can be seen, the graphene oxide (GO)-modified glassy carbon electrode (GCE) exhibits wrinkled structure. When the reaction is carried out in CHIT solution, the obtained film is stacked on GO/GCE. When both IL and CHIT are present, the obtained hybrid film is similar to that without IL. But with the concentration of IL, increasing the hybrid film tends to roll out. The result indicates that the concentration of IL can influence the morphology of hybrid film. IL acts as a capping agent that is selectively adsorbed on a specific crystal surface of AuNP. At the same time, CHIT, with a large number of amino and hydroxyl groups, enables the simultaneous synthesis and surface modification of AuNP in one pot. Importantly, when the hybrid film is dried on GO/GCE, the CHIT is easy to dry and shrink to form agglomerated and stacked shape. On the contrary, IL is difficult to dry and it can prevent the shrink of CHIT. Therefore, the morphology of hybrid film should be related to the interaction of AuNP, IL, and CHIT. The preparation method can overcome the agglomeration of the dropping mixture and produce three-dimensional and mountain-like shape. Thus, the hybrid film shows larger surface area than the agglomerated and the smooth one.

When the hybrid film is prepared with low concentration of $HAuCl_4$, the diameters of AuNPs are about 50–70 nm and AuNPs are sparse. When the concentration of $HAuCl_4$ increases (i.e., 3 mmol dm^{-3}), the diameters of AuNPs become smaller (about 40–50 nm), the density of AuNP become higher. When the concentration of $HAuCl_4$ is 4 mmol dm^{-3}, the diameters of AuNPs are about 5–30 nm, the density of AuNP is high, and the layout of AuNP is compact. Comparing with other hybrid film reported [254], the small and dense AuNP-decorated hybrid film is easy to be obtained. The AuNPs are spherical and their diameters are about 30 nm when the reaction is completed in water. When the reaction is performed in CHIT aqueous solution, anisotropic AuNPs are obtained, and the diameters are 30–50 nm, indicating that CHIT is a critical factor to make AuNP to form an anisotropic structure. When the reaction is performed in CHIT–IL aqueous solution, the diameters of major nanoparticles are 5–30 nm, which means that IL plays an important role to control the diameter of AuNP [253].

Furthermore, it has been observed that foreign ions (metal, halides, etc.) play important roles in the morphology control of the NMNPs [230, 255]. They generally adsorb on a certain set of facets of the growing particle more strongly than others. Such preferential adsorption affects the growth rate of a particle in an anisotropic fashion or may influence the formation of defect structure of the seeds, resulting in the modification of the final crystal shape [255]. However, the actual roles of most of these additives or impurities in morphology control are neither clearly understood nor always recognized. For instance, two schools of thought (viz., soft template and preferential-surface adsorption) exist regarding the roles of surfactant (or their mixtures) in the silver- and gold-nanorod formations [218, 256]. It is worth pointing out here that the impurities present in many chemical reagents can play a vital role in controlling the shape of the nanoparticles. For example, Smith and Korgel recently reported that the yield of gold nanorods varied strongly

depending on the different batches of CTAB obtained from different manufacturers [257]. Millstone et al. also reported a similar observation [230]. They claimed that CTAB, depending upon the supplier, has an iodide contaminant, which acts as a key shape-directing element. One should be careful about the changing behavior of the additives under different reaction conditions (e.g., temperature) [258]. For example, Miyazaki and Nakano reported that the temperature-dependent conformation change of poly(N-isopropylacrylamide) affected the shape of platinum nanoparticles formed upon the reduction of K_2PtCl_4 by hydrogen [259]. Nature of solvent may also be important in the control of nanoparticle morphology. Later, Gao et al. found that in the presence of the same capping agent, PVPo, the formation of gold crystals with {111} facets was more favorable, which changed to the {100}-type in ethylene glycol [260].

Since the very first SERS investigations in silver hydrosols, a lot of interest arose about the influence of the addition of halide anions on SERS spectra. For most of the adsorbed molecules, an increase of 2 or 3 orders of magnitude of the SERS signal is observed upon addition of the halide anions to silver colloids. It is necessary, however, that halide anions are specifically adsorbed on silver particles and this generally occurs for chloride, bromide, and iodide anions. Later, this "activation" effect has been thoroughly investigated, because single-molecule SERS signals have been only detected in the case of activated silver colloids. Several explanations of the SERS activation due to the addition of halide anions were proposed, essentially based on the formation of Ag^+–halide-ligand surface complexes with a large charge transfer between adsorbate and metal or on the increase of the local electromagnetic field by aggregation of metal colloidal particles. Moreover, it is of note that both the adsorption mechanism and the surface coverage of an organic ligand are strongly affected by the addition of halide anions. This could explain why the SERS spectra of some adsorbates are markedly enhanced by the addition of halide anions [261], whereas others are negatively affected by it [262]. The silver colloid activation is still a controversial point. Aggregation of the silver and gold nanoparticles upon addition of halide anions has been observed by microscopic and UV-Vis absorption measurements. However, no significant increase in the SERS enhancement of 1,2,3-triazole (hereafter TZ3) has been detected in both silver and gold hydrosols by addition of chloride or bromide anions, as, instead, expected on the basis of the electromagnetic mechanism after colloidal aggregation [263]. In the case of gold hydrosols at their usual pH (6), no difference is observed between the SERS spectra with or without halide addition. In the case of silver and basified gold colloids, instead, the presence of coadsorbed halide anions induces the adsorption of TZ3 as neutral molecule through one nitrogen atom. The occurrence of several bands in the SERS spectra of TZ3 adsorbed on Ag/halide or Au/halide colloids is due to the adsorption of both tautomers of TZ3, as deduced by the spectral and computational results [264].

Ethanol as well as water was suggested to act as very weak reducer agents [87]. Thus, tetrachloroauric acid was mildly stirred in ethanol at 35 °C for a couple of days, but no changes in the color were observed. However, as the temperature was increased to 68 °C the color changed immediately from yellow pale to pink,

indicating that the gold salt was completely reduced and the atoms nucleated forming small gold nanoparticles. Therefore, considering that the synthesis was carried out at temperature lower than 45 °C, the ethanol can also be discarded as reductant at the working temperature. In a similar experiment, $HAuCl_4$ was mildly stirred in water at 35 °C for one day. Unlike what happens with ethanol, smooth changes in color were observed after one day, indicating that water is a weak reductant at the working temperature.

Most of the methods used to produce gold nanoparticles involve the reduction of Au(III) using strong reducing agents such as $NaBH_4$ which generates gold nanoparticles very rapidly [110, 265]. The introduction of strong capping agents during nanoparticle synthesis has the effect of stopping the growth of the NPs whereas weakly associated ligands allow for continued growth [266]. As a result, the presence of the capping agent whether strongly or weakly binding is essential during the nanoparticle synthesis in order to control the nanoparticle size and shape and to prevent aggregation. However, use of strong capping agents makes further surface modification with alternative ligands challenging [267]. In addition, the sizes of the nanoparticles produced using strong capping agents, e.g., alkylthiols, vary from batch to batch [268]. In order to synthesize AuNPs without the use of strong capping agents, the synthetic method requires a reducing agent to generate nanoparticles at a slow rate with the resulting particles stabilized by coordinating ions or ligands which are already present in the reaction mixture from the gold salt precursor.

Ligand exchange reactions have proven a particularly powerful approach to incorporate functionality in the ligand shell of thiol-stabilized nanoparticles and are widely used to produce organic- and water-soluble nanoparticles with various core sizes and functional groups. However, this approach continues to be limited by a number of challenges, including difficulties incorporating charged ligands into the ligand shell, controlling the core size independent of the ligand used, and driving complete replacement of the original ligand shell. Direct synthesis approaches have also been employed to prepare functionalized nanoparticles but most of these methods suffer from the incompatibility of functionalized ligands with the reaction conditions and show a strong dependence of the core size on the stabilizing ligand used during synthesis [269]. This novel approach has been developed for the preparation of diverse libraries of ligand-stabilized metal nanoparticles that address the challenges stated above. It consists of a straightforward two-step procedure, involving (i) preparation of well-defined phosphine-stabilized precursor particles (d_{CORE}) and (ii) functionalization of these particles through ligand exchange reactions with functionalized thiols. The small set of thiols previously used in this approach suggested that the method might be extended to provide general, convenient access to functionalized, thiol-stabilized gold nanoparticles with a controlled core size. The studies mainly explore the dynamics of ligand exchange reactions between thiol-stabilized gold nanoparticles and other thiols [270]. The results demonstrated that different thiol molecules have different reactivity for bonding with gold in the formation of the nanoparticles. Possible causes for the reactivity difference include (1) difference in the electron density of sulfur atom (–

S–) and (2) presence or absence of a metal chelation effect. The electron-withdrawing carbonyl group (–C=O) in tiopronin (for example) makes its sulfur atom less electron dense compared with the sulfur in EG$_3$-SH. According to the nanoparticle formation mechanism proposed by Shiffrin et al. [18], as shown in Eqs. 2.10 and 2.11, the more electron-rich thiol group (HS–) in EG$_3$-SH reacts faster with AuCl$_4^-$ in the polymer formation step. After the polymer was reduced by BH$_4^-$, the nanoparticle surface is bound more favorably to EG$_3$-SH. In addition, the tiopronin molecule has an acid group (–COOH) that could chelate to Au^{3+} metal salt to prevent the formation of Au(I)–S–R, resulting in low reactivity [271]:

$$AuCl_4{}^- + HSR \rightarrow (-Au^I SR-)n (\text{Polymer}) \tag{2.10}$$

$$\left(- Au^I SR-\right)_n + BH^- \rightarrow Au_p(SR)_q \tag{2.11}$$
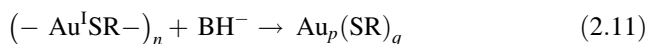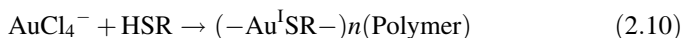
Graphene oxide (GO), a derivative of graphene, is obtained through the intense oxidation of natural graphite [272]. Since GO sheets have large surface areas and the edges are covered with epoxy, hydroxyl, and carboxyl groups, GO has many potential applications, such as adsorption [273], the separation of pollutants [274], and catalytic supports for chemical reactions [275, 276]. Its structure also endows GO with the ability to be functionalized. GO is viewed as an amphiphile with a largely hydrophobic basal plane and hydrophilic edges, which make it behave like a colloidal surfactant [277]. GO has been used as a functional surfactant in a Pickering emulsion polymerization to fabricate a poly(methyl methacrylate)/GO composite [278]. The method is a soap-free environmentally benign process that produces high-quality polymer graphene composites. The GO sheets are both hydrophilic and hydrophobic due to the basal planes of the carbon networks and oxygen-containing functional groups on those planes. With the amphipathicity, GO sheets act like a functional surfactant and can participate in Pickering emulsions as the stabilizer [279]. Similarly, Pickering emulsion can be also stabilized by AuNP/GO [280].

To obtain metal nanoparticle composites through the efficient, convenient, and easy way, Liu et al. have developed a one-step approach based on the interfacial thiol−ene photopolymerization, in which microcapsules (MCs) and metal nanoparticles are generated simultaneously by irradiation of ultraviolet (UV) light [281]. The in situ photoreduction of metal ions can minimize the number of processing steps in fabrication of metal nanoparticles [282]. Using thiol groups containing POSS (PTPS) as a reactive surfactant, Li et al. recently fabricated the uniform-sized microcapsules through the one-step toluene/water interfacial thiol−ene photopolymerization [283]. This emulsion-based approach is very appealing for the large-scale fabrication of microcapsules. Through adding a metal precursor into the water phase, this approach can be successfully modified to prepare MC@NMNPs. In the presence of amphiphilic polyhedral oligomeric silsesquioxane (POSS) containing thiol groups (PTPS) as a reactive surfactant and trimethylol-propane triacrylate (TMPTA) as a cross-linker, the oil phase of toluene dissolved with a photoinitiator was emulsified into a water phase containing a metal precursor to form an oil-in-water (o/w) emulsion. Upon irradiation of ultraviolet (UV) light,

the thiol−ene photopolymerization and photoreduction at the interface of toluene/water lead to the formation of the cross-linked wall and metal nanoparticles, respectively. A series of gold, silver, and platinum nanoparticle-decorated micro-capsules (MC@AuNPs, MC@AgNPs, and MC@PtNPs) were prepared through this one-step interfacial thiol−ene photopolymerization.

Montmorillonite (MMT) is a multilayered material consisting of many parallel arrays of broken plates [284], and the nanomaterials exhibited similar morphologies upon silver functionalization [Scheme 2.15 and Chap. 5 (Scheme 5.2)]. With increased $AgNO_3$ ratio on MMT, the surface becomes shiny due to the presence of AgNPs and homogeneous fraction surface was detected during the synthetic processes; $AgNO_3$ is intercalated into the gallery regions of montmorillonite/polymer and formed hybrid framework. It can also be seen that the AgNPs@MMT and/or MMT@AgNPs nanocomposites exhibited card-like and ball-like homogeneous
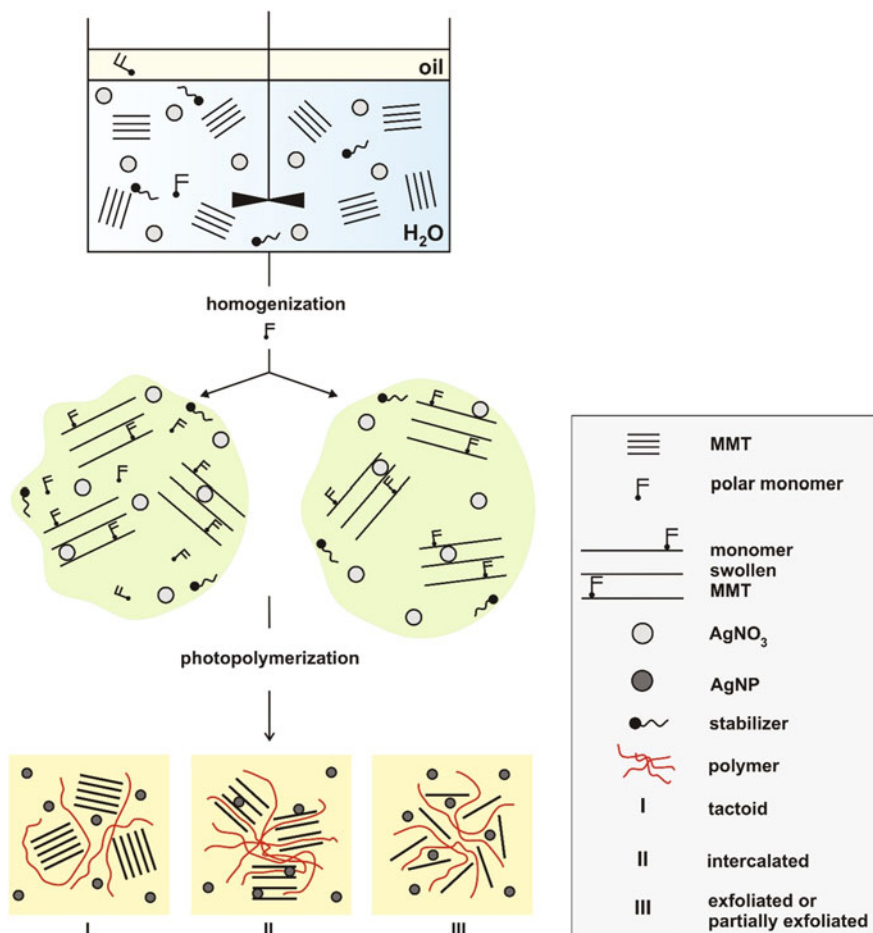
Scheme 2.15 The mechanistic routes of clay (montmorillonite, MMT) polymer—nanocomposites formation in the thermally- and photoinduced reduction of silver salts

surface fractions and form one-phase morphology. The HRTEM images revealed that the AgNPs are well dispersed on both MMT surface and pores, and the dark region is increased with increasing silver content, which is in good agreement with XRD analysis [179].

Typical XRD peaks for all samples of trioctahedral subgroup of 2:1 phyllosilicates are observed, which are ascribed to (110), (020), (004), (130), (200), (330), and (060) diffractions. The results indicate that the crystalline structure of the clay sheets had not been destroyed after preparation processes, with observed low intensities peak closely matching those of pure silver (reflections at 38.36°, 44.49°, 64.81°, 77.71°, and 81.81°). The silver-peak (111) is indicating that the silver grains were oriented along the [111] direction, where (111) plane corresponds to the cubic system in the thin films' growth [285]. Despite the intensities of reflections corresponding to the planes in different samples are low, the 5% AgNP@MMT sample shows more reflection intensity indicates more crystallites corresponding to the (111) plane of cubic Ag ($a = 0.4132$ nm). Indeed, the reflection peaks of AgNPs have low intensities owing to their high dispersion on the inner surface of MMT, which is consistent with other report [286]. The crystal grain size was estimated from the full width at half maximum of the Ag (111) peak using the Scherrer equation. The crystallite size for 1, 3, and 5% Ag in AgNP@MMT nanocomposite samples is found to be in the range of ~ 7.4, ~ 10.7, and ~ 19 nm, respectively.

MMT is porous material and according to [286], the low intensity of some metal in the porous structure resulted from high diffusion of this metal inside pores. The degree AgNPs dispersion on MMT surface is a function of color intensity and its homogeneity. However, more congregating of the silver nanoparticles is inhibited due to the paraformaldehyde (polyoxymethylene) molecule escaping on the surfaces of the silver particles, then forming a steric hindrance to prevent them from aggregation [287]. Compared to AgNPs [288], MMT@AgNPs exhibit a redshifted peak at 421, 433, and 442 nm for 1, 3, and 5 MMT@AgNPs nanocomposites, respectively. This redshift in the absorption spectra reflects a decrease band gap of the semiconductor, which arises from the size quantization effect, and may be caused by the MMT shell [289]. It was reported that the absorption bands correspond to silver nanoparticles smaller than 15 nm were detected at around 404–415 nm [290]. The symmetric absorption peaks indicate surface plasmon resonance of uniform spherical silver nanoparticles [291]. This implies that when the concentration of silver ions was increased, the size increased. This could be due to different nucleation mechanisms operating at lower and higher Ag^+ concentrations attached to MMT at constant ratio of stabilizing agent.

The corresponding findings for traditionally studied ensembles of palladium nanoparticles includes lowering of the critical temperature for separation of the α- and β-phases with decreasing particle size [292], narrowing of the two-phase region [293], decreasing absorption–desorption hysteresis, increasing slope of the plateau of the corresponding loop [294], and apparent compensation for the influence of surface tension by absorption at subsurface sites [295]. The influence of the particle size/shape distribution on these findings is, however, not fully clear [296]. Other frequent complicating factors are different types of surfactants, polymeric

stabilizers, or strong interactions with the support/host matrix that may affect lattice strain and its relaxation during hydrogenation [297].

With the development of nanoplasmonic sensing, it recently became possible to advance from studies of confinement effects in Pd thin films and arrays/ensembles of Pd nanoparticles to the investigation of hydrogen sorption at the single-nanoparticle level, eliminating ensemble-averaging artifacts [140]. However, these initial single-particle studies did not provide deeper insight into the corresponding physics. The first detailed single-particle experiments were performed by Baldi et al. with individual Pd nanocubes at low pressure and temperature by means of electron energy loss spectroscopy [298]. Instead of a slope in the plateau region observed earlier at the ensemble level for Pd nanocubes by Bardhan et al. [299], they found a sharp phase transition and a size-dependent absorption plateau pressure (the thermodynamics was not quantified). This was explained by a model assuming phase coherence and tensile strain in the particle core, induced by a thin 1-nm subsurface hydride layer, which mediates the phase transition [298]. In contrast, the treatment by Bardhan et al. invoked a thermal-fluctuation-mediated phase transition to explain the observed size-dependent thermodynamic parameters [299].

Syrenova et al. have applied noninvasive single-particle plasmonic nanospectroscopy for the comprehensive experimental assessment of both hydrogenation thermodynamics and hysteresis in individual, surfactant-free, palladium nanocrystals over an unprecedented size (from 17 nm to over 100 nm) and shape range (single-crystalline nanocubes, nano-octahedra, and twinned nanorods) [300]. They rely on wet-chemically synthesized Pd–Au heterodimers, created by electrostatic self-assembly of plasmonic gold nanoantennas and shape-selected Pd nanocrystals we have introduced earlier [301]. Hydrogen sorption is tracked by measuring the spectral shifts of the plasmonic scattering peak of individual dimers, which is proportional to the hydrogen concentration in a Pd particle [302] as here also confirmed specifically by finite-difference time-domain (FDTD) simulations for the three investigated Pd nanoparticle shapes. Plasmonic nanospectroscopy is effective for probing individual functional nanoparticles in situ and in eliminating ensemble averaging to unearth single-particle-specific effects. Here, the authors have employed this approach to investigate in detail the thermodynamics of the hydride formation, and to analyze the hysteresis in the metal-to-hydride phase transition in individual Pd nanocrystals with different sizes and shapes. It was found that hydride formation enthalpy and entropy in the considered size range are nearly independent of particle size or shape. This result is in agreement with the general understanding that particle sizes below 10 nm are required to significantly reduce ΔH [303]. They also observed a sharp hydride phase transition with flat plateaux and with hysteresis (much) wider than for single- and polycrystalline bulk Pd, thin-film, and polycrystalline nanoparticle systems. Moreover, they reported an asymmetric size dependence of the hysteresis through decreasing absorption plateau pressures for decreasing particle size (in agreement with Baldi et al. [298]). At the same time, they found that desorption plateau pressures are constant for all investigated particle sizes and shapes, and in excellent agreement with bulk Pd data. These findings were

explained within the established picture of a first-order phase transition, and the energetic interplay between dislocation formation and coherency strain at the metal–hydride interface during hydride formation. Finally, direct comparison between ensemble and single-particle measurements clearly reveals for the first time that the typical slope on equilibrium plateaus observed for nanoparticle ensembles is not only due to inhomogeneous particle size (as commonly put forward), but also a direct consequences of the specific defect structure of the individual particles—that is, the availability of dislocations to accommodate lattice strain. The latter becomes clear from the fact that nanocrystals with nominally identical size can exhibit hysteresis with widely varying width.

2.2.1   Particle Nucleation and Growth

The understanding and control of crystal (particle) growth are critical to modern nanoscience and nanotechnology [304]. A general strategy for producing high-quality crystals is to maintain the growth solution slightly supersaturated in the atomic or molecular species to be deposited so that the lowest energy equilibrium positions can be attained. Often modifiers (e.g., surfactants) are added to moderate the growth rate or influence the final crystal habit. Growth of gold nanocrystals in solution also relies on surfactants to control unwanted cluster aggregation during chemical reduction of ionic precursors or thermal decomposition of metalorganics. In the case of chemical reduction of a metal salt, for example, the nucleation event may be localized uniformly in space and time by the presence of nanometer size cavities or by creating a microheterogeneous solution. The latter strategy is the basis for nanocrystal growth in the interior of surfactant aggregates (micelles or vesicles). In both cases, the diffusion of new material and its deposition onto the seed nuclei will be much slower than would occur in a continuous phase such as a liquid or gas. In the latter case, the aggregation kinetics as described by the Smoluchowski equation predicts a power law (or log-normal) size distribution in the final product. Such strong polydispersity is generally unwanted. In the case of slow, controlled growth of small nanocrystals in a microheterogeneous environment, one anticipates that facile surface diffusion of atoms deposited on the initial nuclei may create structures controlled by thermodynamic considerations rather than kinetic ones as in classical colloidal (microemulsion) growth. As the growing clusters undergo diffusion and collisions in the solution, intercluster exchange of atoms may even occur in order to achieve a structure with the most thermodynamically stable structure [305].

Models of particle (crystal) development consider two basic steps: nucleation and growth [306]. The creation of a new phase from a metastable (supersaturated or supercooled) state is nucleation. Nucleation occurs via embryos, or germs, which are small, transient clusters, or some entities approximating it, of the new phase. Continuous fluctuations in the sizes of these clusters occur via the incorporation of additional atoms or molecules and their detachment. Where the incorporation event

becomes overwhelmingly more probable than decay, it may result in an embryo growing large enough to become stable, i.e., the energy barrier for its structural fluctuations becomes sufficiently high and a new moiety with well-defined structure is formed [307]. During the nucleation, two opposing energy factors come into play simultaneously. Creation of (new) surface at the boundaries of a nucleus costs energy. On the other hand, there is an energy release due to creation of a new volume [306]. Depending on the surface-to-volume ratio of a developing particle, the resultant energy varies and, therefore, there will be an energy barrier for nucleation. The energy barrier for homogeneous nucleation (spontaneous and random nucleation occurring throughout the solution) is high and hence requires higher degree of metastability (e.g., supersaturation) compared to heterogeneous nucleation. In the case of heterogeneous nucleation, nucleation occurs on surfaces of preexisting foreign bodies or solid structures; hence, some energy is released by the partial elimination of those preexisting interface. This energy gain diminishes the free-energy barrier and facilitates nucleation. Therefore, heterogeneous nucleation occurs much more often and at the lower saturation level compared to the homogeneous nucleation [307, 308].

In the embryonic stage of the metal nanoparticle nucleation, atoms (formed via reduction of metal precursors) or the combined atom–metal precursor systems assemble to form clusters such as dimers, trimers, tetramers, in solution. These clusters may disassemble or collide with further metal ions/atoms, finally forming an irreversible seed. Nucleation ceases when the concentration of growth units falls below the minimum supersaturation level. Once the seed forms, it acts as a convergence point for growth units (ions/atoms) as long as they are available and grows in dimension. Morphology and growth rate of the seed (which are again functions of thermodynamic and kinetic factors) play major roles in determining the final nanoparticle morphology.

The homogeneous nucleation of nanoparticles is based on the supersaturation of solution by reactants such as precursors, reducing agent, stabilizers, costabilizers, and additives. The increased solubility of component in the continuous phase can be reached by the rising in temperature. The supersaturation state can be then reached by the reduction in temperature. Generation of supersaturation through in situ chemical reactions by converting highly soluble chemicals into less soluble chemicals is a good example of this approach. In a typical homogeneous nucleation synthesis consisting of one step process in which precursor (s), stabilizer(s) and other additives are stirred in the oil- or water-continuous phase and then treated by the heat [309]. The heterogeneous nucleation of metal particles consists of several-step process [310]. In a typical heterogeneous nucleation, the first step is the formation of the primary (seed) metal particles and then the growth of particles is achieved via further steps, for example, by the further addition of precursor(s), stabilizer(s), and additives. Meanwhile, some stabilizers, like sodium dodecyl sulfate [311], sugar ball [312], and polymer (e.g., poly(vinylpyrrolidone)) [313], were used, and some stabilization technologies of thiol-ligand coatings [314] and polymer capping agents [315] were developed to prevent the prepared (sub)nanoparticles from aggregating. At room temperature, citric acid, oxidizable solvents (such

as alcohols or DMF), and polymers (e.g., poly(vinyl alcohol) (PVA), PVPo, PVP, etc.) show weak reducing properties toward most of the metal precursors. However, they are capable of reducing a number of metal ions at elevated temperatures [316–318]. In most of the cases, these reducing agents play simultaneous roles of solvents and stabilizers. Depending on the reduction potentials of the metal precursor and the reducing-agent systems, the temperature required for reduction varies.

In the case of homogeneous nucleation, the shape of a (seed) crystal under equilibrium (thermodynamic) conditions can be predicted on the basis of Gibbs–Wulff theorem. The equilibrium (or Gibbs–Wulff) shape of a crystal is one that minimizes surface energy for a given enclosed volume. If the surface energy is isotropic (as for a liquid), the equilibrium shape will be spherical as the sphere has the minimum surface area for a given volume. In the case of crystalline solids, the surface energy is anisotropic. Therefore, total surface energy is not only determined by the surface area but also by the nature of the surface facets. Therefore, the energy-minimizing shape is obtained by enclosing the crystal with the facets of the lowest possible surface energy as well as truncating the facets in order to give minimum possible surface area for a given volume, which results in a polyhedron shape. For a face-centered-cubic (fcc) crystal structure, the surface energies (γ) of the low-index crystallographic facets are given in the order [307, 319]:

$$\gamma\{111\} < \gamma\{100\} < \gamma\{110\} \tag{2.12}$$

Based on this facet energy, minimum surface-energy requirement predicts that the seed crystals of fcc metals should show a tendency to adopt a tetrahedral or an octahedral shape enclosed by {111} facets. But tetrahedron or octahedron shapes are not the minimum area shapes for a given volume. Therefore, the Gibbs–Wulff shape for an fcc crystal structure is a truncated octahedron, which is enclosed by eight hexagonal {111} facets and six square {100} facets. Though truncation introduces a relatively high-energy {100} facet but generates nearly spherical shape, thereby decreasing the total surface area and free energy. At very small (nanometer) sizes, the equilibrium shape is an octahedron, corresponding to the disappearance of the {100} facets [320]. The regular polyhedron shapes can be obtained only at 0 K, where the surface-energy anisotropy is maximal. The surface-energy anisotropy decreases at high temperatures and rounded parts appear in the equilibrium shape [321].

In the case of heterogeneous nucleation, the seed can grow in an epitaxial or nonepitaxial way. Epitaxy is the technique of growing a crystal (called deposit or overgrowth), layer-by-layer, on another crystal (substrate). In the epitaxial growth, the deposited metal takes on a lattice structure and orientation identical to those of the substrate. Chemical compositions of the deposit and the substrate may be the same (when it is termed as homoepitaxy, e.g., gold seed to gold nanorod), or different (in the case of heteroepitaxy of the different metals). The deposit and substrate may differ in the nature and strength of their chemical bonds as well as in their lattice structures. The chemical bond between the deposit and substrate determines the degree of interaction that can occur between the two, while the

lattice mismatch determines the spatial variation of the interaction. A strong deposit–substrate interaction and small lattice mismatch stimulate epitaxial growth. According to the Wulff–Kaischew theorem, the equilibrium shape of a supported (macroscopic) crystal is determined not only by the surface energy (γ) of the facets but also by its adhesion energy (β) with the support [320]. Depending on the magnitude of γ as compared to β, various degrees of truncation of epitaxially formed nuclei (as compared to homogeneously formed nuclei) may result. The presence of strain at the interface due to a mismatch (misfit) between the lattice parameters of the support and the deposit crystal may cause deviation from the equilibrium shape. When the crystal structures are the same, the mismatch (m) between the two lattices is defined by [307]

$$m = (a_\mathrm{d} - a_\mathrm{s})/a_\mathrm{s} \qquad (2.13)$$

where a_d and a_s are the lattice parameters of the deposit and the substrate, respectively. For zero mismatch ($m = 0$), edges between the top facet (parallel to the substrate) and the lateral facets (perpendicular) follow a straight line with crystal growth, meaning that the shape is self-similar (the Wulff–Kaischew case). But for nonzero mismatch ($m \neq 0$), the deposit crystal grows faster in height than laterally when the height-to-width aspect ratio is no longer constant and larger aspect ratios (i.e., taller crystal) are obtained with the larger mismatch. The equilibrium shape then deviates from the Wulff–Kaischew case. Qualitatively, as the depositing crystal layer is strained at the interface, it prefers to decrease the interface area and to grow at the top to relax more easily. However, the elastic energy increases with the size of the crystal and at a given size the system will partially relax the strain by introduction of dislocation. In the case of formation of an epitaxial phase, mechanisms of nucleation and overgrowth have been categorized into three types, namely the Frank–van der Merwe mode, the Stranski–Krastanov mode, and the Volmer–Weber mode [322, 323]. These modes have been deduced from equilibrium considerations of the energy balance between the surface energy and the interfacial energy for lattice-matched systems. The Frank–van der Merwe mode, where 2D layer-by-layer growth is observed, occurs under lattice-matched or slightly mismatched conditions with high interfacial bond energies and low supersaturation to suppress 3D nucleation [322, 323]. In Stranski–Krastanov mode, a 2D layer of adsorbed atoms is formed under conditions of undersaturation, which turns into 3D growth under conditions of supersaturation (2D layer followed by 3D islands on top). In the Volmer–Weber mode, which occurs under highly lattice mismatched conditions, 3D nucleation occurs under conditions of supersaturation, followed by growth of 3D islands leading to their coalescence [322, 323].

From crystallography, we know that for crystals grown under surface-control conditions, the mechanism of crystal growth can be determined by the structure of the crystal face. It is known that closely packed flat faces (F-faces) grow more slowly than stepped faces (S-faces) or kinked faces (K-faces). Thus, in a growing crystal, F-facets will be exposed more and more, while S-faces and K-faces will gradually disappear. This results in a shrinkage in area (or elimination) of

higher-energy facets, while the area of lower-energy facets increases [231]. Consequently, in contrast to the unique equilibrium shape (at a given temperature) of a macroscopic crystal, several polyhedral growth shapes, including highly anisotropic ones, can be obtained by fine-tuning the relative growth rates of the different facets. The surface energy of a facet can be modified by the adsorption of various additives.

Mass-transport-limited growth is another source of anisometric development of nanoparticles. If interfacial processes are extremely fast during a crystal growth process, the long-range transport of mass controls the rate of growth. Crystals grown under such far-from-equilibrium (high-supersaturation) conditions often show complex shapes, dendritic or branch formation. Fast interfacial process creates a depletion zone around a crystal at the crystal–solution interface due to fast accommodation of the growth units (atoms, ions, molecules), and the supersaturation increases with distance into the parent phase. When a depletion zone is formed around a crystal with polyhedron shape, the apexes of the crystal protrude into the region of higher concentration [231]. Consequently, the rate of growth of any apex (protrusion) will be greater than the growth rate of the rest of the crystal facets, leading to the formation of branches. The diffusive nature of long-range transport processes gives rise to such morphological instabilities, leading to shapes like dendrites [324]. One can summarize different growth conditions as follows: (i) At or near equilibrium growth conditions, faces with the lowest surface energies dominate the crystal habit. (ii) In crystals grown under surface-control conditions, faces with the slowest growth rate dominate the resulting habit. (iii) For diffusion-controlled continuous growth conditions, the crystal habits tend to be rounded, as all crystal faces are rough and predicted to grow at the same rate. (iv) At very high supersaturations, morphological instability can occur and dendritic, cellular, hopper, etc., growth forms may appear.

In general, colloidal particles in a dispersion medium are subject to Brownian motion, and this produces frequent collisions between particles [325]. During such a collision, there are two basic interactions between the particles that determine their stability: one being the attractive forces (van der Waals attractive forces often dominated by a metallic core) and the other being the repulsive forces (mainly electrostatic and steric hindrance). If the attractive forces dominate, the particles will aggregate; in contrast, if the repulsive forces dominate, the system will remain in a dispersed, stable state. For nanoparticles in solution, due to the van der Waals attractive forces acting continuously between them, it is necessary to introduce a repulsive force to maintain particle stability [326]. For example, gold nanoparticles are commonly synthesized through the reduction of auric acids in water using trisodium citrate, with the citrate ions also serving as stabilizing ligands providing surface-bound negative charges, repulsive electrostatic forces around the gold nanoparticles [327]. Upon the chemisorption of electrostatically neutral small molecules, the molecules displace citrate ions from the AuNP surface, reducing or eliminating the surface charges [328]. Without strong charge–charge repulsions, these monolayer-coated AuNPs can be driven to each other by van der Waals attractions, leading to aggregation. In most cases, aggregation of AuNPs is an

irreversible process, and the presence of irreversibly aggregated AuNPs changes the particle size distribution, optical properties, and the surface-to-volume ratio for the AuNPs in solution, making it difficult or impossible to employ them in various applications [329].

In liquid-phase synthesis of NMNPs, nucleation and growth depend on the nature of the reducing agent and stabilizing ligands, the identity of the metal ion precursor, and reaction temperature [266]. In a typical liquid-phase synthesis, the nanoparticle formation process undergoes three distinct stages as follows: (1) reduction and generation of active nuclei, (2) formation of seed particles upon collision of active nuclei, and (3) formation of larger nanoparticles via a growth process, which may be Ostwald ripening or aggregation. In liquid-phase synthesis of nanoparticles, sodium citrate and sodium borohydride are the most commonly used reducing agents. The synthesis of nanoparticles via the citrate reduction method is generally performed at elevated temperatures (85–100 °C) [19, 330]. However, sodium citrate alters the solution pH due to its weakly basic character and influences nucleation and growth [331], causing conditions under which the nanoparticle formation mechanisms contradictory and uncertain [332]. In the case of sodium borohydride-based synthesis of nanoparticles, nucleation and growth take place on a millisecond timescale [333]. As a result, direct time-resolved measurements are extremely challenging and required special instrumentation [334]. Although real-time TEM (tTEM) techniques have been recently introduced to monitor nanoparticle growth [335], characterization of the early stages of nucleation and growth still remains elusive. In addition to using TEM, mass spectrometry was introduced to investigate the formation of thiolate-stabilized gold nanoparticles [336]. However, this method did not provide information about the nucleation and growth processes during nanoparticle formation. A separate study reported aggregative growth by evaluating precursor decomposition at elevated temperature [337]. However, this method required additional cleaning to purify the nanoparticles for each step of data analysis, which could alter the nanoparticle size distribution adding ambiguity to the proposed nanoparticle formation mechanism. Furthermore, LSPR properties of nanoparticles are strongly dependent on their local dielectric environment [338].

The NMNP growth, thus, is generally categorized by two processes: diffusion-controlled Ostwald ripening and aggregation/coalescence. The diffusion-controlled Ostwald-ripening growth can be differentiated from the aggregative/coalescence growth by three distinct observable characteristics during the nanoparticle formation as follows [266, 339]: (1) The final nanoparticles should be single crystalline in nature (2) the nanoparticle growth kinetics should be nonsigmoidal, and (3) the early reduction process should not involve a bimodal size distribution. It was reported that the evolution of the LSPR peak with time during silver nanoparticle formation was nonsigmoidal. Moreover, it was also found single crystallinity of the final AgNPs and the absence of a bimodal size distribution at the early stage of nanoparticle formation. These data are consistent with diffusion-controlled Ostwald-ripening growth during the slow reduction and formation of AgNPs [340].

The digestive-ripening process contributes to the regulation of the particle growth and particle distribution. The entire process from an as-prepared colloid to a digestively ripened one can be categorized into three steps, namely (1) addition of the ligand to the as-prepared colloid to break the bigger particles into smaller ligand-capped particles (2) isolation of the ligand-capped particles from reaction side products, and (3) refluxing the isolated colloid from step 2 with additional ligand to obtain the digestively ripened colloid. There are two important steps in the above process, which differentiate useful ligands from the rest. In the first step, the ligands (except alkanes) break the big prismatic-shaped as-prepared particles into nearly spherical and relatively monodisperse colloids. The next step involves the isolation of these ligand-stabilized small spherical particles from the reaction side products. Two slightly different protocols were employed for this. In the first one, the ligand-stabilized colloids were precipitated by adding excessive amounts of ethanol or acetone. This worked well for thiol-, amine-, and silane-coated particles. In all the other cases, the ligands were probably not securely attached to the particle surface, leading to the coagulation of particles when ethanol or acetone was added, and they could not be redispersed in toluene. Alternative methods like extracting the side products and surfactants with water were effective for only phosphine-stabilized particles. In all the other cases, shaking with water-formed emulsions and the colloids decomposed rapidly, making them useless for digestive ripening. The successfully isolated colloids were either redispersed in toluene (thiol-, amine-, and silane-capped) or were taken as it is (phosphine); a second dose of ligand was added to them and they were subjected to reflux, resulting in the formation of a nearly monodisperse gold nanoparticles in all the cases [340].

Furthermore, to fully utilize the functional properties of the nanoparticles, well-dispersed systems are desirable. Recently, solvents and the soft templates have been widely used to control the synthesis of metal nanomaterials because their coordination interaction with metal ions provides a good way to control the size and, more importantly, the size distribution of nanocrystals. By changing the reaction conditions, for example, the concentration of starting materials, the nature of the solvents, and the suitable capping/stabilizing agents, it is possible to synthesize a variety of nanocrystallites with different sizes. In the solvothermal process, the capping agent can covalently bind to the surface atoms of the nanocrystallite and can thus prevent them from forming bulk materials. Therefore, solvothermal process has recently been extensively applied to the synthesis and design of nanomaterials of new structures and properties.

Gold nanoparticles show distinct absorption in the visible region due to surface plasmon resonance, and their fundamental optical properties are studied using continuous white light. On another front, pulsed laser light enables us to inject much energy into materials and expand the research field. Studies on ultrafast energy relaxation dynamics in gold nanoparticles induced by femtosecond laser pulses are good examples. Irradiation of intense pulsed laser light to gold nanoparticles induces their size reduction, size enlargement, and morphological

changes [341]. The photothermal process in which the absorbed photon energy heats the particles in a few picoseconds is considered to cause enlargement and morphological changes. Morphological changes of ellipsoidal gold nanoparticles with low aspect ratios to spheres occurred ca. 100 °C lower than the melting point because of surface melting. However, for laser-induced size reduction, two kinetic processes are proposed; one is the vaporization of particles induced by a photothermal process in which particles vaporize at the boiling point [342], and the other is a kind of Coulomb explosion of particles induced by electron ejection from particles. For femtosecond laser irradiation to gold nanorods, experimental results are in contrast with the hypothesis based on the photothermal process since the size reduction of gold nanorods occurred without correlating with the fact that the temperature of the particles reached the boiling point. However, Inasawa et al. [341] suggested a semiquantitative model that explained the maximum diameter of particles, existing in the system after sufficient laser irradiation, reported by Takami et al. [342]. Their model was based on the heat balance, including the heat dissipation from a particle to the surrounding media, because the heat dissipation occurred in 100–200 ps (shorter than the pulse width used by Takami et al.; they used nanosecond laser pulses [342]). Their work supports the photothermal process as its mechanism. In addition to the contrasting experimental results above, phenomenological details, such as to what extent particles reduce their sizes per one pulse and what is the main factor determining the size of small particles, which are generated by laser-induced size reduction, are not yet known. It was revealed that the size reduction of gold nanoparticles under picosecond laser pulses occurred even below the boiling point because of the gold vapor formation around hot liquid gold drops. With sufficient laser energy for the boiling of particles, gold vapor can also be formed inside liquid gold drops, and such bubbles go to the outside of the drops with some volume of liquid gold around the bubbles, resulting in the formation of particles with gold strings on their surfaces. Our results also indicate that the important factor that determines the phenomenon is not temperature but the vapor pressure at the liquid interface [343].

Modifications in temperature influence the reaction by changing the stabilization of the complexes formed between metal precursors and the surface modifiers, e.g., PVPo, and the nucleation rate of the reduced metallic atoms. Characterization of these systems has been a difficult process where researchers have employed indirect measurements to identify the localization of the elements within the nanoparticles. A novel approach to study this kind of particles is based on the use of a high-angle annular dark-field (HAADF) technique, in a TEM, which allows the observation of the interfaces between layers of different elements due to differences in atomic number, densities, or the presence of strain fields due to differences in lattice parameters. This is mainly useful when the structure of the particles is of the core@shell type. On the other hand, it is known that small metallic particles show characteristic absorption bands in the UV-Vis region of the electromagnetic spectrum, but their spectrum can be modified depending on the characteristics of the

suspending medium, composition of the metallic structure, the presence of surfactants or any other surface modifier besides the size of the particle. Reaction proceeds in general as an oxidation of the ethylene glycol reducing the metallic precursor to its zero-valence state:

$$OH-CH_2-CH_2-OH- \text{ oxidize} \rightarrow CH_3-CHO \ + \ H_2O \tag{2.14}$$

$$4(CH_3-CHO) + H_2PtCl_6 \rightarrow 2(CH_3-CO-CO-CH_3) + Pt^0 + 6HCl \tag{2.15}$$
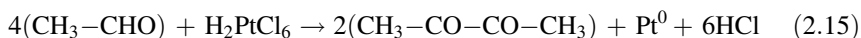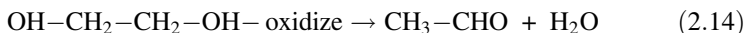
This is the reaction involved in the reduction of Pt^{4+} to Pt^0

$$OH-CH_2-CH_2-OH- \text{ oxidize} \rightarrow CH_3-CHO + H_2O \tag{2.16}$$

$$6(CH_3-CHO) + 2HAuCl_4 \rightarrow 3(CH_3-CO-CO-CH_3) + 2Au^0 + 8HCl \tag{2.17}$$
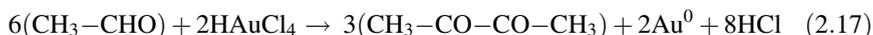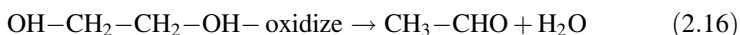
This reaction describes the reduction of Au^{3+} to Au^0. In the presence of a surface modifier, the reaction changes depending on the ability of the metal to coordinate with it, as in the case of PVPo where the metallic precursor could coordinate with the oxygen of the pyrrolidone group, when the particles are in the nanometer size range, while when they are in the micrometer size range the coordination is mainly with the nitrogen, as reported by Bonet et al. [344].

The analysis of the bimetallic synthesis suggests that at lower temperatures (100 and 110 °C) the gold reduces and nucleates much faster than the platinum and that an interaction between Pt and PVPo is strong enough to prevent the two elements from forming bimetallic structures. However, at 120 °C there seems to be a balance between the reduction and nucleation rates of Pt and Au, considering Pt was given one more minute in the reaction. This is why we observe an interaction between the elements and the formation of bimetallic structures. However, at this temperature there is a combination of a few Au@Pt nanoparticles (particles > 10 nm) with a combination of Pt@Au nanoparticles (particles < 10 nm) and eutectic alloyed nanoparticles. In the temperature range between 130 and 170 °C, Pt@Au particles were obtained. And in the last two temperatures (180 and 190 °C), Pt@Au nanoparticles with thicker Au shells were synthesized, as observed in the HAADF images. In all the temperatures above 110 °C, the presence of eutectic alloyed nanoparticles was also detected [345].

The growth of metals on oxide surfaces is important in numerous technologies including electronic device fabrication and heterogeneous catalysis. With respect to the latter, the activity and selectivity of metal-catalyzed reactions are often sensitive to the metal particle morphology. For example, the catalytic activity of gold supported on certain oxides depends critically on the morphology of the clusters. In general, the morphology of metal particles on oxide surfaces depends to a large extent on defects, particularly point defects such as oxygen vacancies. The research has been addressed to the relationship between metal cluster nucleation/growth on oxide surfaces and defects; however, many questions remain unanswered. Using scanning tunneling microscopy showed that bridging oxygen vacancies on TiO_2 are

active nucleation sites for gold clusters. In addition, this was suggested that the diffusion of a vacancy–cluster complex plays an important role in the formation of larger gold clusters. Using atomic force microscopy, point defects in MgO have been quantified by estimating the Pd cluster density as a function of the deposition surface temperature. In a theoretical study, the binding energies of various metals to MgO have been calculated and showed that dimers of noble metals are more stable at oxygen vacancies. Using STM, preferential decoration of Pd and Rh metal particles on line defects of Al_2O_3 has been discussed. Furthermore, defects in crystalline SiO_2 thin films have been studied using ultraviolet photoelectron spectroscopy (UPS) and metastable impact electron spectroscopy techniques (MIES). On the basis of STM studies, gold nanoclusters can be used to highlight defects in SiO_2 thin films with cluster growth related to a specific defect feature. On a well-prepared SiO_2 thin film, gold nanoclusters preferentially decorate line defects. However, higher densities of Au nanoclusters are observed on the terrace sites of a SiO_2 thin film prepared at a lower annealing temperature. A plot of the number density of gold clusters with respect to Au coverage shows that the nucleation and growth of Au clusters is initially dominated by oxygen vacancy complexes [346].

Seed-mediated growth method [24] has been demonstrated to be a powerful synthetic route to generate a range of different types of metal nanoparticles [347]. This method separates the nucleation and growth stage of nanoparticle syntheses by introducing presynthesized small seed particles into a growth solution typically containing a metal precursor, reducing agent, surfactants, and some additives. It has been shown that various shapes of gold and silver nanoparticles (e.g., rods, spheres, cubes, and octahedra) can be synthesized using the method, depending on the type of surfactants and ionic additives (e.g., silver ions, halides, and hydroxide) in the growth solution [347]. This approach with hydroquinone can reduce $HAuCl_4$ in an aqueous solution that contains 15-nm gold nanoparticle seeds. This seed-based method of synthesis is similar to that used in photographic film development, in which silver grains within the film grow through addition of reduced silver onto their surface. Likewise, gold nanoparticles can act in conjunction with hydroquinone to catalyze reduction of ionic gold onto their surface. The presence of a stabilizer such as citrate results in controlled deposition of gold atoms onto the particles and growth. Typically, the nanoparticle seeds are produced using the citrate method. The hydroquinone method extends the range of monodispersed spherical particle sizes that can be produced. Furthermore, the hydroquinone method can produce particles of at least 30–300 nm.

Dissolution is one of the main processes that controls metal nanoparticles behavior in aquatic systems. This is not the case for the metal microparticles or bulk metal fragments. Dissolution of silver nanoparticles, for example, occurs through oxidation of metallic silver and release of Ag^+ into solution (or dissolution rate is accelerated) [348]. Release of Ag^+ is determined by intrinsic physicochemical properties of silver nanoparticles and by those of the solution. Parameters that either enhance or suppress silver nanoparticle dissolution are ionic strength, pH, dissolved oxygen concentration, temperature, dissolved complexing ligands (organic matter, sulfur, chlorine), silver surface coating, shape, and size [349]. Often dissolution of

silver (AgNPs) is controlled by a combination of solution and intrinsic properties making it challenging to evaluate contribution of each parameter to dissolution. Studies of silver nanoparticle dissolution in natural and synthetic waters revealed that particle size might have a dominant effect on AgNP dissolution. For instance, studies of AgNP dissolution in acetate buffer (pH 4) revealed more Ag^+ release from 4.8 nm than from 60 nm particles. Nevertheless, surface-area-normalized Ag^+ release was similar for both sizes suggesting that AgNP dissolution is size-controlled [350]. In general, the particle size has an inverse effect on AgNP dissolution: small nanoparticles (<15 nm) release more Ag^+ than large ones because particles of the smaller radius are energetically unfavorable due to higher surface-to-volume ratio and consequently more soluble [351].

Studies of PEG-SH-coated silver nanoparticle dissolution revealed that solubility of nanoparticles was larger in acetic acid than in water. The proposed mechanisms of silver nanoparticle dissolution are oxidative dissolution through reaction of metallic silver with dissolved oxygen and protons [348] following reactions:

$$4Ag_{(s)} + O_2 \rightarrow 2Ag_2O_{(s)} \tag{2.18}$$

$$Ag_2O_{(s)} + 2H^+ \rightarrow 2Ag^+ + H_2O \tag{2.19}$$

Dissolution is initiated by oxidation of metallic Ag on the surface of AgNP by dissolved O_2 and formation a 1–2 atomic layer thick silver(I) oxide (Ag_2O) [352]. The layer of Ag_2O dissolves releasing Ag^+ into solution until Ag_2O is extinguished [349]. Once the Ag_2O layer is completely dissolved, further oxidation of metallic Ag to Ag_2O might occur, and AgNP dissolution will continue. Our observation of increase of AgNP dissolution when pH decreased from 7 (water) to 3 (acetic acid) might further support formation of Ag_2O surface layer. In the presence of water, the surface of Ag_2O is covered with surface hydroxyl groups (Ag–OH) which undergo protonation at acidic pH (Ag–OH_2^{2+}). Protonation tends to weaken and break surface Ag–O bonds, resulting in larger Ag^+ release into solution at acidic than at neutral pH.

According to thermodynamic calculations, silver nanoparticles are not stable in aerobic waters with pH ranging from 4 to 12 and will dissolve completely [348]. The extent of dissolution varied between 3 and 15% in water and between 6 and 41% in acetic acid. Similar silver nanoparticle behavior was observed in other dissolution studies that found an extent of AgNP dissolution of 30% in acetate buffer (pH 4) [348], 10−27% in Hoagland medium (pH 5.6) [353], 11−52% in water (pH not reported) [352], and 1−60% in 1 M $NaHCO_3$ solution (pH 8) [354]. The results indicate that kinetic factors play an important role in inhibiting complete AgNP dissolution. Incomplete dissolution could be due to Ag^+ adsorption on AgNP, limited diffusivity of O_2 and protons to reaction sites, AgNP stabilization by PEG-SH, and particle aggregation. It was hypothesized that the partial dissolution of AgNP observed is due to an increase in the particle size leading to a solubility decrease. Analysis of AgNP by TEM revealed that the average diameter increased after dissolution of AgNP6, AgNP9, and AgNP13 and remained unchanged in

nondissolving AgNP70 (70 nm). The absence of size increase in the nondissolving AgNP70 suggested that release of Ag^+ during AgNP dissolution was necessary for the nanoparticle growth. Two possible mechanisms of AgNP size growth were considered: (1) precipitation of dissolved Ag^+ on the surface of AgNP and (2) Ostwald ripening. The first hypothesis was evaluated based on the XRD analysis of the 80 d-dissolved AgNP6, calculations of mass increase due to Ag^+ precipitation and saturation index calculations. The AgNP6 size increased from ~ 6.2 to ~ 10.6 nm by the end of dissolution experiment. Increase in dissolved Ag^+ concentration might shift Eq (2.18) equilibrium toward Ag_2O precipitation.

Experimental evidence of increase in average particle size as well as broadening of size distribution might indicate that Ostwald ripening was responsible for silver nanoparticle size growth [355]. Ostwald ripening is explained by the fact that larger particles with small surface-to-volume ratios are more stable than smaller particles with large surface-to-volume ratios, leading to dissolution of smallest particles and redeposition of the released atoms at larger particles. Growth of AgNP follows oxidation−reduction mechanisms, first smaller AgNPs are oxidized by O_2, Ag^+ is then dissolved, followed by Ag^+ reduction and Ag deposition on larger AgNP [356]. Such mechanism would likely lead to a decrease in concentration of dissolved Ag^+ with time as observed in AgNP6 and AgNP9 samples. However, the dissolved Ag^+ concentration decrease, 5 and 0.8 μM, would result in an average size growth to 7.2 and 9.5 nm in AgNP6 and AgNP9, respectively, which is smaller than the observed diameters at the end of dissolution experiment. The discrepancies in concentration changes and size growth suggest that oxidation of metallic silver and reduction of Ag^+ occurred simultaneously after reaching equilibrium. Similar observations were reported by Jang et al. [357] for Ostwald ripening of gold nanoparticles during which dissolved gold concentration did not change while particles increased in size. However, they were not able to determine what reducing agent was responsible for Ag(I) to Ag(0) transformation in the dissolution studies.

Jang et al. [357] studied Ostwald ripening of gold nanoparticles in the presence of H_2O_2 and Br^-. It was demonstrated that H_2O_2 induced both oxidation of smaller AuNP to Au(III) and Au(III) reduction leading to the increase in size of larger ones. Hydrogen peroxide production was detected during dissolution of citrate-coated AgNP in air-saturated water [348]. It was revealed that after a 3-h dissolution experiment, up to 0.4 μM H_2O_2 was produced in the presence of AgNP, while no H_2O_2 was detected in a control $AgClO_4$ solution. In the study of AgNP behavior in the presence of H_2O_2, He et al. [358] observed reduction of Ag^+ at pH > 5.5. They demonstrated that the final AgNP increased in size, and the morphology changed from spherical to more irregular shape [358]. Thus, oxidative dissolution of AgNP might catalyze production of H_2O_2, which further reduced Ag^+ to Ag atoms. Deposition of silver atoms on the AgNP surface resulted in the particle growth.

2.3 Biohybrids

QAC are the most extensively studied surface-active agents. They are mainly used as slimicides in swimming pools, antistatic agents in hair conditioners and wetting agents in nasal sprays. Moreover, they also find use shampoos and dishwashing materials [359]. The used surfactants find their way to various environmental segments and thus pose serious health hazards. They have the ability to adsorb strongly onto negatively charged suspended particulates and sludge. Intensive investigations have been carried out on their behavior, fate, and biological effects [143]. Long exposure to QACs can cause sensitization, hemolysis, and toxic effects by all routes of exposure including inhalation, ingestion, dermal application, and irrigation of body cavities. The concentrated solutions of QACs result in allergic reactions, hypersalivation, vomiting, hematemesis, and diarrhea. In severe cases, they may cause respiratory paralysis, convulsions, coma, and cardiorespiratory arrest [360].

Didodecyldimethylammonium bromide (DDAB) is toxic as well as cancer-preventing agent [361]. Toxicity is a major nuisance of anticancer drugs. Most of the clinically used anticancer drugs have a narrow therapeutic index, with a small difference in their dose for antitumor effect and toxicity. Therefore, the doses recommended for such compounds are determined according to their toxicity endpoints. Considerable research work has been carried out on the cancer prevention ability of DAAB but the mechanism of action has not been explored. The main cause of several diseases such as diabetes, hemophilia, and cancer is related to the alteration in the replication machinery of DNA. Therefore, drug interactions, with DNA which can affect the replication processes, are potential treatments for such ailments [362].

Polymer-based drug delivery systems emerged from the laboratory bench in the 1990s as a promising therapeutic strategy for the treatment of cancer and other devastating diseases [144]. Polymer–drug conjugates are nanosized hybrid constructs that covalently combine a bioactive agent with a polymer to ensure not only its efficient delivery to the required intracellular compartment but also its availability within a specific period of time. It has already been demonstrated that polymer–drug conjugation promotes tumor targeting by the enhanced permeability and retention effect and its capability of escaping from reticuloendothelial system. One promising example of such polymer nanomaterials is presented by a class of pluronic block copolymers (also known under nonproprietary name poloxamers). These block copolymers consist of hydrophilic poly(ethylene oxide) (PEO) and

Chart 2.2 ABA tri-block structure of pluronic block copolymers

hydrophobic poly(propylene oxide) (PPO) blocks arranged in ABA tri-block structure: PEO-PPO-PEO (Chart 2.2) [363].

As outlined in a large number of previous reports, passive drug targeting is a validated method for improving the delivery of low molecular weight (chemo-) therapeutic agents to tumors [364]. Several different polymer-based anticancer agents have been approved for clinical use, including, e.g., Gliadel (i.e., carmustine-containing polymeric wafers, for surgical implantation in case of brain cancer), Lupron Depot (i.e., LHRH-containing polymeric microspheres, for local prostate cancer therapy), and Oncaspar (i.e., PEG-L-asparaginase, for the treatment of leukemia) [365]. For passive tumor targeting, however, essentially only Abraxane, i.e., albumin-based paclitaxel, has managed to be used (for metastatic breast cancer) [366]. This is in spite of the large number of passively tumor-targeted polymeric drug carriers that have been evaluated in animal models and in patients in the past two decades.

Prominent examples of macromolecular drug carrier systems evaluated in patients are albumin, poly(ethylene glycol), dextran, poly(L-glutamic acid), poly[N-(2-hydroxypropyl)methacrylamide], and others [367]. The most advanced of these formulations currently are, i.e., poly(L-glutamic acid)-based paclitaxel, which are in phase III trials for breast, ovarian, and lung cancers [368]. Copolymers based on N-(2-hydroxypropyl) methacrylamide (HPMA) were used to improve the tumor-directed delivery of doxorubicin and they demonstrated that long-circulating and passively tumor-targeted polymeric drug carriers are able to beneficially affect the therapeutic index of doxorubicin-based chemotherapy. These formulations were found to be 4–5 times higher than that of free doxorubicin, no cardiotoxicity was detected (in spite of the relatively high overall doses administered), and several clear responses were observed, in patients with nonsmall cell lung cancer, with colon cancer and with doxorubicin-resistant breast cancer [369].

At the preclinical level, a large number of additional HPMA-based nanodiagnostics and nanotherapeutics have been evaluated over the years, functionalized besides with standard chemotherapeutics, such as doxorubicin, cisplatin, and paclitaxel, also with more recently developed (and more sophisticatedly acting) drugs, such as the heat-shock protein inhibitor geldanamycin [370]. Moreover, besides passively tumor-targeted polymeric nanomedicines, also a large number of actively targeted HPMA copolymers have been designed and evaluated [371]. And furthermore, significant progress has also been made with respect to the development of novel drug linkers, such as pH-sensitive hydrazone spacers, which are much more effective than GFLG spacers in releasing doxorubicin, and which consequently much more strongly inhibit tumor growth [372].

HPMA copolymers have also been used for overcoming multidrug resistance [373], for coating viral and nonviral gene delivery systems [374], for imaging purposes [375], and for making block copolymer micelles, which can be core-cross-linked to improve their circulation times [376]. Furthermore, HPMA copolymers have also been employed to improve the treatment of noncancerous disorders, such as rheumatoid arthritis and bacterial infections, which are also characterized by a strong inflammation component and leaky blood vessels, and

which are therefore also highly amenable to EPR-mediated passive drug targeting [377]. And a significant number of studies have focused on the combination of HPMA copolymer-based nanomedicine formulations with other treatment modalities, such as with surgery, with radiotherapy, with hyperthermia, with photodynamic therapy, and with chemotherapy [378]. Together, these insights and efforts, HPMA copolymers are highly suitable systems for drug targeting to tumors. In addition, they indicate that by improving the pharmacokinetic and biodistributional properties of attached diagnostic and therapeutic active agents, long-circulating and passively tumor-targeted polymeric drug carriers might be suitable systems for image-guided drug delivery, as well as for improving the efficacy of combined modality anticancer therapy.

2.4   Conclusion

The field of NMNPs has been an extremely exciting research area for chemists, biologists, physicists, and materials scientists. This chapter attempted to give an outline of the colloid-chemical synthesis approach for controlling morphology in NMNPs. These nanoparticles with intriguing and novel morphologies, and sometimes with near-perfect shape control, have been produced by colloid-chemical synthesis. The influences of various synthesis parameters, processes, and approaches in manipulating the nanometer features in all three dimensions of nanoparticles have been discussed. Several viewpoints on how the particle morphology can be understood in terms of the precursor types and particle nucleation and growth have been compared and contrasted. This information will help to look at different aspects of particle morphology control in a more systematical way. We have touched upon some of the experimental tools and reaction mechanisms that provide the needed characterization of complex NMNPs.

Factors such as the nature and concentration of metal precursor and reducing agent, molar ratio of precursor to additives, the selective adsorption of additives to different crystal facets, contact with an external support, are all capable of influencing the nucleation and kinetics of particle growth. The proper choice of parameters for the reaction, including the temperature, radiation, the reducing method, the stabilizers (capping agent, surfactant, surface-active additive) and additives, plays a crucial role in the successful synthesis of metal nanoclusters. The metal ions from dissolved can be reduced, either by a chemical reductant (e.g., sodium borohydride, sodium hypophosphite), by light (photoreduction with visible or ultraviolet light), or by γ-rays (by radiolysis of water). Thus, the preparation of NMNPs by chemical reduction contains two major parts: (i) reduction using agents such as borohydrides, aminoboranes, hydrazine, formaldehyde, hydroxylamine, saturated and unsaturated alcohols, citric and oxalic acids, polyols, sugars, hydrogen peroxide, sulfites, carbon monoxide, hydrogen, acetylene, and monoelectronic reducing agents including electron-rich transition-metal sandwich complexes; and (ii) stabilization by agents such as trisodium citrate dihydrate, sulfur ligands (in

particular thiolates), phosphorus ligands, nitrogen-based ligands (including hete-rocycles), oxygen-based ligands, dendrimers, polymers, copolymers, and surfac-tants. Spectroscopic and microscopic techniques support a three-stage mechanism of NMNP formation. In the initial stage, simultaneous reduction and active nuclei formation are involved. This is followed by concurrent reduction, nucleation, and growth, and finally, single-crystalline nanoparticles are formed via growth by slow Ostwald ripening. The amount of stabilizing ligand influences the final nanoparticle size but has less effect on the nucleation and growth processes. The overall nanoparticle formation process becomes faster as the solution temperature increa-ses, and the Ostwald-ripening growth mechanism is maintained.

It was reported that using citric acid as a reducing agent made the reduction reaction take one week longer and led to a wide size distribution. As far as stabi-lizers are concerned, citrate ions can bind on silver surfaces for shape control, but their ability to stabilize silver particles is weaker than thiols. Nowadays, a molecule which can act both as a reducing and capping agent is preferred so that the reaction takes place in one step and there is no need for an external reducing agent. This will reduce the number of steps involved in metal nanoparticle synthesis. The physical method involves radiation reduction of silver ions by γ-ray, microwave, ultraviolet, or visible light. Chemical reduction in solution is advantageous over other pro-cesses, because of its simplicity, low reaction temperature, and solubility of metal salts in water. Silver nanoparticles can be prepared in DMF without adding any reductant. It has been suggested that the reduction rate can be enhanced at high temperatures. Formamide is one of the most common solvents used to study various processes such as formation of metal nanoparticles, interaction with alcohols. The reducing power of the amines of several different structures was confirmed and showed, very clearly, that the oxidation potential of the reducing agent should lie between the oxidation of Au(0)–Au(I) and the reduction of Au(III)–Au(0) for the reaction to proceed. Multifunctional amines and nitrogen-containing polymers have also been tested for the synthesis of AuNPs. Ketyl radicals formed by the photolysis of carbonyl-based initiator acted as reductants of silver salt leading to the formation of AgNPs. This approach is based on the Norrish Type I photocleavage of pho-toinitiator leading to ketyl radicals. Silver cations, Ag^+, scavenge the $(CH_3)_2\dot{C}OH$ radical (ketyl) and reduce Ag^+ to Ag^0. It was postulated that this protecting effect depends on the number of available NH_2 groups, rather than the macromolecule conformation.

Poly(ethylene oxide)-poly(propylene oxide)-poly(ethylene oxide) (PEO-PPO-PEO) block copolymers are well known as dispersion stabilizers and templates for the synthesis of mesoporous materials and nanoparticles. Variation of the PEO-PPO-PEO block copolymer molecular characteristics, concentration, and temperature allows for unique tunability of block copolymer self-assembly in the presence of selective solvents such as water. It was found that PEO-PPO-PEO block copolymers can act as very efficient reductants/stabilizers in the single-step syn-thesis and stabilization of gold nanoparticles from gold salts. Formation of gold nanoparticles from $AuCl_4^-$ in aqueous PEO-PPO-PEO block copolymer solutions includes three main steps: (1) reduction of metal ions in aqueous block copolymer

solution (2) absorption of block copolymer on gold clusters because of amphiphilic character (hydrophobicity of PPO) and reduction of further metal ions on the surface of gold clusters, and (3) growth of gold particles and stabilization by block copolymers. Furthermore, copolymers (as capping agents) with stimulus responsibility have attracted growing attention due to their diverse self-assembly behavior in response to stimuli, such as pH, temperature, salt. The stimulus responsibility allows for tailoring the supramolecular aggregates with desirable morphologies and properties from the same precursory copolymers. Poly(N-isopropylacrylamide) is a stimulus responsive polymer that undergoes a reversible, inverse phase transition at a lower critical solution temperature in pure water. In addition to temperature, cosolvents can also cause an inverse phase transition in pNIPAM. The functionality of pNIPAM on surfaces can be separated into two categories: (1) triggered changes in polymer conformation and (2) triggered changes in polymer surface energetics.

Coordination chemistry offers simplicity, stable bonding, and ligand-metal specificity, enabling ligand-bearing components to be assembled into supramolecular structures using appropriate metal ions. This approach is particularly compatible with surface chemistry, as binding of metal ions activates the surface toward ligand binding, and vice versa. The reactive ligands approach highlights that (i) the ligands decorated on a spatially limited surface can be used for further chemistry, and the rest of the ligands can be selected to remain unreactive during the coupling process. (ii) It was applicable to a wide size range of nanoparticles, e.g., the functionalization of AuNPs with the diameter of 16–41 nm was demonstrated.

In addition to the stabilizing ability of some stabilizing agents, BSA and HSA, these additives can also be used as a reducing agent. A protein macromolecule contains several amino acids such as cysteine, tryptophan, lysine which can act as weak reducing agents. All these amino acids can reduce gold or silver ions independently even at room temperature. However, when amino acid is present in a protein macromolecule, the reducing ability is significantly compromised by the steric screening of other nonreducing amino acids in the vicinity. Then, the reducing ability of a particular amino acid is purely related to its location in the native state of protein.

In the pullulan- and chitosan-mediated synthesis procedure, these modified nanoparticles were first produced and gold layers were then added to promote the anisotropic growth, which is indeed, substantially sensitive to the presence of the chitosan matrix. Their reducing and stabilizing activities led to the one-pot procedure. The appropriate amounts of iron particles and chitosan solution enabled the fine control of the chitosan-mediated approach leading to a high product yield of anisotropic nanoparticles. The proposed synthesis procedure remains simple, and the reaction carried out at room temperature allows to obtain core–shell nanoparticles of around ~ 90 nm diameters with narrow size distribution. Chitosan acts as a soft template in the formation of multibranched magnetic nanoparticles, and gold coating process was carried out in the presence of chitosan to give better particle dispersity and to avoid agglomeration problems.

A novel approach has been developed for the preparation of diverse libraries of ligand-stabilized metal nanoparticles that address the challenges stated above. It

consists of a straightforward two-step procedure, involving (i) preparation of well-defined phosphine-stabilized precursor particles (d_{CORE}) and (ii) functionalization of these particles through ligand exchange reactions with functionalized thiols.

In a typical liquid-phase synthesis, the nanoparticle formation process undergoes three distinct stages as follows: (1) reduction and generation of active nuclei, (2) formation of seed particles upon collision of active nuclei, and (3) formation of larger nanoparticles via a growth process, which may be Ostwald ripening or aggregation. The NMNP growth is generally categorized by two processes: diffusion-controlled Ostwald ripening and aggregation/coalescence. The diffusion-controlled Ostwald-ripening growth can be differentiated from the aggregative/coalescence growth by three distinct observable characteristics during the nanoparticle formation as follows: (1) The final nanoparticles should be single crystalline in nature, (2) the nanoparticle growth kinetics should be nonsigmoidal, and (3) the early reduction process should not involve a bimodal size distribution.

Dissolution of silver nanoparticles, for example, occurs through oxidation of metallic Ag and release of Ag^+ into solution (or dissolution rate is accelerated). Release of Ag^+ is determined by intrinsic physicochemical properties of AgNP and by those of the solution. Parameters that either enhance or suppress AgNP dissolution are ionic strength, pH, dissolved oxygen concentration, temperature, dissolved complexing ligands (organic matter, sulfur, chlorine), silver surface coating, shape, and size. The proposed mechanisms of AgNP dissolution are oxidative dissolution through reaction of metallic Ag with dissolved oxygen and protons. Protonation tends to weaken and break surface Ag–O bonds, resulting in larger Ag^+ release into solution at acidic than at neutral pH. Two possible mechanisms of AgNP size growth were considered: (1) precipitation of dissolved Ag^+ on the surface of AgNP and (2) Ostwald ripening. Growth of AgNP follows oxidation–reduction mechanisms, first smaller AgNPs are oxidized by O_2, Ag^+ is then dissolved, followed by Ag^+ reduction and Ag deposition on larger AgNP.

It was found that the temperature plays a decisive role in the synthesis of bimetallic Au–Pt nanoparticles protected with PVPo by the polyol method. It does not only affect the rates of reduction and nucleation of the metals, but it also affects the coordination between the metals and the polymeric protective agent, the distribution of elements in the nanoparticles, and the final particle size.

We have demonstrated the synthesis of silver nanoparticles in formamide at room temperature without adding any reductant from outside. In the presence of a proper stabilizer, nanoparticles of silver metal can be stabilized. Surface-modified particles (or films) show optical properties significantly different from those of the primary silver dispersion (or film). The silver nanoparticles also act as redox catalysts due to the shift in the Fermi level toward more negative potential. Moreover, the method described here presents a simple approach for the formation of silver nanoparticles.

To obtain MNP composites through the efficient, convenient, and easy way, a one-step approach based on the interfacial thiol–ene photopolymerization, in which microcapsules (MCs) and metal nanoparticles are generated simultaneously by irradiation of ultraviolet (UV) light, was developed. The in situ photoreduction of metal ions can minimize the number of processing steps in fabrication of metal nanoparticles. A series of gold, silver, and platinum nanoparticle-decorated microcapsules (MC@AuNPs, MC@AgNPs, and MC@PtNPs) were prepared through this one-step interfacial thiol–ene photopolymerization. $AgNO_3$ can be intercalated into the gallery regions of montmorillonite and formed hybrid framework. These MMT@AgNPs nanocomposites exhibited card-like and ball-like homogeneous surface fractions and form one-phase morphology. The degree AgNPs dispersion on MMT surface is a function of color intensity and its homogeneity. The stable AgNP@MMT nanocomposites were synthesized by microwave method. XRD analyses and TEM observations confirmed the formation of nanoparticles on the clay surfaces.

Ionic liquids (ILs) are a viable option as stabilizing agents because of their ionic character and can be easily made task-specific as phase-transfer catalysts due to their tunable nature. They are used to halt aggregation of Au(0) produced in the reduction of tetrachloroauric acid, thus limiting the size of the gold aggregates that form nanoparticles. Room-temperature ionic liquids are attracting much interest in many fields of chemistry and industry, due to their potential as a "green" recyclable alternative to the traditional organic solvents. They are nonvolatile and provide an ultimately polar environment for chemical synthesis. Among various known ionic liquids, ionic liquids containing imidazolium cation and PF_6^- have a particularly useful set of properties, being virtually insoluble in water. We have demonstrated the synthesis of the imidazolium ionic liquid-modified gold nanoparticles.

Well-defined, single, dispersed, structurally unusual, tadpole-shaped gold nanoparticles were synthesized by the reduction of chloroauric acid with tri-sodium citrate in the presence of a capping agent such as sodium dodecylsulfonate. TEM and AFM images show a clear view of its three-dimensional (3D) stereographic structure. It can be easily inferred from these images that the head and tail of the nanotadpole possess different structures (poly- and single-crystalline, respectively), but the tadpole-shaped object as a whole maintains polycrystalline.

The initial monomodal size distribution of gold nanoparticles changed into a bimodal one during pulsed laser irradiation. This modal change was caused by the gradual size reduction of gold nanoparticles. From careful observation by TEM, we extracted a characteristic value for the size-reduction rate per one pulse. It was revealed that the size reduction of gold nanoparticles under picosecond laser pulses occurred even below the boiling point because of the gold vapor formation around hot liquid gold drops. With sufficient laser energy for the boiling of particles, gold vapor can also be formed inside liquid gold drops, and such bubbles go to the outside of the drops with some volume of liquid gold around the bubbles, resulting in the formation of particles with gold strings on their surfaces. Obtained results

also indicate that the important factor that determines the phenomenon is not temperature but the vapor pressure at the liquid interface. The condensation process of gold vapor is thought to be one of the main factors that restricts the sizes of small particles.

The field of NMNPs has been an extremely exciting research area for chemists, biologists, physicists, and materials scientists. This chapter attempted to give an outline of the colloid-chemical synthesis approach for controlling morphology in NMNPs. NMNPs with intriguing and novel morphologies, and sometimes with near-perfect shape control, have been produced by colloid-chemical synthesis. The influences of various synthesis parameters in manipulating the nanometer features in all three dimensions of NMNPs have been discussed. Several viewpoints on how the particle morphology can be understood in terms of the seed structure, surface energies of various crystallographic planes, relative growth rates along various crystallographic directions, and so forth, have been compared and contrasted. This information will help to look at different aspects of particle morphology control in a more systematical way. Reliable characterization of nanoparticles is one of the most important aspects of nanoparticle synthesis. We have touched upon some of the experimental tools that provide the needed characterization of complex NMNPs.

The progress in the NMNP synthesis has been rapid and inspired toward the innovative synthesis methods and sophisticated characterization techniques. However, most of the methods are limited to synthesis in small quantities and often have poor yield of a given morphology. Colloid-chemical synthesis very often results in a mixture of nanoparticles and constant efforts must be directed to gain exquisite control of the size and the shape of various types of nanoparticles. Achieving high yield and successful scaling up of the synthesis process are necessary for the synthesis to be commercially viable. At the same time, there is need for the development of advanced techniques for separation or elimination of the unwanted shapes.

The used precursors (mainly surfactants) find their way to various environmental segments and thus pose serious health hazards. They have the ability to adsorb strongly onto negatively charged suspended particulates and sludge. Intensive investigations have been carried out on their behavior, fate, and biological effects. They can be toxic and used as well as cancer-preventing agent. Toxicity is a major nuisance of anticancer drugs. Most of the clinically used anticancer drugs have a narrow therapeutic index, with a small difference in their dose for antitumor effect and toxicity. Prominent examples of macromolecular drug carrier systems evaluated in patients are albumin, poly(ethylene glycol), dextran, poly(L-glutamic acid), poly [N-(2-hydroxypropyl)methacrylamide], and others. Copolymers based on N-(2-hydroxypropyl)methacrylamide (i.e., HPMA) and PEO-PPO were used to improve the tumor-directed delivery of doxorubicin and they demonstrated that long-circulating and passively tumor-targeted polymeric drug carriers are able to beneficially affect the therapeutic index of doxorubicin-based chemotherapy.

Glossary

Chemotherapy	as a treatment of cancer often relies on the ability of cytotoxic agents to kill or damage cells which are reproducing. This cancer treatment uses one or more anticancer drugs (chemotherapeutic agents) as part of a standardized chemotherapy regimen. Chemotherapy is one of the major categories of medical oncology (the medical discipline specifically devoted to pharmacotherapy for cancer).
Chemotherapeutic agents	are also known as cytotoxic agents. These are generally used to treat cancer. It includes alkylating agents, antimetabolites, antitumor antibiotics, anthracyclines, and topoisomerase inhibitors.
Chemotherapeutics	such as doxorubicin, cisplatin, and paclitaxel are selectively destructive to malignant cells and tissues.
Cross-link	is a bond that links one polymer chain to another. They can be covalent bonds or ionic bonds. When the term "cross-linking" is used in the synthetic polymer science field, it usually refers to the use of cross-links to promote a difference in the polymers' physical properties. When "cross-linking" is used in the biological field, it refers to the use of a probe to link proteins together to check for protein–protein interactions, as well as other creative cross-linking methodologies.
DNA replication	is the biological process of producing two identical replicas of DNA from one original DNA molecule. This process occurs in all living organisms and is the basis for biological inheritance. DNA is made up of a double helix of two complementary strands. During replication, these strands are separated. Each strand of the original DNA molecule then serves as a template for the production of its counterpart. Cellular proofreading and error-checking mechanisms ensure near perfect fidelity for DNA replication.
Hemolysis	or haemolysis, also known by several other names, is the rupturing (lysis) of red blood cells (erythrocytes) and the release of their contents (cytoplasm) into

	surrounding fluid (e.g., blood plasma). Hemolysis may occur in vivo or in vitro (inside or outside the body).
Metastatic cancer, or metastatic tumor,	is one which has spread from the primary site of origin (where it started) into different area(s) of the body. Metastasis is the spread of cancer cells to new areas of the body (often by way of the lymph system or bloodstream).
Photodynamic therapy (PDT)	is a clinically approved and minimally invasive therapy that uses a nontoxic light-sensitive compound (photosynthesizer) that is readily absorbed by abnormal cells. When exposed to a specific wavelength of light, the photosynthesizer is activated to produce changes in endothelial cell integrity that ultimately produces vascular disruption.
Rheumatoid arthritis (RA)	is a long-lasting autoimmune disorder that primarily affects joints. Most commonly, the wrist and hands are involved, with the same joints typically involved on both sides of the body. The disease may also affect other parts of the body. This may result in a low red blood cell count, inflammation around the lungs, and inflammation around the heart slimicide is a chemical that prevents the growth of slime in paper stock.
Spacer	the most developed peptide linker for triggered release of covalently attached drug is the glycylphenylalanylleucylglycine (GFLG) tetra-peptide spacer. This spacer is often employed in published polymer anticancer conjugates based on N-(2-hydroxypropyl) methacrylamide (HPMA).
Therapeutic index (TI)	(also referred to as therapeutic ratio) is a comparison of the amount of a therapeutic agent that causes the therapeutic effect to the amount that causes toxicity. The related terms therapeutic window and safety window refer to a range of doses which optimize between efficacy and toxicity, achieving the greatest therapeutic benefit without resulting in unacceptable side effects or toxicity.

References

1. Nguyen DT, Kim DJ, Kim KS (2011) Controlled synthesis and biomolecular probe application of gold nanoparticles. Micron 42:207–227
2. Parab H, Jung C, Woo MA, Park HG (2011) An anisotropic snowflake-like structural assemblyof polymer-capped gold nanoparticles. J Nanopart Res 13:2173–2180
3. Siegel RW, Ramasamy S, Hahn H, Li Z, Lu T, Gronsky R (1988) Synthesis, characterization, and properties of nanophase TiO_2. J Mat Res 3.1367–1372
4. Fegley BJ, White P, Bowen HK (1985) Processing and characterization of ZrO_2 and Y-doped ZrO_2 powders. Am Ceram Soc Bull 64:1115–1120
5. Fayet P, Wöste L (1986) Experiments on size-selected metal cluster ions in a triple quadrupole arrangement. Zeitschrift für Physik D, Atoms, Mol Clusters 3:177–182
6. Tang ZX, Sorensen CM, Klabunde KJ, Hadjipanayis GC (1991) Preparation of manganese ferrite fine particles from aqueous solution. J Colloid Interface Sci 146:38–52
7. Ma Z, Brown S, Howe JY, Overbury SH, Dai S (2008) Surface modification of Au/TiO_2 catalysts by SiO_2 via atomic layer deposition. J Phys Chem C 112:9448–9457
8. Anandan S, Grieser F, Ashokkumar M (2008) Sonochemical synthesis of Au–Ag core-shell bimetallic nanoparticles. J Phys Chem C 112:15102–15105
9. Hashimoto S, Uwada T, Masuhara H, Asahi T (2008) Fabrication of gold nanoparticle-doped zeolite L crystals and characterization by optical microscopy: laser ablation-and crystallization inclusion-based approach. J Phys Chem C 112:15089–15093
10. Zeng H, Li J, Wang ZL, Liu JP, Sun S (2004) Bimagnetic core/shell $FePt/Fe_3O_4$ nanoparticles. Nano Lett 4:187–190
11. Bendikov TA, Rabinkov A, Karakouz T, Vaskevich A, Rubinstein I (2008) Biological sensing and interface design in gold island film based localized plasmon transducers. Anal Chem 80:7487–7498
12. Delgado JM, Rodes A, Orts JM (2007) B3LYP and in Situ ATR-SEIRAS study of the infrared behavior and bonding mode of adsorbed acetate anions on silver thin-film electrodes. J Phys Chem C 111:14476–14483
13. Liu YC, Lin LH, Chiu WH (2004) Size-controlled synthesis of gold nanoparticles from bulk gold substrates by sonoelectrochemical methods. J Phys Chem B 108:19237–19240
14. Dumestre F, Chaudret B, Amiens C, Fromen MC, Casanove MJ, Renaud P, Zurcher P (2002) Shape control of thermodynamically stable cobalt nanorods through organometallic chemistry. Angew Chem 114:4462–4465
15. Pileni MP (2003) The role of soft colloidal templates in controlling the size and shape of inorganic nanocrystals. Nat Mater 2:145–150
16. Jana NR, Gearheart L, Murphy CJ (2001) Wet chemical synthesis of high aspect ratio cylindrical gold nanorods. J Phys Chem B 105:4065–4067
17. M Green (2005) Organometallic based strategies for metal nanocrystal synthesis. Chem Commun 3002–3011
18. Brust M, Walker M, Bethell D, Schiffrin DJ, Whyman R (1994) Synthesis of thiol-derivatised gold nanoparticles in a two-phase Liquid-Liquid system. J Chem Soc, Chem Commun 801–802
19. Turkevich J, Stevenson PC, Hillier J (1951) A study of the nucleation and growth processes in the synthesis of colloidal gold. Discuss Faraday Soc 11:55–75
20. Hamad-Schifferli K, Schwartz JJ, Santos AT, Zhang S, Jacobson JM (2002) Remote electronic control of DNA hybridization through inductive coupling to an attached metal nanocrystal antenna. Nature 415:152–155
21. Mallin MP, Murphy CJ (2002) Solution-phase synthesis of sub-10 nm Au–Ag alloy nanoparticles. Nano Lett 2:1235–1237
22. Liz-Marzán LM, Kamat PV (eds) (2003) Nanoscale materials. Kluwer Academic, Boston
23. Henglein A, Meisel D (1998) Radiolytic control of the size of colloidal gold nanoparticles. Langmuir 14:7392–7396

24. Jana NR, Gearheart L, Murphy CJ (2001) Wet chemical synthesis of silver nanorods and nanowires of controllable aspect ratio. Chem Commun 7:617–618

25. Jin RC, Cao YW, Mirkin CA, Kelly KL, Schatz GC, Zheng JG (2001) Photoinduced conversion of silver nanospheres to nanoprisms. Science 294:1901–1903

26. Hulteen JC, Treichel DA, Smith MT, Duval ML, Jensen TR, Van Duyne RP (1999) Nanosphere lithography: size-tunable silver nanoparticle and surface cluster arrays. J Phys Chem B 103:3854–3863

27. Sun YG, Mayers B, Herricks T, Xia YN (2003) Polyol synthesis of uniform silver nanowires: a plausible growth mechanism and the supporting evidence. Nano Lett 3:955–960

28. Chen SH, Wang ZL, Ballato J, Foulger SH, Carroll DL (2003) Monopod, bipod, tripod, and tetrapod gold nanocrystals. J Am Chem Soc 125:16186–16187

29. Liz-Marzan LM, Mulvaney P (2003) The assembly of coated nanocrystals. J Phys Chem B 107:7312–7326

30. Daniel MC, Astruc D (2004) Gold nanoparticles: assembly, supramolecular chemistry, quantum-size-related properties, and applications toward biology, catalysis, and nanotechnology. Chem Rev 104:293–346

31. Peyser LA, Vinson AE, Bartko AP, Dickson RM (2001) Photoactivated fluorescence from individual silver nanoclusters. Science 291:103–106

32. Haes AJ, Zou SL, Schatz GC, Van Duyne RP (2004) A nanoscale optical biosensor: the short range distance dependence of the localized surface plasmon resonance of silver and gold nanoparticles. J Phys Chem B 108:6961–6968

33. Yeung LK, Crooks RM (2001) Heck heterocoupling within a dendritic nanoreactor. Nano Lett 1:14–17

34. Maillard M, Giorgio S, Pileni MP (2001) Silver nanodisks. Adv Mater 14:1084–1086

35. Zhang J, Liu Z, Han B, Jiang T, Wu W, Chen J, Li Z, Liu D (2004) Preparation of polystyrene-encapsulated silver nanorods and nanofibers by combination of reverse micelles, gas antisolvent, and ultrasound techniques. J Phys Chem B 108:2200–2204

36. Sun YG, Xia YN (2002) Shape-controlled synthesis of gold and silver nanoparticles. Science 298:2176–2179

37. Metraux GS, Cao YC, Jin R, Mirkin CA (2003) Triangular nanoframes made of gold and silver. Nano Lett 3:519–522

38. Cassagneau T, Caruso F (2002) Contiguous silver nanoparticle coatings on dielectric spheres. Adv Mater 14:732–736

39. El-Sayed MA (2004) Small is different: shape-, size-, and composition-dependent properties of some colloidal semiconductor nanocrystals. Acc Chem Res 37:326–333

40. Andres RP, Bein T, Dorogi M, Feng S, Henderson JJ, Kubiak CP, Mahoney W, Osifchin RG, Reifenberger R (1996) "Coulomb staircase" at root temperature in a self-assembled molecular nanostruc- ture. Science 272:1323–1325

41. Galletto P, Brevet PF, Girault HH, Antoine R, Broyer M (1999) Enhancement of the second harmonic response by adsorbates on gold colloids: the effect of aggregation. J Phys Chem B 103:8706–8710

42. Baschong W, Wrigley NG (1990) Small colloidal gold conjugated to Fab fragments or to immunoglobulin G as high-resolution labels for electron microscopy: a technical overview. J Electron Microsc Tech 14:313–323

43. Maier SA, Brongersma ML, Kik PG, Meltzer S, Requicha AAG, Atwater HA (2001) Plasmonics-A route to nanoscale optical devices. Adv Mater 13:1501–1505

44. Tripathi GNR (2003) p-Benzosemiquinone radical anion on silver nanoparticles in water. J Am Chem Soc 125:1178–1179

45. Xiong Y, Chen J, Wiley B, Xia Y, Aloni S, Yin Y (2005) Understanding the role of oxidative etching in the polyol synthesis of Pd nanoparticles with uniform shape and size. J Am Chem Soc 127:7332–7333

46. Hussain I, Graham S, Wang Z, Tan B, Sherrington DC, Rannard SP, Cooper AI, Brust M (2005) Size-controlled synthesis of near-monodisperse gold nanoparticles in the 1–4 nm range using polymeric stabilizers. J Am Chem Soc 127:16398–16399

47. Murray CB, Kagan CR, Bawendi MG (2000) Synthesis and characterization of monodisperse nanocrystals and close-packed nanocrystal assemblies. Annu Rev Mater Sci 30:545–610

48. Schaaff TG, Knight G, Shafigullin MN, Borkman RF, Whetten RL (1998) Isolation and selected properties of a 104 kDa gold: glutathione cluster compound. J Phys Chem B 102:10643–10646

49. Prasad BLV, Stoeva SI, Sorensen CM, Klabunde KJ (2002) Digestive ripening of thiolated gold nanoparticles: the effect of alkyl chain length. Langmuir 18:7515–7520

50. Stoeva S, Klabunde KJ, Sorensen CM, Dragieva I (2002) Gram-scale synthesis of monodisperse gold colloids by the solvated metal atom dispersion method and digestive ripening and their organization into two- and three-dimensional structures. J Am Chem Soc 124:2305–2311

51. Shah PS, Holmes JD, Johnston KP, Korgel BA (2002) Size-selective dispersion of dodecanethiol-coated nanocrystals in liquid and supercritical ethane by density tuning. J Phys Chem B 106:2545–2551

52. McLeod MC, Anand M, Kitchens CL, Roberts CB (2005) Precise and rapid size selection and targeted deposition of nanoparticle populations using CO_2 gas expanded liquids. Nano Lett 5:461–465

53. Jimenez VL, Leopold MC, Mazzitelli C, Jorgenson JW, Murray RW (2003) HPLC of monolayer-protected gold nanoclusters. Anal Chem 75:199–206

54. Al-Somali AM, Krueger KM, Falkner JC, Colvin VL (2004) Recycling size exclusion chromatography for the analysis and separation of nanocrystalline gold. Anal Chem 76:5903–5910

55. Sweeney SF, Woehrle GH, Hutchison JE (2006) Rapid purification and size separation of gold nanoparticles via diafiltration. J Am Chem Soc 128:3190–3197

56. Novak JP, Nickerson C, Franzen S, Feldheim DL (2001) Purification of molecularly bridged metal nanoparticle arrays by centrifugation and size exclusion chromatography. Anal Chem 73:5758–5761

57. Templeton AC, Cliffel DE, Murray RW (1999) Redox and fluorophore functionalization of water-soluble, tiopronin-protected gold clusters. J Am Chem Soc 121:7081–7089

58. Dillenback LM, Goodrich GP, Keating CD (2006) Temperature-programmed assembly of DNA: Au nanoparticle bioconjugates. Nano Lett 6:16–23

59. Niemeyer CM, Simon U (2005) DNA-based assembly of metal nanoparticles. Eur J Inorg Chem 3641–3655

60. Gole A, Murphy CJ (2005) Biotin-streptavidin-induced aggregation of gold nanorods: tuning rod-rod orientation. Langmuir 21:10756–10762

61. Fendler JH, Meldum FC (1995) Colloid chemistry approach to nanostructured materials. Adv Mater 7:607–632

62. Bourgoing JF, Kergueris C, Lefevre E, Palacin S (1998) Blodgett films of thiol-capped gold nanoclusters: fabrication and electrical properties. s 515:327–329

63. Sastry M, Patil V, Mayya KS, Paranjape DV, Singh P, Sainkar SR (1998) Organization of polymer-capped platinum colloidal particles at the air-water interface. Thin Solid Films 324:239–244

64. Ganguly P, Paranjape DV, Patil KR, Chaudhari SK, Kshirsagar ST (1992) Spreading of C_{60} at air water interface. Ind J Chem A 31:F42–F45

65. Heath JR, Knobler CM, Leff DV (1997) Pressure/temperature phase diagrams and superlattices of organically functionalized metal nanocrystal monolayers: the influence of particle size, size distribution, and surface passivant. J Phys Chem B 101:189–197

66. Gmucová K, Weis M, Nádaždy V, Capek I, Šatka A, Chitu L, Cirák J, Majková E (2008) Effect of charged deep states in hydrogenated amorphous silicon on the behavior of iron oxides nanoparticles deposited on its surface. Appl Surface Sci 254:7008–7013

67. Sastry M, Kumar A, Mukherjee P (2001) Phase transfer of aqueous colloidal gold particles into organic solutions containing fatty amine molecules. Colloids Surf A 181:255–259
68. Zhao WA, Brook MA, Li Y (2008) Design of gold nanoparticle-based colorimetric biosensing assays. ChemBioChem 9:2363–2371
69. Wang C, Chen Y, Wang T, Ma Z, Su Z (2007) Biorecognition-driven self-assembly of gold nanorods: a rapid and sensitive approach toward antibody sensing. Chem Mater 19:5809–5811
70. He W, Huang ZC, Li YF, Xie JP, Yang RG, Zhou PF, Wang J (2008) One-step label-free optical genosensing system for sequence-specific DNA related to the human immunode-ficiency virus based on the measurements of light scattering signals of gold nanorods. Anal Chem 80:8424–8430
71. Perrault SD, Chan WCW (2009) Synthesis and surface modification of highly monodis-persed, spherical gold nanoparticles of 50–200 nm. J Am Chem Soc 131:17042–17043
72. Bastus NG, Comenge J, Puntes V (2011) Kinetically controlled seeded growth synthesis of citrate-stabilized gold nanoparticles of up to 200 nm: size focusing versus Ostwald ripening. Langmuir 27:11098–11105
73. Brown KR, Natan MJ (1998) Hydroxylamine seeding of colloidal Au nanoparticles in solution and on surfaces. Langmuir 14:726–728
74. Jana NR, Gearheart L, Murphy CJ (2001) Seed-mediated growth approach for shape-controlled synthesis of spheroidal and rod-like gold nanoparticles using a surfactant template. Adv Mater 13:1389–1393
75. Busbee BD, Obare SO, Murphy CJ (2003) An improved synthesis of high-aspect-ratio gold nanorods. Adv Mater 15:414–416
76. Nikoobakht B, El-Sayed MA (2003) Preparation and growth mechanism of gold nanorods (NRs) using seed-mediated growth method. Chem Mater 15:1957–1962
77. Brown KR, Walter DG, Natan MJ (2000) Seeding of colloidal Au nanoparticle solutions 2 improved control of particle size and shape. Chem Mater 12:306–313
78. Brown KR, Lyon LA, Fox AP, Reiss BD, Natan MJ (1999) Hydroxylamine seeding of colloidal au nanoparticles 3 controlled formation of conductive Au films. Chem Mater 12:314–323
79. Rodriguez-Fernandez J, Perez-Juste J, Garcia FJ, Liz-Marzan LM (2006) Seeded growth of submicron Au colloids with quadrupole plasmon resonance modes. Langmuir 22:7007–7010
80. Jana NR, Gearheart L, Murphy CJ (2001) Seeding growth for size control of 5–40 nm diameter gold nanoparticles. Langmuir 17:6782–6786
81. Volkert AA, Subramaninam V, Haes AJ (2011) Implications of citrate concentration during the seeded growth synthesis of gold nanoparticles. Chem Commun 47:478–480
82. Kwon K, Lee KY, Lee YW, Kim M, Heo J, Ahn SJ, Han SW (2007) Controlled synthesis of icosahedral gold nanoparticles and their surface-enhanced Raman scattering property. J Phys Chem C 111:1161–1165
83. Zhao P, Li N, Astruc D (2013) State of the art in gold nanoparticle synthesis. Coord Chem Rev 257:638–665
84. Ziegler C, Eychmüller A (2011) Seeded growth synthesis of uniform gold nanoparticles with diameters of 15–300 nm. J Phys Chem C 115:4502–4506
85. Gachard E, Remita H, Khatouri J, Keita B, Nadjo L, Belloni J (1998) Radiation-induced and chemical formation of gold clusters. New J Chem 22:1257–1265
86. Regev O, Backov R, Faure C (2004) Gold nanoparticles spontaneously generated in onion-type multilamellar vesicles Bilayers-particle coupling imaged by cryo-TEM. Chem Mater 16:5280–5285
87. de la Presa P, Rueda T, del Puerto Morales M, Chichón FJ, Arranz R, Valpuesta JM, Hernando A (2009) Gold nanoparticles generated in ethosome bilayers, as revealed by cryo-electron-tomography. J Phys Chem B 113:3051–3057
88. Kamat PV, Flumiani M, Hartland GV (1998) Picosecond dynamics of silver nanoclusters Photoejection of electrons and fragmentation. J Phys Chem B 102:3123–3128

89. Taleb A, Petit C, Pileni MP (1997) Synthesis of highly monodisperse silver nanoparticles from AOT reverse micelles: a way to 2D and 3D self-organization. Chem Mater 9:950–959

90. Naik RR, Stringer SJ, Agarwal G, Jones SE, Stone MO (2002) Biomimetic synthesis and patterning of silver nanoparticles. Nat Mater 1:169–172

91. Gardea-Torresdey JL, Gomez E, Peralta-Videa JR, Parsons JG, Troiani H, Jose-Yacaman M (2003) Alfalfa sprouts: a natural source for the synthesis of silver nanoparticles. Langmuir 19:1357–1361

92. Rodríguez-Sánchez ML, Blanco MC, López-Quintela MA (2000) Electrochemical synthesis of silver nanoparticles. J Phys Chem B 104:9683–9688

93. Henglein A (1998) Colloidal silver nanoparticles: photochemical preparation and interaction with O_2, CCl_4, and some metal ions. Chem Mater 10:444–450

94. Dimitrijevic NM, Bartels DM, Jonah CD, Takahashi K, Rajh T (2001) Radiolytically induced formation and optical absorption spectra of colloidal silver nanoparticles in supercritical ethane. J Phys Chem B 105:954–959

95. Mafuné F, Kohno J, Takeda Y, Kondow T (2000) Structure and stability of silver nanoparticles in aqueous solution produced by laser ablation. J Phys Chem B 104:8333–8337

96. Rodríguez-Gattorno G, Díaz D, Rendón L, Hernández-Segura GO (2002) Metallic nanoparticles from spontaneous reduction of silver(I) in DMSO interaction between nitric oxide and silver nanoparticles. J Phys Chem B 106:2482–2487

97. Pol VG, Srivastava DN, Palchik O, Palchik V, Slifkin MA, Weiss AM, Gedanken A (2002) Sonochemical deposition of silver nanoparticles on silica spheres. Langmuir 18:3352–3357

98. Sarathy KV, Kulkarni GU, Rao CNR (1997) A novel method of preparing thiol-derivatised nanoparticles of gold, platinum and silver forming superstructures. Chem Commun 537–538

99. Evanoff DD, Chumanov G (2005) Synthesis and optical properties of silver nanoparticles and arrays. Chem Phys Chem 6:1221–1231

100. Evanoff DD, Chumanov G (2004) Size-controlled synthesis of nanoparticles 2 measurement of extinction, scattering, and absorption cross sections. J Phys Chem B 108:13957–13962

101. Morones JR, Elechiguerra JL, Camacho A, Holt K, Kouri JB, Ramirez JT, Yacaman MJ (2005) The bactericidal effect of silver nanoparticles. Nanotechnology 16:2346–2353

102. Jeong SH, Hwang YH, Yi SC (2005) Antibacterial properties of padded PP/PE nonwovens incorporating nano-sized silver colloids. J Mater Sci 40:5413–5418

103. Hiramatsu H, Osterloh FE (2004) A simple large-scale synthesis of nearly monodisperse gold and silver nanoparticles with adjustable sizes and with exchangeable surfactants. Chem Mater 16:2509–2511

104. Evanoff DD, Chumanov G (2004) Size-controlled synthesis of nanoparticles 1 "Silver-only" aqueous suspensions via hydrogen reduction. J Phys Chem B 108:13948–13956

105. Germain V, Brioude A, Ingert D, Pileni MP (2005) Silver nanodisks: size selection via centrifugation and optical properties. J Chem Phys 122(12):124707

106. Sarkar A, Kapoor S, Mukherjee T (2005) Synthesis of silver nanoprisms in formamide. J Colloid Interface Sci 287:496–500

107. Jiang LP, Xu S, Zhu JM, Zhang JR, Zhu JJ, Chen HY (2004) Ultrasonic-assisted synthesis of monodisperse single-crystalline silver nanoplates and gold nanorings. Inorg Chem 43:5877–5883

108. Im SH, Lee YT, Wiley B, Xia Y (2005) Large-scale synthesis of silver nanocubes: the role of HCl in promoting cube perfection and monodispersity. Angew Chem, Int Ed 44:2154–2157

109. Shon YS, Cutler E (2004) Aqueous synthesis of alkanethiolate-protected Ag nanoparticles using Bunte salts. Langmuir 20:6626–6630

110. Jana NR, Peng XG (2003) Single-phase and gram-scale routes toward nearly monodisperse Au and other noble metal nanocrystals. J Am Chem Soc 125:14280–14281

111. Yang Q, Wang F, Tang K, Wang C, Chen Z, Qian Y (2002) The formation of fractal Ag nanocrystallites via γ-irradiation route in isopropyl alcohol. Mater Chem Phys 78:495–500

112. Callegari A, Tonti D, Chergui M (2003) Photochemically grown silver nanoparticles with wavelength-controlled size and shape. Nano Lett 3:1565–1568
113. Gao F, Lu QY, Komarneni S (2005) Interface reaction for the self-assembly of silver nanocrystals under microwave-assisted solvothermal conditions. Chem Mater 17:856–860
114. Malandrino G, Finocchiaro ST, Fragala IL (2004) Silver nanowires by a sonoself-reduction template process. J Mater Chem 14:2726–2728
115. Zhang ZP, Han MY (2003) Deposition of CdSe thin films using a novel single-source precursor, [MeCd{(SeP^{i}Pr$_2$)$_2$N}]$_2$. J Mater Chem 13:641–643
116. Yu D, Yam VW (2004) Controlled synthesis of monodisperse silver nanocubes in water. J Am Chem Soc 126:13200–13201
117. Sun Y, Mayers B, Xia Y (2003) Transformation of silver nanospheres into nanobelts and triangular nanoplates through a thermal process. Nano Lett 3:675–679
118. Giersig M, Pastoriza-Santos I, Liz-Marzán LM (2004) Evidence of an aggregative mechanism during the formation of silver nanowires in N,N-dimethylformamide. J Mater Chem 14:607–610
119. Tan YW, Dai XH, Li YF, Zhu DB (2003) Preparation of gold, platinum, palladium and silver nanoparticles by the reduction of their salts with a weak reductant-potassium bitartrate. J Mater Chem 13:1069–1075
120. Lee GJ, Shin SI, Kim YC, Oh SG (2004) Preparation of silver nanorods through the control of temperature and pH of reaction medium. Mater Chem Phys 84:197–204
121. Sun YG, Xia YN (2002) Large-scale synthesis of uniform silver nanowires through a soft, self-seeding, polyol process. Adv Mater 14:833–837
122. Sun YG, Yin YD, Mayers BT, Herricks T, Xia YN (2002) Uniform silver nanowires synthesis by reducing AgNO$_3$ with ethylene glycol in the presence of seeds and poly(vinyl pyrrolidone). Chem Mater 14:4736–4745
123. Tan YW, Li YF, Zhu DB (2003) Preparation of silver nanocrystals in the presence of aniline. J Colloid Interface Sci 258:244–251
124. Raveendran P, Fu J, Wallen SL (2003) Completely "green" synthesis and stabilization of metal nanoparticles. J Am Chem Soc 125:13940–13941
125. Manna A, Imae T, Aoi K, Okada M, Yogo T (2001) Synthesis of dendrimer-passivated noble metal nanoparticles in a polar medium: comparison of size between silver and gold particles. Chem Mater 13:1674–1681
126. Zhang Z, Patel RC, Kothari R, Johnson CP, Friberg SE, Aikens PA (2000) Stable silver clusters and nanoparticles prepared in polyacrylate and inverse micellar solutions. J Phys Chem B 104:1176–1182
127. Zheng J, Dickson RM (2002) Individual water-soluble dendrimer-encapsulated silver nanodot fluorescence. J Am Chem Soc 124:13982–13983
128. Korchev AS, Bozack MJ, Slaten BL, Mills G (2004) Polymer-initiated photogeneration of silver nanoparticles in SPEEK/PVA films: direct metal photopatterning. J Am Chem Soc 126:10–11
129. Shameli K, Ahmad MB, Yunus W, Ibrahim NA, Gharayebi Y, Sedaghat S (2010) Synthesis of silver/montmorillonite nanocomposites using g-irradiation. Int J Nanomed 5:1067–1077
130. Pillai SK, Sinha Ray S, Scriba M, Bandyopadhyay J, Roux-van der Merwe MP, Badenhorst J (2013) Microwave assisted green synthesis and characterization of silver/montmorillonite heterostructures with improved antimicrobial properties. Appl Clay Sci 83–84:315–321
131. Tamer U, Onay A, Ciftci H, Bozkurt AG, Cetin D, Suludere Z, Boyaci IH, Daniel P, Lagarde F, Yaacoub N, Greneche JM (2014) High-yield aqueous synthesis of multi-branched iron oxide core-gold shell nanoparticles: SERS substrate for immobilization and magnetic separation of bacteria. J Nanopart Res 16(2624):1–11
132. Murawala P, Phadnis SM, Bhonde RR, Prasad BLV (2009) In situ synthesis of water dispersible bovine serum albumin capped gold and silver nanoparticles and their cytocompatibility studies. Coll Surf B 73:224–228

133. De-Llanos R, Sánchez-Cortes S, Domingo C, García-Ramos JV, Sevilla P (2011) Surface plasmon effects on the binding of antitumoral drug emodin to bovine serum albumin. J Phys Chem C 115:12419–12429
134. Peters T Jr (ed) (1996) All about albumin: biochemistry. Genetics and Medical Applications Academic Press, San Diego and London
135. Gebauer JS, Malissek M, Simon S, Knauer SK, Maskos M, Stauber RH, Peukert W, Treuel L (2012) Impact of the nanoparticle-protein corona on colloidal stability and protein structure. Langmuir 28:9673–9679
136. Nayak NC, Shin K (2008) Human serum albumin mediated selfassembly of gold nanoparticles into hollow spheres. Nanotechnology 46:265603
137. Schlapbach L, Zuttel A (2001) Hydrogen-storage materials for mobile applications. Nature 414:353–358
138. Felder Hoff M, Bogdanović B (2009) High temperature metal hydrides as heat storage materials for solar and related applications. Int J Mol Sci 10:325–344
139. Oumellal Y, Rougier A, Nazri GA, Tarascon JM, Aymard L (2008) Metal hydrides for lithium-ion batteries. Nature Mater 7:916–921
140. Wadell C, Syrenova S, Langhammer C (2014) Plasmonic hydrogen sensing with nanostructured metal hydrides. ACS Nano 8:11925–11940
141. Yoshimura K, Langhammer C, Dam B (2013) Metal hydrides for smart window and sensor applications. MRS Bull 38:495–503
142. Huiberts JN, Griessen R, Rector JH, Koeman NJ (1996) Yttrium and lanthanum hydride films with switchable optical properties. Nature 380:231–234
143. Boeris PS, Liffourrena AS, Salvano MA, Lucchesi GI (2009) Physiological role of phosphatidylcholine in the Pseudomonas putida A ATCC 12633 Response to tetradecyltrimethylammonium bromide and aluminium. Letters Appl Microbiol 49:491–496
144. Danquah MK, Zhang XA, Mahato RI (2010) Extravasation of polymeric nanomedicines across tumor vasculature. Adv Drug Deliv Rev 63:623–639
145. Bérubé V, Radtke G, Dresselhaus M, Chen G (2007) Size effects on the hydrogen storage properties of nanostructured metal hydrides: a review. Int J Energ Res 31:637–663
146. Díez I, Jiang H, Ras RHA (2010) Enhanced emission of silver nanoclusters through quantitative phase transfer. ChemPhysChem 11:3100–3104
147. Udaya Bhaskara Rao T, Pradeep T (2010) Luminescent Ag7 and Ag8 clusters by interfacial synthesis. Angew Chem Int Ed 49:3925–3929
148. Yu J, Choi S, Richards CI, Antoku Y, Dickson RM (2008) Live cell surface labeling with fluorescent Ag nanocluster conjugates. Photochem Photobiol 84:1435–1439
149. Díez I, Ras RHA (2011) Fluorescent silver nanoclusters. Nanoscale 3:1963–1970
150. Ershov BG, Henglein A (1998) Time-resolved investigation of early processes in the reduction of Ag$^+$ on polyacrylate in aqueous solution. J Phys Chem B 102:10667–10671
151. Sharma J, Yeh HC, Yoo H, Werner JH, Martinez JS (2010) A complementary palette of fluorescent silver nanoclusters. Chem Commun 46:3280–3282
152. Díez I, Pusa M, Kulmala S, Jiang H, Walther A, Goldmann AS, Müller AHE, Ikkala O, Ras RHA (2009) Color tunability and electrochemiluminescence of silver nanoclusters. Angew Chem, Int Ed 48:2122–2125
153. Wu Z, Jin R (2010) On the ligand's role in the fluorescence of gold nanoclusters. Nano Lett 10:2568–2573
154. Pastoriza-Santos I, Liz-Marzán LM (2002) Formation of PVP-protected metal nanoparticles in DMF. Langmuir 18:2888–2894
155. Pastoriza-Santos I, Liz-Marzán LM (2002) Synthesis of silver nanoprisms in DMF. Nano Lett 2:903–905
156. Yu YT, Xu BQ (2006) Shape-controlled synthesis of Pt nanocrystals: an evolution of the tetrahedral shape. Appl Organomet Chem 20:638–647
157. Fu X, Wang Y, Wu N, Gui L, Tang Y (2002) Shape selective preparation and properties of oxalate- stabilized Pt colloid. Langmui 18:4619–4624

158. Ahmadi TS, Wang ZL, Green TC, Henglein A, El-Sayed MA (1996) Shape-controlled synthesis of colloidal platinum nanoparticles. Science 272:1924–1926

159. Shan J, Pickup PG (2000) Characterization of polymer supported catalysts by cyclic voltammetry and rotating disk voltammetry. Electrochim Acta 46:119–125

160. Antolini E, Cardelline F, Giacometti E, Squadrito G (2002) Study on the formation of Pt/C catalysts by non-oxidized active carbon support and a sulfur-based reducing agent. J Mater Sci 37:133–139

161. Andreas HA, Birss VI (2005) Synthesis and characterization of alkoxide-derived Pt nanoparticles. J Phys Chem B 109:3743–3750

162. Lee H, Habas SE, Somorjai GA, Yang P (2008) Localized Pd overgrowth on cubic Pt nanocrystals for enhanced electrocatalytic oxidation of formic acid. J Am Chem Soc 130:5406–5407

163. Sajanlal PR, Pradeep T (2008) Electric-field-assisted growth of highly uniform and oriented gold nanotriangles on conducting glass substrates. Adv Mater 20:980–983

164. Toshima N, Yonezawa T (1998) Bimetallic nanoparticles-novel materials for chemical and physical applications. New J Chem 22:1179–1201

165. Ducamp-Sanguesa C, Herrera-Urbina R, Figlarz M (1992) Synthesis and characterization of fine and monodisperse silver particles of uniform shape. J Solid State Chem 100:272–280

166. Xia Y, Xiong Y, Lim B, Skrabalak SE (2008) Shape-controlled synthesis of metal nanocrystals: simple chemistry meets complex physics? Angew Chem Int Ed 48:60–103

167. Sau TK, Murphy CJ (2007) Role of ions in the colloidal synthesis of gold nanowires. Philos Mag 87:2143–2158

168. Mpourmpakis G, Vlachos DG (2008) Insights into the early stages of metal nanoparticle formation via first-principle calculations: the roles of citrate and water. Langmuir 24:7465–7473

169. Slot JW, Geuze HJ (1985) A new method of preparing gold probes for multiple-labeling cytochemistry. Eur J Cell Biol 38:87–93

170. Brown KR, Fox AP, Natan MJ (1996) Morphology-dependent electrochemistry of cytochrome-c at au colloid-modified SnO$_2$ electrodes. J Am Chem Soc 118:1154–1157

171. Sivaraman SK, Kumar S, Santhanam V (2011) Monodisperse sub-10 nm gold nanoparticles by reversing the order of addition in Turkevich method—the role of chloroauric acid. J Colloid Interface Sci 361:543–547

172. Song W, Zhang X, Yin H, Sa P, Liu Z (2009) Preparation and storage of silver nanoparticles in aqeous polymers. Chin J Chem 27:717–721

173. Jiang XC, Chen CY, Chen WM, Yu AB (2009) Role of citric acid in the formation of silver nanoplates through a synergistic reduction approach. Langmuir 26:4400–4408

174. Ramteke C, Chakrabarti T, Sarangi BK, Pandey RA (2013) Synthesis of silver nanoparticles from the aqueous extract of leaves of Ocimum sanctum for enhanced antibacterial activity. J Chem Article ID 278925, 7 pages

175. Darmanin T, Nativo P, Gilliland D, Ceccone G, Pascual C, De Berardis B, Guittard F, Rossi F (2012) Microwave-assisted synthesis of silver nanoprisms/nanoplates using a modified polyol process. Colloids Surf A 395:145–151

176. da Costa LP, Formiga ALB, Mazali IO, Sigoli FA (2011) Spontaneous formation of highly dispersed spheroidal metallic silver nanoparticles in surfactant-free N,N-dimethylacetamide. Synth Met 161:1517–1521

177. Solanki JN, Murthy ZVP (2011) Controlled size silver nanoparticles synthesis with water-in-oil microemulsion method: a topical review. Ind Eng Chem Res 50:12311–12323

178. Papa M, Pradell T, Crespo D, Calderon-Moreno JM (2007) Stable silver colloidal dispersions using short chain polyethylene glycol. Colloids Surf A 303:184–190

179. Kheiralla ZMH, Rushdy AA, Betiha MA, Yakob NAN (2014) High-performance antibacterial of montmorillonite decorated with silver nanoparticles using microwave-assisted method. J Nanopart Res 16:1–14

180. Ojha AK, Srivastava SK, Koster J, Shukla MK, Leszczynski J, Asthana BP, Kiefer W (2004) Investigation of hydrogen bonding and self-association in neat HCONH$_2$ and the binary

mixture (HCONH$_2$ + CH$_3$OH) by concentration dependent Raman study and ab initio calculations. J Mol Struct 689:127–135

181. Sarkar A, Kapoor S, Mukherjee T (2005) Preparation, characterization, and surface modification of silver nanoparticles in formamide. J Phys Chem B 109:7698–7704

182. Zheng N, Fan J, Stucky GD (2006) One-step one-phase synthesis of monodisperse noble-metallic nanoparticles and their colloidal crystals. J Am Chem Soc 128:6550–6551

183. Newman JDS, Blanchard GJ (2006) Formation of gold nanoparticles using amine reducing agents. Langmuir 22:5882–5887

184. Subramaniam C, Tom RT, Pradeep T (2005) On the formation of protected gold nanoparticles from AuCl$_4$− by the reduction using aromatic amines. J Nanopart Res 7:209–217

185. Goy-López S, Taboada P, Cambón A, Juárez J, Alvarez-Lorenzo C, Concheiro A, Mosquera V (2009) Modulation of size and shape of Au nanoparticles using amino-X-shaped poly(ethylene oxide)-poly(propylene oxide) block copolymers. J Phys Chem B 114:66–76

186. Barros Scaravelli RC, Dazzi R, Giacomelli FC, Machado G, Giacomelli C, Schmidt V (2013) Direct synthesis of coated gold nanoparticles mediated by polymers with amino groups. J Colloid Interface Sci 397:114–121

187. Dahmane S, Lasia A, Zhao Y (2008) Electrochemically active block copolymer micelles containing coumarin moieties. Macromol Chem Phys 209:1065–1072

188. Xiao ZP, Cai ZH, Liang H, Lu J (2010) Amphiphilic block copolymers with aldehyde and ferrocene-functionalized hydrophobic block and their redox-responsive micelles. J Mater Chem 20:8375–8381

189. Liu SY, Armes SP (2003) Synthesis and aqueous solution behavior of a pH-responsive schizophrenic diblock copolymer. Langmuir 19:4432–4438

190. Cabral H, Kataoka K (2010) Multifunctional nanoassemblies of block copolymers for future cancer therapy. Sci Technol Adv Mater 11:014109

191. Wen F, Zhang W, Wei G, Wang Y, Zhang J, Zhang M, Shi L (2008) Synthesis of noble metal nanoparticles embedded in the shell layer of core-shell poly (styrene-co-4-vinylpyridine) micospheres and their application in catalysis. Chem Mater 20:2144–2150

192. Zhang M, Kataoka K (2009) Nano-structured composites based on calcium phosphate for cellular delivery of therapeutic and diagnostic agents. Nano Today 4:508–517

193. Hu Y, Jiang Z, Chen R, Wu W, Jiang X (2010) Degradation and degradation-induced re-assembly of PVP-PCL micelles. Biomacromolecules 11:481–488

194. Yu Y, Wu G, Liu K, Zhang X (2010) Force required to disassemble block copolymer micelles in water. Langmuir 26:9183–9186

195. Bae KH, Lee Y, Park TG (2007) Oil-encapsulating PEO-PPO-PEO/PEG shell cross-linked nanocapsules for target-specific delivery of paclitaxel. Biomacromolecules 8:650–656

196. Bae KH, Choi SH, Park SY, Lee Y, Park TG (2006) Thermosensitive pluronic micelles stabilized by shell cross-linking with gold nanoparticles. Langmuir 22:6380–6384

197. Wang L, Chen X, Zhan J, Sui Z, Zhao J, Sun Z (2004) Controllable morphology formation of gold nano- and micro-plates in amphiphilic block copolymer-based liquid crystalline phase. Chem Lett 33:720–721

198. Sakai T, Alexandridis P (2004) Single-step synthesis and stabilization of metal nanoparticles in aqueous pluronic block copolymer solutions at ambient temperature. Langmuir 20:8426–8430

199. Longenberger L, Mills G (1995) Formation of metal particles in aqueous solutions by reactions of metal complexes with polymers. J Phys Chem 99:475–478

200. Sakai T, Alexandridis P (2005) Mechanism of gold metal ion reduction, nanoparticle growth and size control in aqueous amphiphilic block copolymer solutions at ambient conditions. J Phys Chem B 109:7766–7777

201. Read ES, Armes SP (2007) Recent advances in shell cross-linked micelles. Chem Commun 3021–3035

202. Xu JP, Yang X, Lv LP, Wei Y, Xu FM, Ji J (2010) Gold-nanoparticle-stabilized pluronic micelles exhibiting glutathione triggered morphology evolution properties. Langmuir 26:16841–16847

203. Falletta E, Ridi F, Fratini E, Vannucci C, Canton P, Bianchi S, Castelvetro V, Baglioni P (2011) A tri-block copolymer templated synthesis of gold nanostructures. J Colloid Interface Sci 357:88–94

204. Wang Y, Han P, Xu H, Wang Z, Zhang XV, Kabanov A (2010) Photocontrolled self-assembly and disassembly of block ionomer complex vesicles: a facile approach toward supramolecular polymer nanocontainers. Langmuir 26:709–715

205. Schild HG, Muthukumar M, Tirrell DA (1991) Cononsolvency in mixed aqueous solutions of Poly(N-isopropylacrylamide). Macromolecules 24:948–952

206. Kaholek M, Lee WK, Ahn SJ, Ma H, Caster KC, LaMattina B, Zauscher S (2004) Stimulus-responsive poly(N-isopropylacrylamide) brushes and nanopatterns prepared by surface-initiated polymerization. Chem Mater 16:3688–3696

207. Xiong Y, Washio I, Chen J, Sadilek M, Xia Y (2007) Trimeric clusters of silver in aqueous AgNO$_3$ solutions and their role as nuclei in forming triangular nanoplates of silver. Angew Chem Int Ed 46:4917–4921

208. Goia DV, Matijevic E (1998) Preparation of nanodispersed metal particles. New J Chem 22:1203–1215

209. Dong WF, Kishimura A, Anraku Y, Chuanoi S, Kataoka K (2009) Monodispersed polymeric nanocapsules: spontaneous evolution and morphology transition from reducible hetero-PEG PIC micelles by controlled degradation. J Am Chem Soc 131:3804–3805

210. Sardar R, Tyler B, Shumaker-Parry JS (2007) Versatile solid phase synthesis of gold nanoparticle dimers using an asymmetric functionalization approach. J Am Chem Soc 129:5356–5357

211. Xu Y, Guo L, Huang L, Palanisamy K, Kim D, Chen G (2013) Facile preparation of partially functionalized gold nanoparticles via a surfactant-assisted solid phase approach. J Colloid Interface Sci 409:32–37

212. Templeton AC, Zamborini FP, Wuelfing WP, Murray RW (2000) Controlled and reversible formation of nanoparticle aggregates and films using Cu^{2+}-carboxylate chemistry. Langmuir 16:6682–6688

213. Zamborini FP, Smart LE, Leopold MC, Murray RW (2003) Distance-dependent electron hopping conductivity and nanoscale lithography of chemically-linked gold monolayer protected cluster films. Anal Chim Acta 496:3–16

214. Chen SW, Pei RJ, Zhao TF, Dyer DJ (2002) Gold nanoparticle assemblies by metal ion—pyridine complexation and their rectified quantized charging in aqueous solutions. J Phys Chem B 106:1903–1908

215. Rashid MH, Bhattacharjee RR, Kotal A, Mandal TK (2006) Synthesis of spongy gold nanocrystals with pronounced catalytic activities. Langmuir 22:7141–7143

216. Guo R, Zhang L, Zhu Z, Jiang X (2008) Direct facile approach to the fabrication of chitosan-gold hybrid nanospheres. Langmuir 24:3459–3464

217. Hong R, Han G, Fernandez JM, Kim BJ, Forbes NS, Rotello VM (2006) Glutathione-mediated delivery and release using monolayer protected nanoparticle carriers. J Am Chem Soc 128:1078–1079

218. Murphy CJ, Sau TK, Gole AM, Orendorff CJ, Gao J, Gou L, Hunyadi SE, Li T (2005) Anisotropic metal nanoparticles: synthesis, assembly, and optical applications. J Phys Chem B 109:13857–13870

219. Bakshi MS, Kaur H, Khullar P, Banipal TS, Kaur G, Singh N (2011) Protein films of bovine serum albumen conjugated gold nanoparticles: a synthetic route from bioconjugated nanoparticles to biodegradable protein films. J Phys Chem C 115:2982–2992

220. Kemp MM, Kumar A, Mousa S, Park TJ, Ajayan P, Kubotera N, Mousa SA, Linhardt RJ (2009) Synthesis of gold and silver nanoparticles stabilized with glycosaminoglycans having distinctive biological activities. Biomacromolecules 10:589–595

221. Harmatz D, Blauer G (1975) Optical properties of bilirubin-serum albumin complexes in aqueous solution. A comparison among albumins from different species. Arch Biochem Biophys 170:375–383

222. Alarcon EI, Bueno-Alejo CJ, Noel CW, Stamplecoskie KG, Pacioni NL, Poblete H, Scaiano JC (2013) Human serum albumin as protecting agent of silvernanoparticles: role of the protein conformation and aminegroups in the nanoparticle stabilization. J Nanopart Res 15:1374–1377

223. Jockusch S, Landis MS, Freiermuth B, Turro NJ (2001) Photochemistry and photophysics of a-hydroxy ketones. Macromolecules 34:1619–1626

224. Lynch I, Dawson KA (2008) Protein-nanoparticle interactions. Nano Today 3:40–47

225. Ganeshkumar M, Ponrasu T, Raja MD, Subamekala MK, Suguna L (2014) Green synthesis of pullulan stabilized gold nanoparticles for cancer targeted drug delivery. Spectrochimica Acta Part A: Mol Biomol Spectrosc 130:64–71

226. Yuan H, Khoury CG, Hwang H, Wilson CM, Grant GA, Vo-Dinh T (2012) Gold nanostars: surfactant-free synthesis, 3D modelling, and two-photon photoluminescence imaging. Nanotechnology 23:075102

227. Mahmoud MA, El-Sayed MA (2012) Substrate effect on the plasmonic sensing ability of hollow nanoparticles of different shapes. J Phys Chem B 117:4468–4477

228. Sun Y, Zhang L, Zhou H, Zhu Y, Sutter E, Ji Y, Rafailovich MH, Sokolov JC (2007) Seedless and templateless synthesis of rectangular palladium nanoparticles. Chem Mater 19:2065–2070

229. Skrabalak SE, Au L, Li X, Xia Y (2007) Facile synthesis of Ag nanocubes and Au nanocages. Nat Protoc 2:2182–2190

230. Millstone JE, Wei W, Jones MR, Yoo H, Mirkin CA (2008) Iodide ions control seed-mediated growth of anisotropic gold nanoparticles. Nano Lett 8:2526–2529

231. Choi KS (2008) Shape control of inorganic materials via electrodeposition. Dalton Trans 5432–5438

232. Kou X, Zhang S, Yang Z, Tsung CK, Stucky GD, Sun L, Wang J, Yan C (2007) Glutathione- and cysteine-induced transverse overgrowth on gold nanorods. J Am Chem Soc 129:6402–6404

233. Bakshi MS, Bakshi MS, Sachar S, Kaur G, Bhandari P, Kaur G, Biesinger MC, Possmayer F, Petersen NO (2008) Dependence of s. Cryst Growth Des 8:1713–1719

234. Gao JX, Bender CM, Murphy CJ (2003) Dependence of the gold nanorod aspect ratio on the nature of the directing surfactant in aqueous solution. Langmuir 19:9065–9070

235. Qian Z, Park SJ (2014) Silver seeds and aromatic surfactants facilitate the growth of anisotropic metal nanoparticles: gold triangular nanoprisms and ultrathin nanowires. Chem Mater 26:6172–6177

236. Feng L, Wu X, Ren L, Xiang Y, He W, Zhang K, Zhou W, Xie S (2008) Well-controlled synthesis of Au@ Pt nanostructures by gold-nanorod-seeded growth. Chem Eur J 14:9764–9771

237. Feng X, Li X, Shi H, Huang H, Wu X, Song W (2014) Highly accessible Pt nanodots homogeneously decorated on Au nanorods surface for sensing. Analytica Chimica Acta 852:37–44

238. Wang S, Kristian N, Jiang S, Wang X (2009) Controlled synthesis of dendritic Au@Pt core-shell nanomaterials for use as an effective fuel cell electrocatalyst. Nanotechnology 20:25605

239. Maclennan A, Banerjee A, Scott RW (2013) Aerobic oxidation of α, β-unsaturated alcohols using sequentially-grown AuPd nanoparticles in water and tetraalkylphosphonium ionic liquids. Catal Today 207:170–179

240. Dupont J, Fonseca GS, Umpierre AP, Fichtner PFP, Teixeira SR (2002) Transition-metal nanoparticles in imidazolium ionic liquids: recyclable catalysts for biphasic hydrogenation reactions. J Am Chem Soc 124:4228–4229

241. Itoh H, Naka K, Chujo Y (2004) Synthesis of gold nanoparticles modified with ionic liquid based on the imidazolium cation. J Am Chem Soc 126:3026–3027

242. Tatumi R, Fujihara H (2005) Remarkably stable gold nanoparticles functionalized with a zwitterionic liquid based on imidazolium sulfonate in a high concentration of aqueous electrolyte and ionic liquid. Chem Commun (Camb) 83–85
243. Scheeren CW, Machado G, Dupont J, Fichtner PFP, Texeira SR (2003) Nanoscale Pt (0) particles prepared in imidazolium room temperature ionic liquids: synthesis from an organometallic precursor, characterization, and catalytic properties in hydrogenation reactions. Inorg Chem 42:4738–4742
244. Guo S, Wang E (2007) Synthesis and electrochemical applications of gold nanoparticles. Anal Chim Acta 598:181–192
245. Li Z, Liu Z, Zhang J, Han B, Du J, Gao Y, Jiang T (2005) Synthesis of single-crystal gold nanosheets of large size in ionic liquids. J Phys Chem B 109:14445–14448
246. Zhu J, Shen Y, Xie A, Qiu L, Zhang Q, Zhang S (2007) Photoinduced synthesis of anisotropic gold nanoparticles in room-temperature ionic liquid. J Phys Chem B 111:7629–7633
247. Tsuda T, Seino S, Kuwabata S (2009) Gold nanoparticles prepared with a room-temperature ionic liquid-radiation irradiation method. Chem Commun 6792–6794
248. Yang G, Zhao F, Zeng B (2013) Electrochemical determination of cefotaxime based on a three-dimensional molecularly imprinted film sensor. Biosens Bioelectron C 53:447–452
249. Okitsu K, Mizukoshi Y, Yamamoto TA, Maeda Y, Nagata Y (2007) Sonochemical synthesis of gold nanoparticles on chitosan. Mater Lett 61:3429–3431
250. Jin Y, Li Z, Hu L, Shi X, Guan W, Du Y (2013) Synthesis of chitosan-stabilized gold nanoparticles by atmospheric plasma. Carbohydr Polym 91:152–156
251. Spano F, Massaro A, Blasi L, Malerba M, Cingolani R, Athanassiou A (2012) In situ formation and size control of gold nanoparticles into chitosan for nanocomposite surfaces with tailored wettability. Langmuir 28:3911–3917
252. Di Carlo G, Curulli A, Toro RG, Bianchini C, de Caro T, Padeletti G, Zane D, Ingo GM (2012) Green synthesis of gold-chitosan nanocomposites for caffeic acid sensing. Langmuir 28:5471–5479
253. Yang G, Zhao F, Zeng B (2014) Facile fabrication of a novel anisotropic gold nanoparticle-chitosan-ionic liquid/graphene modified electrode for the determination of theophylline and caffeine. Talanta 127:116–122
254. Wang L, Wen W, Xiong H, Zhang X, Gu H, Wang S (2013) A novel amperometric biosensor for superoxide anion based on superoxide dismutase immobilized on gold nanoparticle-chitosan-ionic liquid biocomposite film. Anal Chim Acta 758:66–71
255. Aherne D, Ledwith DM, Gara M, Kelly JM (2008) Optical properties and growth aspects of silver nanoprisms produced by a highly reproducible and rapid synthesis at room temperature. Adv Funct Mater 18:2005–2016
256. Miranda OR, Dollahon NR, Ahmadi TS (2006) Critical concentrations and role of ascorbic acid (vitamin C) in the crystallization of gold nanorods within hexadecyltrimethyl ammonium bromide (CTAB)/tetraoctyl ammonium bromide (TOAB) micelles. Cryst Growth Des 6:2747–2753
257. Smith DK, Korgel BA (2008) The importance of the CTAB surfactant on the colloidal seed-mediated synthesis of gold nanorods. Langmuir 24:644–649
258. Park HJ, Ah CS, Kim WJ, Choi IS, Lee KP, Yun WS (2006) Temperature-induced control of aspect ratio of gold nanorods. J Vac Sci Technol A 24:1323–1326
259. Miyazaki A, Nakano Y (2000) Morphology of platinum nanoparticles protected by poly(N-isopropylacrylamide). Langmuir 16:7109–7111
260. Gao Y, Jiang P, Song L, Wang JX, Liu LF, Liu DF, Xiang YJ, Zhang ZX, Zhao XW, Dou XY, Luo SD, Zhou WY, Xie SS (2006) Studies on silver nanodecahedrons synthesized by PVP-assisted N, N-dimethylformamide (DMF) reduction. J Cryst Growth 289:376–380
261. Grochala W, Kudelski A, Bukowska J (1998) Anion-induced charge-transfer enhancement in SERS and SERRS spectra of Rhodamine 6G on a silver electrode: how important is it? J Raman Spectrosc 29:681–685
262. Fang Y (1999) Acid with visible and near-infrared excitations. J Raman Spectrosc 30:85–89

263. Pergolese B, Muniz-Miranda M, Bigotto A (2004) Study of the adsorption of 1,2,3-triazole on silver and gold colloidal nanoparticles by means of surface enhanced raman scattering. J Phys Chem B 108:5698–5702
264. Pergolese B, Muniz-Miranda M, Bigotto A (2005) Surface enhanced raman scattering investigation of the halide anion effect on the adsorption of 1,2,3-triazole on silver and gold colloidal nanoparticles. J Phys Chem B 109:9665–9671
265. Sardar R, Shumaker-Parry JS (2009) 9-BBN induced synthesis of nearly monodisperse ω-functionalized alkylthiols stabilized gold nanoparticles. Chem Mater 21:1167–1169
266. Sardar R, Shumaker-Parry JS (2011) Spectroscopic and microscopic investigation of gold nanoparticle formation: ligand and temperature effects on rate and particle size. J Am Chem Soc 133:8179–8190
267. Dahl JA, Maddux BLS, Hutchison JE (2007) Toward greener nanosynthesis. Chem Rev 107:2228–2269
268. Roth PJ, Theato P (2008) Versatile synthesis of functional gold nanoparticles: grafting polymers from and onto. Chem Mater 20:1614–1621
269. Sarathy KV, Raina G, Yadav RT, Kulkarni GU, Rao CNR (1997) Thiol-derivatized nanocrystalline arrays of gold, silver, and platinum. J Phys Chem B 101:9876–9880
270. Woehrle GH, Brown LO, Hutchison JE (2005) Thiol-functionalized, 15-nm gold nanoparticles through ligand exchange reactions: scope and mechanism of ligand exchang. J Am Chem Soc 127:2172–2183
271. Zheng M, Huang X (2004) Nanoparticles comprising a mixed monolayer for specific bindings with biomolecules. J Am Chem Soc 126:12047–12054
272. Park S, Ruoff RS (2009) Chemical methods for the production of graphened. Nat Nanotechnol 4:217–224
273. Muhammad S, Chandra V, Kemp KC, Kim KS (2013) Synthesis of N-doped microporous carbon via chemical activation of polyindole-modified graphene oxide sheets for selective carbon dioxide adsorption. Nanotechnology 24(25):255702
274. Liu Y, Ma J, Wu T, Wang X, Huang G, Liu Y, Qiu H, Li Y, Wang W, Gao J (2013) Cost-effective reduced graphene oxide-coated polyurethane sponge as a highly efficient and reusable oil-absorbent. ACS Appl Mat Interfaces 5:10018–10026
275. Tan R, Li CY, Luo JQ, Kong Y, Zheng WG, Yin DH (2013) An effective heterogeneous L-proline catalyst for the direct asymmetric aldol reaction using graphene oxide as support. J Catal 298:138–147
276. Mayavan S, Jang HS, Lee MJ, Choi SH, Choi SM (2013) Enhancing the catalytic activity of Pt nanoparticles using poly sodium styrene sulfonate stabilized graphene supports for methanol oxidation. J Mater Chem A 1:3489–3494
277. Kim JY, Cote LJ, Kim F, Yuan W, Shull KR, Huang JX (2010) Graphene oxide sheets at interfaces. J Am Chem Soc 132:8180–8186
278. Gudarzi MM, Sharif F (2011) Self assembly of graphene oxide at the liquid–liquid interface: a new route to the fabrication of graphene based composites. Soft Matter 7:3432–3440
279. Zhang LY, Shi TJ, Wu SL, Zhou HO (2013) Sulfonated graphene oxide: the new and effective material for synthesis of polystyrene-based nanocomposites. Colloid Polym Sci 291:2061–2068
280. Tang M, Wang X, Wu F, Liu Y, Zhang S, Pang X, Li X, Qiu H (2014) Au nanoparticle/graphene oxide hybrids as stabilizers for Pickering emulsions and Au nanoparticle/graphene oxide@polystyrene microspheres. Carbon 71:238–248
281. Liu D, Jiang X, Yin J (2014) One-step interfacial thiol-ene photopolymerization for metal nanoparticle-decorated microcapsules (MNP@MCs). Langmuir 30:7213–7220
282. McGilvray KL, Decan MR, Wang D, Scaiano JC (2006) Facile photochemical synthesis of unprotected aqueous gold nanoparticles. J Am Chem Soc 128:15980–15981
283. Liu DD, Yu B, Jiang XS, Yin J (2013) Responsive hybrid microcapsules by the one-step interfacial thiol—ene photopolymerization. Langmuir 29:5307–5314

284. Rehab A, Akelah A, Agag T, Betiha MJ (2007) Polymer-organoclay hybrids by polymerization into montmorillonitevinyl monomer interlayers. J Appl Polym Sci 106:3502–3514
285. Senthil Kumar P, Ray S, Sunandana CS (2001) Sb-assisted AgI nanoparticle growth in thin films. Mater Phys Mech 4:39–41
286. Neri G, Rizzo G, Arico AS, Crisafulli C, de Luca L, Donato A, Musolino MG, Pietropaolo R (2007) One-pot synthesis of naturanol from a-pinene oxide on bifunctional Pt-Sn/SiO$_2$ heterogeneous catalysts (I) the catalytic system. Appl Catal A 325:15–24
287. Xie YW, Ye RQ, Liu HL (2006) Synthesis of silver nanoparticles in reverse micelles stabilized by natural biosurfactant. Colloid Surf A 279:175–178
288. He S, Yao J, Jiang P, Shi D, Zhang H, Xie S, Pang S, Gao H (2001) Formation of silver nanoparticles and self-assembled twodimensional ordered superlattice. Langmuir 17:1571–1575
289. Choi H, Lee JP, Ko SJ, Jung JW, Park H, Yoo S, Park O, Jeong JR, Park S, Kim JY (2013) Multipositional silica-coated silver nanoparticles for high-performance polymer solar cells. Nano Lett 13:2204–2208
290. Aihara N, Torigoe K, Esumi K (1998) Preparation and characterization of gold and silver nanoparticles in layered laponite suspensions. Langmuir 14:4945–4949
291. Vadakkekara R, Chakraborty M, Parikh PA (2012) Catalytic performance of silica-supported silver nanoparticles for liquid-phase oxidation of ethylbenzene. Ind Eng Chem Res 51:5691–5698
292. Narehood DG, Kishore S, Goto H, Adair JH, Nelson JA, Gutierrez HR, Eklund PC (2009) X-ray diffraction and H-storage in ultra-small palladium particles. Int J Hydrogen Energ 34:952–960
293. Yamauchi M, Ikeda R, Kitagawa H, Takata M (2008) Nanosize effects on hydrogen storage in palladium. J Phys Chem C 112:3294–3299
294. Langhammer C, Zhdanov VP, Zori¢ I, Kasemo B (2010) Size-dependent hysteresis in the formation and decomposition of hydride in metal nanoparticles. Chem Phys Lett 488:62–66
295. Wadell C, Pingel T, Olsson E, Zoric I, Zhdanov VP, Langhammer C (2014) Thermodynamics of hydride formation and decomposition in supported sub-10 nm Pd nanoparticles of different sizes. Chem Phys Lett 603:75–81
296. Salomons E, Griessen R, De Groot DG, Magerl A (1988) Surface-tension and subsurface sites of metallic nanocrystals determined from H-absorption. Europhys Lett 5:449–454
297. Suleiman M, Faupel J, Borchers C, Krebs HU, Kirchheim R, Pundt A (2005) Hydrogen absorption behaviour in nanometer sized palladium samples stabilised in soft and hard matrix. J Alloys Compd 404–406:523–528
298. Baldi A, Narayan TC, Koh AL, Dionne JA (2014) In situ detection of hydrogen-induced phase transitions in individual palladium nanocrystals. Nat Mater 13:1143–1148
299. Bardhan R, Hedges LO, Pint CL, Javey A, Whitelam S, Urban JJ (2013) Uncovering the intrinsic size dependence of hydriding phase transformations in nanocrystals. Nat Mater 12:905–912
300. Syrenova S, Wadell C, Nugroho FAA, Gschneidtner TA, Diaz Fernandez YA, Nalin G, Switlik D, Westerlund F, Antosiewicz TJ, Zhdanov VP, Moth-Poulsen K, Langhammer C (2015) Hydride formation thermodynamics and hysteresis in individual Pd nanocrystals with different size and shape. Nat Mat 14:1236–1244
301. Gschneidtner TA, Diaz Fernandez YA, Syrenova S, Westerlund F, Langhammer C, Moth-Poulsen K (2014) A versatile self-assembly strategy for the synthesis of shape-selected colloidal noble metal nanoparticle heterodimers. Langmuir 30:3041–3050
302. Ameen Poyli M, Silkin VM, Chernov IP, Echenique PM, Díez Muiño R, Aizpurua J (2012) Multiscale theoretical modeling of plasmonic sensing of hydrogen uptake in palladium nanodisks. J Phys Chem Lett 3:2556–2561
303. Pundt A (2004) Hydrogen in nano-sized metals. Adv Eng Mater 6:11–21
304. Wilcoxon JP, Provencio PP (2004) Heterogeneous growth of metal clusters from solutions of seed nanoparticles. J Am Chem Soc 126:6402–6408

305. Watzky MA, Finke RG (1997) Nanocluster size-control and "magic mumber" investigations Experimental tests of the "living-metal polymer" concept and of mechanism-based size-control predictions leading to the syntheses of iridium(0) nanoclusters centering about four sequential magic numbers. Chem Mater 9:3083–3095

306. De Yoreo JJ, Vekilov PG (2003) Principles of crystal nucleation and growth. Rev Mineral Geochem 54:57–93

307. Sau TK, Rogach AL (2010) Nonspherical noble metal nanoparticles: colloid-chemical synthesis and morphology control. Adv Mater 22:1781–1804

308. Liu XY (2000) Heterogeneous nucleation or homogeneous nucleation? J Chem Phys 112:9949–9955

309. Hyeon T, Lee SS, Park J, Chung Y, Bin Na H (2001) Synthesis of highly crystalline and monodisperse maghemite nanocrystallites without a size-selection process. J Am Chem Soc 123:12798–12801

310. Sun S, Murray CB, Weller D, Folks L, Moser A (2000) Monodisperse FePt nanoparticles and ferromagnetic FePt nanocrystal superlattices. Science 287:1989–1992

311. Shoji M, Miyajima K, Mafuné F (2008) Ionization of gold nanoparticles in solution by pulse laser excitation as studied by mass spectrometric detection of gold cluster ions. J Phys Chem C 112:1929–1932

312. Esumi K, Hosoya T, Suzuki A, Torigoe K (2000) Spontaneous formation of gold nanoparticles in aqueous solution of sugarpersubstituted poly(amidoamine) dendrimers. Langmuir 16:2978–2980

313. Tsunoyama H, Ichikuni N, Tsukuda T (2008) Microfluidic synthesis and catalytic application of PVP-stabilized, approximately 1 nm gold clusters. Langmuir 24:11327–11330

314. Zhang H, Fung KH, Hartmann J, Chan CT, Wang D (2008) Controlled chainlike agglomeration of charged gold nanoparticles via a deliberate interaction balance. J Phys Chem C 112:16830–16839

315. Yin B, Ma H, Wang S, Chen S (2003) Electrochemical synthesis of silver nanoparticles under protection of Poly(N-vinylpyrrolidone). J Phys Chem B 107:8898–8904

316. Liu X, Huang R, Zhu J (2008) Functional faceted silver nano-hexapods: synthesis, structure characterizations, and optical properties. Chem Mater 20:192–197

317. Wei G, Zhou H, Liu Z, Song Y, Wang L, Sun L, Li Z (2005) One-step synthesis of silver nanoparticles, nanorods, and nanowires on the surface of DNA network. J Phys Chem B 109:8738–8743

318. Zhang J, Liu H, Wang Z, Ming N (2007) Shape-selective synthesis of gold nanoparticles with controlled sizes, shapes, and plasmon resonances. Adv Funct Mater 17:3295–3303

319. Wang ZL (2000) Transmission electron microscopy of shape-controlled nanocrystals and their assemblies. J Phys Chem B 104:1153–1175

320. Henry CR (2005) Morphology of supported nanoparticles. Prog Surf Sci 80:92–116

321. Chen HM, Liu RS, Asakura K, Jang LY, Lee JF (2007) Controlling length of gold nanowires with large-scale: X-ray absorption spectroscopy approaches to the growth process. J Phys Chem C 111:18550–18557

322. Fan FR, Liu DY, Wu YF, Duan S, Xie ZX, Jiang ZY, Tian ZQ (2008) Epitaxial growth of heterogeneous metal nanocrystals: from gold nanooctahedra to palladium and silver nanocubes. J Am Chem Soc 130:6949–6951

323. Seifert W, Carlsson N, Miller M, Pistol ME, Samuelson L, Wallenberg LR (1996) In-situ growth of quantum dot structures by the Stranski-Krastanow growth mode. Prog Cryst Growth Charact 33:423–472

324. Sekerka RF (2005) Equilibrium and growth shapes of crystals: how do they differ and why should we care. Cryst Res Technol 40:291–306

325. Birdi KS (1998) Handbook of surface and colloid chemistry CRC Press, Boca Raton

326. Green SJ, Stokes JJ, Hostetler MJ, Pietron J, Murray RW (1997) Three-dimensional monolayers: nanometer-sized electrodes of alkanethiolate-stabilized gold cluster molecules. J Phys Chem B 101:2663–2668

327. Mirkin CA (2000) Programming the assembly of two- and threedimensional architectures with DNA and nanoscale inorganic building blocks. Inorg Chem 39:2258–2272

328. Oldenburg SJ, Averitt RD, Westcott SL, Halas NJ (1998) Nanoengineering of optical resonances. Chem Phys Lett 288:243–247

329. Resch R, Baur C, Bugacov A, Koel BE, Echternach PM, Madhukar A, Montoya N, Requicha AAG, Will P (1999) Linking and manipulation of gold multinanoparticle structures using dithiols and scanning force microscopy. J Phys Chem B 103:3647–3650

330. Frens G (1973) Controlled nucleation for the regulation of the particle size in monodisperse gold suspension. Nat Phys Sci 241:20–22

331. Ji X, Song X, Li J, Bai Y, Yang W, Peng X (2007) Size control of gold nanocrystals in citrate reduction: the third role of citrate. J Am Chem Soc 129:13939–13948

332. Chow MK, Zukoski CF (1994) Gold sol formation mechanisms: role of colloidal stability. J Colloid Interface Sci 165:97–109

333. Sardar R, Funston AM, Mulvaney P, Murray RW (2009) Gold nanoparticles: past, present, and future. Langmuir 25:13840–13851

334. Polte J, Tuaev X, Wuithschick M, Fischer A, Thuenemann AF, Rademann K, Kraehnert R, Emmerling F (2012) Formation mechanism of colloidal silver nanoparticles: analogies and differences to the growth of gold nanoparticles. ACS Nano 6:5791–5802

335. Yuk JM, Park J, Ercius P, Kim K, Hellebusch DJ, Crommie MF, Lee JY, Zettl A, Alivisatos AP (2012) High-resolution EM of colloidal nanocrystal growth using graphene liquid cells. Science 336(6077):61–64

336. Dharmaratne AC, Krick T, Dass A (2009) Nanocluster size evolution studied by mass spectrometry in room temperature Au25(SR)18 synthesis. J Am Chem Soc 131:13604–13605

337. Richards VN, Rath NP, Buhro WE (2010) Pathway from a molecular precursor to silver nanoparticles: the prominent role of aggregative growth. Chem Mater 22:3556–3567

338. Novo C, Funston AM, Pastoriza-Santos I, Liz-Marzan LM, Mulvaney P (2007) Influence of the medium refractive index on the optical properties of single gold triangular prisms on a substrate. J Phys Chem C 112:3–7

339. Skrdla PJ (2012) Roles of nucleation, denucleation, coarsening, and aggregation kinetics in nanoparticle preparations and neurological disease. Langmuir 28:4842–4857

340. Prasad BLV, Stoeva SI, Sorensen CM, Klabunde KJ (2003) Digestive-ripening agents for gold nanoparticles: alternatives to thiols. Chem Mater 15:935–942

341. Inasawa S, Sugiyama M, Yamaguchi Y (2005) Laser-induced shape transformation of gold nanoparticles below the melting point: the effect of surface melting. J Phys Chem B 109:3104–3111

342. Takami A, Kurita H, Koda S (1999) Laser-induced size reduction of noble metal particles. J Phys Chem B 103:1226–1232

343. Inasawa S, Sugiyama M, Yamaguchi Y (2005) Bimodal size distribution of gold nanoparticles under picosecond laser pulses. J Phys Chem B 109:9404–9410

344. Bonet F, Tekaia-Elhsissen K, Sarathy KV (2000) Study of interaction of ethylene glycol/PVP phase on noble metal powders prepared by polyol process. Bull Mater Sci 23:165–168

345. Garcia-Gutierrez DI, Gutierrez-Wing CE, Giovanetti L, Ramallo-López JM, Requejo FG, Jose-Yacaman M (2005) Temperature effect on the synthesis of Au-Pt bimetallic nanoparticles. J Phys Chem B 109:3813–3821

346. Min BK, Wallace WT, Santra AK, Goodman DW (2004) Role of defects in the nucleation and growth of Au nanoclusters on SiO₂ thin films. J Phys Chem B 108:16339–16343

347. Zhang Q, Yin Y (2013) Beyond spheres: Murphy's silver nanorods and nanowires. Chem Commun 49:215–217

348. Liu J, Hurt RH (2010) Ion release kinetics and particle persistence in aqueous nano-silver colloids. Environ Sci Technol 44:2169–2175

349. Levard C, Hotze EM, Lowry GV, Brown GE Jr (2012) Environmental transformations of silver nanoparticles: impact on stability and toxicity. Environ Sci Technol 46:6900–6914

350. Liu J, Sonshine DA, Shervani S, Hurt RH (2010) Controlled release of biologically active silver from nanosilver surfaces. ACS Nano 4:6903–6913

351. Borm P, Klaessig FC, Landry TD, Moudgil B, Pauluhn J, Thomas K, Trottier R, Wood S (2006) Research strategies for safety evaluation of nanomaterials, Part V: role of dissolution in biological fate and effects of nanoscale particles. Toxicol Sci 90:23–32

352. Sotiriou GA, Meyer A, Knijnenburg JT, Panke S, Pratsinis SE (2012) Quantifying the origin of released Ag^+ ions from nanosilver. Langmuir 28:15929–15936

353. Zhang W, Yao Y, Sullivan N, Chen Y (2011) Modeling the primary size effects of citrate-coated silver nanoparticles on their ion release kinetics. Environ Sci Technol 45:4422–4428

354. Ma R, Levard C, Marinakos SM, Cheng Y, Liu J, Michel FM, Brown GE Jr, Lowry GV (2011) Size-controlled dissolution of organic-coated silver nanoparticles. Environ Sci Technol 46:752–759

355. Iggland M, Mazzotti M (2012) Population balance modeling with size-dependent solubility: Ostwald ripening. Cryst Growth Des 12:1489–1500

356. Zhang Q, Yang Y, Li JR, Iurilli R, Xie S, Qin D (2013) Citratefree synthesis of silver nanoplates and the mechanistic study. ACS Appl Mater Interfaces 5:6333–6345

357. Jang E, Lim EK, Choi J, Park J, Huh YJ, Suh JS, Huh YM, Haam S (2011) Br-assisted Ostwald ripening of Au nanoparticles under H_2O_2 redox. Cryst Growth Des 12:37–39

358. He W, Zhou YT, Wamer WG, Boudreau MD, Yin JJ (2012) Mechanisms of the pH dependent generation of hydroxyl radicals and oxygen induced by Ag nanoparticles. Biomaterials 33:7547–7555

359. Shah A, Nosheen E, Qureshi R, Yasinzai MM, Lunsford SK, Dionysiou DD, Zia–ur–Rehman, Siddiq M, Badshah A, Ali S (2011) Electrochemical characterization, detoxification and anticancer activity of didodecyldimethylammonium bromide. Int J Org Chem 1:183–190

360. Ren R, Liu D, Li K, Sun J, Zhang C (2011) Adsorption of quaternary ammonium compounds onto activated sludge. J Water Res Prot 3:105–113

361. Garcia MT, Campos E, Sanchez-Leal J, Risoba I (2000) Anaerobic degradation and toxicity of commercial Ca–tionic surfactants in anaerobic screening tests. Chemosphere 41:705–710

362. Chifotides HT, Dunbar KR (2005) Interactions of metal–metal–bonded antitumor active complexes with DNA fragments and DNA. Acc Chem Res 38:146–156

363. Sun CZ, Lu CT, Zhao YZ, Guo P, Tian JL, Zhang L, Li XK, Lv HF, Dai DD, Li X (2011) Characterization of the doxorubicin–pluronic F68 conjugate micelles and their effect on doxorubicin resistant human erythroleukemic cancer cells. J Nanomedic Nanotechnol 2:1–6

364. Allen TM, Cullis PR (2004) Drug delivery systems: entering the mainstream. Science 303:1818–1822

365. Moses MA, Brem H, Langer R (2003) Advancing the field of drug delivery: taking aim at cancer. Cancer Cell 4:337–341

366. Gradishar WJ, Tjulandin S, Davidson N, Shaw H, Desai N, Bhar P, Hawkins M, O'Shaughnessy J (2005) Phase III trial of nanoparticle albumin–bound paclitaxel compared with polyethylated castor oil–based paclitaxel in women with breast cancer. J Clin Oncol 23:7794–7803

367. Duncan R (2006) Polymer conjugates as anticancer nanomedicines. Nat Rev Cancer 6688–701

368. Paz-Ares L, Ross H, O'Brien M, Riviere A, Gatzemeier U, Von Pawel J, Kaukel E, Freitag L, Digel W, Bischoff H, García-Campelo R, Iannotti N, Reiterer P, Bover I, Prendiville J, Eisenfeld AJ, Oldham FB, Bandstra B, Singer JW, Bonomi P (2008) Phase III trial comparing paclitaxel poliglumex vs docetaxel in the second–line treatment of non–small–cell lung cancer. Br J Cancer 98:1608–1613

369. Vasey PA, Kaye SB, Morrison R, Twelves C, Wilson P, Duncan R, Thomson AH, Murray LS, Hilditch TE, Murray T, Burtles S, Fraier D, Frigerio E, Cassidy J (1999) Phase I clinical and pharmacokinetic study of PK1 [N–(2–hydroxypropyl)methacrylamide copolymer doxorubicin]: first member of a new class of chemotherapeutic agents–drug–polymer conjugates. Cancer research campaign phase I/II Committee. Clin Cancer Res 5:83–94
370. Nishiyama A, Nori A, Malugin A, Kasuya Y, Kopečková P, Kopeček J (2003) Free and N–(2–hydroxypropyl)methacrylamide copolymer–bound geldanamycin derivative induce different stress responses in A2780 human ovarian carcinoma cells. Cancer Res 63:7876–7882
371. Pike DB, Ghandehari H (2010) HPMA copolymer–cyclic RGD conjugates for tumor targeting. Adv Drug Deliv Rev 62:167–183
372. Ulbrich K, Subr V (2010) Structural and chemical aspects of HPMA copolymers as drug carriers. Adv Drug Deliv Rev 62:150–166
373. Minko T (2010) HPMA copolymers for modulating cellular signaling and overcoming multidrug resistance. Adv Drug Deliv Rev 62:192–202
374. Fisher KD, Seymour LW (2010) HPMA copolymers for masking and retargeting of therapeutic viruses. Adv Drug Deliv Rev 62:240–245
375. Lu ZR (2010) Molecular imaging of HPMA copolymers: visualizing drug delivery in cell, mouse and man. Adv Drug Deliv Rev 62:246–257
376. Talelli M, Rijcken CJ, van Nostrum CF, Storm G, Hennink WE (2010) Micelles based on HPMA copolymers. Adv Drug Deliv Rev 62:231–239
377. Liu XM, Miller SC, Wang D (2010) Beyond oncology—application of HPMA copolymers in non–cancerous diseases. Adv Drug Deliv Rev 62:258–271
378. Lammers T (2010) Improving the efficacy of combined modality anticancer therapy using HPMA copolymer–based nanomedicine formulations. Adv Drug Deliv Rev 62:203–230

Chapter 3
Stabilizers-Mediated Nanoparticles Syntheses

Abstract Of the chemical processes, a reverse micelle (w/o microemulsion, a soft template) synthesis has been demonstrated to be a viable method for producing a wide array of noble metals over a relatively narrow particle size distribution. Noble metal colloids can be prepared in metal salt/(non)ionic surfactant/oil/water microemulsions by using both classical and nontraditional reductants. Reduction of metal ions occurred in microemulsions based on some ionic and nonionic surfactants without adding specific reductants. Mostly, the spherical metal nanoparticles are fabricated. A number of nonspherical nanomaterials of aligned noble metal colloids were found in the prolate ionic surfactants micelles. The citrate reduction method is well known for its simple procedure, yielding stable and reproducible gold nanoparticles of narrow size distribution. The coordination of metal ions with functional groups such as NH_2 in polymer served as weak cross-linkers to attach polymer chains and formation and stabilization of metal colloids. Gold nanoparticles surrounding with silica shells as a support could be a potentially useful method for the preparation of highly active nanoconjugates assemblies. Laser ablation of solvent-suspended metal powders can be used in for synthesis of gold/silver alloy and core@shell nanoparticles of predetermined composition. The generation of polymer coatings for noble metal nanoparticles (NMNPs) may feature stimulus-responsiveness (pH, temperature, ionic strength, and light) and spontaneously form versatile supramolecular structures. Some of the physical and chemical properties of the core nanoparticles are often imparted to the resulting polymeric shell system, producing hybrid materials with novel properties and functions that are not possible from the single-component structure alone. Various reducing agents introduced into polymer-based micelle systems may result in the formation of NMNPs of various sizes. A new method of producing gold nanoparticles is a surfactant-free synthesis, high variability in the introduction of (functionalized) ligands, and good control over the particle size. Soft-ligand-stabilized nanoparticles can be used as precursors to obtain nanoparticles with different surface chemistry by replacing the soft ligands with other desired ligands. The ionic liquids stabilize the metal nanoparticles noncovalently via electrostatic interactions. They initiated the formation of various nanoparticles such as spherical, oblate, nanorods of different aspect ratios, and sharp-edged

nanostructures. The versatility of the micellar nanostructure lies in its capacity to cargo drug molecules and biological macromolecules that are either hydrophilic, therefore entrapped in the liposome inner aqueous core, or hydrophobic, therefore incorporated within the lipid bilayer. PEO-modified noble metal nanomaterials have several attractive characteristics for diagnostic applications, including (1) biocompatibility and stability, (2) unique tunable optical properties, and (3) easy conjugation of biomolecules to the surface for tumor specific targeting.

Keywords Surfactant · Amphiphilic copolymer · Micelles · Droplets · Microemulsion · Noble metal nanoparticles · Solutes · Bioconjugates · Drugs

Abbreviations

1D	One-dimensional
2D	Two-dimensional
9-BBN	9-borabicyclo [3.3.1] nonane
AED	Average esterification degrees
AOT	Sodium bis(2-ethylhexyl)sulfosuccinate
AuNPs	Gold nanoparticles
AuNSs	Gold nanoshells
BAC	Benzyldimethyltetradecylammonium chloride
BE	Binding energy
CMC	Critical micelle concentration
CS	Cysteamine-monochlorhydrat
CTAB	Cetyltrimethylammonium bromide
CTAC	Cetyltrimethylammonium chloride
d_2	Interparticle spacing
DDT	Dodecanethiol
diglyme	Diethylene glycol dimethyl ether
DKSS	Sucrose fatty acids of monoesters and di- and triesters, fatty acid constituent consisting of stearic acid and palmitic acid
DLS	Dynamic light scattering
DT	Dodecanethiol
EDXRF	Energy-dispersive X-ray fluorescence
EPR	Enhanced permeability and retention
fcc	Face-centered cubic
FTIR	Fourier transform infrared spectroscopy
HAc	Acetic acid
HAuNS	Hollow gold nanoshells
hcp	Hexagonal close packed
HDT	1-hexadecanethiol
HER2	Human epidermal growth receptor 2
HLB	Hydrophilic–lipophilic balance
HMTS	Heptamethyltrisiloxane

HRSEM	High-resolution SEM
HRTEM	High-resolution TEM
HTAB	*N*-hexadecyltrimethylammonium bromide
ICP	Inductively coupled plasma
IL	(Ionic liquid)-surfactant
I_{sc}	Total scattered light intensity
LMCT	Ligand-to-metal charge transfer
LPR	Longitudinal plasmonic resonance
LSP	Longitudinal surface plasmon
LSPR	Localized surface plasmon resonance
MDR	Multidrug resistance
N_2H_4	Hydrazine
NIR	Near-infrared
MNPs	Metal nanoparticles
MPA	Mercaptopropionic acid
MPCs	Monolayer-protected clusters
MUA	11-mercaptoundecanoic acid
MUOH	11-mercaptoundecanol
NMNCs	Noble metal nanocrystals
NMNPs	Noble metal nanoparticles
NT	1-nonanethiol
o/w	Oil-in-water
PAM	Polyacrylamide
PBS	Phosphate buffer solution
PDI	Polydispersity index,
PDPAEMA	Poly[2-(diisopropylamino) ethyl methacrylate]
PEG	Poly(ethylene glycole)
PEI-HCA	Polyethylenimine-*g*-hydrocaffeic acid
PEO-*b*-PCL	Poly(ethylene oxide)-*b*-poly(ε-caprolactone)
PEO-*b*-PDHPMA-*b*-PDPAEMA	Poly(ethylene oxide)-*b*-poly(2,3-dihydroxypropyl methacrylate)-*b*-poly[2-(diisopropylamino) ethyl methacrylate]
PEO-PPO-PEO	Poly(ethylene oxide)-poly(propylene oxide)-poly(ethylene oxide)
P-gp	Glycoprotein
PNIPAM	Poly(*N*-isopropylacrylamide)
PSt-*b*-PVP	Poly(styrene)-block-poly(vinylpyridine)
PVPo	Polyvinylpyrrolidone
QD-particles	Quantum dot particles
RI	Refractive index
SAED	Selected area (electron) diffraction
SAXS	Small angle X-ray scattering
SDS	Sodium dodecylsulfate
SM	3–sulfonate mercaptopropan

SP	Surface plasmon
SPR	Surface plasmon resonance
SPRs	Surface plasmon resonances
SPIONs	Superparamagnetic iron oxide nanoparticles
TBAB	Tetrabutylammonium bromide
TDT	1-tetradecanethiol
TEG	Tetra (ethylene glycol)
TEM	Transmission electron microscopy
TEOS	Tetraethylorthosilicate
T_c	Crystallization temperature
T_m	Melting temperature
TOA	Trioctylamine
TOAB	Tetraoctylammonium bromide
TPR	Transverse plasmon resonance
TRITC	Tetramethyl rhodamine isothiocyanate
Tween 20	Sorbitan monolaurate
w/c	Water-in-CO_2 microemulsions
w/o	Water-in-oil
XANES	X-ray absorption near-edge spectroscopy
XPS	X-ray photoelectron spectroscopy
λ_{max}	Absorption maximum

3.1 Introduction

Surfactants are usually organic compounds that are amphiphilic, meaning they contain both hydrophobic groups (their tails) and hydrophilic groups (their heads). Surfactants will diffuse in water and adsorb at interfaces between air and water or at the interface between oil and water, in the case where water is mixed with oil. The water-insoluble hydrophobic group may extend out of the bulk water phase, into the air or into the oil phase, while the water-soluble head group remains in the water phase. The polar "heads" of the surfactant molecules coating the micelle interact more strongly with water, so they form a hydrophilic outer layer that forms a barrier between micelles. This inhibits the oil droplets, the hydrophobic cores of micelles, from merging into fewer, larger droplets ("emulsion breaking") of the micelle. The compounds that coat a micelle are typically amphiphilic in nature, meaning that micelles may be stable either as droplets of aprotic solvents such as oil in water, or as protic solvents such as water in oil. When the droplet is aprotic, it sometimes is known as a reverse micelle. In the bulk aqueous phase, surfactants form aggregates, such as micelles, where the hydrophobic tails form the core of the aggregate and the hydrophilic heads are in contact with the surrounding liquid. Other types of aggregates can also be formed, such as spherical or cylindrical micelles or lipid

bilayers. The shape of the aggregates depends on the chemical structure of the surfactants, namely the balance in size between hydrophilic head and hydrophobic tail. A measure of this is the hydrophilic–lipophilic balance (HLB) . Surfactants reduce the surface tension of water by adsorbing at the liquid–air interface.

Of the chemical processes, a reverse micelle (w/o microemulsion) synthesis has been demonstrated to be a viable method for producing a wide array of noble metal nanoparticles [1] over a relatively narrow particle size distribution in different organic media. A reverse microemulsion (a soft template) utilizes the natural phenomenon involving the formation of spheroidal aggregates in a solution when a surfactant is introduced to an organic solvent, formed either in the presence or in the absence of water [2]. Micromulsions are thermodynamically stable, and surfactants or surface-active polymers are normally used to help form such stable systems. Micelle formation allows for a unique encapsulated volume of controllable size through which reactions and subsequent development of metal nanostructures or nanoparticles proceed in the soft template. This approach presents a novel and straightforward step for the synthesis of NMNP in w/o microemulsion template, in which the reduction of metal cations to atoms takes place under the presence of reductants or UV irradiation. The use of microemulsion template is one of the most advantageous ways to synthesize NMNP in a "bottom–up" approach. Microemulsions are also clear colloidal dispersion comprised of oil, water, and surfactant. Different structure can be formed as such: water-in-oil (w/o) or oil-in-water (o/w) droplets, and bicontinue structure, over a wide range of com-position depending on the properties of the surfactant and the oil. An oil–in–water microemulsion is similar to a direct micelle, while the water-in-oil microemulsion is topological analogous to a reverse micelle.

The w/o microemulsion method offers a lot of advantages with respect to others (coprecipitation in solution, sol-gel, flame–spray pyrolysis, laser evaporation, high-energy milling), namely the use of a simple equipment, homogeneous mixing, high degree of particles size and composition control, formation of NMNPs with high surface area, and the use of soft condition of synthesis near ambient tem-perature and pressure [3]. The first application of w/o microemulsion for noble metal nanoparticles synthesis was reported in 1982 [4]. The main strategy for the NMNP synthesis in w/o microemulsion consists in mixing two microemulsions, one containing the metal precursor solution and the other one containing the reduction agent [5]. Upon mixing procedure, both reactants (metal precursor and reduction agent solutions) will contact each other due to the coalescence and droplet collisions and will react to form NMNP which remain confined to the interior of microemulsion droplets. Even through NMNP obtained by w/o microemulsion shows superior properties and performance, at the industrial level this method has no good acceptance, mainly due to the large amount of solvents (oils) which represent the main component of these systems being the continuous phase [6].

Following early developments in wet chemistry methods, such as the well-known reduction of silver or gold salts by different reducing agents in the presence of low-molecular weight additives (surfactants) to provide colloidal sta-bility and/or specific functionality, the use of (co)polymers is clearly an interesting

route for the fabrication of NMNP systems with a core@shell microgel structure [7, 8]. The external polymeric coating of gold cores defines both the spacing and the interactions in nanoparticle systems with this type of architecture. We can, therefore, take advantage of modern macromolecular engineering knowledge to synthesize next-generation polymer coatings for gold nanoparticles that may feature stimulus-responsiveness (pH, temperature, ionic strength, and light) and spontaneously form versatile supramolecular structures. The fabrication of metal core@polymer shell nanoparticle architectures has been the focus of research owing to potential applications in many fields (optics, electronics, catalysis, drug delivery, etc.) [9].

Incorporation of low-molecular mass drugs into pluronic micelles can increase drug solubility and drug stability, and can improve drug pharmacokinetics and biodistribution. Although doxorubicin (DOX, drug) is easily sequestered and released from pluronic micelles in vitro, this type of micelle is not sufficiently stable to be used in vivo. To enhance stability of micelles in the bloodstream upon dilution, pluronic micelles were cross-linked through their hydrophilic shells. Pluronics cause drastic sensitization of multidrug resistance tumors to various anticancer agents, enhance drug transport across the blood–brain and intestinal barriers, and cause transcriptional activation of gene expression both in vitro and in vivo.

The versatility of the micellar liposomal structure lies in its capacity to cargo drug molecules and biological macromolecules that are either hydrophilic, therefore entrapped in the liposome inner aqueous core (or in the w/o droplet core), or hydrophobic, therefore incorporated within the lipid bilayer (or in o/w droplet core). Al-Jamal et al. have presented the concept of liposome-nanoparticle hybrids as a general methodology, taking advantage of the much more developed and sophisticated liposome technology, to be used as a platform for the delivery of novel nanoparticles [10].

PEO-modified gold nanomaterials except of self-assembling have also several attractive characteristics for diagnostic applications, including (1) biocompatibility and stability, (2) unique tunable optical properties, and (3) easy conjugation of biomolecules to the surface for tumor specific targeting. More complex shapes with excitation wavelengths of 800–1200 nm could absorb the NIR light, and then be converted to heat. By changing the shape of gold nanoparticles to nanorods, the absorption and scattering wavelength changes from the visible to the near-infrared region and their absorption and scattering cross sections also increase. Indeed, the surface plasmon field absorption of gold nanorods is the strongest of all the different shapes of gold and silver nanoparticles [11].

Aptamers are DNA or RNA oligonucleotides or modified DNA or RNA oligonucleotides that fold by intramolecular interaction into unique conformations with ligand-binding characteristics. Their nanoconjugates with metal nanoparticles preferentially accumulate at the tumor sites because of hallmarks of tumors such as the fenestrated vasculature and poorly lymphatic drainage, resulting in an enhanced permeability and retention (EPR) effect [12].

3.2 Micelles and Microemulsion Templates

3.2.1 General

In order to produce metal nanoparticles having suitable sizes and/or shapes, many physical or chemical techniques such as coprecipitation, gas evaporation, sol-gel method and sputtering have been developed so far. Additionally, more attention has been paid on the preparation of metal nanoparticles in reverse micelles [13]. Reverse micelles are thermodynamically stable nanometer-sized aggregates of surfactant molecules dispersed in a hydrophobic organic phase like octane or toluene and can form a w/o (water-in-oil) type microemulsion containing a water pool in its center (core). Metal nanoparticles are synthesized in the water pool, in which most precursors and reactants are dissolved. Water is readily solubilized in the polar core of reverse micelles, forming so-called water pools that play the role of templates for NMNP formation and also prevent the aggregation of metal nanoparticles [14]. As the preparation of metal nanoparticles using reverse micelles does not require a special apparatus and extreme conditions of temperature and pressure, it is comparatively easy to expand the scale of reverse micellar reaction system. However, the productivity of metal nanoparticles per volume of reverse micellar system is limited due to low overall concentration of reactants in the reverse micellar system, since the volumetric ratio of water phase playing a role as the dissolution of reactants and the reaction field to the bulk organic phase is too small.

Besides the electrostatic bonding, surfactants are also used to form reverse micelles for NMNPs synthesis. Reverse micelle solutions are mostly transparent, isotropic, thermodynamically stable water-in-oil microemulsions that are dispersed in a continuous oil phase and stabilized by surfactant molecules at the water/oil interface [15, 16]. The sizes of the NMNPs are defined by the micelle volume. Both low-molecular weight surfactants and copolymer surfactants form reverse micelles for the synthesis of NMNPs. Micelle formation allows for a unique encapsulated volume of controllable size through which reactions and subsequent development of metal nanostructures or nanoparticles proceed in the soft template Aggregates containing ω (=[water]/[surfactant]) of less than 15 can be called as reverse micelles and have hydrodynamic diameters in the range of 4–10 nm [17], whereas ω greater than 15 constitute microemulsions, which have a hydrodynamic diameter range between 5 and 50 nm. Once the right microemulsions are obtained, the method of particle preparation consists in mixing of two microemulsions carrying the appropriate reactants in order to obtain the desired particles [18] (Scheme 3.1).

Sodium bis(2-ethylhexyl) sulfosuccinate (AOT) is a widely used low-molecular weight surfactant in noble metal nanoparticles synthesis. The reverse micelle is thus prepared by adding water/AOT/n-heptane [20] or water/AOT/isooctane [21, 22] into an appropriate amount of $HAuCl_4$ or other metal salts. Then, the reducing agent is added into the mixture to form the AuNPs. Catanionic surfactants (mixture of octanoic acid and octylamine) such as lecithin [23, 24], and trichromophoric
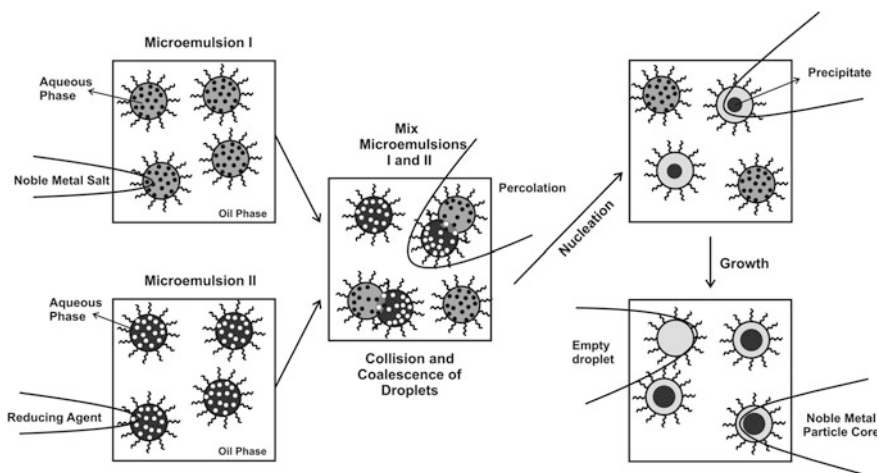
Scheme 3.1 Proposed mechanism for the formation of noble metal nanoparticles by the inverse microemulsion (a soft template) [19]

dye-reverse micelles (in the toluene continuous phase) were reported to fabricate via spontaneous reduction and stabilize AuNPs as shown in Scheme 3.2 [25].

However, the use of water/oil microemulsions for the synthesis of NMNPs has a major drawback. Large amounts of surfactant are required to stabilize the metal NPs, which introduces impurities. In order to solve this problem, Hollamby et al. purified reverse micelle-stabilized NMNPs in a single step. Thus, the metal NPs are stabilized by the microemulsion that forms in water/octane with butanol as coadditive. After adding excess water, the NMNPs are concentrated into the upper octane-rich phase, and the impurities remain in the water-rich lower phase [27].

In order to solubilize reactants in reverse micelles, three solubilization methods are utilized: injection method, liquid-liquid extraction method, and solid-liquid extraction method [28]. First, the injection method is carried out by injecting a few microliters of the concentrated stock solution of reactants into the hydrocarbon solution of surfactants. This method is most commonly used to prepare metal nanoparticles. Second, the liquid-liquid extraction method is carried out by transferring solutes dissolved in an aqueous phase from the aqueous phase into the hydrocarbon phase of surfactants. This method is relatively slow, and the concentration of reactants in the hydrocarbon phase is limited due to the distribution between aqueous and reverse micellar organic phases in thermodynamic equilibrium. Third, the solid–liquid extraction method is carried out by mixing solid reactants with the reverse micellar solution containing already a certain amount of water. This method can dissolve reactants until their dissolution reaches saturation in water pool. Moreover, when using the solid–liquid extraction instead of the conventional injection method to solubilize reactants into reverse micelles, the following benefits are expected. First, the productivity of metal nanoparticles is markedly promoted, since reactants consumed for the formation of metal
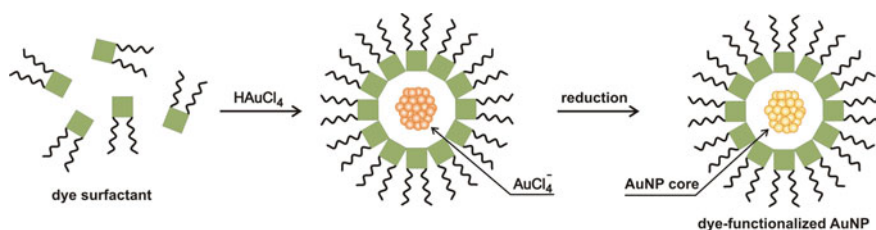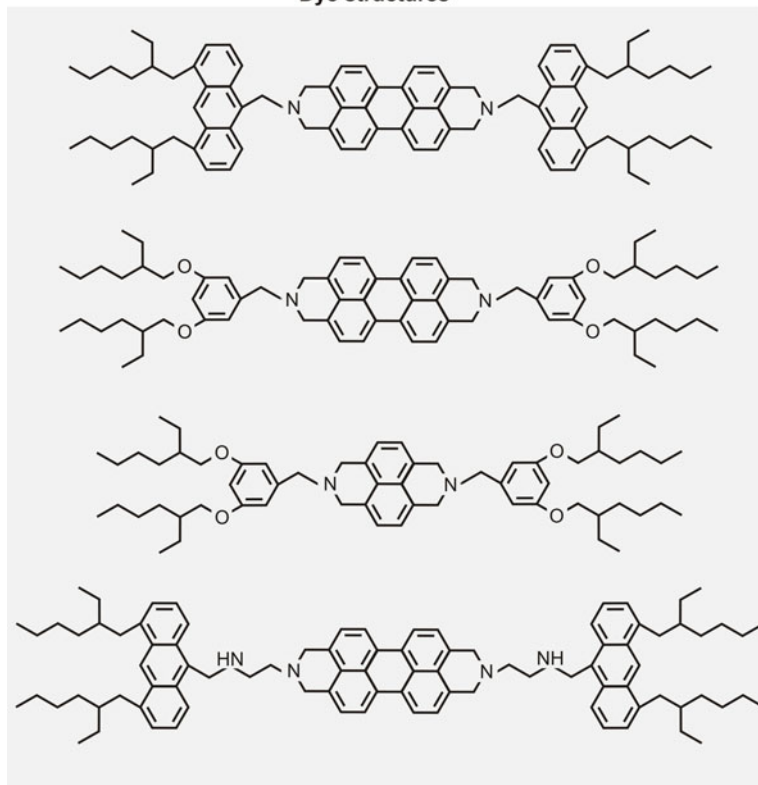
Scheme 3.2 Formation of dye-functionalized AuNPs (*top panel*) and dye structure (*bottom panel*) [25, 26]

nanoparticles are successively supplied from solid reactants already added in large excess, compared to the solubility of the water pool of reverse micelles. Second, only a small amount of water is needed for solid–liquid extraction. Consequently, the aggregation of resultant nanoparticles is inhibited, since the lower water content is kept in reverse micellar system, the more stably nanoparticles are dispersed [29]. The advantage of the reverse micelle is that it can solubilize both the hydrophobic nanoparticle and polar or nonpolar polymer precursor via their polar micelle

interface and reaction can be initiated from homogeneous solution [30]. The initiation and particle growth can proceed at room temperature. A novel and straight forward approach was developed for the synthesis of AuNP in w/o microemulsion template, in which the reduction of Au^{3+} to Au^0 takes place under UV irradiation and keeps the features of template [31].

Different structures can be formed as such: water–in–oil or oil–in–water droplets, and bicontinue structure, over a wide range of composition and reaction conditions. An o/w microemulsion is similar to a direct micelle, while the w/o microemulsion is topological analogous to a reverse micelle [32, 33]. From environmental and applied point of view, the possibility of preparing metal nanoparticles using o/w microemulsion template has several advantages over w/o microemulsion since the major continuous phase is water: the ratio of water and oil phase is far grater than 1, the consumption of organic matter is less, and the cost is relatively low. The main applications of o/w microemulsion were preparation of lipidic and polymeric nanoparticles [34] and in pharmaceuticals and detergent formulations [35]. O/w microemulsion started to be used for the synthesis of inorganic nanoparticles only until recently hence, the literature is not abundant with this subject. Li et al. [36] reported the o/w microemulsion for the synthesis of various inorganic nanoparticles, such as metallic nanoparticles (Ag, Cu), semiconductors (Ag_2S, PbS, CdS, ZnS, CdSe, PbSe, Ag_2Se), fluorides (CaF_2, YF_3, NdF_3, PrF_3), phosphates ($CePO_4$ and $HoPO_4$), and chromates ($BaCrO_4$ and $PbCrO_4$), and all the products were made up of small particles with average size ranging from 2 to 13 nm.

It is known that water is a broadly used continuous and disperse phase. The second most important disperse phase is CO_2. CO_2 is a feeble solvent because of its very low dielectric constant (1.1–1.5) and zero dipole moment, resulting in low solubility of many organic species. The very low polarizability per unit volume and low refractive index of CO_2 results in weaker van der Waals forces than hydrocarbon solvents, making CO_2 more similar to fluorocarbons with respect to solvent strength [37]. Fluorinated surfactants [38] have shown high solubility in CO_2 and some of them have stabilized water in CO_2 microemulsions [39]. Nanoparticles have been formed in CO_2 within water-in-CO_2 (w/c) microemulsions or by arrested precipitation techniques using fluorinated compounds [40]. Both fluorinated surfactants and fluorinated ligands have been used to disperse particles in CO_2. Interactions between the CO_2 solvent and the fluorinated coating on the nanoparticles provide enough repulsive forces to counterbalance the attractive van der Waals forces between the particles. In the w/c microemulsion system, fluorinated surfactant-supported aqueous cores act as a nanoreactor to synthesize and then disperse the particles in a CO_2 phase due to strong interactions between CO_2 and the fluorinated surfactant tails.

3.2.2 Silver Nanoparticles

Among various nanoparticles, silver nanoparticles are of particular interest because of their wide applications resulting from their unique properties [41]. Silver nanoparticles (AgNPs) have been gaining significant research interest due to their unique shape and size-dependent optical [42], antimicrobial [43], and catalytic properties [44]. Silver nitrate aqueous solution was directly used to prepare silver nanoparticles in AOT (sodium bis(2-ethylhexyl)sulfosuccinate)–dodecane–water–silver nitrate–hydrazine microemulsions [45]. The silver nanoparticles were obtained from the reduction of silver nitrate by hydrazine. The particle mean diameter decreased significantly with increasing silver nitrate concentration when silver nitrate concentration is less than 0.2 M. However, it increases when silver nitrate concentration is greater than 0.2 M. When silver nitrate concentration is greater than 0.4 M, the silver colloid is unstable and easy to flocculate. TEM data indicate that there are fewer but larger silver nanoparticles generated in the microemulsion formed by 0.1 M silver nitrate ($d \sim 3.9$ nm). By contraries, there are more but smaller nanoparticles performed in the microemulsion formed by 0.2 M silver nitrate ($d \sim 2.6$ nm), which means that the higher the silver nitrate concentration, the faster the growth of nanoparticles (Fig. 3.1).

In addition, the collision frequency of the formed particles increases significantly with silver nitrate concentration, and then the protection obtained by absorption of AOT molecules on the particles' surface is weakened. Thus, the tiny particles are easy to aggregate into larger particles at the high silver nitrate concentration. These conclusions have also been confirmed by the UV–Vis spectra [46]. At low concentration of $AgNO_3$, the maximum absorption wavelength gives rise to a blueshift, meaning a decrease of the particles size. At high concentration of $AgNO_3$, the maximum absorption gives rise to a redshift, the particles size increased [47], and the large silver aggregates formed. TEM micrograph and size distribution histogram of silver colloidal particles obtained at various ω ([water]/[surfactant]) values (Fig. 3.2):

$$d(nm)/\omega: 1.5/2.5, \ 3.4/7.5, \ 5.0/15.0 \tag{3.1}$$

Fig. 3.1 Size distribution of silver nanoparticles showing the effect of different concentration of silver nitrate: 0.1 M (1), 0.2 M (2) [45–47]
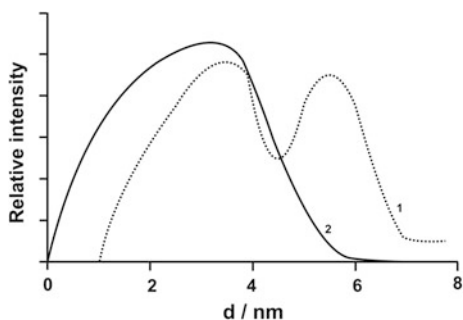
Fig. 3.2 Size distribution of
silver nanoparticles showing
the effect of different molar
ratios of water to AOT (ω):
2.5 (*1*), 7.5 (*2*), 15 (*3*) [45–47]
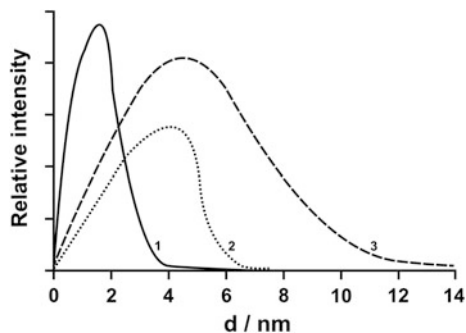
The particles are spherical in shape, and there is narrower in the size distribution
at lower water content than that obtained at higher ω values. Hence, a decrease in
the micellar size, i.e., a decrease in the molar ratio of water to AOT, induces
formation of smaller and more monodisperse silver particles. Because at low water
content, the water solubilized in the polar core is bounded by the surfactant
molecules, which increases the boundary strength and decreases the intermicellar
rate among the reverse micelles. Increasing the water content, the bound water turns
into bulk water, which is benefit for the water pools to exchange their contents by a
collision process and make the chemical reaction or coprecipitation between
compounds solubilized in two different reverse micelles more easily. As a result, the
rate of nucleation and the particle growth begin to be controlled by the collision,
fusion, and split of the droplets. Due to the nature of bulk water drastically different
from bound water, the resultant particle size is relatively bigger and the size dis-
tribution is broader.

The microemulsion approach (the diethyl ether/AOT/water/dodecanethiol sys-
tem) was used to prepare thiol-capped silver particles under simple reaction con-
ditions [48]. Dodecanethiol-capped silver "quantum dot" particles (QD-particles)
have been synthesized using a novel biphasic microemulsion. AOT as the anionic
surfactant due to its higher solubility in organic phase helps to extract metal cations
from the aqueous to reverse micellar phase. FTIR investigations and elemental
analyses support the encapsulation of silver particles by dodecanethiol (DT) , while
the transmission electron micrograph reveals an average size of 11 nm.
A comparison of the FTIR spectra between 400 and 450 c@@@m^{-1} of DT and
encapsulated particles shows all the important bands of pure DT are clearly seen in
the encapsulated particles. The similarity of the features confirms the following:

(1) The presence of thiol as an essential component of the composite nanoparticles;
    and
(2) that the thiol molecule is not leached out during several washings of the
    precipitate.

The ratio of the sum of the percentage of C, H, S, and metallic content reveals
that 3.5 silver atoms associate with 4 alkanethiol molecules. The signals of the XPS

spectra acknowledge the presence of Ag and S in the synthesized nanoparticles. A high-resolution scan over the range 360–380 eV reveals a doublet of the Ag $3d_{5/2}$ peak at 368.4 eV and the Ag $3d_{3/2}$ peak at 374.4 eV, corresponding to peak separation of 6 eV.

For the formation of silver nanoparticles in AOT microemulsion, diverse and sometime conflicting results have been reported. For example, Andersson et al. [49] thought that silver ions were not reduced by AOT surfactant in their reaction system. Petit et al. [50] had not reported whether there were silver nanoparticles formed in AOT microemulsion. However, Monnoyer et al. [51] found there were silver particles formed in AOT microemulsion when they used AOT microemulsion fabricating silver bromide nanoparticles. Liz-Marzán and Lado-Touriño [52] had even synthesized silver sols by reduction of AgNO$_3$ with AOT in ethanol solution, although a very low yield was obtained in the case. Thus, surfactants, which act as both reductant and stabilizer preventing particle aggregation, are known to play an important role in the nucleation and stabilization of silver nanoparticles.

Barnickel et al. [53] have synthesized silver colloids in $C_{12}E_5$/cyclohexane/water microemulsions by using daylight irradiation of the silver nitrate solution. Reduction of silver ions occurred in microemulsion based on cationic and nonionic surfactants without adding specific reductants. The oxo groups from the polyether generated hydroperoxides able to reduce silver ions. The terminal hydroxyl groups of the $C_{12}E_5$ surfactant reduced Ag$^+$ ions upon radiation:

$$Ag^+ + e^-(h\nu, \ C_{12}E_5) \rightarrow Ag^{(0)} \tag{3.2}$$
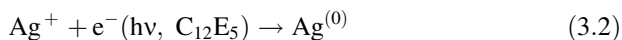
Spherical silver nanoparticles were fabricated in the micellar sodium dodecyl-sulfate (SDS) solutions by the reduction of silver nitrate using ascorbic acid as the reducing agent [54]. The particles are roughly spherical with the characteristic plasmon band. With increase in length of the micelles, the polydispersity of the distribution decreases and the peak of the intensity weighted distribution shifts to larger diameter. This is possibly because of the growth of the nuclei at the expense of smaller particles to reduce the interfacial energy. It is likely that the micellar surface provides a platform for the nucleation and further growth of the particles as the positively charged Ag$^+$ ions can condense on the negatively charged surface of the micelles through electrical double layer formation [55]. An increase in micelle length increases interfacial area of the micelles thereby increasing the local concentration of Ag$^+$ ions. This facilitates easy growth of the nuclei without collision and intermicellar exchange. As the number of counter ions per micelle increases with increase in aggregation number of the micelles, the extent of growth of the particles and its average dimension increases.

An alternative new approach to monodisperse silver nanocubes in water by a HTAB (n-hexadecyltrimethylammonium bromide)-modified silver mirror reaction was reported by Yu and Yam [56, 57]. Controlled synthesis of silver nanocubes could be accomplished by such an "old" reaction by the introduction of HTAB. The synthetic reactions were as follows:

$$\left[\text{Ag}(\text{NH}_3)_2\right]^+ + \text{Br}^- \leftrightarrows \text{AgBr}(s) + 2\text{NH}_3 \tag{3.3}$$

$$\left[\text{Ag}(\text{NH}_3)_2\right]^+ + \text{RCHO (glucose)} \rightarrow \text{AgNPs} + \text{RCOO}^- + \text{NH}_4^+ \tag{3.4}$$
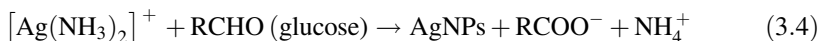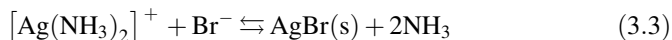
Upon addition of HTAB into the solution containing $[\text{Ag}(\text{NH}_3)_2]^+$, the Br^- from HTAB reacted with $[\text{Ag}(\text{NH}_3)_2]^+$ to form AgBr (solid, insoluble, Eq. 3.3). Reaction 4 proceeded in a more controllable manner at a high temperature (120 °C) to form the nanocubes. With the consumption of $[\text{Ag}(\text{NH}_3)_2]^+$ by reaction 4, the equilibrium reaction 3 shifts to the left until the reactions are completed. XRD peaks of the product were assigned to the diffraction of (111), (200), and (400) planes of face-centered cubic (fcc) silver. The unusual intensity of the (200) diffraction peak is a result of the strong tendency of the AgNPs to assemble into two-dimensional (2D) arrays on the solid surface with the c-axis perpendicular to the substrate upon the evaporation of the water.

A typical TEM image of the silver nanoparticles indicates that the products consisted of a large quantity of uniform nanocubes with smooth faces having a mean edge length of ca. 55 nm. The cubes had a strong tendency to assemble into 2D arrays with regular checked pattern on the TEM grid, and the spacings between adjacent cubes are ca. 5 nm. Such a regular assembly of the cubes is due to the facts that the HTAB adsorbed on the cube surfaces would form a capping shell to generate a regular interparticle spacing and thus to prevent the cubes from random aggregation [58], and that the uniformity of the sample made it possible to manipulate the cubes into a close-packed and ordered array caused by van der Waals forces [59]. The 2D lattice fringes of the HRTEM image were examined to be 0.204 nm, close to the {200} lattice spacing of the fcc silver. On the basis of the TEM and HRTEM analyses, it could be concluded that when these regular nanocubes bounded by {200} facets assembled into a 2D array on a substrate, they, of course, had an identical <001> zone direction, thus resulting in the strongest diffraction of (200) as shown in the XRD pattern. HTAB acted not only as the reaction moderator as described above but also as the shape controller and stabilizing agent. First of all, HTAB micelles directed the silver metal to nucleate and grow into nanoparticles other than the usual silver mirror. An increase in the molar ratio of $\text{HTAB}/[\text{Ag}(\text{NH}_3)_2]^+$ led to a shape evolution of silver nanoparticles from spheres to cubes, which was caused by the anisotropic adsorption of the surfactant on the silver crystal faces, while such adsorption characteristics depended on the molar ratio. When the molar ratio reached ca. 1.5, anisotropic growth of the particles appeared. When the molar ratio increased further to 2.5, the product was dominated by nanocubes. Second, it stabilized the silver nanoparticles to form stable aqueous solutions, the color of which changed from orange to yellow with the increase of the molar ratio. Note that the nanocubes also showed an absorption band at ca. 420 nm, typical of the plasmon resonance of the spherical silver nanoparticles, since the nanocubes assumed bent edges rather than sharp ones such as triangles or prisms [41].

The formation process of the silver nanocubes and their assembling is proposed as illustrated schematically in Scheme 3.3. The growth of silver nanoparticles should be a result of the interplay of the faceting tendency of the stabilizing agent of HTAB and the growth kinetics of silver metal. On one hand, $[Ag(NH_3)_2]^+$ reacted with Br^- from HTAB in reaction 3 to produce AgBr colloids, which were stabilized by HTAB. Subsequently, with the proceeding of reaction 4, silver colloids were formed and temporarily stabilized by HTAB, but they were unstable due to their high energy resulting from the small particle size.

A number of 1D arrays of aligned silver colloids with a size of approximately 4 nm were found in the prolate HTAB micelles. Meanwhile, some nanowires that formed along the arrays were also observed. Of particular, interest is to note that the corresponding spaces left alongside the nanowires suggested that the nanowires were formed probably via the assembly of small spherical particles. Unlike the nanowires that were assembled from silver nanoparticles in a polyol/toluene medium which revealed a polycrystalline texture [60], these nanowires were characterized by the nature of a single crystal. If more than one nanowire were formed along an array of aligned small spheres, strong van der Waals forces would exist between adjacent nanowires because of their closed packing, and may lead to the formation of the 2D alignments of silver nanowires. Since the morphology of the surfactant micelles may range from spherical shape to prolate or rodlike, and lamellar phase, depending on the concentration of the surfactant and additives [61], the assembly of the silver colloids into wires other than the cubes could probably be attributed to the template action of the prolate micelles of HTAB under these experimental conditions.

Because the as-synthesized silver nanoparticles were well-crystallized single crystals, the silver colloids had probably assembled through an adhesion process
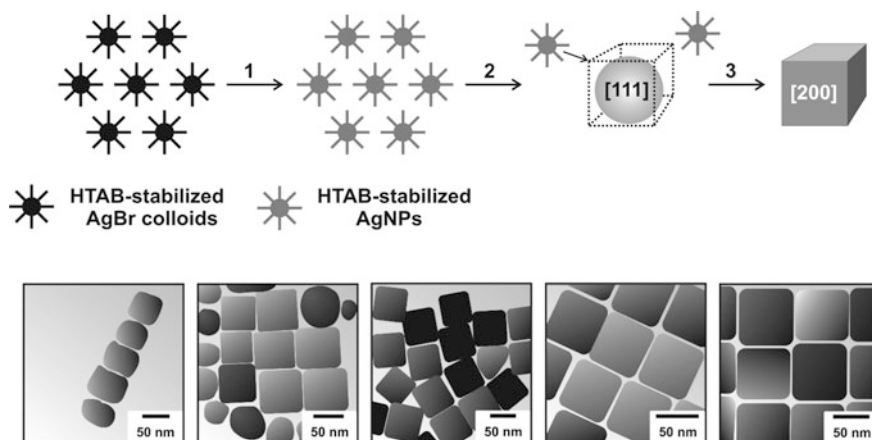
Scheme 3.3 Schematic illustration of the proposed formation process of silver nanocubes (*top panel*) and 1D and 2D possible arrays and assembles (*bottom panel*): *1* reduction step and *2* and *3* assembling steps [57]

followed by a subsequent coalescence process, similar to the 2D silver nanowire array formed by reducing the capping ligand coverage on small silver particles [62]. However, this process was driven by hydrothermal energy, which could be supported by the fact that if the autoclave was cooled to room temperature the assembly of the colloids stopped during the growth process of the nanocubes. Thus, it is proposed that the observed formation of the silver nanoparticles occurs through a hydrothermal-induced assembly mechanism. Similar to other studies [63], the prerequisites for the assembly of small spheres into silver nanoparticles are the formation of the small colloidal particles (<10 nm) and a suitable choice of a surfactant and its concentration, both of which are, to a large extent, determined by the concentrations of HTAB and $[Ag(NH_3)_2]^+$. For example, with a fixed concentration of $[Ag(NH_3)_2]^+$, lowering the concentration of HTAB resulted in large silver colloids (diameter > 10 nm), which could not assemble into the nanoparticles because of their low energy. Although a much higher HTAB concentration would be favorable for the formation of small silver colloids (<5 nm), they could not assemble into the nanoparticles because of a large amount of capping ligand coverage on the colloids which would block the interparticle assembly. Therefore, the successful formation of the multiple silver nanoparticles through the adjustment of the concentrations of HTAB and $[Ag(NH_3)_2]^+$ is believed to be the outcome of their effect on both the formation and the assembly process of the colloidal silver spheres.

Noritomi et al. have reported the preparation of silver nanoparticles in reverse micelles of sucrose fatty acid esters by using the conventional injection method [64]. Sucrose fatty acid esters are commercial food grade nonionic surfactants, and are biodegradable and nonhazardous to the environment [65]. Successive supply reactants consumed for the formation of silver nanoparticles to the water pools of reverse micelles, which are reaction fields, produce silver nanoparticles at high concentration. Noritomi et al. [66] have also employed solid-liquid extraction method instead of the conventional injection method [28]. The colloidal solution of silver nanoparticles prepared by solid-liquid extraction method was much concentrated, compared to that prepared by the injection method examined in their previous method [64]. The concentration of silver nanoparticles obtained by the present approach was about one hundred and thirty times larger than that obtained by the injection method. The color of the solution after dilution was yellow, similar to the case of injection method, and its UV–Visible absorption spectrum exhibited the peak around 403 nm, which corresponds upon the localized surface plasmon resonance (LSPR) of silver nanoparticles [67]. The relationship between surfactant concentration and the absorbance at 403 nm of colloidal solutions of silver nanoparticles preliminarily diluted one hundred-fold with n-butanol is as follows:

Absorbance (a.u.)/DKSS (sucrose fatty acids of 99 wt% monoesters and 1 wt% di- and triesters, fatty acid constituent consisting of 60 wt% stearic acid, and 40 wt% palmitic acid) (wt%) [66]:

$$0.1/10, \ 0.2/20, \ 1.0/30, \ 1.5/40, \ \text{and} \ 2.7/50 \tag{3.5}$$

Any absorbance at 403 nm was not observed without surfactant. On the other hand, the absorbance at 403 nm increased above 20 g/dm^3 of surfactant concentration. The apparent critical micelle concentration in sucrose fatty acid/n-butanol/isooctane system was observed to be around 10 g/dm^3 [68]. Consequently, it is suggested that the preparation of silver nanoparticles proceeds as follows. First, empty reverse micelles containing a small amount of water approach solid reactants added in large excess. When the water pools of reverse micelles contact solid reactants, reactants are solubilized into the water pools. Then, silver nanoparticles are synthesized from reactants solubilized in reverse micelles. Resultant silver nanoparticles are coated by surfactants, and are dispersed in organic solvents. Thus, the production of silver nanoparticles is promoted by repeating the process composed of the extraction of reactants, the synthesis of silver nanoparticles, and the dispersion of resultant silver nanoparticles (AgNPs).

The average particle diameter (d) of AgNPs prepared in the reverse DKSS micellar system at different reaction temperatures increases with temperature as follows:

$$d(\text{nm})/\text{temp.}(^{\circ}\text{C}): 6.8/5, \ 7.3/15, \ 7.8/25, \ 9.6/40 \tag{3.6}$$

The TEM images showed that the obtained silver nanoparticles displayed a wide variety of shapes. The size of resultant AgNPs was almost similar to that prepared in AOT reverse micelles by the conventional injection method [64]. The line in this dependence represents the fitting curve as

$$d = 0.079 \, t + 6.2 \tag{3.7}$$

where d is the mean diameter of silver nanoparticles, and t is the reaction temperature. The solubilization of reactants, the exchange of reactants between reverse micelles, the reduction reaction, and the growth of nanoparticles increase with increasing the reaction temperature [69]. The wavelength in the peaks increases with an increase in the mean diameter of silver nanoparticles. The line in this dependence represents the fitting curve as

$$\lambda = 8.2 \, d + 340 \tag{3.8}$$

where λ is the wavelength of peaks. The position of the plasmon adsorption peak depends upon the particle size and shape, and especially tends to be redshifted with increasing the particle size [69, 70].

The formation and stability of micelles are due to the structure and/or hydrophobic hydrophilic balance (HLB) of surfactants [71]. The structure and HLB of sucrose fatty acid esters alter with the esterification degree [65]. In order to elucidate the effect of those factors on the formation of AgNPs, the synthesis of silver nanoparticles was examined in the reverse micelles of sucrose fatty acid

esters by mixing DKSS (average esterification degree = 1.01, HLB = 19) with DKF20 W (average esterification degree = 3.1, HLB = 2). The more weight fraction of DKF20 W is, the larger the average esterification degree is. When AgNPs were prepared in the reverse micellar system of sucrose fatty acid esters at different average esterification degrees (AED), the particle diameter varies as follows:

$$d(nm)/AED: 7.8/1.01, \ 7.9/1.43, \ 8.2/1.85, \ 9.2/2.68, \ 12.4/3.1 \qquad (3.9)$$

As shown, the mean diameter of silver nanoparticles increases with the average esterification degree [64]. Thus, when the bulkiness of surfactants increased or the HLB value decreased, the size of silver nanoparticles tended to increase.

Driven by thermal movement, the small nanoparticles assembled into larger particles with spherical or near-cubic shapes, on the basis of which nanocubes were eventually formed [57]. Obviously, from the spherical or near-cubic silver particles to the final nanocubes, the {111} and {110} facets of the particles had to grow faster than their {200} facets so as to form the sharp vertexes and edges of the cubes. That is, the silver colloids should have preferential {111} and {110} assembling orientation. Similar to the case of the formation of cubic gold nanoparticles in the presence of cetyltrimethylammonium bromide (CTAB) as reported by Murphy et al. [72], HTAB molecules probably bound more strongly to the {200} than to the {111} and {110} facets, which led to an increase in the growth rate along the $\langle 111 \rangle$ direction and a reduction in the growth rate along the $\langle 100 \rangle$ direction, thus resulting in the formation of the nanocubes [73]. On the other hand, from the kinetics point of view, the lowest energy {111} facets were favorable for the colloids to assemble, leading to their disappearance and the formation of {200} facets till a cubic structure bounded by the six {200} facets was achieved.

In fact, synthesis of silver nanoparticles in the presence of coating agents, such as amino acids or small peptides, often produces nanoparticles with variable dimensions, which depend on the concentration of the coating agent [74], and on reaction conditions [75].

3.2.3   Gold Nanoparticles

Controlled nucleation and separation of nucleation from growth are the keys to synthesizing near-monodisperse gold nanoparticles [76]. This can be achieved either by providing a controlled number of preformed gold nanoparticles as nucleation centers in a growth medium where no secondary nucleation can occur—the seeding growth method [76]—or by varying the ratio of strong and weak reducing agents [77]. Key goals in the synthesis of metal nanostructures are that the synthesis gives nanostructures of a specific size and size distribution and that the synthesis is reproducible [78]. The simplest approaches for isotropic and

anisotropic gold nanoparticle synthesis are various surfactant-based methods, mainly microemulsion approach [79].

Surfactant-based (an)isotropic micelle templates can be easily prepared [80]. For example, the ∼6 nm spherical micelles formed by a dilute (>1 mM) solution of CTAB surfactant convert to cylindrical micelles at higher concentrations (>20 mM), more elongated rodlike micelles in the presence of organic solubilizates [81], and wormlike micelle structures in the presence of salicylate [82]. Surfactant molecules can be used as "simple" capping, soft template, and stabilizing agents as in the organometallic precursor decomposition reactions.

Fu et al. [83] and Jana et al. [84] have proposed a micelle template mechanism that can explain the origin of various shapes of gold nanoparticles (Scheme 3.4). There are three important parts of this mechanism: First, the cylindrical micelle induces breaking of symmetry in the growing nanoparticle; second, symmetry-breaking performance is dependent on nanoparticle size; third, beyond a size limit (>5–10 nm) the nanoparticle detaches from the micelle surface because of its comparatively larger mass, and the micelle template mechanism does not work. Nanorods are obtained in high yield only when the nonseeding method is used or when the smallest seed of 1.5 nm was used in the seeding growth method.

Lower symmetric spheroids, platelets, cubes, and stars were formed if the seed size was between 3 and 5 nm or the gold nanorods were allowed to grow further. If the seed particle size was >5 nm, the anisotropic nanoparticle yield was very low regardless of seed concentration used. According to earlier mechanisms [85], monomers organize on the micelle surface, make a covalent organic shell surrounding the micelle, and these primary core@shell particles are connected to each
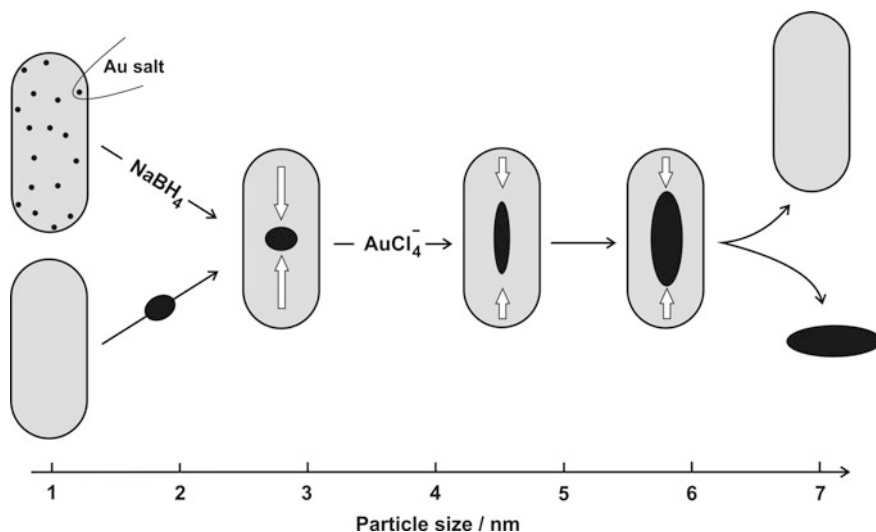
Scheme 3.4 Proposed rodlike micelle template mechanism for (*top*) borohydrate or (*bottom*) gold seed nanoparticles [84]

other via interparticle bonding. Primary rodlike particles are formed while occupying only a part of each micelle surface [84]. When the particle–particle interaction is weak, the primary particles remain isolated during the entire growth processes. The final particle size is dictated by the size of the micelle template and the relative rates of nucleation and growth.

Variations of noble metal nanorods to spheres were initiated by using cyanide as oxidant in the presence of CTAB micelles [86]. Herein, short spheroids with sharp tips dissolve preferentially from the tips, leading to lower aspect ratio nanorods and eventually to spheres. However, for longer nanorods, cyanide oxidation occurred at various spots along the side edges, with no intermediate shorter rods being formed. Rodrıguez-Fernandez et al. have shown that the $AuCl_4^-$ ions are quantitatively bounded to CTAB micelles and can be used to vary the particle size and shape [87]. The crystal growth can be manipulated and spatially controlled by CTAB if the active solution species that deposit onto the growing particle surface is adsorbed to the CTAB micelles. Conversely, in its absence corrosion should be homogeneous over the particle surface. The dissolution of gold nanorods by $AuCl_4^-$ is shown via reaction (3.10)

$$AuCl_4^- + 2Au^0 + 2Cl^- \leftrightharpoons 3AuCl_2^- \tag{3.10}$$

which only takes place in the presence of CTAB because of a change in the reduction potential of $AuCl_4^-$ upon complexation, and leads to gradual oxidation of gold nanoparticles. Careful analysis of this reaction shows that it occurs preferentially at nanoparticle surface sites with higher radius of curvature, and provides an elegant procedure for the narrowing of the nanoparticle size and shape distribution.

If $AuCl_4^-$ is added to the seed gold nanoparticles in the absence of CTAB, no changes in either the optical response (plasmon band position, shape, or intensity) or the morphology of the particles are observed, but if both the seed gold nanoparticles and the gold salt are premixed with CTAB, then upon mixing there is a gradual change in the spectrum [87]. There is a systematic blueshift of the absorption peak, a clear decrease in the peak intensity, a narrowing of the absorption band, and an increase in the symmetry of the band profile. Such spectral changes are consistent with the gradual oxidation of Au^0 since a decrease in particle size will lower the absorbance and cause a blue-shift. Time evolution of the UV–Vis spectra during oxidation of gold nanoparticles before (0) and after addition of $HAuCl_4$ with CTAB and Au:Au(III) molar ratios (a) 1:0.25 and (b) 1:0.5 is as follows [87]:

(a) λ_{max} (nm)/time (min):

$$550/0, \; 545/36, \; 540/131, \; 535/300 \text{ and } 530/1036 \tag{3.11}$$

Absorbance (a.u)/time (min):

$$1.0/0, \ 0.9/36, \ 0.8/131, \ 0.7/300 \text{ and } 0.6/1036 \qquad (3.12)$$

(b) $\lambda_{\max}$ (nm)/time (min):

$$500/0, \ 490/36, \ 478/131, \ 465/300 \text{ and } 450/1036 \qquad (3.13)$$

Absorbance (a.u)/time (min):

$$1.05/0, \ 0.85/36, \ 0.6/131, \ 0.3/300 \text{ and } 0.13/1036 \qquad (3.14)$$

Furthermore, the narrowing and increased symmetry of the surface plasmon (SP) absorption band also suggested that there is a progressive increase in monodispersity [88]. This reaction only takes place in the presence of CTAB micelles which carry complexed $AuCl_4^-$ ions. If the concentration of CTAB is lower than the critical micelle concentration, precipitation of the $AuCl_4^-$ ions complexed with CTAB monomers is observed [89]. Importantly, the different shaped gold nanoparticles expose different crystallographic facets to the solution at the protuberances. Since they all display the same surface smoothing during oxidation, it is concluded that the mechanism that leads to spatially directed oxidation of the particles is independent of the exact crystallographic facets present at the sharply curved points on the particle surface. Hence, it is not determined by the specific binding of CTAB to particular facets, but is a consequence of the high local curvature. This suggests that both reduction of $AuCl_4^-$ to form gold rods and the dissolution of the rods take place at the rod termini. Micellization of the gold salt leads to preferred electron transfer at the tips and implies that the collision frequency of micelles with the gold rods is higher at the tips.

To provide a clear demonstration of the shifts in absorbance band with particle sizes and shapes, Rodrıguez-Fernandez et al. have chosen samples with relatively high aspect ratio (~ 5) [87]. They used a mixture of mostly rods (68%) and cubes (32%). When $HAuCl_4$ is added in the presence of CTAB, absorption spectroscopy [the absorption band shifts from 900 nm before oxidation to 700 nm after oxidation and simultaneously the absorbance decreased from 2.2 to 1.0 (a.u.)] reveals a gradual blueshift and decrease of the longitudinal surface plasmon (LSP) band, indicating the expected decrease in aspect ratio, which is also confirmed by TEM (see Scheme 3.5). TEM images also show that nanocubes present in the sample become more spherical after the oxidation (before: $L = 48$ nm, $W = 10$, $L/W = 5$; after: $L = 29$ nm, $W = 10.4$, $L/W = 2.8$, [Au]:[Au^{III}] = 1:0.25, 0.05 M CTAB, [width (W) and length (L)]). This is probably related to the extreme curvature associated with such acute tips. This cube-to-sphere conversion is also reflected in the UV–Vis spectra, since the band at 545 nm (due to nanocubes) in the spectrum at time zero quickly merges with the absorption band, around 520 nm due to excitation of surface plasmons in spherical nanoparticles.
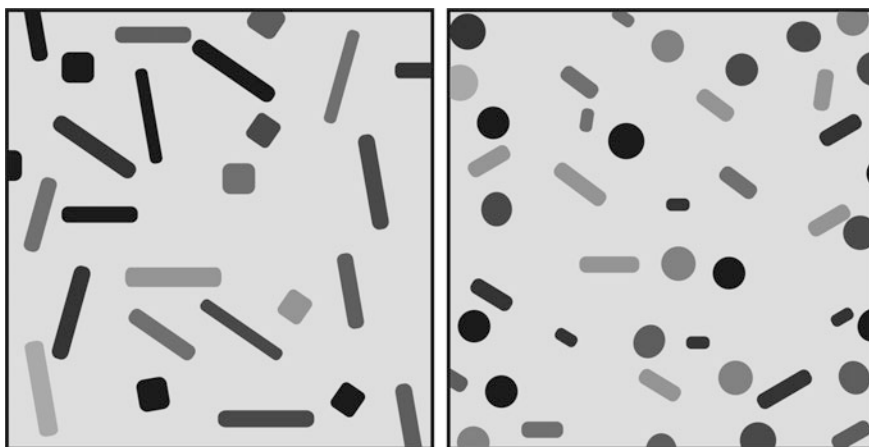
Scheme 3.5 Gold nanorods (*left panel*) before and (*right panel*) after oxidation with HAuCl$_4$ ([Au]:[Au^{III}] = 1:0.25) in the presence of CTAB 0.05 M [87]

The addition of H$_2$O$_2$ to a phosphate buffer solution that includes AuCl$_4$$^-$, gold nanoparticle seeds ($\sim$12 nm stabilized by citrate), and cetyltrimethylammonium chloride (CTAC), as surfactant, results in the immediate increase of the absorbance corresponding to the gold nanoparticle plasmon [90]. Figure 3.3 shows the evolution of the absorbance spectra in the system with variable concentrations of H$_2$O$_2$. As the concentration of H$_2$O$_2$ increases, the absorbance is intensified. Control experiments reveal that no AuNPs are formed in the absence of the AuNP seeds and that added H$_2$O$_2$ is essential to stimulate the absorbance changes. These results suggest that the AuNP seeds act as catalysts for the reduction of AuCl$_4$$^-$ by H$_2$O$_2$, resulting in the enlargement of the particles and the enhanced absorbance features, Eq. 3.15.

Fig. 3.3 Variations of absorbance spectra AuNP seeds ($\sim$12 nm), with the H$_2$O$_2$ concentrations, upon growth in the presence of HAuCl$_4$, in phosphate buffer solution that included CTAC, and using different concentrations of H$_2$O$_2$: *1* 0 M, *2* 5 × 10^{-5} M, *3* 1.8 × 10^{-4} M, *4* 6.0 × 10^{-4} M [90]

$$AuCl_4^- + 3/2H_2O_2 - AuNP \rightarrow Au^0 + 4Cl^- + 3H^+ + 3/2O_2 \qquad (3.15)$$
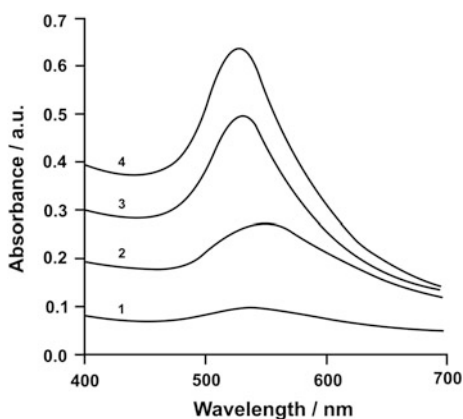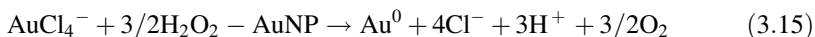
A closer inspection of the spectral changes of the gold nanoparticle seeds upon treatment with H_2O_2, Fig. 3.3, indicates that at low H_2O_2 concentrations a redshift in the absorbance maximum is observed, curve (1), while at higher H_2O_2 concentrations, concomitant to the absorbance growth, a blueshift in the absorbance maxima occurs (curve 4). While the redshift observed at low H_2O_2 concentrations may support the enlargement of the particles [91], the blueshift at higher H_2O_2 concentrations with the concomitant absorbance growth may imply the formation of more AuNPs of lower dimensions or the formation of a mixture of very small crystalline AuNPs together with enlarged AuNPs.

The gold nanoparticles are found to exist in several morphologies (spheres, rhombs, triangles, and polygons) with a very narrow size distribution ~ 12 nm. The gold crystallites are observed to be catalytically grown at the intersection of the faces of the parent seed gold nanoparticles. The HRTEM analysis indicates that the initial AuNP seeds are in the distinct decahedral or icosahedral structures [92, 93]. Upon the enlargement of the particles, gold is deposited on the seeds, and the nanocrystalline flakes are deposited and catalytically enlarged at the sharp intersections of (111)/(111), (100)/(110), and {110}/{210} faces. This mechanism may smooth out the sharp edges of the nanoparticles and decrease their surface energy.

The enlargement of the gold nanoparticles seeds by H_2O_2 was also examined on surfaces. The citrate-capped gold nanoparticles were assembled on an aminopropylsiloxane film that was assembled on glass plates [94]. The resulting plates were then reacted with a solution of $AuCl_4^-$/CTAC in the presence of different concentrations of H_2O_2. The absorbance of the AuNP-modified interface increases as the concentration of H_2O_2 is elevated. Interestingly, however, and in contrast to the spectra in solution, the absorbance bands characteristic to the AuNPs are constantly redshifted. As the H_2O_2 concentration increases, the AuNPs are enlarged. The absorbance spectra of the slides correspond then to the net surface-enlarged AuNPs. HR-SEM measurements support the enlargement process of the AuNPs on the surface. The AuNPs are enlarged from ~ 12 to ~ 18 nm, respectively.

Gold nanopopcorn synthesis was achieved through a two-step process, using seed-mediated growth in the micellar solution. In the first step, very small, reasonably uniform, spherical seed particles were generated using trisodium citrate as stabilizer and sodium borohydride as strong nucleating agent. In the second step, ascorbic acid was used as weak reductant as well as CTAB as shape-templating surfactant so that the seeds grew into larger particles of the particular morphology we desired. $HAuCl_4$ together with gold-seeded nanoparticles and silver salt were also present in the reaction solution. The ascorbic anions transfer electrons to the spherical seed particles, which reduce gold ions to form a gold shell, which grows into different shapes in the presence of CTAB. The solution turned pink immediately after the addition of $NaBH_4$ and became red after it was kept in the dark

overnight. The nanoseeds exhibited absorption spectra with a maximum at 510 nm, which corresponds to a 4.3 nm seed, which was confirmed by TEM [95].

A generated popcorn-shaped gold nanoparticle has only one plasmon bond, like spherical gold nanoparticles, but its λ_{max} is shifted about 60 nm in comparison to that of a spherical gold nanoparticle of the same size. The popcorn-shaped gold nanoparticles concentration was measured using the plasmon absorption peak at 580 nm, given that the popcorn-shaped nanoparticles extinction coefficient is $4.6 \times 10^9\,M^{-1}\,cm^{-1}$. The extinction coefficient was measured by using inductively coupled plasma (ICP) analysis to quantitatively determine the gold concentration in nanoparticle solution and nanoparticle volume measured by TEM [96].

The organic coating was performed in nonionic surfactant (Igepal)-cyclohexane reverse micelle medium [30]. Igepal produces 1–10-nm-size spherical reverse micelles, depending on the water-surfactant molar ratio [97]. This coating method has been extended to different hydrophobic nanoparticles as well as to different imidazole monomers. Although the method works well for gold and silver, and produces water-soluble particles, it did not work for iron oxide nanoparticles (produces water-insoluble particles). Different imidazole monomers such as imidazole, imidazole-4-acetic acid, L-histidine, L-histidinol, and their mixtures were tested, and it was found that imidazole-4-acetic acid and L-histidine produce water-soluble particles that are the most stable. The reaction conditions were optimized by varying the molar ratio of different reactants and other reaction conditions, in order to get the most stable colloidal solution. The possibility of particle aggregation during polymer coating was minimized by examining different experimental conditions and finding conditions that produce water-soluble nanoparticles of smaller size [98].

The o/w microemulsion with gold precursor, $HAuCl_4$, as aqueous phase was subjected to an irradiation process [99]. Initially, before the irradiation, the size of the nanodroplets $HAuCl_4$ containing, in this pristine o/w microemulsion, was around 20 nm. By increasing the irradiation time to 60 min, one can observe that
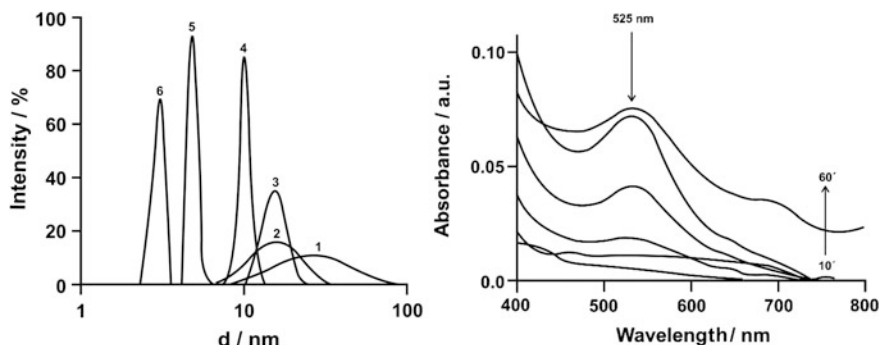
Fig. 3.4 Evolution in time of simple AuNP in pristine microemulsion (mE): DLS spectra; *1* initial mE, irradiation time: *2* 10 min, *3* 20 min, *4* 40 min, *5* 50 min, and *6* 60 min (*left panel*), electronic spectra of mE solution irradiated from 10 to 60 min (*right panel*) [99]

the sizes of the micelles are decreasing very much up to 5 nm (Fig. 3.4). Also, the intensity of the size peak increased substantially and the polydispersity index was high (~ 1) which indicates that polydisperse AuNPs with small size were obtained, but with a high tendency of aggregation.

The UV–Vis electronic spectra in Fig. 3.5 show a maximum absorption peak at 325 nm for initial microemulsion characteristic for [AuCl$_4^-$] ions that disappears after 20 min of irradiation, and the presence of the surface plasmon resonance band at a 525 nm wavelength specific to colloidal gold nanoparticle evolves. These results were similar with AuNPs obtained in w/o microemulsion [31]. The absorbance has limited values as the concentration and the size of the nanoparticles are small. The absorption wavelength offers valuable information about the size of AuNP, and absorbtion at 525 nm wavelength confirms the small size of 5 nm and spherical shape [100].

As the simple AuNPs were not stable in the microemulsion system, thiols (10^{-1} M) were introduced as stabilizer before the microemulsion formation. The volumetric ratio tiol: HAuCl$_4$ was 1:3. The DLS results of the microemulsion system containing sodium 3–sulfonate mercaptopropan (SM)—HAuCl$_4$ irradiated from 0 to 240 min are presented in Fig. 3.5 (right panel). The DLS analysis showed that, in the synthesis process of {Au–SM}NP, the microemulsion template used was very stable since the sizes of the micelles were almost at the same initial value of 20 nm. After the addition of SM thiol, the intensive band specific to [AuCl$_4^-$] at 325 nm disappeared and only a shoulder between 300 and 350 nm remains corresponding to SM derivative. The electronic spectra of AuNP functionalized with SM in a single-phase synthesis in o/w microemulsion were not useful as, during the irradiation process, the color of the microemulsion was yellow and the absorption peak specific for the plasmon resonance band was not visible.

The behavior of cysteamine-monochlorhydrat (CS) thiol was similar with the one of SM as the size of the AuNP stabilized with CS and dispersed in o/w
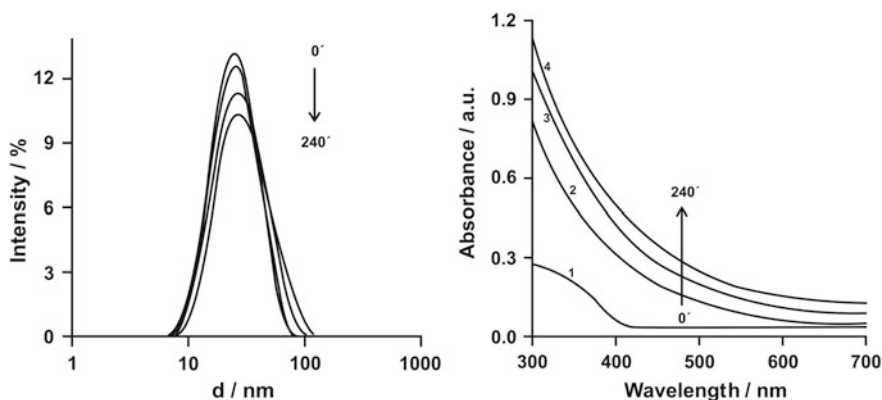
Fig. 3.5 Evolution in time of SM—AuNP in pristine mE: DLS spectra (*left panel*); electronic spectra (*right panel*) [99]

microemulsion was maintained at initial value of 20 nm (similar behavior to Fig. 3.5). The o/w microemulsion containing CS–AuNP having the same behavior and color as pristine SM–AuNP microemulsion. The "masking" behavior can be explained by covering the AuNP surface with SM thiol molecules similar to spectral shape being obtained by Hussain et al. [101] who studied the effect of water-soluble alkyl thioether over AuNP size control.

The narrow shape of the size distribution indicates the homogeneity distribution of the gold precursor in the o/w microemulsion [PDI $\sim$ 0.229 (SM) and $\sim$0.237 (CS)]. After the o/w microemulsion has been formed the gold precursor and thiols molecules are dispersed in continuous water phase, but after the irradiation and formation of Au–S bond between AuNP and thiols, the CS–AuNP is transferred in oil droplets due to the hydrophobic tail of CS thiols. These could be the reason for the AuNP size and geometrical shape similar with the one of oil droplets.

The XRD analysis revealed the presence of the seven diffraction peaks that are attributed to the crystalline phases of gold, similar for both gold nanoparticles stabilized with SM or CS, at 2θ = 38, 44, 64, 78, 82, 98, and 111 °C that correspond to crystalline planes (111), (200), (220), (311), (222), (400), and (311) of gold. The diffraction peaks corresponding to the diffraction planes (111), (200), and (220) were indexed to the gold metal with face-centered cubic [100]. The energy-dispersive X-ray fluorescence (EDXRF) qualitative analysis of the solid sample of AuNP stabilized by SM thiol identified the presence of gold in a percent of 99.41%. EDXRF analysis of the {Au–CS}NP in solid state indicated the presence of gold in a major percent, 99.54%. The overlapping of the two spectra, for the two types of samples, Au–SM and Au–CS nanopartiles, showed they have a similar composition.

HRTEM has shown that all {Au–SM} and {Au–CS}NPs are spherical in shape and well dispersed from each other but size of 5 nm is smaller than the one obtained from DLS measurements. When are dispersed in o/w microemulsion the AuNPs are surrounded by a surfactant molecules layer which increases the size estimated by DLS. The SAED patterns recorded at a camera length of 80 nm consisted of a number of diffraction spots arranged in circular rings, indicating areas of crystalline AuNP structure [99].

Negatively AuNP surface charges were obtained using SM, whereas positively AuNP surface charge using CS, as thiols capping ligands (SM = −28.1 mV and CS = 24.9 mV) of gold precursor, $HAuCl_4$. The negative charge for SM and the positive charge in the case of CS were formed due to the free sulfate, SO_3^- and ammonium, NH_3^+ ions remained at the surface of AuNP, after the strong chemical bond between the gold and sulfur [102]. Positively and negatively gold nanoparticle surface charge has various applications in biological and medicine field such as gene delivery [103], colorimetric detection of glucose [104], inhibition of Alzheimer's amyloid–β fibrillization [105] and binding, and stabilization and delivery of therapeutic DNA, RNA, and other biological macromolecules [106]. Relating to the delivery efficiency the polarity of AuNP is important, due to the highest deliverance potential displayed by positively charged AuNP and grater

cellular uptake showed by negatively charged AuNP than neutral AuNP which was likely because of their affinity for membrane proteins [107].

3.2.4   Hybrid Nanoparticles

Specific supports or templates such as metal oxides [108], or activated carbon [109], have been used to improve the activity in the adsorption of reactants, stability of noble metal nanoparticles, and reusability of conjugates. Significant effort has been made to develop gold nanocatalytic systems that mainly include discovering adequate supports and efficient deposition methodologies [110], fabricating core@shell-type morphologies [111], and integrating active nanoparticles [112]. Therefore, assembling noble metal nanoparticles by surrounding them with polymer or inorganic (silica, SiO_2) shells as a support (template) could be a potentially useful method for the preparation of highly active hybrid nanoconjugates assemblies.

The soft template formed by reverse micelles consisting of CTAB, 1-butanol, and octane as the (co)surfactant, and the oil phase, respectively, was effective to prepare the composite (hybrid) gold-coated iron nanoparticles [113]. The composite nanoparticles were prepared in inverse micelles by reduction of Fe(II) salt with $NaBH_4$, and then Au(III) salt with $NaBH_4$ were added. The typical size of the composite nanoparticles is about 20 nm. Cho et al. have investigated [114] the reverse micelle synthetic method more in detail and have found that the structure of iron@gold (core@shell) nanoparticles is not as simple as either of the previous reports indicated [113]. The gold shell was suggested to grow by nucleating from small nanoparticles on the iron-core surface before it develops the shell structure. These nanoparticle nucleation sites form islands for the growth and coalescence of the thin gold overlayer. Specifically, Au^{3+} is reduced to Au(0) by $NaBH_4$, which initiates minimum nanoscaled seed gold nanoparticles, and they grow larger, resulting in a gold shell (a heterogeneous nucleation).

Laser ablation of solvent-suspended metal powders can be used in for synthesis of gold/silver alloy and core@shell nanoparticles of predetermined composition [115]. Two general routes for synthesis of the Fe@Au nanoparticles have been explored. The first one consists of making both the iron core and the gold shell using the laser ablation method. The second one consists of preparing the iron core by wet chemistry and subsequently coating the core with gold by laser ablation of gold powder. Magnetic extraction and acid washing of nanoparticles constitute the third step in both routes (Scheme 3.6) [116]. The main advantages of the second route are a higher overall yield and better control of the size of the magnetic core.

Lin et al. have more in detail described a heterogeneous growth process in which an organometallic source of atoms is slowly coinjected with a solution containing a metal hydride reductant into a stirred vial containing the nanocluster seed crystals [117]. They grew successive generations of metal particles from seeds formed in cationic inverse micelles using the inverse micelle solution used to grow the seeds
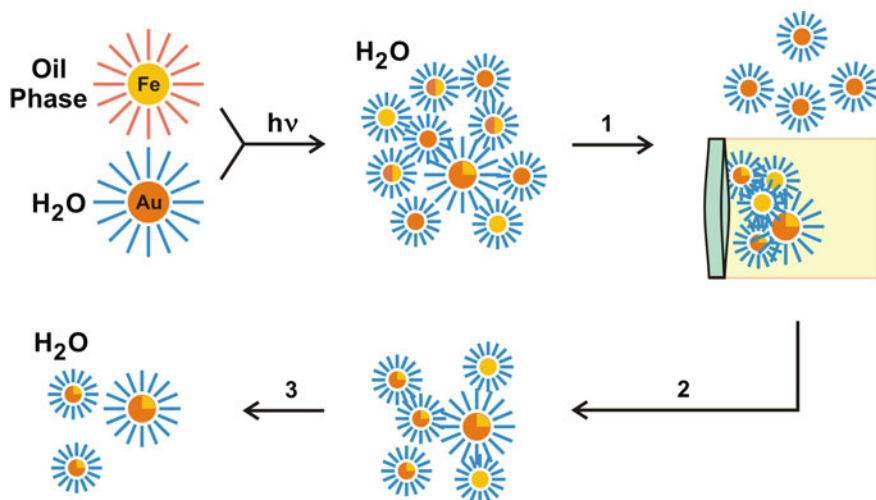
Scheme 3.6 Schematic diagram of the experimental process for fabrication of iron@gold magnetic nanoparticles, *1* magnetic confinement, *2* redispersed in water with surfactant, and *3* remove surfactants; acid washing/redispersed in water with surfactant [116]
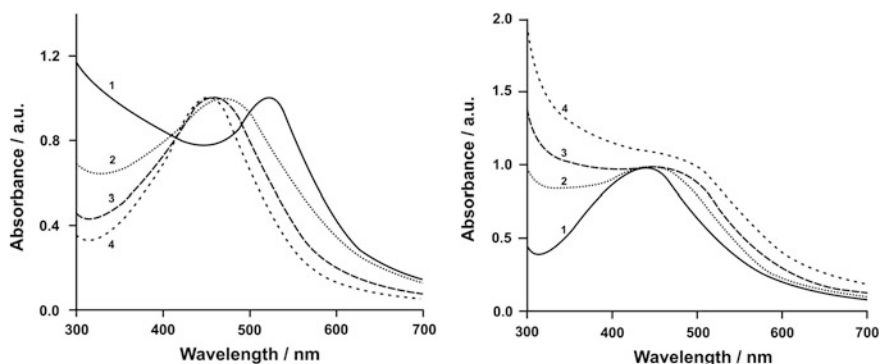
Fig. 3.6 Effect of deposition of progressively larger amounts of Ag on Au seed nanoparticles with a core size of $d = 5.4$ nm (*curve 1*). The atomic ratios of Au:Ag are indicated for each case. The ratios correspond to Ag shell thicknesses (total thicknesses) of ~ 1.4 (*2*), 3.2 (*3*), and 5.3 (*4*) nm, respectively (*left panel*). Effect of deposition of progressively larger amounts of Au on Ag seed nanoparticles with a core size of $d = 4.0$ nm (*curve 1*). The atomic ratios of Au:Ag are indicated for each case. The ratios correspond to Au shell thicknesses (total thicknesses) of ~ 1 (*2*), 2.5 (*3*), 4.6 (*4*), and 8.2 (*4*) nm, respectively (*right panel*) [118]

as the feedstock for each stage of growth. The effect of silver and gold deposition on the absorbance properties of seed nanoparticles is summarized in Fig. 3.6 [118]. The red-colored parent solution with an absorbance peak at 518 nm (AuNPs) blueshifts in a systematic manner as thicker shells of silver are formed around the

core, ultimately resulting in a yellow-colored solution with a narrower symmetrical plasmon typically associated with a silver nanocluster [117]:

$$\lambda_{max}(nm)/\{Au:Ag\,(atomic\,ratio):gold\,seed\,(518\,nm)\};$$
$$480/1{:}1,\;460/1{:}3,\;450/1{:}7 \tag{3.16}$$

In the case of gold deposition onto silver clusters, the absorbance peak shifts in the opposite manner, as shown in the example of Fig. 3.6 (right panel), where a seed population of AgNPs was used:

$$\lambda_{max}(nm)/\{Ag:Au:silver\,seed\,(430\,nm)\}:$$
$$460/1{:}1,\;480/1{:}3,\;500/1{:}7,\;505/1{:}15\;and\;510/1{:}31 \tag{3.17}$$

It is noteworthy that even when the particle has a 31:1 Ag:Au ratio which corresponds to a $d = 4$-nm silver core with a total size of ~ 12 nm, the damping of the gold plasmon is much stronger than is observed in a pure gold particle of the same size. These experiments indicate that, beyond a size of ~ 6 nm, further addition of gold feedstock atoms in the presence of alkanethiols leads to an etching and mass redistribution process. Such a process has already been demonstrated for thiolate-stabilized 8–10-nm-gold nanoparticles grown in nonionic inverse micelles [119]. It is very interesting to note that the same mechanism appears to be causing a size reduction in this case too. In aqueous solution, growth of large-size clusters in the range of 12–100 nm by a seeding technique using relatively monodisperse seeds has been demonstrated [120]. Herein, the clusters were charge stabilized by the presence of citrate ions on their surfaces. This overcomes the requirement of bulky, polymer-like steric stabilizers to prevent particle agglomeration.

In addition to gold nanoparticles, other noble-metallic nanoparticles with a narrow size distribution can be synthesized by substituting gold precursor with other metal precursors (e.g., $AgCF_3COO$, Pd(II) acetylacetone, etc.) [121]. As observed, both mono- and alloyed (Pd/Ag) metallic nanoparticles can be synthesized (~ 5.5 nm AgNP; ~ 6.3 nm PdNP; ~ 3.8 nm 1:1 Pd/Ag alloy). Ayyanppan et al. [122] obtained silver, gold, palladium, and copper nanoparticles by reducing metallic salts in dry ethanol. Longenberger et al. [123] produced Au, Ag, and Pd metal colloids from air-saturated aqueous solutions of poly(ethylene glycol) (PEG). Reduction methods can also be used for the production of Pt, Pd, Cu, Ni, etc., although specific protocols depend on the reduction potential of the source ion [124]. Under certain conditions, the metal particles can be oxidized and, therefore, they require capping ligands to prevent the oxidation.

A useful technique for assembling gold nanoparticles within a silica shell was reported by Park and Yoo research group [125]. Highly spherical nanoparticles with a core comprising multiple gold nanodots and a silica shell ($\{Au@SiO_2\}NPs$) were synthesized via a reverse (water-in-oil) microemulsion-based method. The silica-encapsulated gold nanodots with diameters of 2–5 nm were arranged such that the interparticle gaps were in the subnanometer range. However, the gold

nanodots within multi-Au@SiO$_2$ nanoparticles ({Au@SiO$_2$}NPs) were surrounded by a thick and dense silica shell, which might restrict the potential availability of multiple gold nanodots and the interparticle gaps. To use the physical and structural properties of the gold nanodot assembly of {Au@SiO$_2$}NPs in a variety of applications, further modifications of the silica shell such as imparting porosity were required [126]. Au^{3+} ions were reduced during the formation of silica nanoparticles from tetraethylorthosilicate (TEOS) and NH$_4$OH in a reverse microemulsion, which was generated using polyoxyethylene glycol dodecyl ether [(C$_2$H$_4$O)$_{23}$C$_{12}$H$_{25}$OH, Brij35], n-hexanol, and cyclohexane.

In an endeavor to develop {Au@SiO$_2$}NPs, a "soft-etching" methodology was employed through a thermal treatment without any surface-protective agents. This synthetic method is based on the fact that amorphous silica nanoparticles can be dissolved in the form of monomeric Si(OH)$_4$ in water, and the solubility increases with temperature [127]. Although single gold nanoparticle core@mesoporous silica shell nanoparticles have been fabricated through similar strategies [128], there has been no example of silica etching in types of {Au@SiO$_2$}NPs. It was found that thermal treatment of the {Au@SiO$_2$}NPs in water without adding any other additives leads to generation of mesopores over the silica shell without any change in the size and number of the gold nanodots.

The {Au@SiO$_2$}NPs were transformed to multi-Au@mesoporous-SiO$_2$ NPs by heating and clearly observed in TEM images. Scheme 3.7 (left) is the TEM image of {Au@SiO$_2$}NPs that was acquired before heating, and Scheme (right) is the images of nanoparticles after heating at 90 °C for 12 h. Although both nanoparticles show spherical geometries, the nanoparticles in a right image show much more and larger holes over the silica shells than those in a left image. These empty spaces are attributed to mesopores, which were generated by the etching of silica shells in water at high temperature [128]. The average diameter of individual multi-Au@mesoporous-SiO$_2$ nanoparticles was ~41.1 nm, which was similar to that of multi-Au@SiO$_2$ nanoparticles (~40.8 nm). Importantly, the multiple gold nanodots core was not affected by the thermal treatment; the average size and number of gold nanodots in multi-Au@mesoporous-SiO$_2$ nanoparticles were ~3 and ~4.5 nm, respectively, and these values were not critically different from those of {Au@SiO$_2$}NPs (~3.6 and ~3.4 nm [125]). Therefore, we can conclude that thermal etching in water without adding any other additives is a facile and valuable synthetic strategy to prepare multiple nanoparticles core@mesoporous silica shell nanoparticles, without disturbing the structural motifs of metal nanodot assemblies.

Almost no surface plasmon resonances were observed from the aqueous colloidal solution of multi-Au@SiO$_2$ nanoparticles without any heating [125]. However, by etching the silica shell through thermal treatment, the extinction approximately at 530 nm was gradually improved, and this can be assigned to the SPR of spherical gold nanoparticles within the silica matrix (Fig. 3.7). During the thermal reaction, the silica shell was partly etched out and mesopores were generated, which decreased the refractive index of the silica shell. Therefore, the SPRs of gold nanodots could be detected in multi-Au@mesoporous-SiO$_2$ nanoparticles.
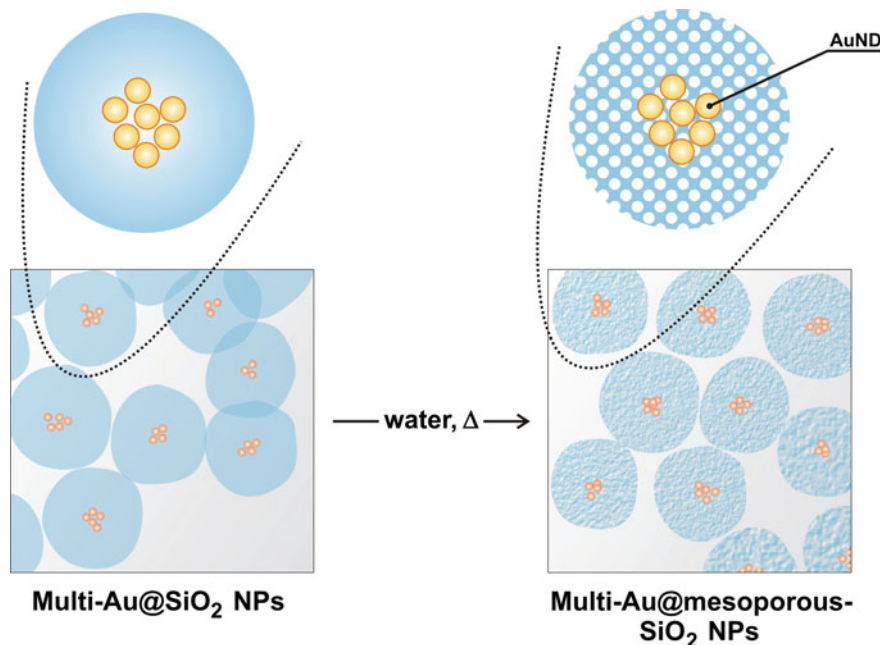
Scheme 3.7 Schematic representation of the formation of multi-Au@mesoporous-SiO$_2$ NPs. TEM image of multi-Au@SiO$_2$ nanoparticles before thermal treatment (*left images*), TEM image of multi-Au@mesoporous-SiO$_2$ nanoparticles formed after thermal treatment of multi-Au@SiO$_2$ NPs in water (*right images*) [125]

Fig. 3.7 UV–Vis spectral changes of multi-Au@SiO$_2$ NPs as a function of heating time 0 (*curve 1*), 12 (*2*), and 36 h (*3*) at 90 °C [129]
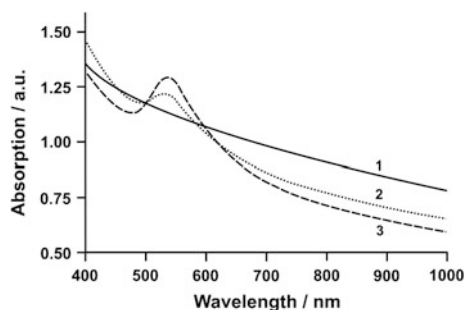
A higher intensity of SPRs was observed after heating, which demonstrates that longer reaction times may lead to greater etching of the silica shell. However, with much longer reaction times, the spherical morphologies of multi-Au@mesoporous-SiO$_2$ nanoparticles were not sustained, and the silica matrix combined to generate wormlike multiple gold nanodots core@silica shell structures. Hence, optimizing the etching reaction time was critical in obtaining highly spherical multi-Au@mesoporous-SiO$_2$ nanoparticles.

The multiple gold nanodots can interact with each other because of their proximity and exhibit interesting collective properties. To understand any collective property of multiple gold nanodots in multi-Au@mesoporous-SiO$_2$ NPs, authors attempted to create single gold nanodot core@silica shell nanoparticles {(single-Au@SiO$_2$)NPs and (single-Au@mesoporous-SiO$_2$)NPs}. Interestingly, when the (multi-Au@SiO$_2$) NPs were stirred in aqueous polyvinylpyrrolidone (PVPo) solution at room temperature, the multiple gold nanodots within the silica matrix were merged together and changed to a single gold nanoparticle. Each silica nanoparticle encapsulated only one gold nanoparticle, which was localized at the center of the silica matrix. The sizes of individual spherical silica nanoparticles were not considerably changed upon aggregating multiple gold nanodots (before: $\sim$40.8 nm, after: $\sim$46.2 nm). On the other hand, the average diameter of the gold nanoparticles within the silica matrix was $\sim$5.50 nm, which increased about 50% from that of each gold nanodot in multi-Au@SiO$_2$ nanoparticles ($d_{avr.} \sim$ 3.60 nm). Furthermore, there was a little empty space between the gold nanoparticle and silica layer in each multi-Au@SiO$_2$ nanoparticle, which made this particle a "york-shell" morphology [130]. Previously, it was reported that PVPo can protect the outmost silica layer to allow selective etching of the inner section preferentially [131, 132]. In the current discoveries, the internal silica matrix around multiple gold nanodots is believed to be much "softer" than the outer sides, therefore could be unevenly etched when PVPo is used as a surface-protective agent. In particular, after the inner silica matrix is firstly etched, a void water environment might be formed on the center of silica nanoparticles. In this condition, multiple gold nanodots could be aggregated to generate a single gold nanoparticle within a hollow silica nanoparticle due to their high surface energies. Similar uneven etchings of silica matrix have been observed in water [128] and in acidic conditions [133].

3.2.5 Polymer-Coated Nanoparticles

The external polymeric coating of gold or silver cores defines both the spacing and the interactions in nanoparticle systems with this type of architecture. We can, therefore, take advantage of modern macromolecular engineering knowledge to synthesize next-generation polymer coatings for noble metal nanoparticles that may feature stimulus-responsiveness (pH, temperature, ionic strength, and light) and spontaneously form versatile supramolecular structures. A number of methods have been described for preparation and stabilizing NMNPs, including soft micelle templates of ionic and nonionic polymeric surfactants such as polyoxyethylene (20) sorbitan monolaurate (Tween 20) [134], direct attachment of bolaamphiphile surfactants [135] or thiolated polymers [136], and layer-by-layer deposition of polymers using charge interactions on the surface of NMNPs as a driving force [137].

The fabrication of metal core@polymer shell nanoparticle architectures in which a layer of polymer material surrounds an inorganic core has been the focus to potential applications in fields of research ranging from optics [138] to electronics [10], to catalysis [11]. Such applications typically involve tailoring the surface properties of the core particles by coating and encapsulating them within a desired polymeric material. Some of the physical and chemical properties of the core nanoparticles are often imparted to the resulting polymeric shell system, producing hybrid materials with novel properties and functions that are not possible from the single-component structure alone. Among the various polymer shell/metal core structures of particular interest is the encapsulation of gold nanoparticles within functional polymers [139, 140]. Such systems are attractive due to their biocompatibility [141], ease of functionalization because of the strong thiol–gold bond [142], and optical properties related to the gold core and its surface plasmon characteristics, which arise from light coupling to the collective oscillation of the conduction band electrons of the metal [143].

The incorporation of amphiphilic copolymers into the gold nanoparticle fabrication process has led to the interesting discovery that both the formation and the stability of colloids are dictated by the chemical structure of macromolecular chains. Environmentally friendly, single-step/single-phase synthesis of core@shell NMNPs can be mediated by surface-active polymers that simultaneously play the roles of reductant and stabilizer while imparting unique properties to the resulting hybrid material. To date, the above strategy has been applied successful mainly to pluronics and polyacrylates with amino groups, which have a strong ability to coordinate on metal surfaces [144, 145]. The reduction of Au(III) species is induced by the poly(propylene oxide) segment and nitrogen atoms, respectively. Polymer chains chemisorb onto the newly generated particle, being consequently tethered from the surface into the solvent phase.

Compared with classical surfactant-formed micelles, the copolymer surfactant-formed micelles have several advantages. First, the critical micelle concentration of copolymers is much smaller, and their kinetic stability is larger than that of low-molecular weight surfactants. Second, the size and shape of copolymer micelles is easily tuned by varying the composition of the copolymer, the length of the constituent blocks, and the architecture of the copolymer. Third, the stability of the AuNPs is enhanced upon increasing the length of the coronal blocks [146, 147]. Poly(styrene)-block-poly(vinylpyridine) (PSt-*b*-PVP) [148, 149] and poly(ethylene oxide)-poly(propylene oxide)-poly(ethylene oxide) (PEO-PPO-PEO) [150, 151] are the most widely used polymer micelles for AuNPs synthesis, and these AuNPs are applied in catalysis [152] and biosensing [151]. PSt-*b*-PVP micelle-stabilized AuNPs are typically synthesized as described by Möller's group [149]. A solution of the block copolymer in toluene is mixed with HAuCl$_4$ in appropriate amount. The reducing agent hydrazine is added under stirring to form the AuNPs (Scheme 3.8) [148].

Various reducing agents introduced into PSt-*b*-PVP micelle systems may result in the formation of AuNPs of various sizes [149]. In addition, microcalorimetry was used to investigate AuNP formation in the copolymer micelles. For instance,
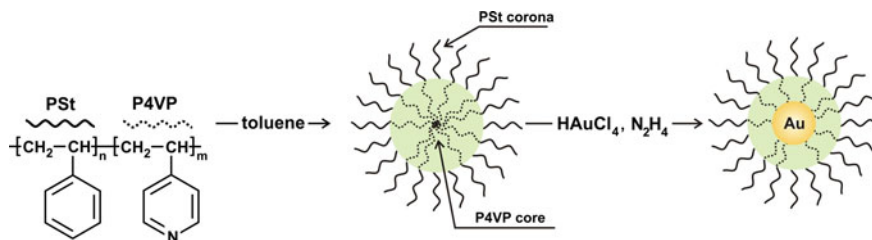
Scheme 3.8 Molecular structure of the PSt-*b*-P4VP (PSt-*b*-P4VP) copolymer and schematic illustration of the micellation process with in situ synthesis of AuNPs by reduction with hydrazine (N_2H_4) in PSt-*b*-P4VP micelles. The molar ratio of $HAuCl_4$:P4VP is 0.1 [26, 148]

PEO-PPO-PEO-stabilized AuNPs were prepared in an efficient one-pot aqueous-phase synthesis from the reduction of gold salts by using PEO-PPO-PEO, both as reducing agent and stabilizer [153]. The formation of AuNPs from gold salts comprises three steps: (i) initial reduction of Au ions in crown ether-like domains formed by block copolymer in solution, (ii) absorption of block copolymer on AuNPs and further reduction of gold ions on the surface of these AuNPs, and (iii) growth of particles stabilized by block copolymers [154]. Increasing the PEO chain length favors the reduction of gold salts and formation of AuNPs [154]. In addition, the temperature [155], micelle environment [150], and shapes and sizes of micelles [150] are also considered to be the main contribution factors in the overall growth kinetics leading to a specific morphology of AuNPs [150]. For example, the smaller micelle size with few surface cavities produced small AuNPs (Scheme 3.9) [150].

Other polymer reverse micelle-stabilized gold nanoparticles were also recently prepared using similar approaches. For example, poly(ethylene oxide)-*b*-poly
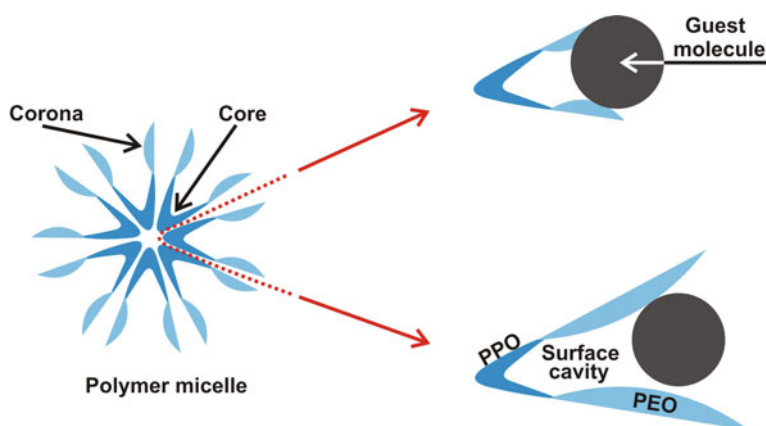
Scheme 3.9 PEO-PPO-PEO micelle with the core occupied by PPO units and the corona constituted by PEO units [26, 150]

(ε-caprolactone) (PEO-*b*-PCL)-stabilized AuNPs with 5–7 nm core size have potential for the exploration of drug delivery systems with biodegradable PCL units and biocompatible PEO units [156]. Polyethylenimine-*g*-hydrocaffeic acid (PEI-*g*-HCA)-covered AuNPs are also the subject of biomedical applications [157].

Despite their simplicity (one-pot, two-reactants, and no workup), this class of reactions still offers a number of possibilities in relation to tweaking the experimental conditions (concentration of reactants, polymer composition and architecture, temperature, and additives) to generate particles with controlled dimensions and properties. Scaravelli et al. have addressed this issue in relation to gold nanoparticle synthesis using the versatile poly(ethylene oxide)-*b*-poly (2,3-dihydroxypropyl methacrylate)-*b*-poly[2-(diisopropylamino) ethyl methacrylate] (PEO-*b*-PDHPMA-*b*-PDPAEMA) triblock copolymer (1) [158]. PEO$_{113}$-*b*-PDHPMA$_{30}$-*b*-PDPAEMA$_{50}$ triblock copolymer can originate pH-responsive, cross-linkable nanostructures in both organic and aqueous media [159]. Molecularly dissolved and positively charged chains in water self-assemble on addition of phosphate buffer solution (PBS) at pH 6.8, owing to the increase in the solution pH to values close to the characteristic pKa of amino groups of the PDPAEMA segment (pKa = 6.8) [160]. Deprotonation of amino groups (50% at pH = pKa = 6.8) renders polymer chains sufficiently amphiphilic to trigger a micellization process, which reduces nonfavorable interactions with the solvent. The resulting self-organized morphology comprises spherical micelles with a three-layer onion-like core@shell–corona architecture, with the PDPAEMA block occupying the micelle core and the PDHPMA and PEO block forming the inner shell and corona, respectively.

The observed absorption at around 530 nm is due to the characteristic localized surface plasmon resonance (LSPR) of gold nanoparticles formed by reduction of Au(III) species in the presence of block copolymer micelles (Fig. 3.8). The nanoparticles also absorb light to a certain extent within the whole range, especially at 300–650 nm. Bands below 400 nm (310 and 320 nm) are assigned to ligand-to-metal charge transfer (LMCT) of chlorohydroxoaurate species $[AuCl_xOH_{4-x}]^-$ (pH dependent) and polymer species, as well as to polymer–$[AuCl_xOH_{4-x}]^-$ complexes [161]. The absorbance of these bands decreases at first with a decrease in Au(III) concentration, eventually increasing owing to the accumulation of Au(0) as nanoparticles. It is worth noting the distinct profile of the first spectrum recorded after buffer addition (*t* = 0 min) as compared to that shown in Fig. 3.8 (*t* = 10 min) (left panel). Clearly, the absorption centered at 320 nm rapidly decreases due to the changes in the coordination environment around the Au (III) metal center that generate absorbing species with lower extension coefficient values. It is ruled out the possibility of Au(III) reduction since the same behavior was also identified in acidic solutions (pH 4.0), where AuNPs cannot be synthesized by the method investigated herein (right panel). There is no evidence of an LSPR band after 48 h at pH 4.0 based on the data provided in Fig. 3.8.

The right panel (Fig. 3.8) highlights the sigmoidal growth kinetics of AuNPs when the only substance used is the triblock 1 copolymer, which, at pH 6.8, is self-assembled into micelles which not only serve as a nanoreactor but also act as a
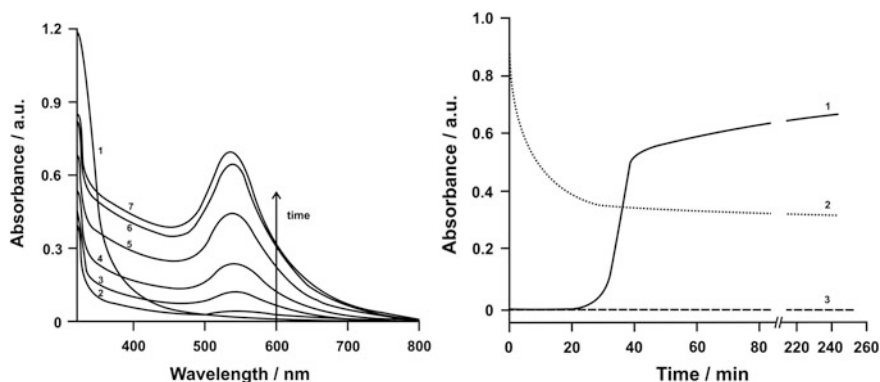
Fig. 3.8 Evolution of UV–Vis spectra during a typical AuNP synthesis procedure involving the reaction between $HAuCl_4$ and triblock 1 copolymer in buffer solution at pH 6.8, time: 0 (*curve 1*), 10 min (7) (*left panel*) and corresponding particle growth kinetics—AuNP: pH = 6.6 (*curve 1*) and 4.0 (3), Au (III) salt: pH = 6.8 (2) (*right panel*) [158]

reducing agent and particle stabilizer [162]. The sigmoidal shape of the curve is typical of an auto-catalytic process often observed in the synthesis of metallic nanoparticles [8], as well as of the so-called aggregative nanocrystal model used to describe gold nanocrystal growth [163]. In general, the process starts with an induction period (t_0) during which absorption at the LSPR is negligible, and the absorption originating from Au(III) species decreases. Au(III) reduction during the induction period t_0 corresponds to the initial nucleation step, which leads to critically sized aggregates [161]. Since the redox-active block of the copolymer is located in the micelle core, these aggregates are formed within the nanoreactor (core) and at the core–shell interface. The interaction between gold species and micelle core is favored by a high concentration of nitrogen atoms.

As the reaction proceeds, nanoparticle growth inside the micelle core occurs by coalescence of very small aggregates [164] or by an auto-catalytic processes [165]. As a result, the micelle diameter ($d_h = 2r_h$) and the total scattered light intensity (I_{sc}) increase as a function of the reaction time (Fig. 3.9, left panel, DLS). Size distribution profiles given in Fig. 3.9 (right panel) confirm the presence of a single population of objects with characteristic diameter of 63 nm in solutions of AuNP@triblock (1) at pH 6. 8. Interestingly, the polymer-coated AuNPs retain their stability at pH 3.0, where micelles are known to disassemble due to the protonation of PDPAEMA [159]. DLS measurements under acidic conditions show an increase in the overall particle size, because the positively charged, water-soluble block copolymer chains that are adsorbed onto the gold surface assume an extended conformation.

The spherical core@shell morphology of the hybrid nanostructures was confirmed by HRTEM images, which generally show that the metal particle is located in the core and surrounded by a polymeric shell of comparatively much lower electron density. According to the thermogravimetric analysis of nanoparticle
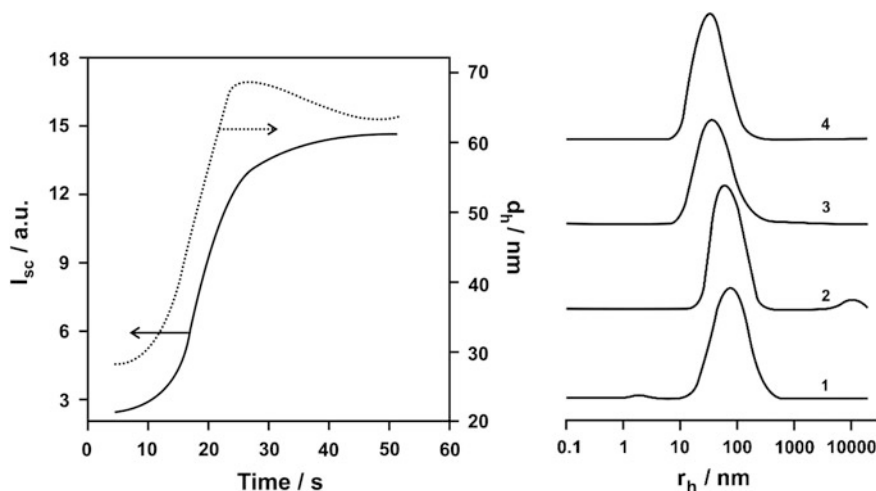
Fig. 3.9 Total scattered light intensity (I_{sc}) and hydrodynamic diameter (d_h) variations during triblock 1@AuNP particle growth in buffered solution (pH 6.8) of 0.275 mM HAuCl$_4$ and 1.0 mg mL^{-1} triblock 1 copolymer (*left panel*), and particle size distribution recorded during selected steps of the synthetic procedure, as indicated (*right panel*) [158]

sediments, the organic content (polymer) was approximately 80%. FTIR spectra of AuNP@triblock (1) revealed a significant shift in the carbonyl group stretching frequency from 1733 to 1720 cm^{-1}, suggesting the adsorption of polymer onto the particle surface, in agreement with previous results obtained by other authors [166]. The results reported above reveal that gold nanoparticle formation only occurs in the presence of triblock 1 when the solution pH is close to, or above, the pKa of the amino groups of the PDPAEMA segment.

Evidently, the PEO block alone or PEO-*b*-PPO-*b*-PEO triblock cannot promote the formation of AuNPs; the characteristic plasmon resonance of AuNPs was not detected. In fact, a much higher concentration is needed to induce AuNP formation via oxidation of the oxyethylene and oxypropylene (if present) segments by the metal center as observed in Fig. 3.10 (left panel). The reason for such an effect is that oxidation is only favorable when these polymers adopt conformations similar to a pseudo-crown-ether structure, which binds with metal ions; the cyclization is caused by ion–dipole interactions between the templating ion and the electron lone pairs of the ethylene oxide linkages, and several oxygen atoms interact with one ion [154]. Therefore, the strength of the attraction is dependent on the concentration. In fact, no electrochemical response was seen at low concentrations. Additional reductants, such as sodium borohydride, may be used in the synthesis, but the polymer will primarily function as a stabilizer while still potentially dictating the size and shape of the nanoparticles [167]. Accordingly, the chemical moiety that effectively mediates the AuNP synthesis is the 2-(dialkylamino)ethyl substituent grafted to the polymethacrylate polymer. This verifies that tertiary amines with
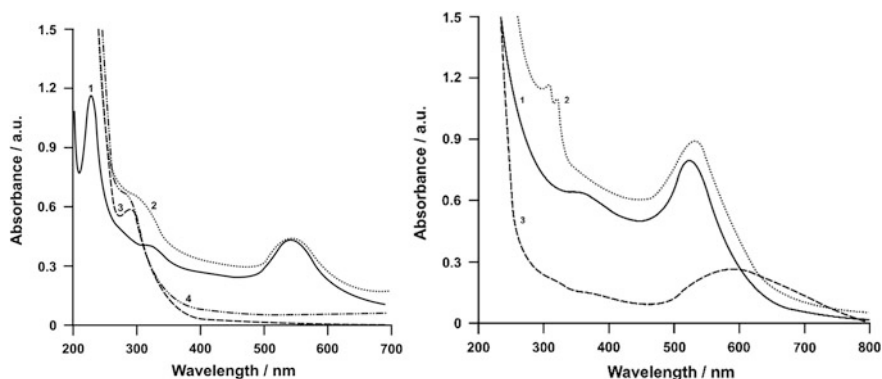
Fig. 3.10 UV–Vis spectra recorded (4 h) after mixing HAuCl$_4$ with selected molecules at concentrations corresponding to the following stoichiometric ratios. PEO-*b*-PPO-*b*-PEO: [EO]/[Au] = 692 (*1*), PEO: [EO]/[Au] = 4132 (*2*), PEO: [EO]/[Au] = 20 (*3*), PEO-*b*-PPO-*b*-PEO: [EO]/[Au] = 20 (*4*) (*left panel*), PEI: [N]/[Au] = 9 (*1*), DPA: [N]/[Au] = 9 (*3*), and PMC-PDPA: [N]/[Au] = 9 (*2*) (*right panel*). All reactions were carried out in buffer solutions (pH 6.8) [158]

aliphatic substituents are good reducing agents for the AuNP preparation, in agreement with the findings of the pioneer work of Yuan et al. [166] and with the electrochemistry results reported by Newman and Blanchard [168] for low molar mass molecules.

The validity of the statement above by conducting reactions was tested with PEO-*b*-PDEAEMA (diblock 2), PMPC-*b*-PDPAEMA (diblock 3), and polyethylenimine (PEI, branched polymer 4) . In the case of 3 and 4, both reactions occurred in a very similar way to 1; λ_{max} and corresponding absorbance values were comparable. In PEI-mediated AuNP synthesis, however, large, dark aggregates were visible within a short period of time because PEI chains are not efficient steric stabilizers of gold colloids. The same comments also apply to the 2-(dialkylamino) ethyl methacrylate monomer, as can be deduced from the corresponding spectra shown in Fig. 3.10 (right panel).

AuNP growth using diblock 2 is feasible, but reactions are characterized by a longer induction time and slower kinetics when compared to triblock 1 system. It should be noted, however, that PDEAEMA and PDPAEMA have distinct pKa values (7.3 and 6.8, respectively) [169]. Thus, the concentration of hydrophobic amino groups is a function of the solution pH, and consequently, the reaction parameters should also vary according to the solution pH. At pH 6.8, the induction period is significantly shorter and the reaction is faster (steeper absorption increase) for triblock 1 (the molar fraction of neutralized amino groups $\alpha = 0.50$) than for diblock 2 ($\alpha = 0.24$) (Fig. 3.11). On increasing the solution pH to 7.4, the α-value of 2 (0.55) becomes comparable to the α-value of 1 at pH 6.8 (0.50), but the kinetics remain vastly different. Therefore, it is not only the degree of neutralization which explains such a behavior, which is ultimately related to the polymer structure–reactivity relationship—PDPAEMA being more efficient than PDEAEMA. The

Fig. 3.11 Kinetic profiles of
typical synthesis procedures
involving the reaction
between 0.275 mM HAuCl$_4$
and triblock 1 (curve (*1*) pH
9.1, α 0.99, (2) 7.4, 0.79, (3)
6.8, 0.5, (4) 4.0, 0.0) or
diblock 2 (closed symbols
curve (*1′*) pH 9.1, α 0.98, (2′)
7.4, 0.55, (3′) 6.8, 0.24, (4′)
4.0, 0.0) at concentrations
corresponding to [N]/
[Au] = 9, in solutions
buffered at different pH values
(indicated) [158]
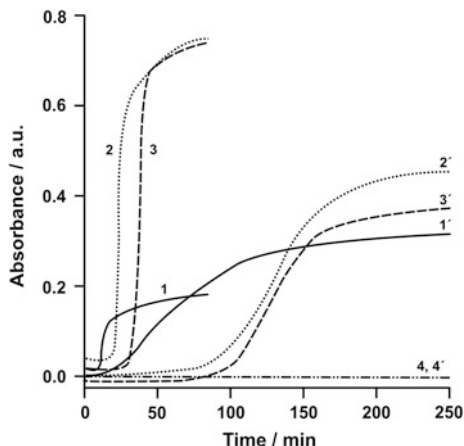
reactions carried out in the presence of triblock 1 featured a short induction period
and led to AuNP solutions with low absorption ($\sim$ fourfold decrease as compared to
pH 7.3). The latter is ascribed to a low concentration of AuNPs since no changes
were observed in the UV–Vis spectrum and LSPR band. Two effects favor a
decrease in the AuNP concentration; firstly, the reduction potential of Au(III)/A(0)
is shifted toward cathodic values at high pH; secondly, the micelle core is highly
dehydrated at pH 9.1 and diffusion of Au(III) species to, and within, this com-
partment during the reaction is more difficult, particularly for PDPAEMA systems.

A linear increase in the SPR absorbance with Au(III) concentration in Fig. 3.12
(left panel), denoting an equally linear variation in the number of particles whose
size is not dependent on the concentrations, and hence, the number of objects is
directly proportional to the concentration. Indeed, UV–Vis spectra recorded after
the synthesis show, in all the cases, a well-defined profile with a constant λ_{max}
value, which suggests similar electronic and morphological properties. The highest
amount of Au(III), which represented the maximum limit, led to the appearance of
stable gold sols. Higher concentrations produced particles that aggregated and, on
standing, subsequently settled out at the bottom of the vial. These experiments also
revealed that at Au(III) concentrations above 0.5 mM, the metal centers can create
cross-linking points, connecting multiple polymer chains and leading to slightly
turbid solutions even under acidic conditions. These solutions show a low back-
ground absorption in the UV–Vis kinetic experiment, and when this was detected,
the induction time was no longer reproducible.

A small amount of unstable AuNPs was produced at the lowest polymer (tri-
block 1) concentration (see broad absorption with a low intensity band at around
530 nm) (Fig. 3.12, right panel, curves 4–6). While the reduced amount of polymer
was sufficient to promote the synthesis, it was not enough to provide colloidal
stability. The threshold for this was 0.4 mg mL^{-1} triblock 1, after which the LSPR
band was well defined and centered at 532 nm. The corresponding absorption
intensity reached a stable plateau when the triblock 1 concentration exceeded
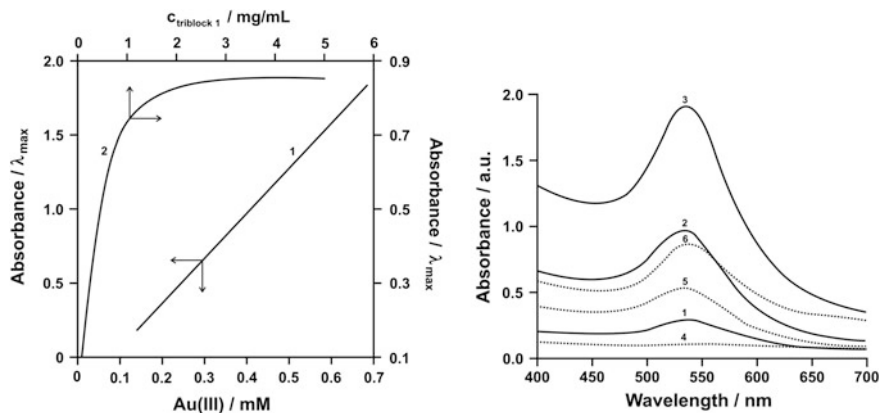
Fig. 3.12 Influence of triblock copolymer 1 and gold precursor concentrations on the AuNP synthesis process, a linear increase in the SPR absorbance with Au(III) concentration (*left panel, curve 1*), corresponding UV–Vis spectra recorded after the synthesis with a constant λ_{max} value (*a right panel, curves 1–3*), an increase in the SPR absorbance with triblock copolymer 1 concentration (*left panel, curve 2*), corresponding UV–Vis spectra recorded after the synthesis with a λ_{max} value (*a right panel, curves 4–6*) [158]

2.0 mg mL^{-1}. However, a background absorption above the LSPR band was evident for 5.0 mg mL^{-1}, which indicates the formation of ill-defined particles. Moreover, the LSPR band is redshifted, thus suggesting the presence of comparatively larger particles.

The reversible aggregation/deaggregation of AuNPs functionalized with adsorbates having various chain lengths of terminal poly(ethylene glycol methyl ether) moieties, thiol head groups, and intervening free radical initiator moieties was reported [170]. For these adsorbates, the thiol group at one end of the chain is utilized to anchor these surfactants to the AuNP surface by Au–S bond formation, and the PEG groups at the other end are used to stabilize the AuNPs via steric hindrance. In a selected example utilizing this architecture, the intervening initiator moieties were shown to promote the growth of poly(*N*-isopropylacrylamide) (PNIPAM) hydrogel coatings on AuNPs [171]. In the present investigation, the stability of the adsorbate-functionalized nanoparticles in water was evaluated as a function of nanoparticle size ($\sim$15, 40, and 90 nm in diameter) as well as PEG chain length (M_n = 350, 750, and 2000). Thus, this process was performed for each of the different lengths of initiator-containing adsorbates (HSPEG$_{350}$, HSPEG$_{750}$, and HSPEG$_{2000}$). AuNPs coated with HS–NN–(but not modified with PEG) aggregated immediately, contrasting with the behavior of those modified with HSPEG$_{350}$, HSPEG$_{750}$, and HSPEG$_{2000}$ (Chart 3.1) (HSPEG$_{350}$-AuNPs, HSPEG$_{750}$-AuNPs, and HSPEG$_{2000}$-AuNPs, respectively).

The spectrum for the as-prepared 15 nm gold sol is also shown for comparison. In each case, the SPR band indicates a gradual redshift from 524 nm for measurements made after the adsorbates were added to the AuNP solutions, regardless
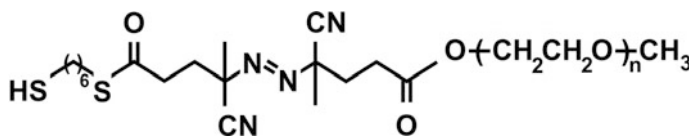
Chart 3.1 Initiators based on HSPEG$_{350}$, HSPEG$_{750}$, and HSPEG$_{2000}$, where $n \sim 7$, ~ 16, and ~ 45, respectively [170]

of the chain length of the adsorbate, indicating the immobilization of the molecules on the surface of the AuNPs (Fig. 3.13). The formation of a dielectric layer around the AuNPs will also result in a redshift of the SPR band, if the dielectric constant of the layer is larger than that of the medium [172]. These observations are consistent with the formation of adsorbed organic layers around the metal nanoparticles in solution [173]. The 15-nm gold core AuNPs coated with the shortest PEG chain (HSPEG$_{350}$-AuNPs) were unstable and all precipitated out of suspension within several days. This aggregation gives rise to the dramatic decrease in the extinction maxima in the SPR bands, as shown in Fig. 3.13. The rate of the aggregation is much slower for the 15-nm-gold core nanoparticles functionalized with longer PEG chain adsorbates when compared to the HSPEG$_{350}$-AuNPs. Interestingly, the 15-nm-gold core nanoparticles with the longest PEG chains, HSPEG$_{2000}$-AuNPs, showed almost no peak broadening or decrease in the intensity of the SPR band, implying that these nanoparticles undergo little or no aggregation for up to five days. Thus, when the AuNPs aggregate and the distance between aggregating particles become small as compared to the particle radius, the SPR band will appear at longer wavelengths than those of the individual particles [174].

The SPR bands of the nanoparticles redshifted from 524 nm after the adsorbates were added to the 40-nm-gold core nanoparticle solutions regardless of the chain lengths of the adsorbates, as also occurred with the HSPEG$_{350}$-AuNPs (Fig. 3.14, left panel). The rate of change for the SPR band appears to be inversely dependent on the PEG chain length (similar to the results obtained for the 15-nm-gold core

Fig. 3.13 UV–Vis extinction spectra of bare and adsorbate-functionalized AuNPs with ~ 15 nm gold cores (Au$_{15}$) as a function of increasing time in solution where the adsorbate is HSPEG$_{350}$ (P$_{350}$), HSPEG$_{750}$ (P$_{750}$), and HSPEG$_{2000}$ (P$_{2000}$): _1_ Au$_{15}$pure, _2_ Au$_{15}$P$_{350}$-24 h, _3_ Au$_{15}$P$_{350}$-5 days, _4_ Au$_{15}$P$_{750}$-5 days, _5_ Au$_{15}$P$_{2000}$-5 days [170]
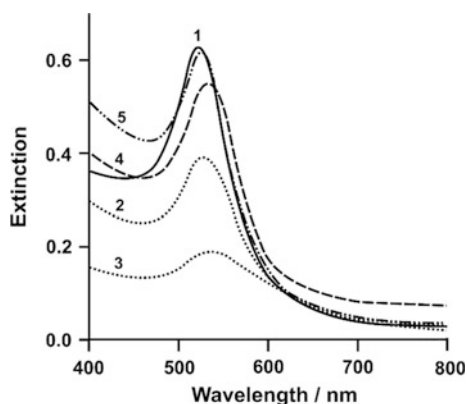
nanoparticle system), exhibiting the largest change with the shortest PEG chain. As shown in Fig. 3.14, a dramatic broadening and redshifting of the SPR band to 585 nm was observed for the 40-nm-gold core HSPEG$_{350}$-AuNPs. The SPR band shifts to 585 nm, thus substantial aggregation occurred as characterized by the broadening and decreased intensity of the SPR band. In contrast, the SPR bands of the 40-nm-gold core HSPEG$_{750}$-AuNPs and HSPEG$_{2000}$-AuNPs show little or no SPR band broadening or diminishment, suggesting that the AuNPs modified with the longer PEG chain adsorbates undergo almost no aggregation after adsorption of these adsorbates. The 90-nm-gold core nanoparticles produced a similar redshifting trend (Fig. 3.14, right panel), and the AuNPs modified with HSPEG$_{350}$ aggregated and precipitated out of suspension within 24 h. However, unlike the other two series, the 90-nm-gold core nanoparticles modified with the longer adsorbates showed signs of diminished stability within five days.

Thus, the SPR bands in the UV–Vis spectra of the HSPEG$_{350}$-AuNPs were significantly broadened and redshifted and exhibited a decrease in intensity. The HSPEG$_{750}$-AuNPs and HSPEG$_{2000}$-AuNPs on the 15 and 40 nm gold cores exhibited little, if any, change in the UV–Vis spectra as a function of time. These observations support the notion that steric stabilization by the PEG moieties surrounding the AuNPs can play a key role in their resistance to aggregation. The PEG$_{750}$ adsorbate was long enough to stabilize these two sizes of AuNPs in water for several days. Indeed, the radius of the HSPEG$_{750}$-AuNPs increased the hydrodynamic radius by 5 nm for the particles in solution, as verified by DLS measurements, and this value is consistent with results reported previously [175]. However, there are indications in the data for the nanoparticles with 90 nm gold cores that the ability of the PEG moieties to prevent the coated AuNPs from aggregation depends on the sterically repulsive layer being of sufficient thickness to offset the underlying attractive van der Waals forces between the metal cores. The
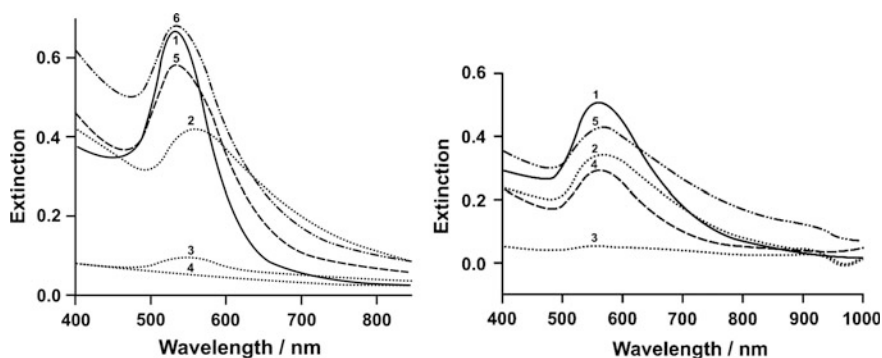
Fig. 3.14 UV–Vis extinction spectra of bare and adsorbate-functionalized AuNPs with ∼40 and ∼90 nm gold cores (Au$_{40}$) as a function of increasing time in solution where the adsorbate is HSPEG$_{350}$, HSPEG$_{750}$, and HSPEG$_{2000}$: *1* Au$_{40}$pure, *2* Au$_{40}$P$_{350}$-1 h, *3* Au$_{40}$P$_{350}$-24 h, *4* Au$_{40}$P$_{750}$-5 days, *5* Au$_{40}$P$_{750}$-5 days, *6* Au$_{40}$P$_{2000}$-5 days (*left panel*), and *1* Au$_{90}$pure, *2* Au$_{90}$P$_{350}$-1 h, *3* Au$_{90}$P$_{350}$-24 h, *5* Au$_{90}$P$_{750}$-5 days, *6* Au$_{90}$P$_{2000}$-5 days (*right panel*) [170]

overall results regarding the stability evolution of the functionalized AuNPs are summarized as follow:

1. $\mathrm{HSPEG}_{750,2000} - \mathrm{AuNPs}_{,15,40 \text{ and } 90 \text{ nm}}$ and HSPEG_{350}
    $- \mathrm{AuNPs}_{,15 \text{ nm}}$ are stable   (3.18)
    and

2. $\mathrm{HSPEG}_{350} - \mathrm{AuNPs}_{,40 \text{ and } 90 \text{ nm}}$ and $\mathrm{HS} - \mathrm{N}$
    $= \mathrm{N} - \mathrm{AuNPs}_{,15,40 \text{ and } 90 \text{ nm}}$ are unstable.   (3.19)

Furthermore, the IR spectra of the HSPEG_{750}-AuNPs are similar to that of pure HSPEG_{750}, providing evidence that HSPEG_{750} is indeed a part of these composite nanoparticles. The prominent peak for the –C–O–C– bending bands associated with the PEG moieties was observed at 1110 cm^{-1}, and the C=O bands of the ester and thioester groups were found at ~ 1700 cm^{-1} [176]. The bands observed at 2930 and 2864 cm^{-1} correspond to the antisymmetric and symmetric stretching vibrations of the –CH$_2$ units in the PEG chain, respectively [177]. Although the IR spectra indicate that the HSPEG_{750} molecules were successfully grafted onto the AuNPs, it is difficult to determine the precise nature of the bonding between the AuNPs and HSPEG_{750} with the FTIR spectra.

The S$_{2p}$ region of the XPS spectra can provide strong evidence for bond formation between sulfur and the gold substrate. This is because the binding energy of the S$_{2p3/2}$ peak for sulfur bound to gold is known to be ~ 162 eV. In contrast, the S$_{2p3/2}$ peak for unbound sulfur appears at around 164 eV in the XPS spectra [178], which is also associated with the S$_{2p3/2}$ peak of thioester [179]. XPS spectra for HSPEG_{750}-AuNPs with gold core sizes of ~ 15, 40, and 90 nm were collected, and the binding energy (BE) scales for the organic layers on the AuNPs were referenced by setting the Au$_{4f7/2}$ BE to 83.8 eV. The presence of the covalent bond (in XPS spectrum of the S$_{2p3/2}$ region) between the HSPEG_{750} and the 40 nm AuNPs was verified with the S$_{2p3/2}$ peak at ~ 162 eV. The strong S$_{2p3/2}$ signal at ~ 164 eV can be rationalized either as an incomplete adsorbate binding of the HSPEG_{750} or confirmation of the presence of the thioester sulfur within the adsorbate chain. It is believed the latter case given the relative attenuation of photoelectrons and their different positions around the modified AuNPs; bound thiol sulfur is at the HSPEG_{750}–AuNP interface, and the thioester sulfur is closer to the outer surface. Attenuation in a layered structure tends to underestimate the elements buried deeper relative to those at the outer surface, resulting in a much smaller XPS intensity for the buried atoms. This would explain the smaller intensity of the S$_{2p3/2}$ peak at 162 eV associated with the bound thiol sulfur. Considering the presence of the S$_{2p3/2}$ peak at 164 eV, we cannot rule out the possibility of the presence of some unbound HSPEG_{750} (unbound thiols); however, the S$_{2p3/2}$ peak at 164 eV is believed to be mainly from the thioester sulfur and that almost all of the HSPEG_{750}s are adsorbed on the surface of the AuNPs.

Both the aqueous solubility and the general stability of these nanoparticles can be attributed to the exposed PEG moieties. The HSPEG$_{750}$-AuNPs were colloidally stable not only in water but also in solvent-free "dried" form and could be readily redispersed in aqueous buffer solutions (pH 4, 7, and 10) and in nonaqueous solvents [(ethanol (EtOH), methanol (MeOH), tetrahydrofuran (THF), and dichloromethane (CH$_2$Cl$_2$)] without any noticeable loss to aggregation. Figure 3.15 provides evidence of this phenomenon, showing HSPEG$_{750}$-AuNPs (curves 1–3) dispersed in aqueous solution and (curves 1'–3') isolated in a solvent-free "dried" form. When dispersed in aqueous solution, the HSPEG$_{750}$-AuNPs exist as discrete species, producing the characteristic color associated with individual AuNPs; ruby red, purple, and brown for the $\sim$15, 40, and 90 nm gold cores, respectively. As the solvents were evaporated, the nanoparticles began to aggregate, revealing the bulk metal color of the gold core, as shown in Fig. 3.15. Moreover, the isolating–redispersing process of these nanoparticles (aggregation/deaggregation) was completely reversible; the HSPEG$_{750}$-AuNPs failed to undergo fusion of the metallic cores even in the solvent-free form. Irreversible aggregation is a notorious problem for large AuNPs (>10 nm) during preparation and purification [180]. Importantly, the dried monolayer-coated AuNPs described here could be redispersed in a variety of solvents without any signs of particle degradation or formation of permanent aggregates.

The aqueous solution of HSPEG$_{750}$-AuNPs exhibits similar features in their extinction spectra with values of λ_{max} at 520, 530, and 600 nm (corresponding to the $\sim$15, 40, and 90-nm-diameter gold cores), which are the characteristic values for spherical AuNPs in aqueous solution (Fig. 3.15) [143]. In accordance with the visual observations, the HSPEG$_{750}$-AuNPs in the solvent-free form show dramatically redshifted SPR bands with values of λ_{max} at 650 and 750 nm, corresponding to the $\sim$15 and 40 nm gold cores, and accompanied with noticeable broadening of the spectra. Additionally, the SPR band for the 90-nm-gold core HSPEG$_{750}$-AuNPs resulted in a broad absorption that stretches from the UV to the IR region, which is a characteristic response expected for a continuous metal film [143]. These results might be attributed to a form of aggregation where the functionalized AuNPs group in aggregate characteristics of their size or to plasmon hybridization between the neighboring nanoparticles. Since simple aggregations of AuNPs in solution showed no similar dramatic redshift ($\Delta\lambda \sim 120$ nm) in their extinction spectra, this phenomenon is believed to be more likely related to the latter case for our system.

For the HSPEG$_{750}$-AuNPs in the solvent-free form, the nanoparticles are in close proximity at a distance determined by the monolayer boundaries between the gold cores. The uniformity of the distances established by the HSPEG$_{750}$ adsorbates gives an average interparticle spacing of about 3 nm as estimated from the SEM and TEM images. The resulting plasmon hybridization between neighboring individual nanoparticles in particle aggregate assemblies produces surface plasmon bands that are more dramatically redshifted [181]. These intermixed, hybridized plasmon bands disperse strongly to lower energies, corresponding to infrared wavelengths of the spectrum for the larger gold cores, leading to a redshift of the surface plasmon band of all three samples. As with the reversible aggregation/

Fig. 3.15 Extinction spectra of the HSPEG$_{750}$-AuNPs in aqueous solution (*curves 1–3*) and d in solvent-free "dried" form (*curves 1'–3'*), the HSPEG$_{750}$-AuNPs with ~15, 40, and 90-nm-diameter gold cores [170]
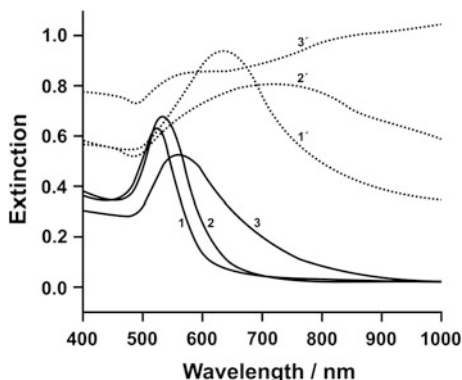
deaggregation observed by the naked eye, these optical properties were found to be completely reversible for this system. This unique reversibility might prove useful for chemical vapor sensing as well as for the self-assembly of monolayer-coated AuNPs in nanoscale electronic devices [170, 182].

3.2.6 Stabilizers, Solutes, and Additives-Mediated Nanoparticle Synthesis

3.2.6.1 Surfactants

Several simpler single-phase syntheses have been presented [77, 183]. They employ the reduction with borohydrides that are soluble in the organic solvent in the presence of a capping ligand. If unpolar solvents (e.g., toluene) are used, additional stabilizers (surfactants) have to be added to render the gold salt soluble. The advantages of all of these methods are (i) good control over the particle size and dispersity by tuning the gold salt-to-ligand ratio and reaction conditions [184], (ii) the possibility of introducing a variety of functionalized ligands, and (iii) simple isolation, cleaning, and redispersion of the particles in different solvents. Disadvantages are the impurities that are introduced by the use of surfactants and the restriction of carrying out the reduction in the presence of the capping ligand. The latter can be partially circumvented if functional ligands are introduced by ligand exchange reactions on stable nanoparticles [185]. However, this approach is generally more elaborated and still suffers some limitations, especially the problem of getting a complete ligand exchange.

Two principal concepts can be distinguished in the solution synthesis of gold nanoparticles. The first, and older one, involves the reduction of tetrachloroaurate ions in aqueous media, employing reducing agents such as sodium citrate [186] or sodium borohydride. This step can be performed in the presence or absence of additional ligands, as the nanoparticles in the resulting hydrosols are stabilized

electrostatically. Functionalization of the nanoparticles can easily be achieved, but is restricted to water-soluble ligands. However, the control over particle size and monodispersity in a particular synthetic protocol is rather poor. The second concept involves the synthesis in organic solvents. The most popular method is the two-phase synthesis reported by Brust et al. [187], which involves the transfer of tetrachloroaurate ions into toluene with the use of tetraalkylammonium bromide and subsequent reduction with sodium borohydride in the presence of thiols.

Surfactants stabilize the gold nanoparticles by electrostatic bonding between the gold surface and the surfactant heads. The surfactant tetraoctylammonium bromide (TOAB) is normally used in the Brust–Schiffrin two-phase method as a phase-transfer agent, and it also acts as metal nanoparticle stabilizer. The TOAB-capped AuNP is obtained by the Brust–Schiffrin two-phase method without adding the additional stabilizer and utilized in further functionalization or self-assembly [188–190]. Another example is Nikoobakht et al. synthesis of CTAB-stabilized AuNPs [191, 192]. The AuNPs are obtained by adding $NaBH_4$ solution into the mixture of CTAB and $HAuCl_4$ solution, yielding AuNPs of average size up to 4 nm with a net positive interfacial charge. It is frequently used as a seed for the preparation of monodispersed gold nanorods (AuNRs) [191] and size- and shape-controlled AuNPs [193].

Farren-Dai et al. [194] have presented gold nanoparticles stabilized by an IL (ionic liquid)-surfactant in solution. The IL used–benzyldimethyltetradecylammonium chloride (BAC) –stabilizes the nanoparticles noncovalently via electrostatic interactions [195], (Scheme 3.10). Ionic liquids are liquid (molten) salts of weakly coordinating cations and anions. By definition, the melting point of ILs has to be below 100 °C. Typical IL cations are 1-alkyl-3-methyl-imidazolium and tetraalkylammonium, and typical anions for ILs are halide anions, tetrafluoroborate BF_4^-, hexafluorophosphate $PF6^-$, trifluoromethanesulfonate (triflate) TfO^-, $CF_3SO_3^-$, and bis(trifluoromethylsulfonyl)amide $Tf2N^-$, $(CF_3SO_2)_2N^-$. ILs have an intrinsic "nanostructure" which is caused by electrostatic, hydrogen bonding, and van der Waals interactions.

Astruc et al. proposed a model based on differential anion stabilization of metal nanoparticles in the following order: polyoxometallate > citrate > polyacrylate $\sim$ chloride. They argue that the anion must be at the surface of the metal, because the stabilization of the nanoparticles correlates with the sterics of the anion [195]. However, some mechanistic descriptions of AuNP stabilization by imidazolium chloride ILs posit that the cation is at the surface of the metal (Scheme 3.11) [196]. Herein, a stabilization is similar to what was proposed by Thomas et al. which was based on the strong association of photo-responsive molecules on the surface of AuNPs (Scheme 3.12) [197].

The IR spectra, however, showed some significant differences between pure BAC and the dried stabilized AuNPs. The most significant change outside the fingerprint region was a new peak at 1562 cm^{-1} in the AuNP IR. The changes seen in the fingerprint region have been attributed to the lengthy alkyl chain gaining more vibrational freedom while in a stabilizing conformation. If BAC IL molecules are surrounding the AuNP in a radial arrangement similar to a micelle, then they

Scheme 3.10 Metal nanoparticle stabilization by an alkyl ammonium chloride mechanism as proposed by Astruc et al. [194, 195]
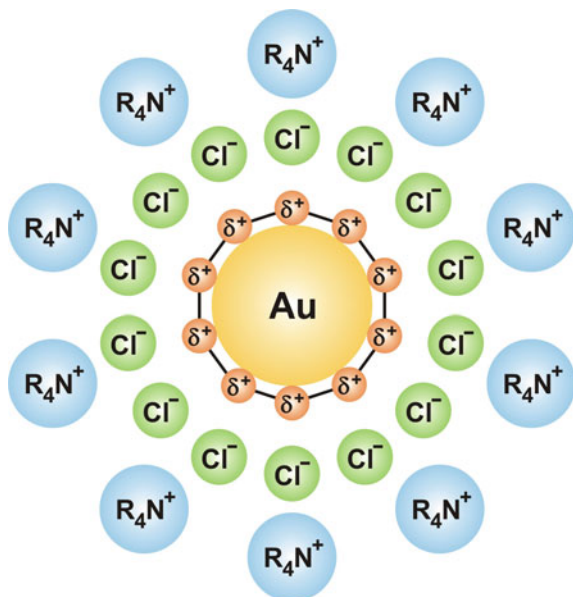
Scheme 3.11 Imidazolium cation coordination and stabilization [194]
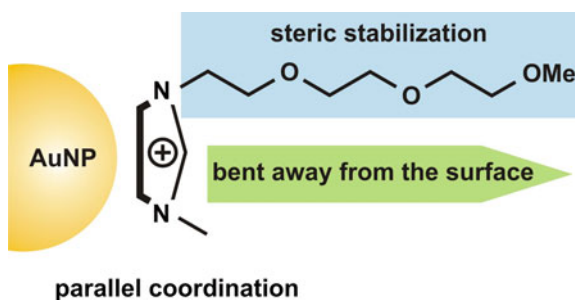
have much more freedom sterically as opposed to the close stacking of solid BAC, as can be seen in its crystal structure [198]. The optimized structure demonstrates that the chloride and cationic head of BAC are both close to the Au(0) atom in a minimum energy structure. Characterization of the synthesized gold nanoparticles suggests that the Au(0) is stabilized at the surface of NPs by both the cation and anion of BAC.

It has been shown that ionic liquids are remarkable and excellent media for the synthesis and stabilization of noble metal nanoparticles without the need of additional stabilizers, surfactants, or capping ligands. ILs can be regarded as supramolecular three-dimensional electrostatic and hydrogen-bonded networks. The stabilization of metal nanoparticles in ILs can be further attributed to effects from the network properties of ILs such as hydrogen bonding, the hydrophobicity, and steric interactions which prevent NMNPs agglomeration (Schemes 3.10, 3.11
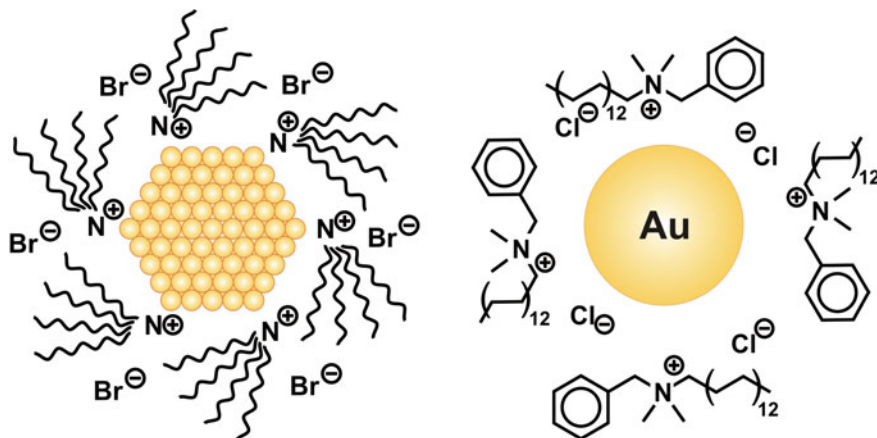
Scheme 3.12 Proposed schematic for a gold nanoparticle stabilized by TOAB (*left panel*) and BAC (*right panel*) [194]

and 3.12). Various methods of chemical synthesis for metal nanoparticles in ILs allow for the design of a variety of NMNP shapes and sizes. The synthesis of ILs-stabilized NMNPs can proceed by chemical reduction, thermolysis, photochemical decomposition, electroreduction, microwave and sonochemical irradiation, and gas-phase deposition methods.

3.2.6.2   Amine-Based Additives

Efforts have also been made to develop one-phase syntheses in which the reduction of metal takes place homogeneously in a selected organic solvent rather than at the two-phase interface as in the Brust method [199]. These one-phase syntheses have been shown to significantly narrow the particle size distribution, and monodisperse metallic particles with size dispersivity <5% can be prepared. Zheng et al. [121] have reported a facile one-step one-phase synthetic route to achieve a variety of metallic nanoparticles by using amine–borane complexes as reducing agents. With the use of different metal sources, both mono- and alloyed metallic nanoparticles with a narrow size distribution can be obtained in a single step. All syntheses were carried out in air by mixing metal source(s) and capping ligand (e.g., thiols) in an organic solvent, such as benzene, toluene, or chloroform. An amine–borane complex was then added to the mixture and stirred until the reduction was complete. As reported, long-range close-packed superlattices of gold nanoparticles can be obtained even without control over the evaporation rate. The synthesized nanoparticles are ready to function as building blocks for the formation of large colloidal crystals directly from the reaction mixtures.

Zheng et al. [121] found that the reducing rate of metal cations by certain amine (phosphines)–borane complexes is dependent on the reaction temperature and

concentration of reactants. The higher the temperature or the concentration of reactants, the faster the reducing reaction. The reaction at lower temperature for a short period typically leads to a relatively broad size distribution due to the existence of small nanoparticles. When the reaction time is long enough or the reaction temperature is increased, these small nanoparticles can grow to reach the size of larger particles. As observed, the reduction of AuPPh$_3$Cl in benzene gave 5.3 nm particles at room temperature, 6.2 nm at 55 °C, 7.1 nm at 85 °C, and 8.3 nm at 100 °C. Reaction solvents can also have a significant effect on determining the average size of nanoparticles. Stable smaller gold nanoparticles can be synthesized by using a polar solvent. The 2.1 nm nanoparticles were produced at room temperature when 3:1 (by volume) chloroform/ethanol was applied as solvent; the reaction in chloroform gave uniform 3.5-nm-gold nanoparticles. The average size and size dispersivity of nanoparticles are mainly controlled by the balance of nucleation and growth rates. Thus, strong ligands, such as thiols, should be avoided in order to get monodisperse gold nanoparticles because they limit the activity of metal precursors [77]. In these syntheses, however, it was found that strong thiol ligands facilitate the formation of monodisperse nanoparticles better than weak ligands (e.g., phosphines, amines). Fortunately, by using low concentration and low temperatures (i.e., room temperature), the reaction rate can be significantly reduced, which allows us to monitor the formation of nanoparticles during the course of reaction. It was found that large nanoparticles formed at the very beginning of the reaction and neither grew nor aggregated with the reaction time. These large-sized nanoparticles can be considered as a thermodynamic metastable state that can be better stabilized by long-chain alkanethiols.

A high-temperature solution-phase synthesis as an inexpensive, versatile, and very reproducible method can be used for the large-scale synthesis of organoamine-protected gold and silver nanoparticles in the 6–21 nm (gold) and 8–32 nm (silver) size ranges and with polydispersities as low as 7% [200]. In terms of achievable particles sizes, polydispersites, and simplicity (only three reagents, tetrachloroauric acid or silver acetate, oleylamine, and a solvent are required), the method is superior to that of Jana et al. [77]. The syntheses are fast, very reproducible, and simple. The particles are stable in dried form, and they can be easily modified with hydrophobic and hydrophilic thiols to afford nanoparticles that are soluble in organic solvents or in water.

Organoamine-protected gold nanoparticles of variable sizes form by refluxing a solution of tetrachloroauric acid and oleylamine in the organic solvent. The reducing equivalents in the reaction are provided by the amine, which can undergo metal ion-induced oxidation to nitriles [201]. The carbon double bond in oleylamine does not play a significant role in this process since other aliphatic amines, for example, 1-dodecylamine, work equally in the reaction. Figure 3.16 (top panel) shows the evolution of the gold nanoparticles size as a function of time. The particle size data can be interpreted in terms of a classical nucleation/diffusional growth model [202]. Here, the initially formed gold atoms self-nucleate to form a fixed number of seeds during the first stage of the reaction, and particles then continue to

grow by diffusion-driven deposition of gold atoms onto these existing seeds
(Fig. 3.16, bottom panels).

Assuming that the rate at which gold atoms are deposited onto the nuclei is
linearly dependent on the concentration of gold precursor in the solution, one
obtains the exponential growth curve shown in Fig. 3.16, which agrees well with
the data. The intersection of the theoretical curve with the *x*-axis indicates that the
end of the particle nucleation phase occurs roughly 300 s after the mixing of the
reactants. By quenching the reaction, it is possible to obtain gold nanoparticles in
the 4–13-nm-size regime. Alternatively, the gold nanoparticle sizes can be regulated
with the concentrations of the gold precursor and of the amine from 15.3 nm (6.7%)
to 21.3 nm (6.9%). Here, the maximum particle size is limited by the solubility of
the nanoparticles. Higher concentrations of the gold precursor give smaller particles
because more seed particles are formed at the beginning of the reaction. While the
surfactant concentration has only a small influence on nanoparticles size, it greatly
influences polydispersity of the formed colloid. Polydispersities below 10% gen-
erally require the larger amount of amine.

Multidomain colloidal crystals of 16–21-nm-oleylamine-ligated gold nanopar-
ticles are routinely obtained as black solids directly from the reaction mixture upon
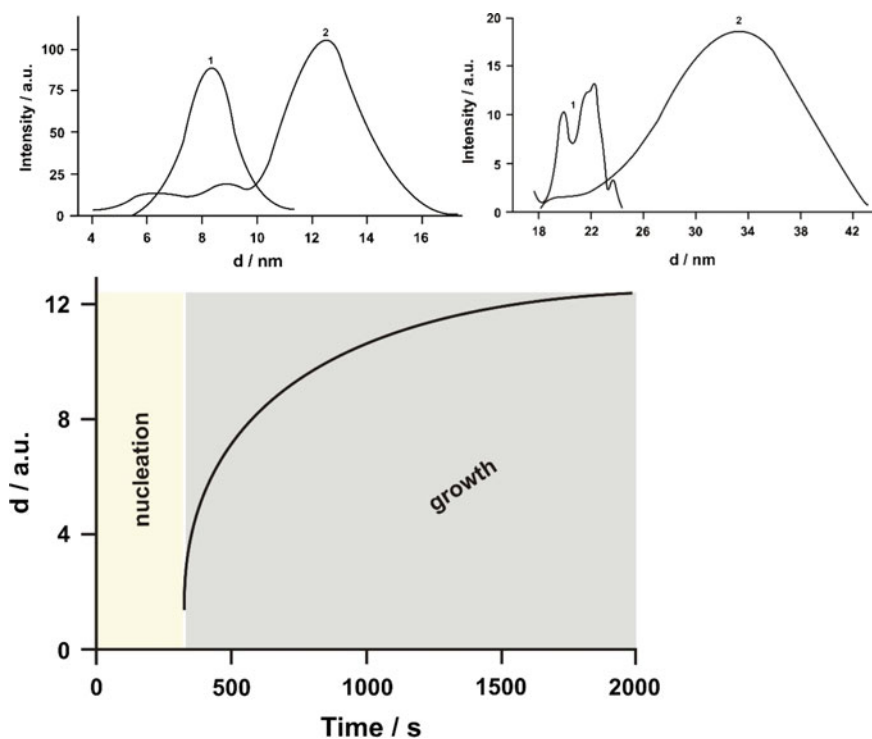
Fig. 3.16 Evolution of the gold nanoparticle size as a function of time (*top panel*). Growth
dynamics (size of nanoparticles) for gold particles from *left to right bottom panel* in toluene [200]

cooling to room temperature, or by slow evaporation of the solvent from the heated solution. Crystals grown at lower temperature show a preference for the hcp (hexagonal close packed) lattice, whereas crystals grown at higher temperature contain an increased number of domains in the fcc (face-centered cubic) structure type. Submicrometer crystals of <10 nm amine [203], thiol [204], and tetraalkylammonium-[205] stabilized gold nanoparticles with fcc and hcp structures have been reported also by other groups.

Li and Wu used alkylamines as stabilizers for silver nanoparticles [206] since they have weaker interactions with silver [200]. These weak interactions can potentially be broken up at significantly lower temperatures, thus enabling the "stripped" silver nanoparticles to coalesce to form a continuous conductive layer. The reduction of silver acetate at lower temperatures could be accelerated if an appropriate reducing agent was added. While reducing agents, such as $NaBH_4$, hydrazine, and aldehyde, provided rapid acceleration leading to large silver aggregates, substituted hydrazines, such as phenylhydrazine, were effective in modulating the reduction to an extent which gave stable silver nanoparticles. Specifically, with just 0.5 molar equiv of phenylhydrazine in the presence of an alkylamine (1-hexadecylamine, 1-dodecylamine, etc.) in toluene, the reduction of silver acetate at 25–60 °C proceeded smoothly yielding a dark brown solution without precipitation. Silver nanoparticles prepared in this manner were soluble in common organic solvents (e.g., hexane, toluene, THF, etc.) and were stable under ambient conditions (the particle size was <10 nm). UV–Vis absorption spectrum exhibited a plasmon band at ∼415 nm, indicative of metallic silver. The present synthesis is facile and offers the following advantages:

(i) one-phase reaction without additional surfactants;
(ii) low reaction temperature and short reaction time;
(iii) less stabilizer and high concentration of silver nanoparticle product; and
(iv) relatively inexpensive starting materials.

A reddish-brown thin film with a thickness of ∼70 nm spin cast from a solution of 1-hexadecylamine-stabilized silver nanoparticles [(Ag@C16)NPs] in cyclohexane on a glass substrate turned to a shiny silvery film upon heating on a hot plate. Use of a shorter alkylamine, such as 1-dodecylamine, as a stabilizer further lowered the metallization temperature. X-ray diffraction pattern of the resulting silver film showed diffraction peaks at

$$2\theta = 38.1°, \ 44.2°, \ 64.34°, \ \text{and} \ 77.39°, \tag{3.20}$$

which are identical to those of a vacuum-deposited silver thin film. SEM image revealed formation of a continuous layer comprising of larger coalesced particles of 100–500 nm. The electrical conductivity of the resulting silver film was in the range of 2–4×10^4 S c@@@m^{-1}, which is in the same order as that of a vapor-deposited silver thin film of similar thickness (4–6×10^4 S c@@@m^{-1}). This high level of conductivity is more than sufficient for application in any electronic devices. In addition, the alkylamine-stabilized silver nanoparticles prepared

by the present procedure exhibited good shelf-life stability both in powder and in solution forms, and this is of critical important in electronic circuit manufacturing.

The concentration and chain length of the surfactants (and/or the weak ligands) played a key role in determining the concentration of the nuclei formed in the solution, judged by the final average particle size, a high concentration of ligands, or ligands with a bulky tail suppressed the activity of the monomers [207, 208]. Consequently, the number of nuclei formed was low, which results in relatively large nanocrystals. This strategy yields nearly monodisperse gold nanocrystals between 1.5 and 7 nm in size. Control experiments with thiols in place of the weak ligands (amines or fatty acids) were performed. The average nanocrystal size was limited in the range between 1 and 3 nm, which is similar to the Brust method. The size distribution of very small-sized gold nanocrystals synthesized using thiols was decent, but the samples for relatively large nanocrystals all showed a significantly broader size distribution (Fig. 3.17). These control experiments verified the hypothesis that very strong ligands should be avoided for the synthesis of noble metal nanocrystals. When the formed nanocrystals were coated by strong ligands, the subsequent growth at room temperature was hindered, and the remaining monomers in the solution supported a continuous nucleation process, which resulted in samples being rich with very small particles (Fig. 3.17).

The final size achievable through the first strategy was limited to roughly smaller than 7 nm. The second strategy was developed for the synthesis of large nanocrystals, 6–15 nm in size, by decreasing the reducing power of the reducing reagents. This was done by replacing a part of TBABs and strong reducing reagents with hydrazine that is relatively weak at room temperature. Presumably, TBAB (tetrabutylammonium bromide) was mostly used for the nucleation, and hydrazine was consumed in the growth stage. As a result, the final size of the resulting nanocrystals increased by decreasing the relative concentration of TBAB.

In the third strategy, small-sized nanocrystals were formed first, after that, more metal precursor and reducing reagents were added into the growth solution in a dropwise fashion. The volume increase of the nanocrystals grown by this strategy roughly matched the amount of the metal precursors added in each injection, indicating an insignificant secondary nucleation. Different from the seeding growth

Fig. 3.17 Size distribution of Au nanocrystals formed with thiol (*curve 1*) and amine (*curve 2*) as the ligands [77]
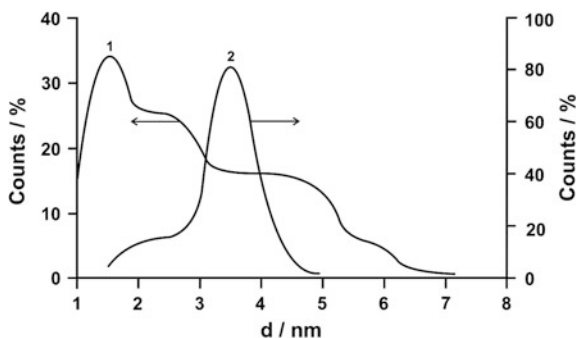
[76], the entire synthesis was conducted in a one-pot fashion although multiple-pot schemes also worked. The nanocrystals obtained in this way were similar to the ones grown by the second strategy.

After reduction, the nanoparticles are presumably stabilized only by solvent molecules, which should be easily replaced by ligands that offer stronger binding groups, such as thiols or amines, and an enduring stabilization of the nanoparticles. The average size of the nanoparticles increases with increasing amounts of reduction solution, which was already suggested by the evolution of the surface plasmon resonance. For example, the size of the dodecanethiol-capped nanoparticles could be tuned within the range of 1.9–5.2 nm. Addition of a high excess of reduction solution did not result in larger particles. The achieved dispersities of 15–20% are narrow and comparable to the leading methods in the field. Ligands with thiol or amine binding groups that lead to gold nanoparticles that are soluble in organic solvents were added as a solution in diglyme or toluene to the weakly stabilized nanoparticle solutions, and the ligand-capped nanoparticles were isolated. Water-soluble gold nanoparticles (d ca. 5 nm) were obtained by the use of 2-(dimethylamino)ethanethiol hydrochloride as a ligand.

The characteristic surface plasmon resonance in the absorption spectra of gold nanoparticles capped with different types of ligands (dodecanethiol capped, d ca. 4.7 nm, toluene; dodecylamine, 4.2 nm, toluene and 2-(dimethylamino)ethanethiol hydrochloride, 5.3 nm, water) was observed at ca. 520 nm. Notably, larger particles could be obtained with amine ligands than with thiol ligands (4–5 nm). 8.9 nm dodecylamine-capped nanoparticles exhibit a narrow dispersity, as indicated by the formation of 2D hexagonal close-packed arrays. This implies a significant particle growth during the ligand-binding process of the weaker amine ligands as compared to the stronger thiol ligands.

In the next study, a water-soluble acrylamide or polyacrylamide was used to prepare silver nanoparticles [209]. Neither a commonly used reducing agent for the reduction of silver ions nor an initiator for the polymerization of monomer acrylamide (AM) was employed. The solution containing only silver nitrate in water was heated to above 150 °C, which is much lower than the decomposition temperature of silver nitrate (440 °C), and no silver particles were found. Meanwhile, heating the solution of neat acrylamide in water at 100 °C could not initiate the polymerization reaction of monomer but the spontaneous polymerization of acrylamide could take place at 120 °C or above and a certain pressure. Colorless floccular precipitates formed when commercial polyacrylamide was added into aqueous solution including silver nitrate at room temperature, which indicated the coordination of silver ions with NH_2 groups in polyacrylamide (PAM) , and silver ions served as weak cross-linkers to attach polymer chains. Fast formation of silver nanoparticles occurred upon exposing the above mixture to ambient (indoor) light. No such process happened with the solution of acrylamide and silver nitrate in water, even when light irradiated for several days. These observations highlighted the significant role that the polymer plays in the photoreactions and also in the present preparation.

Chen et al. have suggested two possible mechanisms for the formation of silver colloids [209]. One involves the electron transfer from the water or acrylamide molecules to silver ions at a certain temperature, similar to that for the photolysis of silver ions in aqueous solution [210]. This mechanism can be proven by the formation of large black silver particles visible by the naked eye when the aqueous solution of silver nitrate and acrylamide was heated to above 100 °C, in which no obvious polyacrylamide was found. The other one is related to the reduction of silver ions by the organic radicals [211] produced in the thermal polymerization of acrylamide, which is possibly initiated by the thermal homolysis of impurities (including peroxides or hydroperoxides formed due to O_2) present in the monomer [212].

The presence of the above two kinds of mechanisms could also be further supported by the formation of PAM-stabilized silver nanoparticles with bimodal size distribution. A small amount of silver nanoparticles formed with the first kind of mechanism in the presence of acrylamide when the temperature was less than 150 °C and grew into larger ones when the reaction proceeded. Smaller silver nanoparticles formed at the same time with the polymerization of acrylamide. As we know, thermal polymerization of olefin at relatively high temperature is a free radical chain polymerization with a fast reaction rate. A large number of organic radicals thus formed could reduce silver ions and produce silver nanoparticles in a very short time [211]. Furthermore, reduction of silver ions and thermal polymerization of acrylamide occurred almost simultaneously and resulted in well-dispersed silver nanoparticles protected by polyacrylamide. Nearly, spherical silver nanoparticles about 5.0 nm but also large individual silver nanoparticles with sizes between 10 and 30 nm are observed. There are still a few large silver nanoparticles with an average size of 50 nm besides a large amount of small particles in the size range of ~ 17 nm.

In the presence of HNO_3 the appeared distinct broad peak, which is located at ca. 450 nm belongs to Ag@Ag2O (core@shell) nanoparticles. However, this peak vanished gradually with increasing amount of HNO_3 and merged into the shoulder band that belongs only to silver nanoparticles, and formed a relatively symmetric peak whose location is eventually blueshifted to 413 nm (Fig. 3.18). At the same time, another peak at 300 nm appeared and its intensity increased with the HNO_3 concentration increasing, which inferred the gradual dissolution of silver oxide layer and some of neat silver nanoparticles and the formation of silver ions. The intensity, on the other hand, of the absorption peak at around 413 nm increased as the HNO_3 concentration increased, and then decreased with the HNO_3 concentration increased; meanwhile, a significant increase in intensity of the peak at 300 nm was also observed. The intensity variation of both peaks depending on the HNO_3 concentration reveals the following conclusions: (1) The removing of silver oxide layers from the surfaces of silver nanoparticles resulted in the increase of the intensity of the SPR peak for silver nanoparticles. (2) Dissolution of silver nanoparticles led to the decrease of the intensity of the SPR peak for silver nanoparticles and the increase of the intensity of silver ions. The variation of the position of the absorption peak indicated that the thickness of Ag_2O layers was

increased with the addition of a small amount of very dilute HNO_3 solution (shown in Eq. 3.21), and then part of Ag_2O layers was removed when more HNO_3 was used (shown in Eq. 3.22).

$$2Ag + 2HNO_3 \rightarrow Ag_2O \downarrow + 2NO_2 \uparrow + H_2O \tag{3.21}$$

$$Ag_2O + 2HNO_3 \rightarrow 2AgNO_3 + H_2O \tag{3.22}$$
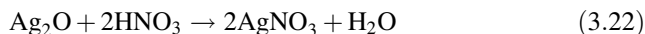
To fully prove the existence of silver nanoparticles covered with Ag_2O layers, HNO_3 was replaced with acetic acid (HAc) and NaCl solution (Fig. 3.19). AM-stabilized silver colloids were added to NaCl solutions. The broad SPR bands between 350 and 550 nm disappeared, and a relatively symmetric peak at around 412 nm could be observed, indicating that the Ag_2O layers were completely removed and the AM-stabilized pure silver nanoparticles were present. In addition, a small shoulder at ca. 280 nm was also seen owing to the formation of AgCl particles [213]. The mechanism for the formation of AgCl might involve the following chemical reaction:

$$Ag_2O + H_2O + 2NaCl \rightarrow 2AgCl \downarrow + 2NaOH \tag{3.23}$$

3.2.6.3 Thiol-Based Additives

Nanoparticles with a narrow size distribution can further function as building blocks for the construction of higher-ordered superlattices that exhibit collective properties of individual nanoparticles [214]. Although several synthetic routes of noble-metallic nanoparticles have been developed, the challenge remains of obtaining monodisperse nanoparticles with size <10 nm on a large scale. Since the first report in 1994, the syntheses of metallic nanoparticles with size less than 10 nm have been dominated by the Brust method, a two-phase protocol that can be easily scaled up to gram scale. However, the nanoparticles prepared by the Brust

Fig. 3.18 UV–Vis absorption spectra of the colloidal silver solution prepared by dropping of AM-stabilized silver colloids into HNO_3 solutions with concentrations of 0 (*curve 1*), 1 mM (*2*), 2 mM (*3*), 0.1 M (*4*), and 2 M (*5*) [209]
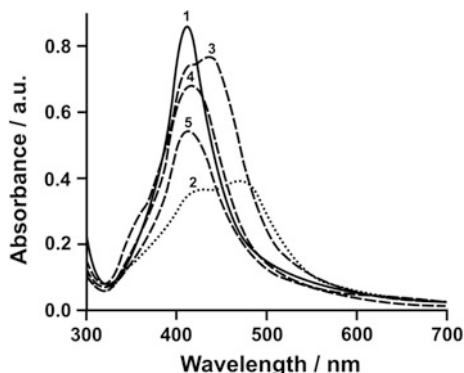
method and its variations typically have a continuous and broad size distribution
[187, 215].

The Brust–Schriffin in situ biphasic gold nanoparticle synthesis introduced the
use of TOAB (tetraoctylammonium bromide)—a quaternary ammonium ion sta-
bilized by a bromide anion—as a stabilizing agent, and phase-transfer catalyst in the
production of colloidal gold from chloroauric acid. When reducing $HAuCl_4$ with
sodium borohydride, TOAB stabilizes the precipitating colloidal gold in the
aqueous phase. This stabilizing interaction allows the AuNPs to solvate into an
organic phase, with TOAB effectively acting as a phase-transfer catalyst. However,
TOAB does not bind gold particularly strongly and thus only provides temporary
stabilization, with gold aggregating in the long term. Thus, usually a subsequent
covalent stabilizer such as a thiol is added [195]. Thus, tetrachloroaurate (III) is
transferred to toluene using TOAB as the phase-transfer reagent and reduced by
$NaBH_4$ in the presence of dodecanethiol (DDT). Larger thiol/gold mole ratios give
smaller average core sizes, and fast reductant addition and cooled solutions pro-
duced smaller, more monodisperse particles. Following the Brust–Schiffrin method,
gold nanoparticles with a variety of functional thiol ligands have been synthesized.
Later, a simple protocol for the one-step aqueous preparation of highly monodis-
perse gold nanoparticles with diameters below 5 nm using thioether- or
thiol-functionalized polymer ligands, such as alkyl thioether end-functionalized
poly(methacrylic acid), has been developed by Hussain and coworkers [216, 217].
In this approach, the particle size and size distribution is controlled by subtle
variation of the polymer structure, concentration and "denticity." By varying sys-
tematically the polymer to gold ratio, the size of the nanoparticles can be finely
tuned and a transition from nonfluorescent to fluorescent nanoparticles is observed
for core diameters between 1.1 and 1.7 nm [218]. Most hydrophobic gold
nanoparticles [also sometimes called monolayer-protected clusters (MPCs)] with
diameters in 1 to ca. 8 nm ranges are prepared by the Brust–Schiffrin method: The
gold (III) derivatives are reduced by sodium borohydride in an organic solvent in
the presence of thiol-capping ligands using either a two-phase liquid/liquid system
or a suitable single-phase solvent [187, 219]. Its high impact is due to:

  (i)   facile synthesis in ambient condition;

 (ii)   relative high thermal and air stability of the AuNPs prepared in this way;

(iii)   repeated isolation and re-dissolution without aggregation or decomposition;

(iv)   control of the small size with narrow dispersity; and

 (v)   relatively easily functionalization and modification by ligand substitution.

These AuNPs are stabilized by relatively strong Au-S bonds, their diameters are in the 2–5 nm range, and their shapes are cuboctahedral and icosahedral. Due to the nucleation-growth-passivation kinetics model by which the sulfur-containing agents inhibit the growth process [215, 220], larger S/Au mole ratios give smaller average core sizes. Fast $NaBH_4$ addition and cooled solutions also produce smaller, more monodispersed AuNPs. During the reaction of the thiol with growing AuNPs, the H atom of the thiol is lost, presumably by oxidative addition of the S–H bond onto two contiguous Au^0 atoms of the AuNP surface. The fluxional properties of the Au–H bonds on the AuNP surface can provide the fast walking path of the H atoms on the surface until two Au–H bonds become contiguous for H_2 reductive elimination. Later, the formation surface Au–S bonds were shown using Raman spectroscopy by Li et al. who actually demonstrated the overall mechanism including all the steps of the Brust–Schiffrin AuNP synthesis. In particular, they disclosed that, interestingly, these Au–S bonds are formed only after adding $NaBH_4$ as indicated in Scheme 3.13. This work brings about a key understanding of the mechanism of this synthesis [221], while a previous widely accepted assumption had been that the thiol reduced Au(III) to Au(I) and formed $[Au(I)SR]_n$ [222].

Given the above advantages, the Brust–Schiffrin method is now much in use for the preparation and application on thiolate-liganded AuNPs [223, 224]. This method was improved by procedure upon which the *p*-mercaptophenol-stabilized AuNPs were synthesized in methanol solution without the phase-transfer agent TAOB [219]. Any thiol that is soluble in the same solvent as $HAuCl_4$ such as methanol, ethanol, or water allows the use of a single-phase system for AuNP synthesis. Brust's group further prepared biocompatible and water-soluble AuNPs capped by (1-mercaptoundec-11-yl) tetraethylene glycol [225] with less than 10 nm. Due inter alia to the hydrophobic alkanethiol interior and tetra (ethylene glycol) (TEG) hydrophilic shell, AuNPs are of great biomedical interest [226], in particular in the form of AuNPs capped with thiolated poly(ethylene glycol)s (PEGs) [227].

Thiol-capped silver nanoparticles are obtained analogously at room temperature in chloroform [200]. When thiols with ionizable carboxylic acid groups, such as 11-mercaptoundecanoic acid (MUA), are employed in the reaction, one obtains water-soluble nanoparticles with virtually unchanged UV/vis spectra (Fig. 3.20) in the case of silver and with slightly redshifted bands in the case of gold. Aliphatic thiols, on the other hand, lead to particles that are soluble in nonpolar organic solvents. Apart from the altered solubility, successful ligand exchange is also supported by the FTIR spectra on the products.

The surface ligands of noble metal nanocrystals may need to be varied for certain purposes. For instance, biomedical applications [228] require water-soluble
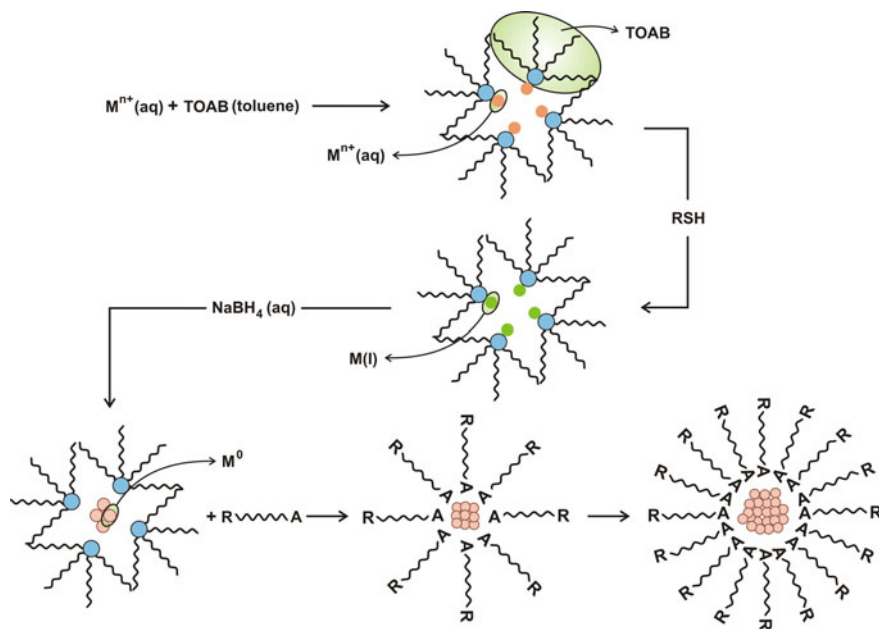
Scheme 3.13 Mechanism for chalcogenate-protected noble metal NP synthesis by the Brust–Schiffrin method [26, 221]

Fig. 3.20 UV–Vis spectra of oleylamine [OA, Ag (*curve 2*), Au (4)] and 11-mercaptoundecanoic acid [MUA, Ag (*curve 1*), Au (3)] ligated gold (13 nm) and silver (8.5 nm) nanoparticles in toluene (OA) and water (MUA) [200]
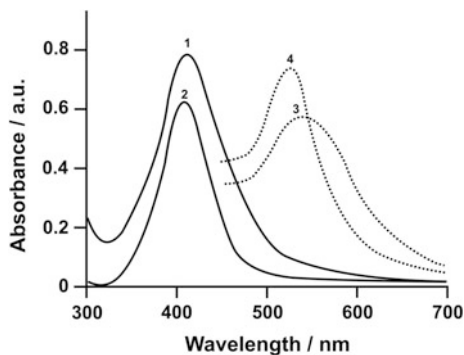
nanocrystals. Using weak ligands in the synthetic schemes, then the surface modification of the gold nanocrystals is quite straightforward by reacting the synthesized nanocrystals with strong ligands, such as thiols. Depending on the terminal groups of the thiols used, gold nanocrystals can be made to either maintain its hydrophobic nature or become water soluble (Scheme 3.14). The influence of alkylthiol chain lengths on the colloidal properties of the AuNPs [$H_3C–(CH_2)_n–SH$ where n represents the number of methylene ($–CH_2$) groups] led to the following results. For this study, the alkylthiols used were 1-nonanethiol (NT, $n = 8$) ,
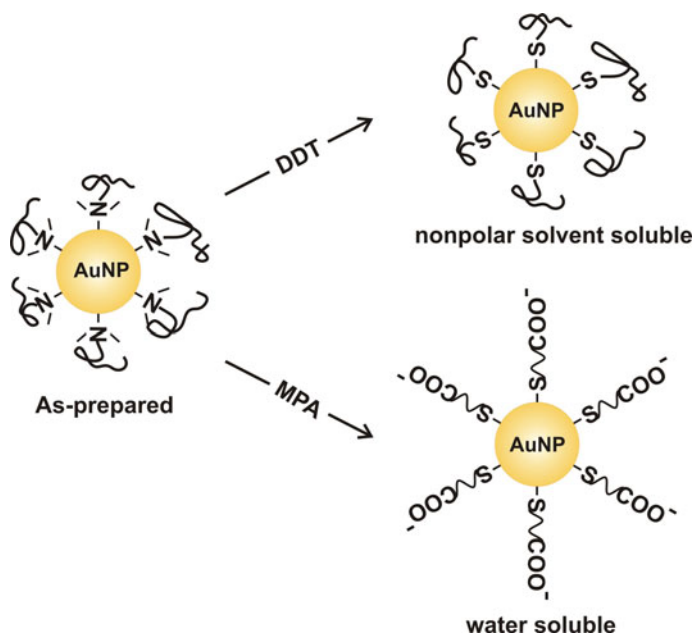
Scheme 3.14 Schemes of the surface modification of Au nanocrystals with dodecanethiol (DTT) and mercaptopropionic acid (MPA) [77]

1-dodecanethiol (DDT, $n = 11$) , 1-tetradecanethiol (TDT, $n = 13$) , and 1-hexadecanethiol (HDT, $n = 15$). TEM images confirm the formation of the thiol coated nearly monodisperse AuNPs with an average particle diameter of ~ 3.9 nm, ~ 3.7 nm, ~ 3.6 nm, and ~ 4.0 nm for NT-, DDT-, TDT-, and HDT-functionalized AuNPs, respectively [229].

The TEM images show organization of the alkylthiolate-functionalized AuNPs into a 2D assembly. The growth termination through addition of the alkylthiols ligands helps in producing nearly monodisperse AuNPs and contributes to formation of the 2D assembly. Interestingly, the particles form a pseudo-hexagonal arrangement with regular interparticle spacing (edge–edge, d_1). The theoretical spacing (d_2) was calculated using the equation:

$$d_2 = 0.25 + 0.127n, \tag{3.24}$$

where n is the number of –CH$_2$ groups in the alkyl chain, 0.127 is the length per –CH$_2$, and 0.25 is the contribution of the terminal methyl group and carbon–sulfur bond of the thiol [230, 231]. Close inspection of the TEM images reveals that the interparticle spacing increases from A to D as the number of methylene groups increases from 8 to 15, respectively, from NT to HDT.

The theoretical interparticle spacing (d_2) is larger in comparison to the experimentally observed spacing (d_1) for nanoparticles coated with different chain length

alkylthiols (Fig. 3.21). For example, the calculated spacing for NT-AuNPs was ~ 2.1 nm which is slightly lower than the theoretical calculation (d_2) of 2.5 nm that is twice the length $(NT)_2$ chain. The slightly shorter observed particle spacing for thiolate-stabilized AuNPs could be due to alkyl chain interdigitation of the molecules adsorbed on the two adjacent surfaces of the nanoparticles as shown in Scheme 3.15. Another possibility could be the microscopic analysis of the samples. TEM analyses were performed on a 2D surface of a 3D structure (thiolate-protected AuNPs) where variation of height could be lost during the measurement resulting in shorter apparent interparticle distances [232].

It has been shown that alkylthiolate-coated nanoparticles form a 2D assembly due to a combination of electrostatic repulsion and van der Waals interaction. 2D assemblies of the alkylthiolate-stabilized AuNPs were observed on the TEM grids. The fact that the different alkylthiol stabilized AuNPs show different spacings in TEM indicates that their LSPR properties would be different due to the change in the short-range coupling distance. The NT-functionalized AuNPs showed a LSPR peak absorption maxima (λ_{max}) at 560 nm as shown in Fig. 3.21 (curves 1–4). This LSPR peak is redshifted by 36 nm in comparison to the Et_3P- and Cl^--stabilized AuNPs (λ_{max}) at 524 nm before addition of NT. The values of LSPR peak (λ_{max}) shifts are 26, 20, and 18 nm for DDT, TDT, and HDT, respectively. The LSPR bands are clearly dependent on the thiol chain length, where the largest LSPR shift (36 nm) was observed for the shorter chain thiol (NT, $H_3C–(CH_2)_8–SH$) and lowest LSPR peak shift (18 nm) was exhibited when the longer chain thiol (HDT, $H_3C–(CH_2)_{15}–SH$) was used.

There are two possible causes of such a noticeable shift of the LSPR λ_{max}. The first is the influence of local dielectric environment around the particles, which includes change of solvent refractive index and the shell of stabilizing ligands around the particles [233]. As thiol was added to NP solution, the change of solvent refractive index (RI) is negligible (acetonitrile has RI ~ 1.334 and THF ~ 1.40) and should not be responsible for such a large redshift of the LSPR λ_{max}. In addition, the amount of thiols introduced to the acetonitrile: THF mixture was small

Fig. 3.21 UV–Vis absorption spectra of different alkylthiol stabilized AuNPs showing the dependence of the LSPR wavelength on the thiol chain length (DDT (*curve 1*), TDT (*2*), HDT (*3*), and NT (*4*). Interparticle spacing (d_1) of the AuNPs functionalized with different thiols (*5*) [229]
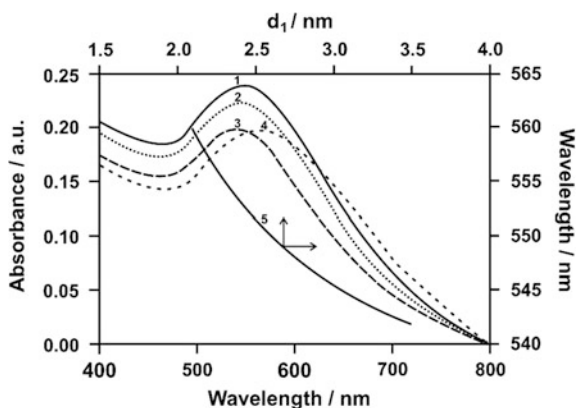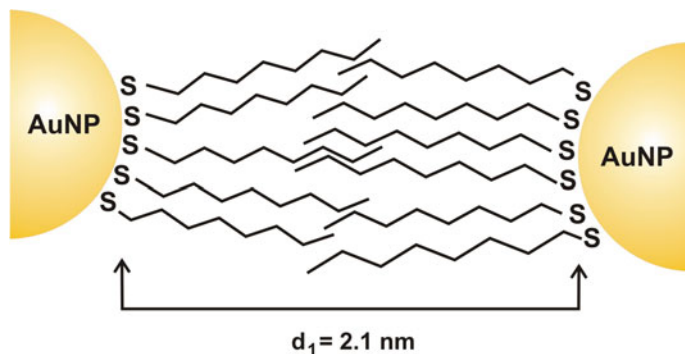
Scheme 3.15 Schematic representation of alkyl chains interdigitation of thiolated ligand (NT) adsorbed on the AuNP surface [229]

and should not alter the bulk RI. However, Mulvaney and coworkers have theoretically shown that when uncoated 5.2 nm AuNPs were coated with alkylthiols, the LSPR band redshifted [233]. According to their results, a 7 nm redshift could be feasible for a 2.0-nm-thick monolayer shell on ∼5.0 nm AuNPs. A much larger 36-nm LSPR peak shift for 4.0 nm AuNPs containing a shell of 1.25 nm alkanethiols was observed. In a further report, it was shown that adsorption of different chain length alkylthiol does not change the local dielectric environment of AuNPs significantly [234]. Such a noticeable LSPR shift observed in the present study implies that, rather than a change of local dielectric environment around the particles due to thiol functionalization, other factors are also playing a significant role in LSPR λ_{max} shift for the functionalized AuNPs.

The other possible cause of the LSPR λ_{max} shift is near-field plasmon coupling between the AuNPs. The spherical metal nanoparticles possess strong electromagnetic fields around the particle surface due to the LSPRs and when the electromagnetic fields couple in the near-field region, the LSPR properties of the NPs are strongly influenced [235]. We could conclude that the shifts of LSPR wavelength (λ_{max}) ranging from 36 to 18 nm, depending on the thiol chain length, occurred due to the electromagnetic coupling between nearby AuNPs in the near-field region. Both the theoretical and experimental results showed that LSPR interactions in the near-field region strongly depend on interparticle spacing. As the spacing between the adjacent NP decreases, larger redshifts of LSPR wavelength would occur [235]. This could be related to the observation of the 2D assembly of the AuNPs in the TEM images. It may be the case that the trend in the LSPR λ_{max} shift correlates with interparticle spacing which changes in the 2D assemblies based on the length of the alkylthiolate ligand. The values of λ_{max} dependent on interparticle spacing taking into account the presence of different thiolated ligand are shown in Fig. 3.21 (curve 5), where the LSPR wavelength decays exponentially with an increase of the interparticle spacing. A similar interparticle spacing dependent LSPR shift has been previously observed for alkanethiolate

protected >10.0 nm AuNPs [234] and lithographically fabricated gold nanostructure (>70.0 nm) on a solid surface.

A series of thiolate-stabilized AuNPs were prepared by a modified single-phase method. Sardar and Shumaker-Parry introduced 9-borabicyclo [3.3.1] nonane (9-BBN) as a mild reducing agent for the synthesis of a series of functionalized alkylthiolate-stabilized AuNPs [236]. Other thiolate ligands such as bifunctional alkanethiolate [237], arenethiolate [238, 239], and other functional thiolate-stabilized have been used to synthesize functional AuNPs [240] from the corresponding thiols.

The method based on the solvated metal atom dispersion technique is suitable for preparation of metal nanoparticles on the gram scale [241], but postheat treatment is generally required for good size dispersivity. Some postsynthesis treatments, such as ligand exchange [242] and thermal annealing [243], are reported to improve the size distribution of the gold nanocrystals formed through either the mentioned Brust method or other synthetic approaches. The other drawback of the Brust method is that the resulting nanocrystals are coated with a monolayer of strong ligands, thiols, which makes it difficult to carry out the surface modification and functionalization needed for certain purposes.

3.2.6.4 Various Additives

LSPR-based optical spectroscopy and electron microscopy were correlated to investigate the formation of silver nanoparticles by reduction of $AgClO_4$ in toluene using the mild reducing agent heptamethyltrisiloxane (HMTS) in the presence of the weak stabilizing ligand trioctylamine (TOA) [244]. AgNPs were synthesized in toluene from $AgClO_4$ using HMTS as a reducing agent in the presence of the stabilizing ligand TOA at room temperature. After the addition of TOA, the color of the solution was faint yellow and displayed a diffuse LSPR peak at 434 nm, which can be attributed to the formation of ultrasmall silver nanocrystals [245] (Fig. 3.22, curves 1–6). Over the next few minutes, the LSPR peak amplitude increased rapidly with a concurrent redshift reaching a maximum at 439 nm followed by a monotonic decrease to 431 nm over the remaining 150 min. The LSPR peak intensity increased throughout the entire 160 min, but was biphasic with rate change near 50 min. A similar LSPR blueshift was previously reported during the synthesis of thiolate-stabilized gold nanoparticles under mild reduction and was explained by a decrease in the dispersity of the nanoparticles [246]. Approximately 160 min after the addition of TOA, the amplitude of the LSPR peak approached its maximum. Figure 3.22 (curves 7 and 8) summarizes the time dependence of the LSPR peak intensity and position during the AgNP formation, and the plot reflects a slow reduction process with a much slower rate of formation of nanoparticles relative to sodium borohydride [247, 248]. The complete conversion of Ag^+ ions to Ag^0 was confirmed by XPS analysis. The XPS survey scan of TOA-stabilized AgNPs confirms the expanded silver 3d region. The signals at 368, 532, 285, and 402 eV represent the silver 3d, oxygen 1s, carbon 1s, and nitrogen 1s binding energies,

respectively. The peak position of the Ag 3d doublet [$3d_{5/2}$ (368.2 eV) and $3d_{3/2}$ (374.2 eV)] with peak-to-peak separation of 6.0 eV confirmed that silver was present only in the Ag^0 oxidation state [249].

Thiols used are strong, stabilizing ligands, and the formation of thiolate-protected gold nanoparticles is very complex [250–252], and unrelated to the process described here for AgNPs. Two minutes after addition of TOA, formation of ~ 1.7-nm average diameter AgNPs was observed, which increased to 2.1 nm within another ~ 12 min of the reaction. As the reaction continued, AgNPs grew larger and by 50 and 90 min after addition of TOA, the particles had grown to average diameters of ~ 2.5 and ~ 2.8 nm, respectively. Over the remaining time, a gradual increase in nanoparticle size was observed, with the final AgNPs ~ 3.1 nm in diameter at 160 min. The diameter change was biphasic and exhibited an initial rapid increase, which was completed at approximately 10–15 min similar to that found with the wavelength maximum in Fig. 3.22, and a more gradual increase thereafter extending through 160 min. The data represent the slow, continuous growth (increase in size) of AgNPs at time >50 min in agreement with the biphasic nature of the LSPR amplitude increase previously discussed. Additionally, the TEM analysis revealed that at the early stage of the reaction (<15 min) the dispersity of the AgNPs increased from 35% at 2 min to 42% at 8 min, which is in agreement with the redshift of LSPR peak illustrated in Fig. 3.22 (curves 7 and 8). After reaching maximum dispersity, the AgNPs exhibited a gradual decrease of dispersity to 19% at 160 min. This conversion of polydispersed AgNPs to nearly monodispersed nanoparticles by TEM analysis is also in agreement with a previous observed blueshift of the LSPR peak over this time period [244].

It is known that hydrosiloxanes are weak reductants due to their slow liberation of hydrides in the presence of metal ions [253] suggesting that in the present investigation, reduction of Ag^+ by HMTS was slow and continuous. Based on time-dependent UV–Visible absorption studies and TEM analysis, the following mechanism of TOA-stabilized AgNP formation was suggested:

Fig. 3.22 Time dependence of synthesis of TOA-stabilized AgNPs. UV–Visible absorption spectra at different times (from 2 to 160 min, *curves 1–6*) after addition of TOA to AgClO$_4$ at room temperature with HMTS as reductant. Solution absorbance and position of LSPR peak as a function of reaction time (*curves 7 and 8*) [244]
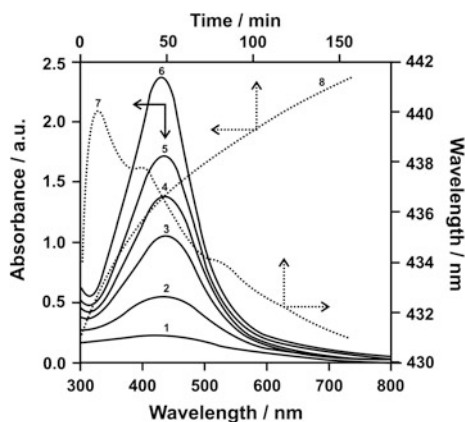
(1) Immediately after the addition of TOA, the solution color turned from colorless to faint yellow, indicating the very rapid formation of ultrasmall nanocrystals which serve as "active nuclei".

(2) With time, these active nuclei grow to form seeds. Simultaneously, more active nuclei are formed from the reduction of Ag^+ to Ag^0, as evident by the increasing LSPR peak intensity (Fig. 3.22). These seeds continue to grow forming larger nanoparticles via Ostwald-ripening growth. The biphasic behavior of the LSPR peak (Fig. 3.22) is interpreted as the result of simultaneously continuous reduction, nucleation, and growth processes until approximately 50 min after the addition of TOA.

(3) The final stage of nanoparticle formation is almost exclusively dominated by slow Ostwald-ripening growth as evident by the plot of nanoparticle volume versus time. In the ideal case of Ostwald-ripening growth $\{\overline{V}(t)\}$, the change in average AgNP volume should be linear with respect to time [254]. Based on the time-resolved TEM size analysis, linear nanoparticle growth kinetics, and single crystallinity of the final AgNP structure, it is concluded that under the slow reduction condition, nanoparticle growth is controlled by Ostwaldripening [244].

The peak shape and LSPR wavelength maximum (~ 431 nm) were comparable when 1.5 and 2.0 mmol of TOA were used for synthesis; however, with 0.2 mmol, the peak width was broader (Fig. 3.23). This figure (curves 1 and 2) shows that the rate of absorbance change for 0.2 mmol TOA was faster than that with 1.5 or 2.0 mmol TOA. The average diameters determined by TEM of AgNPs were ~ 2.9 and ~ 3.0 nm for 1.5 and 2.0 mmol of TOA, respectively. However, when nanoparticles were synthesized using 0.2 mmol of TOA, large-size polydispersed AgNPs were formed (~ 7.3 nm) in agreement with the broader LSPR peak and faster rate of formation [245].

Beside its stabilizing ability, TOA may also act as a catalyst for the Ag^+ reduction process. Over the following 3-h period, the colorless solution turned to a faint murky yellow which displayed a very weak, broad absorption band centered at approximately 423 nm, indicative of silver nanocluster formation [245, 255]. However, the normalized intensity of the nanoparticle solution was $\sim 2.0 \times 10^2$ times lower than that what was achieved for reduction of Ag^+ to Ag^0 at 160 min. Furthermore, amines can readily coordinate to a tetravalent silicon center and form pentavalent silicon species, as illustrated in Scheme 3.16 [256, 257]. Immediately after addition, the solution turned yellow and displayed an intense and broad LSPR peak at 429 nm indicating the formation of AgNPs in high concentration. The peak intensity gradually increased over time and approximately 130 min after TOA addition, a stable LSPR peak at 435 nm was observed. The above experimental results strongly suggest that TOA plays dual roles in the formation of AgNPs.

The LSPR time course at 35 and 45 °C displayed qualitatively the same behavior as observed when the synthesis was performed at room temperature with reaction rates at 45 > 35 > 24 °C (Figs. 3.23 and 3.24). The increase of peak intensity over time at both elevated temperatures suggests continuous formation of
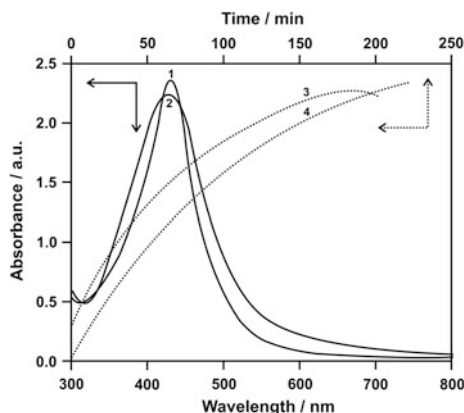
Fig. 3.23 UV–Visible absorption spectra of AgNPs synthesized using different TOA concentrations at room temperature. *Lines 1 and 2* represent 0.2 and 2.0 mM of TOA, respectively, added to 0.1 mmol AgClO$_4$ with HMTS as the reducing agent. The rate of nanoparticle formation represented by absorbance increases in presence of 0.2 (*curve 3*) and 2.0 (*4*) mM of TOA, respectively [244]

nanoparticles following the Ostwald-ripening growth mechanism. The average sizes of the AgNPs synthesized at 35 and 45 °C were ∼3.8 and ∼4.0 nm in diameter, respectively, which were greater than the AgNPs synthesized at room temperature (∼3.1 nm) [258]. More specifically, when the AgNPs were synthesized at room temperature, a sharp LSPR peak at 431 nm was observed. When the synthesis was performed at 35 and 45 °C, the LSPR peaks were centered at 436 and 443 nm, respectively. Previously, it was reported that the LSPR properties of metal nanoparticles are strongly correlated with particle size, and as the size of the nanoparticles increases, the LSPR peak redshifts [245, 259]. In this investigation, a 12 nm redshift was observed when the AgNPs were synthesized 45 °C compared to nanoparticles made at room temperature. The observed increases in particle size and
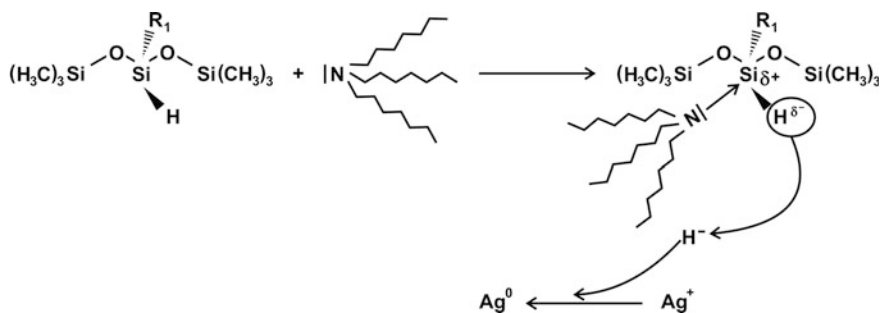
Scheme 3.16 Proposed mechanism of trioctylamine (TOA)-induced pentavalent silicon species formation and liberation of hydride, which facilitate the reduction of Ag$^+$ to Ag^0 [244]

dispersity also suggest that TOA is a weak stabilizing ligand at elevated temperatures. In addition, solution temperature is expected to effect the concentration of available reductant, in that the hydride generation rate in the reaction mixture should increase with increasing temperature. Therefore, the concentration of active nuclei in solution should increase more quickly at higher temperature, and the newly formed active nuclei should undergo faster nucleation and growth resulting in relatively larger nanoparticles than those formed at room temperature with slower active nuclei formation. Figure 3.24 shows that after the reaction mixture displayed stable LSPR peak absorptivity, continued heating caused it to decrease. Apparently, continued heating produced nanoparticles of sufficiently large sizes that they became unstable in solution, and then aggregated and precipitated. This behavior is consistent with TOA being a weakly stabilizing ligand and unable to control AgNP growth at elevated temperature.

Some of previous nanoparticle synthesis and growth studies were performed in aqueous phase using the strong reducing agent sodium borohydride. In these studies, the reduction and nucleation processes take place very rapidly, resulting in almost immediate aggregation and coalescence. In contrast, some authors have also reported that reduction, nucleation, and growth processes are occurring simultaneously over a period of time. Moreover, in sodium borohydride-based reduction and formation of NMNPs, aggregative growth of nanoparticles is the most common formation pathway [248], whereas the researchers observed predominantly Ostwald-ripening growth. Sodium citrate is the second most commonly used reducing agent for nanoparticle synthesis and growth studies. [254, 260, 261]. However, the growth kinetics found for HMTS-induced synthesis of AgNPs are different than classical citrate-mediate nanoparticle formation, even though both HMTS and citrate are mild reductants. One major difference between these two reductants is the resulting reaction medium. As mentioned earlier, the presence of citrate in aqueous medium can alter the solution pH and influence the growth mechanism [262]. Such behavior is negligible for hydrosiloxane-induced synthesis of AgNPs due its stable structure in organic solvents. In addition, aggregative growth of NMNPs was reported for citrate-based synthesis, in contrast to what was observed.

The introduction of strong capping agents during nanoparticle synthesis has the effect of stopping the growth of the NPs, whereas weakly associated ligands allow for continued growth [246]. As a result, the presence of the capping agent whether

Fig. 3.24 Dependence of AgNP synthesis on reaction temperature. The rate of AgNPs formation represented by absorbance increases as a function of time at 35 °C (*curve 2*) and 45 °C (*1*) after reduction of 0.4 mmol TOA to 0.1 mM of AgClO$_4$ [244]
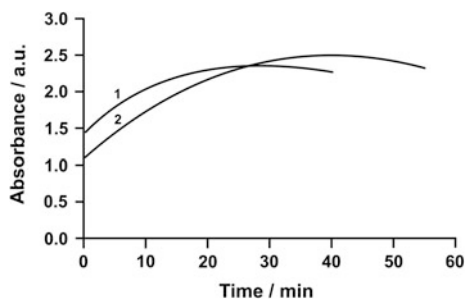
strongly or weakly binding is essential during the nanoparticle synthesis in order to control the nanoparticle size and shape and to prevent aggregation. However, use of strong capping agents makes further surface modification with alternative ligands challenging [263]. In addition, the sizes of the nanoparticles produced using strong capping agents, e.g., alkylthiols, vary from batch to batch [264].

In order to synthesize gold nanoparticles without the use of strong capping agents, the synthetic method requires a reducing agent to generate nanoparticles at a slow rate with the resulting particles stabilized by coordinating ions or ligands which are already present in the reaction mixture from the gold salt precursor. Shem et al. have demonstrated this approach based on the reducing agent 9-borabicyclo [3.3.1] nonane (BBN) [229]. BBN was used to prepare various x-terminated (acid, amide, or alcohol) alkylthiolate-functionalized AuNPs, azide-terminated disulfide-protected AuNPs, triphenylphosphine-stabilized AuNPs, and other noble metal nanoparticles, specifically, silver, palladium, and platinum nanoparticles [236, 246, 265]. This approach was used for preparation of AuNPs with a size smaller than 5 nm without a need for strong ligands. Additionally, postsynthetic surface modification of the soft-ligand-stabilized NPs with more strongly interacting ligands such as bipyridyls and thiols is important in tuning the optical and electronic properties of the AuNPs for applications. Shem et al. [229] have used the BBN synthesis as the basis of a synthetic strategy for producing soft-ligand-stabilized AuNPs via a surfactant-free synthesis. The advantage of this synthetic procedure is that during NP synthesis, no additional capping agents are added as the NPs are produced at a slow rate and stabilized by soft ligands, Et_3P molecules, and Cl^- ions, which are introduced through the precursor materials. The soft ligands offer the potential for easy displacement after synthesis by the desired stronger binding ligands. In addition to changing functionality through control of surface chemistry, the introduction of stronger binding ligands at specific time points during synthesis prevents continued growth and produces AuNPs with a much more narrow size dispersion. Furthermore, stronger ligands also lead to long-term stability of the AuNPs.

The versatility and usefulness of soft-ligand-coated AuNPs are further demonstrated by replacing the soft ligands with alkylthiols, which results in 2D assembly of the AuNPs. Control of the size and assembly of the NPs is important because these two properties modulate the near-field optical coupling and LSPR properties of the NPs [234]. To date, most 2D assemblies have been prepared either at the air–water interface or on a solid surface [266]. In the latter case, a dewetting process was used where nanoparticles were dispersed in solvent. When the nanoparticle solution was placed on a substrate, the solvent slowly evaporated leaving a film of thiol-capped NPs. Interfacial or dewetting techniques typically focus on AuNPs larger than 10 nm; however, much progress has been made in applying these approaches to small nanoparticles [267]. Such small NPs are of particular interest in optoelectronic device fabrication [268]. One important requirement for formation of 2D assemblies is that the building blocks or individual NPs should be highly monodisperse to ensure regular packing, and this is achieved through the described synthesis.

Soft-ligand-stabilized AuNPs were prepared as shown in Scheme 3.17. No additional surfactants were introduced in the reaction mixture besides Et₃PAuCl which was present as the gold salt precursor and BBN as the reducing agent. On addition of BBN, the color of the solution changed from colorless to light brown to reddish-brown. A broad featureless response in the UV–Vis spectrum between 400 and 600 nm was observed, indicating that AuNPs were being formed.

When the reaction solution was stirred mechanically using a magnetic stir bar, the absorption spectra changed very little as shown in Fig. 3.25. The color of the solution also did not change from the light brown color first observed on addition of BBN. The lack of change was an indication that continued growth beyond a certain size was not taking place during the course of the reaction. However, when stirring was stopped, the NPs rapidly aggregated as evidenced by the appearance of a broad LSPR peak (Fig. 3.25, curve 3). TEM analysis of this sample showed aggregated NPs.

For the unstirred solution, the LSPR peak shifted to longer wavelengths with time as the nanoparticle growth process progressed as shown in Fig. 3.25 (curves 2, 4–6). This plasmon band shift was an indication that the NP size was increasing [246]. The color of the solution changed from colorless, to reddish-brown, purple, and finally bluish purple, indicating that the growth of the NPs continued during the course of the reaction. A close examination of the spectra in Fig. 3.25 reveals that between 10 and 20 min after addition of BBN, there was very little change in the absorbance amplitude and the absorption wavelength did not shift. After 20 min, there was a marked redshift and broadening of the absorbance band indicating either formation of large NPs or NPs undergoing an aggregation process. When the reaction was allowed to proceed for 60 min, a decrease in amplitude and broadening of the absorption spectrum was observed along with nanoparticle precipitation.

Mechanical agitation introduced by the stirring alters the nucleation and growth processes of the gold nanoparticles. Stirring introduces shear forces to the solution and, while shear-induced enhancement of nucleation has been reported, mechanical
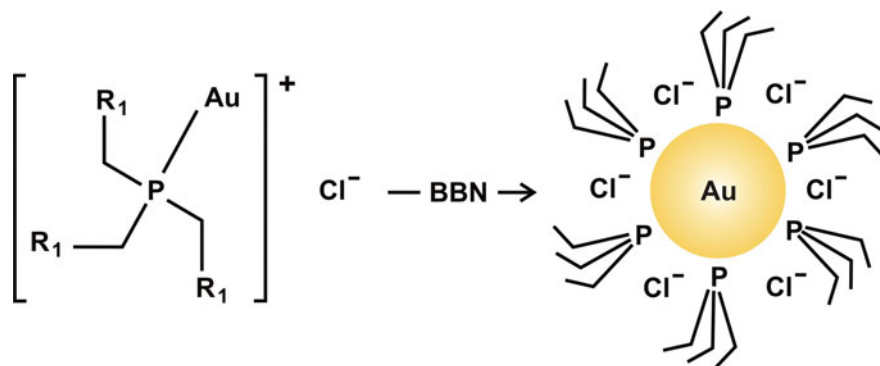
Scheme 3.17 Synthetic approach for soft-ligand (triethylphosphine)-stabilized AuNPs [229]

Fig. 3.25 UV–Vis absorption spectra of the stirred NPs (*curve 1*), the broad peak was recorded 5 min after stirring was stopped (*curve 3*) and unstirred TPP-AuNPs solution over the time course [2–60 min, *curves 2* (2 min), *4* (10), *5* (40), and *6* (60)] of the synthesis [229]
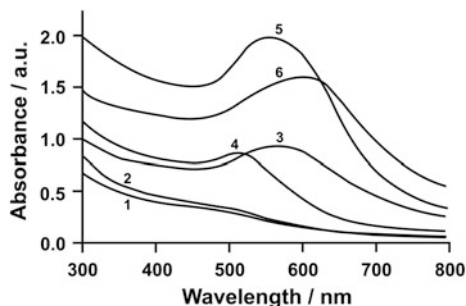
shear also has been found to suppress growth by breaking up aggregated NPs [269]. It seems that stirring enhanced the nuclei concentration leading to smaller NPs produced while larger particles resulted when the solution was not stirred [270]. Analysis of the TEM images indicates that the nanoparticles had a broad size distribution at early times, with two populations of small and large NPs being observed. This size distribution narrowed with time to form a uniform size distribution after 20 min. At $\sim$20 min, the absorbance peak position and amplitude of the NPs do not change (Fig. 3.25). The size of the AuNPs at this point was determined to be $\sim$3.6 nm. The AuNPs formed larger aggregates when the stirring was stopped and the solution was allowed to stand for 60 min. HRTEM shows NPs with well-defined lattice fringes, which were indexed to Au fcc lattice using SAED. HRTEM analysis shows the shape and faceting of the AuNPs and indicates that the NPs are not single crystals. The particles are made up of smaller NP units likely formed by coalescence of individual, smaller NPs along common facets to form twinned particles. Contrast differences in HRTEM images, where some regions are darker than others, are an indication of twinning [271, 272]. The SAED pattern of the AuNPs was indexed to the (111), (200), (220), and (311) planes of a face-centered cubic gold lattice. The spotty diffraction rings observed in the SAED pattern also support the presence of twins.

Bimodal distribution of AuNPs as observed in the early stage of synthesis is evidence for aggregative growth [164]. This indicates particle–particle interactions leading to coalescence, or an aggregative growth mechanism. Coalescence stopped when all the particles had been consumed, leading to the end of the growth process and the establishment of a narrow size distribution of the AuNPs [273]. Polte et al. [247] observed that in the absence of a stabilizing agent, growth can continue for long periods of time (in their case, 24 h) driven entirely by coalescence and not monomer addition [247]. The nonstirring approach resulted in nearly monodisperse AuNPs with a size of $\sim$4 nm at the approximately 20-min time point during the synthesis.

The XPS spectrum in Fig. 3.26 shows the peak positions of the Au 4f doublet, $4f_{5/2}$ (87.8 eV), $4f_{7/2}$, (84.1 eV) with peak-to-peak distance of 3.7 eV. The peak positions verify that most of the gold was present in the Au^0 oxidation [274]. Peaks associated with P (2p) at 131.6 eV from Et_3P and Cl (2P) at 198 eV also were

observed [265]. In both of the experiments, XPS evidence of the presence of P and Cl is consistent with the soft ligands acting as the nanoparticle-capping agents, providing stability to the AuNPs in organic solvent and preventing agglomeration.

Soft-ligand-stabilized nanoparticles can be used as precursors to obtain AuNPs with different surface chemistry by replacing the soft ligands with other desired ligands [265, 275]. The AuNPs surface was also modified with 11-mercaptoundecanol (MUOH) and analyzed the surface chemistry after the exchange process using XPS. Interestingly, XPS high-resolution scans for the P (2p) region for the particles before and after ligand exchange with MUOH showed that phosphorus was absent after ligand exchange. An observed peak for sulfur, S (2p) at 162.4 eV, indicates a sulfur–Au interaction through a thiolate bond along with Au 4f doublets $4f_{5/2}$ (87.8 eV) and $4f_{7/2}$, (84.1 eV). The absence of peaks for P and Cl and appearance of a peak for sulfur suggest that when the AuNPs stabilized by Et_3P and Cl^- ions were incubated in the MUOH solution, the higher affinity thiol ligands replaced the weakly associated Et_3P and Cl^- from the surface and produced thiolate-functionalized AuNPs.

Thus, an in situ ligand exchange reaction can be used to replace the soft ligands with bipyridyls according to Scheme 3.18. If the ligands were introduced at a later time point, TEM analysis indicated that the particles would undergo further uncontrolled growth to produce polydisperse particles.

The color change is an indication that the bipyridyls attached to the AuNP surface [276]. The bipyridyl-stabilized AuNPs were dissolved only in polar solvents. The UV–Vis spectra of the solution of soft-ligand-stabilized AuNPs had maximum absorbance (λ_{max}) at ∼530 nm, while the 2,2′-bipyridyl and 4,4′-bipyridyl AuNPs exhibited maximum absorbance at 535 and 545 nm, respectively (Fig. 3.27, curves 1–3). As the AuNP size changed very little after addition of the bipyridyls, the different absorption peak wavelength positions are attributed to different orientations of 2,2′-bipyridyl and 4,4′-bipyridyl on the surface of the AuNPs as shown in Scheme 3.18 [277, 278]. One can note that there was no

Fig. 3.26 XPS high-resolution scan for the Au 4f [peak 1 (87.8 eV) and peak 2 (84.1 eV)] photoelectron peak for the AuNPs immobilized on MPTES functionalized glass. The Au 4f peak was fitted using Gaussian–Lorentzian line shapes. The peak position and peak-to-peak distance of the doublet is consistent with Au^0 [229]
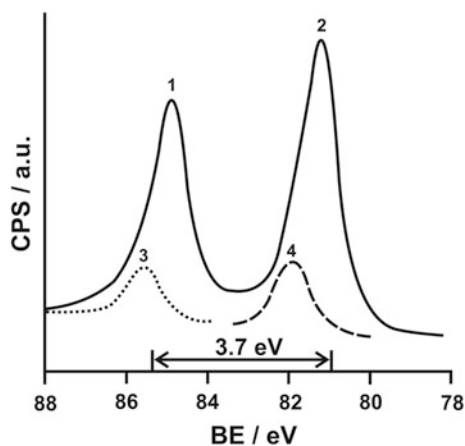
significant change in the sizes of the NPs after functionalization with the bipyridyl ligands. The average size of the AuNPs before functionalization with the bipyridyl ligands was ~ 3.6 nm (TEM). The sizes of the 4,4′-bipyridyl and 2,2′-bipyridyl AuNPs were determined to be ~ 3.5 and ~ 3.1 nm, respectively.

The N 1s spectra (XPS) were resolved by fitting into three components at 399.5, 401.4 and 403.4 eV for 2,2′-bipyridyl AuNPs, and 399.6, 400.3 and 402.8 eV for 4,4′-bipyridyl AuNPs. The peaks at 399 eV indicate that the bipyridyls are coordinated to the AuNPs compared to the expectation to observe a peak at 398 eV for free ligands [279, 280]. The shift to higher binding energy occurs because the bipyridyls donate electrons to the Au atoms via the nitrogen atom [281]. The peaks at 401–403 eV are due to the protonation of the bipyridyl nitrogen. Therefore, the high binding energy peaks indicate the presence of a N^+ species. The C 1s spectra for both 2,2′- and 4,4′-bipyridyl AuNPs exhibit peaks at 285.9 and 285.2 eV, respectively. These peaks are attributed to the aromatic carbons of the bipyridyl ligands [279]. The peaks at 284.8 eV are assigned to adventitious carbon. The peaks at a higher binding energy of 287.8 and 288.3 eV for 2,2′- and 4,4′-bipyridyl AuNPs, respectively, are due to hydrogen bonding of the bipyridyl nitrogen [282]. The Au 4f spectra indicate that Au exists primarily as Au atoms. These XPS results confirm that the bipyridyl ligands are attached to the AuNPs through interactions with the nitrogen atoms [229].

Duraiswamy and Khare were able to synthesize spherical gold nanoparticles (Fig. 3.28, curve 1), oblate particles (curve 2, both left panel), gold nanorods of varying aspect ratios (Fig. 3.28, curves 1–3), and sharp-edged nanostructures
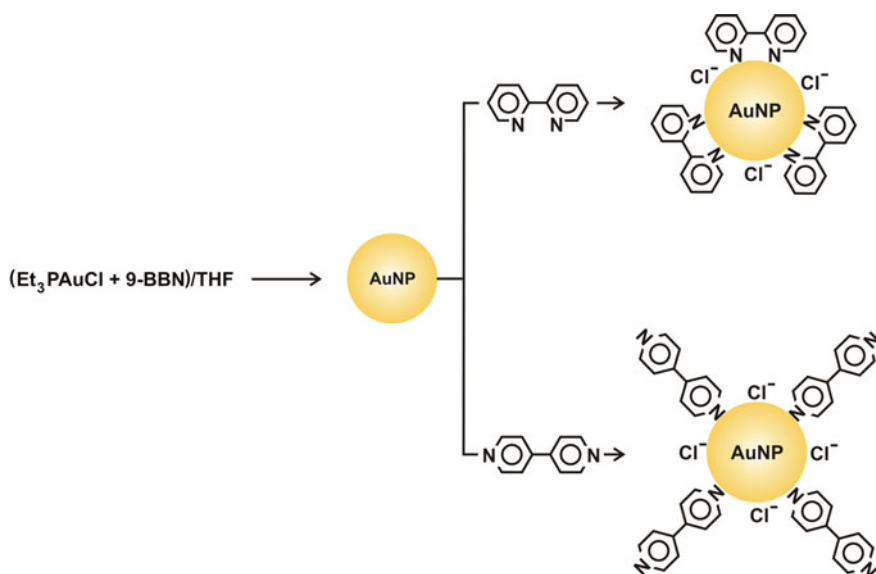
Scheme 3.18 Synthesis of 2,2′- and 4,4′-bipyridyl-stabilized AuNPs [229]

(Fig. 3.28, curve 4) by simply varying solution flow rates in the two reaction stages (Scheme 3.19) [283]. Spherical gold exhibits a sharp absorption peak at the characteristic wavelength of 520 nm, while oblate/spheroidal particles exhibit two plasmon resonances at 520 nm and ~660 nm. They also obtained nanorods with two characteristic plasmon resonances: transverse plasmon resonance (TPR) caused by their short axes and longitudinal plasmonic resonance (LPR) caused by their long axes. All three samples yielded short nanorods with average length ~35 nm and width ~12 nm; these measured nanorod sizes typically followed skewed, nonnormal distributions. Interestingly, measured aspect ratios under the conditions in Fig. 3.28 (right panel, curve 1) (~3.6) were different from those in Fig. 3.28, curves 2 and 3 (~2.8 and 2.5 respectively). Finally, all three samples had different LPRs: 700 nm (curve 1), a broad peak between 650 and 720 nm (curve 2), and 680 nm (curve 3), respectively. The obtained plasmon resonance signature results highlight an important point relevant to flow synthesis schemes, namely that changes in operating conditions can yield sufficiently different nanocrystal populations with different overall plasmon signatures. These differences arise due to changes in

  (i)   particle sizes and shapes;
 (ii)   size distributions; and
(iii)   the relative numbers of particles of various shapes under different operating conditions.

   The different shapes and sizes of anisotropic particles are obtained by tuning the relative flow rates, which in turn affect the relative concentrations of the gold precursor (Au^{3+}), shape directing agent (Ag^+), and the surfactant solution [72, 284–286].

   Obtained ultrasmall (<5 nm) nanoparticle seeds with the corresponding UV–Vis spectra (in Fig. 3.28, curve 3, left panel) exhibiting no prominent peak but a slight hump around 520 nm, characteristic of particles of size <5 nm [216, 287, 288]. In

Fig. 3.27 UV–Vis absorption spectra of the 2,2′-bipyridyl and 4,4′-bipyridyl-functionalized AuNPs, *curve 3*: bare AuNPs, curve 2: 2,2′bipy-stabilized AuNPs and *curve 3*: 4,4′ bipy-stabilized AuNPs [229]
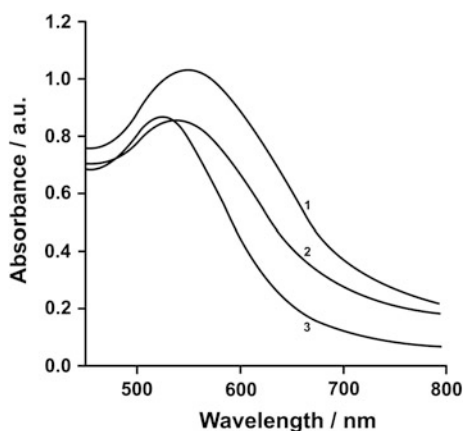
this case, the on-chip residence time of reagents is ~ 5 min, while the off-chip growth time is ~ 1 h (sample collection time). In contrast, under normal operating conditions described in the above paragraphs, the residence time for nanoparticle seed nucleation and growth is restricted to ~ 90 s in Stage 1, which is likely insufficient for the seed formation to proceed to completion. The spectrum does not exhibit the characteristic spectrum of the seeds; furthermore, the solution is not colored, whereas gold precursor solution is golden yellow and a suspension of seeds is typically golden brown in color. The absence of brown color indicates that the seeds have not completely formed, while the absence of yellow color indicates that the reduction of Au^{3+} to Au^0 has proceeded to some extent and random cluster formation, leading to incipient "nuclei" has been initiated. Polte et al. [248, 289] have reported detailed in situ time-resolved small angle X-ray scattering (SAXS) and X-ray absorption near-edge spectroscopy (XANES) measurements on gold and silver nanoparticle growth by chemical reduction. Their studies have shed light on several key phenomena that are also relevant to work [283]: Au^{3+} is not instantaneously reduced to Au^0; furthermore, particle growth typically occurs via a four-step growth mechanism, in which small nuclei (Step 1) first grow by coalescence (Step 2) followed by slower diffusion controlled growth (Step 3) and finally by a fast growth burst (Step 4) accompanied by complete consumption of precursor. It is likely that the short residence time in Stage 1 of present reactor leads to incomplete growth of nanoparticle seeds, probably arrested in Step 2 of the mechanism. The incompletely grown seeds interact minimally with the channel wall, leading to robust operation of Stage 1 without wall deposition [290] for over 12 h of continuous operation.
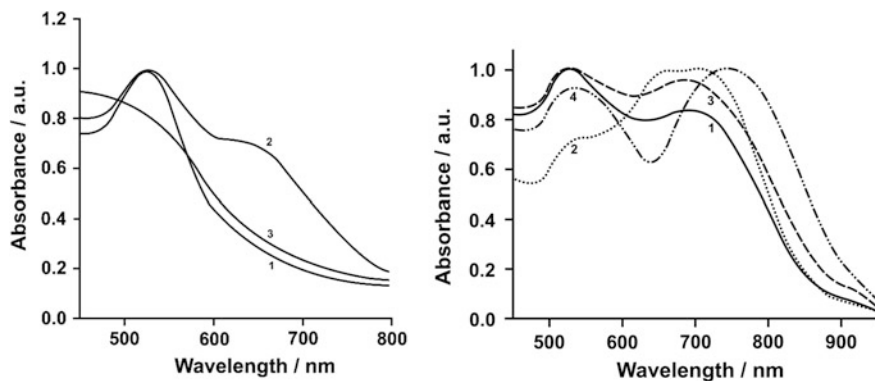
Fig. 3.28 UV–Vis absorbance spectra of spherical gold nanoparticles (*curve 1*) and oblate/spheroidal particles (*2*), seed nanoparticles (*3*) (*left panel*) and gold nanorods of varying aspect ratios (*curves 1–3*), and sharp-edged nanostructures (*curve 4*) (*right panel*) [283]
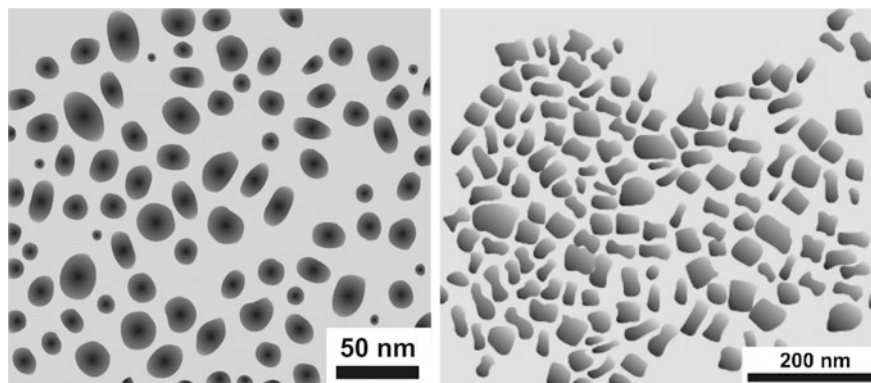
Scheme 3.19 TEM images of oblate and nonspheroidal gold particles [283]

3.2.6.5 Surfactant-Free Syntheses

A new method of producing gold nanoparticles is a surfactant-free synthesis, high variability in the introduction of (functionalized) ligands, and good control over the particle size [199]. It was found that a solution of hydrogen tetrachloroaurate in diethylene glycol dimethyl ether (diglyme) can be reduced by a solution of sodium naphthalenide in diglyme to form gold nanoparticles. In this reaction, no further stabilizing surfactant is necessary, although sodium naphthalenide can be considered a rather harsh reducing agent. The resulting, weakly protected nanoparticles can straightforwardly be stabilized and functionalized by the addition of a variety of ligands. Upon dropwise addition of the sodium naphthalenide solution to the yellow aurate solution, for example, the latter turns slightly green followed by a deep brown color, indicating the formation of gold nanoparticles. On further addition of the reducing agent, a dark purple color is arising, which can be attributed to the surface plasmon resonance, suggesting an increase in particle size above 2 nm [259]. The nanoparticle growth is slow in diglyme, but, on standing, they tend to agglomerate and form a loose purple precipitate within the course of several hours to 1 day.

Among all the in situ syntheses of gold nanoparticles by reduction of $HAuCl_4$, citrate-stabilized AuNPs have been regarded as the most popular ones for a long time, since their introduction by Turkevich in 1951 [186]. The $HAuCl_4$ solution is boiled, and the trisodium citrate dihydrate is then added under stirring. The wine-red colloidal suspension is then obtained, and the AuNP size is about 20 nm. Frens [291] later published an approach giving a broad size range of AuNPs (from 15 to 150 nm) by controlling the trisodium citrate to gold ratio. The citrate reduction method is well known for its simple procedure, yielding stable and reproducible gold nanoparticles of narrow size distribution [292]. The citrate method produces nearly monodisperse gold nanoparticles in the size range from 2 to 100 nm [293]. Problems of the citrate method are a low gold nanoparticle content

of the resulting solutions (<0.01 M) and the restriction to water as a solvent. Because the charge-stabilized particles easily undergo irreversible aggregation upon addition of electrolytes and nonpolar surfactants, particles cannot be surface-derivatized with hydrophobic surfactants. The improved approaches with various mechanisms of AuNPs formation using this synthetic route have been examined in details [262, 289]. Kimling et al. [294] indicated that a high concentration of citrate more rapidly stabilizes AuNPs of smaller sizes, whereas a low concentration of citrate leads to large-size AuNPs and even to the aggregation of AuNPs.

Remarkable research on the mechanism of the Turkevich-Frens method in multiple-step process was published by Kumar's group [295]. The initial step of this multiple-step process, with reactions occurring in series and parallel, is the oxidation of citrate that yields dicarboxy acetone. Then, the auric salt is reduced to aurous salt and Au^0, and the aurous salt is assembled on the Au^0 clusters to form the AuNP (Scheme 3.20). Thus, in the Turkevich-Frens method, the actual AuNP stabilizer is dicarboxy acetone resulting from the oxidation of citrate, rather than citrate itself.

In addition, the presence of a citrate salt modifies the pH of the system and influences the size and size distribution of the AuNPs [262]. On this basis, nearly monodispersed AuNPs with sizes ranging from 20 to 40 nm have been synthesized upon variation of the solution pH [296, 297]. Other improvements of the Turkevich method involved the control of the reaction temperature [298], the introduction of fluorescent light irradiation [299], and the use of high-power ultrasound [300]. Citrate-stabilized AuNPs are always larger than 10 nm, due to the very modest reducing ability of trisodium citrate dihydrate. An intriguing result from Puntes's group [301] concerning citrate-stabilized AuNPs is the use of D_2O as the solvent instead of H_2O during the synthesis of AuNPs. As shown in Fig. 3.29, the size of the AuNPs was tailored to 5 nm. It was concluded that D_2O increased the reducing strength of citrate:

absorbance (a.u)/wavelength (nm):

$$0.47/512.5(100\% \, D_2O, \text{ curve } (1))$$
$$0.35/514.5(50\% \, D_2O : 50\% \, H_2O, (2)) \tag{3.25}$$
$$0.48/519(100\% \, H_2O, (3))$$

3.3 Bioconjugates

Due to their amphiphilic character, the pluronic block (PEO-PPO-PEO) copolymers display surfactant properties including ability to interact with hydrophobic surfaces and biological membranes. The pluronic block copolymers self-assemble into micelles in aqueous solutions at concentrations above critical micelle concentration (CMC) . Incorporation of low-molecular mass drugs (such as
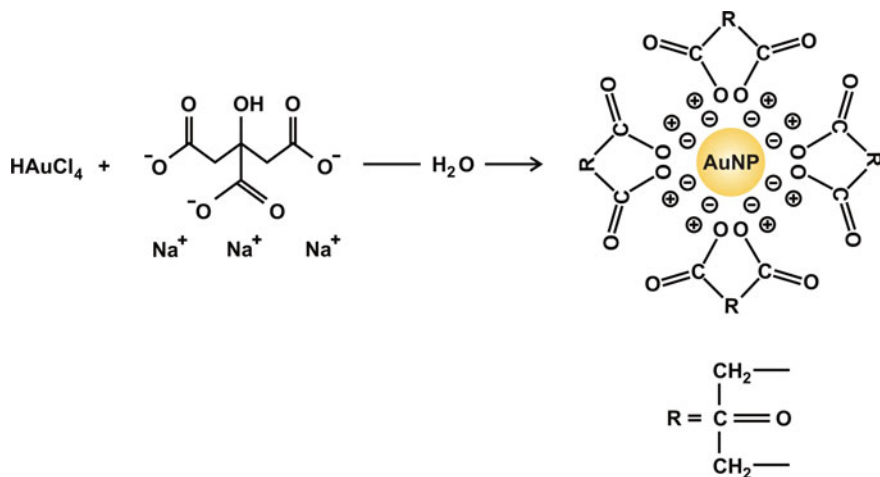
Scheme 3.20 AuNP synthesis using the Turkevich method [26]

doxorubicin (DOX) which is a topoisomerase inhibitor and a widely used anti-cancer drug in the treatment of many types of cancer) into pluronic micelles can increase drug solubility and drug stability, and can improve drug pharmacokinetics and biodistribution. Although DOX is easily sequestered and released from pluronic micelles in vitro, this type of micelle is not sufficiently stable to be used in vivo. Dilution in the blood upon injection would quickly dissolve the micelle and prematurely release the drug into the bloodstream, which limits their practical uses for systemic delivery of DOX. To enhance stability of micelles in the bloodstream upon dilution, pluronic L121 micelles were cross-linked through their hydrophilic shells [302]. This greatly reduced the CMC and diameters of the micelles and enhanced the micelle stability. Recent developments indicate that pluronic block
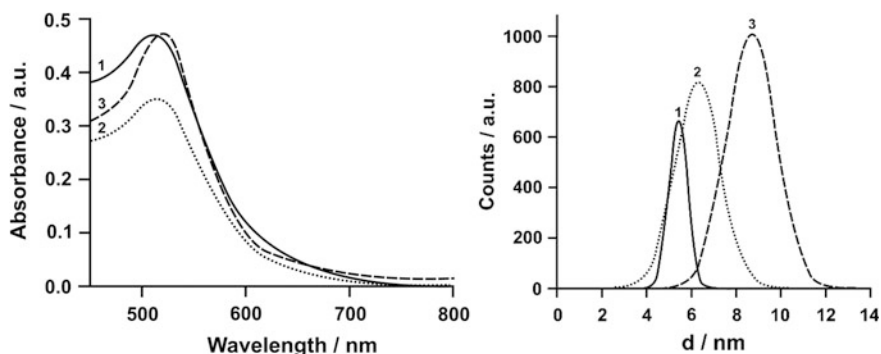
Fig. 3.29 Optical (UV–Vis. spectroscopy) and morphological (TEM) characterization of AuNPs synthesized using various solvents: 100% D_2O (*1*), 50% D_2O/H_2O (*2*), and 100% H_2O (*3*). TEM images show the size distribution measurements of AuNPs [26, 301]

copolymers can implement more than only inert carrier functions by being biological response modifiers [303]. Pluronics cause drastic sensitization of multidrug resistance (MDR) tumors to various anticancer agents, enhance drug transport across the blood–brain and intestinal barriers, and cause transcriptional activation of gene expression both in vitro and in vivo. Pluronics have a broad spectrum of biological response modifying activities which make it one of the most potent drug targeting systems available, resulting in a remarkable impact on the emergent field of nanomedicine.

Differential scanning calorimetry can be used to measure a number of characteristic properties of nanoparticles based on pluronics. With this technique, it is possible to observe fusion and crystallization characteristics of polymers. As the temperature increases, the sample eventually reaches its melting temperature (T_m). The melting process results in an endothermic peak in the DSC curve. The transition at crystallization temperature (T_c) from amorphous solid to crystalline solid is an exothermic process, and results in a peak in the DSC signal. The T_m and T_c of DOX-pluronic F68 comparing with pluronic F68 were both declined from 53.37 to 48.04 °C and 30.83 to 24.47 °C. The decrease of T_m and T_c might be resulted from the connection of DOX to pluronic F68.

As shown in TEM, pluronic F68 micelles were irregular in shape and showed an average size of about 50 nm. However, DOX-conjugated pluronic F68 (DOX-P) micelles showed tightly packed nanospheres with an average size of about 20 nm. It was likely that hydrophobic interaction stacking of conjugated DOX molecules in the core was responsible for the self-assembling core/shell structure of DOX-P micelles, which would make the micelles more stable in theory [302]. It is known that drug encapsulation in micelles can diminish drug extravasation into normal tissues and provide for a passive drug targeting to tumors via the enhanced permeability and retention (EPR) effect. The EPR effect is realized due to abnormally high permeability of tumor blood vessels combined with prolonged circulation of the micelles due to their decreased extravasations in normal vessels and lack of renal clearance [304].

The side chain hydrolysis of polymers related to the drug release depends on the strength and chemical nature of the polymer–drug bonds, the structure of polymer, and medium conditions. As shown in Fig. 3.30, hydrolysis behavior of DOX-P micelles in vitro was studied in buffer solutions with different pHs (pH 6.0, 7.4, and 8.5) at 37 °C. Under different pH conditions, DOX release profiles showed similar increasing trend with time. In 14 day, up to 70–100% of the loaded DOX could be released from DOX–P conjugate, which was attributed to the gradual hydrolysis of the amide and ester bond between DOX and the side chain of the polymer. The difference of DOX release with pH was remarkable. The release of DOX from the micelles was accelerated when the pH was reduced to 6.0 or increased to 8.5 comparing with pH 7.4's condition. The sustained release of DOX from DOX-P was similarly observed in formulations of microspheres and nanoparticles that were prepared by the conjugation of various hydrophilic drugs to polymers [305]. The efficacy of chemotherapy treatment in many types of cancers is severely limited by multidrug resistance (MDR) . Cancers with the MDR phenotype overexpress efflux

transporters belonging to a superfamily of ATP binding cassette proteins, such as P-gp and MDR associated proteins that pump drugs out of cells. It is reported that pluronic copolymers can inhibit P-gp function [307].

The cellular uptake of DOX by K562 and K562/AO2 cell lines at 37 °C for distinct durations was investigated, and there was no significant difference in the cellular uptake of DOX from different formulations ($P > 0.05$). Free DOX might transport across the cell membrane through diffusion in K562 cells, a pathway that was affected in K562/AO2 cells by P-gp [308]. After exposure of K562/AO2 cells to DOX solution, the accumulation of DOX in cells was limited throughout the entire course of the study. It suggested that entered DOX could be extruded out of K562/AO2 cells by the P-gp efflux pump. In DOX-P solution, however, the accumulation of DOX in K562/AO2 cells enhanced with increased duration of incubation. It indicated that pluronic copolymers could effectively inhibit P-gp function [304] and therefore help to circumvent the DOX resistance of K562/AO2 cells. DOX-P solution showed more cytotoxic effect upon K562/AO2 cells than DOX solution ($P < 0.05$, in vitro). However, there is little difference for the viability of K562 cells from DOX-P solution and DOX solution ($P > 0.05$). This result confirmed the enhancement effect of DOX-P micelles for DOX uptake and DOX resistant inhibition [306].

The versatility of the micellar liposomal structure lies in its capacity to cargo drug molecules and biological macromolecules that are either hydrophilic, therefore entrapped in the liposome inner aqueous core (or in the w/o droplet core), or hydrophobic, therefore incorporated within the lipid bilayer (or in o/w droplet core). Al-Jamal and Kostarelos [10] have presented the concept of liposome-nanoparticle hybrids as a general methodology, taking advantage of the much more developed and sophisticated liposome technology, to be used as a platform for the delivery of novel nanoparticles. Encapsulation of various types of nanoparticles within liposomes can lead to enhanced nanoparticle hydrophilicity, stability in plasma, better control of the pharmacological fate, and an overall improvement in their biocompatibility. The three different approaches for the engineering of liposome-nanoparticle hybrids are schematically shown in Scheme 3.21 [309]. Hydrophobic nanoparticles can be embedded in the lipid bilayer, whereas

Fig. 3.30 In vitro release profiles of DOX from DOX-P micelles depending on the pH value of environment: (*1*) pH 8.5, (*3*) pH 7.4, and (*2*) pH 6.0, temp. = 37 °C [306]
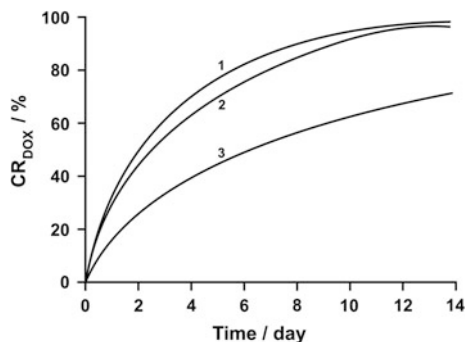
hydrophilic nanoparticles can be encapsulated within the internal liposome aqueous core. Alternatively, various types of nanoparticles can be chemically or physically adsorbed onto the external liposome surface.

The liposome-nanoparticle hybrids have been designed for use as diagnostic probes. In addition, various types of liposome-nanoparticle hybrids have shown promise in significantly stabilizing colloidal dispersions of otherwise unstable nanoparticle systems in vitro and in vivo. Recently, some studies have shown that incorporation of metallic nanoparticles in liposomes can also trigger release of encapsulated contents using external stimuli, such as magnetic fields, laser irradiation, or electromagnetic radiation at different radio frequencies. There are multiple examples of liposome systems with diverse characteristics and capabilities that incorporate therapeutics or imaging agents [310]. Grange et al. [311] showed combined delivery and magnetic resonance imaging (MRI) of doxorubicin-containing liposomes in a Kaposi's sarcoma model in vivo. MRI was exploited not only to track the liposome tissue distribution but also to monitor drug delivery and release. Encapsulation of doxorubicin and MRI contrast agents in temperature-sensitive liposomes allowed noninvasive and dynamic imaging of drug release during hyperthermia application [312]. In these studies, the MRI imaging agents were either ProHance [Gd(HPDO3A)-(H$_2$O)] or manganese sulfate (MnSO$_4$); therefore, no nanoparticles were used. Previously, cationic magnetoliposomes (iron oxide nanoparticle-containing liposomes) were used for gene delivery, since they were able to complex nucleic acids (plasmid DNA), and consequently to allow the isolation of the transfected cells using a magnetic field [313]. In other studies, magnetoliposomes were used to accumulate the vesicles to a desired tissue or to induce hyperthermia in response to a magnetic field. Despite the fact that such liposome-nanoparticle hybrids exhibited therapeutic activity, the magnetic nanoparticles were not used as imaging agents. We can speculate to combine liposomes with nanoparticles with the intention to design liposome-nanoparticle hybrids that could achieve therapeutic and imaging capabilities.

The magnetic (composite) nanoparticles based on superparamagnetic iron oxide nanoparticles (SPIONs) are controlled by three principal forces:

(a) hydrophobic–hydrophilic;
(b) magnetic; and
(c) van der Waals.

SPIONs tend to aggregate to micron size clusters in suspension due to the hydrophobic interactions between the sub-nm-size particles. Micron size clusters further aggregate due to the magnetic dipole–dipole interactions and become magnetized by neighboring clusters. In the presence of an external magnetic field, further magnetization of these clusters can occur increasing their aggregation [314]. In general, nanometer size particles aggregate in suspension due to the attractive van der Waals forces in order to minimize the total surface or interfacial energy. Consequently, such aggregation can hamper the efficacy of SPIONs in drug
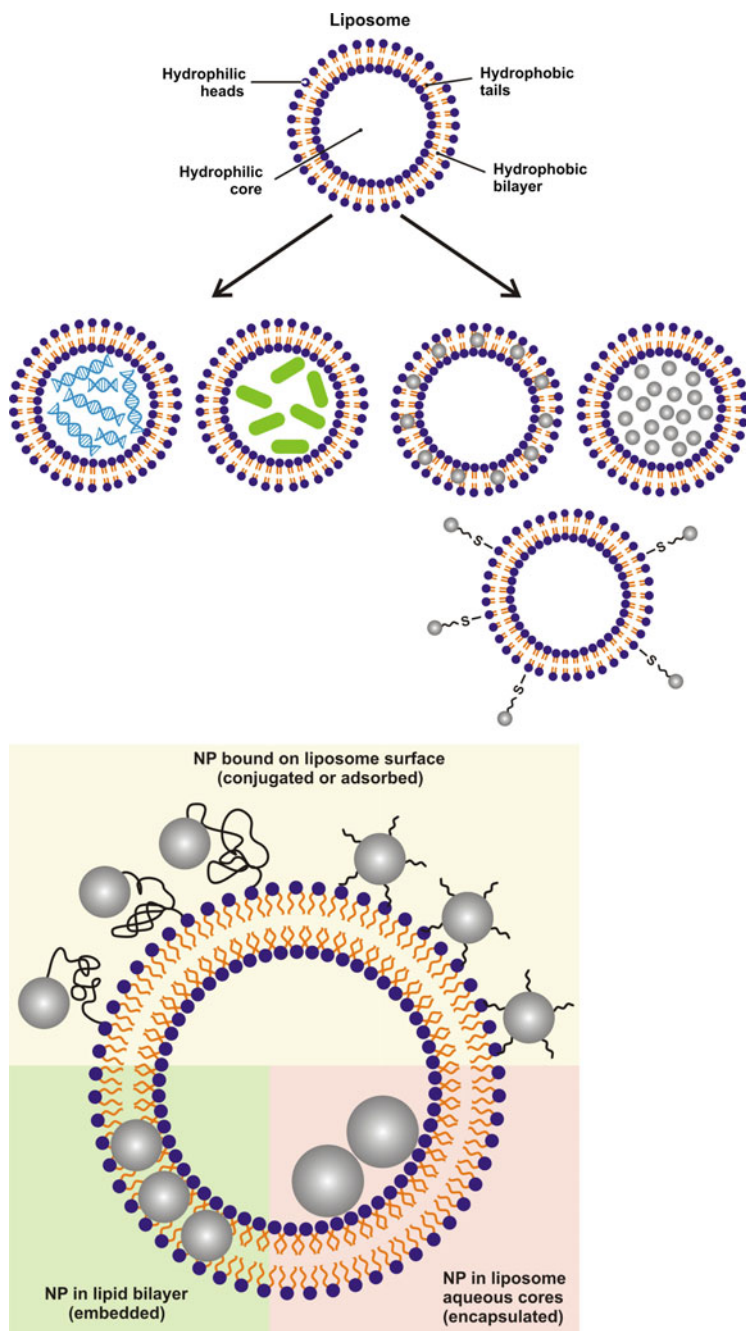
◀**Scheme 3.21**   Schematic diagram of three different approaches to engineer liposome-biomolecules (DNA, proteins, enzymes …) conjugates and liposome-nanoparticle hybrids (*top panel*). Hydrophobic nanoparticles embedded in the lipid bilayer (*left bottom*); hydrophilic nanoparticles encapsulated in the aqueous core (*right bottom*); and nanoparticles chemically conjugated or physically adsorbed/complexed to the liposome surface (*top*) (*bottom panel*) [309]

delivery (less drug loading) due to their low surface area and larger sizes. Hence, the stabilization of SPIONs in suspension by modifying their surface is an important issue in the context of drug delivery.

PEO-modified gold nanomaterials except of self-assembling have also several attractive characteristics for diagnostic applications, including

1. biocompatibility and stability;
2. unique tunable optical properties (LSPR) ; and
3. easy conjugation of biomolecules (i.e., ssDNA) to the surface for tumor specific targeting. More complex shapes with excitation wavelengths of 800–1200 nm could absorb the NIR light, and then be converted to heat. By changing the shape of gold nanoparticles to nanorods, the absorption and scattering wavelength changes from the visible to the (near-infrared) NIR region and their absorption and scattering cross sections also increase. Indeed, the surface plasmon field absorption of gold nanorods is the strongest of all the different shapes of gold and silver nanoparticles [11]. Unlike gold nanospheres with one visible absorption band around 520 nm, gold nanorods showed two surface plasmon absorption bands: a strong long-wavelength band due to the longitudinal oscillation of electrons (above 700 nm) and a weak short-wavelength band around 520 nm due to the transverse electronic oscillation. According to the increase of the rods' aspect ratio, the longitudinal absorption band shifts from the visible to the NIR region. For this reason, gold nanorods can be used as a novel contrast agent for dual molecular imaging using simple dark-field microscopy and selective photothermal therapy using a NIR laser. In UV–Vis spectra, there are two clear surface plasma absorption bands at 520 and 782 nm without irradiation, whereas the decrease of the peak intensity at ca 780 nm and the increase at 520 nm were observed after NIR irradiation, indicating that the shape of some gold nanorods was changed to gold nanospheres. Indeed, SEM images clearly demonstrated that the DNA–gold modified nanorods changed their shapes and sizes after the exposure to NIR irradiation. The transformation of gold nanorods into nanospheres by NIR irradiation could be DNA released from the nanorods. From the result of electrophoresis, free DNA was detected after irradiation treatment, whereas without irradiation the release of DNA was not detected. The release of DNA from nanorods might be due to the breakage of the Au–S bond between the nanorod surface and DNA during the irradiation-induced atomic rearrangement process [315].

Another type of multifunctional nanoparticles is the combination of metallic nanoparticles and magnetic nanoparticles, which likely will lead new applications in biomedicine because metallic nanoparticles hold the intrinsic properties and functions as optical contrast agents and probes. The plasmonic magnetic Fe_3O_4–Au heterodimer structure offers the particles with two distinct surfaces, thus, different kinds of functional molecules can covalently bind to the specific parts of the heterodimers. Together with their own distinct functionalities, Fe_3O_4–Au multifunctional heterodimers can respond to external magnetic fields, show enhanced resonance absorption and scattering, and be able to bind with specific receptors. Using EGFRA-conjugated Fe_3O_4–Au heterodimer nanoparticles, Xu et al. demonstrated their dualfunctional probing property for cell tracking [316]. The A431 cells labeled with Fe_3O_4–Au heterodimer nanoparticles showed strong MR contrast enhancement signal. Because of the strong reflectance, the A431 cells labeled with Fe_3O_4–Au heterodimer nanoparticles can be also visualized by a scanning confocal microscope. Furthermore, under the optical microscope, it is possible to track the movement of labeled A431 cells by an external magnetic field due to the magnetic property of the heterodimer nanoparticles. This type of heterodimer nanoparticles may have the great potential in multimodal biomedical applications, especially for multiplexed probing and multimodality molecular imaging [317, 318].

Gold nanoparticles are more commonly used for hyperthermia than other heavy metals (such as silver or cobalt) due to the unique interaction of gold with light, which results in surface plasmon resonance (SPR). In the presence of oscillating electromagnetic radiations at a particular resonance frequency, free electrons in gold undergo collective coherent oscillations (SPR oscillations) which can decay via heat emission [319, 320]. Changing the size, shape, and refractive index (RI) of the material changes its SPR frequency. Ideally, this frequency is tuned in the NIR region. At NIR wavelengths, the absorption of innate biological fluorochromes and water is low [321], and thus, the light can penetrate deeper into tissues without causing damage to surrounding healthy cells. Hyperthermia, also called photothermal ablation, is a physical treatment for cancer involving the killing of cancer cells in the presence of heat. Hyperthermia leads to apoptotic cell death caused by heating of surrounding tissues or cells to a temperature of 42–46 °C; above 46 °C, photothermal ablation causes undesirable necrosis of the surrounding cells [322]. With no chemical payload to deliver, hyperthermia is less prone to toxic side effects that often accompany chemotherapeutic agents.

To combine imaging and therapy in the case of gold-containing nanoparticles, architectures with iron oxide cores and gold shells have been explored widely. Gold nanoparticles with iron oxide cores, such as magnetite (Fe_2O_4) or maghemite (γ-Fe_2O_4), can be imaged using MRI. The layer of gold surrounding the magnetic iron oxide particles helps to stabilize them from in vivo aggregation and reduces their toxicity. The desired NIR absorption frequency for gold nanoparticles can be achieved by coating them with silica, which has a high dielectric constant and, thus, helps to lower the absorption frequency toward NIR wavelengths [319]. Iron oxide particles impart a high T_2 relaxivity (good negative contrast for MRI) and, in the

presence of a magnetic field, can be localized to the site of interest. This therapeutic targeting strategy is known as magnetic field-directed hyperthermia [323].

As an example of magnetic field-directed hyperthermia, researchers have developed human epidermal growth receptor 2 (HER2)-targeted gold nanoparticles for breast cancer treatment. Kim et al. [324] designed magnetic gold nanoshells (Mag-AuNSs) consisting of a magnetic iron oxide (Fe_2O_4) and silica core surrounded by a 15 nm gold shell. For breast cancer targeting, Mag-AuNS functionalized with an antibody targeting HER-2/neu receptor ($Ab_{HER2/neu}$), a cell surface molecule that is overexpressed on breast cancer cells. SKBR3 breast cancer cells and lung cancer cells (H520 cells, which do not overexpress HER2/neu) were treated with $Ab_{HER2/neu}$–containing Mag-AuNS. Upon subsequent exposure to a femtosecond-long laser (800 nm) pulse, Mag-AuNS-transfected SKBR3 cells exhibited significant cell death. T_2-weighted MR images of transfected SKBR3 cells and H520 cells showed higher image contrast for targeted particles than untransfected cells (Scheme 3.22), with SKBR3 cells exhibiting enhanced contrast relative to H520 cells, as expected.

In a related study, Lim et al. [326] synthesized core@shell-type structures in which 9–11 nm magnetic iron oxide cores were covered with 2–3-nm-hollow gold
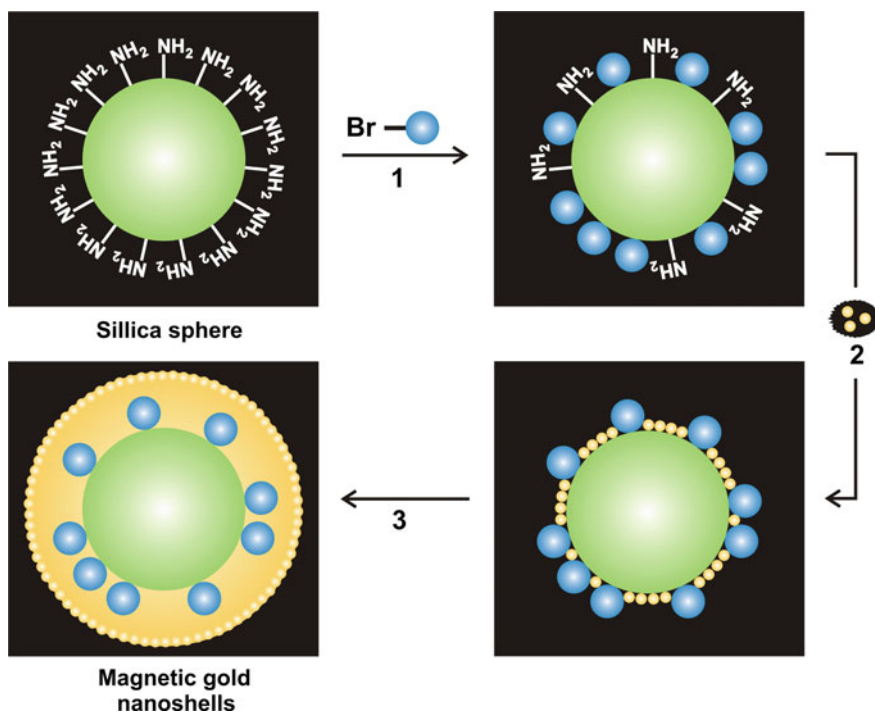
Scheme 3.22 Schematic of synthesis of magnetic gold nanoshells (Mag-AuNSs): *1* BMPA-stabilized magnetic nanoparticles, *2* seed AuNPs, and *3* gold shell growth [324, 325]
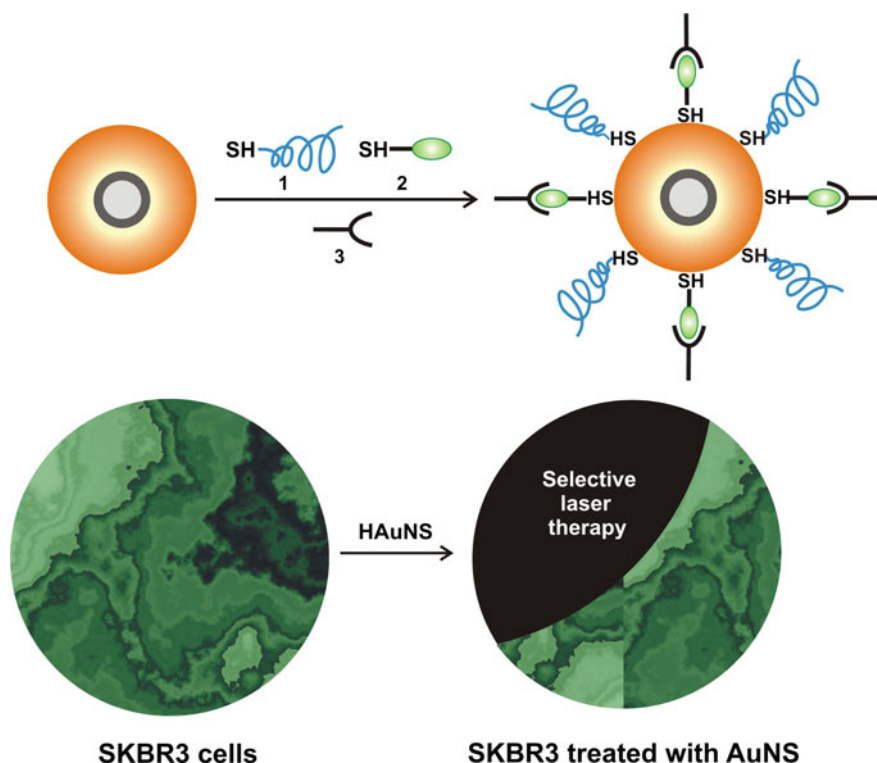
Scheme 3.23 Schematic of the synthesis of hollow gold nanoshells functionalized with iron oxide, poly(ethylene glycol) (PEG, *1*), protein G (*2*), and a HER2-targeting antibody (*3*) (*top panel*). SKBR3 cells incubated with the targeted HAuNS (Fe$_2$O$_3$@Au) and stained with calcein-AM (*green*). Irradiation with an 808 nm laser resulted in a significant decrease in survival of treated cells [326]

nanoshells (HAuNS); the resulting materials (Fe$_3$O$_4$@Au) were surface-functionalized with anti-HER2 monoclonal antibodies (Scheme 3.23, top). The specificity of the antibody attached on the surface of HAuNS (Fe$_2$O$_3$@Au) was tested in SKBR3 (HER2-positive) and MCF-7 (HER2-negative) cancer cells by further labeling these particles with tetramethyl rhodamine isothiocyanate (TRITC); TRITC fluorescence was only seen in SKBR3 cells, implicating HER2 engagement in the uptake of these nanoparticles. Photothermal therapy performed on treated SKBR3 cells with an 808 nm laser resulted in cell death without causing any damage to unexposed cells (Scheme 3.23, bottom).

A novel class of molecules, referred to as nucleic acid ligands (aptamers) , has been developed for noble metal stabilization and therapeutic and diagnostic applications [327]. Aptamers are DNA or RNA oligonucleotides or modified DNA or RNA oligonucleotides that fold by intramolecular interaction into unique conformations with ligand-binding characteristics. Since the DNA-covered gold

nanoparticles are 100- to 10,000-fold smaller than cancer cells, they can easily pass through cell barriers. In addition, they preferentially accumulate at the tumor sites because of hallmarks of tumors such as the fenestrated vasculature and poorly lymphatic drainage, resulting in an enhanced permeability and retention (EPR) effect [12]. In contrast with the conventional nanocarriers, however, the biopolymer (chitosan, DNA …)-based and modified nanoparticles progressively accumulated in the tumor tissues by the EPR effect with considerably low uptake in the liver and spleen [328].

3.4 Conclusion

A large number of variants have been developed, corresponding to various combinations of metal precursors, solvents, reducing agents, stabilizing molecules, complexing agents, and reaction conditions. A reverse micelle synthesis, for example, has been recently demonstrated to be a viable method for producing a wide array of metal nanoparticles over a relatively narrow particle size distribution. Micelle formation allows for a unique encapsulated volume of controllable size through which reactions and subsequent development of metal and metallic compounds can be produced. Thus, by mixing microemulsions containing different reactants, it is possible to perform chemical reactions inside the reverse micelle water pool, using it as a nanoreactor. If this reaction results in a solid compound, nanoparticles are created and their growth is limited by the micelle size. By controlling the experimental parameters such as the concentration of the surfactant, the water content, and reaction temperature, inorganic nanostructures with morphologies of bundles of rods, ellipsoids, spheres, dipyramids, and nanoparticles can be efficiently achieved by the microemulsion approach, respectively. The advantage of the reverse micelle is that it can solubilize both the hydrophobic nanoparticle and polar or nonpolar polymer precursor via their polar micelle interface, and polymerization can be initiated from homogeneous solution. Large amounts of surfactant are required to stabilize the AuNPs, which introduces impurities (a major drawback). Different structures can be formed as such: water–in–oil (w/o) or oil–in–water (o/w) droplets, and bicontinue structure, over a wide range of composition depending on the properties of the surfactant and the oil. The intermicellar interactions, the capping with surfactant, and the reducing agent concentration govern the growth processes. As for the shape, it can be controlled by using nonspherical templates. In this way, elongated noble metal nanocrystals can be obtained when the synthesis takes place in cylindrical reverse micelles or in an interconnected cylinder phase. By combining the strategy of the surfactant-based template with the capping involving salts or specific molecules, it appears that the particle shape can be more efficiently controlled. Nonspherical shapes can also be obtained in spherical reverse micelles. In this case, the synthesis takes place in a large excess (the use reverse micelles in a supersaturated regime) either of reducing agent or of one of the reagents. The results showed that the cetyltrimethylammonium bromide

(CTAB) was the best candidate for the formation of anisotropic nanoparticles such as nanorods, nanowhiskers, nanofibers, or nanocables among all the used surfactants. It was postulated that the CTAB preferentially binds to the {100} faces, along the length of the rods, compared to the end {111} Au faces, due to the size of the CTAB head group, although the hydrocarbon tail of CTAB also plays a role in the growth of gold nanorods via a postulated "zipping" mechanism. Generally, the face with a higher density of surface atoms is blocked by the adsorption of surfactants during the crystal growth of nanocrystals, and the growth along this facet is, therefore, considerably restricted, which means that the nuclei grow in a one- or two-dimensional mode to produce nanorods, nanotubes … or nanoplates. Catanionic surfactants such as lecithin and trichromophoric dye-reverse micelles were also shown to stabilize AuNPs. The microemulsion approach was used to prepare thiol-capped silver particles under simple reaction conditions. Silver colloids have synthesized silver in $C_{12}E_5$/cyclohexane/water microemulsions by using daylight irradiation. An alternative new approach to monodisperse silver nanocubes in water is by a HTAB (n-hexadecyltrimethylammonium bromide)-modified silver mirror reaction at 120 °C. The preparation of silver nanoparticles in reverse micelles of sucrose fatty acid esters by using the conventional injection method was reported. Variations of noble metal nanorods to spheres were initiated by using cyanide as oxidant in the presence of CTAB micelles. Herein, short spheroids with sharp tips dissolve preferentially from the tips, leading to lower aspect ratio nanorods and eventually to spheres. It was shown that the $AuCl_4^-$ ions are quantitatively bounded to CTAB micelles and can be used to vary the particle size and shape. The crystal growth can be manipulated and spatially controlled by CTAB if the active solution species that deposits onto the growing particle surface is adsorbed to the CTAB micelles. When $HAuCl_4$ is added in the presence of CTAB, absorption spectroscopy reveals a gradual blueshift and decrease of the longitudinal surface plasmon (LSP) band, indicating the expected decrease in aspect ratio. The gold nanoparticles are found to exist in several morphologies (spheres, rhombs, triangles, and polygons) with a very narrow size distribution ∼ 12 nm. Gold nanopopcorn synthesis was achieved through a two-step process, using seed-mediated growth in the micellar solution. Laser ablation of solvent-suspended metal powders can be used in for synthesis of gold/silver alloy and core@shell nanoparticles of predetermined composition. Highly spherical nanoparticles with a core comprising multiple gold nanodots and a silica shell ($\{Au@SiO_2\}NPs$) were synthesized via a reverse (water-in-oil) microemulsion-based method. It was found that thermal treatment of the $\{Au@SiO_2\}NPs$ in water without adding any other additives leads to generation of mesopores over the silica shell without any change in the size and number of the gold nanodots. Hence, optimizing the etching reaction time was critical in obtaining highly spherical multi-Au@mesoporous-SiO_2 nanoparticles. Interestingly, when the multi-Au@SiO_2 nanoparticles were stirred in aqueous polyvinylpyrrolidone (PVPo) solution at room temperature, the multiple Au nanodots within the silica matrix were merged together and changed to a single-Au nanoparticle. Stable NMNPs with spherical shape and size of 5 nm were

successfully prepared by combining the soft chemical o/w microemulsion template with physical photoreduction technique.

Among the various polymer shell/metal core structures of particular interest is the encapsulation of gold nanoparticles within functional polymers. Strongly basic media lead to highly dehydrated micelle cores within which the diffusion of gold species is hindered and, as a result, the concentration of AuNPs produced at high pH decreases significantly. These surface-functionalized gold nanoparticles are expected to offer new possibilities in nanomedicine, and particularly in catalysis applications, provided that control over the interaction between the gold catalyst and the substrate is possible through the selection of the coating polymer. Compared with classical surfactant-formed micelles, the copolymer surfactant-formed micelles have several advantages. The formation of a dielectric layer around the AuNPs will also result in a redshift of the SPR band, if the dielectric constant of the layer is larger than that of the medium. The Brust–Schriffin in situ biphasic gold nanoparticle synthesis introduced the use of tetraoctylammonium bromide (TOAB)—a quaternary ammonium ion stabilized by a bromide anion—as a stabilizing agent, and phase-transfer catalyst in the production of colloidal gold from chloroauric acid. When reducing $HAuCl_4$ with sodium borohydride, TOAB stabilizes the precipitating colloidal gold in the aqueous phase. This stabilizing interaction allows the AuNPs to solvate into an organic phase, with TOAB effectively acting as a phase-transfer catalyst. Organoamine-protected gold nanoparticles of variable sizes form by refluxing a solution of tetrachloroauric acid and oleylamine in the organic solvent. The reducing equivalents in the reaction are provided by the amine, which can undergo metal ion-induced oxidation to nitriles. Alkylamines were also used as stabilizers for silver nanoparticles since they have weaker interactions with silver. These weak interactions can potentially be broken up at significantly lower temperatures, thus enabling the "stripped" silver nanoparticles to coalesce to form a continuous conductive layer. The reduction of silver acetate at lower temperatures could be accelerated if an appropriate reducing agent was added. The concentration and chain length of the surfactants (and/or the weak ligands) played a key role in determining the concentration of the nuclei formed in the solution, judged by the final average particle size, a high concentration of ligands or ligands with a bulky tail suppressed the activity of the monomers. This strategy yields nearly monodisperse gold nanocrystals. A new method of producing gold nanoparticles is a surfactant-free synthesis, high variability in the introduction of (functionalized) ligands, and good control over the particle size. It was found that a solution of hydrogen tetrachloroaurate in diethylene glycol dimethyl ether (diglyme) can be reduced by a solution of sodium naphthalenide in diglyme to form gold nanoparticles. In this reaction, no further stabilizing surfactant is necessary, although sodium naphthalenide can be considered a rather harsh reducing agent. The resulting, weakly protected nanoparticles can straightforwardly be stabilized and functionalized by the addition of a variety of ligands. The introduction of strong capping agents during nanoparticle synthesis has the effect of stopping the growth of the NPs, whereas weakly associated ligands allow for continued growth. As a

result, the presence of the capping agent whether strongly or weakly binding is essential during the nanoparticle synthesis in order to control the nanoparticle size and shape and to prevent aggregation. However, use of strong capping agents makes further surface modification with alternative ligands challenging. The versatility and usefulness of soft-ligand-coated AuNPs are further demonstrated by replacing the soft ligands with alkylthiols, which results in 2D assembly of the AuNPs. Control of the size and assembly of the NPs is important because these two properties modulate the near-field optical coupling and LSPR properties of the NPs. Soft-ligand-stabilized nanoparticles can be used as precursors to obtain NPs with different surface chemistry by replacing the soft ligands with other desired ligands. The IL used stabilizes the nanoparticles noncovalently via electrostatic interactions. A proposed model was based on differential anion stabilization of metal nanoparticles in the following order: polyoxometallate > citrate > polyacrylate $\sim$ chloride. The anion should be at the surface of the metal, because the stabilization of the nanoparticles correlates with the sterics of the anion. Spherical gold nanoparticles, oblate particles, gold nanorods of varying aspect ratios, and sharp-edged nanostructures were obtained by simply varying solution flow rates in the two reaction stages. Spherical gold exhibits a sharp absorption peak at the characteristic wavelength of 520 nm, while oblate/spheroidal particles exhibit two plasmon resonances at 520 nm and $\sim$660 nm. Among all the in situ syntheses of gold nanoparticles by reduction of $HAuCl_4$, citrate-stabilized AuNPs have been regarded as the most popular ones for a long time. The citrate reduction method is well known for its simple procedure, yielding stable and reproducible gold nanoparticles of narrow size distribution. Other improvements of the Turkevich method involved the control of the reaction temperature, the introduction of fluorescent light irradiation, and the use of high-power ultrasound.

Some of previous nanoparticle synthesis and growth studies were performed in aqueous phase using the strong reducing agent sodium borohydride. In these studies, the reduction and nucleation processes take place very rapidly, resulting in almost immediate aggregation and coalescence. Moreover, sodium borohydride-based reduction/formation of NMNPs, aggregative growth of nanoparticles is the most common formation pathway, whereas some researches observed predominantly Ostwald-ripening growth.

Solutes-mediated synthesis to produce NMNPs by in situ and ex situ surface modification of the NPs without incorporating additional stabilizing agents in the reaction mixture allows good control over the synthetic process and the surface chemistry of the NPs. Experimental evidence shows that the soft ligands can be displaced by stronger ligands. It was demonstrated that addition of some capping ligands to replace the soft ligands restricts NP growth and narrows the size dispersion of the NPs. The bipyridyl-functionalized AuNPs can have a wide range of applications including nanoscale electronics, solar energy conversion, and redox indicators. The addition of thiols also led to AuNPs with a narrow size dispersion by controlling the growth process. The thiolated ligands-stabilized AuNPs produced 2D assemblies with regular interparticle (edge-to-edge) spacing on TEM grids. UV–Vis spectroscopy analysis indicated that the alkylthiolate ligands may also

influence AuNP interactions in solution. Evidence indicates a possible correlation of a redshift of the LSPR λ_{max} with near-field plasmonic coupling of AuNPs in close proximity in solution.

CT-pluronic F68 was used to synthesize a new doxorubicin–pluronic F68 conjugate (DOX-P). Its related characterization and cell cytotoxicity were investigated. The structures of CT-pluronic F68 and DOX-P were confirmed by FTIR and 1H-NMR spectra. The T_m and T_c of DOX-P were lower than pluronic F68 resulted from the connection of DOX to pluronic F68.

DOX-P micelles showed tightly packed nanospheres with an average size of about 20 nm. Drug release profile showed that the DOX-P conjugate maintained a sustained DOX release. From cell experiment in vitro, DOX-P micelles could circumvent the DOX resistance of K562/AO2 cells. With advantages of EPR effect and reducing tumor resistance, DOX-P micelles might develop as new tumor targeted delivery system for chemotherapy.

A novel class of (bio)molecules, referred to as nucleic acid, protein, targeting antibody, and enzyme ligands, has been developed for noble metal stabilization and therapeutic and diagnostic applications. DNA aptamers, for example, fold by intramolecular interaction into unique conformations with ligand-binding characteristics. Since the DNA-covered gold nanoparticles are 100- to 10,000-fold smaller than cancer cells, they can easily pass through cell barriers. In addition, they preferentially accumulate at the tumor sites because of hallmarks of tumors such as the fenestrated vasculature and poorly lymphatic drainage, resulting in an enhanced permeability and retention (EPR) effect. In contrast with the conventional nanocarriers, however, the biopolymer (chitosan, DNA, etc.)-based and modified NMNPs progressively accumulated in the tumor tissues by the EPR effect with considerably low uptake in the liver and spleen.

Glossary

Chemotherapy is a category of cancer treatment that uses one or more anticancer drugs (chemotherapeutic agents) as part of a standardized chemotherapy regimen. Chemotherapy may be given with a curative intent (which almost always involves combinations of drugs), or it may aim to prolong life or to reduce symptoms (palliative chemotherapy). Chemotherapy is one of the major categories of medical oncology (the medical discipline specifically devoted to pharmacotherapy for cancer).

Enhanced permeability and retention (EPR)	effect is the property by which molecules of certain sizes (typically liposomes, nanoparticles, and macromolecular drugs) tend to accumulate in tumor tissue much more than they do in normal tissues.
Hyperthermia	is elevated body temperature due to failed thermoregulation that occurs when a body produces or absorbs more heat than it dissipates. Extreme temperature elevation then becomes a medical emergency requiring immediate treatment to prevent disability or death.
Liposome	is a spherical vesicle having at least one lipid bilayer. The liposome can be used as a vehicle for administration of nutrients and pharmaceutical drugs. Liposomes can be prepared by disrupting biological membranes (such as by sonication).
Multiple drug resistance (MDR),	multidrug resistance, or multiresistance is antimicrobial resistance shown by a species of microorganism to multiple antimicrobial drugs.
Receptor tyrosine-protein kinase erbB-2	also known as CD340 (cluster of differentiation 340), proto-oncogene Neu, Erbb2 (rodent), or ERBB2 (human). It is a protein that in humans is encoded by the ERBB2 gene, and it is also frequently called HER2 (from human epidermal growth factor receptor 2) or HER2/neu. Amplification or overexpression of this oncogene has been shown to play an important role in the development and progression of certain aggressive types of breast cancer. In recent years, the protein has become an important biomarker and target of therapy for approximately 30% of breast cancer patients.

References

1. Capek I (2006) Nanocomposite structures and dispersions. In: D. Mobius, R. Muller (eds). Elsevier, London
2. Misra RDK, Gubbala S, Kale A, Egelhoff WF (2004) A comparison of the magnetic characteristics of nanocrystalline nickel, zinc, and manganese ferrites synthesized by reverse micelle technique. J Mater Sci Eng B 111:164–174
3. Sanchez-Dominguez M, Pemartin K, Boutonnet M (2012) Preparation of inorganic nanoparticles in oil-in-water microemulsions: a soft and versatile approach. Curr Opin Colloid Interface Sci 17:297–305

4. Boutonnet M, Kizling J, Stenius P (1982) The preparation of monodisperse colloidal metal particles from microemulsions. Colloids Surf 5:209–225

5. Thikett K, Brice H, Myakonkaya O, Eastoe J, Rogers SE, Heenan RK, Grillo I (2010) Microemulsion-based organogels containing inorganic nanoparticles. Soft Matter 6:1291–1296

6. Boutonnet M, Lögdberg S, Svensson E (2008) Recent developments in the application of nanoparticles prepared from w/o microemulsions in heterogeneous catalysis. Curr Opin Colloid Interface Sci 13:270–286

7. Liu S, Weaver JVM, Save M, Armes SP (2002) Synthesis of pH-responsive shell cross-linked micelles and their use as nanoreactors for the preparation of gold nanoparticles. Langmuir 18:8350–8357

8. Tatarchuk V, Sergievskaya A, Druzhinina I, Zaikovsky V (2011) Kinetics and mechanism of the growth of gold nanoparticles by reduction of tetrachloroauric acid by hydrazine in Triton N-42 reverse micelles. J Nanopart Res 13:4997–5007

9. Chen S, Sommers JM (2001) Alkanethiolate-protected copper nanoparticles: spectroscopy, electrochemistry, and solid-state morphological evolution. J Phys Chem B 105:8816–8820

10. Al–Jamal WT, Kostarelos K (2007) Liposome–nanoparticle hybrids for multimodal diagnostic and therapeutic applications. Nanomedicine 2:85–98

11. Hao E, Schatz GC, Hupp JT (2004) Synthesis and optical properties of anisotropic metal nanoparticles. J Fluoresc 14:331–341

12. Maeda H, Wu J, Sawa T, Matsumura Y, Hori K (2000) Tumor vascular permeability and the EPR effect in macromolecular therapeutics: a review. J Control Release 65:271–284

13. Uskokovic V, Drofenik M (2005) Synthesis of materials within reverse micelles. Surf Rev Lett 12:239–277

14. Murphy CJ, Sau TK, Gole A, Orendorff CJ (2005) Surfactant-directed synthesis and optical properties of one-dimensional plasmonic metallic nanostructures. MRS Bull 30:349–355

15. Pileni MP (1993) Reverse micelles: a microreactors. J Phys Chem 97:6961–6973

16. Wu M, Chen D, Huang T (2001) Synthesis of Au/Pd bimetallic nanoparticles in reverse micelles. Langmuir 17:3877–3883

17. McLeod MC, McHenry RS, Beckman EJ, Roberts CB (2003) Synthesis and stabilization of silver metallic nanoparticles and premetallic intermediates in perfluoropolyether/CO_2 reverse micelle systems. J Phys Chem B 107:2693–2700

18. Jain TK, Cassin G, Badiali JP, Pileni MP (1996) Relation between exchange process and structure of AOT reverse micellar system. Langmuir 12:2408–2411

19. Capek I (2004) Preparation of metal nanoparticles in water-in-oil (w/o) microemulsions. Adv Colloid Interface Sci 110:49–74

20. Aliotta F, Arcoleo V, Buccoleri S, La Manna G, Turco Liveri V (1995) Calorimetric investigation on the formation of gold nanoparticles in water/AOT/*n*-heptane microemulsions. Thermochim Acta 265:15–23

21. Chiang CL (2000) Controlled growth of gold nanoparticles in aerosol-OT/sorbitan monooleate/isooctane mixed reverse micelles. J Colloid Interface Sci 230:60–66

22. Herrera AP, Resto O, Briano JG, Rinaldi C (2005) Synthesis and agglomeration of gold nanoparticles in reverse micelles. Nanotechnology 16:S618–S625

23. Calandra P, Giordano C, Longo A, Turco Liveri V (2006) Physicochemical investigation of surfactant-coated gold nanoparticles synthesized in the confined space of dry reversed micelles. Mater Chem Phys 98:494–499

24. Abecassis B, Testard F, Zemb T (2009) Gold nanoparticle synthesis in worm-like catanionic micelles: microstructure conservation and temperature induced recovery. Soft Matter 5:974–978

25. Takahashi M, Ohno S, Fujita N, Sengoku T, Yoda H (2011) Spontaneous formation of dye-functionalized gold nanoparticles using reverse micellar systems. J Colloid Interf Sci 356:536–542

26. Zhao P, Li N, Astruc D (2013) State of the art in gold nanoparticle synthesis. Coord Chem Rev 257:638–665

27. Hollamby MJ, Eastoe J, Chemelli A, Glatter O, Rogers S, Heenan RK, Grillo I (2010) Separation and purification of nanoparticles in a single step. Langmuir 26:6989–6994

28. Luisi PL (1985) Enzymes hosted in reverse micelles in hydrocarbon solution. Angew Chem 24:439–450

29. Kitahara A, Tamura T, Matsumura S (1979) Effect of water on stability of carbon black dispersed in nonaqueous aerosol OT solutions. Chem Lett 8:1127–1128

30. Moffat BA, Reddy GR, McConville P, Hall DE, Chenevert TL, Kopelman RR, Philbert M, Weissleder R, Rehemtulla A, Ross BD (2003) A novel polyacrylamide magnetic nanoparticle contrast agent for molecular imaging using MRI. Mol Imag 2:324–332

31. Mihaly M, Fleancu MC, Olteanu NL, Bojin D, Meghea A, Enachescu M (2012) Synthesis of gold nanoparticles by microemulsion assisted photoreduction method. C R Chim 15:1012–1021

32. Malik MA, Wani MY, Hashim MA (2012) Microemulsion method: a novel route to synthesize organic and inorganic nanomaterials. Arab J Chem 5:397–417

33. Eastoe J, Hollamby MJ, Hudson L (2006) Recent advances in nanoparticle synthesis with reversed micelles. Adv Colloid Interface Sci 128–130:5

34. Hentze HP, Kaler EW (2003) Polymerization of and within self-organized media. Curr Opin Colloid Interface Sci 8:164–178

35. Lawrence MJ, Rees GD (2000) Microemulsion-based media as novel drug delivery systems. Adv Drug Deliv Rev 45:89–121

36. Ge JP, Chen W, Liu LP, Li YD (2006) Formation of disperse nanoparticles at the oil/water interface in normal microemulsions. Chem Eur J 12:6552–6558

37. Johnston KP, Harrison KL, Clarke MJ, Howdle SM, Heitz MP, Bright FV, Carlier C, Randolph TW (1996) Water-in-carbon dioxide microemulsions: an environment for hydrophiles including proteins. Science 271:624–526

38. Hoefling TA, Beitle RR, Enick RM, Beckman EJ (1993) Design and synthesis of highly CO_2-soluble surfactants and chelating agents. Fluid Phase Equilib 83:203–212

39. Clarke MJ, Harrison KL, Johnston KP, Howdle SM (1997) Water in supercritical carbon dioxide microemulsions: spectroscopic investigation of a new environment for aqueous inorganic chemistry. J Am Chem Soc 119:6399–6406

40. Shah PS, Hanrath T, Johnston KP, Korgel BA (2004) Nanocrystal and nanowire synthesis and dispersibility in supercritical fluids. J Phys Chem B 108:9574–9587

41. Jin R, Cao YC, Hao E, Métraux GS, Schatz GZ, Mirkin CA (2003) Controlling anisotropic nanoparticle growth through plasmon excitation. Nature 425:487–490

42. El-Sayed MA (2001) Some interesting properties of metals confined in time and nanometer space of different shapes. Acc Chem Res 34:257–264

43. Wang L, Luo J, Shan S, Crew E, Yin J, Zhong CJ, Wallek B, Wong SS (2011) Bacterial inactivation using silver-coated magnetic nanoparticles as functional antimicrobial agents. Anal Chem 83:8688–8695

44. Tang S, Vongehr S, Meng X (2010) Carbon spheres with controllable silver nanoparticle doping. J Phys Chem C 114:977–982

45. Zhang W, Qiao X, Chen J (2007) Synthesis of nanosilver colloidal particles in water/oil microemulsion. Colloids Surf A: Physicochem Eng Aspects 299:22–28

46. Zhang W, Qiao X, Chen J, Wang HS (2006) Preparation of silver nanoparticles in water-in-oil AOT reverse micelles. J Colloid Interface Sci 302:370–373

47. He BL, Tan JJ, Kong YL, Liu HF (2004) Synthesis of size controlled Ag nanoparticles. J Mol Catal A: Chem 221:121–126

48. Manna A, Kulkarni BD, Bandyopadhyay K, Vijayamohanan K (1997) Synthesis and characterization of hydrophobic, approtically-dispersible, silver nanoparticles in winsor II type microemulsions. Chem Mater 9:3032–3036

49. Andersson M, Pedersen JS, Palmqvist AEC (2005) Silver nanoparticle formation in microemulsions acting both as template and reducing agent. Langmuir 21:11387–11396

50. Petit C, Lixon P, Pileni MP (1993) In situ synthesis of silver nanocluster in AOT reverse micelles. J Phys Chem 97:12974–12983

51. Monnoyer P, Fonseca A, Nagy JB (1995) Preparation of colloidal AgBr particles from microemulsions. Colloids Surf A 100:233–243

52. Liz-Marzan LM, Lado-Touriño I (1996) Reduction and stabilization of silver nanoparticles in ethanol by nonionic surfactants. Langmuir 12:3585–3589

53. Barnickel P, Wokaun A, Sager W, Eiche HF (1992) Size tailoring of silver colloids by reduction in WO microemulsions. J Colloid Interface Sci 148:80–90

54. Chaudhari VR, Haram SK, Kulshreshtha SK, Bellare JR, Hassan PA (2007) Micelle assisted morphological evolution of silver nanoparticles. Colloids Surf A: Physicochem Eng Aspects 301:475–480

55. Pileni MP, Gulik-Krzywick T, Tanori J, Filankembo A, Dedieu JC (1998) Template design of microreactors with colloidal assemblies: control the growth of copper metal rods. Langmuir 14:7359–7363

56. Yu D, Yam VWW (2004) Controlled synthesis of monodisperse silver nanocubes in water. J Am Chem Soc 126:13200–13201

57. Yu D, Yam VWW (2005) Hydrothermal-induced assembly of colloidal silver spheres into various nanoparticles on the basis of HTAB-modified silver mirror reaction. J Phys Chem B 109:5497–5503

58. Murray CB, Kagan CR, Bawendi MG (2000) Synthesis and characterization of monodisperse nanocrystals and close-packed nanocrystal assemblies. Annu Rev Mater Sci 30:545–610

59. Collier CP, Vossmeyer T, Heath JR (1998) Nanocrystal superlattices. Annu ReV Phys Chem 49:371–404

60. Viau G, Piquemal JY, Esparrica M, Ung G, Chakroune N, Warmont F, Fiévet F (2003) Formation of assembled silver nanowires by reduction of silver thiolate in polyol/toluene medium. Chem Commun 2216–2217

61. Lindman B, Wennerström H (1980) Miceles amphiphile aggregation in aqueous solution. Top Curr Chem 87:1–87

62. Korgel BA, Fitzmaurice D (1998) Self-assembly of silver nanocrystals into two-dimensional nanowire arrays. Adv Mater 10:661–665

63. Jin RC, Egusa S, Scherer NF (2004) Thermally-induced formation of atomic Au clusters and conversion into nanocubes. J Am Chem Soc 126:9900–9901

64. Noritomi H, Igari N, Kagitani K, Umezawa Y, Muratsubaki Y, Kato S (2010) Synthesis and size control of silver nanoparticles using reverse micelles of sucrose fatty acid esters. Colloid Polym Sci 288:887–891

65. Otomo N (2003) Self-organized structures of food emulsifiers and their applications. Jpn J Food Eng 4:1–9

66. Noritomi H, Umezawa Y, Miyagawa S, Kato S (2011) Preparation of highly concentrated silver nanoparticles in reverse micelles of sucrose fatty acid esters through solid-liquid extraction method. Adv Chem Eng Sci 1:299–304

67. Henglein A (1993) Physicochemical properties of small metal particles in solution: "microelectrode" reactions, chemisorption, composite metal particles, and the atom-to-metal transition. J Phys Chem 97:5457–5471

68. Noritomi H, Ito S, Kojima N, Kato S, Nagahama K (2006) Forward and backward extractions of cytochrome c using reverse micellar system of sucrose fatty acid ester. Colloid Polym Sci 284:604–610

69. Bagwe RP, Khilar KC (2000) Effects of intermicellar exchange rate on the formation of silver nanoparticles in reverse microemulsions of AOT. Langmuir 16:905–910

70. Taleb A, Petit C, Pileni MP (1997) Synthesis of highly monodisperse silver nanoparticles from AOT reverse micelles: a way to 2D and 3D self-organization. Chem Mater 9:950–959

71. Mitchell DJ, Ninham BW (1981) Micelles, vesicles, and microemulsions. J Chem Soc, Faraday Trans 2: Mol Chem Phys 77:601–629
72. Sau TK, Murphy CJ (2004) Room temperature, high-yield synthesis of multiple shapes of gold nanoparticles in aqueous solution. J Am Chem Soc 126:8648–8649
73. Sun YG, Xia YN (2002) Shape-controlled synthesis of gold and silver nanoparticles. Science 298:2176–2179
74. Wu Q, Cao H, Luan Q, Zhang J, Wang Z, Warner JH, Watt AAR (2008) Biomolecule-assisted synthesis of water-soluble silver nanoparticles and their biomedical applications. Inorg Chem 47:5882–5888
75. Graf P, Mantion A, Foelske A, Shkilnyy A, Masic A, Thunemann AE, Taubert A (2009) Peptide-coated silver nanoparticles: synthesis, surface chemistry, and pH-triggered, reversible assembly into particle assemblies. Chem-Eur J 15:5831–5844
76. Murphy CJ, Jana NR (2002) Controlling the aspect ratio of inorganic nanorods and nanowires. Adv Mater 14:80–82
77. Jana NR, Peng XG (2003) Single-phase and gram-scale routes toward nearly monodisperse Au and other noble metal nanocrystals. J Am Chem Soc 125:14280–14281
78. Roucoux A, Schultz J, Patin H (2002) Reduced transition metal colloids: a novel family of reusable catalysts? Chem Rev 102:3757–3778
79. Jana NR (2004) Shape effect in nanoparticle self-assembly. Angew Chem 116:1562–1566
80. Jana NR, Pal T (2001) Acid-base equilibria in aqueous micellar medium: a comprehensive review. J Surf Sci Technol 17:191–212
81. Toernblom M, Henriksson U (1997) Effect of solubilization of aliphatic hydrocarbons on size and shape of rodlike C16TABr micelles studied by 2H NMR relaxation. J Phys Chem B 101:6028–6035
82. Lin Z, Cai JJ, Scriven LE, Davis HT (1994) Spherical-to-wormlike micelle transition in CTAB solutions. J Phys Chem 98:5984–5993
83. Fu H, Xiao D, Yao J, Yang G (2003) You have full text access to this content Nanofibers of 1,3-Diphenyl-2-pyrazoline induced by cetyltrimethylammonium bromide micelles. Angew Chem 115:2989–2992
84. Jana NR (2005) Gram-scale synthesis of soluble, near-monodisperse gold nanorods and other anisotropic nanoparticles. Small 1:875–882
85. Fu H, Xiao D, Yao J, Yang G (2003) Nanofibers of 1,3-diphenyl-2-pyrazoline induced by cetyltrimethylammonium Bromide micelles. Angew Chem Int Ed 42:2883–2886
86. Jana NR, Gearheart L, Obare SO, Murphy CJ (2002) Anisotropic chemical reactivity of gold spheroids and nanorods. Langmuir 18:922–927
87. Rodriguez-Fernandez J, Perez-Juste J, Mulvaney P, Liz-Marzan LM (2005) Spatially-directed oxidation of gold nanoparticles by Au(III)-CTAB complexes. J Phys Chem B 109:14257–14261
88. Link S, El-Sayed MA (1999) Spectral properties and relaxation dynamics of surface plasmon electronic oscillations in gold and silver nanodots and nanorods. J Phys Chem B 103:8410–8426
89. Esumi K, Matsuhisa K, Torigoe K (1995) Preparation of rodlike gold particles by UV irradiation using cationic micelles as a template. Langmuir 11:3285–3287
90. Zayats M, Baron R, Popov I, Willner I (2005) Biocatalytic growth of Au nanoparticles: from mechanistic aspects to biosensors design. Nano Lett 5:21–25
91. Xiao Y, Pavlov V, Levine S, Niazov T, Markovitch G, Willner I (2004) Catalytic growth of Au nanoparticles by NAD(P)H cofactors: optical sensors for NADP(+)-dependent biocatalyzed transformations. Angew Chem Int Ed 43:4519–4522
92. Marks LD (1994) Experimental studies of small particle structures. Rep Prog Phys 57:603–649
93. Wang ZL, Mohamed MB, Link S, El-Sayed MA (1999) Crystallographic facets and shapes of gold nanorods of different aspect ratios. Surf Sci 440:809–814

94. Doron A, Katz E, Willner I (1995) Organization of Au colloids as monolayer films onto ITO glass surfaces: application of the metal colloid films as base interfaces to construct redox-active monolayers. Langmuir 11:1313–1317

95. Lu W, Singh AK, Khan SA, Senapati D, Yu H, Ray PC (2010) Gold nano-popcorn-based targeted diagnosis, nanotherapy treatment, and in situ monitoring of photothermal therapy response of prostate cancer cells using surface-enhanced Raman spectroscopy. J Am Chem Soc 132:18103–18114

96. Orendorff CJ, Murphy CJ (2006) Quantitation of metal content in the silver-assisted growth of gold nanorods. J Phys Chem B 110:3990–3994

97. Lipgens S, Schubel D, Schlicht L, Spilgies JH, Ilgenfritz G (1998) Percolation in nonionic water-in-oil—microemulsion systems: a small angle neutron scattering study. Langmuir 14:1041–1049

98. Jana NR, Patra PK, Saha A, Basiruddin SK, Pradhan N (2009) Imidazole based biocompatible polymer coating in deriving <25 nm functional nanoparticle probe for cellular imaging and detection. J Phys Chem C 113:21484–21492

99. Olteanu NL, Meghea A, Enachescu M, Mihaly M (2013) Tunning gold nanoparticles size and surface charge by oil-in-water microemulsion template. Dig J Nanomaterials Biostructures 8:1687–1697

100. Long NN, Vu LV, Kiem CD, Doanh SC, Nguyet CT, Hang PT, Thien ND, Quynh LM (2009) Synthesis and optical properties of colloidal gold nanoparticles. J Phys: Conf Series 187:1

101. Yang S, Wang Y, Wang Q, Zhang R, Ding B (2005) UV irradiation induced formation of Au nanoparticles at room temperature: the case of pH values. Colloid Surf A 301:174–183

102. Zhou J, Ralston J, Sedev R, Beatie DA (2009) Functionalized gold nanoparticles: synthesis, structure and colloid stability. J Coll Intef Sci 331:251–262

103. Chen G, Takezawa M, Kawazoe N, Tateishi T (2008) Preparation of cationic gold nanoparticles for gene delivery. Open Biotech J 2:152–156

104. Yun JV, Li B, Cao R (2010) Positively-charged gold nanoparticles as peroxidiase mimic and their application in hydrogen peroxide and glucose detection. Chem Commun 46:8017–8019

105. Liao YH, Chang YJ, Chen YR (2012) Negatively charged gold nanoparticles inhibit Alzheimer's amyloid-β fibrillization, induce fibril dissociation, and mitigate neurotoxicity. Small 8:3631–3639

106. DeLong RK, Reynolds CM, Malcom Y, Schaeffer A, Severs T, Wanekaya A (2010) Functionalized gold nanoparticles for the binding, stabilization, and delivery of therapeutic DNA, RNA, and other biological macromolecules. Nanotechnol Sci Appl 3:53–63

107. Ahmed M, Deng Z (2009) Study of transfection efficiencies of cationic glyconanoparticles of different sizes in human cell line. ACS Appl Mater Interf 1:1980–1987

108. Gong J (2012) Structure and surface chemistry of gold-based model catalysts. Chem Rev 112:2987–3054

109. Önal Y, Schimpf S, Claus P (2004) Structure sensitivity and kinetics of d-glucose oxidation to d-gluconic acid over carbon-supported gold catalysts. J Catal 223:122–133

110. Bond GC, Louis C, Thompson DT (eds) (2006) Catalysis by gold. Imperial College Press, London

111. Zhang Q, Lee I, Joo JB, Zaera F, Yin Y (2013) Core-shell nanostructured catalysts. Acc Chem Res 46:1816–1824

112. Zeng HC (2013) Integrated nanocatalysts. Acc Chem Res 46:226–235

113. Cho SJ, Kauzlarich SM, Olamit J, Liu K, Grandjean F, Rebbouh L, Long GJ (2004) Characterization and magnetic properties of core/shell structured Fe/Au nanoparticles. J Appl Phys 95:6804–6806

114. Cho SJ, Idrobo JC, Olamit J, Liu K, Browning ND, Kauzlarich SM (2005) Growth mechanisms and oxidation resistance of gold-coated iron nanoparticles. Chem Mater 17:3181–3186

115. Zhang J, Worley J, Denommee S, Kingston C, Jakubek ZJ, Deslandes Y, Post M, Simard B (2003) Synthesis of metal alloy nanoparticles in solution by laser irradiation of a metal powder suspension. J Phys Chem B 107:6920–6923

116. Zhang J, Post M, Veres T, Jakubek ZJ, Guan J, Wang D, Normandin F, Deslandes Y, Simard B (2006) Laser-assisted synthesis of superparamagnetic Fe@Au core-shell nanoparticles. J Phys Chem B 110:7122–7128

117. Lin XM, Sorensen CM, Klabunde KJ, Hajupanayis GC (1999) Control of cobalt nanoparticle size by the germ growth method in inverse micelle system: size dependent magnetic properties. J Mater Res 14:1542–1547

118. Wilcoxon JP, Provencio PP (2004) Heterogeneous growth of metal clusters from solutions of seed nanoparticles. J Am Chem Soc 126:6402–6408

119. Wilcoxon JP, Provencio P (2003) Etching and aging effects in nanosize Au clusters investigated using high-resolution size-exclusion chromatography. J Phys Chem B 107:12949–12957

120. Jana NR, Gearheart L, Murphy CJ (2001) Seeding growth for size control of 5–40 nm diameter gold nanoparticles. Langmuir 17:6782–6786

121. Zheng N, Fan J, Stucky GD (2006) One-step one-phase synthesis of monodisperse noble-metallic nanoparticles and their colloidal crystals. J Am Chem Soc 128:6550–6551

122. Ayyappan S, Srinivasa GR, Subbanna GN, Rao CNR (1997) Nanoparticles of Ag, Au, Pd, and Cu produced by alcohol reduction of the salts. J Mater Res 12:398–401

123. Longenberger L, Mills G (1995) Formation of metal particles in aqueous solutions by reactions of metal complexes with polymers. J Phys Chem 99:475–478

124. Scott RWJ, Ye H, Henriquez RR, Crooks RM (2003) Synthesis, characterization, and stability of dendrimer-encapsulated palladium nanoparticles. Chem Mater 15:3873–3878

125. Pak J, Yoo H (2013) Facile synthesis of spherical nanoparticles with a silica shell and multiple Au nanodots as the core. J Mater Chem A 1:5408–5413

126. Shenhar R, Norsten TB, Rotello VM (2005) Polymer-mediated nanoparticle assembly: structural control and applications. Adv Mater 17:657–669

127. Fournier RO, Rowe JJ (1977) The solubility of amorphousilica in water at high temperatures and high pressure. Am Mineral 62:1052–1056

128. Wong YJ, Zhu L, Teo WS, Tan YW, Yang Y, Wang C, Chen H (2011) Revisiting the Stöber method: inhomogeneity in silica shells. J Am Chem Soc 113:11422–11425

129. Pak J, Yoo H (2014) Synthesis and catalytic performance of multiple gold nanodots core-mesoporous silica shell nanoparticles. Microporous Mesoporous Mater 185:107–112

130. Park JC, Song H (2011) Metal@Silica yolk-shell nanostructures as versatile bifunctional nanocatalysts. Nano Res 4:33–49

131. Hu Y, Zhang Q, Goebl J, Zhang T, Yin Y (2010) Control over the permeation of silica nanoshells by surface-protected etching with water. Phys Chem Chem Phys 12:11836–11842

132. Zhang Q, Lee I, Ge J, Zaera F, Yin Y (2010) Surface-protected etching of mesoporous oxide shells for the stabilization of metal nanocatalysts. Adv Funct Mater 20:2201–2214

133. Yu Q, Wang P, Hu S, Hui J, Zhuang J, Wang X (2011) Hydrothermal synthesis of hollow silica spheres under acidic conditions. Langmuir 27:7185–7191

134. Aslan K, Perez-Luna VH (2002) Surface modification of colloidal gold by chemisorption of alkanethiols in the presence of a nonionic surfactant. Langmuir 18:6059–6065

135. Sistach S, Rahme K, Perignon N, Marty JD, Viguerie NLD, Gauffre F, Mingotaud C (2008) Bolaamphiphile surfactants as nanoparticle stabilizers: application to reversible aggregation of gold nanoparticles. Chem Mater 20:1221–1223

136. Wuelfing WP, Gross SM, Miles DT, Murray RW (1998) Nanometer gold clusters protected by surface-bound monolayers of thiolated poly(ethylene glycol) polymer electrolyte. J Am Chem Soc 120:12696–12697

137. Schneider G, Decher G (2008) Functional core/shell nanoparticles via layer-by-layer assembly Investigation of the experimental parameters for controlling particle aggregation and for enhancing dispersion stability. Langmuir 24:1778–1789

138. Quaroni L, Chumanov G (1999) Preparation of polymer-coated functionalized silver nanoparticles. J Am Chem Soc 121:10642–10643

139. Raula J, Shan J, Nuopponen M, Niskanen A, Jiang H, Kauppinen EI, Tenhu H (2003) Synthesis of gold nanoparticles grafted with a thermoresponsive polymer by surface-induced reversible-additionfragmentation chain-transfer polymerization. Langmuir 19:3499–3504

140. Ohno K, Koh K, Tsujii Y, Fukuda T (2002) Synthesis of gold nanoparticles coated with well-defined, high-density polymer brushes by surface-initiated living radical polymerization. Macromolecules 35:8989–8993

141. Phillips MA, Gran ML, Peppas NA (2010) Targeted nanodelivery of drugs and diagnostics. Nano Today 5:143–159

142. Daniel MC, Astruc D (2004) Gold nanoparticles: assembly, supramolecular chemistry, quantum-size-related properties, and applications toward biology, catalysis, and nanotechnology. Chem Rev 104:293–346

143. Liz-Marzán LM (2006) Tailoring surface plasmons through the morphology and assembly of metal nanoparticles. Langmuir 22:32–41

144. Shou Q, Guo C, Yang L, Jia L, Liu C, Liu H (2011) Effect of pH on the single-step synthesis of gold nanoparticles using PEO–PPO–PEO triblock copolymers in aqueous media. J Colloid Interface Sci 363:481–489

145. Falletta E, Ridi F, Fratini E, Vannucci C, Canton P, Bianchi S, Castelvetro V, Baglioni P (2011) A tri-block copolymer templated synthesis of gold nanostructures. J Colloid Interface Sci 357:88–94

146. Fustin CA, Colard C, Filali M, Guillet P, Duwez AS, Meier MAR, Schubert US, Gohy JF (2006) Tuning the hydrophilicity of gold nanoparticles templated in star block copolymers. Langmuir 22:6690–6695

147. Riess G (2003) Micellization of block copolymers. Prog Polym Sci 28:1107–1170

148. Leong WL, Lee PS, Lohani A, Lan YM, Chen T (2008) Non-volatile organic memory applications enabled by in situ synthesis of gold nanoparticles in a self-assembled block copolymer. Adv Mater 20:2325–2331

149. Papp S, Korösi L, Gool B, Dederichs T, Mela P, Möller M, Dékány I (2010) Formation of gold nanoparticles in diblock copolymer micelles with various reducing agents. J Therm Anal Calorim 101:865–872

150. Khullar P, Singh V, Mahal A, Kaur H, Singh V, Banipal TS, Kaur G, Bakshi MS (2011) Tuning shape and size of gold nanoparticles with triblock polymer micelle structure transitions and environments. J Phys Chem C 115:10442–10454

151. Liu J, Niu J, Yin L, Jiang F (2011) In situ encapsulation of laccase in nanofibers by electrospinning for development of enzyme biosensors for chlorophenol monitoring. Analyst 136:4802–4808

152. Cuenya BR, Baeck SH, Jaramillo TF, McFarland EW (2003) Size-and support-dependent electronic and catalytic properties of $Au0/Au^{3+}$ nanoparticles synthesized from block copolymer micelles. J Am Chem Soc 125:12928–12934

153. Lopez SG, Castro E, Taboada P, Mosquera V (2008) Block copolymer-mediated synthesis of size-tunable gold nanospheres and nanoplates. Langmuir 24:13186–13196

154. Sakai T, Alexandridis P (2005) Mechanism of gold metal ion reduction, nanoparticle growth and size control in aqueous amphiphilic block copolymer solutions at ambient conditions. J Phys Chem B 109:7766–7777

155. Khullar P, Mahal A, Singh V, Banipal TS, Kaur G, Bakshi MS (2010) How PEO–PPO–PEO triblock polymer micelles control the synthesis of gold nanoparticles: temperature and hydrophobic effects. Langmuir 26:11363–11371

156. Azzam T, Eisenberg A (2007) Monolayer-protected gold nanoparticles by the self-assembly of micellar poly(ethylene oxide)-b-poly(epsilon-caprolactone) block copolymer. Langmuir 23:2126–2132

157. Lee Y, Park TG (2011) Facile fabrication of branched gold nanoparticles by reductive hydroxyphenol derivatives. Langmuir 27:2965–2971

158. Barros Scaravelli RC, Dazzi R, Giacomelli FC, Machado G, Giacomelli C, Schmidt V (2013) Direct synthesis of coated gold nanoparticles mediated by polymers with amino groups. J Colloid Interf Sci 397:114–121

159. Schmidt V, Borsali R, Giacomelli C (2009) Aggregation of a versatile triblock copolymer into pH-responsive cross-linkable nanostructures in both organic and aqueous media. Langmuir 25:13361–13367

160. Giacomelli FC, Stepanek P, Giacomelli C, Schmidt V, Jager E, Jager A, Ulbrich K (2011) pH-triggered block copolymer micelles based on a pH-responsive PDPA (poly[2-(diisopropylamino)ethyl methacrylate]) inner core and a PEO (poly(ethylene oxide)) outer shell as a potential tool for the cancer therapy. Soft Matter 7:9316–9325

161. Sabir TS, Yan D, Milligan JR, Aruni AW, Nick KE, Ramon RH, Hughes JA, Chen Q, Kurti RS, Perry CC (2012) Kinetics of gold nanoparticle formation facilitated by triblock copolymers. J Phys Chem C 116:4431–4441

162. Liu S, Weaver JVM, Tang Y, Billingham NC, Armes SP, Tribe K (2002) Synthesis of shell cross-linked micelles with pH-responsive cores using ABC triblock copolymers. Macromolecules 35:6121–6131

163. Njoki PN, Luo J, Kamundi MM, Lim S, Zhong CJ (2010) Aggregative growth in the size-controlled growth of monodispersed gold nanoparticles. Langmuir 26:13622–13629

164. Shields SP, Richards VN, Buhro WE (2010) Nucleation control of size and dispersity in aggregative nanoparticle growth A study of the coarsening kinetics of thiolate-capped gold nanocrystals. Chem Mater 22:3212–3225

165. Streszewski B, Jaworski W, Paclawski K, Csapó E, Dékány I, Fitzner K (2012) Gold nanoparticles formation in the aqueous system of gold (III) chloride complex ions and hydrazine sulfate-kinetic studies. Colloids Surf A 397:63–72

166. Yuan JJ, Schmid A, Armes SP, Lewis AL (2006) Facile synthesis of highly biocompatible poly(2-(methacryloyloxy)ethyl phosphorylcholine)-coated gold nanoparticles in aqueous solution. Langmuir 22:11022–11027

167. Ray D, Aswal VK, Kohlbrecher J (2011) Synthesis and characterization of high concentration block copolymer-mediated gold nanoparticles. Langmuir 27:4048–4056

168. Newman JDS, Blanchard GJ (2006) Formation of gold nanoparticles using amine reducing agents. Langmuir 22:5882–5887

169. Vo CD, Armes SP, Randall DP, Sakai K, Biggs S (2006) Synthesis of zwitterionic diblock copolymers without protecting group chemistry. Macromolecules 40:157–167

170. Park HH, Park H, Jamison AC, Lee TR (2014) Colloidal stability evolution and completely reversible aggregation of gold nanoparticles functionalized with rationally designed free radical initiators. Coll Polym Sci 292:411–421

171. Park HH, Lee TR (2011) Thermo- and pH-responsive hydrogelcoated gold nanoparticles prepared from rationally designed surface-confined initiators. J Nanopart Res 13:2909–2918

172. Stuart DA, Haes AJ, Yonzon CR, Hicks EM, Van Duyne RP (2005) Biological applications of localised surface plasmonic phenomenae. IEE Proc Nanobiotechnol 152:13–32

173. Eck D, Helm CA, Wagner NJ, Vaynberg KA (2001) Plasmon resonance measurements of the adsorption and adsorption kinetics of a biopolymer onto gold nanocolloids. Langmuir 17:957–960

174. Rahme K, Gauffre F, Marty JD, Payre B, Mingotaud C (2007) A systematic study of the stabilization in water of gold nanoparticles by poly(ethylene oxide)-poly(propylene oxide)-poly(ethylene oxide) triblock copolymers. J Phys Chem C 111:7273–7279

175. Liu YL, Shipton MK, Ryan J, Kaufman ED, Franzen S, Feldheim DL (2007) Synthesis, stability, and cellular internalization of gold nanoparticles containing mixed peptide-poly(ethylene glycol) monolayers. Anal Chem 79:2221–2229

176. Li DX, He Q, Zhu HF, Tao C, Li JB (2007) Enhanced dispersity of gold nanoparticles modified by omega-carboxyl alkanethiols under the impact of poly(ethylene glycol)s. J Nanosci Nanotechnol 7:3089–3094

177. Manna A, Imae T, Yogo T, Aoi K, Okazaki M (2002) Synthesis of gold nanoparticles in a winsor ii type microemulsion and their characterization. J Colloid Interface Sci 256:297–303

178. Castner DG, Hinds K, Grainger DW (1996) X-ray photoelectron spectroscopy sulfur 2p study of organic thiol and disulfide binding interactions with gold surfaces. Langmuir 12:5083–5086

179. Wenzler LA, Moyes GL, Raikar GN, Hansen RL, Harris JM, Beebe TP, Wood LL, Saavedra SS (1997) Measurements of single-molecule bond rupture forces between self-assembled monolayers of organosilanes with the atomic force microscope. Langmuir 13:3761–3768

180. Resch R, Baur C, Bugacov A, Koel BE, Echternach PM, Madhukar A, Montoya N, Requicha AAG, Will P (1999) Linking and manipulation of gold multinanoparticle structures using dithiols and scanning force microscopy. J Phys Chem B 103:3647–3650

181. Wang H, Kundu J, Halas NJ (2007) Plasmonic nanoshell arrays combine surface-enhanced vibrational spectroscopies on a single substrate. Angew Chem Int Ed 46:9040–9044

182. Jin CM, Zhou HH, Wei W, Narayan R (2006) Three-dimensional self-organization of crystalline gold nanoparticles in amorphous alumina. Appl Phys Lett 89:261103/1–261103/3

183. Rowe MP, Plass KE, Kim K, Kurdak C, Zellers ET, Matzger AJ (2004) Single-phase synthesis of functionalized gold nanoparticles. Chem Mater 16:3513–3517

184. Hostetler MJ, Wingate JE, Zhong CJ, Harris JE, Vachet RW, Clark MR, Londono JD, Green SJ, Stokes JJ, Wignall GD, Glish GL, Porter MD, Evans ND, Murray RW (1998) Alkanethiolate gold cluster molecules with core diameters from 15 to 52 nm: core and monolayer properties as a function of core size. Langmuir 14:17–30

185. Woehrle GH, Brown LO, Hutchison JE (2005) Thiol-functionalized, 15-nm gold nanoparticles through ligand exchange reactions: scope and mechanism of ligand exchange. J Am Chem Soc 127:2172–2183

186. Turkevich J, Stevenson PC, Hillier J (1951) A study of the nucleation and growth processes in the synthesis of colloidal gold. Discuss Faraday Soc 11:55–75

187. Brust M, Walker M, Bethell D, Schiffrin DJ, Whyman R (1994) Synthesis of thiol-derivatised gold nanoparticles in a two-phase Liquid-Liquid system. J Chem Soc, Chem Commun 801–802

188. Chaikin Y, Leader H, Popovitz-Biro R, Vaskevich A, Rubinstein I (2011) Versatile scheme for the step-by-step assembly of nanoparticle multilayers. Langmuir 27:1298–1307

189. Nair SS, John SA, Sagara T (2009) Simultaneous determination of paracetamol and ascorbic acid using tetraoctylammonium bromide capped gold nanoparticles immobilized on 1,6-hexanedithiol modified Au electrode. Electrochim Acta 54:6837–6843

190. Brust M, Etchenique R, Calvo EJ, Gordillo GJ (1996) The self-assembly of gold and SCd nanoparticle multilayer structures studied by quartz crystal microgravimetry. Chem Commun 1949–1950

191. Edgar JA, McDonaph AM, Cortie MB (2012) Formation of gold nanorods by a stochastic "popcorn" mechanism. ACS Nano 6:1116–1125

192. Yong KT, Swihart MT, Ding H, Prasad PN (2009) Preparation of gold nanoparticles and their applications in anisotropic nanoparticle synthesis and bioimaging. Plasmonics 4:79–93

193. Moon SY, Kusunose T, Sekino T (2009) CTAB-assisted synthesis of size- and shape-controlled gold nanoparticles in SDS aqueous solution. Mater Lett 63:2038–2040

194. Farren-Dai M, Awoonor-Williams E, MacNeil CS, Mahimwalla Z, Ghandi K (2014) A novel gold nanoparticle stabilization and its muon chemistry. Chem Phys Lett 610–611:331–334

195. Astruc D, Lu F, Aranzaes JR (2005) Nanoparticles as recyclable catalysts: the frontier between homogeneous and heterogeneous catalysis. Angew Chem Int Ed Engl 44:7852–7872

196. Schrekker HS, Gelesky MA, Stracke MP, Schrekker CML, Machado G, Teixeira SR, Rubim JC, Dupont J (2007) Disclosure of the imidazolium cation coordination and stabilization mode in ionic liquid stabilized gold(0) nanoparticles. J Colloid Interface Sci 316:189–195

197. Thomas KG, Kamat PV (2003) Chromophore-functionalized gold nanoparticles. Acc Chem Res 36:888–898

198. Rao CNR, Matte HSSR, Voggu R, Govindaraj A (2012) Recent progress in the synthesis of inorganic nanoparticles. Dalton Trans 41:5089–5120
199. Schulz-Dobrick M, Sarathy KV, Jansen M (2005) Surfactant-free synthesis and functionalization of gold nanoparticles. J Am Chem Soc 127:12816–12817
200. Hiramatsu H, Osterloh FE (2004) A simple large-scale synthesis of nearly monodisperse gold and silver nanoparticles with adjustable sizes and with exchangeable surfactants. Chem Mater 16:2509–2511
201. Capdevielle P, Lavigne A, Sparfel D, Baranne-Lafont J, Cuong NK, Maumy M (1990) Mechanism of primary aliphatic amines oxidation to nitriles by the cuprouschloride-dioxygen-pyridine system. Tetrahedron Lett 31:3305–3308
202. Privman V, Goia DV, Park J, Matijevic E (1999) Mechanism of formation of monodispersed colloids by aggregation of nanosize precursors. J Colloid Interface Sci 213:36–45
203. Brown LO, Hutchison JE (2001) Formation and electron diffraction studies of ordered 2-D and 3-D superlattices of amine-stabilized gold nanoparticles. J Phys Chem B 105:8911–8916
204. Stoeva S, Klabunde KJ, Sorensen CM, Dragieva I (2002) Gram-scale synthesis of monodisperse gold colloids by the solvated metal atom dispersion method and digestive ripening and their organization into two- and three-dimensional structures. J Am Chem Soc 124:2305–2311
205. Fink J, Kiely CJ, Bethell D, Schiffrin DJ (1998) Self-organization of nanosized gold particles. Chem Mater 10:922–926
206. Li Y, Wu Y, Ong BS (2005) Facile synthesis of silver nanoparticles useful for fabrication of high-conductivity elements for printed electronics. J Am Chem Soc 127:3266–3267
207. Peng ZA, Peng X (2001) Formation of high-quality CdTe, CdSe, and CdS nanocrystals using CdO as precursor. J Am Chem Soc 123:183–184
208. Yu WW, Peng X (2002) Formation of high-quality CdS and other II-VI semiconductor nanocrystals in noncoordinating solvents: Tunable reactivity of monomers. Angew Chem Int Ed 41:2368–2371
209. Chen M, Wang LY, Han JT, Zhang JY, Li ZY, Qian DJ (2006) Preparation and study of polyacryamide-stabilized silver nanoparticles through a one-pot process. J Phys Chem B 110:11224–11231
210. Hada H, Yonezawa Y, Yoshida A, Kurakake A (1976) Photoreduction of silver ion in aqueous and alcoholic solutions. J Phys Chem 80:2728–2731
211. Henglein A, Giersig M (1999) Formation of colloidal silver nanoparticles: capping action of citrate. J Phys Chem B 103:9533–9539
212. Odian G (2004) Principles of Polymerization, 4th Ed. Wiley, New Jersey, p 297
213. Cheng DM, Xia HB, Chan HSO (2004) Facile fabrication of AgCl@polypyrrole-chitosan core-shell nanoparticles and polymeric hollow nanospheres. Langmuir 20:9909–9912
214. Shevchenko EV, Talapin DV, Kotov NA, O'Brien S, Murray CB (2006) Structural diversity in binary nanoparticle superlattices. Nature 439:55–59
215. Templeton AC, Wuelfing WP, Murray RW (2000) Monolayer-protected cluster molecules. Acc Chem Res 33:27–36
216. Hussain I, Graham S, Wang ZX, Tan B, Sherrington DC, Rannard SP, Cooper AI, Brust M (2005) Size-controlled synthesis of near-monodisperse gold nanoparticles in the 1–4 nm range using polymeric stabilizers. J Am Chem Soc 127:16398–16399
217. Wang ZX, Tan B, Hussain I, Schaeffer N, Wyatt MF, Brust M, Cooper AI (2007) Design of polymeric stabilizers for size-controlled synthesis of monodisperse gold nanoparticles in water. Langmuir 23:885–895
218. Schaeffer N, Tan B, Dickinson C, Rosseinsky MJ, Laromaine A, McComb DW, Stevens MM, Wang Y, Petit L, Barentin C, Spiller DG, Cooper AI, Levy R (2008) Fluorescent or not? Size-dependent fluorescence switching for polymer-stabilized gold clusters in the 11–17 nm size range. Chem Commun 3986–3988
219. Brust M, Fink J, Bethell D, Schiffrin DJ, Kiely CJ (1995) Synthesis and reactions of functionalised gold nanoparticles. J Chem Soc, Chem Commun 1655–1656

220. Hostetler MJ, Green SJ, Stockes JJ, Murray RW (1996) Monolayers in three dimensions: synthesis and electrochemistry of omega-functionalized alkanethiolate-stabilized gold cluster compounds. J Am Chem Soc 118:4212–4213
221. Li Y, Zaluzhna O, Xu B, Gao Y, Modest JM, Tong YJ (2011) Mechanistic insights into the Brust-Schiffrin two-phase synthesis of organo-chalcogenate-protected metal nanoparticles. J Am Chem Soc 133:2092–2095
222. Jin R (2010) Quantum sized, thiolate-protected gold nanoclusters. Nanoscale 2:343–362
223. Zaluzhna O, Li Y, Zangmeister C, Alison TC, Tong YJ (2012) Mechanistic insights on one-phase vs two-phase Brust-Schiffrin method synthesis of Au nanoparticles with dioctyl-diselenides. Chem Commun 48:362–364
224. Vitale F, Fratoddi I, Battocchio C, Piscopiello E, Tapfer L, Russo MV, Polzonetti G, Giannini C (2011) Mono- and bi-functional arenethiols as surfactants for gold nanoparticles: synthesis and characterization. Nanoscale Res Lett 6:103
225. Kanaras AG, Kamounah FS, Schaumburg K, Kiely CJ, Brust M (2002) Thioalkylated tetraethylene glycol: a new ligand for water soluble monolayer protected gold clusters. Chem Commun 2294–2295
226. Miesch C, Kosif I, Lee E, Kim JK, Russell TP, Hayward RC, Emrick T (2012) Nanoparticle-stabilized double emulsions and compressed droplets. Angew Chem Int Ed 51:145–149
227. Hao Y, Yang X, Song S, Huang M, He C, Cui M, Chen J (2012) Exploring the cell uptake mechanism of phospholipid and polyethylene glycol coated gold nanoparticles. Nanotechnology 23:045103
228. Hamad-Schifferli K, Schwartz JJ, Santos AT, Zhang S, Jacobson JM (2000) Remote electronic control of DNA hybridization through inductive coupling to an attached metal nanocrystal antenna. Nature 415:152–155
229. Shem PM, Sardar R, Shumaker-Parry JS (2014) Soft ligand stabilized gold nanoparticles: Incorporation of bipyridyls and two-dimensional assembly. J Colloid Interf Sci 426:107–116
230. Bain CD, Troughton EB, Tao YT, Evall J, Whitesides GM, Nuzzo RG (1989) Formation of monolayer films by the spontaneous assembly of organic thiols from solution onto gold. J Am Chem Soc 111:321–335
231. Motte L, Pileni MP (1998) Influence of length of alkyl chains used to passivate silver sulfide nanoparticles on two- and three-dimensional self-organization. J Phys Chem B 102:4104–4109
232. Woehrle GH, Warner MG, Hutchison JE (2004) Molecular-level control of feature separation in one-dimensional nanostructure assemblies formed by biomolecular nano-lithography. Langmuir 20:5982–5988
233. Templeton AC, Pietron JJ, Murray RW, Mulvaney P (2000) Solvent refractive index and core charge influences on the surface plasmon absorbance of alkanethiolate monolayer-protected gold clusters. J Phys Chem B 104:564–570
234. Chen CF, Tzeng SD, Chen HY, Lin KJ, Gwo S (2008) Tunable plasmonic response from alkanethiolate-stabilized gold nanoparticle superlattices: Evidence of near-field coupling. J Am Chem Soc 130:824–826
235. Bukasov R, Shumaker-Parry JS (2007) Highly tunable infrared extinction properties of gold nanocrescents. Nano Lett 7:1113–1118
236. Sardar R, Shumaker-Parry JS (2009) 9-BBN induced synthesis of nearly monodisperse ω-functionalized alkylthiols stabilized gold nanoparticles. Chem Mater 21:1167–1169
237. Leontowich AFG, Calver CF, Dasog M, Scott RWJ (2010) Surface properties of water-soluble glycine-cysteamine-protected gold clusters. Langmuir 26:1285–1290
238. Gupta RK, Srinivasan MP, Dharmarajan R (2011) Synthesis of short chain thiol capped gold nanoparticles, their stabilization and immobilization on silicon surface. Colloid Surf A 390:149–156
239. Ackerson CJ, Jadzinsky PD, Sexton JZ, Bushnell DA, Kornberg RD (2010) Synthesis and bioconjugation of 2 and 3 nm-diameter gold nanoparticles. Bioconjugate Chem 21:214–218

240. Müller CI, Lambert C (2011) Electrochemical and optical characterization of triarylamine functionalized gold nanoparticles. Langmuir 27:5029–5039
241. Stoeva SI, Prasad BLV, Uma S, Stoimenov PK, Zaikovski V, Sorensen CM, Klabunde KJ (2003) Face-centered cubic and hexagonal closed-packed nanocrystal superlattices of gold nanoparticles prepared by different methods. J Phys Chem B 107:7441–7448
242. Brown LO, Hutchison JE (1999) Controlled growth of gold nanoparticles during ligand exchange. J Am Chem Soc 121:882–883
243. Shimizu T, Teranishi T, Hasegawa S, Miyake M (2003) Size evolution of alkanethiol-protected gold nanoparticles by heat treatment in the solid state. J Phys Chem B 107:2719–2724
244. Dennis NW, Muhoberac BB, Newton JC, Kumbhar A, Sardar R (2014) Correlated optical spectroscopy and electron microscopy studies of the slow Ostwald-ripening growth of silver nanoparticles under controlled reducing conditions. Plasmonics 9:111–120
245. Mulvaney P (1996) Surface plasmon spectroscopy of nano sized metal particles. Langmuir 12:788–800
246. Sardar R, Shumaker-Parry JS (2011) Spectroscopic and microscopic investigation of gold nanoparticle formation: ligand and temperature effects on rate and particle size. J Am Chem Soc 133:8179–8190
247. Polte J, Erler R, Thunemann AF, Sokolov S, Ahner TT, Rademann K, Emmerling F, Kraehnert R (2010) Nucleation and growth of gold nanoparticles studied via in situ small angle X-ray scattering at millisecond time resolution. ACS Nano 4:1076–1082
248. Polte J, Tuaev X, Wuithschick M, Fischer A, Thuenemann AF, Rademann K, Kraehnert R, Emmerling F (2012) Formation mechanism of colloidal silver nanoparticles: analogies and differences to the growth of gold nanoparticles. ACS Nano 6:5791–5802
249. Bootharaju MS, Pradeep T (2010) Uptake of toxic metal ions from water by naked and monolayer protected silver nanoparticles: an Xray photoelectron spectroscopic investigation. J Phys Chem C 114:8328–8336
250. Qian H, Zhu M, Wu Z, Jin R (2012) Quantumsized gold nanoclusters with atomic precision. Acc Chem Res 45:1470–1479
251. Gronbeck H (2012) The bonding in thiolate protected gold nanoparticles from Au4f photoemission core level shifts. Nanoscale 4:4178–4182
252. Hakkinen H (2012) The gold-sulfur interface at the nanoscale. Nat Chem 4:443–455
253. Shankar R, Shahi V, Sahoo U (2010) Comparative study of linear poly(alkylarylsilane)s as reducing agents toward Ag(I) and Pd(II) ions, synthesis of polymer, metal nanocomposites with variable size domains of metal nanoparticles. Chem Mater 22:1367–1375
254. Skrdla PJ (2012) Roles of nucleation, denucleation, coarsening, and aggregation kinetics in nanoparticle preparations and neurological disease. Langmuir 28:4842–4857
255. Van Hyning DL, Klemperer WG, Zukoski CF (2001) Silver nanoparticle formation: predictions and verification of the aggregative growthmodel. Langmuir 17:3128–3135
256. Chuit C, Corriu RJP, Reye C, Young JC (1993) Reactivity of pentaand hexacoordinate silicon compounds and their role as reaction intermediates. Chem Rev 93:1371–1448
257. Kano N, Komatsu F, Yamamura M, Kawashima T (2006) Reversible photoswitching of the coordination numbers of silicon in organosilicon compounds bearing a 2-(Phenylazo)phenyl group. J Am Chem Soc 128:7097–7109
258. Yeshchenko O, Dmitruk I, Alexeenko A, Kotko A, Verdal J, Pinchuk A (2012) Size and temperature effects on the surface plasmon resonance in silver nanoparticles. Plasmonics 7:685–694
259. Alvarez MM, Khoury JT, Schaaff TG, Shafigullin MN, Vezmar I, Whetten RL (1997) Optical absorption spectra of nanocrystal gold molecules. J Phys Chem B 101:3706–3712
260. Ojea-Jimenez I, Bastus NG, Puntes V (2011) Influence of the sequence of the reagents addition in the citrate-mediated synthesis of gold nanoparticles. J Phys Chem C 115:15752–15757

261. Bastus NG, Comenge J, Puntes V (2011) Kinetically controlled seeded growth synthesis of citrate-stabilized gold nanoparticles of up to 200 nm: size focusing versus Ostwald ripening. Langmuir 27:11098–11105
262. Ji X, Song X, Li J, Bai Y, Yang W, Peng X (2007) Size control of gold nanocrystals in citrate reduction: the third role of citrate. J Am Chem Soc 129:13939–13948
263. Dahl JA, Maddux BLS, Hutchison JE (2007) Toward greener nanosynthesis. Chem Rev 107:2228–2269
264. Roth PJ, Theato P (2008) Versatile synthesis of functional gold nanoparticles: grafting polymers from and onto. Chem Mater 20:1614–1621
265. Shem PM, Sardar R, Shumaker-Parry JS (2009) One-step synthesis of phosphine-stabilized gold nanoparticles using the mild reducing agent 9-BBN. Langmuir 25:13279–13283
266. Huang J, Kim F, Tao AR, Connor S, Yang P (2005) Spontaneous formation of nanoparticle stripe patterns through dewetting. Nat Mater 4:896–900
267. Prasad BLV, Sorensen CM, Klabunde KJ (2008) Gold nanoparticle superlattices. Chem Soc Rev 37:1871–1883
268. Chen S, Ingram RS, Hostetler MJ, Pietron JJ, Murray RW, Schaaff TG, Khoury JT, Alvarez MM, Whetten RL (1998) Gold nanoelectrodes of varied size: transition to molecule-like charging. Science 280:2098–2101
269. Li D, Kaner RB (2005) Shape and aggregation control of nanofibers: not shaken, not stirred. J Am Chem Soc 128:968–975
270. Liu X, Worden JG, Huo Q, Brennan JP (2006) Kinetic study of gold nanoparticle growth in solution by Brust-Schiffrin reaction. J Nanosci Nanotechnol 6:1054–1059
271. Wang ZL (2000) Transmission electron microscopy of shape-controlled nanocrystals and their assemblies. J Phys Chem B 104:1153–1175
272. Liu X, Atwater M, Wang J, Dai Q, Zou J, Brennan JP, Huo Q (2007) A study on gold nanoparticle synthesis using oleylamine as both reducing agent and protecting ligand. J Nanosci Nanotechnol 7:3126–3133
273. Sugimoto T (2000) Fine particles-synthesis, characterization, and mechanism of growth. Surfactant Sci Ser 92, Marcel Dekker, New York
274. Leff DV, Brandt L, Heath JR (1996) Synthesis and characterization of hydrophobic, organically-soluble gold nanocrystals functionalized with primary amines. Langmuir 12:4723–4730
275. Brown LO, Hutchison JE (1997) Convenient preparation of stable, narrow-dispersity, gold nanocrystals by ligand exchange reactions. J Am Chem Soc 119:12384–12385
276. Joo SW (2006) Adsorption of bipyridine compounds on gold nanoparticle surfaces investigated by UV-Vis absorbance spectroscopy and surface enhanced Raman scattering. Spectrosc Lett 39:85–96
277. Wandlowski T, Ataka K, Mayer D (2002) In situ infrared study of 4,4′-bipyridine adsorption on thin gold films. Langmuir 18:4331–4341
278. Noda H, Minoha T, Wan LJ, Osawa M (2000) Adsorption and ordered phase formation of 2,2′-bypyridine on Au(111): a combined surface-enhanced infrared and STM study. J Electroanal Chem 481:62–68
279. Chong SV, Tallon JL (2010) Aqueous electrochemical insertion of Na^+ into the tungsten oxide hybrid $WO_3(4,4′-bipyridyl)_{05}$. J Phys Chem Solids 71:303–308
280. Hamoudi H, Döring K, Chesneau F, Lang H, Zharnikov M (2012) Self-assembly of pyridine-substituted alkanethiols on gold: the electronic structure puzzle in the ortho- and para-attachment of pyridine to the molecular chain. J Phys Chem C 116:861–870
281. Liu W, Yang X, Xie L (2007) Size-controlled gold nanocolloids on polymer microsphere-stabilizer via interaction between functional groups and gold nanocolloids. J Colloid Interface Sci 313:494–502
282. Zubavichus Y, Zharnikov M, Yang Y, Fuchs O, Umbach E, Heske C, Ulman A, Grunze M (2004) XPS and NEXAFS study of water adsorption on the pyridine-terminated thiolate self-assembled monolayer. Langmuir 20:11022–11029

283. Duraiswamy S, Khan SA (2014) Dual-stage continuous-flow seedless microfluidic synthesis of anisotropic gold nanocrystals. Part Part Syst Charact 31:429–432

284. Nikoobakht B, El-Sayed MA (2003) Preparation and growth mechanism of gold nanorods (NRs) using seed-mediated growth method. Chem Mater 15:1957–1962

285. Jana NR, Gearheart L, Murphy CJ (2001) Evidence for seed-mediated nucleation in the chemical reduction of gold salts to gold nanoparticles. Chem Mater 13:2313–2322

286. Gou L, Murphy CJ (2005) Fine-tuning the shape of gold nanorods. Chem Mater 17:3668–3672

287. Duff DG, Baiker A, Edwards PP (1993) A new hydrosol of gold clusters 1 formation and particle size variation. Langmuir 9:2301–2309

288. Khan SA, Duraiswamy S (2012) Controlling bubbles using bubbles-microfluidic synthesis of ultra-small gold nanocrystals with gas-evolving reducing agents. Lab Chip 12:1807–1812

289. Polte J, Ahner TT, Delissen F, Sokolov S, Emmerling F, Thünemann AF, Kraehnert R (2010) Mechanism of gold nanoparticle formation in the classical citrate synthesis method derived from coupled in situ XANES and SAXS evaluation. J Am Chem Soc 132:1296–1301

290. Wagner J, Kohler JM (2005) Continuous synthesis of gold nanoparticles in a microreactor. Nano Lett 5:685–691

291. Frens G (1973) Controlled nucleation for the regulation of the particle size in monodisperse gold suspensions. Nature: Phys Sci 241:20–22

292. Gross S Colloidal dispersion of gold nanoparticles In: Schubert U, Hüsing N, Laine RM (eds) (2008) Materials syntheses. SpringerWien, New York, pp 155–161

293. Wilcoxon JP, Williamson RL, Baughman R (1993) Optical-properties of gold colloids formed in inverse micelles. J Chem Phys 98:9933–9950

294. Kimling J, Maier M, Okenve B, Kotaidis V, Ballot H, Plech A (2006) Turkevich method for gold nanoparticle synthesis revisited. J Phys Chem B 110:15700–15707

295. Kumar S, Gandhi KS, Kumar R (2007) Modeling of formation of gold nanoparticles by citrate method. Ind Eng Chem Res 46:3128–3136

296. Li C, Li D, Wan G, Xu J, Hou W (2011) Facile synthesis of concentrated gold nanoparticles with low size-distribution in water: temperature and pH controls. Nanoscale Res Lett 6:440

297. Rahman MR, Saleh FS, Okajima T, Ohsaka T (2011) pH Dependence of the size and crystallographic orientation of the gold nanoparticles prepared by seed-mediated growth. Langmuir 27:5126–5135

298. Rohiman A, Anshori I, Surawijaya A, Idris I (2011) Study of colloidal gold synthesis using turkevich method. AIP Conf Proc 1415:39–42

299. Kim JH, Lavin BW, Burnett RD, Boote BW (2011) Controlled synthesis of gold nanoparticles by fluorescent light irradiation. Nanotechnology 22:285602

300. Aguilera LMC, Romano MF, Gil MLA, Rodriguez IN, Hidalgo-Hidalgo de Cisneros JL, Santander JMP (2011) New, fast and green procedure of gold nanoparticles based on sonocatalysis. Untrason Sonochem 18:789–794

301. Ojea-Jimenez I, Romero FM, Bastus NG, Puntes V (2010) Small gold nanoparticles synthesized with sodium citrate and heavy water: insights into the reaction mechanism. J Phys Chem C 114:1800–1804

302. Yang TF, Chen CN, Chen MC, Lai CH, Liang HF, Sung HW (2007) Shell–crosslinked Pluronic L121 micelles as a drug delivery vehicle. Biomaterials 28:725–734

303. Huang J, Si L, Jiang L, Fan Z, Qiu J, Li G (2008) Effect of pluronic F68 block copolymer on P-glycoprotein transport and CYP3A4 metabolism. Int J Pharm 356:351–353

304. Batrakova EV, Kabanov AV (2008) Pluronic block copolymers: Evolution of drug delivery concept from inert nanocarriers to biological response modifiers. J Control Release 130:98–106

305. Yoo HS, Park TG (2000) In vitro and in vivo anti-tumor activities of nanoparticles based on DOX–PLGA conjugates. J Control Release 68:419–431

306. Sun CZ, Lu CT, Zhao YZ, Guo P, Tian JL, Zhang L, Li XK, Lv HF, Dai DD, Li X (2011) Characterization of the doxorubicin-pluronic F68 conjugate micelles and their effect on doxorubicin resistant human erythroleukemic cancer cells. J Nanomed Nanotechnol 2:2–6

307. Kabanov A, Alakhov VY (2002) Pluronic block copolymers in drug delivery: from micellar nanocontainers to biological response modifiers. Crit Rev Ther Drug Carr Syst 19:1–72

308. Mahmud A, Lavasanifar A (2005) The effect of block copolymer structure on the internalization of polymeric micelles by human breast cancer cells. Colloids Surf B Biointerfaces 45:82–89

309. Al–Jamal WT, Kostarelos K (2011) Liposomes: from a clinically established drug delivery system to a nanoparticle platform for theranostic nanomedicine. Accounts of Chemical Research 44:1094–1104

310. Sajja HK, East MP, Mao H, Wang YA, Nie S, Yang L (2009) Development of multifunctional nanoparticles for targeted drug delivery and noninvasive imaging of therapeutic effect. Curr Drug Discov Technol 6:43–51

311. Grange C, Geninatti-Crich S, Esposito G, Alberti D, Tei L, Bussolati B, Aime S, Camussi G (2010) Combined delivery and magnetic resonance imaging of neural cell adhesion molecule–targeted doxorubicin–containing liposomes in experimentally induced Kaposi's sarcoma. Cancer Res 70:2180–2190

312. de Smet M, Heijman E, Langereis S, Hijnen NM, Grüll H (2011) Magnetic resonance imaging of high intensity focused ultrasound mediated drug delivery from temperature–sensitive liposomes: an in vivo proof–of–concept study. J Control Release 150:102–110

313. Margolis LB, Namiot VA, Kljukin LM (1983) Magnetoliposomes: another principle of cell sortingBiochim. Biophys Acta 735:193–195

314. Hamley IW (2003) Nanotechnology with soft materials. Angew Chem Int Ed 42:1692–1712

315. Chen CC, Lin YP, Wang CW, Tzeng HC, Wu CH, Chen YC, Chen CP, Chen LC, Wu YC (2006) DNA–gold nanorod conjugates for remote control of localized gene expression by near infrared irradiation. J Am Chem Soc 128:3709–3715

316. Xu C, Xie J, Ho D, Wang C, Kohler N, Walsh EG, Morgan JR, Chin YE, Sun S (2008) Au–Fe$_3$O$_4$ dumbbell nanoparticles as dual–functional probes. Angew Chem Int Ed Engl 47:173–176

317. Jiang J, Gu HW, Shao HL, Devlin E, Papaefthymiou GC, Ying JY (2008) Bifunctional Fe$_3$O$_4$–Ag heterodimer nanoparticles for two-photon fluorescence imaging and magnetic manipulation. Adv Mater 20:4403–4407

318. Xie J, Zhang F, Aronova M, Zhu L, Lin X, Quan Q, Liu G, Zhang G, Choi KY, Kim K, Sun X, Lee S, Sun S, Leapman R, Chen X (2011) Manipulating the power of an additional phase: a flower-like Au–Fe$_3$O$_4$ optical nanosensor for imaging protease expressions in vivo. ACS Nano 5:3043–3051

319. Jain PK, Huang X, El–Sayed IH, El–Sayed MA (2008) Noble metals on the nanoscale: optical and photothermal properties and some applications in imaging, sensing, biology, and medicine. Acc Chem Res 41:1578–1586

320. Melancon MP, Lu W, Li C (2009) Gold–based magneto–optical nanostructures: challenges for in vivo applications in cancer diagnostics and therapy. MRS Bull 34:415–421

321. Mahmood U, Weissleder R (2003) Near–infrared optical imaging of proteases in cancer. Mol Cancer Ther 2:489–496

322. Hilger I, Fruhauf K, Andra W, Hiergeist R, Hergt R, Kaiser WA (2002) Heating potential of iron oxides for therapeutic purposes in interventional radiology. Acad Radiol 9:198–202

323. Gilchrist RK, Medal R, Shorey WD, Hanselman RC, Parrott JC, Taylor CB (1957) Selective inductive heating of lymph nodes. Ann Surg 146:596–606

324. Kim J, Park S, Lee JE, Jin SM, Lee JH, Lee IS, Yang I, Kim JS, Kim SK, Cho MH, Hyeon T (2006) Designed fabrication of multifunctional magnetic gold nanoshells and their application to magnetic resonance imaging and photothermal therapy. Angew Chem Int Ed 45:7754–7758

325. Kelkar SS, Reineke TM (2011) Theranostics: combining imaging and therapy. Bioconjug Chem 22:1879–1903
326. Lim YT, Cho MY, Kim JK, Hwangbo S, Chung BH (2007) Plasmonic magnetic nanostructure for bimodal imaging and photonic-based therapy of cancer cells. ChemBioChem 8:2204–2209
327. Jayasena SD (1999) Aptamers: an emerging class of molecules that rival antibodies in diagnostics. Clin Chem 45:1628–1650
328. Kim K, Kim JH, Park H, Kim YS, Park K, Nam H, Lee S, Park JH, Park RW, Kim IS, Choi K, Kim SY, Park K, Kwon IC (2010) Tumor–homing multifunctional nanoparticles for cancer theragnosis: simultaneous diagnosis, drug delivery, and therapeutic monitoring. J Control Release 146:219–227

Chapter 4
Polymer Template-Directed Synthesis

Abstract The use of spatially and dimensionally constrained (co)polymers as templates is an effective method to prepare metal nanocrystals. These spatially and dimensionally constrained polymers can serve as reaction cages to control the growth of the particles, leading to the formation of nanoparticles with a morphology complementary to that of the template. By varying the shape of the sacrificial template nanoparticle and its ratio to the more noble metal precursor added, one can obtain a variety of morphologies such as, for example, triangular rings, wires, tubes, boxes, or cages. Block copolymers, especially amphiphilic, have been used to prepare aggregation-free noble metal nanoparticles. New template methods based on a synergistic soft-hard template mechanism were suggested for the preparation of flexible noble metal/cross-linked nanomaterials. Infinite coordination polymer particles are a class of emerging functional materials that are formed by bridging repeating organic ligands with metallic nodes. Noble metal nanoparticles have also been synthesised using biopolymer template such as proteins, nucleic acids, and polysaccharides known as polyelectrolytes. The synthetic polymers known as polyelectrolytes can be used as reducing/stabilizing agents in one single-step syntheses. Highly branched macromolecules-dendrimers are well defined with hollow cores and dense shells. They are constructed from an initiator core to which radially branched layers are covalently attached. Most of the dendritic containers reported so far use the concept of closing the dendritic box in order to keep the guest metal particle inside the dendrimer host. Dendrimer-entrapped nanoparticles are often formed using fast reduction and nucleation chemistry. With PAMAM dendrimers as templates, dendrimer-entrapped metal nanoparticles can be formed with each noble metal nanoparticle entrapped within each dendrimer molecule. Likewise, bimetallic core@shell or alloy dendrimer-(stabilized) entrapped metal nanoparticles can be prepared by coreduction of the metal ions within the dendrimer templates. Colloidally stable and water-soluble functional nanoparticles can be formed with plasmonic and fluorescent activities. The functionalized plasmonic-fluorescent nanoparticles have been used as cell imaging and plasmon-based optical detection probe. Dendrimers find many applications in drug delivery due to the opportunity of their internal niches to host a variety of molecules. They have also been reported to enter tumors and carry either chemotherapeutic agents or genetic therapeutics.

Incorporation of photoactive components in either the core or the periphery of these nanostructures enriches them with new functionalities opening new perspectives in nanomedicine.

Keywords Polymers · Polyelectrolytes and dendrimers templates · Amphiphilic copolymers and bioconjugates

Abbreviations

{Au@DMAP}NP	Gold nanoparticle decorated with DMAP
{Au@MUA}NP	Gold nanoparticle decorated with MUA
0D	Zero dimensional
1D	One dimensional
3T6C	Thiophene dendrons
ABCs	Amphiphilic block copolymers
AFM	Atomic force microscopy
AgDENPs	Dendrimer-entrapped silver nanoparticles
AgDSNPs	Dendrimer-stabilized silver nanoparticles
AgNP/THI/ICP	Silver nanoparticles capped with thionine and ICP
AgNPs/THI/ICP/GCE	Conjugate AgNPs/THI/ICP on GCE
ALT	Alanine transaminase
AM	Acrylamide
ATRP	Atom transfer radical polymerization
AuDENPs	Dendrimer-encapsulated (entrapped) gold nanoparticles
AuDSNPs	Dendrimer-stabilized gold nanoparticles
B-PEI	Branched poly(ethylenimine)
CD	Cyclodextrin
CEA	Carcinoembryonic antigen
Con A	Concanavalin A
CTAB	Cetyltrimethylammonium bromide,
DANPs	Dendrimer-assembled nanoparticles
DBG	T-BOC-protected glycine-coated dendrimer
DBPA	T-BOC-protected phenylalanine-coated dendrimer
DENPs	Dendrimer-encapsulated (entrapped) nanoparticles
DEN	Dendrimer
DLS	Dynamic light scattering technique
DMAEMA	Dimethylaminoethyl methacrylate
DPV	Differential pulse voltammetry
DSNPs	Dendrimer-stabilized nanoparticles
EDA	Ethylenediamine
EDS	Energy-dispersed spectrum
EG	Ethylene glycol
EIS	Electrochemical impedance spectroscopy

EMCH	Heterobifunctional cross-linker N-(ε-maleimidocaproic acid)-hydrazide
FA	Folic acid
FAR	Folic acid receptor
FI	Fluorescein isothiocyanate
FRTEM	Freeze-etching replication transmission electron microscopy
FTIR	Fourier transform infrared spectroscopy
fwhm	Full width at half maximum
G4(3T6C)	Thiophene dendron-functionalized PAMAM
G5·NGlyOH	Glycidol hydroxyl-terminated G5 dendrimers
GCE	Glassy carbon electrode
Hb	Hemoglobin
HCT	Hematocrit
HEPES	4-(2-hydroxyethyl)-1-piperazineethanesulfonic acid
HFOTAI	$CF_3(CF_2)_7$–SO_2NH–$(CH_2)_3N^+(CH_3)_3$ I^-
HOMO	Highest occupied molecular orbital
HOPG	Highly ordered (oriented) pyrolytic graphite
I907	IRGACURE 907
ICPs	Infinite coordination polymer particles
ITX	2-isopropylthioxanthone
i.v.	Intravenously
i.p.	Intraperitoneal
L-PPI	Lactose-coated PPI dendrimer
LBL	Layer-by-layer
LC-SPDP	Heterobifunctional cross-linking agent succinimidyl 6-(3′-[2-pyridyl-dithio] propionamido) hexanoate
LCST	Lower critical solution temperature
L-PEI	Linear poly(ethyleneimine)
LUMO	Lowest unoccupied molecular orbital
MA	Methyl acrylate
MCH	Mean corpuscular hemoglobin
MC@MNPs	Metal nanoparticles-decorated microcapsule
MOCVD	Metal organic chemical vapor deposition
MOFs	Metal-organic frameworks
MPC	Monolayer-protected cluster
M-PPI	Mannose-coated PPI dendrimer
MUA	Mercaptoundecanoic acid
MW	Microwave
Mw	Molecular weight
NICISS	Neutral impact collision ion scattering spectroscopy
Nip	4-nitrophenol
OEG	Oligo(ethylene glycol)
OEGMA	Oligo (ethylene glycol) methacrylate

PA	Polyamino oxanorbornene
PAcrA	Poly(acrylic acid)
PAH	Poly(allylamine hydrochloride)
PAlA	Poly(allylamine)
PAM	Polyacrylamide
PAMAM	Poly(amidoamine)
PAN	Polyacrylonitrile
PC	Phosphorylcholine
PCP	Porous coordination polymer
PDADMAC	Poly(diallyl dimethylammonium chloride)
PDI	Polydispersion (polydispersity) index
PE	Polyelectrolyte
PEG	Poly(ethylene glycol)
PEG-*b*-P4VP-*b*-PNIPAM	Poly(ethylene glycol)-*b*-poly(4-vinylpyridine)-*b*-poly(*N*-isopropylacrylamide)
PEI	Poly(ethylenimine)
PEO	Poly(ethylene oxide)
PEO-PPO-PEO	Poly(ethylene oxide)-poly(propylene oxide)-poly(ethylene oxide)
PEs	Polyelectrolytes
PG	Polyguanidino oxanorbornene
PGA	Poly(γ-glutamic acid)
PISA	Polymerization-induced self-assembled
PMMA	Poly(methyl methacrylate)
PNG	Polyelectrolyte gold nanoparticle
PNIPAM	Poly(*N*-isopropylacrylamide)
POEGMA-*b*-PDMAEMA	Diblock copolymer of oligo (ethylene glycol) methacrylate and dimethylaminoethyl methacrylate
POSS	Polyhedral oligomeric silsesquioxane
PPI	Poly(propylene imine)
PPI-5.0G	5 PPI dendrimer
PPy	Polypyrole
PSt	Polystyrene
PSt-*b*-PAcrA	Poly(styrene-block-acrylic acid)
PSt-*b*-PAcrA	Polystyrene-block-poly(acrylic acid)
PSt-*b*-PEO	Polystyrene-block-poly(ethylene oxide)
PSt-*b*-PVP	Polystyrene-block-poly(vinyl pyridine)
PStS	Poly (sodium 4-styrenesulfonate)
PStS	Polystyrene-sulfonic acid, sodium salt
PTPS	POSS containing thiol groups
PVA	Poly(vinyl alcohol)
PVM/MAn	Poly(methyl vinyl ether-co-maleic anhydride)
PVP	Poly(4-vinylpyridine)
PVPo	Poly(vinylpyrrolidone)

RAFT	Reversible addition–fragmentation chain transfer
RBCs	Red blood cells
Ret	Electron-transfer resistance
RGD (Arg-Gly-Asp)	Arginine-glycine-aspartic acid
ROMP	Ring-opening metathesis polymerization
SAED	Selected area electron diffraction
SAMs	Self-assembled monolayers
SERS	Surface-enhanced Raman scattering
SFS	Sodium formaldehyde sulfoxylate
Si-PEI	N-[3-(trimethoxysilyl)propyl] poly(ethylenimine)
SPR	Surface plasmon resonance
SSHM	Synergistic soft-hard template mechanism
TG	Thermogravimetric
TGA	Thermogravimetric analysis
THF	Tetrahydrofuran
TMPTA	Trimethylolpropane triacrylate
TRIS	Tris(hydroxymethyl)aminomethane,
WBCs	White blood corpuscles
XPS	X-ray photoelectron spectroscopy
XRD	X-ray diffraction

4.1 Introduction

Many methods (e.g., chemical reduction, polyol process, template and radiolytic approaches, etc.) [1–3] have been developed for the synthesis of noble metal nanoparticles. These methods are expected to result in a very narrow particle size distribution and particles of uniform shape. Most synthesis describes the use of suitable surface-capping agents in addition to the reducing agents for synthesis of nanoparticles. Frequent use of organic compounds as well as polymers has been described for obtaining redispersible nanoparticles. Among the many functional (co)polymers, carboxylic acids have found special mention for their ease of handling, effective capping, mild reducing ability, and human-friendly nature [4, 5]. Since aggregates of the metal colloid tend to coagulate, which makes them unstable and difficult to use, resulting in poor reproducibility of spectral signals. This problem can be largely overcome by transferring the metal nanoparticles on to a polymer template [6]. Poly(vinyl alcohol) could be considered as a good host material for metal nanoparticles, due to good thermostability and chemical resistance. Sodium poly(γ-glutamic acid) (PGA) is a water-soluble and biodegradable polymer. Each repeating unit of PGA contained one carboxyl group with specific affinity, which is useful for tissue culture and many food, biomedical, and industrial applications [7].

The use of spatially and dimensionally constrained polymers as templates is an effective method to prepare metal nanocrystals with morphology similar or complementary to that of the template. Both soft and hard templates can be employed for the shape-controlled synthesis of metal nanocrystals. For example, some flexible structures assembled by polymers and biopolymers can be utilized as soft templates for synthesizing 0D and 1D noble metal nanoparticles. As a representative example, single-crystal gold nanowires with a diameter below 2 nm were synthesized by aging the oleylamine solution of $HAuCl_4$ at room temperature, where the mesostructures formed by cooperative assembly between the Au^+ ions and oleylamine were believed to serve as growth templates and govern anisotropic growth in the nanoscale [8].

The template can also serve as a scaffold. The metal ions are reduced within or around the confined volume or space of the template. These spatially and dimensionally constrained structures can serve as reaction cages to control the nucleation and growth of the particles. Self-assembled, biological, and synthetic structures such as liposomes and vesicles, biological macromolecules, and viruses belong also to the soft templates [9–11]. Liquid-crystalline media have been used as templates in the synthesis of anisotropic nanoparticles. For example, hexagonal liquid-crystalline phases formed by cylindrical reverse micelles containing long water channels were used as templates in the synthesis of silver nanowires [12]. The authors reported the synthesis of triangular or hexagonal-shaped gold nano- and microplates by reduction of $HAuCl_4$ in lyotropic liquid crystals made of poly(ethylene oxide)-poly(propylene oxide)-poly(ethylene oxide) block copolymers, water, and a small amount of surfactant (cetyltrimethylammonium bromide, CTAB) . According to these data, however, the lyotropic liquid crystals did not act as a true template, rather it provided an ordered structure confining CTAB as well as the nascent metal nuclei, which enhances the oriented attachment of nuclei and, thus, the consequent growth of single-crystal plates [13].

Metal-core polymer-shell nanoparticles were synthesized by a method in which block copolymer surfactant micelles are assembled around bare nanoparticles and then permanently fixed by chemical cross-linking of the copolymer [14]. For example, amphiphilic poly(styrene-block-acrylic acid) (PSt_{100}-b-$PAcrA_{13}$) copolymer [15] and dodecanethiol-capped gold nanoparticles ($d \sim 31$ nm) were initially dissolved together in a good solvent for both the hydrophobic (PSt) and hydrophilic (PAcrA) polymer blocks and the nanoparticles [16]. Gradual addition of water to this mixture induced the formation of a surfactant micelle around each nanoparticle. These gold-core@micelle-shell structures were then made permanent by cross-linking the polyacrylate block of the micelles. TEM images of the resulting nanoparticles dried from aqueous suspension show that each polymer shell contains exactly one nanoparticle and has uniform thickness. The polyacrylate is on the outside of the polymer shell because the system is in water and the polyacrylate block is hydrophilic or water soluble. This assumption is further supported by NMR data on encapsulated nanotubes [17] which show that the polyacrylate block is solvated in water and the polystyrene block is not. This cross-linked layer insures that, as the polystyrene shell swells or desolvates in response to changes in the

surrounding solvent, the polymer layer does not dissociate from the particle surface and the particles do not precipitate from suspension.

Templating can also be done against existing nanoparticles with a well-controlled shape. It is appropriate here to point out a difference between the preformed-seed-mediated method and the template method. In the preformed-seed-mediated method, a similar or identical seed particle becomes part of the resultant nanoparticle, whereas the template is often a dissimilar material that does not become part of the nanoparticle. For example, Djalali et al. [18] fabricated gold nanowires by using sequenced histidine-rich peptide nanowires as templates. The sequenced histidine-rich peptide molecules were assembled as nanowires, and monodispersed gold nanocrystals were uniformly coated on the histidine peptide nanowires with the high-density coverage.

Templating synthesis is a powerful method for the controlled synthesis of shaped nanocrystals; however, the available templates for colloidal synthesis of noble metal nanocrystals are still rather limited. In the classical seed-mediated synthesis of gold nanorods in the presence of CTAB, originally it was thought that the rodlike micelles formed by CTAB in aqueous solution would play the role of soft templates [19] but later on a more reasonable mechanism based on the preferential binding of CTAB to certain crystal faces of gold nanorods was put forward and became widely accepted [20]. It is worthwhile to search for other feasible colloidal templates for the shape-controlled synthesis of gold nanocrystals. In this regard, metal–surfactant complexes with desirable morphologies, which are formed by Au(I) or Au(III) and surfactants through binding interactions (e.g., aurophilic attraction and electrostatic combination), can be employed as reactive sacrificial templates for the shape-controlled synthesis of gold nanocrystals (metal–surfactant complex-templated synthesis).

Dendrimers are highly branched macromolecules with successive layers or generations of branch units surrounding a central core [21]. The characteristic tree-like structural attributes of this class of compounds give rise to unique intramolecular and intermolecular associations and templates. These functionalized materials have been utilized in the synthesis of nanoparticles [22, 23] and polymer nanocomposites [24]. The special properties of dendritic boxes make them useful in many applications, such as in drug release, molecular labels, probe moieties, and chemical sensors. Most of the dendritic containers reported so far use the concept of closing the dendritic box in order to keep the guest molecules inside the dendrimer host. Thus, many researchers have addressed this kind of core@shell structure by modifying the dendrimer surface, so that molecules can be reversibly imprisoned in internal cavities of the dendrimer and then site-selectively liberated by a suitable external or internal stimulus. For such applications, a shell should be "opened" and "closed" reversibly controlled by means of a simple external or internal stimulus, such as light, pH, or ionic strength [25]. Preformed nanoparticles that are modified with dendrimers or functionalized dendrimers could have improved biocompatibility, stability, and specific functionalities for biomedical application. Similarly, the dendrimer molecules assembled onto the preformed nanoparticles could be further chemically modified to achieve desired biofunctionalities for biomedical

applications. Depending on the dendrimer type and generation, they carry a positive, neutral, or negative charge on the surface. Once introduced into the systemic circulation, positively charged dendrimers and cationic macromolecules have been found to interact with blood components, destabilize cell membranes, and cause cell lysis [26].

4.2   Polymer

4.2.1   Polymer-Decorated NMNPs

4.2.1.1   Homopolymers

Direct synthesis of nanoparticles in solid matrixes is attracting increasing interest in terms of practical applications and synthetic challenges. Multilayered polymer films and block copolymer films [27] were used as stabilizers, templates, and/or nanoreactors for formation of noble metal nanoparticles. However, in some cases, these metal nanoparticles must be stabilized by ligands or surfactants in order to prevent their coagulation [28, 29]. Thiol chemistry has widely been used to modify the surface of gold nanoparticles with synthetic and natural polymers and biomacromolecules [30–33]. The gold–thiol bonds commonly used to attach biomolecules to noble metal nanoparticle surfaces are stable at room temperature but unstable to high temperature, competing biological thiols, and chemical cleaving agents [34, 35]. Therefore, metal@polymer nanoparticles of core@shell structures, which are stable in a variety of environments, including organic solvents and buffers, are extensively attractive.

Polymers such as poly(vinylpyrrolidone) (PVPo) [36], poly(amidoamine) [37], polyacrylate [38], polyacrylonitrile (PAN) [39], and polyacrylamide (PAM) [40] are also popular stabilizing agents. For example, Song et al. [41] used cationic polymer nanofibers to embed silver nanoparticles to reinforce the antimicrobial activity of the embedded silver nanoparticles. Tan and coworkers reported [42] the use of branched polyethylenimine (B-PEI) and 4-(2-hydroxyethyl)-1-piperazineethanesulfonic acid (HEPES) together to reduce silver nitrate under UV irradiation for the synthesis of silver nanoparticles. The resultant silver nanoparticles are positively charged as the B-PEI amino groups are protonated in the process. A few other polymer systems have been also developed for the stabilization of nanoparticles [43].

Another class of polymer (silver/polypyrole (PPy))-based silver composites were produced using microwave (MW) energy on the basis of interfacial polymerization. A water–chloroform interface was used under MW irradiation with no oxidizing agent. The silver nanoparticles produced were spherical, well dispersed, and approximately 20 nm in size [44]. $AgNO_3$ provided Ag^+ ions for the thermal polymerization of pyrrole. The ions were converted to PPy/Ag nanocomposites.

TEM images proved that the particles were about 5–10 nm in size. The PPy/Ag had a thick film, which could sense ammonia, hydrogen sulfide, and carbon dioxide at 100, 250, and 350 °C, respectively [45]. MW radiation and ethylene glycol can be used to synthesize silver powders from $AgNO_3$ at temperatures of 100–200 °C. After treatment, the powdered form was obtained in high yield (99%) with the diameters ranging from 0.15 to 1.8 µm; they grew in size and also aggregated. However, when poly(vinylpyrrolidone) was used in the mixture of $AgNO_3$, the particles ranged from 62 to 78 nm in diameter [46]. Citrate and PVPo are two popular surface-capping agents for silver nanoparticles and have different stabilization mechanisms [47], resulting in different behaviors in solution. For example, PVPo-capped AgNPs have been found to be more stable than citrate-capped AgNPs in both simple NaCl and $CaCl_2$ solutions [48]. Another unique attribute of silver nanoparticles is their dissolution when in aqueous solution, resulting in the potential release of bioavailable Ag^+ free ions [49, 50]. Relative to capping agents, PVPo-capped AgNPs are more prone to Ag^+ release than are citrate-capped AgNPs in river and lake water [51].

Another classic example is iron–silver bimetallic nanoparticles, which could be synthesized using microwave heating and an oil-soluble silver salt [52]. The silver nanoparticles were characterized through a series of tests, such as freeze-etching replication transmission electron microscopy (FRTEM), which revealed the nanoparticle diameter and distribution. Centrifuge tests (both normal and high speed) were conducted in order to determine the dispersion stability of the synthesized particles. The AgNPs were spherical in shape and had an average, uniform size of 30 nm [53]. Alcohols like ethanol coupled with poly(vinylpyrrolidone), at temperatures that exceed 120 °C, show that silver salts can be reduced into nanoparticles under MW irradiation.

$AgNO_3$ in an ethanolic medium along with PVPo under microwave irradiation was used to synthesize silver nanoparticles; a surface plasmon band at 416 nm indicated that silver nanoparticles have been produced after being exposed to MW irradiation. The nanoparticles were spherical in shape and had a diameter of ~ 10 nm. Their fluorescence band was noticed at 491 nm [54]. MW synthesis was used to prepare different kinds of nanosilver colloids. $AgNO_3$ was mixed with sodium citrate and then heated for varying durations of time at different temperatures. It was determined that the nanosilver colloids had a negatively charged surface when heated for a long period of time and a positively charged surface when heated for a short period of time [55]. UV–Vis and XRD analyses confirmed the formation of silver nanoparticles. Their phase was found to be an fcc system. The nanoparticles ranged from 15 to 25 nm and were evenly spread out in the PVPo matrix [56].

Poly(ethylene glycol) (PEG) was used to prepare stable silver colloids because it is eco-friendly reducing agent as well as a stabilizer. The particles produced were monodispersed with a diameter of less than 10 nm. These silver colloids worked against bacteria and fungi that were Gram-positive and Gram-negative [57].

Tan et al. [42] reported a synthesis of positively charged silver nanoparticles via photoreduction of silver nitrate in B-PEI/HEPES solution. Importantly, these

positively charged silver nanoparticles demonstrate superior surface-enhanced Raman scattering (SERS) activity over negatively charged silver nanoparticles for the detection of a variety of negatively charged analytes in aqueous solutions. Irzh et al. [58] proposed a method to prepare microwave-assisted coating of poly(methyl methacrylate) (PMMA) beads by silver nanoparticles. Microwave irradiation was found to be a new technique for coating of AgNPs onto the surface of PMMA beads. Bimetallic alloy nanoparticles consisting of two noble metals platinum–silver supported on carbon with a variable dimension were successfully prepared by ethylene glycol (EG), as reported by Hwang et al. [59].

Luo et al. have reported a new template method for the preparation of flexible silver/cross-linked poly(vinyl alcohol) (PVA) nanocables via one-step in situ reduction of Ag^+ and Ag^+-catalyzed cross-linking of PVA chains under hydrothermal conditions [60]. It is well known that PVA chains will turn to cross-link after treatment at high temperature (250 °C); however, hydrothermal treatment of PVA solution at 160 °C or even 200 °C cannot make it cross-linked. The cross-linked reaction that occurred at relatively low temperature in the presence of silver ions could be due to the close hydrothermal reaction conditions. The default experiments in the absence of silver nitrate show that PVA cannot be cross-linked, even under identical conditions. In addition, the rapid reduction of $AgNO_3$ into silver nanoparticles in the same solution with an identical concentration of PVA and then hydrothermal treatment at the same temperature for the same reaction period cannot produce such cables. These results demonstrated that the presence of $AgNO_3$ is essential for the formation of cables, and $AgNO_3$ indeed plays a key role as a catalyst for oxidation-reduction reactions such as that occurring in this system. In this process, PVA can be oxidized by $AgNO_3$ at 160 °C into cross-linked PVA, which is insoluble in water with a deep yellow brown color. The detailed time-dependent experiments indicated that the silver nanowires and irregular AgCl particles are formed in the early stage and then converted to Ag/cross-linked PVA nanocables.

The FTIR spectrum of the obtained nanocables is almost the same as that of pure PVA, which shows several absorption peaks located at about 3430, 2820, and 1600 cm^{-1}. However, there is a wide absorption peak from 1050 to 1100 cm^{-1}, which can be assigned as the absorption peak of σ_{as}(C–O–C) of the cross-linked PVA. It has to be pointed out that there may exist some ester in the product due to the presence of a peak at 1737 cm^{-1}. On the basis of the above analysis, the reaction that occurred under the present hydrothermal conditions can be illustrated as follows (Scheme 4.1).

For comparison, the reaction of $AgNO_3$ with less PVA under similar hydrothermal conditions leads to the formation of only silver nanoparticles with irregular shapes. Moreover, if less $AgNO_3$ was used and the amount of PVA was kept the same, no cables were obtained. In fact, the formation of such elegant nanocables is controlled by a synergistic growth mechanism, which was called as a synergistic soft-hard template mechanism (SSHM) (Scheme 4.2). It is clear that PVA is responsible for both the formation of silver nanoparticles and further oriented growth of silver nanowires stabilized by PVA; in turn, the silver wires act as a
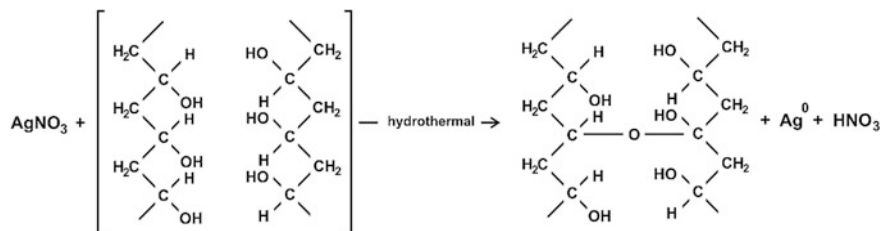
Scheme 4.1 Hydrothermal reaction scheme for the nucleation of silver nanoparticles [60]

backbone on which cross-linked PVA will form. In addition, the newly formed cross-linked PVA will act as an effective bridge to connect nearby single cables to form raft-like cable bundles in a parallel fashion, as observed.

The coordination of silver ions with NH_2 groups and its effect on the silver particle formation were studied in the next work in which silver ions served as weak cross-linkers to attach polymer chains [61]. Colorless floccular precipitates formed when commercial polyacrylamide (PAM) was added into the aqueous solution of silver nitrate at room temperature. Fast formation of silver nanoparticles occurred
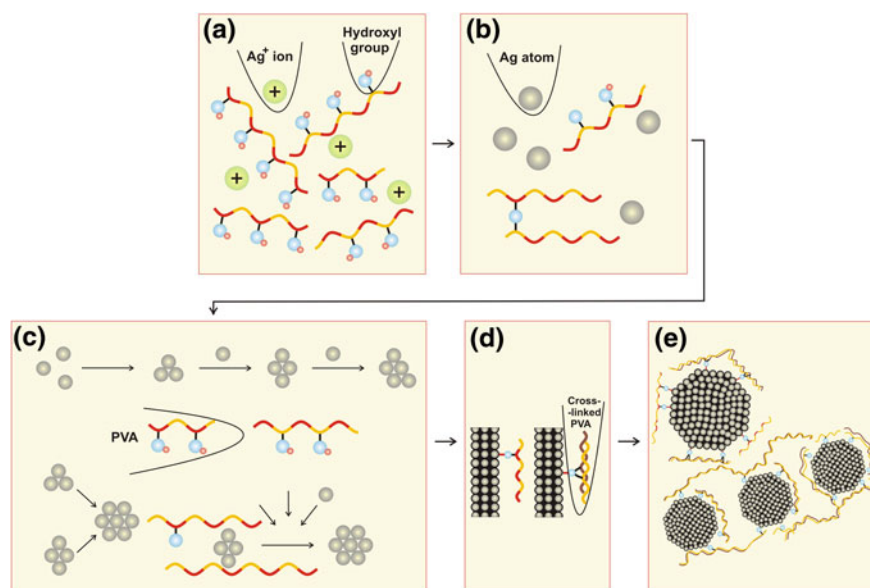
Scheme 4.2 Illustration of the formation mechanism of silver/cross-linked PVA nanocables. **a** The association of silver ions with PVA, **b** the formation of silver nanoclusters stabilized by PVA, **c** the aggregation of Ag nanoclusters stabilized by PVA , **d** the formation of Ag nanowires and the entangled cross-linked PVA on the backbone of nanowires (*side view*), and **e** further cross-linking of PVA results in the formation of single cables or parallel cables with bundle structure (viewed along the cable axis) [60]

upon exposing the above mixture to ambient (indoor) light. These observations highlighted the significant role that the polymer plays in the photoreactions during the particle preparation. Examination of the FTIR spectra confirmed that the product contained the PAM and excluded the presence of monomer acrylamide (AM). For the spectrum of the PAM-stabilized silver nanoparticles, the N–H stretching vibrations were observed at 3414 and 3188 cm^{-1}. The strong absorption at 1659 cm^{-1} can be attributed to the C=O stretching in the-$CONH_2$ group, and the shoulder around 1610 cm^{-1} to the NH_2 bending, which also indicates that PAM is stable under the reaction conditions. The frequency of the C=O stretching in Ag/PAM nanocomposites is shifted to 1659 cm^{-1} from 1670 cm^{-1} of that in commercial PAM or neat PAM, which implies the presence of coordination of silver atoms with the oxygen atoms in carbonyl group [62]. But no obvious shift of the absorption peak of N–H at 1610 cm^{-1} was observed. On the basis of the reports about surface chemistry of colloidal silver in aqueous solution [63], the silver atoms on the surface of nanoparticles are coordinatively unsaturated, and polyacrylamide serving as a nucleophilic reagent can donate an electron pair into unoccupied orbitals that exist on the surface [61]. Silver nanoparticles with nucleophilic molecules on the surface are very reactive toward oxygen and oxidative reagents, which lead to further complexation of surface atoms until the particle is whole or partly oxidized.

The XRD pattern of as-prepared particles shows broad peaks around 38° and 44° corresponding to (111) and (200) of the cubic silver structures. With increasing $AgNO_3$ content in the starting solution, the characteristic peaks of the resultant product became stronger. The broad peak at 2θ less than 40° is attributed to the noncrystalline polymer PAM, which also causes the higher uneven baseline. The XRD analysis further proved that Ag/PAM nanocomposites had been achieved with the simple route. The XPS spectra of the stabilized silver nanoparticles with all of the binding energies were referenced to C 1s (284.8 eV). The survey spectrum reveals the existence of C and O, which are, from reference, polymer stabilizer and absorbed gaseous molecules, respectively. Higher resolution spectra were also taken of the Ag 3d region. The binding energies of Ag $3d_{5/2}$ and Ag $3d_{3/2}$ of the passivated silver nanoparticles are 368.5 and 374.5 eV. No impurity peaks of pure Ag^+ and Ag_2O particles were observed.

The thermogravimetric (TG) analysis curves the AgNPs/PAM samples showed that there were three stages of mass loss for the thermal degradation of polyacrylamide, which is in agreement with that reported [64]. The first one involved a slight weight loss with temperature below 220 °C for the synthesized pure PAM, which is probably due to absorbed water from the environment and other volatile impurities [65]. For the composite samples with silver nanoparticles, a weight loss of around 15% could be observed in this region. Vilcu et al. [66] observed an 11% weight loss up to 200 °C, which they attributed to the release of both surface and matrix-bound water from the polymer. Herein, it is most likely that the presence of silver nanoparticles enhanced the water absorbance of PAM. The second one appeared in the range of 220–340 °C with the decomposition of pendant amide groups and the intactness of polymer main chains [67]. The observed values of weight loss are

around 20, 17, and 17% for samples a, b, and c (0 (sample a), 0.1 (sample b), and 1.0 g (sample c) of AgNO$_3$), respectively. The third one (340–450 °C) with 48, 32, and 30% of weight loss for the different samples, respectively, could be ascribed to the breakdown of the polymer backbones [67]. It is reasonable that the remaining weight increased with increasing the AgNO$_3$ content in the starting solutions.

A thermosensitive water-soluble polymer, poly(*N*-isopropylacrylamide) (PNIPAM) was also used for the immobilization, encapsulation, and stabilization of noble metal nanoparticles. Tenhu et al. used the grafting-onto method to coat gold nanoparticles with PNIPAM (molar mass 5000 g Mol^{-1}) chains of end-functionalized with SH groups [68]. Different reaction conditions were employed for the grafting, and it was found that again the single-step procedure, i.e., simply reducing HAuCl$_4$ and forming nanoparticles in presence of the PNIPAM-SH, was the most facile and successful way, leading to 2 nm gold cores covered with a dense layer of PNIPAM chains of thickness about 4.5 nm. This value is a bit higher than expected for a random coil confirmation of the PNIPAM chains, indicating that the grafted PNIPAM adopts an extended coil configuration. The small size of the gold nanoparticles formed under these conditions, corresponding to a large surface curvature and high surface area, underlines the efficiency of the PNIPAM-SH polymer chains as a stabilizer compared to conventional alkane thiols. Also, comparison with PEG-SH showed that the PNIPAM-SH is an even better ligand and stabilizer. It should be noted, however, that these PNIPAM-coated gold nanoparticles were not stable but still tended to aggregate even in highly dilute aqueous dispersions.

A similar core@shell particle architecture with a nanoscopic gold core and thermosensitive PNIPAM polymer shell was presented by Li and coworkers, who instead of grafting-onto used the grafting-from approach in terms of surface-initiated atom transfer radical polymerization (ATRP) as a controlled polymerization technique to grow a defined polymer layer from a gold nanoparticle surface [69, 70]. Here, the citrate on the gold particle surface first has to be replaced with a disulfide ATRP initiator via ligand exchange, before the polymer layer is grown by ATRP. Using this grafting-from approach, Li et al. prepared a very interesting multifunctional core@shell system: spherical gold nanoparticles with a thermoresponsive PNIPAM and poly(methoxy oligo(ethylene glycol) methacrylate) copolymer shell, which in aqueous dispersion show two transition temperatures near 33 and 55 °C, respectively [71]. It should be noted that also pH-responsive core@shell gold nanoparticles were prepared in the Li group by surface-initiated ATRP grafting-from of poly(4-vinylpyridine) (PVP) chains [72, 73].

In particular, two main strategies can be identified for the preparation of charged polymer (polyelectrolyte (PE)) template for gold nanoparticles, as illustrated in Scheme 4.3. In the first strategy (top panel), the gold salt is reduced in the presence of the polyelectrolyte—one-step route; in the second route (bottom panel), gold nanoparticles previously prepared are subsequently functionalized with the polyelectrolyte [74].
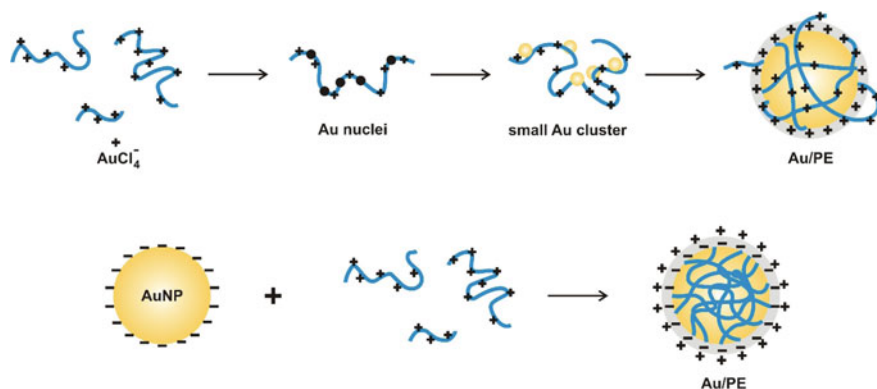
Scheme 4.3 Schematic representation of the two main strategies for the preparation of Au/polyelectrolyte (PE) assemblies [74]

Herein polymers have been used in one-step synthesis of polyelectrolyte-decorated gold nanoparticles either as reducing agents and/or colloidal stabilizers. In this case, the polymer chains form a protective shell around the nanoparticles preventing particle aggregation. There is a great diversity of polymers that can be used to produce surface-capped AuNPs with adequate chemical functionalities toward a specific (bio)application. Dumur et al. [75] listed the most used polymers in gold nanoparticles synthesis and stabilization, including poly(ethylene oxide), diamine-terminated poly(ethylene oxide), linear poly(ethyleneimine) (L-PEI) , amine-functionalised poly(propylene imine)dendrimers, poly(dimethyl-siloxane), PVPo, PVP, poly(allylamine) (PAlA) , and poly(allylamine hydrochloride) (PAH) . All these polymers are water soluble thus allowing the preparation of hydrosols of AuNPs. Gold nanoparticles have also been synthesized using biopolymers such as proteins [76] and polysaccharides (e.g., chitosan) [77]. These polymers are known as polyelectrolytes (PEs) and can be used as reducing/ stabilizing agents in one single-step syntheses. For example, PAH, PEI, and poly (diallyl dimethylammonium chloride) (PDADMAC) are cationic polymers commonly used to build shells around negatively surface-charged gold nanoparticles. However, these polyamines can also reduce the $HAuCl_4$ precursor and stabilize the resulting gold nanoparticles in a single-step process. Newman et al. [78] have shown that gold nanoparticles can be prepared using several amines: primary, secondary, and tertiary amines including aliphatic, aromatic, and aryl systems. The authors have also assessed the effect of the redox properties of the reducing agent on the thermodynamics and the kinetics involved. It was concluded that amines having a reduction potential between the potential of oxidation of Au^0 to Au^{+1} and the reduction potential of $HAuCl_4$ to Au^0 are good candidates to be used as reducing agents. It was proposed that for Au(III) reduction, three amine groups are necessary to transfer three electrons per metal ion, resulting in the formation of Au^0 (Eq. 1).

$$HAuCl_4 + 3NR_3 \rightarrow Au^0 + 3NR_3^{\cdot+} + H^+ + 4Cl^- \tag{1}$$
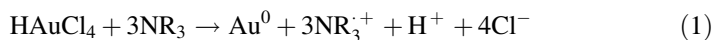
However, amines with reduction potential outside this range will not react with $HAuCl_4$ to form AuNPs.

In 2006, Sun et al. [79] reported the synthesis of gold nanoparticles using a series of polyelectrolytes: N-[3-(trimethoxysilyl)propyl] poly(ethylenimine) (Si-PEI), B-PEI, L-PEI, and PAH (Chart 4.1) with a molar ratio 4:1 of polyelectrolyte to $HAuCl_4$. The surface plasmon resonances ascribed to the ensuing AuNPs were observed at 519 nm (Si-PEI), 523 nm (B-PEI), 527 nm (L-PEI), and 524 nm (PAH), and the TEM images showed average particle sizes of

$$d_{Si-PEI} \approx 6\,nm; \quad d_{B-PEI} \approx 7\,nm; \quad d_{L-PEI} \approx 25\,nm \quad and \quad d_{PAH} \approx 9\,nm, \tag{2}$$

respectively. The different sizes of the nanoparticles prepared using these polyelectrolytes were attributed to the nature of the ions of the polyelectrolytes which create distinct confined microenvironments for the nucleation and growth kinetics of gold nanoparticles. A pictorial description for this mechanism is shown in Scheme 4.4 [79].

Besides the nature of the ions, the size of gold nanoparticles obtained by these methods also depends on the molar ratio of the polyelectrolyte and gold salt. Newman et al. [80] have also demonstrated the influence of the ratio [PAH]: [$HAuCl_4$] on the average particle size and have shown the influence of the concentration and ratio of PAH and $HAuCl_4$ on the kinetics of AuNPs formation. Depending on the reaction conditions, the generation of AuNPs was well controlled whose diameters varied from 5 to 50 nm and have also observed that by increasing the concentration of PAH, the rate of AuNPs formation increased. While for a 4.5:1 molar ratio, the particles ranged from 5 to 15 nm in diameter and exhibited a narrow SPR band at 530 nm, and for a 20.4:1 molar ratio, the particle diameter ranged from 35 to 50 nm and the respective optical spectrum showed a broad SPR band peaked at 600 nm. Sardar et al. have also reported the use of poly(acrylic acid) (PAcrA) as reducing agent to produce AuNPs with diameter about 2 nm whose SPR band was observed at 524 nm [81].

Chen et al. [82] have prepared gold nanoparticles with average diameter about 12 nm (λ_{SPR} = 522 nm) using PDADMAC as reducing/stabilizing agent.
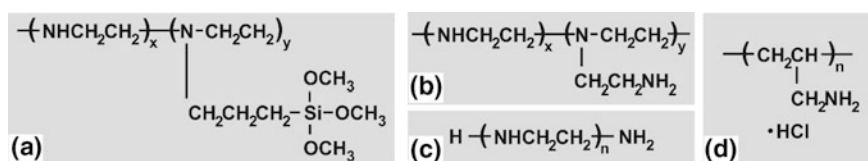
Chart 4.1 a Si-PEI, **b** B-PEI, **c** L-PEI, and **d** PAH
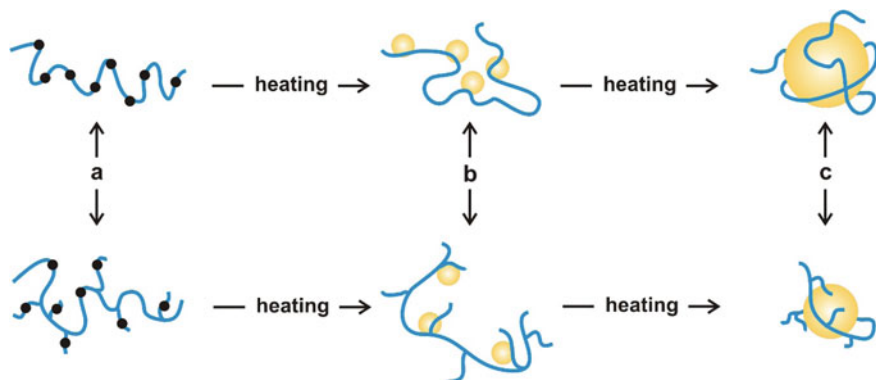
Scheme 4.4 Possible mechanisms of nucleation and growth of nanoparticles in distinct polyelectrolyte-confined microenvironments [74, 79]

Furthermore, the alkaline conditions were required for a successful synthesis. The rate formation of Au/PDADMAC nanoparticles was markedly influenced by reaction temperature. The one-step synthesis of AuNPs using polyelectrolytes shows that the AuNPs average size depends on the molar ratio between the polyelectrolyte and the gold salt. An increase of the particles' size is generally observed by increasing that ratio because the number of reducing agents available in the PE also increases. Thus, and according to the mechanism depicted in Scheme 4.4, the gold nuclei formed during the reaction grow into bigger nanoparticles. It has also been observed that the formation of AuNPs depends on the nature of the repeating units of the PE molecules. This is because the polyelectrolyte molecules can adopt different conformations and therefore the confined space available for particle nucleation and growth also varies.

The colloidal stability of gold nanoparticles can be achieved during the synthesis using stabilizers that also act as reducing agents or by postsynthesis treatment of those stabilizing agents. However, for bioapplications of AuNPs, further surface modification is required not only to provide higher stabilization in physiological medium but also to add functional groups necessary for biofunctionalization. The surface modification of particles using PE attached via electrostatic interactions is a very convenient method to promote the chemical functionalization of AuNPs. Indeed, the nanoparticle surface remains in this case coated with PE multilayers rendering stable colloids in aqueous medium. Möhwald and Caruso have reported pioneering work on this method using polystyrene latexes about 640 nm diameter as substrates [83–85]. Gittins and Caruso have also applied this method to AuNPs in order to obtain stratified shells of PE layers [86]. This stratified coating is obtained by a layer-by-layer deposition process using polyelectrolytes of opposite charges mediated by electrostatic interactions. Briefly, the coating of negatively charged AuNPs is performed by attaching a layer of a polycation onto the particles' surfaces followed by the deposition of polyanions. This deposition cycle is repeated until the required number of layers has been achieved in order to produce a

core@shell type structure (Scheme 4.5). A washing procedure in between each deposition step is employed in order to remove excess of polyions.

The resulting structures are typically characterized by zeta potential measurements because opposite zeta values after each layer deposition indicate the reversal of surface charge; visible spectroscopy can be also used to monitor the SPR band during the polyelectrolyte deposition because a small shift of the SPR band is associated with changes of the refractive index, which depends on the polyelectrolyte used [74]. However, a larger redshift of the SPR band ($\Delta\lambda > 80$ nm) might indicate interparticle interaction and aggregation. The building-up of stratified PE multilayers at the particles surface is mainly based on electrostatic interactions though it has been argued that other types of interactions may also be involved [85]. For example, some authors argue that the first deposited layer of polyamine displaces the protective surface species, such as citrate ions [87] or hexadecyltrimethylammonium bromide [88], due to the interaction between the gold nanoparticles and the groups of PE that are in excess. However, according to Dorris et al. [89], this does not always happen. Despite of the discussion regarding the mechanistic aspects involved in the adsorption of the first layer, this versatile and nonexpensive method has been employed using other types of substrates in which both the core and the PE can be combined into a variety of core@shell particles.

With regard to the polyelectrolyte, several combinations of polyanions and polycations both from natural resources and synthetic ones can be used to form the surface shells. The most common polycations are PAH, PDADMAC, and PEI, and commonly used polyanions are poly (sodium 4-styrenesulfonate) (PStS) and poly (acrylic acid) (PAcrA; see Chart 4.2) [74]. The shell thickness is adjusted by varying the number of PE layers coating the particle [90, 91]. This is clearly advantageous in developing optical-active gold nanodevices in which the optical signal depends on the distance of the particle to a specific target [92]. Similarly, ionized biomacromolecules can be used to functionalize the gold particles via electrostatic interactions at the surfaces, examples include polysaccharides [93], proteins [94], and nucleic acids [95, 96].

The optimal coating/stabilization of nanoparticles, i.e., the best adsorption of the polyelectrolyte onto the oppositely charged nanoparticles, depends on some key parameters such as the PE molecular weight (chain length), the nature of the
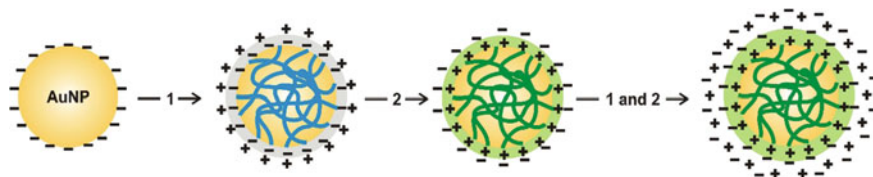
Scheme 4.5 Surface modification of nanoparticles using PE treatment, (*1*) polycation wash and (*2*) polyanion wash [74]
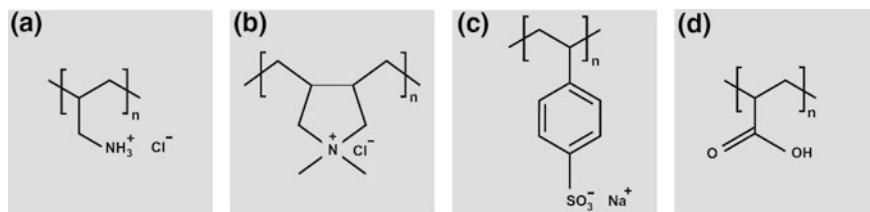
Chart 4.2 Common polyelectrolytes used in multilayered coated colloidal particles [74]: **a** PAH,
b PDADMAC, **c** PStS and **d** PAcrA

repeating units, the concentration and charge density of the polyelectrolyte, particle
size, concentration and surface properties (e.g., charge density) of the nanoparticle,
as well as the ionic strength, pH, and temperature of the medium. Understanding the
effects of the experimental conditions on the final assembly is a critical requirement
to yield stable colloids and to insure an efficient dispersion of nanoparticles after
coating and functionalization [97, 98]. Schneider et al. [99] have made significant
contributions to understand the influence of several parameters on the deposition of
PE onto AuNPs.

It has been observed that both short chains of polyelectrolyte and lower con-
centration of nanoparticles yield lower number of aggregates because bridging
flocculation is limited, while longer chains promote bridges between the coated
particles. On the other hand, high concentration of nanoparticles causes flocculation
via bridge formation due to shorter distances between the high number of
nanoparticles. Regardless of the molecular weight of PStS, for a high excess of PE,
a small shift on the SPR band has been observed while a decrease of the PEs/NP
ratio induced particle aggregation. This effect is monitored by determining the
recovery yield of nanoparticles after each adsorption step, i.e., the percentage of
isolated nanoparticles that can be obtained after centrifugation, and which decreased
when the PEs/NP ratio decreased and increased when the PEs/NP ratio was
increased. Moreover, as expected, for short chains of polyelectrolyte, fewer bridges
were formed but the recovery yield of NPs was smaller as well as the amount of
adsorbed polymer onto NPs. On the other hand, extensive particle aggregation
induced by bridging flocculation was observed for longer chains, lower polymer
concentration, and high content on NPs. As regards the influence of the ionic
strength on the colloidal stability of PE-coated (ten layers) AuNPs, this parameter
was investigated using NaCl solutions. The increase of the ionic strength caused
changes on the optical spectra of the gold colloids, by shifting the SPR band to
higher wavelength ($\Delta\lambda \sim 5$ nm) and by decreasing the optical absorbance, due to
aggregation induced by electrostatic screening effects. The magnitude of such
optical shift is higher for nanoparticles coated with fewer layers because the shell
thickness allows shorter interparticle distances and therefore stronger plasmon
coupling [74].

Although the AuNPs/PE assemblies are very often destabilized in solution of
high ionic strength, a number of bioapplications require the use of saline solutions

(physiological serum). Mandal et al. [87] have studied the dependence of poly-electrolyte conformation in systems of variable ionic strength used for multilayer deposition. The authors have prepared stable AuNPs/PE nanostructures and in Ringer's solution (a well-known medicinal solution) by promoting a multilayer coating based on PE dissolved in solutions of different ionic strengths (Scheme 4.6). First, gold@citrate nanoparticles dispersed in ultra-pure water were coated with five layers of PAH (M_w = 15,000 Da) and PStS (M_w = 4300 Da); in a second step, the subsequent layers were deposited using NaCl aqueous solutions containing the same PE. The increase of the ionic strength of the solutions used in the second step induced changes in the polyelectrolyte conformation, thus the PAH chains collapsed into a random coiled structure, which was found more effective in preventing bridging flocculation (Scheme 4.6) [74].

Another critical parameter to bear in mind in the preparation of AuNPs/PE assemblies is the pH due to the fact that the polyelectrolytes charge depends on pH. Indeed, this parameter plays a major role during the deposition of the layers as well as on the stability of the ensuing assemblies. Nevertheless, it must be emphasized that the medium pH during the layer deposition depends on the chemical surface of AuNPs (e.g., {Au@citrate}NPs, {Au@MUA}NPs, or {Au@DMAP}NPs) as well as on the type of PE used. Thus, Dorris et al. [89] have studied the influence of pH during the deposition of PStS on {Au@DMAP}NPs concluding that Au@DMAP were stable in the pH 5–12 range but optimum PE adsorption was found at pH 10. Also, Mayya et al. [100] have dispersed {Au@MUA}NPs in TRIS buffer pH 9 (MUA $pK_a \sim 4.6$) prior adsorption of PE (PDADMAC and PStS) in order to insure that the carboxylic groups of the surface coating (11-mercaptoundecanoic acid (MUA)) were fully ionized.

The building-up of multifunctional core@shell nanostructures is one of the great advantages of using PE assemblies [74]. A scheme of a multifunctional nanoparticle-based core@shell system is illustrated in Scheme 4.7 [101]. In this case, the PE forming the multilayers can be functionalized with drugs, organic dyes, contrast agents, radionuclides, catalysts, organic dyes, and proteins, namely anti-bodies, allowing the application of the ensuing structures in areas such as drug/gene delivery, biosensing, bioimaging, and photodynamic therapy [102–104]. Additionally, the core of the assemblies can be removed to produce hollow particles for the encapsulation of drugs and subsequent controlled drug delivery [105].
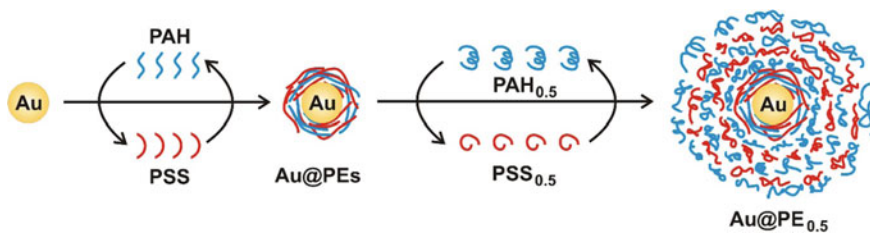
Scheme 4.6 Scheme of multilayer coating on AuNP (Au@PE—polyelectrolyte-covered gold nanoparticle) based on PE dissolved in solutions of different ionic strengths [74, 87]

In the next report, the ability of two chemically different polynorbornenes to stabilize silver nanoparticles was studied. The two cationic polymers, at two different molecular weights each, shown in Scheme 4.8, were made from oxanorbornene monomers via ring-opening metathesis polymerization (ROMP) following reports by Tew and coworkers [106, 107]. Polyguanidino oxanorbornene (PG) has a remarkable combination of potent antimicrobial activity and low membrane-disruptive properties. Its amino counterpart, polyamino oxanorbornene (PA), interestingly does not possess these properties [106]. Additionally, the cell-permeating activities of polyarginines [108], synthetic guanidinium-containing polymers [109], and, in particular, the PG reported here [110] have recently led to the development of several other polynorbornene derivatives that efficiently act as protein transduction mimics [111].

The size and the higher-order organization of the nanoparticles appear to be dependent on the type of cationic moiety present and the length of the polymer. Importantly, the silver nanoparticles synthesized in this report are also effective in catalyzing the reduction [113] of 4-nitrophenol to 4-aminophenol in the presence of excess $NaBH_4$ following pseudo-first-order kinetics. This reduction is unfeasible in the presence of the strong reducing agent, $NaBH_4$ without the nanoparticle catalyst. Since PG is water soluble and biocompatible [111].

Four different polymer-stabilized silver nanoparticles AgNP-PG-5K, AgNP-PG-25K, AgNP-PA-3K,, and AgNP-PA-15K were simply synthesized by reducing silver ion in aqueous solutions of the PA- or PG-type polymer. The absorbance maximum observed at 392–420 nm is characteristic of silver surface plasmon resonance [114]. Figure 4.1 (a left panel) shows the UV–Vis spectra of $AgNO_3$ (curve 1), aqueous PG-5K (curve 2), aqueous PG-25K (curve 3), colloidal
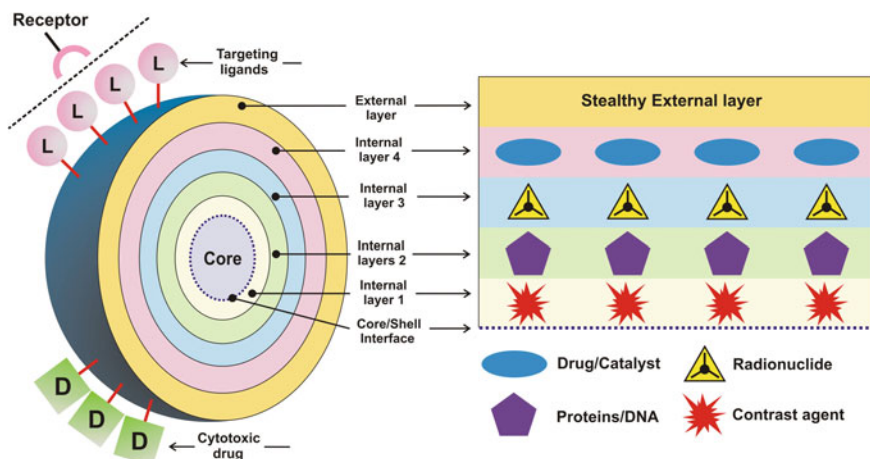
Scheme 4.7 Scheme of a multifunctional nanoparticle coated with PE multilayers (external and internal layers, template for various agents) saturated with various additives: drugs, contrast agents, radionuclides, proteins, DNAs, etc. [74, 101]
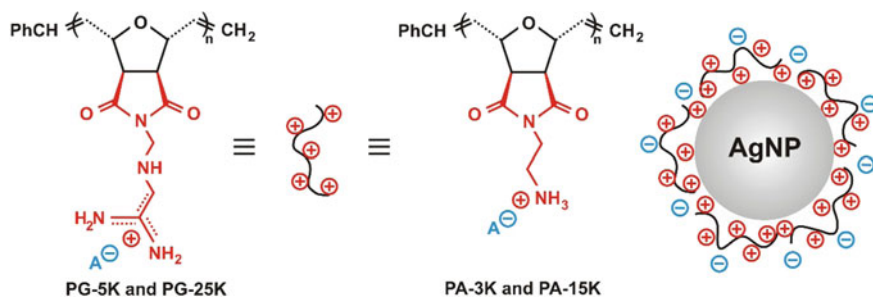
Scheme 4.8 Structures of polyguanidino oxanorbornene (PG, a *left cartoon*), polyamino oxanorbornene (PA, a *right cartoon*), and a cartoon of the AgNP stabilized by PG or PA. Counteranion (A⁻) = trifluoroacetate [112]

AgNP-PG-5K (curve 4), and colloidal AgNP-PG-25K (curve 5). In curve 1, there is only one signal at 301 nm characteristic of silver ion (Ag^+) in aqueous solution; in curve 2, the signal at 250 nm is characteristic of PG-5K in aqueous solution, and in curve 3, the signal at 250 nm is characteristic of PG-25K. For curves 4 and 5, there is only a dominant absorption maximum at 399 nm (absorbance 0.54) and 400 nm (absorbance 0.46), respectively, characteristic of colloidal AgNPs. This is indicative of AgNP-PG-5K (curve 4) and AgNP-PG-25K (curve 5) nanoparticles being formed. The dispersity of AgNPs was evaluated by comparing the full width at half maximum (fwhm) [115] from the UV–Vis spectra. The fwhm of colloidal AgNP-PG-5K and AgNP-PG-25K are ∼65 and ∼80 nm, respectively. This indicates that AgNP-PG-5K was relatively monodispersed and AgNP-PG-25K was relatively polydispersed [115]. Curve 1 is for silver ion (Ag^+) in aqueous solution, curve 2 is for PA-3K in aqueous solution with a characteristic signal at 250 nm, and curve 3 is for PA-1K in aqueous solution with a characteristic signal at 248 nm (Fig. 4.1, a right panel). For curve 4, there is one dominant absorption maximum at 410 nm (absorbance 0.50) characteristic of the colloidal AgNPs. The fwhm of colloidal AgNP-PA-3K is ∼85 nm. This indicates that the sample was relatively polydispersed [115]. For curve 5, the absorption maximum is at 393 nm (absorbance 0.07) with an additional shoulder at 485 nm. There is no evidence of the presence of Ag^+ ions in solution from the spectrum. However, the fwhm of colloidal AgNP-PA-15K is ∼130. This is indicative of the fact the AgNP-PA-15K (curve 5) is relatively polydispersed [116].

UV–Vis spectra shown in Fig. 4.2 demonstrate the stability of colloidal nanoparticles in aqueous solutions. Colloidal AgNPs have inherent tendency to oxidize in the presence of oxygen making them less attractive from the point of view of stability and shelf life [117]. In the presence of the PG polymers, AgNPs were moderately stable compared to PA-3K and PA-15K. In Fig. 4.2 (a left panel), the UV–Vis spectra of AgNP-PG-5K (curve 1), AgNP-PG-25K (curve 2), AgNP-PG-5K-1m (curve 3, sample 1 after 1 month), and AgNP-PG-25K-1m (curve 4, sample in curve 2 after 1 month) are shown. Absorption maximum of AgNP-PG-5K (curve 1) at 399 nm (absorbance 0.54) changes to 398 nm
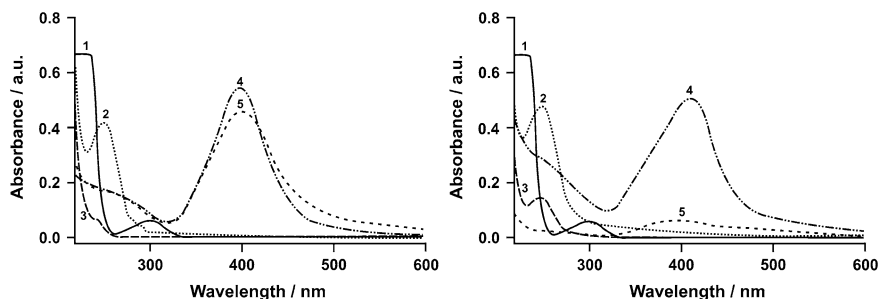
Fig. 4.1 UV–Vis spectra of (*1*) 10 mM AgNO$_3$, (*2*) aqueous PG-5K, (*3*) aqueous PG-25K, (*4*) AgNP-PG-5K, and (*5*) AgNP-PG-25K (*left panel*); (*1*) 10 mM AgNO$_3$, (*2*) aqueous PA-3K, (*3*) aqueous PA-15K, (*4*) AgNP-PA-3K, and (*5*) AgNP-PA-15K (*right panel*) [112]

(absorbance 0.48) (curve 3) after a month. In addition, the fwhm of colloidal AgNP-PG-5K changes from ∼65 to ∼61 nm after a month. Absorption maximum of AgNP-PG-25K (curve 2) at 400 nm (absorbance 0.46) changes to 398 nm (absorbance 0.39) (curve 4) after a month. In addition, the fwhm of colloidal AgNP-PG-25K changes from ∼80 to ∼75 nm after a month. The decrease in absorbance is about 0.06 units, and the shift in absorption position is not more than 2 nm in both cases. These slight changes indicate that some of the surface silver atoms are oxidized over the course of 1 month [118], but there is minimal size decrease and the AgNPs essentially remain relatively monodispersed. In Fig. 4.2 (right panel), the UV–Vis spectra of AgNP-PA-3K (curve 1), AgNP-PA-15K (curve 2), AgNP-PA-3K-1m (curve 3, sample 1 after 1 month), and AgNP-PA-15K-1m (curve 4, sample in curve 2 after 1 month) are shown. Absorption maximum of AgNP-PA-3K (curve 1) at 410 nm (absorbance 0.50) changes to 400 nm (absorbance 0.36) (curve 3) after a month. In addition, the fwhm of colloidal AgNP-PA-3K changes from ∼85 to ∼73 nm after a month. The decrease in absorbance is 0.14 units, and the shift in absorption position is 10 nm. These larger shifts indicate that surface silver atoms are oxidized significantly over the course of 1 month [118]. However, AgNP-PA-3K essentially remains relatively polydispersed. The absorption maximum of AgNP-PA-15K (curve 2) at 393 nm (absorbance 0.07) changes to 403 nm (absorbance 0.034) (curve 4), and the shoulder at 485 nm disappears after a month. In addition, the fwhm of colloidal AgNP-PA-15K changes from ∼130 to ∼74 nm after a month. This change indicates that in the course of a month, the large aggregates were dispersed to relatively larger AgNPs, and some surface silver atoms are also lost as Ag$^+$ ions due to oxidation [118]. It is worthwhile to mention here that we do not observe any absorption maximum for the dissociated silver ions (Ag$^+$) in Fig. 4.2 as they are under the detection limit.

The hydrodynamic diameter of AgNP-PG-5K was estimated to be equal to ∼18 nm (DLS). Three populations of the AgNP-PG-25K were found to be located in 0.6 nm (at 2% intensity), 2.0 nm (at 23% intensity), and 30 nm (75% intensity)
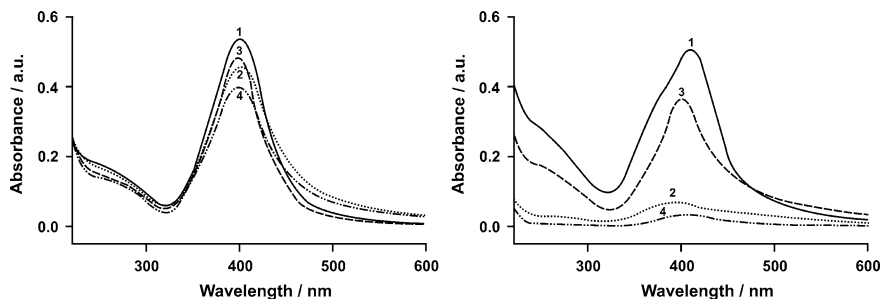
Fig. 4.2 UV–Vis spectra of: (*1*) AgNP-PG-5K, (*2*) AgNP-PG-25K, a month old solution of (*3*) AgNP-PG-5K-1m, and a month old solution of (*4*) AgNP-PG-25K-1m (*left panel*); (*1*) AgNP-PA-3K, (*2*) AgNP-PA-15K, a month old solution of (*3*) AgNP-PA-3K-1m, and a month old solution of (*4*) AgNP-PA-15K-1m (*right panel*) [112]

with a polydispersity index (PDI) of 0.175. Two populations were found for AgNP-PA-3K in 30 nm (at 88% intensity) and 158 nm (at 12% intensity) with a PDI of 0.339. Similarly, two populations were found for AgNP-PA-15K in 35 nm (at 68% intensity) and 2.0 nm (at 32% intensity) with a PDI of 0.090. The TEM images support all these distributions.

The surface plasmon resonance (SPR band) corresponds to the AgNPs size, and the redshift in the SPR band qualitatively indicates an increase in AgNPs size [119]. The absorption maxima of 399 nm for AgNP-PG-5K (Fig. 4.2) indicate the presence of roughly spherical AgNPs, and the corresponding DLS signal displays a size of 18 nm. Previous literature reports indicate that an SPR band of 402 nm corresponds to a diameter of $\sim$21 nm AgNPs [119]. Thus, UV–Vis absorption maximum of AgNP-PG-5K provides qualitative size distributions. However, the TEM image for the dried samples show agglomerates of small grains and some dispersed nanoparticles. In contrast, the other three sets of AgNPs reported here have two size distributions with wide polydispersity as indicated by DLS and therefore do not follow a clear trend corresponding to the SPR absorption maxima.

The changes in specific stretching and bending vibrations of molecules due to conjugation with nanoparticles can be observed by FTIR spectroscopy [120]. The characteristic signals responsible for the polymer–AgNPs interaction are C−N stretching (alkyl), N−H stretching, C–N stretching (aryl), and C=O stretching. The band at 1177 cm^{-1} in PG-5K is due to C−N stretching vibration of guanidino group and this band shift to 1198 cm^{-1} in AgNP-PG-5K. Only two N−H stretching vibrations of guanidino group appear at 3189 and 3364 cm^{-1} in PG-5K. In the corresponding AgNP-PG-5K conjugates, there are three distinct N−H signals which are seen at 3216, 3359, and 3437 cm^{-1}. The band at 1273 cm^{-1} in PG-5K is due to C−N stretching vibration of cyclic amido group and this band shift to 1319 cm^{-1} in AgNP-PG-5K. The C=O stretching vibrations of cyclic amido group appear at 1665 cm^{-1} in PG-5K. In the corresponding AgNP-PG-5K conjugates, this signal appears at 1675 cm^{-1}. The observed shifts, especially in guanidino C−N and N−H stretches, are indicative of the fact that PG-5K binds to the AgNPs surface facing

the guanidino group [120]. For PG-25K, the signals are C−N stretching vibration at 1180 cm^{-1}, N−H stretching vibrations at 3183 and 3357 cm^{-1}, C−N stretching vibration at 1275 cm^{-1}, and C=O stretching vibration at 1665 cm^{-1}. In AgNP-PG-25, the corresponding signals are C−N stretching vibration at 1198 cm^{-1}, N−H stretching vibrations at 3340 cm^{-1}, C−N stretching vibration at 1308 cm^{-1}, and C=O stretching vibration at 1658 cm^{-1}. These changes in the FTIR signals of PG-25 while bound to the AgNPs account for the interaction of the polymer with AgNPs [120]. Similar results were observed in AgNP-PA systems. The changes in the FTIR signals of PA are due to the complexation with the nanoparticles' surface [121].

The problem concerning of particle aggregation within the solution can be largely overcome by transferring the metal nanoparticles on to a polymer template [6]. Poly(vinyl alcohol) (PVA, Chart 4.3) could be considered as a good host material for metal nanoparticles, due to good thermostability and chemical resistance. Sodium poly(γ-glutamic acid) (PGA, Chart 4.3) , a water-soluble and biodegradable polymer, is a linear homopolypeptide made of only glutamic acid residuals in γ-peptide bond linkages with the degree of polymerization ranging from 1000 to 12,000. Each repeating unit of PGA contained one carboxyl group with specific affinity, which is useful for tissue culture and many food, biomedical, and industrial applications [7].

When the merely AgNO$_3$ precursor injected into the PVA solution, a very broad UV–Vis band appeared [122]. When the PGA-capped AgNO$_3$ solution added, it could be seen that the SPR absorption band exhibited sharper, peaking at about 380 nm (10 wt% PGA). The redshift of SPR peaks increased with the increasing PGA addition. The similar effect occurred in the silver/PVA nanoparticle film. However, the observed SPR peaks of films were higher than those of silver solution. As we know, from the shape of the SPR absorption peak, we can bear witness to the changes of the size distribution. If the nanoparticle in polymer is monodisperse, the peak shape is symmetric and the fwhm is small [123]. It is shown in Fig. 4.3, the PGA/PVA/Ag nanocomposite exhibited more symmetric band and narrower fwhm, suggesting that the size distribution of the silver nanoparticles is uniform and well dispersed. The redshift to the longer wavelengths and narrowing of the SPR

Poly(vinyl alcohol)   Sodium γ-PGA
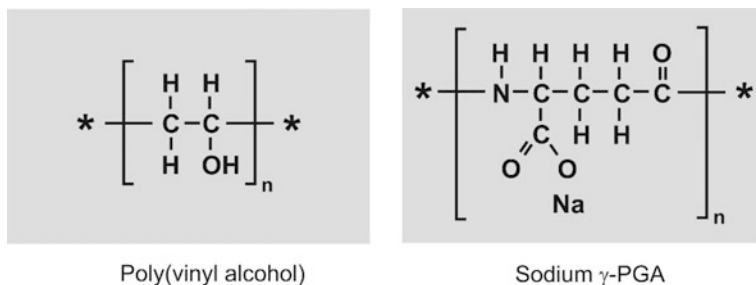
Chart 4.3 Chemical structure of PVA and PGA

absorption band upon incorporation of silver nanoparticles into PVA matrix could be induced by regular agglomeration in the presence of macromolecular PGA stabilizer.

The mechanism of silver nanoparticle-embedded PVA nanocomposite could be summarized as three steps. In the first step, the cationic silver ions (Ag^+) interact with negative carboxylic PGA–COO$^-$. In the next step, metallic complex into PVA solution is reduced to silver atoms and then nearby silver atoms aggregate at close range. The aggregates are the primary nanoparticles. Finally, the primary nanoparticles coalesce with other nearby primary nanoparticles or interact with PGA to form larger aggregates, which are the secondary (final) nanoparticles. During this process, PGA is expected to inhibit the further aggregation of silver nanoparticles and to stabilize the dispersed Ag nanoparticles in silver colloidal solution. That is, the silver nanoparticles should be encapsulated into macromolecular polymer-PGA. When PGA in the solution is varied from 5 to 10 wt% at constant AgNO$_3$ concentration, the number of silver ions that can interact with a molecule of PGA increases as the amount of PGA in the solution increases. As a result, the number of silver atoms presented at close range increases, hence increasing the average size of the silver nanoparticles. Manna et al. [124] described the silver nanoparticle formation mechanism using N-hexadecylethylenediamine as stabilizer. The result showed the more stabilizer induced, the bigger silver nanoparticle formed. The silver nanoparticles remain monodispersed and spheroid, due to the encapsulated effect of PGA. However, the status is dynamic, especially in the solution environment. The as-fabricated silver nanoparticles were easy to disassemble or reaggregate in the diluted solution, although stabilized with PGA. The presence of spherical silver particles with an average diameter of about 20 nm can be seen in a TEM image. Of all silver colloidal solution indicated no significant difference. The dissociation process of silver nanoparticles as the function of the extent of dilution was also described in Shin et al. [125] study. In a word, the reduction of silver salts with PVA in the presence of PGA with a longer chain leads to the formation of silver nanoparticles that are stable in solution. In particular,

Fig. 4.3 Absorption spectra of as-prepared silver/PVA solution (*1–4*) and nanocomposite films: (*1′*) PVA; (*2′*) PVA/Ag; (*3′*) 5PGA/PVA/Ag; and (*4′*) 10PGA/PVA/Ag [122]
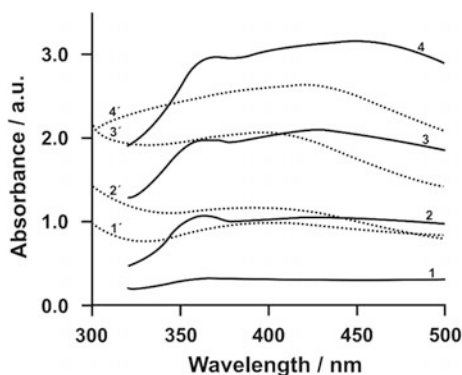
fabricated gel film results in sharper and more symmetrical UV–Vis spectra as well as to more stable dispersions.

In the UV–Vis spectra of the composite film (Fig. 4.3), the absorption band at around 414 and 421 nm appeared for 5PGA/PVA/Ag and 10PGA/PVA/Ag, respectively, which indicates that the $AgNO_3$ precursor in the film has changed into silver nanoparticles and agglomerated. Both of the silver/PVA nanocomposite films exhibited more symmetric band than that of PVA/Ag, suggesting that the size distribution of the Ag nanoparticles is uniform and monodispersed.

The SERS signals from the PGA/PVA/Ag were much stronger than that of PVA/Ag. Furthermore, the enhancement ability of 10PGA/PVA/Ag is estimated to be about 1.5 times higher than that of 5PGA/PVA/Ag. This result demonstrates that the SERS activity is related to the size and shape of the Ag nanoparticles. It has been reported that the largest achievable SERS enhancement was obtained for an average particle size in the range 100–150 nm [126]. The diameter of most spherical Ag particles on the 10PGA/PVA/Ag surface was in the range 80–100 nm, whereas irregular silver particles with 40–70 nm for PVA/Ag. This is an important reason for the strong SERS signals from the Ag nanocomposite film.

The prominent peaks at 2θ values of about 38° and 44° represented the (111) and (200) Bragg's reflections of face-centered cubic structure of silver, respectively. It could be seen that the PVA/Ag did not show the significant appearance of Ag^0 phase in the absence of PGA. Furthermore, the XRD intensity of PGA/PVA/Ag composite increased with the increasing PGA amount, thereby indicating PGA should be beneficial to form the Ag nanocrystal and responsible for the SERS performance.

The refluxing of the as-prepared powder to about 100 °C for a few minutes is considered good enough to generate desired colloidal solution. This, thus, avoided the generation of surface defects and the alteration in morphology. The word chemical treatment was still valid as the organic capping on the surface of the big particles would start dissociating in water (being water friendly in nature) and would start acting as growth terminating agent to smaller particles that would result from the loosely held outer surfaces or being trapped in the defective sites of the big particles. Thus, clear yellow solution indicated the initial formation of nanosilver which showed excellent absorption phenomenon under visible light. In view of this, surface-capped powder can be effectively converted to colloidal state via redispersion approach and can be subsequently loaded in polymer. Thus, synthesis of silver nanopowder by use of sodium citrate and sodium formaldehyde sulfoxylate (SFS) was carried out and the so-obtained powder was redispersed in water to generate silver colloids [127]. Sodium formaldehyde sulfoxylate is known to be a mild reducing agent with a sulfoxylate group that helps in terminating the particle growth and its use in the formation of fine silver powder. The use of these two reducing-cum-capping agents has resulted in the powder that has a crystallite size typically in the range of about 30–50 nm as confirmed by X-ray diffraction pattern. To stabilize these colloidal particles, it is again necessary to use suitable surfactants. In view of this, one can apply the polymeric matrices such as poly(vinyl alcohol) and polyvinylpyrrolidone to isolate the nanoparticles. It is observed that even when

the colloidal solution is loaded in PVA, the band at 275 nm remains unaffected thus further indicating that the capping is not affected adversely by loading the nanoparticles in polymer. Similar loading in PVPo, however, leads to broadening of the band at 400 nm and disappearance of the peak at 275 nm due to the fact that nitrogen hetero-atom present in the polymer may coordinate with silver ions because of the vacancy in the d-orbital of silver. The loan pair available in the nitrogen atom of PVPo would tend to make a temporary chemical bond thus reducing the number of silver ions, and, therefore, broadened absorption patterns at about 275 nm due to suppressed surface plasmon resonance are observed.

The UV–Visible spectrum (Fig. 4.4) of the yellow solution showed a well-defined surface plasmon resonance at ~ 400 nm in addition to a prominent band at about 275 nm. The band at higher energy, i.e., 275 nm is reported to be due to the formation of various types of silver ions such as Ag^{2+} and Ag^{3+} due to clustering. Such presence of silver ions in the present study confirms that the capping of the nanoparticles by citrate ion leads to better quality of the silver nanoparticles. The dispersion of the powder if leads to such multiple bands hints toward the effectiveness of the method. Ershov and Henglein [128] have reported the reduction of Ag^+ on polyacrylate in the aqueous solution and have studied the kinetic behavior of the reaction during the formation of Ag^+ ions. It was reported that the in situ produced Ag^+ ions were bound to the acrylate polymer through a chemical bonding which later helps the Ag^+ ions to get converted into the Ag^0.

The clear yellow solution produced can be casted into film easily to study the optical properties of silver nanoparticles. Thus, initial big particles can be loaded into the polymeric matrices leading to optical grade nanosilver via such as a dispersion chemical approach. The absorption spectrum of the film in PVA also showed the peaks due to silver ions at about 280 nm and a surface plasmon resonance band at about 420 nm which is shifted by about 20 nm in comparison with the values that are obtained in solution. The redshift of the absorption values in films is normally considered due to the aggregation of the particles during the film formation.

TEM analysis of as-isolated silver nanoparticles from the present method showed the particle size to be less than 30 nm. The morphology of the particles is

Fig. 4.4 UV–Visible spectra of silver nanoparticles generated by the redispersion of the powder in water alone and loaded in polymers, (*1*) Ag in water, (*2*) Ag@PVA, and (*3*) Ag@PVPo [122–125]
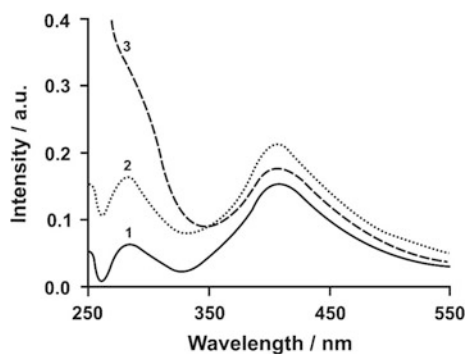
spherical with homogeneous distribution yet some clustering was observed due to the presence of capping agent. The electron diffraction analysis revealed all dull rings indicative of poor Bragg's reflections conforming to the amorphous nature of AgNPs. Particle size analysis was performed to understand the size distribution in as-prepared silver nanoparticles by the current method. Particle size distribution by dynamic light scattering technique (DLS) is in the range of 10–40 nm. The particles are monodispersed within a narrow range of about 25 nm without the presence of polymer. It is seen that the distribution of particles further narrows down between 5 and 10 nm showing that the particle nucleation can be controlled by the use of suitable polymers such as PVA and PVPo. The role of polymer for better surface protection of the nanoparticles is therefore highlighted.

4.2.1.2 Copolymers

Copolymers that have ion-exchangeable capacity can be used in many fields of science. These copolymers often used contained phosphonic acid groups and had a low molecular weight. The preparation route was based on an initial complexation of the polymer to metal cations, and then, the metal ions were reduced into nanoparticles. The metal nanoparticles were stabilized by an ion-exchange polymer. The surface morphology indicated that cubes and rectangular prism structures of silver were formed [129]. Copolymers such as cyclodextrin grafted with poly (acrylic acid) can be used to produce nanosized noble metal nanoparticles particles. These copolymers reduce and stabilize the silver ions that yielded AgNPs. The concentration of the alkali, $AgNO_3$, the copolymer, and the method of heating all played a role in determining the size of the gathered nanoparticles. Further experimentation proved that the silver nanoparticles had antibacterial properties [130]. Poly(methyl vinyl ether-co-maleic anhydride) (PVM/MAn) could be used as a reducing and stabilizing agent as well. The nanoparticles synthesized were stable at room temperature for up to a month and had a 5–8 nm coat of PVM/MAh surrounding them [131]. MAn-based copolymers consist of a wide variety of copolymers with diverse applications including compatibilizers and coupling agents with polyolefins and as thickeners, dispersants, and stabilizing agents. Herein factors involved in the synthesis, such as the acidity, initial concentrations of starting materials, and the molar ratio of the reactants were all varied. Some dispersing agents were used to keep the nanoparticles from accumulating and were analyzed for morphology, particle size, the elemental composition, etc. It was also determined that the nanoparticles were fcc structures, not aggregating, and very spherical in shape. The average particle was 10.2–13.7 nm in size, depending on what was used to reduce the ions (citrate or ascorbic acid). The zeta potential was from −40 to −42 mV and was influenced mainly by the nanoparticles acidity and size [115]. Formaldehyde, when reacted with ammonium hydroxide, forms a polymer that influences the way in which the silver attaches to the substrate, as well as the way it coats it. When there are no favorable conditions for the synthesis of the polymer, the nanoparticles formed will be concentric and will have a plasmon

resonance between that of gold and silver which occurs at 498 nm. By knowing this, the amount of formaldehyde used can be drastically decreased, by 100-fold, which would lead to a more environmentally friendly synthesis [132].

Poly(ethylene oxide) (PEO), poly(*N*-isopropylacrylamide) (PNIPAM), amine-functionalized polymeric dendrimer, template block copolymers, etc., have been used for the synthesis of core@shell gold nanoparticles structures [133–136]. Block copolymers, especially amphiphilic polystyrene-block-poly(ethylene oxide) (PSt-*b*-PEO) [137], polystyrene-block-poly(vinyl pyridine) (PSt-*b*-PVP) [138], and polystyrene-block-poly(acrylic acid) (PSt-*b*-PAcrA) [139, 140], have been used to prepare aggregation-free AuNPs. For example, poly(block comacromonomer)s consisting of a poly(2-vinylpyridine) and of a polystyrene block with the methacryloyl group attached to the poly(vinylpyridine) end were synthesized by the Schmidt group and used as templates for the formation of gold clusters and nanowires [141]. Arborescent polystyrene-graft-[poly(2-vinylpyridine)-block-polystyrene] copolymers were also applied to the preparation of gold nanoparticles [142]. Taton et al. prepared gold@polymer nanoparticles with cross-linked block copolymer micelles [14]. Shi et al. reported the synthesis of gold@polymer nanoparticles mediated with a triblock copolymer of poly(ethylene glycol)-*b*-poly(4-vinylpyridine)-*b*-poly(*N*-isopropylacrylamide) (PEG-*b*-P4VP-*b*-PNIPAM) by changing the pH or temperature of the triblock copolymer aqueous solution [143]. Yoo et al. [144] reported a simple, one-pot process for hydroxyl-functionalized gold nanocrystals with precise morphology control by a surface-regulating copolymer, poly(vinyl pyrrolidone-ran-vinyl acetate). A new class of amphiphilic polystyrene-block-polycysteine copolymers was synthesized and used to conjugate with AuNPs to inhibit particle aggregation [43]. Watson et al. [145] prepared hybrid nanoparticles with block copolymer shell structures by the use of transition-metal catalyzed ring-opening metathesis polymerization and surface-functionalized AuNPs. To enhance the stability of the surfactant layer of the AuNPs, chemically cross-linking the surfactant molecules has been investigated [34, 139, 146]. For example, PSt-*b*-PAcrA and PMMA-*b*-PAcrA were used as encapsulating amphiphiles, and the hydrophilic poly(acrylic acid) block of the assembled polymer layer was cross-linked using aqueous carbodiimide/diamine coupling [147]. Up to date, although many approaches have been suggested, there is still a strong demand for a simple, facile route to prepare stable gold@polymer nanoparticles.

Claiming that a high density of COOH-groups benefits the formation of fluorescent silver nanoclusters compared with short linear polymers, a star-like polymer with 36 arms, polyglycerol-block-poly(acrylic acid), was later used to prepare silver nanoclusters under similar conditions [148]. Nevertheless, also linear polyacrylates or polymethacrylates such as poly(methacrylic acid) can act as an excellent scaffold for the preparation of silver nanoclusters in water solution, by photoreduction with visible light [149], UV light [150] or sonochemically [151]. Molar ratios COOH: silver can be very flexible, 1:0.15–1:3, when using visible light as reported by Ras et al. [149]. Poly(methacrylic acid)-stabilized nanoclusters have an excellent stability (no visible changes for 3-year-old samples) [149], a high

quantum yield ($\sim$18.6%) [150] and can be transferred to other scaffolds [152] or solvents [153] and can sense the local environment [149]. The sonochemical process was as well successfully used with scaffolds as poly(acrylic acid) and poly-(acrylic acid-co-maleic acid) [151]. Silver nanoclusters formed in (meth)acrylates present in general a single emission band centered in the region from about 550 to 650 nm. Silver nanoclusters prepared in poly(methacrylic acid) exhibit electrochemiluminescence, also called electrogenerated chemiluminescence [149].

A PEO-based nonionic block copolymer (poly(ethylene oxide)-poly(propylene oxide)-poly(ethylene oxide) (PEO-PPO-PEO)) templates the synthesis of luminescent silver particles, with a mean diameter below 10 nm. The fluorescence can be observed even in the absence of the block copolymer, but the fluorescence intensity increases with the polymer concentration. It is claimed that the emission is caused by silver nanoclusters chemo-adsorbed on the nanoparticle surface [154]. For instance, silver nanoparticles with diameters of 10 nm can be coated by poly (4-vinylphenylboronic acid-co-2-(dimethylamino)ethyl acrylate) to obtain a fluorescent nanocomposite gel capable of sensing glucose [155]. The gel exhibits volume phase transitions induced by glucose, thereby changing the local refractive index of the medium surrounding the silver particles and producing changes in their fluorescent properties [155]. Another example of fluorescent metal nanoparticles are silver/gold bimetallic cores coated by a PEG-based hydrogel prepared with 2-(2-methoxyethoxy)ethyl methacrylate as monomer and poly(ethylene glycol) dimethacrylate as cross-linker. The reversible thermoresponsive volume phase transition of the PEG-based gel can modify the environment of the metal nanoparticles and hence their fluorescence intensity, facilitating application for sensing environmental temperature increases, offering a thermotriggered drug release and fluorescently imaging of cancer cells [156].

Oligo (ethylene glycol) methacrylate (OEGMA, M_n = 300 g mol^{-1}) was polymerized by reversible addition-fragmentation chain transfer (RAFT) polymerization [157, 158], yielding POEGMA ($M_{n,SEC}$ = 7300 g mol^{-1} and PDI = 1.08). The POEGMA was then chain extended in the presence of dimethylaminoethyl methacrylate (DMAEMA) in toluene (Scheme 4.9, Chart 4.4), yielding a diblock polymer (constituted by 15 units of DMAEMA). The diblock copolymer was then chain extended using RAFT dispersion polymerization of styrene to yield a triblock copolymer (Scheme 4.10). Similar copolymers were also used for the stabilization/reduction events and the formation of noble metal nanoparticles. The molecular weight shoulders of POEGMA-b-PDMAEMA-b-PSt triblock copolymers were observed at different polymerization times and were attributed to the formation of PSt—PSt radical coupling during the dispersion polymerization. All radical generated in these reaction systems take part in the reduction of metal salts. Similar observations were also noted in previous publication using dispersion polymerization [159].

SEC analysis confirmed the successful chain extension of POEGMA-b-PDMAEMA with a gradual increase of the molecular weight as the dispersion polymerization progressed (Figs. 4.5 and 4.6) [160]. The POEGMA homopolymer, POEGMA-b-PDMAEMA diblock copolymer, and POEGMA-b-PDMAEMA-b-PSt

triblock copolymers were all characterized by ^{1}H NMR. Characteristic signals of POEGMA homopolymer were observed between 4.3 and 3.3 ppm with dithiobenzoate end groups at 7.2, 7.5, and 7.8 ppm. After chain extension with PDMAEMA, new signals appeared at 2.55 and 2.30 ppm, consistent with methylene protons adjacent to the tertiary amino group and methyl protons on the tertiary amine besides POEGMA peaks in the mid-spectrum. After the final chain extension, the presence of aromatic protons of polystyrene at around 6.6 and 7.1 ppm confirmed triblock copolymer formation. ^{1}H NMR was also employed to estimate the molecular weight of the triblock copolymers. The molecular weight values determined by SEC were slightly lower than the values calculated via NMR:

$$M_{\text{n,NMR}} \times 10^{-4}/(\text{g/mol})/\text{time (h)} : 3.2/6,\ 3.7/12,\ 4.3/18,\ 4.4/24,\ 5.6/32 \text{ and } 5.7/40 \tag{3}$$

$$M_{\text{n,SEC}} \times 10^{-4}/(\text{g/mol})/\text{time (h)} : 2.2/6,\ 2.4/12,\ 2.9/18,\ 3.2/24,\ 3.7/32 \text{ and } 3.8/40 \tag{4}$$

$$\text{PDI/time (h)} : 1.3/6,\ 1.43/12,\ 1.45/18,\ 1.41/24,\ 1.43/32 \text{ and } 1.45/40 \tag{5}$$

The morphologies that formed during the dispersion polymerization were investigated by TEM and DLS measurements. Number-average particle sizes of the triblock copolymers were measured as 34 nm after 6-h polymerization time and 436 nm after 40 h:

$$d\,(\text{nm})/\text{time (h)} : 34/6,\ 45/12,\ 67/18,\ 78/24,\ 210/32 \text{ and } 436/40. \tag{6}$$

TEM images revealed morphology transitions with increasing monomer conversion (time), going from micelles to rodlike structures and then to vesicles (Fig. 4.7). The morphology progression was mainly influenced by the DPn of the PSt block (Fig. 4.7). Micelles were observed after the PSt block reached 200 repeating units, and finally, vesicles were formed with 440 PSt repeating units.

Di- and triblock nonionic copolymers based on poly(ethylene oxide) and poly (propylene oxide) were studied for the stabilization of nanoparticles in water at high ionic strength [161]. The effect of the molecular architecture (di- vs. triblock) of
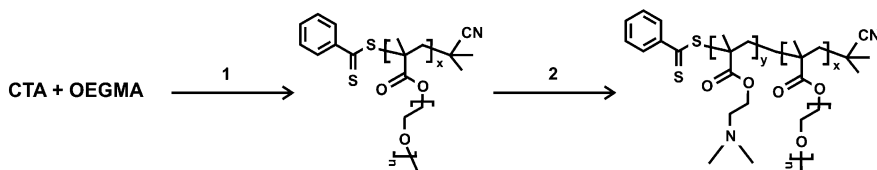
Scheme 4.9 Schematic illustration of POEGMA homopolymer (*1*, M/CTA/AIBN = 50/1/0.125, in acetonitrile) and POEGMA-*b*-PDMAEMA diblock copolymer synthesis (*2*, M-CTA/DMAEMA/AIBN = 1/500/0.2, in toluene, 70 °C) [157, 158]
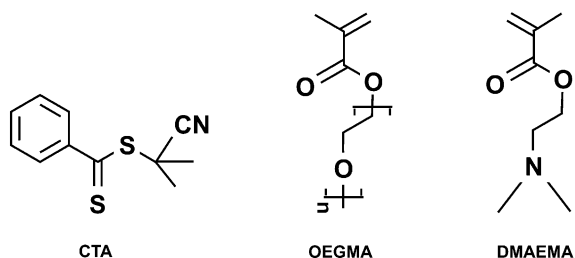
Chart 4.4 Chain transfer agent (CTA) (*1*), oligo (ethylene glycol) methacrylate (OEGMA) (*2*), and dimethylaminoethyl methacrylate (DMAEMA) (*3*)
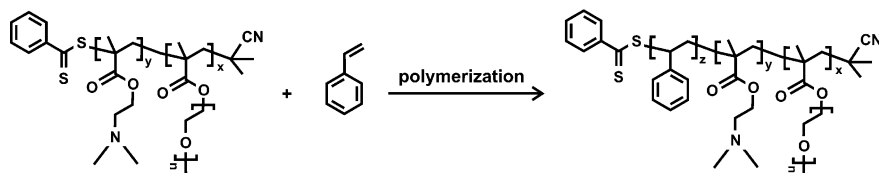
Scheme 4.10 Schematic illustration of dispersion polymerization of styrene initiated by AIBN in acetonitrile in the presence of POEGMA-*b*-PDMAEMA (M-CTA/St/AIBN=1/500/0.2) [157, 158]

these amphiphilic copolymers was investigated by using gold nanoparticles (AuNPs) as probes for colloidal stability. The results demonstrate that both di- and triblock copolymers can provide long-term stability and that in both cases AuNPs are individually embedded within globules of polymers. However, in the case of diblock copolymers, the colloidal stability was related to the formation of micelles, in contrast with the case of triblock copolymers, which were previously shown to provide good stability even at concentrations at which micelles do not form. Quartz crystal microbalance (QCM) experiments showed that the presence of the hydrophobic block in the structure of the polymer is important to insure quantitative adsorption upon a gold surface and to limit desorption. It was demonstrated that with an appropriate choice of polymer, the polymer/AuNP hybrids can also undergo filtration and freeze-drying without noticeable aggregation, which can be very convenient for further applications. Finally, preliminary studies of the cytotoxicity effect on fibroblast cells show that the polymer/AuNP hybrids were not cytotoxic. TEM micrographs on ultrathin sections of cells after incubation with the colloidal solutions showed that the nanoparticles were internalized into the cells, conserving their initial size and shape.

A thiol-reactive amphiphilic block copolymer poly(ethylene oxide)-block-poly (pyridyldisulfide ethyl methacrylate) (PEO-*b*-PPDSM) was used for coating gold nanoparticles [162]. The resultant polymer-coated AuNPs have almost neutral surfaces with slightly negative zeta potentials from −10 to 0 mV over a wide pH range from 2 to 12. Although the zeta potential is close to zero, the PEO-*b*-PPDSM

Fig. 4.5 SEC traces (*curve 1*: POEGMA, *curve 2*: POEGMA-*b*-PDMAEMA) [157, 158]
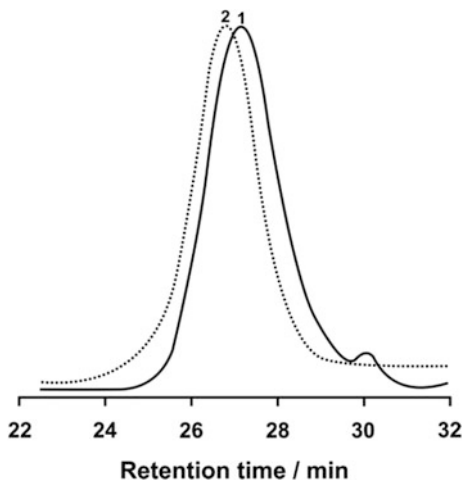
copolymer-coated AuNPs was shown to have both good stability in various physiological conditions and reduced nonspecific adsorption of proteins/biomolecules. It was reported that this copolymer confers three desirable characteristics. First, the multiple PDS groups on the PPDSM block interact with AuNPs through multiple Au–S binding sites so that stable and individually dispersed AuNPs in aqueous solution could be formed. Second, the resultant nanoparticles have neutral surfaces since there are no charged groups on polymer. Third, because of the multiple pyridyldisulfide groups on the PPDSM block, these individually dispersed nanocomplexes with an overall hydrodynamic size around 43.8 nm can be directly functionalized via disulfide–thiol exchange chemistry.
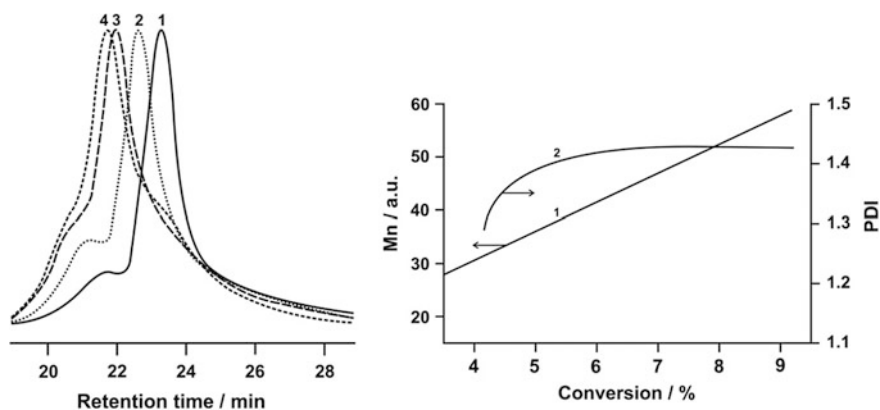
Fig. 4.6 SEC traces of the POEGMA-*b*-PDMAEMA-*b*-PSt triblock copolymers at different polymerization times (*curves 1–4*) (*left panel*); Evolution of molecular weight (*curve 1*) and PDI (*2*) versus monomer conversion (*right panel*) [160]
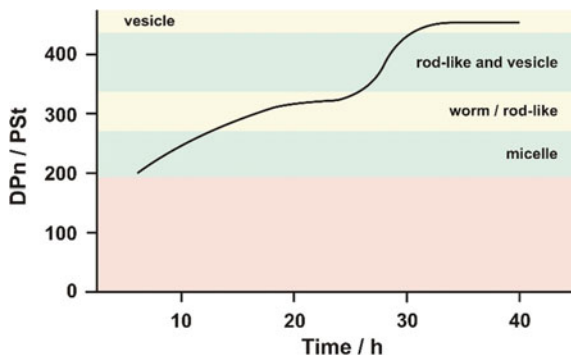
Fig. 4.7 Morphology progression by the DPn of the PSt block [160]

Two types of amphiphilic gold nanoparticles (AuNP-1 and -2) grafted with a mixture of poly(*N*-isopropylacrylamide) (PNIPAM) and polystyrene (PSt) chains in two different compositions have been successfully prepared with the "grafting-to" method in a homogeneous THF phase [31]. Langmuir monolayer experiments at the air–water interface of the two types of AuNPs revealed different compression isotherms of the surface pressure versus particle area (π–A curve) conducted at 20 °C. These amphiphilic gold nanoparticles can be regarded as analogues of amphiphilic diblock copolymers at the air–water interface. The compression isotherm of AuNP-2 with a PNIPAM:PSt ratio of 2:1 showed several characteristic regions that can be attributed to the polymer conformational transitions from the pancake, the pancake to brush transition, to the brush. However, the monolayer of AuNP-1, with a ratio of 5:1 of PNIPAM:PSt, never reaches a brush stage but showed an extension of the pseudo-plateau region upon compression. These differences may be due to the more hydrophilic nature and the more stretched PNIPAM chains. Furthermore, the sessile drop contact angle measurements, conducted at room temperature on both upper and lower surfaces of the AuNP-2 monolayer transferred at 35 mN/m onto either hydrophilic or hydrophobic substrates, are slightly different, $\sim$82° and $\sim$77°, respectively. After comparing with the literature data of the contact angles of water on either the pure PSt film or the PNIPAM brush, it was concluded that the chemically different PNIPAM and PSt chains grafted on the surface of the gold core tend to be phase-separated [31].

4.2.2 NMNPs-Decorated Polymer Structures

This structure consisting of the polymer core and metal shell is reverse to that was discussed above. Microgels of poly(*N*-isopropylacrylamide-co-acrylic acid-co-acrylamide), for example, can be used to template the formation of fluorescent silver nanoparticles [163]. The polyacrylamide fragments serve as

stabilizing ligands. Poly(acrylic acid) fragments induce a pH-sensitive volume phase transition of the gel by shrinking during protonation, resulting in an enhancement of the photoluminescence intensity. Whereas the PNIPAM component is used to induce temperature-responsive volume phase transition to control the size particle, it is suggested that the small silver nanoclusters can coexist with the large silver nanoparticles [163].

Poly(*N*-isopropylacrylamide-acrylic acid-co-2-hydroxyethyl acrylate) microgel particles as a scaffold were also used to form fluorescent silver nanoclusters. The microgel particles contain not only OH-groups but also COOH-groups. However, the acrylates only are claimed to be critical for the formation of nanoclusters. Additionally, the scaffold exhibits stimuli-responsive volume changes under variation of external factors such as temperature and pH, facilitating the application of nanoclusters. The nanoclusters were prepared with UV irradiation in molar ratio COOH:Ag of 1:1 [164]. Acrylates were already used for the synthesis of small silver nanoclusters by γ-irradiation, but no fluorescence was reported [128].

Infinite coordination polymer particles (ICPs) are a class of emerging functional materials that are formed by bridging repeating organic ligands with metallic nodes [165]. Over the past decades, the ICPs have attracted enormous research interest in chemistry and materials science, because they can be made from readily available and highly tailorable metal and ligand precursors, have chemically adjustable porosities and high internal surface areas, and provide with a network structure that can be deliberately and easily modified for many applications [166, 167]. The outstanding properties acquired have promised potential applications across various technological fields including various templates, gas sorption and separation, molecular sieving, drug delivery, photonics, heterogeneous catalysis, and biosensing [168–170]. A new path to design multifunctional ICPs materials has been opened up by the incorporation or integration of other functional materials into ICPs. However, few research involving in different types of metal nanoparticles (Au, Ag, Pt, etc.) incorporated into different ICPs structures has been reported. Accordingly, the key challenge herein is to determine appropriate methods that can help to generate the interaction between the incorporated metal nanoparticles and ICPs materials.

Lu et al. have explored a novel nanocomposite (AgNP-decorated thionine/ICP fibers)-based biosensor for detecting carcinoembryonic antigen (CEA) with low detection limit, and to developed a stable, sensitive, simple, and low-cost label-free immunosensor [171]. Infinite coordination polymer fibers were prepared by mixing aqueous $HAuCl_4$ solution, $AgNO_3$ solution, and ethanol solution of 1,10-phenanthroline at room temperature. The AgNP-decorated thionine/ICP (AgNP/THI/ICP) fibers are prepared by direct adsorption of preformed, negatively charged AgNPs onto the surface of ICP fibers. Thionine is used to adhere the AgNPs to the ICP fibers and acts as the redox probe. The AgNP/THI/ICP fibers not only favor the immobilization of antibody but also facilitate the electron transfer. The low magnification SEM image of the ICP fibers indicated that they consist of a large amount of one-dimensional (1D) structures about several tens of micrometers in length. The high magnification SEM image reveals that these 1D nanostructures

are fibers with widths in the range of 50–200 nm. The peaks of C, N, Au, and Ag determined by the energy-dispersed spectrum (EDS) indicate that they are formed from 1,10-phenanthroline, thionine, $HAuCl_4$, and $AgNO_3$. It is well known that nitrogen ligand can coordinate with Au(III) and Ag(I) [172]. The formation of such nanobelts can be attributed to coordination-induced assembly from Au(III) and Ag (I). The low magnification SEM image of the AgNPs/THI/ICP fibers indicates that they consist of a large amount of 1D structures about several tens of micrometers in length. The high magnification SEM image further reveals that such 1D fibers shrink together after the adding of thionine solution, due to the π–π stacking interactions of thionine. It is important to note that small nanoparticles are observed on the fibers, indicating that the citrate-stabilized AgNPs are adsorbed on the surface of the ICP fibers.

A large amount of very small silver nanoparticles is also observed on the THI/ICP fibers. The interplane distance calculated from the HRTEM image taken from one nanoparticle is 0.235 nm, corresponding to the (111) lattice space of metallic silver, indicating the nanoparticles are AgNPs [173]. It is observed that discrete dots in the electron diffraction pattern show that the silver nanoparticles are crystalline in nature [174]. The selected area electron diffraction (SAED) pattern has also been obtained by directing the electron beam perpendicular to one of the small particles. The hexagonal symmetry of diffraction spot pattern shown confirms that the particles are well crystalline, and its face is mainly indexed to (111) planes [175]. Both HRTEM image and SAED pattern confirm that the silver nanoparticles on AgNPs/THI/ICP fibers are single crystals.

The FTIR peak at 723 cm^{-1} is assigned to the in-planar swing of $(-CH_2-)_n$ ($n > 4$) [176]. The peak observed at 1414 cm^{-1} can be attributed to a totally symmetric stretching of the phenazine heterocyclic ring [177]. The characteristic N–H symmetric absorption bands in 1,10-phenanthroline occur at 3380 cm^{-1} [178]. These observations are consistent with the original composition of 1,10-phenanthroline. FTIR spectra of AgNPs/THI/ICP fibers are also measured. The characteristic N–H asymmetric absorption bands in 1,10-phenanthroline occur at 3526 cm^{-1}. The peaks at 2919 and 2851 cm^{-1} can be assigned to the symmetric stretching vibrations of $-CH_3$ group and $-CH_2$ groups, respectively [179]. The peak at 1330 cm^{-1} is attributed to the stretch of hydroxyl (–OH) of the carboxylic group [180], which is attributed to the citrate-stabilized AgNPs. As a result, FTIR spectra have demonstrated that the AgNPs/THI/ICP fibers contain the carboxylic group and primary amines ($-NH_2$), which can provide a favorable microenvironment for immobilization of various biomolecules or their fragments without additional immobilized reagent [171].

The differential pulse voltammetry (DPV) responses of bare glassy carbon electrode (GCE) , AgNPs/THI/ICP fibers-modified GCE (AgNPs/THI/ICP/GCE), anti-CEA-modified AgNPs/THI/ICP/GCE (anti-CEA/AgNPs/THI/ICP/GCE), BSA-modified anti-CEA/AgNPs/THI/ICP/GCE (BSA/anti-CEA/AgNPs/THI/ICP/GCE), and CEA-modified BSA/anti-CEA/AgNPs/THI/ICP/GCE were reported. The bare GCE exhibits a remarkable current peak about −100 μA in intensity at 0.16 V versus Ag/AgCl. After the AgNPs/THI/ICP fibers are coated on the surface of

bare GCE, the current peak is significantly increased to approximately $-112\ \mu A$, exhibiting the excellent conductivity of AgNPs/THI/ICP fibers. In contrast, when the electrode is modified with anti-CEA, the peak current is decreased due to the formation of an electron-blocking layer. Subsequently, the immunosensor is blocked with 1% BSA solution and then incubates in a solution containing CEA. It can be attributed to the insulating BSA and CEA protein layers on the electrode that retards the electron transfer [171].

Electrochemical impedance spectroscopy (EIS) is an effective tool for monitoring the interfacial properties of electrode during the modification process [181]. In the Nyquist diagram, the linear portion at the low frequencies and the semicircle portion at the high frequencies correspond to the diffusion-limited process and the electron transfer-limited process, respectively. The electron-transfer resistance (Ret) can be estimated from the diameter of a semicircle in an impedance spectrum. It is observed that the bare GCE exhibits a small semicircle at high frequencies with a diameter of 488 Ω and a linear part at low frequencies, which is characteristic of a diffusional limiting step of the electrochemical process on a bare GCE. After deposition of AgNPs/THI/ICP fibers, the Ret of 306 Ω is much smaller than that of the bare GCE, indicating that the AgNPs/THI/ICP fibers can promote the electron transfer. When the anti-CEA is adsorbed to the AgNPs/THI/ICP/GCE (anti-CEA/AgNPs/THI/ICP/GCE), the value of Ret increased to 867 Ω. The result is ascribed to the nonconductive properties of anti-CEA which insulates the conductive support and blocks the electron transfer. Similarly, after the capture of BSA and CEA, the values of Ret increase to 1328 and 1570 Ω, respectively. It is suggested that the formation of hydrophobic immunocomplex layer hinders the electron transfer. All these observations demonstrate that the AgNPs/THI/ICP fibers, anti-CEA, BSA, and CEA have been successfully assembled on to the GCE [171].

Metal-organic frameworks (MOFs) are another form of mesoporous materials that are thermally robust and in many cases highly porous. It is expected that the crystalline porous structures of MOFs limit the migration and aggregation of AuNPs. Thus, MOF-supported AuNPs have gained progressive attention since the first report by Fisher and coworkers in 2005 [182]. In Fisher's method, the precursor AuNPs are mixed with MOF-5 and loaded into MOF-5 both by thermal metal organic chemical vapor deposition (MOCVD) and photo-MOCVD. In addition, the MOF-5-encapsulated AuNPs were also prepared by solid grinding without organic solvent (Scheme 4.11) [183].

Such noble metal nanoparticles-decorated microcapsule (MC@NMNPs) structures are of both scientific and technological importance because of the wide range of potential applications [185–187], such as catalyst, controlled delivery of drugs, sensor, and imaging. The incorporation of metal nanoparticles in polymer microcapsules is an effective way to combine the unique optical, electrical, and catalytic properties of metal nanoparticles [188–190] with the novel encapsulation of microcapsules. Furthermore, the synergistic effect between metal nanoparticles and polymer microcapsules can overcome the shortcomings derived from nanoparticles and polymer materials and brings some positive impacts to the

resulting MC@NMNPs [191, 192]. The metal nanoparticle–polymer-decorated structures were shown to improve the mechanical and thermal performance of microcapsules, while MCs as the platform can enhance the stability and amphiphilicity of NMNPs, which significantly decreases the known aggregation of NMNPs [193]. For example, the Parak group incorporated both gold and Fe$_2$O$_3$ nanoparticles into the wall of a polyelectrolyte capsule to synthesize the light- and magnetic-responsive microcapsules, which was well-suited for in vitro delivery of drugs inside cells [194]. Because of the outstanding performance in catalysis, stability to oxidation, and surface plasmon resonance, noble metal nanoparticles, such as gold, silver, and platinum, are widely decorated on polymer microcapsules for the desired function. The remote control of bioreaction in the microcapsule modified by AgNPs or AuNPs was demonstrated by the Skirtach group [195].

As a result, much effort has been devoted to fabricate MC@NMNPs. Among the established methodologies, the typical way is usually composed of two steps: microcapsules were first prepared, and then metal nanoparticles were incorporated into microcapsules through in situ reduction or electrostatic-driven adsorption. Through the layer-by-layer (LBL) assembly, the Tsukruk group [196] and the Caruso group [197] prepared the polyelectrolyte microcapsules, which can adsorb the precursor of gold, and then embedded AuNPs into the wall of microcapsules through in situ reduction. Using AuNP with carboxy groups on the surface as a building block, Geest fabricated the stimuli-responsive multilayer AuNP/polyelectrolyte microcapsules through LBL [198].

To obtain MC@NMNPs structures through the efficient, convenient, and easy way, Liu et al. have developed a one-step approach based on the interfacial thiol–ene photopolymerization, in which microcapsules and metal nanoparticles are generated simultaneously by irradiation of ultraviolet (UV) light (Scheme 4.12, Chart 4.5) [199]. The in situ photoreduction of metal ions can minimize the number of processing steps in fabrication of metal nanoparticles [200, 201]. Using thiol groups containing POSS (PTPS) as a reactive surfactant, we fabricated the uniform-sized microcapsules through the one-step toluene/water interfacial thiol–ene photopolymerization (polyhedral oligomeric silsesquioxane (POSS) containing
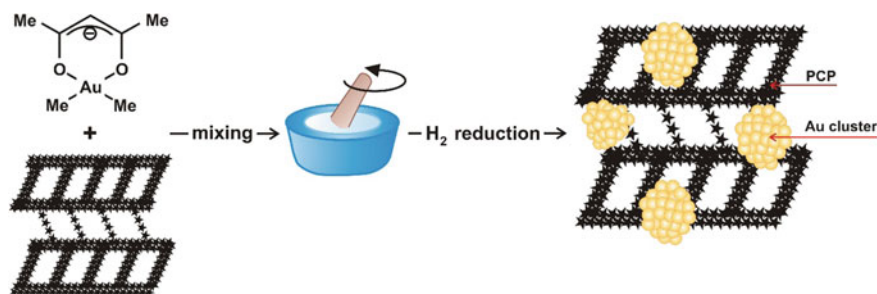
Scheme 4.11 Synthetic procedure of MOF-5-encapsulated AuNPs (*PCP* Porous coordination polymer) [183, 184]

thiol groups (PTPS)) [202]. This emulsion-based approach is very appealing for the large-scale fabrication of microcapsules. Through adding a metal precursor into the water phase, this approach can be successfully modified to prepare MC@NMNPs, which were fully characterized by SEM and TEM.

The whole strategy for the fabrication of MC@NMNPs is illustrated in Scheme 4.12. Toluene containing multifunctional trimethylolpropane acrylate (TMPTA) and photoinitiator IRGACURE 907 (I907) or ITX (2-isopropylthioxanthone) serves as the oil phase, while the metal precursor aqueous solution is used as the water phase (Chart 4.5). In the presence of PTPS as a reactive surfactant, the oil phase of toluene is emulsified into a water phase containing a metal precursor to obtain an oil-in-water (o/w) emulsion. As the reactive surfactant, amphiphilic PTPS is composed of the POSS skeleton, hydrophobic alkyl chains, hydrophilic poly(ethylene glycol) (PEG) chains, and thiol groups, which can participate in the thiol–ene polymerization. The star structure and high molecular weight provide amphiphilic PTPS as the excellent surfactant, which distributed at the interface of toluene/water. Upon exposure of 365-nm UV light, the radicals generated from photoinitiator system I907/ITX can be trapped quickly by the thiol groups of PTPS to form sulfur radicals, which then initiate polymerization of TMPTA (cross-linker) to form the cross-linked wall. Simultaneously, metal ions diffusing to the interface and adsorbed by the thiol groups of PTPS can be in situ reduced by the radicals to generate nanoparticles in the wall. Thus, NMNPs located at the outer layer of the wall of the microcapsule are covered by the hydrophilic PEG chains, while the thiol–ene cross-linked network of TMPTA forms the hydrophobic inner layer of the wall of the microcapsule. In this strategy, the emulsion droplets can serve as templates and guide the thiol–ene photopolymerization and photoreduction on their surface, resulting in the formation of MC@NMNPs structures.

Taking the formulation PTPS/TMPTA/toluene/HAuCl$_4$ = 1:0.85:48:5.0 as an example, the resulting MC-1@AuNPs aqueous solution turned wine-red and exhibited the characteristic plasmonic band absorption at around 526 nm, suggesting the formation of AuNPs [203]. SEM images revealed that MC-1@AuNPs took the typical morphology of the microcapsule and nanoparticles distributed at
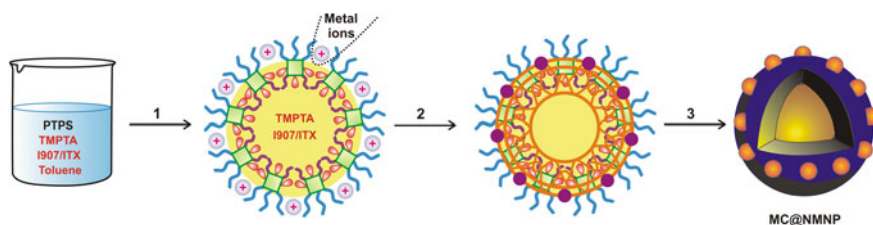
Scheme 4.12 Whole strategy to fabricate the microcapsules containing metal nanoparticles (MC@NMNPs): (*1*) formation of emulsion by adding metal salt aqueous solution and mixing of reaction solution, (*2*) UV irradiation starts the thiolene photopolymerization—in situ photoreduction, (*3*) toluene removing [199]

the surface of the microcapsule (Fig. 4.8). The average size of MC-1@AuNP is ~2.2 μm in diameter, with a low polydispersity index (PDI) of 0.10, and the wall is about 70 nm in thickness, which is determined by SEM analysis. The aspect ratio between the diameter of MC-1@AuNPs and the thickness of the wall is as high as around 30, indicating the thin wall. Generally, microcapsules with a thin wall always collapse and deform under the extreme vacuum conditions of SEM measurement [204]. The typical microcapsule morphology of MC-1@AuNPs is further supported by the atomic force microscopy (AFM) image. Even under the experiment condition of AFM without vacuum, AuNPs-MC-1 took the deformed morphology of microcapsules, which might be ascribed to the thin wall and high aspect ratio between the diameter and the thickness of the wall. DLS was also used to check the size distribution of MC-1@AuNPs in tetrahydrofuran (THF). As shown in Fig. 4.8, only one peak related to the microscale appeared in DLS curves, indicating that there are no free AuNPs in the solution and all AuNPs are fixed on the surface of microcapsules. The average diameter of MC-1@AuNPs determined by DLS is around 1.5 μm, with a low PDI of 0.05. DLS experiments revealed that MC-1@AuNPs is uniform, which is in good agreement with SEM observation. The size of MC-1@AuNPs determined by DLS is smaller than that determined by SEM, which might be explained by the deformed and flattened morphology of microcapsules in the SEM measurement.

The typical morphology of the microcapsule decorated with nanoparticles was further confirmed by TEM images. As shown in panels of Fig. 4.8, the deformed
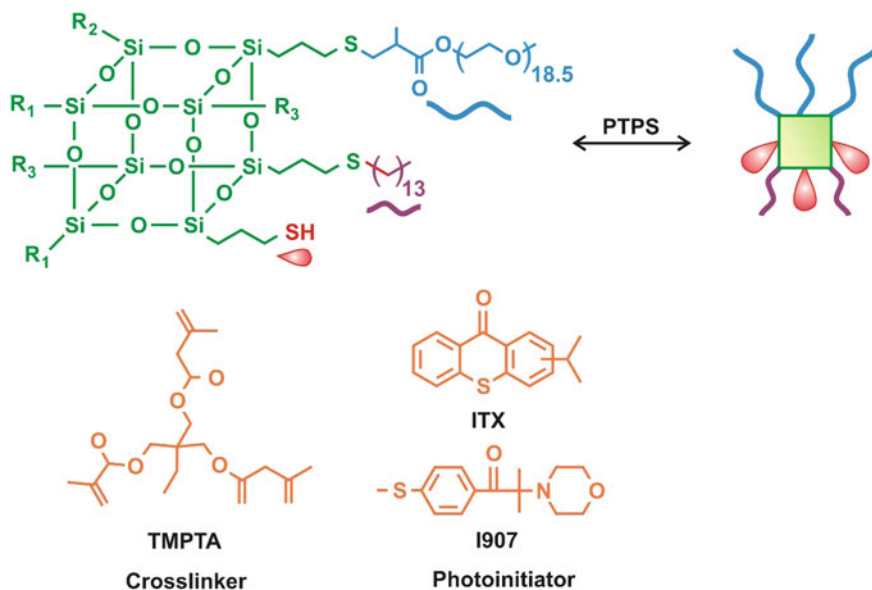
Chart 4.5 Chemical structure of the reactive surfactant (PTPS), acrylate cross-linker (TMPTA), and photoinitiator system (ITX/I907, I_{photo}) [199]

microcapsules are covered by gold nanoparticles with a size of ∼25 nm. No nanoparticles appear in the background of the TEM image, and all nanoparticles are completely fixed in the microcapsules, which are in good agreement with DLS results. This might be ascribed to the advantages of in situ photoreduction of Au ions in the wall of the microcapsule [200, 201]. Because radicals are produced only in the toluene phase and trapped by PTPS at the interface, ions cannot be reduced in the water phase and metal nanoparticles are generated only in the wall of microcapsules. It should be noted that, although the thickness of the wall is thin, MC-1@AuNPs kept the well-defined morphology and was not destroyed, even under the extreme vacuum conditions in SEM and TEM measurements.

During the formation of MC-1@AuNPs, the thiol−ene photopolymerization of TMPTA and the photoreduction of gold ions were traced by Fourier transform infrared spectroscopy (FTIR) and UV–Vis spectra, respectively (Fig. 4.9). After irradiation of 365 nm of UV light for 2 h, the peak of 1636 cm^{-1} assigned to C=C of TMPTA almost disappeared, indicating that the cross-linked wall of the microcapsule can form in 2 h. As shown in Fig. 4.9, the characteristic plasmonic
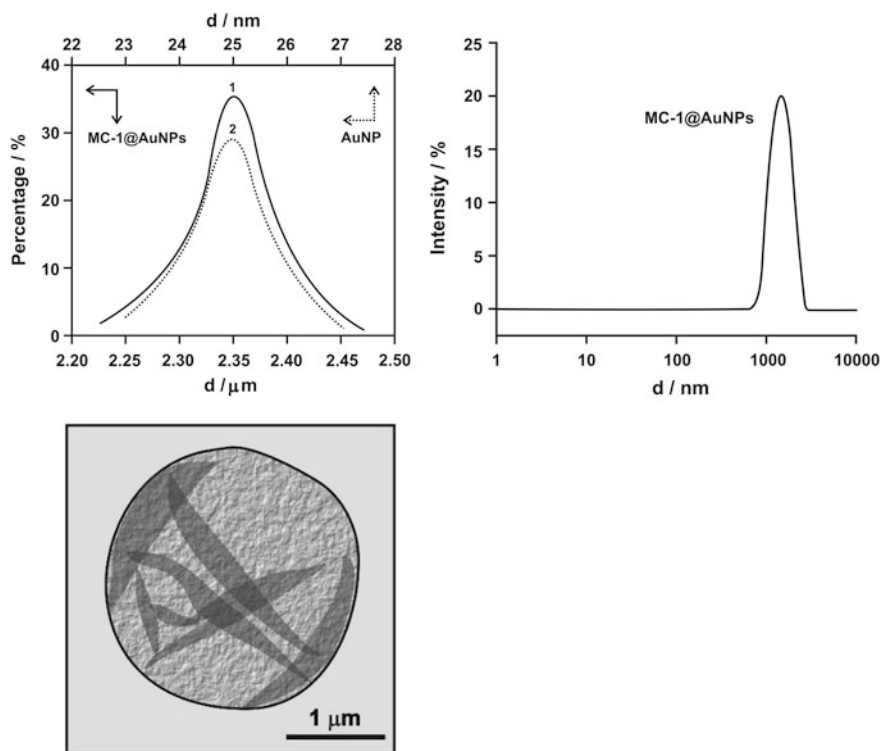
Fig. 4.8 Size distribution histograms of MC-1@AuNPs determined by SEM images and AuNPs determined by TEM images (*top left*, *curves 1* and *2*). Size distribution of MC-1@AuNPs in THF determined by DLS (*right panel*). TEM image of MC-1@AuNPs (*bottom panel*) [199]

bond absorption of AuNPs at 526 nm did not appear at the beginning of UV irradiation for 1 h and then increased gradually with the continuing irradiation in the following 5 h. The in situ photoreduction of gold ions is obviously slower than the thiol–ene photopolymerization. This can be explained by the fact that the active radicals generated by irradiation first participated in thiol–ene photopolymerization to produce the cross-linked wall then reduced gold ions to generate AuNP.

The possible mechanism for the preparation of MC-1@AuNPs via one step involving the thiol–ene polymerization and photoreduction was proposed in Scheme 4.13. As the good type II photoinitiator and photosensitizer, ITX was excited to the excited state by 365 nm UV light irradiation, which can produce radicals through two approaches (Scheme 4.13a). In the presence of the hydrogen donor, such as amino and thiol groups, the excited state of ITX can abstract hydrogen to produce the active radical derived from amine, thiol, and another ketyl radical from ITX. Because of the steric hindrance and delocalization of the unpaired electron, the ketyl radical is usually not reactive to the vinyl monomer and cannot initiate polymerization of TMPTA. The type I photoinitiator I907 can also be sensitized by the excited state of ITX to produce two types of active radicals. Except for ketyl radicals, all active radicals can be quickly trapped by –SH of PTPS (Scheme 4.13b). The thiol–ene reaction proceeds only at the interface via a radical step-growth polymerization manner, and the excess acrylate continues to polymerize through homopolymerization. After almost all acrylate groups are polymerized, the active radicals as well as ketyl radicals reduce gold ions to produce AuNPs (Scheme 4.13c). The reduction happens at the water–toluene interface, where the gold ions in the water phase can diffuse to the interface because of the complexity between sulfur of PTPS in the interface and Au ions. Although the ketyl radical of ITX is not active, Galian et al. [201, 205, 206] have proven that it can reduce noble metal ions and change back into the ketone. As for this point, ITX can diffuse to the interface and act as a catalyst for the photogeneration of AuNPs.
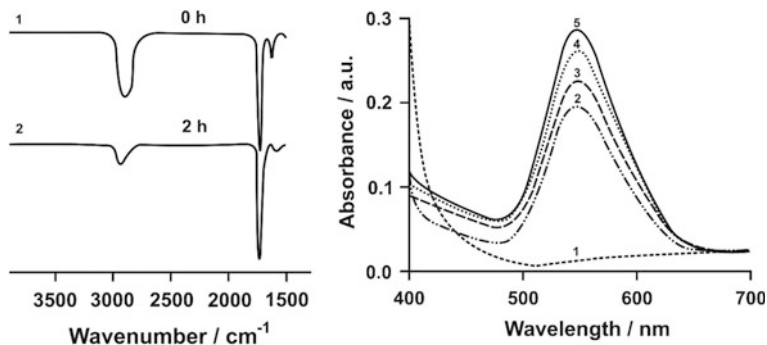
Fig. 4.9 FTIR spectra of MC-1@AuNPs exposed under a 365-nm UV light for different times: 0 and 1 h (*left panel*), UV–Vis kinetics curves [50 min (*curve 1*), 110 (*2*), 230 (*3*), 320 (*4*), and 440 (*5*)] of the preparation of MC-1@AuNPs under irradiation by 365-nm UV light (*right panel*) [199]
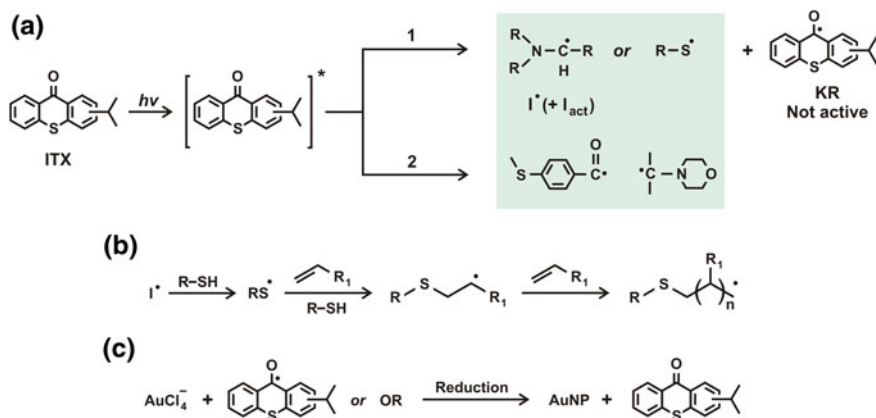
Scheme 4.13 Proposed mechanism involving in the processes for generation of MCs@NMNPs:
a Toluene phase: Generation of free radicals from the photoinitiator system I907/ITX, Interface:
b Radical mediated thiol–ene polymerization for the formation of the cross-linked wall of
microcapsules, and **c** Generation of metal nanoparticles through the reduction of metal ions by free
radicals, I_{act}—active radicals, OR—other radicals [199]

Therefore, both photopolymerization and photoreduction take place only at the
water–toluene interface, which is the key factor to the successful preparation of
MC@AuNPs through a one-step approach.

Through changing the concentration of HAuCl$_4$ or replacing HAuCl$_4$ with
AgNO$_3$ or H$_2$PtCl$_6$, microcapsules decorated with AgNP, PtNP, and the smaller
AuNP can be obtained. As for all MC@NMNPs, the formulation, size in diameter
and thickness of the wall for the MCs, and size of NMNPs varied as follows: size of
AuNPs varied from 3.1 to 25.2 nm, MCs from 2.2 to 2.7 μm, and wall thickness
from 40 to 70 nm. SEM and TEM images showed that the typical morphology of
the microcapsule is covered with the nanoparticles and all metal nanoparticles are
fixed on the surface of microcapsules. The diameter of AuNP and the thickness of
the wall for MC-0.5@AuNPs (1:0.85:48:2.5, the feed ratio refers to the weight ratio
of PTPS/TMPT/toluene/metal precursor) are ∼5.9 and about 50 nm, respectively.
In comparison with MC-1@AuNP, (1:0.85:48:5.0) the less and smaller AuNP for
MC-0.5@AuNPs should be ascribed to the low concentration of HAuCl$_4$ in
preparation, which is also reflected by the thinner wall of MC-0.5@AuNPs. This
indicated that the size and amount of AuNP on the surface of the microcapsule
might be tunable by this strategy. The solutions of MC-1@AuNPs and
MC-0.5@AuNPs are wine-red and purple-red, respectively, suggesting the different
sizes of AuNP.

As for MC-0.5@AgNPs, the diameter of AgNP and the thickness of the wall are
∼13 and ∼45 nm, respectively. Upon exposure of UV light, the solution of
MC-0.5@AgNPs became orange and exhibited the characteristic SPR of Ag
nanoparticles, suggesting the generation of AgNPs (Fig. 4.10). The size of PtNP in
diameter and the thickness of the wall for MC-0.5@PtNPs are ∼3.1 and 40 nm,

respectively. Because of the weak SPR of PtNP, the color of MC-0.5@PtNPs solution is yellow and does not change obviously with the irradiation of UV light. The size dependence of NMNPs upon the different metals might be ascribed to the difference in the ability of the sulfur radicals at the interface to reduce different metal ions. The other factor might be that the diffusion of metal ions from the water phase to the interface is dependent upon the type of metal ions or the numbers of NMNPs in each capsule. These factors might mainly cause the different sizes of various metal nanoparticles. The signals assigned to Au, Ag, and Pt observed in the X-ray photoelectron spectroscopy (XPS) spectra of MC-0.5@AuNPs, MC-0.5@AgNPs, and MC-0.5@PtNPs confirm the presence of metal nanoparticles. In comparison with AuNP@MC-0.5, the higher weight retention in the thermogravimetric analysis (TGA) curve of MC-1@AuNPs suggested the high content of gold nanoparticles, which is in good agreement with the observation in SEM and TEM images.

Because of the hydrophilic outer layer of PEG, the obtained MC@NMNPs can be well dispersed in aqueous solution. For example, no obvious aggregation occurred in MC-1@AuNPs aqueous solution when it was kept for 1 month at room temperature. To test the catalysis performance of MC-1@AuNPs, the reduction of 4-nitrophenol (Nip) was chosen as the model reaction (Scheme 4.14) [112, 207, 208]. As shown in Fig. 4.11 (left panel), the strong absorption peak of 4-nitro-3-(trifluoromethyl)-phenol (CF$_3$Nip) at 394 nm decreased gradually after adding MC-1@AuNPs, while simultaneously, a new peak appeared at 317 nm, which should be assigned to the product 4-amino-3-(trifluoromethyl)phenol. Because the concentration of sodium borohydride largely exceeds the concentration of nitrophenol, first-order rate kinetics with regard to the nitrophenol concentration could be used to evaluate the catalytic rate [112]. The conversion of the catalytic reduction process can be obtained by the ratio of the respective absorption A/A$_0$, and the apparent rate constant k_{app} is calculated from the linear plot of ln(A/A$_0$) versus reduction time. As shown in Fig. 4.11 (right panel), k_{app} for CF$_3$Nip and Nip
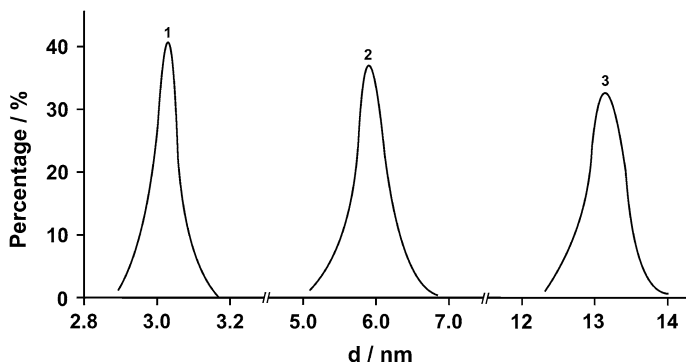
Fig. 4.10 Size distribution histogram of NMNPs decorated on PtNP@MC-0.5 (*1*), AuNP@MC-0.5 (*2*), and AgNP@MC-0.5 (*3*), respectively [199]

Scheme 4.14 Proposed scheme of the reduction of Nip and CF3Nip by a reducing agent in the presence of MC-1@AuNPs [199]
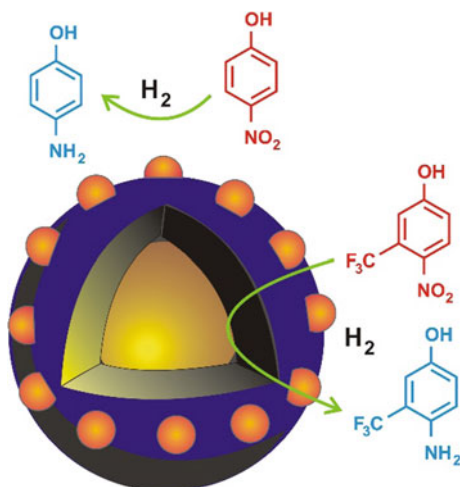
are 0.29 and 0.25 min^{-1}, respectively. The higher k_{app} for CF$_3$Nip might be ascribed to the encapsulation of the hydrophobic CF$_3$Nip by MC-1@AuNPs in aqueous solution. As proposed in Fig. 4.11, the encapsulation of CF$_3$Nip can increase the local concentration of CF$_3$Nip and accelerate its adsorption on the surface of AuNPs, resulting in the enhancement of the reduction speed. The excellent catalytic stability might be explained by the fact that AuNPs are well decorated in the wall of the microcapsule, which can decrease their aggregation during reaction (Scheme 4.14).

4.3 Dendrimer

Dendrimers (DENs) can be prepared with a level of control not attainable with most linear polymers, leading to nearly monodisperse, globular macromolecules with a large number of peripheral groups. DENs, also called arboroles or cascade polymers, are highly branched, nearly size monodisperse polymers with several structural properties [209]. These structural features include the incorporation of metal nanoparticles with precise control over the nanoparticle size [210, 211] and a defined number of terminal groups for each generation with multiple branch ends, which can be available for consecutive conjugation reactions [212]. Moreover, they are able to form stable, dense, well-organized, and close-packed arrays on surfaces. Indeed, dendrimers are emerging as promising candidates for novel diagnostic platforms [213, 214]. Dendrimers are highly branched macromolecules with successive layers or generations of branch units surrounding a central core. The characteristic tree-like structural attributes of this class of compounds give rise to unique intramolecular and intermolecular associations. These functionalized materials have been utilized in the synthesis of nanoparticles and their
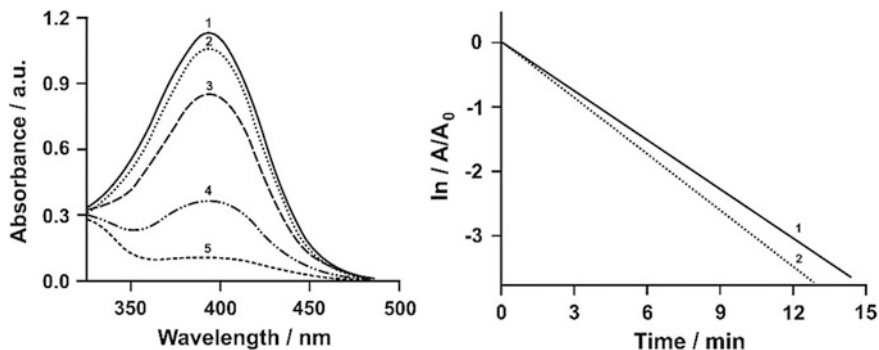
Fig. 4.11 UV–Vis absorption spectra of the CF₃Nip solution as a function of time during the reduction catalyzed by MC-1@AuNPs at 25 °C: #/time (min) 1/0, 2/2, 3/4, 4/8, and 5/12 (*left panel*). Time-conversion plot of the reduction of Nip (*curve 1*) and CF₃Nip (*curve 2*) catalyzed by MC-1@AuNPs at 25 °C (*right panel*) [199]

nanocomposites. The dendrimer can be grown outward from a central core, a process known as the divergent method, or it can be prepared by convergent method by which the dendrimer is synthesized from the periphery inward, terminating at the core [215]. In the divergent method, synthesis starts with a multifunctional core followed by repeated addition of monomers and increase in molecular weight with exponential increase in surface termini. By contrast, the convergent method starts from the dendrimer surface and proceeds inward to a multivalent core where the dendrimer segments are joined together. In the divergent approach, starting from a core molecule (e.g., EDA, ethylenediamine) , poly(amido amine) (PAMAM) dendrimers are synthesized via alternating reiterations of exhaustive Michael addition with methyl acrylate (MA) followed by amidation with EDA [216, 217]. Using the same strategy, nanoparticle core@dendrimer shell composite particles can be synthesized via a divergent ''grafting-from'' method starting from a nanoparticle core [218].

The branching units are described by generation, starting with the central branched core molecule as generation 0 (G0) and increasing with each successive addition of branching points (i.e., G1, G2, etc.); dendrimers are often characterized by their terminal generation, such that a G5 dendrimer refers to a polymer with four generations of branch points emanating from a central branched core. With each successive generation, the number of end groups increases exponentially. Dendritic macromolecules tend to linearly increase in diameter and adopt a more globular shape with increasing dendrimer generation [219]. As a consequence, dendrimers have become an ideal delivery vehicle candidate for explicit study of the effects of polymer size, charge, and composition on biologically relevant properties such as lipid bilayer interactions, cytotoxicity, internalization, blood plasma retention time, biodistribution, and filtration. The majority of studies have been performed on modified polyamidoamine (PAMAM) dendrimer, in part because PAMAM generations 0 through 10 (G0–G10) are commercially available featuring a wide

number of peripheral groups (4–4096), end-group functionality (e.g., amine, carboxylic acid, hydroxyl) and molecular weights (657–935,000 g/mol). Other dendritic molecules under active investigation include poly(propyleneimine), poly (glycerol-co-succinic acid), poly(L-lysine), poly(glycerol), poly(2,2-bis-(hydroxymethyl)propionic acid), and melamine dendrimers (Scheme 4.15). All together, these dendrimers represent a collection of macromolecules which possess varied chemical structures and properties (e.g., basicity, hydrogen bonding capability, charge, etc.) that can be manipulated by increasing dendrimer generation or modifying surface groups. Over the last few years, mechanistic and systematic studies have been taken to understand the relationships between the composition, architecture, and properties of dendrimers toward improved biocompatibility from cell to tissue and pharmacokinetic considerations including biodistribution and excretion.

The first component in DEN synthesis is the dendrimer itself. By using different sizes, or generations, of dendrimers, it is possible to control the size of the nanoparticle to be synthesized. Although there are many types of dendrimers, the most common is the PAMAM dendrimer. These types of dendrimers are predominantly terminated with either amine or hydroxyl groups. The notation for these dendrimers are in the form of Gx-R, where x is generation of the dendrimer and R is the terminal group of the dendrimer (in most cases $R = -OH$ or $-NH_2$). When metal ions are introduced to a dendrimer in aqueous solution, they form a complex with the tertiary amines of the dendrimer notated as $Gx-R(M^{p+})_n$, where M^{p+} refers to the metal ions used and n refers to the average number of metal ions complexed within each dendrimer. After a complex has formed, a reducing agent is introduced in a high molar excess and the metal ions are reduced to their zerovalent form and come together within the dendrimer to form the DEN notated as $Gx-R(M_n)$ where M is the zerovalent metal used and n is the number of metal atoms.

Dendrimer- or dendron-stabilized noble metal nanoparticles are classified in three parts [220]: (i) NMNPs that are entrapped into the dendrimers or dendrons by the functional groups (containing S, N, P, and O) and the steric embedding effects. These nanoparticles are also called dendrimer-encapsulated nanoparticles (DENPs) and are sometimes used in electrocatalysis [221–223], (ii) NMNPs that are surrounded by several small dendrimers at their periphery are called dendrimer-stabilized nanoparticles (DSNPs), and (iii) NMNPs prepared as dendrimer cores and stabilized by coordinating ligands located at the focal points of dendrons (dendrimer-assembled nanoparticles (DANPs)). The major difference between DANPs and DSNPs that are generally formed via an in situ process is that the DANPs are formed on the basis of preformed NPs. With functional groups located at the dendron periphery, the NMNP assembly provides NMNP-cored dendrimers containing peripheral functional groups such as redox groups that are broadly used as redox sensors [224, 225].

Dendrimer-stabilized nanoparticles (DSNPs), thus, are referred to a nanostructure, where one metal or other inorganic nanoparticle is surrounded with multiple dendrimer molecules. In general, the DSNPs are formed in the presence of dendrimers and the formation process under appropriate conditions is in situ. Compared with DENPs that generally have a size smaller than 5 nm, the size of DSNPs is
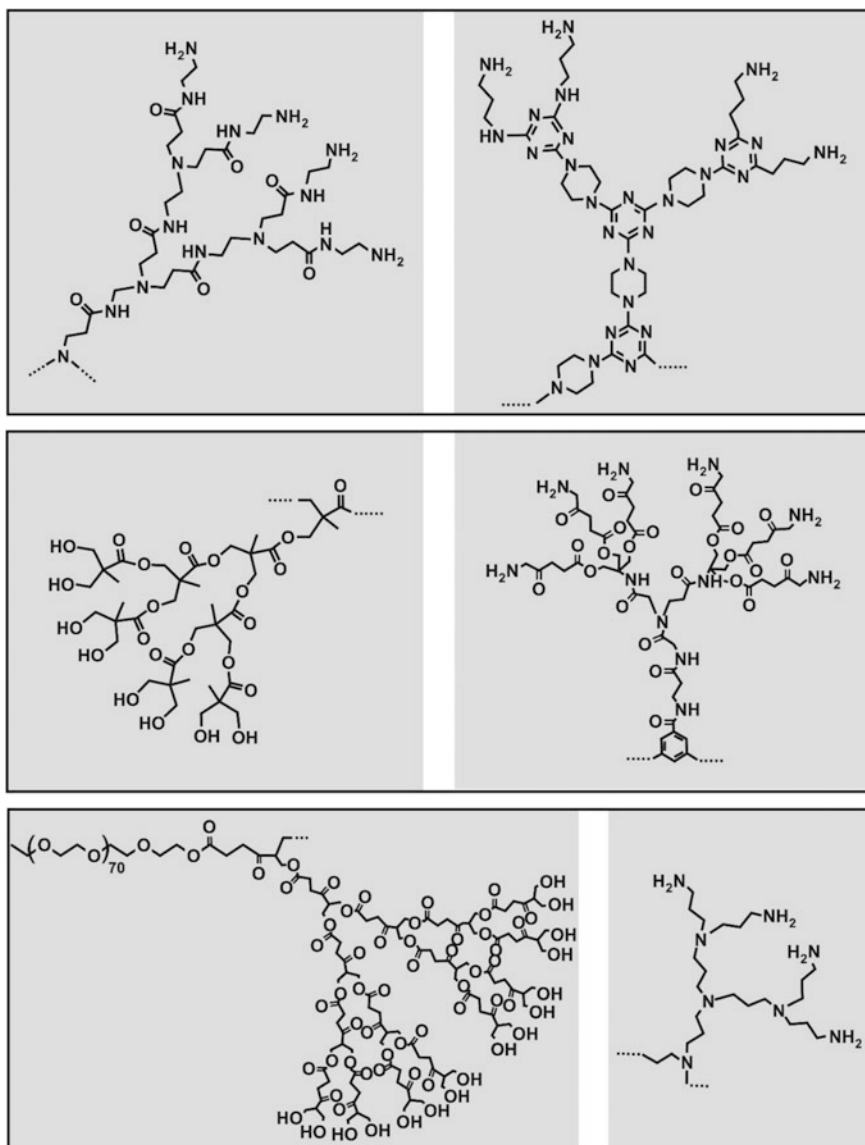
Scheme 4.15 Structures of several dendrimers: Top: (*1*) PAMAM (left panel), (*2*) melamine-based dendrimer (right panel), Center: (*3*) dendrimer based on 2,2-bis(hydroxymethyl) propionic acid (left panel), (*4*) dendrimer based on 5-aminolaevulinic acid (right panel), Bottom: (*5*) dendrimer based on glycerol and succinic acid with a PEG core (left panel), and (*6*) PPI (right panel) [215]

often larger than 5 nm. Metal DSNPs are usually formed under mild reduction conditions to assist slow nucleation of the particles. The formation of metal DSNPs also depends on the structure of dendrimers used. In some cases, if low generation
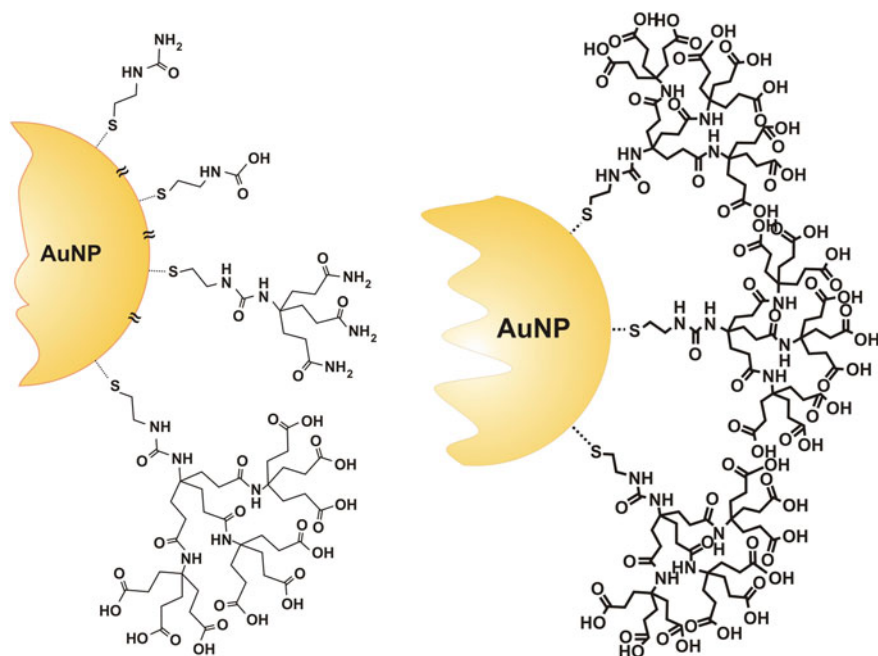
Scheme 4.16 Newkome-type dendron-stabilized AuNPs [184, 237]

dendrimers (G1–G3) are used as templates, even fast reduction and nucleation can still afford the formation of metal DSNPs (instead of DENPs) because the limited terminal amines and open structures of dendrimers cannot entrap metal nanoparticles inside the dendrimers [226, 227].

Dendrimer-encapsulated gold nanoparticles (AuDENPs) were first published by Crooks's and Tomalia's groups using the polyamidoamine dendrimers as stabilizers [228], followed by a number of reports dealing with the preparation of dendrimer-stabilized AuNPs of various kinds. The size distribution of dendrimer-stabilized AuNPs depends on the initial dendrimer-to-gold ratio [229, 230] and dendrimer generation [231]. Other sulfur groups, hydroxyl groups [232], benzyl ethers [233], and amine groups [234], allow the synthesis of dendrimer-stabilized AuNPs [235–237] (Schemes 4.15 and 4.16). In "click" PEG dendrimer-stabilized AuNPs, stabilization is provided by 1,2,3-triazole coordination, and the AuNPs are encapsulated in the dendrimers when the latter are large enough or surrounded by several dendrimers when the latter are too small (zeroth generation) [211].

Dendrimer-entrapped nanoparticles (DENPs) are often formed using fast reduction (e.g., sodium borohydride reduction) and nucleation chemistry. The formation of DENPs consists of two steps. In the first step, metal ions are preorganized by the dendrimer host through ligand–metal ion interactions, salt formation, acid–base and donor–acceptor interactions, covalent bond formation, steric
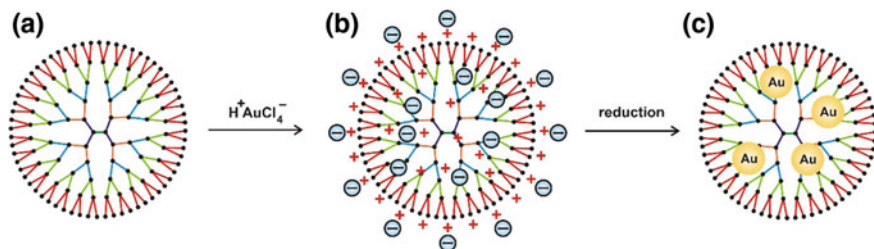
Scheme 4.17 Dendrimer nanotemplating in aqueous solution: **a** bare PAMAM dendrimer, **b** charged dendrimer loaded with gold salt, and **c** dendrimer with gold nanoparticles inside [240, 241]

confinement, various types of weaker forces (van der Waals, hydrogen bonding, etc.), and combinations thereof [238]. Meanwhile, due to many possible overlapping equilibrium processes, the binding of metal ions within dendrimer host usually appears as a nonstoichiometric process. The preorganization results in dendrimer–metal complexes, which are in dynamic equilibrium with the template and metal ions. The dynamic equilibrium permits equal distribution of the metal ions between all the equivalent ligands in the dendrimer molecules, and diffusion provides a homogenous distribution of metal ions among the dendrimer template. In the second step, a reduction of preorganized metal ions results in the formation of DENPs. A scheme for the synthesis of AuDENPs [37, 239] (Scheme 4.17) gives an example how the two steps lead to the formation of metal DENPs. In the first step, the dendrimer is loaded with a precursor salt ($H^+AuCl_4^-$), resulting in a charged dendrimer with the precursor as counterions. In the second step, the chemical reduction is performed which yields a colloid inside the dendrimer [240].

With PAMAM dendrimers as templates, dendrimer-entrapped gold nanoparticles (AuDENPs) can be formed with each AuNP entrapped within each dendrimer molecule [242]. Bimetallic palladium-platinum-DENPs (PdPtDENPs) can be prepared by cocomplexation of the two corresponding metal complexes by interior amines of hydroxyl-terminated PAMAM dendrimers, followed by reduction [243]. The size and composition of the resulting DENPs were found to depend on the metal complex-to-dendrimer ratio and the relative percentages of each metal complex, respectively. Similar results have been reported by Chung and Rhee for PdPt and PdRh bimetallic DENPs [244]. It was demonstrated that core@shell Pd@Au bimetallic DENPs can be prepared using a sequential-loading approach [245]. This dendrimer-templating technique involves selective reduction of the shell metal onto a core or seed of the first metal. By choosing a weak reducing agent for the second step, the reduction can be efficiently catalyzed by the seed of the first metal. This approach insures that the shell metal only deposits onto the preexisting cores [246]. A wide range of metal ions including Cu^{2+}, Au^{3+}, Ag^+, Pd^{2+}, Pt^{2+}, Ni^{2+}, and Ru^{3+} can be preorganized with dendrimers, especially PAMAM dendrimers to form metal DENPs [238, 247, 248]. Likewise, bimetallic core@shell or

alloy DENPs (e.g., NiAu with a size of 3 nm) can be prepared by coreduction of the metal ions in the presence of dendrimer templates [249]. In general, the nanoparticle cores are firstly modified to have a number of primary amine groups, rendering the reaction with MA possible. Compared with DENPs, DSNPs, and DANPs that are formed in the presence of preformed dendrimers, the dendrimer part in this type of hybrid nanoparticles is synthesized via a step-by-step manner, similar to the conventional divergent approach used to synthesize dendrimers.

Thus, the use of PAMAM dendrimers is a unique approach to the preparation of gold nanoparticles and their hybrids as discussed below [242, 250]. Fourth-generation poly(amidoamine) (G4-PAMAM) dendrimers have been used for DNA and protein immobilization [251, 252]. However, to reduce nonspecific protein adsorption and to use the modified surface in the analysis of complex matrixes, several strategies were attempted [253, 254]. In this field, oligo(ethylene glycol) (OEG) and peptide-based self-assembled monolayers are well-known biomaterials providing low specific protein adsorption on a variety of surfaces, mainly due to steric repulsion and excluded volume effects [254]. The protein resistance of a SAM-modified surface is dependent on the conformation chain length, mobility, and surface density of OEG-terminated alkanethiol chains [255, 256].

In recent years, dendrimer-based organic/inorganic hybrid nanoparticles have received immense scientific and technological interest because of their promising applications in a broad range of fields, such as catalysis, optics, electronics, and biomedical applications. The unique properties of dendrimers as well as their excellent biocompatibility and nonimmunogenicity [257] lead to the synthesis of various dendrimer-based organic/inorganic hybrid composite nanoparticles for a range of various applications. The major advantage of using dendrimers to generate organic/inorganic hybrid nanoparticles is their tunable surface chemistry, providing many opportunities for the functionalization of the nanoparticle surfaces.

The tunable surface chemistry of dendrimers allows their assembly onto various nanoparticles. For example, through electrostatic interaction, dendrimers or biofunctionalized dendrimers can be assembled onto magnetic nanoparticles to stabilize or functionalize the nanoparticles [258, 259]. The dendrimer molecules assembled onto nanoparticles can be further modified or functionalized, rendering the particles good colloidal stability, biocompatibility, and biofunctionality [260]. In addition, amine-functionalized nanoparticles can be used as cores for step-by-step divergent growth of dendrimers of different generations onto the particle surfaces [261]. The formed nanoparticle core@dendrimer shell composite particles can be further used as a platform for biomedical applications [262].

Bifunctional hydroxyl/thiol-functionalized G4-polyamidoamine dendrimer-encapsulated gold nanoparticle conjugates, for example, were synthesized and immobilized on a mixed SAM of alkanethiolates on gold generated from the (2-(2-(2-(11-mercaptoundecyl-oxy)-ethoxy)ethoxy) ethyl alcohol, (*a1*), (HS $(CH_2)_{11}(OCH_2CH_2)_3OH$) and the (2-(2-(2-(2-(2-(2-(2-(11-mercaptoundecyl-oxy) ethoxy)ethoxy)ethoxy)ethoxy)-ethoxy)ethoxy) acetic acid, (*b1*), (HS(CH_2)$_{11}^-$ $(OCH_2CH_2)_6OCH_2CO_2H$) [263]. Furthermore, the dendrimer density on the surface

tuned the surface coverage of gold nanoparticles and, thus, the near-field coupling effects. G4-PAMAM dendrimers were employed as nanotemplates for the formation of inorganic–organic hybrid colloids in aqueous solution. The addition of $HAuCl_4$ to the neutral G4-PAMAM dendrimers results in a protonated dendrimer with $AuCl_4^-$ counterions, which were then reduced to metallic gold. The stable brown-red solution of the resulting colloidal gold formed indicates that the metal colloids were stabilized by the dendrimer. Furthermore, amine-terminated G4-PAMAM dendrimers-encapsulated AuNPs were surface modified with a bioactive functionality, to immobilize proteins, and a bioinert one, to minimize nonspecific adsorption of proteins. The $AuNP-G4-NH_2$ dendrimer was conjugated with the heterobifunctional cross-linking agent succinimidyl 6-(3′-[2-pyridyl-dithio] propionamido)hexanoate (LC-SPDP) through a stable amide bond to provide a protected thiol in the form of a disulfide bond for dendrimer immobilization and antibody conjugation. Herein, an average of 13 disulfide groups per dendrimer was estimated [212]. Remaining amino groups were converted to hydroxyl groups by reacting with 4-isothiocyanato-1-butanol forming stable thiourea linkages to give hydroxyl/LC-SPDP-conjugated G4(AuNPs). A stable colloidal solution is formed. The size distribution indicates that the average diameter of these particles is ca. 1.7 nm.

Mixed self-assembled monolayers (SAMs) comprising the tri(ethylene glycol)-terminated thiol, *a1*, and the hexa(ethylene glycol) carboxylic acid-terminated thiol, *b1*, were used for modification of sensor chip, by immersing the gold-coated substrates in solutions of mixtures of *a1* and *b1* at the stated mole fraction. Carboxylic acid groups of the modified surface were activated by the activation reagents (EDC (carbodiimide) /HOBT (1-hydroxybenzotriazole monohydrate)), and the resulting HOBT-activated groups were conjugated to the heterobifunctional cross-linker EMCH (Scheme 4.18). The maleimide groups of the SAM-modified surface were conjugated to the thiol groups in AuNP-G4-OH/SH to immobilize the dendrimer. The remaining free thiol groups of the immobilized dendrimer were activated by the heterobifunctional cross-linker *N*-(ε-maleimidocaproic acid)-hydrazide (EMCH), which was used to attach the protein.

Dendrimer immobilization onto the activated self-assembled monolayer-modified surface was probed in situ by the SPR shift of the surface. SPR experiments evidenced that the amount of immobilized dendrimer is controlled by the composition of the mixed SAM (as the mole fraction between carboxylic acid-terminated thiol, *b1*, and hydroxyl-terminated thiol, *a1*, used to prepare the SAM). A low density of activated carboxylic acid on the surface induces a small amount of AuNP-G4-OH/SH dendrimer to attach onto the SAM-modified platform, resulting in a small angle shift. As the mole fraction of carboxyl SAM increases, the change in the angle position of the minimum reflectance becomes larger, attaining the largest plasmon shift for a ratio of carboxylic and hydroxyl SAM close to 0.12, exhibiting an ellipsometric thickness of ca. 2.4 nm. The initial change in plasmon angle evolves linearly with the amount of immobilized AuNP-G4-OH/SH dendrimer; this is consistent with previously reported phenomenon indicating that SPR shift is roughly linear with AuNP coverage [264]. A significantly higher shift in
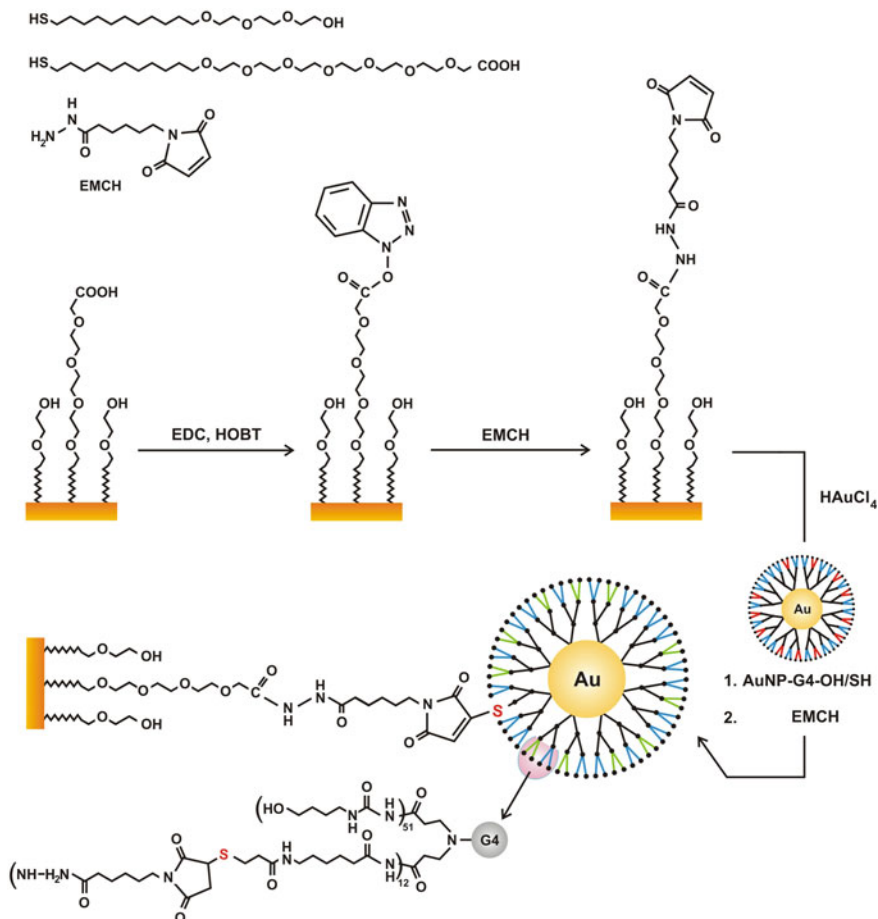
Scheme 4.18 Immobilization of hydroxyl/LC-PDP-functionalized G4-PAMAM dendrimer-encapsulated AuNP onto mixed SAMs of alkanethiolates on gold derived from tri (ethylene glycol)-terminated thiol and the hexa(ethylene glycol) carboxylic acid-terminated thiol (MES buffer, pH 6.5) [263]

plasmon angle was observed upon the immobilization of AuNP-G4-OH/SH dendrimer onto a SAM-modified gold surface; in addition, the AuNPs introduced to the surface with the dendrimers resulted in an increase in the minimum reflectance and noticeable broadening of the SPR curve, as a result of the localized coupling. The results of theoretical modeling studies, performed with a Cauchy dispersion relationship [265], to fit raw experimental data suggested that the thickness of the AuNP-G4-OH/SH immobilized onto mixed SAM-modified gold surfaces was 2.9 nm. When compared with different generations of neutral PAMAM, synthesized with the same procedure reported for the AuNP-G4-OH/SH, without the

encapsulated AuNP, the thickness of the modified surface increased with the generation number of the dendrimer [263].

Ellipsometric thickness (nm)/RSD (%) {SAM, G2-OH SAM, G4-OH SAM, G6-OH SAM, and AuNP- G4-OH SAM}:

$$2.4/4.2, \ 2.6/4.8, \ 2.8/7.0, \ 3.3/6.5 \ \text{and} \ 2.9/5.1 \tag{7}$$

The measured thickness was quite smaller than the bulk phase diameter for the G2-OH dendrimer that showed a disk-like three-dimensional structure, as opposed to spherical shapes of G4-OH and G6-OH, that fits the diameters based on modeled geometry [266]. The surface analysis performed indicates the formation of a dendrimer monolayer on SAM-modified gold surface as reported with a different dendrimer-modified surface [252]. The measured value of refractive index of 1.38 obtained for the AuNP-G4-OH dendrimer is within the range of refractive index reported previously for a G4-OH dendrimer monolayer on gold ($n = 1.46$) [266].

Using the same strategy, dendrimer-entrapped silver nanoparticles (AgDENPs) can be acetylated to influence the nanoparticles generation process [267]. In sharp contrast to the acetylation of AuDENPs, AgDENPs are more sensitive to the acetylation reaction. The size and size distribution significantly change when different degrees of acetylation reaction were applied. Herein the size of partially acetylated AgDENPs displays a bimodal distribution (2.9 and 11.0 nm), whereas the pristine amine-terminated AgDENPs and the completely acetylated AgDENPs are relatively monodisperse with a size of 2.9 and 11.0 nm, respectively. It indicates that complete acetylation transfers AgDENPs to dendrimer-stabilized AgNPs (AgDSNPs). This study suggests that changing the terminal amine groups of the host dendrimers to acetamide groups significantly affects the reorganization and nucleation of AgNPs entrapped in the dendrimers. In contrast, in the case of AuDENPs with similar metal/dendrimer molar feed ratio, even after different acetylation, the size and size distribution do not change. This difference is presumably due to the higher reactivity of the silver (Ag^0) than the gold (Au^0). The higher reactivity of the silver clusters favors aggregation, resulting in the formation of larger nanoparticles compared to those of the gold [37, 268].

Shi et al. [269] have utilized amine-terminated PAMAM dendrimers of generation 2 through 6 as stabilizers to synthesize AuDSNPs by hydrazine reduction chemistry. For all AuDSNPs, the molar ratios between dendrimer terminal amines and gold atoms were kept consistent at 1:0.4. Figure 4.12 (left panel) shows the UV–Vis spectra of AuDSNPs prepared using $G2 \cdot NH_2$ through $G6 \cdot NH_2$ as stabilizers. The plasmon peak at around 525 nm, which is attributed to collective oscillation of free electrons in gold nanoparticles [270], is clearly observed for all samples. Figure 4.12 (right) shows the fluorescence spectra of AuDSNPs and commercial gold colloid particles (5 and 100 nm). All AuDSNPs were found to be fluorescent and display strong blue photoluminescence. The maximum excitation and emission wavelengths were around 397 and 458 nm, respectively, in agreement with the literature data [271]. In contrast, commercial gold colloids (5 and 100 nm) that are prepared using citric acid reduction and protection approach do not exhibit
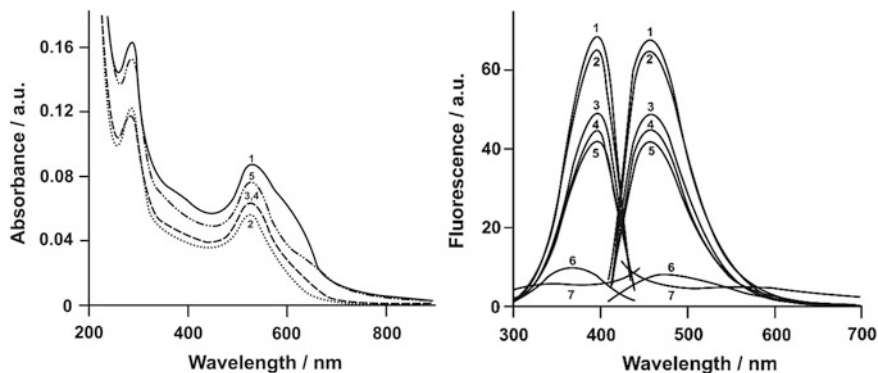
Fig. 4.12 UV–Vis and fluorescence (*right*) spectra of AuDSNPs. *Curve 1, 2, 3, 4*, and *5* correspond to $\{(Au^0)_6\text{-G2}\cdot NH_2\}$, $\{(Au^0)_{12}\text{-G3}\cdot NH_2\}$, $\{(Au^0)_{24}\text{-G4}\cdot NH_2\}$, $\{(Au^0)_{57}\text{-G5}\cdot NH_2\}$, and $\{(Au^0)_{98}\text{-G6}\cdot NH_2\}$, respectively (*left panel*). *Curves 6* and *7* indicate gold colloids with diameter of 5 and 100 nm, respectively (*right panel*) [241, 269]

fluorescence emission, suggesting that the dendrimer stabilizers contribute to the fluorescence properties of the formed AuDSNPs [272].

The sizes of the formed AuDSNPs for $\{(Au^0)_6\text{-G2}\cdot NH_2\}$, $\{(Au^0)_{12}\text{-G3}\cdot NH_2\}$, $\{(Au^0)_{24}\text{-G4}\cdot NH_2\}$, $\{(Au^0)_{57}\text{-G5}\cdot NH_2\}$, and $\{(Au^0)_{98}\text{-G6}\cdot NH_2\}$, respectively, are as follows. It is clear that all the AuDSNPs are relatively monodispersed except $\{(Au^0)_6\text{-}G2\cdot NH_2\}$:

$$d\,(\mathrm{nm})/G_{\mathrm{generation}} : 15.4/2,\ 12.0/3,\ 9.1/4,\ 8.6/5,\ 7.1/6 \tag{8}$$

The first one displays larger size and higher polydispersity, which is attributed to limited number of amines of G2·NH$_2$ dendrimers to stabilize AuNPs [273]. The size of the AuDSNPs decreases with the increase of the number of dendrimer generations, suggesting the different nucleation and growth mechanisms for gold nanocrystals in the presence of PAMAM dendrimers. At basic pH conditions (pH ≈ 10.4 when dendrimers are dissolved in water), $AuCl_4^-$ anions bind preferably to the protonated amines of PAMAM dendrimers through electrostatic interaction. Larger generation PAMAM dendrimers have denser structures that would significantly limit the nucleation, movement, and growth of gold nanocrystals. In contrast, smaller generation PAMAMs have relatively open structures, which hinder the growth of gold nanocrystals less significantly than larger generation PAMAMs. The present AuDSNPs are significantly larger than AuDENPs previously reported [239, 242, 273]. This is because the reduction potential of NH_2–NH_2 (−0.09 V) used in this work is significantly smaller than NaBH$_4$ (−0.48 V). Therefore, the slower reaction rate favors the formation of larger AuDSNPs. The size dispersity of AuDSNPs synthesized using hydrazine reduction chemistry is comparable with those synthesized under UV or laser radiation [274, 275]. All the synthesized AuDSNPs are highly polycrystalline as demonstrated by both the high-resolution

TEM images and selected area electron diffraction patterns [241, 269]. Zeta potential measurements confirmed that all the synthesized AuDSNPs are positively charged with zeta potentials ranging from ~ 26 to ~ 41 mV. This further indicates that after the formation of the hybrid nanostructures, the terminal amines of dendrimers are still available to be protonated. The surface charge polarity of AuDSNPs is similar to the protonated corresponding dendrimers, which was confirmed by polyacrylamide gel electrophoresis measurements [269].

AgDSNPs synthesized using amino-, hydroxyl-, and carboxyl-terminated EDA core generation 5 PAMAM dendrimers (G5·NH$_2$, G5·NGlyOH, and G5·NSAH) as stabilizers are biocompatible, fluorescent, and can be used as cell-labeling markers [276]. The AgDSNPs were synthesized by UV irradiation of Ag(I)–dendrimer complexes and are water soluble and stable. The fluorescent properties of AgDSNPs are from the dendrimer templates, which have been demonstrated by some researchers [269, 272]. The {(Ag^0)$_{25}$-PAMAM G5·NH$_2$}, {(Ag^0)$_{25}$-PAMAM G5·NGlyOH}, and {(Ag^0)-PAMAM G5·NSAH} DSNPs are fluorescent in the wavelength range of 400–500 nm. The fluorescence properties of AgDSNPs allow us to image the intracellular uptake of AgDSNPs using confocal microscopy, while the high electron density contrast of silver metal allows one to image the cellular localization of the nanoparticles using TEM.

Shi et al. have [277] shown that acetamide-functionalized AuDSNPs (diameter ca 13 nm) can be formed by acetylation of amine-terminated G5·NH$_2$ PAMAM dendrimers complexed with Au(III) ions (AuCl$_4^-$). In addition, hydroxyl-functionalized AuDSNPs (diameter ca. 8.5 nm) can be formed by simply mixing the glycidol hydroxyl-terminated G5 dendrimers (G5·NGlyOH) with HAuCl$_4$. In both cases, no additional reducing agents were needed and the reactions were completed at room temperature. Alexa Fluor 594 dye-functionalized AuDSNPs (diameter ca. 16 nm) can be formed by acetylation of Alexa Fluor 594-conjugated, amine-terminated G5 dendrimers complexed with HAuCl$_4$. Fluorescence spectroscopy studies reveal that the Alexa Fluor 594-functionalized AuDSNPs retain similar fluorescence intensity to the Alexa Fluor 594-functionalized dendrimers that lack AuNPs. The formed acetylated AuDSNPs displayed a zeta potential value of +9.8 mV, which is close to neutral. These preparations of AuDSNPs provide a straightforward approach to synthesizing functionalized metal nanoparticles for biomedical applications.

In comparison with AuDENP nanostructures composed of one or more metal nanoparticles within one dendrimer molecule [240], it is possible to modify AuDSNPs with many more targeting ligands than those of AuDENPs, which significantly increases their targeting sensitivity and polyvalency effect [278–280].

Specifically, unique bimetallic materials can be synthesized by dendrimer-templating method (Scheme 4.19) such as AuAg alloys, core@shell Au@Ag and AuAg alloy@Ag structures [245]. The model was proposed to explain extraction involves insertion of the thiol group into the dendrimer, partial functionalization of the AuDENP surface with *n*-alkanethiols, extraction of the DENP as a monolayer-protected cluster (MPC) [28], and then additional passivation of the MPC surface with *n*-alkanethiol ligands [282, 283]. These Au/Ag materials display
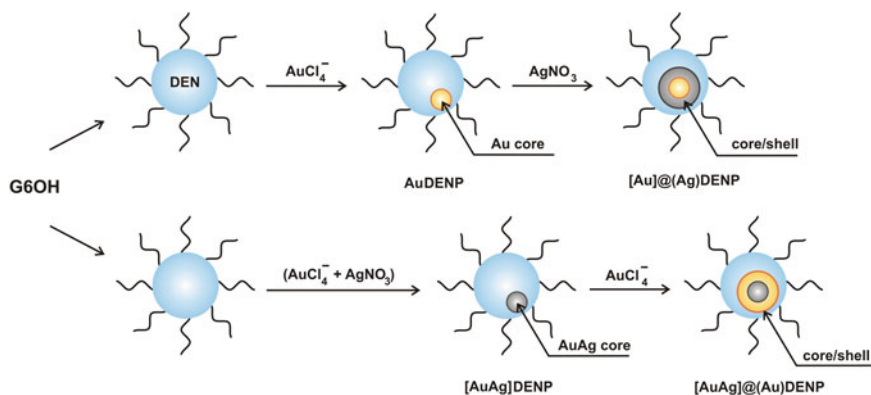
Scheme 4.19 Dendrimer-templating method used to prepare core@shell ([Au$_{55}$]@(Ag$_n$) and [AuAg]$_{55}$@(Au$_n$)) nanoparticles and AuAg alloys (for structured materials, brackets indicate the core metal and parentheses indicate the shell metal), reducing agent: ascorbic acid [281]

interesting optical properties that are dependent not only on the percentage elemental composition of the component elements but also on their geometrical arrangement, specifically, whether the nanoparticle is composed of a random alloy or has a core@shell structure [284]. AuAg alloy nanoparticles are usually synthesized by the simultaneous reduction of both salts in solution [285, 286], while Au@Ag or Ag@Au (core@shell) nanoparticles have been synthesized by controlled deposition of the shell metal onto a seed of the core metal [287].

The spectrum of $(Au^0)_{55}$-G6-OH (Au$_{55}$@G6-OH) exhibits a monotonically increasing absorbance toward higher energies (Fig. 4.13) [239]. This spectrum is suggestive of gold nanoparticles that are less than 2 nm in diameter [288], because larger gold particles give rise to a characteristic surface plasmon band at ~ 520 nm. The UV–Vis spectrum of the G6-OH[Au$_{27.5}$Ag$_{27.5}$]DENPs $\{((Au^0Ag^0)_{27.5}@G6-OH)$ DENPs} in Fig. 4.13 reveals a broad peak centered at ~ 450 nm. However, the spectrum of silver-only nanoparticles having a diameter of ~ 3 nm consists of a single,

Fig. 4.13 UV–Vis spectra of Au$_{55}$@G6-OH (G6-OH [Au$_{55}$]) (*1*) and (AuAg)$_{27.5}$@G6-OH (G6-OH [Au$_{27.5}$Ag$_{27.5}$]) DENP (*2*) seeds [281]
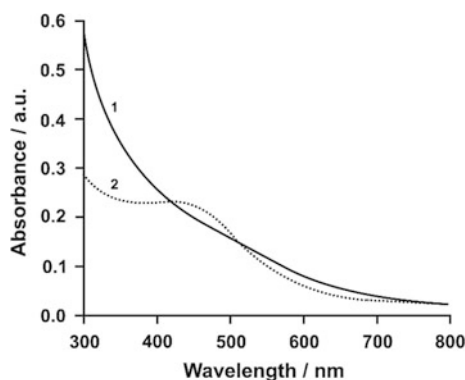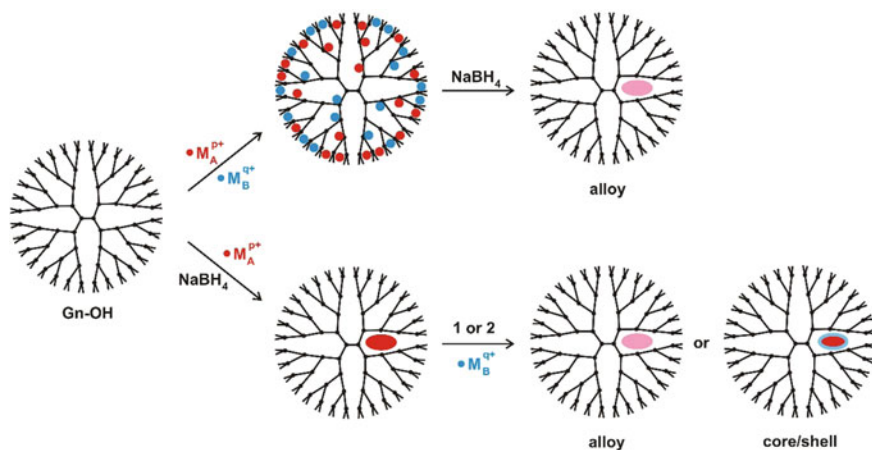
Scheme 4.20 Cartoon depicting the synthesis of various metal nanoparticles using dendrimers as capping ligands, top structure—alloy: cocomplexation approach, bottom structures—alloy or core@shell: sequential approach (weak reducing agent, *1*) and partial displacement approach (more noble metal salt, *2*) [210, 291]

narrow plasmon band that appears at 390 nm [289]. An early report of the absorption spectra of AuAg alloys [290], which were synthesized by melting gold and silver, showed that there is a linear dependence of λ_{max} on the composition of the nanoparticles. Subsequently, this relationship was found to apply to AuAg alloys formed by core-duction [285]. What this means is that AuAg alloys exhibit a single peak in their absorption spectra, and the position shifts continuously from that of pure gold ($\sim$520 nm) to that of pure silver ($\sim$390 nm) as the Ag/Au molar ratio in the nanoparticles increases [285]. Accordingly, λ_{max} for a AuAg alloy containing 50% of each metal was found to occur in the range of 450–460 nm [285]. The position of λ_{max} in Fig. 4.13 ($\sim$450 nm) is within this range, and thus the optical spectroscopy results are consistent with the presence of AuAg bimetallic DENPs containing equal percentages of gold and silver. The Au_{55}@G6-OH DENPs have a diameter of $\sim$1.4 nm, while the $(AuAg)_{27.5}$@G6-OH DENPs have an average size of 1.5 nm. These values agree with previously reported results [282] although both are slightly larger than the calculated value of 1.2 nm.

Various dendrimer molecules have already been mentioned to stabilize (noble) metal nanoparticles. Pioneering work by Crooks et al. [291] substantially defined the nanoparticle stability inside the dendritic network and its further utilization (Scheme 4.20). The advantages of the dendrimer approach include the following:

(1) The completeness of reduction of the metal ions sequestered inside the dendrimer yields some stoichiometric control over the nanoparticle size. The dendrimer arms are very effective at preventing nanoparticle aggregation.
(2) The loose steric aspects of dendrimers also allow the encapsulated nanoparticles to participate in various catalytic reactions.

(3) The terminal groups on the dendrimer periphery can be modified for purposes
    of nanoparticle solubility in different media, among other goals.

The encapsulation of metal ions inside dendrimers involves, variously, electrostatic and complexation interactions—the dendrimer interior includes coordinating groups such as –OH, NH_2, or –COOH. Stable monodisperse gold nanoparticles can be synthesized using quaternary ammonium-terminated fourth- and sixth-generation (G4, G6) dendrimers without further purification steps. Water-soluble Au_8 nanodots have also been prepared within hydroxy-terminated second- and fourth-generation (G2-OH and G4-OH) dendrimers [271], and they fluoresce at short wavelengths that change with the size of the gold nanoparticle. In contrast, thiolated gold subnanoparticles do not emit at shorter wavelengths but instead emit at relatively size-independent near-infrared wavelengths.

Recently, there has been a lot of interest in hybrid composites of organic and inorganic material systems utilizing dendrimers. In particular, their role in templating nanoparticle growth has been explored. Crooks et al. have shown that PAMAM can be used as templates for preparing nearly monodispersed intradendrimer metal nanoparticles using a "ship-in-a-bottle" approach [248]. These hybrid dendrimer-encapsulated metal nanoparticles (DEMNPs) are useful for applications in catalysis and electrocatalysis. However, it has been difficult to immobilize and stabilize PdDEMNPs on highly ordered pyrolytic graphite (HOPG) for applications such as carbon-supported electrocatalysts in the development of fuel cells. This is largely due to the poor adhesion properties of the DEMNPs on graphite and their strong tendency toward aggregation.

The coupling of energy and electron-transfer phenomena between inorganic nanoparticles and organic molecules is also of great interest. The difference between the HOMO and LUMO levels between nanoparticles and organic dyes/conjugated polymers has resulted in both energy-transfer and quenching mechanisms. This was discussed with a new type of conjugated dendrimers based on thiophene and demonstrated interesting 2D supramolecular assembly on graphite [292]. Besides their excellent assembly properties on graphite, thiophene dendrimers also have very strong absorption in the region of 250–400 nm and are good candidates as light-harvesting antenna macromolecules.

Deng et al. [293] have reported the synthesis of PAMAM dendrimers functionalized with thiophene dendrons (3T6C) on their periphery (Scheme 4.21) and the preparation of dendrimer-encapsulated metal nanoparticles. In general, the hybrid nanoparticles based on thiophene dendron-functionalized PAMAM G4 (3T6C) can be prepared by the so-called ship-in-a-bottle approach. The first step is the loading of metal ions into the interior of dendrimers. The second step is the reduction of metal ions and consequent Ostwald-ripening process. The changes in absorption spectra of the dendrimers G4(3T6C)-$(Pd^{2+})_{24}$ and G4(3T6C)$(Pd)_{24}$ are consistent with the formation of dendrimer-encapsulated Pd nanoparticles. The surface plasmon peak of G4(3T6C)$(Au^{3+})_8$ at about 530 nm is not observable because of the overlap with the absorption of G4(3T6C). Therefore, to prove the existence of gold nanoparticles inside the dendrimer, the authors decided to
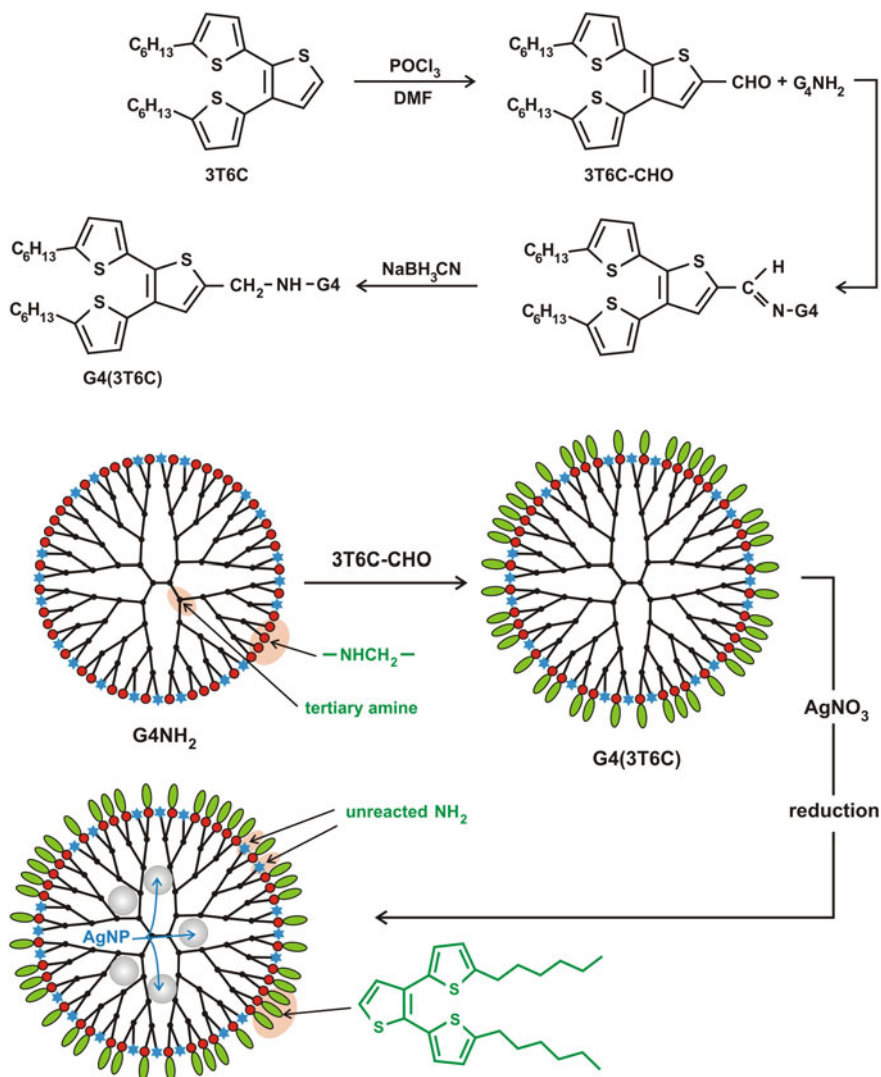
Scheme 4.21 Cartoon depicting the modification of G4 PAMAM with thiophene dendrons (3T6C) and the preparation of dendrimer-encapsulated metal nanoparticles [293]

synthesize larger Au nanoparticles $G4(3T6C)(Au^{3+})_{24}$, where the surface plasmon peak at 562 nm was easily observed. The resulting Pd hybrid nanoparticles are very stable. Even after several months, no agglomeration was observed and the solution spectra remained the same. However, the gold hybrid nanoparticles are not as stable as Pd. A black precipitate was formed after several weeks.

In general, both the loading of metal ions and the presence of nanoparticles shift the amide bands to a larger wave number. The amide I band is more sensitive (from

-4 to 12 cm^{-1}) than that of amide II (from 0 to 12), and metal ions have a stronger effect than their corresponding nanoparticles. Thus, the shift of amide bands is an indication of complexation. A stronger complexation results in a larger shift. Therefore, the metal ions will complex with PAMAM more strongly than their corresponding nanoparticles. This is expected because of the electrostatic charge present on the metal ions. As indicated by the significant shift of amide bands, it is very clear that amide groups are involved in the complexation and stabilization of both Pd^{2+} and Pd nanoparticles, although it is not fully understood at present why the amide I of G4(3T6C)(Pd)$_{24}$ shifts to a shorter wave number. However, the loading of Au^{3+} does not change the amide II band, which is a combination of C–N stretching and N–H bending. This indicates that Au^{3+} does not or very weakly binds to the NH of the amide group as compared to Pd^{2+}. Also, Au^{3+} does not shift the amide I as much as does Pd^{2+}. Therefore, amide groups do not contribute significantly to the complexation of Au^{3+} with PAMAM, partially explaining the weak complexation between Au^{3+} and PAMAM. Upon the formation of gold nanoparticles, both amide I and II bands are at the exact wave number as for G4(3T6C). If there were weak interactions between Au^{3+} with amide groups, Au nanoparticles do not interact with it at all. This can partially explain why the Au hybrid nanoparticles are not as stable as Pd nanoparticles.

Dendrimer G4(3T6C) showed three characteristic absorption bands of 3T6C at about 245, 270, and 315 nm. The loading of metal ions shifts the absorption maxima to shorter wavelengths and increases the intensity of absorption at 245 nm, making the absorption peak at 270 nm not very resolvable. Upon formation of metal clusters, the absorption maxima are further blueshifted. This hypsochromic effect is the result of increased rigidity of the dendrimer caused by metal ions and nanoparticles. As compared to Au^{3+} and Au clusters, Pd^{2+} and Pd clusters have a stronger binding effect. This is consistent with the results from FTIR spectra that Pd^{2+} binds more strongly to PAMAM and therefore the Pd hybrid nanoparticles are more stable. The hypsochromic effect is not obvious for fluorescence. Interestingly, the fluorescence of G4(3T6C) is enhanced by gold nanoparticles due to a surface enhancement effect. The mechanism for this enhancement involves the interaction of the emission dipole moment of the gold surface plasmon resonance with the emission dipole moment of the dendrimer G4(3T6C). The surface plasmon band of G4(3T6C)(Au)$_8$ (at about 530 nm) has a better overlap with the emission of G4 (3T6C) than does that of G4(3T6C)(Au)$_{24}$ (at 562 nm). Therefore, the fact that G4 (3T6C)(Au)$_8$ enhances the fluorescence of G4(3T6C) more than does G4(3T6C) (Au)$_{24}$ provides direct evidence for this mechanism. Surface-enhanced fluorescence is rarely observed directly in a nanoparticle and organic fluorophore system.

G4(3T6C) tends to form very large aggregates. This is due to the increased hydrophobicity caused by thiophene dendrons on the periphery. However, highly oriented pyrolytic graphite (HOPG) surfaces turned out to be a very good substrate for G4(3T6C). In the AFM images, one can see many separate and randomly deposited globular particles on the HOPG surface. In each image, the particles appeared to be substantially uniform in size. There are a few large irregular clusters, perhaps caused by dendrimer aggregation. According to the structure of dendrimer

G4(3T6C), it has approximately the same size of G6NH$_2$ (diameter 6.7 nm). However, a strong dendrimer–graphite interaction causes a spherically symmetric dendrimer to adopt an oblate shape on the surface. This is due to the strong ð–ð stacking and interaction of the terthiophene moieties with graphite. This strong stabilization was discussed along with an order with thiophene dendrimers on HOPG as a function of dendrimer generation and alkyl chain length [292]. G4 (3T6C)(Pd)$_{24}$ has an average height of 1.5 nm and full width at baseline of 50 nm. Dendrimers with metal clusters inside tend to form more uniform aggregates. The presence of hydrophilic metal ions may decrease the interaction between the dendrimer and hydrophobic graphite, resulting in more irregular aggregates for dendrimer loaded with metal ions. It should be pointed out that G4(3T6C) provides essentially a monodispersed size and strong adhesion of Pd hybrid nanoparticles to HOPG. Thus, the driving force to assemble dendrimers onto preformed nanostructures could be electrostatic interaction [294], covalent bonding [295], and the combination of different weak forces [296].

Pang et al. have demonstrated a facile wet chemical method for the synthesis of dendrimer-like structures that are spontaneously assembled using gold nanoparticles by a one-pot route, wherein a novel surfactant solution of CF$_3$(CF$_2$)$_7$–SO$_2$NH–(CH$_2$)$_3$N$^+$(CH$_3$)$_3$ I$^-$ (HFOTAI) is used not only as a reducing agent, but also as an assembling agent [297]. In the spectra of the mixed solution of HFOTAI and HAuCl$_4$, new bands at 520 and 670 nm appeared (Fig. 4.14). These band intensities increased for early incubation times, but they decreased after 3 days due to the sedimentation of the products. The band at 520 nm can be attributed to the surface plasmon band of gold particles. The band at 670 nm is probably due to aggregated particles and/or larger particles of Au. Thus, the UV–Vis spectra indicate that Au particles were formed by the reaction of HAuCl$_4$ with HFOTAI, though the details of the chemical reaction of HFOTAI are still unknown. The formation of Au particles was also confirmed by the XRD patterns of the precipitates of the products, for which the [111] and [199] diffraction peaks of a gold crystal were observed at 38.0° and 44.2°, respectively. Scheme 4.22 shows a schematic illustration of the evolution process estimated from the experimental results. For the whole concentration (from 4.6 to 18.6 mg) of HFOTAI, Au particles only exist in the early stages and in the final stages of the evolution process. The structures of the assemblies at high concentrations of HFOTAI for short incubation times are similar to those of the evolved assemblies for lower concentrations of HFOTAI for longer incubation times. In other words, the assemblies for higher concentrations in the evolution process follow the evolved assemblies produced at lower concentrations. In addition, the formation rate of a younger assembly increases with increasing concentration of HFOTAI.

The very slow evolution process of the assemblies shows that the supply of gold is constant for a long time. Possible sources of the gold are (a) the reduction product of HAuCl$_4$ and (b) gold nanoparticles produced during the early period evolution. In the present system, iodine ions, which are the counterions of HFOTAI, probably affect the evolution of the gold nanoparticles. That is, the iodine ions enhance the rate of the Ostwald-ripening process. Thus, a selected gold particle or assembly
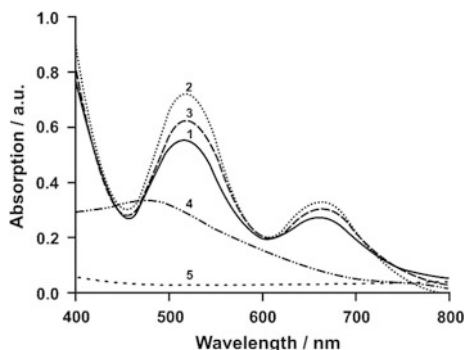
Fig. 4.14 UV–Vis spectra of the reaction solution (0.48 mM HAuCl$_4$ with 11.4 mg HFOTAI) for different incubation times: (*1*) just after mixing, (*2*) after 3 days, (*3*) after 21 days, (*4*) HFOTAI and (*5*) HAuCl$_4$ [297]
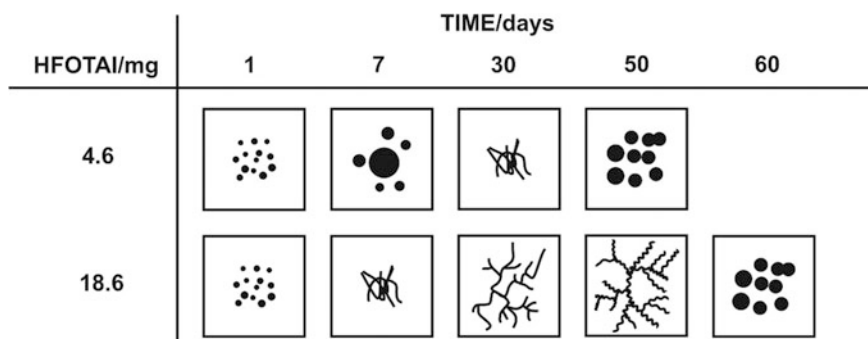
Scheme 4.22 Schematic illustration of the microstructural evolution process for various HFOTAI concentrations [297]

grows due to the supply of atomic gold generated by the slow reduction of HAuCl$_4$ and/or gold nanoparticles produced in a short incubation time.

An important factor for the possible explanation of the dendritic assembly formation is the role of HFOTAI. TEM observations confirmed that HFOTAI formed vesicles in an aqueous solution. Since, in the mixture solution of HAuCl$_4$ and HFOTAI, surfactant assemblies of HFOTAI were not observed in TEM micrographs, HFOTAI molecules probably interacted with the gold nanoparticles. The IR spectra indicate that the gold particles are covered with HFOTAI molecules and that the dendritic assemblies consist of gold particles and HFOTAI. Thus, HFOTAI molecules probably serve as a binder of the gold particles. The gold nanoparticles were prepared by the traditional sodium citrate reduction method, wherein the gold nanoparticles were covered by citrate ions. The resulting product was not dendritic assemblies of Au particles but larger spherical and cubic particles. Thus, HFOTAI

molecules covering the gold particles play an important role for the formation of the dendritic assembly structures.

De Jong et al. [298] have prepared cyclodextrin (CD) self-assembled monolayers (SAMs) on gold surfaces onto which stable positioning and patterning of molecules has been achieved by means of multiple supramolecular interactions. Therefore, these CD SAMs constitute a molecular printboard for the positioning of thermo-dynamically and kinetically stable assemblies of multivalent systems, for example, dendrimers. It was reported that an analogous ferrocene-terminated dendrimer (generation 5, 64 ferrocene end groups) binds to CD SAMs on gold with approximately seven interactions to the surface [299] leaving multiple guest groups exposed to the solution available for complexation of hosts from solution. These molecules bind to the CD printboards with different numbers of interactions depending on the number of functional groups present in the dendrimer [299]. Herein the complexation-induced aggregation in solution of CD-modified gold nanoparticles (CD-AuNPs) and adamantyl-functionalized dendrimers was studied. The addition of such a dendrimer to a solution containing AuNP@CDs led to pronounced and irreversible precipitation of the dendrimer/CD-AuNP aggregates.

Crespo-Biel et al. [300] have described the stepwise construction of a novel kind of self-assembled organic/metal nanoparticle multilayers on the basis of multivalent supramolecular host–guest interactions between dendritic guest molecules and host-modified gold nanoparticles. Adamantyl-terminated poly(propylene imine) dendrimers were chosen because the CD–adamantyl interaction is one of the strongest, the number of adamantyl units (ranging from 4 to 64) can be easily varied, and the spherical shape of the dendrimers allows the multivalent display of these guest functionalities. Dendrimer (Scheme 4.23) has 64 adamantyl groups, and the complexation with CD takes place in solution. Adamantyl-terminated poly (propylene imine) (PPI) dendrimers were insoluble in water, but by complexation of the adamantyl end groups by slight excess of cyclodextrin and by the protonation of the dendrimer core amine functionalities, they could be brought into aqueous (pH = 2) solution. However, at pH > 7, precipitation of generations 3–5 of these PPI dendrimers occurs. Conversely, AuNP@CDs are not stable in acidic solution. Therefore, the LBL assembly was typically accomplished by alternately dipping the substrate into an aqueous acidic CD (pH = 2) solution, followed by rinsing the substrate with the same CD (pH = 2) solution, and into an aqueous CD-AuNPs solution, followed by rinsing with water. The delivery of the dendrimers from solution-phase CD complexes to the CD SAMs makes use of the competition between the solution and the surface host sites, as well as the multivalency of the surface host sites emerging from the surface immobilization (Scheme 4.24).

UV–Vis spectroscopy was used to monitor the supramolecular assembly of the CD-decorated AuNPs (AuNP@CDs nanostructures). Dendrimer adsorption was not visible in the visible region. When CD-AuNPs were adsorbed onto the film, the CD-AuNPs plasmon absorption band in the visible region emerged at around 525 nm similar to the CD-AuNPs in solution. The UV–Vis absorption spectra of the multilayer PPI/CD-AuNPs films for different numbers of bilayers on a CD SAM show the increase in absorption at 525 nm, and this increase was a function of the
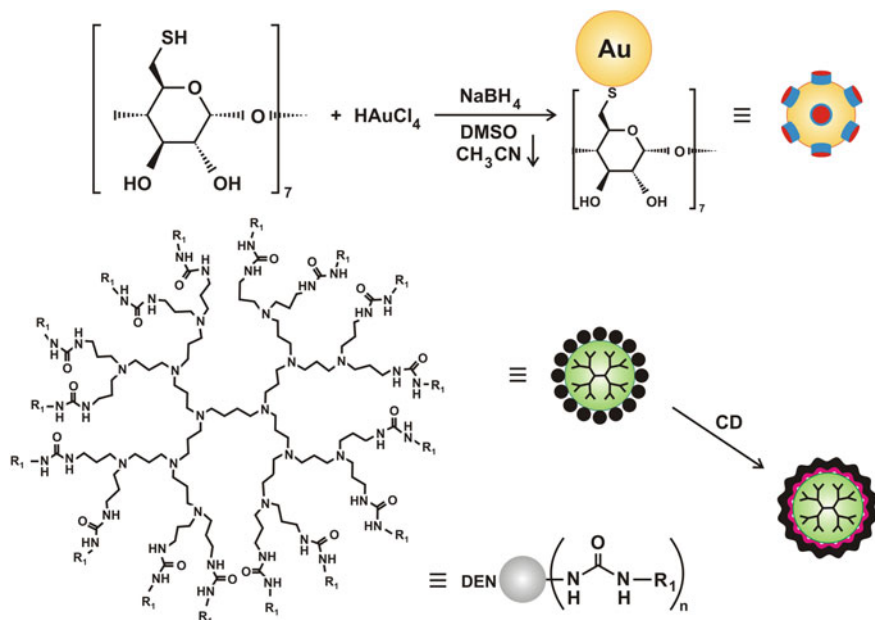
Scheme 4.23 Chemical structures of the CD-AuNPs and adamantyl-terminated PPI Dendrimers [300]
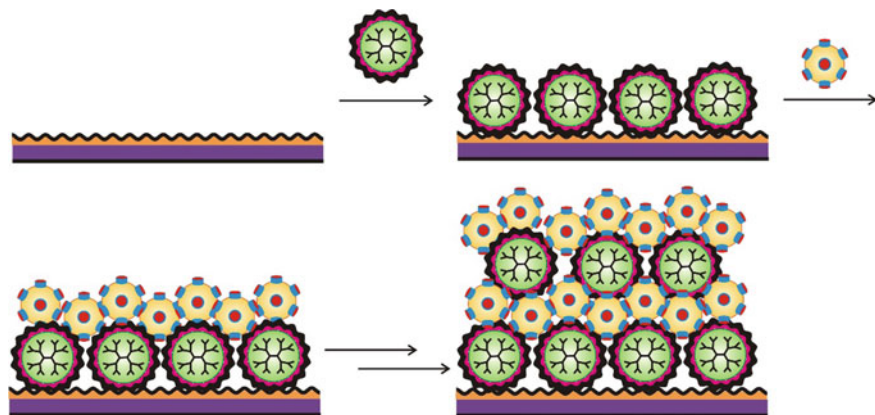
Scheme 4.24 Layer-by-layer assembly scheme for the alternating adsorption of adamantyl-terminated PPI dendrimer and CD-covered AuNPs onto CD SAMs [300]

number of bilayers deposited on the CD surface. An essentially linear dependence was found, confirming the SPR and ellipsometry data. The linearity was shown to last up to 18 bilayers, which is a strong indication of a well-defined deposition process.

From the absorption at 525 nm of a solution of CD-AuNPs, the extinction coefficient was calculated to be 0.586 cm^2/mg using the Lambert-Beer law. The surface coverage for one layer of CD-AuNPs was calculated to be 3.1 μg/cm^2. A theoretical value of 1.7 μg/cm^2 was estimated on the basis of the formation of a monolayer of CD-AuNPs in a hexagonal packing with a lattice periodicity of a gold nanoparticle core summed with twice the CD cavity height and taking into account that the gold core contributes 62% of the total weight of the AuNPs. Thus, the experimental value is a factor 1.8 larger than the crude theoretical estimate obtained assuming a hexagonal packing of monodisperse particles. Most of this difference can probably be attributed to the slight physisorption of the CD-AuNPs at the relatively high concentration employed in the UV–Vis experiments. Nevertheless, the fair comparison between the experimental and the theoretical values clearly indicates that close to a monolayer of AuNPs is deposited after each deposition cycle. The multilayer thickness as a function of the number of deposited bilayers demonstrating that the thickness of the film is linearly related to the number of deposited bilayers (AFM). An estimate of the multilayer thickness of 2 nm/bilayer was obtained in congruence with the ellipsometry results.

Most of the dendritic containers reported so far use the concept of closing the dendritic box in order to keep the guest molecules (particles) inside the dendrimer host. Thus, many researchers have addressed this kind of core@shell structure by modifying the dendrimer surface, so that molecules can be reversibly imprisoned in internal cavities of the dendrimer and then site-selectively liberated by a suitable external or internal stimulus. For such applications, a shell should be "opened" and "closed" reversibly—controlled by means of a simple external or internal stimulus, such as light, pH, or ionic strength. Vogtie and coworkers prepared a photo-switchable dendritic box by modifying terminal groups with light-switchable units [301]. PNIPAM is a well-known water-soluble polymer that shows reversible hydration–dehydration changes in response to small solution-temperature changes. Okano and coworkers have already reported thermally controlled surface attachment and detachment of cells using a surface-grafted PNIPAM. The thermally responsive polymeric micelles maintain passive targeting of tissue sites via their small size, and the potential for active targeting via their PNIPAM-switchable physicochemical character [302]. Jiang and coworkers have achieved reversible switching between superhydrophilicity and superhydrophobicity by grafting PNIPAM to a surface [303]. PNIPAM and its copolymers have found several applications, such as extraction, controlled release, and enzyme-activity control. Thus, attaching a sensitive PNIPAM shell onto a dendrimer surface will produce dendritic core@shell nanostructures with special properties for applications in smart nanostructure synthesis, drug delivery, and smart catalysis. However, it has been very difficult to link a PNIPAM chain to the dendrimer surface to form a dendritic core@shell nanostructure, although some kinds of core@shell structures have been successfully prepared by polymer-chain modification of the dendrimer surface. You et al. have reported that the average hydrodynamic radius (r_h) decreases from 19 to 10 nm when the temperature increases from 24 to 38 °C, due to the shell shrinking [304]. Conversely, r_h increases from 10 to 19 nm as the temperature decreases from

38 to 24 °C, resulting from the shell expanding. This is because, at temperatures below the lower critical solution temperature (LCST) , the predominantly intermolecular hydrogen bonding between the PNIPAM chains and water molecules results in the PNIPAM chains adopting a water-soluble coiled structure. At temperatures above the LCST, intramolecular hydrogen bonding between C=0 and N–H groups in the PNIPAM chains causes the chains to become compact and collapse, reducing their water solubility. To compensate, the PNIPAM chains collapse onto the surface of the dendrimer to form a shell at the periphery of the dendritic core; the (r_h) (10 nm) of the core-shell nanostructure is much smaller than that (19 nm) at temperatures below the LCST. In addition, PNIPAM chains in aqueous solution collapsing to a globular state from the expanded state can result in changes in transmittance; that is, the aqueous-transmittance changes reflect the PNIPAM-chain conformation in aqueous solution. An aqueous solution of dendrimer is transparent when the PNIPAM chains are expanded, but it becomes turbid when the chains collapse above the LCST. The solution became turbid in response to increasing the temperature to 32 °C, which indicates that the PNIPAM chains collapsed above 32 °C. On the other hand, the radius of gyration r_g can be measured to calculate r_g/r_h, which reflects the density of the polymer segments. A smaller value of r_g/r_h corresponds to a higher segment density. For example, for linear, flexible macromolecules, r_g/r_h is around 1.5–2.0, but for a hard sphere, the ratio falls to 0.78. A ratio of 0.8–1.5 is found for hyperbranched or dendritic macromolecules. The value of r_g/r_h decreased from 1.05 to 0.88 when the temperature increased from 25 to 35 °C, which indicates that the PNIPAM chains collapsed onto the core to form a barrier-like shell. Therefore, a dendritic core@-shell nanostructure, whose shell is sensitive to temperature, has been successfully synthesized by grafting PNIPAM chains to the dendrimer surface.

The supramolecular cages generated by hydrophilic dendritic polyols can be utilized as templates for the kinetically controlled growth of faceted silver nanoparticles with low aspect ratios [305]. These polyester-type polyols consist of a multifunctional core, and the large number of terminal hydroxyl groups makes them hydrophilic (Scheme 4.24). A "green" advantage of using hydrophilic polymers is that one can avoid using hazardous organic solvents for nanoparticle synthesis. A hydrazine/ethanol solution was added dropwise with stirring to the Ag+–dendrimer solution until the reduction to silver was initiated, indicated by the appearance of a light yellow color. Experiments using the H20 dendrimer produced a broad size range of particles from 10 to 100 nm. The majority of particles ($\sim$60%) was in the 40–60 nm size range and was in general characterized by low aspect ratios. The measured surface plasmon band (λ_{max} = 416 nm) is characteristic of silver nanoparticles, confirming the reduction and formation of Ag(0) particles. It was found that the particles grow (measured by TEM) in these matrices to form well-defined large particles over time. When the same nanoparticle dispersion was analyzed after three months, larger particles in the size range of 200–600 nm with well-defined facets and shapes were observed in addition to the smaller particles observed previously. Most of the large particles are octahedral, and some of them are cubes. Of the analyzed particles using the TEM images, only a small percent

($\sim$5%) of the large particles were found to be cubes while the remaining were general polyhedra with well-defined facets.

The high density of hydroxyl groups (Scheme 4.25) in the Boltorn dendrimers leads to extensive inter- and intramolecular hydrogen bonding, making them unique in their ability to form supramolecular assemblies with nanosized cores. These supramolecular cages are dynamic in their structural attributes since intermolecular hydrogen bonds can act as dynamic gates for the controlled passage of ions as well as small nanoparticles into and out of the cages. By virtue of the high density of hydroxyl groups, the interior of these cages is polar and hydrophilic, making it possible to transport and reduce metal ions in the cages. Also, the ester and the hydroxyl groups help passivate the surfaces of the metal nanoparticle formed inside these nanocavities. The stability of these supramolecular cages would depend largely on the generation number of the dendrimer and the nature of the solvent with the higher generations possessing greater stabilities. While Scheme 4.24 refers to one focal point for the growth, it is possible that several extended structures of various shapes, containing several intercluster aggregations, by virtue of the possibility for extended hydrogen bonding. Protic solvents such as water or ethanol can also affect the stability of these polymer associations by solvent bridging.

It is noteworthy that the experiments conducted with larger generation dendrimers (H30 and H40) did not yield particles with well-defined faces. Most of the particles formed from these dispersions were spherical in general, and over a period of time aggregated randomly without any significant variation in the individual particle sizes. For example, the particle sizes varied from 50 to 190 nm. Thus, the functionalized dendrimers can act as host molecules for metal ions and that the reduction of these metal ions yield metal nanoparticles stabilized within the inter-
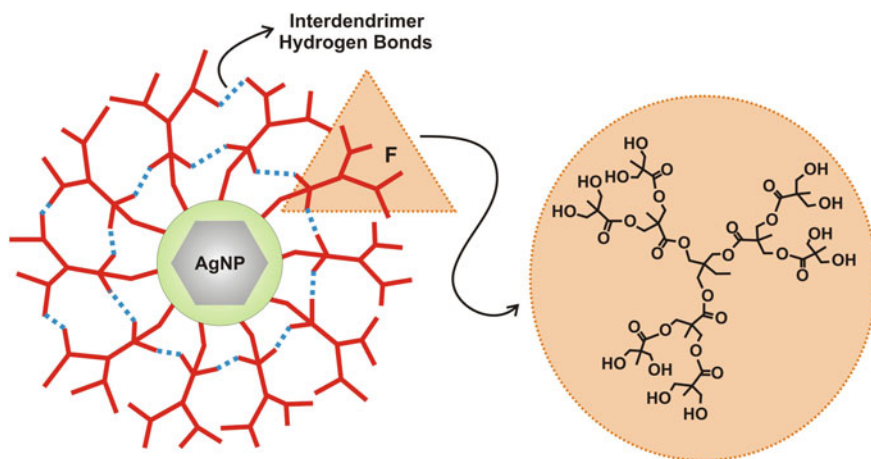
Scheme 4.25 Structural motif of the hyperbranched dendritic polyols. A cartoon illustrating the formation of metal nanoparticles in the size-confined pools formed by the intermolecular association of the dendritic polyols. "*F*" represents the focal point of an individual dendrimer [305]

and intradendrimer cavities. Wang et al. [306] showed that focally modified dendrons with metal coordinating functionalities can be utilized as a stabilizing medium for the controlled growth of nanoparticles. They reported [306] that the average size of the resulting nanoparticles is a direct function of the generation number of the passivating dendrons with the higher generation dendrons yielding larger particles. However, the growth of large nanocrystals was observed to be specific to the case of the H20 templates.

Upon considering the growth of nanoparticles in dendrimer dispersions, one should consider two important aspects that govern the plausible mechanisms—the ability of the individual molecular units to undergo intermolecular association and the effect of increasing the generation of the dendrimer. Higher generation dendrimers will have better defined intramolecular structures compared to their lower analogues. It is hypothesized that nanoparticle formation in the lower generation dendrimers occurs in the intermolecular cavities as shown in Scheme 4.25. For the higher generation dendrimers, both the intermolecular and intramolecular cavities can act as size-confined pools for nanoparticle formation. However, a comparison of the particle size with the size of the dendrimer molecule reveals that most of the particles in the present view are formed in intermolecular cavities. The particle growth, however, is observed only in the case H20. This may be attributed to two factors. First, the self-structuring of higher generation dendrimers (H30 and H40) is more defined in comparison with H20. This will reduce diffusion of small nanoparticles from one nanocapsule to another as well as the dynamic restructuring of the nanocapsules for H30 and H40. Another factor may be the shape of the initial particles. It is plausible that the well-defined faces of the nanoparticles formed in the H20 sample are significant in the further growth of the nanocrystals. The face-to-face joining of individual nanoparticles minimizes the overall surface energy allowing the formation larger, stabilized, and nanosized single crystals. The view presented here reveals that functional dendritic structures and dispersions can serve as a medium for the growth of nanocrystals with well-defined facets, and the influence of the dendrimer generation on particle growth and morphology.

4.4 Bioconjugates

The coated particles prepared by different approaches have amine, hydroxyl, or carboxyl groups. A primary amine on their surface, for example, comes from aminopropyl methacrylamide. The presence of such primary amine is tested by reaction with fluorescamine and also reflected from positive surface charge of the particle [307]. This primary amine group was used for covalent linking of different molecules of interest, such as glucosamine, oleylamine, and TAT peptide. Glutaraldehyde can be used as the conjugation reagent that has primary amine-reactive two aldehyde groups at the two ends [308]. Similarly, TAT (TAT peptide with sequence CGRKKRRQRRR) peptide functionalization was achieved using N-succinimidyl 4-(maleimidomethyl) cyclohexanecarboxylate (SMCC) as a

conjugation reagent. Colloidally stable and water-soluble functional nanoparticles formed retained plasmonic and fluorescent properties, suggesting that various other functionalizations can also be achieved.

The functionalized plasmonic-fluorescent nanoparticle has been used as cell imaging and plasmon-based optical detection probe. The oleyl and TAT-functionalized gold nanoparticle was used to label COS-7, EAC, and Neuro2a cells. The oleyl group has a strong interaction to the cell membrane that helps the particle to target the cell membrane [309]. Similarly, TAT-functionalized nanoparticles induce increased cellular interaction and labeling [307]. It was observed that oleylated and TAT-functionalized particles label the cell and labeled cells are successfully imaged with a fluorescence microscopes using the fluorescence property of plasmonic-fluorescent nanoparticles. The positive surface charge and multiple oleyl/TAT functionality in each particle induce strong interactions of particles with cell membranes, and thus the nanomolar concentration of the particle is sufficient to observe such labeling under fluorescence microscope. Sample solution or labeled cells were also exposed under continuous UV irradiation. The result shows that the fluorescence decrease of the sample solution is insignificant and the fluorescence image of the labeled cells fades only partially, even after 5–10 min of UV light exposure. Usually, molecular fluorescence of fluorescein bleaches rapidly within minutes under continuous UV light, and for that reason, the fluorescence image faded upon long-term imaging. In present composite probe, several fluoresceins are attached in each particle and thus bleaching becomes partial and slow. A similar stable fluorescence of fluorescein and other fluorophore-conjugated silica particles was observed earlier [310]. This result suggests that the fluorescence property of the composite nanoprobe is stable enough for relatively long-term imaging applications [311].

Glucose-functionalized plasmonic-fluorescent composite particles show their biochemical activity toward Concanavalin A (Con A) . Con A is a glycoprotein that has four glucose binding sites at pH 7.5. As a result, it induces cross-linking between glucose-functionalized particles [312]. This effect is seen as visible precipitate formation of particles after Con A addition. The particle aggregation and precipitate formation can be monitored using the surface plasmon of the plasmonic-fluorescent particle. As the particle size is small, the formation of coupled plasmon at the long wavelength due to the particle aggregation is not dominant. However, optically clear solutions turn cloudy, and then a pink/yellow precipitate appears, leaving a colorless supernatant. This result shows that the plasmonic property of the composite particle can also be used for optical detection applications [311].

Among the myriad possibilities, dendrimers can find applications in drug delivery due to the opportunity of their internal niches to host a variety of molecules [209]. DEMs have also been reported to enter tumors and carry either chemotherapeutic agents or genetic therapeutics [313]. Incorporation of photoactive components in either the core or the periphery of these nanostructures enriches them with new functionalities opening new perspectives in nanomedicine.

Roberts et al. [314] studied the toxicity of cationic PAMAM Starburst® in mice. Cationic dendrimers of generation 3 (G3, Mw 5147, diameter 3.1 nm, 24 amine termini), generation 5 (G5, Mw 21,563, diameter 5.3 nm, 96 amine termini), and generation 7 (G7, Mw 87,227, diameter 8.0 nm, 768 amine termini) were given i. p. with doses ranging from 0.026 to 45 mg/kg either as a single dose or once a week for 10 weeks. No significant behavioral abnormality or weight loss was observed through the study. However, one out of five mice died at about 24 h after dendrimer injection in the G7 group with highest dose of 45 mg/kg. These studies suggest that low generation cationic dendrimers ($G < 7$) even at high doses do not cause adverse effects. However, Heiden et al. found cationic PAMAM dendrimers (G4, amine termini) were toxic to zebra fish embryos, and the toxicity was dose and exposure duration dependent [315]. A mortality of 100% was observed by 24-h postfertilization when the dendrimer concentration exceeded 20 μM. In the same study by contrast, anionic PAMAM dendrimers (G3.5, carboxylic acid termini) were not toxic and showed no signs of attenuating embryo development. G4 dendrimers conjugated to Arg-Gly-Asp (RGD) were much less toxic compared to unconjugated G4 dendrimers. Malik et al. [316] also found that 95 mg/kg daily doses of anionic PAMAM dendrimers (G3.5, carboxylic acid termini) administered i.p. led to no mortalities and no weight change in B16F10 tumor-bearing mice. Overall, these studies indicated that dendrimer toxicity is dose and generation dependent with higher dose and higher generation dendrimers leading to more toxicity in vivo. The toxicity profiles also depend greatly on the surface charge of the dendrimers, that is, anionic dendrimers are less toxic compared to cationic dendrimers.

Photoactivated DEMs for the targeted delivery of an anticancer drug were also developed based on the photocaging strategy [317]. Fifth-generation polyamidoamine (PAMAM) DEMs of ca. 5 nm in diameter were conjugated with the anticancer drug doxorubicin caged with the *o*-nitrobenzyl photocage. Furthermore, folic acid (FA) appendages were also introduced at the DEM exterior as suitable targeting ligands. These bifunctional DEMs were effectively taken up by cancer cells expressing a high level of folate receptors. Note that the presence of the FA chromophores, spatially close to the photocage, does not influence the photochemical properties of this latter. In fact photolysis of the tailored DEMs with 365 nm light produces a clean photochemical reaction which leads to release of the anticancer drug in the cell compartment with a precise time control, inducing a remarkable level of cell mortality strictly dependent on the light exposure time.

Hematologic toxicity is one of the most important concerns for dendrimers given intravenously. Cationic dendrimers such as $-NH_2$ PAMAM have shown concentration- and generation-dependent hemolysis and induced morphology changes in red blood cells after 1-h incubation at a low concentration of 10 μg/mL; whereas, anionic dendrimers were not hemolytic at concentrations up to 2 mg/mL [318]. Agashe et al. examined the hematologic toxicities of generation 5 PPI dendrimer (PPI-5.0G), t-BOC-protected glycine-coated dendrimer (DBG), t-BOC-protected phenylalanine-coated dendrimer (DBPA), mannose-coated dendrimer (M-PPI), and lactose-coated dendrimer (L-PPI) [319]. Dendrimers were administered intravenously (i.v) into male albino rats, and blood samples were collected and analyzed

to determine hematologic parameters such as white blood corpuscles (WBCs), red blood cells (RBCs), hemoglobin (Hb), hematocrit (HCT), and mean corpuscular hemoglobin (MCH). Compared to the control group, there were significantly higher WBC counts and lower RBC, HCT, Hb, and MCH values for the PPI-5.0G group, probably due to the polycationic nature of the dendrimers. Surface-modified dendrimers (DBG, DBPA, M-PPI and L-PPI) showed no difference in terms of hematologic parameters compared to the control group.

Immunogenicity is the ability of antigens to induce humoral or cell-mediated immune responses. Immunogenicity should be avoided if the immune system is not the intended target of the dendrimer drug delivery system. The immunogenicity of PAMAM (G3, G5, and G7) dendrimers was studied in rabbits, and no evidence of immunogenicity was found 10 days after i.p. injection by the immunoprecipitation assay or the Ouchterlony double diffusion assay [314]. Five PPI-based dendrimers (PPI-5.0G, DBG, DBPA, M-PPI, and L-PPI) were injected intramuscularly into Balb/C mice at dose levels of 1–4 mg of dendrimer [319]. The antibody (IgG) level in blood was nondetectable, which indicated no sign of humoral immune response triggered by the dendrimers. However, these studies only tested short-term immunogenicity. The in vivo studies of cell-medicated immune response and complement activation have not been reported though a G5 PAMAM dendrimer has been seen to induce strong complement activation in vitro [320].

Nephrotoxicity and hepatotoxicity have been reported consistent with biodistribution studies that revealed high kidney and liver accumulation for G3 PAMAM dendrimers (intraperitoneal–i.p.) [314], G3 and G4 PAMAM dendrimers (i.v. or i.p.) [318], biotinylated-PAMAM dendrimers (G0-4) (i.v.) [321], and PEG-polyester dendritic hybrids (i.v.) [322]. Roberts et al. [314] noticed liver cell vacuolization of the cytoplasm in a 6-month toxicity study group after administration of G7 PAMAM dendrimers by i.p. route once a week for 10 weeks. A third-generation melamine dendrimer (MW 8067, 24 amine termini) was evaluated for in vivo acute (single dose) and subchronic (three i.p. injections) toxicities [323]. The acute study indicated the lethal dose was 160 mg/kg, giving rise to 100% mortality 6–12-h postinjection. In both acute and subchronic studies, there was no significant renal damage in all dose ranges as determined by blood urea nitrogen levels. Hepatic function was normal at up to 10 mg/kg dendrimer as evaluated by changes in serum alanine transaminase (ALT) activity. However, a significant increase in ALT activity noticed for both acute and subchronic groups at the 40 mg/kg dose level, and the histopathological investigation showed extensive liver necrosis.

Dendrimer modification with chemically inert polyethylene glycol (PEG) or fatty acids is one of the most attractive ways to reduce dendrimer toxicities in vitro [26]. PEG-polyester dendritic hybrids (3-arm PEG star and G2 polyester dendrons, Mw 23,500 Da) were injected into mice as an i.v. bolus dose of 1.3 g/kg [322]. Mice survived after 24 h, and no changes of organ pathology were observed in the liver, lungs, heart, kidney, or intestine. PEGylated melamine dendrimer (G3, PEG 2000 termini) was administered at doses of 2.56 g/kg i.p. and 1.28 g/kg i.v. into C3H mice, and all mice survived after 24 and 48 h after i.p. and i.v. administration, respectively, with no liver or kidney toxicity noted [324].

The nonbiodegradability of PAMAM/PPI-type dendrimers is of major concern for their medical use. Biodistribution studies of magnetic resonance imaging (MRI) contrast agents based on PAMAM/PPI dendrimer-gadolinium (Gd) chelates have been reported. Lower generations of PAMAM-Gd (diameter < 10 nm) were excreted via kidney, and the renal elimination rate decreased with increasing dendrimer size. Minimal renal excretion and high RES uptake were observed when PAMAM-Gd size exceeded 10 nm [325]. It was also noticed that only less than 15% of the injected PAMAM-Gd agents (PAMAM G4, G5, and G6) was excreted within 2 days [326]. Dendrimer core structure also influences the biodistribution of the dendrimer MRI agents. Compared to the PAMAM-Gd, a less hydrophilic PPI diaminobutane core contributes to the dramatic increase in liver accumulation [327]. Although PEGylation and other surface modification schemes may reduce the potential of harmful biological interactions, the dendrimer core material must be biodegradable or readily eliminated by the renal or hepatic system. Otherwise, the long-term toxicity is difficult to predict. The amide core of PAMAM- and PPI-type dendrimers cannot undergo hydrolysis or enzymatic degradation. Newer dendrimers where the core is structured from amino acids, oligonucleotides, or polyesters may overcome these toxicity concerns [328].

In a further study [329], fluorescein-doped magnetic mesoporous silica nanoparticles were modified with 3-(triethoxysily)proplyl isocyanate-activated G2·NH$_2$ PAMAM dendrimers and the amino terminal groups of the assembled dendrimers can be further neutralized by reacting with methyl acrylate to form esters. The formed composite nanoparticles are biocompatible even at a NP concentration of 650 μg mL^{-1} and can be used as both drug delivery vehicles and fluorescent imaging agents.

For targeted imaging of cancer cells in vitro and in vivo, it would be ideal to assemble targeting ligand-modified dendrimer molecules onto the nanoparticles (e.g., iron oxide, NMNPs, etc.). In the study [294], Shi et al. synthesized and characterized a group of FA-modified carboxyl-functionalized G3 PAMAM dendrimers that were used to assemble onto the superparamagnetic iron oxide (Fe$_3$O$_4$) NPs. The Fe$_3$O$_4$NPs synthesized using controlled coprecipitation of Fe(II) and Fe (III) ions were assembled with the FA-modified dendrimers through electrostatic interaction in order to achieve specific targeting to KB cells that overexpress FAR. It appears that carboxyl-terminated PAMAM dendrimer-assembled Fe$_3$O$_4$NPs can be uptaken by KB cells regardless of the repelling force between the negatively charged cells and the negatively charged particles. In the presence of a large amount of carboxyl terminal groups on the dendrimer surface, the receptor-mediated endocytosis of Fe$_3$O$_4$NPs assembled by FA-modified dendrimers was not facilitated. This implies that the surface charge of dendrimer-stabilized magnetic iron oxide NPs in a biological medium is an important factor influencing their biological performance.

The first methods for preparing metal-encapsulated dendrimers for use in biomedical applications were reported within the last decade with the goal of adding a finer degree of control for tuning the biological interactions elicited by the metal particles, including improved biocompatibility, retention, and ease of surface

modification for potential use as biomarkers, contrast agents, and for photothermal therapy [242, 330]. Gold-based nanoparticles have been developed that strongly absorb light in the near-infrared region, facilitating deep optical penetration into tissues, generating a localized lethal dose of heat at the site of a tumor [330].

The advantage of using dendrimers as templates to prepare gold nanoparticles lies in the fact that the surface of the particles can be modified with various functional moieties (e.g., targeting ligands and dyes) through dendrimer chemistry for practical biomedical applications [331, 332]. AuDENPs with a size of 2 nm prepared with amine-terminated generation 5 PAMAM dendrimers (G5·NH₂'s) can be modified with folic acid and fluorescein isothiocyanate for the subsequent targeting and imaging of cancer cells overexpressing high-affinity folic acid receptors [279, 332]. Arginine-glycine-aspartic acid (RGD) peptide-functionalized generation 5 (G5) dendrimers can be used as templates to form AuDENPs with a size of 3 nm, which can specifically target tumor vasculature-related endothelial cells overexpressing $\alpha_v\beta_3$ integrin [331]. RGD peptides are well known to bind preferentially to the $\alpha_v\beta_3$ integrin. In this context, targeting tumor cells or tumor vasculature by RGD-based strategies is a promising approach for delivering anticancer drugs or contrast agents for cancer therapy and diagnosis. RGD-based strategies include antagonist drugs (peptidic or peptidomimetic) of the RGD sequence, RGD-conjugates, and the grafting of the RGD peptide or peptidomimetic, as targeting ligand, at the surface of nanocarriers. These studies have clearly indicated that PAMAM dendrimers are promising templates for the generation of multifunctional AuDENP-based nanoplatforms for various biomedical applications. One of the key steps in the preparation of AuDENPs for ready use for biological applications is the rendering of the particle surface charge to neutral. This can be achieved by the acetylation of dendrimer terminal amines [267]. Shi et al. [267] have shown that AuDENPs formed with G5. NH₂ dendrimers as templates with a gold salt/dendrimer molar ratio of 51.2:1 can be acetylated to render particles with a similar size and size distribution to those before acetylation. The acetylated AuDENPs, having neutral surface charges, are water soluble, colloidally stable, and biocompatible at a concentration up to 2 μM.

Phosphorylcholine (PC)-functionalized dendrimers provide another example of noble metal particle stabilizer. Their stability and controllable surface properties indicated potential use in biosensing (Scheme 4.26) [333]. AFM and TEM were used to demonstrate the morphology and size distribution of the AuNPs formed. Later, Voelcker's use of the neutral impact collision ion scattering spectroscopy (NICISS) technique proved useful to understand the inner structure of dendrimer-stabilized AuNPs [231].

Furthermore, dendrimer-encapsulated gold nanoparticles have been prepared and identified for their potential use toward the photothermal treatment of malignant tissue (Scheme 4.27). Amine-terminated G5-PAMAM dendrimer-entrapped gold nanoparticles were prepared and covalently conjugated to fluorescein and folic acid for targeted delivery to tumor cells overexpressing folic acid receptors, as reported by the Baker group [332]. The dendrimers were shown to specifically bind to KB cells in vitro and were internalized into lysosomes. The applicability of these
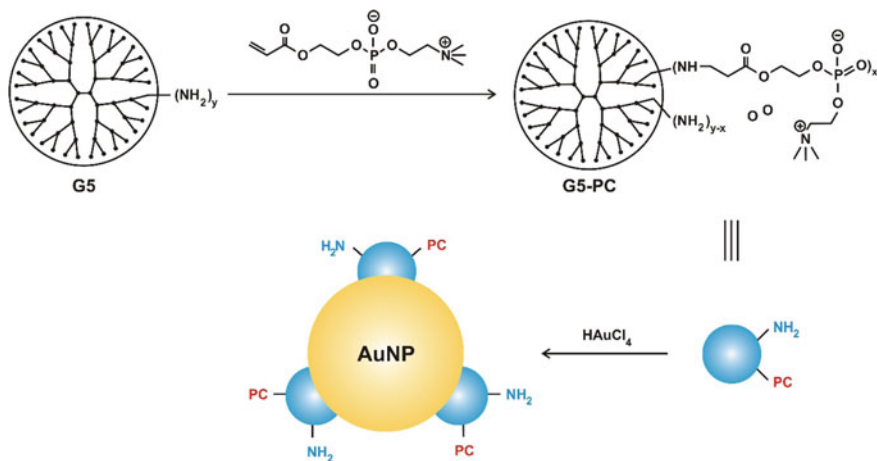
Scheme 4.26 Schematic representation of the synthesis of AuDSNs saturated with reactive amine groups (NH_2) for bioconjugation and phosphorylcholine groups (PC) for stability [184, 333]

particles for targeted hyperthermia treatment and as electron-dense contrast agents was recognized, and in vivo performance studies are currently underway. The photothermal properties of gold-encapsulated PEGylated and non-PEGylated G4-PAMAM dendrimers as reported by Haba et al., were evaluated and compared to conventionally used gold nanoparticles prepared with sodium citrate [334]. Gold was encapsulated by first introducing $HAuCl_4$ and then chemically reducing the gold inside the dendrimers. PEGylated gold-encapsulated dendrimers demonstrated superior photostability compared to non-PEGylated, with the non-PEGylated absorbance decreasing to almost negligible levels by three days, whereas the PEGylated nanoparticle absorbance was relatively unchanged over five days. It was noted that the non-PEGylated gold particles tended to aggregate. The photothermal properties of the PEGylated particles were only slightly lower compared to conventional gold particles.

Scheme 4.27 Photothermal therapy. Conceptual representation of photothermal therapy using dendrimer-entrapped gold nanoparticles. The nanoparticles would be targeted to tumor cells via folic acid receptors, and upon exposure to near-infrared light, the gold particles would emit heat and kill the host cell [334]
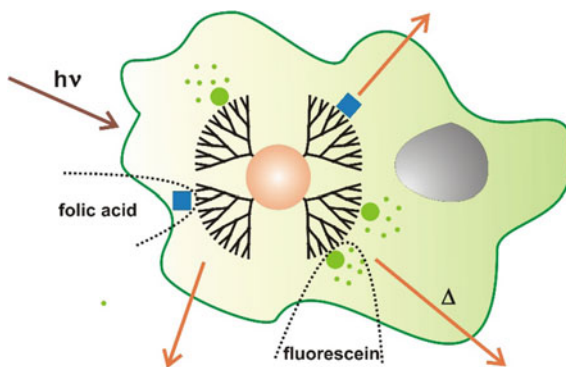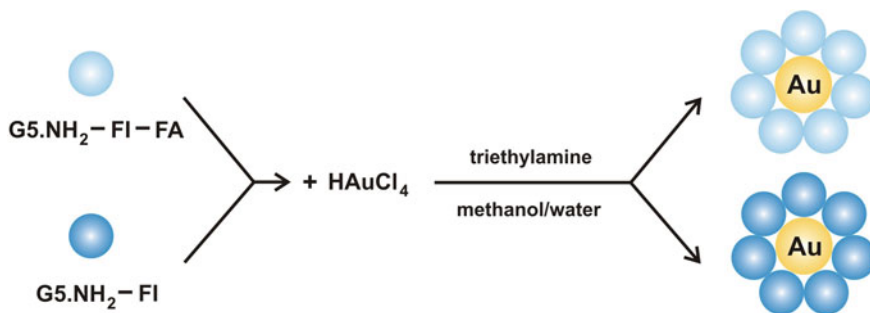
Scheme 4.28 Schematic representation of the approaches to synthesizing $\{(Au^0)_7\text{-}$ G5·NHAc-FI-FA$\}$ and $\{(Au^0)_7\text{-}G5\cdot NHAc\text{-}FI\}$ DSNPs [241, 280]

It is known that folic acid (FA)- and fluorescein isothiocyanate (FI)-modified G5 dendrimers with neutral surface charge can specifically target to some cells over-expressing folic acid receptor (FAR) [279]. It is anticipated that using FA- and FI-modified G5 dendrimers to synthesize AuDSNPs using the developed spontaneous approach [277] may provide a means to create an AuNP-based multifunctional nanoplatform for cancer cell targeting and imaging. In Shi et al.'s work [280], amine-terminated G5 PAMAM dendrimers prefunctionalized with FA and FI moieties were complexed with Au(III) ions, followed by acetylation of the amine groups on the dendrimer surfaces (Scheme 4.28). This one-step process led to the spontaneous formation of 6 nm-sized AuNPs stabilized by multifunctional dendrimers bearing both targeting and imaging functionalities. The formed AuDSNPs are water soluble, stable, and biocompatible. Combined flow cytometry, confocal microscopy, silver staining, and inductively coupled plasma-mass spectrometry analyses show that the FA- and FI-functionalized AuDSNPs can specifically target to cancer cells expressing high-affinity FAR in vitro. The tunable dendrimer surface chemistry (e.g., surface functionalization and bioconjugation) in conjunction with the facile approach developed to form AuDSNPs open a new avenue to developing various biofunctionalized AuDSNPs for a range of interesting biomedical applications.

4.5   Conclusion

Some templates can be employed for the shape-controlled synthesis of metal nanocrystals. These spatially and dimensionally constrained structures can serve as reaction cages to control the nucleation and growth of the particles (and impart stability), leading to the formation of nanoparticles with a morphology complementary to that of the template. Thiol chemistry has widely been used to modify the surface of NMNPs with synthetic polymers and biomacromolecules. Block copolymers (di- and triblock), especially amphiphilic, have been used to prepare

aggregation-free NMNPs. A new class of amphiphilic polystyrene-block-polycysteine copolymers was synthesized and used to conjugate with AuNPs to inhibit particle aggregation. A synthesis of positively charged silver nanoparticles via photoreduction of silver nitrate in branched copolymers demonstrated superior surface-enhanced Raman scattering (SERS) activity. Microwave irradiation was found to be a new technique for coating of AgNPs onto the surface of PMMA beads. Bimetallic alloy nanoparticles consisting of two noble metals platinum–silver supported on carbon with a variable dimension were successfully prepared by ethylene glycol (EG). A PEG-based nonionic block copolymer templates were used for the synthesis of luminescent silver nanoparticles. Another example of fluorescent metal nanoparticles are Ag/Au bimetallic cores coated by a PEG-based hydrogel prepared with 2-(2-methoxyethoxy)ethyl methacrylate as monomer and poly(ethylene glycol) dimethacrylate as cross-linker. A new path to design multifunctional infinite coordination polymer particles (ICPs) materials has been opened up by the incorporation or integration of other functional materials into ICPs. Gold nanoparticles have also been synthesized using biopolymers such as proteins and polysaccharides. These polymers are known as polyelectrolytes (PE) and can be used as reducing/stabilizing agents in one single-step syntheses. The building-up of multifunctional core@shell nanostructures is one of the great advantages of using PE assemblies. In this case, the PE forming the multilayers can be functionalised with drugs, organic dyes, contrast agents, radionucleids, catalysts, organic dyes, and proteins, namely antibodies, allowing the application of the ensuing structures in areas such as drug/gene delivery, biosensing, bioimaging, and photodynamic therapy. Copolymers based on cyclodextrin can be used to produce nanosized silver particles where potassium persulfate was used as the initiator.

Through the layer-by-layer (LBL) assembly, the polyelectrolyte microcapsules can adsorb the precursor of metal and then embedded NMNPs into the wall of microcapsules through in situ reduction. Nontraditional nanostructures consisting of noble metals are often fabricated by depositing thin layers of metals (or their precursors) on some silica beads existing templates, followed by calcination or wet chemical etching to remove the solid cores. Another method was based on the layer-by-layer adsorption of polyelectrolytes and charged gold nanoparticles to build shell-like structures around colloidal templates whose surfaces had been derivatized with appropriately charged groups. A supramolecular procedure was introduced for the stepwise construction of multilayer thin films. The procedure, based on the LBL assembly of guest-functionalized dendrimers and CD-AuNPs (AuNP@CDs), was demonstrated to yield multilayer thin films with thickness control at the nm level. Characterization by means of SPR, UV–Vis spectroscopy, ellipsometry, and AFM showed a well-defined multilayer formation, an accurate thickness control, and the need of specific host–guest interactions. Such protocols can potentially be used for obtaining various structures, whose assembly is driven by multiple supramolecular interactions. This constitutes a general nanofabrication paradigm for the integration of organic, inorganic, metallic, and biomolecular components while retaining the interfacing supramolecular specificity.

We have reported an environment-friendly in situ polyol process for developing a well-distribution and uniform shape of silver nanoparticles in PVA films stabilized with PGA polypeptide. The application of the Ag films to SERS shows great enhancement, needs low excitation power, is easy to prepare, and is convenient to use. Using benzoic acid as a probe molecule, we obtained much stronger SERS signals, indicating that for silver nanoparticles capped by stabilizer molecules such as PGA, the in situ reducing method provides a new vision of PVA to fabricate SERS-active substrates. As compared the effects of the silver colloid aggregation on the silver/PVA nanocomposite, we can therefore confirm that the size, shape, and spacing of silver nanostructures is related to SERS enhancement.

Colloids of Ag were obtained from the powder that has bigger particles (typically between 30 and 50 nm) via a chemical redispersion method. The studies revealed that the powder has about 20–25% redispersibility in aqueous medium. It is highlighted that one can prepare large surface-capped particles in the first place and then isolate particles of smaller dimension i.e., typically in the nanometer regime via a colloidal stage. The nanoparticles via colloids can be loaded in various matrices including the polymers. The absorption wavelength can be altered by the selection of water-friendly polymers. The nanoparticles so obtained can have potential applications in household items, electronics as well as in optoelectronics.

Amphiphilic block copolymers (ABCs) highlighted here have been used extensively in pharmaceutical applications ranging from sustained-release technologies to gene delivery. The utility of ABCs for delivery of therapeutic agents results from their unique chemical composition, which is characterized by a hydrophilic block that is chemically tethered to a hydrophobic block. In aqueous solution, polymeric micelles are formed via the association of ABCs into nanoscopic core/shell structures at or above the critical micelle concentration. Upon micellization, the hydrophobic core regions serve as reservoirs for hydrophobic drugs, which may be loaded by chemical, physical, or electrostatic means, depending on the specific functionalities of the core-forming block and the solubilizate. Although the Pluronics® are the most widely studied ABC system, copolymers containing poly(L-amino acid) and poly(ester) hydrophobic blocks have also shown great promise in delivery applications. Because each ABC has unique advantages with respect to drug delivery, it may be possible to choose appropriate block copolymers for specific purposes, such as prolonging circulation time, introduction of targeting moieties, and modification of the drug-release profile. ABCs have been used for numerous pharmaceutical applications including drug solubilization/stabilization, alteration of the pharmacokinetic profile of encapsulated substances, and suppression of multidrug resistance and herein highlighted the formation of metal nanoparticles.

With PAMAM dendrimers as templates, dendrimer-entrapped gold nanoparticles (AuDENPs) can be formed with each AuNP entrapped within each dendrimer molecule. A wide range of metal ions can be preorganized with dendrimers, especially PAMAM dendrimers to form metal DENPs. Likewise, bimetallic core@shell or alloy DENPs can be prepared by coreduction of the metal ions in the presence of dendrimer templates. AuDSNPs (dendrimer-stabilized) were found to

be fluorescent and display strong blue photoluminescence. The size of the AuDSNPs decreases with the increase of the number of dendrimer generations, suggesting the different nucleation and growth mechanisms for gold nanocrystals in the presence of PAMAM dendrimers. Specifically, unique bimetallic materials can be synthesized by dendrimer-templating method such as AuAg alloys, core@shell Au@Ag, and AuAg alloy@Ag structures. The encapsulation of metal ions inside dendrimers involves, variously, electrostatic and complexation interactions—the dendrimer interior includes coordinating groups such as –OH, NH$_2$, or –COOH.

Amine-terminated fourth-generation PAMAM dendrimers functionalized with thiophene dendrons are synthesized, and their application in the preparation of dendrimer-encapsulated nanoparticles has been demonstrated. FTIR and UV–Vis spectroscopies show evidence that Pd hybrid nanoparticles are more stable than Au nanoparticles. Fluorescence spectra indicate that thiophene dendrons interact with the encapsulated nanoparticles and their emission can even be enhanced by gold nanoparticles through energy transfer. AFM images reveal that the functionalized PAMAM dendrimer is an efficient host for immobilizing and stabilizing hybrid nanoparticles on HOPG. The complex dendrimer-like gold assembly was spontaneously formed.

The functionalized plasmonic nanoparticle has been used as cell imaging and plasmon-based optical detection probe. Biomolecule (lucose…)-functionalized plasmonic-fluorescent composite particles show their biochemical activity toward, for example, Concanavalin A (Con A). This effect is seen as visible precipitate formation of particles after Con A addition. The particle aggregation and precipitate formation can be monitored using the surface plasmon of the plasmonic-fluorescent particle.

Among the myriad possibilities, dendrimers (DEMs) can find applications in drug delivery due to the opportunity of their internal niches to host a variety of molecules. DEMs have also been reported to enter tumors and carry either chemotherapeutic agents or genetic therapeutics. Incorporation of photoactive components in either the core or the periphery of these nanostructures enriches them with new functionalities opening new perspectives in nanomedicine. Dendrimer modification with chemically inert polyethylene glycol or fatty acids is one of the most attractive ways to reduce dendrimer toxicities in vitro.

For targeted imaging of cancer cells in vitro and in vivo, it would be ideal to assemble targeting ligand-modified dendrimer molecules onto the metal nanoparticles. The advantage of using dendrimers as templates to prepare gold nanoparticles lies in the fact that the surface of the particles can be modified with various functional moieties (e.g., targeting ligands and dyes) through dendrimer chemistry for practical biomedical applications. Gold-based nanoparticles have been developed that strongly absorb light in the near-infrared region, facilitating deep optical penetration into tissues, generating a localized lethal dose of heat at the site of a tumor.

Glossary

Boltorn polyols	and their derivatives are hyperbranched polymers which are widely used in material and medicinal chemistry to prepare polymers with improved mechanical properties, to modify the properties of membranes, and to control drug delivery. A characteristic example of such hyperbranched molecules, which can now be produced on an industrial scale, belongs to the aliphatic polyester family bearing the commercial name Boltorn®. The hyperbranched Boltorn polymers can be aliphatic polyesters constructed with ethoxylated pentaerythritol as central cores and 2,2-bis(methylol)propionic acid (bisMPA) as dendritic units. For example, Boltorn H20 should contain 16 hydroxyl end groups per molecule indicating that it contains on average two generations of MPA. Similarly Boltorn H30 and H40, respectively, are third and fourth generation containing 32 hydroxyl and 64 hydroxyl per molecule.
Folic acid	another form of which is known as folate, is one of the B vitamins. It is used as a supplement by women to prevent neural tube defects (NTDs) developing during pregnancy. It is also used to treat anemia caused by folic acid deficiency. Long-term supplementation is also associated with small reductions in the risk of stroke and cardiovascular disease. Folate targeting is a method utilized in biotechnology for drug delivery purposes. Based on the natural high affinity of folate for the folate receptor protein (FAR), which is commonly expressed on the surface of many human cancers, folate–drug conjugates also bind tightly to the FR and trigger cellular uptake via endocytosis. $\alpha_v\beta_3$ is a type of integrin that is a receptor for vitronectin. It consists of two components, integrin alpha V and integrin beta 3 (CD61), and is expressed by platelets. Furthermore, it is a receptor for phagocytosis on macrophages or dendritic cells.
Hematologic toxicity	is a common treatment complication of chronic hepatitis C virus (HCV) infection, especially when interferon (IFN) and ribavirin are used. The side effects of treatment are often augmented in cancer patients due to baseline cytopenias. These adverse events often lead to dose reduction or discontinuation of antivirals.
Hepatotoxicity	(from hepatic toxicity) implies chemical-driven liver damage. Drug-induced liver injury is a cause of acute and chronic liver disease.

| HOMO and LUMO | are acronyms for highest occupied molecular orbital and lowest unoccupied molecular orbital, respectively. The energy difference between the HOMO and LUMO is termed the HOMO–LUMO gap. HOMO and LUMO are sometimes referred to as frontier orbitals. The difference in energy between these two frontier orbitals can be used to predict the strength and stability of transition metal complexes, as well as the colors they produce in solution. Roughly, the HOMO level is to organic semiconductors and that the valence band maximum is to inorganic semiconductors and quantum dots. The same analogy exists between the LUMO level and the conduction band minimum. In organometallic chemistry, the size of the LUMO lobe can help predict where addition to pi ligands will occur. Each molecular orbital has a calculated energy level. Chemists sort the molecular orbitals (MOs) by energy levels. Chemists assume that the electrons will occupy the lowest energy level MOs first. The difference in the HOMO's energy level and the LUMO's energy level is called the band gap. The band gap can sometimes serve as a measure of the excitability of the molecule: the smaller the energy, the more easily a molecule's electrons will be excited. For example, this can help predict whether a substance will have luminescence. As MOs for larger molecules tend to be more complicated (the electrons are spread out all over the big molecule). At this point, we generally no longer focus on a comparison between the MOs and the AOs but instead just take the MOs as a set of orbitals for the whole molecule. There are many such orbitals (an infinite number), but we will always focus simply on the electrons that are most important for the chemistry.In immunology, the mononuclear phagocyte system or mononuclear phagocytic system (MPS) (also known as the reticuloendothelial system or macrophage system) is a part of the immune system that consists of the phagocytic cells located in reticular connective tissue. The cells are primarily monocytes and macrophages, and they accumulate in lymph nodes and the spleen. The Kupffer cells of the liver and tissue histiocytes are also part of the MPS. The mononuclear phagocyte system and the monocyte macrophage system refer to two different entities, often mistakenly understood as one.Immunogenicity is the ability of a particular substance, such as an antigen or epitope, to provoke an immune response in the body of a human or animal. In other words, immunogenicity is the ability to induce a humoral and/or cell-mediated immune responses.Nephrotoxicity is toxicity in the kidneys. It is a poisonous effect of some substances, |

both toxic chemicals and medications, on renal function. There
are various forms, and some drugs may affect renal function in
more than one way. Nephrotoxins are substances displaying
nephrotoxicity.

Zebra fish   (Danio rerio) is a tropical freshwater fish belonging to the
                       minnow family (Cyprinidae) of the order Cypriniformes.

References

1. Kim TG, Kim YW, Kim JS, Park B (2004) Silver-nanoparticle dispersion from the consolidation of Ag-attached silica colloid. J Mater Res 19:1400–1407
2. Khanna PK, Singh N, Charan S, Subbarao VVVS, Gokhale R, Mulik UP (2005) Synthesis and characterization of Ag/PVA nanocomposite by chemical reduction method. Mater Chem Phys 93:117–121
3. Muniz-Miranda M (2004) SERS-active Ag/SiO$_2$ colloids: photoreduction mechanism of the silver ions and catalytic activity of the colloidal nanoparticles. J Raman Spectrosc 35: 839–842
4. He J, Kunitake T, Nakao A (2003) Facile in situ synthesis of noble metal nanoparticles in porous cellulose fibers. Chem Mater 15:4401–4406
5. Adhyapak PV, Khanna PK, Dadge JW, Aiyer RC (2006) Tuned optical properties of in-situ synthesized m-nitroaniline doped Ag/PVA nano-composites. J Nanosci Nanotechnol 6:2141–2146
6. Mbhele ZH, Salemane MG, van Sittert CGCE, Nedeljkovic JM, Djokovic V, Luyt AS (2003) Fabrication and characterization of silver-polyvinyl alcohol nanocomposites. Chem Mater 15:5019–5024
7. Lin YH, Chung CK, Chen CT, Liang HF, Chen SC, Sung HW (2005) Preparation of nanoparticles composed of chitosan/poly-gamma-glutamic acid and evaluation of their permeability through Caco-2 cells. Biomacromol 6:1104–1112
8. Huo Z, Tsung C, Huang W, Zhang X, Yang P (2008) Sub-two nanometer single crystal Au nanowires. Nano Lett 8:2041–2044
9. Yener DO, Sindel J, Randall CA, Adair JH (2002) Synthesis of nanosized silver platelets in octylamine-water bilayer systems. Langmuir 18:8692–8699
10. Wei G, Zhou H, Liu Z, Song Y, Wang L, Sun L, Li Z (2005) One-step synthesis of silver nanoparticles, nanorods, and nanowires on the surface of DNA network. J Phys Chem B 109:8738–8743
11. Zhang J, Liu H, Wang Z, Ming N (2007) Shape-selective synthesis of gold nanoparticles with controlled sizes, shapes, and plasmon resonances. Adv Funct Mater 17:3295–3303
12. Huang LM, Wang HT, Wang ZB, Mitra A, Bozhilov KN, Yan YS (2002) Nanowire arrays electrodeposited from liquid crystalline phases. Adv Mater 14:61–64
13. Wang L, Chen X, Zhan J, Chai Y, Yang C, Xu L, Zhuang W, Jing B (2005) Synthesis of gold nano-and microplates in hexagonal liquid crystals. J Phys Chem B 109:3189–3194
14. Kang Y, Taton TA (2005) Core/Shell gold nanoparticles by self-assembly and crosslinking of micellar, block-copolymer shells. Angew Chem Int Ed Engl 44:409–412
15. Huang HY, Kowalewski T, Remsen EE, Gertzmann R, Wooley KL (1997) Hydrogel-coated glassy nanospheres: A novel method for the synthesis of shell cross-linked knedels. J Am Chem Soc 119:11653–11659
16. Ge Z, Kang Y, Taton TA, Braun PV, Cahill DG (2005) Thermal transport in Au-core polymer-shell nanoparticles. Nano Lett 3:531–535

17. Kang Y, Taton TA (2003) Micelle-encapsulated carbon nanotubes: a route to nanotube composites. J Am Chem Soc 125:5650–5651
18. Djalali R, Chen YF, Matsui H (2002) Au nanowire fabrication from sequenced histidine-rich peptide. J Am Chem Soc 124:13660–13661
19. Jana NR, Gearheart L, Murphy CJ (2001) Seed-mediated growth approach for shape-controlled synthesis of spheroidal and rod-like gold nanoparticles using a surfactant template. Adv Mater 13:1389–1393
20. Murphy CJ, Sau TK, Gole AM, Orendorff CJ, Gao J, Gou L, Hunyadi SE, Li T (2005) Anisotropic metal nanoparticles: synthesis, assembly, and optical applications. J Phys Chem B 109:13857–13870
21. Newkome GR, Yao ZQ, Baker GR, Gupta VK (1985) Micelles. Part 1. Cascade molecules—a new approach to micelles. A [27]-arborol. J Org Chem 50:2003–2004
22. Chechik V, Crooks RM (2000) Dendrimer-encapsulated Pd nanoparticles as fluorous-phase-soluble catalysts. J Am Chem Soc 122:1243–1244
23. Ispasoiu RG, Balogh L, Varnavski OP, Tomalia DA, Goodson T (2000) Large optical limiting from novel metal-dendrimer nanocomposite materials. J Am Chem Soc 122:11005–11006
24. Zheng J, Stevenson MS, Hikida RS, Van Patten PG (2002) Influence of pH on dendrimer-protected nanoparticles. J Phys Chem B 106:1252–1255
25. Weener JW, Meijer EW (2000) Photoresponsive dendritic monolayers. Adv Mater 72:741–746
26. Stasko NA, Johnson CB, Schoenfisch MH, Johnson TA, Holmuhamedov EL (2007) Cytotoxicity of polypropylenimine dendrimer conjugates on cultured endothelial cells. Biomacromol 8:3853–3859
27. Horiuchi S, Fujita T, Hayakawa T, Nakao Y (2003) Three-dimensional nanoscale alignment of metal nanoparticles using block copolymer films as nanoreactors. Langmuir 19:2963–2973
28. Templeton AC, Wuelfing WP, Murray RW (2000) Monolayer-protected cluster molecules. Acc Chem Res 33:27–36
29. Brust M, Walker M, Bethell D, Schiffrin DJ, Whyman R (1994) Synthesis of thiol-derivatised gold nanoparticles in a two-phase Liquid-Liquid system. Chem Commun (7):801–802
30. Lowe AB, Sumerlin BS, Donovan MS, McCormack CL (2002) Facile preparation of transition metal nanoparticles stabilized by well-defined (co)polymers synthesized via aqueous reversible addition-fragmentation chain transfer polymerization. J Am Chem Soc 124:11562–11563
31. Shan J, Nuopponen M, Jiang H, Viitala T, Kauppinen E, Kontturi K, Tenhu H (2005) Amphiphilic gold nanoparticles grafted with poly (N-isopropylacrylamide) and polystyrene. Macromolecules 38:2918–2926
32. Mirkin CA, Letsinger RL, Mucic RC, Storhoff JJ (1996) A DNA-based method for rationally assembling nanoparticles into macroscopic materials. Nature 382:607–609
33. Li Z, Jin R, Mirkin CA, Letsinger RL (2002) Multiple thiol-anchor capped DNA-gold nanoparticle conjugates. Nucleic Acids Res 30:1558–1562
34. Chen Y, Cho J, Young A, Taton TA (2007) Enhanced stability and bioconjugation of photo-cross-linked polystyrene-shell, Au-core nanoparticles. Langmuir 23:7491–7497
35. Hong R, Han G, Fernandez JM, Kim BJ, Forbes NS, Rotello VM (2006) Glutathione-mediated delivery and release using monolayer protected nanoparticle carriers. J Am Chem Soc 128:1078–1079
36. Sun Y, Yin Y, Mayers BT, Herricks T, Xia Y (2002) Uniform silver nanowires synthesis by reducing $AgNO_3$ with ethylene glycol in the presence of seeds and poly(vinyl pyrrolidone). Chem Mater 14:4736–4745
37. Manna A, Imae T, Aoi K, Okada M, Yogo T (2001) Synthesis of dendrimer-passivated noble metal nanoparticles in a polar medium: comparison of size between silver and gold particles. Chem Mater 13:1674–1681

38. Zhang Z, Patel RC, Kothari R, Johnson CP, Friberg SE, Aikens PA (2000) Stable silver clusters and nanoparticles prepared in polyacrylate and inverse micellar solutions. J Phys Chem B 104:1176–1182
39. Zhang Z, Han M (2003) One-step preparation of size-selected and well-dispersed silver nanocrystals in polyacrylonitrile by simultaneous reduction and polymerization. J Mater Chem 13:641–643
40. Zhu Y, Qian Y, Li X, Zhang M (1997) γ-radiation synthesis and characterization of polyacrylamide-silver nanocomposites. Chem Commun (12):1081–1082
41. Song J, Kang H, Lee C, Hwang SH, Jang J (2012) Aqueous synthesis of silver nanoparticle embedded cationic polymer nanofibers and their antibacterial activity. ACS Appl Mater Interfaces 4:460–465
42. Tan S, Erol M, Attygalle A, Du H, Sukhishvili S (2007) Synthesis of positively charged silver nanoparticles via photoreduction of $AgNO_3$ in branched polyethyleneimine/HEPES solutions. Langmuir 23:9836–9843
43. Abraham S, Kim I, Batt CA (2007) A facile preparative method for aggregation-free gold nanoparticles using poly(styrene-block-cysteine). Angew Chem Int Ed 46:5720–5723
44. Kate KH, Singh K, Khanna PK (2011) Microwave formation of Polypyrrole/Ag nano-composite based on interfacial polymerization by use of $AgNO_3$. Synth React Inorg Met-Org Chem 41:199–202
45. Kate KH, Damkale SR, Khanna PK, Jain GH (2011) Nano-silver mediated polymerization of pyrrole: synthesis and gas sensing properties of polypyrrole (PPy)/Ag nano-composite. J Nanosci Nanotechnol 11:7863–7869
46. Katouki H, Komarneni S (2003) Nano- and micro- meter sized silver metal powders by microwave-polyol process. J Jpn Soc Powder Powder Metall 50:745–750
47. El Badawy AM, Luxton TP, Silva RG, Scheckel CK, Suidan MT, Tolaymat TM (2010) Impact of environmental conditions (pH, ionic strength, and electrolyte type) on the surface charge and aggregation of silver nanoparticles suspensions. Environ Sci Technol 44:1260–1266
48. Huynh KA, Chen KL (2011) Aggregation kinetics of citrate and polyvinylpyrrolidone coated silver nanoparticles in monovalent and divalent electrolyte solutions. Environ Sci Technol 45:5564–5571
49. El Badawy AM, Silva RG, Morris B, Scheckel KG, Suidan MT, Tolaymat TM (2011) Surface charge-dependent toxicity of silver nanoparticles. Environ Sci Technol 45:283–287
50. Hoheisel SM, Diamond S, Mount D (2012) Comparison of nanosilver and ionic silver toxicity in Daphnia magna and Pimephales promelas. Environ Toxicol Chem 31:2557–2563
51. Dobias J, Bernier-Latmani R (2013) Silver release from silver nanoparticles in natural waters. Environ Sci Technol 47:4140–4146
52. Luo S, Yang S, Sun C, Gu JD (2012) Improved debromination of polybrominated diphenyl ethers by bimetallic iron-silver nanoparticles coupled with microwave energy. Sci Total Environ 429:300–308
53. Ma SN, Ou ZW, Sun XF, Bai M, Liu ZH (2009) In-situ synthesis of ultra-dispersion-stability nano-Ag in epoxy resin and toughening modification to resin. J Funct Mater 40:1029–1032
54. Pal A, Shah S, Devi S (2009) Microwave-assisted synthesis of silver nanoparticles using ethanol as a reducing agent. Mater Chem Phys 114:530–532
55. Si MZ, Fang Y, Dong G (2008) Research on nano-silver colloids prepared by microwave synthesis method and its SERS activity. Acta Photon Sin 37:1034–1036
56. Yao BH, Xu GC, Zhang HY, Han X (2010) Synthesis of nanosilver with polyvinylpyrrolidone (PVP) by microwave method. Chin J Inorg Chem 26:1629–1632
57. Bo L, Yang W, Chen M, Gao J, Xue Q (2009) A simple and 'green' synthesis of polymer-based silver colloids and their antibacterial properties. Chem Biodivers 6:111–116
58. Irzh A, Perkas N, Gedanken A (2007) Microwave-assisted coating of PMMA beads by silver nanoparticles. Langmuir 23:9891–9897

59. Hwang BJ, Kumar SMS, Chen CH, Chang RW, Liu DG, Lee JF (2008) Size and alloying extent dependent physiochemical properties of Pt-Ag/C nanoparticles synthesized ethylene glycol method. J Phys Chem C 112:2370–2377

60. Luo LB, Yu SH, Qian HS, Zhou T (2005) Large-scale fabrication of flexible silver/cross-linked poly(vinyl alcohol) coaxial nanocables by a facile solution approach. J Am Chem Soc 127:2822–2823

61. Chen M, Wang LY, Han JT, Zhang JY, Li ZY, Qian DJ (2006) Preparation and study of polyacrylamide-stabilized silver nanoparticles through a one-pot process. J Phys Chem B 110:11224–11231

62. Yang Q, Wang F, Tang KB, Wang CR, Chen ZW, Qian YT (2002) The formation of fractal Ag nanocrystallites via γ-irradiation route in isopropyl alcohol. Mater Chem Phys 78: 495–500

63. Vukovic VV, Nedeljkovic JM (1993) Surface modification of nanometer-scale silver particles by imidazole. Langmuir 9:980–983

64. Caulfield MJ, Qiao GG, Solomon DH (2002) Some aspects of the properties and degradation of polyacrylamides. Chem Rev 102:3067–3083

65. Silva M, Dutra ER, Mano V, Machado JC (2000) Polymer degradation and stability. Polym Degrad Stab 67:491–495

66. Vilcu R, Irinei F, Ionescu-Bujor J, Olteanu M, Demetrescu I (1985) Kinetic parameters obtained from TG and DTG curves of acrylamide-maleic anhydride copolymers. J Therm Anal 30:495–502

67. Vandyke JD, Kasperski KL (1993) Thermogravimetric study of polyacrylamide with evolved gas-analysis. J Polym Sci Part A Polym Chem 31:1807–1823

68. Shan J, Nuopponen M, Jiang H, Kauppinen E, Tenhu H (2003) Preparation of poly (N-isopropylacrylamide)-monolayer-protected gold clusters: synthesis methods, core size, and thickness of monolayer. Macromolecules 36:4526–4533

69. Li DX, He Q, Cui Y, Wang KW, Zhang XM, Li JB (2007) Thermosensitive copolymer networks modified gold nanoparticles for nanocomposite entrapment. Chem-Eur J 13: 2224–2229

70. Li DX, He QA, Li JB (2009) Smart Core/Shell nanocomposites: polymers modified gold nanoparticles. Adv Colloid Interface Sci 149:28–38

71. Li DX, Cui Y, Wang KW, He Q, Yan XH, Li JB (2007) Binary thermosensitive nanostructures of gold nanoparticles grafted with block copolymer: fabrication, characterization and catalyst applications. Adv Funct Mater 17:3134–3138

72. Li DX, He Q, Yang Y, Mohwald H, Li JB (2008) Two-Stage pH response of poly (4-vinylpyridine) grafted gold nanoparticles. Macromolecules 41:7254–7256

73. Li DX, He Q, Cui Y, Li JB (2007) Fabrication of pH-responsive nanocomposites of gold nanoparticles/poly(4-vinylpyridine). Chem Mater 19:412–417

74. Pereira SO, Barros-Timmons A, Trindade T (2014) Biofunctionalisation of colloidal gold nanoparticles via polyelectrolytes assemblies. Colloid Polym Sci 292:33–50

75. Dumur F, Guerlin A, Dumas E, Bertin D, Gigmes D, Mayer CR (2011) Controlled spontaneous generation of gold nanoparticles assisted by dual reducing and capping agents. Gold Bull 44:119–137

76. Tran NTT, Wang TH, Lin CY, Tsai YC, Lai CH, Tai Y, Yung BYM (2011) Direct synthesis of rev peptide-conjugated gold nanoparticles and their application in cancer therapeutics. Bioconjugate Chem 22:1394–1401

77. Huang H, Yang X (2004) Synthesis of polysaccharide-stabilized gold and silver nanoparticles: a green method. Carbohydr Res 339:2627–2631

78. Newman JDS, Blanchard GJ (2006) Formation of gold nanoparticles using amine reducing agents. Langmuir 22:5882–5887

79. Sun X, Dong S, Wang E (2006) One-step polyelectrolyte-based route to well-dispersed gold nanoparticles: synthesis and insight. Mater Chem Phys 96:29–33

80. Newman J, Blanchard G (2007) Formation and encapsulation of gold nanoparticles using a polymeric amine reducing agent. J Nanopart Res 9:861–868

81. Sardar R, Park JW, Shumaker-Parry JS (2007) Polymer-induced synthesis of stable gold and silver nanoparticles and subsequent ligand exchange in water. Langmuir 23:11883–11889
82. Chen H, Wang Y, Wang Y, Dong S, Wang E (2006) One-step preparation and characterization of PDDA-protected gold nanoparticles. Polymer 47:763–766
83. Caruso F, Caruso RA, Mohwald H (1998) Nanoengineering of inorganic and hybrid hollow spheres by colloidal templating. Science 282:1111–1114
84. Caruso F (2000) Hollow capsule processing through colloidal templating and self-assembly. Chem Eur J 6:413–419
85. Caruso F (2001) Nanoengineering of particle surfaces. Adv Mater 13:11–22
86. Gittins DI, Caruso F (2000) Multilayered polymer nanocapsules derived from gold nanoparticle templates. Adv Mater 12:1947–1949
87. Mandal S, Bonifacio A, Zanuttin F, Sergo V, Krol S (2011) Synthesis and multidisciplinary characterization of polyelectrolyte multilayer-coated nanogold with improved stability toward aggregation. Colloid Polym Sci 289:269–280
88. Djoumessi Lekeufack D, Brioude A, Lalatonne Y, Motte L, Coleman A, Miele P (2012) Reversible multi polyelectrolyte layers on gold nanoparticles. J Nanopart Res 14:1–7
89. Dorris A, Rucareanu S, Reven L, Barrett CJ, Lennox RB (2008) Preparation and characterization of polyelectrolyte-coated gold nanoparticles. Langmuir 24:2532–2538
90. Gittins DI, Caruso F (2001) Tailoring the polyelectrolyte coating of metal nanoparticles. J Phys Chem B 105:6846–6852
91. Schonhoff M (2003) Self-assembled polyelectrolyte multilayers. Curr Opin Colloid Interface Sci 8:86–95
92. Vergaro V, Scarlino F, Bellomo C, Rinaldi R, Vergara D, MaffiaM Baldassarre F, Giannelli G, Zhang X, Lvov YM, Leporatti S (2011) Drug-loaded polyelectrolyte microcapsules for sustained targeting of cancer cells. Adv Drug Delivery Rev 63:847–864
93. Tan WB, Zhang Y (2005) Surface modification of gold and quantum dot nanoparticles with chitosan for bioapplications. J Biomed Mater Res Part A 75A:56–62
94. Ma Z, Ding T (2009) Bioconjugates of glucose oxidase and gold nanorods based on electrostatic interaction with enhanced thermostability. Nanoscale Res Lett 4:1236–1240
95. Zhao E, Zhao Z, Wang J, Yang C, Chen C, Gao L, Feng Q, HouW Gao M, Zhang Q (2012) Surface engineering of gold nanoparticles for in vitro siRNA delivery. Nanoscale 4:5102–5109
96. Lee SK, Han MS, Asokan S, Tung CH (2011) Effective gene silencing by multilayered siRNA-coated gold nanoparticles. Small 7:364–370
97. Schneider G, Decher G (2004) From functional core/shell nanoparticles prepared via layer-by-layer deposition to empty nanospheres. Nano Lett 4:1833–1839
98. Labouta HI, Schneider M (2010) Tailor-made biofunctionalized nanoparticles using layer-by-layer technology. Int J Pharm 395:236–242
99. Schneider G, Decher G (2008) Functional core/shell nanoparticles via layer-by-layer assembly investigation of the experimental parameters for controlling particle aggregation and for enhancing dispersion stability. Langmuir 24:1778–1789
100. Mayya KS, Schoeler B, Caruso F (2003) Preparation and organization of nanoscale polyelectrolyte-coated gold nanoparticles. Adv Funct Mater 13:183–188
101. Schneider G, Subr V, Ulbrich K, Decher G (2009) Multifunctional cytotoxic stealth nanoparticles. A model approach with potential for cancer therapy. Nano Lett 9:636–642
102. Reum N, Fink-Straube C, Klein T, Hartmann RW, Lehr CM, Schneider M (2010) Multilayer coating of gold nanoparticles with drug-polymer coadsorbates. Langmuir 26:16901–16908
103. Masereel B, Dinguizli M, Bouzin C, Moniotte N, Feron O, Gallez B, Vander Borght T, Michiels C, Lucas S (2011) Antibody immobilization on gold nanoparticles coated layer-by-layer with polyelectrolytes. J Nanopart Res 13:1573–1580
104. Guo S, Huang Y, Jiang Q, Sun Y, Deng L, Liang Z, Du Q, Xing J, Zhao Y, Wang PC, Dong A, Liang X-J (2010) Enhanced gene delivery and siRNA silencing by gold nanoparticles coated with charge-reversal polyelectrolyte. ACS Nano 4:5505–5511

105. Schneider G, Decher G, Nerambourg N, Praho R, Werts MHV, Blanchard-Desce M (2006) Distance-dependent fluorescence quenching on gold nanoparticles ensheathed with layer-by-layer assembled polyelectrolytes. Nano Lett 6:530–536

106. Gabriel GJ, Madkour AE, Dabkowski JM, Nelson CF, Nusslein K, Tew GN (2008) Synthetic mimic of antimicrobial peptide with nonmembrane-disrupting antibacterial properties. Biomacromol 9:2980–2983

107. Ilker MF, Nuesslein K, Tew GN, Coughlin EB (2004) Tuning the hemolytic and antibacterial activities of amphiphilic polynorbornene derivatives. J Am Chem Soc 126:15870–15875

108. Sakai N, Futaki S, Matile S (2006) Anion hopping of (and on) functional oligoarginines: from chloroform to cells. Soft Matter 2:636–641

109. Kolonko EM, Pontrello JK, Mangold SL, Kiessling LL (2009) General synthetic route to cell-permeable block copolymers via ROMP. J Am Chem Soc 131:7327–7333

110. Hennig A, Gabriel GJ, Tew GN, Matile S (2008) Stimuli- responsive polyguanidino-oxanorbornene membrane transporters as multicomponent sensors in complex matrices. J Am Chem Soc 130:10338–10344

111. Som A, Reuter A, Tew GN (2012) Protein transduction domain mimics: the role of aromatic functionality. Angew Chem Int Ed 51:980–983

112. Baruah B, Gabriel GJ, Akbashev MJ, Booher ME (2013) Facile synthesis of silver nanoparticles stabilized by cationic polynorbornenes and their catalytic activity in 4-nitrophenol reduction. Langmuir 29:4225–4234

113. Murugadoss A, Chattopadhyay A (2008) Surface area controlled differential catalytic activities of one-dimensional chain-like arrays of gold nanoparticles. J Phys Chem C 112:11265–11271

114. Goia DV (2004) Preparation and formation mechanisms of uniform metallic particles in homogeneous solutions. J Mater Chem 14:451–458

115. Medina-Ramirez I, Bashir S, Luo Z, Liu JL (2009) Green synthesis and characterization of polymer-stabilized silver nanoparticles. Colloids Surf B 73:185–191

116. Michna A, Adamczyk Z, Owieja M, Bielaska E (2011) Kinetics of silver nanoparticle deposition onto poly(ethylene imine) modified mica determined by AFM and SEM measurements. Colloids Surf A 377:261–268

117. Yap FL, Thoniyot P, Krishnan S, Krishnamoorthy S (2012) Nanoparticle cluster arrays for high-performance SERS through directed self-assembly on flat substrates and on optical fibers. ACS Nano 6:2056–2070

118. Kim YK, Han SW, Min DH (2012) Graphene oxide sheath on Ag nanoparticle/graphene hybrid films as an antioxidative coating and enhancer of surface-enhanced raman scattering. ACS Appl Mater Interfaces 4:6545–6551

119. Stamplecoskie KG, Scaiano JC, Tiwari VS, Anis H (2011) Optimal size of silver nanoparticles for surface-enhanced raman spectroscopy. J Phys Chem C 115:1403–1409

120. Mahato M, Pal P, Tah B, Ghosh M, Talapatra GB (2011) Study of silver nanoparticle-hemoglobin interaction and composite formation. Colloids Surf B 88:141–149

121. Gole A, Orendorff CJ, Murphy CJ (2004) Immobilization of gold nanorods onto acid-terminated self-assembled monolayers via electrostatic interactions. Langmuir 20:7117–7122

122. Yu DG, Lin WC, Lin CH, Chang LM, Yang MC (2007) An in situ reduction method for preparing silver/poly(vinyl alcohol) nanocomposite as surface-enhanced Raman scattering (SERS)-active substrates. Mater Chem Phys 101:93–98

123. Porel S, Singh S, Harsha SS, Rao DN, Radhakrishnan TR (2005) Nanoparticle-embedded polymer: in situ synthesis, free-standing films with highly monodisperse silver nanoparticles and optical limiting. Chem Mater 17:9–12

124. Manna A, Imae T, Iida M, Hisamatsu N (2001) Formation of silver nanoparticles from a N-Hexadecylethylenediamine silver nitrate complex. Langmuir 17:6000–6004

125. Shin HS, Yang HJ, Kim SB, Lee MS (2004) Mechanism of growth of colloidal silver nanoparticles stabilized by polyvinyl pyrrolidone in gamma-irradiated silver nitrate solution. J Colloid Interface Sci 274:89–94

126. Liu YC, Chuang TC (2003) Synthesis and characterization of gold/polypyrrole core-shell nanocomposites and elemental gold nanoparticles based on the gold-containing nanocomplexes prepared by electrochemical methods in aqueous solutions. J Phys Chem B 107:12383–12386

127. Khanna PK, Singh N, Kulkarni D, Deshmukh S, Charan S, Adhyapak PV (2007) Water based simple synthesis of re-dispersible silver nano-particles. Mater Lett 61:3366–3370

128. Ershov BG, Henglein A (1998) Time-resolved investigation of early processes in the reduction of Ag$^+$ on polyacrylate in aqueous solution. J Phys Chem B 102:10667–10671

129. García-Serrano J, Herrera AM, Ocampo-Fernández M (2011) Synthesis of Ag particles using an ion-exchange polymer with phosphonic acid groups. Mater Sci Forum 691:113–118

130. Hebeish A, El-Shafei A, Sharaf S, Zaghloul S (2011) Novel precursors for green synthesis and application of silver nanoparticles in the realm of cotton finishing. Carbohyd Polym 84:605–613

131. Maity D, Kanti Bain M, Bhowmick B, Sarkar J, Saha S, Acharya K, Chakraborty M, Chattopadhyay D (2011) In situ synthesis, characterization, and antimicrobial activity of silver nanoparticles using water soluble polymer. J Appl Polym Sci 122:2189–2196

132. Norris CB, Joseph PR, Mackiewicz MR, Reed SM (2010) Minimizing formaldehyde use in the synthesis of gold-silver core-shell nanoparticles. Chem Mater 22:3637–3645

133. Kundu S, Wang K, Liang H (2009) Size-selective synthesis and catalytic application of polyelectrolyte encapsulated gold nanoparticles using microwave irradiation. J Phys Chem C 113:5157–5163

134. Luo Y (2007) Size-controlled preparation of polyelectrolyte-protected gold nanoparticles by natural sunlight radiation. Mater Lett 61:2164–2166

135. Han DH, Pan C (2008) Synthesis and characterization of water-soluble gold nanoparticles stabilized by comb-shaped copolymers. J Polym Sci A Poly Chem 46:341–352

136. Kim JH, Lee TR (2004) Thermo- and pH-responsive hydrogel-coated gold nanoparticles. Chem Mater 16:3647–3651

137. Spatz JP, Roescher A, Möller M (1996) Gold nanoparticles in micellar poly(styrene)-b-poly (ethylene oxide) films-size and interparticle distance control in monoparticulate films. Adv Mater 8:337–340

138. Spatz JP, Mössmer S, Hartmann C, Möller M, Herzog T, Krieger M, Boyen HG, Ziemann P, Kabius B (2000) Ordered deposition of inorganic clusters from micellar block copolymer films. Langmuir 16:407–415

139. Kang Y, Taton TA (2005) Controlling shell thickness in core-shell gold nanoparticles via surface-templated adsorption of block-copolymer surfactants. Macromolecules 38:6115–6121

140. Zubarev ER, Xu J, Sayyad A, Gibson JD (2006) Amphiphilic gold nanoparticles with V-shaped arms. J Am Chem Soc 128:4958–4959

141. Djalali R, Li SY, Schmidt M (2002) Amphipolar core-shell cylindrical brushes as templates for the formation of gold clusters and nanowires. Macromolecules 35:4282–4288

142. Dockendorff J, Gauthier M, Mourran A, Möller M (2008) Arborescent amphiphilic copolymers as templates for the preparation of gold nanoparticles. Macromolecules 41:6621–6623

143. Zheng P, Jiang X, Zhang X, Zhang W, Shi L (2006) Formation of gold@polymer core-shell particles and gold particle clusters on a template of thermoresponsive and pH-responsive coordination triblock copolymer. Langmuir 22:9393–9396

144. Yoo C, Seo D, Chung BH, Chung IS, Song H (2009) A facile one-pot synthesis of hydroxyl-functionalized gold polyhedrons by a surface regulating copolymer. Chem Mater 21:939–944

145. Watson KJ, Zhu J, Nguyen ST, Mirkin CA (1999) Hybrid nanoparticles with block copolymer shell structures. J Am Chem Soc 121:462–463

146. Kang Y, Erickson KJ, Taton TA (2005) Plasmonic nanoparticle chains via a morphological, sphere-to-string transition. J Am Chem Soc 127:13800–13801

147. Huang HY, Remsen EE, Kowalewski T, Wooley KL (1999) Nanocages derived from shell cross-linked micelle templates. J Am Chem Soc 121:3805–3806

148. Shen Z, Duan H, Frey H (2007) Water-soluble fluorescent Ag nanoclusters obtained from multiarm star poly (acrylic acid) as "molecular hydrogel" templates. Adv Mater 19:349–352

149. Díez I, Pusa M, Kulmala S, Jiang H, Walther A, Goldmann AS, Müller AHE, Ikkala O, Ras RHA (2009) Color tunability and electrochemiluminescence of silver nanoclusters. Angew Chem Int Ed 48:2122–2125

150. Shang L, Dong S (2008) Facile preparation of water-soluble fluorescent silver nanoclusters using a polyelectrolyte template. Chem Commun (9):1088–1090

151. Xu H, Suslick KS (2010) Sonochemical synthesis of highly fluorescent Ag nanoclusters. Nano ACS 4:3209–3214

152. Díez I, Hahn H, Ikkala O, Börner HG, Ras RA (2010) Controlled growth of silver nanoparticle arrays guided by a self-assembled polymer-peptide conjugate. Soft Matter 6:3160–3162

153. Díez I, Jiang H, Ras RHA (2010) Enhanced emission of silver nanoclusters through quantitative phase transfer. ChemPhysChem 11:3100–3104

154. Angelescu DG, Vasilescu M, Somoghi R, Donescu D, Teodorescu VS (2010) Kinetics and optical properties of the silver nanoparticles in aqueous L64 block copolymer solutions. Colloids Surf A 366:155–162

155. Wu W, Mitra N, Yan ECY, Zhou S (2010) Multifunctional hybrid nanogel for integration of optical glucose sensing and self-regulated insulin release at physiological pH. ACS Nano 4:4831–4839

156. Wu W, Shen J, Banerjee P, Zhou S (2010) Core-shell hybrid nanogels for integration of optical temperature-sensing, targeted tumor cell imaging, and combined chemo-photothermal treatment. Biomaterials 31:7555–7566

157. Boyer C, Bulmus V, Davis TP, Ladmiral V, Liu J, Perrier S (2009) Bioapplications of RAFT polymerization. Chem Rev 109:5402–5436

158. Boyer C, Stenzel MH, Davis TP (2011) Building nanostructures using RAFT polymerization. J Polym Sci Part A Polym Chem 49:551–595

159. Blanazs A, Ryan AJ, Armes SP (2012) Predictive phase diagrams for RAFT aqueous dispersion polymerization: effect of block copolymer composition, molecular weight, and copolymer concentration. Macromolecules 45:5099–5107

160. Bleach R, Karagoz B, Prakash SM, Davis TP, Boyer C (2014) In situ formation of polymer-gold composite nanoparticles with tunable morphologies. ACS Macro Lett 3: 591–596

161. Rahme K, Vicendo P, Ayela C, Gaillard C, Payré B, Mingotaud C, Gauffre F (2009) A simple protocol to stabilize gold nanoparticles using amphiphilic block copolymers: stability studies and viable cellular uptake. Chemistry 15:11151–11159

162. Chen H, Zou H, Paholak HJ, Ito M, Qian W, Chec Y, Sun D (2014) Thiol-reactive amphiphilic block copolymer for coating gold nanoparticles with neutral and functionable surfaces. Polym Chem 5:2768–2773

163. Wu W, Zhou T, Zhou S (2009) Tunable photoluminescence of Ag nanocrystals in multiple-sensitive hybrid microgels. Chem Mater 21:2851–2861

164. Zhang J, Xu S, Kumacheva E (2005) Photogeneration of fluorescent silver nanoclusters in polymer microgels. Adv Mater 17:2336–2340

165. Oh M, Mirkin CA (2005) Chemically tailorable colloidal particles from infinite coordination polymers. Nature 438:651–654

166. Lu X, Cheng H, Huang P, Yang L, Yu P, Mao L (2013) Hybridization of bioelectrochemically functional infinite coordination polymer nanoparticles with carbon nanotubes for highly sensitive and selective in vivo electrochemical monitoring. Anal Chem 85:4007–4013

167. Ballesteros-Rivas M, Ota A, Reinheimer E, Prosvirin A, Valdes-Martinez J, Dunbar KR (2011) Highly conducting coordination polymers based on infinite M(4,4′-bpy) chains flanked by regular stacks of non-integer TCNQ radicals. Angew Chem Int Ed 50:9703–9707

168. Zhang L, Gao X, Yang L, Yu P, Mao L (2013) Photodecomposition of ferrocenedicarboxylic acid in methanol to form an electroactive infinite coordination polymer and its application in bioelectrochemistry. ACS Appl Mater Interface 5:8120–8124

169. Bae YS, Farha OK, Spokoyny AM, Mirkin CA, Hupp JT, Snurr RQ (2008) Carborane-based metal-organic frameworks as highly selective sorbents for CO_2 over methane. Chem Commun (35):4135–4137

170. Li Z, Zeng HC (2013) Surface and bulk integrations of single-layered Au or Ag nanoparticles onto designated crystal planes 110 or 100 of ZIF-8. Chem Mater 25: 1761–1768

171. Lu W, Cao X, Tao L, Ge J, Dong J, Qian W (2014) A novel label-free amperometric immunosensor for carcinoembryonic antigen based on Ag nanoparticle decorated infinite coordination. Biosens Bioelectron 57:219–225

172. Li H, Zhai J, Sun X (2011) Electrostatic-assembly-driven formation of supramolecular rhombus microparticles and their application for fluorescent nucleic acid detection. PLoS ONE 6:e18958

173. Navaladian S, Viswanathan B, Varadarajan TK, Viswananth RP (2008) Microwave-assisted rapid synthesis of anisotropic Ag nanoparticles by solid state transformation. Nanotechnology 19:045603

174. Khan MAM, Kumar S, Ahamed M, Alrokayan SA, Alsalhi MS (2011) Structural and thermal studies of silver nanoparticles and electrical transport study of their thin films. Nanoscale Res Lett 6:434–441

175. Mendoza-Reséndez R, Núñez NO, Barriga-Castro ED, Luna C (2013) Synthesis of metallic silver nanoparticles and silver organometallic nanodisks mediated by extracts of Capsicum annuum var aviculare (piquin) fruits. RSC Adv 3:20765–20771

176. Zhang XM, Quan ZW, Yang J, Yang PP, Lian HZ, Lin J (2008) Solvothermal synthesis of well-dispersed MF2 (M = Ca, Sr, Ba) nanocrystals and their optical properties. Nanotechnology 19:075603

177. Stejskal J, Sapurina I, Trchova M, Konyushenko EN, Holler P (2006) The genesis of polyaniline nanotubes. Polymer 47:8253–8262

178. Li L, Weng J (2010) Enzymatic synthesis of gold nanoflowers with trypsin. Nanotechnology 21:305603

179. Gai S, Yang G, Li X, Li C, Dai Y, He F, Yang P (2012) Facile synthesis and up-conversion properties of monodisperse rare earth fluoride nanocrystals. Dalton Trans 41:11716–11724

180. Beegum MF, Kumari LU, Harikumar B, Varghese HT, Panicker CY (2008) Vibrational spectroscopic studies of 4-cyanobenzoic acid. Rasayan J Chem 2:258–262

181. Katz E, Willner I (2003) Probing biomolecular interactions at conductive and semiconductive surfaces by impedance spectroscopy: routes to impedimetric immunosensors, dna-sensors, and enzyme biosensors. Electroanalysis 15:913–947

182. Hermes S, Schroter MK, Schmid R, Khodeir L, Muhler M, Tissler A, Fischer RW, Fischer RA (2005) Metal@MOF: loading of highly porous coordination polymers host lattices by metal organic chemical vapor deposition. Angew Chem Int Ed 44:6237–6241

183. Ishida T, Nagaoka M, Akita T, Haruta M (2008) Deposition of gold clusters on porous coordination polymers by solid grinding and their catalytic activity in aerobic oxidation of alcohols. Chem Eur J 14:8456–8460

184. Zhao P, Li N, Astruc D (2013) State of the art in gold nanoparticle synthesis. Coord Chem Rev 257:638–665

185. Alvarez-Paino M, Marcelo G, Munoz-Bonilla A, Fernandez-Garcia M (2013) Catecholic chemistry to obtain recyclable and reusable hybrid polymeric particles as catalytic systems. Macromolecules 46:2951–2962

186. He J, Liu Y, Hood TC, Zhang P, Gong J, Nie Z (2013) Asymmetric organic/metal(oxide) hybrid nanoparticles: synthesis and applications. Nanoscale 5:5151–5166

187. Song J, Zhou J, Duan H (2012) Self-Assembled plasmonic vesicles of SERS-encoded amphiphilic gold nanoparticles for cancer cell targeting and traceable intracellular drug delivery. J Am Chem Soc 134:13458–13469

188. Kao J, Thorkelsson K, Bai P, Rancatore BJ, Xu T (2013) Toward functional nanocomposites: Taking the best of nanoparticles, polymers, and small molecules. Chem Soc Rev 42:2654–2678

189. Hu J, Wu T, Zhang G, Liu S (2012) Effcient synthesis of single gold nanoparticle hybrid amphiphilic triblock copolymers and their controlled self-assembly. J Am Chem Soc 134:7624–7627

190. Mieszawska AJ, Mulder WJM, Fayad ZA, Cormode DP (2013) Multifunctional gold nanoparticles for diagnosis and therapy of disease. Mol Pharm 10:831–847

191. Mercato LL, Gonzalez E, Abbasi AZ, Parak WJ, Puntes V (2011) Synthesis and evaluation of gold nanoparticle-modified polyelectrolyte capsules under microwave irradiation for remotely controlled release for cargo. J Mater Chem 21:11468–11471

192. Hickey RJ, Haynes AS, Kikkawa JM, Park SJ (2011) Controlling the self-assembly structure of magnetic nanoparticles and amphiphilic block-copolymers: From micelles to vesicles. J Am Chem Soc 133:1517–1525

193. Tian J, Yuan L, Zhang M, Zheng F, Xiong Q, Zhao H (2012) Interface-directed self-assembly of gold nanoparticles and fabrication of hybrid hollow capsules by interfacial cross-linking polymerization. Langmuir 28:9365–9371

194. Ochs M, Carregal-Romero S, Rejman J, Braeckmans K, De Smedt SC, Parak WJ (2013) Light-addressable capsules as caged compound matrix for controlled triggering of cytosolic reactions. Angew Chem Int Ed 52:695–699

195. Kreft O, Skirtach AG, Sukhorukov GB, Möhwald H (2007) Remote control of bioreactions in multicompartment capsules. Adv Mater 19:3142–3145

196. Kozlovskaya V, Kharlampieva E, Chang S, Muhlbauer R, Tsukruk VV (2009) pH-Responsive layered hydrogel microcapsules as gold nanoreactors. Chem Mater 21:2158–2167

197. Angelatos AS, Radt B, Caruso F (2005) Light-responsive polyelectrolyte/gold nanoparticle microcapsules. J Phys Chem B 109:3071–3076

198. De Geest BG, Skirtach AG, De Beer TRM, Sukhorukov GB, Bracke L, Baeyens WRG, Demeester J, De Smedt SC (2007) Stimuli-responsive multilayered hybrid nanoparticle/polyelectrolyte capsules. Macromol Rapid Commun 28:88–95

199. Liu D, Jiang X, Yin J (2014) One-step interfacial thiol-ene photopolymerization for metal nanoparticle-decorated microcapsules (MNP@MCs). Langmuir 30:7213–7220

200. McGilvray KL, Decan MR, Wang D, Scaiano JC (2006) Facile photochemical synthesis of unprotected aqueous gold nanoparticles. J Am Chem Soc 128:15980–15981

201. Marin ML, McGilvray KL, Scaiano JC (2008) Photochemical strategies for the synthesis of gold nanoparticles from Au(III) and Au(I) using photoinduced free radical generation. J Am Chem Soc 130:16572–16584

202. Liu DD, Yu B, Jiang XS, Yin J (2013) Responsive hybrid microcapsules by the one-step interfacial thiol-ene photopolymerization. Langmuir 29:5307–5314

203. Song J, Cheng L, Liu A, Yin J, Kuang M, Duan H (2011) Plasmonic vesicles of amphiphilic gold nanocrystals: self-assembly and external-stimuli-triggered destruction. J Am Chem Soc 133:10760–10763

204. Yu B, Jiang XS, Qin N, Yin J (2011) Thiol-ene photocrosslinked hybrid vesicles from co-assembly of POSS and poly(ether amine) (PEA). Chem Commun 47:12110–12112

205. Galian RE, Guardia M, Pérez-Prieto J (2011) Size reduction of CdSe/ZnS core-shell quantum dots photosensitized by benzophenone: Where does the Cd(0) go? Langmuir 27:1942–1945

206. Consuelo Cuquerella M, Pocoví-Martínez S, Pérez-Prieto J (2009) Photocatalytic coalescence of functionalized gold nanoparticles. Langmuir 26:1548–1550

207. Wang R, Jiang XS, Yu B, Yin J (2011) Stimuli-responsive microgels formed by hyperbranched poly(ether amine) decorated with platinum nanoparticles. Soft Matter 7:8619–8627
208. Xia B, He F, Li L (2013) Preparation of bimetallic nanoparticles using a facile green synthesis method and their application. Langmuir 29:4901–4907
209. Astruc D, Boisselies E, Ornelas C (2010) Dendrimers designed for functions: from physical, photophysical, and supramolecular properties to applications in sensing, catalysis, molecular electronics, photonics, and nanomedicine. Chem Rev 110:1857–1959
210. Sandar R, Funston AM, Mulvaney P, Murray RW (2009) Gold nanoparticles: past, present and future. Langmuir 25:13840–13851
211. Boisselier E, Diallo AK, Salmon L, Ornelas C, Ruiz J, Astruc D (2010) Encapsulation and stabilization of gold nanoparticles with "click" polyethyleneglycol dendrimers. J Am Chem Soc 132:2729–2742
212. Han HJ, Kannan RM, Wang S, Mao G, Kusanovic JP, Romero R (2010) Multifunctional dendrimer-templated antibody presentation on biosensor surfaces for improved biomarker detection. Adv Funct Mater 20:409–421
213. Benters R, Niemeyer CM, Wöhrle D (2001) Dendrimer-activated solid supports for nucleic acid and protein microarrays. ChemBioChem 2:686–694
214. Ajikumar PK, Ng JK, Tang YC, Lee JY, Stephanopoulos G, Too HP (2007) Carboxyl-terminated dendrimer-coated bioactive interface for protein microarray: high-sensitivity detection of antigen in complex biological samples. Langmuir 23:5670–5677
215. Tomalia DA, Frechet JMJ (eds) (2001) Dendrimers and other dendritic polymers. Wiley, New York
216. Tomalia DA, Baker H, Dewald JR, Hall M, Kallos G, Martin S, Roeck J, Ryder J, Smith P (1986) Dendritic macromolecules: synthesis of starburst dendrimers. Macromolecules 19:2466–2468
217. Tomalia DA, Naylor AM, Goddard WA III (1990) Starburst dendrimers: molecular-level control of size, shape, surface chemistry, topology, and flexibility from atoms to macroscopic matter. Angew Chem Int Ed Engl 29:138–175
218. Pan B, Cui D, Gao F, He R (2006) Growth of multi-amine terminated poly (amidoamine) dendrimers on the surface of carbon nanotubes. Nanotechnology 17:2483–2489
219. Svenson S, Tomalia DA (2005) Dendrimers in biomedical applications–reflections on the field. Adv Drug Deliv Rev 57:2106–2129
220. Newkome GR, Shreiner CD (2010) Dendrimers derived from 1→3 branching motifs. Chem Rev 110:6338–6442
221. Liu H, Sun K, Zhao J, Guo R, Shen M, Cao X, Zhang G, Shi X (2012) Dendrimer-mediated synthesis and shape evolution of gold-silver alloy nanoparticles. Colloid Surf A 405:22–29
222. Yancey DF, Carino EV, Crooks RM (2010) Electrochemical synthesis and electrocatalytic properties of Au@Pt dendrimer-encapsulated nanoparticles. J Am Chem Soc 132:10988–10989
223. Ornelas C, Méry D, Cloutet E, Ruiz J, Astruc D (2008) Cross olefin metathesis for the selective functionalization, ferrocenylation, and solubilization in water of olefin-terminated dendrimers, polymers, and gold nanoparticles and for a divergent dendrimer construction. J Am Chem Soc 130:1495–1506
224. Astruc D (2012) Electron-transfer processes in dendrimers and their implication in biology, catalysis, sensing and nanotechnology. Nat Chem 4:255–267
225. Kaewtong C, Jiang G, Ponnapati R, Pulpoka B, Advincula R (2010) Redox nanoreactor dendrimer boxes: in situ hybrid gold nanoparticles via terthiophene and carbazole peripheral dendrimer oxidation. Soft Matter 6:5316–5319
226. Esumi K (2003) Dendrimers for nanoparticle synthesis and dispersion stabilization. Top Curr Chem 227:31–52
227. Esumi K, Isono R, Yoshimura T (2004) Preparation of PAMAM- and PPI-metal (silver, platinum, and palladium) nanocomposites and their catalytic activities for reduction of 4-nitrophenol. Langmuir 20:237–243

228. Balogh L, Valluzzi R, Laverdure KS, Gido SP, Hagnauer GL, Tomalia DA (1999) Formation of silver and gold dendrimer nanocomposites. J Nanopart Res 1:353–368

229. Shan Y, Luo T, Peng C, Sehng R, Cao X, Cao H, Shen M, Guo R, Tomas H, Shi X (2012) Gene delivery using dendrimer-entrapped gold nanoparticles as nonviral vectors. Biomaterials 33:3025–3035

230. Peng C, Zheng L, Chen Q, Shen M, Guo R, Wang H, Cao X, Zhang G, Shi X (2012) PEGylated dendrimer-entrapped gold nanoparticles for in vivo blood pool and tumor imaging by computed tomography. Biomaterials 33:1107–1119

231. Hoffman LW, Andersson GG, Sharma A, Clarke SR, Voelcker NH (2011) New insights into the structure of PAMAM dendrimer/gold nanoparticle nanocomposites. Langmuir 27: 6759–6767

232. Namazi H, Fard AMP (2011) Preparation of gold nanoparticles in the presence of citric acid-based dendrimers containing periphery hydroxyl groups. Mater Chem Phys 129: 189–194

233. Jiang G, Wang L, Chen T, Yu H, Chen C (2006) Preparation of gold nanoparticles in the presence of poly (benzyl ether) alcohol dendrons. Mater Chem Phys 98:76–82

234. Murugan E, Rangasamy R (2010) Synthesis, characterization, and heterogeneous catalysis of polymer-supported poly(propyleneimine) dendrimer stabilized gold nanoparticle catalyst. J Polym Sci A Polym Chem 48:2525–2532

235. Astruc D, Liang L, Rapakousiou A, Ruiz J (2012) Click dendrimers and triazole-related aspects: catalysts, mechanism, synthesis, and functions A bridge between dendritic architectures and nanomaterials. Acc Chem Res 45:630–640

236. Thompson D, Hermes JP, Quinn AJ, Mayor M (2012) Scanning the potential energy surface for synthesis of dendrimer-wrapped gold clusters: design rules for true single-molecule nanostructures. ACS Nano 6:3007–3017

237. Cho TJ, Zangmeister RA, Mac-Cuspie RI, Patri AK, Hackley VA (2011) Newkome-type dendron stabilized gold nanoparticles: synthesis, reactivity, and stability. Chem Mater 23:2665–2676

238. Crooks RM, Zhao M, Sun L, Chechik V, Yeung LK (2001) Dendrimer-encapsulated metal nanoparticles: synthesis, characterization, and applications to catalysis. Acc Chem Res 34:181–190

239. Kim YG, Oh SK, Crooks RM (2004) Preparation and characterization of 1-2 nm dendrimer-encapsulated gold nanoparticles having very narrow size-distributions. Chem Mater 16:167–172

240. Grohn F, Bauer BJ, Akpalu YA, Jackson CL, Amis EJ (2000) Dendrimer templates for the formation of gold nanoclusters. Macromolecules 33:6042–6050

241. Shen M, Shi X (2010) Dendrimer-based organic/inorganic hybrid nanoparticles in biomedical applications. Nanoscale 2:1596–1610

242. Shi X, Wang SH, Sun H, Baker JR Jr (2007) Improved biocompatibility of surface functionalized dendrimer entrapped gold nanoparticles. Soft Matter 3:71–74

243. Scott RWJ, Datye AK, Crooks RM (2003) Bimetallic palladium-platinum dendrimer-encapsulated catalysts. J Am Chem Soc 125:3708–3709

244. Chung YM, Rhee HK (2003) Partial hydrogenation of 1,3-cyclooctadiene using dendrimer-encapsulated Pd-Rh bimetallic nanoparticles. J Mol Catal A 206:291–298

245. Scott RWJ, Wilson OM, Oh SK, Kenik EA, Crooks RM (2004) Bimetallic palladium-gold dendrimer-encapsulated catalysts. J Am Chem Soc 126:15583–15591

246. Jana NR, Gearheart L, Murphy CJ (2001) Wet chemical synthesis of silver nanorods and nanowires of controllable aspect ratioElectronic supplementary information (ESI) available: UV-VIS spectra of silver nanorods. Chem Commun 7:617–618

247. Balogh L, Tomalia DA (1998) Poly(amidoamine) dendrimer-templated nanocomposites 1 synthesis of zerovalent copper nanoclusters. J Am Chem Soc 120:7355–7356

248. Zhao M, Sun L, Crooks RM (1998) Preparation of Cu nanoclusters within dendrimer templates. J Am Chem Soc 120:4877–4878

249. Auten BJ, Hahn BP, Vijayaraghavan G, Stevenson KJ, Chandler BD (2008) Preparation and characterization of 3 nm magnetic NiAu nanoparticles. J Phys Chem C 112:5365–5372

250. Guo R, Wang H, Peng C, Shen M, Pan M, Cao X, Zhang G, Shi X (2010) X-ray attenuation property of dendrimer-entrapped gold nanoparticles. J Phys Chem C 114:50–56

251. Pathak S, Singh AK, McElhanon JR, Dentiger PM (2004) Dendrimer-activated surfaces for high density and high activity protein chip applications. Langmuir 20:6075–6079

252. Hong MY, Lee D, Kim HS (2005) Kinetic and equilibrium binding analysis of protein-ligand interactions at poly(amidoamine) dendrimer monolayers. Anal Chem 77:7326–7334

253. Bolduc OR, Masson JF (2008) Monolayers of 3-mercaptopropyl-amino acid to reduce the nonspecific adsorption of serum proteins on the surface of biosensors. Langmuir 24:12085–12091

254. Bolduc OR, Clouthier CM, Pelletier JN, Masson JF (2009) Peptide self-assembled monolayers for label-free and unamplified surface plasmon resonance biosensing in crude cell lysate. Anal Chem 81:6779–6788

255. Uchida K, Otsuka H, Kaneko M, Kataoka K, Nagasaki Y (2005) A reactive poly(ethylene glycol) layer to achieve specific surface plasmon resonance sensing with a high S/N ratio: the substantial role of a short underbrushed PEG layer in minimizing nonspecific adsorption. Anal Chem 77:1075–1080

256. Yam CM, Deluge M, Tang D, Kumar A, Cai C (2006) Preparation, characterization, resistance to protein adsorption, and specific avidin-biotin binding of poly (amidoamine) dendrimers functionalized with oligo (ethylene glycol) on gold. J Colloid Interface Sci 296:118–130

257. Medina SH, El-Sayed MEH (2009) Dendrimers as carriers for delivery of chemotherapeutic agents. Chem Rev 109:3141–3157

258. Landmark KJ, DiMaggio S, Ward J, Kelly C, Vogt S, Hong S, Kotlyar A, Myc A, Thomas TP, Penner-Hahn JE, Baker JR Jr, Banaszak Holl MM, Orr BG (2008) Synthesis, characterization, and in vitro testing of superparamagnetic iron oxide nanoparticles targeted using folic acid-conjugated dendrimers. ACS Nano 2:773–783

259. Shi X, Wang SH, Swanson SD, Ge S, Cao Z, Van Antwerp ME, Landmark KJ, Baker JR Jr (2008) Dendrimer-functionalized shell-crosslinked iron oxide nanoparticles for in vivo magnetic resonance imaging of tumors. Adv Mater 20:1671–1678

260. Li Z, Huang P, Zhang X, Lin J, Yang S, Liu B, Gao F, Xi P, Ren Q, Cui D (2010) RGD-conjugated dendrimer-modified gold nanorods for in vivo tumor targeting and photothermal therapy. Mol Pharmaceutics 7:94–104

261. Abu-Reziq R, Alper H, Wang D, Post ML (2006) Metal supported on dendronized magnetic nanoparticles: highly selective hydroformylation catalysts. J Am Chem Soc 128:5279–5282

262. Pan B, Cui D, Sheng Y, Ozkan C, Gao F, He R, Li Q, Xu P, Huang T (2007) Dendrimer-modified magnetic nanoparticles enhance efficiency of gene delivery system. Cancer Res 67:8156–8163

263. Frasconi M, Tortolini C, Botré F, Mazzei F (2010) Multifunctional Au nanoparticle dendrimer-based surface plasmon resonance biosensor and its application for improved insulin detection. Anal Chem 82:7335–7342

264. Zhou XC, O'Shea SJ, Li S (2000) Amplified microgravimetric gene sensor using Au nanoparticle modified oligonucleotides. Chem Commun (11):953–954

265. Tompkins HG, McGahan WA (1999) spectroscopic ellipsometry and reflectometry: a user's guide. Wiley, New York

266. Tokuhisa H, Zhao M, Baker LA, Phan VT, Dermody DL, Garcia ME, Peez RF, Crooks RM, Mayer TM (1998) Preparation and characterization of dendrimer monolayers and dendrimer-alkanethiol mixed monolayers adsorbed to gold. J Am Chem Soc 120:4492–4501

267. Shi X, Lee I, Baker JR Jr (2008) Acetylation of dendrimer-entrapped gold and silver nanoparticles. J Mater Chem 18:586–593

268. Laibinis PE, Whitesides GM, Allara DL, Tao YT, Parikh AN, Nuzzo RG (1991) Comparison of the structures and wetting properties of self-assembled monolayers of

n-alkanethiols on the coinage metal surfaces, copper, silver, and gold. J Am Chem Soc 113:7152–7167

269. Shi X, Ganser TR, Sun K, Balogh LP, Baker JR Jr (2006) Characterization of crystalline dendrimer-stabilized gold nanoparticles. Nanotechnology 17:1072–1078

270. Alvarez MM, Khoury JT, Schaaff TG, Shafigullin MN, Vezmar I, Whetten RL (1997) Optical absorption spectra of nanocrystal gold molecules. J Phys Chem B 101:3706–3712

271. Zheng J, Petty JT, Dickson RM (2003) High quantum yield blue emission from water-soluble Au8 nanodots. J Am Chem Soc 125:7780–7781

272. Wang D, Imae T (2004) Fluorescence emission from dendrimers and its pH dependence. J Am Chem Soc 126:13204–13205

273. Esumi K, Suzuki A, Yamahira A, Torigoe K (2000) Role of poly(amidoamine) dendrimers for preparing nanoparticles of gold, platinum, and silver. Langmuir 16:2604–2608

274. Esumi K, Suzuki A, Aihara N, Usui K, Torigoe K (1998) Preparation of gold colloids with UV irradiation using dendrimers as stabilizer. Langmuir 14:3157–3159

275. Hayakawa K, Yoshimura T, Esumi K (2003) Preparation of gold-dendrimer nanocomposites by laser irradiation and their catalytic reduction of 4-nitrophenol. Langmuir 19:5517–5521

276. Lesniak W, Bielinska AU, Sun K, Janczak KW, Shi X, Baker JR Jr, Balogh LP (2005) Silver/dendrimer nanocomposites as biomarkers: fabrication, characterization, in vitro toxicity, and intracellular detection. Nano Lett 5:2123–2130

277. Shi X, Sun K, Baker JR Jr (2008) Spontaneous formation of functionalized dendrimer-stabilized gold nanoparticles. J Phys Chem C 112:8251–8258

278. Hong S, Leroueil PR, Majoros IJ, Orr BG, Baker JR Jr, Banaszak Holl MM (2007) The binding avidity of a nanoparticle-based multivalent targeted drug delivery platform. Chem Biol 14:107–115

279. Thomas TP, Majoros IJ, Kotlyar A, Kukowska-Latallo JF, Bielinska A, Myc A, Baker JR Jr (2005) Targeting and inhibition of cell growth by an engineered dendritic nanodevice. J Med Chem 48:3729–3735

280. Shi X, Wang SH, Van Antwerp ME, Chen X, Baker JR Jr (2009) Targeting and detecting cancer cells using spontaneously formed multifunctional dendrimer-stabilized gold nanoparticles. Analyst 134:1373–1379

281. Wilson OM, Scott RWJ, Garcia-Martinez JC, Crooks RM (2005) Synthesis, characterization, and structure-selective extraction of 1-3-nm diameter AuAg dendrimer-encapsulated bimetallic nanoparticles. J Am Chem Soc 127:1015–1024

282. Garcia-Martinez JC, Crooks RM (2004) Extraction of Au nanoparticles having narrow size distributions from within dendrimer templates. J Am Chem Soc 126:16170–16178

283. Garcia-Martinez JC, Scott RWJ, Crooks RM (2003) Extraction of monodisperse palladium nanoparticles from dendrimer templates. J Am Chem Soc 125:11190–11191

284. Hodak JH, Henglein A, Giersig M, Hartland GV (2000) Laser-induced inter-diffusion in AuAg core-shell nanoparticles. J Phys Chem B 104:11708–11718

285. Mallin MP, Murphy CJ (2002) Solution-phase synthesis of sub-10 nm Au-Ag alloy nanoparticles. Nano Lett 2:1235–1237

286. Gonzalez-Rodriguez B, Iglesias-Sanchez A, Giersig M, Liz-Marzan LM (2004) AuAg bimetallic nanoparticles: formation, silica-coating and selective etching. Faraday Discuss 125:133–144

287. Mandal S, Selvakannan PR, Pasricha R, Sastry M (2003) Keggin ions as UV-switchable reducing agents in the synthesis of Au core-Ag shell nanoparticles. J Am Chem Soc 125:8440–8441

288. Daniel MC, Astruc D (2004) Gold nanoparticles: assembly, supramolecular chemistry, quantum-size-related properties, and applications toward biology, catalysis, and nanotechnology. Chem Rev 104:293–346

289. Henglein A, Mulvaney P, Linnert T (1991) Chemistry of Agn aggregates in aqueous solution: non-metallic oligomeric clusters and metallic particles. Faraday Discuss 92:31–44

290. Papavassiliou GC (1976) Surface plasmons in small Au-Ag particles. J Phys F 6:L103–L105

291. Scott RW, Wilson OM, Crooks RM (2005) Synthesis, characterization, and applications of dendrimer-encapsulated nanoparticles. J Phys Chem B 109:692–704

292. Xia C, Fan X, Locklin J, Advincula RC, Gies A, Nonidez W (2004) Characterization, supramolecular assembly, and nanostructures of thiophene dendrimers. J Am Chem Soc 126:8735–8743

293. Deng S, Locklin J, Patton D, Baba A, Advincula RC (2005) Thiophene dendron jacketed poly(amidoamine) dendrimers: nanoparticle synthesis and adsorption on graphite. J Am Chem Soc 127:1744–1751

294. Shi X, Thomas TP, Myc LA, Kotlyar A, Baker JR Jr (2007) Synthesis, characterization, and intracellular uptake of carboxyl-terminated poly(amidoamine) dendrimer-stabilized iron oxide nanoparticles. Phys Chem Chem Phys 9:5712–5720

295. Li Z, Huang P, Lin J, He R, Liu B, Zhang X, Yang S, Xi P, Zhang X, Ren Q, Cui D (2010) Arginine-glycine-aspartic acid-conjugated dendrimer-modified quantum dots for targeting and imaging melanoma. J Nanosci Nanotechnol 10:1–9

296. Kobayashi M, Maskawa T (1973) CP-Violation in the renormalizable theory of weak interaction. Progress Theoret Phys 49:652–657

297. Melde BJ, Johnson BJ (2010) Mesoporous materials in sensing: morphology and functionality at the meso-interface. Anal Bioanal Chem 398:1565–1573

298. De Jong MR, Huskens J, Reinhoudt DN (2001) Influencing the binding selectivity of self-assembled cyclodextrin monolayers on gold through their architecture. Chem Eur J 7:4164–4170

299. Nijhuis CA, Huskens J, Reinhoudt DN (2004) Binding control and stoichiometry of ferrocenyl dendrimers at a molecular printboard. J Am Chem Soc 126:12266–12267

300. Crespo-Biel O, Dordi B, Reinhoudt DN, Huskens J (2005) Supramolecular layer-by-layer assembly: alternating adsorptions of guest- and host-functionalized molecules and particles using multivalent supramolecular interactions. J Am Chem Soc 127:7594–7600

301. Archut A, Azzellini GC, Balzani V, DeCola L, Vogtie F (1998) Toward photoswitchable dendritic hosts interaction between azobenzene-functionalized dendrimers and eosin. J Am Chem Soc 720:12187–12191

302. Okano T, Yamada N, Sakai H, Sakurai Y (1993) A novel recovery system for cultured cells using plasma-treated polystyrene dishes grafted with poly(N-isopropylacrylamide). J Biomed Mater Res 27:1243–1251

303. Sun TL, Wang GJ, Feng L, Liu BQ, Ma YM, Jiang L, Zhu DB (2004) Reversible switching between superhydrophilicity and superhydrophobicity. Angew Chem Int Ed 43:357–360

304. You YZ, Hong CY, Pan CY, Wang PH (2004) Synthesis of a dendritic core-shell nanostructure with a temperature-sensitive shell. Adv Mater 16:1953–1957

305. Raveendran P, Goyal A, Blatchford MA, Wallen SL (2006) Stabilization and growth of silver nanocrystals in dendritic polyol dispersions. Mater Lett 60:897–900

306. Wang R, Yang J, Zheng Z, Carducci MD, Jiao J, Seraphin S (2001) Dendron-controlled nucleation and growth of gold nanoparticles. Angew Chem Int Ed 40:549–552

307. Wei Y, Jana NR, Tan SJ, Ying JY (2009) Surface coating directed cellular delivery of TAT-functionalized quantum dots. Bioconjug Chem 20:1752–1758

308. Wartlick H, Spankuch-Schmitt B, Strebhardt K, Kreuter J, Langer K (2004) Tumour cell delivery of antisense oligonucleotides by human serum albumin nanoparticles. J Controlled Release 96:483–495

309. Selvan ST, Patra PK, Ang CY, Ying JY (2007) Synthesis of silica-coated semiconductor and magnetic quantum dots and their use in the imaging of live cells. Angew Chem Int Ed Engl 46:2448–2452

310. Ow H, Larson DR, Srivastava M, Baird BA, Webb WW, Wiesner U (2005) Bright and stable core-shell fluorescent silica nanoparticles. Nano Lett 5:113–117

311. Saha A, Basiruddin SK, Sarkar R, Pradhan N, Jana NR (2009) Functionalized plasmonic–fluorescent nanoparticles for imaging and detection. J Phys Chem C 113:18492–18498

312. Earhart C, Jana NR, Erathodiyil N, Ying JY (2008) Synthesis of carbohydrate-conjugated nanoparticles and quantum dots. Langmuir 24:6215–6219

313. Baker JR Jr (2009) Dendrimer-based nanoparticles for cancer therapy. Hematology Am Soc Hematol Educ Program 2009(1):708–719

314. Roberts JC, Bhalgat MK, Zera RT (1996) Preliminary biological evaluation of polyamidoamine (PAMAM) Starburst (TM) dendrimers. J Biomed Mater Res A 30:53–65

315. Heiden TCK, Dengler E, Kao WJ, Heideman W, Peterson RE (2007) Developmental toxicity of low generation PAMAM dendrimers in zebrafish. Toxicol Appl Pharmacol 225:70–79

316. Malik N, Evagorou EG, Duncan R (1999) Dendrimer-platinate: a novel approach to cancer chemotherapy. Anticancer Drugs 10:767–776

317. Choi SK, Thomas T, Li M, Kotlyar A, Desai A, Baker JR Jr (2010) Light-controlled release of caged doxorubicin from folate receptor-targeting PAMAM dendrimer nanoconjugate. Chem Commun 46:2632–2634

318. Malik N, Wiwattanapatapee R, Klopsch R, Lorenz K, Frey H, Weener JW, Meijer EW, Paulus W, Duncan R (2000) Dendrimers: relationship between structure and biocompatibility in vitro, and preliminary studies on the biodistribution of I-125-labelled polyamidoamine dendrimers in vivo. J Control Release 65:133–148

319. Agashe HB, Dutta T, Garg M, Jain NK (2006) Investigations on the toxicological profile of functionalized fifth-generation poly(propylene imine) dendrimer. J Pharm Pharmacol 58:1491–1498

320. Plank C, Mechtler K, Szoka FC, Wagner E (1996) Activation of the complement system by synthetic DNA complexes: a potential barrier for intravenous gene delivery. Hum Gene Ther 7:1437–1446

321. Wilbur DS, Pathare PM, Hamlin DK, Buhler KR, Vessella RL (1998) Biotin reagents for antibody pretargeting. 3. Synthesis, radioiodination, and evaluation of biotinylated starburst dendrimers. Bioconjug Chem 9:813–825

322. De Jesus OLP, Ihre HR, Gagne L, Frechet JMJ, Szoka FC (2002) Polyester dendritic systems for drug delivery applications: In vitro and in vivo evaluation. Bioconjug Chem 13:453–461

323. Neerman MF, Zhang W, Parrish AR, Simanek EE (2004) In vitro and in vivo evaluation of a melamine dendrimer as a vehicle for drug delivery. Int J Pharm 281:129–132

324. Chen HT, Neerman MF, Parrish AR, Simanek EE (2004) Cytotoxicity, hemolysis, and acute in vivo toxicity of dendrimers based on melamine, candidate vehicles for drug delivery. J Am Chem Soc 126:10044–10048

325. Kobayashi H, Brechbiel MW (2005) Nano-sized MRI contrast agents with dendrimer cores. Adv Drug Deliv Rev 57:2271–2286

326. Sato N, Kobayashi H, Hiraga A, Saga T, Togashi K, Konishi J, Brechbiel MW (2001) Pharmacokinetics and enhancement patterns of macromolecular MR contrast agents with various sizes of polyamidoamine dendrimer cores. Magn Reson Med 46:1169–1173

327. Kobayashi H, Kawamoto S, Saga T, Sato N, Hiraga A, Ishimori T, Akita Y, Mamede MH, Konishi J, Togashi K, Brechbiel MW (2001) Novel liver macromolecular MR contrast agents with a polypropyleneimine diaminobutyl dendrimer core: comparison to the vascular MR contrast agent with the polyamidoamine dendrimer core. Magn Reson Med 46:795–802

328. Al-Jamal KT, Ruenraroengsak P, Hartell N, Florence AT (2006) An intrinsically fluorescent dendrimer as a nanoprobe of cell transport. J Drug Target 14:405–412

329. Yu J, Zhao H, Ye L, Yang H, Ku S, Yang N, Xiao N (2009) Effect of surface functionality of magnetic silica nanoparticles on the cellular uptake by glioma cells in vitro. J Mater Chem 19:1265–1270

330. Hirsch LR, Gobin AM, Lowery AR, Tam F, Drezek RA, Halas NJ, West JL (2006) Metal nanoshells. Ann Biomed Eng 34:15–22

331. Shukla R, Hill E, Shi X, Kim J, Muniz MC, Sun K, Baker JR Jr (2008) Tumor microvasculature targeting with dendrimer-entrapped gold nanoparticles. Soft Matter 4:2160–2163

332. Shi X, Wang SH, Meshinchi S, Van Antwerp ME, Bi X, Lee I, Baker JR Jr (2007) Dendrimer-entrapped gold nanoparticles as a platform for cancer-cell targeting and imaging. Small 3:1245–1252
333. Jia L, Lv LP, Xu JP, Ji J (2011) Phosphorylcholine functionalized dendrimers for the formation of highly stable and reactive gold nanoparticles and their glucose conjugation for biosensing. J Nanopart Res 13:4075–4083
334. Haba Y, Kojima C, Harada A, Ura T, Horinaka H, Kono K (2007) Preparation of poly (ethylene glycol)-modified poly(amido amine) dendrimers encapsulating gold nanoparticles and their heat-generating ability. Langmuir 23:5243–5246

Chapter 5
Hard Template-Directed Synthesis

Abstract Silica is presently widely used as a template for the development of various nanostructures due to its characteristic high surface area, thermal and chemical resistance, the presence of reactive silanol groups (Si–OH), and nano-pores. Nontraditional nanostructures consisting of noble metals are often fabricated by depositing thin layers of metals (or their precursors) on some silica beads existing templates. A straightforward sol-gel method can be utilized for the preparation of noble metal nanoparticles and their composites via in situ-doped silica aerogels. The metal dispersion and size distribution obtained by this approach depends on the kind of metal, the reaction conditions, and the metal loading. Another approach consisted of making use of the pore channels of hexagonal mesoporous silica, as matrixes for controlling the nanoparticles size. It was demonstrated that noble metal nanoparticles could be coated with a silica shell via the reaction of citrate-stabilized gold nanoparticles and alkylaminotrimethoxysilane, followed by polymerization after the addition of a sodium silicate solution. The spherical silica nanoparticles were used as the templates of interior cores of metal nanoshells and as the templates for the deposition of the external noble metal shell layer by layer. A controlled growth of silver nanoparticles on TiO_2 templates is expected in tuning the optical response of the silver–TiO_2 hybrids. The growth model can explain the phenomenon of silver nanoplates lying on the small silver nanoparticles. A simple and reproducible method for the activation of monodis-persed silver nanoparticles was insertion of the concentrated NaCl, NaBr, and NaI solution into the silver nanoparticle dispersion. It was also demonstrated the entrapment of thiol-coated gold particles, and believe that the technique is straightforwardly applicable also for other hydrophobically coated nanoparticles. The presence of a substrate influences the resultant frequency and bandwidth of the surface plasmon resonance and more generally its multipole distribution. By combining two different materials or different particle shapes of the same material within the same single nanostructure, new properties of the coupled system can be obtained. An interesting approach to introduce theranostic functionalities into a nanosystem is to covalently attach a metal-porphyrin chelate to mesoporous silica nanoparticles (MSNs) which are readily taken up by cells. Bioconjugates based on MSNs are used in a wide array of applications, including chemical catalysis, drug

delivery, controlled release of therapeutics, and cell labeling and killing. UV-photoexcited TiO_2 nanoparticles and their conjugates in aqueous solution form various reactive oxygen species, mainly highly reactive hydroxyl (OH), peroxy (HO_2) radicals, and singlet oxygen, highly reactive hydroxyl radicals, electrons and superoxide ions able to deactivate of bacteria, algae, viruses and kill cancer cells.

Keywords Silica and TiO_2 templates · Mesoporous silica nanoparticles · Composites · Deposition · Bioconjugates · Reactive oxygen species · Cell killing

Abbreviations

1D	One-dimensional
AAS	Atomic absorption spectrometry
AFM	Atomic force microscopy
APS	Aminopropyltrimethoxysilane
APTES	(aminopropyl)triethoxysilane
APTMS	Aldehyde propyltrimethoxysilane
Asm	Aspartame
AuNP	Gold nanoparticle
AuNR	Gold nanorod
BDAC	Benzyldimethylhexadecylammonium chloride
BET	Brunauer–Emmett–Teller
BJH	Barrett–Joyner–Halenda
CEA	Carcinoembryonic antigen
CNS	Central nervous system
CTAB	Cetyltrimethylammonium bromide
CTAC	Cetyltrimethylammonium chloride
CVD	Chemical vapor deposition
CVs	Cyclic voltammograms
DA	Dopamine
DBTA	Dibenzoyl tartaric acid
DCC	Dicyclohexylcarbodiimide
DLS	Dynamic light scattering
DMAP	Dimethylamino pyridine
DNA	Deoxyribonucleic acid
DOPAC	3,4-dihydroxyphenylacetic acid
DOX	Doxorubicin
DTG	Differential thermogravimetry
EDC	N-(3-dimethylaminopropyl)-N-ethylcarbodiimide hydrochloride
EDS	Energy-dispersive spectra
EDX	Energy-dispersive X-ray spectroscopy
EFPL	Enhancement factor
EF_{SERS}	Raman enhancement factor
EI	Extinction intensity
ELs	Edge lengths

F	Fluorescein
Fcc	Face-centered cubic
FESEM	Field emission scanning electron microscopy
FSM	Folded-sheet mesoporous material
FTIR	Fourier transform infrared spectroscopy
GCE	Glassy carbon electrode
HAADF	High-angle annular dark field
HD-PtNDs	Highly dispersed platinum nanodots
HF	Hydrofluoric acid
HRTEM	High-resolution TEM
ICP-AES	Inductively coupled plasma atomic emission spectrometry
LSPR	Local surface plasmon resonance
MCM	Mobil composition of matter, mobil crystalline materials
MCN	Mesoporous carbon nitride
MESNa	Sodium 2-mercaptoethanesulfonate
MIES	Metastable impact electron spectroscopy techniques
ML	Monolayer
MMT	Montmorillonite clay
M-O-M′	M and M′, metals; O, oxygen
MPTMS	3-mercaptopropyltrimethoxysilane
MSN	Mesoporous silica nanoparticle
MSN-PdTPP	Pd-meso-tetra (4-carboxyphenyl) porphyrin (PdTPP) covalently embedded in MSNs
MTT	3-(4,5-dimethylthiazol-2-yl)-2,5-diphenyltetrazolium bromide
MW	Microwave
Nbx	Nanobox
Ncg	Nanocage
Ncb	Nanocube
NCls	Nanoclusters
NCs	Nanocrystals
Nf	Nanoframes
NHA	Normal human astrocytes
NMNP	Noble metal nanoparticle
OA	Oriented attachment
OR	Ostwald ripening
OTS	Octadecyltrimethoxysilane
PDT	Photodynamic therapy
PdTPP	Pd-meso-tetra (4-carboxyphenyl) porphyrin
PL	Photoluminescence
PLE	Photoluminescence excitation
PLGA	Poly(L-glutamic acid)
PLL	Poly(L-lysine)
PSA	Prostate-specific antigen
PVPo	Polyvinylpyrrolidone

QD	Quantum dot
RBS	Rutherford backscattering spectrometry
RF	Radio frequency
Rh	Rhodamine
Rh6G	Rhodamine 6G
RhB	Rhodamine B
SBA-15	Mesoporous silica nanoparticles
SEM	Scanning electron microscope
SERS	Surface-enhanced Raman scattering
SG	Sol-gel
SHE	Standard hydrogen electrode
SiNWs	Silicon nanowires
Si–OH	Silanol groups
SPO	Scanning probe oxidation
SPR	Surface plasmon resonance
STM	Scanning tunneling microscopy
TEM	Transmission electron microscope
TEOS	Tetraethoxysilane, tetraethyl orthosilicate
TGA	Thermal gravimetric analysis
THF	Tetrahydrofuran
TSPR	Transverse SPR
UPD	Underpotential deposition
UPS	Ultraviolet photoelectron spectroscopy
UVA	UV light
XRD	X-ray diffraction
ΔE	Given temperature
κ	Dielectric constant decreases the value
ζ	Zeta potential

5.1 Introduction

Hard templates can be employed for the shape-controlled synthesis of metal nanocrystals. The metal ions are reduced within or around the confined volume or space of the template. These spatially and dimensionally constrained structures can serve as reaction cages to control the nucleation and growth of the particles (and impart stability). Templating can also be done against existing nanoparticles with a well-controlled shape. It is appropriate here to point out a difference between the preformed-seed-mediated method and the template method. In the preformed-seed-mediated method, a similar or identical seed particle becomes part of the resultant nanoparticle, whereas the template is often a dissimilar material that does not become part of the nanoparticle. There are reports on the deposition of

various inorganic nanoparticles onto silica microspheres, including metals [1], metal oxides [2] and sulfides [3].

Nanoscale dispersions of metal in silicate and other metal matrixes have attracted great interest because of their unique size-dependent optical, electrical, and chemical properties [4]. Several general strategies were reported for the encapsulation of metallic colloids in sol-gel matrixes. With use of an inverse micelle technique, spherical nanosized metal-silica composite particles were prepared via a sol-gel reaction within the metal alkoxide microemulsion [5]. Martino et al. reported the synthesis of metal nanocluster-dispersed silica monoliths by diffusing the metal clusters into pre-existing wet monoliths formed through a sol-gel reaction [6]. Silica thin films and bulk materials containing metal colloids were also prepared by diffusing metal salt solution into silica matrixes, followed by a reduction of the metal salt, which could be chemical, photochemical, or sonochemical reduction [7]. Using a two-step sol-gel procedure, Whilton et al. [8] synthesized porous silica-supported metal nanoparticles. Prefabricated metal-polymer microgel hybrids were incorporated in a silica matrix. In this method, the spherical functionalized polymer microgels function as both nanosized exotemplates for controlled growth of metal colloids and as endotemplates for porous sol-gel silica. From all these works, it has been noticed that the morphology and properties of the metal-silica composite were greatly affected by the preparation methods.

In addition to the soft and hard templates, there is another kind of nanoparticle template, called sacrificial template that has been used, where the template particle sacrifices itself in the process of templated particle formation. Sacrificial template mechanism is based on the principles of galvanic displacement reactions. The morphology of sacrificial nanoparticle acts as a reference and guides the nucleation and growth of the depositing metal and final morphology of the resultant particle. By varying the shape of the sacrificial template nanoparticle and its ratio to the more-noble metal precursor added, one can obtain a variety of morphologies such as, for example, triangular rings, wires, tubes, boxes, or cages [9, 10].

Porous metal-oxide membranes containing uniform cylindrical pores can be used as hard templates for the electrochemical preparation of noble metal nanorods, which may represent one of the first major developments in high-yield, solution-phase synthesis of anisotropic metallic nanostructures [11]. This membrane-based approach is very useful for synthesizing metal nanorods with control over both diameter and length. Recently, novel plasmonic nanorod metal materials for biosensing were prepared by electrochemical growth of gold nanorod arrays using a substrate supported, thin-film porous aluminum oxide template [12]. In addition to the synthesis of 1D gold nanostructures, gold nanocrystals with complex morphologies, such as branched [13] and cap-like [14] particles, can be produced by employing suitable hard templates. Examples of hard templates include silicas and porous nanoparticles membranes, such as polymer films containing track-etched channels and alumina films containing anodically etched pores. This approach is commonly used for the synthesis of high-density, ordered arrays of nanorods, nanowires, and nanotubes. Preparation of nanoparticles in these templates involves infiltration of the pores with a precursor solution, which is then

allowed to undergo reduction and recovery of the metallic nanoparticles by selectively removing the template. The pore size and shape and the amount of metal deposited within the pores of the membrane control the nanoparticle diameter, size, and morphology [15, 16]. Metals can be deposited inside the pores of the templates by either chemical ("electroless") or electrochemical reduction of the appropriate metal ion [15, 17]. Electroless metal deposition involves the use of a chemical-reducing agent to generate electrons and to deposit a metal from solution onto a desired surface without any circuitry. Metal nanotubules and wires can be prepared by using this technique [15, 18].

A suitable scaffold for the synthesis of noble metal nanoclusters typically allows multiple and strong interactions with metal ions by complexation or by ionic bonds. Special care is needed to avoid aggregation, since all the suitable scaffolds can also be used for the nucleation and growth of large nonfluorescent silver nanoparticles, for example, in acrylates [19, 20], dendrimers [21] or DNA [22]. To limit the size to few-atom nanoclusters, proper scaffolds thus must be combined with suitable concentrations and with appropriate reduction methods.

In the classical seed-mediated synthesis of gold nanorods in the presence of CTAB, originally it was thought that the rod-like micelles formed by CTAB in aqueous solution would play the role of soft templates [23] but later on a more reasonable mechanism based on the preferential binding of CTAB to certain crystal faces of gold nanorods was put forward and became widely accepted [24]. It is worthwhile to search for other feasible colloidal templates for the shape-controlled synthesis of gold nanocrystals. In this regard, metal–surfactant complexes with desirable morphologies, which are formed by Au(I) or Au(III) and surfactants through binding interactions (e.g., aurophilic attraction and electrostatic combination), can be employed as reactive sacrificial templates for the shape-controlled synthesis of gold nanocrystals (metal–surfactant complex-templated synthesis).

Modification of the nanoparticle surface is a suitable and still almost unexplored path to constrain a set of smart units into an organized network. Fluorescent nanoparticles, for example, are in fact very promising for the design of labels and sensors for the relative ease of their synthesis and for their peculiar properties. Silica nanoparticles can be prepared in a very straightforward way and their surface can be easily modified by means of alchoxysilane derivatives. This versatility makes silica nanoparticles a good choice as a scaffolding structure for a network of dye moieties (metal nanoparticles), especially considering that in addition these materials are transparent to visible light and inert as far as energy and electron-transfer processes are concerned [25]. As a consequence, dye-coated silica nanoparticles constitute a suitable system to characterize intermolecular photophysical processes at their surface, avoiding any interference from the particle nucleus.

Composites of nanometer-sized metal particles with a narrow particle size distribution homogeneously dispersed in a SiO_2 matrix have been reported based on the incorporation of preformed nanoparticles within silica [26] or by sol-gel processing of the metal complex [27]. The metal dispersion and size distribution obtained by this approach depend on the kind of metal, the reaction conditions, and the metal loading. Another approach consisted of making use of the pore channels

of hexagonal mesoporous silica [28], as matrixes for controlling the nanoparticles size. Thus, the ordered mesoporous silica materials, MCM (mobil composition of matter or mobil crystalline materials) and FSM (folded-sheet mesoporous material) types, have been used as templates for the growth of metal nanoparticles [29]. The general procedure used was based on impregnating the metallic precursor onto the support followed by calcination to generate the nanoparticles. The final size of the nanoparticles is dependent on both the pore size and the calcination temperature. Guari et al. [30] have described a new methodology consisting of coordination of an organogold precursor within the pore channels of functionalized mesoporous silica followed by metal nanoparticles growth under mild chemical reduction. Other research groups seeking gold nanoparticles growth using, respectively, thiol- or amino-functionalized mesoporous silica materials have also explored this approach [31]. This methodology should prevent outer pores growth and allow a good control of the size of the particles [32].

Several other literature data concerning gold encapsulated in SiO_2 can be included. Caruso described some methods for the engineering of nanoparticle surfaces [33]. It was demonstrated that gold nanoparticles could be coated with a silica shell via the reaction of citrate-stabilized gold nanoparticles and alkylaminotrimethoxysilane, followed by polymerization after the addition of a sodium silicate solution. Liz- Marzan et al. [34] have claimed that the preparation of a silica coating on gold nanoparticles was successful only when the gold complexing and silane-coupling agent ((3-aminopropyl)trimethoxysilane) were previously attached to the particle surface. Mann et al. [35] prepared functionalized silica shells over gold nanoparticles and showed that the colloidal solutions of these particles were stable for up to 2 months. Methods for covering the surface of gold nanoparticles with polymers have also been discussed [36]. It was also reported the homogeneous incorporation of silica-coated gold particles into a transparent silica gel without any aggregation of particles [37]. These core@shell nanoparticles are stable and ready for further applications; however, they generally have a nonordered porous shell. Later, Konya et al. [38] have proposed a simple but very promising method to synthesize controlled size and shape Pt nanoparticles containing mesoporous materials.

The nanoscale dispersions of noble metal particles in mesoporous sol-gel materials are of great interest. With a size range of 2–50 nm, the mesopores permit ingress by molecules and guests physically excluded from microporous materials and provide a high surface area available for sensing and catalysis. In comparison to macroporous materials, the pore size can be made small enough to prevent the active species (i.e., nanosized particles) from leaking out of the matrixes. Since the early 1990s, numerous kinds of mesoporous silicate have been prepared using neutral or ionic surfactant as the template or pore-forming agent [39]. Wei et al. [40] have developed a novel, low-cost, biocompatible nonsurfactant pathway for preparing mesoporous materials. With use of small nonsurfactant molecules such as glucose, fructose, dibenzoyl tartaric acid (DBTA), and urea as a pore-forming agent, silica mesoporous materials have been prepared with high surface area and

pore volume. The pore size is in the range of 2–6 nm with narrow distributions [41].

There has been major progress in methods for controlling the growth of nanocrystals (NCs) of metallic materials. Shape control has enabled obtaining nanoparticles in forms such as dots, rods, tetrapods, and more [42]. Earlier work on NCs in sol-gel materials focused primarily on hydrophilic, water-soluble NCs. Additional types of water-soluble semiconductor NCs were entrapped in silica particles by a sol-gel process, forming "raisin bun"-type particles [43]. The general method for the entrapment of hydrophobically coated NCs inside micrometer- and submicrometer-sized composite silica spheres is based on the work [44]. The NC entrapment method is demonstrated for a variety of nanocrystals, primarily semiconductors covering different spectral bands, and of different shapes including spheres and rods. Authors also demonstrated the entrapment of thiol-coated gold particles and believe the technique is straightforwardly applicable also for other hydrophobically coated NCs. They term the micrometer-sized particles which contain nanoparticles "nano@micro" or "micro@nano" composites [45]. The size-, composition-, and shape-dependent properties of such NCs can be harnessed for a variety of applications in areas ranging from biological fluorescent tagging to light-emitting diodes, lasers, and catalysts.

The development of new bioactive materials able to bond to living tissues is a promising alternative for the production of implants and scaffolds for tissue engineering. Many bioactive materials are prepared by a sol-gel method, including glasses and organic–inorganic hybrids. When in contact with physiological fluids, they form carbonated hydroxyapatite nanocrystals similar in composition and structure to biological apatites. This was considered an essential stage in the formation of a bond between the bioactive glasses and the living tissues [46].

Inorganic gel materials prepared by the so-called "sol-gel method" using metal alkoxides as starting materials are generally porous and have a large specific surface area, so that the gel materials can easily react with water vapor and/or water liquid in a much shorter time. In the case of multicomponent inorganic gel materials, hetero-bondings like M–O–M′ (M and M′, metals; O, oxygen), which are often not stable from a thermodynamic point of view, are readily hydrolyzed, and specific components dissolve and recrystallize in water.

The growth of metals on oxide surfaces is important in numerous technologies including electronic device fabrication and nanoparticle formation. In general, the morphology of metal particles on oxide surfaces depends to a large extent on defects, particularly point defects like oxygen vacancies [47]. Several studies have addressed the relationship between metal cluster nucleation/growth on oxide surfaces and defects; however, many questions remain unanswered. A study by Besenbacher and coworkers using scanning tunneling microscopy (STM) showed that bridging oxygen vacancies on TiO_2 are active nucleation sites for gold clusters [48]. In addition, the authors suggested that the diffusion of a vacancy–cluster complex plays an important role in the formation of larger gold clusters. Using atomic force microscopy (AFM), Barth and coworkers have quantified point defects on MgO by estimating the Pd cluster density as a function of the deposition surface

temperature [49]. In a theoretical study, Bogicevic and Jennison have calculated the binding energies of various metals to MgO and showed that dimers of noble metals are more stable at oxygen vacancies [47]. Using STM, Freund and coworkers have demonstrated preferential decoration of Pd and Rh metal particles on line defects of Al_2O_3 [50]. Furthermore, defects on crystalline SiO_2 thin films can be studied using ultraviolet photoelectron spectroscopy (UPS) and metastable impact electron spectroscopy techniques (MIES) [51].

Precise position of nanomaterials produced by various chemical routines is critically required for ultimate nanostructuring. The mainstream methodologies for this involve direct manipulation of the nano-objects by AFM or guided self-assembly on a well-defined template via capillary interaction, electrostatic attraction, or covalent bonding [52]. Compared with low-throughput AFM manipulation, flexible and high-throughput self-assembly strategies are more amenable to large-scale nanostructuring. Employing nanometer-resolution lithography, sub-100-nm nanomaterials were precisely positioned [53]. Particularly, using scanning probe oxidation (SPO), which directly oxidizes a substrate by applying an intensive electrical field at tip-sample junction, a template of patterned oxide domains, nanoparticles, were fabricated on a silicon substrate. Deriving the oxide domains with aminopropyltrimethoxysilane (APS) led to precise position of single gold nanoparticles that were perfectly guided by the template. This strategy does not apply any principle limitation to the choice of other organosilanes possessing specific affinities for various colloids; in general, any nano-object that could self-assemble on silicon surfaces has the chance to be patterned by the combination of SPO and self-assembly involving versatile layer-by-layer assembly.

A spherical, isotropic, homogeneous particle has isotropic optical characteristics (e.g., polarizability, extinction cross section). The same particle placed in the vicinity of a substrate (template) reveals anisotropic optical response due to the polarizability of the substrate material, which may be described as electromagnetic coupling with the image charges induced in the substrate. The presence of a substrate influences the resultant frequency and bandwidth of the surface plasmon resonance and more generally its multipole distribution. The problem of the induced image charges and their influence on the optical properties of nanoparticles was first considered by Yamaguchi [54]. Wind et al. [55] developed a general expression for the polarizability of a sphere on a substrate. Gozhenko et al. [56] developed a theory for a multipole response of an arbitrary aggregate of nanospheres placed in the vicinity of a plane substrate with particle sizes smaller than the wavelength of light. Most of the experimental and theoretical investigations were devoted to the optical response of metallic nanoparticles deposited on a dielectric substrate. The system of a layer of metallic nanoparticles placed in the vicinity of a plane metallic substrate may be used to investigate the coupling of the localized surface particle and propagating surface plasmon polaritons at the interface between the plane substrate and the ambient medium. The coupling of localized and propagating surface plasmon polaritons may reveal interesting physical phenomena, which, in turn, may find numerous technological applications.

The core-shell nanomaterials, as one of the complex nanostructures, have been widely studied. Inorganic nanoparticles can obtain improved chemical stability and size monodispersity through deposition onto the inert supports in this type of nanostructure. There are also some reports on the deposition of various inorganic nanoparticles onto silica microspheres, including metals [1], metal oxides [2], and sulfides [3]. Gold nanoparticles are widely used metal nanoparticles for the deposition onto silica microspheres. The typical method contains three steps: the synthesis of silica microspheres; the surface functionalization of silica microspheres with silane-coupling agents; deposition of AuNPs onto the functionalized silica microspheres by simply mixing the two kinds of particles. Obviously, the three-step method has been widely used for its convenient manipulation. However, the process is tedious, and the Au coverage on silica microspheres is not dense. Halas and coworkers [57] already made a detailed study for the three-step method. They found that the surface functionalization of silica microspheres with different terminal groups had a significant influence on the gold coverage. The hydrophilic groups, such as amino (NH_2) and mercapto (SH) groups, promoted the attachment of AuNPs, while the hydrophobic groups, such as methyl (CH_3) and diphenylphosphine (PPh_2) groups, could not favor the attachment of AuNPs. They also studied the impact of mixture of organosilanes and mixture of solvents on the coverage and morphologies of the attached AuNPs. There is a great effort to optimize the reaction conditions of the three-step method and to explore novel methods to improve the gold coverage on silica microspheres. In addition, sonochemical deposition [58], electroless deposition [59], and seeded growth [60] have been successfully used for the deposition of AuNPs onto silica microspheres. Seed-mediated template-growth method has been demonstrated to be a powerful synthetic route to generate a range of different types of metal nanoparticles [61]. This method separates the nucleation and growth stage of nanoparticle syntheses by introducing presynthesized small seed particles into a growth solution typically containing a metal precursor, reducing agent, surfactants, and some additives. It has been shown that various shapes of gold and silver nanoparticles (e.g., rods, spheres, cubes, and octahedra) can be synthesized using the method, depending on the type of surfactants and ionic additives (e.g., silver ions, halides, and hydroxide) in the growth solution [62].

Alcohol reduction method [63] has been known as a chemical-reducing-agent-free-preparation method for colloidal dispersion of metal nanoparticles. In this method, metal ions are mainly reduced by alcohol via redox reaction between the metallic precursor and alcohol; the reduction of metal ions is greatly governed by the difference between the oxidation potential of alcohol and the reduction potential of metal species at a given temperature (ΔE) [64]. Generally, monoalcohol aqueous solutions such as ethanol/water mixture are frequently used as a reducing agent and a solvent for the reduction reaction in alcohol reduction method. In a typical procedure, the metal precursors are suspended or dissolved in an ethanol/water mixed solvent. The resultant metal precursor suspensions or solutions are heated with reflux at a given temperature for a few hours in the presence of water-soluble polymeric stabilizer like poly(N-vinyl-2-pyrrolidone), and then colloidal metallic particles are formed. This method seems to be proper for attaching metal

nanoparticles to the surface of the support materials due to its slower reduction rate compared to the direct reduction method by a chemical-reducing agent in solution. It is well known that the fast reduction rate makes it difficult to control the system. In order to easily prepare the nanocomposite materials, novel preparation routes were suggested including the polyol process or alcohol reduction method [65].

It was demonstrated that ion irradiation can also be used to modify the shape of nanomaterials [66]. For example, silica colloids with diameters in the 100–1000 nm range show dramatic anisotropic plastic deformation under mega-electron-volt ion irradiation, changing their shape from spherical into oblate ellipsoidal. This ion-beam-induced anisotropic deformation effect is known to occur for a broad range of amorphous materials [67] but has not been observed for crystalline materials, including metals.

Although small platinum (Pt) nanostructures are particularly important for the efficient catalysis and sensitive detection [68], the ease of aggregation often leads to performance deterioration [69]. To obtain the dispersed Pt nanostructures, one of the effective routes is to chemically fabricate Pt on preformed nanostructured surfaces, to form a core@shell structure. Gold nanorods have been extensively investigated as support, due to their well-established synthesis routes, tunable surface plasmon resonance property, and super catalytical activity. The Au@Pt nanostructure has been synthesized by using Au nanorods as support [70], which can catalyze the oxidation of some organic compounds [71].

By combining two different materials or different particle shapes of the same material within the same single nanostructure, new properties of the coupled system can be obtained [72]. One potential route to produce such nanoparticle arrangements is by self-assembly of the components. The mechanisms driving the self-assembly of nanoparticles have been presented [73]. Exploiting the balance between repulsive and attractive interactions in colloidal systems, it has been possible to control the self-assembly of nanoparticles into discrete structures [74]. In this context, the assembly of NP homodimers, that is dimeric structures of the same metal, and their optical properties have been studied before [75]. Examples in which NPs in solution were selectively assembled have been presented by Mirkin et al. [76] and Alivisatos et al. [77] using DNA as linker molecules. Enrichment of the dimer population has been achieved by different methods [78].

5.2   Silica

5.2.1   General

Silica is a robust, hydrophilic, and biocompatible material that can be readily modified with diverse chemical functionality. As a consequence, it is widely used as an inorganic coating and templates for nanoparticles of different composition, e.g., quantum dots (QDs) [79], magnetic nanoparticles [80], lanthanide nanoparticles

[81], and noble metal nanoparticles (NMNPs) [82], or as a nanoparticle-based carrier of functional molecules [83]. Using the diversity of silane chemistry [84], a silica shell, coating, or template can be tailored to have functional groups that can include, but are not limited to, amine, aldehyde, carboxyl, epoxy, and thiol groups. In addition to the use of silica as a structural shell on other template materials, nanoparticles composed of silica can be prepared with sizes that typically range between tens and hundreds of nanometers. The Stöber or reverse microemulsion methods are most commonly used for the synthesis of silica-based nanomaterials [85].

Silica is presently widely used as a template for the development of various nanostructures to its characteristic high surface area, thermal and chemical resistance, the presence of reactive silanol groups (Si–OH), and pores with diameters between 2 and 50 nm. Thus, the process of mass transfer is favored by its mesoporous structure, providing smart nanostructures with high sensitivity [86–88]. Therefore, the formation of a hybrid material containing mesoporous silica provides an excellent substrate for the development of smart nontraditional structures. The nanostructures consisting of noble metals are often fabricated by depositing thin layers of metals (or their precursors) on some silica beads existing templates, followed by calcination or wet chemical etching to remove the solid cores. As demonstrated by Halas and coworkers [89], small gold nanoparticles (with diameter of 1–2 nm) could be adsorbed onto the surfaces of silica spheres that had been premodified with self-assembled monolayers of (3-aminopropyl)triethoxysilane. These adsorbed gold colloids could then serve as the nucleation sites for the subsequent electroless plating of gold (or other metals), leading to the formation of complete metal shells. Another method developed by Caruso and coworkers was based on the layer-by-layer adsorption of polyelectrolytes and charged gold nanoparticles to build shell-like structures around colloidal templates whose surfaces had been derivatized with appropriately charged groups [90].

As a general rule, the functional performances of noble metal nanoparticles/SiO$_2$ materials are strongly dependent on the gold particle size and distribution and hence on the adopted synthetic procedure. Generally, these systems have been prepared by both physical and chemical routes, including ion implantation, ionized cluster beam, evaporation, sputtering, chemical vapor deposition (CVD), wet chemical methods, polyol process, and sol-gel (SG) routes. A report concerning the preparation of Ag–SiO$_2$ composites by a combined pulsed laser deposition/SG approach has also appeared in the literature [91]. Among these synthesis routes, the sol-gel process is a versatile low-temperature approach to glass coatings and powdered samples incorporating nanoclusters in various matrixes [92]. Moreover, under suitable conditions, the formation of the host and guest phases in the composite system can be performed by a single-step process. This peculiarity, together with the mild synthesis conditions (soft chemistry), makes the sol-gel method particularly suitable for yielding thin films with good control over composition and microstructure. The plasma-/liquid-phase hybrid approach also appears as an interesting route. In particular, the peculiar characteristics of radio frequency (RF)-sputtering are the flexibility that permits the fabrication of composite films of

various metals and dielectric materials and the capability to produce uniformly distributed metal clusters [93]. Moreover, the synergic competition between characterizing sputtering processes from glow discharges is a key step in order to obtain nanoparticles with tailored size and distribution. In these processes, plasma activation of both gas-phase species and growth surface can induce intermixing processes between the host matrix and the guest phase. Such effects are further enhanced by the properties of $SiO_x(OH)_y(OR)_z$ gels, i.e., the porous structure and the presence of nonbridging groups, allowing, in principle, an optimal dispersion of the deposited gold nanoparticles. These features might result in unexpected and/or improved functional properties. Moreover, an important advantage of the proposed synthetic pathway is its versatility and feasibility for the preparation of a wide range of host/guest systems, featuring properties hardly attainable by conventional synthetic routes.

The production of the mesoporous silica material-supported gold nanoparticles types of nanocomposites leads to high surface area systems, in which the shape-selective behavior of mesoporous materials can be combined with the catalytic action of metal particles. This shape selectivity cannot be achieved with amorphous oxide-supported metal catalysts [94, 95]. Among all the mesoporous materials, the mesoporous silicas have gained great attention due to the properties of MCM-41 (mobil composition of matters) and related materials, including highly ordered mesopores, controlled pore size, specific surface areas, and pore volumes [96, 97]. Mulvaney group published an early synthesis of silica-coated AuNPs in 1996. The silane-coupling agent (3-aminopropyl)trimethoxysilane was used to render the gold surface vitreophilic. After the formation of a thin silica layer in aqueous solution, the particles were transferred into ethanol for further growth using the Stober method. Varying the silica shell thickness and the refractive index of the solvent allowed control over the optical properties of the dispersions [34].

Noble metal nanoparticles can be synthesized in mesoporous silica films [30] and in ultrathin nanoporous particle films [98]. Silver particles of narrow size distribution were produced upon reversible chemical transformation between metallic and oxide states in the titania matrix [99] and in mesoporous silica that was grafted with hydrophobic $Si(CH_3)_3$ groups at the pore surface [100]. It is well known that gold nanoparticles are typically red or pink [101]. In addition, the refractive index of aerogel deeply influences the color of gold particles [102]. The high refractive index materials induced the gold fine particles to take on a blue color. In the case of the silica matrix with low refractive index, the gold-doped silica aerogel samples showed a pink color. Since the change after supercritical drying was only related to the volatilization of solvent, a process that does not destroy the silica matrix, the color of gold-doped silica aerogel was retained as pink.

Montmorillonite clay (MMT), as lamellar clay, has been used as templates for noble metal nanoparticles with good results because their high ion-exchange capacity, high surface area and sportive capacity, chemical lifelessness, and low or null toxicity [103] lead to high antimicrobial activity compared to bulk silver metal [104]. MMT@AgNPs-based structures are supposed to be new generations of antimicrobials as they are being used in many antimicrobial preparations [105].

Several methods have been reported for the synthesis of nanostructures based on silica/noble metals, e.g., photochemical reduction, microwave, chemical reduction, irradiation [106]. Microwaves are electromagnetic waves and being used for the development of different materials. In microwave applications, heating is caused by the interaction of permanent dipole moment of molecules with high-frequency electromagnetic radiation. In comparison with conventional heating, this method shortens reaction time by factor of approximately 20 with uniformly spread through the entire bulk of the reaction medium. Silver nanoparticles were synthesized onto the surface of MMT by a simple-microwave-assisted process from an aqueous solution of silver nitrate; silver nanoparticles with a narrow size distribution on MMT surface were obtained without using any reducing agents [107].

5.2.2 Silver Nanoparticles

Silver nanoparticles were successfully immobilized onto the 3-mercaptopropyltrimethoxy-silane (MPTMS)-functionalized silica particles by polyol process [108, 109]. Thiol groups tend to interact with silver ions by the cleavage of an S–H bond and the spontaneous formation of an S–Ag bond [110]. As a result of unique behavior of thiol groups containing sulfur atom, chemicals containing thiol groups have been widely used as chemical protocols to make various metal–metal-oxide composites [111]. Thiol groups can be introduced by graft reaction between surface silanol groups of silica and MPTMS [112]. In this procedure, monodispersed silica particles with spherical shape and an average particles size of about ~ 300 nm in diameter are observed. Herein, polyol process was applied to form and immobilize silver nanoparticles onto the silica surface functionalized with thiol groups. Generally, polyvinylpyrrolidone (PVPo) acts not only as a nucleation-promoting agent for silver ions but also as a stabilizer for silver nanoparticles in polyol process. When ethylene glycol solution containing silver ions and silica particles functionalized with thiol groups was heated with reflux in the absence of PVPo, few particles were formed and immobilized onto the silica surface. On the contrary, when the same reaction proceeded in the presence of PVPo, silver nanoparticles were successfully formed and immobilized onto the surface of silica particles. Thus, the reduction potential of this system consisting of $AgNO_3$, silica particles, and ethylene glycol is insufficient to reduce $AgNO_3$ and stabilize the silica@Ag nanostructures at a given reaction temperature in the absence of PVPo.

In Fig. 5.1, curves 1 and 2 indicate the UV–Vis absorption spectra of resulting composite particles prepared in the absence of PVPo and in the presence of PVPo, respectively. Curve 1 shows very weak absorption intensity, whereas curve 2 shows a broad absorption band about 520 nm, redshifted compared to the general absorbance band of silver nanoparticles observed at about 400 nm. This is discussed in terms of the fact that absorption and scattering of light by the particle

depend on its chemical composition, size, shape, surrounding dielectric medium, and coupling of the colloids and adsorbed solutes [113].

Especially, in the case of composite (core@shell) particles consisting of dielectric core and metal layer such as shell or particles, when the thickness and coverage of silver layer are increased, the plasmon peak broadens, redshifts, and depresses the scattering peak greatly [114, 115]. From these facts, it is thought that redshift and broadening of plasmon peak were attributed to the high degree of silver coverage on the silica surface, which means that the silver nanoparticles were completely immobilized onto the silica particles with a high degree of coverage. Therefore, it is obviously concluded that PVPo molecules successfully promoted the formation of silver nanoparticles without interference of formation of combined structure between silver nanoparticles and silica surface. On the other hand, it is worth to notice that though the degree of apparent silver coverage is high, actually, a small number of silver particles with a large size and a wide size distribution are immobilized onto the silica surface. It is thought that nucleation period was not enough and nucleation and growth steps occurred simultaneously during the formation of silver particles. In order to obtain small particles having a narrow size distribution, nucleation and growth steps are completely separated. In addition, it is more advantageous to perform the preparation procedure in steps during the preparation of composite particles consisting of dielectric core and metallic shell to prevent the formation of large aggregates or particles [116].

The generation of silica–silver composite particles at different stages of immobilization process is shown in Fig. 5.2. In curve 1, a broad absorption peak appears about 490 nm, which indicates that very small silver nanoparticles are immobilized onto the silica surface.

After additional growth of silver particles, much higher and broader peak was observed as shown in Fig. 5.2 (curves 1 and 2). This means that small silver particles grow to larger ones. Moreover, it is thought that the thickness of silver layer increased after additional growth process. Similar behavior was confirmed by the FESEM observation. Therefore, it can be concluded that when polyol process is

Fig. 5.1 UV–Vis absorption spectra of the silica–silver composite particles prepared by polyol process at 120 °C for 4 h with silver concentration of 1000 ppm in the absence of PVPo (*1*) and in the presence of PVPo (*2*) [113]
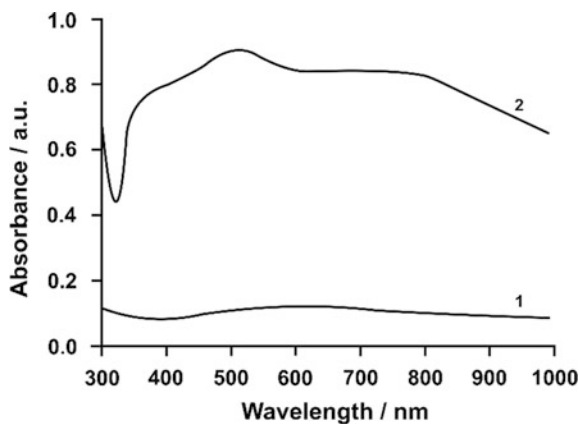
Fig. 5.2 UV–Vis absorption spectra of the silica–silver composite particles prepared by polyol process at 25 °C for 12 h (*curve 1*, *solid line*) and after additional growth for 7 h (*curve 2*, *solid line*) and at higher silver concentration of 10,000 ppm for 12 h (*curve 1**, *dotted line*) reaction and after additional growth for 7 h (*2**) [113]

applied for the immobilization of silver nanoparticles onto the large supports, it is possible to obtain extremely small silver particles and to control the size of silver particles and the thickness of silver layer by control of reaction temperature and time. This size-controlled immobilization route is explained by following two steps; (1) small silver particles are firstly formed on the silica surface and (2) these small silver particles homogeneously grow to larger ones. These two steps are completely conducted in one-pot by polyol process, which is attributed to the slower and more easily controllable reaction rate of the polyol reduction method than that of general chemical reduction method using reducing agent such as hydrazine or sodium borohydride. Especially, first step is more easily conducted by polyol process in the present system; extremely small silver particles are easily immobilized onto the supports by polyol process at a low reaction temperature for a relatively long reaction time.

At higher concentration of $AgNO_3$ (10,000 ppm), this trend was more clearly proven. When the reaction proceeded at 120 °C, few silver particles with extremely large size were immobilized on the surface of silica particles, whereas when the reaction was conducted at 25 °C at a sufficient nucleation time, many small silver particles are immobilized onto the silica surface. As a result, it is obvious that small silver particles with narrow size distribution are easily formed on the silica surface at a low reaction temperature. Subsequently, additional growth step proceeded with increasing reaction temperature up to 120 °C according to the same schedule as already mentioned. After the additional reduction process, the size of individual silver particles immobilized onto the surface of silica particles increased irregularly and the number of silver particles greatly decreased. This fact means that despite slow reaction rate of the polyol process, the reaction rate of growth process is so fast that immobilized small silver particles homogeneously grow to larger ones because too high concentration of silver precursor accelerates the reaction rate. It is thought that they are finally detached from the surface of silica particles because they are too large to be immobilized onto the surface by thiol groups. It is experimentally well known that when silver nanoparticles are prepared by polyol process, large particles

about over 50 nm in size are more easily deposited on the surface of inside wall of glass reactor than small one. From these facts, it is obvious that large particles growing over than about 50 nm during the growth process were detached from the silica surface and deposited on the inside wall of glass reactor. This can be more clearly explained by UV–Vis absorption spectra of the samples discussed above. In two curves of Fig. 5.2 (dotted lines, curves 1* and 2*), it was observed that the maximum peak intensity was decreased after growth process, which indicates that the concentration of the silver particles in the solution decreased as a reaction proceeded. This result agrees with the glass wall coating phenomenon and FESEM images. As a result, it is clearly concluded that too high silver precursor concentration interferes with the immobilization of well-defined silver nanoparticles due to the fast reduction rate of silver precursor.

The mechanism for the immobilization of the silver nanoparticles onto the silica surface by polyol process is shown in Scheme 5.1. At the initial stage of the reaction, MPTMS-functionalized silica particles and PVPo are dissolved into the ethylene glycol. After complete dissolution of PVPo, $AgNO_3$ is added into the system. In this stage, silver ions are bonded with thiol groups of the silica surface by the cleavage of an S–H bond and the spontaneous formation of an S–Ag bond [110], and excess silver ions form complex with PVPo by interaction between the hydrophilic pendant rings of PVPo and the silver ions [117]. In the second stage, Ag^+ ions are reduced to Ag^0 metal state by ethylene glycol and PVPo, and silver nuclei are formed on the surface of the MPTMS-functionalized silica particles; nuclei are created at the silver ions bound to the thiol groups of the silica surface by the nucleation site role of Ag^+ ions bound to thiol groups [114], similar with the role of seed materials. Finally, silver nanoparticles are formed on the silica surface by growth of nuclei [33]; reduced silver species such as silver atoms or clusters in the solution are deposited on the nuclei immobilized on the silica surface, which is attributed to the slower reduction rate of polyol process than that of general chemical reduction method using reducing agent.
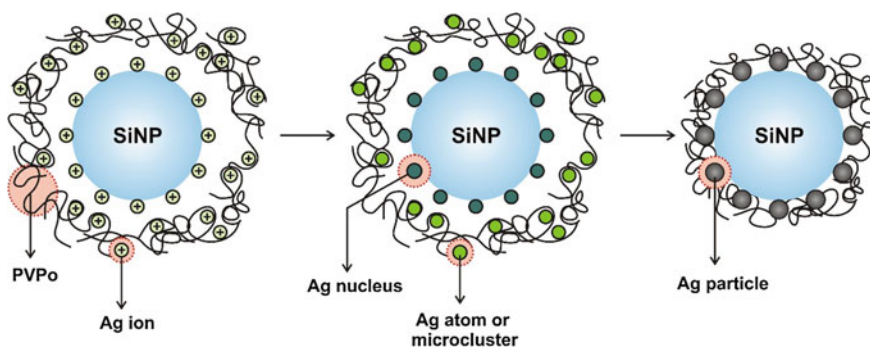
Scheme 5.1 A schematic representation of the mechanism for the immobilization of the silver nanoparticles onto the silica surface by polyol process [113–115]

Silver nanoparticles can be also synthesized by using thermal decomposition method. Ag–SiO$_2$ (SiO$_2$@AgNPs) composite (or core@shell) nanoparticles are synthesized by using well-known Stöber method at low-temperature route for coating SiO$_2$ particles with silver nanoparticles [118]. This synthesis was done completely without external reducing agents or media, adhesive aids or functionalizing agents. Composition or structure of these nanocomposites can be obtained by weight loss (thermal gravimetric analysis, TGA) analysis during heat treatment under airflow. Data reveal, for example, the formation of silver–oleate complex (Fig. 5.3). A very strong endothermic peak was observed at 295 °C. The peak is related to the evaporation of oleate molecules by the decomposition of silver–oleate complex. In the case of CTAB, the weight loss occurred from 220, revealing that CTAB molecules were decomposed thermally [119].

No peak of silver in the pristine silver–oleate complex has been observed in the XRD analysis which indicates that the complex is amorphous. However, peaks of silver have been observed in the aging of silver–oleate complex at 300 °C. Peaks are broadened due to the nanocrystalline nature of silver. Herein the XRD shows three peaks at 2θ values of 38.2°, 44.5°, and 64.5° corresponding to (111), (200), and (220) planes of silver, respectively. No impurity peak is observed in the XRD spectrum. The mean size of silver nanoclusters was determined as ~ 8.0 nm (TEM). The silver nanoparticles have very narrow size distribution. The EDX spectra of silver nanoparticles excited by an electron beam. There is no impurity atom in the nanoparticles except silver atom. Accordingly, from the EDX spectra, we could confirm that the nanoparticles in TEM images are pure silver particles.

Figure 5.4 (left panel) shows UV–Vis spectrum of Ag nanoparticle ($\lambda_{max} =$ 410 nm) dispersed in isooctane solution. Ag nanoparticles display an optical absorption band at 410 nm (~ 3 eV), typical of absorption at metallic silver nanoparticle, due to the surface plasmon resonance (SPR) [120]. The colloidal suspensions of silver particles were a bright yellow-greenish color, due to the intense bands around the excitation of SPR [121]. This absorption band is a little

Fig. 5.3 TGA (1)/DTG (2) curves of silver–oleate complex during heat treatment under airflow [118, 119]
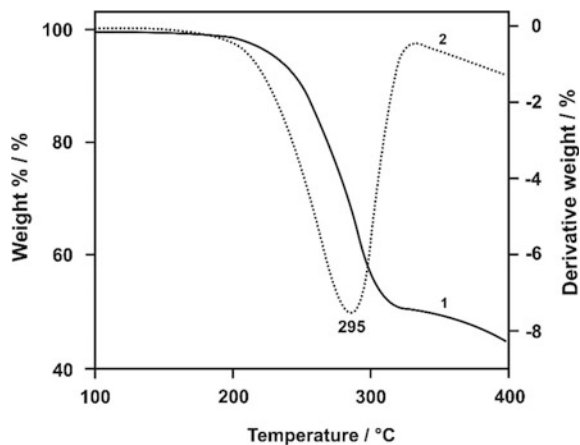
blueshifted compared with the plasmon absorption band of silver colloids prepared by citrate reduction method (λ_{max} = 434 nm) [122]. It is caused that silver nanoparticles have narrower size distribution and smaller diameter than silver nanoparticles prepared by citrate reduction method.

UV–Vis spectrum of Ag–SiO$_2$ nanoparticles shows absorption band at 420 nm whereas that of silver nanoparticles prepared is shown at 410 nm (Fig. 5.4). This absorption band is rather broad and redshifted compared with the plasmon absorption band of Ag nanoparticle. As discussed earlier, the position and shape of the plasmon absorption of silver nanoparticles are strongly dependent on the particle size, dielectric medium, and surface-adsorbed species. This is concerned with redshifted absorption band of Ag–SiO$_2$ [123]. EDX (energy-dispersive X-ray spectroscopy) spectrum shows that this product consists of Ag and Si components.

Figure 5.4 (right panel) shows TEM image of SiO$_2$@AgNPs nanostructures whose SiO$_2$ nanoparticle size is about 200 nm and silver nanoparticle size is below 10 nm. Silica nanoparticles were synthesized by hydrolysis and condensation of tetraethylorthosilicate (TEOS) in a mixture of ethanol with water, using ammonia as catalyst to initiate the reaction. TEM image shows SiO$_2$ nanoparticles were homogeneously impregnated with silver nanoparticles.

Further silica–silver heterogeneous nanocomposite structures have been prepared by alcohol reduction method [124]. Silver nanoparticles with narrow size distribution were homogeneously and quickly immobilized onto the silica surface with thiol groups. The spherical silica particles were prepared by the sol-gel process on the basis of the Stöber method [125]. Thiol groups were used as a chemical protocol to attach the silver nanoparticles to the silica surface [110]. Therein, in the case of silver ion reduction by alcohol reduction method, the degree of reduction can be monitored by the change in color of the solution during the reaction. Transparent ethanol solution containing AgNO$_3$ and PVPo shows a color change
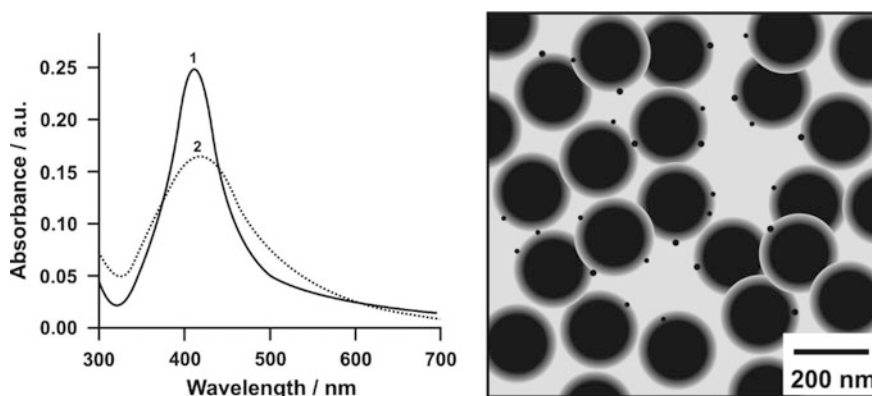
Fig. 5.4 UV–Vis spectra of Ag nanoparticle (λ_{max} = 410 nm, *curve 1*) and Ag–SiO$_2$ nanoparticle (λ_{max} = 420 nm, *curve 2*) (*left panel*). Schematic picture of SiO$_2$@Ag nanoparticles (*right panel*) [120]

between light brownish yellow and dark brownish yellow according to reaction factors (e.g., precursor concentration, stabilizer concentration, reaction temperature and time). The appearance of the yellow color reveals the formation of colloidal silver nanoparticles. In this system, the color of the solution changed to light brownish yellow at about 90s and became darker to thick brownish yellow as the reaction proceeded.

In the UV–Vis graph (Fig. 5.5, left panel), well-defined peaks are shown at around 405 nm, which is attributed to the surface plasma excitation of silver nanoparticles. The peak intensity slowly increased as the reaction proceeded and the formation of silver particles is almost ended within 10 min.

It was observed (TEM, 10 min, Fig. 5.5, left panel, curve 1) that the silver nanoparticles with an average size of 6.9 nm are homogeneously immobilized onto the silica surface. After 2 h, the silver nanoparticles on the surface of silica grow to larger ones with an average size of 10.6 nm in diameter. Figure 5.5 (right panel, curves 1 and 2) shows the particle size distribution for silver particles immobilized on the surface of silica particles. These results show a good agreement with that of the color change of the solution and UV–Vis absorption spectra of the resulting nanocomposite particles.

The Si, S, and Ag peaks (2 h, EDX elemental analysis) were obtained, which indicates that the silver nanoparticles were successfully immobilized onto the silica surface. The XRD diffraction peaks for the nanocomposite particles prepared at the reaction time of 10 min are broadened and small. This fact suggests that their particle size was extremely small. After an additional reaction for 2 h, the diffraction peaks clearly appeared and the intensity was increased. This result is attributed to the increase of crystallinity of the silver nanoparticles due to the increase of the particles size. The formation of face-centered cubic (fcc) phase of silver was confirmed; diffraction peaks at $2\theta = 38.10°$, $44.30°$, $64.35°$, and $77.35°$
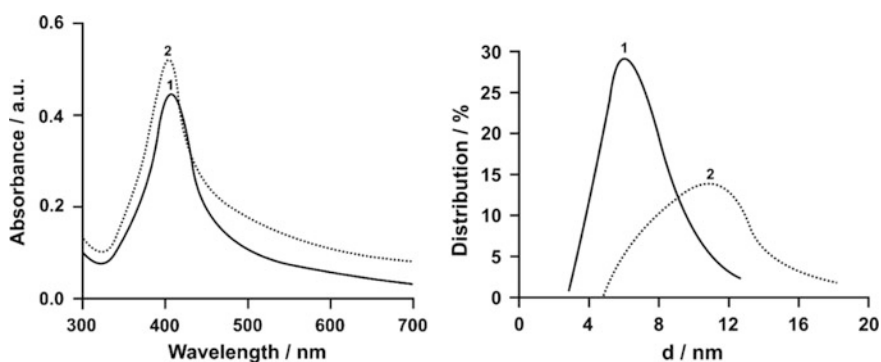
Fig. 5.5 UV–Vis absorption spectra of the silica–silver nanocomposite particles prepared by the alcohol reduction method at different reaction times: 10 min (*curve 1*) and 2 h (2) (*left panel*). Particle size distribution for the silica–silver nanocomposite particles prepared by the alcohol reduction method at different reaction times: (*curve 1*) 10 min and (2) 2 h (*right panel*) [124]

are assigned as the (111), (200), (220), and (311) reflection lines, respectively, of the fcc phase of silver.

To verify the role of the thiol groups on the surface of silica particles, the preparation of the silica–silver nanocomposite particles was tried in ethanol medium using bare silica particles without thiol groups. In TEM figure, it was not clear whether the silver nanoparticles are immobilized on the silica surface or only overlapped in the image. However, it is clearly observed that the number of silver nanoparticles is smaller compared to the case using silica particles with thiol groups on the surface. This fact can be explained by the nucleation site role of the thiol groups. In this system, silver ions are bound to the sulfur of the thiol groups before being reduced due to the strong interaction between the sulfur and metal ions. These combined sites on the silica surface (S–Ag) act as nucleation sites during the reduction process, similar to the heterogeneous nucleation technique. As a result, thiol groups on the silica surface act as a chemical protocol and a nucleation-promoting agent.

Furthermore, free silver nanoparticles below 3 nm are observed in solution. Particularly, free silver nanoparticles are obviously smaller in size than that of immobilized silver nanoparticles. In spite of the additional reaction for 2 h, the size of the free silver nanoparticles did not grow larger; only silver nanoparticles immobilized on the silica surface grew to larger ones. From this fact, it is thought that silver species with ~ 3 nm in size such as nuclei, microclusters, and particles were continuously formed in the solution, and these silver species were deposited on the nuclei immobilized on the silica surface. This is attributed to the slower reduction rate of the alcohol reduction method than that of the general chemical reduction method using a reducing agent. In consequence, the preparation mechanism is explained by two steps; (1) silver nuclei were mostly created on the surface of silica by a nucleation site role of thiol groups on the silica surface, and (2) these nuclei grew to larger ones by deposition of reduced silver species to the immobilized nuclei, similar to the seed-growth mechanism.

The effect of surfactant and solvent (reducing agent) on the formation of AgNPs-silica was studied in several papers [126, 127]. On addition of silver salt in formamide, evolution of gas was observed. This was attributed to the reduction of silver ions or oxidation of formamide. The process involves the evolution of NH_3, CO_2, and H_2 gases [126, 127]. When a stabilizing agent such as SiO_2 or PVPo was added to formamide before addition of silver salt, stable clear dispersions were obtained. However, no adsorption of metallic silver on the walls of the container was observed in the presence of SiO_2 or PVPo. Silica seed nanoparticles (13 nm) were used to provide support for silver nanoparticles. The evolution of silver nanoparticles stabilized by SiO_2 is given by the following dependence (Fig. 5.6):

$$\text{Absorbance}_{450}/\text{time (min)} : 0.6/15, \ 1.0/30, \ 1.5/60 \text{ and } 3.3/210 \qquad (5.1)$$

On comparison with the results obtained without SiO_2, it can be noted that in the presence of silica, the rate of formation of silver particles decreases drastically. It is important to clarify here that this difference is due to the fact that in absence of SiO_2

Fig. 5.6 Time-dependent UV–Visible absorption spectra of silver nanoparticles in formamide in the presence of 1.5 g/dm^3 SiO$_2$: *curve 1* (15 min), *2* (60), and *3* (210) [126]
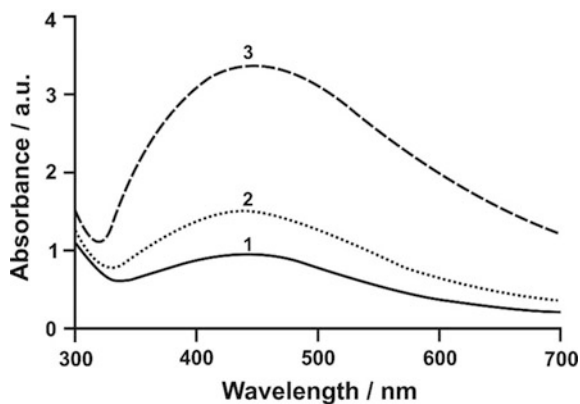
silver particles got deposited on the walls of the container. The particle size (determined by DLS) was around 38 nm for 0.01 mol dm^{-3} AgNO$_3$ solution containing 1.5 g/dm^3 SiO$_2$. The variation in the size of the particles with [Ag$^+$] keeping the amount of SiO$_2$ constant was also determined. It can be noted that as the concentration of Ag$^+$ ions increased the size of the particles decreased. This can be explained by assuming that, to generate small and monodispersed particles, the nucleation and particle growth processes should occur on different timescales [128]. As the rate of evolution of silver particles increases with the concentration of silver ions, it appears that this could be the reason for observing smaller particles at higher concentration of Ag$^+$ ions.

It was noted that the charge on colloidal SiO$_2$ in formamide becomes more negative (−56.7 mV) as compared to that in water (−37.3 mV). The zeta potential, ζ, of colloid particles is sensitive to the inverse Debye screening length (κ) of the medium, which in turn is decided by the ionic strength and dielectric constant of the medium. An increase in dielectric constant decreases the value of κ, thereby increasing the effective potential of the particle at the shear plane. This explains the observed increase in the charge of colloidal SiO$_2$ in formamide as compared to that in water. Due to negative charge on the surface of SiO$_2$ particles, the encounters between the particles are inhibited. This helps in stabilizing small silver particles on its surface.

Microwave-assisted synthesis of different silver nanoparticles to MMT ratios nanocomposite was developed by Kheiralla et al. [129] (Scheme 5.2).

The aqueous AgNO$_3$ solution was contacted with MMT, and then paraformaldehyde citric acid was added. The resulting solution was then placed in a conventional microwave. The obtained AgNPs@MMT powder materials were labeled as 1, 3, and 5% AgNPs@MMT nanocomposites, where 1, 3, and 5 represented the weight ratio of silver metal at MMT. Paraformaldehyde and citric acid are used as stabilizing and reducing agent for synthesizing silver nanoparticles through the reduction in silver ions by the oxidation of hydroxyl groups of paraformaldehyde to aldehyde groups using strong base, NaOH. The addition of
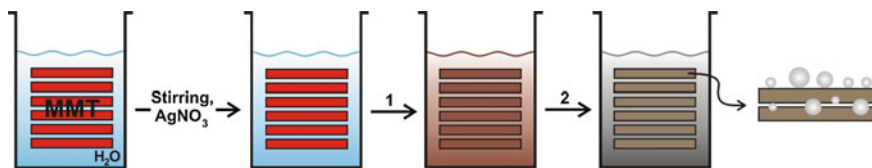
Scheme 5.2 Schematic diagram for the synthesis of AgNPs@MMT nanocomposite, (*1*) paraformaldehyde/NaOH, (*2*) MW/citric acid [129]

silver nitrate to the NaOH solution (Scheme 5.2; Chap. 2, Scheme 2.15) leads to the formation of Ag^+ as $[Ag(H_2O)^4]^+$, which then change to silver oxide (Ag_2O) through the reaction of OH^- ions with Ag^+ ions. A dark cream solution is produced because of the formation of a large amount of silver oxide (Ag_2O) sediment [130]. Paraformaldehyde is deprotonated $[-O(CH_2O)_nH]$, and electrostatic interaction between silver ions and free deprotonated paraformaldehyde shielded the formed nanoparticles and grabbed silver clusters to the nanoparticles. Increasing temperature using microwave in presence of NaOH solution (pH 12) leads to fast hydrolysis paraformaldehyde to oligomers that capped more Ag^+ ions and causes high dispersion on MMT surface. The addition of citric is obligatory because of the removal silver ions by NaOH (redox reaction), which inhibits further reduction reaction of the silver particle surface (Chap. 2, Eqs. 2.2–2.5).

Typical XRD peaks for all samples of trioctahedral subgroup of 2:1 phyllosilicates are observed, which are ascribed to (110), (020), (004), (130), (2 0), (330), and (060) diffractions. The results indicate that the crystalline structure of the clay sheets had not been destroyed after preparation processes, with observed low intensities peak closely matching those of pure silver (reflections at 38.36°, 44.49°, 64.81°, 77.71°, and 81.81°). The Ag peak (111) is indicating that the Ag grains were oriented along the [111] direction, where (111) plane corresponds to the cubic system in the thin films' growth [131]. Despite the intensities of reflections corresponding to the planes in different samples are low, the 5% AgNP@MMT sample shows more reflection intensity indicates more crystallites corresponding to the (111) plane of cubic Ag ($a = 0.4132$ nm). Indeed, the reflection peaks of AgNPs have low intensities owing to their high dispersion on the inner surface of MMT, which is consistent with other report [132]. The crystal grain size (*d*) was estimated from the full width at half-maximum of the Ag (111) peak using the following Scherrer equation. The crystallite size for 1, 3, and 5% AgNPs@MMT nanocomposite samples is found to be in the range of 7.4, 10.7, and 19 nm, respectively.

The FESEM (field emission scanning electron microscopy) morphologies of MMT@AgNPs nanocomposite show MMT as a multilayered material consisting of many parallel arrays of broken plates [133, 134], and the nanomaterials exhibited similar morphologies upon silver functionalization. With increase $AgNO_3$ ratio on MMT, the surface becomes shiny due to the presence of AgNPs, and homogeneous fraction surface was detected during the synthetic processes; $AgNO_3$ is intercalated into the gallery regions of montmorillonite and formed hybrid framework. It can

also be seen that the AgNPs@MMT nanocomposites exhibited card-like and ball-like homogeneous surface fractions and form one-phase morphology. The HRTEM images revealed that the AgNPs are well dispersed on both MMT surface and pores, and the dark region is increased with increasing silver content, which is in good agreement with XRD analysis. MMT is porous material and according to [132], the low intensity of some metal in the porous structure resulted from high diffusion of this metal inside pores. The degree AgNPs dispersion on MMT surface is a function of color intensity and its homogeneity. However, more congregating of the silver nanoparticles is inhibited due to the paraformaldehyde (polyoxymethylene) molecule escaping on the surfaces of the silver particles, then forming a steric hindrance to prevent them from aggregation [135]. Furthermore, the inductively coupled plasma atomic emission spectrometry (ICP-AES) measurements confirmed that the silver nanoparticles have been well distributing in the MMT, as it was observed by TEM.

The UV–Vis absorption spectrum of 1, 3, and 5% AgNPs@MMT nanocomposite is shown in Fig. 5.7. Compared to AgNPs [136], AgNP@MMT exhibit a redshifted peak at 421, 433, and 442 nm for 1, 3, and 5 AgNP@MMT nanocomposites, respectively. This redshift in the absorption spectra reflects a decrease band gap of the semiconductor, which arises from the size quantization effect, and may be caused by the MMT shell [137]. It was reported that the absorption bands correspond to AgNPs smaller than 15 nm were detected at around 404–415 nm [138]. The symmetric absorption peaks indicate surface plasmon resonance of uniform spherical silver nanoparticles [139]. This implies that when the concentration of silver ions was increased, the size increased. This could be due to different nucleation mechanisms operating at lower and higher Ag^+ concentrations attached to MMT at constant ratio of stabilizing agent.

Fig. 5.7 Typical UV–Vis spectrum of the 1–5% (*curves 1, 2,* and *3*) AgNPs@MMT nanocomposites [129]
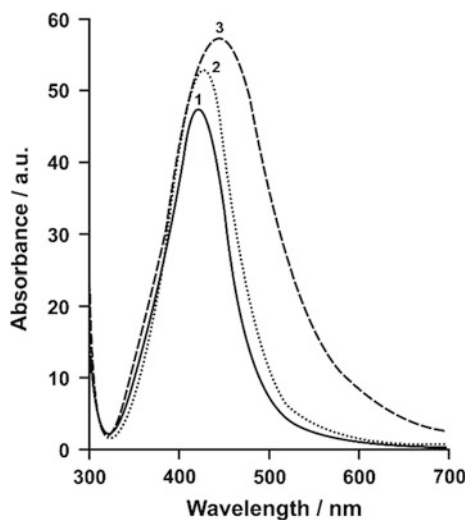
The band at 518 cm^{-1} (FTIR spectra) was observed in the pristine clay, which is attributed to the Al–O–Si (in the octahedral sheets) bending vibration. The band at ≈800 cm^{-1} is associated with δ SiO–H, and the sharp band at ≈1050 cm^{-1} suggests the asymmetric Si–O stretching modes of gallery silica framework and MMT layers [140]. The band at 3640 is assigned to O–H group along with stretching Al–OH [141]. The bands in the 2930–2856 cm^{-1} and band at 1380 cm^{-1} regions, which assigned to the different C–H stretching vibrations of the reducing agent, are almost disappear indicating that these materials have been removed [134]. The broad bands around 3475 cm^{-1} may be attributed to surface silanols group and the adsorbed water molecules, while deformational vibrations of adsorbed water molecules cause band at ≈1640 cm^{-1}. The shoulder at ≈1223 cm^{-1} is due to asymmetric stretching vibrations of Si–O–Si bridges, while the 960–965 cm^{-1} bands are due to Si–O–Ag^{+} vibrations in metal-incorporated silanols [141], and the intensity of these bands is increased with increasing the silver content. Moreover, the high intense band at 3475 and 1625 cm^{-1} due to more of van der Waals interactions between the oxygen groups of MMT and AgNPs [142].

The prepared materials exhibited well-defined hysteresis loops of type H3 with capillary condensation isotherms, which with aggregates of plate-like particles giving rise to slit-shaped pores [143]. A gradual increase in N_2 adsorption at low-to-medium partial pressures (P/P_0 of 0.05–0.25 and >3) suggests that these materials possess supermicropores and mesopores [141]. Moreover, these N_2 sorption isotherms and pore size [Barrett–Joyner–Halenda (BJH)] distributions are similar to MMT. The isotherm hysteresis for AgNPs-MMT nanocomposites extend to very low pressure, which may arise from the irreversible uptake of N_2 in the narrowed channels. These results should mean that the pores of AgNPs-MMT nanocomposites may have been partially clogged by nanosilver molecules. Depending on the loading of the nanosilver molecules, MMT has surface areas of 249 m^2 g^{-1}, pore volumes of 0.342 cm^3 g^{-1}, and the framework pore sizes are of 1.87 nm, decreasing gradually with increasing the concentration of AgNPs in the reactant mixture (5% AgNPs-MMT: 172 m^2 g^{-1}, 0.289 cm^3 g^{-1}, and 1.82 nm). One reasonable explanation is that the increased silver particles result in intensified occupation of the gallery channel space and increase in wall thickness of the pore [144].

Silica−alumina can be used to synthesize silver nanoparticles with precursors like Ag_2O or $AgNO_3$. By coupling MW-plasma with fluidized bed technologies, the precursors could be decomposed and evaporated; the ensuing nanoparticles were spread over the support in a uniform manner. The particles were as small as 3 nm in diameter or as big as 50 nm. They were not oxidized, and the particles were well spread out [145]. Hydrolysis of alkoxysilanes along with the silver salt, in the presence of MW irradiation, can produce Ag/SiO_2 composite sols, which displayed antimicrobial properties [146]. Vongehr et al. [147] reviewed advances in the utilization of various water-based synthesis routes toward the shape-controlled synthesis of silver nanoparticles and microstructures. Several one-pot methods employing commercial MW ovens, inexpensive/low power ultrasound cleaners, or

two-electrode electrochemistry were described. Synthesis of silver nanostructures with various shapes and their doping on unmodified silica proceeded in solution.

Pinchuk et al. have studied the system of silver nanoparticles located in the vicinity of plane metallic (silver or aluminum) and semiconductor (GeSe4) substrates [148]. The experimental dependence of the particle resonance frequency on the distance from the substrate was described using an image-charge model to account for the substrate influence. The silver clusters were deposited on the top of the sample with a small oxide Al_2O_3 gap between the aluminum film and the silver clusters. The thickness of the alumina film was estimated to be as $d \approx 2$ nm [149]. The measured resonance frequency of the absorption band coincides quite well with the theoretical one. Concerning the bandwidth, the agreement between the experimental results and the theory, based on image charges induced at the interface between the aluminum film and the oxide film, was not as good as in the case of the GeSe4 substrate. A possible reason is the topological and stoichiometric irregularity of the thin aluminum film, and its only estimated thickness [150]. The absorption cross section of the light linearly polarized with the electric field parallel to the substrate was numerically simulated. At the distance $d \sim 2r$ (the mean radius of the clusters) between the center of the sphere and the substrate, the influence of the mirror-induced charges vanishes and the resonant absorption approaches the limit of the single sphere in the matrix. When the sphere approaches the substrate $d < 2r$, one observes an increased redshift of the plasmon resonance both for parallel and perpendicular components of the electric field (polarization) of the incident light beam. The amplitude of the absorption is slightly increased when approaching the substrate. The influence of the substrate is more pronounced in the case of the perpendicular field, because the induced dipole field is larger. The frequency shift of the resonance absorption and its increase are less pronounced in the case of a glass substrate as compared to a metallic substrate.

Inorganic glasses provide a solid matrix that stabilizes silver nanoclusters by immobilization, and thus preventing their tendency to aggregate to large nanoparticles. In general, the process to make the silver nanoclusters in a glass consists of two steps. First a Ag^+-doped glass is prepared, either by melting $AgNO_3$ together with the other raw materials, or by immersion of a glass slide in a molten salt bath containing the silver salt, so that Ag^+ replaces Na^+ in an ion-exchange reaction, or by ion implantation. In the second step, the Ag^+-doped glass is activated to form the fluorescent nanoclusters. Activation is achieved by laser irradiation [151], synchrotron irradiation [152], thermal annealing or controlled quenching of the melt [153]. The nanoclusters are reported to be very stable against photobleaching, have short lifetimes, and have a high quantum yield up to 20%. The glass matrix is transparent, and therefore these fluorescent glasses could find applications as optical components in the form of thin films and fibers. Furthermore, direct laser writing on the Ag^+-doped glass enables fabrication of 3D fluorescent structures at the nanometer scale opening up applications in optical data storage and nanophotonics [154]. The recorded images do not photobleach and are claimed to have temperature, aging, and humidity tolerance, making silver cluster glasses suitable as a perennial storage medium over many centuries [154].

5.2.3 Gold Nanoparticles

5.2.3.1 Monolayer Templates

Gold nanoparticles, formed by the reduction of $AuCl_4^-$ with trisodium citrate, are negatively charged because of the adsorption of anions such as citrate, chloride, gold chloride ($AuCl_4^-$), and hydroxide [155]. When aminopropyltrimethoxysilane (APS) monolayers were immersed into the suspension of gold nanoparticles, their top amino groups were protonated since the pKa [156] of amino groups of aminopropyltrimethoxysilane monolayers is smaller than the pH of the suspension. Therefore, negatively charged gold nanoparticles can be assembled on APS monolayers with positively charged amino groups by electrostatic interaction [157]. Using this concept, a binary pattern can be generated with two groups with different affinities for gold nanoparticles. For example, a pattern composed of amino and methyl groups would restrict assembly of gold nanoparticles to predetermined domains of positively charged amino groups [158]. It would even be possible to position single gold nanoparticles by employing scanning probe oxidation (SPO) to produce a pattern of domains each of a size comparable to a single AuNP. However, without careful control of surface properties of oxide domains, low-quality APS films were usually prepared on these domains, which reduced the reproducibility of positioning AuNPs. High-quality APS films on oxide domains, on the other hand, are expected to have gold nanoparticles, with an interparticle distance nearly double that of the particle diameter, homogeneously distributed on the entire surface of these domains. Therefore, for an oxide domain diameter of ~ 70 nm, at least two or three 15-nm-diameter gold nanoparticles (in triangular conformation) would be on top of it; for a 28-nm-diameter domain, it would always have one gold nanoparticle. With only such a saturated coverage of gold nanoparticles realized on oxide domains of different sizes, the precise control of particle number on domains by modulating the domain size could be reproducibly applied.

Using gold nanoparticles for aminopropyltrimethoxysilane labeling, Ling et al. performed detailed investigations on the deposition of APS on silicon oxide domains produced by scanning probe oxidation [159]. APS located preferentially at the domain boundaries possibly because of asymmetrically distributed hydroxyl groups, which led to the incomplete coverage of gold nanoparticles on the domains. To facilitate complete coverage of oxide domains with gold nanoparticles, a homogeneous coverage of silanol on these domains was necessary. To obtain rich content of hydroxyl groups on oxide, instead of separately manipulating the operation parameters for each probe, oxide domains produced under different conditions were simply subjected to etching and oxidation in two stages. This two-step treatment generated uniformly distributed hydroxyl groups on those domains, which led to complete coverage of gold nanoparticles on the domain surfaces.

A possible mechanism for water-mediated deposition of aminopropyltrimethoxysilane (APS) on inert surfaces, such as the above methyl-terminated monolayers, is as follows. First, APS rapidly binds top layers of surface water through hydrogen bonds, such as $-H_2N \cdots HOH$ or $-Si-OH \cdots HOH$. This is followed by further hydrolysis of APS by underlying surface water and condensation to form polymeric siloxane [160]. Because of the increased van der Waals attraction between the methyl-terminated surface and polymeric APS, their removal becomes difficult. For the gold substrate modified sequentially with octanethiol, APS, and Au nanoparticles, no obvious detachment of AuNPs was observed after short sonication. This was only achieved by sonication in water for longer period probably because of hydrolysis and dissolution of polymeric APS during sonication. Removal of APS adsorbed on methyl-terminated surface by sonication in water, however, damaged adsorbed APS on oxide. A strategy, to inhibit APS deposition outside oxide domains by reducing physisorbed water at these regions, only produced good results on high-quality OTS monolayers, which were more resistive to the damage of etching and oxidation. For samples of relatively low-contact angles, possibly indicating the presence of unreacted $Si-OH$ or $Si-OCH_3$ groups on OTS monolayers, a large number of gold nanoparticles adsorbed outside oxide domains. The compact and ordered packing of OTS molecules would be disrupted by these groups, making them more susceptible to etching and acid-catalyzed hydrolysis to produce more $Si-OH$ groups. In OTS monolayers, these reactive groups could form covalent bonds with APS, which would be difficult to remove by sonication without damaging those adsorbed on oxide domains. Such APS molecules would determine the attachment of gold nanoparticles outside of oxide domains.

Min et al. [161] have demonstrated that gold clusters nucleate and grow at defect sites on SiO_2 thin films. Consequently, the nucleation and growth of the gold clusters allow assessment of the defect density and type. Frequently, defects play a key role in the nucleation and growth of metals on oxide surfaces, and in the electronic and chemical properties of metal-oxide systems. Defects on oxide surfaces are usually classified as extended defects (e.g., steps), line defects (e.g., antiphase domain boundaries), and point defects (e.g., oxygen vacancies) [162]. Defects in the SiO_2 film are evident in the scanning tunneling microscopy (STM) images. This STM image shows three distinct regions corresponding to gold coverages of <0.17, 0.17–0.33, and >0.33 monolayer (ML). Up to ~ 0.17 ML, the cluster density is essentially independent of the gold coverage. The cluster density rapidly increases between ~ 0.17 and 0.33 ML, after which the cluster density remains essentially constant. These results suggest that the low coverage region with a constant density of gold clusters correlates with the number of point defects (oxygen vacancies). However, the precise number of neighboring oxygen vacancies required for nucleation and growth of clusters is difficult to assess. According to some results, single oxygen vacancies on TiO_2 bind approximately three gold atoms, whereas larger gold clusters require several oxygen vacancies. According to this model, the number of Au atoms in a 1.4-nm cluster is ~ 20 and would require ~ 7 oxygen vacancies. Thus, the density of Au clusters above 0.1 ML increases and

saturates between 0.3 and 0.6 ML. The increase in cluster density from 0.1 to 0.3 ML indicates that there are nucleation sites in addition to the point defects described above. After reaching saturation, the gold cluster density is essentially constant whereas the average cluster size increases. This suggests that deposited adatoms are captured by existing Au clusters within the saturation coverage range up to 1.3 ML. However, gold clusters do not preferentially decorate step edge sites even during deposition at a high surface temperature. Therefore, point defects with several oxygen vacancies (oxygen vacancy complexes) [163] are more stable for cluster growth than step edges. In addition, as mentioned previously, step edges are more stable sites than line defects for cluster growth. It should be noted that cluster growth related to point defects disappears upon an anneal to 1150–1200 K in an oxygen environment and cluster nucleation changes to decoration of line defects, although oxygen vacancies are still expected to be present. However, most vacancies are single oxygen vacancies and therefore do not play a role as active nucleation and growth sites for Au clusters. These do, however, compete with line defects, which are more stable sites for Au nanoclusters. On the basis of these results, the stability of gold nanoclusters on various defect sites is anticipated to be (from high to low): oxygen vacancy complexes > step edges > line defects > single oxygen vacancies.

5.2.3.2 Core@Shell Structures

Ren and Zhang have described a straightforward sol-gel method for the preparation of gold nanoparticles via in situ-doped silica aerogels using hydroxylamine as a reducing agent [164]. The monolithic gold-doped silica aerogels were comprised of crystalline gold nanoparticles with sizes at the 5–7 nm range. Samples possessed high surface area and pore diameters of about 15 nm. From the UV–Vis spectrum, the absorbance properties of Au^{3+} altered after the addition of hydroxylamine (NH_2OH). An absorbance peak can be observed at 325 nm, which is evidently dependent on reaction time. When the peak disappeared, the reaction was completed, thus, the gold ion concentration in the system gradually decreased until Au^{3+} ions no longer existed in the system. In the system, NH_2OH was thermodynamically capable of reducing Au^{3+} to bulk metal, and the reaction was dramatically accelerated by gold surfaces. This process is referred to as a self-catalyzed reaction [165]:

$$Au^{3+} + NH_2OH + H^+ - \text{the catalyzed surface} \rightarrow Au^0 + N_2 + H_2O \qquad (5.2)$$
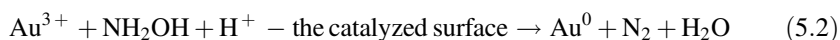
Zhang et al. [166] have used a simplified method [167] to prepare SiO_2@Au (core@shell) composite nanoparticles. Firstly, silica microspheres were prepared and then functionalized with the silane-coupling agent. Secondly, hydrochloroauric acid was reduced to gold nanoparticles with sodium citrate in the presence of the functionalized silica microspheres. By contrast with the general three-step method, the procedure was simplified, the reaction time was remarkably shortened, and the

gold coverage on silica microspheres was denser. The general three-step method to prepare the SiO_2@Au composite nanoparticles is shown in Scheme 5.3. The SEM images revealed the morphologies of the SiO_2@Au composite nanoparticles, which showed distinctly that AuNPs were attached to the surfaces of the functionalized silica microspheres (Fig. 5.8). At lower pH values, sparse AuNPs were distributed on the functionalized silica microspheres. As the pH values were adjusted to lower levels gradually under acidic condition, the Au coverage was decreased correspondingly. Especially when the pH value of the treatment solution fell to around 4, very few AuNPs were attached onto the functionalized silica microspheres. Under basic condition (pH > 7), a denser gold coverage was achieved on silica microspheres. As the pH values were adjusted to higher levels gradually under basic condition, the gold coverage was increased correspondingly. Obviously, the coverage of AuNPs achieved under basic condition was denser than that under acidic condition. Moreover, the atomic absorption spectrometry (AAS) measurement revealed that the sample prepared at 3.8 contained 5.2 wt% Au, while the sample at 10.2 contained 8.8 wt% Au. This result was consistent with the above qualitative analysis. It indicated that for the three-step method, the SiO_2@Au composite nanoparticles achieved a denser Au coverage on silica microspheres under basic condition than that under acidic condition. AuNPs were attached to surfaces of the functionalized silica microspheres through the coordination bonds between empty orbits of gold atoms and lone-pair electrons of nitrogen atoms. Under acidic
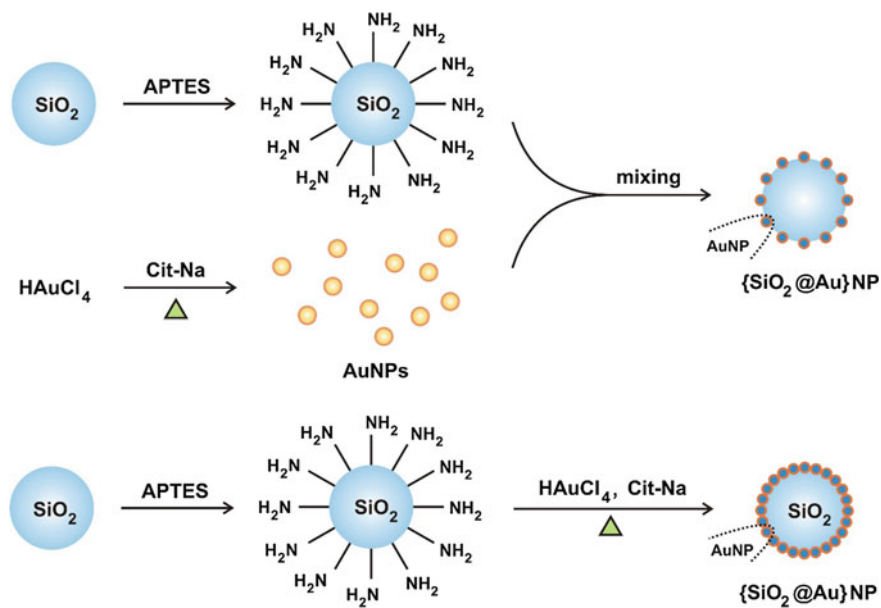
Scheme 5.3 Schematic illustration of the deposition of AuNPs onto silica microspheres by three-step (I) (*top panel*) and simplified (II) (*bottom panel*) methods [166]
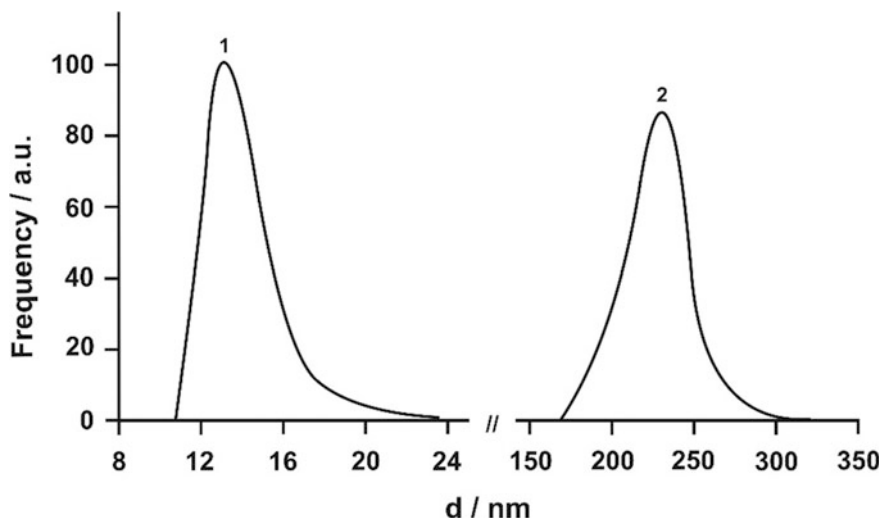
Fig. 5.8 Histograms for the size distribution of AuNPs (*1*) and silica microspheres (*2*) [166]

condition, most of the amino groups on surfaces of silica microspheres were probably bound with protons so that the Au–N coordinating interaction was broken.

The UV–Vis spectra of the pure AuNPs reduced by sodium citrate exhibited a plasmon absorption peak at 530 nm (Fig. 5.9, left panel). The absorption peak of the $\{SiO_2@Au\}$NPs structures obtained at higher pH values had a redshift of about 10 nm relative to that of the pure AuNPs. The redshift could be induced by the transfer of most of AuNPs from the solution to surfaces of the functionalized silica microspheres. The absorption peak of $\{SiO_2@Au\}$NPs structure obtained at lower pH values had little shift relative to that of the pure AuNPs, which was because few AuNPs were attached to surfaces of silica microspheres, and most were still dispersed in the solution. The results of UV–Vis spectra were in agreement with the Au coverage shown in the SEM images. In addition, the indented shapes of the absorption peaks were possibly due to the existence of silica microspheres.

The TEM characterization had given us a clearer image that most of the functionalized silica microspheres were covered with a dense gold layer when the pH value was adjusted to 3.85 (Scheme 5.4). But the amount of the attached AuNPs decreased to a much lower level as the pH value was adjusted to nearly 9. Furthermore, the results of AAS measurement showed us that the higher gold content of 12.6 wt% was gained in the sample at 3.8, and the lower Au content of 10.6 wt% in the sample at 8.9. This result was in agreement with that of SEM observation.

The results revealed that the lower pH values led to a denser gold layer on silica microspheres, while the higher pH values led to a lower gold coverage. Under acidic condition, most of the amino groups on the surfaces of silica microspheres were probably bound with protons originally. However, this binding might be
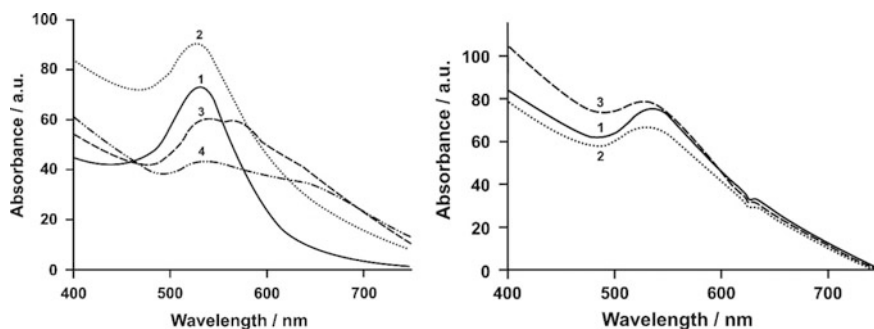
Fig. 5.9 UV–Vis spectra of pure AuNPs (*curve 1*), SiO$_2$@Au composite nanoparticles [*curve 2* (pH 3.8), 3 (7.8), and 4 (10.2)] prepared by the first method (I) (*left panel*) and SiO$_2$@Au nanoparticles [*curve 1* (pH 3.8), 2 (7.9), and 3 (8.9)] prepared by the simplified method (II) with various pH values (*right panel*) [166]

Scheme 5.4 TEM image of SiO$_2$@Au composite nanoparticles II at the pH value of 3.85 [166]
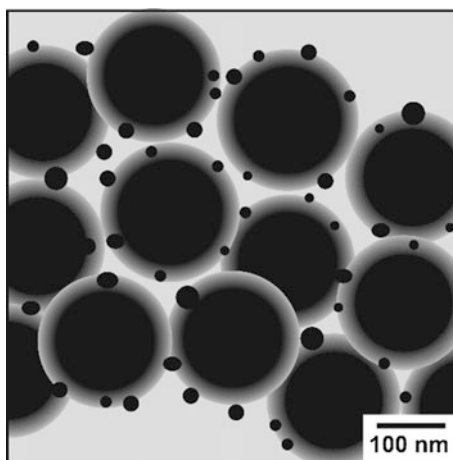
reduced greatly in the following step of heating the mixture of silica microspheres and HAuCl$_4$ to reflux. Thus, it was not the major factor for the effect of the pH values on the gold coverage any longer. This phenomenon for the pH effect could be accounted for qualitatively by the pH values of the treatment solutions relative to the isoelectric points of silica microspheres and AuNPs. The reported values of the isoelectric point were around 2 for SiO$_2$, and about 6 for AuNPs [168]. It indicated that the silica surfaces were negatively charged, respectively, at pH 3.8, 4.8, and 5.4, while AuNPs synthesized by citrate reduction had a positive surface charge. Apparently, AuNPs experienced a significant electrostatic attraction to the silica surfaces with negative charge. Thus, most of AuNPs were deposited by this electrostatic attraction on silica microspheres as soon as they were formed. As the pH value of the treatment solution was increased over 7, the electrostatic attraction

referred above was remarkably lowered. Furthermore, the reduction of $AuCl_4$ ions to AuNPs could not be carried out completely at higher pH values (pH > 7). As a result, a relatively smaller amount of AuNPs were attached.

The spectra of the results obtained at lower pH values all exhibited a plasmon absorption peak at 538 nm, having a redshift relative to that of the pure AuNPs [Fig. 5.9, prepared by the simplified method (II)]. It could be due to the transfer of most of AuNPs from the solution to the surfaces of the functionalized silica microspheres. The spectra of the results obtained at higher pH values exhibited a plasmon absorption peak at 529 nm, having no distinct shift. The reason could be that few AuNPs were attached to the surfaces of the functionalized silica microspheres.

The SiO_2@Au composite nanoparticles, prepared by simple mixing AuNPs with the functionalized silica microspheres at room temperature, were transferred into the aqueous solution of $HAuCl_4$, and the mixture was heated to react with a certain reductant. The final products achieved an evidently denser Au coverage than the original SiO_2@Au composite nanoparticles prepared at room temperature. Moreover, the TEM image obviously revealed that the SiO_2@Au composite nanoparticles prepared using formaldehyde as the reductant achieved a denser Au layer on the functionalized silica microspheres. In this method, three reductants had been used: sodium citrate, formaldehyde, and sodium hypophosphite. The SiO_2@Au composite nanoparticles prepared at room temperature had a low Au coverage. The Au coverage was improved as the further reduction of $AuCl_4$ ions was carried out with any of the three reductants. The improvement of the Au coverage was partly supported as the Au content was measured for 15.7 wt% in the sample using formaldehyde as the reductant, which was apparently higher than that in the sample prepared by the three-step method. The major reason was based on the seeded growth. The whole reaction consisted of two parts. In the first part where the three-step method was used, AuNPs were tethered on the functionalized silica microspheres by virtue of the aminophilic nature of AuNPs. In the second part where the simplified method was used, the pre-attached AuNPs were used as seeds immobilized on silica microspheres, which provided more nucleation sites for the growth of an Au layer. Obviously, these growing seeds played a role as the link between the silica cores and the freshly formed AuNPs during this process. Another possible reason was the formation of the hydrogen bonds. In the first part of the reaction, the hydrogen bonds could be formed in the solution, which consumed many amino groups on silica microspheres and caused a low coverage of AuNPs. But in the second part, the hydrogen bonds had the possibility to be broken under the higher temperature (100 °C). Thus, the consumed amino groups could be reformed on silica microspheres, which could be coupled with freshly formed AuNPs. The final Au coverage on silica microspheres was enhanced.

The prepared SiO_2@Au composite nanoparticles using various reductants exhibited the plasmon absorption peaks at 551 nm for sodium citrate, 551 nm for formaldehyde, and 548 nm for sodium hypophosphite (Fig. 5.10). They all had a little blueshift compared with the absorption peak of the SiO_2@Au composite particles prepared at room temperature (Fig. 5.10, curve 1). It could be caused by
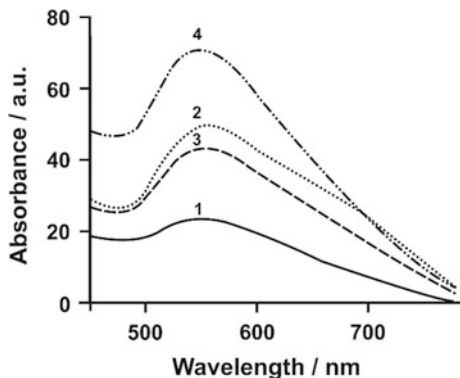
the increase of the Au coverage after further reduction of HAuCl$_4$. Furthermore, the
position and shape of the plasmon absorption of silver nanoparticles are strongly
dependent on the particle size, dielectric medium, and surface-adsorbed species.

Mercapto-functionalized ordered mesoporous silica with pore sizes ranging from
2.1/2.1 to 7.2/5.9 nm (adsorption/desorption branch) are used as matrixes for gest
noble metal nanoparticles [169]. The silica materials are prepared following the
direct synthesis method, which consists of processing by the sol-gel method a
solution of 3-mercaptopropyltrimethoxysilane (MPTMS) with tetraethyl orthosili-
cate (TEOS) in the presence of a surfactant. These materials were prepared by the
cocondensation route of MPTMS with z equivalents of TEOS in the presence of a
structure-directing agent: n-hexadecylamine for HS-HMS-C16 materials 1 ($z = 41$)
and 2 ($z = 19$), and pluronic 123 for HS-SBA-15 materials 3 ($z = 19$) and 4 ($z = 9$)
according to following reaction:

$$HS(CH_2)_3Si(OMe)_3 + z\,Si(OEt)_4 - surfactant \rightarrow HS(CH_2)_3SiO_{1.5}/zSiO_2 \quad (5.3)$$
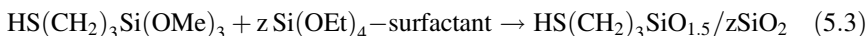
As the composition of the final materials is directly linked to the amount of
reactants introduced, this direct synthesis method of functionalization of ordered
mesoporous silica allows a strict control of the organic content incorporated within
the hybrid material. Furthermore, by increasing the amount of organic content, a
decrease in the pore size is obtained from 7.2/5.9 (adsorption/desorption branch) for
3 to 5.3/4.6 for 4. The gold precursor (HAuCl$_4$) was stirred in the presence of
material 4 and NaBH$_4$ to allow complete diffusion within the channels before
isolation of material. All the materials exhibited intense plasmon band absorbance
at 520 nm, indicative of gold (0) nanoparticles. The XRD pattern of gold samples
displayed for the high-angle region ($2\theta = 20$–70) broad reflections characteristic of
gold (0) nanoparticles.

For the materials ([Au]/[SR] = 0.2), the gold (0) nanoparticles size derived from
TEM measurements are in good agreement with the pore size values obtained from
BET measurements whatever the method followed (Fig. 5.11). TEM photographs
clearly show a single distribution even for [A1, 0.2] and [A2, 0.2] materials

Fig. 5.11 Correlation between the pore diameter (*dotted* (*curve 2*)/*dashed* (*3*) *lines* for adsorption/desorption data from N_2 studies) and the gold nanoparticles size (*1*) for [A4, 0.2] (variations of pore surface (Pore$_{surf}$) /number of nanoparticles (N_{NPs}) with pore diameter) [169]
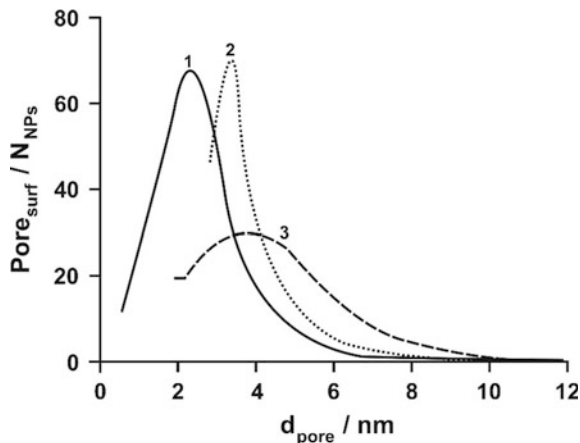
obtained, respectively, from 1 and 2 following method A (in water suspension). However, in both cases, the large size distribution observed results from the modification of the silica matrix during the first step of the process. A narrower size distribution was obtained for the gold (0) nanoparticles included in materials, [A3,0.2], [A4, 0.2], and [B3, 0.2], whatever the method adopted (B in THF suspension). For [Au]/[SR] = 2, the excess of organogold precursor, which could not be stabilized by the thiol functions, gave rise to the formation of nanoparticles at the surface of the grains in large quantities. This is consistent with the necessity of the complexation of the organogold precursor onto the thiol function prior to chemical reduction in order to control the size distribution of the as-obtained nanoparticles. Furthermore, these thiol functions interact strongly with the gold nanoparticle surface, which retains the nanoparticles within the pores.

Material containing 16.1 wt% of gold as given by elemental analysis displays a high density of nanoparticles located exclusively within the channels of the mesoporous material, as showed TEM measurements. Following this method, the amount of organic functions incorporated, which plays a crucial role in the process leading to gold (0) nanoparticles containing materials with a narrow size distribution, can be finely tuned from 0.49 to 1.57 Mmol g^{-1}. The amount of gold incorporated within the materials is linked to the amount of mercapto functions and varies from 1.05 to 16.1 wt%.

5.2.3.3 Interior Templates

Cheng et al. [170] have successfully applied the convenient nonsurfactant-templating approach to the synthesis of mesoporous gold–silica nanocomposites. Instead of using a postdiffusion process, monolithic gold–silica nanocomposites were synthesized through a one-step sol-gel reaction in the presence of a colloidal gold sol and a nonsurfactant template in the starting precursor sol mixtures. After

the template was removed through calcinations, the materials exhibited meso-porosity with a high surface area up to 600 m^2/g, a pore volume of 0.5 cm^3/g, and relatively narrow pore size distributions with a pore diameter of 3–4 nm. Gold nanoparticles ranging in diameters of 2–8 nm were homogeneously dispersed throughout the silica matrix [41]. The gold–silica composites are nanoscopic materials in which the optical and physical/chemical properties of gold nanoparti-cles are coupled with the high surface area and the high porosity of the silica framework.

With the gold content at 10.1 wt% or lower, the pore structures of the composite samples are comparable to the control sample in the absence of gold. These materials exhibit mesoporosity with a pore diameter of 3–4 nm, a high Brunauer–Emmett–Teller (BET) surface area up to 630 m^2/g, and a large pore volume of ~ 0.5 cm^3/g. It should be noted that, with the gold content as low as 6.9 wt%, the composite sample (i.e., GS50-10: 50 wt% DBTA template containing 10 wt% gold sol) shows a higher BET surface area than the gold-free control sample (i.e., GS50-0). During the sol-gel process, the organic moieties in the starting liquid gold sol might be trapped in the gold–silica matrix and may function as "cotemplates" with dibenzoyl tartaric acid (DBTA). As the gold concentration is further increased, the BET surface area of the composite samples tends to decrease. When the gold content is increased to 11.4 wt%, the pore diameter remains at 3.5 nm. However, the surface area decreases to ~ 210 m^2/g, and a smaller value of pore volume (~ 0.17 cm^3/g) was observed. There could be several factors that might contribute to the observed decrease in the specific area and pore volume. First of all, more gold nanoparticles should result in smaller specific area and pore volume because of the physical occupation of the internal space by the gold particles. The gold particle size is slightly greater than the pore size, indicating that in some area the gold particles could have partially extruded into the pore walls made of relatively "soft" amorphous sol-gel silica. In such a case, the pore or channel in the silica matrix would be blocked and become inaccessible to the pore volume and surface area measurement. This should also contribute significantly to the observed low pore volume and specific area in the samples with high gold loadings. In addition, the presence of gold may also affect the interactions, for example, hydrogen bonding, between the nonsurfactant template (i.e., DBTA) and silicate species during the mesophase formation, which could result in modified pore parameters. Furthermore, it is possible that the introduction of gold into the silica matrix also brings complexities in porosity measurement with nitrogen sorptions, among which electrostatic forces between an adsorbate (i.e., nitrogen) and metallic surface and increased material density may affect the measured values to some extent.

In all, with the introduction of gold sol, there simultaneously exist two factors affecting, in an opposite way, the porosity of the composite materials. One results from cotemplates, which increase the total pore surface area. The other factor is "the presence of gold" that reduces the surface area. The outcome depends on the compromise of these two factors: At low gold content, the pore surface area reduced by the gold coating is compensated, or even overcome, by the cotemplating effect. As a result, the composite materials persist in a relatively high surface area and pore

volume. While as the gold content increases, the cotemplate effect gradually becomes negligible, giving rise to decreased surface area.

All the mesoporous gold–silica samples exhibit a similar powder XRD profile. The XRD pattern shows an intense peak at a d-spacing of 6.3 nm along with a broad shoulder at low-angle range. A broad diffraction peak centered at 2θ of $21°$ was observed at high-angle range. This pattern is characteristic of a mesoporous structure lacking a long-range order, which is reminiscent of the disordered wormhole-like mesoporous silicas prepared by a nonsurfactant-templating pathway [41].

The analogous XRD patterns were also observed from some mesoporous materials obtained with neutral and cationic surfactant templates [171]. In the wormhole-like porous structure, d-spacing obtained from XRD could be approximately the repeating distance from one layer of silica wall to the next layer of silica wall crossing a mesopore space. From the difference of the repeating distance (6.3 nm) and the average pore diameter (3.0 nm), the thickness of pore wall can be estimated to be ~ 3.3 nm, which is comparable with those of the mesoporous materials prepared by a nonionic surfactant-templating route [172] or cationic surfactant-templated multiprecursors sol-gel method [171]. The presence of a single broad peak centered at a 2θ value of $21°$ is attributed to the amorphous structure of sol-gel silica [40].

The annealed gold–silica nanocomposites retain a distinctive wine-red color, which arises from the surface plasmon resonance of gold particles. SPR is characteristic of mesoscale (2–50 nm) particle surfaces because, at this dimension, the electron cloud can oscillate on the particle surfaces and absorb electromagnetic radiation at a particular level of energy [173]. However, smaller nanoparticles (<1–2 nm) do not display this phenomenon because their electrons exist in discrete energy levels, and bulk gold has a continuous absorbance in the UV–Vis–IR region. The UV–Visible spectra of as-synthesized composite samples show broad plasmon absorbance peaks at around 520 nm with full width at half-maximum of 160 nm. The peak position and the shape are not significantly affected by the gold concentration. The absorption maxima obtained in this work are comparable with reported spectra of nanosized gold particles dispersed in silica aerogel prepared with other methods [174]. Though dominated by the particle size, the exact wavelength and shape of the plasmon absorbance maximum are also known to be affected by particle shape, orientation, and the environment [175]. Therefore, the presence of such a well-defined plasmon absorption not only reveals the size scale of gold particles in the nanocomposites but also contributes to some other morphological information: The colloidal gold particles in the composites are more likely to be confined in the pore cages, or if coforming the pore wall with silica, they are more likely to be exposed to the pore surface rather than embedded in the silica matrixes [174].

Surface area, average pore size, and pore volume were determined for silica aerogels and gold-doped silica aerogels [164]. The nitrogen adsorption–desorption isotherm is classified as type IV with desorption branch hysteresis, which reveals that the gold-doped silica aerogel is a typical mesoporous material. BET surface

areas of gold-doped silica aerogels, derived from their isotherm, are <850 m^2/g, as opposed to 10^{10} m^2/g for the silica aerogel. These results are consistent with the current understanding that gold nanoparticles are adhered to the inner surface of silica, which leads to the decrease of BET surface. All samples possess the approximate average pore diameters (16.1 nm for silica aerogel; 14.3, 15.2, and 17.1 nm for gold-doped silica aerogels). However, the doped gold influenced the pore volumes of the aerogels. Typically, the pore volume of silica aerogel is 4.09 cm^3/g. In contrast, the gold-doped samples only exhibited pore volumes of <3.5 cm^3/g. It may be that the gold nanoparticles were locked into the pores of the silica aerogel. The presence of gold nanoparticles in the aerogel induced shrinkage of the silica matrix.

The spherical silica nanoparticles were used as the templates of interior cores of metal nanoshells. Three kinds of metal–ligand complexes, Ru(Phen-NH$_2$)$_3^{2+}$, Ru (bpy)$_3^{2+}$, and Ru(dpp)$_3^{2+}$, were absorbed in silica for fluorescence purposes, which was shown by the color of formed silica spheres, although the absorbance spectra could be determined because of their strong light scattering. According to the changes in complex concentrations in solution before and after reactions, it was estimated that there were ca. 5×10^{-4} M Ru(Phen-NH$_2$)$_3^{2+}$, 4×10^{-4} M Ru(bpy)$_3^{2+}$, and 3×10^{-4} M Ru(dpp)$_3^{2+}$ complexes in the silica spheres. According to the TEM images, the silica spheres were observed to have an average diameter of 40 nm. Per silica sphere thus was estimated to contain approximately 150 Ru(Phen-NH$_2$)$_3^{2+}$, 120 Ru(bpy)$_3^{2+}$, or 90 Ru(dpp)$_3^{2+}$ complexes. These Ru(II) complexes were strongly absorbed in the silica spheres, and no significant release was observed during store or reaction [176]. The silica spheres were used as the interior temples for the deposition of the external noble metal shell layer by layer [176, 177]. On the TEM images, the silver shells that were built on three kinds of silica spheres were observed to have similar sizes of 60 nm. The silica spheres are known to have an average diameter of 40 nm. The metal shells thus were estimated to be approximately 10 nm thick. These silver nanoshells also had homogeneous size distributions [178]. Their absorbance spectra showed almost the same plasmon resonances at 430 nm. Upon excitation at 450 nm, the Ru(Phen-NH$_2$)$_3^{2+}$-Ag, Ru-(bpy)$_3^{2+}$-Ag, and Ru(dpp)$_3^{2+}$-Ag nanoshells displayed the emission maxima at 596, 605, and 608 nm, respectively, close to the emission maxima of free Ru(II) complexes or silica spheres. Similar excitation and emission maxima of three metal nanoshells may promise that their emission signals can be detected in a single imaging test when they are bound with multiple target molecules in the cells.

To increase the chemical stability of as-prepared metal nanoshells in buffer solution, they were capped with the monolayers of glycol-like organic ligand [179]. The metal nanoshells were partially substituted with the carboxylate-terminal ligands and subsequently bound with the avidin molecules in the presence of an excess amount of EDC in solution [180]. To verify the occurrence of binding and determine the binding number, the silica spheres without the Ru(II) complexes were also made and the metal shells were deposited in the same manner. Under the same conditions, the Rhodamine 6G-avidin conjugates were covalently bound on the metal nanoshells without fluorescence as the control [181]. The concentration of

metal nanoshell was determined by the intensity of plasmon resonance before metal dissolution, and the concentration of the avidin conjugate was determined by the emission intensity after metal dissolution. The binding number on per metal nanoshell thus was estimated by the molar ratio of avidin conjugate over metal nanoshell, which was 6.4 in this case. With the same reaction conditions, the Ru(II) complex-Ag nanoshells were regarded to have approximately similar binding numbers.

Representative intensity/lifetime emission images showed that the avidin-Ag complexes were much brighter than the metal-free silica spheres. The lifetimes of Ru(II) complexes in silica were also observed to be shortened by the metal shells. Compared with the silica spheres, the avidin–silver complexes showed approximately sixfold enhancements on the emission intensities almost independent of Ru (II) complexes (Fig. 5.12). On the contrary, even though all lifetimes of Ru(II) complexes were dramatically shortened by the metal shells, the scales of decrease were variable depending on the Ru(II) complexes. The lifetime of Ru(Phen-NH$_2$)$_3^{2+}$-Ag shells was shortened from 100 to 10 ns, a tenfold decrease, and the lifetime of Ru(bpy)$_3^{2+}$-Ag shells was shortened from 600 to 45 ns, a 13-fold decrease (Fig. 5.13). According to the literature, the lifetime of Ru(dpp)$_3^{2+}$ in aqueous solution is over 3 μs [182–184]. As immobilized in silica, the lifetime should be increased. Even though the lifetime of 3 μs was used as the Ru(dpp)$_3^{2+}$ in silica, there was an approximately 17-fold decrease when the lifetime of Ru(dpp)$_3^{2+}$-Ag complexes was determined to be 180 ns. Thus, we can conclude that a longer lifetime complex may result in a greater decrease of the lifetime by the metal shell. Enhanced emission intensity is regarded from the coupling interaction of the fluorophore with the plasmon resonance of the metal nanoparticle on excitation and emission. Three Ru(II) complexes are known to have close excitation and emission maxima, and the plasmon resonances from three metal nanoshells are also found to have similar maxima. Consequently, three Ru(II) complexes should have similar coupling interactions with the metal shells, resulting in close enhancement efficiencies on the emission intensity. In contrast, a decreased lifetime by the metal nanoshell results in an increase of the radiative rate of the fluorophore [185, 186]. It is a dynamic process and thus is relevant to the lifetime of the fluorophore prior to binding with the metal. Consequently, the change in lifetime for the fluorescence metal nanoshells cannot be completely consistent with that on the emission intensity.

5.2.3.4   Composites

Mesoporous carbon-supported gold nanoparticles have been obtained by replication of gold-containing mesoporous silicas [188]. Mesoporous silica is a mesoporous form of silica. The most common types of mesoporous nanoparticles are MCM-41 and SBA-15. Au/SiO$_2$ templates were prepared by contacting a functionalized SBA-15 silica material with an aqueous solution of HAuCl$_4$, followed by chemical reduction (Scheme 5.5). Alkylammonium grafts led to the direct formation of gold
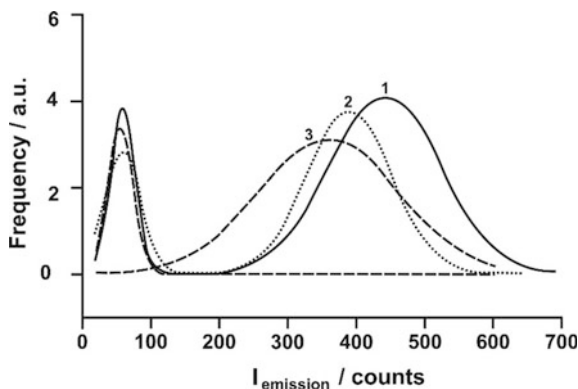
Fig. 5.12 Histograms of emission intensities (I_{emission}) from (*curve 1*) Ru(Phen-NH$_2$)$_3^{2+}$/silica sphere and Ru(Phen-NH$_2$)$_3^{2+}$-Ag shell, (2) Ru-(bpy)$_3^{2+}$/silica sphere and Ru(bpy)$_3^{2+}$-Ag shell, and (*3*) Ru-(dpp)$_3^{2+}$/silica sphere and Ru(dpp)$_3^{2+}$-Ag shell [187]
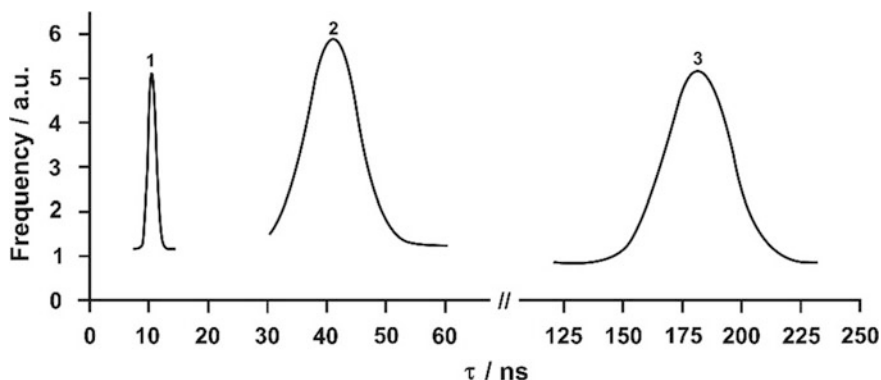
Fig. 5.13 Histograms of lifetimes from (*curve 1*) Ru(Phen-NH$_2$)$_3^{2+}$-Ag shells, (2) Ru(bpy)$_3^{2+}$-Ag shells, and (*3*) Ru(dpp)$_3^{2+}$-Ag shells that were collected from the single nanoprobe images [187]

nanoparticles located in the pores of SBA-15, with a size limited by the pore opening. Thus, gold-containing mesostructured carbons by replication of gold-supported mesoporous silicas were prepared. The strategy consists in a functionalization of SBA-15 followed by addition of a cationic gold precursor HAuCl$_4$ and in situ reduction with sodium borohydride to form gold particles inside the porosity. The XRD pattern of the template (SBA-15) is characteristic of silicas with regular mesopores arranged in a 2D hexagonal structure. The physical confinement is expected to limit the growth of the gold particles at this stage, to a uniform size defined by the size of the pore. After impregnation with sucrose, the composite material is carbonized at high temperature and silica is finally removed in HF (Scheme 5.5). Control of the particle size is expected from sterical hindrance by the forming carbon.
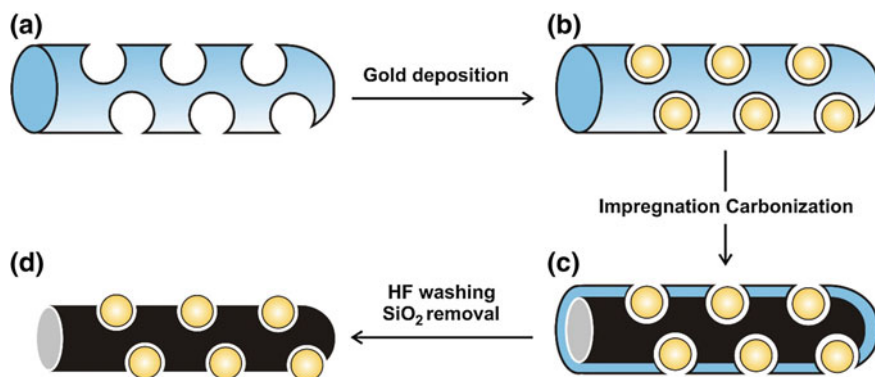
Scheme 5.5 Elemental steps for the preparation of gold-containing ordered mesoporous carbons, **a** functionalized silica, **b** AuNPs inside silica pores, **c** carbon-impregnated silica, and **d** mesoporous carbon with partially encapsulated particles [188]

Two series of Au/SiO$_2$ templates were prepared and used, depending on the nature of the functionalization molecule. While ammonium-functionalized silicas gave gold rod particles with size determined by the pores of the silica support, the use of MPTMS as grafting molecule afforded the possibility to control the particle size inside the mesopores. Both series gave highly ordered mesoporous carbons with gold nanoparticles incorporated in the carbon nanorods. However, the gold particle size in mesoporous carbons was the same for both series and apparently did not depend on the nature of the silica template. By contrast, chemical reduction of MPTMS-modified silicas by NaBH$_4$ and sodium citrate was not sufficient to reduce completely gold species in the metallic state. Gold nanoparticles were only formed after heating the solids in air, and the particle size could be controlled by temperature. Ordered mesoporous carbons obtained by replication of these gold-containing SBA-15 samples incorporate small gold particles with an average size independent of the template and determined only by the porosity of the silica support. It was assumed that very small gold particles melt down and form larger aggregates in the mesopores prior to complete carbonization of sucrose. After carbonization, the presence of carbon in the silica pores provided gold particles with a very high thermal stability, since no large crystals were observed on the outer surface even after heating at 900 °C under inert atmosphere. Gold-containing mesoporous carbons show less activity in the aerobic oxidation of olefins than the corresponding silica-supported catalysts. Besides a difference in mean particle size, hence lower dispersion of gold in mesoporous carbons, the low activity of replicas could also result from the confinement of gold particles in carbon nanorods, which limits their accessibility to reactants.

The use of task-specific ligands with calcining as post-treatment provides AuNPs that are encapsulated into the mesoporous channels or loaded on the surface of silica spheres [189, 190]. For example, Corma's group [191] showed that task-specific ligands containing a cetylammonium moiety act as structure-directing
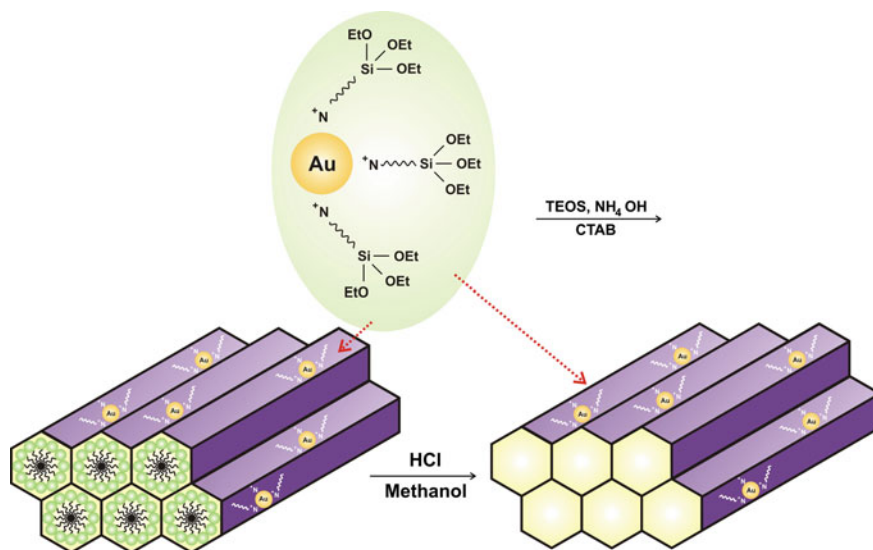
Scheme 5.6 Synthesis of AuNPs encapsulated in mesoporous silica [191, 192]

agent with AuNPs containing a trialkoxysilyl group. The latter cocondenses with TEOS to form mesoporous silica (Scheme 5.6). In another recent example [191], NH_2 and –NH functionalized mesoporous carbon nitride (MCN) was shown to stabilize AuNPs. The synthesis involved the reduction of $AuCl_4$ by $NaBH_4$ in water suspension in the presence of MCN.

Besides task-specific ligands, the AuNPs are also coated with polymers and then encapsulated by mesoporous materials as core@shell AuNPs. For instance, according to Jan et al. [193], a preparation of AuNP/mesoporous silica tubular nanostructures proceeded with some polymers. Poly(L-lysine) (PLL) and poly(L-glutamic acid) (PLGA) multilayer-coated membranes could be immersed in a $HAuCl_4$ solution to form AuNP/PLL/PLGA multilayers. Subsequently, the membranes were taken out from the solution and inserted in a freshly prepared orthosilicic acid solution for 6–12 h, to allow precipitation of silica in this multilayer. After thoroughly rinsing with water and drying at room temperature, the as-prepared AuNP/meso-SiO_2/PLL/PLGA multilayer was obtained and purified by calcination (Scheme 5.7).

5.2.3.5 Re-shaping

Citrate-capped gold zero-dimensional (0D) nanoparticles 1 (3–5 nm average diameter) were attached to the p-type Si(100) substrate modified by (aminopropyl) triethoxysilane (APTES), dicyclohexylcarbodiimide (DCC), and dimethylamino pyridine (DMAP) to unreacted amine groups through electrostatic or Au–NH_2
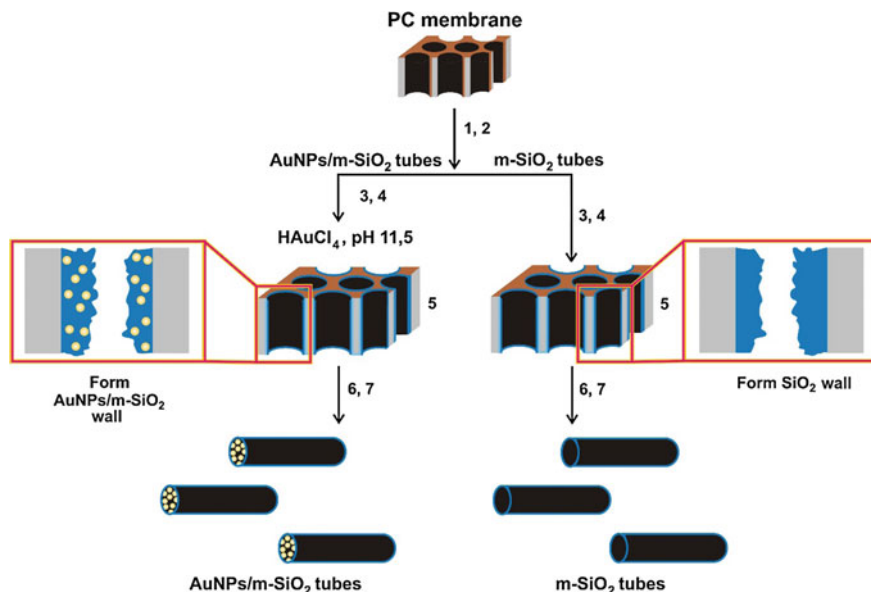
Scheme 5.7 Procedure used for preparing mesoporous silica and AuNP/meso-silica tubes consists of following steps: (*1*) PLL, (*2*) PLGA, (*3*) orthosilicic acid, (*4*) remove surface coating, (*5*) silicified (PLL/PLGA)$_n$-coated PC membrane, (*6*) remove PC membrane, (*7*) remove polypeptides [192, 193]

interactions [194, 195]. The substrate was then placed into a growth solution of CTAB, AuCl$_4^-$, and ascorbic acid [196, 197]. This step [196] leads to the growth of surface-bound AuSNP seeds into AuNRs via seed-mediated growth (Scheme 5.8).

Gold nanostructures grown on a Si(100)/APTES surface imaged by SEM showed that the surface was not functionalized with acetic acid. The surface exhibits a high density of gold nanoparticles (175 μm^2) with just a very few unaligned short rods on the surface. Gold nanorods were observed to grow on a Si(100)
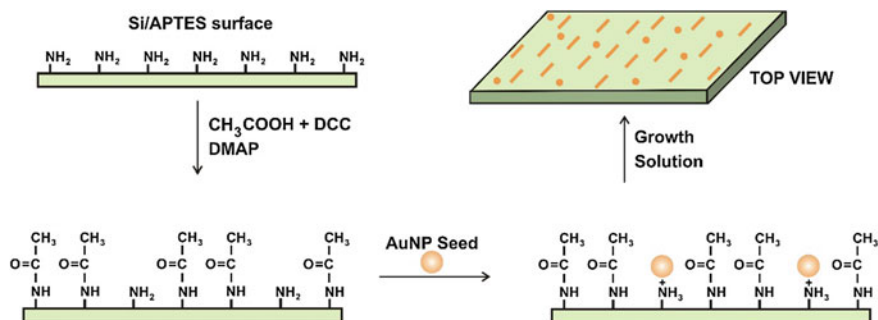
Scheme 5.8 Method for growing aligned AuNRs [194]

surface functionalized with mercaptopropyltrimethoxysilane (MPTMS) [198, 199]. The surface contains a lower overall density of gold nanostructures (18 μm^2) compared to Si(100)/APTES and high aspect ratio AuNRs exhibiting no particular alignment. AuNRs were also produced on Si(100)/APTES functionalized with acetic acid as in Scheme 5.8. These surfaces show a more reduced nanostructure density on the surface (3 μm^2), and more importantly, the nanorods show an incredible propensity for parallel alignment to one another. The yield of AuNRs is ∼19%, the diameter is 25–30 nm, and the average length is ca. 580 nm (AR ∼ 20) [194].

Surface functionality on alignment by growing AuNRs on Si(100)/APTES samples reacted with succinic acid, which terminates the surface with COOH instead of CH$_3$ groups. The SEM image shows that this also leads to AuNR alignment. The SEM image shows that AgNRs grown on Si(100)/APTES/acetic acid surfaces using a similar seed-mediated growth procedure [200] are also aligned (∼60%), but not to the extent of AuNRs. The fact that alignment is not observed on MPTMS, and APTES-functionalized or bare Si(100) shows that surface chemistry plays a major role, but it is not clear how the amidation reaction leads to alignment. The aspect ratio of AuNRs can be controlled not only during synthesis but also by resizing after growth. Size reduction of AuNRs has been demonstrated with thermal/laser heating [201] and cyanide/Au(III) dissolution [202].

Roorda et al. [203] have showed that polycrystalline gold colloids can be deformed by ion irradiation indirectly, if they are embedded in an amorphous silica glass matrix that does deform under the ion beam. To do so, colloidal core@shell particles composed of a 14-nm-diameter Au core surrounded by a 72-nm-thick SiO$_2$ shell have been irradiated with Cu or Se ions. By irradiating ensembles of these particles, they were able to fabricate arrays of aligned gold nanorods that showed evidence for split plasmon bands that are characteristic for anisotropic metal nanoparticles.

TEM image of a gold@silica particle before irradiation showed spherically shaped, with the 14-nm-diameter gold core centered inside. A TEM image after Se irradiation showed neither the silica shell nor the Au core are spherically shaped. The deformation of the silica shell is consistent with other work on ion beam deformation of pure silica colloids (i.e., formation of an oblate particle, with the minor axis parallel and two major axes perpendicular to the ion beam) [204]. TEM also shows that the gold core has deformed, but in an entirely different manner: A major axis is observed along the ion beam and a minor axis perpendicular to the beam. The initially 14-nm-diameter Au core has deformed into a rod with apparent dimensions of 6 nm by 38 nm. Correcting for the 45° projection of the TEM image relative to the ion beam direction, the major axis is as large as 54 nm (size aspect ratio ∼9). Assuming cylindrical symmetry, we can derive from the TEM image that the volume of the Au particle does not change during the deformation. Reference measurements were also performed, in which 14-nm-diameter Au colloids, not surrounded by a silica shell, were irradiated with Se ions, and no deformation was observed. These data indicate that the deformation of the Au core is related to an effect imposed by the silica shell.

To study this in more detail, a series of core@shell particles was made with different silica shell thicknesses (and identical Au cores) in the range 15–72 nm. No measurable deformation of the Au core was observed for silica shells thinner than 26 nm. A second additional observation, of similar nature, is that for core@shell particles of equal size and shell thickness, the deformation of the metal core depends on the local surroundings of the particles; particles that are stacked two or three layers thick and are in contact before irradiation exhibit significantly larger deformation of the metal core than isolated particles. An array of aligned nanorods is observed, with size aspect ratios that vary across the image, due to the varying degree of interparticle contact throughout the structure. From these two independent experiments (varying shell thickness and varying colloid contact), one concludes that the Au core deforms more efficiently as more silica surrounds it.

To explain the shape change of the gold core due to the silica shell, the following indirect deformation scenario was proposed. Each individual ion impact in silica leads to the formation of a thermal spike that leads to an in-plane strain perpendicular to the ion beam [205]. In planar (constrained) films, the combined strain of all individual ion impacts leads to the build up of a macroscopic stress that can be as large as several hundreds of mega-pascals [206]. In free-standing silica colloids, this leads to anisotropic expansion perpendicular to the beam, as also observed here for the silica colloid. In the core@shell colloids studied here, the lateral stress fields surrounding each individual ion track in silica also act on the Au core. Metals are known to be relatively soft under ion irradiation, as evidenced, e.g., from the low radiation-induced viscosity [207]. Thus, with an in-plane stress acting on the soft core, it may flow in the out-of-plane direction, i.e., along the direction of the ion beam. A TEM image of an isolated core@shell particle showed the deformation after Se irradiation. The metal core has evolved into a dumbbell-like structure, i.e., two small spheres connected by a thin rod. The rod is aligned along the ion beam axis. Due to the contact, larger deformation of the Au core is induced, and in this case the Au core has broken up into a collection of smaller spheres, randomly distributed in the silica colloid.

Preliminary optical transmission measurements were made under normal-incidence conditions on core@shell colloids, with 14-nm-diameter Au cores and 39-nm-thick shells, that were allowed to dry on a fused silica substrate (0.5 mm thick) to a thickness of 10–20 layers. The sample was immersed in an index-matching fluid to avoid light scattering due to the silica shells, so that only the extinction due to the Au cores remains. Fitting a Lorentzian line shape to the main peak for the unirradiated sample gives a central wavelength of 529 nm. This is in good agreement with the surface plasmon resonance of Au nanoparticles embedded in a silica matrix. After irradiation, a broad shoulder has developed on the long-wavelength side (600–650 nm). In addition, the central wavelength of the main feature has slightly blueshifted to a wavelength of 521 nm. The small blueshift and large redshift are characteristic for elongated gold nanoparticles. The size aspect ratio estimated from the shifts [208] is 4.6, taking into account the 20° viewing angle.

Gold nanodots deposited on silicon are of significant importance because this material presents a large number of applications like as subwavelength antennas in plasmonic applications, or as catalysts for the growth of silicon nanowires (SiNWs) , or even as electrical contacts in Si nanodevices. In the first example, the gold nanoparticles are exploited to increase light absorption in solar cells, thanks to the surface plasmon resonances, when they are in contact with the active surface of semiconductor. But most of the experimental results [209, 210] demonstrate that these mechanisms, and consequently the cell performance, are strongly dependent on the geometrical characteristics of the dot, such as size and shape. Another field of application for gold nanodots is in the synthesis of SiNWs, where they can be used either as catalyst seeds in a bottom-up approach like the vapor–liquid–solid process, or as etching initiator in a top-down process like the metal chemical etching [211, 212]. Also, in these cases, the main morphological characteristics of the final SiNWs such as diameter and growth (/etching) direction are determined by the size of the catalyst and their interconnection, i.e., by the original gold dot characteristics [213–215]. The SiAu system has been also studied from the point of view of the electrical stability in metallic contacts. Akhtari-Zavareh et al. [216] studied the morphological and electrical characteristic of an Au/Si diode. They found that after air exposure, there is a formation of a continuous interfacial layer due to an interaction between Au and Si. This surface or interfacial interaction leads to the degradation of the rectifying diode properties.

The evidence of an interaction between gold and silicon is shown in many works for several annealing temperatures. At $T = 150$ °C, i.e., below the Au–Si eutectic point (363 °C), Rutherford backscattering spectrometry (RBS) analysis demonstrated that in a Si sample covered with an evaporated gold layer, Si atoms migrate through the gold film, accumulate on its surface, and oxidize after air exposure [217]. Room temperature evolution of continuous gold layers evaporated on Si (111) has been investigated too [218]. The gold films were evaporated in this case at $T < 50$ °C on clean silicon and characterized in situ by using electron loss spectroscopy and Auger electron spectroscopy. The interacted regions have been identified as metastable alloys or silicides [219, 220]. A critical thickness below which the gold seems inert and not able to create alloying has been identified, and, if it is less than 2 ML, gold and Si do not intermix even at temperatures as high as 800 °C [218]. For a thickness larger than 5 ML, gold reacts with silicon also at room temperature [218]. The critical thickness has been in this case estimated as the plateau exhibited by the growth rate measured by an oscillating quartz, but no morphological analysis is shown. A lower value of 1 ML for the critical thickness has also been found by Auger spectroscopy studies for gold evaporated on clean Si (111) at room temperature [219]. Experiments of minute amounts of gold deposited on NaCl demonstrated that a considerable surface mobility and coalescence are present also at room temperature. Since the diffusion coefficient of gold in silicon cannot explain this rapid interdiffusion, it was concluded that the intermixing of gold into the silicon was a chemically driven process. However, TEM analysis has been indicated as an improper technique to study the early stages of the deposition of gold on Si because early film growth can be detected only after the adatoms have

formed small metal nuclei with sizes exceeding the resolving power of the technique. The top region of the interacted material has been investigated too, and in literature, a controversy is present, some papers referring to an alloy [221], some to a gold-rich material [218], others to a Si rich one [222]. The interaction can be inhibited if the Si surface is covered by SiO_2 or impurities such as carbon, water, or oxygen prior to the gold deposition [218]. The effects of the substrate orientation have been explored, and the (100) Si surface exhibits higher interaction rates than the (111), due to the larger Si dangling bonds density, available for bonding to gold, present in the first [222]. The role of the deposition technique has been investigated too, and it has been found that in sputtered samples, the interaction is more active than in evaporated films due to the knock-off mechanism inferred by the energetic ions during the sputtering on the Si surface, which remove more efficiently oxide residuals and improve the Au/Si contact [222].

The TEM analysis after the HF etch and gold deposition shows two zones: white regions representing the silicon substrate and black regions that represent the gold nanodots [223]. The analysis performed on the sample a few hours after the deposition shows three zones: white regions representing the silicon substrate, black regions that represent gold nanodots, and an intermediate zone of gray color. The corresponding electron diffraction patterns of the samples are shown. The blue square is superimposed to the pattern of the (100) Si substrate zone axis. The indexes refer to the Si spots 004 and 022. The Au spots, indicated by the red indexes, correspond to two Au patterns rotated by 90° relative to each other with the same zone axis [110] on Si [100]. As observed, the diffraction analysis shows an in-plane alignment of the Au nanostructures. The orientation relationship is Au (110)∥Si(100) with Au[002]∥Si[022] and Au[002]∥Si[022]. High-resolution TEM analysis coupled to diffraction analysis indicates that the cloudy gray region corresponds to an amorphous mixture of gold and silicon, thus indicating that here gold has intermixed with silicon. Since the characterization is ex situ, it is not possible to establish whether the interaction has proceeded during the deposition because of the energetic plasma, or right after the deposition because of the few hours of room temperature exposure. However, it is reasonable to think that the plasma has contributed to it, as in case of sputtered continuous films [218].

The interaction between Si and Au is known for thin continuous films annealed at $T < 150$ °C [218]. The agglomeration of gold in nanodots is presumably due to some local residual or regrown Si–O bonds or C atoms that prevent the Si/Au intermixing [224]. From a preliminary observation, it is possible to understand that the evolution of the gold nanodots does not show drastic changes, while the amorphous Au/Si agglomerates, corresponding to the gray areas, evidence a morphological modification because they shrink in density and size leaving room to Si uncovered areas. In some cases, these areas exhibit the fringes typical of a crystalline phase lying over a crystalline substrate, indicating that these nanostructures after aging are crystalline. This result demonstrates that to ensure the accuracy of the results, besides than properly preparing the sample for analysis, it is crucial to analyze the samples immediately after the gold deposition. The next results refer to the characterization performed on the nanodots first, and then to the amorphous

agglomerates. The size distribution of the Au nanodots as a function of their radius for the several days of observation varies as follows [223]:

evolution time (days)/dot radius (nm)/dot density (#/cm^2 × 10^{-12}):

$$0/1.7/2.2, \ 14/1.6/2.6, \ 43/1.8/1.7, \ \text{and} \ 99/1.7/1. \tag{5.4}$$

From these data, we can say that the size distribution of the Au nanodots as a function of the radius presents a shape that is maintained all over the time with small differences in the peak value and in the centroid. The quantitative analysis of the data then confirms the previous observations, i.e., the nanodots morphological characteristics do not show appreciable evolution over time, supporting the hypothesis that at the interface, the presence of residual or regrown SiO$_x$, or even carbon atoms, have inhibited the intermixing between Au and Si.

Bal and Hazra [224] have studied the room temperature diffusion of continuous thin layers of gold on Si (001) substrates and have observed that in samples whose surface was initially treated with HF to remove the native oxide, gold interacts with silicon diffusing through the surface. The amount of diffusing gold saturated after about 2 weeks from the date of deposition due to the regrowth of an oxide layer, which slows or prevents the intermixing Au–Si. Relatively to the Au–Si interaction, it is known that the intermixing between Au and Si even at low temperatures produces a gold-rich (70%) amorphous surface alloy [225]. Kim et al. [226] proposed a structural model, indicating the arrangement of atoms in the layers as they are deposited. The proposed model shows that at the interface between the deposited material and the substrate, the system Au/Si tends to reach the concentration of a 50–50 of compound Au–Si. Once reached this level, the system tends to preserve this condition, so it behaves as a "stable" condition.

It was also concluded that the Au/Si interdiffusion in the as-deposited samples takes place also in case of nano-islands, when in contact with Si-producing amorphous alloys of about 70:30 Au:Si composition and that after aging, it tends to the 100% Au composition realigned in both <100> and <200> orientations. From further results, it can also be concluded that the coverage of Au interacted with Si decreases after aging, and this is correlated to the relatively slow spinodal decomposition kinetics occurring at RT (which is well below the eutectic temperature T_e = 363 °C). Considering the equilibrium phases diagram and the Au–Si system, this process should cause after a certain time the complete separation of the mixed Au–Si region in the two elemental phases which nucleate and grow at expenses of the intermixed region.

The formation of nanocomposites one can see as follows: (a) First, gold is deposited on clean Si, and the gold atoms are randomly placed over the surface. (b) Gold starts mixing with Si by interdiffusion. Due to some residual or regrown local SiO$_x$, the gold deposited on the oxide does not interact with Si and form nuclei for stable crystalline dots. (c) The intermixing creates a surface Si layer and sub-surface amorphous islands of mixed Au–Si, which tend to form a stable stoichiometry of 70% [227]. After the sample is taken out of the chamber, gold starts to diffuse segregating in crystalline islands aligned with some crystallographic

orientations of Si and occupying smaller and less dense areas through a process similar to ripening. The exchange of gold atoms between the crystalline dots and the subsurface agglomerates is inhibited by the presence of contaminants.

It was reported that nearly monodisperse gold nanoparticles can be prepared by carrying out a digestive ripening (refluxing a polydisperse colloid suspended in a solvent with a suitable capping agent) protocol with different ligands such as alkanethiols, phosphines, amines, and silanes [228]. Among these ligands, it was clearly established by Banaszak Holl and coworkers that when silanes are attached to gold surfaces, they lose hydrogen, resulting in weak Au–Si covalent bonds [229]. It has also been demonstrated that large amounts of gold and other metal colloids can be prepared in polar solvents such as acetone, butanone, and pentanone. TEM pictures of the as-prepared colloids reveal that the gold nanoparticles are highly polydisperse and also highly defective in nature. In an effort to make narrower size-distributed colloids, researchers have been trying to digestively ripen these Au-ketone-stabilized colloids with various ligands. Indeed, it was shown that digestively ripening these colloids with ligands such as dodecanethiol leads to a highly monodisperse colloid which forms beautiful superlattices [230]. Similarly, digestive ripening of a Au-butanone or Au-pentanone colloid with $C_{18}H_{37}SiH_3$ leads to a decrease in the size of the as-prepared gold nanoparticles with a narrower size distribution. However, when the same reaction (refluxing a Au-butanone or Au-pentanone colloid with $C_{18}H_{37}SiH_3$) was carried out in the presence of small amounts of water, a dramatic formation of nanowires, filaments, and tubes is observed. The average diameters of these wires and tubes are in the 50–100 nm range, and the lengths are almost into millimeters. Interestingly, many of these nanostructures adopt highly helical structures. HRTEM micrographs clearly reveal the presence of a gold nanoparticle at the tip of each of these nanostructures (Fig. 5.14). Elemental and energy-dispersive X-ray studies suggest the elemental composition of these nanostructures to be $C1_8H_{37}SiO_{1.5}$, with trace amounts of gold. HRTEM photographs and selected area electron diffractions also suggest these structures to be without any crystalline order. Indeed, when the powder X-ray pattern of these structures was recorded, a peak other than that corresponding to SiO_2 was not found [231].

5.3 Inorganic Scaffolds

5.3.1 General

Inorganic scaffolds were the first type of stabilizers available for noble metal nanoclusters. Under suitable conditions, they can produce nanoclusters (NCls) of a well-defined number of atoms, and they can cover a wide emission wavelength range from UV to near-IR. Silver nanoparticles were used as sacrificial templates to react with an aqueous $HAuCl_4$ solution, resulting in the formation of gold

Fig. 5.14 Schematic picture clearly depicting a gold nanoparticle at the tip of the nanowires [229, 230]
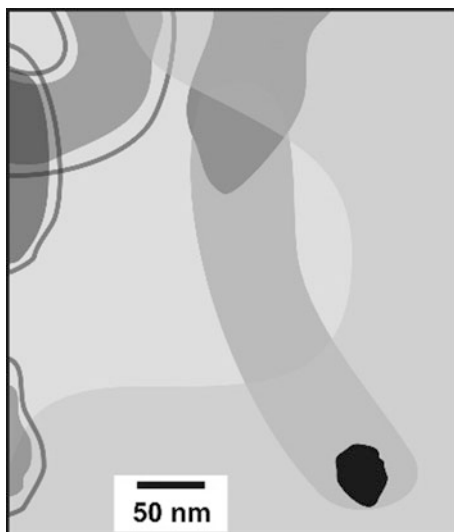
50 nm

nanoshells with hollow interiors and smooth and pinhole-free surfaces, as well as homogeneous and highly crystalline walls [232, 233]. In addition, recent success in synthesizing silver nanostructures with well-defined shapes and surfaces [e.g., nanocubes bounded by {100} (crystallographic planes)] also provides a number of model systems to systematically investigate the template-engaged replacement reaction on the nanometer scale nanocubes [234], triangular nanoplates [235], circular nanodisks [236], nanorods [200], and nanowires [237]. These results showed that the template-engaged replacement reaction proceeded through two distinctive steps:

(i) the formation of seamless hollow structures (with the walls made of gold-silver alloys) via a combination of galvanic replacement (between silver and HAuCl$_4$) and alloying (between gold and silver) and

(ii) the formation of hollow structures with slightly reconstructed shapes and porous walls via dealloying.

Rodriguez-Lopez et al. [238] reported a very elegant treatment on the shape or morphology transition of some mono- and bimetallic particles with evolving size. According to this approach, evolving from the very small size range of both mono- and binary metallic nanoparticles, a sequence of structures is formed. At small sizes, particles tend to be Platonic-(shape) solids. The particles tend to adopt Archimedean-related shapes at a slightly greater particle size. When the particle size is even larger, they tend to adopt shapes corresponding to Kepler–Poinsot solids, defect structures (twins, stacking faults, etc.), and finally bulklike structures.

Matrix isolation is a method to produce few-atom ligand-free metal nanoclusters, and since the early work by Ozin in the 1970s, it has provided lots of insight in the photophysical properties of oligomeric silver and was used to verify the outcome of

computational studies [239, 240]. In matrix isolation, the silver atoms are thermally evaporated and transported by a flow of noble gas (e.g., Ar) followed by their deposition on a cooled transparent substrate, like quartz. The cooling of the gas at the cold walls leads to nucleation and growth of the nanoclusters. Parameters that allow control of the cluster size distribution include the gas-to-metal ratio and the temperature of the substrate. At temperatures approaching 50 K, silver atoms are able to diffuse throughout the Ar matrix to form nanoclusters, whereas at lower temperatures, clustering is limited to the surface of the growing matrix layer [241]. Alternatively, the bulk diffusion and subsequent cluster formation can also be induced by light [242]. The group of Ertl reported that the aggregation of silver atoms to nanoclusters is accompanied with emission of light (chemiluminescence) [243]. Although cryogenic matrix isolation is a good tool to study metal nanoclusters, it is not suitable for applications in ambient conditions.

Fleischmann's 1974 discovery of surface-enhanced Raman scattering (SERS) [244], and especially its rediscovery on colloidal silver particles in 1977 by Creighton [245], started the extensive development of a new and very sensitive analytical method [246] enabling to detect molecules in the concentration range from pico- to femtomoles [247]. High enhancements of SERS even allowed the detection of individual molecules adsorbed on a single silver particle [248, 249]. Some studies have shown that the highest value of enhancement is achieved only on the silver particles of a certain size which are referred to as "hot particles". The optimal size of these hot particles depends on the wavelength of the laser used for excitation and ranges from approximately 70–200 nm for excitation wavelengths between 488 and 647 nm [250]. For the commonly used argon laser with a wavelength of 514.5 nm, the "hot particle size" is reported from 80 to 100 nm [247, 251]. For a use of lasers with an excitation wavelength in the red region ($\sim$785 nm), and especially in the NIR region ($\sim$1064 nm), we can assume that the highest enhancement of the Raman signal would be achieved with particles of around 400 nm in diameter. Nevertheless, the preparation of such large particles represents a hard task from the synthetic viewpoint. Moreover, particles of these dimensions are unstable and usually settle within a few hours. Silver nanoparticles of 20–30 nm in sizes can be stable for several months or years, even without any extra stabilization. However, these small particles themselves usually do not provide enhancement of the Raman signal. For this purpose, they must be activated for example by the addition of some inorganic ions [252, 253]. The most frequently used activation agents of the silver nanoparticles prepared by the common reduction procedures [254] include halide ions, particularly chlorides [255, 256]. However, the mechanism of the activation has not yet been fully explained [257, 258]. One possible explanation is based on the formation of silver particle aggregates [259]. It has been shown that a very strong increase in the Raman signal is achieved in nanocrystal junction sites between two nanoparticles [260].

The most widely used procedure for the preparation of gold nanoparticles supported on the insoluble oxides solids is the precipitation–deposition method. Starting from an aqueous solution of $HAuCl_4$, addition of a base leads to precipitation of a mixture of $Au(OH)_4$ or $Au(OH)_x^-Cl_{4-x}^-$. Related gold oxy/hydroxides

that adsorb into the solid are then reduced to metallic gold by boiling the adsorbed species in methanol or any other alcohol. After adsorption on the solid surface, AuNP formation occurs by nucleation and growth. The pH of the precipitation and the other experimental conditions (nature of the alcohol, temperature and time of the reduction, calcination procedure, etc.) provides a certain control of the particle size of the resulting nanoparticles [261]. The ideal solid oxide support should have a high density of hydroxyl groups and a large surface area according to the deposition–precipitation mechanism in order to achieve the formation of AuNPs with narrow size distribution [262–264].

Rigid templates such as membranes [265, 266] have been used wherein metal ions are reduced/reacted inside their nanoscale pores. Reaction temperature seemed to play the most important role in determining the morphology of the template and the diffusion coefficient of metal atoms are both strongly dependent on this parameter [267]. Similar changes in morphology, composition, and structure were observed no matter whether silver nanocubes, nanowires, or nanospheres were used as the templates.

An alternative method for the synthesis of metal hybrids lies in the use of bimetallic nanocrystals by means of seed-grow processes to obtain heterogeneous nanoparticles. Following this approach, Xia et al. [268] described the overgrowing of gold structures on presynthesized palladium cubes. Zhang et al. [269] reported the synthesis of gold nanorods on Ag and CdSe seeds, while Lombardi et al. [270] demonstrated direct self-assembly of heterodimers formed by Au and {Ag@SiO$_2$} NPs, highlighting the relevance of this method to investigate single nanoparticle spectroscopic properties.

5.3.2   Silver Nanostructures

Prucek et al. have reported a simple and reproducible method for the activation of monodispersed silver nanoparticles by introducing the concentrated NaCl solution into the AgNP dispersion [271]. Immediately after the addition of NaCl solution to AgNPs, there was a considerable change in the color of the dispersion of AgNPs with corresponding changes in its absorption spectrum (Fig. 5.15, curves 2–6). The average particle size was observed to increase with the reaction time (Fig. 5.15 curve 1). The color of the dispersion changes immediately from yellow to violet. The original absorption peak with the maximum at 410 nm, corresponding to the surface plasmon of the original nanoparticles, was considerably suppressed, while at the same time, the secondary peak with the maximum at 570 nm has emerged. The secondary peak with the similar maximum was previously reported for silver particles with dimensions of 100–110 nm [272, 273]. The addition of chloride ions further decreased the absorption maximum at 410 nm and a shift of the secondary absorption maximum to 650 nm, which moved to 680 nm was observed. This shift in the position of the secondary absorption peak can be considered as a confirmation of the gradual increase in the average size of silver particles. After several

Fig. 5.15 Time dependence of average size of AgNPs (*curve 1*) and the representative UV–Vis absorption spectra [*curves 2* (without NaCl), *3* (0.1 min), *4* (2), *5* (5), and *6* (20)] recorded during 20 min after the addition of the NaCl solution (the final concentration of 400 mM) [271]
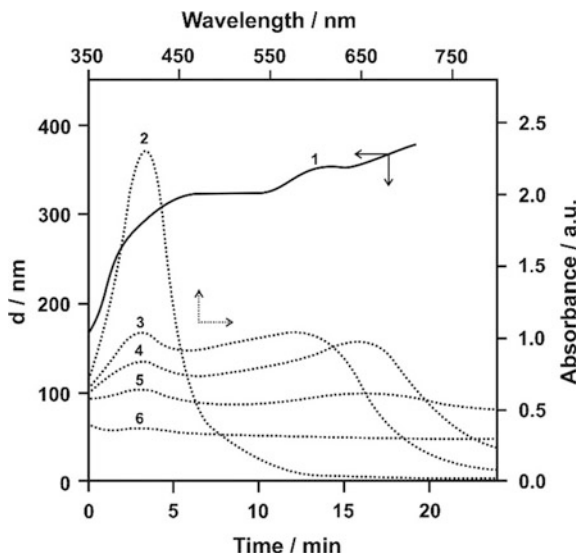
minutes, the absorption spectra already had a very flat course without any pronounced maximum, which is characteristic of silver particles with dimensions of about 200 nm and larger [273].

For example, $d = 24$ nm determined by TEM is in a good accordance with the value determined by the DLS method 28 nm (at the given time). After 30 s, TEM image revealed considerable amount of silver nanoparticles with the size of equal to or below 25 nm ($\sim 90\%$). However, a certain number of particles ($\sim 10\%$) had dimensions ranging from 50 to 100 nm. In the sample taken 2 min after the addition of NaCl solution, the presence of Ag particles with a size of around 150 nm was observed, and the particles of dimensions of around 25 nm were almost not present. After 15 min, the large Ag particles with the size of around 350–400 nm were found in the dispersion, while any smaller particles and/or their aggregates were not detected. Approximately 20% of the AgNPs were present in the form of well-defined crystalline shapes, such as hexagonal (Fig. 5.16 a), rod-like (b), and triangular (c). The miscellaneous morphologies of recrystallized particles are probably related to the presence of particles with different shapes already present in the original dispersion (Fig. 5.16d–f). The single-crystal character and typical cubic structure of these recrystallized silver particles were confirmed by the selected area electron diffraction.

Similar experiments were performed with NaBr and NaI solutions. In all cases, the yellow coloring changed to the gray color within several seconds. However, this color change, implying for a disappearance of the original well-dispersed nanoparticles, is not due to the recrystallization of silver nanoparticles as observed after the NaCl addition. In the case of NaBr and NaI additions, the primary dissolution followed by a secondary precipitation of silver halogenides is a competitive process, which was proved by detailed TEM (Fig. 5.17) and UV–Vis
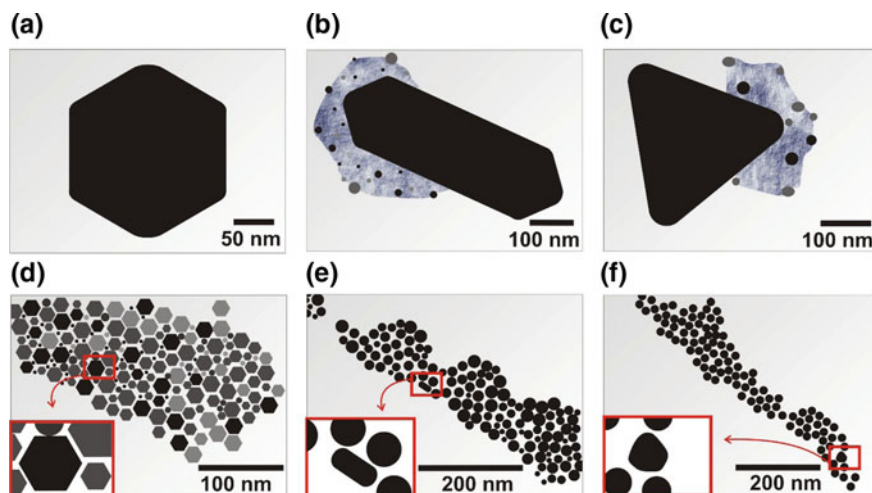
Fig. 5.16 Schematic pictures taken 15 min after the addition of the 4 M NaCl solution exhibiting recrystallized silver particles with various morphologies (**a**, **b**, and **c**), and images of primary nonactivated AgNPs of the same crystal shapes (**d**, **e**, and **f**) [271]

measurements. TEM images of the objects formed after NaBr (NaI) addition revealed presence of aggregates (particles) with the sizes of several tens to hundreds of nanometers (Fig. 5.17a, c). These objects were, after the radiation by electrons in TEM, subjects to partial (Fig. 5.17b) or almost total destruction (Fig. 5.17d). This might be a proof of the formation of a certain amount of AgBr (in the case of NaBr addition) or even prevailing amount of AgI (in the case of NaI addition). The different action of iodide ions in comparison with chloride ions is also reflected in the obtained absorption spectra when almost zero absorbance, between wavelengths of 500–900 nm, registered after 20 min since the NaI addition, gives further support for an absence of metallic nanoparticles in the system. Evidently, the highly concentrated solutions of bromides and iodides are not applicable for activation of silver nanoparticle dispersion due to the precipitation of silver halogenides. It is well known that halide anions can serve as a precipitant of Ag^+ ions at a low concentration and a complexing agent at a high concentration of halides. The halide ions can react with the silver atoms and dissociate them from the surface of Ag particles. This phenomenon is known as the oxidative etching process [274, 275]. Henglein et al. [276] have reported that oxidative etching of silver particles is accelerated through the presence of complexing agents. They observed that ligands that coordinated more strongly with silver induced the oxidative etching at much faster rates. The suggested mechanism underlying this phenomenon was that the silver atoms on the surface are coordinated by halide ions, and this action is accompanied with a simultaneous pickup of the electrons by oxygen. Under such conditions, the varying behavior of Br^- and I^- ions compared to Cl^- is therefore given by significantly higher stability constants of AgX_2^- complexes with Br^- and
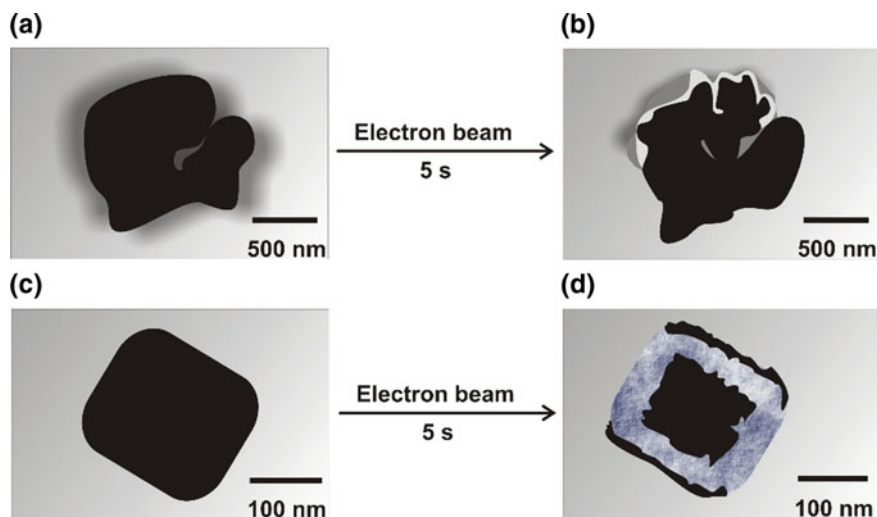
Fig. 5.17 Schematic pictures demonstrating the electron beam-induced transformation of particles formed after 15 min since the addition of the NaBr (**a**, **b**) and NaI (**c**, **d**) [271]

I^- ions. In the case of bromides and iodides, etched Ag^+ ions are more firmly tied up into a respective complex compound and the subsequent recrystallization of particles proceeds with a greater difficulty (Br^-) or almost not at all (I^-).

The original silver nanoparticles (~ 30 nm), as well as the recrystallized silver particles transformed after the addition of NaCl (~ 400 nm) were tested for application in surface-enhanced Raman spectroscopy with adenine as an model analyte.

The enhancement of the Raman signal was monitored depending on the period of time that elapsed since the addition of the NaCl solution to the diluted dispersion of original AgNPs (Fig. 5.18). The increase in the enhancement during the first 12 min can be explained by an increase in the particle size caused by the recrystallization process. After the mentioned time elapsed since the addition of sodium chloride, the particle size reached a value of around 400 nm, which is in good agreement with the prediction of optimal size of silver particles based on previously published results regarding the dependence of enhancement of the Raman signal on the particle size for the given excitation wavelength [250]. In the case of excitation at 488 nm, a considerable enhancement was achieved within two minutes after the addition of the NaCl solution. The size of silver particles reached approximately 150 nm at this moment. Surprisingly, the enhancement grew further with the increasing particle size. This fact can be probably connected to the irregular surface of most silver particles providing active sites for the enhancement. Generally, it is well known that chloride anions, in low concentrations (about 10 mM) [256, 257, 277], induce the aggregation process, and the junctions among silver nanoparticles (tens of nanometers) represent the active sites for the Raman signal enhancement.

Fig. 5.18 Time dependence
of enhancement of Raman
signal (SERS) of adenine after
the addition of chloride ions
for the excitation wavelengths
of 1064 nm (*2*) and 488 nm
(*1*). The enhancement factor
was determined by comparing
the intensities of the most
intensive peak in spectrum at
734 cm^{-1} [271]
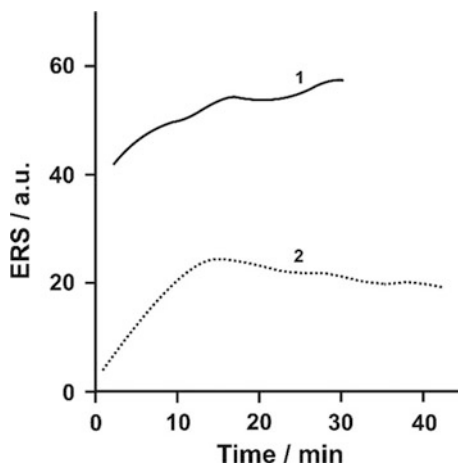
However, data presented in this work indicate that chloride ions cause the formation
of large silver particles (hundreds of nanometers), which are very efficient for the
Raman signal enhancement [250].

5.3.3 Gold Nanostructures

Depending upon composition and desired dimensions, certain types of prisms can
be prepared either thermally or photochemically [235, 278]. The photochemical
routes, thus far, have been used to synthesize silver nanoprisms with excellent size
control. Gold nanoprisms, on the other hand, have been synthesized exclusively by
thermal methods with varying degrees of success regarding purity and size control
[279]. Both prism compositions are particularly attractive for their enhancing
properties with respect to Raman spectroscopy. The optical spectra of nanoprisms
should exhibit a distinct dipole resonance as observed in isotropic spherical
structures in addition to weaker higher order resonances [280]. In the case of silver,
where bulk preparations of high-quality and relatively pure nanoprisms can be
realized, these plasmons have been identified and assigned through experiment and
computation [278].

Millstone et al. have presented a synthetic approach and separation procedure for
synthesizing and isolating large quantities of gold nanoprisms with uniform edge
lengths and thicknesses, which has allowed them to use UV–Vis–NIR spectroscopy
to observe an in-plane quadrupole resonance mode of such structures for [281].
This synthetic procedure builds off the work of Sau and Murphy [282] and involves
the preparation of small gold seed nanoparticles ($d \sim 5$ nm) and the subsequent
three-step growth of seeds in an aqueous solution containing the capping agent
(CTAB), gold ions ($AuCl_4^-$), reducing agent (ascorbic acid), and NaOH. This
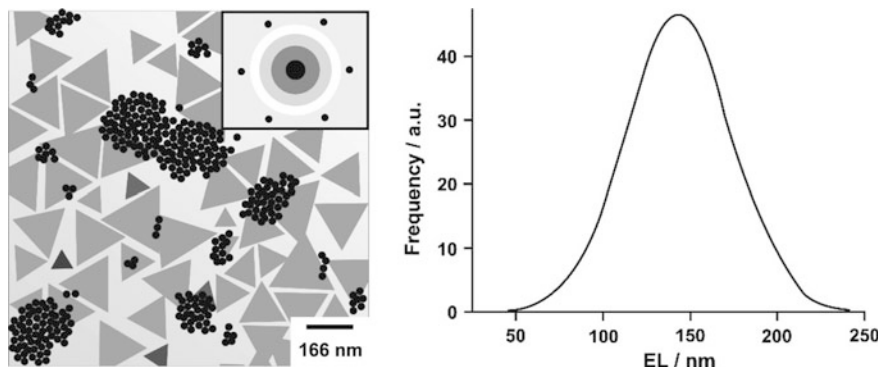
Fig. 5.19 Schematic picture of gold spherical and triangular nanoparticles (*left panel*). *Inset* shows the electron diffraction pattern of the *top* of a single prism. Histogram of nanoprism edge lengths (ELs) (*right panel*) [281]

synthetic procedure produces a mixture of spherical and triangular gold nanoparticles, each with a relatively homogeneous size distribution (Fig. 5.19). In contrast with many other similar synthetic routes for gold nanostructures utilizing CTAB, a present synthetic method produced no rods, cubes, or branched structures [282].

The average edge length of the nanoprisms is ca. 144 nm, and the average spherical nanoparticle diameter is ca. 35 nm. Interestingly, electron diffraction analysis of an individual gold nanoprism shows that, unlike lithographically generated structures, they are single crystalline and that the large, flat top and bottom faces are (111) facets (Fig. 5.19). Atomic force microscope images of the gold nanoprisms confirm that their top and bottom faces are atomically flat with a uniform thickness of ca. 7.8 nm. This thickness is approximately equal to the average diameter of the seed nanoparticles when the thickness of the two layers of CTAB on the top and bottom surfaces of nanoprisms is taken into account. This suggests that growth of prisms occurs in two dimensions from the isotropic seed to form the anisotropic prism.

Wang et al. have reported a facile, high-yield synthesis of unique porous gold nanobelts by morphology-preserved transformation from metal–surfactant complex precursor nanobelts formed by $HAuCl_4$ and Br^- $[(CH_3)_3N^+–(CH_2)_{12}–N^+(CH_3)_3]$ Br^- (N-C_{12}–NBr_2), a bolaform surfactant containing two quaternary ammonium head groups [283]. Typical SEM and TEM images of the porous gold nanobelts were obtained from the product generated by adding $NaBH_4$ to a solution containing N–C_{12}–NBr_2 and $HAuCl_4$. It was observed that the product consists of curled, porous gold nanobelts arrays with a thickness of about 10–20 nm, and width about 100–200 nm (Scheme 5.9). Such porous gold nanobelts combine the advantages of both 1D structures and nanoporous structures and may be an appealing material in application areas including catalysis. Further study showed that curled nanobelts of ∼500 nm in width and 50–100 nm in thickness appeared soon after mixing N–C_{12}–NBr_2 and $HAuCl_4$ in solution without $NaBH_4$.
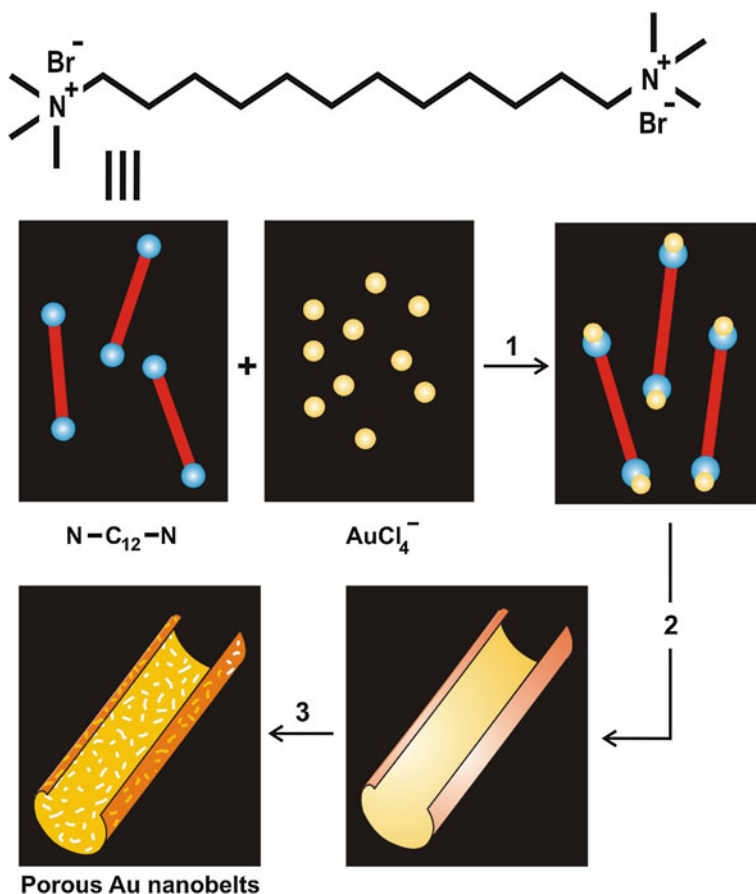
Scheme 5.9 Schematic illustration of the formation mechanism of porous gold nanobelts via an N–C$_{12}$–N(AuCl$_4$)$_2$ complex template and following steps: (*1*) electrostatic combining, (*2*) crystallization, and (*3*) morphology-preserved reduction [283, 284]

Accordingly, the formation process of the porous gold nanobelts is tentatively proposed as follows: When N–C$_{12}$–NBr$_2$ was mixed with HAuCl$_4$, a stoichiometric N–C$_{12}$–N(AuCl$_4$)$_2$ complex formed immediately via electrostatic interaction as well as van der Waals interaction between the positively charged head groups and the negatively charged AuCl$_4^-$ ions, which quickly self-assembled and crystallized into curled nanobelts. As the reductant NaBH$_4$ was added, the N–C$_{12}$–N(AuCl$_4$)$_2$ complex was reduced to gold nanocrystals, resulting in the formation of porous gold nanobelts arrays with shrunken sizes.

5.3.4 Composites

Fasciani et al. have presented the remarkable behavior of core@shell gold@silver nanostructures stabilized with aspartame (Asm), a common artificial sweetener (Charts 5.1 and 5.2) [285, 361, 363, 369].

The material presented in this contribution consists of a gold core, encapsulated in a silver shell [286] and stabilized with a dipeptide, specifically aspartame. AuNP seeds (~12 nm) were used for seed-mediated growth of core@shell nanoparticles [287]. Briefly, an aqueous solution of $HAuCl_4$ and I-2959 was irradiated with UVA light, using a Luzchem LZC-4 photoirradiator (Chap. 2, Scheme 2.11). A seed-mediated growth procedure was employed for the formation of Au@Ag nanoparticles according to a reported procedure [286], but by replacing the citrate stabilizer with two biocompatible stabilizing agents, aspartame. Ketyl radicals formed by the decomposition of excited I-2959 reduce Au ions via two steps: Au (III) to Au(I) and then to Au(0)

The surface protection with aspartame leads to excellent aqueous stabilization with a long shelf life. Moreover, in addition to the synthesis and characterization of aspartame-stabilized Au@Ag nanostructures ((Au@Ag)@Asm), representative in vitro experiments were carried out as a first indication of their antibacterial properties. Formation of (Au@Ag)@Asm nanostructure led to the spectral changes in Fig. 5.20. Note that after irradiation with $AgNO_3$, the band corresponding to the gold plasmon absorption is shifted to the blue, while a new band, corresponding to the silver plasmon absorption and centered at 405 nm, appears. The intensity of the two absorptions is consistent with the presence of comparable amounts of Au and Ag. Moreover, after the initial stabilization of the particles formed, the UV spectra did not change with time, showing very high stability. The analysis of the UV–vis spectra furnished a clear indication that core@shell structures are formed as opposed to separate nanoparticles or alloys. Indeed, in those cases we would have had no shift of the plasmon maximum (single particles) or a single band between the two metal plasmon absorptions (alloy) [288].

The TEM images obtained clearly reveal that (Au@Ag)@Asm particles are spherical with an average diameter of ~16.6 nm. The particles present a darker central region, attributed to the gold core, as well a lighter section around it, representing the silver shell; see Fig. 5.21.

Chart 5.1 Aspartame molecular structure [285]
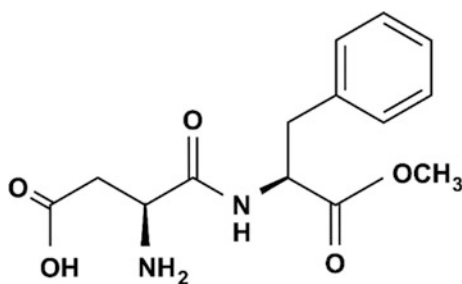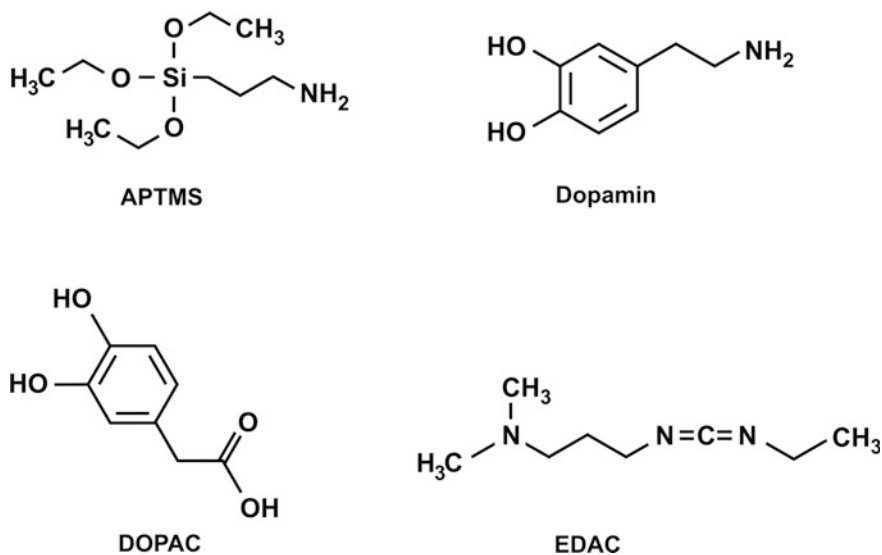
Chart 5.2 DOPAC (3,4-dihydroxyphenylacetic acid), EDAC (1-ethyl-3-(-3-dimethylaminopropyl) carbodiimide), APTMS ((3-aminopropyl) trimethoxysilane), dopamine [361, 363, 369]

EDS analysis was performed for Au@Ag@AsmNP, and the relative average percent (%) composition revealed ∼45.8% silver and ∼54.2% gold, similar to the anticipated composition based on the amount of $HAuCl_4$ (110 μM) and silver nitrate (110 μM), respectively. The EDS spectra confirmed the metal composition of the core@shell particles formed.

Sun et al. have also focused on silver nanocubes because this class of nanostructures provides a model system with monodispersed size and well-defined facets

Fig. 5.20 Absorption spectra for core@shell nanoparticles stabilized with aspartame ((AuNP@Ag)@Asm), recorded before irradiation (*curve 1*), right after irradiation in the presence of $AgNO_3$ (2), and at different times (5–10 days) after the irradiation was completed (3). The maxima of the two bands obtained after irradiation are centered at 405 and 510 nm [285]
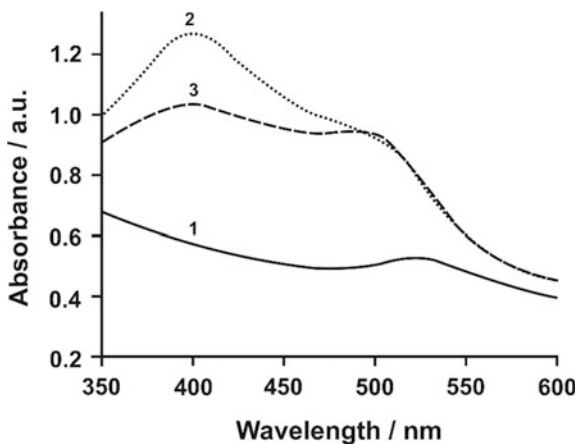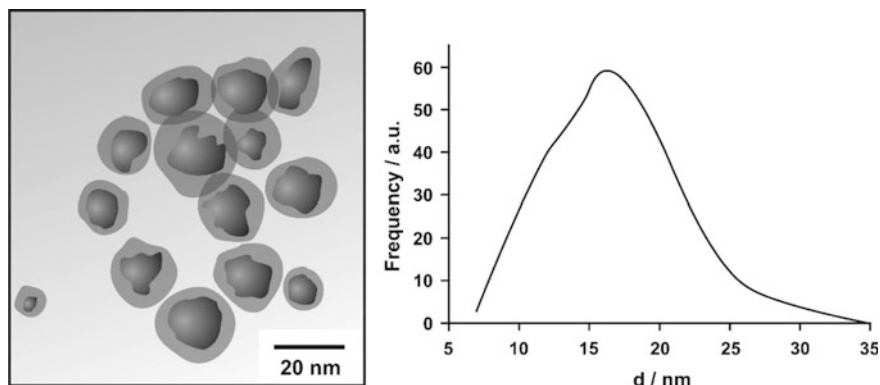
Fig. 5.21 Schematic picture for (AuNP@Ag)@Asm. Core@shell nature of the nanoparticles can be easily visualized (*left panel*). The *right panel* shows a histogram of the size distribution of the nanoparticles, which yields a mean diameter of ~ 17 nm [285]

[289]. Since the standard reduction potential of $AuCl_4^-$/Au pair (0.99 V vs. standard hydrogen electrode, SHE) is higher than that of the Ag^+/Ag pair (0.80 V vs. SHE), silver would be oxidized into Ag^+ when silver nanostructures and $HAuCl_4$ are mixed in an aqueous medium:

$$3Ag(s) + AuCl_4^-(aq) \rightarrow Au(s) + 3Ag^+(aq) + 4Cl^- \quad (aq) \qquad (5.5)$$

Two distinctive steps have been resolved: In the first step, the silver nanostructures were continuously dissolved, and the resultant elemental gold was epitaxially deposited on the surface of each template. At the same time, the gold layer was transformed into AuAg alloy because of the fast interdiffusion between gold and silver at 100 °C. A combination of these two processes led to the formation of well-defined nanostructures which had hollow interiors, smooth surfaces, and homogeneous walls consisting of the AuAg alloy. In the second step, the Au–Ag walls were dealloyed as the replacement reaction continued to proceed, and processes such as Ostwald ripening would induce morphological reconstruction, as well as the formation and enlargement of pinholes in the walls. Complete dealloying eventually forced the porous nanostructures to collapse into gold fragments characterized by irregular shapes. The reaction temperature was found to play a critical role in determining the final morphology of the product. At room temperature, for example, the simultaneous formation of AgCl solid could disrupt the epitaxial deposition of gold atoms on the surfaces of silver templates. The slow diffusion of silver and gold atoms at such a low temperature also prevents the resultant nanostructures from smoothening their surfaces via processes such as alloying and Ostwald ripening.

In addition to the traditional templates acting as spatially confined reaction media, certain reactive solids with a specific shape can be used as sacrificial templates for the production of metal nanocrystals, which adopt the underlying shape of

the template. In particular, silver nanocubes can be used as sacrificial templates for the fabrication of novel gold composite nanocages and nanoframes through a galvanic displacement reaction (Scheme 5.10) [290]. With the addition of $HAuCl_4$ solution into a boiling suspension of silver nanocubes, a pinhole is formed on one of the six faces, and gold is deposited epitaxially on the surface of the silver cube. As the gold layer forms, the initial pinhole serves as the site for silver dissolution, facilitating the conversion of the nanocube into a Au/Ag-alloyed nanobox. With the addition of more $HAuCl_4$ solution, dealloying occurs, resulting in the formation of a porous gold nanocage with an underlying cubic form. By using the wet etchant Fe $(NO_3)_3$ to selectively dissolve silver from the Au/Ag-alloyed nanobox (Nbx), a unique gold nanoframe is obtained. Representative SEM and TEM images of the obtained gold nanocages and nanoframes are shown in Scheme 5.10.

The introduction of silver seeds can lead to fast and high-yield syntheses of two highly anisotropic metal nanoparticles: ultrathin metal nanowires and triangular gold nanoprisms [291]. Ultrathin metal nanowires are of great interest owing to their unusual transport properties and potential applications in electronics [292]. Triangular nanoprisms have also attracted a great deal of attention for their tunable surface plasmon resonance (SPR) and field enhancement at sharp corners [293]. Here, we show that such low-dimensional nanoparticles can be readily synthesized in high yields by adopting silver seed particles in combination with an aromatic surfactant, benzyldimethylhexadecylammonium chloride (BDAC), in the growth solution. The sizes of prepared gold and silver seed particles were determined to be ~ 2.5 and ~ 3.6 nm, respectively. Subsequently, the seed solution was added into solution containing BDAC, $HAuCl_4$ or $AgNO_3$, and ascorbic acid [291].
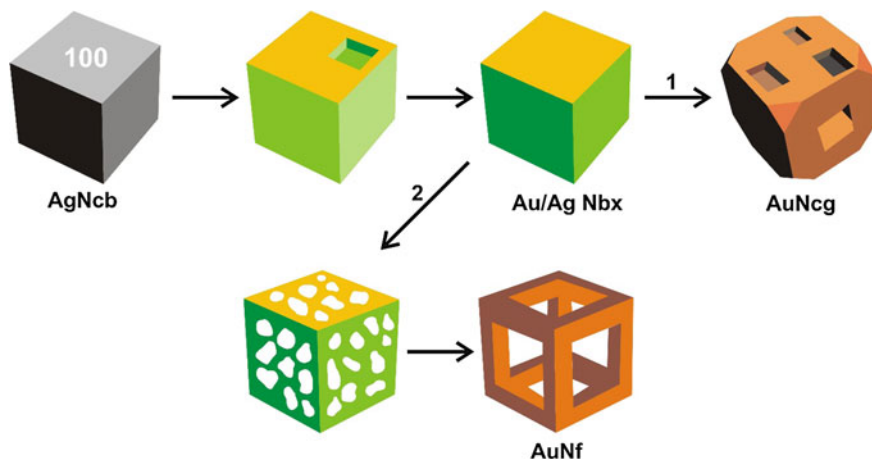
Scheme 5.10 Schematic illustration of the formation of gold nanocages (Ncg) and nanoframes (Nf) from a silver nanocube (Ncb) that serves as a template. Coloration indicates the conversion of a silver nanocube into an Au/Ag nanocage via galvanic replacement, and then into gold nanocages via continued galvanic replacement (*1*) or an Au nanoframe via selective etching with a wet etchant (*2*). SEM and TEM images of Au nanocages and nanoframes [284, 290]

Scheme 5.11 presents TEM images of nanoparticles synthesized with silver seed particles and varying amount of silver nitrate in the growth solution. In the absence of silver nitrate, quasispherical particles with an average diameter of ~ 19.0 nm were formed. The particles show an SPR band position at 530 nm (Fig. 5.22, right panel, curve 2), indicating that the particles synthesized in this condition are not completely spherical [294]. When a small amount of silver nitrate was added to the growth solution ([AgNO$_3$]/[HAuCl$_4$] ratio of 0.15), triangular prisms and truncated prisms (about 50%) were formed in high yields as shown in Scheme 5.11. The edge length and the height of triangular prisms were measured to be ~ 33.5 nm (Fig. 5.22, left panel, curve 3) and ~ 5.4 nm, respectively. The edge length was controllable from 23 to 46 nm by varying the volume ratio between the seed and the growth solution or by using small triangular prisms as seed particles, while the height of the triangular nanoprisms remained almost constant in the series of different synthetic conditions.

The silver mole percentage in triangular nanoprisms was determined to be 5 and 4% by energy-dispersive spectra (EDS) and inductively coupled plasma atomic emission spectroscopy (ICP-AES), respectively, indicating that the triangular nanoprisms are made of mainly gold. The extinction spectra of the triangular nanoprisms exhibited a dominant SPR peak at 750 nm (Fig. 5.22, right panel, curve 3), which is assigned to in-plane dipole resonance. The main peak position of calculated spectra of snipped triangular gold nanoprisms with the dimension from the TEM analyses matches well with the experimentally obtained extinction
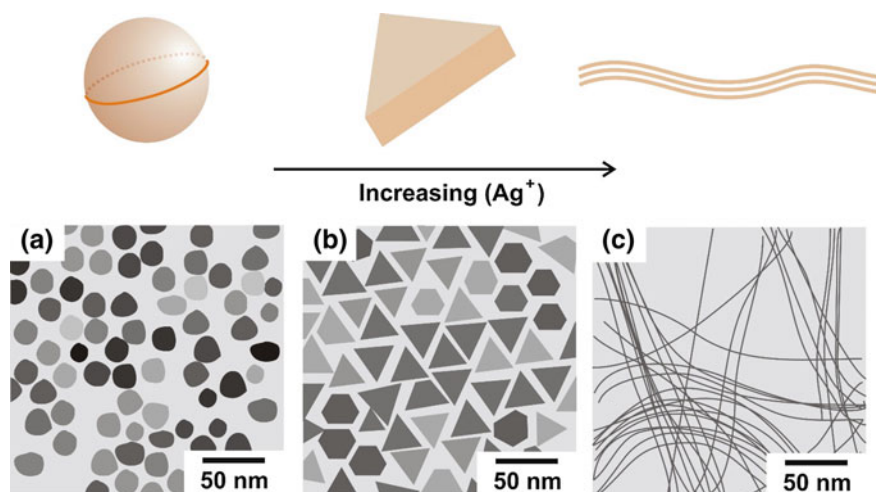
Scheme 5.11 Pictorial description showing the shape of nanoparticles synthesized by the seed-growth method using silver seed particles and BDAC. The shape evolved from quasi-spheres to triangular nanoprisms and ultrathin nanowires with increasing the concentration of AgNO$_3$ in the growth solution. The [AgNO$_3$]/[HAuCl$_4$] ratio in the growth solution was 0, 0.15, and 1.2 for quasi-spheres, triangles, and nanowires, respectively. TEM images of quasi-spheres (**a**), triangular nanoprisms (**b**), and ultrathin nanowires (**c**) [291]
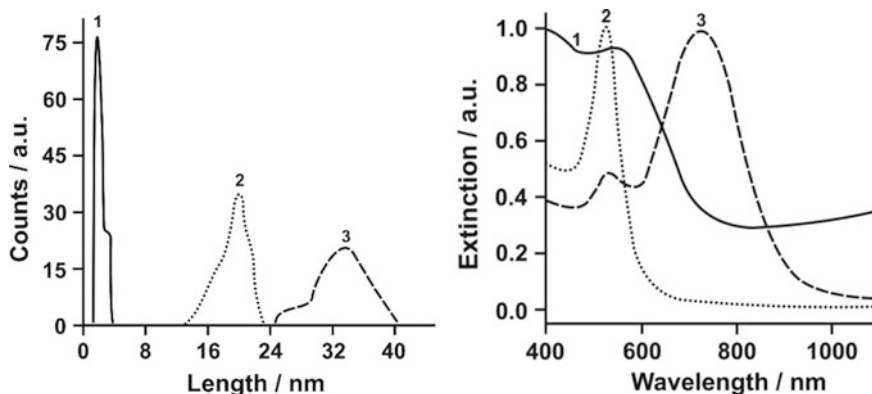
Fig. 5.22 Size histogram of ultrathin nanowires (*curve 1*, diameter (*d*)), quasi-spheres (*2, d*), and triangular nanoprisms (*3*, edge length) (*left panel*). UV−Vis spectra of ultrathin nanowires (*curve 1*), quasi-spheres (*2*), and triangular nanoprisms (*3*) (*right panel*) [291]

spectra, supporting the theory that the triangular nanoprisms are made of gold. The weak peak at 534 nm was assigned to the small amount of polyhedron (decahedron and icosahedron)-shaped particles formed along with triangles ($\sim 15\%$). When the [AgNO$_3$]/[HAuCl$_4$] ratio in the growth solution was increased to 1.2, extremely uniform ultrathin nanowires were formed (Scheme 5.11). The silver mole percentage in the ultrathin nanowires was determined to be 21 and 14% by EDS and ICP-AES, respectively. The nanowires had a uniform diameter of 1.6 nm and can grow up to several micrometers in length.

In the absence of silver nitrate, spherical gold nanoparticles (Scheme 5.12 a) with a diameter of ~ 40.9 nm and an SPR band at 526 nm (Fig. 5.23, right panel, curve 2) were synthesized [294]. At an intermediate silver nitrate concentration ([AgNO$_3$]/[HAuCl$_4$] ratio of 0.15), small spheres were primarily formed along with a small amount of rods and triangles (Scheme 5.12b), which is also evident in the extinction spectra (Fig. 5.23, curve 3). Note that, for silver seeds, triangular nanoprisms were formed at the same condition (Scheme 5.11b). At a higher [AgNO$_3$]/[HAuCl$_4$] ratio of 1.2, ultrathin nanowires were formed, similarly to the synthesis with silver seed particles (Scheme 5.12c). The silver mole percentage in the ultrathin nanowires was determined to be 21 and 20% by EDS and ICP-AES, respectively, which is similar to the silver content found in nanowires synthesized with silver seeds.

The data presented in Figs. 5.22 and 5.23 reveal that silver seeds play more important role than gold seeds for the high-yield formation of anisotropic triangular nanoprisms. This result was unexpected as silver seeds have a larger size distribution than gold seeds. A small light dot was observed in almost every triangular nanoprism in TEM images, indicating the position of silver seed particles. Similar light dot features were observed in a previous study on the syntheses of gold nanospheres from small silver seeds [295]. The dot area in triangular nanoprisms
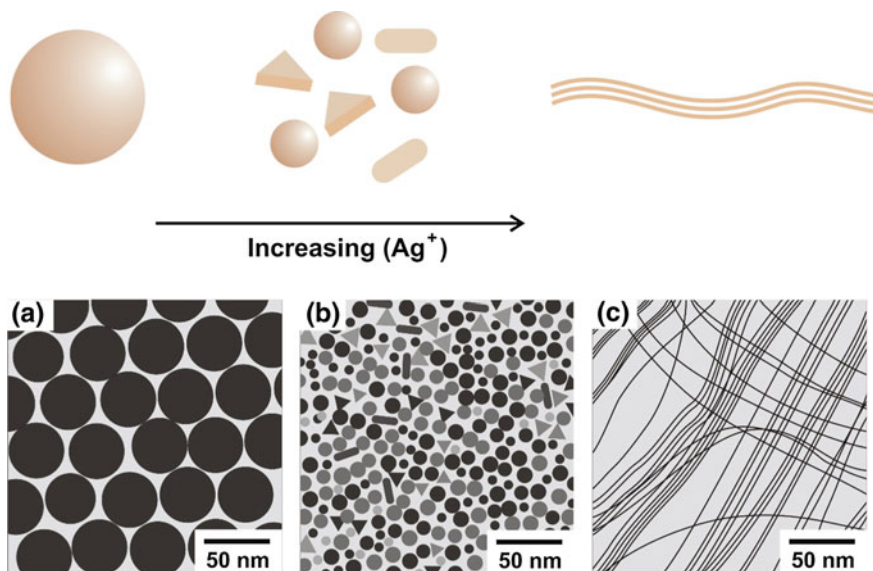
Scheme 5.12 Pictorial description showing the shape of nanoparticles synthesized by the seed-growth method using gold seed particles and BDAC. TEM images of nanoparticles formed at the [AgNO$_3$]/[HAuCl$_4$] ratio of 0 (**a**), 0.15 (**b**), and 1.2 (**c**). TEM images of spheres (*left panel* **a**), spheres, rods, and triangles (*middle panel* **b**) and ultrathin nanowires (*right panel* **c**) [291]

Fig. 5.23 Nanoparticles synthesized by the seed-growth method using gold seed particles and BDAC. Extinction spectra of nanoparticles shown in Scheme 5.12 **a** (*curve 2*, spheres), **b** (*3*), and (**c** *1*, ultrathin nanowires) [291]
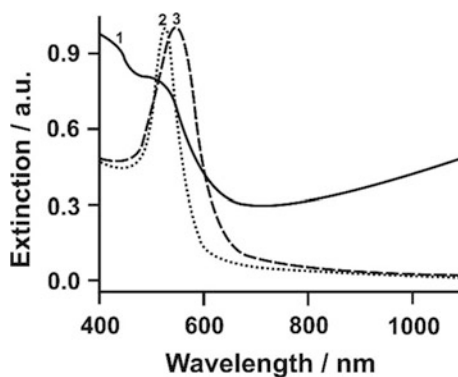
appeared dark in high-angle annular dark field (HAADF) images, as expected. EDS line scan across the dot showed an increase in the silver content and a decrease of gold content in the dot area (Fig. 5.24), which indicates that the initial silver seeds are not completely consumed during the reaction [296].

We attribute the growth of triangles from silver seeds to the relatively more reactive nature of silver compared to gold. In general, silver is more prone to atomic rearrangement than gold due to the relatively lower bond energy compared to that

Fig. 5.24 EDS intensity line
profile for Au Mα (*curve 1*)
and Ag Lα (*2*) peaks [291]
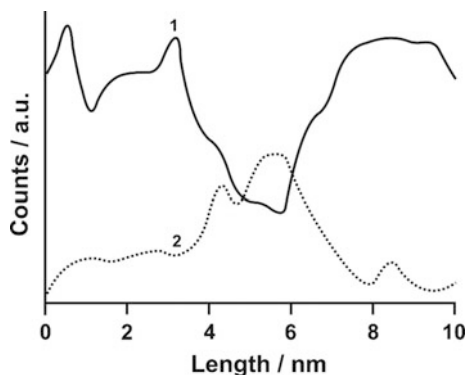
of gold. Also, silver seeds are relatively more reactive than gold seeds, and they can undergo structure reconfiguration and repopulation through various mechanisms such as oxidative etching [297]. In present synthesis, an additional reaction of galvanic replacement can occur between silver seeds and gold complexes upon mixing the seeds and the growth solution [298]. The galvanic replacement reaction can provide a mechanism for atomic rearrangements and facilitate the structure evolution of seeds into planar-twined Ag/Au particles covered with thermodynamically stable (111) facets (Scheme 5.13) [299]. This intermediate structure can grow into thin triangular nanoprisms in the presence of silver nitrate through silver underpotential deposition (UPD) on (111) facets [300], which slows down the growth of (111) facets (Scheme 5.13). The silver ions released from the galvanic replacement reaction can also contribute to the stabilization of (111) facets of the initially formed Ag/Au particles [298]. Gold seeds, on the other hand, generate a mixture of nanoparticles with different shapes due to the lack of shape reconfiguration mechanism. It is worth noting that the quasispherical gold particles formed from silver seeds, and silver-free growth solution shows very little defects, while gold spheres made from gold seeds at the same condition show many defect-induced contrasts. These observations support that silver seed particles can evolve into more stable particles with less defects. Other possible reactions such as oxidative etching of silver by dissolved oxygen can contribute to the defect reduction [297]. However, etching by oxygen did not appear to be the main driving force, as the purging of the reaction media with nitrogen or oxygen gas did not make significant differences in final products.

In the case of silver seeds, the nanowire growth was almost instantaneous. This was not the case with gold seeds (Fig. 5.25, curves 1–6). The fast growth kinetics with silver seeds (slow with gol seeds) was further verified by the sudden initial jump of the extinction in the UV–vis spectra (Fig. 5.25, curves 1 and 2, see also Chap. 2, Scheme 2.13, Figs. 2.5 and 2.6).

The type of surfactant discussed in Chap. 2 was observed to be critical for the formation of highly anisotropic particles. While triangular nanoprisms could be generated with cetyltrimethylammonium chloride (CTAC), the yield of nanoprisms
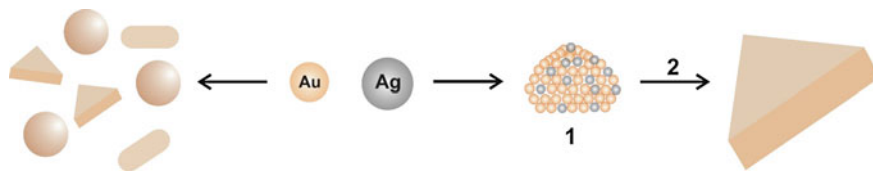
Scheme 5.13 Schematic description showing how silver seeds and gold seeds grow into nanoparticles of different shapes: (*1*) plate-like structure and (*2*) silver UPD [291]
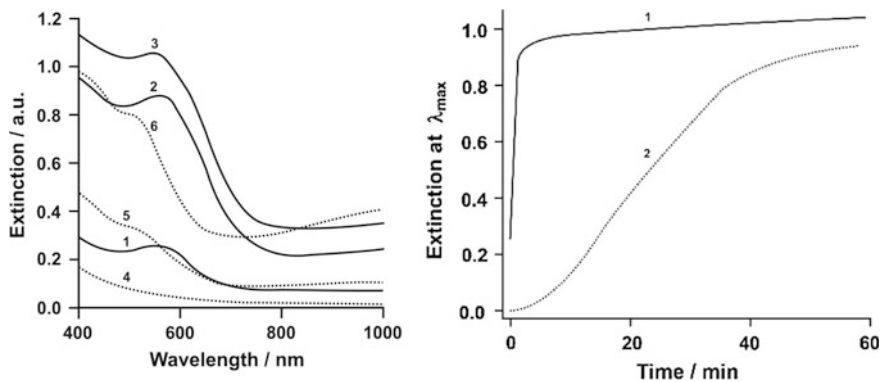
Fig. 5.25 Extinction spectra showing the growth process for Ag seed particles [*curves 1* (1 min), *2* (3), and *3* (60)] and Au seed particles [*curves 4* (1 min), *5* (10), and *6* (60)] (*left panel*). Plot of time-dependent maximum extinction change for the two syntheses shown in (*curve 1*, Ag seed) and (*2*, Au seed) (*right panel*) [291]

was lower and the size distribution was broader with CTAC (Chap. 2, Scheme 2.13, Fig. 2.5). The use of BDAC was particularly important for the formation of nanowires; nanowires were rarely observed in CTAC samples (Chap. 2, Scheme 2.13, Fig. 2.5).

Highly dispersed platinum nanodots (HD-PtNDs) that are densely decorated on gold nanorods (AuNR@PtNDs) with mimetic peroxidase activity were prepared through the seed-mediated growth strategy, which was designed as an active electrode modifier to fabricate the H_2O_2 electrochemical sensor. The synthetic route is shown in Chap. 2 (Scheme 2.14) [301]. Figure 5.26 shows the comparative UV–Vis spectra of PtNPs, AuNRs, and PtNDs-AuNRs. The as-prepared PtNPs had no UV–Vis absorption (Fig. 5.26, curve 1), which was consistent with previous data [302]. The purple AuNRs solution presented two surface plasmon resonance (SPR) bands (curve 2), a strong longitudinal SPR (LSPR) band centered at 760 nm, and a weak transverse SPR (TSPR) at around 512 nm. After PtNDs were decorated on the surface of AuNRs, the LSPR band obviously redshifted, accompanied by a dramatic reduction in intensity and an evident broadening in width (curve 3). The deposition of the PtNDs on the surface of AuNRs was reported to enhance the
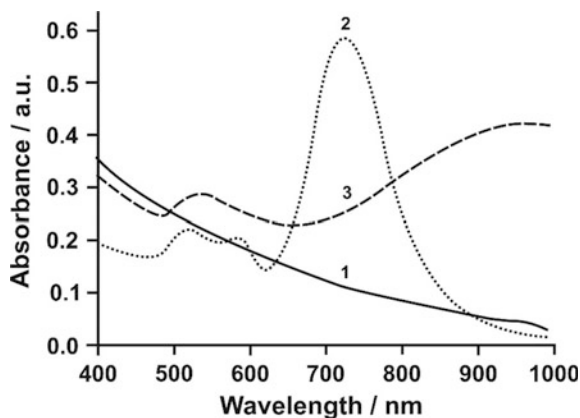
damping to the AuNRs, which led to an obvious redshift of the LSPR band of the AuNRs [70]. These results strongly proved the formation of core@shell nanostructure of AuNR@HD-PtNDs via the above-mentioned as-synthetic route.

Two main peaks (Au and Pt) were observed in the EDX spectrum, indicating a chemical composition of Au and Pt in the core@shell nanostructure. The other peaks (C and Br) that appeared in the EDX spectrum indicated the existence of CTAB on the surface of AuNR@PtNDs nanostructures. The quantitative analysis indicated that the loading amount of PtNDs on AuNRs was 0.21, which was slightly smaller than the theoretical feeding ratio of 0.25.

In a further report, the CTAB was confirmed to be as the most suitable reagent to control the formation of AuNRs [303]. Thus, the CTAB was involved in the synthesis of the AuNRs@HD-PtNDs nanocomposites. Furthermore, the CTAB covered the special lattice plane of the AuNRs though a moderate combination of bromide ion with metal; the long hydrocarbon chains of the absorbed CTAB formed a very stable bilayer on the AuNRs, which acted as the directing agents for growing PtNDs on AuNRs. The interaction between the CTAB and Pt surface was significantly weaker, which offered a possibility to control the morphology and preserve the catalytic activity of the PtNDs [304].

Figure 5.27 shows the corresponding cyclic voltammograms (CVs) of the AuNRs/GCE (curves 1 and 2) and the AuNR@HD-PtNDs/GCE (curves 3 and 4). For the AuNRs/GCE (Fig. 5.27, curves 1 and 2), a (single) oxidation peak at +1.03 V and a reduction peak at +0.45 V were observed, corresponding to the Au oxide formation and its reduction. After the decoration of the PtNDs, typical characteristic hydrogen adsorption/desorption peaks appeared in the potential range of +0.05 V to −0.20 V in the H_2SO_4 solution at the HD-PtNDs-AuNRs/GCE (Fig. 5.27, curves 3 and 4). The difference of the surface information between the AuNRs/GCE and AuNR@HD-PtNDs/GCE strongly proved the formation of the core@shell nanostructures.

The redox probe $Fe(CN)_6^{3-/4-}$ was sensitive to the surface chemical of the electrode, which was utilized to evaluate the electrochemical properties of the

Fig. 5.27 CVs of AuNRs/GCE (*curves 1* and *2*) and HD-PtND/AuNRs/GCE (*curves 3* and *4*) in the N$_2$-saturated H$_2$SO$_4$ solution [301]
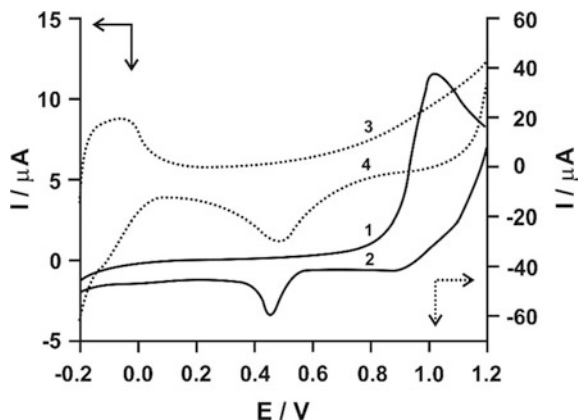
AuNRs/GCE and AuNRs@HD-PtNDs/GCE. An enhanced current response of Fe $(CN)_6^{3-/4-}$ was observed at the AuNR@HD-PtNDs/GCE than that of AuNRs/GCE, indicating an effective increase in the electroactive surface area by modifying the AuNR@HD-PtNDs on the GCE. The decoration of the PtNDs on the surface of the AuNRs effectively enlarged the electroactive surface areas of the modified electrode.

The situation for the assembly of heterodimer structures is a very different and further synthetic route. While a plethora of methods for synthesis of NPs of different sizes, shapes, and materials exist [305], just a few methods for controlled assembly of nanoparticles into well-defined heteroaggregates have been established [306]. Specifically, the selective formation of heterodimers from NPs of different materials remains a challenging goal. Chen et al. [307] synthesized bimetallic nanostructures by using nanoscopic phase separation of different metals due to the embedment of surface ligands. Pietryga et al. [308] described the synthesis of quantum dot–dielectric–metal hybrids where a silicon shell on top of the gold nanostructure was used to attach quantum dots.

Gschneidtner et al. [309] have developed a versatile synthetic strategy for combining two different metal nanoparticles (of the same metal or two different metals) via electrostatic interaction. By using oppositely charged particles, heterodimer combinations of individual nanoparticles of different sizes, shapes, and compositions, as exemplified in Scheme 5.14, were obtained. The aggregation process can be controlled to produce the highest possible yield of dimers by tuning the ratio between the two kinds of NP components.

Starting from two classes of nanoparticles, here called NP-A (negatively charged) and NP-B (positively charged), controlled aggregation can be achieved by tuning the experimental conditions (Scheme 5.15).

Class NP-A constitutes negatively charged nanoparticles capped by MESNa in trisodium citrate (90 nm). The second class, NP-B, is composed by NPs capped with a cationic surfactant CTAB or chloride (CTAC). The controlled electrostatic self-assembly of NP heterodimers can occur only under experimental conditions
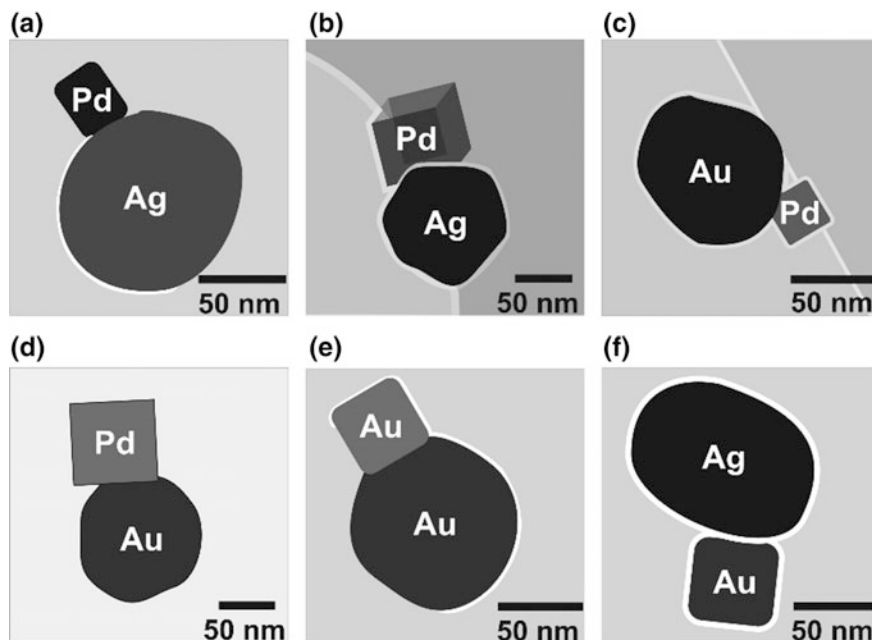
Scheme 5.14 TEM images of different nanoparticle heterodimers prepared by electrostatic self-assembly: **a** Ag (spherical$_{90\ nm}$) and Pd (cube$_{25\ nm}$); **b** Ag (spherical$_{90\ nm}$) and Pd (cube$_{70\ nm}$); **c** Au (spherical$_{90\ nm}$) and Pd (cube$_{25\ nm}$); **d** Au (spherical$_{90\ nm}$) and Pd (cube$_{70\ nm}$); **e** Au (spherical$_{90\ nm}$) and Au (cube$_{35\ nm}$); and **f** Ag (spherical$_{90\ nm}$) and Au (cube$_{35\ nm}$) [309]

that guarantee the mutual stability of the two kinds of nanoparticles used. It was observed that the presence of cationic surfactants destabilizes the negatively charged NP-A. Similarly, positively charged NP-Bs are destabilized by citrate, which is negatively charged. For this reason, in a wide range of capping agent concentrations, each type of NP is incompatible with the capping agent of the other type. In order to facilitate the differentiation between heterodimers and self-aggregates, NP-A and NP-B were combined with distinctly different shapes and sizes (Scheme 5.14, panels a–f). The average gap between the NPs in the heterodimers was found to be between 0.8 and 1.9 nm, suggesting that these structures can be used in sensing and plasmonic applications. The maximum yields of heterodimers were ranging from 30 to 40% for the combinations of NPs investigated. The self-assembly of Pd-NPs particles with Au spheres (NP-A) into heterodimers was successful with yields of about 30%. In high-magnification SEM images, the three-dimensional features of the Pd surfaces can clearly be observed.

The surface potential data suggest that the absolute value of the surface electric potential of NP-A is reduced in the presence of cationic surfactant molecules, leading to destabilization of the colloidal solution if the concentration of surfactant is sufficiently high. Similarly, the zeta potential for NP-B is decreased by addition of citrate ions. Combining these two results, we can infer that the appropriate ratio
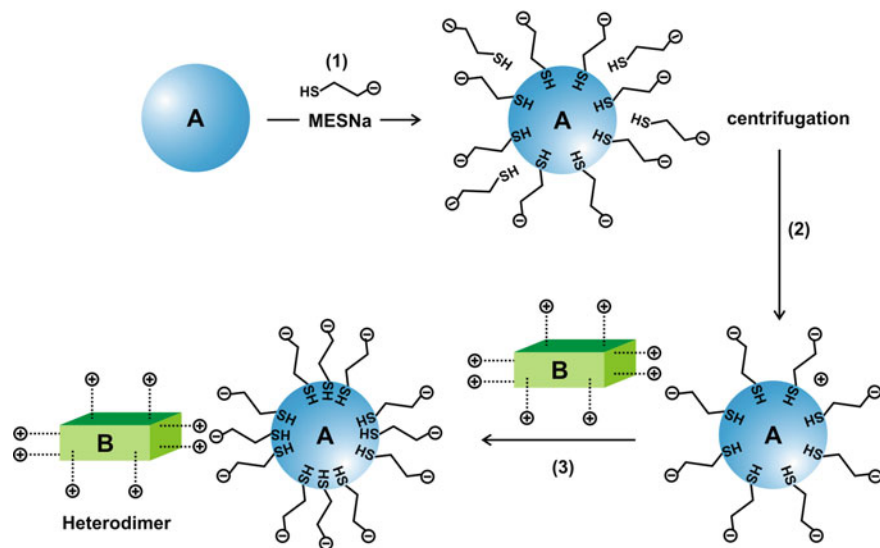
Scheme 5.15 Synthetic procedure used to prepare NPs heterodimers via electrostatic interactions. *Step 1* Functionalization of NP-A with sodium 2-mercaptoethanesulfonate (MESNa) through ligand exchange. *Step 2* Purification of functionalized NP-A from excess of coating agent by centrifugation. *Step 3* Controlled self-assembly of NP-A and NP-B through electrostatic interactions [309, 310]

between the particle stabilizers, CTAB/CTAC and citrate, leads to conditions in which both kinds of nanoparticles are stable. It is generally accepted that there is a minimum residual concentration of surfactant needed to achieve stability of CTAB or CTAC-capped nanoparticles [311]. At the same time, according to stability experiments, there is also a maximum concentration threshold of cationic surfactant above which negatively charged NP-A colloids undergo self-aggregation. Considering the concentration of citrate, there is also a maximum concentration of this salt above which the NPs stabilized by cationic surfactants become unstable. Therefore, we can define a stability concentration zone in which NP-A and NP-B are both stable. For the case of Au sphere$_{90\ nm}$ with Pd cube$_{25\ nm}$, the stability zone is very narrow and is delimited by the stability curve of AuNPs and Pd-NPs (Fig. 5.28, curves 1 and 2) at different concentrations of citrate and CTAB, respectively. Dimer formation area is the stability-phase diagram of the binary system of NPs as a function of the concentrations of their respective stabilization agents. Controlled self-aggregation occurs only within the stability zone, and therefore, the determination of these experimental conditions is crucial to achieve high yields of dimeric structures formed by electrostatic self-assembly.

The colloidal solution-phase diagrams presented in Fig. 5.28 can be rationalized considering the interaction energy involved in self- and heteroaggregation processes. Since van der Waals and London forces are short-range attractive
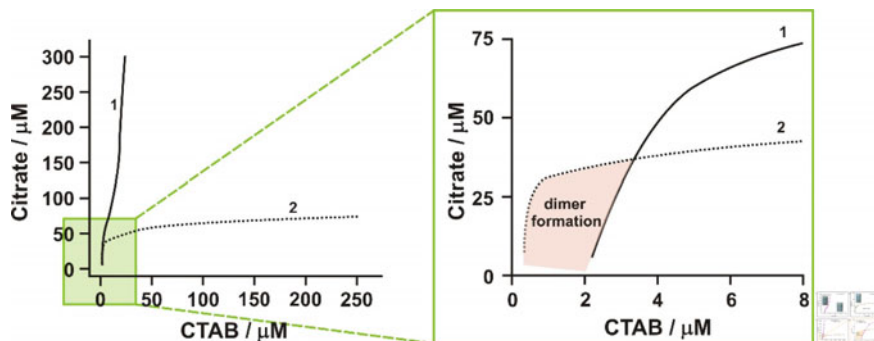
Fig. 5.28 Stability-phase diagrams as a function of concentration of capping agents for (*curve 1*) Au sphere$_{90 \text{ nm}}$, (2) Pd cube$_{25 \text{ nm}}$, and the combination of Au sphere$_{90 \text{ nm}}$ and Pd cube$_{25 \text{ nm}}$. Detailed view of the stability zone (the *green square* or *pink area*) [309]

interactions, the electrostatic potential energy constitutes the long-range driving force for the formation of aggregates for NPs of different charge (heteroaggregates) and generates the energy barrier for aggregation of NPs of the same charge (homoaggregates). This is the situation it was observed within the stability zone leading to controlled self-assembly. Conversely, if the electrostatic repulsion potential is not enough to create an aggregation barrier higher than the thermal energy, the system undergoes massive aggregation, as observed experimentally outside the stability zone in Fig. 5.28.

The next analysis provides additional information regarding the specific conditions that lead to controlled self-assembly. The homopair interaction profiles describe predominantly repulsive interactions for large interparticle distance, accounting for the dominant effect of the electrostatic contribution (Fig. 5.29, curves 5 and 6). For short distances, the potential energy for homodimers reaches a maximum and drops into the attraction regime due to the van der Waals forces operating at short range. The energy barrier for homoaggregation is higher than the thermal energy for both kinds of NPs, and for this reason, under present experimental conditions, the formation of aggregates of the same kind of particles is disfavored. Conversely, the heteropair interactions are predominantly attractive at every distance (Fig. 5.29, curves 1 or/and 2); therefore, the formation of heteroaggregates has no energy barrier and occurs spontaneously. Furthermore, considering that the depth of the attractive potential at short distances is more than $10 \text{ k}_B\text{T}$, the aggregation process can be considered irreversible. Hence, in this case, the formation of aggregates can be understood as a kinetic process that is controlled by the collision rate of the nanoparticles in the solution.

The electrostatic self-assembly of two kinds of oppositely charged nanoparticles should predominantly lead to the formation of heteroaggregates. In principle, the number and composition of these heteroassemblies of NPs depend on the entity of the interactions involved and on the density number of each kind of particle in solution. The analyzed TEM and SEM images of the samples produced by
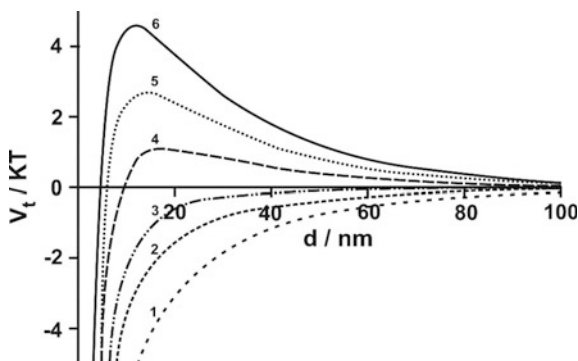
Fig. 5.29 Interaction energy versus interparticle separation for representative NPs: (*curves 4–5*) homodimer Pd cube$_{25\ nm}$ with Pd cube$_{25\ nm}$; (*6*) homodimer Au sphere$_{90\ nm}$ with Au sphere$_{90\ nm}$; (*1–2*) heterodimer Au sphere$_{90\ nm}$ with Pd cube$_{25\ nm}$; The *curves 1–6* describe the composition of the multimers considering one NP-A (Au sphere$_{90\ nm}$) and different numbers of NPs B (Pd cube$_{25\ nm}$) [309]

self-assembly experiments showed populations of aggregates containing different numbers of NP-A and NP-B (Scheme 5.15). For all the combinations of nanoparticles investigated here, the fraction of homoaggregates was very low, reflecting the repulsive nature of the interactions among NPs of the same type. Similarly, more than 95% of the NP heteroaggregates in the samples contained only one NP-A. These results are supported by the analysis of the repulsion energy barriers for Au spheres$_{90\ nm}$ and Pd cubes$_{25\ nm}$, suggesting that homoaggregates and heteroaggregates containing more than one NP-A are energetically disfavored. Taking these facts into account, three statistical classes of clusters based on aggregates containing one NP-A were defined (Scheme 5.16).

The first class is called "singles" and consists of isolated NP-As. The second class is heterodimers, containing one NP-A and one NP-B. The third class accounts for small aggregates containing one NP-A and more than one NP-B, here called multimers.

Representative yields for the three classes of aggregates, in self-assembly experiments using different ratios of NP-B and NP-A, are presented in Fig. 5.30. Aggregates containing more than one NP-A were considered large aggregates and
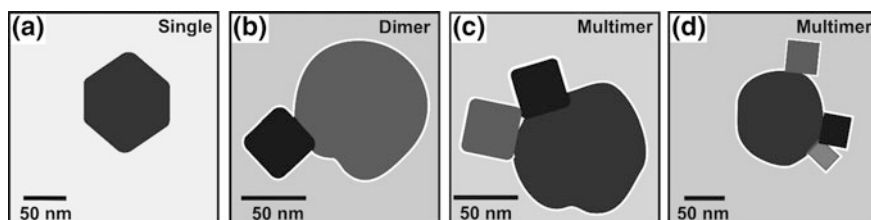
Scheme 5.16 TEM-like images of representative single, dimer, and multimers [309]
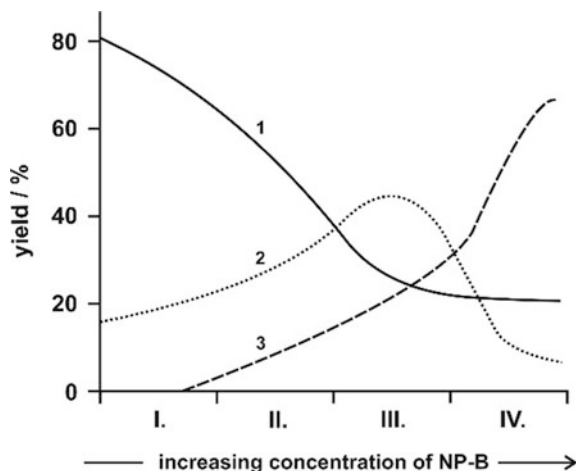
counted separately. For the NP combinations investigated here, these large aggregates accounted for less than 5% of the populations. Using this approach, a broad range of concentrations of NPs was explored in order to determine the concentration ratio for NP-A and NP-B leading to the highest yield of heterodimers for each combination of NPs. Considering, for example, the combination of spherical AuNPs (sphere$_{90 \text{ nm}}$, NP-A) and Pd nanocubes$_{25 \text{ nm}}$, (NP-B), single AuNPs were mostly observed for low concentrations of palladium cubes (Fig. 5.30). Increasing the concentration of palladium cubes, a highest yield of 43% dimers was obtained. Further increase of the concentration of NP-B leads to larger amounts of multimeric structures in which several Pd-NPs surround the spherical AuNP.

5.3.5 TiO$_2$-Based Nanostructures

TiO$_2$ is the most promising material in the field of photocatalysis because of its superior photocatalytic activity, chemical stability, low cost, and nontoxicity. As such, its performances in photocatalytic degradation of chemical pollutants and solar energy conversion have been widely studied in the past decades, and its practical application has been seriously considered [312]. TiO$_2$ assembled with noble metal nanoparticles has received much attention because such a hybrid can effectively separate the charges and redshift the absorption to visible light via plasmonic resonance [313]. For example, Awazu et al. combined TiO$_2$ and Ag core/SiO$_2$-shell nanoparticles in a heterostructure, and the photocatalytic activity was enhanced by a factor of 7 under near-ultraviolet (NUV) irradiation [314]. TiO$_2$ assisted by the localized surface plasmon resonance (LSPR) is promising in applications such as photocatalysis [313], photovoltaic cells [315] reversible imaging [316], LSPR sensors [317]. Since Haruta' seminal discovery [261] in the

1980s of CO oxidation by O_2 to CO_2 at low temperature using TiO_2-supported gold nanoparticles that are smaller than 5 nm, these oxide-stabilized AuNPs are widely studied in catalysis for aerobic oxidations of various substrates including alcohol oxidation, CO oxidation, and hydrolytic dehydrogenation and for hydrogenation reactions [262, 264].

Under UV light, electrons in the valence band of TiO_2 are excited to the conduction band, resulting in generation of holes in the valence band. It is known that Ag^+ ions are reduced by the excited electrons of TiO_2 to silver nanoparticles [318]. It is also known that silver nanoparticles absorb visible light of various wavelengths due to surface plasmon resonance and that the wavelength depends on particle size, particle shape, and local-refractive index. Thus, the brownish-gray color of the Ag-TiO_2 film should be ascribed to silver nanoparticles with various sizes and shapes deposited in the nanopores of the TiO_2 film. These nanoparticles can absorb the light of different wavelengths, and the characteristic broad absorption band appears in the visible range. When the brownish-gray film is irradiated with a colored light, the absorption at around the excitation wavelength decreases. Thus, an "absorption hole" is formed. This is probably because electrons of AgNPs are excited only when they are irradiated with the light of their resonance wavelength. The excited electrons transfer to oxygen in air, and thus the silver nanoparticles are oxidized to colorless Ag^+ ion. As a result, only the light of the excitation wavelength is reflected or transmitted, while the remaining particles absorb the lights of the other wavelengths. Thus, the color corresponding to the excitation wavelength appears [316].

Naoi et al. have also reported that Ag-TiO_2 material can display various colors by irradiating the thick film with various excitation lights [319]. Thus, silver nanoparticles of various sizes and shapes should be prerequisite to displaying various colors. Furthermore, nanopores of various sizes and shapes present in the TiO_2 films act as molds for silver nanoparticles with various sizes and shapes. We call this a "molding effect". If this effect holds, the nanopores may determine sizes, shapes, and thereby resonance wavelengths of AgNPs. A specific nanopore may produce silver nanoparticles with the same specific resonance wavelength repeatedly, in repeated writing–erasing cycles. Various nanoparticles are generated under UV light. Assume that this sample is irradiated with green light. Only the Ag nanoparticles that absorb the green light are excited. The excited electrons are transferred to oxygen, and the nanoparticles are oxidized to Ag^+ ion. As a result, the Ag-TiO_2 film turns green, since the green light is not absorbed but reflected (or transmitted). In this case, if the Ag^+ ions generated during the green light irradiation are removed, the film should stay green even if it is irradiated with UV light. If this sample is irradiated with white light, all the Ag nanoparticles left are also photooxidized to Ag^+ ions, and the film becomes colorless. In this stage, the nanopores that produce silver nanoparticles absorbing green light contain no Ag^+ ions. Therefore, even when the film is irradiated with UV light again, silver particles that absorb green light may not be formed, while the other particles, which absorb blue and red lights, are generated. Thus, the film turns green again. The color information is kept as a "latent image," although the film is colorless. However, if the

molding effect does not hold, regenerated particles are not specific, and the film should turn brownish-gray under UV light.

It is assumed that the silver nanoparticles are formed at the gas–solid interface between TiO_2 and air. Herein, the Ag nanoparticles are probably in contact with not only TiO_2 but also air. The absorption wavelength is redshifted as the refractive index increases [320]. Therefore, the absorption wavelength of the Ag nanoparticles would depend on the local composition of the matrix, namely, the TiO_2/air ratio. This might be one of the origins of the diversity in the absorption wavelengths of the Ag particles. If so, the absorption wavelength should be redshifted, when the air filling the vacant nanospaces is replaced with a solvent whose refractive index is higher than that of air. An absorption hole generated by a colored light should also be redshifted. However, if no shift is observed, we should conclude that the Ag nanoparticles are surrounded only by TiO_2. To examine this, the thin Ag-TiO_2 film in brownish-gray was irradiated with a blue light, and the film was impregnated with ethanol (refractive index = 1.36). This redshifted the absorption hole by about 30 nm. As the ethanol was evaporated, the absorption hole reverted to the original wavelength again. A larger peak shift (by about 50 nm) was observed when quinoline (refractive index = 1.63) was used instead of ethanol. Such solvatochromic characteristics indicate that the absorption wavelength of the silver nanoparticles before the impregnation depends not only on the refractive index of TiO_2 but also on that of air. The particles must be in contact with TiO_2 and air at various ratios. The diversity in the ratio should contribute to the diversity in the resonance wavelength of the AgNPs to some extent. These results suggest that chromogenic properties of this material can be controlled by tuning the refractive index of the matrix. Also, the present solvatochromic property might be exploited for new functions, such as optical sensing of chemical species.

A controlled growth of silver nanoparticles on TiO_2 templates is expected in tuning the optical response of the Ag–TiO_2 hybrids. The photocatalytic growth of anisotropic AgNPs on the nanoparticulate TiO_2 films in the $AgNO_3$ ethanol solution was reported, and the vertical growth of silver nanoplates was attributed to the surface roughness and random features of the substrate [321]. Using an annealed single-crystalline TiO_2 substrate, Kazuma et al. [322] reported the bi- and uniaxially

Fig. 5.31 The size distribution of AgNPs grown on fresh TiO_2 films in the $AgNO_3$ solution (3200 mg/dm^3) varies with time (min) as follows : *1* (10), *2* (16), *3* (30), and *4* (60) [324]
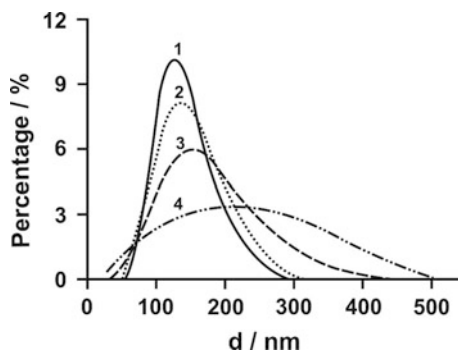
oriented growth of AgNPs. They found that the preferential orientation and morphology of these AgNPs depend on the presence of ethanol, acetaldehyde, and UV exposure conditions. Similar to the previous report [323], the AgNPs on the fresh films show the irregular spherical shapes of isotropic growth, irrespective of the $AgNO_3$ concentration (Fig. 5.31) [324].

The growth behavior of silver nanoparticles on the oil-decorated TiO_2 films was varied. In the initial growth stage, AgNPs show sphere-like shapes that are similar to those grown on the fresh films, but their sizes are smaller. By increasing the growth time to 2 and 4 min, the anisotropic AgNPs, or the small Ag nanoplates, appear in the products. At 8-min growth time, the well-defined Ag nanoplates, upright standing or tiled, were popularly observed in the product. The formation of Ag nanoplates is likely due to the aggregation of the primary particles (nuclei) in the nucleation stage. As indicated by the circles in the figure, the spherical AgNPs in some regions aggregate together or form Ag nanochains, and then the small silver nanoplates are gradually developed to be the perfect regular triangles or hexagons. Such nanoplates have three major LSPR modes, namely, out-of-plane mode and in-plane longitudinal and transverse modes, and respond selectively to light polarized in a specific angle. Thereby, the silver nanoplates can be applied to the fields such as stereoscopic visions, storing multiple information, certification, and anticounterfeit technologies and polarizers [325]. Using the upright standing and the tiled Ag nanoplates, the thickness of the Ag nanoplates was estimated to be 30–40 nm, whereas the lengths of their edges ranged from 0.1 to 1 μm. TEM analysis reveals that the silver nanoplates are faced with (111) planes. The above results indicate that the oil-decorated TiO_2 films successfully induce the anisotropic growth of AgNPs.

With an increase in the growth time, the feature size of the distribution does not obviously increase, but the percentage of large AgNPs increases considerably, forming a distribution tail, as shown in Fig. 5.32 (left panel, curve 3–5). This type of evolution is much different from that of AgNPs on the fresh films. When compared with the SEM images, the feature sizes were found to be determined by the distributions of irregularly spherical AgNPs in the products, and the appearance of the silver nanoplates results in the formation of distribution tails. Because the feature size was not increased by increasing the growth time, it was concluded that the isotropic growth of AgNPs on the oil-decorated films is restrained. The change in growth behavior was also observed in the in situ extinction spectra, as shown in Fig. 5.32 (right panel). The extinction intensities in the visible region slowly increase by increasing the growth time, whereas the extinction in the NIR region is quickly enhanced. The small peak at ∼340 nm, which was first observed at 8 min, is due to the out-of-plane quadrupole resonance of the Ag nanoplates in $AgNO_3$ solution, and the peak position is associated with the thickness of the Ag nanoplates [326]. According to the effective medium theory [327], isotropic AgNPs contribute to the extinction in the visible region, and Ag nanoplates give rise to an enhancement of the extinction in the NIR region. Thus, it is concluded that the oil-decorated films play a role in restraining the isotropic growth of the AgNPs.
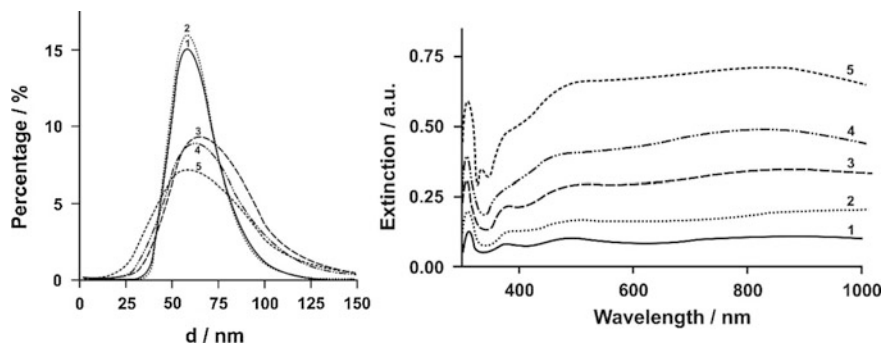
Fig. 5.32 Size distribution of AgNPs grown on the oil-decorated TiO_2 films in the $AgNO_3$ solution (3200 mg/dm³) *curve 1* (1 min, 58 nm), *2* (2, 58), *3* (4, 63), *4* (8, 60), and *5* (16, 59) (*left panel*) and the corresponding extinction spectra (*right panel*) [324]

The silver nanoplates in the product were found to be dependent on the oil-decoration time of the TiO_2 film. The number of silver nanoplates increases with an increase in the oil-decoration time until 4 min, and then no obvious difference is observed. In addition, it was reported that a shorter time of oil decoration leads to the production of smaller Ag nanoplates. Besides the oil-decoration time, the $AgNO_3$ concentration is found to be important in determining the formation of Ag nanoplates on the oil-decorated films. Ag nanoplates cannot be synthesized in the $AgNO_3$ solution below 200 mg/dm³. In $AgNO_3$ solutions with concentration >400 mg/dm³, the density of the Ag nanoplates increases with an increase in the $AgNO_3$ concentration, indicating that a critical $AgNO_3$ concentration is required for the formation of Ag nanoplates on the oil-decorated films. The critical concentration is necessary to induce the formation of Ag nanoplates on the oil-decorated films, irrespective of the decoration time.

First, two kinds of AgNPs, isotropic nanoparticles ($\sim$ 60 nm size) and anisotropic nanoplates (30–40 nm thickness), were obtained using the oil-decorated films. However, the initial nucleation of AgNPs on the oil-decorated films is similar to that on the fresh film except that the size of the primary particle is smaller. According to the nucleation theory of crystal growth [328], high supersaturation of the neutral atom leads to the small size and high density of the primary particles (nuclei). Thereby, the formation of Ag nanoplates is related to the increase in the density of Ag atoms. In other words, the reduction rate of Ag atoms on the oil-decorated films is likely higher than that on the fresh film. The critical $AgNO_3$ concentration for the formation of Ag nanoplates also suggests that the anisotropic growth needs a high Ag reduction rate, which is proportional to the concentration of Ag ions in solution. The increase in the Ag reduction rate can be attributed to the efficient charge separation of photocatalysis due to the introduction of the oil layer on TiO_2 films. As is well known, two kinds of photo-induced carriers, electron and hole, are generated in the TiO_2 film and are transferred to its surface. The electron reduces the ions in solution, and the hole oxidates the neutral particles into ions.

Thus, the reoxidation of the reduced Ag atoms decreases the Ag reduction rate. The oil layer on the TiO$_2$ film is the substitute for the reduced Ag atoms. Because the Ag atoms avoid reoxidation with the oil layer, the net reduction rate of the Ag atoms is increased.

Second, it was reported that most of the Ag nanoplates pile up over each other or lay over the irregularly shaped AgNPs. In addition, these Ag nanoplates are mobile and easily stripped from the substrates. These observations suggest that the formation of Ag nanoplates likely took place in the area adjacent to the film surface, and they adhered to the surface when they were taken out from the solution. On the basis of the given observation, the authors suggest a scenario for the growth of AgNPs via photocatalytic reduction with TiO$_2$ film, as shown in Scheme 5.17. Considering Ag atom mobility and reoxidation, a specific Ag atom distribution is suggested. Depending on the nucleation free energy and the supersaturation, self-nucleation (homogeneous nucleation) in the solution and heterogeneous nucleation on the film surface are both possible. After nucleation, the AgNPs grow through two mechanisms, Ostwald ripening (OR, Scheme 5.18) and oriented attachment (OA). The OR mechanism often leads to an isotropic growth, whereas the OA mechanism results in the formation of nanoplates, nanorods, and nanosheets, etc. Thus, the formation of the Ag nanoplates is likely related to the OA growth.

The oriented attachment (OA) mechanism is a particle-mediated mesoscopic transformation process [329] and has been demonstrated to be one of the important mechanisms leading to the anisotropic growth of AgNPs in solution-phase synthesis. Yin et al. [330] found that both OA and OR mechanisms coexist in the growth of nanoparticles. At the initial stage, increasing the concentration of the primary particles facilitates the OA-based growth, and the OR growth is restrained. The HRTEM observation also implies that the OA growth is likely responsible for the formation of Ag nanoplates on the oil-decorated films. The contacted AgNPs
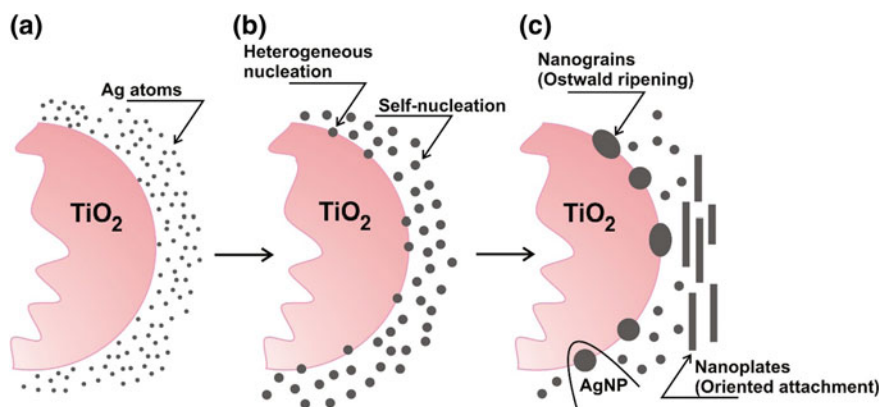
Scheme 5.17 Photocatalytic growth model of Ag NPs in AgNO$_3$ solution with TiO$_2$ films **a** reduction of Ag atoms, **b** nucleation of Ag primary particles, and **c** formation of AgNPs or nanoplates [324]
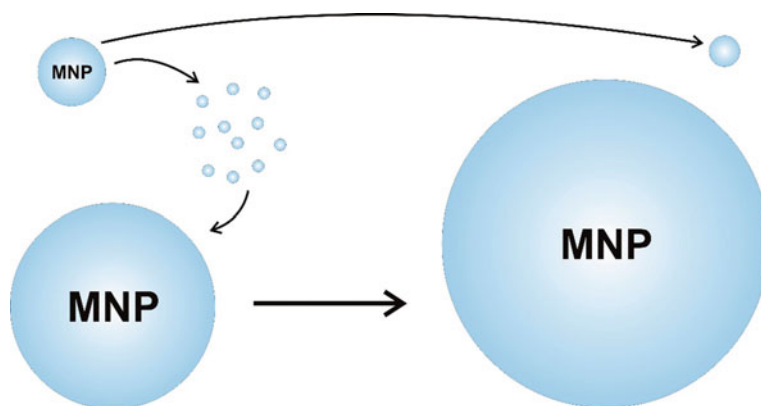
Scheme 5.18 Ostwald-ripening mechanism [324]

exhibit the lattice spacings of 0.24–0.25 nm, which are closed to the spacing of Ag (111) plane (0.2361 nm). Similar AgNPs in contact were never observed on the fresh films. In the in situ HRTEM study of crystal growth controlled by the OA mechanism in solution-phase synthesis [331], Li et al. [324] took a series of TEM images of the NPs in contact, which are interpreted as the particles undergoing continuous rotation and interaction before they find a perfect match.

Using TiO_2 films as the photocatalytic reduction media, the Ag^+ ions in the $AgNO_3$ solution are reduced on TiO_2 films under UV irradiation, forming TiO_2-catalyzed AgNP films, which have been used as the substrates for surface-enhanced Raman scattering [323]. AgNPs synthesized by photocatalytic reduction generally exhibit irregular sphere-like shapes. The photocatalytic growth of anisotropic AgNPs on the TiO_2 films in the $AgNO_3$ ethanol solution was reported, and the vertical growth of Ag nanoplates was attributed to the surface roughness and random features of substrate [321]. Using an annealed single-crystalline TiO_2 substrate, Kazuma et al. reported the bi- and uniaxially oriented growth of AgNPs [322]. The preferential orientation and morphology of these AgNPs were found depending on the presence of ethanol, acetaldehyde, and UV exposure conditions.

Figure 5.33 and Scheme 5.19 show the typical morphology of isotropic AgNPs, which were grown in the $AgNO_3$ solution. The SEM images show that the AgNPs at the growth time of 2, 4, 8, 16, and 120 min exhibited irregularly spherical shapes. At a 2-min growth time, the AgNPs are ~ 27 nm of average size and $\sim 4 \times 10^9/cm^2$ of density (Fig. 5.33, left panel, curve 1). When increasing the growth time to 4 min, the AgNP density dramatically reduced to $\sim 2.3 \times 10^6/cm^2$, and the size increased to ~ 97 nm (curve 2), indicating that the coalescence process took place between silver primary particles at a growth time in between 2 and 4 min. By fitting the time dependence of average size (d) after the coalescence phenomenon, the dependence
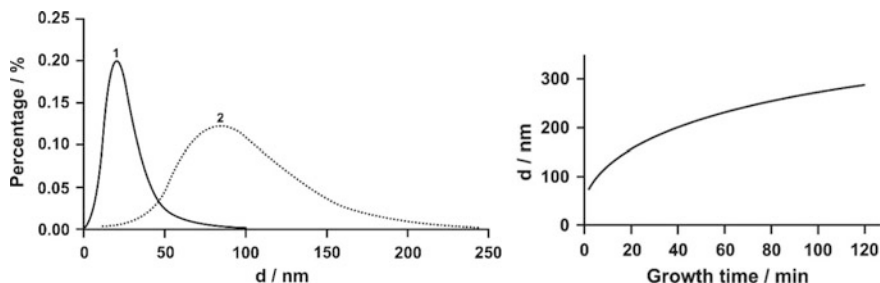
Fig. 5.33 The size distributions of AgNPs, *curve 1* (2 min) and *2* (4) (*left panel*), and growth-time dependence of AgNP size (*right panel*) [333]
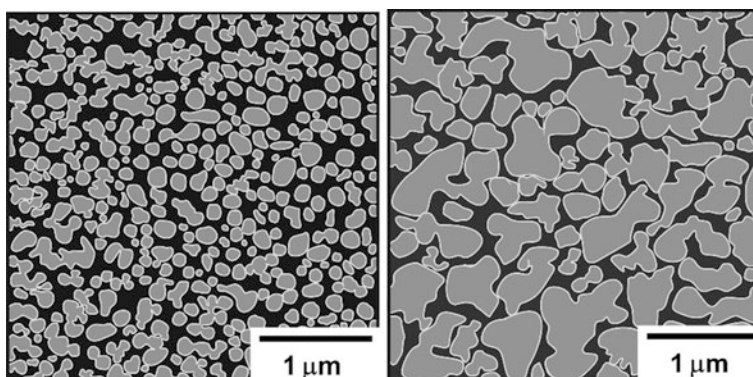
Scheme 5.19 SEM images of Ag–TiO$_2$ films grown in 180 mg/L AgNO$_3$ solution at the growth time of 2–120 min [321, 322]

$$d^3 \propto t \qquad\qquad (5.6)$$

was observed. Such a relationship is an indication of diffusion-limited growth. In other words, Ostwald ripening [332] dominates the coarsening process of AgNPs.

As shown in Fig. 5.34 (left panel), extinction peak, which is associated with Ag primary particle density and size, appeared at $\sim$400 nm. By plotting the extinction intensity at $\sim$400 nm as a function of growth time, as shown in Fig. 5.34 (right panel), the formation of silver primary particles was extrapolated to a time as early as <1 s after the photocatalytic beginning (the extinction was defined by $\ln(I_0/I)$, where I_0 is the transmitted intensity before photocatalytic reduction and I is the intensity during photocatalytic reduction). The extinction spectra show that the number of AgNPs is increasing with the irradiation time, whereas the change in sizes is not obvious. The formation of silver primary particles originates from supersaturated silver atoms, which are related to the photocatalytic reduction ability of TiO$_2$ films.
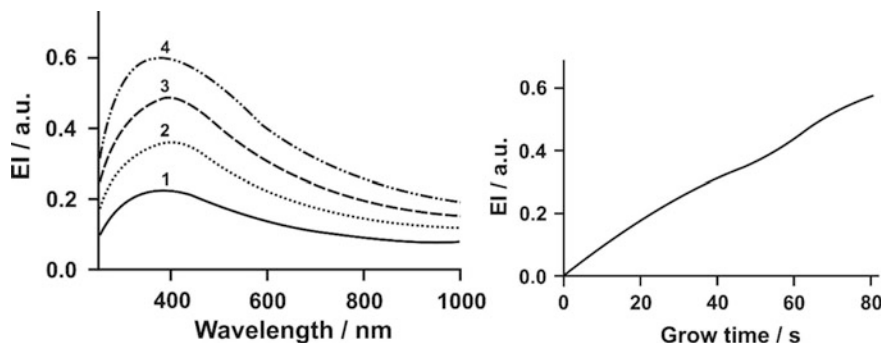
Fig. 5.34 In situ extinction spectra of AgNPs grown in 180 mg/dm³ AgNO₃ solution from the photocatalytic beginning to 80 s (*left panel*). Growth-time dependence of extinction intensity (EI) at ∼ 380 nm (*right panel*) [333]

By increasing the AgNO₃ concentration, it was found that the increased Ag reduction rate gave rise to a change in AgNP growth, resulting in the formation of Ag nanoplates in the product. A large amount of thin Ag nanoplates were produced at the growth time as early as 2 min. The silver nanoplates were ∼ 10 nm thick and 0.1–1 µl of edge length. With an increase in the growth time, the sizes of Ag nanoplates were not varied obviously, but the thickness increased. TEM analysis shows that the nanoplates are faced with Ag (111) planes. At a 120-min growth time, the Ag nanoplates were rarely observed, instead evolved into three-dimensional AgNPs with the well-defined shapes, which are a little different from the irregular AgNPs grown in the 180 mg/L AgNO₃ solution. The SEM images reveal that the increased AgNO₃ concentration promoted an early coalescence resulting in the formation of Ag nanoplates. SEM images show that Ag nanoplates and irregularly spherical AgNPs were co-existed in the photocatalytic growth using 2800 mg/L AgNO₃ solution, whereas the isotropic growth of AgNPs was restrained. The Ag reduction rate in 2800 mg/L AgNO₃ solution was estimated to be ∼ 2 × 10¹⁴ cm⁻² s⁻¹, which is ∼ 10 times of that in 180 mg/L AgNO₃ solution. Therefore, it was concluded that the increased reduction rate promotes the formation of Ag nanoplates and their applications [334].

To understand the formation mechanism of AgNPs and Ag nanoplates, a growth model was proposed by taking Ag atom and Ag⁺ ion diffusion into consideration [328]. The growth model can explain the phenomenon of Ag nanoplates lying on the small AgNPs [333]. On the other hand, the growth model is consistent with the conclusion of Yin et al. that the OA growth is facilitated in high-density primary particles [330]. Similarly, the formation of Ag nanoplates using AgNO₃ ethanol solution [335] or using oil-decorated TiO₂ films [324] can also be attributed to the increase in the silver reduction rate due to the photodegradation of organic molecules. It should be emphasized that the growth model suggested the importance of surface roughness in the formation of Ag nanoplates, which is consistent with the observation of Tanabe et al. that the growth of Ag nanoplates was related to the

surface roughness and random features of substrate [335]. According to the growth model [333], a smooth TiO_2 film facilitates the formation of large-scale Ag nanoplates.

With an increase in the growth time, the UV peak was blueshifted and the blue–green peak was redshifted (Fig. 5.35 exhibits a UV extinction peak at ∼380 nm and a blue–green extinction peak at ∼450 nm). The two extinction peaks are very like the quadrupole and dipole resonances of Ag spheroids [280]; however, they are more likely due to a combination of factors because visible quadrupoles require extreme size, shape, and external medium regularity in a typical macrogeometry which averages over thousands of particles. In other words, the extinction spectra are the hybridized plasmon response of the complex nanostructures [336] or due to an asymmetric dielectric environment [337]. When increasing the growth time, the extinction peak at ∼380 nm was rapidly enhanced, and the extinction peak at ∼450 nm was weakened. The extinction peak at ∼450 nm was no more observed for the Ag–TiO_2 film at a 120-min growth time.

For the Ag–TiO_2 film grown in the 2800 mg/L $AgNO_3$ solution at 2-min growth time, the extinction spectrum is something like that of a smooth and compact Ag film, and no particle-like extinction peak was observed, as shown in Fig. 5.35, indicating that the Ag nanoplates with various sizes dominate the extinction of the Ag–TiO_2 film. With the increase in the growth time, the particle-like extinction emerges and gradually changes to be visible. By observing the SEM images, authors suggested that the particle-like extinction results from the transition of Ag nanoplates to the AgNPs with well-defined shapes. At 120-min growth time, the extinction spectrum changed to be similar to that of the Ag–TiO_2 film grown in 180 mg/L $AgNO_3$ solution, which is in accordance with SEM observation.

Using Rhodamine 6G (Rh6G) as the probe molecule, the SERS activity of the Ag–TiO_2 conjugates was evaluated. Two kinds of electromagnetic "hot spots", the sub-10-nm "feed-gaps" between metal NPs and the "lightning rods" [338–341],
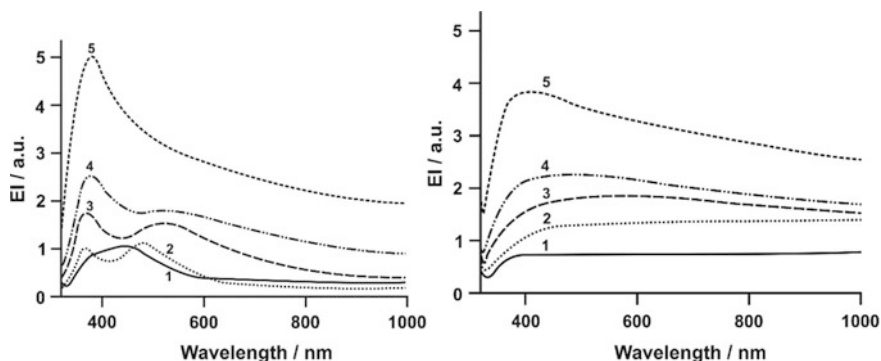
Fig. 5.35 Extinction spectra of Ag–TiO_2 films at the given growth times: *curves 1* (2 min), *2* (4), *3* (8), *4* (16), and *5* (12), Ag–TiO_2 films grown in 180 mg/dm^3 $AgNO_3$ solution (*left panel*) and Ag–TiO_2 films grown in 2800 mg/dm^3 $AgNO_3$ solution (*right panel*) [333]

have been known making the important contributions to SERS. Based on the SEM observation, the "feed-gaps" were excluded because the adjacent AgNPs are generally separated by a distance larger than 10 nm. Thus, "lightning rods" are proposed to be the SERS mechanism of Ag–TiO$_2$ films. To demonstrate this proposal, AFM was used to quantitatively measure the roughness of Ag–TiO$_2$ films, and the roughness dependence of EF$_{SERS}$ is plotted in Fig. 5.36 (left panel). EF$_{SERS}$ increased with the roughness of Ag–TiO$_2$ films, indicating that the enhanced Raman signals can be attributed to the "lightning rods" effect at the sharp edges of AgNPs, similar to the SERS mechanism on a rough Ag metal surface.

Figure 5.36 (right panel) shows the growth-time dependence of SERS enhancement factor, and the EF$_{SERS}$ (Raman enhancement factor) values of the Ag–TiO$_2$ films grown in 180 mg/L AgNO$_3$ solution are also plotted for comparison. The Ag–TiO$_2$ films dominated by Ag nanoplates, which are the two samples grown in 2800 mg/L AgNO$_3$ solution for 2 and 4 min, produced a $\sim 1 \times 10^5$ Raman enhancement, which is larger than that of Ag–TiO$_2$ films with small AgNPs, but smaller than that of Ag–TiO$_2$ films with large AgNPs. With the increase in the growth time, the EF$_{SERS}$ values increased. The increase of EF$_{SERS}$ values can be ascribed to the transition of Ag nanoplates to AgNPs with well-defined shapes, increasing the density of large AgNPs. However, the production of large AgNPs in 2800 mg/L AgNO$_3$ solution is lower than that in 180 mg/L AgNO$_3$ solution. Therefore, the increase in Raman enhancement is limited when the growth time was extended to 120 min. The results suggest that using a high concentration solution cannot bring large SERS values due to the formation of Ag nanoplates.

The fluorophore of RhB (Rhodamine B) in TiO$_2$ sol-gel was coated on the surface of Ag–TiO$_2$ films to avoid the fluorescence quenching. As shown in Fig. 5.37 (left panel), the photoluminescence (PL) excitation (PLE) spectrum was found essentially superposed with the absorption, and the maximum PLE at 554 nm
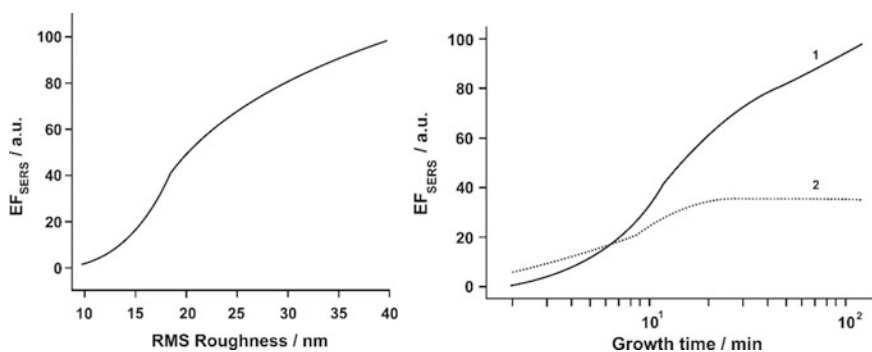
Fig. 5.36 SERS enhancement factor as a function of the film surface roughness (Raman spectra of R6G molecules on Ag–TiO$_2$ films that were grown in 180 mg/dm^3 AgNO$_3$ solution at the given growth time) (*left panel*) and SERS enhancement factor as a function of the growth time (Raman spectra of Rh6G molecules on Ag–TiO$_2$ films that were grown in 180 (*curve 1*) and 2800 mg/dm^3 (*curve 2*) AgNO$_3$ solution at the given growth time) [333]
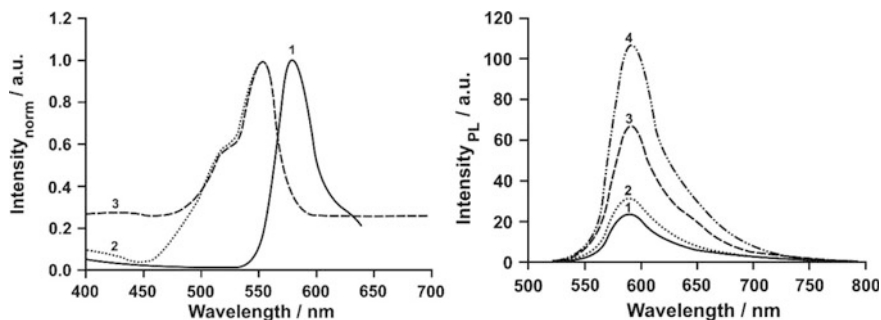
Fig. 5.37 Photoluminescence (*curve 1*), PLE (*2*), and absorption (*3*) spectra of RhB solution. The PL spectrum was excited by 330 nm light, and the PLE spectrum was detected at 578 nm (left panel). RhB PL spectra on Ag–TiO$_2$ films that were grown in 180 mg/dm^3 AgNO$_3$ solution at the given growth time [*1* (2 min), *2* (4), *3* (8), and *4* (32)] (*right panel*) [333]

partially overlapped with PL emission, thus the excitation light for PL measurement was set at the wavelength of 500 nm. Similar RhB PL spectra on the pure TiO$_2$ films were obtained, and the PL intensity did not obviously depend on the thickness of fluorophore layer. Compared to the RhB fluorescence on the pure TiO$_2$ films, the PL intensity of RhB on the Ag–TiO$_2$ films was enhanced, and the enhancement strongly depends on the growth time of AgNPs, as shown in Fig. 5.37 (right panel). Using the RhB PL spectra on the pure TiO$_2$ as the reference, the enhancement factor (EFPL) was determined to be 1.5–6.9. The enhancement is consistent with the measurement for the other fluorophore on the silver island films [342].

Fluorescence enhancement results primarily from two processes, an increase of the localized electromagnetic fields near the metal NPs and an increase of radiative decay rate [343]. Thus,

$$EF_{PL} = G_{exc} \times G_{QY}, \tag{5.7}$$

where G_{exc} is the enhancement of the localized electromagnetic field, and G_{QY} is the increase in quantum yield of the fluorophore, which can be estimated with the PL lifetime. For the RhB molecules on the pure TiO$_2$ films, the determined average lifetime was ∼0.63 ns. The RhB PL lifetime on the Ag–TiO$_2$ films was found to be ∼0.35–0.58 ns and did not obviously depend on the growth time of AgNPs. Considering that the quantum yield of a fluorophore in solid cannot exceed a few percents, G_{QY} was estimated smaller than 2. Thus, the localized electromagnetic field and/or the increased scattering of the Ag–TiO$_2$ films play an important role in the PL enhancement of RhB besides the increase in quantum yield. In addition, the increased roughness of the Ag–TiO$_2$ film by deposition time might result in larger surface area allowing more dye molecules located in the near field of the Ag nanostructures, thus leading to more enhancement of PL intensity.

5.4   Bioconjugates

An interesting approach to introduce theranostic functionalities into a nanosystem is to covalently attach a palladium (Pd)-porphyrin chelate to mesoporous silica nanoparticles (MSNs) which are readily taken up by cells. Some of the important properties of MSNs are large surface area (~ 1000 m^2/g), uniform pore size (~ 3 nm), particle size (in the range ~ 70–100 nm), ease of functionalization, large payload capacity, high cellular uptake, and low cytotoxicity. Because of these properties, MSNs have several advantages over normal silica nanoparticles and, thus, are used in a wide array of applications, including chemical catalysis, drug delivery, controlled release of therapeutics, and cell labeling. Pd-porphyrin has a long phosphorescence lifetime and has been used for in vivo oxygen sensing and imaging [344, 345]. Cheng et al. [346] synthesized (Scheme 5.20) phosphorescent Pd-meso-tetra (4-carboxyphenyl) porphyrin (PdTPP) covalently embedded in MSNs (MSN-PdTPP) as theranostic agents for the imaging and treatment of breast cancer. The energy required for phosphorescence imaging is only 10^{-4}–10^{-5} times that required for conventional PDT. Also, the concentration of singlet oxygen species generated during oxygen sensing/imaging is much lower compared to that during conventional photodynamic therapy (PDT) and, thus, by changing the energy of photoirradiation, the functionalities of MSN-PdTPP can be "switched" between a phosphorescence probe for oxygen sensing/imaging (diagnostics) and a photosensitizer for PDT (therapy). Breast cancer cells (MDA-MB-231) transfected with MSN-PdTPP, followed by photoirradiation (532 nm wavelength), showed a significant change in cell morphology and large extent of cell death indicated by high propidium iodide fluorescence.

In a further example of metal-containing theranostic nanoparticles, Kim et al. [348] have developed a facile synthetic route (Scheme 5.21) with good control over size to synthesize monodisperse, discrete mesoporous silica materials (smaller than 100 nm) containing a single Fe$_3$O$_4$ nanocrystal as a core (Fe$_3$O$_4$@mSiO$_2$).
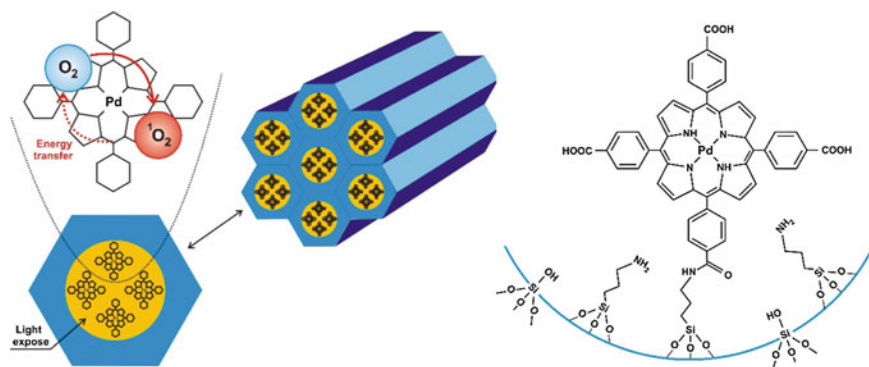
Scheme 5.20 Schematic of the mechanism of PDT with MSN-PdTPP (*left panel*). Chemical structure of PdTPP covalently attached to MSN (*right panel*) [347]

Fluorescent dyes, rhodamine (Rh) or fluorescein (F) isothiocyanate, were covalently attached to the silica surface, and doxorubicin (DOX) was encapsulated within the silica matrix. Next, the surface of the rhodamine-containing nanoparticles was functionalized with PEG groups (Fe_3O_4@$mSiO_2$ (Rh)-PEG) to minimize non-specific interactions and lengthen the blood circulation half-life. DOX-induced cytotoxicity was studied by transfecting SK-BR-3 cells with DOX-loaded Fe_3O_4@$mSiO_2$ (Rh)-PEG nanoparticles. In vivo studies were performed by sub-cutaneously injecting MCF-7 cells pretreated with Fe_3O_4@$mSiO_2$ (Rh)-PEG particles into the dorsal shoulder of nude mice. The MCF-7 cells containing Fe_3O_4@$mSiO_2$ (Rh)-PEG particles were easily detectable as dark spots on T2-weighted MR images and elicited significant rhodamine fluorescence when examined by fluorescence imaging.

It is well established that UV-photoexcitation of bare TiO_2 particles in aqueous solution results in the formation of various reactive oxygen species (ROS), mainly hydroxyl (OH), peroxy (HO_2) radicals, and singlet oxygen ($^1O_2$) [349]. Under UV radiation, the photogenerated holes on the TiO_2 nanoparticles can react with absorbed H_2O or OH in aqueous environment to form highly reactive hydroxyl radicals, and electrons can react with oxygen to produce superoxide ions [350]. TiO_2 is well known as a ultraviolet light (UV)-inducible catalyst in the photooxidation of organic substrates and the deactivation of bacteria, algae, and viruses [351, 352]. Under UV excitation, TiO_2 nanoparticles of various sizes and morphologies have been reported to exhibit cytotoxicity toward some tumors [353].

This approach can be used to treat tumor cells due to cell membrane peroxidation [354]. It has been known that the photocatalytic activity of TiO_2
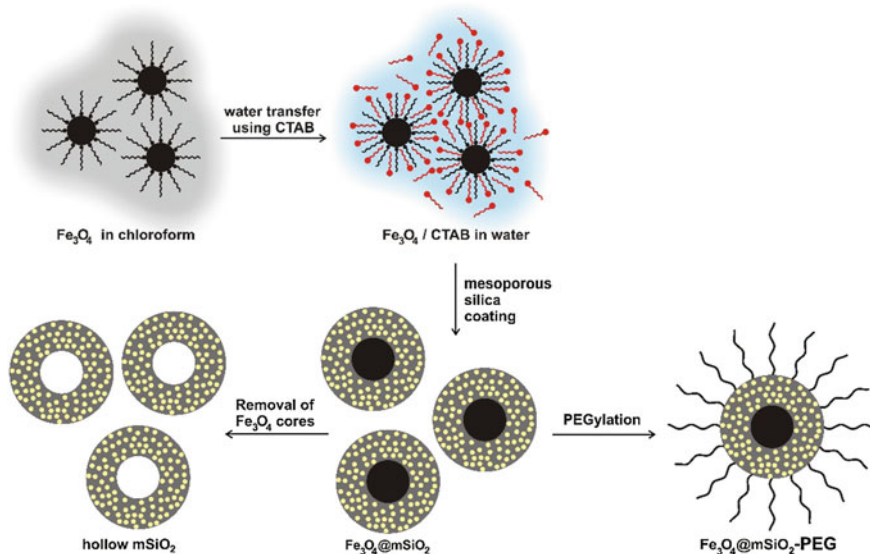
Scheme 5.21 Schematic for synthesis of Fe_3O_4@$mSiO_2$-PEG [347, 348]

nanoparticles depends not only on the properties of the TiO_2 material itself, but also on the modifications of the TiO_2 material [355]. Therefore, the TiO_2 nanoparticles modified with noble metal Pt was chosen as the composite [356] for cancer-cell treatment. Furthermore, Pt nanoparticles on the surface of TiO_2 nanoparticles may significantly enhance the photocatalytic activity of the semiconductor nanoparticles because of better charge separation between the electrons which accumulate on the metal and holes remaining on the photocatalyst surface [357]. Furthermore, Pt nanoparticles are more stable than the commonly used Au nanoparticles, and they can be stored more easily and longer [358].

The TEM image that the TiO_2 nanoparticles are single-crystalline with the average size of 10 nm, and the surfaces of the TiO_2 crystals are smooth, while most of the surfaces of Pt/TiO_2 and Au/TiO_2 nanocomposites are rough. Meanwhile, with careful observation, there are some fuscous points on the TiO_2 nanoparticle surfaces. So, Pt and Au nanoparticles have been deposited on the surfaces of the TiO_2 nanoparticles. The metal/TiO_2 nanocomposites have been also identified with UV–Vis adsorption spectra. As is shown in Fig. 5.38, the TiO_2 nanoparticles show an absorption edge near 400 nm due to the band gap absorption of TiO_2. As Pt nanoparticles are modified on the surfaces of the nano-TiO_2 particles, there is a large increase in the absorption wavelength of Pt/TiO_2. On the other hand, if Au metal is employed, a broad spectral band at approximately 550 nm can be observed in the UV–Vis absorption spectra, which is attributed to the Au nanoparticles. It was further demonstrated that the Pt/TiO_2 nanocomposite can show significant stableness for several months at room temperature, while Au/TiO_2 nanoparticles congregate within several hours. So Pt/TiO_2 nanomaterial might be more useful in reality.

The morphological changes of HeLa cells obtained by optical microscopy may give us direct images about the photodynamic killing effect of the Pt/TiO_2
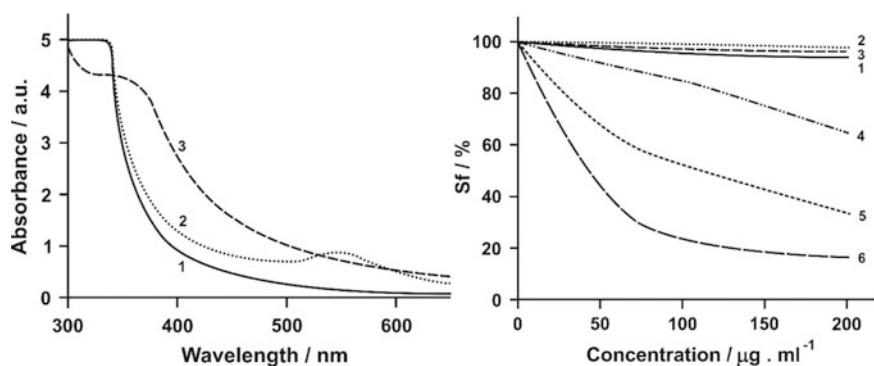
Fig. 5.38 The UV absorption spectra of TiO_2 (*curve 1*), Pt/TiO_2 (*3*), and Au/TiO_2 (*2*) nanocomposites (*left panel*) and relationship between the surviving fraction (Sf) of the HeLa cells and the TiO_2-based nanomaterials [TiO_2–non-UV, Au/TiO_2–non-UV, Pt/TiO_2–non-UV (*curves 1–3*), TiO_2–UV (*4*), Au/TiO_2–UV (*5*), Pt/TiO_2–UV (*6*) (*right panel*)]

nanocomposite on the cancer cells. The live HeLa cells treated in the absence of Pt/TiO$_2$ nanocomposite may remain attached to the substrate with elongated shapes, so UV irradiation on the cells with no Pt/TiO$_2$ nanocomposite involved is harmless to the cancer cells. However, treated by UV irradiation in the presence of the nanomaterial, some of the cells will detach from the substrate and present a death morphology. The higher the concentration of the Pt/TiO$_2$ nanocomposite, the more the abnormal or dead cells. At the concentration of 200 μg ml^{-1} Pt/TiO$_2$, most of the cancer cells have been detached from the substrate and have been dead. Since the UV intensity is rather weak, the Pt/TiO$_2$ nanocomposite should have shown a very high photodynamic effect to kill cancer cells. Figure 5.38 (right panel) shows the comparison of the MTT (3-(4,5-dimethylthiazol-2-yl)-2,5-diphenyltetrazolium bromide) assay. Without UV irradiation, the Pt/TiO$_2$ nanocomposite with different concentrations is found to have no cytotoxicity, and a nearly 100% surviving fraction shows that the Pt/TiO$_2$ nanoparticles are relatively biocompatible (Fig. 5.38, curve 2). In contrast, with the treatment of 2 h UV irradiation, as the concentration of the Pt/TiO$_2$ nanocomposite is increased, the surviving fraction of the cells displays a significant decline (Fig. 5.38, 6). At the concentration of 25, 50, 100, and 200 μg ml^{-1}, the surviving fractions of the cancer cells are 70, 36, 20, and 15%, respectively. For the cases of TiO$_2$ and Au/TiO$_2$ nanoparticles, without UV irradiation, TiO$_2$ and Au/TiO$_2$ nanoparticles with different concentrations have nearly no cytotoxicity as well. After a 2-h treatment of UV irradiation in the presence of TiO$_2$ or Au/TiO$_2$ nanoparticles, the surviving fractions of cancer cells are also decreased for the both cases. Nevertheless, there are more cells that can survive. For the case of TiO$_2$ alone nanoparticles, at the concentration of 25, 50, 100, and 200 μg ml^{-1}, the surviving fractions of the cancer cells are separately decreased to be 94, 88, 85, and 65% (Fig. 5.38, 4). For the case of Au/TiO$_2$ nanocomposite, they are 83, 60, 50, and 33%, respectively (Fig. 5.38, 5). Obviously, at the same concentration, metal/TiO$_2$ nanocomposite particles can kill more cancer cells than TiO$_2$ nanoparticles alone, and the Pt/TiO$_2$ nanocomposite can show a stronger power to kill cancer cells.

The electrical characteristics of Au and Pt nanoparticles have tiny differences [359], while Au nanoparticles show a strong tendency to form large clusters on nano-TiO$_2$ surfaces than Pt nanoparticles [360]. So, we propose that the reason why Pt/TiO$_2$ nanocomposite may have a better photodynamic efficiency to kill cancer cells than Au/TiO$_2$ nanocomposite is that Pt/TiO$_2$ nanocomposite is much more stable. Furthermore, TiO$_2$-based colloid particles, and their composites, have been successfully applied for destruction of brain cancer cells [361]. One recent example [353] describes 50-nm rhodamine-labeled TiO$_2$/PEG constructs able to be internalized into rat glioma C6 cells. Although the essential question regarding accumulation selectivity of the photocatalyst in cancerous cells over healthy astrocytes remains to be answered, the antiglioma activity of these hydrophilic nanoconstructs was found to be remarkable. The antitumor performance was evaluated in glioma cell spheroids representing a provisional three-dimensional model valuable for translation to animal xenografted models. The cytotoxic effect of the UV-irradiated photocatalyst depended on the concentration of TiO$_2$/PEG and the light exposure

time, as shown in Fig. 5.39. More than 90% of cells were killed by a UV dose of
13.5 J cm^{-2} in the presence of the nanocatalyst at a concentration of 0.5 mg/mL.
The irradiated spheroids in the presence of TiO$_2$/PEG showed growth suppression
compared with control groups. Moreover, fluorescent images of the
photocatalyst-treated spheroids costained with apoptosis and necrosis markers,
Annexin V-FITC and propidium iodide (PI) reveal the prevalence of induced
apoptotic cell death within first 6 h.

   Another work [361] suggests approaches to resolve the two main concerns
regarding the use of small TiO$_2$ nanocrystals in biological systems–nonspecific
distribution within cancer and healthy cells, and UV light photoreactivity. Although
nanoscale materials tend to passively accumulate in tumors due to enhanced per-
meability and retention effects, and often serve as "nanocarriers" for chemothera-
peutics, this passive strategy has limitations because of the risk of random delivery.
The problem of passive transport can be improved by integrating hard inorganic
nanomaterials with biological targeting vehicles—for example, an antibody.
Functionalization of 5-nm high-crystalline TiO$_2$ nanoparticles with a monoclonal
antibody recognizing IL13R fostered nanoparticle delivery specifically to
glioblastoma cells in a manner dependent upon cellular membrane IL13R expres-
sion. Since visualization of 5-nm TiO$_2$ nanocrystals within cells without additional
labeling represents a challenge for conventional microscopies, direct visualization
of the TiO$_2$-antibody/receptor interaction and mapping of the IL13R location and
distribution throughout a single A172 brain cancer cell were demonstrated using
synchrotron-based X-ray fluorescence microscopy [361]. PDT using the nanobio
hybrid photocatalyst resulted in the destruction of over 80% of A172 glioma cells
with high levels of IL13R expression, whereas in the case of U87 cells charac-
terized by lower antigen presentation, cytotoxicity at the same conditions reached a
plateau of $\sim 50\%$ and did not increase at higher photocatalyst concentrations.
Moreover, no cytotoxicity was observed for normal human astrocytes (NHA)
known to be not IL13R-expressing. It must be noted that 5-nm TiO$_2$ nanocrystals

Fig. 5.39 Surviving fraction
(Sf) of C6 cells as a function
of UV irradiation in the
presence of different
concentrations of TiO$_2$/PEG
(*curve 1* (0), *2* (100), *3* (250),
4 (500 µg/mM) [362]
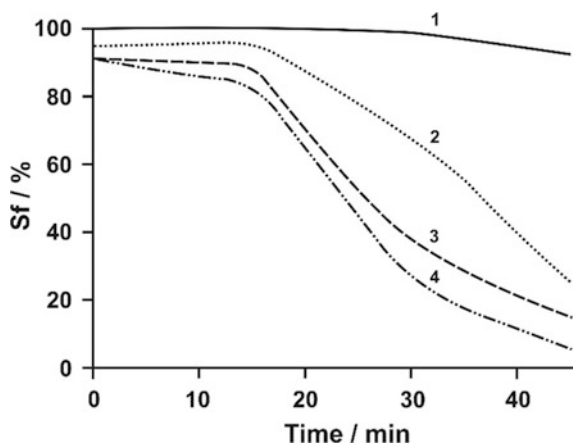
not functionalized with an antibody demonstrated slight (<20%) nonspecific light-driven toxicity for all types of cells; this fact must be considered when any small nanoparticles are applied to biological systems [361].

Another challenge for bioapplication of TiO_2 semiconductor nanocrystals is in tailoring of the photochemical properties and extending reactivity toward the visible light region. While common approaches for shifting TiO_2 reactivity include doping inorganic elements—for example, rare earth ions—another method developed by Rajh et al. [363] is based upon chemisorption of organic molecules, such as dihydroxybenzenes (e.g., dopamine, DA), upon the surface of the semiconductor particles. As a result of the presence of two OH groups in the ortho position, the catecholate group forms a strong bidentate complex with coordinatively unsaturated Ti atoms at the nanoparticle surface. It has furthermore been shown that DA creates electronic coupling between TiO_2 and DNA, allowing transport of photogenerated holes to biomolecules [364]. Modification of TiO_2 particles with electron-donating enediol ligands results in significant improvements to the outer crystal structure and photoreactivity of the particles, narrowing the band gap to 1.6 eV and redshifting the absorption edge to the visible part of the solar spectrum below $\sim$750 nm [365]. As was reported, the application of polychromatic visible light, with an incident intensity of 60 mW/cm^2, with UV and IR cutoff wavelengths filters, led to instant morphological changes in A172 cells. However, in the case of DA- and DA-antibody-modified TiO_2 particles, ROS arise from multiple, mechanically distinct redox chemistries, and the principal ROS produced is the superoxide anion, formed by reaction of photogenerated electrons with molecular oxygen [363]. Further studies of photo-induced cytotoxicity toward A172 glioma cells in the presence of selective ROS quenchers were consistent with these results, as shown in Fig. 5.40 [361]. ROS cause cell membrane damage, permeability changes, and cell death. Induced apoptosis was proposed as a foremost pathway in TiO_2-DOPAC (3,4-dihydroxyphenylacetic acid)-antibody-catalyzed cell phototoxicity [361] (Scheme 5.22). Nanostructured porous TiO_2 has been developed as a biocompatible nanodevice for constant chemotherapy drug release into the central nervous system (CNS) [366]. A porous titania carrier uploaded with low concentrations of a cytostatic platinum complex was capable of inducing DNA fragmentation, possibly via a strong interaction between nitrogen atoms in nucleotides, and Lewis acid sites on both the titania surface, and the platinum complex coordination sphere. Application of this material directly on to C6 glioma xenografted into Wistar rats resulted in a significant decrease in tumor size and growth rate. Although no light stimulus was employed in these trials [349], this photoreactive material served as the scaffold for release of a cytostatic agent. The overall potential of this porous material remains to be explored in combined brain cancer chemo- and phototherapies.

Devices based on nanowires are emerging as a powerful and general platform for ultrasensitive, direct electrical detection of biological and chemical species. Lieber's group developed the silicon (Si) nanowire field-effect devices in which distinct nanowires and surface receptors are incorporated into arrays. The surface chemistry of nanowire devices can affect the electric changes, which is the basic
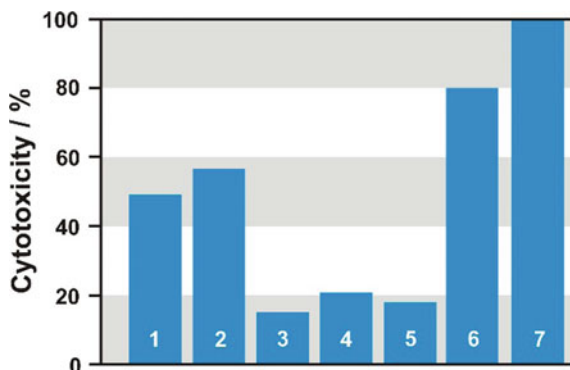
Fig. 5.40 Photoexcitation of the nanobio hybrid in an aqueous solution results in the formation of various ROS. Cytotoxicity of the TiO_2–antibody hybrid is reduced in the presence of ROS quenchers, mainly superoxide anion. Mannitol (*1*), histidine (*2*), NaN_3 (*3*), catalase (*4*), SOD (*5*), TiO_2-mAb/light (*6*), and lysis solution (*7*) [362]

mechanism of this approach for the development of a viable multiplexed detection technology. The Si-nanowire probes have been used for detection of various biological species and their interactions, including small molecules, proteins, DNAs, viruses, and even neuronal signals [367, 368]. There are three key steps for the fabrication of a nanowire device array: first, the couple of aldehyde propyltrimethoxysilane (APTMS) and Si-nanowires to present terminal aldehyde groups at the nanowire surface; second, the conjugation of aldehyde groups with monoclonal antibodies (mAbs) to endow with the specificity; third, the block of unreacted free aldehyde groups by reaction with ethanolamine [369]. Selective interaction of cancer biomarkers with surface-linked mAbs will produce a conductance change in the corresponding receptor-modified Si-nanowire devices but not in devices lacking of the specific antibodies. For example, the results showed that the conductance change was directly proportional to the solution of prostate-specific antigen (PSA) concentration from ∼5 ng/mL down to 90 fg/mL (Fig. 5.41). Using Si-nanowire devices functionalized with mAbs for PSA, carcinoembryonic antigen (CEA), and mucin-1, respectively, one can achieve the multiplexed, real-time, label-free biomarker detection with sensitivity to the femtomolar level (conductance vs. time data can be used for the simultaneous multiplexed detection of proteins on p-type Si-nanowire arrays). The nanodevices were also successful for the detection of PSA in donkey and human serum samples with high sensitivity and selectivity (the detection of PSA-containing donkey serum samples on an array in which NW1 was functionalized with Ab1 and NW2 was passivated with ethanolamine) [369]. The capability of Si-nanowire probes for multiplexed real-time monitoring of protein markers with high sensitivity and selectivity in clinically relevant samples opens up substantial possibilities for diagnosis and treatment of cancer and other complex diseases. For example, the combination of Si nanoprobes and microfluidic purification chips may provide
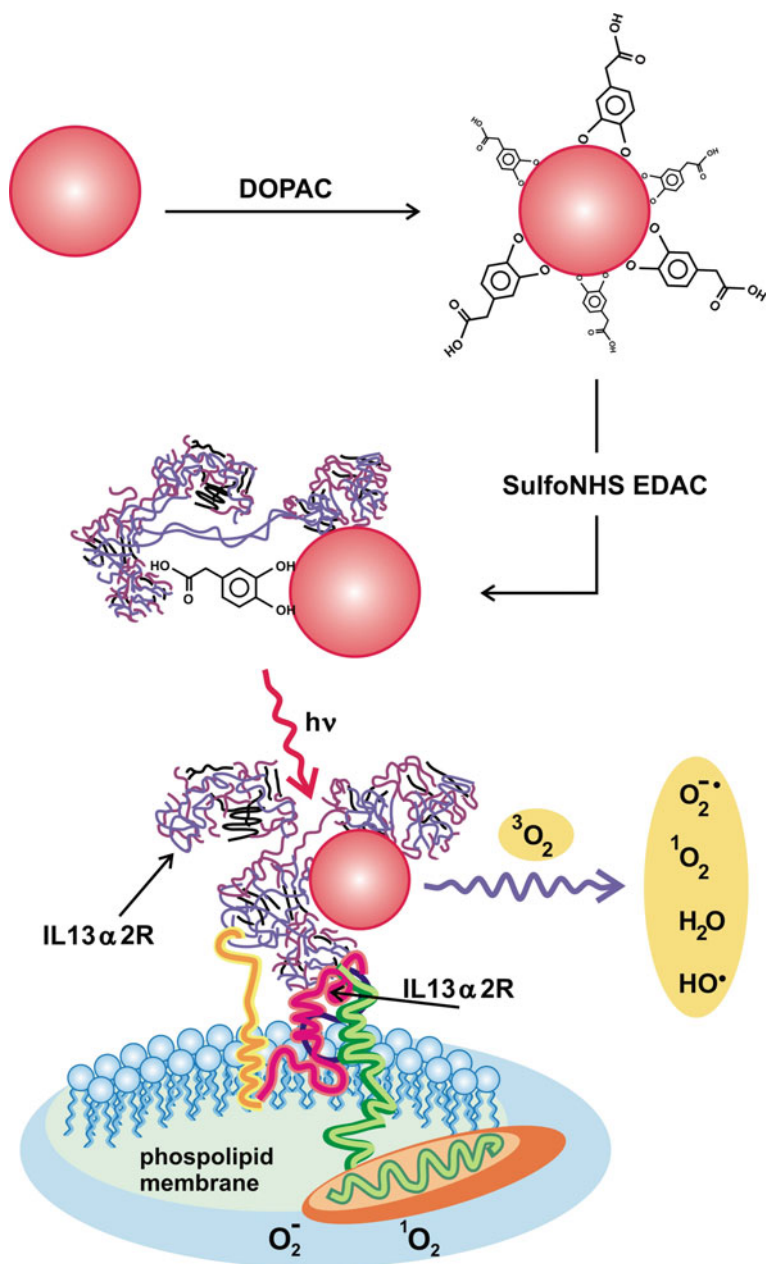
Scheme 5.22 Modification of 5 nm TiO$_2$ semiconductor particles with electron-donating endiol ligands results in narrowing the band gap to 1.6 eV and redshifting the absorption edge to the visible part of the solar spectrum [361]

Fig. 5.41 Si-nanowire field-effect devices. Change in conductance versus concentration of PSA for a p-type Si-nanowire modified with PSA-Ab1 receptor [371]
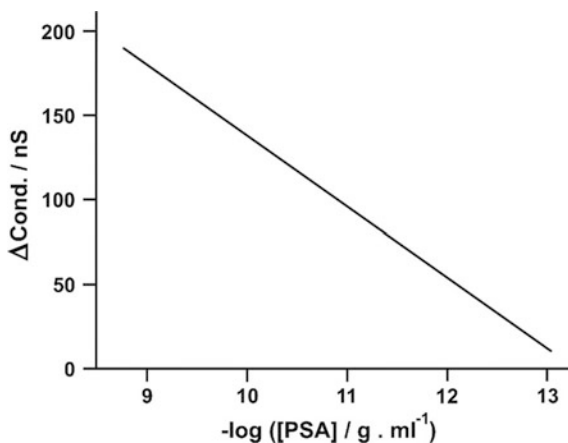
point-of-care diagnostics for the specific and quantitative detection of disease biomarkers in physiological fluid samples, positioning this technology for rapid translation to clinical settings [370].

5.5   Conclusion

Some templates can be employed for the shape-controlled synthesis of metal nanocrystals. These spatially and dimensionally constrained structures can serve as reaction cages to control the nucleation and growth of the particles (and impart stability), leading to the formation of nanoparticles with a morphology complementary to that of the template. Liquid-crystalline media have also been used as templates in the synthesis of anisotropic nanoparticles. Porous membranes containing uniform cylindrical pores can be used as hard templates. Examples of other hard templates include porous nanoparticles membranes. In addition to the soft and hard templates, there is another kind of nanoparticle template, called sacrificial template, that has been used, where the template particle sacrifices itself in the process of templated particle formation. By varying the shape of the sacrificial template nanoparticle and its ratio to the more-noble metal precursor added, one can obtain a variety of morphologies, such as triangular rings, wires, tubes, boxes, or cages. Nontraditional nanostructures consisting of noble metals are often fabricated by depositing thin layers of metals (or their precursors) on some silica beads existing templates, followed by calcination or wet chemical etching to remove the solid cores. Small gold nanoparticles could be adsorbed onto the surfaces of silica spheres that had been premodified with self-assembled monolayers of (3-aminopropyl)triethoxysilane. Another method was based on the layer-by-layer adsorption of polyelectrolytes and charged gold nanoparticles to build shell-like structures around colloidal templates whose surfaces had been derivatized with

appropriately charged groups. Noble metal nanoparticles can be synthesized in mesoporous silica films and in ultrathin nanoporous films. Surface area, average pore size, and pore volume were determined for silica aerogels and gold-doped silica aerogels. On comparison with the results obtained without SiO_2, it can be noted that in the presence of silica, the rate of formation of silver particles decreases drastically. The use of task-specific ligands with calcining as post-treatment provides AuNPs that are encapsulated into the mesoporous channels or loaded on the surface of silica spheres. Task-specific ligands containing a cetylammonium moiety act as structure-directing agent with AuNPs containing a trialkoxysilyl group. The latter cocondenses with tetraethoxysilane (TEOS) to form mesoporous silica. Poly (L-lysine) (PLL) and poly(L-glutamic acid) (PLGA) multilayer-coated membranes could be immersed in a $HAuCl_4$ solution to form AuNP/PLL/PLGA multilayers. The silica nanoparticles were used as the templates of interior cores of metal nanoshells and as the interior templates for the deposition of the external noble metal shell layer by layer. A straightforward sol-gel method can be utilized for the preparation of gold nanoparticles via in situ-doped silica aerogels using a reducing agent. Metal nanoparticles were used as sacrificial templates to react with an aqueous gold salt solution, resulting in the formation of gold nanoshells with hollow interiors and smooth and pinhole-free surfaces, as well as homogeneous and highly crystalline walls. Similar changes in morphology, composition, and structure were observed no matter whether silver nanocubes, nanowires, or nanospheres were used as the templates. The discovery of surface-enhanced Raman scattering (SERS) on colloidal silver particles started the extensive development of a new and very sensitive analytical method enabling to detect molecules in the concentration range from pico- to femtomoles. Some studies have shown that the highest value of enhancement is achieved only on the silver particles of a certain size which are referred to as "hot particles." The most frequently used activation agents of the silver nanoparticles prepared by the common reduction procedures include halide ions, particularly chlorides. A simple and reproducible method for the activation of monodispersed AgNPs was insertion of the concentrated NaCl solution into the AgNP dispersion. The halide ions can react with the silver atoms and dissociate them from the surface of Ag particles. This phenomenon is known as the oxidative etching process. The most widely used procedure for the preparation of AuNPs supported on these insoluble oxides solids is the precipitation–deposition method. A controlled growth of AgNPs on TiO_2 templates is expected in tuning the optical response of the Ag–TiO_2 hybrids. In addition, these Ag nanoplates are mobile and easily stripped from the substrates. After nucleation, the AgNPs grow through two mechanisms, Ostwald ripening (OR) and oriented attachment (OA). It was also reported that both OA and OR mechanisms coexist in the growth of nanoparticles. At the initial stage, increasing the concentration of the primary particles facilitates the OA-based growth, and the OR growth is restrained. TiO_2 assembled with Ag nanoparticles has received much attention because such a hybrid can effectively separate the charges and redshift the absorption to visible light via plasmonic resonance. The Ag reduction rate is determined by the parameters related to UV irradiation, reduction activity of TiO_2 film, $AgNO_3$ concentration of solution, etc.

The growth model can explain the phenomenon of Ag nanoplates lying on the small AgNPs. According to this growth model, a smooth TiO_2 film facilitates the formation of large-scale Ag nanoplates.

The morphological and structural data have thus shown that gold deposited by sputtering on clean Si shows two phases: gold agglomerated as nanodots of a few nanometers in size and amorphous Au/Si agglomerates. The latter evolves at room temperature and tends to form smaller and fewer crystalline regions of pure gold aligned with some crystallographic orientations of the silicon substrate. The preparation of gold (0) nanoparticles within channels of mesoporous materials functionalized with mercaptopropyl groups is also reported. These materials prepared using the so-called direct method contain various and controlled numbers of thiol functions, which are homogeneously distributed exclusively within the pore channels. The regular distribution of organic groups allows the exclusive growth of nanoparticles with a narrow size distribution within the pores of the materials with a high gold content. The good control of size distribution of the nanoparticles obtained, due to their exclusive location within the channels of the materials, demonstrates the crucial role of the thiol functions both for (i) the complexation of the organogold precursor prior to the reduction step and for (ii) their strong interaction with the gold nanoparticle surface during and after the nanoparticle growth process. We have also presented a facile synthesis of mesoporous gold–silica nanocomposites through a one-step sol-gel reaction. With use of a nonsurfactant compound DBTA as the pore structure-directing template, the synthesis process is environment friendly and convenient. The pore size and pore structure of the nanocomposite are able to be fine-tuned by varying the amount of template or using different template compounds. Combining both high porosity of the silica framework and the unique physical/chemical properties (such as conductivity and optical behavior) of the second material phase, nanosized gold particles, the mesoporous gold–silica nanocomposite materials are potentially useful for sensors and catalysts. On the basis of STM studies, silver nanoclusters can be used to highlight defects on SiO_2 thin films with cluster growth related to a specific defect feature. On a well-prepared SiO_2 thin film, gold nanoclusters preferentially decorate line defects. However, higher densities of Au nanoclusters are observed on the terrace sites of a SiO_2 thin film prepared at a lower annealing temperature. We have used a simplified method to prepare $SiO_2@Au$ composite nanoparticles and compared it with the general three-step method. The results indicated that the simplified method achieved a denser Au layer on silica microspheres. Silver nanoparticles were successfully immobilized onto the surface of silica particles by novel method involving polyol process. Thiol groups at the surface of the silica particles were used as a chemical protocol to immobilize the silver nanoparticles onto the surface of silica particles. On the basis of experimental results, it has been concluded that when polyol process is applied for the immobilization of silver nanoparticles onto the large supports, it is possible to obtain extremely small silver particles and to control the size of silver particles and the thickness of silver layer by control of reaction temperature and time. This size-controlled immobilization route is explained by following two steps; (1) small silver nanoparticles are firstly formed on the silica

surface, and (2) these small silver nanoparticles homogeneously grow to larger ones. These two steps are completely conducted in one-pot by polyol process, which is attributed to the slower and more easily controllable reaction rate of the polyol reduction method than that of general chemical reduction method using reducing agent such as hydrazine or sodium borohydride. Silica–silver heterogeneous nanocomposite particles were prepared by facile route involving alcohol reduction method. On the basis of the experimental results, the role of thiol groups was investigated; in this system, thiol groups acted as a chemical protocol and a nucleation-promoting agent. The reaction mechanism was briefly suggested as: (1) the formation of nuclei and (2) the growth of nuclei. Mega-electron-volt ion irradiation of colloidal silica particles containing an Au core leads to a deformation of the shell into an oblate ellipsoid and of the Au core into a nanorod. The Au deformation is attributed to the in-plane mechanical stress in the silica shell acting on the radiation-softened Au core. The Au nanorods have size aspect ratios as large as nine for intermediate fluences; they break up for higher fluences. Preliminary optical extinction data show surface plasmon resonance shifts characteristic for anisotropic Au nanorods. As anisotropic deformation is known to occur in a variety of (amorphous) hosts, several other combinations of core and shell materials may be ion-beam-shaped as well. Bimetallic core−shell nanoparticles allow for the exploitation of properties characteristic for monometallic (Au and Ag) nanoparticles. We suggest that thanks to the core−shell nanoparticles' synergistic properties, the material proposed represents an attractive photothermal properties. Aspartame stabilization provides a good shelf life for particles with a material that is nontoxic, inexpensive, and water-soluble. The stable AgNP@MMT nanocomposites were synthesized by microwave method. XRD analyses and TEM observations confirmed the formation of nanoparticles on the clay surfaces. The FTIR analysis suggested that the interaction between AgNPs and the MMT surfaces was weak due to the presence of van der Waals interactions. The synthesized MMT@AgNPs suspensions were found to be stable over a long time without any sign of precipitation (or detachment). Therefore, the silver ions released explain the antimicrobial properties found in the investigated MMT@AgNPs nanocomposites. We have reported that ultrathin gold/silver nanowires and sub-50-nm gold triangular nanoprisms can be readily synthesized by adopting small silver seeds and BDAC in the seed-growth method. Here, we demonstrated that small silver seeds are a versatile choice for generating anisotropic gold nanostructures because they can undergo structure evolution through various mechanisms including galvanic replacement reaction. The seed shape repopulation along with the structure-directing ability of silver UPD and BDAC is responsible for the formation of uniform triangular nanoprisms. These results underscore the importance of the chemical nature of seeds in controlling the shape of metal nanoparticles in the seed-growth method. We also show that silver seeds can significantly speed up the growth rate of ultrathin nanowires. A majority of existing synthetic procedures for ultrathin nanowires take much longer times ranging from hours to days because they rely on slow processes to ensure the formation of highly anisotropic wires. The introduction of silver seeds and BDAC (benzylhexadecylammonium chloride) in

the seed-growth method reported here opens a new pathway to high-yield syntheses of anisotropic metal nanoparticles. We have developed a versatile colloidal synthesis method to assemble noble metal NP heterodimers based on electrostatic interactions. The phase diagrams of the relevant individual dimer components were investigated to derive a stability zone where both components were stable in solution despite opposite surface charge, in order to find the optimal conditions for selective self-assembly of the targeted heterodimers. Using this approach, we have successfully assembled plasmonic heterodimers of Au and Ag spheres$_{90\,nm}$ paired with Au$_{30\,nm}$ cubes and Au$_{50\,nm}$ rhombic dodecahedron. Furthermore, we have also combined catalytic Pd-NPs of different sizes and shapes (cubes$_{25\,nm}$/$_{70\,nm}$; rhombic dodecahedron$_{110\,nm}$, truncated cubes$_{120\,nm}$, octahedron$_{130\,nm}$) with plasmonic spherical AuNPs (90 nm).

The SiO$_2$@Au composite microspheres were prepared by the reduction of HAuCl$_4$ in the presence of the functionalized silica microspheres. SEM images of the SiO$_2$@AuNPs spheres illustrated the differences in the morphologies of the composite particles obtained at different pH values. There was an overall trend to the reduction of the Au coverage when the pH values of the treatment solutions were increased gradually. As the pH value was lowered to around 4, almost each functionalized silica sphere was overlaid with a large amount of AuNPs, forming a dense and uniform gold monolayer.

If the brownish-gray Ag-TiO$_2$ film is irradiated with colored (e.g., red) light in air, the photooxidatively generated Ag$^+$ is retained in the nanopores, so that the colored (e.g., red) film turns original brownish-gray under UV light. This should be because the Ag nanoparticles absorbing the colored (e.g., red) light form again in the nanopores. In contrast, if the Ag-TiO$_2$ film is irradiated with colored (e.g., red) light in water, the generated Ag$^+$ is removed from the pores, so that the film retains its color (e.g., red) even under UV light. We have achieved the improvement of the chromogenic properties of the Ag-TiO$_2$ film and the introduction of new functions, namely, nonvolatilization and solvatochromism. In addition, an evidence for the molding effect of the nanopores in the TiO$_2$ film was described.

An interesting approach to introduce theranostic functionalities into a nanosystem is to covalently attach a palladium (Pd)-porphyrin chelate to mesoporous silica nanoparticles (MSNs) which are readily taken up by cells. Pd-meso-tetra (4-carboxyphenyl) porphyrin (PdTPP) covalently embedded in MSNs (MSN-PdTPP) was used as theranostic agents for the imaging and treatment of breast cancer. Also, the concentration of singlet oxygen species generated during oxygen sensing/imaging is much lower compared to that during conventional photodynamic therapy (PDT) and, thus, by changing the energy of photoirradiation, the functionalities of MSN-PdTPP can be "switched" between a phosphorescence probe for oxygen sensing/imaging (diagnostics) and a photosensitizer for PDT (therapy). UV-photoexcited TiO$_2$ nanoparticles in aqueous solution form various reactive oxygen species, mainly highly reactive hydroxyl (OH), peroxy (HO$_2$) radicals, and singlet oxygen, highly reactive hydroxyl radicals, electrons and superoxide ions able to deactivate bacteria, algae, viruses and kill cancer cells. Pt/TiO$_2$ nanocomposites were found to have a better photodynamic efficiency to kill

cancer cells than TiO_2NPs or Au/TiO_2 nanocomposites. Nanostructured porous TiO_2 has been developed as a biocompatible nanodevice for constant chemotherapy drug release. A porous titania carrier uploaded with a cytostatic platinum complex was capable of inducing DNA fragmentation, possibly via a strong interaction between nitrogen atoms in nucleotides, and Lewis acid sites on both the titania surface and the platinum complex coordination sphere.

Glossary

Antibody (Ab)	is a large, Y-shaped protein produced mainly by plasma cells that is used by the immune system to identify and neutralize pathogens such as bacteria and viruses. The antibody recognizes a unique molecule of the harmful agent, called an antigen, via the Fab's variable region. Each tip of the "Y" of an antibody contains a paratope (analogous to a lock) that is specific for one particular epitope (similarly analogous to a key) on an antigen, allowing these two structures to bind together with precision. Using this binding mechanism, an antibody can tag a microbe or an infected cell for attack by other parts of the immune system, or can neutralize its target directly (e.g., by blocking a part of a microbe that is essential for its invasion and survival). Depending on the antigen, the binding may impede the biological process causing the disease or may activate macrophages to destroy the foreign substance. The ability of an antibody to communicate with the other components of the immune system is mediated via its Fc region (located at the base of the "Y"), which contains a conserved glycosylation site involved in these interactions. The production of antibodies is the main function of the humoral immune system.
Antigen	is a molecule capable of inducing an immune response on the part of the host organism, though sometimes antigens can be part of the host itself. Each antibody is specifically produced by the immune system to match an antigen after cells in the immune system come

	into contact with it; this allows a precise identification of the antigen and the initiation of a tailored response. The antibody is said to "match" the antigen in the sense that it can bind to it thanks to adaptations performed to a region of the antibody; because of this, many different antibodies can be produced, with specificity to bind many different antigens while sharing the same basic structure.
Apoptosis	is a process of programmed cell death that occurs in multicellular organisms. Biochemical events lead to characteristic cell changes (morphology) and death. These changes include blebbing, cell shrinkage, nuclear fragmentation, chromatin condensation, chromosomal DNA fragmentation, and global mRNA decay. Between 50 and 70 billion cells die each day due to apoptosis in the average human adult. Apoptosis is a highly regulated and controlled process that confers advantages during an organism's lifecycle. Apoptosis produces cell fragments called apoptotic bodies that phagocytic cells are able to engulf and quickly remove before the contents of the cell can spill out onto surrounding cells and cause damage to the neighboring cells.
Astrocytes	are characteristic star-shaped glial cells in the brain and spinal cord. They perform many functions, including biochemical support of endothelial cells that form the blood–brain barrier, provision of nutrients to the nervous tissue, maintenance of extracellular ion balance, and a role in the repair and scarring process of the brain and spinal cord following traumatic injuries.
Cancer cells	are cells that divide relentlessly, forming solid tumors or flooding the blood with abnormal cells. Cell division is a normal process used by the body for growth and repair. A parent cell divides to form two daughter cells, and these daughter cells are used to build new tissue, or to replace cells that have died as a result of aging or damage. Healthy cells stop dividing

when there is no longer a need for more daughter cells, but cancer cells continue to produce copies. They are also able to spread from one part of the body to another in a process known as metastasis.

Carcinoembryonic antigen (CEA)
describe a set of highly related glycoproteins involved in cell adhesion. CEA is usually present only at very low levels in the blood of healthy adults. However, the serum levels are raised in some types of cancer, which means that it can be used as a tumor marker in clinical tests. Serum levels can also be elevated in heavy smokers. CEA are glycosyl phosphatidyl inositol (GPI) cell-surface-anchored glycoproteins whose specialized sialofucosylated glycoforms serve as functional colon carcinoma L-selectin and E-selectin ligands, which may be critical to the metastatic dissemination of colon carcinoma cells.

Central nervous system (CNS)
is the part of the nervous system consisting of the brain and spinal cord. The central nervous system is so named because it integrates information it receives from and coordinates and influences the activity of all parts of the bodies of bilaterally symmetric animals—that is, all multicellular animals except sponges and radially symmetric animals such as jellyfish—and it contains the majority of the nervous system.

Chemotherapy
as a treatment of cancer often relies on the ability of cytotoxic agents to kill or damage cells which are reproducing; this preferentially targets rapidly dividing cancer cells. This cancer treatment uses one or more anticancer drugs (chemotherapeutic agents) as part of a standardized chemotherapy regimen. It may be given with a curative intent (which almost always involves combinations of drugs), or it may aim to prolong life or to reduce symptoms (palliative chemotherapy). Chemotherapy is one of the major categories of medical oncology (the medical discipline specifically devoted to pharmacotherapy for cancer).

Cytotoxicity	is the quality of being toxic to cells. Examples of toxic agents are an immune cell or some types of venom, e.g., from the puff adder (Bitis arietans) or brown recluse spider (Loxosceles reclusa).
Dopamine (3,4-dihydroxyphenethylamine)	is an organic chemical of the catecholamine and phenethylamine families that plays several important roles in the brain and body. It is an amine synthesized by removing a carboxyl group from a molecule of its precursor chemical L-DOPA, which is synthesized in the brain and kidneys. Dopamine is also synthesized in plants and most multicellular animals. In the brain, dopamine functions as a neurotransmitter —a chemical released by neurons (nerve cells) to send signals to other nerve cells. The brain includes several distinct dopamine pathways, one of which plays a major role in reward-motivated behavior. Most types of reward increase the level of dopamine in the brain, and many addictive drugs increase dopamine neuronal activity. Other brain dopamine pathways are involved in motor control and in controlling the release of various hormones. These pathways and cell groups form a dopamine system which is neuromodulatory.
Doxorubicin	is a medication used in cancer chemotherapy. It is commonly used in the treatment of a wide range of cancers, including hematological malignancies (blood cancers, like leukemia and lymphoma), many types of carcinoma (solid tumors), and soft tissue sarcomas. It is often used in combination chemotherapy as a component of various chemotherapy regimens.
Imaging agents	are chemicals designed to allow clinicians to improve the imaging of specific organs, tissues, diseases, and physiological functions.
Interleukin (IL),	any of a group of naturally occurring proteins that mediate communication between cells. Interleukins regulate cell growth, differentiation, and motility. They are particularly important in stimulating immune responses, such as inflammation. Interleukins are a group

of cytokines (secreted proteins and signal molecules) that were first seen to be expressed by white blood cells (leukocytes). The interleukin-13 receptor (IL13R) is a type I cytokine receptor, binding Interleukin-13. It consists of two subunits, encoded by IL13RA1 and IL4R, respectively. These two genes encode the proteins IL-13Rα1 and IL-4Rα. These form a dimer with IL-13 binding to the IL-13Rα1 chain, and IL-4Rα stabilizes this interaction. This IL-13 receptor can also instigate IL-4 signaling. In both cases, this occurs via activation of the Janus kinase (JAK)/Signal Transducer and Activator of Transcription (STAT) pathway, resulting in phosphorylation of STAT6. Phosphorylated STAT6 dimerises and acts as a transcription factor activating many genes.

Monoclonal antibodies (mAb or moAb) are antibodies that are made by identical immune cells that are all clones of a unique parent cell. Monoclonal antibodies can have monovalent affinity, in that they bind to the same epitope (the part of an antigen that is recognized by the antibody). In contrast, polyclonal antibodies bind to multiple epitopes and are usually made by several different plasma cell (antibody secreting immune cell) lineages. Bispecific monoclonal antibodies can also be engineered, by increasing the therapeutic targets of one single monoclonal antibody to two epitopes. Given almost any substance, it is possible to produce monoclonal antibodies that specifically bind to that substance; they can then serve to detect or purify that substance. This has become an important tool in biochemistry, molecular biology, and medicine. Monoclonal antibodies (mAbs) have become a successful therapeutic drug class due to their specificity, efficacy, and the low level of adverse effects they induce. They are single-targeting molecules meaning that all antibodies in a drug product are identical and therefore bind specifically to only one binding site on one target. Such single-targeting

molecules offer specificity but not diversity, which may help explain why a recombinant mAb drug is less likely to completely neutralize or eliminate targets involved in disease, and consequently why mAbs may provide limited clinical benefit.

Photodynamic therapy (PDT)	is a clinically approved and minimally invasive therapy that uses a nontoxic light-sensitive compound (photosynthesizer) that is readily absorbed by abnormal cells. When exposed to a specific wavelength of light, the photosynthesizer is activated to produce changes in endothelial cell integrity that ultimately produce vascular disruption.
Prostate-specific antigen (PSA),	also known as gamma-seminoprotein or kallikrein-3 (KLK3), is a glycoprotein enzyme encoded in humans by the KLK3 gene. PSA is a member of the kallikrein-related peptidase family and is secreted by the epithelial cells of the prostate gland. PSA is present in small quantities in the serum of men with healthy prostates, but is often elevated in the presence of prostate cancer or other prostate disorders.
Therapeutic agent	is a structure of natural or synthetic origin used for its specific action against disease, usually against infection. A therapeutic effect is a consequence of a medical treatment of any kind, the results of which are judged to be desirable and beneficial.
Therapy agents	are used to modify the relationship between tumor and host, altering the host's biological response to tumor cells, with a resultant therapeutic effect. Most therapy agents are designed to activate the patient's immune system and induce it to attack cancer cells. Common biological agents that have been approved for use in treating specific types of cancer are interferons, monoclonal antibodies, interleukins, tumor vaccines, etc.

References

1. Gao J, Tang FQ, Ren J (2005) Electroless nickel deposition on amino-functionalized silica spheres. Surf Coat Technol 200:2249–2252

2. Dun HJ, Zhang WQ, Wei Y, Song XQ, Li YM, Chen LR (2004) Layer-by-layer self-assembly of multilayer zirconia nanoparticles on silica spheres for HPLC packings. Anal Chem 76:5016–5023

3. Dhas NA, Zaban A, Gedanken A (1999) Surface synthesis of zinc sulfide nanoparticles on silica microspheres: sonochemical preparation, characterization, and optical properties. Chem Mater 11:806–813

4. Khushalani D, Hasenzahl S, Mann S (2001) Synthesis of mesoporous silica monoliths with embedded nanoparticles. J Nanosci Nanotechnol 1:129–132

5. Li T, Moon J, Morrone AA, Mecholsky JJ, Talham DR, Adair JH (1999) Preparation of Ag/SiO$_2$ nanosize composites by a reverse micelle and sol−gel technique. Langmuir 15:4328–4334

6. Martino A, Yamamaka SA, Kawola JS, Loy DL (1997) Encapsulation of gold nanoclusters in silica materials via an inverse micelle/sol−gel synthesis. Chem Mater 9:423–429

7. Chen W, Cai WP, Liang CH, Zhang LD (2001) Synthesis of gold nanoparticles dispersed within pores of mesoporous silica induced by ultrasonic irradiation and its characterization. Mater Res Bull 36:335–342

8. Whilton NT, Berton B, Bronstein L, Hentze HP, Antonietti M (1999) Organized functionalization of mesoporous silica supports using prefabricated metal–polymer modules. Adv Mater 11:1014–1018

9. Mayers B, Jiang X, Sunderland D, Cattle B, Xia Y (2003) Hollow nanostructures of platinum with controllable dimensions can be synthesized by templating against selenium nanowires and colloids. J Am Chem Soc 125:13364–13365

10. Yin Y, Erdonmez C, Aloni S, Alivisatos AP (2006) Faceting of nanocrystals during chemical transformation: From solid silver spheres to hollow gold octahedra. J Am Chem Soc 128:12671–12673

11. Martin CR (1994) Nanomaterials: a membrane-based synthetic approach. Science 266:1961–1966

12. Kabashin AV, Evans P, Pastkovsky S, Hendren W, Wurtz GA, Atkinson R, Pollard R, Podolskiy VA, Zayats AV (2009) Plasmonic nanorod metamaterials for biosensing. Nat Mater 8:867–871

13. Li Z, Li W, Camargo PHC, Xia Y (2008) Facile synthesis of branched an nanostructures by templating against a self-destructive lattice of magnetic Fe nanoparticles. Angew Chem Int Ed 47:9653–9656

14. Zhao N, Li L, Huang T, Qi L (2010) Controlled synthesis of PbS–Au nanostar–nanoparticle heterodimers and cap-like Au nanoparticles. Nanoscale 2:2418–2423

15. Wirtz M, Martin CR (2003) Template-fabricated gold nanowires and nanotubes. Adv Mater 15:455–458

16. Hurst SJ, Payne EK, Qin L, Mirkin CA (2006) Multisegmented one-dimensional nanorods prepared by hard-template synthetic methods. Angew Chem Int Ed 45:2672–2692

17. Piquemal JY, Viau G, Beaunier P, Bozon-Verduraz F, Fiévet F (2003) One-step construction of silver nanowires in hexagonal mesoporous silica using the polyol process. Mater Res Bull 38:389–394

18. Nishizawa M, Menon VP, Martin CR (1995) Metal nanotubule membranes with electrochemically switchable ion-transport selectivity. Science 268:700–702

19. Mitra A, Bhaumik A (2007) Nanoscale silver cluster embedded in artificial heterogeneous matrix consisting protein and sodium polyacrylate. Mater Lett 61:659–662

20. Hu Y, Ge J, Lim D, Zhang T, Yin Y (2008) Size-controlled synthesis of highly water-soluble silver nanocrystals. J Solid State Chem 181:1524–1529

21. Guoping L, Yunjun L, Wenting L, Jie L, Yujuan J, Sufang G (2010) Dependence of property of silver nanoparticles within dendrimer-template on molar ratios of Ag$^+$ to PAMAM dendrimers. Chin J Chem 28:633–638

22. Kumar A, Ramakrishnan V, Gonnade R, Ganesh KN, Sastry M (2002) Electrostatically entrapped DNA molecules in lipid thin films as templates for the in situ growth of silver nanoparticles. Nanotechnology 13:597–600

23. Jana NR, Gearheart L, Murphy CJ (2001) Seed-mediated growth approach for shape-controlled synthesis of spheroidal and rod-like gold nanoparticles using a surfactant template. Adv Mater 13:1389–1393

24. Murphy CJ, Sau TK, Gole AM, Orendorff CJ, Gao J, Gou L, Hunyadi SE, Li T (2005) Anisotropic metal nanoparticles: synthesis, assembly, and optical applications. J Phys Chem B 109:13857–13870

25. Heimer TA, Meyer GJ (1996) Luminescence of charge transfer sensitizers anchored to metal oxide nanoparticles. J Lumin 70:468–478

26. Selvan ST, Nogami M, Nakamura A, Hamanaka Y (1999) A facile sol-gel method for the encapsulation of gold nanoclusters in silica gels and their optical properties. J Non-Cryst 255 (2–3):254–258

27. Lembacher C, Schubert U (1998) Nanosized platinum particles by sol-gel processing of tethered metal complexes: influence of the precursors and the organic group removal method on the particle size. New J Chem 22(7):721–724

28. Moller K, Bein T (1998) Inclusion chemistry in periodic mesoporous hosts. Chem Mater 10:2950–2963

29. Schweyer F, Braunstein P, Estournés C, Guille J, Kessler H, Paillaud HL, Rosé J (2000) Metallic nanoparticles from heterometallic Co-Ru carbonyl clusters in mesoporous silica xerogels and MCM-41-type materials. Chem Commun (14):1271–1272

30. Guari Y, Thieuleux C, Mehdi A, Reyé C, Corriu RJP, Gomez-Gallardo S, Philippot K, Chaudret B, Dutartre R (2001) In situ formation of gold nanoparticles within functionalised ordered mesoporous silica via an organometallic 'chimie douce' approach. Chem Commun (15):1374–1375

31. Mukherjee P, Patra CR, Kumar R, Sastry M (2001) Entrapment and catalytic activity of gold nanoparticles in amine-functionalized MCM-41 matrices synthesized by spontaneous reduction of aqueous chloroaurate ions. Phys Chem Comm 4:24–25

32. Gomez S, Philippot K, Colliére V, Chaudret B, Senocq F, Lecante P (2000) Gold nanoparticles from self-assembled gold(I) amine precursors. Chem Commun (19):1945–1946

33. Caruso F (2001) Nanoengineering of particle surfaces. Adv Mater 13:11–22

34. Liz-Marzan LM, Griersig M, Mulvaney P (1996) Synthesis of nanosized gold–silica core shell particles. Langmuir 12:4329–4335

35. Hall SR, Davis SA, Mann S (2000) Nanoparticle templating of organo-silica shells as a route to functionalized core-shell colloids. Langmuir 16:1454–1456

36. Marinakos SM, Novak JP, Brousseau LC, House AB, Edeki EM, Feldhaus JC, Feldheim DL (1999) Gold particles as templates for the synthesis of hollow polymer capsules. Control of capsule dimensions and guest encapsulation. J Am Chem Soc 121:8518–8522

37. Kobayashi Y, Correra-Duarte MA, Liz-Marzán LM (2001) Sol−gel processing of silica-coated gold nanoparticles. Langmuir 17:6375–6379

38. Konya Z, Puntes VF, Kiricsi I, Zhu J, Alivisatos AP, Somorjai GA (2002) Nanocrystal templating of silica mesopores with tunable pore sizes. Nano Lett 2:907–910

39. Stein A, Melde BJ (2001) The role of surfactants and amphiphiles in the synthesis of porous inorganic solids. Surf Sci Ser 100:819–851

40. Wei Y, Jin D, Ding T, Shih WH, Liu X, Cheng SZD, Fu Q (1998) A non-surfactant templating route to mesoporous silica materials. Adv Mater 10:313–316

41. Wei Y, Dong H, Xu J, Feng Q (2002) Simultaneous immobilization of horseradish peroxidase and glucose oxidase in mesoporous sol–gel host materials. ChemPhysChem 3:802–808

42. Dumestre F, Chaudret B, Amiens C, Renaud P, Fejes P (2004) Superlattices of iron nanocubes synthesized from Fe[N(SiMe3)2]2. Science 303:821–823

43. Rogach AL, Nagesha D, Koktysh D, Kotov NA (2000) Synthesis of "Raisin-Bun"-type composite nanoparticle spheres. Chem Mater 12:2676–2685

44. Sertchook H, Avnir D (2003) Submicron silica/polystyrene composite particles prepared by a one-step sol-gel process. Chem Mater 15:1690–1694

45. Mokari T, Sertchook H, Aharoni A, Ebenstein Y, Avnir D, Banin U (2005) Nano@micro: general method for entrapment of nanocrystals in sol-gel-derived composite hydrophobic silica spheres. Chem Mater 17:258–263

46. Vallet-Regı M (2001) Ceramics for medical applications. J Chem Soc Dalton Trans 2:97–108

47. Bogicevic A, Jennison DR (2002) Effect of oxide vacancies on metal island nucleation. Surf Sci 515:L481–L486

48. Wahlström E, Lopez N, Schaub R, Thostrup P, Ronnau A, Africh C, Laegsgaard E, Norskov JK, Besenbacher F (2003) Bonding of gold nanoclusters to oxygen vacancies on rutile TiO2(110). Phys Rev Lett 90:026101

49. Haas G, Menck A, Brune H, Barth JV (2000) Nucleation and growth of supported clusters at defect sites: Pd/MgO(001). Phys ReV B 61:11105–11108

50. Bäumer M, Frank M, Heemeier M, Kuhnemuth R, Stempel S, Freund HJ (2000) Nucleation and growth of transition metals on a thin alumina film. Surf Sci 454–456:957

51. Kim YD, Wei T, Goodman DW (2003) Identification of defect sites on SiO2 thin films grown on Mo(112). Langmuir 19:354–357

52. Liu ST, Maoz R, Schmid G, Sagiv J (2002) Template guided self-assembly of [Au55] clusters on nanolithographically defined monolayer patterns. Nano Lett 2:1055–1060

53. Wouters D, Schubert US (2004) Nanolithography and nanochemistry: probe-related patterning techniques and chemical modification for nanometer-sized devices. Angew Chem Int Ed 43:2480–2495

54. Yamaguchi T, Zoshida S, Kinbara A (1974) Optical effect of the substrate on the anomalous absorption of aggregated silver films. Thin Solid Films 21:173–187

55. Wind MM, Vlieger J, Bedeaux D (1987) The polarizability of a truncated sphere on a substrate I. Phys A 141:33–57

56. Gozhenko VV, Grechko LG, Whites KW (2003) Electrodynamics of spatial clusters of spheres: substrate effects. Phys Rev B 68:125422

57. Westcott SL, Oldenburg SJ, Lee TR, Halas NJ (1998) Formation and adsorption of clusters of gold nanoparticles onto functionalized silica nanoparticle surfaces. Langmuir 14:5396–5401

58. Pol VG, Gedanken A, Calderon-Moreno J (2003) Deposition of gold nanoparticles on silica spheres: a sonochemical approach. Chem Mater 15:1111–1118

59. Kobayashi Y, Tadaki Y, Nagao D, Konno M (2005) Deposition of gold nanoparticles on silica spheres by electroless metal plating technique. J Colloid Interface Sci 283:601–604

60. Lim YT, Park OO, Jung HT (2003) Gold nanolayer-encapsulated silica particles synthesized by surface seeding and shell growing method: near infrared responsive materials. J Colloid Interface Sci 263:449–453

61. Zhang Q, Yin Y (2013) Beyond spheres: Murphy's silver nanorods and nanowires. Chem Commun 49:215–217

62. Sanchez-Gaytan BL, Qian Z, Hastings SP, Reca ML, Fakhraai Z, Park SJ (2013) Controlling the topography and surface plasmon resonance of gold nanoshells by a templated surfactant-assisted seed growth method. J Phys Chem C 117:8916–8923

63. Toshima N (2000) In: Sugimoto T (ed) Fine Particles: synthesis, characterization, and mechanisms of growth, vol 92. Marcel Dekker, New York, USA, Chap 9, p. 430

64. Bonet F, Guéry C, Guyomard D, Herrera-Urbina R, Tekaia-Elhsissen K, Tarascon JM (1999) Electrochemical reduction of noble metal compounds in ethylene glycol. Int Inorg Mater 1:47–51

65. Kim DW, Lee JM, Oh C, Kim DS, Oh SG (2006) A novel preparation route for platinum–polystyrene heterogeneous nanocomposite particles using alcohol-reduction method. J Colloid Interface Sci 297:365–369

66. Snoeks E, van Blaaderen A, van Dillen T, van Kats CM, Brongersma ML, Polman A (2000) Colloidal ellipsoids with continuously variable shape. Adv Mater 12:1511–1514

67. Benyagoub A, Klaumiinzer S, Thome L, Dran JC, Garrido F, Dunlop A (1992) Ion-beam induced plastic deformation in amorphous materials investigated by marker implantation and RBS. Nucl Instr Methods B64:684–686

68. Liu J, Hu X, Hou S, Wen T, Liu W, Zhu X, Yin JJ, Wu X (2012) Au@Pt core/shell nanorods with peroxidase-and ascorbate oxidase-like activities for improved detection of glucose. Sens Actuators B 166:708–714

69. Bo X, Bai J, Qi B, Guo L (2011) Ultra-fine Pt nanoparticles supported on ionic liquid polymer-functionalized ordered mesoporous carbons for nonenzymatic hydrogen peroxide detection. Biosens Bioelectron 28:77–83

70. Feng L, Wu X, Ren L, Xiang Y, He W, Zhang K, Zhou W, Xie S (2008) Well-controlled synthesis of Au@ Pt nanostructures by gold-nanorod-seeded growth. Chem Eur J 14:9764–9771

71. He W, Liu Y, Yuan J, Yin JJ, Wu X, Hu X, Zhang K, Liu J, Chen C, Ji Y (2011) Au@Pt nanostructures as oxidase and peroxidase mimetics for use in immunoassays. Biomaterials 32:1139–1147

72. Tedsree K, Li T, Jones S, Chan CWA, Yu KMK, Bagot PAJ, Marquis EA, Smith GDW, Tsang SCE (2011) Hydrogen production from formic acid decomposition at room temperature using a Ag-Pd core-shell nanocatalyst. Nat Nanotechnol 6:302–307

73. Wang J, Xia H, Zhang Y, Lu H, Kamat R, Dobrynin AV, Cheng J, Lin Y (2013) Nucleation-controlled polymerization of nanoparticles into supramolecular structures. J Am Chem Soc 135:11417–11420

74. Lattuada M, Hatton TA (2011) Synthesis, properties and applications of janus nanoparticles. Nano Today 6:286–308

75. Reinhard BM, Siu M, Agarwal H, Alivisatos AP, Liphardt J (2005) Calibration of dynamic molecular rulers based on plasmon coupling between gold nanoparticles. Nano Lett 5:2246–2252

76. Mucic RC, Storhoff JJ, Mirkin CA, Letsinger RL (1998) DNA-directed synthesis of binary nanoparticle network materials. J Am Chem Soc 120:12674–12675

77. Loweth CJ, Caldwell WB, Peng X, Alivisatos AP, Schultz PG (1999) DNA-based assembly of gold nanocrystals. Angew Chem Int Ed 38:1808–1812

78. Busson MP, Rolly B, Stout B, Bonod N, Larquet E, Polman A, Bidault S (2011) Optical and topological characterization of gold nanoparticle dimers linked by a single dna double strand. Nano Lett 11:5060–5065

79. Wolcott A, Gerion D, Visconte M, Sun J, Schwartzberg A, Chen SW, Zhang JZ (2006) Silica-coated CdTe quantum dots functionalized with thiols for bioconjugation to IgG proteins. J Phys Chem B 110:5779–5789

80. Lee DC, Mikulec FV, Pelaez JM, Koo B, Korgel BA (2006) Synthesis and magnetic properties of silica-coated FePt nanocrystals. J Phys Chem B 110:11160–11166

81. Sivakumar S, Diamente PR, Veggel FC (2006) Silica coated Ln^{3+}-doped LaF3 nanoparticles as robust down-and upconverting biolabels. Chem Eur J 12:5878–5884

82. Liu S, Han MY (2010) Silica-coated metal nanoparticles. Chem Asian J 5:36–45

83. Burns A, Ow H, Wiesner U (2006) Fluorescent coreshell silica nanoparticles: towards "Lab on a Particle" architectures for nanobiotechnology. Chem Soc Rev 35:1028–1042

84. Haensch C, Hoeppener S, Schubert US (2010) Chemical modification of self-assembled silane based monolayers by surface reactions. Chem Soc Rev 39:2323–2334

85. Knopp D, Tang D, Niessner R (2009) Review: bioanalytical applications of biomolecule-functionalized nanometersized doped silica particles. Anal Chim Acta 647:14–30

86. Melde BJ, Johnson BJ (2010) Mesoporous materials in sensing: morphology and functionality at the meso-interface. Anal Bioanal Chem 398:1565–1573

87. Lee CH, Lin TS, Mou CY (2009) Mesoporous materials for encapsulating enzymes. Nano Today 4:165–179

88. Walcarius A, Kuhn A (2008) Ordered porous thin films in electrochemical analysis. TrAC Trends Anal Chem 27:593–603

89. Jackson JB, Halas NJ (2001) Silver nanoshells: variations in morphologies and optical properties. J Phys Chem B 105:2743–2746

90. Caruso F, Spasova M, Salgueiriño-Maceira V, Liz-Marzán LM (2001) Multilayer assemblies of silica-encapsulated gold nanoparticles on decomposable colloid templates. Adv Mater 13:1090–1094

91. Renard C, Ricolleau C, Fort E, Besson S, Gacoin T, Boilot JP (2002) Coupled technique to produce two-dimensional superlattices of nanoparticles. Appl Phys Lett 80:300–302

92. Gurin VS, Alexeenko AA, Yumashev KV, Prokoshin R, Zolotovskaya SA, Zhavnerko GA (2003) Structure and optical properties of Cu_xO- and Cu_xSe-doped sol-gel silica glasses. Mater Sci Eng C 23:1063–1067

93. Cho S, Lee S, Oh SG, Park SJ, Kim WM, Cheong BK, Chung M, Song KB, Lee TS, Kim SG (2000) Optical properties of Au nanocluster embedded dielectric films. Thin Solid Films 377:97–102

94. Konya Z, Puntes VF, Kiricsi I, Zhu J, Ager JW, Ko MK, Frei H, Alivisatos P, Somorjai GA (2003) Synthetic insertion of gold nanoparticles into mesoporous silica. Chem Mater 15:1242–1248

95. McMorn P, Htchings GJ (2004) Heterogeneous enantioselective catalysts: strategies for the immobilisation of homogeneous catalysts. Chem Soc Rev 33:108–122

96. Kresge CT, Leonowicz ME, Roth WJ, Varuli JC, Beck JS (1992) Ordered mesoporous molecular sieves synthesized by a lipid-crystal template mechanism. Nature 359:710–712

97. Mishra GS, Kumar A (2012) Hydroisomerization of saturated hydrocarbons with novel MCM-41 immobilized Re(V) complex catalysts. Appl Catal A Gen 429–430:1–8

98. He J, Ichinose I, Kunitake T, Nakao A (2002) In situ synthesis of noble metal nanoparticles in ultrathin TiO_2−gel films by a combination of ion-exchange and reduction processes. Langmuir 18:10005–10010

99. He J, Ichinose I, Fujikawa S, Kunitake T, Nakao A (2002) Reversible conversion of nanoparticles of metallic silver and silver oxide in ultrathin TiO_2 films: a chemical transformation in nano-space. Chem Commun (17):1910–1911

100. Besson S, Gacoin T, Ricolleau C, Boilot JP (2003) Silver nanoparticle growth in 3D-hexagonal mesoporous silica films. Chem Commun (3):360–361

101. Pinto RJB, Marques PAAP, Martins MA, Neto CP, Trindade T (2007) Electrostatic assembly and growth of gold nanoparticles in cellulosic fibres. J Colloid Interface Sci 312:506–512

102. Kawazu M, Nara M. Tsujino T (2004) Preparation of Au-TiO_2 hybrid nano particles in silicate film made by sol-gel method. J Sol-Gel Sci Technol 31:109–112

103. Shameli K, Bin Ahmad M, Yunus WMZW, Ibrahim NA, Gharayebi Y, Sedaghat S (2010) Synthesis of silver/montmorillonite nanocomposites using γ-irradiation. Int J Nanomed 5:1067–1077

104. Cho KH, Park JE, Osaka T, Park SG (2005) The study of antimicrobial activity and preservative effects of nanosilver ingredient. Electrochim Acta 51:956–960

105. Rai M, Yadav A, Gade A (2009) Silver nanoparticles as a new generation of antimicrobials. Biotechnol Adv 27:76–83

106. Ahmad MB, Shameli K, Yunus WMZW, Ibrahim NA, Darroudi M (2010) Synthesis and characterization of silver/clay/ starch bionanocomposites by green method. Aust J Basic Appl Sci 4:2158–2165

107. Pillai SK, Ray SS, Scriba M, Bandyopadhyay J, Van der Merwe MPR, Badenhorst J (2013) Microwave assisted green synthesis and characterization of silver/montmorillonite heterostructures with improved antimicrobial properties. Appl Clay Sci 83–84:315–321

108. Lee JM, Kim DW, Jun YD, Oh SG (2006) Preparation of silica-silver heterogeneous nanocomposite particles by one-pot preparation strategy using polyol process: size-controlled immobilization of silver nanoparticles. Mater Res Bull 41:1407–1416

109. Lee JM, Kim DW, Lee YH, Oh SG (2005) New approach for preparation of silver-polystyrene heterogeneous nanocomposite by polyol process. Chem Lett 34:928–929

110. Cao Y, Li YS, Tseng JL, Desiderio DM (2001) Interfacial study of benzenesulfinate chemisorbed on silver. Apectrochim Acta Part A 57:27–34

111. Park JH, Kim YG, Oh C, Shin SI, Kim YC, Oh SG, Kong SH (2005) Fabrication of hollow silver spheres by MPTMS-functionalized hollow silica spheres as templates. Mater Res Bull 40:271–280

112. Badley RD, Ford WT, McEnroe JJ, Assink RA (1990) Surface modification of colloidal silica. Langmuir 6:792–801

113. Slistan-Grijalva A, Herrera-Urbina R, Rivas-Silva JF, Ávalos-Borja M, Castillón-Barraza FF, Posada-Amarillas A (2005) Classical theoretical characterization of the surface plasmon absorption band for silver spherical nanoparticles suspended in water and ethylene glycol. Physica E 27:104–112

114. Zhang J, Liu J, Wang S, Zhan P, Wang Z, Ming N (2004) Facile methods to coat polystyrene and silica colloids with metal. Adv Funct Mater 14:1089–1096

115. Wang DS, Kerker M, Chew H (1980) Raman and fluorescent scattering by molecules embedded in dielectric spheroids. Appl Opt 19:2135–2328

116. Schierhorn M, Liz-Marzán LM (2002) Synthesis of bimetallic colloids with tailored intermetallic separation. Nano Lett 2:13–16

117. Shin HS, Yang HJ, Kim SB, Lee MS (2004) Mechanism of growth of colloidal silver nanoparticles stabilized by polyvinyl pyrrolidone in gamma-irradiated silver nitrate solution. J Colloid Interface Sci 274:89–94

118. Kim YH, Lee DK, Kang YS (2005) Synthesis and characterization of Ag and Ag–SiO$_2$ nanoparticles. Colloids Surf A Physicochem Eng Aspects 257–258:273–276

119. Wu SH, Chen DH (2004) Synthesis of high-concentration Cu nanoparticles in aqueous CTAB solutions. J Colloids Interface Sci 273:165–169

120. Magudapathy P, Gangopadhyay BK (2001) Electrical transport studies of Ag nanoclusters embedded in glass matrix. Phys B 299:142–146

121. George C, Konstantin S, Therese MC (1996) Unusual extinction spectra of nanometer-sized silver particles arranged in two dimensional arrays. J Phys Chem 100:5166–5168

122. Rivas L, Sanchez-Cortes S, Garcia-Ramos JV, Morcillo G (2001) Growth of silver colloidal particles obtained by citrate reduction to increase the raman enhancement factor. Langmuir 17:574–577

123. Mulvaney P (1996) Surface plasmon spectroscopy of nanosized metal particles. Langmuir 12:788–800

124. Lee JM, Kim DW, Kim TH, Oh SG (2007) Facile route for preparation of silica-silver heterogeneous nanocomposite particles using alcohol reduction method. Mater Lett 61:1558–1562

125. Stöber W, Fink A, Bohn E (1968) Controlled growth of monodisperse silica spheres in the micron size range. J Colloid Interface Sci 26:62–69

126. Sarkar A, Kapoor S, Mukherjee T (2005) Preparation, characterization, and surface modification of silver nanoparticles in formamide. J Phys Chem B 109:7698–7704

127. Yu JY, Schreiner S, Vaska L (1990) Homogeneous catalytic production of hydrogen and other molecules from water-DMF solutions. Inorg Chim Acta 170:145–147

128. Tojo T, Blanco MC, Rivadulla F, Lopez-Quintela MM (1997) Kinetics of the formation of particles in microemulsions. Langmuir 13:1970–1977

129. Kheiralla ZH, Rushdy AA, Betiha MA, Yakob NAN (2014) High-performance antibacterial of montmorillonite decorated with silver nanoparticles using microwave-assisted method. J Nanopart Res 16:2560

130. Papa M, Pradell T, Crespo D, Calderon-Moreno JM (2007) Stable silver colloidal dispersions using short chain polyethylene glycol. Colloids Surf A 303:184–190

131. Senthil Kumar P, Ray S, Sunandana CS (2001) Sb-assisted AgI nanoparticle growth in thin films. Mater Phys Mech 4:39–41
132. Neri G, Rizzo G, Arico AS, Crisafulli C, de Luca L, Donato A, Musolino MG, Pietropaolo R (2007) One-pot synthesis of naturanol from a-pinene oxide on bifunctional Pt-Sn/SiO2 heterogeneous catalysts (I) the catalytic system. Appl Catal A 325:15–24
133. Akelah A, Rehab A, Agag T, Betiha M (2007) Polystyrene nanocomposite materials by in situ polymerization into montmorillonite-vinyl monomer interlayers. J Appl Polym Sci 103:3739–3750
134. Rehab A, Akelah A, Agag T, Betiha MJ (2007) Polymer-organoclay hybrids by polymerization into montmorillonitevinyl monomer interlayers. J Appl Polym Sci 106:3502–3514
135. Xie YW, Ye RQ, Liu HL (2006) Synthesis of silver nanoparticles in re-verse micelles stabilized by natural biosurfactant. Colloid Surf A 279:175–178
136. He S, Yao J, Jiang P, Shi D, Zhang H, Xie S, Pang S, Gao H (2001) Formation of silver nanoparticles and self-assembled twodimensional ordered superlattice. Langmuir 17:1571–1575
137. Choi H, Lee JP, Ko SJ, Jung JW, Park H, Yoo S, Park O, Jeong JR, Park S, Kim JY (2013) Multipositional silica-coated silver nanoparticles for high-performance polymer solar cells. Nano Lett 13:2204–2208
138. Aihara N, Torigoe K, Esumi K (1998) Preparation and characterization of gold and silver nanoparticles in layered laponite suspensions. Langmuir 14:4945–4949
139. Vadakkekara R, Chakraborty M, Parikh PA (2012) Catalytic performance of silica-supported silver nanoparticles for liquid-phase oxidation of ethylbenzene. Ind Eng Chem Res 51:5691–5698
140. Mao H, Gao X, Yang J, Li B (2011) A novel one-step synthesis of meso-structured silica-pillared clay with highly ordered gallery organic-inorganic hybrid frame. Appl Surf Sci 257:4655–4662
141. Betiha MA, Hassan HMA, Al-Sabagh AM, Khder AS, Ahmed EA (2012) Direct synthesis and the morphological control of highly ordered mesoporous AlSBA-15 using urea-tetrachloroaluminate as a novel aluminum source. J Mater Chem 22:17551–17559
142. Shameli K, Bin Ahmad M, Zargar M, Yunus WMZW, Rustaiyan A, Ibrahim NA (2011) Synthesis of silver nanoparticles in montmorillonite and their antibacterial behaviour. Int J Nanomed 6:581–590
143. Sing KSW, Everett DH, Haul RAW, Moscou L, Pierotti RA, Rouquérol J, Siemieniewska T (1985) Reporting physisorption data for gas/solid systems with special reference to the determination of surface area and porosity. Pure Appl Chem 57:603–619
144. Stein A, Melde BJ, Schroden RC (2000) Hybrid inorganic-organic mesoporous silicates-nanoscopic reactors coming of age. Adv Mater 12:1403–1419
145. Soto G, Tiznado H, Contreras O, Pérez-Tijerina E, Cruz-Reyes J, Del Valle M, Portillo A (2011) Preparation of a Ag/SiO$_2$ nanocomposite using a fluidized bed microwave plasma reactor, and its hydrodesulphurization and *Escherichia coli* bactericidal activities. Powder Technol 213:55–62
146. Mahltig B, Gutmann E, Reibold M, Meyer DC, Böttcher H (2009) Synthesis of Ag and Ag/SiO$_2$ sols by solvothermal method and their bactericidal activity. J Sol-Gel Sci Technol 51:204–214
147. Meng XK, Tang SC, Vongehr S (2010) A review on diverse silver nanostructures. J Mater Sci Technol 26:487–522
148. Pinchuk A, Hilger A, von Plessen G, Kreibig U (2004) Substrate effect on the optical response of silver nanoparticles. Nanotechnology 15:1890–1896
149. Starodub D, Gustafsson T, Garfunkel E (2004) The reaction of O$_2$ with Al(110): a medium energy ion scattering study of nano-scale oxidation. Surf Sci 552:199–214
150. Hilger A, Tenfelde M, Kreibig U (2001) Silver nanoparticles deposited on dielectric surfaces. Appl Phys B 73:361–372

151. Bellec M, Royon A, Bourhis K, Choi J, Bousquet B, Treguer M, Cardinal T, Videau JJ, Richardson M, Canioni L (2010) 3D patterning at the nanoscale of fluorescent emitters in glass. J Phys Chem C 114:15584–15588

152. Eichelbaum M, Rademann K, Hoell A, Tatchev DM, Weigel W, Stößer R, Pacchioni G (2008) Photoluminescence of atomic gold and silver particles in soda-lime silicate glasses. Nanotechnology 19:135701–135709

153. Tikhomirov VK, Rodríguez VD, Kuznetsov A, Kirilenko D, Van Tendeloo G, Moshchalkov VV (2010) Preparation and luminescence of bulk oxyfluoride glasses doped with Ag nanoclusters. Opt Express 18:22032–22040

154. Royon A, Bourhis K, Bellec M, Papon G, Bousquet B, Deshayes Y, Cardinal T, Canioni L (2010) Silver clusters embedded in glass as a perennial high capacity optical recording medium. Adv Mater 22:5282–5286

155. Sandroff CJ, Herschbach DR (1985) Kinetics of displacement and charge transfer reactions probed by SERS: evidence for distinct donor and acceptor sites on colloidal gold surfaces. Langmuir 1:131–135

156. Zhang H, He HX, Wang J, Mu T, Liu ZF (1998) Force titration of amino group-terminated self-assembled monolayers using chemical force microscopy. Appl Phys A 66:S269–S271

157. Zhu T, Fu XY, Mu T, Wang J, Liu ZF (1999) pH-dependent adsorption of gold nanoparticles on p-aminothiophenol-modified gold substrates. Langmuir 15:5197–5199

158. Zheng JW, Zhu ZH, Chen HF, Liu ZF (2000) Nanopatterned assembling of colloidal gold nanoparticles on silicon. Langmuir 16:4409–4412

159. Ling X, Zhu X, Zhang J, Zhu T, Liu M, Tong L, Liu Z (2005) Reproducible patterning of single Au nanoparticles on silicon substrates by scanning probe oxidation and self-assembly. J Phys Chem B 109:2657–2665

160. Rye RR, Nelson GC, Dugger MT (1997) Mechanistic aspects of alkylchlorosilane coupling reactions. Langmuir 13:2965–2972

161. Min BK, Wallace WT, Santra AK, Goodman DW (2004) Role of defects in the nucleation and growth of Au nanoclusters on SiO_2 thin films. J Phys Chem B 108:16339–16343

162. Pacchioni G, Ierano G (1998) Ab initio theory of optical transitions of point defects in SiO_2. Phys Rev B 57:818–832

163. Namai Y, Fukui KI, Iwasawa Y (2003) Atom-resolved noncontact atomic force microscopic observations of $CeO_2(111)$ surfaces with different oxidation states: surface structure and behavior of surface oxygen atoms. J Phys Chem B 107:11666–11673

164. Ren H, Zhang L (2010) In situ growth approach for preparation of Au nanoparticle-doped silica aerogel. Colloids Surf A Physicochem Eng Aspects 372(1–3):98–101

165. Koyanaka H, Takeuchi K, Loong CK (2005) Gold recovery from parts-per-trillion level aqueous solutions by a nanostructure Mn_2O_2 adsorbent. Sep Purif Technol 43:9–15

166. Zhang L, Feng YG, Wang LY, Zhang JY, Chen M, Qian DJ (2007) Comparative studies between synthetic routes of SiO_2@Au composite nanoparticles. Mater Res Bull 42:1457–1467

167. Wang W, Ruan CM, Gu BH (2006) Development of gold-silica composite nanoparticle substrates for perchlorate detection by surface-enhanced Raman spectroscopy. Anal Chim Acta 567:121–126

168. Hussain I, Brust M, Papworth AJ, Cooper AI (2003) Preparation of acrylate-stabilized gold and silver hydrosols and gold-polymer composite films. Langmuir 19:4831–4835

169. Guari Y, Thieuleux C, Mehdi A, Reyé C, Corriu RJP, Gomez-Gallardo S, Philippot K, Chaudret B (2003) In situ formation of gold nanoparticles within thiol functionalized HMS-C16 and SBA-15 type materials via an organometallic two-step approach. Chem Mater 15:2017–2024

170. Cheng S, Wei Y, Feng QW, Qiu KY, Pang JB, Jansen SA, Yin R, Ong K (2003) Facile synthesis of mesoporous gold-silica nanocomposite materials via sol-gel process with nonsurfactant templates. Chem Mater 15:1560–1566

171. Joo J, Hyeon T, Hyeon-Lee J (2000) Fabrication of novel mesoporous dimethylsiloxane-incorporated silicas. Chem Commun 16:1487–1488

172. Zhao D, Hou Q, Feng J, Chmelka BF, Stucky GD (1998) Nonionic triblock and star diblock copolymer and oligomeric surfactant syntheses of highly ordered, hydrothermally stable, mesoporous silica structures. J Am Chem Soc 120:6024–6036

173. Shipway AN, Katz E, Willner I (2000) Nanoparticle arrays on surfaces for electronic, optical, and sensor applications. ChemPhysChem 1:18–52

174. Smith DD, Sibille L, Ignont E, Cronise RJ, Noever DA (2000) Noble metal immersion spectroscopy of silica alcogels and aerogels. J Porous Mater 7:499–508

175. Bloemer MJ, Haus JW, Ashley PR (1990) Degenerate four-wave mixing in colloidal gold as a function of particle size. J Opt Soc Am B 7:790–795

176. Stoermer RL, Keating CD (2006) Distance-dependent emission from dye-labeled oligonu-cleotides on striped Au/Ag nanowires: effect of secondary structure and hybridization efficiency. J Am Chem Soc 128:13243–13254

177. Zhang J, Fu Y, Lakowicz JR (2007) Emission behavior of fluorescently labeled silver nanoshell: enhanced self-quenching by metal nanostructure. J Phys Chem C 111:1955–1961

178. Zhang J, Fu Y, Mei Y, Jiang F, Lakowicz JR (2010) Fluorescent metal nanoshell probe to detect single miRNA in lung cancer cell. Anal Chem 82:4464–4471

179. Huang X, Peng X, Wang Y, Wang Y, Shin DM, El-Sayed MA, Nie S (2010) A reexamination of active and passive tumor targeting by using rod-shaped gold nanocrystals and covalently conjugated peptide ligands. ACS Nano 4:5887–5896

180. Templeton AC, Wuelfing WP, Murray RW (2000) Monolayer-protected cluster molecules. Acc Chem Res 33:27–36

181. Brinkley M (1992) A brief survey of methods for preparing protein conjugates with dyes, haptens and crosslinking reagents. Bioconjugate Chem 3:2–13

182. Lal S, Clare SE, Halas NJ (2008) Nanoshell-enabled photothermal cancer therapy: impending clinical impact. Acc Chem Res 41:1842–1851

183. Enderlein J (2002) Spectral properties of a fluorescing molecule within a spherical metallic cavity. Phys Chem Chem Phys 4:2780–2786

184. Enderlein J (2002) Theoretical study of single molecule fluorescence in a metallic nanocavity. Appl Phys Letts 80:315–317

185. Zhang J, Fu Y, Liang D, Nowaczyk K, Zhao RY, Lakowicz JR (2008) Single-cell fluorescence imaging using metal plasmon-coupled probe 2: single-molecule counting on lifetime image. Nano Lett 8:1179–1186

186. Zhang J, Fu Y, Chowdhury MH, Lakowicz JR (2008) Single-molecule studies on fluorescently labeled silver particles: effects of particle size. J Phys Chem C 112:18–26

187. Zhang J, Fu Y, Lakowicz JR (2011) Fluorescent metal nanoshells: lifetime-tunable molecular probes in fluorescent cell imaging. J Phys Chem C 115:7255–7260

188. Kerdi F, Caps V, Tuel A (2011) Mesostructured Au/C materials obtained by replication of functionalized SBA-15 silica containing highly dispersed gold nanoparticles. Microporous Mesoporous Mater 140:89–96

189. Corma A, García H (2008) Supported gold nanoparticles as catalysts for organic reactions. Chem Soc Rev 37:2096–2126

190. Hu JC, Chen LF, Zhu K, Suchopar A, Richards R (2007) Aerobic oxidation of alcohols catalyzed by gold nano-particles confined in the walls of mesoporous silica. Catal Today 122:277–283

191. Aprile C, Abad A, Garcia H, Corma A (2005) Synthesis and catalytic activity of periodic mesoporous materials incorporating gold nanoparticles. J Mater Chem 15:4408–4413

192. Zhao P, Li N, Astruc D (2013) State of the art in gold nanoparticle synthesis. Coord Chem Rev 257:638–665

193. Jan JS, Chuang TH, Chen PJ, Teng H (2011) Layer-by-layer polypeptide macromolecular assemblies-mediated synthesis of mesoporous silica and gold nanoparticle/mesoporous silica tubular nanostructures. Langmuir 27:2834–2843

194. Mieszawska AJ, Slawinski GW, Zamborini FP (2006) Directing the growth of highly-aligned gold nanorods by a surface chemical amidation reaction. J Am Chem Soc 128:5622–5623

195. Taub N, Krichevski O, Markovich G (2003) Growth of gold nanorods on surfaces. J Phys Chem B 107:11579–11582
196. Mieszawska AJ, Jalilian R, Sumanasekera GU, Zamborini FP (2005) Synthesis of gold nanorod/single wall carbon nanotube heterojunctions directly on surfaces. J Am Chem Soc 127:10822–10823
197. Mieszawska AJ, Zamborini FP (2005) Gold nanorods grown directly on surfaces from microscale patterns of gold seeds. Chem Mater 17:3415–3420
198. Wei Z, Mieszawska AJ, Zamborini FP (2004) Synthesis and manipulation of high aspect ratio gold nanorods grown directly on surfaces. Langmuir 20:4322–4326
199. Wei Z, Zamborini FP (2004) Directly monitoring the growth of gold nanoparticle seeds into gold nanorods. Langmuir 20:11301–11304
200. Jana NR, Gearheart L, Murphy CJ (2001) Wet chemical synthesis of silver nanorods and nanowires of controllable aspect ratio. Chem Commun 7:617–618
201. Link S, Burda C, Nikoobakht B, El-Sayed MA (2000) Laser-induced shape changes of colloidal gold nanorods using femtosecond and nanosecond laser pulses. J Phys Chem B 104:6152–6163
202. Rodriguez-Fernandez J, Perez-Juste J, Mulvaney P, Liz-Marzan LM (2005) Spatially-directed oxidation of gold nanoparticles by Au(III)-CTAB complexes. J Phys Chem B 109:14257–14261
203. Roorda S, van Dillen T, Polman A, Graf C, van Blaaderen A, Kooi BJ (2004) Aligned gold nanorods in silica made by ion irradiation of core-shell colloidal particles. Adv Mater 16:235–237
204. van Dillen T, van Blaaderen A, Fukarek W, Polman A (2001) Energy-dependent anisotropic deformation of colloidal silica particles under MeV Au irradiation. Appl Phys Lett 78:910–912
205. Trinkaus H, Ryazanov AI (1995) Viscoelastic model for the plastic flow of amorphous solids under energetic ion bombardment. Phys Rev Lett 74:5072–5075
206. Brongersma ML, Snoeks E, van Dillen T, Polman A (2000) Origin of MeV ion irradiation-induced stress changes in SiO_2. J Appl Phys 88:59–64
207. Snoeks E, Boutros KS, Barone J (1997) Stress relaxation in tungsten films by ion irradiation. Appl Phys Lett 71:267–269
208. Bohren CF, Huffman DR (1983) Absorption and scattering of light by small particles. Wiley, New York (Chapter 12), pp 336–338
209. Atwater HA, Polman A (2010) Plasmonics for improved photovoltaic devices. Nat Mater 9:205–213
210. Catchpole KR, Polman A (2008) Design principles for particle plasmon enhanced solar cells. Appl Phys Lett 93:191113–1–191113-3
211. Garozzo C, Puglisi RA, Bongiorno C, Scalese S, Rimini E, Lombardo S (2011) Selective diffusion of gold nanodots on nanopatterned substrates realized by self-assembly of diblock copolymers. J Mater Res 26:240–246
212. Garozzo C, La Magna A, Mannino G, Privitera V, Scalese S, Sberna PM, Simone F, Puglisi RA (2013) Competition between uncatalyzed and catalyzed growth during the plasma synthesis of Si nanowires and its role on their optical properties. J Appl Phys 113:214313
213. Huang Z, Shimizu T, Senz S, Zhang ZX, Lee W, Geyer N, Gösele U (2009) Ordered arrays of vertically aligned [110] silicon nanowires by suppressing the crystallographically preferred <100> etching directions. Nano Lett 9:2519–2525
214. Chang SW, Chuang VP, Boles ST, Thompson CV (2010) Metalcatalyzed etching of vertically aligned polysilicon and amorphous silicon nanowire arrays by etching direction confinement. Adv Funct Mater 20:4364–4370
215. Milazzo RG, D'Arrigo G, Spinella C, GrimaldiMG Rimini E (2012) Ag-assisted chemical etching of (100) and (111) n-type silicon substrates by varying the amount of deposited metal. J Electrochem Soc 159:D521–D525

216. Akhtari-Zavareh A, Li W, Maroun F, Allongue P, Kavanagh KL (2013) Improved chemical and electrical stability of gold silicon contacts via epitaxial electrodeposition. J Appl Phys 113:063708
217. Hiraki A, Lugujjo E, Mayer JW (1972) Formation of silicon oxide over gold layers on silicon substrates. J Appl Phys 43:3643
218. Okuno K, Ito T, Iwami M, Hiraki A (1980) Presence of critical Au film thickness for room temperature interfacial reaction between Au(film) and Si(crystal substrate). Solid State Commun 34:493–497
219. Andersson TG (1982) The initial growth of vapour deposited gold films. Gold Bull 15:7–18
220. Hiraki A, Kim SC, Imura T, Iwami M (1979) Si(LMM) Auger electron emission from Si alloys by keV Ar$^+$ ion bombardment, new effect and application. Jpn J Appl Phys 18:1767–1772
221. Braicovich L, Garner CM, Skeath PR, Su CY, Chye PW, Lindau I, Spicer WE (1979) Photoemission studies of the silicon-gold interface. Phys Rev B 20:5131–5141
222. Chang CA, Ottaviani G (1984) Outdiffusion of Si through gold films: the effects of Si orientation, gold deposition techniques and rates, and annealing ambients. Appl Phys Lett 44:901–903
223. Garozzo C, Filetti A, Bongiorn C, La Magna A, Simone F, Puglisi RA (2014) Room temperature evolution of gold nanodots deposited on silicon. Gold Bull 47:185–193
224. Bal JK, Hazra S (2007) Interfacial role in room-temperature diffusion of Au into Si substrates. Phys Rev B 75:20541
225. Hiraki A, Shimizu A, Iwami M, Narusawa T, Komiya S (1975) Metallic state of Si in Si noble metal vapor quenched alloys studied by Auger electron spectroscopy. Appl Phys Lett 26:57–60
226. Kim JH, Yang G, Yang S, Weiss AH (2001) Study of the growth and stability of ultra-thin films of Au deposited on Si(100) and Si(111). Surf Sci 475:37–46
227. Hiraki A, Iwami M (1974) Electronic structure of thin gold film deposited on silicon substrate studied by Auger electron and X-ray photoelectron spectroscopies. Jpn J Appl Phys 2(Supplement 2–2):749–752
228. Prasad BLV, Stoeva SI, Sorensen CM, Klabunde KJ (2003) Digestive-ripening agents for gold nanoparticles: alternatives to thiols. Chem Mater 15:935–942
229. Owens TM, Nicholson KT, Banaszak Holl MM, Suzer S (2002) Formation of alkylsilane based monolayers on gold. J Am Chem Soc 124:6800–6801
230. Stoeva SI, Klabunde KJ, Sorensen CM, Dragieva I (2002) Gram-scale synthesis of monodisperse gold colloids by the solvated metal atom dispersion method and digestive ripening and their organization into two- and three-dimensional structures. J Am Chem Soc 124:2305–2311
231. Prasad BLV, Stoeva SI, Sorensen CM, Zaikovski V, Klabunde KJ (2003) Gold nanoparticles as catalysts for polymerization of alkylsilanes to siloxane nanowires, filaments, and tubes. J Am Chem Soc 125:10488–10489
232. Metraux GS, Cao YC, Jin R, Mirkin CA (2003) Triangular nanoframes made of gold and silver. Nano Lett 3:519–522
233. Sun Y, Xia Y (2004) Multiple-walled nanotubes made of metals. Adv Mater 16:264–268
234. Sun YG, Xia YN (2002) Shape-controlled synthesis of gold and silver nanoparticles. Science 298:2176–2179
235. Sun YG, Mayers B, Xia YN (2003) Transformation of silver nanospheres into nanobelts and triangular nanoplates through a thermal process. Nano Lett 3:675–679
236. Sun Y, Xia Y (2003) Gold and silver nanoparticles: A class of chromophores with colors tunable in the range form 400 to 750 nm. Analyst 128:686–691
237. Sun Y, Mayers B, Herricks T, Xia Y (2003) Polyol synthesis of uniform silver nanowires: a plausible growth mechanism and the supporting evidence. Nano Lett 3:955–960
238. Rodriguez-Lopez JL, Montejano-Carrizales JM, Jose-Yacaman M (2006) Low dimensional non-crystallographic metallic nanostructures: HRTEM simulation, models and experimental results. Mod Phys Lett B 20:725–751

239. Ozin GA, Mitchell SA (1983) Ligand-free metal clusters. Angew Chem Int Ed Engl 22:674–694

240. Harbich W, Fedrigo S, Meyer F, Lindsay DM, Lignieres J, Rivoal JC, Kreisle D (1990) Deposition of mass selected silver clusters in rare gas matrices. J Chem Phys 93:8535–8543

241. Rabin I, Schulze W, Ertl G (1999) On the structural transformation of the reconstructed Pt (100) in electrolyte solutions. Chem Phys Lett 312:394–398

242. Ozin GA, Huber H (1978) Cryophotoclustering techniques for synthesizing very small, naked silver clusters Ag, of known size (where n = 2–5). Inorg Chem 17:155–163

243. König L, Rabin I, Schulze W, Ertl G (1996) Chemiluminescence in the agglomeration of metal clusters. Science 274:1353–1355

244. Fleischmann M, Hendra PJ, McQuillan AJ (1974) Raman spectra of pyridine adsorbed at a silver electrode. Chem Phys Lett 26:163–166

245. Creighton JA, Blatchford CG, Albrecht MG (1979) Plasma resonance enhancement of Raman scattering by pyridine adsorbed on silver or gold sol particles of size comparable to the excitation wavelength. J Chem Soc Faraday Trans 2(75):790–798

246. Xu W, Zhang JX, Zhang LD, Hu XY, Cao XL (2009) Ultrasensitive detection using surface enhanced raman scattering from silver nanowire arrays in anodic alumina membranes. J Nanosci Nanotechnol 9:4812–4816

247. Kneipp K, Wang Y, Dasari RR, Feld MS (1995) Approach to single-molecule detection using surface-enhanced resonance raman-scattering (serrs)—a study using rhodamine 6 g on colloidal silver. Appl Spectrosc 49:780–784

248. Nie SM, Emery SR (1997) Probing single molecules and single nanoparticles by surface-enhanced raman scattering. Science 275:1102–1106

249. Kneipp J, Kneipp H, Kneipp K (2008) SERS-a single-molecule and nanoscale tool for bioanalytics. Chem Soc Rev 37:1052–1060

250. Emory SR, Haskins WE, Nie SM (1998) Direct observation of size-dependent optical enhancement in single metal nanoparticles. J Am Chem Soc 120:8009–8010

251. Garrell RL (1989) Surface-enhanced Raman spectroscopy. Anal Chem 61:401A–411A

252. Yaffe NR, Blanch EW (2008) Effects and anomalies that can occur in SERS spectra of biological molecules when using a wide range of aggregating agents for hydroxylamine-reduced and citrate-reduced silver colloids. Vib Spectrosc 48:196–201

253. Cañamares MV, Garcia-Ramos JV, Sanchez-Cortes S, Castillejo M, Oujja M (2008) Comparative SERS effectiveness of silver nanoparticles prepared by different methods: a study of the enhancement factor and interfacial properties. J Colloid Interface Sci 326:103–109

254. Leopold N, Lendl B (2003) A new method for fast preparation of highly surface-enhanced Raman scattering (SERS) active silver colloids at room temperature by reduction of silver nitrate with hydroxylamine hydrochloride. J Phys Chem B 107:5723–5727

255. Zou XQ, Dong SJ (2006) Surface-enhanced Raman scattering studies on aggregated silver nanoplates in aqueous solution. J Phys Chem B 110:21545–21550

256. Leng WN, Woo HY, Vak D, Bazan GC, Kelley AM (2006) Surface-enhanced resonance raman and hyper-raman spectroscopy of water-soluble substituted stilbene and distyrylbenzene chromophores. J Raman Spectrosc 37:132–141

257. Doering WE, Nie SM (2002) Single-molecule and single-nanoparticle SERS: examining the roles of surface active sites and chemical enhancement. J Phys Chem B 106:311–314

258. Bengter H, Tengroth C, Jacobsson SP (2005) New light on Ag-colloid preparation for surface-enhanced FT-Raman spectroscopy: the role of aggregation. J Raman Spectrosc 36:1015–1022

259. Otto A, Bruckbauer A, Chen YX (2003) On the chloride activation in SERS and single molecule SERS. J Mol Struct 661–662:501–514

260. Li WY, Camargo PHC, Lu XM, Xia YN (2009) Dimers of silver nanospheres: facile synthesis and their use as hot spots for surface-enhanced Raman scattering. Nano Lett 9 (1):485–490

261. Haruta M, Yamada N, Kobayashi T, Iijima S (1989) Gold catalysts prepared by coprecipitation for low-temperature oxidation of hydrogen and of carbon monoxide. J Catal 115:301–309

262. Yoshida H, Kuwauchi Y, Jinschek JR, Sun K, Tanaka S, Kohyama M, Shimada S, Haruta M, Takeda S (2012) Visualizing gas molecules interacting with supported nanoparticulate catalysts at reaction conditions. Science 335:317–319

263. Wei Y, Liu J, Zhao Z, Duan A, Jiang G (2012) The catalysts of three-dimensionally ordered macroporous $Ce_{1-x}Zr_xO_2$-supported gold nanoparticles for soot combustion: the metal–support interaction. J Catal 287:13–29

264. Kim HY, Lee HM, Henkelman G (2012) CO oxidation mechanism on CeO_2-Supported Au nanoparticles. J Am Chem Soc 134:1560–1570

265. Martin CR (1996) Membrane-based synthesis of nanomaterials. Chem Mater 8:1739–1746

266. Wu CG, Bein T (1994) Conducting carbon wires in ordered, nanometer-sized channels. Science 266:1013–1015

267. Dick K, Dhanasekaran T, Zhang Z, Meisel D (2002) Size-dependent melting of silica-encapsulated gold nanoparticles. J Am Chem Soc 124:2312–2317

268. Lim B, Kobayashi H, Yu T, Wang J, Kim MJ, Li ZY, Rycenga M, Xia Y (2010) Synthesis of Pd-Au bimetallic nanocrystals via controlled overgrowth. J Am Chem Soc 132:2506–2507

269. Liang S, Liu XL, Yang YZ, Wang YL, Wang JH, Yang ZJ, Wang LB, Jia SF, Yu XF, Zhou L, Wang JB, Zeng J, Wang QQ, Zhang Z (2012) Symmetric and asymmetric Au-AgCdSe hybrid nanorods. Nano Lett 12:5281–5286

270. Lombardi A, Grzelczak MP, Crut A, Maioli P, Pastoriza-Santos I, Liz-Marzán LM, Fatti N, Del Vallée F (2013) Optical response of individual Au-Ag@SiO_2 heterodimers. ACS Nano 7:2522–2531

271. Prucek R, Panáček A, Fargašová A, Ranc V, Mašek V, Kvítek L, Zbořil R (2011) Re-crystallization of silver nanoparticles in a highly concentrated NaCl environment-a new substrate for surface enhanced IR-visible Raman spectroscopy. Cryst Eng Comm 13:2242–2248

272. Jensen T, Kelly L, Lazarides A, Schatz GC (1999) Electrodynamics of noble metal nanoparticles and nanoparticle clusters. J Cluster Sci 10:295–317

273. Schneider S, Halbig P, Grau H, Nickel U (1994) Reproducible preparation of silver sols with uniform particle size for application in surface-enhanced raman spectroscopy. Photochem Photobiol 60:605–610

274. Cobley CM, Rycenga M, Zhou F, Li ZY, Xia YN (2009) Etching and growth: an intertwined pathway to silver nanocrystals with exotic shapes. Angew Chem Int Ed 48:4824–4827

275. Yang J, Zhang QB, Lee JY, Too HP (2007) Dissolution-recrystallization mechanism for the conversion of silver nanospheres to triangular nanoplates. J Colloid Interface Sci 308:157–161

276. Henglein A, Linnert T, Mulvaney P (1990) Reduction of Ag^+ in aqueous polyanion solution—some properties and reactions of long-lived oligomeric silver clusters and metallic silver particles. Ber Bunsen-Ges Phys Chem Chem Phys 94:1449–1457

277. Michaels AM, Nirmal M, Brus LE (1999) Surface enhanced raman spectroscopy of individual rhodamine 6G molecules on large Ag nanocrystals. J Am Chem Soc 121:9932–9939

278. Jin R, Cao Y, Mirkin CA, Kelly KL, Schatz GC, Zheng JG (2001) Photoinduced conversion of silver nanospheres to nanoprisms. Science 294:1901–1903

279. Shankar SS, Rai A, Ankamwar B, Singh A, Ahmad A, Sastry M (2004) Biological synthesis of triangular gold nanoprisms. Nature Mater 3:482–488

280. Kelly KL, Coronado E, Zhao LL, Schatz GC (2003) The optical properties of metal nanoparticles: the influence of size, shape, and dielectric environment. J Phys Chem B 107:668–677

281. Millstone JE, Park S, Shuford KL, Qin L, Schatz GC, Mirkin CA (2005) Observation of a quadrupole plasmon mode for a colloidal solution of gold nanoprisms. J Am Chem Soc 127:5312–5313
282. Sau TK, Murphy CJ (2004) Room temperature, high-yield synthesis of multiple shapes of gold nanoparticles in aqueous solution. J Am Chem Soc 126:8648–8649
283. Li L, Wang Z, Huang T, Xie J, Qi L (2010) Porous gold nanobelts templated by metal–surfactant complex nanobelts. Langmuir 26:12330–12335
284. Xiao J, Qi L (2011) Surfactant-assisted, shape-controlled synthesis of gold nanocrystals. Nanoscale 3:1383–1396
285. Fasciani C, Silvero MJ, Anghel MA, Argüello GA, Becerra MC, Scaiano JC (2014) Aspartame-stabilized gold–silver bimetallic biocompatible nanostructures with plasmonic photothermal properties, antibacterial activity, and long-term stability. J Am Chem Soc 136:17394–17397
286. McGilvray KL, Fasciani C, Bueno-Alejo CJ, Schwartz-Narbonne R, Scaiano JC (2012) Photochemical strategies for the seed-mediated growth of gold and gold–silver nanoparticles. Langmuir 28:16148–16155
287. McGilvray KL, Decan MR, Wang D, Scaiano JC (2006) Facile photochemical synthesis of unprotected aqueous gold nanoparticles. J Am Chem Soc 128:15980–15981
288. Scaiano JC, Billone P, Gonzalez CM, Maretti L, Marin ML, McGilvray KL, Yuan N (2009) Photochemical routes to silver and gold nanoparticles. Pure Appl Chem 81:635–647
289. Sun Y, Xia Y (2004) Mechanistic study on the replacement reaction between silver nanostructures and chloroauric acid in aqueous medium. J Am Chem Soc 126:3892–3901
290. Skrabalak SE, Chen J, Sun Y, Lu X, Au L, Cobley CM, Xia Y (2008) Gold nanocages: synthesis, properties, and applications. Acc Chem Res 41:1587–1595
291. Qian Z, Park SJ (2014) Silver seeds and aromatic surfactants facilitate the growth of anisotropic metal nanoparticles: gold triangular nanoprisms and ultrathin nanowires. Chem Mater 26:6172–6177
292. Pud S, Kisner A, Heggen M, Belaineh D, Temirov R, Simon U, Offenhäusser A, Mourzina Y, Vitusevich S (2012) Features of transport in ultrathin gold nanowire structures. Small 9:846–852
293. Straney PJ, Andolina CM, Millstone JE (2013) Seedless initiation as an efficient, sustainable route to anisotropic gold nanoparticles. Langmuir 29:4396–4403
294. Njoki PN, Lim IIS, Mott D, Park HY, Khan B, Mishra S, Sujakumar R, Luo J, Zhong CJ (2007) Size correlation of optical and spectroscopic properties for gold nanoparticles. J Phys Chem C 111:14664–14669
295. Zhi-Chuan X, Cheng-Min S, Cong-Wen X, Tian-Zhong Y, Huai-Ruo Z, Jian-Qi L, Hu-Lin L, Hong-Jun G (2007) Wet chemical synthesis of gold nanoparticles using silver seeds: a shape control from nanorods to hollow spherical nanoparticles. Nanotechnology 18:115608
296. Aherne D, Gara M, Kelly JM, Gun'ko YK (2010) From Ag nanoprisms to triangular AuAg nanoboxes. Adv Funct Mater 20:1329–1338
297. Zheng Y, Zeng J, Ruditskiy A, Liu M, Xia Y (2013) Oxidative etching and its role in manipulating the nucleation and growth of noble-metal nanocrystals. Chem Mater 26:22–33
298. Personick ML, Langille MR, Wu J, Mirkin CA (2013) Synthesis of gold hexagonal bipyramids directed by planar-twinned silver triangular nanoprisms. J Am Chem Soc 135:3800–3803
299. Aherne D, Ledwith DM, Gara M, Kelly JM (2008) Optical properties and growth aspects of silver nanoprisms produced by a highly reproducible and rapid synthesis at room temperature. Adv Funct Mater 18:2005–2016
300. Langille MR, Personick ML, Zhang J, Mirkin CA (2011) Bottom-up synthesis of gold octahedra with tailorable hollow features. J Am Chem Soc 133:10414–10417
301. Feng X, Li X, Shi H, Huang H, Wu X, Song W (2014) Highly accessible Pt nanodots homogeneously decorated on Au nanorods surface for sensing. Anal Chim Acta 852:37–44
302. Ongartkit A, Ananta S, Srisombat L (2014) Preparation of Ag/Au/Pt nanoparticles and their catalytic properties. Chem Phys Lett 605:85–88

303. Gao JX, Bender CM, Murphy CJ (2003) Dependence of the gold nanorod aspect ratio on the nature of the directing surfactant in aqueous solution. Langmuir 19:9065–9070

304. Wang S, Kristian N, Jiang S, Wang X (2009) Controlled synthesis of dendritic Au@Pt core-shell nanomaterials for use as an effective fuel cell electrocatalyst. Nanotechnology 20:25605

305. Lohse SE, Burrows ND, Scarabelli L, Liz-Marzán LM, Murphy CJ (2014) Anisotropic noble metal nanocrystal growth: the role of halides. Chem Mater 26:34–43

306. Sheikholeslami S, Jun YW, Jain PK, Alivisatos AP (2010) Coupling of optical resonances in a compositionally asymmetric plasmonic nanoparticle dimer. Nano Lett 10:2655–2660

307. Feng Y, He J, Wang H, Tay YY, Sun H, Zhu L, Chen H (2012) An unconventional role of ligand in continuously tuning of metal- metal interfacial strain. J Am Chem Soc 134:2004–2007

308. Khanal BP, Pandey A, Li L, Lin Q, Bae WK, Luo H, Klimov VI, Pietryga JM (2012) Generalized synthesis of hybrid metal- semiconductor nanostructures tunable from the visible to the infrared. ACS Nano 6:3832–3840

309. Gschneidtner TA, Fernandez YAD, Syrenova S, Westerlund F, Langhammer C, Moth-Poulsen K (2014) A versatile self-assembly strategy for the synthesis of shape-selected colloidal noble metal nanoparticle heterodimers. Langmuir 30:3041–3050

310. Wu HL, Kuo CH, Huang MH (2010) Seed-mediated synthesis of gold nanocrystals with systematic shape evolution from cubic to trisoctahedral and rhombic dodecahedral structures. Langmuir 26:12307–12313

311. Becker R, Liedberg B, Käll PO (2010) CTAB promoted synthesis of Au nanorods-temperature effects and stability considerations. J Colloid Interface Sci 343:25–30

312. Chen X, Mao SS (2007) Titanium dioxide nanomaterials: synthesis, properties, modifications, and applications. Chem Rev 107:2891–2959

313. Hou W, Cronin SB (2013) A review of surface plasmon resonance enhanced photocatalysis. Adv Funct Mater 23:1612–1619

314. Awazu K, Fujimaki M, Rockstuhl C, Tominaga J (2008) A plasmonic photocatalyst consisting of silver nanoparticles embedded in titanium dioxide. J Am Chem Soc 130:1676–1680

315. Liu Z, Hou W, Pavaskar P, Aykol M, Cronin SB (2011) Plasmon resonant enhancement of photocatalytic water splitting under visible illumination. Nano Lett 11:1111–1116

316. Ohko Y, Tatsuma T, Fujii T, Naoi K, Niwa C, Kubota Y, Fujishima A (2003) Multicolour photochromism of TiO_2 films loaded with silver nanoparticles. Nat Mater 2:29–31

317. Tanahashi I, Iwagishi H, Chang G (2008) Localized surface plasmon resonance sensing properties of photocatalytically prepared Au/TiO_2 films. Mater Lett 62:2714–2716

318. Ohtani B, Okugawa Y, Nishimoto S, Kagiya T (1987) Photocatalytic activity of TiO_2 powders suspended in aqueous silver nitrate solution-correlation with pH dependent surface structures. J Phys Chem 91:3550–3555

319. Naoi K, Ohko Y, Tatsuma T (2004) TiO_2 films loaded with silver nanoparticles: control of multicolor photochromic behavior. J Am Chem Soc 126:3664–3668

320. Doremus RH (1965) Optical properties of small silver particles. J Chem Phys 42:414–417

321. Matsubara K, Kelly KL, Sakai N, Tatsuma T (2009) Plasmon resonance-based photoelectrochemical tailoring of spectrum, morphology and orientation of Ag nanoparticles on TiO_2 single crystals. J Mater Chem 19:5526–5532

322. Kazuma E, Matsubara K, Kelly KL, Sakai N, Tatsuma T (2009) Bi- and uniaxially oriented growth and plasmon resonance properties of anisotropic Ag nanoparticles on single crystalline TiO_2 surfaces. J Phys Chem C 113:4758–4762

323. Li D, Pan L, Li S, Liu K, Wu S, Peng W (2013) Controlled preparation of uniform TiO_2-catalyzed silver nanoparticle films for surface-enhanced Raman scattering. J Phys Chem C 117:6861–6871

324. Li S, Tao Q, Li D, Zhang Q (2014) Controlled anisotropic growth of Ag nanoparticles on oil-decorated TiO_2 films with photocatalytic reduction method. J Mater Res 29:2497–2504

325. Sakai Y, Tanabe I, Tatsuma T (2011) Orientation-selective removal of upright Ag nanoplates from a TiO$_2$ film. Nanoscale 3:4101–4103

326. Jin R, Cao YC, Hao E, Me GS, Schatz GC, Mirkin CA (2004) Controlling anisotropic nanoparticles growth through plasmon excitation. Science 425:487–490

327. Moores A, Goettmann F (2006) The plasmon band in noble metal nanoparticles: An introduction to theory and applications. New J Chem 30:1121–1132

328. Ohring M (2002) Materials science of thin films, Deposition and structure. Academic Press, San Diego, USA

329. Zhang J, Huang F, Lin Z (2010) Progress of nanocrystalline growth kinetics based on oriented attachment. Nanoscale 2:18–34

330. Yin S, Huang F, Zhang J, Zheng J, Lin Z (2011) The effects of particle concentration and surface charge on the oriented attachment growth kinetics of CdTe nanocrystals in H$_2$O. J Phys Chem C 115:10357–10364

331. Li DS, Nielsen MH, Lee JRI, Frandsen C, Banfield JF, De Yoreo JJ (2012) Direction-specific interactions control crystal growth by oriented attachment. Science 336:1014–1018

332. Viswanatha R, Santra PK, Dasgupta C, Sarma DD (2007) Growth mechanism of nanocrystals in solution: ZnO, a case study. Phys Rev Lett 98:255501

333. Chookajorn T, Park M, Schuh CA (2015) Duplex nanocrystalline alloys: entropic nanostructure stabilization and a case study on W–Cr. J Mater Res 30:151–163

334. Tanabe I, Matsubara K, Sakai N, Tatsuma T (2011) Photoelectrochemical and optical behavior of single upright Ag nanoplates on a TiO$_2$ film. J Phys Chem C 115:1695–1701

335. Tanabe I, Matsubara K, Standridge SD, Kazuma E, Kelly KL, Sakai N, Tatsuma T (2009) Photocatalytic growth and plasmon resonance-assisted photoelectrochemical toppling of upright Ag nanoplates on a nanoparticulate TiO$_2$ film. Chem Commun 24:3621–3623

336. Prodan E, Radloff C, Halas NJ, Nordlander P (2003) A hybridization model for the plasmon response of complex nanostructures. Science 302:419–422

337. Beck FJ, Verhagen E, Mokkapati S, Polman, A Catchpole KR (2011) Resonant SPP modes supported by discrete metal nanoparticles on high-index substrates. Opt Express 19:A146–A156

338. Hildebrandt P, Stockburger M (1984) Surface-enhanced resonance Raman-spectroscopy of rhodamine-6G adsorbed on colloidal silver. J Phys Chem 88:5935–5944

339. Tao Q, Li S, Zhang QY, Kang DW, Yang JS, Qiu WW, Liu K (2014) Controlled growth of ZnO nanorods on textured silicon wafer and the application for highly effective and recyclable SERS substrate by decorating Ag nanoparticles. Mater Res Bull 54:6–12

340. Garcia-Vidal FJ, Pendry JB (1996) Collective theory for surface enhanced Raman scattering. Phys Rev Lett 77:1163–1166

341. Yang Y, Matsubara S, Xiong LM, Hayakawa T, Nogami M (2007) Solvothermal synthesis of multiple shapes of silver nanoparticles and their SERS properties. J Phys Chem C 111:9095–9104

342. Lakowicz JR, Geddes CD, Gryczynski I, Malicka J, Gryczynski Z, Aslan K, Lukomska J, Matveeva E, Zhang J, Badugu R, Huang JJ (2004) Advances in surface-enhanced fluorescence. J Fluoresc 14:425–441

343. Lakowicz JR (2005) Radiative decay engineering 5: metal-enhanced fluorescence and plasmon emission. Anal Biochem 337:171–194

344. Lo LW, Koch CJ, Wilson DF (1996) Calibration of oxygen-dependent quenching of the phosphorescence of Pd-meso-tetra (4-carboxyphenyl) porphine: a phosphor with general application for measuring oxygen concentration in biological systems. Anal Biochem 236:153–160

345. Vinogradov SA, Wilson DF (1994) Phosphorescence lifetime analysis with a quadratic programming algorithm for determining quencher distributions in heterogeneous systems. Biophys J 67:2048–2059

346. Cheng SH, Lee CH, Yang CS, Tseng FG, Mou CY, Lo LW (2009) Mesoporous silica nanoparticles functionalized with an oxygen-sensing probe for cell photodynamic therapy: potential cancer theranostics. J Mater Chem 19:1252–1257

347. Kelkar SS, Reineke TM (2011) Theranostics: combining imaging and therapy. Bioconjug Chem 22:1879–1903

348. Kim J, Kim HS, Lee N, Kim T, Kim H, Yu T, Song IC, Moon WK, Hyeon T (2008) Multifunctional uniform nanoparticles composed of a magnetite nanocrystal core and a mesoporous silica shell for magnetic resonance and fluorescence imaging and for drug delivery. Angew Chem Int Ed 47:8438–8441

349. Lopez T, Recillas S, Guevara P, Sotelo J, Alvarez M, Odriozola JA (2008) Pt/TiO2 brain biocompatible nanoparticles: GBM treatment using the C6 model in Wistar rats. Acta Biomater 4:2037–2044

350. Fu GF, Vary PS, Lin CT (2005) Anatase TiO$_2$ nanocomposites for antimicrobial coatings. J Phys Chem B 109:8889–8898

351. Theron J, Walker JA, Cloete TE (2008) Nanotechnology and water treatment: applications and emerging opportunities. Crit Rev Microbiol 34:43–69

352. Yamaguchi K, Sugiyama T, Kato S, Kondo Y, Ageyama N, Kanekiyo M, Iwata M, Koyanagi Y, Yamamoto N, Honda M (2008) A novel CD4-conjugated ultraviolet light-activated photocatalyst inactivates HIV-1 and SIV efficiently. J Med Virol 80:1322–1331

353. Yamaguchi S, Kobayashi H, Narita T, Kanehira K, Sonezaki S, Kubota Y, Terasaka S, Iwasaki Y (2010) Novel photodynamic therapy using water-dispersed TiO2-polyethylene glycol compound: evaluation of antitumor effect on glioma cells and spheroids in vitro. Photochem Photobiol 86:964–971

354. Seo JW, Chung H, Kim MY, Lee J, Choi IH, Cheon J (2007) Development of water soluble single-crystalline TiO$_2$ nanoparticles for photocatalytic cancer-cell treatment. Small 3:850–853

355. Kawahara T, Konishi Y, Tada H, Tohge N, Nishii J, Ito S (2002) A patterned TiO$_2$(anatase)/TiO$_2$(rutile) bilayer-type photocatalyst: effect of the anatase/rutile junction on the photocatalytic activity. Angew Chem Int Ed 41:2811–2813

356. Liu L, Miao P, Xu Y, Tian Z, Zou Z, Li G (2010) Study of Pt/TiO$_2$ nanocomposite for cancer-cell treatment. J Photochem Photobiol B 98:207–210

357. Kasarevic-Popovic Z, Behar D, Rabani J (2004) Role of excess electrons in TiO$_2$ nanoparticles coated with Pt in reduction reactions studied in radiolysis of aqueous solutions. J Phys Chem B 108:20291–20295

358. Xu J, Chen ZD, Sun Y, Chen CM, Jiang ZY (2008) Photocatalytic killing effect of gold-doped TiO$_2$ nanocomposites on human colon carcinoma LoVo cells. Acta Chim Sin 66:1163–1167

359. Lee CH, Meteer J, Narayanan V, Kan EC (2005) Self-assembly of metal nanocrystals on ultrathin oxide for nonvolatile memory applications. J Electron Mater 34:1–11

360. Gong XQ, Selloni A, Dulub O, Jacobson P, Diebold U (2008) Small Au and Pt clusters at the anatase TiO$_2$(101) surface: behavior at terraces, steps, and surface oxygen vacancies. J Am Chem Soc 130:370–381

361. Rozhkova EA, Ulasov I, Lai B, Dimitrijevic NM, Lesniak MS, Rajh T (2009) A high-performance nanobio photocatalyst for targeted brain cancer therapy. Nano Lett 9:3337–3342

362. Rozhkova EA (2011) Nanoscale materials for tackling brain cancer: recent progress and outlook. Adv Mater 23:H136–H150

363. Dimitrijevic NM, Rozhkova EA, Rajh T (2009) Dynamics of localized charges in dopamine-modified TiO(2) and their effect on the formation of reactive oxygen species. J Am Chem Soc 131:2893–2899

364. Dimitrijevic NM, Saponjic Z, Rabatic BM, Rajh T (2005) Assembly and charge transfer in hybrid TiO(2) architectures using biotin-avidin as a connector. J Am Chem Soc 127:1344–1345

365. de la Garza L, Saponjic ZV, Dimitrijevic NM, Thurnauer MC, Rajh T (2006) Surface states of titanium dioxide nanoparticles modified with enediol ligands. J Phys Chem B 110:680–686

366. Lopez T, Figueras F, Manjarrez J, Bustos J, Alvarez M, Silvestre-Albero J, Rodriguez-Reinoso F, Martinez-Ferre A, Martinez E (2010) Catalytic nanomedicine: a new field in antitumor treatment using supported platinum nanoparticles. In vitro DNA degradation and in vivo tests with C6 animal model on Wistar rats. Eur J Med Chem 45:1982–1990

367. Patolsky F, Zheng G, Lieber CM (2006) Nanowire sensors for medicine and the life sciences. Nanomedicine 1:51–65

368. Tian BZ, Cohen-Karni T, Qing QA, Duan XJ, Xie P, Lieber CM (2010) Three-dimensional, flexible nanoscale field-effect transistors as localized bioprobes. Science 329:830–834

369. Zheng G, Patolsky F, Cui Y, Wang WU, Lieber CM (2005) Multiplexed electrical detection of cancer markers with nanowire sensor arrays. Nat Biotechnol 23:1294–1301

370. Stern E, Vacic A, Rajan NK, Criscione JM, Park J, Ilic BR, Mooney DJ, Reed MA, Fahmy TM (2010) Label-free biomarker detection from whole blood. Nat Nanotechnol 5:138–142

371. Chi X, Huang D, Zhao Z, Zhou Z, Yin Z, Gao J (2012) Nanoprobes for in vitro diagnostics of cancer and infectious diseases. Biomaterials 33:189–206

Index